

Lecture Notes in Mechanical Engineering

Rohit Sharma

Ravindra Kannojiya

Naveen Garg

Sachin S. Gautam *Editors*

# Advances in Engineering Design

Select Proceedings of FLAME 2022



Springer

# Lecture Notes in Mechanical Engineering

## Series Editors


Fakher Chaari, National School of Engineers, University of Sfax, Sfax, Tunisia

Francesco Gherardini , Dipartimento di Ingegneria “Enzo Ferrari”, Università di Modena e Reggio Emilia, Modena, Italy

Vitalii Ivanov, Department of Manufacturing Engineering, Machines and Tools, Sumy State University, Sumy, Ukraine

Mohamed Haddar, National School of Engineers of Sfax (ENIS), Sfax, Tunisia

## Editorial Board

Francisco Cavas-Martínez , Departamento de Estructuras, Construcción y Expresión Gráfica Universidad Politécnica de Cartagena, Cartagena, Murcia, Spain

Francesca di Mare, Institute of Energy Technology, Ruhr-Universität Bochum, Bochum, Nordrhein-Westfalen, Germany

Young W. Kwon, Department of Manufacturing Engineering and Aerospace Engineering, Graduate School of Engineering and Applied Science, Monterey, CA, USA

Justyna Trojanowska, Poznan University of Technology, Poznan, Poland

Jinyang Xu, School of Mechanical Engineering, Shanghai Jiao Tong University, Shanghai, China

**Lecture Notes in Mechanical Engineering (LNME)** publishes the latest developments in Mechanical Engineering—quickly, informally and with high quality. Original research reported in proceedings and post-proceedings represents the core of LNME. Volumes published in LNME embrace all aspects, subfields and new challenges of mechanical engineering.

To submit a proposal or request further information, please contact the Springer Editor of your location:

**Europe, USA, Africa:** Leontina Di Cecco at [Leontina.dicecco@springer.com](mailto:Leontina.dicecco@springer.com)

**China:** Ella Zhang at [ella.zhang@springer.com](mailto:ella.zhang@springer.com)

**India:** Priya Vyas at [priya.vyas@springer.com](mailto:priya.vyas@springer.com)

**Rest of Asia, Australia, New Zealand:** Swati Meherishi at [swati.meherishi@springer.com](mailto:swati.meherishi@springer.com)

Topics in the series include:

- Engineering Design
- Machinery and Machine Elements
- Mechanical Structures and Stress Analysis
- Automotive Engineering
- Engine Technology
- Aerospace Technology and Astronautics
- Nanotechnology and Microengineering
- Control, Robotics, Mechatronics
- MEMS
- Theoretical and Applied Mechanics
- Dynamical Systems, Control
- Fluid Mechanics
- Engineering Thermodynamics, Heat and Mass Transfer
- Manufacturing
- Precision Engineering, Instrumentation, Measurement
- Materials Engineering
- Tribology and Surface Technology

**Indexed by SCOPUS, EI Compendex, and INSPEC**

All books published in the series are evaluated by Web of Science for the Conference Proceedings Citation Index (CPCI)

To submit a proposal for a monograph, please check our Springer Tracts in Mechanical Engineering at <https://link.springer.com/bookseries/11693>

Rohit Sharma · Ravindra Kannojiya ·  
Naveen Garg · Sachin S. Gautam  
Editors

# Advances in Engineering Design

Select Proceedings of FLAME 2022

 Springer



*Editors*

Rohit Sharma  
Department of Mechanical Engineering  
Amity University  
Noida, Uttar Pradesh, India

Ravindra Kannojiya  
Department of Mechanical Engineering  
Amity University  
Noida, Uttar Pradesh, India

Naveen Garg  
Acoustics and Vibration Standards  
CSIR-National Physical Laboratory  
New Delhi, Delhi, India

Sachin S. Gautam  
Department of Mechanical Engineering  
Indian Institute of Technology Guwahati  
Guwahati, Assam, India

ISSN 2195-4356

ISSN 2195-4364 (electronic)

Lecture Notes in Mechanical Engineering

ISBN 978-981-99-3032-6

ISBN 978-981-99-3033-3 (eBook)

<https://doi.org/10.1007/978-981-99-3033-3>

© The Editor(s) (if applicable) and The Author(s), under exclusive license to Springer Nature Singapore Pte Ltd. 2023

This work is subject to copyright. All rights are solely and exclusively licensed by the Publisher, whether the whole or part of the material is concerned, specifically the rights of translation, reprinting, reuse of illustrations, recitation, broadcasting, reproduction on microfilms or in any other physical way, and transmission or information storage and retrieval, electronic adaptation, computer software, or by similar or dissimilar methodology now known or hereafter developed.

The use of general descriptive names, registered names, trademarks, service marks, etc. in this publication does not imply, even in the absence of a specific statement, that such names are exempt from the relevant protective laws and regulations and therefore free for general use.

The publisher, the authors, and the editors are safe to assume that the advice and information in this book are believed to be true and accurate at the date of publication. Neither the publisher nor the authors or the editors give a warranty, expressed or implied, with respect to the material contained herein or for any errors or omissions that may have been made. The publisher remains neutral with regard to jurisdictional claims in published maps and institutional affiliations.

This Springer imprint is published by the registered company Springer Nature Singapore Pte Ltd. The registered company address is: 152 Beach Road, #21-01/04 Gateway East, Singapore 189721, Singapore

# Preface

This book presents a pool of research articles on different aspects of engineering design from the 3rd International Conference on Future Learning Aspects for Mechanical Engineering (FLAME), which was organized by Amity University, Uttar Pradesh, Noida, India, from 3 to 5 August 2022. The conference aims to provide a platform for academicians, scientists, and researchers across the globe to share their scientific ideas and vision in the areas of thermal, design, industrial, production, and interdisciplinary areas of mechanical engineering. The FLAME 2022 conference played a key role in setting up a bridge between academics and industry. Almost 600 people attended the conference to exchange scientific ideas. During the three-day conference, the researchers from academia and industry offered the most recent cutting-edge findings, went through several scientific brainstorming sessions, and exchanged ideas on practical socioeconomic topics. This conference also provided an opportunity to establish a network for joint collaboration between academicians and industry. Major emphasis was placed on the recent developments and innovations in various fields of mechanical engineering through plenary lectures. The book covers mechanical design areas such as computational mechanics, finite element modelling, computer-aided design, tribology, fracture mechanics, and vibration. The book brings together different aspects of engineering design and will be useful for researchers and professionals working in this field. The editors would like to acknowledge all the participants who have contributed to this volume. We also deeply express our gratitude for the generous support provided by Amity University, Noida. The editors also thank the publishers and every member of the department and institute staff who have directly or indirectly assisted in accomplishing this goal. Finally, the editors would also like to express gratitude to the respected founder president of Amity University, Dr. Ashok K. Chauhan, for providing all kinds of support and blessings.

In spite of sincere care, there might be typos, and there is always room for improvement. The editors would appreciate any suggestions from the reader for further improvements to this book.

Noida, India  
Noida, India  
New Delhi, India  
Guwahati, India

Rohit Sharma  
Ravindra Kannojiya  
Naveen Garg  
Sachin S. Gautam

# Contents

<b>Estimation of Lacunar Permeability in Anatomical Regions of Femoral Cortex: Endocortical Versus Periosteal</b> .....	1
Saurabh Tiwari, Rakesh Kumar, Abhishek Kumar Tiwari, Dharmendra Tripathi, Ram Naresh Yadav, Navin Kumar, and Sonu Ambwani	
<b>Design of Efficient Finite Elements Using Deep Learning Approach</b> ....	11
Sekhori S. Nath, Dipjyoti Nath, and Sachin S. Gautam	
<b>Design of Efficient Quadrature Scheme in Finite Element Using Deep Learning</b> .....	21
Rohan Chinchkar, Dipjyoti Nath, and Sachin S. Gautam	
<b>Accelerating Finite Element Assembly on a GPU</b> .....	31
Utpal Kiran, Sachin S. Gautam, and Deepak Sharma	
<b>Design and Fabrication of PLA-Printed Wearable Exoskeleton with 7 DOF for Upper Limb Physiotherapy Training and Rehabilitation</b> .....	43
Gaurav Gupta, Karan Agarwal, Ayush Yadav, Ashok Kumar Yadav, and Devendra Kumar Sinha	
<b>Framework for Design and Control of Automatic Stone—Glass Separator</b> .....	57
Priyank Srivastava, Siddharth, Vipul, Anmol, Shivam, Amartya, and Sanjeev Kumar Sharma	
<b>Buckling Analysis of Piston Rod for Hydraulic Cylinder of Cotton Bale Press Machine</b> .....	67
S. G. Mahakalkar and Neeraj Sunheriya	

<b>Manufacturing Process-Related Challenges of Additive Manufactured Parts: A Review</b> .....	75
Siddharth Pradeep Kumar Samgeetha, Neethesh Maharaj, and Bhupendra Prakash Sharma	
<b>Modelling of Kinematic Chains and Mechanisms with Special Emphasis on Multi-Linked Jointed Chain Mechanisms</b> .....	83
Ojasvi Rajeev Sharma, Shaurya Bhatnagar, Shivam Verma, Jatin Mahallawat, Vipin Kaushik, and Sumit Sharma	
<b>Design and Analysis of a Spherical Joint Mechanism for Robotic Manipulators</b> .....	93
B. L. S. Gopal and Rohit Singla	
<b>Recent Progress in the Design of Solar Still: An Understanding and Comparison</b> .....	103
Priyansh Gupta, Gopal Nandan, Syed M. I. Nakshbandi, Vishal Gaur, Anoop Kumar Shukla, Ramakant Shrivastava, and Arnav Kumar	
<b>Aerodynamic Performance Analysis of Formula-Based Vehicle Through Ansys</b> .....	121
Venkata Siva Sainath Bavapuram, Surya Narayanan Suresh, Sumit Sharma, and Vipin Kaushik	
<b>Numerical Estimation of Base Reactions of an Underwater Manipulator with Variable Drag Coefficients</b> .....	133
Chandan Kumar, N. Srinivasa Reddy, Dipankar Chatterjee, Pratik Saha, Sambhunath Nandy, and Soumen Sen	
<b>A Study on the Reflection Coefficient of Higher Modes of Torsional Wave by Theoretical and Numerical Method</b> .....	145
I. Boris, Sunil Kumar Sharma, and Jaesun Lee	
<b>A Comparative Study on Ultrasonic Propagation Characteristics and Defect Detection of Metal Material Additive Manufacturing Using Deep Learning Algorithm</b> .....	157
Hyeonsu Song, Junpil Park, Sunil Kumar Sharma, and Jaesun Lee	
<b>Design and Fabrication of an Atmospheric Water Generator for Water Harvesting from Moist Air</b> .....	169
Uhinee Banerjee, Harsh Kaushik, Harshit Garg, and Basant Singh Sikarwar	
<b>A Comprehensive Survey on Visualization of Human Action Recognition: By Hidden Markov Model and Convolution Neural Network</b> .....	179
Aleem Ahmed, Garima Jain, Amritanshu Sharma, Md. Hashim, and Aditya Raj	

**Design and Modal Analysis of an Impact Energy Absorption System for a Four-Wheeler Vehicle** ..... 197  
 Angat Singh, Surendra Nath Banerjee, Ujjwal Kumar, Rohit Sharma, and Vikas Kumar

**Analysis of a Steering Upright for a Three-Wheel Solar Electric Car** ... 209  
 Vinayak H. Khatawate, Burhanuddin H. Telwala, and Ayush P. Shah

**Advanced Helmet System** ..... 225  
 Rupam Dahe and Ram Bansal

**Modelling and Stress Analysis of Connecting Rod Using Fusion 360** .... 235  
 Riya Pal, Shweta Mitra, Rahul, and Neetu Kanaujia

**Numerical and Experimental Study of Vortex Generator** ..... 249  
 K. Balaji, Mayuri R. Gore, and S. V. Khandal

**Performance Comparison of Cryptographic Algorithms Used in Cloud Computing** ..... 261  
 Neha Juyal, Eeshita Deepta, and Dolly Sharma

**Modern Generative Design Tools: Siemens NX’s Algorithmic Feature and Rhinoceros 3D’s Grasshopper** ..... 275  
 Amit Singh Rawat and Gaurav Tiwari

**Farming System: Quadcopter Fabrication and Development** ..... 285  
 Rajat Yadava and Anas Aslam

**Development of a Drone with Spraying Mechanism for Agricultural Work** ..... 295  
 Pratejas Tomar and Sumit Krishnan

**Modeling and Performance Evaluation of Pelamis Wave Energy Converter Considering Indian Economic Estimates** ..... 309  
 Krishnakant Dixit and Kanchan Yadav

**Review and Development of Thermal Design of a Cryogenic Dewar** .... 319  
 Pranav Pandharpatte, Kartik Kurkure, Sandeep Kore, Avinash Shinde, and K. V. Shrinivasan

**Static Analysis of a Low-Pressure Stage Blade of a Steam Turbine Using ANSYS** ..... 333  
 Pooja Rani and Atul Kumar Agrawal

**Behavioral Simulation of Biological Neuron Using VHDL** ..... 343  
 Sarthak Sharma and V. K. Tomar

**Flexible Manufacturing System By Mechanized Guided Vehicles Through Genetic Algorithms Approach** ..... 351  
 Aman Sharma and Rishabh Chaturvedi

<b>Investigation of Two-Stage Epicyclic Gearbox for an Automobile for Energy Regeneration</b> .....	363
Aditi Namdeo, Ashok Atulkar, and R. K. Porwal	
<b>Securing Network Address in PingER and IOS Application Development</b> .....	377
Palak Gupta and Purushottam Sharma	
<b>Atlas Generation of Planar Flapping Wing Mechanism with Higher Pair</b> .....	391
Pankaj Vinayak Dorlikar, Nikhil Belhekar, and Sujit Suresh Pardeshi	
<b>Structural and Dynamic Analysis of an Aluminium Alloy Piston Using Finite Element Method</b> .....	401
Prayas Gupta, Manish Kumar, Kuldeep Narwat, and Vivek Kumar	
<b>Design and Simulation of PV Solar Cell System with Microgrid and Fuel Cell Using Discrete PID and FUZZY Controller</b> .....	427
Gunjan Taneja, Vijay Kumar Tayal, and Kamlesh Pandey	
<b>Modeling, Analysis, and Comparison of Two Materials for Universal Joint by Using Ansys Software</b> .....	439
Bishnu Bishwakarma, Devyanshu Raj Singh, Rohit Chaudhary, and Brahma Nand Agrawal	
<b>Small-Scale Electricity Generation from Biogas in Third World Countries</b> .....	449
Coddell Tanaka Mutate, Artwell Jairos Kanjanda, and Gitanjali Mehta	
<b>Design and Implementation of a Gesture-Controlled Car with Arduino Nano Board</b> .....	461
Pawan Kumar, Prabhat Kumar Singh, Vaibhav Nijhawan, and Harsh Khanna	
<b>Design and Fabrication of a Solar-Powered Unmanned Aerial Vehicle (UAV)</b> .....	473
Izhaan Shaikh, Mahmoud Abdelrazag Salih Suliman, Nour Alaa Elsonbaty, Sarath Raj Nadarajan Assari Syamala, and Apurv Yadav	
<b>Screw-Based Extruder Design for 3D Printing of Food Using Food Layered Technology</b> .....	479
Moin Khan, Abid Haleem, Mohd Javaid, Shashi Bahl, Chander Prakash, Rajesh Singh, and Ashok Kumar Bagha	
<b>Finite Element Analysis of Residual Stresses During Incremental Sheet Forming of Ti-6Al-4V Alloys Using Different Tool Path Profiles</b> .....	493
Gianender Kajal, M. R. Tyagi, and Gulshan Kumar	

**A Comparative Analysis of Plane and Corrugated Designs of Soft Pneumatic Actuators Based on Finite Element Method** ..... 507  
 Narendra Gariya and Pushpendra Kumar

**Study of Anti-Tetra Chiral Auxetic Cluster Under Biaxial Loading Using FEM** ..... 519  
 G. Siva Prasad, Ch Jaya Krishna, and M. P. Hariprasad

**Cross-Correlation of Schlieren Images to Retrieve Velocity Information** ..... 529  
 Louther Charl Flores David, Jhoffanel Pazo, Efstratios L. Ntantis, and Kizhakkelan Sudhakaran Siddharth

**Design and Fabrication of a Small-Scale Solar Aircraft** ..... 541  
 Chaithanya Reddy, Mohammed Hisham, and Kizhakkelan Sudhakaran Siddharth

**Numerical Study on the Influence of Shape Parameters on Aerodynamic Performance of a Trapezoidal Cylinder** ..... 551  
 S Aiswarya Lakshmi, Parvathy Rajeev, Manu Sivan, and Ajith Kumar S

**Transosonde Balloon Aerial Mapping with APRS Module and GPS Tracking** ..... 563  
 Sarath Raj, Ali Asgher, Mohamed Sufyan Shafi, and Nour Alaa Elsonbaty

**Analysis of Water Indices’ Level in Nile River over the City of Cairo Using Landsat 8 Satellite Imagery** ..... 573  
 Sarath Raj, Anusha Santhosh, and Sathiyagayathiri Ramamoorthy

**Design and Analysis of Load Stiffness Tester for Dual Applications in Measurement of Spring Stiffness and Walnut Shell Stiffness** ..... 605  
 Shivam Aggarwal, M. L. Aggarwal, and Krishan Verma

**A Review of Vehicle Automation Using Artificial Intelligence** ..... 613  
 Sudhanshu Sharma, S. A. Khan, Sachin Sharma, Vishal Gupta, Yatharth Rajput, and Surya Pratap Singh

**Ultra-Broadband with High Absorption Rate Metamaterial Absorber on Thin Substrate for Airborne Radar Applications** ..... 629  
 Maxon Okramcha and Malay Ranjan Tripathy

**Experimental Design of a Novel Winglet for Aircraft** ..... 639  
 Sarath Raj, Shone George Kurian, and Sathiyagayathiri Ramamoorthy

**Design and Analysis of PLA and Carbon Fiber Mono Leaf Spring for Small Commercial Vehicles** ..... 663  
 Lavepreet Singh, Shreyansh Gupta, and Rahul Katiyar

**Design and Analysis of a Compliant Microgripper** ..... 673  
 Anurag T. Vidap, Bhagyesh D. Deshmukh, and Sujit. S. Pardeshi



<b>Water Logging Analysis over Dubai Using Sentinel-2 Satellite Imagery</b> .....	683
Sarath Raj, Ayush Harish, and Sathiyagayathiri Ramamoorthy	
<b>Comparative Deflection Analysis of a Cantilever Beam Fixed at One End by Using Finite Element and Analytical Method</b> .....	697
Aditya Pratap Singh, Shrikant Vidya, P. Suresh, and Amresh Kumar	
<b>Application of Compliant Mechanisms in Various Fields—A Review</b> ...	707
Pooja K. Jambhale and Bhagyesh B. Deshmukh	
<b>Enhancement of the Machine Safety Using OpenCV</b> .....	717
Sumit Raut, Vishal Hase, Shreyas Kotgire, Swapnil Dalvi, and Abhijeet Malge	
<b>Implementation of Artificial Neural Network for Prognosis of Photovoltaic Panel Using Python</b> .....	725
Neeraj Khera, Komal Rukshar Begum, and Farheen Khan	
<b>A Methodology for Optimal Scaling of Unguided and Guided Rockets in a Military Formation</b> .....	733
N. Ranjana and Indra Deo Kumar	
<b>Static Analysis of Pick-and-Place Robotic Arm Based on ANSYS</b> .....	743
Shikkha Sood and Pramod Kumar	
<b>Experimental Reduction of Coke Oven Gas by Adjustment of Gas Flow in Pushing and Charging Schedule of Coke Oven Plant</b> .....	753
Niranjan Mahato, Himanshu Agarwal, and Jainendra Jain	
<b>Studying Current Safety Systems for Accident Prevention and Wellbeing of Powered Two-Wheeler Community: Prevalence of Safety Components</b> .....	767
Gaurav Gupta, Riya Mariam Babu, Ashok Kumar Yadav, Devendra Kumar Sinha, R. K. Tyagi, Sanjeev Kumar Sharma, and Srinivasa Rao Gorrepati	
<b>Design and Temperature Measurement of Axisymmetric Heater for Rotor–Stator System</b> .....	781
Rakesh Kumar Yadu and Achhaibar Singh	
<b>Formulating and Analysing the Effect of Suspension Parameters on Critical Speeds for Various DOFs in Rail Vehicle</b> .....	791
Prem Narayan Vishwakarma, Pankaj Mishra, Sunil Kumar Sharma, and Anoop Kumar Shukla	

<b>Detection of Biofilm on Steel and Plastic Surfaces Using Image Analysis</b> .....	803
Manoj Kumar Dewangan, Pulkit Jain, and Gurmeet Singh	
<b>Artificial Hip Prostheses Design and Its Evaluation by Using Ansys Under Static Loading Condition</b> .....	815
Gyan Prakash Tripathi, Sumit Agarwal, Ankita Awasthi, and Vanya Arun	

## About the Editors



**Dr. Rohit Sharma** is presently working as an Assistant Professor in the Department of Mechanical Engineering, Amity University, India. He completed his B.Tech. and M.Tech. from Kurukshetra University, India. Dr. Sharma received his Ph.D. degree in 2014 from Dayalbagh Educational Institute, India. He has over ten years of teaching and research experience. His area of research is ergonomics, design, hand arm vibration, whole body vibration, and metal matrix composites. He has published forty research papers in peer-reviewed SCI and Scopus indexed journals and conferences. He has presented more than twenty research papers at international and national conferences.



**Dr. Ravindra Kannojiya** is working as a full-time academician since the last 8 years. He has a Ph.D. in Mechanical Engineering from Delhi Technological University, India, and M.Tech. (Thermal Engineering) from the National Institute of Technology (NIT) Silchar, India. He also holds B.Tech. (Mechanical and Automation Engineering) from Govind Ballabh Pant Government Engineering College, GGSIPU, Delhi. He has published research papers in reputed international journals and conferences. He has also published patents from his research work. He is working in the area of thermal engineering, optimization algorithms, energy management, and intelligent systems.



**Dr. Naveen Garg** is Sr. Principal Scientist and Head, Acoustics and Vibration Standards in CSIR-National Physical Laboratory, New Delhi working in the field of sound and vibrations since past 18 years. He is a mechanical engineer specializing in machine design, vibrations and acoustics, measurement science. He is currently working in development and up-gradation of primary standards of sound pressure and vibration amplitude and R&D in applied acoustics. He has done his Doctorate in Mechanical Engineering from Delhi Technological University (DTU) India, and M.Tech. in Machine Design from Indian Institute of Technology (IIT) Delhi. He has been involved in many consultancy and sponsored projects pertaining to Environmental Impact Assessment studies in respect of noise and vibration for government bodies like Central Pollution Control Board (CPCB), Archaeological Survey of India (ASI), Delhi Metro Rail Corporation (DMRC), Bangalore Metro Rail Corporation Limited (BMRCL), India etc. He has published many papers in national and international journals in the field of acoustics and vibrations and has been actively involved in the Key Comparison exercises in Acoustics and Vibration metrology with other National Metrology Institutes (NMIs) of the world. He has been Managing Editor of *MAPAN Journal of Metrology Society of India* published by Springer and reviewer of many international journals and has enormously contributed towards evaluation, analysis and control of noise pollution. He was awarded APMP Iizuka Young Metrologist Prize for Developing Economies by Asia Pacific Metrology Programme (APMP) Secretariat, Japan in November, 2017 for his notable contributions to acoustics and vibration metrology.



**Dr. Sachin S. Gautam** is currently an Assistant professor in the Department of Mechanical Engineering, Indian Institute of Technology (IIT) Guwahati. He carried out his post-doctoral research at AICES, RWTH Aachen University, Germany. He finished his Ph.D. and M.Tech. in the area of high velocity impact problems from IIT Kanpur. Dr. Gautam has undertaken projects from SERB, DST and VSSC, ISRO. He has recently received funding to enhance the functionalities of ISRO's structural analysis software tool FEASTSMT. Also, his students have been working on research projects in joint collaboration with Siemens and Cummins. He has guided two Ph.D. students and further supervised eight students. He has guided 19 M.Tech. students. He has published around 15 book chapters, 22 journal papers, and 50 national/international; conference publications. His current area of research is in computational contact mechanics, isogeometric analysis, GPU computing, application of machine learning in computational mechanics.

# Estimation of Lacunar Permeability in Anatomical Regions of Femoral Cortex: Endocortical Versus Periosteal



**Saurabh Tiwari, Rakesh Kumar, Abhishek Kumar Tiwari, Dharmendra Tripathi, Ram Naresh Yadav, Navin Kumar, and Sonu Ambwani**

**Abstract** Bone's adaptation occurs in response to mechanical loads. In vivo experimental studies explained that cortical bone envelopes (periosteal and endocortical) and their anatomical regions (anterior, posterior, lateral, medial) experience differential loading-induced osteogenesis. It has always been a challenge to establish a computer model to precisely predict such non-uniform new bone formation at the cortex due to mechanobiological stimuli such as strain or canalicular fluid flow. Lacunar permeability governs canalicular fluid velocity magnitude in bone-cross section. Anatomical variations of permeability could be the reason of differential fluid flow response which causes distinct site-specific bone formation. Therefore, it is important to compute poromechanical properties which are required to compute flow distribution. Lacunar canalicular permeability of the periosteal and endosteal surfaces in different anatomical locations has not been well reported. Thus, this paper estimates the poromechanical properties of cortical bone specially the permeability at periosteal and endocortical envelopes in their different anatomical regions, i.e. medial, lateral, anterior and posterior. Nanoindentation technique in combination with poroelastic optimization technique was employed. The result indicates that

---

S. Tiwari · R. Kumar

Department of Mechanical Engineering, Manipal University Jaipur, Jaipur, Rajasthan 303007, India

A. K. Tiwari (✉)

Department of Applied Mechanics, Motilal Nehru National Institute of Technology, Allahabad, Prayagraj, Uttar Pradesh 211004, India  
e-mail: [aktiwari@mnnit.ac.in](mailto:aktiwari@mnnit.ac.in)

D. Tripathi

Department of Mathematics, National Institute of Technology, Srinagar, Uttarakhand 246174, India

R. N. Yadav · N. Kumar

Department of Mechanical Engineering, Indian Institute of Technology Ropar, 140001, Roopnagar, Punjab, India

S. Ambwani

Department of Molecular Biology and Genetic Engineering, G.B. Pant University of Agriculture and Technology, Pantnagar, Uttarakhand 263145, India

the endocortical surface was found to be more permeable than periosteal surface. Moreover, medial and lateral sides were also found more permeable than the other two regions, namely anterior and posterior. A clear understanding on cortical bone permeability will help researchers to precisely simulate the site-specific osteogenesis.

**Keywords** Bone adaptation · Periosteal and endocortical surfaces · Shear modulus · Lacunar Canalicular permeability · Nanoindentation

## 1 Introduction

Bone's microarchitectural adaptation to loading-induced mechanical environment is a well-known phenomenon [1, 2]. Dynamic mechanical loading especially of low magnitude promotes new bone formation where normal strain magnitude was elevated above osteogenic threshold [3, 4]. Loading parameters such as strain magnitude, frequency, cycles, and strain rate (depending on loading waveform) affect the new bone formation [5–8]. However, these models fail to predict osteogenesis at several instances. For example, computer modelling studies [4, 9] on bone adaptation observed the bone formation also occurs near the minimal sites of strain distribution, which is an anomaly. Experimental as well as computational works identified canalicular fluid motion as a potential mechanical signal of new bone formation [10–14]. Price et al. [15] also substantiated that the canalicular fluid flow induced wall shear stress is responsible for new bone formation. Further, Carriero et al. [16] noticed osteogenesis at those sites where fluid flow in the cortex of long bone was high as compared to the sites of elevated strain energy density. This challenges the establishment of strain energy as a sole osteogenic stimulus.

It is noticed that cortical bone surfaces (periosteal and endocortical) experience distinct new bone formation in response to exogenous mechanical stimulation [8, 17]. Moreover, anatomical regions of the cortex also experience different new bone especially medial–lateral regions of the cortex had greater bone formation. It is worth mentioning that loading on bone tissue induces pore pressure which causes fluid flow velocity in LCS which excites the mechanosensory cells osteocytes for osteogenesis [13, 18]. It is quite possible that cortical surface and their anatomical regions may be subjected to a variable fluid motion and thus experience different mechanoresponsiveness and osteogenesis [19, 20]. A major reason is that microarchitectural properties such as canalicular permeability and porosity vary with respect to cortical surfaces and anatomical regions. Microstructural properties such as lacunar canalicular permeability typically governs the fluid flow in the cortical bone which decides the fluid dynamics within the bone tissue.

There are a few studies which have reported cortical bone permeability in a range of  $10^{-22}$  to  $10^{-19}$  m<sup>2</sup> [21]. Age, species, anatomical locations, and bone disorder-related mechanical properties change within the same at different anatomical location. However, poromechanical properties of cortical bone tissue with respect to cortical surface (periosteal vs. endocortical) and their anatomical regions are not well

investigated. This motivated us to characterize the poroelastic properties of cortical envelopes, i.e. periosteal and endosteal surfaces across their anatomical locations. Nanoindentation technique [22–24] in combination with optimization is employed to estimate the permeability of cortical tissue. The estimated permeability of the periosteal and endocortical envelopes is compared in their anatomical regions. The present work will allow the better assessment of loading-induced fluid flow in the cortex and will also help in precise prediction of site-specific osteogenesis.

## 2 Methodology

### 2.1 Sample Preparation

Six Wistar skeletally mature rats (7 months) were involved in the study. Right knee joint was detached to separate the femur at animal house facility of G.B. Pant University of Agriculture and Technology, Uttarakhand, India. Standard protocols were followed as prescribed in the Institutional Ethics Committee of G. B. Pant University of Agriculture and Technology, India. Soft tissues around the bone tissue were removed using water jet and ultrasonic bath, and femur is preserved in phosphate buffer saline wrapping in gauze at -20 °C as suggested in the literature [19]. Femur mid-diaphysis is sliced into 3–4 mm thick sections (Fig. 1a) with the help of Buehler IsoMet™ low-speed saw. Epoxy resin (EPOTHIN, Buehler, Illinois, USA) was used to embed this section in presence of the hardener. These cortical bone sections are then polished with different grades of carbide papers and diamond slurries in presence of ionized water jet to avoid dehydration. Superior sample finish is achieved using a constant pressure before nanoindentation [20].

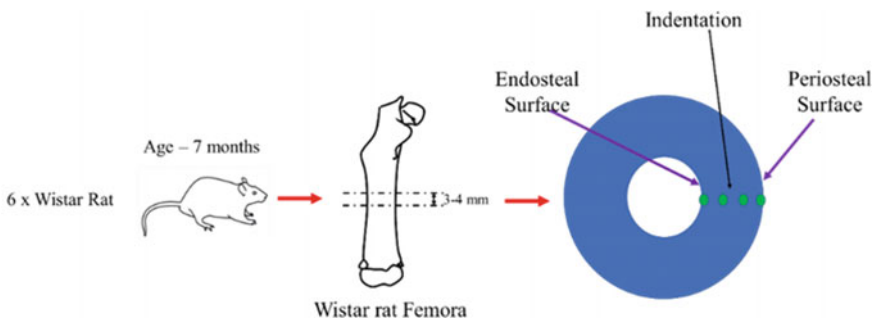
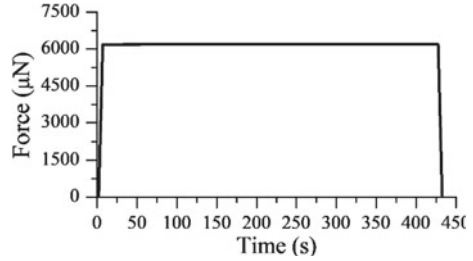


Fig. 1 Wistar rat femora cortex with nano-indentation scheme



**Fig. 2** Trapezoidal loading waveform for indentation



## 2.2 Nanoindentation

This study employs nanoindentation to compute permeability using the method proposed by Oyen [25]. Tissues were hydrated (distal water) and kept at room the temperature before the indentation. Nanoindentation is done using Triboindenter 950 (Hysitron Inc. Minneapolis, USA) using spherical indenter of 200  $\mu\text{m}$  in load control mode. Trapezoidal loading waveform as shown in Fig. 2 is used for indentation.

## 2.3 Indentation Scheme

Nanoindentation was performed in different anatomical regions, namely anterior, posterior, medial and lateral, which are identified through attached microscope (Fig. 1). Indents were performed in these regions radially starting from periosteal surface to endosteal envelope. Loading waveform remained same in all anatomical regions.  $P-h-t$  data obtained from indentation were supplied in MATLAB (MathWorks, Natick, MA, USA).

## 2.4 Poroelastic and Statistical Analysis

The present work estimates the poromechanical properties such as shear modulus ( $G$ ), drained ( $\nu$ ), Poisson's ratio ( $\nu$ ), and intrinsic permeability ( $k$ ) which are important parameters to compute the poroelastic response [21]. Poroelastic properties are measured using creep analysis of hydrated porous biological material using nanoindentation as mentioned in the studies of Oyen [25] and Galli and Oyen [26]. Time-dependent response, i.e.  $P-h-t$ , obtained from nanoindentation supplied in standard poroelastic optimization algorithm which computes poromechanical properties (Fig. 3).

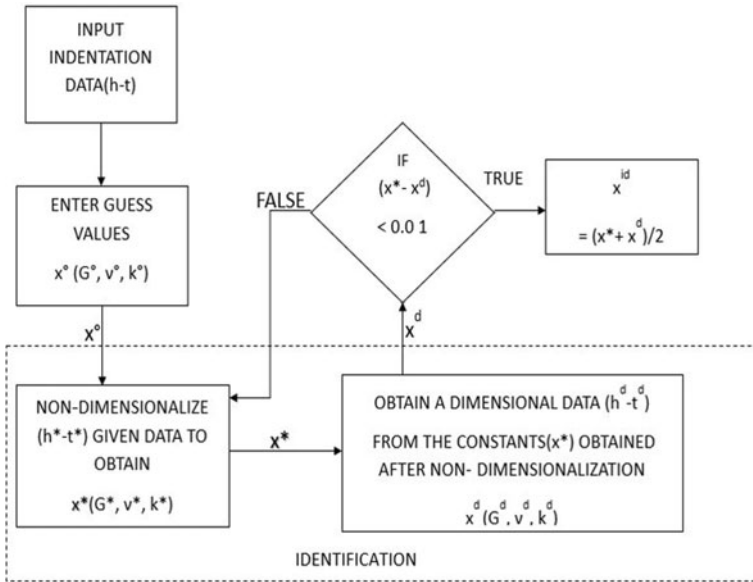


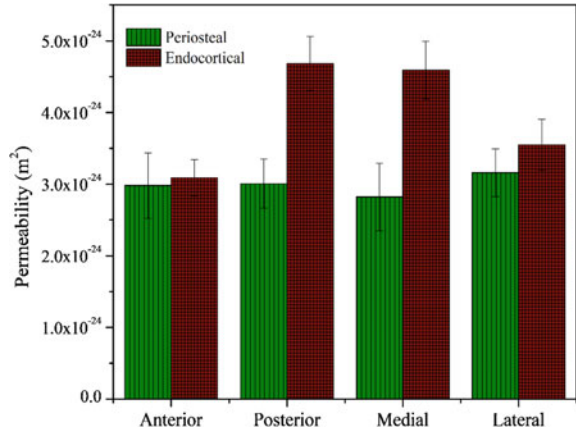
Fig. 3 Optimization algorithm based on Oyen et al. [25]

### 3 Results and Discussion

#### 3.1 Lacunar Canalicular Permeability

Lacunar canalicular permeability decides the amount of fluid flows through the canalicular channel [27, 28]. Usually, higher the lacunar permeability of the LCS channel the fluid can flow easily, while low permeability resists the fluid flow. Lacunar canalicular permeability was measured at the mid-cortex in anterior, posterior, medial, and lateral regions. Figure 4 indicates that endocortical surface seems more permeable in comparison to periosteal surface in all anatomical regions. The computed lacunar canalicular permeability varies from  $3 \times 10^{-24} \text{ m}^3$  to  $4.8 \times 10^{-24} \text{ m}^3$ . These permeability values also align with the previous experiment [20, 21]. For example, Rodriguez-Florez et al. [21] computed the permeability of lacunar space in C57BL/6 mice of different age groups. They have noticed that the permeability decreases as the age increases. In addition, Birkhold et al. [17] substantiated that the endocortical surface is more mechanoresponsive in comparison to periosteal surface.

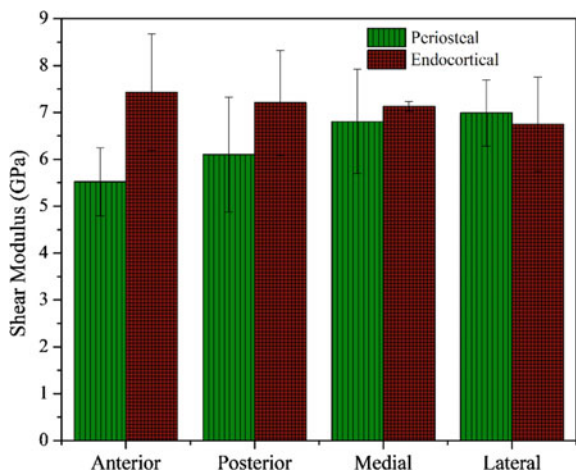
**Fig. 4** Permeability distribution in different anatomical location of femur with standard deviation



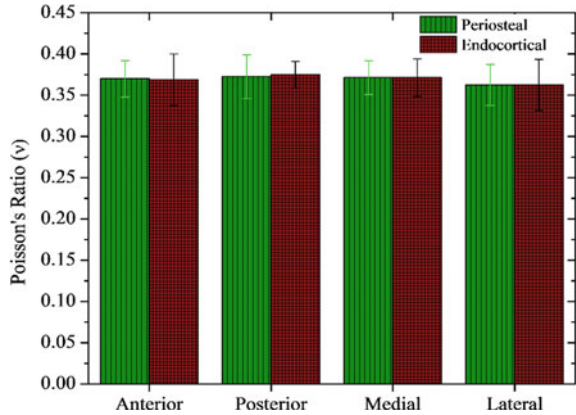
### 3.2 Shear Modulus

Present section compares shear modulus in anatomical regions of femoral bone cortex. It is noticeable that the endocortical surface has greater shear modulus in comparison to the periosteal surface except in the lateral region (Fig. 5). Shear modulus with standard deviation was also plotted at periosteal and endocortical surfaces. The magnitude of shear modulus is found to be in the range of 5–7 GPa. Rodriguez-Florez et al. [21] reported that the shear modulus does not depend upon the indenter tip cross section and size, whereas it may also depend upon the condition in which the bone tissue is kept, i.e. hydrated or dehydrated. They have also reported that the shear modulus may decrease due to spherical indenter in comparison to the use of Bercovich indenter.

**Fig. 5** Shear modulus distribution in different anatomical location of femur with standard deviation



**Fig. 6** Poisson’s ratio distribution in different anatomical location of femur with standard deviation



### 3.3 Poisson’s Ratio

Poisson’s ratio for femoral cortex at the different anatomical location is presented in Fig. 6 which clearly indicates that no significant variation occurs at both the cortical boundaries, i.e. periosteal and endosteal. No significant difference is also observed across different anatomical reasons. Poisson’s ration at all the place lies nearly in the range of 0.34. Similar values of Poisson’s ratio are also observed in Rodriguez-Florez et al. [21].

## 4 Conclusions

The present study estimates shear modulus, lacunar canalicular permeability, and Poisson’s ratio of periosteal and endosteal surfaces of Wistar rat femora at different anatomical regions. The results of present work are quite suggestive of the fact that periosteal region of the cortical bone has less permeability than endocortical region which reasserts the fact that endocortical region is more mechanoresponsive than the periosteal region. The results also suggest that permeability and shear modulus vary at different sites. The outcomes of the present work will improve the information on the role of fluid flow in bone remodelling and adaptation. Moreover, the findings will ultimately help in the identification of alterations in bone adaptation and remodelling.

**Compliance with Ethical Standards:** All procedures performed in this study were in accordance with the prescribed Institutional Ethics Committee of G. B. Pant University of Agriculture and Technology, India.

## References

1. Kumar R, Tiwari AK, Tripathi D, Mishra A (2022) Electromagnetic field induced alterations in fluid flow through lacuno-canalicular system of bone. *Int J Mech Sci* 217:107036
2. Willie BM, Zimmermann EA, Vitiene I, Main RP, Komarova SV (2020) Bone adaptation: safety factors and load predictability in shaping skeletal form. *Bone* 131:115114
3. Lanyon LE, Rubin C (1984) Static vs dynamic loads as an influence on bone remodelling. *J Biomech* 17:897–905
4. Tiwari AK, Prasad J (2016) Computer modelling of bone's adaptation: the role of normal strain, shear strain and fluid flow. *Biomech Model Mechanobiol* 1–16. <https://doi.org/10.1007/s10237-016-0824-z>
5. Srinivasan S, Weimer DA, Agans SC, Bain SD, Gross TS (2002) Low-Magnitude mechanical loading becomes osteogenic when rest is inserted between each load cycle. *J Bone Miner Res* 17:1613–1620
6. Srinivasan S, Ausk BJ, Poliachik SL, Warner SE, Richardson TS, Gross TS (2007) Rest-inserted loading rapidly amplifies the response of bone to small increases in strain and load cycles. *J Appl Physiol* 102:1945–1952. <https://doi.org/10.1152/jappphysiol.00507.2006>
7. Cullen D, Smith R, Akhter M (2001) Bone-loading response varies with strain magnitude and cycle number. *J Appl Physiol* 91:1971–1976
8. Tiwari AK, Kumar R, Tripathi D, Badhyal S (2018) In silico modeling of bone adaptation to rest-inserted loading: strain energy density versus fluid flow as stimulus. *J Theor Biol* 446:110–127
9. Kumar R, Tiwari AK, Tripathi D, Shrivastava NV, Nizam F (2019) Canalicular fluid flow induced by loading waveforms: a comparative analysis. *J Theor Biol* 471:59–73
10. Srinivasan S, Gross T (1999) Canalicular fluid flow in bone: a basis for bone formation at sites of minimal strain. 45th Ann Meet Orthop Res Soc Poster
11. Gardinier JD, Townend CW, Jen K-P, Wu Q, Duncan RL, Wang L (2010) In situ permeability measurement of the mammalian lacunar–canalicular system. *Bone* 46:1075–1081
12. Wang B, Zhou X, Price C, Li W, Pan J, Wang L (2013) Quantifying load-induced solute transport and solute–matrix interaction within the osteocyte lacunar–canalicular system. *J Bone Miner Res* 28:1075–1086
13. Wang L (2018) Solute transport in the bone lacunar–canalicular system (LCS). *Curr Osteoporos Rep* 16:32–41
14. Kumar R, Tiwari AK, Tripathi D, Sharma NN (2020) Signalling molecule transport analysis in lacunar–canalicular system. *Biomech Model Mechanobiol* 19:1879–1896
15. Price C, Zhou X, Li W, Wang L (2011) Real-time measurement of solute transport within the lacunar–canalicular system of mechanically loaded bone: direct evidence for load-induced fluid flow. *J Bone Miner Res* 26:277–285
16. Carriero A, Pereira A, Wilson A, Castagno S, Javaheri B, Pitsillides A, Marenzana M, Shefelbine S (2018) Spatial relationship between bone formation and mechanical stimulus within cortical bone: combining 3D fluorochrome mapping and poroelastic finite element modelling. *Bone Rep* 8:72–80
17. Birkhold AI, Razi H, Duda GN, Weinkamer R, Checa S, Willie BM (2016) The periosteal bone surface is less mechano-responsive than the endocortical. *Sci Rep* 6:23480
18. Fritton SP, Weinbaum S (2009) Fluid and solute transport in bone: flow-induced mechanotransduction. *Annu Rev Fluid Mech* 41:347–374
19. Kumar R, Tiwari AK, Sihota P, Tripathi D, Kumar N, Ahmad A, Ambwani S (2017) Investigation on viscoelastic properties of cortical surfaces using dynamic mechanical analysis. In: International conference on advances in thermal systems, materials and design engineering (ATSMDE2017)
20. Kumar R, Tiwari AK, Tripathi D, Main RP, Kumar N, Sihota P, Ambwani S, Sharma NN (2021) Anatomical variations in cortical bone surface permeability: tibia versus femur. *J Mech Behav Biomed Mater* 113:104122

21. Rodriguez-Florez N, Oyen ML, Shefelbine SJ (2014) Age-related changes in mouse bone permeability. *J Biomech* 47:1110–1116
22. Rodriguez-Florez N, Oyen ML, Shefelbine SJ (2013) Multi-scale permeability of murine bone measured by nanoindentation. In: *Poromechanics V: proceedings of the fifth biot conference on poromechanics*, pp 1145–1151
23. Casanova M, Balmelli A, Carnelli D, Courty D, Schneider P, Müller R (2017) Nanoindentation analysis of the micromechanical anisotropy in mouse cortical bone. *R Soc Open Sci* 4:160971
24. Pathak S, Swadener JG, Kalidindi SR, Courtland H-W, Jepsen KJ, Goldman HM (2011) Measuring the dynamic mechanical response of hydrated mouse bone by nanoindentation. *J Mech Behav Biomed Mater* 4:34–43
25. Oyen ML (2008) Poroelastic nanoindentation responses of hydrated bone. *J Mater Res* 23:1307–1314
26. Galli M, Oyen M (2009) Fast identification of poroelastic parameters from indentation tests. *Cmes-Comput Model Eng Sci* 48:241–269
27. Gatti V, Azoulay EM, Fritton SP (2018) Microstructural changes associated with osteoporosis negatively affect loading-induced fluid flow around osteocytes in cortical bone. *J Biomech* 66:127–136
28. van Tol AF, Roschger A, Repp F, Chen J, Roschger P, Berzlanovich A, Gruber G, Fratzl P, Weinkamer R (2019) Network architecture strongly influences the fluid flow pattern through the lacunocanalicular network in human osteons. *Biomech Model Mechanobiol* 1–18

# Design of Efficient Finite Elements Using Deep Learning Approach



Sekhor S. Nath, Dipjyoti Nath, and Sachin S. Gautam

**Abstract** The finite element method (FEM) is a well-known method for numerically solving partial differential equations (PDEs) over a physical domain. It has been applied successfully to solve various problems in the field of structural analysis, electromagnetics, heat transfer, fluid flows, etc. However, the issue of improving FEM has been going on for the last 50 years. The objective of the study is to create an artificial neural network (ANN) model that can learn to predict the stiffness matrices of 2D finite elements, such as the 8-node quadrilateral element. The computational efficiency and accuracy of the finite elements generated through the ANN model are also checked with existing finite elements through some numerical examples. The results have been found to be consistent with available literature.

**Keywords** Deep learning · Finite element method · 8-node quadrilateral element · Stiffness matrix

## 1 Introduction

FEM is commonly used as a technique for numerically solving differential equations encountered in engineering and mathematical modeling [23]. It has been successfully applied in several areas such as structural analysis, fluid flows, electromagnetics, and heat transfer. The FEM procedure involves discretization of a continuum into smaller parts known as finite elements. This is accomplished by constructing a mesh of the domain, i.e., a set of discretized points in the domain. The solution of the complete system can then be found by the assembly of all the finite elements present in the mesh.

Deep learning is a field of machine learning which primarily deals with artificial neural networks (ANNs) containing many hidden layers [4]. ANN is an algorithm which is loosely modeled after the human brain. An ANN model is a collection of densely interconnected units known as artificial neurons [14]. Due to the rapid

---

S. S. Nath · D. Nath · S. S. Gautam (✉)  
Indian Institute of Technology Guwahati, Guwahati 781039, India  
e-mail: [ssg@iitg.ac.in](mailto:ssg@iitg.ac.in)

© The Author(s), under exclusive license to Springer Nature Singapore Pte Ltd. 2023  
R. Sharma et al. (eds.), *Advances in Engineering Design*, Lecture Notes in Mechanical Engineering, [https://doi.org/10.1007/978-981-99-3033-3\\_2](https://doi.org/10.1007/978-981-99-3033-3_2)

increase in computational power in the last two decades, deep learning has become very popular and has been widely implemented in various fields of computational mechanics. It has been applied extensively in the field of PDEs [11, 19], fracture mechanics [13, 18], fatigue [2, 15, 22], contact mechanics [5, 17], finite element quadrature [16, 21], and stress recovery [9, 12]. Recently, there has also been an attempt to develop a neural network to predict the element stiffness matrices of 2D finite elements [8].

In the present work, the idea of Jung et al. [8] is explored in a different way. The ANN model used in the current work is different as it uses a different cost function than the one used by Jung et al. [8]. Moreover, an exponentially decaying learning rate was used in this paper, which is different from the one used in [8]. The neural network predicts the strain–displacement matrix at all the Gauss points of the finite element, which can be used further to evaluate the stiffness matrix. The nodal coordinates of the finite element and the material properties constitute the neural network’s input signal. The strain–displacement matrices obtained from the ANN model are then post-processed to form the stiffness matrices of actual finite elements. The accuracy and computational efficiency of the finite elements are then measured through two numerical examples.

The rest of the paper is organized as follows. The isoparametric finite element procedure is covered in Sect. 2. Section 3 describes the data generation method and neural network configuration. The results and discussion are described in Sect. 4. Finally, Sect. 5 concludes the paper.

## 2 Isoparametric FEM

In this section, the isoparametric FEM procedure for a 2D solid quadrilateral element with  $n$  nodes [23] is reviewed in a brief manner. In isoparametric FEM, the same interpolation functions (or shape functions) are used for domain and dependent variable interpolation, such as displacement and temperature, as shown below,

$$\mathbf{x} = \sum_{i=1}^n N_i(\xi, \eta) \mathbf{x}_i \quad \text{and} \quad \mathbf{u} = \sum_{i=1}^n N_i(\xi, \eta) \mathbf{u}_i \quad (1)$$

where  $\mathbf{x}_i$  is the  $2 \times 1$  position vector of the  $i^{\text{th}}$  node,  $N_i(\xi, \eta)$  are the shape functions of the element at Gauss point  $(\xi, \eta)$ , and  $\mathbf{u}_i$  is the displacement vector at the  $i^{\text{th}}$  node. The strain–displacement matrix  $\mathbf{B}$  is used to calculate the strains at the Gauss points.

$$\boldsymbol{\epsilon} = \mathbf{B}(\xi, \eta) \hat{\mathbf{u}} \quad (2)$$

with

$$\boldsymbol{\epsilon} = [\epsilon_{xx} \ \epsilon_{yy} \ \gamma_{xy}]^T \quad \text{with} \quad \gamma_{xy} = 2\epsilon_{xy} \quad (3)$$



$$\hat{\mathbf{u}} = [u_1 \ u_2 \ \dots \ u_n \ v_1 \ v_2 \ \dots \ v_n]^T \quad (4)$$

Then the element stiffness matrix is obtained as follows:

$$\mathbf{K} = \sum_{i=1}^p \sum_{j=1}^p w_{i,j} \mathbf{B}_{i,j}^T \mathbf{D} \mathbf{B}_{i,j} \mathbf{J}_{i,j} \quad (5)$$

where  $w_{i,j}$  is the weight associated with the Gauss–Legendre quadrature rule,  $\mathbf{J}_{i,j} = \det \mathbf{J}(\xi_i, \eta_j)$ ,  $\mathbf{B}_{i,j} = \mathbf{B}(\xi_i, \eta_j)$ , and  $\mathbf{D}$  is the constitutive matrix which is a function of material parameters.

### 3 Implementation of Deep Learned Finite Elements

The mathematical formulation for constructing the strain–displacement matrices of a two-dimensional 8-node quadrilateral finite element using a deep learning model [8] is shown here.

#### 3.1 Data Generation

The first step in building an ANN model is to generate a large amount of data. To effectively generate data containing a variety of shapes, normalized data is generated to train the model. The  $n^{\text{th}}$  normalized geometry is a quadrilateral with four nodes at the corners and the remaining four nodes lying at the mid-point of each side. The base of the quadrilateral is fixed such that the node 1 lies at the origin and the node 2 is located on the  $x$ -axis with coordinates (1, 0). The other two nodal coordinates  $\mathbf{x}_3^{(n)}$  and  $\mathbf{x}_4^{(n)}$  are generated at random in such a way that the side lengths of the quadrilateral excluding the base are always less than 1.0.

To avoid nearly singular Jacobian matrix ( $J$ ) during generation of random elements, severely distorted geometries are excluded. Hence, the interior angles of the quadrilateral are constrained to lie between  $10^\circ$  and  $170^\circ$ , and the length of the other sides of the quadrilateral must be between 0.1 and 1.0. Young's modulus of the material is taken as  $E = 2.0 \times 10^{11}$  units, and the Poisson's ratio ( $\nu^{(n)}$ ) is sampled such that  $\nu^{(n)} \sim \mathcal{U}(0, 0.499999)$ .

To generate the strain data for the randomly generated normalized element, a *reference data model* is created. First of all, the random element geometry is discretized into uniform  $N \times N$  mesh using 4-node quadrilateral elements (Q4) [23].  $N = 50$  is used for constructing the reference model. Then, the nodal displacements are generated at all the 8 nodes of the elements from a uniform probability distribution lying in the range  $[-0.25, 0.25]$ . Then the displacements at the outer nodes of the element are found by using the shape function interpolation formula given in Eq. (1). The

outer displacements are then mapped to a data model, and the nodal displacement vector is split into inner and outer displacements. The inner displacements are then found out by using the standard FEM procedure. After calculating the inner and outer displacements, the strains are computed at the Gauss points. To avoid rank deficiency of stiffness matrices, a  $3 \times 3$  quadrature rule is used. The  $n^{\text{th}}$  row of the data matrix  $(\mathbf{x}^{(n)}, \mathbf{y}^{(n)})$  is constructed as follows:

$$[\mathbf{x}^{(n)}, \mathbf{y}^{(n)}] = [v^{(n)} \quad \mathbf{X}^{(n)} \quad \mathbf{U}^{(n)} \quad \mathbf{S}^{(n)}] \quad (6)$$

where  $\mathbf{X}^{(n)}$  contains the coordinates of node 3 and node 4 of the element,  $\mathbf{U}^{(n)}$  is a row vector containing the nodal displacements at the 8 nodes of the element, and  $\mathbf{S}^{(n)}$  contains the strain components at all the 9 Gauss points of the element. Thus, there are 48 columns in the data matrix.

### 3.2 Architecture of the Neural Network and Training

The ANN model has five inputs in the input layer, i.e.,  $v^{(n)}$  and  $\mathbf{X}^{(n)}$ . The neural network outputs the normalized strain–displacement matrices computed at all the Gauss point locations of the element. In the present work, the cost function shown below is used for training the ANN model.

$$C(\boldsymbol{\theta}) = \frac{1}{27M} \sum_{n=1}^M \sum_{i=1}^3 \sum_{j=1}^3 \left( \mathbf{B}_{i,j}^{(n)}(\boldsymbol{\theta}) \mathbf{u}^{(n)} - \boldsymbol{\epsilon}_{i,j}^{(n)} \right)^2 \quad (7)$$

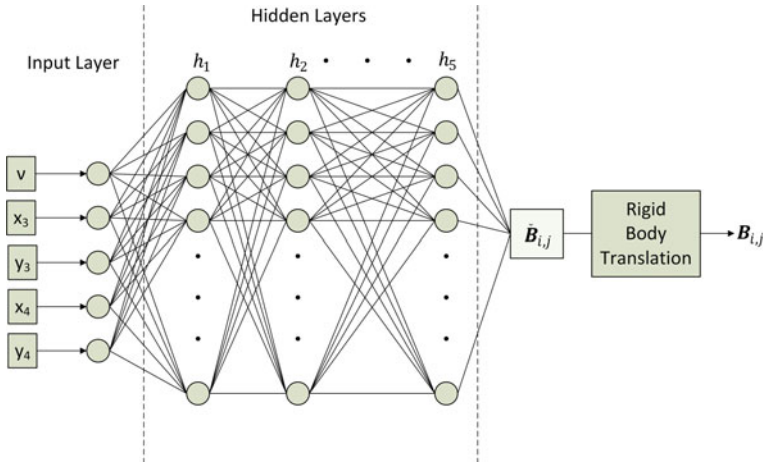
Here,  $\boldsymbol{\theta}$  is the weights of the ANN model, and  $M$  is the number of training examples.

The finite elements produced from the deep learned model may not produce zero strain energy in rigid body motion. This is ensured by enforcing the condition given by,

$$\mathbf{B}_{i,j}^{(n)}(\boldsymbol{\theta}) \Delta \mathbf{u} = 0 \quad (8)$$

where  $\Delta \mathbf{u}$  is the vector that contains the rigid body translation displacements in the order mentioned in Eq. (4).

The deep neural network configuration consists of five hidden layers (Fig. 1). In each hidden layer, batch normalization [7] is applied before the activation function to normalize the weighted sum of the previous layer activations, and then exponential linear unit (ELU) activation function is used to apply some nonlinearity to the activations. Each hidden layer of the ANN model contains 378 neurons ( $= 9 \times 3 \times 14$ ), which is equal to the number of values to be predicted. Then the 378 outputs are rearranged to form the intermediate matrices  $(\widetilde{\mathbf{B}}_{i,j}(\boldsymbol{\theta}))$  at all the nine Gauss points. After that, the condition given in Eq. (8) is imposed on these intermediate matrices



**Fig. 1** Architecture of the neural network used.  $h_1, h_2, \dots, h_5$  represent the hidden layers of the ANN model

to get the final strain–displacement matrices at all the Gauss points of the element. The Adam optimization algorithm [10] is used as an optimizer to minimize the cost function, and Xavier normal initialization [3] is used to initialize the weights of the neural network randomly. An exponentially decaying learning rate with initial value of 0.01 is used during training of the network. The network is trained using  $M = 3,00,000$  data points with a batch size of 50,000, and 50,000 data points are used for the testing set. To model pure shearing problems, additional 3000 data points are generated for training and 1200 data points for testing in  $x$  and  $y$  directions. The training and testing error (Eq. (7)) of the deep learning model is obtained as  $4.3320 \times 10^{-4}$  and  $5.7183 \times 10^{-4}$ , respectively.

### 3.3 Computation of the Stiffness Matrix

During the testing phase, the actual physical finite element geometries have to be preprocessed to convert them to the normalized element geometries. Before doing this, the element connectivity in the finite element mesh is assigned in such a way that the longest side always lies between the nodes 1 and 2. After that, the normalized element coordinates are obtained as given below,

$$X_i = \frac{1}{l_{\max}} \mathbf{R}^T \begin{Bmatrix} x_i - x_1 \\ y_i - y_1 \end{Bmatrix} \quad \text{where } i = 1, 2, 3, 4 \quad (9)$$

and

$$\mathbf{R} = \begin{bmatrix} \cos \psi & -\sin \psi \\ \sin \psi & \cos \psi \end{bmatrix} \quad (10)$$

where  $\psi$  is the angle between the side having the maximum length in the physical finite element and the  $x$ -axis. The coordinates obtained from Eq. (9) are used as inputs to the neural network.

To get the strain–displacement matrices of the original element from those of the normalized elements, the results obtained from the neural network must be post-processed as given below,

$${}_{\text{ANN}}\mathbf{B}_{i,j} = \frac{1}{l_{\max}} \mathbf{T} {}_{\text{output}}\mathbf{B}_{i,j} \mathbf{Q}^T \quad (11)$$

where  $\mathbf{T}$  is the matrix used for transformation of strains [20],  ${}_{\text{output}}\mathbf{B}_{i,j}$  is the output of the neural network, and  $\mathbf{Q}$  is the rotation matrix which is arranged according in the way given below [8].

$$\mathbf{Q} = \begin{bmatrix} \cos \psi & 0 & \dots & -\sin \psi & 0 & \dots \\ 0 & \ddots & \vdots & 0 & \ddots & 0 \\ \vdots & 0 & \cos \psi & \vdots & 0 & -\sin \psi \\ \sin \psi & 0 & \dots & \cos \psi & 0 & \dots \\ 0 & \ddots & 0 & 0 & \ddots & 0 \\ 0 & 0 & \sin \psi & 0 & \dots & \cos \psi \end{bmatrix}_{(16 \times 16)} \quad (12)$$

The strain–displacement matrices are then corrected by using the B-bar method [6] as shown below,

$${}_{\text{ANN}}\bar{\mathbf{B}}_{i,j} = {}_{\text{ANN}}\mathbf{B}_{i,j} + {}_{\text{ANN}}\tilde{\mathbf{B}}_{i,j} \quad (13)$$

where

$${}_{\text{ANN}}\tilde{\mathbf{B}}_{i,j} = \frac{1}{V} \int_V ({}_{\text{ANN}}\mathbf{B}_{i,j} - {}_{\text{Q8}}\mathbf{B}_{i,j}) dV \quad (14)$$

Here,  $V$  is the volume of the element, and  ${}_{\text{Q8}}\mathbf{B}_{i,j}$  denotes the strain–displacement matrix of the 8-node quadrilateral (Q8) element [23]. The stiffness matrix is finally computed as shown below,

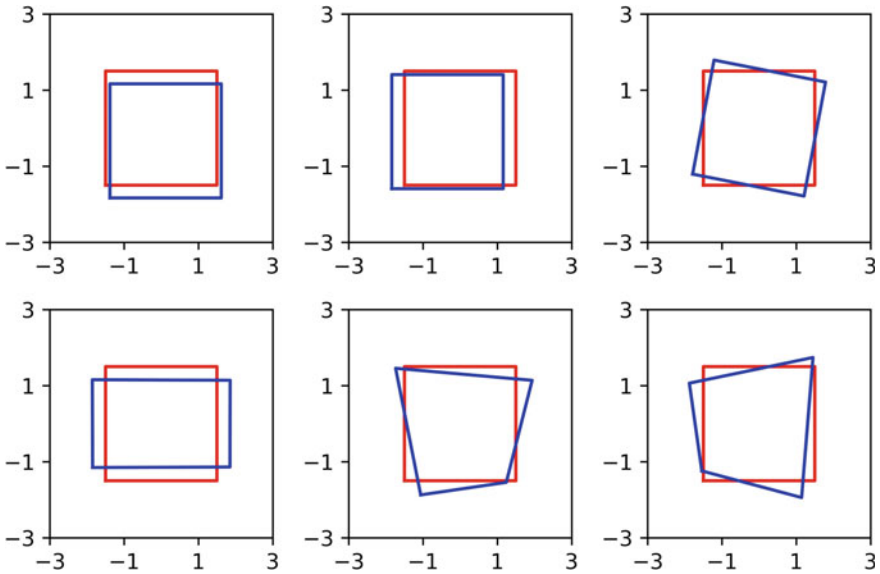
$$\mathbf{K} = \sum_{i=1}^p \sum_{j=1}^p w_{i,j} {}_{\text{ANN}}\bar{\mathbf{B}}_{i,j}^T \mathbf{D}_{\text{ANN}} \bar{\mathbf{B}}_{i,j} \mathbf{J}_{i,j} \quad (15)$$

## 4 Results and Discussion

In this section, the performance of the finite elements generated by deep learning is measured through two numerical examples, the zero-energy mode test [8] and the Cook’s membrane problem [1].

### 4.1 Zero-Energy Mode Tests

The zero-energy modes of a single unconstrained element without any boundary conditions are calculated which helps to evaluate the performance of a single element. A homogeneous and isotropic elastic material having  $E = 1.5 \times 10^3$  units and  $\nu = 0.3$  are taken for conducting this test. The eigenvalues and eigenvectors of the stiffness matrix of the element are obtained up to the sixth strain energy mode. The deformed configuration for the first six deformation modes of the element is plotted as shown in Fig. 2. This confirms that the physical element does not contain any extra zero-energy modes apart from the rigid body modes. Hence, it can be shown that the finite element can accurately capture the physics of the problem.

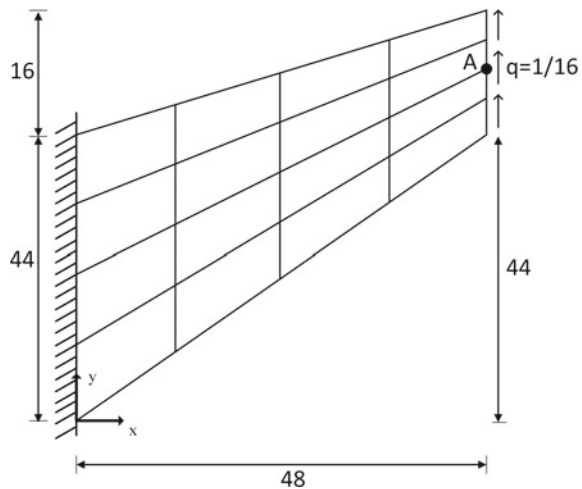


**Fig. 2** First six modes of the element. Red represents the undeformed geometry, and blue represents the deformed geometry of the element

## 4.2 Cook's Membrane Problem

To assess the performance of the 8-node quadrilateral element generated from the neural network, the Cook's membrane problem [1] is considered. The description of the problem is mentioned in Fig. 3. The condition of plane stress with  $E = 1.0$  and  $\nu = 1/3$  is used for solving the problem. The uniform meshing strategy of  $N \times N$  is used for discretizing the beam. The vertical deflections at point A ( $v_A$ ) are computed by using the deep learned element to mesh the domain. The reference solution of  $v = 23.9662$  is obtained by using a uniform mesh containing 100 elements in each direction. The results obtained are then compared with those obtained by using 4-node quadrilateral (Q4), 8-node quadrilateral (Q8), and 9-node quadrilateral (Q9) elements for different mesh sizes of  $N = 2, 4, 8, 16, 32$ . The absolute percentage error is shown in Table 1. The values of absolute percentage error in Table 1 show that the DL8 element performed better than the 4-node quadrilateral element for coarse mesh sizes, and the displacements obtained are close to the solution obtained through various standard finite elements.

**Fig. 3** Cook's membrane problem discretized with a uniform mesh with  $N$  elements in each direction



**Table 1** Absolute percentage error in the displacement in y-direction computed at point A (shown in Fig. 3) in the Cook's membrane problem [1]

Mesh	Q4	Q8	Q9	DL8
$2 \times 2$	50.7531	5.2090	2.8269	17.0573
$4 \times 4$	23.6904	1.0761	0.5278	6.0251
$8 \times 8$	7.8790	0.3442	0.1702	3.9389
$16 \times 16$	2.2361	0.1318	0.0701	3.3585
$32 \times 32$	0.6200	0.0463	0.0225	3.1407

## 5 Conclusion

In this work, the deep learning approach is used to generate stiffness matrices for 2D 8-node quadrilateral solid finite element. The work also focused on normalized data generation for efficient training of the model, preprocessing of the inputs to the network, and finally post-processing of the output obtained from the ANN model to get the element stiffness matrices. The finite elements generated from the ANN model are also formulated in such a way as to represent rigid body motions by including a separate layer of neurons in the ANN model. The performance of the generated finite elements was also measured with the help of a numerical example. This also shows that artificial intelligence and machine learning can be used in modeling finite elements to solve 2D elasticity problems. This can pave the way for the future incorporation of AI- and ML-based algorithms for fast and high-performance FEM simulations. The work is also being presently extended to the domain of three-dimensional hexahedral finite elements.

**Acknowledgements** The authors gratefully acknowledge the support from SERB, DST under project IMP/2019/000276, and VSSC, ISRO, through MoU No.: ISRO:2020:MOU:NO: 480.

## References

1. Cook RD, Malkus DS, Plesha ME, Witt RJ (2007) Concepts and applications of finite element analysis. John Wiley & Sons
2. Gautam SS, Khan K (2020) Detection of fretting fatigue using machine learning algorithms. In: Proceedings of the 3rd structural integrity conference and exhibition (SICE 2020)—“structural integrity at multiple length scales” (e-Conference). IIT Bombay
3. Glorot X, Bengio Y (2010) Understanding the difficulty of training deep feedforward neural networks. In: Proceedings of the thirteenth international conference on artificial intelligence and statistics. JMLR workshop and conference proceedings, pp 249–256
4. Goodfellow I, Bengio Y, Courville A (2016) Deep learning. MIT Press
5. Gouravaraju S, Narayan J, Sauer RA, Gautam SS (2023) A Bayesian regularization-backpropagation neural network model for peeling computations. *J Adhesion* 99(1):92–115
6. Hughes TJ (1980) Generalization of selective integration procedures to anisotropic and nonlinear media. *Int J Numer Meth Eng* 15(9):1413–1418
7. Ioffe S, Szegedy C (2015) Batch normalization: accelerating deep network training by reducing internal covariate shift. In: Bach F, Blei D (eds) Proceedings of the 32nd international conference on machine learning. Proceedings of machine learning research, vol 37. PMLR, Lille, France, pp 448–456
8. Jung J, Yoon K, Lee PS (2020) Deep learned finite elements. *Comput Methods Appl Mech Eng* 372:113401
9. Khoei A, Moslemi H, Seddighian M (2020) An efficient stress recovery technique in adaptive finite element method using artificial neural network. *Eng Fract Mech* 237:107231
10. Kingma DP, Ba J (2014) Adam: a method for stochastic optimization. arXiv preprint [arXiv:1412.6980](https://arxiv.org/abs/1412.6980)
11. Lagaris IE, Likas A, Fotiadis DI (1998) Artificial neural networks for solving ordinary and partial differential equations. *IEEE Trans Neural Networks* 9(5):987–1000

12. Liang L, Liu M, Martin C, Sun W (2018) A deep learning approach to estimate stress distribution: a fast and accurate surrogate of finite-element analysis. *J R Soc Interface* 15(138):20170844
13. Liu X, Athanasiou CE, Padture NP, Sheldon BW, Gao H (2020) A machine learning approach to fracture mechanics problems. *Acta Mater* 190:105–112
14. Mitchell T (1997) *Machine learning*. McGraw-Hill Education
15. Nowell D, Nowell P (2020) A machine learning approach to the prediction of fretting fatigue life. *Tribol Int* 141:105913
16. Oishi A, Yagawa G (2017) Computational mechanics enhanced by deep learning. *Comput Methods Appl Mech Eng* 327:327–351
17. Oishi A, Yagawa G (2020) A surface-to-surface contact search method enhanced by deep learning. *Comput Mech* 65:1125–1147
18. Ozarde AP, Narayan J, Yadav D, McNay GH, Gautam SS (2020) Optimization of diesel engine's liner geometry to reduce head gasket's fretting damage. *SAE Int J Engines* 14(1):81–97
19. Raissi M, Perdikaris P, Karniadakis GE (2019) Physics-informed neural networks: a deep learning framework for solving forward and inverse problems involving nonlinear partial differential equations. *J Comput Phys* 378:686–707
20. Roylance D (2001) Transformation of stresses and strains. *Lecture notes for mechanics of materials*
21. Vithalbhair SK, Nath D, Agrawal V, Gautam SS (2022) Artificial neural network assisted numerical quadrature in finite element analysis in mechanics. *Mat Today Proc* 66:1645-1650
22. Vithalbhair S, Gautam SS (2021) A machine learning approach to fretting fatigue problem. In: *Proceedings of the international conference on futuristic technologies (e-Conference)—structural health monitoring, energy harvesting, Green Material and Biomechanics*. IIT Delhi
23. Zienkiewicz OC, Taylor RL, Zhu JZ (2005) *The finite element method: its basis and fundamentals*. Elsevier



# Design of Efficient Quadrature Scheme in Finite Element Using Deep Learning



Rohan Chinchkar, Dipjyoti Nath, and Sachin S. Gautam

**Abstract** The advancement of computers has led to collection and handling of huge data from various resources. The inherent properties of computational mechanics application can be extracted from the appropriate data using different techniques of machine learning (ML). The present work enlightens a method to employ machine learning in the field of finite element method (FEM) where evaluation of sufficient number of integrals has to be carried out. This calculation of integral by the standard Gauss–Legendre quadrature rule requires specific number of Gauss quadrature points for getting the desired accuracy which minimizes the computational cost. Whereas the element stiffness matrix is calculated numerically with required number of Gauss quadrature points for different element with respect to the material properties. Most of the auto-mesh software consider constant number of Gauss quadrature points for all the elements irrespective of their distortion and material behaviour. The main motivation of this work is to build an accurate and computationally efficient quadrature scheme with the help of standard Gauss–Legendre quadrature rule for computing elemental stiffness matrix. An efficient method is developed using a deep neural network to predict respective number of Gauss quadrature points for given element coordinates and the material properties.

**Keywords** Finite element method · Stiffness matrix · Deep learning · Quadrature scheme

## 1 Introduction

Machine learning (ML) is a discipline which addresses the mapping between the input and output parameters using available data. Over the past decade, a prodigious rise of ML-based techniques is impacting in many areas such as database mining [1], healthcare [2], engineering [3], autonomous driving [4], computer vision [5],

---

R. Chinchkar · D. Nath · S. S. Gautam (✉)  
Department of Mechanical Engineering, Indian Institute of Technology Guwahati, Guwahati,  
Assam 781039, India  
e-mail: [ssg@iitg.ac.in](mailto:ssg@iitg.ac.in)

and many more. ML approach has been used in various mechanical problems such as to identify a small driving force for a fatigue crack observed in a polycrystalline material [6], and also, predict the growth of a fatigue crack [7–9]. Deep learning approach is used by Liang et al. [10] to estimate stress distribution in main artery of the body using deep learning. Stress concentration factor of an infinite panel under uniaxial and biaxial loading conditions was calculated using artificial neural network (ANN) by Ozkan and Erdemir [11]. Gouravaraju et al. [12] have predicted pull-off force and applied displacement using a neural network at detachment for peeling angle. Oishi and Yagawa [13] used an ANN to predict the Gauss quadrature points for given irregular distorted element of a single material in FEM. Weinan and Yu [14] introduced a deep learning-based method to solve variational problem called as Deep Ritz method (DRM).

FEM is one of the promising numerical techniques, widely used in solving partial differential equations of engineering problems by discretizing the geometry with different kinds of elements. These elements can be of different types such as linear, triangular or quadrilateral, and tetrahedral or hexahedral element. Depending upon the nature of problem and the required accuracy, the type of element can be chosen. Moreover, the operations performed to get the numerical integration of partial differential equation mainly consist of Gauss–Legendre quadrature scheme. An auto-mesh software considers an equal number of Gauss quadrature points for all the meshed elements irrespective of their shape. However, the work done till now is limited to usage of single material [13]. Cheng et al. [15] have prepared a neural network to find numerical integration scheme for boundary element method.

Enlightened by reported works, herein a neural network is made to handle multiple engineering materials to predict the respective number of Gauss quadrature points. Complex architecture of deep neural network is prepared to attain higher accuracy with larger number of examples incorporated with dropout and batch normalization techniques different than Oishi and Kashyap. Also, the work comprises usage of only regular finite elements generated by a method different than the Oishi's method of data generation. The following section describes the Gauss quadrature implemented in FEM. Section 3 briefly reviews artificial neural network. The details about deep neural network are discussed in Sect. 4. Outcome of DNN model is given in Sect. 5, and finally, Sect. 6 summarizes the faster computation of elemental stiffness matrix for multiple engineering materials.

## 2 Gauss Quadrature Scheme in FEM

The evaluation of elemental stiffness matrix in FEM is carried out numerically through Gauss quadrature rule. The general equation of elemental stiffness matrix  $[k^e]$  is given as

$$[k^e] = \int_V [\mathbf{B}]^T [\mathbf{D}] [\mathbf{B}] dV \quad (1)$$

where the  $[\mathbf{B}]$  and  $[\mathbf{D}]$  matrices are called as strain–displacement matrix and material elastic tensor, respectively.  $\mathbf{J}$  is the Jacobian matrix calculated for the given 8-noded hexahedral element. The numerical integration of a function using Gauss–Legendre quadrature formula for three-dimensional space is evaluated by using following formula (Eq. 2).

$$I = \int_{-1}^1 \int_{-1}^1 \int_{-1}^1 f(u, v, w) du dv dw \approx \sum \sum \sum f(\xi_i, \eta_j, \zeta_k) \cdot W_i \cdot W_j \cdot W_k \quad (2)$$

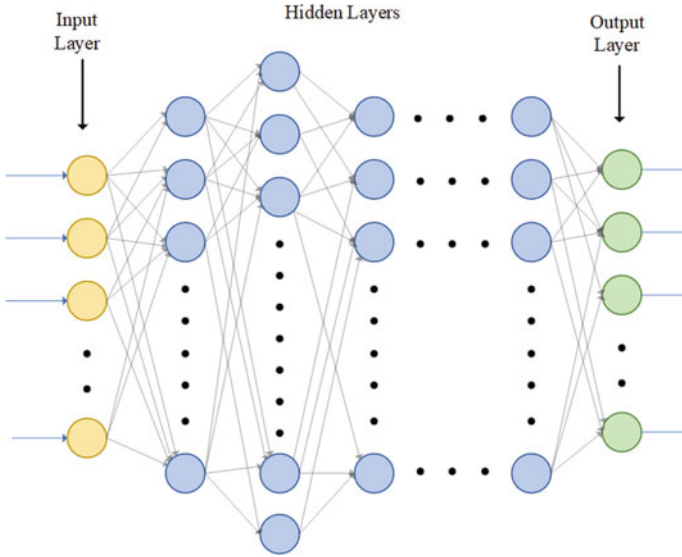
where  $\xi_i, \eta_j, \zeta_k$  are the integration points related to  $i^{\text{th}}, j^{\text{th}},$  and  $k^{\text{th}}$  integration points and the weights  $W_i, W_j,$  and  $W_k$  corresponding to the  $\xi_i^{\text{th}}, \eta_j^{\text{th}},$  and  $\zeta_k^{\text{th}}$  Gauss points. The numerical solution of the Eq. (1) using Gauss–Legendre quadrature rule is given in following Eq. (3).

$$[k^e] \approx \sum_{j=1}^{n_\xi} \sum_{k=1}^{n_\eta} \sum_{l=1}^{n_\zeta} [\mathbf{B}]^T [\mathbf{D}] [\mathbf{B}] |\mathbf{J}| \cdot w_\xi w_\eta w_\zeta \quad (3)$$

where  $n_\xi, n_\eta,$  and  $n_\zeta$  are the number of Gauss quadrature points in respective  $x, y,$  and  $z$ -axis and  $w_\xi, w_\eta,$  and  $w_\zeta$  are the weights related to  $\xi, \eta,$  and  $\zeta,$  respectively. Hence, the total number of Gauss quadrature points is denoted by  $N_{gp},$  and it would be  $n_\xi \times n_\eta \times n_\zeta.$  For regular perfect 8-noded hexahedral element, 2 number of Gauss quadrature points are taken in each axis.

$$\begin{aligned} \text{Total Gauss points} &= N_{gp} = n_\xi \times n_\eta \times n_\zeta \\ &= 2 \times 2 \times 2 = 8 \end{aligned} \quad (4)$$

The motivation could be justified in finite element analysis of crash experiments or contact impulse problems where gradient of primary variable, i.e. displacement is very high. This necessity takes higher number of Gauss quadrature points to accurately integrate the displacement field. Depending upon the deformation of element, adaptive number of Gauss quadrature points should be considered and that is possible with the help of machine learning algorithms.



**Fig. 1** Basic architecture of deep neural network

### 3 Artificial Neural Network

An artificial neural network (ANN) is one of the machine learning technique that mimics the working of human brain and can be used in any complex problem with deeper neural network [16]. The basic architecture of deep neural network is illustrated through Fig. 1. Moreover, addition of advanced optimization techniques such as dropout method [17] and batch normalization [18] for particular layer of ANN model can be applied to reduce the variance and improve the performance of the model [19].

Pointing towards the architecture of neural network, the number of neurons in input and output layer represents number of input and output parameters, respectively. Further, the number of hidden layers and hidden neurons depends upon the complexity of the problem and can be decided using various ML tuning procedures.

### 4 Deep Neural Network for Quadrature Scheme

Procedure for preparing deep neural network (DNN) consists of several sophisticated steps such as data preparation, data preprocessing, hyperparameter tuning, results analysis, and the implementation of the DNN on new dataset. In this work, a number of Gauss quadrature points are calculated considering geometric and material properties of 8-noded hexahedral element.

Coordinates of regular 8-noded hexahedral elements (Fig. 2) are obtained randomly and respective number of Gauss quadrature points are calculated. Dataset used for training and testing of neural network consists of the input parameters such as material properties and coordinates of the element. The training dataset consists of the examples with hypothetical data of materials with young’s modulus ranging from 80 to 200 GPa and Poisson’s ratio from 0.2 to 0.325 with six regular intervals. The testing dataset consists of an example with material properties of carbon steel having young’s modulus of 200 GPa and Poisson’s ratio of 0.3. Similarly, the output parameter is the number of minimum Gauss quadrature points required to get certain accuracy with relative error value of  $10^{-3}$  using following Eq. (5).

$$\text{Relative error} = \frac{\sum_{i,j} |k_{i,j}^p - k_{i,j}^{p_{\max}}|}{\max_{i,j} |k_{i,j}^{p_{\max}}|} \tag{5}$$

where  $k_{i,j}$  represents the  $(i, j)^{\text{th}}$  entry in the elemental stiffness matrix; also, the  $p$  is the number of Gauss quadrature points used to obtain elemental stiffness matrix.  $p_{\max}$  is the maximum number of Gauss points taken as a reference to get accurate elemental stiffness matrix and considered as 20 along each axis. After preparing the training dataset, the overview of the data is given in the following Fig. 3.

One example of each element is given in the following figure (Fig. 4) to present the number of Gauss quadrature points required for observed distortion in the element.

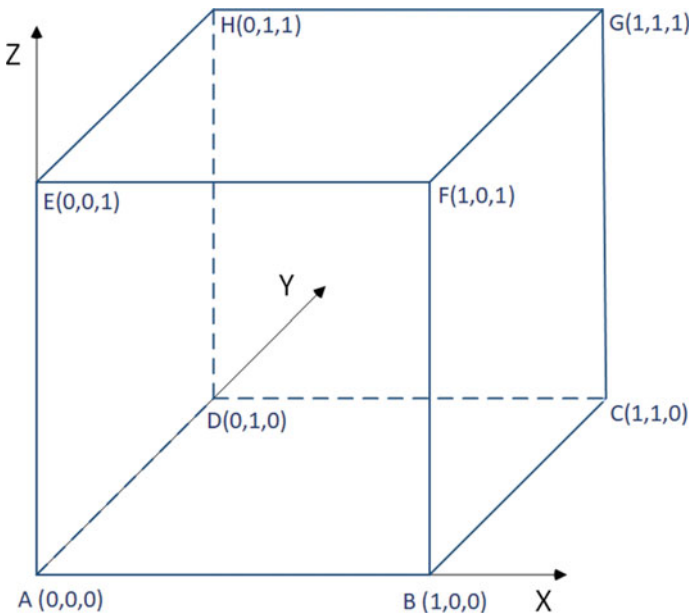


Fig. 2 Reference regular 8-noded hexahedral element

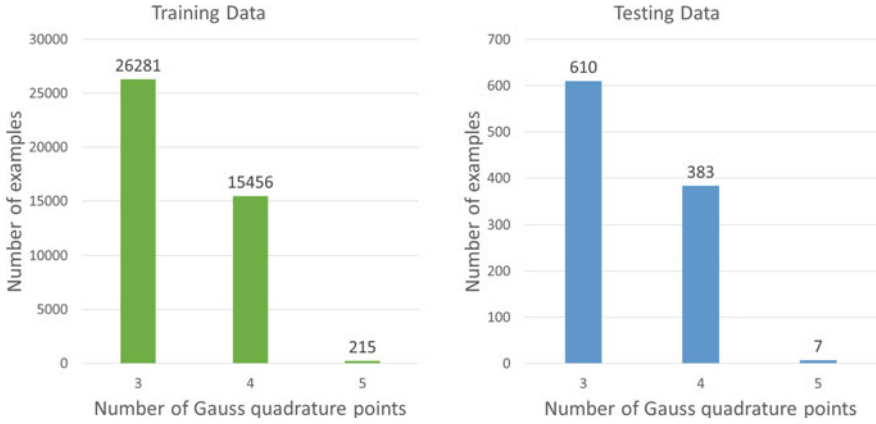


Fig. 3 Data insight according to output parameter

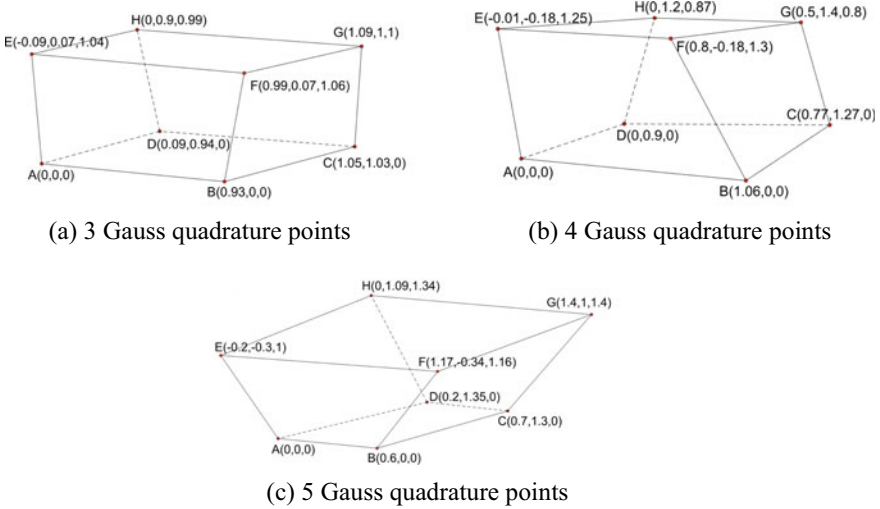


Fig. 4 Distorted regular elements classified with requirement of number of Gauss quadrature points

As prepared, DNN model has 20 input parameters including nonzero coordinate information of the distorted element and the material properties such as young's modulus and Poisson's ratio. The DNN has one output parameter with four hidden neurons predicting the number of optimal Gauss quadrature points for given input. It is further tuned for optimal hyperparameters like seven hidden layers and also integrated with the advanced training techniques such as dropout method and batch normalization technique.

## 5 Results and Discussion

Our work reveals training accuracy of 99% for multiple engineering materials, and the testing has been done through the mentioned real material data to validate the training data. The testing accuracy of the DNN observed is 92% which is better than the basic model of Oishi et al. [13] and the advanced model of Kashyap et al. [19], where both models consider single material. This is achieved with the help of complex neural network architecture and batch normalization technique. Outcome of the neural network is helpful for directly choosing required number of Gauss quadrature points to calculate accurate elemental stiffness matrix. Obtained results of our neural network for multi-class classification problem is discussed through the following Table 1.

The number of Gauss quadrature points associated with the deformed element plays major role in accuracy of elemental stiffness matrix. An overall comparison of the error obtained by using different number of Gauss quadrature points is done to get intuition regarding relative error (Eq. 5) and represented through the following Table 2.

where the left-side column indicates the actual requirement of Gauss quadrature points for a particular selected hexahedral element and the subsequent columns represent the error term observed during evaluation of elemental stiffness matrix compared to reference number of Gauss quadrature points. For initial distortion of the perfect element, percentage of error is less for lower values of Gauss quadrature points, but as the requirement increases, respective error percentage also increases.

**Table 1** Accuracy of DNN

Gauss points in each axis	Training accuracy (%)	Testing accuracy (%)
3	99	92
4	99	91
5	96	75

**Table 2** Relative error analysis with respect to Gauss quadrature points

Required number of Gauss quadrature points	Error found for number of Gauss quadrature points (%)			
	2	3	4	5
3	1.621	<b>8.914 × 10<sup>-04</sup></b>	6.22 × 10 <sup>-07</sup>	4.998 × 10 <sup>-10</sup>
4	11.7358	0.1116	<b>1.076 × 10<sup>-03</sup></b>	1.033 × 10 <sup>-05</sup>
5	44.64	2.0439	0.0959	<b>4.53 × 10<sup>-03</sup></b>

## 6 Conclusion

This work highlights the capability of DNN model predicting the Gauss quadrature point required to accurately calculate elemental stiffness matrix. However, our as described model is capable of handling multiple engineering materials. This could avoid further fine meshing of the object and will give better results with suitable Gauss quadrature points with consideration of material behaviour. Significantly, using predicted Gaussian quadrature points directly into the calculation of elemental stiffness matrix while solving a FEM problem reduces computational cost as well as operational time of Gauss–Legendre integral. Hence, this enables faster computation of elemental stiffness matrix with required accuracy.

**Acknowledgements** The authors gratefully acknowledge the support from SERB, DST under project IMP/2019/000276 and VSSC, ISRO through MoU No.: ISRO:2020:MOU:NO: 480.

## References

1. Alizadehsani R, Roshanzamir M, Abdar M, Beykikhoshk A, Khosravi A, Panahiazar M, Sarrafzadegan N (2019) A database for using machine learning and data mining techniques for coronary artery disease diagnosis. *Scientific Data* 6(1):1–13
2. Chen PHC, Liu Y, Peng L (2019) How to develop machine learning models for healthcare. *Nat Mater* 18(5):410–414
3. Capuano G, Rimoli JJ (2019) Smart finite elements: a novel machine learning application. *Comput Methods Appl Mech Eng* 345:363–381
4. Dogan Ü, Edelbrunner J, Iossifidis I (2011) Autonomous driving: a comparison of machine learning techniques by means of the prediction of lane change behavior. In: 2011 IEEE international conference on robotics and biomimetics. IEEE, pp 1837–1843
5. Khan AI, Al-Habsi S (2020) Machine learning in computer vision. *Proc Comput Sci* 167:1444–1451
6. Rovinelli A, Sangid MD, Proudhon H, Ludwig W (2018) Using machine learning and a data-driven approach to identify the small fatigue crack driving force in polycrystalline materials. *NPJ Comput Mater* 4(1):1–10
7. Ozarde AP, Narayan J, Yadav D, McNay GH, Gautam SS (2021) Optimization of diesel engine's liner geometry to reduce head gasket's fretting damage. *SAE Int J Eng* 14(1)
8. Gautam SS, Khan KM (2020) Detection of fretting fatigue using machine learning algorithms, 3rd structural integrity conference and exhibition (SICE 2020)—“structural integrity at multiple length scales” (e-Conference), IIT Bombay
9. Vithalbhai SK, Gautam SS (2021) A machine learning approach to fretting fatigue problem. In: International conference on futuristic technologies (e-Conference)—structural health monitoring, energy harvesting, green material and biomechanics, IIT Delhi
10. Liang L, Liu M, Martin C, Sun W (2018) A deep learning approach to estimate stress distribution: a fast and accurate surrogate of finite-element analysis. *J R Soc Interface* 15(138):20170844
11. Ozkan MT, Erdemir F (2021) Determination of theoretical stress concentration factor for circular/elliptical holes with reinforcement using analytical, finite element method and artificial neural network techniques. *Neural Comput Appl* 33(19):12641–12659
12. Gouravaraju S, Narayan J, Sauer RA, Gautam SS (2023) A Bayesian regularization-backpropagation neural network model for peeling computations. *J Adhesion* 99(1):92–115



13. Oishi A, Yagawa G (2017) Computational mechanics enhanced by deep learning. *Comput Methods Appl Mech Eng* 327:327–351
14. Yu B (2018) The deep Ritz method: a deep learning-based numerical algorithm for solving variational problems. *Commun Math Stat* 6(1):1–12
15. Cheng R, Xiaomeng Y, Chen L (2022) Machine learning enhanced boundary element method: prediction of Gaussian quadrature points. *CMES-Comput Model Eng Sci* 131(1):445–464
16. Funahashi KI (1989) On the approximate realization of continuous mappings by neural networks. *Neural Netw* 2(3):183–192
17. Srivastava N, Hinton G, Krizhevsky A, Sutskever I, Salakhutdinov R (2014) Dropout: a simple way to prevent neural networks from overfitting. *J Mach Learn Res* 15(1):1929–1958
18. Ioffe S, Szegedy C (2015) Batch normalization: accelerating deep network training by reducing internal covariate shift. In: *International conference on machine learning*. PMLR, pp 448–456
19. Vithalbai SK, Nath D, Agrawal V, Gautam SS (2022) Artificial neural network assisted numerical quadrature in finite element analysis in mechanics. *Materials Today: Proceedings* 66:1645–1650

# Accelerating Finite Element Assembly on a GPU



Utpal Kiran, Sachin S. Gautam, and Deepak Sharma

**Abstract** In this paper, a parallel strategy for assembly of finite element matrices on graphics processing unit (GPU) is presented. Considering the limited memory size of a GPU, the proposed strategy doesn't store the elemental matrices into memory but performs on-the-fly computation and stores the data directly into a global stiffness matrix, reducing memory requirement and preventing overhead due to a separate assembly step. The global stiffness matrix is stored in compressed sparse row (CSR) storage format, commonly used by GPU-accelerated linear solver libraries. However, the assembly of elemental matrices directly into a sparse storage format requires prior knowledge of locations of nonzeros. The current work presents an efficient strategy to pre-compute indices for assembly into CSR sparse storage format. The proposed strategy has been implemented on both CPU and GPU. The performance characteristic of the proposed finite element solver is measured by solving large-scale three-dimensional (3D) elasticity problem involving a maximum of 4.7 million degrees of freedom (DOFs). A comparison is made with the standard assembly implementation in Eigen C++ library, which first stores the nonzero values in the form of triplets and then assembles into CSR sparse format. For the finest mesh with 4.7 million DOFs, the proposed CPU-based assembly strategy achieves  $9.3\times$  speedup over Eigen library. The computation of indices for assembly into CSR format takes 15.7 s on CPU and 2.4 s on GPU for 4.7 million DOFs. The computation of elemental matrices and their assembly, implemented on GPU as a single compute kernel, is found to be up to  $24.3\times$  faster than optimized CPU implementation. In terms of wall-clock time, the GPU-accelerated finite element solver is found to have up to  $4\times$  speedup over CPU solver.

---

U. Kiran · S. S. Gautam · D. Sharma (✉)  
Department of Mechanical Engineering, Indian Institute of Technology Guwahati, Guwahati,  
Assam 781039, India  
e-mail: [dsharma@iitg.ac.in](mailto:dsharma@iitg.ac.in)

U. Kiran  
e-mail: [ukiran@iitg.ac.in](mailto:ukiran@iitg.ac.in)

S. S. Gautam  
e-mail: [ssg@iitg.ac.in](mailto:ssg@iitg.ac.in)

**Keywords** Finite element method · Parallel computing · Sparse matrix assembly · GPU

## 1 Introduction

Finite element method (FEM) is a popular numerical approach for finding approximate solutions to a wide range of scientific problems. Originally, developed for structural mechanics problem, FEM has spread to almost every discipline of engineering, including aerospace, bio-mechanics, fluid mechanics, electromagnetics and weather prediction [1]. However, numerical procedure to obtain solutions with FEM is computationally expensive. Depending on the nature of the problem, the time spent in FEM simulation might vary from hours to months. As the computational power of computer processors has increased in recent times, there is an increasing interest in performing realistic simulation with high accuracy. Therefore, it becomes extremely important to address the issue of high simulation time associated with the FEM. Parallel computers are often employed to handle the high computation cost associated with FEM-based simulation. A recently developed hardware to perform parallel computing is GPU. The hardware like GPUs has become quite popular due to high computational power, massive parallelism and high memory bandwidth. The current work attempts to find an efficient strategy to implement FEM on a GPU.

FEM solver consists of three expensive steps: computation of the elemental matrices, assembly of global stiffness matrix and solution of a system of linear equations given by the global stiffness matrix. Among these, the solution of the system of equations is often the most time-consuming step in FEM. Consequently, GPU implementations of linear solvers have been studied the most [2–5]. The overhead in computation of elemental matrices and their assembly can be significantly high for large-scale problems involving complex differential operators and higher-order finite elements. In nonlinear problems, the computation of elemental matrices and assembly is required multiple times, and therefore, it can contribute to high simulation timings [6].

The global stiffness matrix obtained in FEM is sparse as elements are locally connected to each other in discretized domain. The sparse matrix contains a mix of zero and nonzero values. Since zero values are not useful for computation, only nonzero values are stored in memory. For this purpose, different sparse storage formats like coordinate format (COO), ELLPACK format (ELL), CSR, etc. [7] have been used in the past implying different levels of memory utilization. However, working with a sparse storage format is not a trivial task as each format introduces a unique data structure, which might not be efficient for other computational steps of FEM. The assembly into global stiffness matrix must take into account the data structure of underlying sparse storage format and accordingly adopt an efficient strategy. The most popular way of constructing a sparse matrix in FEM is a two-step procedure. The first step assembles the elemental contribution in COO format where three arrays are used to store nonzero values, row indices and column indices of a matrix.

However, the value array usually contains multiple entries for the same values of row and column indices. In second step, each of the arrays are sorted and entries having repeated values in row and column arrays are consolidated. The global stiffness matrix obtained in COO format can now be converted into any other sparse format, if required. This approach works well for CPU and has been implemented by libraries like [8, 9]. However, this approach does not suit well to the GPU architecture. GPUs have limited memory, and performance of GPU-based code is highly dictated by the amount of memory access. The first step of assembly into COO format allocates more memory than required by the actual number of nonzeros. This puts pressure on GPU memory and limits the size of the problem. The second step of assembly into COO format involves sorting and accumulation of repeated entries. These operations are memory intensive and require a lot of data movement, which is not favorable for the best performance on GPU. Additionally, the COO format is not considered efficient for iterative linear solvers and most of the GPU accelerated libraries recommend other sparse formats like CSR for better performance. There are few related works in literature that attempts to implement finite element assembly on GPU through various approaches. In [10], assembly into COO format is demonstrated on GPU and compared with direct assembly into CSR storage format. It was reported that direct assembly into CSR format is slower than assembly into COO format. However, some recent literatures [11–13] demonstrate the excellent GPU performance for direct assembly into CSR sparse formats. In [11], the assembly process for structured mesh is decomposed into two steps where the location into CSR storage format is computed by performing some pre-processing with mesh connectivity. In [13], the assembly for unstructured mesh is performed over GPU in three compute kernels which includes computation of elemental matrices. The direct assembly into CSR format is presented in [12], where simultaneous computation of elemental matrices and assembly is performed in a single compute kernel.

The current work presents a GPU-based parallel strategy to assemble elemental matrices directly into CSR sparse storage format. The assembly is performed by pre-computing the locations into value array of CSR format for each nonzero values using mesh connectivity. The proposed strategy does not require any additional memory in GPU and provides global stiffness matrix in CSR format to use in linear solvers. The elemental matrices are computed on-the-fly without storing explicitly in GPU memory. The proposed strategy is applicable to unstructured mesh.

The paper is organized as follows. Section 2 provides a brief overview of problem formulations. Section 3 discusses the GPU strategy for finite element assembly. Section 4 presents the results of computational experiments and discusses the parallel performance. Finally, the conclusion is given in Sect. 5.

## 2 Problem Formulation

Consider an elastic body  $\Omega$  subjected to body force  $\mathbf{b}$  and surface traction  $\mathbf{t}$ . The governing differential equation over the body is given as

$$\nabla \cdot \boldsymbol{\sigma} + \mathbf{b} = 0, \quad \forall \mathbf{x} \in \Omega, \quad (1)$$

where  $\boldsymbol{\sigma}$  is the Cauchy stress. The governing equation must satisfy the given values of displacement and traction at the boundary, which is given as

$$\begin{aligned} \mathbf{u} &= \mathbf{u}_0, \quad \forall \mathbf{x} \in \Gamma_u, \\ \mathbf{t} &= \mathbf{t}_0, \quad \forall \mathbf{x} \in \Gamma_f, \end{aligned}$$

where  $\mathbf{u}_0$  is the given displacement on boundary  $\Gamma_u$  and  $\mathbf{t}_0$  is the given traction on surface  $\Gamma_f$ . The Cauchy stress is related to strain  $\boldsymbol{\epsilon}$  through the constitutive relation, which is given as

$$\boldsymbol{\sigma} = \mathbf{D}\boldsymbol{\epsilon}. \quad (2)$$

The relationship between strain and displacement is given by,

$$\boldsymbol{\epsilon} = \frac{1}{2}[\nabla \mathbf{u} + \nabla \mathbf{u}^T]. \quad (3)$$

The geometry of the problem is subdivided into a number of smaller entities called as elements. The displacement over an element is given by

$$\mathbf{u}(\mathbf{x}) = \mathbf{u}_i N_i(\mathbf{x}),$$

where  $\mathbf{u}_i$  is the vector of nodal displacement and  $N_i$  is the interpolation function associated with  $i^{\text{th}}$  node. The above equation can be rewritten as

$$\mathbf{u} = \mathbf{N}\mathbf{u}. \quad (4)$$

where  $\mathbf{N}$  is the shape function matrix and  $\mathbf{u}$  is the elemental displacement vector (refer to [1] for more details). The substitution of discrete variables into weak form gives finite element equation as

$$\mathbf{K}\mathbf{U} = \mathbf{F}, \quad (5)$$

where  $\mathbf{K} = \sum_e \mathbf{K}^e$ ,  $\mathbf{F} = \sum_e \mathbf{F}^e$ , and  $\mathbf{U}$  is the global vector of unknown nodal displacements. The elemental quantities are given as

$$\mathbf{K}^e = \int \mathbf{B}^T \mathbf{D} \mathbf{B} \, dv, \quad \mathbf{F}^e = \int \mathbf{N}^T \mathbf{b} \, dv + \int \mathbf{N}^T \mathbf{t} \, ds.$$

where  $\mathbf{B}$  is the strain–displacement matrix and  $\mathbf{D}$  is the elastic constitutive matrix. The computation of elemental matrices is done by computing the integral numerically using Gauss quadrature rule. Please refer to [1] for further details.

### 3 GPU Implementation of Finite Element Assembly

#### 3.1 *Parallel Computing on a GPU*

GPUs are specialized processor architecture that provides massive parallelism, high memory bandwidth and massive threading capability. Compared to CPUs, which are designed to reduce latency of an operation, GPUs are built to handle data parallel task and provide high computational throughput.

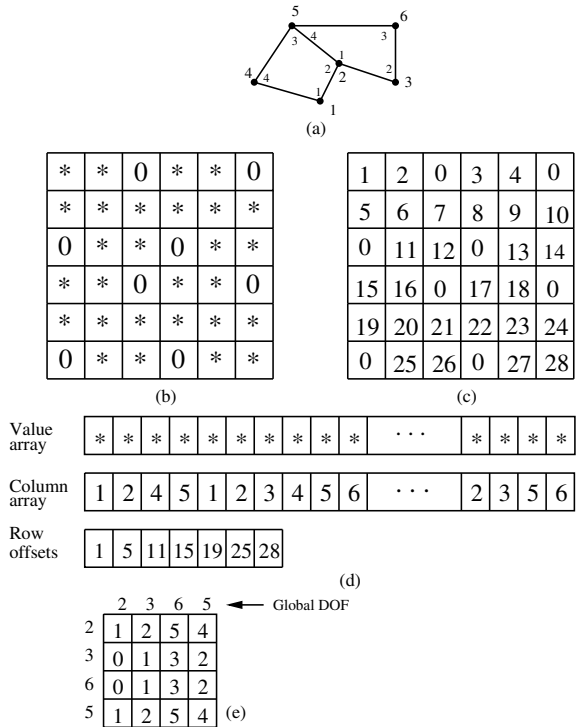
Compute Unified Device Architecture (CUDA) is a parallel programming model for general-purpose computation on NVIDIA GPUs. A typical CUDA program consists of CPU code with desired number of function calls to CUDA kernels. A kernel in CUDA is a function that uses GPU resources to perform computation in parallel. CUDA provides an elegant way to access different types of memory available in a GPU. The global memory is an off-chip memory in a GPU and has the highest latency and the largest size. The on-chip memories named as shared memory and registers are smaller in size and have the lowest latency. Readers are referred to [14] for more details on the CUDA programming model.

#### 3.2 *Pre-Computing Indices into CSR Matrix*

The CSR sparse storage format uses three arrays to store a sparse matrix. These arrays are: value array to store nonzero values, column indices array to store column indices of nonzero values and row offsets array to store the locations of beginning of each row. The row offset array has size equal to size of the matrix incremented by one, the last entry contains the total number of nonzero values. Figure 1a shows an example mesh consisting of quadrilateral elements with a single degree of freedom per node. The full global stiffness matrix corresponding to Fig. 1a is displayed in Fig. 1b, where \* denotes nonzero values, numbered row-wise (as stored in CSR format) as shown in Fig. 1c. The global matrix has a total of 28 nonzero values, and therefore, the value and the column arrays are allotted space for 28 values. The row offsets array is assigned the size of seven values. Figure 1d shows the global stiffness matrix in CSR format where the values of column array are displayed for first, second and last rows.

The local to global mapping of elemental DOFs only provides rows and column indices for a particular nonzero value. While this information is sufficient to find the exact position in full global matrix, the locations into compressed global matrix cannot be found. The direct assembly of elemental matrices into CSR format requires prior knowledge of locations of nonzero values in value array. For example, let's assume that values corresponding to third node in element two are accumulated in the global matrix. The corresponding global DOF number is six, which means that the values should be modified in sixth row of the global matrix. Figure 1d shows the row offset value for 6th row as 25, indicating that the values corresponding to 6th row

**Fig. 1** CSR storage format and pre-computing locations into the value array



lie at locations starting from 25th position in column and value arrays. However, if one wants to modify the value in 5th column of 6th row, the location for 5th column needs to be searched in column array. As shown in column array of Fig. 1d, the 5th column comes at 3rd position in column indices for 6th row. Therefore, to modify a value at 6th row and 5th column in global stiffness matrix, one has to make changes at 27th (25 + 2) position in value array. The exact location is obtained by adding relative position of desired column with respect to the first column in the corresponding row. Whenever the assembly is performed, the relative position of the column index of a nonzero value needs to be searched in the column array, which can be expensive for unstructured meshes in three dimensions (3D). It is to be noted that the relative position of column indices remains fixed as long as a mesh is fixed. This implies that expensive search operations into column array can be done prior to the assembly step, and relative positions of column indices can be pre-computed and stored for later use. Figure 1e shows a 4 × 4 matrix that contains relative positions of column indices for each nodes in element 2 (see Fig. 1a). The relative position of a column index depends on the immediate neighborhood of the node and elements with which it is connected. If a node is associate with multiple elements, the relative position is found for each element. If a node has multiple DOF associated with it, the same relative position can be used for all DOFs. For example, the same 4 × 4 matrix as shown in Fig. 1e is sufficient if quadrilateral elements in Fig. 1a had two DOFs per

node. The relative positions of column indices are referred as CSR indices in the following discussions.

The flowchart for the computation of CSR indices is shown in Fig. 2. In the first step, for each node in the finite element mesh, a list of immediate neighboring elements is obtained. This list is transformed into a neighboring nodes list by including the connectivity of each element. The neighboring nodes list is then sorted in ascending order, and duplicate entries are removed. This procedure is repeated for all nodes, and the final sorted node list is stored in an array. For each node, its neighboring nodes list denotes the position of nonzero values in corresponding rows of global stiffness matrix. The neighboring nodes list can be easily used to generate column indices of nonzero values for each row of global matrix in CSR format. Now, the position of any nonzero value can be obtained by performing a search into the neighboring nodes list instead of column indices. As shown in Fig. 2, the CSR indices are computed for each element in a loop by retrieving neighboring node list for each of its node. The position of all other nodes in the connectivity list is searched, and relative position is stored in an array. In GPU implementation, loop over nodes and loop over elements are parallelized by allocating one thread to each node and element, respectively.

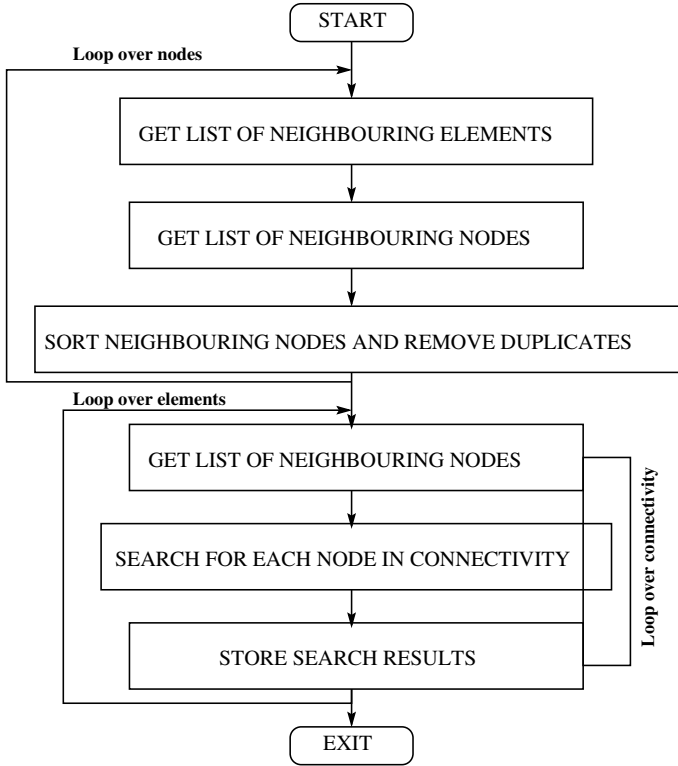
### ***3.3 Computation of Elemental Matrices and Assembly***

The computation of elemental matrices is an embarrassingly parallel operation as each element is independent of others in terms of input data and computation. Each GPU thread is assigned the task to compute the elemental matrix of one element. The respective thread reads the input data for each element such that collective memory access for a warp is coalesced. The Gauss quadrature rule is implemented for numerical integration of fully integrated 8-noded hexahedral element. Since, on-chip memories are limited for a GPU thread, each thread makes extensive use of local memory to store intermediate variables and final output.

The assembly in FEM is not amenable for parallelization due to data read–write conflict among threads. Each DOF in the finite element mesh has a corresponding row in the global stiffness matrix. Since a DOF is shared by multiple elements, each row in global stiffness matrix receives contribution from multiple elemental matrices. When assembly is done in parallel, threads assigned to different elements may try to read or write values simultaneously to the same memory locations. Such operations are conflicting and create an issue of data race condition.

In this paper, mesh coloring method [12] is employed to manage data race among conflicting threads. The mesh coloring is a popular and robust method in which finite element mesh is divided into multiple sets, identified with a color. The elements belonging to a colored set do not have any common node/DOF. The computation for elements belonging to a color can be performed in parallel without any conflict. The computation for all colors is done in sequence.





**Fig. 2** Flowchart indicating steps in computation of CSR indices

The same CUDA kernel that computes elemental matrix also performs assembly into global stiffness matrix in CSR format. Each thread reads global connectivity, corresponding row offsets and CSR indices to locate the position of nonzero values into the global matrix stored in CSR format. The assembled global matrix in CSR format can be directly used in any linear solver after the application of boundary condition. This assembly strategy is similar to the one presented in [12].

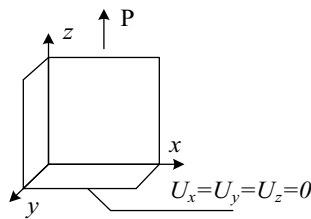
## 4 Results and Discussion

To assess the performance of the proposed strategy, numerical experiment is conducted over a large-scale 3D linear elasticity problem. The numerical experiment is conducted on a machine with the configuration given as: CPU—Intel Xeon® E5-2650 clocked at 2.6 GHz and 128 GB RAM, GPU—NVIDIA Tesla K40c clocked at 745 MHz with 12 GB of DRAM. The solution of the linear system of equations is done by conjugate gradient iterative solver from GPU-based CUSP library [15]. Since

the focus of the current work is not on acceleration of linear solver step of FEM, the same solver is used in both CPU and GPU implementations. The meshes for computational examples are generated in ABAQUS software package with 8-noded hexahedral elements.

A unit cube is taken with boundary conditions as shown in Fig. 3. All DOFs at the bottom are constrained while a distributed load is applied at the top surface. The problem is solved with the following parameters: Young's modulus ( $E$ ) = 200 GPa, Poisson's ratio ( $\nu$ ) = 0.3 and Load ( $P$ ) = 400 MPa. The cube is discretized with different number of elements to get different sizes of mesh, as shown in Table 1.

The computational time for CSR indices on CPU and GPU is presented in Fig. 4. For the coarsest mesh M1, the CPU takes 1.14 s to compute CSR indices which increases almost linearly up to 15.67 s for the finest mesh. The GPU-based implementation achieves speedup in the range  $4.98\times$  to  $6.48\times$  for all the meshes. On GPU, the computation of CSR indices for the finest mesh is completed in just 2.42 s. In order to assess the proposed strategy for direct assembly into CSR format, a comparison is made with sparse assembly feature of the Eigen library. The functions `tripletList.push_back()` and `setFromTriplets()` from Eigen are used for assembly which collect elemental contributions in COO format and transform into CSR format, respectively. As shown in Fig. 5, the assembly with Eigen consumes large amount of time compared to the proposed strategy on CPU. The proposed strategy achieves approximately  $9.3\times$  speedup over Eigen, performing assembly for the finest mesh in 35.08 s, including the time spent in computation for CSR indices. Figure 6 shows the combined computational time of elemental matrices and assembly by the proposed strategy on CPU and GPU. It can be observed that expensive numerical integration adds a significant amount of time to the assembly. The GPU solver achieves speedup



**Fig. 3** A unit cube with boundary conditions

**Table 1** Mesh for cube problem

Mesh	Elements	Nodes	Degrees of freedom
M1	110,592	117,649	352,947
M2	216,000	226,981	680,943
M3	438,976	456,533	1,369,599
M4	884,736	912,673	2,738,019
M5	1,520,875	1,560,896	4,682,688

in the range from  $21.18\times$  to  $24.25\times$  for all the mesh sizes. For 4.7 million DOFs, the GPU solver takes only 6.59 s to perform computation of elemental matrices and their assembly (including time for CSR indices). The wall-clock time for the CPU solver, GPU solver and CPU solver with Eigen library is presented in Fig. 7. Due to huge overhead in assembly, the CPU solver using Eigen library performs poorly and consumes the highest amount of time. The proposed CPU solver consumes moderate amount of time and performs linear elastic analysis of cube for the finest mesh in 213.95 s. The proposed GPU solver achieves speedup in the range from  $8.13\times$  to  $10.14\times$  over CPU solver using Eigen and  $3.34\times$  to  $4.01\times$  speedup over the proposed CPU solver for all mesh sizes. It should be noted that CPU solvers use GPU-based linear solver.

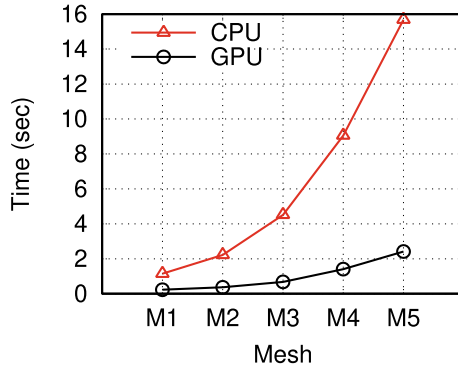


Fig. 4 Computation of CSR indices

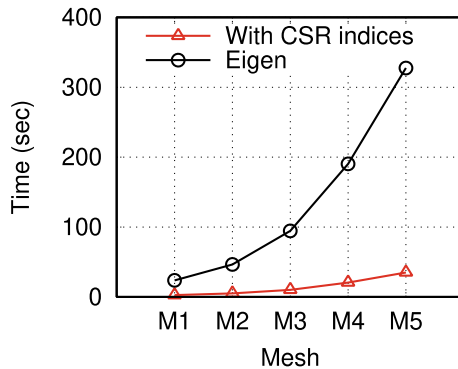
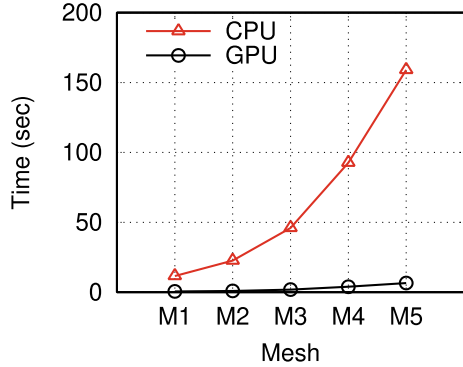
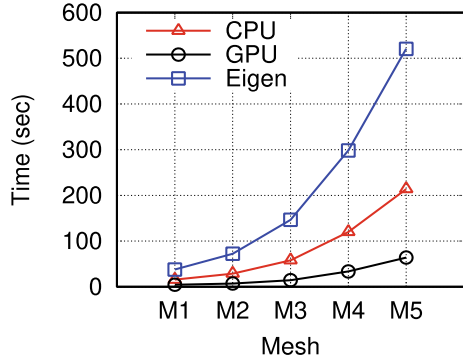


Fig. 5 Assembly with CSR indices on CPU compared with Eigen library

**Fig. 6** Numerical integration and assembly on CPU and GPU



**Fig. 7** Wall-clock time for CPU, GPU and CPU solver using Eigen for assembly



## 5 Conclusion

FEM is widely used numerical method to find solution of engineering problems. However, computation in FEM can be expensive and often leads to high execution time for real-world problems. In this paper, we have addressed the issue of high computational time associated with assembly step of FEM and proposed parallel strategy to perform assembly on the GPU. The proposed assembly strategy uses pre-computed indices into the value array of CSR sparse format to assemble elemental matrices into global matrix. The performance characteristic of the proposed assembly strategy is assessed by solving a linear elasticity problem. For the finest mesh with 4.7 million degrees of freedom, the pre-computing of indices into CSR format takes 15.67 s on CPU and 2.42 s on GPU. On CPU, the proposed assembly strategy is found  $9.3\times$  faster than the sparse assembly function from Eigen library. The proposed GPU assembly strategy achieves speedup in the range from  $21.18\times$  to  $24.25\times$  over the proposed CPU strategy for all mesh sizes in computation of elemental matrices and assembly. As a result of GPU acceleration, an overall speedup of  $3.34\times$  to  $4.01\times$  is obtained with respect to the CPU implementation.

**Acknowledgements** This work was supported by the Science and Engineering Research Board [IMP/2019/000276, SB/FTP/ETA- 0008/2014].

## References

1. Zienkiewicz OC, Taylor RL, Zhu JZ (2005) The finite element method: its basis and fundamentals, 6th edn. Butterworth-Heinemann, Oxford
2. Georgescu S, Chow P, Okuda H (2013) GPU acceleration for FEM-based structural analysis. *Archiv Comput Methods Eng* 20(2):111–121
3. Filippone S, Cardellini V, Barbieri D, Fanfarillo A (2017) Sparse matrix-vector multiplication on GPGPUs. *ACM Trans Math Softw (TOMS)* 43(4):1–49
4. Kiran U, Sanfui S, Ratnakar SK, Gautam SS, Sharma D (2019) Comparative analysis of GPU-based solver libraries for a sparse linear system of equations. In: *Advances in computational methods in manufacturing*. Springer, Singapore, pp 889–897
5. Kiran U, Gautam SS, Sharma D (2020) GPU-based matrix-free finite element solver exploiting symmetry of elemental matrices. *Computing* 102(9):1941–1965
6. Kiran U, Agrawal V, Sharma D, Gautam SS (2019) A GPU based acceleration of finite element and isogeometric analysis. In: Liu GR, Xiangguo GX (eds) *Proceedings at the 10th international conference on computational methods (ICCM2019)*. ScienTech Publisher, Singapore, pp 641–651
7. Bell N, Garland M (2008) Efficient sparse matrix-vector multiplication on CUDA. Nvidia Technical Report NVR-2008-004, Nvidia Corporation
8. Guennebaud G, Jacob B (2021) Eigen V3, <http://www.eigen.tuxfamily.org>
9. The MathWorks. Inc. (2021) MATLAB version R2021a. Natick, Massachusetts
10. Dziekonski A, Sypek P, Lamecki A, Mrozowski M (2012) Finite element matrix generation on a GPU. *Progress Electromagn Res* 128:249–265
11. Sanfui S, Sharma D (2017) A two-kernel based strategy for performing assembly in FEA on the graphics processing unit. In: *International conference on advances in mechanical, industrial, automation and management systems (AMIAMS)*, pp 1–9. IEEE
12. Kiran U, Sharma D, Gautam SS (2019) GPU-warp based finite element matrices generation and assembly using coloring method. *J Comput Des Eng* 6(4):705–718
13. Sanfui S, Sharma D (2020) A three-stage graphics processing unit-based finite element analyses matrix generation strategy for unstructured meshes. *Int J Numer Meth Eng* 121(17):3824–3848
14. NVIDIA Corporation. NVIDIA CUDA C++ programming guide, version 11.6 (2022)
15. Dalton S, Bell N, Olson L, Garland M (2014) Cusp: generic parallel algorithms for sparse matrix and graph computations. version 0.5.0, <http://cusplibrary.github.io>

# Design and Fabrication of PLA-Printed Wearable Exoskeleton with 7 DOF for Upper Limb Physiotherapy Training and Rehabilitation



Gaurav Gupta, Karan Agarwal, Ayush Yadav, Ashok Kumar Yadav, and Devendra Kumar Sinha

**Abstract** Most upper limb exoskeletons that have been presented in the literature are either intended for rehabilitation or for some type of industrial or Military work. However, there are a select few breakthroughs that offer both characteristics and aid with everyday life tasks. This study describes a wearable upper limb exoskeleton that can help people who have lost their ability to move and are undergoing rehabilitation. The exoskeleton arm has a maximum load lifting capacity of 50 kg and can lift that much weight with a 150-psi compressor pressure, which can help people with daily activities and provide mobility. In this study, a pneumatic exoskeleton arm with seven degrees of freedom (DOF) and flex sensors is used to control the extension and retraction of the arm using portable pneumatic pumps. This enables us to carry out the rehabilitation motion as exactly as possible and prevents us from adopting unfavourable postures while searching for the necessary answers. Promising findings were obtained through fabrication and testing that were done to validate our concept.

**Keywords** Exoskeleton · Pneumatic arm · Robotic arm · Rehabilitation · Assistive technology

## 1 Introduction

Since ancient times, human races have attempted to transcend human limitations by inventing a variety of aids, from crutches to future disability suits or defence mechanisms like knives, swords, or other contemporary fighting vehicles. In the

---

G. Gupta (✉) · K. Agarwal · A. Yadav  
Amity University, Noida 201304, India  
e-mail: [15.gaurav@gmail.com](mailto:15.gaurav@gmail.com)

A. K. Yadav  
Raj Kumar Goel Institute of Technology, Ghaziabad, India

D. K. Sinha  
Adama Science and Technology University, Adama, Ethiopia

pursuit of excellence, a state-of-the-art professional exoskeletons and orthoses are currently accessible and becoming more and more necessary to aid, facilitate, and speed up the training and recuperation of weak and wounded persons as robotic assistance and rehabilitative training have lately become more prevalent.

Robot is a mechanical device that can perform physical tasks. One of the types of robots which is very popular and simple is the robotic arm system. A mechanical system known as a robotic arm is utilised to lift, move, and manipulate the work-piece in order to lessen the workload placed on humans. A mobile machine made mostly of an outer framework worn by a human and driven by a system of levers, motors, hydraulics or pneumatics that aid's in limb movement is known as a robotic exoskeleton, also known as exoframe, powered armour or exosuit [1].

The number of handicapped persons has grown alarmingly during the past several decades. According to studies, the majority of handicapped persons are elderly. According to World Health Organization data, more than 20.5 million individuals worldwide experience a stroke or cardiovascular illness each year [2], Of these victims, 85% experience acute arm impairment following a stroke, and 40% experience chronic impairment or permanent disability [3]. Because of the deterioration of their physical and muscular power, elderly individuals, stroke patients, hemiplegic subjects, paralysed people, and those who have had spinal cord injuries all experience various types of locomotional handicaps. The major strategy for encouraging functional recovery in these patients is rehabilitation programmes. Exoskeleton robotic arms might greatly aid in the success of these initiatives because the prevalence of such instances is rising, and therapy is lengthy.

In many industrialised nations, including America, China, and India, musculoskeletal illnesses are the most prevalent ailments. These illnesses have a significant negative influence on the productivity of businesses as well as the quality of life for workers. In the logistics, construction, and medical rehabilitation sectors, there are 67%, 84%, and 75% workers with lumbar issues, respectively [4]. This issue has developed into a societal danger. There have been several methods put out to address this issue. The study of the lumbar exoskeleton is one of those that deserves attention. Statistics show that when users are wearing these, the lumbar spine's muscular activity might be decreased by as much as 30% [5]. Many colleges and research organisations are creating lighter and more potent lumbar exoskeletons to enhance its force-assisted performance.

Exoskeleton arms that are utilised in industry to carry big objects cannot be employed in daily life. It is difficult to reduce the size and weight of exoskeleton arms that are already on the commercial market. On how to enhance exoskeleton technology, there is ongoing discussion. By including a pneumatic cylinder as energiser, it is feasible to greatly minimise the muscle work required by a person. Many effective haptic interfaces have been developed recently as a result of advancements in processing power, control systems, and sensor and actuation technologies [6]. Despite the fact that there have been several high-performance hand controllers. The first exoskeleton arm and glove were created at ARTS Laboratory, [7] for the reconstruction of touch and impact feelings. The 7-DOF ungrounded ARTS arm, sometimes referred to as the PERCRO exoskeleton, is linked to the operator's torso

and shoulder [8]. With his or her palm, the operator grips the gadget. Therefore, the gadget can only apply forces on the user's palm. Prosthetics for the lower limbs and upper limbs are becoming increasingly prevalent. Lower limbs devices like "Lokomat" and upper limbs devices like "PHANTOM, WAM, PUMA (MIME), MIT-MANUS" are utilised to demonstrate the therapeutic effectiveness of physical therapy for movement dysfunction arising due to neurological illnesses and stroke [5].

Exoskeletons, unlike the Sarcos design, which would lighten the load for troops and other people who carry large packs and equipment [9]. According to recent research, even though the weight carried by the wearer's back was significantly smaller, the person carrying the load nevertheless used 10% more oxygen than normal because of the extra effort needed to make up for the gait disturbance. There is one obstacle, nevertheless, that every creator or researcher of exoskeletons says must be cleared first: the price. Each powered exoskeleton costs between \$75,000 and \$130,000 [10]. The price does not include servicing or maintenance. If we add the initial cost to its upkeep and service, the total comes to \$205,000 [11], which is astronomically costly.

Since wearable exoskeletons are so expensive, posing challenges and competitors are a losing proposition. Exoskeleton manufacturing is coming to an end because of its high cost. Exoskeleton development may be considerably accelerated with more funds and resources. The investors aren't keen on getting involved in a market where powered exoskeletons seldom goes beyond few hundred units a year. A profit hasn't been made in years, too. Without making improvements to the product, the annual number of exoskeleton units sold cannot be increased, and the cycle continues. The use of exoskeleton arms is also declining as a result of other well-established sectors, such as wheelchairs.

There are two types of haptic display devices: grounded and ungrounded. A stiff base is attached to a grounded haptic device, which transmits response forces to the ground. Only the operator's body is connected to an ungrounded haptic device, which applies response forces to the user where it is linked. Rehabilitation robots may generally be divided into three categories: (1) supporting structures for posture, (2) rehabilitation approaches, (3) robots to support or take the place of bodily functions [12]. Posture support mechanism is done with the help of a back support robotic exoskeleton as the body posture is controlled by the spinal cord. Rehabilitation mechanism robots help as a support system for a semi functional part which needs a push to regain the muscle strength completely. Lastly, the robots which replace a body function consists of a prosthetic assisted with a robot connected with neurons for the brain to send the signals to the prosthetic. In this work, the focus has been put on a robot assisted exoskeleton for rehabilitation purpose. Based on hand control assist system, developed using electronic and mechanical arrangement controlled by a microcontroller, the exoskeleton/prosthetic prototype is sufficiently powered by a pack of 48 V battery and weighs around 12 kg [11]. Knowledge of rebuilding exoskeletons has been systematically established, and majority of them are intended to empower paraplegic clients to leave the wheelchair and walk upstanding with the help of the gadget. Some of the efforts have been scrutinised critically in Table 1.



**Table 1** Work performed by peer groups in related exohands

DOF	SHOULDER	6	3	3	4	7	4	1	1
	ELBOW	1	1	1	3				
	WRIST	2	3	3	-				
Research group	Tsai et al. [13]		Jiafan et al. [14]	Wen et al. [15]	Moubarak et al. [16]	Garrec [17]	Ruoyin et al. [18]	Lara et al. [19]	Ngai [20]
Technology	Gear drives—dc motor	Crank-Slider mechanism and Links—Pneumatic actuators	Force and position sensors	Gear drives—dc motor	Gear drives—dc motor Brushless	Ball Screw and cables—motor	Cables—actuators	Shape memory alloy	Gear system—stepper motor
Control method	Electromyography			-	Force controlling with position feedback	Indigenous system		Force Controlling	Two push-button sensors—switch based
Special feature	Avoid going through the ill-postured configurations	Produce the vivid feeling in addition to the soft control interface		Controller guarantees the asymptotic stability, for this class of robotic manipulators	Relatively lightweight with a high ratio of DOF/weight	Allows true joint torque control without force sensor	Can accommodate variety of hand sizes to some extent	Compact and portable	Motion was assumed to be axial, but forearm was resisting the axial rotation of
Application	Rehabilitation	Teleoperation	Assistance	Rehabilitation	Assistance	Rehabilitation	Assistance	Assistance	Assistance

Few Applications of exoskeletons are as follows:

**Automotive industries**—It provides the workers with ease of ability to walk and stand on their own, decreases the fatigue level and also prevents injury for the workers who have a prolonged use of the same muscle every day for hours.

**Logistics Department**—Logistics workers use their lower and upper muscles for the lifting of the goods, and thus, this exoskeleton arm can lower their risk of injury.

**Construction**—Construction industry has a large number of workers who work on daily basis and are very much prone to disabilities and injuries faced by them at work.

**Large and small warehouses**—In warehouses, the main function will be of transportation of the goods, and thus, it has a high application rate.

**Prosthetics**—It will be a boon for the prosthetics industry to afford an effective and ergonomic exoskeleton.

**Rehabilitation**—The majority of rehabilitation robots fall into the category of rehabilitation exoskeletons, which are wearable and can regulate entire joint motion during training.

**Physical Therapy**—Use of flex sensors can also make it very easy for a single person to have a rehabilitation session of his own.

All major industries—Currently being widely used by major businesses in the logistics, automotive, aerospace, and construction industries.

## 2 Exoskeleton—Rehabilitation Purpose

It may be summed up based on the examination of pertinent material that was done that—The exoskeleton arm can be used in medical rehabilitation and can be used as prosthetics Exoskeletons are used in industries for assistance lifting and can lighten the load on the worker. The exoskeleton arm can be utilised for prosthetics and medical rehabilitation. Although the exoskeleton arm may be controlled by a variety of cutting-edge technologies, including electromyography and brain wave methods, the pneumatic system is the most secure, affordable, and adaptable power source and offers sufficient strength for lifting weights.

The suggested design comprises a low-cost, ergonomic tool that lifts various loads for accident-prone logistics workers, individuals with disabilities, and others with no physical strain or with little effort actuated by suitable sensors installed capable of measuring the user's action. Prototype which shall be a wearable powered exoskeleton is based on hand control assist system, which is controlled by signals from the user. This whole three major stages.

- (i) Design of a working and effective robotic exoskeleton with 7 DOF
- (ii) Analysis of design for failure

(iii) Fabrication of designed robotic exoskeleton to assist in upper extremities.

**A. Design**

Exoskeletons may be used for a broad range of activities, but their application is limited by their high cost. Any industry, including industrial operations, medical technology, and military might, will find considerable value for such an economical solution. The design proposed is based on average built human being as given in Table 2.

The anatomical ranges and related exoskeleton range are shown in Table 3 as biomechanical models can be employed for the prototype’s design and control in robotic rehabilitation to make the human–robot interaction mechanism simpler.

Table 4 shows range of motion (ROM) for mechanical joints used in exoskeleton inspired by date from Table 2 and Table 3 also establishing against activities of daily living (AOL).

There are four distinct elements that make up the exoskeleton unit.

- (a) Structure
- (b) Power supply
- (c) Control system and
- (d) Electronic firmware.

**Table 2** Statistical data of average human dimensions [3, 4, 21]

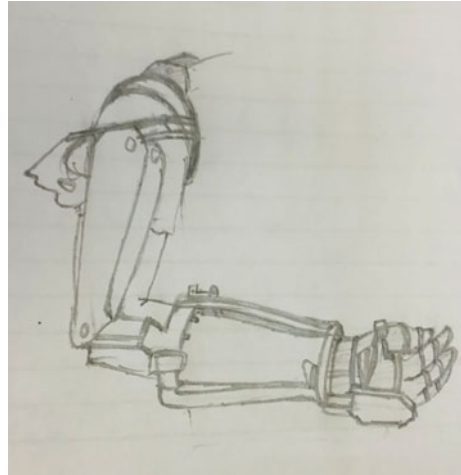
	Minimum	Medium	Maximum
Age (years)	22	30	Above 30
Weight (kg)	60	67	Above 70
Height (cm)	160	170	185

**Table 3** Anatomical range versus exoskeleton range [1, 20, 22, 23]

Motions required	Anatomical range	Exoskeleton range
<i>Elbow and forearm</i>		
Supination	80°–90°	90°
Pronation	80°–90°	80°
Extension	0°–5°	0°
Flexion	140°–145°	140°
<i>Shoulder joint</i>		
Internal rotation	80°–90°	90°
External rotation	60°–90°	90°
Flexion	170°–180°	170°
Extension	30°–60°	50°
Abduction	170°–180°	170°
Adduction	0°–50°	0°

**Table 4** Mechanical joint range of motion [17]

Joint	Motion	ADL ROM (deg)	EXO ROM (deg)
Shoulder	Fle-Ext	110	140
	Int-Ext Rot	135	145
Sternoclavicular	Ele-Dep	35	30
Elbow	Fle-Ext	150	155
	SupPron	90	90

**Fig. 1** Prototype model sketch showing three major parts

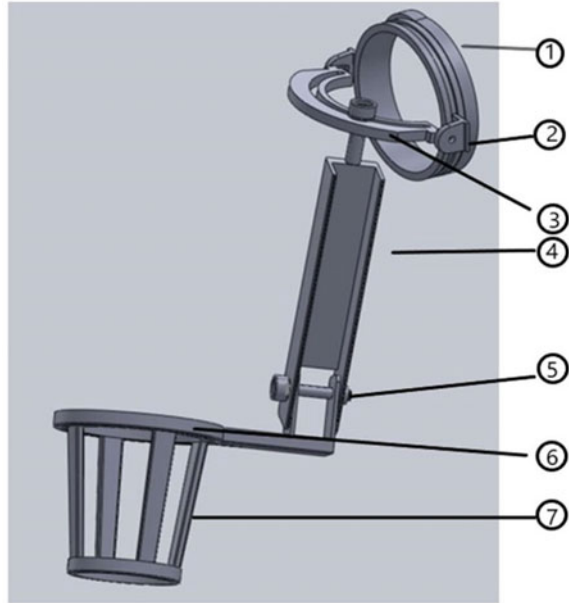
The whole structure of arm as shown in Fig. 1 is divided into three stages, i.e. forearm, elbow and shoulder, and the mechanical design consists of the following parts:

This arm majorly consists of mechanical links joined together and working in tandem by activation of actuators.

- (a) Mechanical links—Links are modelled as a network of rigid links and an ideal pair, called kinematic chains to manage forces and movements.
- (b) Joints—A mechanical joint used to connect one or more mechanical parts to another yet allow the relative movement to a certain degree of freedom and limit movement in one or more direction.
- (c) Pneumatic actuators—A pneumatic actuator consisting of a piston, cylinders and valves or connections can turn energy into linear or rotating mechanical movements.

Exoskeleton arm modelled on software is shown in Fig. 2.

1. Shoulder cover (200 mm diameter)
2. Slider
3. Abduction movement plate

**Fig. 2** Arm design

4. Elbow support (330 mm length)
5. Connecting bolt (7 mm diameter)
6. Ball bearing (200 mm diameter)
7. Lower arm case

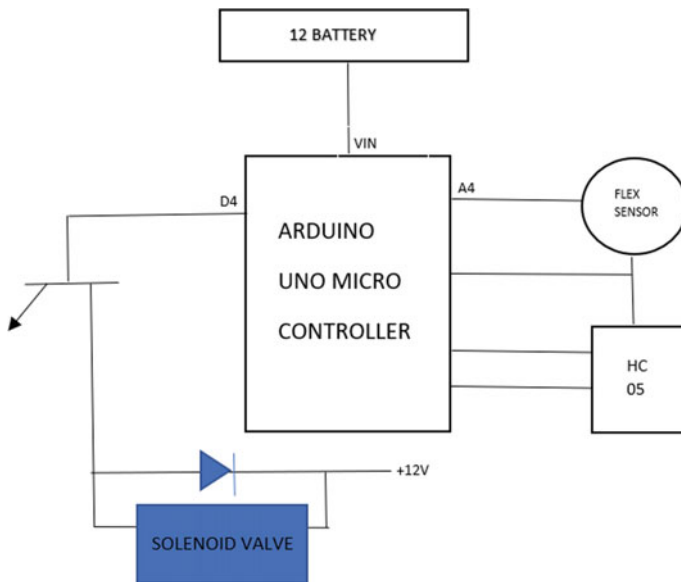
Wearable battery pack is modified rechargeable power source that powers the primary actuators in addition to the microprocessor. The actuators are made up of pneumatic and motor systems. They both attempt to support the exoskeleton arm in providing the desired torque increase.

Control of robotic exoskeleton arm with a transmitting device or wireless controller can be done by just sending a signal via a transmitting device or wireless controller for the required movement of arm or hand, and once the signal is transmitted, signal is processed by arduino and executed on either hand via pneumatic cylinders or the hand via servo motors [24]. This paper is based on hand control assist system, developed using electronic and mechanical arrangement controlled by a microcontroller.

Sensor interface circuitry majorly makes up the exoskeleton. Rechargeable batteries cascaded to power it along with a voltage regulator are used. Together, they feed the microcontroller with a steady DC supply. Flex sensors, which the user wears to identify his motions and operate the arm, are mounted on the forearm. Any bending of the user's hand is detected by the flex sensor glove, which then has an impact on the exoskeleton structure in a comparable way. For instance, the user can activate the exoskeleton arm to automatically lift an object just by keeping it in place without hitting any buttons (or any other indication) [22].

The exoskeleton arm enables the transmission of external load to the stronger part of the body through precisely positioned links in joints. The robotic exoskeleton arm in this paper is controlled by hand a transmitting device which can be any Bluetooth transmitter device. It is hypothesised that the lumbar spine is a hard, non-deformable body since its distortion during movement is so little. The mechanical design would be made of aluminium [25, 26] so that it goes not only light weight but also have much strength. The amount of muscular effort needed by a person can be greatly reduced by adding a pneumatic cylinder to the system. Then main thing in designing a prosthetics model is its control. Flex sensor would be connected to the body of the operator. A microcontroller would get signal from the flex sensor and would actuate the motors accordingly [4, 7]. Components used as shown in Fig. 3 with a brief description are:

- Microcontroller**—Widely used open-source microcontroller board used is Arduino Uno. The Arduino Uno is a microcontroller board based on the ATmega328. External power supply that is other than USB, can be of AC or DC supply with the adaptor or a battery. This adapter will be linked to the board power jack by plugging it into a 2.1 mm centre-positive plug. The circuit board might be capable to operate up to 6–20 V when connected to an external supply. But if the supply is below 7 V the 5 V pin may not function properly, and the board may get unstable and if the supply is more than 12 V the board may get overheated and damaged. The safe and prescribed range should be between 7 and 12 V.



**Fig. 3** Circuit diagram of the mechanism used

- **Flex sensor**—A flex sensor, sometimes known as a bend sensor, is a device with variable resistors that gauges how much something is bending or deflecting. Typically, the sensor is adhered to the surface, and the surface's bending changes the sensor element's resistance.
- **Compressor**—Air compressors are used to produce compressed air. A power tool that produces and transports compressed air is an air compressor. When air is compressed, it produces a powerful force that may be utilised to power a variety of equipment.
- **Solenoid Valves**—An electromechanical device that controls, regulates and keeps track of flow, pressure and other factors. A 5/3 double-solenoid valve is used made it feasible to accomplish intermediate postures and make distinct arm motions.
- **Pneumatic cylinders**—Mechanical devices that use the force of compressed gas to produce power in a responsive linear movement are sometimes referred to as “air cylinders”.
- **Hc-05 Bluetooth modules**—A simple Bluetooth SPP (Serial Port Protocol) module called the HC-05 is made for setting up transparent wireless serial connections.

## B. Stress Analysis of every part

This design has the capability to lift **50 kg** of weight from a single arm, and thus, the load taken for calculations is  $50 * 9.8 = 500 \text{ N}$  (approx.). Stress analysis using ANSYS was found out to be well within the limits Fig. 4. Above these limits the PLA material can break as the individual part is constructed using the 3D printer with different parameters such as ink weight, strength-to-weight ratio.

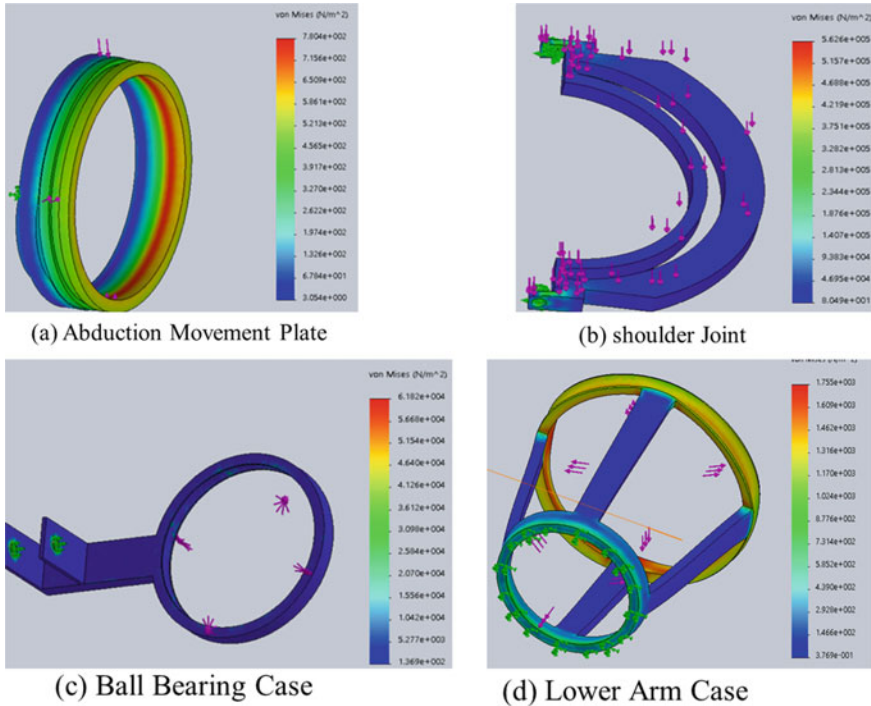
## C. Fabrication

The fabrication of the parts is done by using a 3D printer (CubeX, Fig. 5.), and the material [27] used was PLA which is very durable, light and strong. Free conversion software is included with every CubeX 3D printer. This programme layers slices of a 3D object so they may be printed on your device. Other characteristics and applications of CubeX software include interface that is simple to use and familiar movement, rotation and scaling of components on a virtual print bed. Part and toolpath viewer combined STL file verification built-in profiles for various materials and supports.

Few fabricated parts of exohand are shown in Fig. 6.

## 3 Results and Discussions

Push-button switches located at the wrist section are operated utilising flex sensors to control the arms. This sensor can help the old people as their muscle power is low, so the flex sensor is able to detect a small strain on forearm muscles during flexing or relaxing arm and functions easily with the help of the pneumatic.



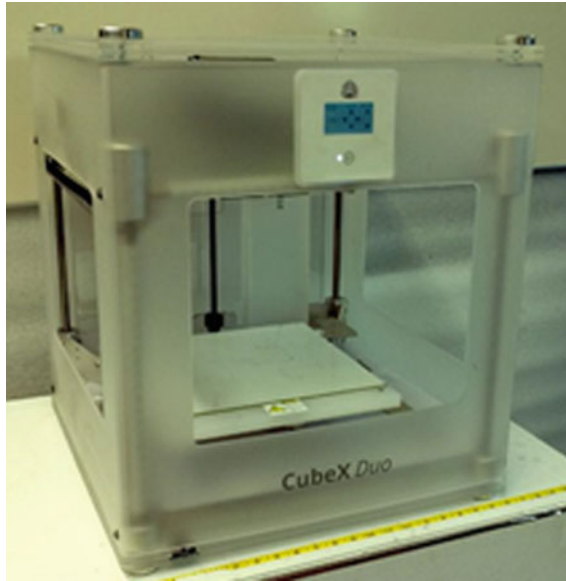
**Fig. 4** **a** Abduction movement plate—maximum stress –  $8.049 \times 10^1$ , **b** shoulder joint—maximum stress –  $7.804 \times 10^2$ , **c** ball bearing case—maximum stress –  $1.369 \times 10^2$ , **d** lower arm case—maximum stress –  $1.755 \times 10^3$

After several trials, the exoskeleton proved to be capable of lifting 50 kg of weight with ease at a compressor pressure of 150 psi. It was able to achieve intermediate positions and distinct arm motions owing to 5/3 double-solenoid valves. Increasing the compressor pressure supplied can enhance the lifting capability. At extremely high compressor pressures, the movement becomes more challenging to regulate.

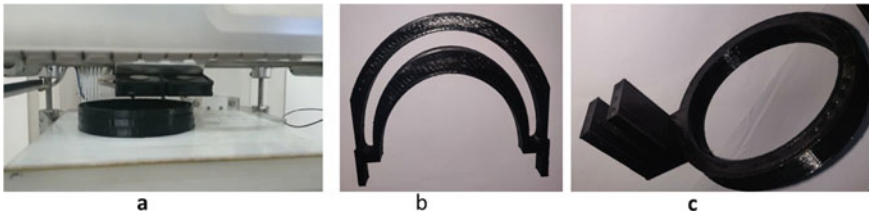
The design is very flexible for all types of users, and it allows a worker to move freely in a restricted free environment and also with the use of portable compressor it can be used for prosthetics and rehabilitation purpose. Selection of Aluminium series 7 material for the fabrication has brought light weight, high strength and easily workability. Exoskeleton evenly distributed the load throughout the upper body with almost no human effort requirement for load lifting.

Future extension of current work could be an exoskeleton for the lower body attached to the main body. The weight will be more easily transferred to the ground with the addition of the lower body to the upper body. Because of this, the user won't be able to feel the weight of their body or the burden they are carrying. Pneumatic systems might be employed in a similar design to help with leg mobility.





**Fig. 5** CubeX duo 3D printer



**Fig. 6** a 3D printing of shoulder part of the exoskeleton, b 3D-printed sliding pair part, c 3D-printed forearm outer cage part

## References

1. Chay KH, Lee JV, Chuah YD, Chong YZ, Tunku Abdul Rahman U, Lumpur K (2014) Upper extremity robotics exoskeleton: application, structure and actuation. *Int J Biomed Eng Sci* 1(1)
2. “WHO EMRO | Stroke, Cerebrovascular accident | Health topics.” [Online]. Available: <https://www.emro.who.int/health-topics/stroke-cerebrovascular-accident/index.html>. Accessed 25 Sep 2022
3. Sui D, Fan J, Jin H, Cai X, Zhao J, Zhu Y (2017) Design of a wearable upper-limb exoskeleton for activities assistance of daily living. In: *IEEE/ASME international conference on advance on intelligent mechatronics, AIM*, pp 845–850
4. Jha P, Savla K, Shah D (2018) Exoskeleton arm. In: *2018 International conference on smart city emerging technology ICSCET 2018*
5. Zhang JF, Yang CJ, Chen Y, Zhang Y, Dong YM (2008) Modeling and control of a curved pneumatic muscle actuator for wearable elbow exoskeleton. *Mechatronics* 18(8):448–457

6. Gupta G, Tyagi RK (2019) Investigation of titanium as thin film deposited material thereon effect on mechanical properties. In: *Advances in industrial and production engineering*, Springer, Singapore, pp 315–323
7. Saqib DA, Arif U, Islam JZ, Qasim M (2018) Prosthetic arm and hand design. *Int J Mater Mech Manuf* 6(4):273–276
8. Gupta A, O'Malley MK (2006) Design of a haptic arm exoskeleton for training and rehabilitation. *IEEE/ASME Trans Mechatronics* 11(3):280–289
9. Riskin J (2003) Eighteenth-century wetware. *Representations* 83:97–125
10. Ji X, Wang D, Li P, Zheng L, Sun J, Wu X (2020) SIAT-WEXV2: a wearable exoskeleton for reducing lumbar load during lifting tasks. *Complexity* 2020
11. Bogue R (2009) Exoskeletons and robotic prosthetics: a review of recent developments. *Ind Rob* 36(5):421–427
12. Dellon B, Matsuoka Y (2007) Prosthetics, exoskeletons, and rehabilitation [grand challenges of robotics]. *IEEE Robot Autom Mag* 14(1):30–34
13. Tsai BC, Wang WW, Hsu LC, Fu LC, Lai JS (2010) An articulated rehabilitation robot for upper limb physiotherapy and training. In: *IEEE/RSJ 2010 international conference on intelligent robots system IROS 2010—conference proceedings*, pp 1470–1475
14. Zhang J (2008) Novel 6-DOF Wearable exoskeleton arm with pneumatic force-feedback for bilateral teleoperation. *Chinese J Mech Eng* 21(03):58
15. Yu W, Rosen J (2010) A novel linear PID controller for an upper limb exoskeleton. In: *Proceedings of IEEE conference decision control*, pp 3548–3553
16. Moubarak S, Pham MT, Pajdla T, Redarce T, Design and modeling of an upper extremity exoskeleton
17. Garrec P (2010) Design of an anthropomorphic upper limb exoskeleton actuated by ball-screws and cables. *Bull Acad Sci Ussr-Phys Ser* 72(2)
18. Zheng R, Li J (2010) Kinematics and workspace analysis of an exoskeleton for thumb and index finger rehabilitation. In: *2010 IEEE international conference on robots biomimetics ROBIO 2010*, pp 80–84
19. Ammar LI, Kaddouh BY, Mohanna MK, Elhadj IH (2010) SAS: SMA aiding sleeve. In: *2010 IEEE international conference robots biomimetics, ROBIO 2010*, pp 1596–1599
20. Ngai M (2010) Design of a forearm exoskeleton for supination/pronation assistance in daily activities. *McMaster University Hamilton, Ontario, Canada*
21. Moubarak S, Pham MT, Pajdla T, Redarce T (2009) Design and modeling of an upper extremity exoskeleton. *25(9):476–479*
22. Rahman MH, Saad M, Kenné JP, Archambault PS (2009) Modeling and control of a 7DOF exoskeleton robot for arm movements. In: *2009 IEEE international conference on robots biomimetics, ROBIO 2009*, pp 245–250
23. Shuayb Ali S, Das S, Kumar Nunia P, Graduate Students U (2019) Study and fabrication of low-cost upper limb exoskeleton. *Int J Res Anal Rev*
24. Gupta G, Tyagi RK (2021) A newer universal model for attaining thin film of varied composition during sputtering. *Lect Notes Mech Eng* 629–638
25. Gupta G, Tyagi RK (2019) An experimental evaluation of mechanical properties and microstructure change on thin-film-coated AISI-1020 steel. *Mater Perform Charact* 8(3):20180143
26. Zeiaee A, Soltani-Zarrin R, Langari R, Tafreshi R (2017) Design and kinematic analysis of a novel upper limb exoskeleton for rehabilitation of stroke patients. *IEEE international conference on rehabilitation robots*, pp 759–764
27. Esposito D et al (2022) Design of a 3D-printed hand exoskeleton based on force-myography control for assistance and rehabilitation *10(1):57*

# Framework for Design and Control of Automatic Stone—Glass Separator



Priyank Srivastava , Siddharth, Vipul, Anmol, Shivam, Amartya, and Sanjeev Kumar Sharma

**Abstract** Nowadays, the technology that has been into the industry revolves around the use of sensors and motors to segregate the waste that is put into the machine/bins. Machine automatically senses the type of waste being put into it and it segregates and pushes down the waste into the respective bin, but these machines have been built on an industrial scale which uses massive conveyer belts and more advanced technology to sense the type of the waste, and these machines are quick but very expensive. The automation in these machines is of utmost importance, and different controls are required for temperature management, operation, and other specific variable control. The present work is the effort of making a scalable model of stone and gas segregator machine. The objective is to segregate glass with similar materials having similar properties. In this study, a framework is proposed for designing and controlling the various sensors that will be used in machine.

**Keywords** Segregation · Waste · Sensor · Microprocessor

## 1 Introduction

Appropriate waste management can be a gigantic reason for worry inside the current world. The removal strategy for a lot of produced squanders has established an unfriendly impact on the climate. The dumping at landfill is the typical technique for removal of waste. Human wellbeing, plant, and creature life are influenced because of this technique. The unsafe strategy for garbage removal spoils surface and the groundwater [1]. It can produce disease vectors which spread harmful infections. It also degrades the value of natural environment, and it is an unavailing use of natural resource. In India, rag pickers play a crucial role within the recycling of urban solid

---

P. Srivastava (✉) · Siddharth · Vipul · Anmol · Shivam · Amartya · S. K. Sharma (✉)  
Amity University, Noida, India  
e-mail: [priyanksrivastava\\_me@yahoo.in](mailto:priyanksrivastava_me@yahoo.in); [psrivastava5@amity.edu](mailto:psrivastava5@amity.edu)

S. K. Sharma  
e-mail: [sksharma.me@gmail.com](mailto:sksharma.me@gmail.com); [sksharma6@amity.edu](mailto:sksharma6@amity.edu)

waste. In India, rag pickers are assumed to be a vital part of the system inside in reusing of metropolitan strong waste. The facts of the hour are that Indian non-rural areas produce around 6.2 crore tonnes of waste out of which only 4.3 crore tonnes of waste are collected, 1.19 crore tonnes are disposed off properly, and the 3.1 crore tonnes of sent off to the landfills and land dumps. Basically, only 70% of the total municipal waste that is produced is collected, and 50% is sent to the landfills and only 20% of it is actually treated. Municipal solid waste (MSW) basically refers to the day-to-day waste that the people throw out [2]. Many methods have been proposed by the researchers for MSW segregation [3–6]

In the present work, an approach has been suggested and investigated to segregate the glass wastes with ceramics and stones or with the wastes having approximately similar properties. Hence, a concept schematic is designed to achieve the goal. In this direction, taking the benefit of few behaviours of selected metal/alloy/metal matrix composite surface and different glasses, pieces of plaster of Paris, tiles, marbles, granites bricks, stones, [7–9] etc., a method has been developed and investigated successfully at certain parameters without significant change of its structural properties. Specific aim of this proposal is to develop an option for segregating glass waste particle from the MSW to improve the recyclability which will directly help in the improvement of circular economy of any country.

## 2 Literature Review

This section presents comprehensive literature review for the MSW, its management, segregation process, impact of MSW on health and environment, and melting point of glasses. For extracting the relevant literature, search engines of Web of sciences and Google scholar were used. The extraction was done using protocol. The PRISMA flowchart [10] (refer Fig. 1) was used for literature review. The keywords of “municipal solid waste AND segregation”; “segregation process”; and “recovered material” were used for the analysis.

From the review, it is quite clear that lots of research is going on for recovery or separation of heavy material, plastic material, even glass but of large size. But there is no reported literature on segregation of glass from the materials that exhibit similar mechanical and electrical properties. This becomes the motivation of doing research, and research questions of “how the glass can be recovered or separated from materials exhibiting same mechanical and electrical properties”? become pertinent. With this objective in mind, design and control framework was developed for stone-glass separator device.

## 3 Research Flow

The research flow is shown in Fig. 2.

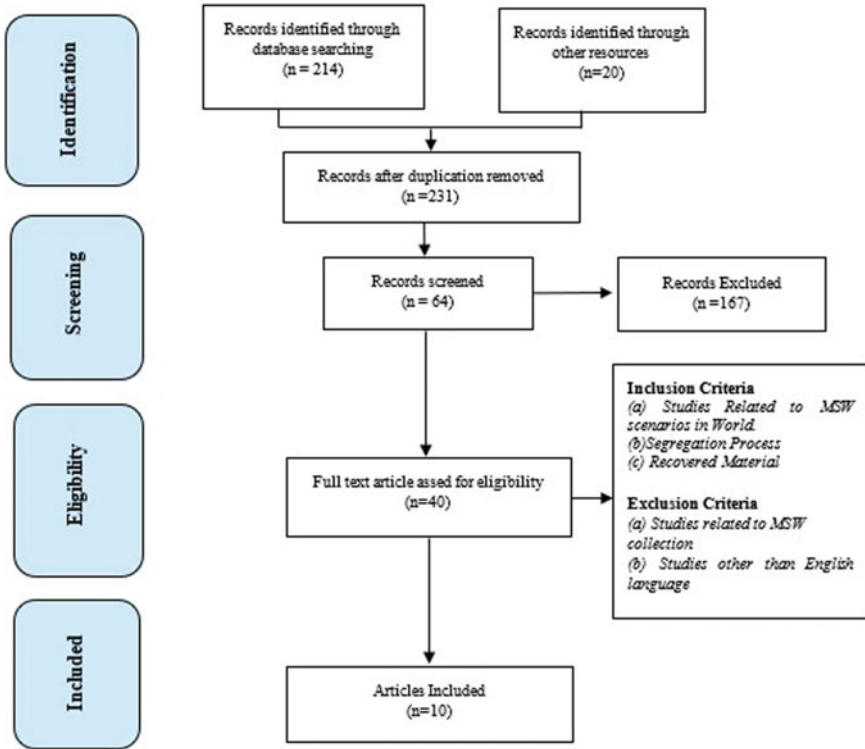


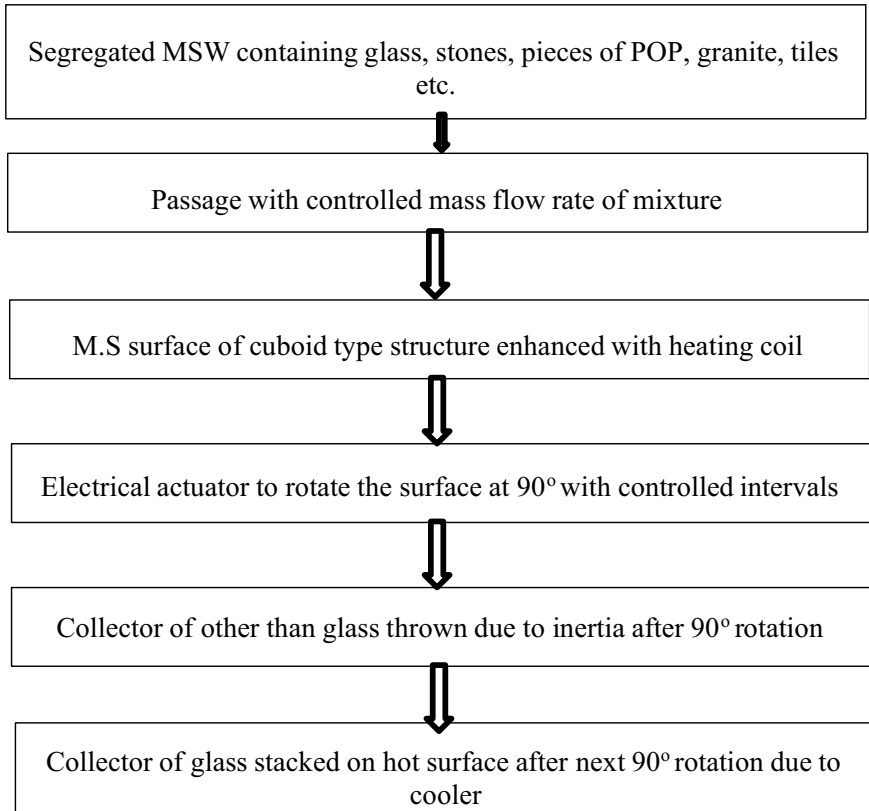
Fig. 1 Literature review

### 4 Prototype Design

This chapter shows the design of prototype. The design components are as follow:

- (i) Ball bearings (7755N17 Tapered Bore Self-Aligning Ball Bearing)
- (ii) Mild steel box
- (iii) Mild steel hollow shaft
- (iv) Custom rings with 25% copper 75% carbon v. Heating coils
- (v) “V” shaped stand
- (vi) Conducting brushes
- (vii) Geneva motor system (90°) (Figs. 3 and 4).

In mild steel rectangular box of size 12 \* 6 inch., with a 5 mm thick sheet, the box is customed with side boundary at 45° which enables the waste to fall but Fig.5 immediately, the box has custom heating coils from underneath Fig. 5, and the box is made up of mild steel which conducts off heat with the melting point 1350 °C which is far away from 700 °C; sticky temperature of glass (Figs. 6, 7, 8, 9, and 10).



**Fig. 2** Research flow

There are 4 such conducting brushes which are connected to the coil at tapered end, and the base is connected to the coil, thereby forming a closed connection (Fig. 11).

Geneva mechanism is one of the most widely used devices for making intermittent rotary motion, characterized by alternate periods of motion and rest with no reversal in direction.

The rotation drive wheel has a pin that reaches into a slot of driven wheel, the drive wheel also has a raised circular blocking disc that locks the driven wheel in position between steps, and the motion is well scrutinized during the working of the mechanism with under controlled rpm.

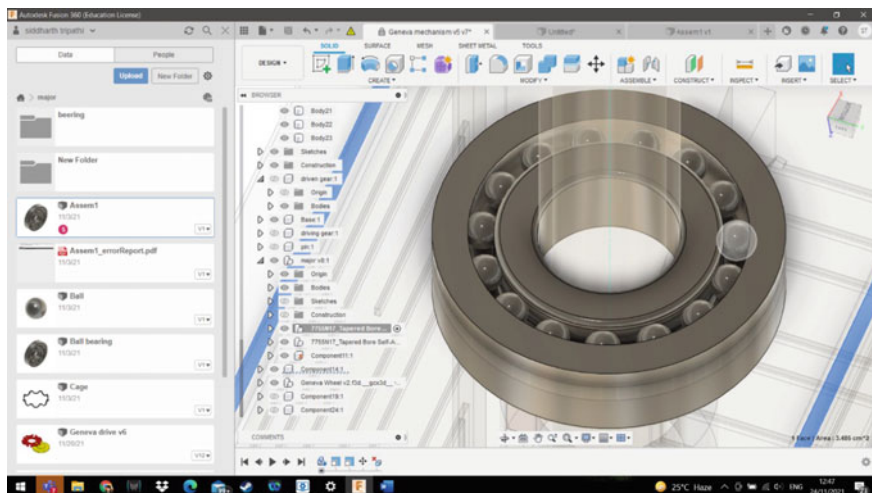


Fig. 3 Bearing

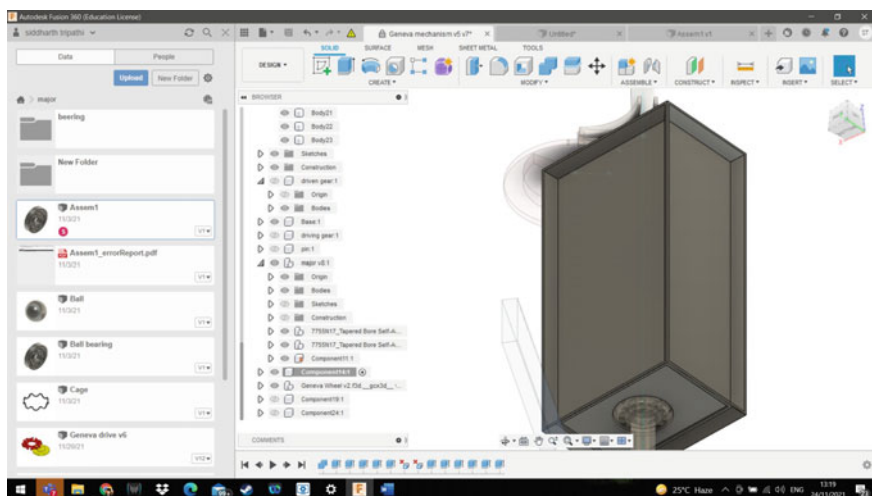


Fig. 4 Box

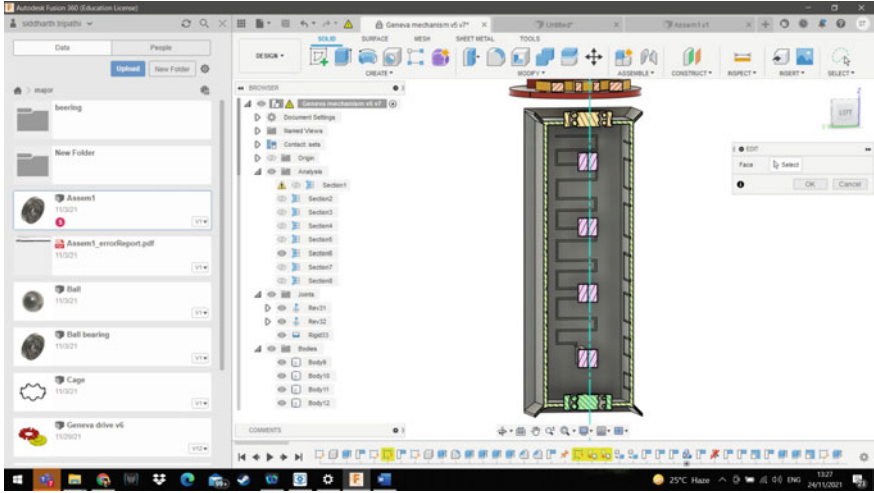


Fig. 5 Internal section

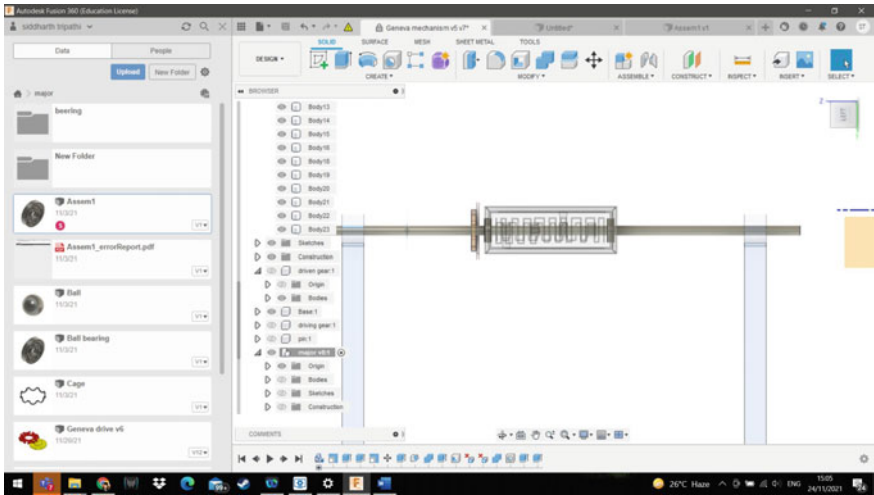


Fig. 6 Hollow section

## 5 Proposed Framework for Control

There are three most important activities that need control. These are as follows:

- (i) Control of rotation and stay of the box at 90° positions.
- (ii) Control of temperature for coils.



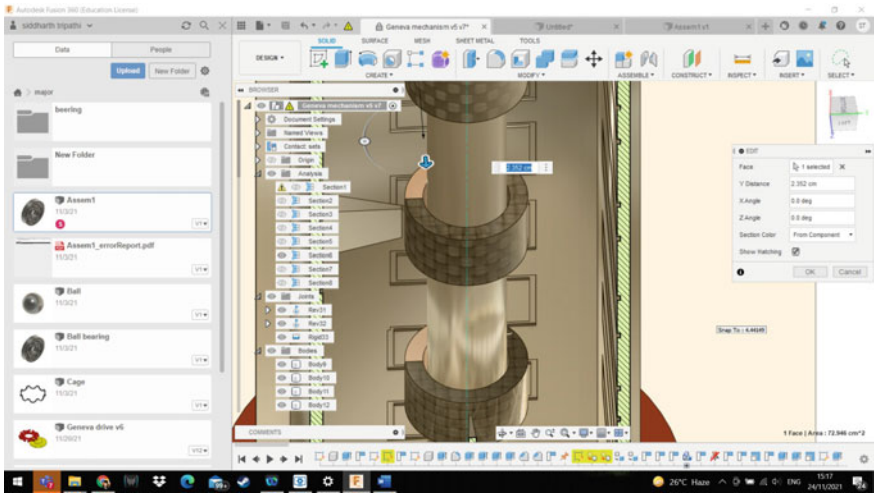


Fig. 7 Custom rings

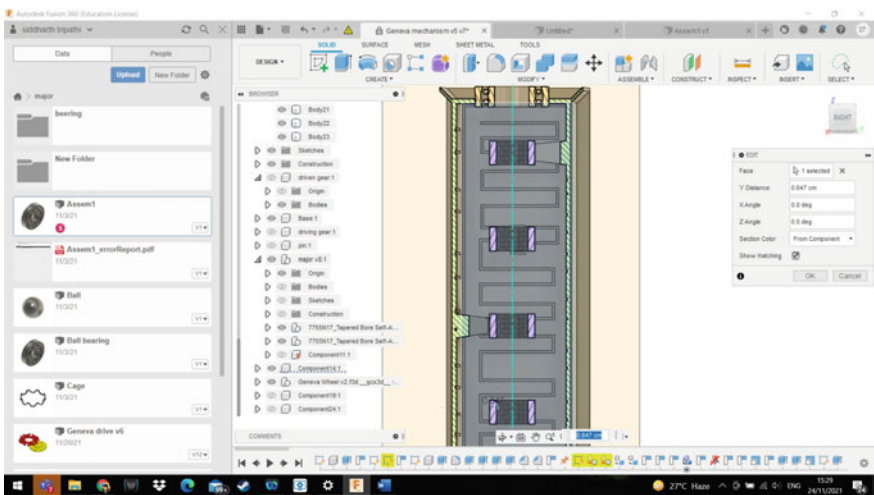


Fig. 8 Heating coils

For controlling the rotation and stay of blocks, pulse width modulation (PMV) method is proposed. It is a technique for controlling the amount of power going to the motor, and hence, how fast or slow it will rotate. Also, rpm of the motor can be controlled. For the above two objectives, it is proposed to use temperature sensor, and it is proposed to use A250 FO-PL pyrometer temperature sensor. It is proposed to use either Raspberry Pi or Arduino microcontroller for control of rotation and safety.

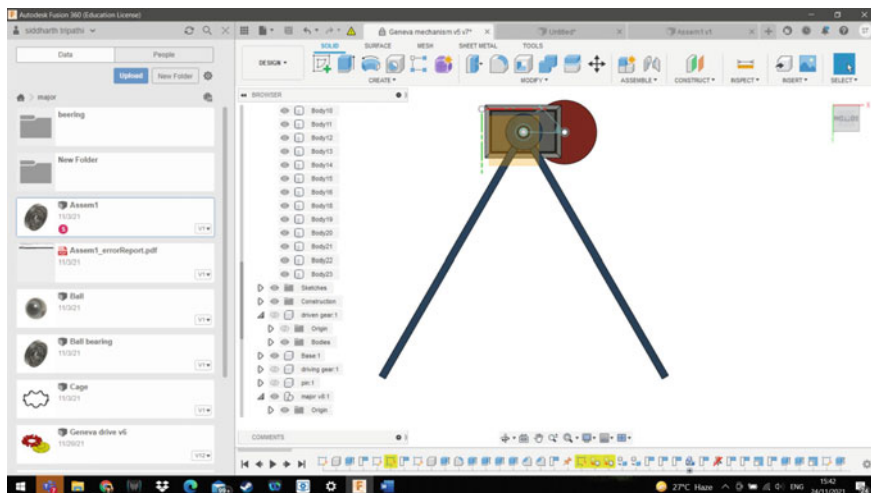


Fig. 9 Stand

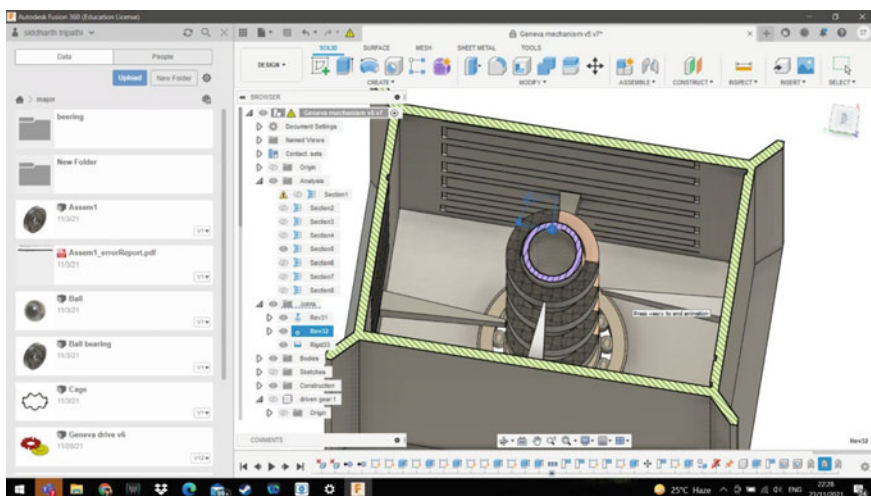


Fig. 10 Conducting brush

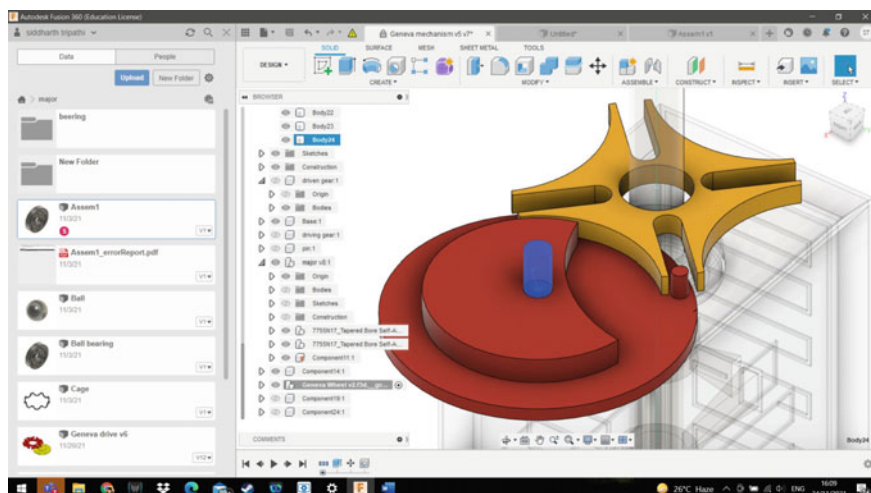


Fig. 11 Geneva mechanism

## 6 Conclusion

The design of the prototype is already developed. The fabrication work is in process. Once fabricated, the prototype will be equipped with the proposed sensors. The efficiency of prototype will be tested for amount of glass recovered and ease of controlling temperature and motor rpm.

## References

1. Lou Z, Bilitewski B, Zhu N, Chai X, Li B, Zhao Y (2015) Environmental impacts of a large-scale incinerator with mixed MSW of highwater content from a LCA perspective. *J Environ Sci* 30:173–179. <https://doi.org/10.1016/j.jes.2014.10.004>
2. Priti, Mandal K (2019) Review on evolution of municipal solid waste management in India: practices, challenges and policy implications. *J Mater Cycles Waste Manag* 21(6):1263–1279. <https://doi.org/10.1007/s10163-019-00880-y>
3. Gundupalli SP, Hait S, Thakur A (2017) Multi-material classification of dry recyclables from municipal solid waste based on thermal imaging. *Waste Manage* 70:13–21. <https://doi.org/10.1016/j.wasman.2017.09.019>
4. Subramanian PM (2000) Plastics recycling and waste management in the US. *Resour Conserv Recycl* 28(3–4):253–263. [https://doi.org/10.1016/S0921-3449\(99\)00049-X](https://doi.org/10.1016/S0921-3449(99)00049-X)
5. Srivastava P, Sindhwani R, Sharma BP, Singla AV, Gupta R, Goyal A (2021) Development of automatic waste identification and segregation system. *Mater Today Proc* 47:3943–3946. <https://doi.org/10.1016/j.matpr.2021.03.648>
6. Thanawala D, Sarin A, Verma P (2020) An approach to waste segregation and management using convolutional neural networks, pp 139–150. [https://doi.org/10.1007/978-981-15-6634-9\\_14](https://doi.org/10.1007/978-981-15-6634-9_14)

7. Ramachandran V, Gilbert SR (1995) Recovering metals from wastes. *JOM* 47(2):64–64. <https://doi.org/10.1007/BF03221412>
8. Zhang G et al (2017) New technology for recovering residual metals from nonmetallic fractions of waste printed circuit boards. *Waste Manage* 64:228–235. <https://doi.org/10.1016/j.wasman.2017.03.030>
9. Vasilyev AM, Kuskov VB (2017) Regularities of fine-grained materials separation process on concentrating table. *Obogashchenie Rud*, pp 63–68. <https://doi.org/10.17580/or.2017.03.10>
10. Moher DA, David, Liberati A, Tetzlaff J, Altman DG, Altman D, Antes G (2009) Preferred reporting items for systematic reviews and meta-analyses: the PRISMA statement. *J Chinese Integ Med* 7(9):889–896

# Buckling Analysis of Piston Rod for Hydraulic Cylinder of Cotton Bale Press Machine



S. G. Mahakalkar and Neeraj Sunheriya 

**Abstract** Buckling is characterized as the sudden sideways failure of a member when subjected to axial compressive stresses. The load is eccentric, which introduces a secondary bending movement that is not part of the primarily applied forces. Buckling analysis is performed on the piston rod of the hydraulic cylinder which compresses huge volumes of cotton. The piston rod, according to its slenderness ratio, falls under the category of long columns, which makes it extremely vulnerable to buckling. A comparative study is performed based on Euler's formula as well as the finite element method. Results using the software approach are obtained for up to three modes. Mathematically, it has been found that the rod is operating with a factor of safety of 2.30, whereas in finite element analysis, the factor of safety turned out to be 7.12. Furthermore, the paper also focuses on different techniques that can be incorporated into piston rods to increase their buckling resistance.

**Keywords** Buckling · Piston rod · Hydraulic cylinder · Finite element method

## 1 Introduction

A cotton bale press machine is used to form bales of finely processed cotton. Cotton bales are compressed and properly shaped blocks. The weight standards vary internationally. In India, a typical cotton bale weighs around 170 kg. The hydraulic cylinder, which the machine uses to compress huge volumes of cotton, is known as a tramper cylinder. One end of the tramper cylinder's piston rod has a ram that compresses cotton with successive strokes. The length of this piston rod is 2627 mm, and its diameter is 70 mm. However, with this design the piston rod while performing its practical application tends to buckle after a period of 6–8 months.

The mathematical analysis of buckling makes use of an axial compressive eccentric load that introduces secondary bending movement. The maximum load that a member can take before buckling is known as a crippling load. The most important

---

S. G. Mahakalkar · N. Sunheriya (✉)  
Yeshwantrao Chavan College of Engineering, Nagpur, India  
e-mail: [neeraj.sunheriya@gmail.com](mailto:neeraj.sunheriya@gmail.com)

© The Author(s), under exclusive license to Springer Nature Singapore Pte Ltd. 2023  
R. Sharma et al. (eds.), *Advances in Engineering Design*, Lecture Notes in Mechanical Engineering, [https://doi.org/10.1007/978-981-99-3033-3\\_7](https://doi.org/10.1007/978-981-99-3033-3_7)

thing in determining the buckling tendency of the member is calculating its slenderness ratio, which is the ratio of the effective length of the column to the least radius of gyration. The slenderness ratio of the piston rod, according to its dimensions, comes out to be 154.28, which propels it in the category of long columns. This makes it vulnerable to buckling.

The goal of this work is to study the current design of this piston rod through mathematical analysis by Euler's formula for buckling and also by finite element analysis using ANSYS software of member to determine its maximum load-carrying capacity and deformation. Furthermore, from studies and research done by researchers, different techniques will be considered and suggested to the manufacturer to reduce the tendency of the member toward buckling.

## 2 Literature Review

Many researchers and investigators have proposed consideration of different parameters while designing members for buckling. Gamez-Montero et al. [1] concluded that working conditions together with boundary conditions considerably modify the actuator's behavior by introducing friction moments which should be considered while designing members for buckling. Gamez-Montero et al. [2] through other research concluded that factors such as manufacturing tolerances, wear of guide rings, and cylindrical tube pressure introduce an imperfection angle in a loaded condition. Equivalent load to these factors should be considered while calculating the load on the cylinder. Awad et al. [3] concluded that induction hardening increases the buckling resistance of the rod. Lee et al. [4] concluded that when weight reduction of connection rod shank is attempted, buckling should be considered as an essential factor along with the other criteria such as yield and fatigue. Because of the enhanced rigidity and strength of composite materials, composite structures have several advantages. Ravi [5] focused on the replacement of conventional steel drive shafts with a hybrid aluminum/carbon fiber propeller shaft for an automotive application, and it was created using a new manufacturing method in which the carbon fiber layers are wrapped around the aluminum tube to achieve maximum strength. An attempt was made to estimate the deflection, stresses, and natural frequencies under applied loads using FEA (ANSYS) for hybrid shaft, and a comparison with traditional steel drive shaft was done to validate the best findings. For static, modal, and buckling analysis, a finite element model of a composite drive shaft consisting of Steel SMC45, Kevlar49/Epoxy, and HM Carbon Composite is constructed by Madhu et al. [6]. According to the data, composites have higher shear strength and bending natural frequency than steel, and Kevlar/Epoxy has a higher buckling strength capacity than other composites. When the finite element analysis findings are compared to the analytical values, it is discovered that the single-piece composite drive shaft is more appropriate for driveline applications. Preetha et al. [7] worked on the buckling analysis of a column with variable cross-sectional dimensions and its critical load-bearing capability. The

elastic instability of a column with changing the length and cross-sectional dimensions is caused by the critical load capacity. The critical load solution was established using Euler’s buckling load theory, and the theoretical findings were compared to simulation tests performed with the ANSYS 19.2 finite element analysis software.

### 3 Methodology

The evaluation of different parameters is evaluated with the help of mathematical analysis and numerical simulations. Results of mathematical and numerical solutions are then compared. A flowchart of the proposed methodology is represented in Fig. 1.

#### 3.1 Mathematical Analysis

For mathematical analysis of buckling, the most suitable and widely used technique is an evaluation by Euler’s equation for long columns. According to Euler’s equation,

$$P_c = \frac{\pi^2 EI}{L_e^2}, \tag{1}$$

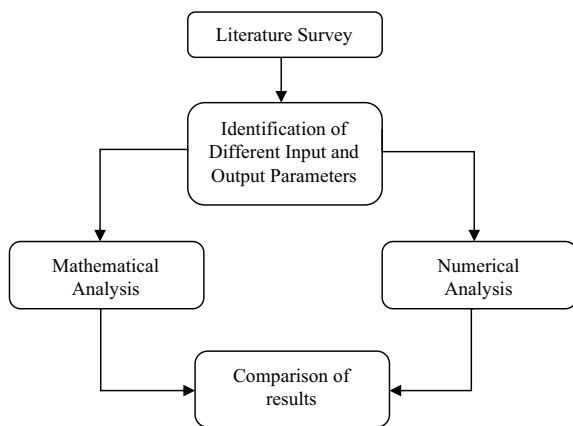
where  $P_c$  is the crippling load or the buckling load,

$E$  is the modulus of elasticity if the material,

$I$  is the moment of inertia of the member under consideration, and

$L_e$  is the effective length of the member.

**Fig. 1** Flowchart of the proposed methodology



The effective length of the member depends upon end conditions during application. In this case, on one end, we have the application of load through fluid pressure, and on another side, the reaction force is applied from compressed cotton. In both cases, the member has some slight displacement in one or more than one direction. Therefore, the condition of ‘both ends hinged’ is considered, according to which effective length turns out to be equal to the actual length of the member ( $L_e = L$ ), i.e.,  $L_e = 2627$  mm.

Moment of inertia:

$$I = \frac{\pi}{64} * 70^4 = 1178588.11 \text{ mm}^4$$

$$P_c = \frac{\pi^2 * 210000 * 1178588.11}{2700^2}$$

$$P_c = 34.15 \text{ tones.}$$

During the operation, the member is subjected to the fluid pressure of about 180 bars inside the cylinder having an internal diameter of 100 mm. Then applied force is

$$\text{Force} = \text{pressure} * \text{area}$$

$$\text{Force} = 180 * 1.03 * 10^{-1} * \frac{\pi}{4} * 100^2$$

$$\text{Force} = 14.83 \text{ tones.} \quad (2)$$

The factor of safety is given by

$$\text{FOS} = \frac{\text{cripling load}}{\text{actual load}} = \frac{34.15}{14.83}$$

$$\text{FOS} = 2.30. \quad (3)$$

Stresses generated are given by

$$\sigma = \frac{145539}{3848.45} = 37.81 \frac{\text{N}}{\text{mm}^2} \quad (4)$$

### 3.2 Numerical Analysis

These analyses are made in a linear buckling module under the ANSYS Workbench 15.0. The CAD model of the piston rod is created using CATIA software. Geometry is then imported into ANSYS for analysis. The material of the piston rod, EN8, is created in ANSYS by defining necessary properties. For meshing, the automatic mesh method is used. The mesh size is kept as 10 mm (Table 1).



**Table 1** Values of properties of material EN8

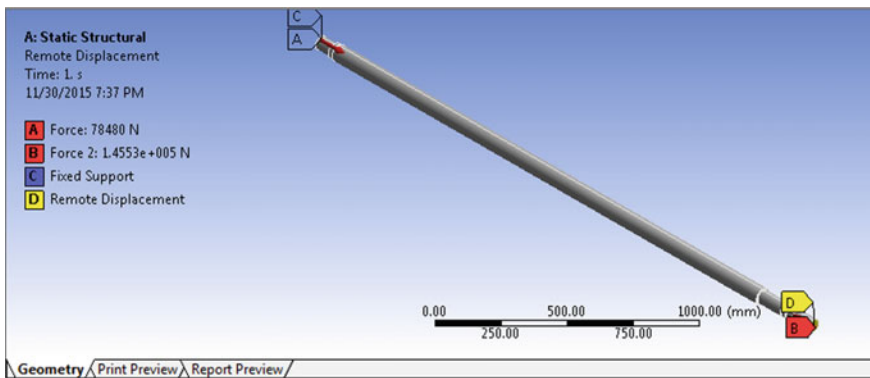
Modulus of elasticity; $E$	210 GPa
Poisons' ratio; $\nu$	0.3
Density	7860 kg/m <sup>3</sup>

### 3.3 Boundary Conditions

Boundary conditions play a vital role in evaluating the results of the analysis. The correctness of analysis depends upon how well boundary conditions are defined for analysis. Figure 2 represents various boundary conditions at different sections of the shaft (A, B, C, and D points). Force 1 is designated with the tag 'B'. It is the force applied to the member by the fluid during the extension of the cylinder. Its magnitude is 145530 N. Force 2 is designated with the tag 'A'. It is the reaction force offered by cotton. In this case, the reaction force is not equal and opposite because the reaction force is shared by three members. One is the piston rod itself, and the other two are the tie rods, which are not part of this analysis. The magnitude of this force is 78480 N. Fixed support is designated with the tag 'C'. The end of the rod which takes reaction force has a RAM attached through threading; hence, there is no chance of the rod's relative movement.

In the figure, remote displacement is designated with the tag 'D'. It is applied at the end where the rod has to take the fluid pressure. It is tabulated below (Table 2).

Here X-axis is the axial direction of the applied load.



**Fig. 2** Boundary conditions for analysis

**Table 2** Remote displacement for piston rod

	Linear	Rotational
X-axis	Free	Free
Y-axis	Constant	Constant
Z-axis	Constant	Constant

### 4 Results and Discussions

The analysis is carried out for three modes to obtain more accurate results regarding load multiplier and maximum deformation of the rod. Response of member for applied force and generated reaction is determined by analyzing shapes resulting from various modes. The result figures for the various modes are displayed below (Figs. 3, 4 and 5).

The results obtained from the above three modes are summarized in Table 3.

It can be seen that the shapes of the member are almost similar; hence, only for FEA we can conclude that the load multiplier of 7.12, which is the least of three, can be taken as a crippling load factor for the member. It indicates that the member can withstand a load of about 7.12 times the applied load before the failure.

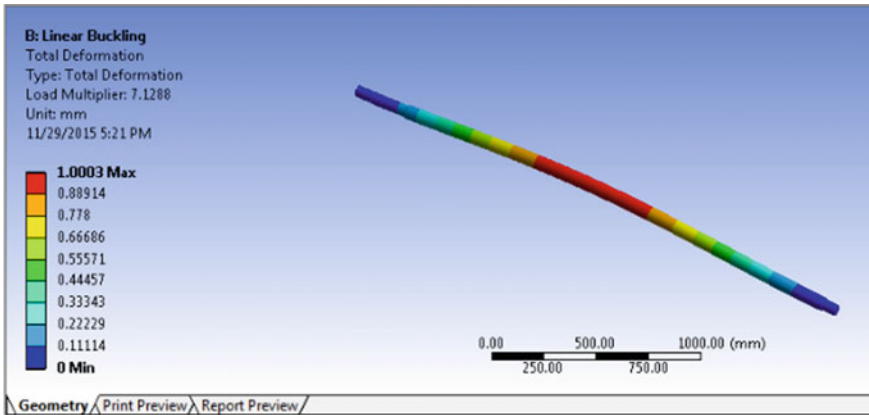


Fig. 3 Load multiplier and deformation in mode 1

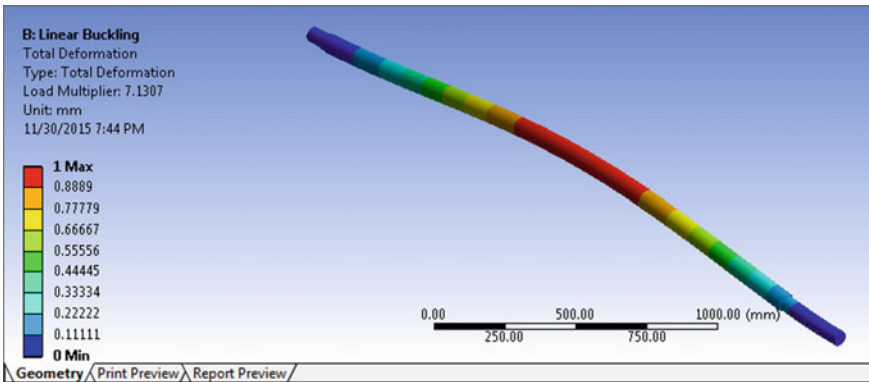


Fig. 4 Load multiplier and deformation in mode 2

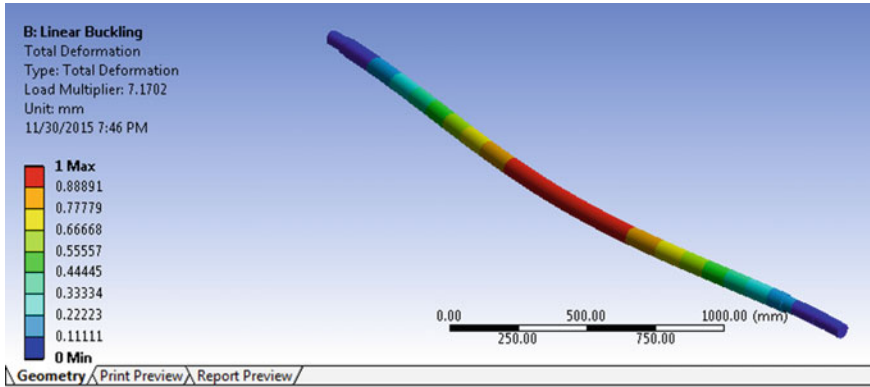


Fig. 5 Load multiplier and deformation in mode 3

Table 3 Results for three modes

	Mode 1	Mode 2	Mode 3
Load multiplier	7.12	7.13	7.17
Max. deflection (mm)	1.0003	1	1
Mini. deflection (mm)	0	0	0

Such a large difference in both the values is because of the discontinuous design of the piston rod. For mathematical analysis, a rod with a uniform cross section, i.e., 70 mm, is considered, whereas, in FEA, the geometry has a slight variation in its diameter in some parts of its length. It also has some groves at both of its ends which reduces the stress concentration and also its buckling tendency. Also, during the application, the piston rod has to take jerk loads. This justifies the heavily designing of the piston rod.

## 5 Conclusion

Analysis of current design of piston rod both mathematically and by finite element analysis has been done. In mathematical analysis, it has been found that the rod is operating with the factor of safety of 2.30, whereas in finite element analysis, the factor of safety turned out to be 7.12. Still with these results, during the practical application, it has a slight tendency to buckle. This tendency can be further reduced by performing precipitation hardening followed by induction hardening to it.

## References

1. Gamez-Montero PJ, Salazar E, Castilla R, Freire J, Khamashta M, Codina E (2009) Friction effects on the load capacity of a column and a hydraulic cylinder. *Int J Mech Sci* 51(2):145–151. <https://doi.org/10.1016/j.ijmecsci.2008.12.007>
2. Gamez-Montero PJ, Salazar E, Castilla R, Freire J, Khamashta M, Codina E (2009) Misalignment effects on the load capacity of a hydraulic cylinder. *Int J Mech Sci* 51(2):105–113. <https://doi.org/10.1016/j.ijmecsci.2009.01.001>
3. Awad M, Hultgren J, Roberts W (n.d.) Increasing the resistance to buckling of piston rods through induction hardening
4. Lee MK, Lee H, Lee TS, Jang H (2010) Buckling sensitivity of a connecting rod to the shank sectional area reduction. *Mater Des* 31(6):2796–2803. <https://doi.org/10.1016/j.matdes.2010.01.010>
5. Ravi T (2018) Numerical and buckling analysis of composite, Nov 2015
6. Madhu KS, Darshan BH, Manjunath K (2013) Buckling Analysis of Composite Drive Shaft for 1:63–70
7. Preetha V, Kalaivani K, Navaneetha S, Senthilkumar V (n.d.) Buckling Analysis of Columns. [www.iosrjen.org](http://www.iosrjen.org)

# Manufacturing Process-Related Challenges of Additive Manufactured Parts: A Review



Siddharth Pradeep Kumar Samgeetha , Neethesh Maharaj, and Bhupendra Prakash Sharma

**Abstract** Additive manufacturing is an integral part of the upcoming digital era and is still developing to become more effective and affordable. Various challenges are faced during the making of additive manufactured parts. Even after extensively using high-tech designing software to design the parts, we are not able to attain the desired product finish after manufacturing due to some design challenges. Manufacturing using additive technology is new and is slowly evolving. This evolution has been faced with a lot of challenges from various aspects. The challenges are mainly formation of stair steps, void in the packing formation, porosity, limited additive manufacturing material palette, and large-scale building capacity, limiting to personal fabrication and rheological scaling of powder dispersed in thermoplastics. These challenges were identified and reviewed to study its formation and the reason for its occurrence. Review is done in detail about these and manufacturing process-related challenges and their effect on additive manufactured parts.

**Keywords** Additive manufacturing · Manufacturing · 3D printing

## 1 Introduction

Manufacturing is the process of transforming raw materials into finished goods by using various machining processes that involve heating and cooling methods. Solid-type additive manufacturing is the type of the manufacturing where direct fabrication and machining are done between the workpieces like fused deposition modelling process uses a thermoplastic material made of continuous filament. This continuous filament is then fed from the spool to a moving component that heats the printer extruder head, and as it moves to the specified location, it deposits on the part being manufactured [1–3]. The freeze-form extrusion fabrication process uses colloidal paste to extrude and deposit layer-by-layer 3D parts using computer control for the

---

S. P. K. Samgeetha · N. Maharaj · B. P. Sharma (✉)  
Amity University Uttar Pradesh, Noida, UP 201313, India  
e-mail: [bpsharma@amity.edu](mailto:bpsharma@amity.edu)

extrusion and deposition. It is environmentally friendly. Laminated object manufacturing technology process uses adhesive-coated paper/metal laminates to glue together layer by layer and then laser cut to form the 3D object. This adhesive-coated paper and the metal laminate act as a 3D printing medium [2]. This process also allows the 3D manufactured parts to be modified post-production for any drilling or machining. Dark ink writing and robocasting process use filament that is paste like material; it is extruded from a small nozzle and moved on the platform to create the 3D manufactured part. This process dies by layer-by-layer manufacturing [4].

Liquid-type additive manufacturing processes use liquid or liquid like materials to create a 3D component. The processes are as follows. Stereolithography process uses a photochemical process to create polymers and is made layer by layer [2, 5]. This photochemical process is achieved by causing chemical monomers and oligomers to form cross-linking together to form polymer [1]. This process is used to make 3D models, prototypes, and various production parts. Rapid freezing prototyping (RFP) process uses rapid freezing of water to form layer-by-layer 3D parts. This process can create freeform parts because it uses a layer-by-layer technique. Multi-jet modelling process uses liquid form acrylic to manufacture 3D parts that can create fine detailed objects with smooth surface and detail rich. The digital light processing process uses liquid resin and light to create 3D parts. The digital light is projected to a digital micro-mirror which focuses the rays to the specific portion, we want to control, the resin that gets stuck on the moving platform. This helps create the 3D part [4].

Powder-based additive manufacturing processes use powder material and bond with a heating/binding agent or reaction. The processes are as follows: the 3D binder jet printing process uses powder particles, and then the binder liquid is sprayed onto the powder by jet to form 3D part [1, 2]. The binder is an adhesive between the powdered particle layers. Electron beam additive manufacturing, or electron beam melting (EBM) process uses an electron beam to heat the metal powder that is kept under vacuum and fused together to form a 3D component. In this process, the raw material is the metal powder, it is completely melted, and this differentiates the electron beam from the selective laser sintering. The selective laser sintering (SLS) process uses a laser beam to selectively heat the powder to form a 3D component [1]. This is done by aiming the laser at parts of the powder according to the instructions, and this helps to create a solid structure by binding the material together. Laser powder forming process uses a metal powder and injected into the molten pool, and then a high-powered laser is focused to create the design. This process uses the CAD file to create a solid model. Selective laser melting (SLM) process completely melts the metal powder using laser and forms the 3D component [1]. It is also known as direct metal laser melting (DMLM). Laser metal deposition (LMD) process uses laser beam to create a melt pool to which metallic powder is added to form deposits that are bonded from fusion layer by layer [2–4].

Complete review of the identified challenges and its effect on the parts are addressed while orienting pre- and post-effects on additive manufactured parts. The review takes angle of the manufacturing perspective for analysis and review.

The review analyses the effect of the most common and repetitively affected challenges and reviews their effects in detail. The challenges are recurrently affecting the advancement of additive manufacturing into a large-scale production capacity.

## 2 Literature Review

We have done our review by analyses and reviewing in the following format to create these papers and reach to our final conclusions (Fig. 1).

The challenges in the manufacturing process start with stair step. According to Abdulhameed et al., the stair steps in additive manufacturing processes are layer-by-layer process, where there might be a layering error which might cause misalignment in layer, thus forming small stair-like surfaces. This error might not affect the structure internally, but externally the error will show. This could be fixed by post-production sanding. Surface irregularities, such as waviness, are caused due to the stair stepping effect. This effect is a primary concern in the manufacturing process of a complex

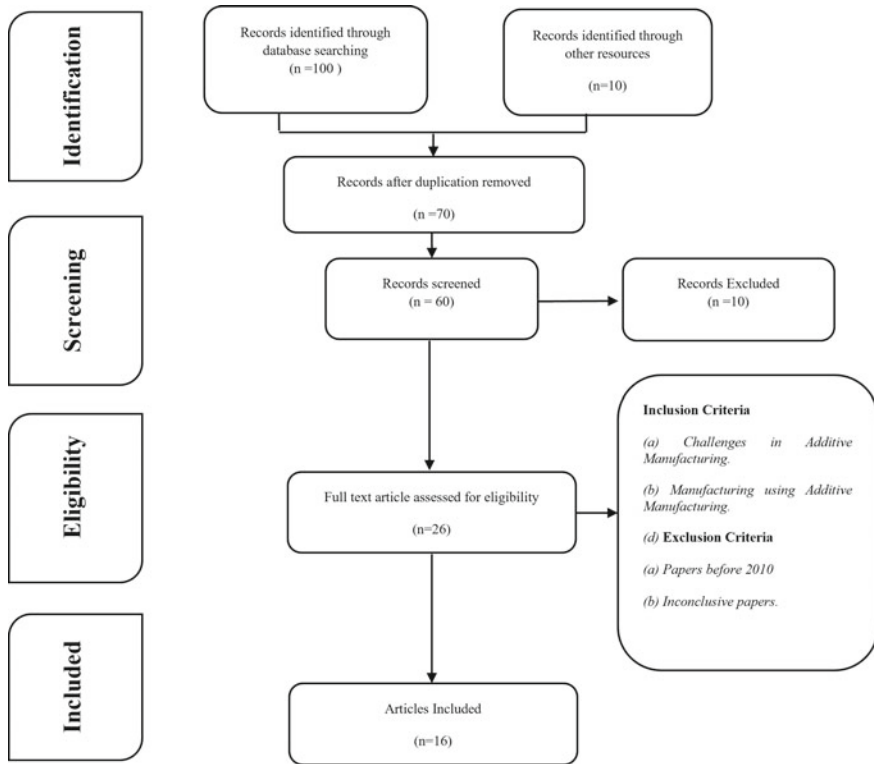


Fig. 1 Methodology of Literature Review

working mechanism such as the aeroplane engine, which is the specific propellers of the engine. If any form of waviness is formed out of the specified design, then it will tamper with the overall working of the component. The surface quality of such parts should be as accurate and error-free as possible to avoid any complications during performance [4, 6, 7].

According to Tronvoll et al., void formation in FDM method includes voids between layers that are formed. This results in low mechanical performance caused by reduced interfacial bonding of printed layers, and the chance for void formation is high in additive manufacturing. The extent of this porosity can only be determined by the material used in the printing and the method of printing. The high porosity of 3D printed parts can be exploited for controlled creation of porosity. This can be used in tissue engineering. This can be used in parts with high requirement of hygroscopic properties [8].

According to Stopyra et al., porosity problems were generally found in additive manufacturing techniques like laser sintering method. Here, if the overall heat that is applied during the process is very high, then the energy density in the workpiece tends to be high, so the porosity tends to generate at the same time. If the total heat that is applied during the process is low, then it is not fully melted. Hence, irregularities in the powder are created again. Artificial kinds of porosity are being generated at the surface levels. So, these things are to be optimized based on laser power, scanning speed, hatch spacing, and layer thickness. This factor is very much related to the problems that are being mentioned before. Apart from it, a specific focused beam is to be avoided, and the more blunt and bigger the radius of beam and the chances of getting porous will also decrease automatically. Here the same method of applying the laser to the workpiece is used; when heat is experienced, then it can be switched off after it is normalized again. It can be applied with this energy density as it will reduce the power utilized and oscillating time intervals can be calculated [5, 9–11].

According to Bourell et al., and Lu and Wong, the limited material palette is how every day we discover new materials and their properties. We learn about their applications and its pros and cons, so we can evaluate how we can utilize them in the most appropriate way possible. Similarly, we also experiment how we can make our everyday material compatible in the additive manufacturing process. Additive manufacturing has a very narrow selection of materials due to material functionality. This also means that most additive manufacturing devices can only process one material at a time and cannot process multiple materials at the same time due to its uncertain behaviour in material interaction. Additive manufacturing has various processes that involve multiple forms of material that are used for the manufacturing process. The larger the variety of material pallets, the larger we can expand our scope of design and manufacturability. This also ensures that we can produce the best possible 3D component of our requirements [12, 13].

According to Gao et al., building scalability is our traditional manufacturing process involved binding two or more objects or subtractive manufacturing techniques. But this is not the case with additive manufacturing; here we must make objects with the addition of the material. This addition is made with the help of



powder, liquid, or solid materials. Additive manufacturing uses layer-by-layer fabrication technique; thus, each layer is made according to the required resolution or the quality. Higher resolution requires higher build time and vice versa. To adapt to high-resolution manufacturing, we must optimize our design to match the manufacturing quality and requirement. Building scalability also depends on a few subfactors like total manufacturing time, storage capability, logistics, and material choice [1, 4, 14].

According to Gao et al., personal fabrication and mass production are the major challenge in some processes like sintering laser beam. In these methods, some preheated powders are being deposited, and then through the conveyor belt, a slow cooling process can occur to prevent all kinds of defects. Now in any other additive manufacturing while doing mass production level of products, any post-processing cannot be done at such a large scale. This is because it will be a time-consuming task, so all preventive defect methods should only be found which can be included in the assembly line. This was only the major focus of the project in addition to optimization of the process parameters. Most of the changes that occur during the additive manufacturing are only around microstructure levels only [1, 4].

According to Hasib et al., rheological scaling of spherical powder dispersed in thermoplastics is generally used in selective laser sintering. The powder is melted and added to the workpieces. Here, rheology means the amount of flow of powder when formed in the form of liquid because this is an essential criterion. If the melting of powder is too large, then due to the formation of an extremely thin liquid, the deposition of the powder can get swept inside the workpiece. At the same time, if powder is not properly melted, then there is a chance that the flowability or the ability of the powder to get dispersed across the workpiece cannot happen as more time has to be spent on it. Moreover, surface roughness can happen if the powder can itself generate the irregularity to some extent. So, here the amount of time that is required to melt and the power applied to the amount of powder that is going to be melted will be the dependent factors that are to be formulated based on which viscosity will somewhat can be determined. And the powders that need to be used needed to be one whose viscosity decreases with an increase in force, so that the flow can be increased gradually when flowing across the surface of the workpieces, and the production process can also be completed quickly. Now there is a further solution towards it, which is that we can add certain adhesive coatings to it so that it can easily bond to the workpiece. The appropriate grain size is to be established that can be universally added to any kind of workpiece because the reason is related, which is being mentioned before [15, 16] (Table 1).

### 3 Conclusion

From the overall review, we can understand that surface roughness is on a key point as its variation can completely alter the design and overall aesthetics of the parts. The tensile property is overall influenced by parameters like print speed, print density, and layer heights. The same parameter can also cause void formations. Such formation



can decrease the overall strength of the part, and the mass is also less. Porosity is a defect that can be better understood under the microscope. These microstructures provide a better understanding of porosity, and the porosity varies with the fill density. In general, additive manufacturing has a limited material choice, and this must be improved for better print quality and applications. This also limits the build scalability. All the challenges are the reason personal fabrication and mass production seem like a challenge, and these must be rectified by changing industry practices.

## References

1. Gao W, Zhang Y, Ramanujan D, Ramani K, Chen Y, Williams CB, Zavattieri PD (2015) The status, challenges, and future of additive manufacturing in engineering. *Comput Aided Des* 69:65–89
2. Kumar MB, Sathiya P (2021) Methods and materials for additive manufacturing: a critical review on advancements and challenges. *Thin-Walled Structures* 159:107228
3. Paolini A, Kollmannsberger S, Rank E (2019) Additive manufacturing in construction: a review on processes, applications, and digital planning methods. *Addit Manuf* 30:100894
4. Abdulhameed O, Al-Ahmari A, Ameen W, Mian SH (2019) Additive manufacturing: challenges, trends, and applications. *Adv Mech Eng* 11(2):1687814018822880
5. Emminghaus N, Hoff C, Hermsdorf J, Kaierle S (2021) Residual oxygen content and powder recycling: effects on surface roughness and porosity of additively manufactured Ti-6Al-4V. *Addit Manuf* 46:102093
6. Ngo TD, Kashani A, Imbalzano G, Nguyen KT, Hui D (2018) Additive manufacturing (3D printing): a review of materials, methods, applications and challenges. *Compos B Eng* 143:172–196
7. Yasa E, Poyraz O, Solakoglu EU, Akbulut G, Oren S (2016) A study on the stair stepping effect in direct metal laser sintering of a nickel-based superalloy. *Procedia Cirp* 45:175–178
8. Tronvoll SA, Welo T, Elverum CW (2018) The effects of voids on structural properties of fused deposition modelled parts: a probabilistic approach. *Int J Adv Manuf Technol* 97(9):3607–3618
9. Stopyra W, Gruber K, Smolina I, Kurzynowski T, Kuźnicka B (2020) Laser powder bed fusion of AA7075 alloy: influence of process parameters on porosity and hot cracking. *Addit Manuf* 35:101270
10. Biswal R, Zhang X, Shamir M, Al Mamun A, Awd M, Walther F, Syed AK (2019) Interrupted fatigue testing with periodic tomography to monitor porosity defects in wire+ arc additive manufactured Ti-6Al-4V. *Addit Manuf* 28:517–527
11. Mancisidor AM, Garciandia F, San Sebastian M, Álvarez P, Díaz J, Unanue I (2016) Reduction of the residual porosity in parts manufactured by selective laser melting using skywriting and high focus offset strategies. *Phys Procedia* 83:864–873
12. Lu QY, Wong CH (2018) Additive manufacturing process monitoring and control by non-destructive testing techniques: challenges and in-process monitoring. *Virtual Phys Prototyping* 13(2):39–48
13. Bourell D, Kruth JP, Leu M, Levy G, Rosen D, Beese AM, Clare A (2017) Materials for additive manufacturing. *CIRP Ann* 66(2):659–681
14. Abdulrahman A, Swash M, Seyed G (2018) Scalable additive manufacturing solution for construction
15. Hasib AG, Niazorou S, Xu W, Niverty S, Kublik N, Williams J, Azeredo B (2021) Rheology scaling of spherical metal powders dispersed in thermoplastics and its correlation to the extrudability of filaments for 3D printing. *Addit Manuf* 41:101967
16. Mackay ME (2018) The importance of rheological behavior in the additive manufacturing technique material extrusion. *J Rheol* 62(6):1549–1561

# Modelling of Kinematic Chains and Mechanisms with Special Emphasis on Multi-Linked Jointed Chain Mechanisms



Ojasvi Rajeev Sharma, Shaurya Bhatnagar, Shivam Verma,  
Jatin Mahallawat, Vipin Kaushik, and Sumit Sharma

**Abstract** The amalgamation of the kinematic chain needs to acquire the data of the kinematic chain precisely and thoroughly. Isomorphism recognition is a fundamental stage in kinematic chain blend. In this article, a clever isomorphism assurance technique for planar kinematic chains with different joints dependent on joint-joint matrix portrayal was proposed. Initially, a joint-joint matrix is introduced to portray the kinematic chain, which can exceptionally address the kinematic chain structure. Then, at that point, connections and joints data were extricated from the matrix. The isomorphism of kinematic chain is distinguished by looking at connections, joints and matrices. Furthermore, the connection between the connections and the joints comparing to the isomorphic kinematic is not really settled. At long last, the models show that the technique is novel and proficient. The mechanisms can be formed by fixing different links and joints in a particular order or a random order.

**Keywords** Matrix · Isomorphism · Kinematic chains

## 1 Introduction

In terms of kinematic synthesis, the designer's task is to create a new collection of kinematic structures that satisfy particular or desired motion characteristics in terms of output link. The production of a product with a specified set of motion

---

O. R. Sharma · S. Bhatnagar · S. Verma · J. Mahallawat  
Amity School of Engineering and Technology, Amity University, Noida,  
Uttar Pradesh, India

V. Kaushik (✉) · S. Sharma  
Department of Mechanical Engineering, Amity University Noida  
Uttar Pradesh, Noida, Uttar Pradesh, India  
e-mail: [vkaushik@amity.edu](mailto:vkaushik@amity.edu)

S. Sharma  
e-mail: [ssharma03@amity.edu](mailto:ssharma03@amity.edu)

characteristics or mechanism is the subject of type synthesis. During the early stages of settling on an idea, a designer is tasked with researching as many different types of mechanisms as possible and then selecting the mechanism that best represents the best possible potential in respect to the design objectives. The number synthesis is based on determining the number of links, joint type and the desired degree of freedom corresponding to the joints required for a certain mechanism class.

## 2 Literature Review

Many researchers felt the need to represent the kinematic structures in the abstract form that is both computationally efficient and as well as easily understandable. Few of them are as under.

Reuleaux [1] was the pioneer and paved a logical way to analyse and represent the mechanism in the symbolic form.

Closely [2] introduces algorithm for calculating the number of links for the possible constrained kinematic chain using Grubler's equation.

Mruthyunjya and Raghvan [3] have proposed a method which is based upon the Bocher's formulae in determining characteristic polynomial.

Mruthyunjya and Raghvan [4] make use of link-link incidence matrix in order to represent a simple-jointed kinematic chain, thereby an algebraic procedure was developed to determine its structural characteristics, i.e. type of degrees of freedom of kinematic chain, number of distinct mechanisms and the mechanisms which are derived from the chain.

Mruthyunjaya [5] developed a fully computerized methodology dependent upon the transformation of binary chain for finding novel aspects dedicated to structural synthesis of kinematic chains

Mruthyunjya and Bala Subramaniam [6] have discussed a reliable computation test for detection of isomorphism in chain.

Ambedkar and Agrawal [7] devoted the study to minimum code concepts and the properties enshrined in it with respect to kinematic chains. Based upon graph theory concepts, an algorithm is elaborated for demonstrating the applicability of minimum code in kinematic chains with simple joints. The minimum code being considered unique for different kinematic chains provides a substantive method found suitable for testing isomorphism.

Ambedkar and Agrawal [8] showed the minimum code, as canonical number to give a unique identification characteristic number for kinematic chains with simple joints, thereby suggesting a method to identify mechanisms, path and function generators through a set of identification numbers.

Agrawal and Rao [9] made use of loop connectivity properties of multi-loop kinematic chains in order to develop a seven-step hierarchical classification scheme of any kinematic structure.

Hong-Sen and Hwang [10] proposed the methodology on the basis of concepts of combinatorial theory. The methodology was found to be suitable for synthesizing all

the non-isomorphic mechanisms pertaining to a given kinematic structure. Principles of permutations were implemented for developing the chain corresponding to marked “Link-Adjacency matrix”, thereby developing new algorithmic approach for generation of distinct set of mechanisms by marking different links and kinematic pairs of the KC. In this way, labelled “Link-Adjacency Matrix” was used to determine the permutation groups of kinematic chains. As a result, building an effective algorithm requires a full grasp of structural properties for a certain type of linkage. The dimensions or proportions of the linkages corresponding to a mechanism are determined by dimensional synthesis. The suggested method has the capacity to create various jointed kinematic chains and distinguish distinct mechanisms that result from these chains.

### 3 Objectives

- OBJECTIVE-I: Development of multiple jointed kinematic chains from given family of simple-jointed kinematic chains.
- OBJECTIVE-II: Modelling of multiple jointed kinematic chains and detection of isomorphism among these chains.
- OBJECTIVE-III: Identification of distinct mechanisms from the given family of multiple jointed kinematic chains.

### 4 Methodology

In structural synthesis, all possible kinematic chains with “ $n$ ” links and “ $F$ ” degree of freedom are derived. Initially, binary links are ignored, and skeletons are developed considering each assortment of polygonal links. Finally, possible assortments of multiple jointed kinematic chains are developed by transforming polygonal links. The multiple jointed kinematic chains are actually developed by transforming the ternary and quaternary link into binary link. The different possible combinations of multiple jointed kinematic chains are obtained by Eq. (1) given below:

$${}^nC_r = n!/r!(n - r)!, \quad (1)$$

where

$n$  = Number of polygonal links, e.g. ternary, quaternary, etc., and

$r$  = Number of polygonal links to be transformed into binary links simultaneously.

**Step 1:** Find all possible assortments by transforming the ternary and quaternary link into binary link. The different possible combinations of multiple jointed kinematic chains are obtained by Eq. (1).

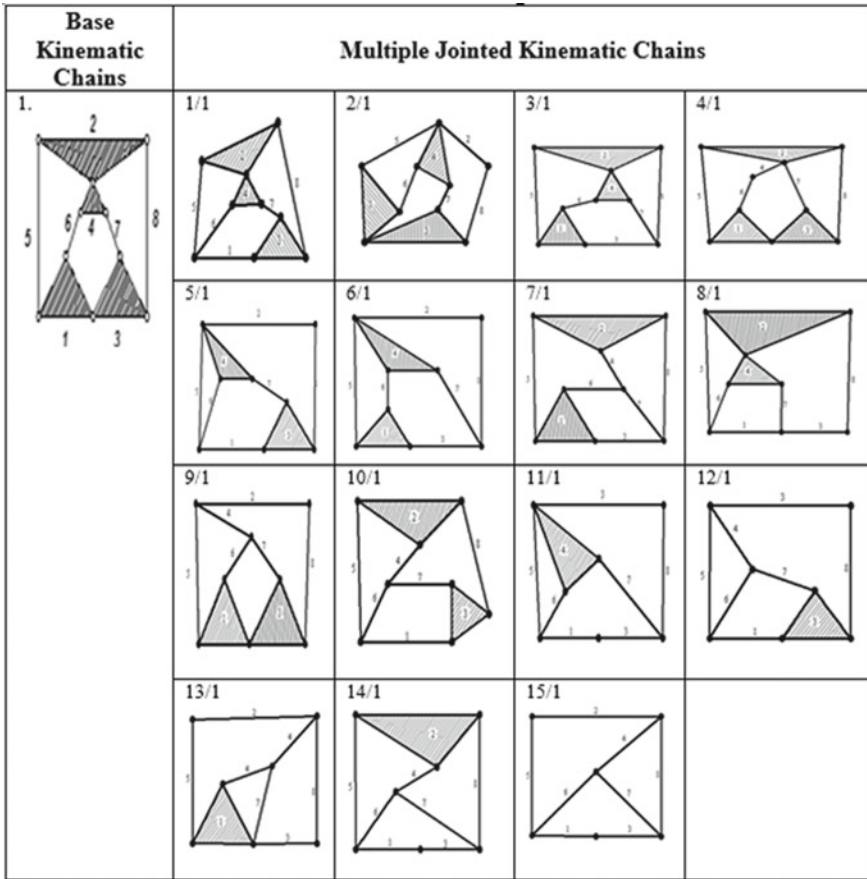


Fig. 1 Kinematic chain and its invariants

**Step 2:** Calculation of joint value for all possible assortments. For the existence of kinematic chains with multiple joints, sum of the value of the edges is supposed to be equal to the no. of joints as existing in kinematic chains with simple joints.

**Step 3:** The procedure as illustrated above is carried out for one of the 16 base kinematic chains with simple joints and the resulting possible assortments of multiple jointed kinematic chains (Fig. 1).

## 5 Results

See Figs. 2, 3, 4, and 5.

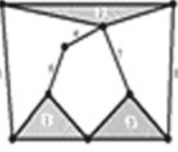
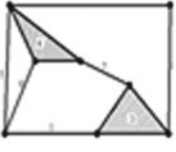
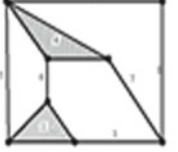
<p>4. KC 04/01</p>  <p>1. -19, 146.63, -591.07, 1329.3, -1642.6, 1010.3, -227.48, -1.4252</p>	FL	EL	Polynomial Coefficients	DM
	1	--	1. -16, 102.15, -333.91, 595.05, -566.75, 258.74, -41.42, 0	
	2	--	1. -16, 101.98, -331, 576.49, -510.58, 179.1, 0.68593, 0	
	3	--	1. -17, 115.8, -405.89, 782.18, -819.56, 426.26, -83.46, -4.2746e-014	
	4	--	1. -16, 100.68, -316.06, 514.83, -402.49, 111.11, 0.6921, -1.921e-017	
	5	--	1. -17, 114.98, -393.98, 717.91, -659.67, 246.32, -8.6473, -3.8402e-015	
	6	--	1. -17, 114.78, -391.34, 705.73, -640.16, 250.28, -31.303, 1.7377e-014	
	7	--	1. -17, 114.61, -390.26, 706.42, -654.71, 275.58, -40.945, -1.461e-028	
8	--	1. -17, 114.8, -392.89, 718.45, -674, 273.28, -23.682, 0		
<p>5. KC 05/01</p>  <p>1. -18, 131.3, -500.42, 1068.5, -1271.8, 795.12, -233.53, 23.46</p>	FL	EL	Polynomial Coefficients	DM
	1	--	1. -16, 101.28, -324.29, 555.42, -491.51, 195.93, -25.292, 0	
	2	--	1. -16, 101.28, -324.29, 554.49, -486.02, 187.16, -22.242, 0	
	3	--	1. -15, 89.701, -274.82, 458.92, -407.93, 172.61, -26.13, -1.4505e-015	
	4	--	1. -15, 89.701, -274.82, 459.88, -413.17, 181.27, -29.941, 9.9725e-015	
	5	--	1. -16, 101.28, -324.29, 555.34, -492.77, 201.63, -28.73, 3.1897e-015	
	6	--	1. -16, 101.45, -325.2, 557.19, -499.6, 218.44, -36.476, -2.4298e-014	
	7	--	1. -16, 101.65, -327.64, 567.33, -515.6, 225.04, -36.761, -2.1813e-027	
8	--	1. -16, 101.47, -326.73, 565.42, -508.67, 208.18, -27.955, 0		
<p>6. KC 06/01</p>  <p>1. -18, 131.28, -500.19, 1067.9, -1271.2, 790.81, -222.42, 19.521</p>	FL	EL	Polynomial Coefficients	DM
	1		1. -15, 89.804, -276.55, 468.29, -428.8, 190.92, -30.226, 0	
	2		1. -16, 101.26, -324.1, 555.08, -492.58, 196.94, -23.027, -2.3114e-030	
	3		1. -16, 101.35, -324.7, 554.41, -482.94, 183.4, -22.197, 9.2414e-016	
	4		1. -15, 89.684, -274.64, 459.71, -413.96, 182.21, -30.174, 6.6999e-015	
	5		1. -16, 101.43, -325.01, 556.01, -493.37, 202.85, -27.533, -1.3373e-015	
	6		1. -16, 101.63, -327.44, 567.21, -518.18, 230.63, -38.772, -2.2599e-014	
	7		1. -16, 101.35, -324.7, 555.33, -488.99, 193.22, -24.112, 1.0708e-014	
8		1. -16, 101.18, -323.79, 555.43, -494.89, 201.45, -26.38, 0		

Fig. 2 Distinct mechanisms obtained from the invariants




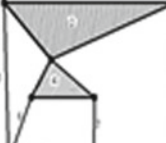

<p>7. KC 07/01</p>  <p>1. -18, 131.26, -499.95, 1068, -1276.6, 801.89, - 226.22, 20.756</p>	FL	EL	Polynomial Coefficients	DM
	1	2	1. -15, 89.786, -276.37, 468.04, -429.34, 191.12, -29.079, 0	
	--	--	1. -15, 89.786, -276.37, 468.04, -429.34, 191.12, -29.079, 0	
	3	4	1. -16, 101.34, -324.51, 555.94, -494.68, 201.5, -25.976, -1.1536e-014	
	--	--	1. -16, 101.34, -324.51, 555.94, -494.68, 201.5, -25.976, 1.1536e-014	
	5	--	1. -16, 101.61, -327.24, 566.01, -512.21, 219.05, -34.645, -1.1113e-027	
	6	8	1. -16, 101.34, -324.51, 555.94, -494.68, 201.5, -25.976, -2.1269e-014	
	7	--	1. -16, 101.06, -321.77, 546.26, -480.28, 196.52, -29.509, -1.6381e-014	
--	--	1. -16, 101.34, -324.51, 555.94, -494.68, 201.5, -25.976, 0		
<p>8. KC 08/01</p>  <p>1. -18, 131.61, -504.47, 1089, -1322.6, 855.05, - 259.59, 26.192</p>	FL	EL	Polynomial Coefficients	DM
	1	--	1. -16, 101.51, -327.42, 569.01, -515.42, 211.29, -26.388, 0	
	2	--	1. -15, 89.959, -277.1, 467.97, -427.73, 194.01, -33.676, 0	
	3	--	1. -16, 101.41, -325.59, 559.13, -494.34, 194.87, -24.838, -5.5151e-015	
	4	--	1. -15, 89.959, -277.1, 468.9, -432.27, 199.6, -35.279, -7.1381e-029	
	5	--	1. -16, 101.79, -330.15, 579.66, -537.28, 235.15, -35, -2.3314e-014	
	6	--	1. -16, 101.68, -328.33, 569.75, -515.56, 217.27, -30.203, -8.3829e-015	
	7	--	1. -16, 101.68, -328.33, 571.4, -526.56, 238.97, -41.409, 9.1947e-015	
--	--	1. -16, 101.68, -328.33, 570.35, -518.09, 218.95, -32.799, 0		
<p>9. KC 10/01</p>  <p>1. -18, 131.28, -501.24, 1080.9, -1327.9, 896.21, - 302.05, 38.832</p>	FL	EL	Polynomial Coefficients	DM
	1	--	1. -16, 101.26, -325.15, 565.85, -527.33, 240.48, -41.133, 0	
	2	--	1. -15, 89.804, -277.6, 476.38, -451.19, 216.63, -40.371, 0	
	3	--	1. -15, 89.684, -274.64, 459.56, -413.21, 180.12, -28.175, -3.1281e-015	
	4	--	1. -16, 101.35, -325.76, 566.07, -523.43, 234.46, -39.611, 1.7591e-014	
	5	--	1. -16, 101.46, -327.53, 576.26, -548.25, 261.39, -48.529, 3.6993e-014	
	6	--	1. -16, 101.16, -322.27, 546.16, -478.09, 195.42, -28.722, -1.5944e-015	
	7	--	1. -16, 101.35, -324.7, 557.16, -500.9, 216.45, -34.263, -8.8392e-027	
8	--	1. -16, 101.63, -328.49, 576.33, -541.2, 247.46, -41.241, 0		

Fig. 3 Distinct mechanisms obtained from the invariants

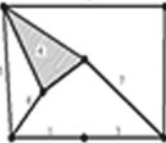


10. KC 11/01	FL	EL	Polynomial Coefficients	DM
 <p>1, -17, 117.98, -431.86, 897.44, -1060.9, 679.08, -210.48, 23.173</p>	1	--	1, -15, 89.881, -276.17, 461.49, -406.1, 164.25, -21.442, 0	§
	2	--	1, -15, 89.959, -277.1, 467.97, -427.73, 194.01, -33.676, 0	
	3	--	1, -15, 89.779, -274.45, 453.65, -392.73, 156.3, -20.962, 4.6545e-015	
	4	--	1, -14, 78.858, -229.78, 370.74, -328.65, 147.52, -25.825, 1.1469e-014	
	5	--	1, -15, 89.433, -271.84, 447.26, -388.55, 159.3, -22.887, -1.6674e-026	
	6	--	1, -15, 90.055, -276.91, 462.26, -408.55, 172.04, -25.492, -2.8302e-015	
	7	--	1, -15, 90.055, -276.91, 463.31, -415.57, 185.75, -32.268, -3.0685e-028	
	8	--	1, -15, 89.881, -276.17, 463.03, -414.88, 178.98, -28.424, 0	
11. KC 12/01	FL	EL	Polynomial Coefficients	DM
 <p>1, -17, 117.46, -427.3, 885.44, -1057.5, 705.27, -240.56, 32.47</p>	1	--	1, -15, 89.433, -272.89, 457.02, -417.93, 192.17, -34.133, 0	§
	2	--	1, -15, 89.355, -272.66, 456.16, -413.07, 184.72, -31.457, 0	
	3	--	1, -14, 78.858, -229.78, 370.18, -325.8, 143.4, -24.269, -1.2945e-029	
	4	--	1, -15, 89.252, -270.94, 447.89, -397.24, 172.13, -28.356, 1.5741e-015	
	5	--	1, -15, 89.355, -272.66, 456.57, -416.01, 190.3, -33.634, -3.7342e-015	
	6	--	1, -15, 89.33, -270.11, 439.94, -379.53, 161.47, -26.491, -5.8821e-015	
	7	--	1, -15, 89.528, -272.35, 448.73, -393.15, 167.64, -27.11, -1.4785e-027	
	8	--	1, -15, 89.63, -275.12, 465.28, -429.77, 198.7, -35.122, 0	
12. KC 13/01	FL	EL	Polynomial Coefficients	DM
 <p>1, -17, 117.89, -431.27, 897.29, -1065.1, 684.1, -208.32, 22.805</p>	1	--	1, -14, 79.409, -235.29, 390.19, -357.73, 164.21, -27.696, 0	§
	2	--	1, -15, 89.786, -276.37, 468.04, -429.34, 191.12, -29.079, 0	
	3	--	1, -15, 89.959, -276.5, 463.49, -415.31, 178.86, -27.341, 1.5177e-015	
	4	--	1, -15, 89.235, -269.7, 439.01, -373.94, 147.59, -19.673, -2.1542e-015	
	5	--	1, -15, 89.51, -272.17, 447.68, -389.33, 161.96, -25.14, 1.9189e-015	
	6	--	1, -15, 89.959, -276.5, 463.24, -414.26, 178.24, -27.632, -2.6843e-015	
	7	--	1, -15, 89.684, -274.04, 454.5, -399.71, 168.46, -26.396, 5.861e-015	
	8	--	1, -15, 89.786, -275.77, 463.03, -415.8, 177.77, -25.368, 0	

Fig. 4 Distinct mechanisms obtained from the invariants

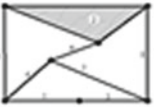

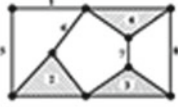
13. KC 14/01		Fl.	El.	Polynomial Coefficients	DM
 <p>1, -17, 117.44, -426.63, 880.78, -1042.6, 678.19, -214.09, 22.745</p>	1	--	1	-15, 89.337, -272.03, 453.08, -406.22, 176, -26.378, 0	6
	2	--	1	-14, 78.96, -232.01, 382.6, -353.66, 169.83, -32.74, 0	
	3	6	1	-15, 89.235, -269.7, 438.86, -373.19, 145.69, -17.533, -3.8932e-015	
	4	8	1	-15, 89.51, -272.77, 453.87, -408.53, 181.54, -29.932, -1.3292e-014	
	5	--	1	-15, 89.613, -274.49, 461.98, -423.93, 195.71, -34.548, -3.7235e-025	
	--	--	1	-15, 89.235, -269.7, 438.86, -373.19, 145.69, -17.533, -3.8932e-015	
	7	--	1	-15, 89.235, -269.7, 439.99, -380.48, 160.39, -25.193, -5.594e-015	
	--	--	1	-15, 89.51, -272.77, 453.87, -408.53, 181.54, -29.932, 0	
14. KC 15/01		Fl.	El.	Polynomial Coefficients	DM
 <p>1, -16, 105.51, -373.36, 772.37, -953.14, 683.31, -259.42, 39.705</p>	1	--	1	-14, 79.409, -236.71, 400.8, -386.13, 196.42, -40.829, 0	8
	2	--	1	-14, 79.409, -235.59, 392.44, -365.78, 171.6, -31.175, 0	
	3	--	1	-14, 79.307, -234.79, 390.03, -360.38, 169.39, -30.673, 0	
	4	--	1	-14, 78.858, -230.75, 377.65, -345.57, 163.91, -31.226, 0	
	5	--	1	-14, 79.409, -236.71, 400.95, -386.64, 196.99, -41.025, 0	
	6	--	1	-14, 78.888, -230.9, 378.6, -347.5, 165.4, -31.54, 0	
	7	--	1	-14, 78.409, -225.29, 353.64, -298.87, 125.29, -20.206, -4.4867e-015	
	8	--	1	-14, 79.409, -236.04, 395.39, -370.55, 177.62, -32.744, 0	
15. KC 01/02		Fl.	El.	Polynomial Coefficients	DM
 <p>1, -19, 147.63, -606.07, 1416.4, -1586.9, 1347.8, -440.84, 45.143</p>	1	--	1	-17, 115.61, -403.26, 769.24, -790.32, 398.36, -76.563, 0	8
	2	--	1	-16, 102.98, -343, 632.43, -637.53, 320.18, -60.954, 0	
	3	--	1	-16, 101.8, -330.09, 579.28, -534.21, 227.84, -33.326, 3.7e-015	
	4	--	1	-16, 103.03, -343.88, 634.44, -629.7, 291.18, -37.947, -9.789e-030	
	5	--	1	-17, 115.8, -405.89, 782.14, -819.16, 426.87, -84.952, -1.8548e-025	
	6	--	1	-17, 115.78, -404.34, 769.53, -780.98, 377.93, -62.186, -1.3808e-014	
	7	--	1	-17, 114.8, -392.89, 715.67, -676.99, 283.43, -33.705, -7.4541e-015	
	8	--	1	-17, 115.98, -406.98, 779.88, -791.69, 369.73, -51.201, 0	

Fig. 5 Distinct mechanisms obtained from the invariants

### 6 Conclusion

- The multiple jointed kinematic chains are developed by transforming the ternary and quaternary link into binary link.
- In transforming ternary and quaternary link into binary link, the no. of joints is reduced physically. Thus, to obtain the actual no. of joints, a graph is drawn pertaining to multiple jointed kinematic chain.
- The values pertaining to edges of the graph become equal to the no. of joints as represented in simple-jointed chain.

- Invariants in terms of polynomial coefficients are obtained which identified the existence of isomorphism in kinematic chains with multiple joints.
- These invariants are generally obtained after representing the chains in their respective kinematic graphs.
- Polynomial coefficients so obtained are same for equivalent mechanisms but found to be different for distinct mechanisms.
- Analysing these polynomial coefficients pertaining to mechanisms of a particular multiple jointed kinematic chain, the distinct mechanisms are obtained.
- The approach is implemented to multiple jointed kinematic chains derived from kinematic chains with simple joints.
- The approach does not consider different combination of kinematic pairs and implemented on pin-jointed kinematic chains.

## References

1. Kennedy AB (1876) Book review: the kinematics of machinery; outlines of a theory of machines, Reuleaux, translated by ABW Kennedy
2. Haas SL, Crossley FRE (1969) A contribution to grubler's theory in the number synthesis of plane mechanisms. *Trans ASME J Eng Ind* 91:240–250
3. Mruthyunjaya TS, Raghavan MR (1979) Structural analysis of kinematic chains and mechanisms based on matrix representation, pp 488–494
4. Mruthyunjaya TS, Raghavan MR (1984) Computer-aided analysis of the structure of kinematic chains. *Mech Mach Theory* 19(3):357–368
5. Mruthyunjaya TS (1984) A computerized methodology for structural synthesis of kinematic chains: part 1—formulation. *Mech Mach Theory* 19(6):487–495
6. Mruthyunjaya TS, Balasubramanian HR (1987) In quest of a reliable and efficient computational test for detection of isomorphism in kinematic chains. *Mech Mach Theory* 22(2):131–139
7. Ambedkar AG, Agrawal VP (1987) Canonical numbering of kinematic chains and isomorphism problem: min code. *Mech Mach Theory* 22(5):453–461
8. Ambedkar AG, Agrawal VP (1987) Identification of kinematic chains, mechanisms, path generators and function generators using min codes. *Mech Mach Theory* 22(5):463–471
9. Agrawal VP, Rao JS (1989) Identification and isomorphism of kinematic chains and mechanisms. *Mech Mach Theory* 24(4):309–321
10. Yan HS, Hwang YW (1991) The specialization of mechanisms. *Mech Mach Theory* 26(6):541–551

# Design and Analysis of a Spherical Joint Mechanism for Robotic Manipulators



B. L. S. Gopal and Rohit Singla 

**Abstract** A spherical joint, also known as a ball-and-socket joint, allows three degrees of rotational freedom about the center of the joint between the two connected segments. Recent trends in the mechanical design of manipulators that have been targeted as essential and have the required reduction of moving masses have resulted in an increase in rigidity. By placing a spherical joint at the base of a manipulator, we can eliminate the number of links and joints (e.g., in the articulated manipulator, we can eliminate the twisting joint at the base and revolute joint at the shoulder) in the configuration of the manipulator by achieving a similar workspace. In the present study, an attempt was made to visualize a new spherical manipulator joint mechanism.

**Keywords** Manipulator · Spherical joint · Mechanism · Linear actuators

## 1 Introduction

A spherical joint is a constraint element that allows the relative rotation of the two bodies. It is sometimes referred to as a “ball-and-socket joint”. Based on the results of many scientific analyses of different mechanisms, we can conclude that the lower the number of moving masses, the higher is the rigidity and stiffness. Cantilever-like manipulators such as PUMA and SCARA are not as rigid owing to the less stiffness seen in the structure and therefore have comparatively poor dynamic performance when operated at high-speed conditions with higher dynamic loading owing to many factors such as the number of links and joints, vibrations in structures, and internal and external loading. By decreasing the number of (moving mass) links, we can increase the rigidity of the manipulator. The mechanical rigidity of a manipulator is considered one of the most important indicators when deriving the performance evaluation for any robotic system. We have observed that for any industrial robot that

---

B. L. S. Gopal · R. Singla (✉)

Department of Mechanical Engineering, Amity School of Engineering and Technology, Amity University, Noida, Uttar Pradesh, India  
e-mail: [rsingla1@amity.edu](mailto:rsingla1@amity.edu)

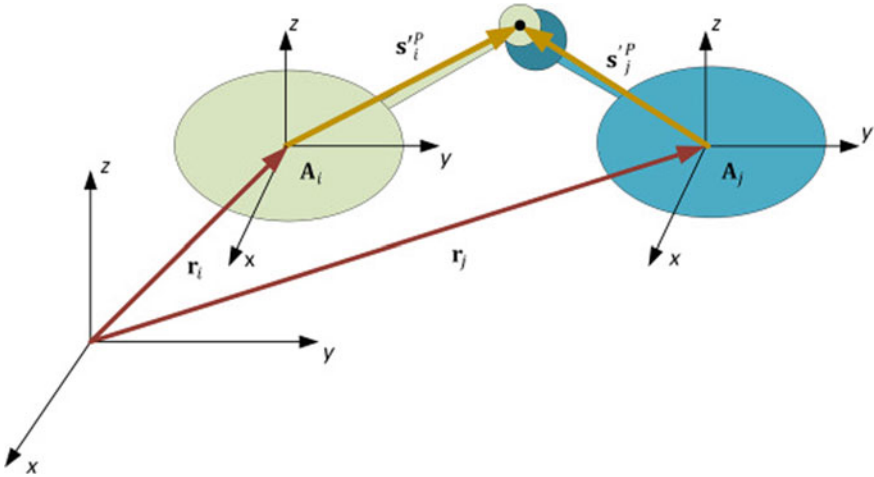
has the primary target to obtain more precise manipulation of any technological tool, the manipulator stiffness helps in defining the positioning errors caused mostly by external and internal loading. Recent trends in the mechanical design of manipulators that have been targeted as essential and have the required reduction of moving masses have resulted in an increase in rigidity.

## 2 Related Work

The development of multi-DOF mechanisms, actuators, and integrated robot joints is ongoing and is responsive to social needs. Robots will become smaller, less expensive, and more functional if many degrees of freedom (DOF) can be operated in a single joint. Several methods and actuators for integrating several DOF in a single joint (contact surface) have been proposed. A sphere and multiple strategically arranged friction wheels constitute a traditional system that employs friction to transmit force [1–4]. Conventional methods allow for limitless motion with three rotational degrees of freedom (R-DoF), but the frictional losses are insignificant. This problem has been resolved in recent years by replacing the friction wheel with an omni-wheel [5–9]. However, slippage prevents the effective transfer of high torque and precise positioning without external three-dimensional sensors. The gear-based joint drove three R-DoFs without slippage. These capabilities were inspired by the unique interactions between two different innovative gears [the cross-spherical gear (CS-gear) and monopole gear (MP-gear)] and the superimposition of those interactions by the quadrature spherical tooth structure of the CS-gear [8]. However, without external three-dimensional sensors, slippage restricts the effective transfer of high torque and precise positioning. High-frequency vibrations from piezoelectric or magneto-strictive elements are used in other methods [10–15]. These designs admit a wide velocity range and compact design owing to their simple construction, but they do not address the concerns mentioned in earlier mechanisms. There have also been proposals for noncontact transmissive spherical actuators, which are three-dimensional expansions of induction or stepping motors [16–21]. Design, analysis, and novel spherical actuator development, and techniques for optimal solution to differential equations involved are shown in [22–26]. Nonlinear random fluctuations in the feedback controller and a rotor orientation measurement principle technique discussed in [27, 28].

## 3 Spherical Joint Geometry

The spherical joint model is illustrated in Fig. 1. Constraint equations are formulated based on the location of the joint center relative to the two segments to ensure that the global positions of these points are the same:



**Fig. 1** Model of a spherical joint between the *i*th and *j*th segments connected at a point with local coordinates for the *i*th and *j*th segments [29]

$$\Phi^{(s,3)}(q, d) = r_i + A_i S_i^P - (r_j + A_j S_j^P) = 0$$

The superscript (*s*, 3) denotes that the constraint equation is for spherical joint *s*, and it contains three constraints [29].

### 4 Design of Joint

When a spherical joint was placed at the base of the manipulator, we reduced the number of links and joints in the configuration of the conventional manipulator while maintaining a similar workspace. SolidWorks is used for 3D modeling and to perform strength analyses of components, and the Fusion 360 package is used for animation of the assembly (Table 1).

The angle between the actuating unit (piston) and the top mount increases in proportion to the stroke of the piston by 28.5° (0.25 × 112). The design of the spherical joint consists of eight parts, as follows (Table 2).

**Table 1** Modeling parameters for workspace maintenance

Parameters	Description	Value
Length of piston	Length of piston	20 mm
Stroke length	Stroke length of piston	05 mm
Ratio	5/20	0.25
Piston-mount angle	The maximum angle between the actuating unit and top mount	112°

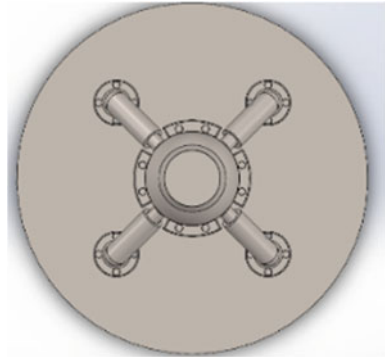
**Table 2** Parts of spherical joint

Part name	Description
Top mount	Next joint will be connected to this part
Bottom	Attaches top mount with actuators
Piston	Maneuvers the joint with relative stroke length
Piston cylinder	Holds the piston
Base plate	Supports and holds the joint together
Bolt	5 mm, 1 mm
Nut	5 mm

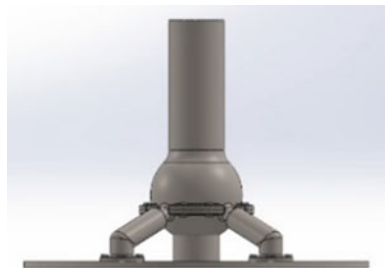
### 5 3D Model: Isometric Views of Spherical Joint

See Figs. 2, 3, and 4.

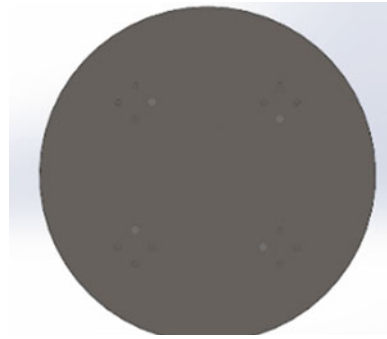
**Fig. 2** Top view



**Fig. 3** Front view





**Fig. 4** Bottom view**Table 3** Mass properties of assembly

Parameter	Value
Material	Mild steel
Yield strength	620.42 MPa
Factor of safety	1.2
Mass	1007.37 g
Volume	130,827.86 mm <sup>3</sup>
Surface area	64,897.50 mm <sup>2</sup>

## 6 Mass Properties of Assembly

Mass of the assembly is determined using mass properties feature in Solidworks software (Table 3).

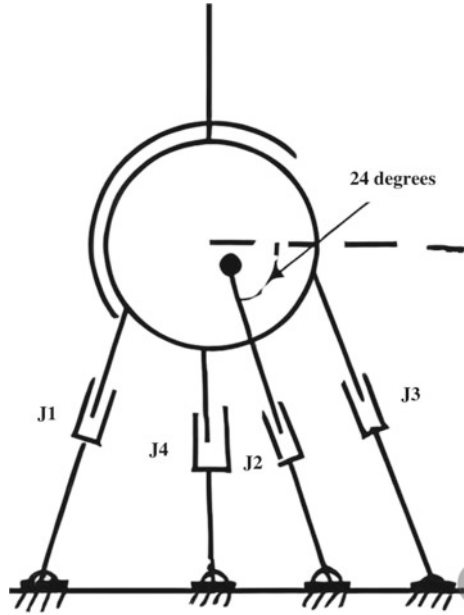
## 7 Kinematic Representation of Assembly

The connectivity of the links and joints in the mechanism is expressed in a kinematic diagram (Fig. 5) rather than the dimensions or shapes of the elements. The stroke lengths of the four linear actuators ( $J_1$ ,  $J_2$ ,  $J_3$ , and  $J_4$ ) are set relative to the position of the top mount required in the workspace.

## 8 Workspace Evaluation

The joint workspace is the region in which the mechanism operates. Figures 6 and 7 show the workspace generated and section view for the spherical joint.

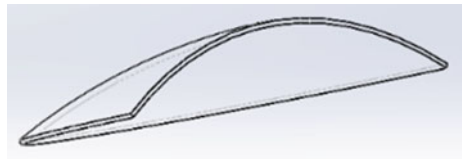
**Fig. 5** Kinematic representation



**Fig. 6** Workspace generated

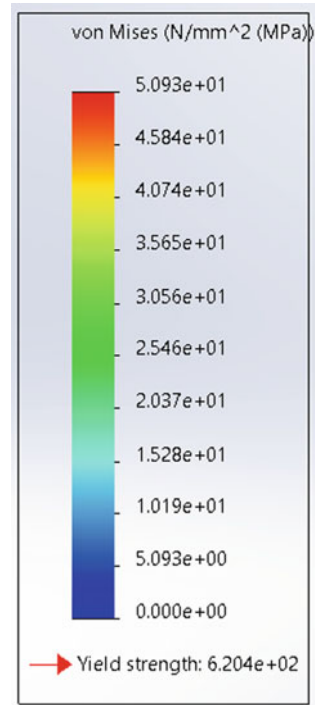


**Fig. 7** Section view of the workspace



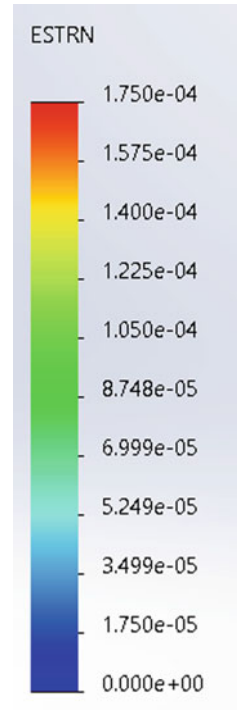
## 9 Strength Analysis Result of Assembly

We consider the case of joint orientation at a maximum value of  $28.5^\circ$ . The permissible design stress value was 513.9 MPa, and the permissible force limit was 1273 N. The angle between the top mount and the actuating unit is  $114^\circ$ . The strength analysis results of the assembly are shown in Figs. 8 and 9, respectively.

**Fig. 8** Stress analysis

## 10 Conclusion and Future Scope

This study proposes a new spherical joint mechanism based on linear actuators. This mechanism can actively drive the three R-DoFs. The interaction of linear displacement of actuating units was imposed on the top mount. The force-acting points of the linear actuators were selected as design parameters. The linear actuators were determined based on the workspace evaluation. The aimed position of the top mount was achieved using the relative displacements of the actuating units. The functional design and strength analyses have been previously described. By changing the joint configuration, two new types of mechanisms were obtained. Future work will be focused on the rotary actuation-based mechanism analysis, and a complete dynamic analysis of the manipulator is required.

**Fig. 9** Strain analysis

## References

1. Deninson JZA (1930) Vericle. U.S. Patent US1928412 A, Jan 1930
2. Isely WH (1964) Control apparatus. U.S. Patent US3267755 A, Apr 1964
3. Kimura A, Matsuzaki M, Tanaka A, Inoue M (1992) Lens frame supporting mechanism. U.S. Patent US5502598 A, Nov 1992
4. Keshtkar S, Moreno JA, Kojima H, Hernández E (2018) Design concept and development of a new spherical attitude stabilizer for small satellites. *IEEE Access* 6:57353–57365
5. Robinson J, Holland J, Hayes M, Langlois R (2005) Velocity-level kinematics of the atlas spherical orienting device using omni-wheels. *Trans Can Soc Mech Eng* 29(4):691–700
6. Kumagai M, Ochiai T (2009) Development of a robot balanced on a ball—application of passive motion to transport. In: *IEEE international conference on robotics and automation*, pp 4106–4111
7. Tsumaki Y, Ohgi T, Niiyama A (2010) A spherical haptic interface with unlimited workspace. *Int J Smart Sens Intell Syst* 3(3):691–700
8. Abe K, Tadakuma K, Tadakuma R (2021) ABENICS: Active ball joint mechanism with Three-DoF based on spherical gear meshings. *IEEE Transactions on Robotics*. 37(5):1806–1825
9. Ueno T, Saito C, Imaizumi N, Higuchi T (2018) Miniature spherical motor using bimetal of magnetostrictive materials. In: *Proceedings of the Japan joint automatic control conference*, vol 50, pp 18–18
10. Lu B, Aoyagi M (2012) Examination of an outer-rotor-type multidegree-of-freedom spherical ultrasonic motor. In: *Proceedings 15th international conference electrical machines systems*, pp 1–5
11. Paku H, Uchiyama K (2015) Satellite attitude control system using a spherical reaction wheel. *Appl Mechanics Mater* 798:256–260

12. Williams FC, Laithwaite ER, Eastham JF (1959) Development and design of spherical induction motors. *Proc IEE—Part A: Power Eng* 106(30):471–484
13. Kaneko K, Yamada I, Itao K (1989) A spherical DC servo motor with three degrees of freedom. *J Dyn Syst Meas Control* 111(3):398–402
14. Lee K, Kwan C (1991) Design concept development of a spherical stepper for robotic applications. *IEEE Trans Robot Automat* 7(1):175–181
15. Lee K, Son H, Joni J (2005) Concept development and design of a spherical wheel motor (SWM). In: *Proceedings IEEE international conference on robotics and automation*, pp 3652–3657
16. Yano T, Suzuki T, Sonoda M, Kaneko M (1999) Basic characteristics of the developed spherical stepping motor. In: *Proceedings 1999 IEEE/RSJ international conference on intelligent robots and systems. Human and environment friendly robots with high intelligence and emotional quotients*, vol 3, pp 1393–1398
17. Gofuku A, Sasaki R, Yano T, Wada Y, Shibata M (2012) Development of a spherical stepping motor rotating around six axes. *Int J Appl Electromagn Mechanics* 39(1/4):905–911
18. Kumagai M, Hollis RL (2013) Development and control of a three DOF spherical induction motor. In: *Proceedings IEEE international conference on robotics and automation*, pp 1528–1533
19. Kim H, Kim H, Ahn D, Gweon D (2013) Design of a new type of spherical voice coil actuator. *Sens Act A: Phys* 203:181–188
20. Nagarajan U, Kantor G, Hollis R (2014) The ballbot: an omnidirectional balancing mobile robot. *Int J Robot Res* 33(6):917–930
21. Gupta B, Singla R (2022) On singular surface theory to study steepening of waves in non-ideal magnetogasdynamics. *Ricerche mat* 71:253–263
22. Kim HY, Kim H, Gweon D, Jeong J (2015) Development of a novel spherical actuator with two degrees of freedom. *IEEE/ASME Trans Mechatronics* 20(2):532–540
23. Fernandes JFP, Branco PJC (2016) The shell-like spherical induction motor for low-speed traction: electromagnetic design, analysis, and experimental tests. *IEEE Trans Ind Electron* 63(7):4325–4335
24. Gupta B, Jena J, Singla R (2022) Propagation, and interaction of waves in non-ideal magnetogasdynamics. *Ricerche mat*. <https://doi.org/10.1007/s11587-022-00734-0>
25. Li H, Li T (2018) End-effect magnetic field analysis of the Halbach array permanent magnet spherical motor. *IEEE Trans Magn* 54(4):1–9
26. Souza KN, Pontes RS, Oliveira AP, Barreto GA (2009) Design and control of a three-coil permanent magnet spherical motor. *Energies* 11(8), Art no 2009
27. Singla R, Agarwal V, Parthasarathy H (2015) Nonlinear robot teleoperation with random fluctuations in the feedback controller. In: *International conference on computer, communication and control (IC4)*, pp 1–6. <https://doi.org/10.1109/IC4.2015.7375514>
28. Chai F, Gan L, Chen L (2020) A novel tiered type permanent magnet spherical motor and its rotor orientation measurement principle. *IEEE Access* 8:15303–15312
29. Andersen MS (2021) Introduction to musculoskeletal modelling. In: *Computational modelling of biomechanics and bio tribology in the musculoskeletal system*, 2nd ed, pp 41–80

# Recent Progress in the Design of Solar Still: An Understanding and Comparison



Priyansh Gupta, Gopal Nandan, Syed M. I. Nakshbandi, Vishal Gaur, Anoop Kumar Shukla, Ramakant Shrivastava, and Arnav Kumar

**Abstract** In last two decades, significant efforts have been done to utilize solar energy for the production of drinkable water from saline or dirty water. This is preferred due its availability and renewability. Solar desalination concept is preferred due to its availability and renewability. This has potential to provide sustainable solution to solve water at the lowest cost and lower maintenance expenses. Sustained and concerted efforts are done worldwide to tap the available solar energy because of its free availability and also our conventional energy resources are depleted at faster rate. Continuous concerted endeavour is being taken by the researcher to further improve desalinated water yield per day. Convectional solar still has lower yield rate. The daily water yield can be increased further by using additional heat in the solar still by employing addition solar collectors. In this paper, application of addition solar collector has been modelled. Application of additional solar collector to further enhance the productivity of the solar still. Different modifications and the effect of modifications on the productivity of single as well as double slope solar still are vividly discussed. Application of phase change material in the basin has been also preferred by the researchers to utilize the solar still when the solar energy is not available.

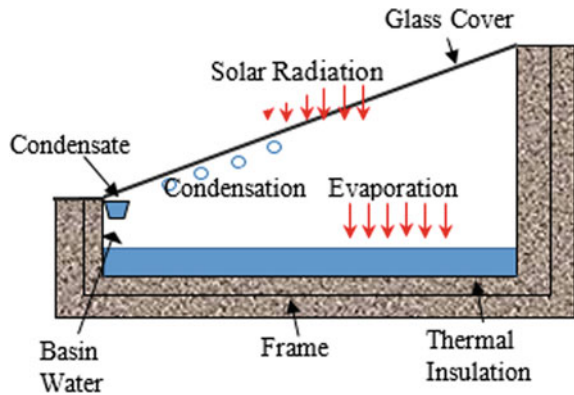
**Keywords** Water treatment · Desalination technologies · Solar collector

---

P. Gupta · G. Nandan (✉) · S. M. I. Nakshbandi · V. Gaur · A. K. Shukla  
Department of Mechanical Engineering, Amity University, Noida, Uttar Pradesh 201313, India  
e-mail: [gopalnandan@gmail.com](mailto:gopalnandan@gmail.com)

R. Shrivastava  
Government College of Engineering, Karad 415124, India

A. Kumar  
B. P. Mandal College of Engineering, Madhepura 852113, India

**Fig. 1** Solar desalination

## 1 Introduction

Water is the most abundant resources on the planet, covering over 75% of its surface. In the oceans, however, around 97% of it is salt water, and only about 3% is fresh water. Only about 1% of the pure water available is appropriate for human and animal consumption. A traditional solar still's maximum thermal efficiency can be as high as 30%, depending on sun intensity, location, time, and weather conditions [1–4]. From the literature, it has also been observed that it requires very little maintenance, with only cleaning, filling, and gathering of produce being required. The cost of distilled water is very low [5, 6]. The saline water in the trough absorbs most of the solar energy that passes through the cover. The lid and the trough absorb the remainder. As a result, the saline water becomes hot enough to evaporate as shown in Fig. 1.

Due to heat entry into the solar basin, evaporation takes place at the water-free surface and rises. Once vapour rises and touches the inner surface of the glass slope where it is condensed, water droplets are formed by releasing its latent heat. Finally, gravity causes the condensed water to flow down and collect in a collector.

## 2 Design of Solar Desalination System

Solar desalination is the process of eradicating salt from saline water that involves evaporation of saline water by utilizing solar energy [7]. Post evaporation, the vapour is condensed into pure freshwater as shown in Fig. 1. In solar still, salt and other contaminants are left behind. This technology can be used to achieve desalination in two ways: direct and indirect. Sunlight can generate heat for evaporative desalination procedure. In passive solar still, solar energy is utilized for evaporation at low temperatures, whereas active solar still, extra energy is utilized to speed up evaporation in the basin. Many researchers are investigating active techniques to increase solar still

production [8, 9]. In the majority of the works, the usage of solar concentrating collectors has been employed.

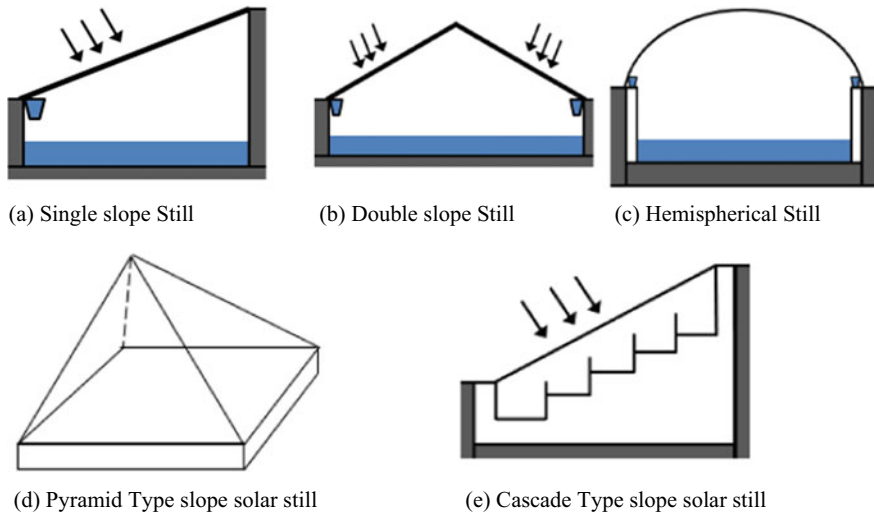
### 2.1 *The Essential Materials for Solar Desalination*

- I. Glazing should have a high solar transmittance, be opaque to heat radiation, be resistant to abrasion, have a long life, be inexpensive, have a good wet ability for water, be lightweight, easy to handle and apply, and be widely available. Glass or processed plastic was employed as the primary materials.
- II. Liner: It should absorb more solar radiation, be robust, watertight, easy to clean, low in cost, and able to tolerate temperatures of around 100 °C. Asphalt matt, black butyl rubber, black polyethylene, and other materials were used.
- III. Sealant should be able to withstand extremely low temperatures, be inexpensive, long-lasting, and simple to apply. Putty, tars, tapes, silicon, and sealer are among the materials utilized.
- IV. Basin tray: It should have a long lifespan, be corrosion resistant, and be inexpensive.
- V. Aluminium galvanized iron, concrete, plastic material, and other materials are utilized in the condensate channel.
- VI. Aluminium foil, mirror, high-grade PVC solar reflector cloth, grey polyester, and customized polycarbonate are examples of reflectors.

## 3 Classification Based on Type of Slope

- (a) **Single slope:** consists of a blackened basin filled with saline water at a shallow depth, with a transparent airtight cover that entirely encloses the space above the basin, shown in Fig. 2a. It is shaped like a roof. The cover, which is normally made of glass but can also be made of plastic, is angled towards a collection trough. Solar energy flows through the cover, absorbing and converting it to heat on the black surface. The vapour produced by heating the impure water in the basin or tray is condensed into purified water on the roof's cooler interior. The translucent roof material (mostly glass) broadcasts nearly all of the radiation it receives and absorbs very little, allowing the water vapour to condense. Condensed water runs down the slanted roof and collects in troughs at the bottom.
- (b) **Double slope:** This solar still is depicted in Fig. 2b. Two glasses are angled in a way that radiation comes from both sides in the basin. The productivity improves with the wind velocity due to cooling of glass cover in the double slope still.





**Fig. 2** Designs of solar stills

- (c) **Hemispherical solar still:** In the hemispherical, glass slope is changed to hemispherical shape as depicted in Fig. 2c. Condensation performance is improved with wind velocity, ambient temperature due to cooling of the glass cover.
- (d) **Pyramid solar still:** Its construction is very simple. The single glass top cover is replaced by triangular-shaped plane in the form of pyramid as shown in Fig. 2d. The basin area remains same, but condensing area increases several times as compared to the single slope [10, 11].

In Tamil Nadu, India, Prakash et al. [12] experimented with a single basin square pyramid solar still with wick material to boost yield. A saline water storage tank with four slanted portions was constructed in the still's basin, and selectively coated jute wick painted black was dispersed over the tilted portions, as illustrated in Fig. 2d. The production of this sort of still was found to be 17.68% higher than a simple pyramid solar still without a wick in the trial. The average still efficiency was 50.25%, while the new pyramid wick-type solar still produced 4.82 L/m<sup>2</sup> day.

- (e) **Cascade-type solar still:** A cascade-type solar still where the absorber is used with a covering of glass on top of still to construct a desalination chamber [13, 14]. A typical design of cascade type still is shown in Fig. 2e. The basin surface is painted black with a mixture of synthetic paint and black oxide so that it can absorb a greater amount of radiated energy from the sun. A reservoir holding brackish water was kept above the still, and water is fed in the chamber with an inlet port situated at the middle of the top edge. To collect condensed water from the still there was an outlet at the bottom right corner together with a small window with a removable glass cover to clean the dissipated salts in the still. Still at bottom of the device was insulated with sawdust and cock sheet.

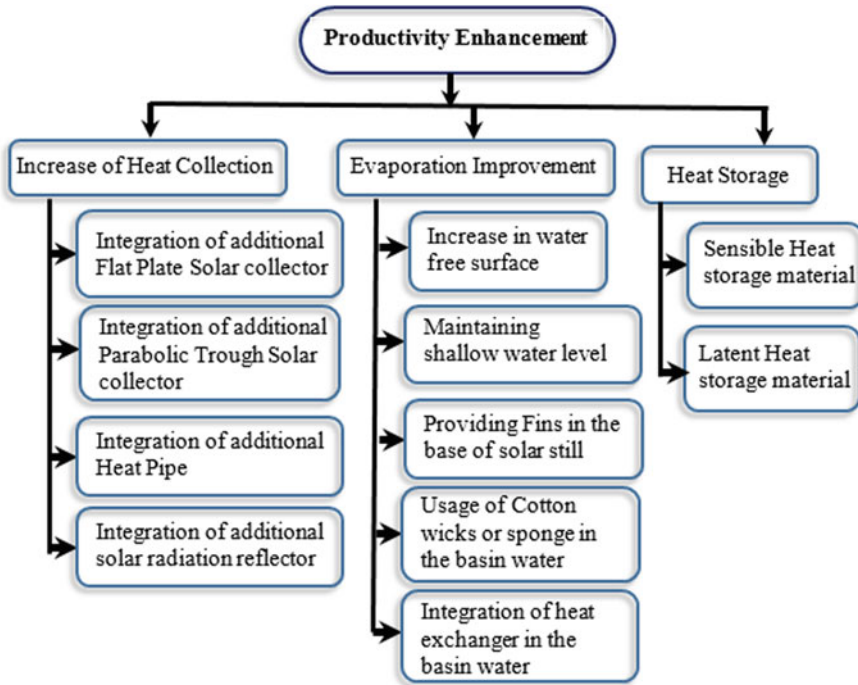
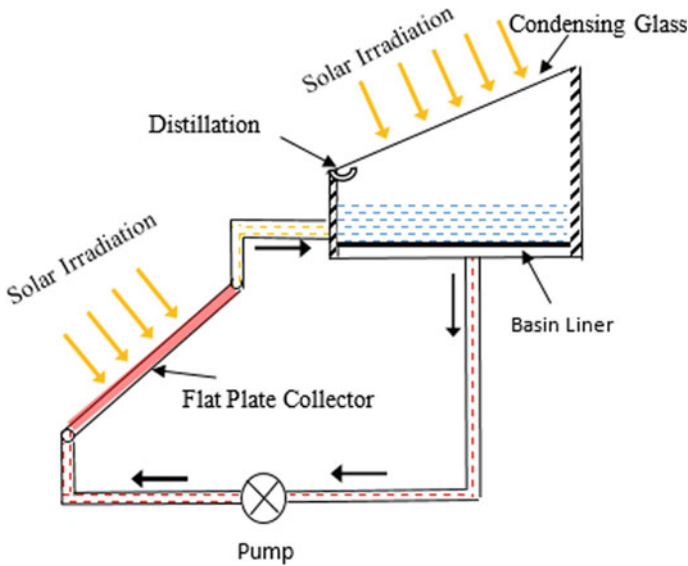


Fig. 3 Modification in the solar still to improve the productivity

- (f) **Productivity enhancement of solar still:** Daily production of the fresh water can be increased by (a) increase in the heat gain, (b) evaporation improvement, and (c) usage of heat storage material in the solar still. This has been depicted in Fig. 3.

#### 4 Increase in the Heat Collection

Evaporation rate in conventional or passive desalination systems is very low. The amount of heat required to facilitate the evaporation process in solar still basin is not sufficient in passive system. Due to low evaporation process, productivity of system is very low that’s why additional solar collector is attached to the system so that large amount of heat is available in the basin. Water is transported outside the basin where water is heated by passing through one of the collectors mainly (a) flat plate collector (FPC) and (b) parabolic trough collector (PTC). Sometimes, integration of more than one type of collector also has been done. Application of different collectors is discussed in the next section:



**Fig. 4** Integration of flat plate solar collector

#### **4.1 Integration of FPC**

The FPC integration with solar still will expedite heat gain in the basin (Fig. 4). Boukar and Harmim [15] attached additional FPC with still to increase heat supply in the still. Due to continual heating of basin water using additional heat by combining a solar flat plate increased the distillation many folds in a 24-h period. Production rate is higher at night in comparison with the day production rate because at night there is a stark difference between the water and the inner glass cover. Hot water as well as desalted water was collected, and the all-day productivity in this system is quite high. Integration of additional solar collector has been summarized in Table 1.

#### **4.2 Integration of PTC**

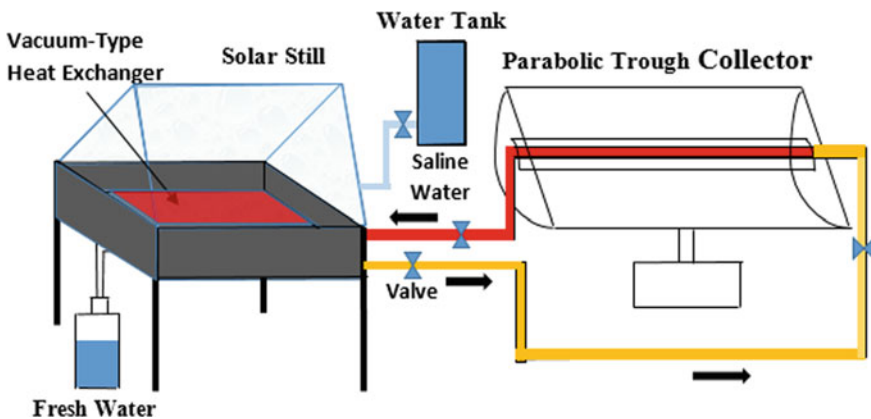
The heat collection at high temperature (less than 300 °C) can be attained using PTC. Researchers used addition PTC to heat the saline water in the basin. Using PTC, more heat collation at higher temperature can be achieved [20, 21]. The arrangement for the integration of additional PTC is depicted in Fig. 5. For heat transmission from the PTC to the basin water is done either by thermo-syphoning technique or by the forced convection by the application of addition fluid pump to circulate fluid in the heat receiver tube of the PTC. In the basin water, heat exchanger is kept submerged to proper heat transfer. The effectiveness of the heat exchange is important in the

**Table 1** Integration of external solar collectors

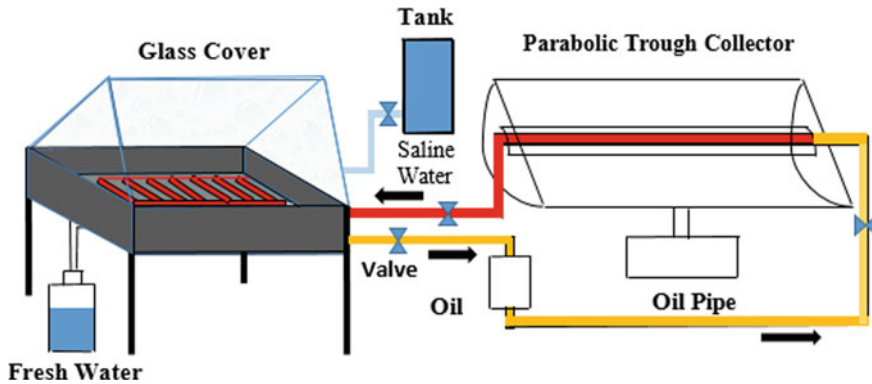
Ref. No.	Details of work	Salient observation
[16]	Heat exchanger having oil pinned-serpentine loop integrated with PTC	<ul style="list-style-type: none"> <li>Productivity in this modification increased by about 28% in reference with CSSS integrated with PTC</li> <li>Exergy as well as energy efficiencies both increased by significant amount</li> </ul>
[17]	Additional photo-voltaic thermal compound	Productivity improved
[18]	Integration of PTC and heat exchanger	Productivity improved
[19]	Integration with heat pipe, evacuated tube and PTC	<ul style="list-style-type: none"> <li>Hourly water production increased from 0.48 to 1.68 kg when oil is used as the additional fluid in gap of ETC and heat pipe in place of aluminium foil</li> <li>Higher evaporation rate is visible in this modification</li> </ul>

basin water. Normal surface heater has been replaced by the serpentine loop heat exchanger by Kabeel and Abdelgaied [22] as shown in Fig. 6. A still having double slope along with PTC make up this system. To maximize the basin’s absorptivity of solar radiation, all interior surfaces are painted of black colour—the basin dimension, 0.03 m thickness, 20 cm height timber frame, 170 cm length, 120 cm breadth [16]. A foam layer which helps to insulate the heat loss to the environment from the bottom and side walls is added.

Instead of plane tube, evacuated tube collectors (ETCs) are preferred for heat gain and reduce heat loss. The ETC can reach temperature beyond 200 °C. It is available in a variety of shapes and sizes. They are commonly built with twin glass tubes arranged in form of row which seems to be parallel, each having heat pipe of metal which is attached to an absorber fin. The fluid between the two glass tubes annulus



**Fig. 5** Integration a solar collector and a vacuum-type heat exchanger



**Fig. 6** Integration a solar PTC collector and serpentine loop heat exchanger

is extracted to create the vacuum for heat loss reduction. ETCs with a single wall are also prevalent. The air in the entire space within the tube is evacuated in this arrangement. As it does not require a metal-to-glass seal, the double-walled design is superior at maintaining vacuum, but the single-walled design absorbs more light and hence has higher thermal performance.

The heat was subsequently transmitted to water flowing via a manifold, and the condensed fluid descends to the heat pipe's bottom, where the cycle is repeated. In general, ETCs outperform the FPC in cold areas because their efficiency does not decline as quickly as FPC when the outside air temperature drops. ETC is used in the forced convection mode also to further increase the heat gain in the solar basin. In forced convection mode, an addition fluid pump is employed [23]. The glass cover transmits 95% of the sun light (short wave) inside, absorbed mainly by absorber (blackened) liner. The water pump draws water from the solar still and returns it after passing it via evacuated tubes. An ETC consists of a series of tubes of material borosilicate which is concentric having inclination of a  $45^\circ$  to horizontal, and annular space is vacuum in nature. Outside surface of inner glass tube is painted black and some special coating has applied over it to absorb maximum radiation of sun. Radiation absorbs by these tubes must be transferred to water within the tubes.

### **4.3 Integration of Additional Heat Pipe**

This setup contains a collector of parabolic shape which collect sun rays at the line which is in focus plane. In addition, to absorb radiation, a heat pipe in which ethanol is partially filled is inserted within a twin glass evacuated tube collector (TETC) and placed along focal line of collector [24]. Rays which are parallel falling on the reflector got reflected back to the TETC, when the parabola is pointed towards the sun. The TETC's inner blackened surface is heated by the concentrated radiation that

reaches it. To maximize absorption of heat, blackened TETC from inside is preferred. Because high rate of heat absorption is there, ethanol evaporates within the heat pipe and moves upward, eventually reaching the heat pipe's condenser. The heat pipe's condenser section is placed within a basin having brackish water, forcing condenser to provide heat to the basin water and facilitate boiling to occur.

#### 4.4 Additional Solar Radiation Reflector

Integration of radiation reflector and external condenser improved performance [25]. The heat exchanger is utilized in still basin to ramp up the evaporation process. Thermo-syphoning is used in transported the heat exchanger via evacuated tubes. To increase condensation rate of the vapours, condenser which is external and having copper pipes is used. Copper pipe having spiral in shape is fully immersed in a saline water. Heat gain the solar still is further enhanced by modifications in the reflector reported by the researchers (Refer Table 2).

### 5 Evaporation Improvement

Productivity of the solar still depends on the evaporation rate of the saline water. The evaporation takes place at water free surface. Hence, increase in the water free surface area will increase the evaporation. This also has been observed that maintaining shallow water level in the water tank also improves the desalination. In cascade-type solar still, very thin water layer can be maintained. Table 3 summarizes the various design modification to further increase in the evaporation rate due increase in the

**Table 2** Summary of design modifications

Researchers	Modifications	Results
Omara et al. [26]	With internal reflector	<ul style="list-style-type: none"> <li>Without internal reflector productivity is 57%, whereas with integration the productivity increased by 75%</li> <li>Daily efficiency increased by 56 and 53%, respectively</li> </ul>
Srivastava and Agrawal [27]	Single slope still with blackened jute cloth in basin and external reflector	<ul style="list-style-type: none"> <li>With the modified still, the distillate gain was 68%, and with the dual reflectors, the distillate increase was 79%</li> <li>Application of absorber plate and two-side reflectors improved productivity</li> </ul>
Tanaka et al. [28]	Single slope still with varying in the inclination angle of external reflector	<ul style="list-style-type: none"> <li>Optimum inclination angle for reflector for spring, summer, and winter seasons is different</li> </ul>

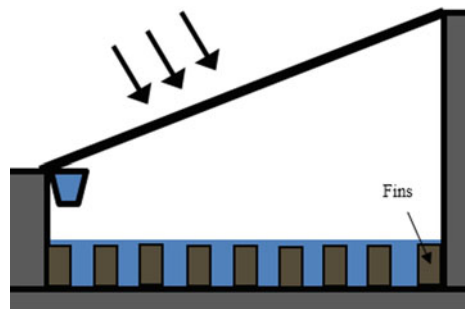
overall heat gain. Ziabri et al. [29] obtained 6.7 L/m<sup>2</sup> day distillate with cascade-type with varying condensing cover inclination. With double-slope CSS by varying glass cover thickness Boodhan and Haraksingh [30] conducted experiment and found average daily efficiency of 29.28%. It has been found that when finned body is kept at the bottom of the solar basin, productivity improved [31]. Usage of fin integration in the basin base is shown in Fig. 7. The parametric effects of the fin geometry are:

- (i) Effect of fin: The use of fins at bottom of solar still basin. It improves the evaporation of water and consequently productivity increases. Productivity is directly influenced by fin geometry. Total distillate yield and efficiency are improved by increasing fin height while fin thickness, and number of fins decreases overall distillate output and efficiency. When the volume of basin water is raised, it has

**Table 3** Design modification to increase heat gain

Researchers	Modifications	Results
Rajamanickam and Ragupathy [32]	Water depth variation with double slope still	<ul style="list-style-type: none"> <li>• Productivity decreases with water depth increase</li> </ul>
Sathyamurthy et al. [33]	Triangular pyramid with paraffin wax in the basin	<ul style="list-style-type: none"> <li>• Productivity increased by 20% due to PCM application</li> </ul>
Ahsan et al. [34]	Tubular solar still with polythene film as condensing cover material	<ul style="list-style-type: none"> <li>• The fabrication cost and weight of the new TSS were reduced by 92 and 61%, respectively</li> <li>• Temperature differential inside the still was found to be equal to distillate output</li> </ul>
Abdul Jabbar N Khalifa [35]	Single and double slope with ideal tilt angle	<ul style="list-style-type: none"> <li>• Ideal cover tilt angle is close to the latitude angle</li> </ul>
Arjunan et al. [36]	Various types of heat energy storage material	<ul style="list-style-type: none"> <li>• Black granite gravel is more efficient energy storage medium, which provided 9.7% more as compared to the standard solar panels</li> </ul>

**Fig. 7** Single slope solar still with fin



an impact on productivity. Because of the greater shadow area of the fin, the solar still improves as the height of the fins increases.

- (ii) Effect of Various Frameworks on Solar Still: The efficiency and productivity of declines with upliftment in a mass of water during daytime and increases throughout night hours due to increase in water mass due to increase in basin water’s heat capacity, which increases temperature between water and glass.
- (iii) Effect of Fin Height: Surface area of the finned plate increases with the up-gradation of the height of the fins which overall increases the area for absorption of solar radiation, the transfer of heat from finned plate to basin water is increased as well.
- (iv) Effect of Fin Thickness: The yield of fin is affected by fin thickness as it decreases the process of evaporation as it declines the horizontal effective area of the basin due to which, amount of sunlight entrapped by basin liner reduces.
- (v) Effect of Number of fins: Distillate output is dependent upon fins number that are employed in the basin. Water production continues to decline with an increase in fin number as there is upliftment in shadow area when fin number increases.

### 5.1 Usage of Heat Storage Material

Use of phase change materials (PCMs) by placing in the basin water, may increase the time of operation of the solar still. The PCM stores heat energy by meting during daytime when excess heat energy is available and release the heat energy in the absence of sun [37–39]. These ways, the still will work in the night-time also. The PCM is employed directly in basin or in the form of capsule. The PCM suitable for solar distillation process has been summarized in Fig. 8 by classifying it into three categories. Table 4, presents thermal properties of PCM, which has been applied by several researchers.

A CSS provides fresh water only in daytime when the sun is available. Tiwari et al. [40] described suitable PCM used in the solar still. The tray is designed with

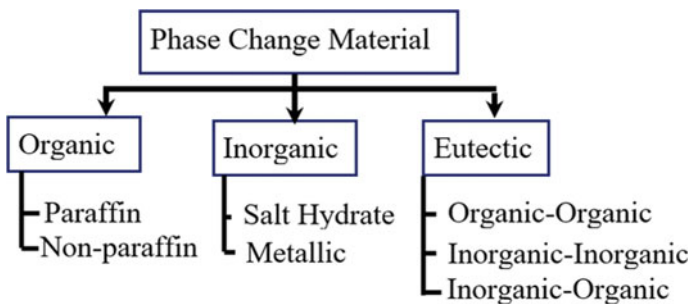


Fig. 8 Classification of PCM



**Table 4** Properties of PCM

Properties	Stearic acid	Paraffin wax	Sodium thiosulphate pentahydrate	Capric palmitic	CaCl <sub>2</sub> ·0.6H <sub>2</sub> O
Melting temperature (°C)	52	56	48.5	22.5	29.8
Thermal conductivity (W/mK)	0.29	0.24	0.57	0.14	1.08
Specific heat (kJ/kg-K for solid)	1.59	2.51–2.95	–	2	1.4
Latent heat of fusion (kJ/kg)	169	226	208.5	173	191
Density (kg/m <sup>3</sup> )	847	760–818	1730	870	1710

vertical pipes to allow the melted PCM to overflow. This occurs when the volume increases due to melting. Thermo-physical characteristics which are possessed by PCM in desalination systems are summarized in Table 4.

Other than the top cover, the other sides are thermally insulated to decrease heat loss. The basin water absorbs incident sunlight. The PCM is on the other side of the linings. As a result, heat is transported to the PCM via convection in saline water, followed by conduction in the liner. The heat in the PCM is intelligently stored before it reaches its melting temperature. The heat is then stored as sensible heat once it changes phase [41–43]. When the sun's radiation falls (in the afternoon), so does the temperature. The PCM provides heat throughout this time. This is referred to as discharging, and solidification occurs. The operation is repeated until complete solidification occurs.

Incorporating PCM into solar stills guarantees continuous operation, i.e., the solar still will operate regardless of the presence of the sun. To increase performance, researchers attached different solar collectors. The flat plate is used to gather heat energy at temperatures up to 90 °C [44]. Heat transfer fluids in PTC can reach temperatures of up to 350 °C [45]. Heat energy which is collected is transferred to the water (saline) preset in still to increase evaporation. The heat energy which is not used must be trapped in the PCM in the form of latent heat. The use of twisted tubes in the tube, the use of designed working fluids, and other techniques improve heat collection in the collector. According to various researchers, heat transport from the collector to the sun is still done using either active or passive methods. The usage of PTC and flat plate collectors increased heat transfer rate without using any tracing device and boosted productivity [9].

### 5.1.1 Integration of PCM and FPC

A FPC is attached to solar still, a glass cover cooling unit, and tubes of PCM which are immersed in basin [46]. The only work of solar collector here is to increase the temperature of water of still basin by heating up the water flows through FPC. Concurrently, the water present in the still absorbed the sun energy that after passing the glass cover reaches up to still basin water. Then comes the role of PCM, as the temperature of basin falls below the melting point of PCM, the PCM helps the system to continue evaporation process by providing energy, which is stored in it earlier, the stored energy in the PCM is consumed. The heat lost by the system is subsidized in this situation by the fusion heat emitted as the PCM solidifies. After nightfall, the PCM maintains production steady, while the evaporation process proceeds. The solar still's inner glass ought to cool because the temperatures achieved in the heat up process are very high. The linked cooling unit performs this job. As solar collector along with cooling unit is present, the examined system has the capacity to achieve significant evaporation rate as well as condensation flow rates. Furthermore, even with the cooling of the system started in the afternoon and after nightfall, its output continues.

Al-harashsheh et al. [47] used external solar radiation reflector in the study. The basin features a multilayer glass cover with two 1 cm separated glass layers. To increase the productivity, evaporation and condensation rate is equally important, that's why in this double-glass layer is fabricated and between the gap the cooled water is passed so that the temperature of inner side of glass on which condensation supposed to take place remain cooled. So, after facilitating the condensation, more and more condensate formed and drip down to the channel present at the end of glass surface and from that channel water is collected in a vessel. A distilled water tub is affixed to the bottom of the solar still in stainless steel. The PCM was poured into each tube. The unit's functioning consists of process: heat addition and heat removal. Heat addition process is heating of water present in the basin from direct solar irradiation, and store the remaining energy with the help of PCM throughout the day. Heat discharge, on the other hand, governs for recollecting the energy stored in the PCM backwater for heating at night. As a result, operations can run continuously for 24 h.

### 5.1.2 Integration of PCM Additional PTC and Heat Exchanger

The gap available between the vessel of absorber and basin was filled by PCM of thickness 3 cm [22, 47, 48]. PCM is a thermal energy storage media that is both latent and sensible. So aluminium sheet highly polished is used which concentrate sunlight on the tube passes parallel to PTC at a distance of focus with help of a parabolic concentrator of cylindrical shape. This aluminium reflector has solar coating which is unique. The receiver is made of a copper absorber tube covered by a glass evacuated tube, in such a way that vacuum must be present in the space between tube (copper) and the glass tube in order to minimize loss due to natural convection. The serpentine

loop is there with 12 passes, and oil is flowing within it and the material of which it is made up of is copper. The heat exchanger must be immersed in the water of basin then only it can serve its purpose. Black paint coat is also applied on copper tube, to increase absorption rate of solar radiation during sunshine.

## 6 Conclusion

Based on the recent research paper available, the following conclusions are drawn:

- Sun tracking systems improve solar collection in the solar still. Use of additional internal and exterior reflectors also increases heat collection in the still.
- A solar still's distillate output is greatly improved by increase in the evaporation rate, condensation rate, condensation cover cooling, and the use of wicks.
- Environmental factors such as solar radiation, temperature, and wind speed have a direct impact on distillate output.
- The basin water depth has a significant impact on the solar stills' production. Freshwater production continues to decline as the basin's water depth rises. The maximum productivity was found observed at a water depth of 40 cm in the basin.
- Due to the lower water layer and more exposed area for evaporation, solar still of cascade-type has a more productivity rate than a flat horizontal collector.
- The depth of water in the basin has a significant impact on production of still. In the CSSS basin, decrement in freshwater productivity has been observed as depth of water in basin rises.
- The use of ETC in conjunction with solar still having single slope increased temps and yields of water. For 0.01 m depth of water in basin and a flow rate (mass) of 0.006 kg/s, per day yield come out as 3.47 kg/m<sup>2</sup>. Yearly yield per m<sup>2</sup> attained is 567.3 kg.
- Adding the second and third collectors to a solar still basin having single slope increased output by 48 and 23% in the summer.
- Application PCM and integration of solar collector further improvement daily freshwater production.
- When water vapour is travelling through long path, the everyday yield falls as between the cover of glass and absorber the air gap increases. Depth of water, inclination of condensing cover, and area of collector each affect annual yield.

## References

1. Hamed O, Eisa E, Abdalla W (1993) Overview of solar desalination. *Desalination* 93:563–579
2. Taghvaei H, Taghvaei H, Jafarpur K, Estahbanati MK, Feilizadeh M, Feilizadeh M, Ardekani AS (2014) A thorough investigation of the effects of water depth on the performance of active solar stills. *Desalination* 347:77–85

3. Singh AK, Dwivedi G, Srivastava BK, Tiwari BK, Kumar P, Yadav R, Singh M, Shukla AK, Nandan G (2021) Study of analytical observations on energy matrix for solar stills. *Mater Today: Proc*
4. Hedayatizadeh M, Sarhaddi F, Pugsley A (2020) A detailed thermal modeling of a passive single-slope solar still with improved accuracy. *Groundw Sustain Dev* 11:100384
5. Wani NA, Nandan G (2019) Modelling of solar parabolic trough collector considering unsymmetrical heat flux. In: 3rd International conference on recent developments in control, automation and power engineering (RDCAPE). IEEE
6. Singh AK, Srivastava B, Shankar V, Prasad R, Yadav R, Shukla AK, Nandan G, Kumar P (2021) Energy matrices and enviroeconomical perspective of solar decontamination system. *Mater Today: Proc* 46:5464–5468
7. Bachchan AA, Nakshbandi SMI, Nandan G, Shukla AK, Dwivedi G, Singh AK (2020) Productivity enhancement of solar still with phase change materials and water-absorbing material. *Mater Today: Proc*
8. Singh AK, Kumar P, Kishore R, Singh P, Kant N, Singh P, Nandan G, Jaiswal A, Prasad R (2021) Stumpy-paced green power generation system. In: 2021 4th International conference on recent developments in control, automation and power engineering (RDCAPE). IEEE
9. Nandan G (2019) Performance of solar photovoltaic panel using forced convection of water-based CuO nanofluid: an understanding. *IOP Conf Ser: Mater Sci Eng* 691:012088
10. Sathyamurthy R, Kennady HJ, Nagarajan P, Ahsan A (2014) Factors affecting the performance of triangular pyramid solar still. *Desalination* 344:383–390
11. Kumar PN, Manokar AM, Madhu B, Kabeel A, Arunkumar T, Panchal H, Sathyamurthy R (2017) Experimental investigation on the effect of water mass in triangular pyramid solar still integrated to inclined solar still. *Groundwater Sustain Dev* 5:229–234
12. Prakash A, Jayaprakash R, Kumar S (2016) Experimental analysis of pyramid wick-type solar still. *Int J Sci Eng Res* 7:1797–1804
13. Dashtban M, Tabrizi FF (2011) Thermal analysis of a weir-type cascade solar still integrated with PCM storage. *Desalination* 279:415–422
14. Sarhaddi F (2018) Exergy analysis of a weir-type cascade solar still connected to PV/t collectors. *IET Renew Power Gener* 12:1336–1344
15. Boukar M, Harmim A (2001) Effect of climatic conditions on the performance of a simple basin solar still: a comparative study. *Desalination* 137:15–22
16. Fathy M, Hassan H, Ahmed MS (2018) Experimental study on the effect of coupling parabolic trough collector with double slope solar still on its performance. *Sol Energy* 163:54–61
17. Singh D, Tiwari G (2016) Effect of energy matrices on life cycle cost analysis of partially covered photovoltaic compound parabolic concentrator collector active solar distillation system. *Desalination* 397:75–91
18. Hosseini A, Banakar A, Gorjian S (2018) Development and performance evaluation of an active solar distillation system integrated with a vacuum-type heat exchanger. *Desalination* 435:45–59
19. Rufuss DDW, Arulvel S, Kumar VA, Davies P, Arunkumar T, Sathyamurthy R, Kabeel A, Vishwanath MA, Reddy DSC, Dutta A, Agrawal M, Hiwarkar VV (2021) Combined effects of composite thermal energy storage and magnetic field to enhance productivity in solar desalination. *Renew Energy*
20. Tiwari GN, Dimri V, Singh U, Chel A, Sarkar B (2007) Comparative thermal performance evaluation of an active solar distillation system. *Int J Energy Res* 31:1465–1482
21. Sekhar TVR, Nandan G, Prakash R, Muthuraman M (2018) Modeling a Renewable Energy Collector and Prediction in Different Flow Regimes Using CFD. *Materials Today: Proceedings* 5(2):4563–4574
22. Kabeel A, Abdelgaied M (2017) Observational study of modified solar still coupled with oil serpentine loop from cylindrical parabolic concentrator and phase changing material under basin. *Sol Energy* 144:71–78
23. Kumar S, Dubey A, Tiwari G (2014) A solar still augmented with an evacuated tube collector in forced mode. *Desalination* 347:15–24

24. Mosleh HJ, Mamouri SJ, Shafii M, Sima AH (2015) A new desalination system using a combination of heat pipe, evacuated tube and parabolic trough collector. *Energy Convers Manage* 99:141–150
25. Bhargva M, Yadav A (2019) Productivity augmentation of single-slope solar still using evacuated tubes, heat exchanger, internal reflectors and external condenser. *Energy Sour Part A: Recov Util Environ Effects*:1–21
26. Omara Z, Kabeel A, Younes M (2014) Enhancing the stepped solar still performance using internal and external reflectors. *Energy Convers Manage* 78:876–881
27. Srivastava PK, Agrawal S (2013) Experimental and theoretical analysis of single sloped basin type solar still consisting of multiple low thermal inertia floating porous absorbers. *Desalination* 311:198–205
28. Tanaka H (2011) A theoretical analysis of basin type solar still with flat plate external bottom reflector. *Desalination* 279:243–251
29. Ziabari FB, Sharak AZ, Moghadam H, Tabrizi FF (2013) Theoretical and experimental study of cascade solar stills. *Sol Energy* 90:205–211
30. Boodhan MK, Haraksingh I (2014) An investigation into the effect on the productivity of cascade-type solar distillation systems with varying cover thicknesses and still orientations under tropical Caribbean climatic conditions. *Desalin Water Treat* 55:3295–3302
31. Xiong J, Xie G, Zheng H (2013) Experimental and numerical study on a new multi-effect solar still with enhanced condensation surface. *Energy Convers Manage* 73:176–185
32. Rajamanickam MR, Ragupathy A (2012) Influence of water depth on internal heat and mass transfer in a double slope solar still. *Energy Procedia* 14: 1701–1708
33. Sathyamurthy R, Nagarajan P, Kennady HJ, Ravikumar T, Paulson V, Ahsan A (2014) Enhancing the heat transfer of triangular pyramid solar still using phase change material as storage material. *Front Heat Mass Transf* 5
34. Ahsan A, Imteaz M, Rahman A, Yusuf B, Fukuhara T (2012) Design, fabrication and performance analysis of an improved solar still. *Desalination* 292:105–112
35. Khalifa AJN (2011) On the effect of cover tilt angle of the simple solar still on its productivity in different seasons and latitudes. *Energy Convers Manage* 52:431–436
36. Arjunan TV, Aybar HS, Sadagopan P, Chandran BS, Neelakrishnan S, Nedunchezian N (2013) The effect of energy storage materials on the performance of a simple solar still. *Energy Sour Part A: Recov Util Environ Effects* 36:131–141
37. Vadhera J, Sura A, Nandan G, Dwivedi G (2018) Study of phase change materials and its domestic application. *Mater Today: Proc* 5(2):3411–3417
38. Shalaby S, El-Bialy E, El-Sebaei A (2016) An experimental investigation of a v-corrugated absorber single-basin solar still using PCM. *Desalination* 398:247–255
39. Naveenkumar R, Divakaran S, Aravinthasamy P, Eswaraaravinth R, Ganesan N, Ravichandran M (2020) Role of phase changing materials and other parameters to enhance the thermal performance of solar still. *Mater Today: Proc*
40. Tiwari AK, Nandan G, Sharma SK, Shrivastava R, Singh AK, Kumar S (2021) Productivity enhancement of solar still using phase change material. In: 2021 4th International conference on recent developments in control, automation and power engineering (RDCAPE), IEEE
41. Mousa H, Gujarathi AM (2016) Modeling and analysis the productivity of solar desalination units with phase change materials. *Renew Energy* 95:225–232
42. El-Sebaei A, Al-Ghamdi A, Al-Hazmi F, Faidah AS (2009) Thermal performance of a single basin solar still with PCM as a storage medium. *Appl Energy* 86:1187–1195
43. Radhwan AM (2005) Transient performance of a stepped solar still with built-in latent heat thermal energy storage. *Desalination* 171:61–76
44. Sharma S, Tiwari S, Tiwari AK, Nandan G, Prakash R (2020) Thermal performance enhancement of flat-plate solar collector using CeO<sub>2</sub> water nanofluid. In: *Advances in solar power generation and energy harvesting*. Springer Singapore, pp 109–118
45. Sekhar TVR, Prakash R, Nandan G, Muthuraman M (2018) Performance enhancement of a renewable thermal energy collector using metallic oxide nanofluids. *Micro & Nano Lett* 13:248–251

46. Abu-Arabi M, Al-harashsheh M, Ahmad M, Mousa H (2020) Theoretical modeling of a glass-cooled solar still incorporating PCM and coupled to flat plate solar collector. *J Energy Storage* 29:101372
47. Al-harashsheh M, Abu-Arabi M, Mousa H, Alzghoul Z (2018) Solar desalination using solar still enhanced by external solar collector and PCM. *Appl Therm Eng* 128:1030–1040
48. Faegh M, Shafii MB (2017) Experimental investigation of a solar still equipped with an external heat storage system using phase change materials and heat pipes. *Desalination* 409:128–135

# Aerodynamic Performance Analysis of Formula-Based Vehicle Through Ansys



Venkata Siva Sainath Bavapuram, Surya Narayanan Suresh, Sumit Sharma, and Vipin Kaushik

**Abstract** The method to enhance the performance of race cars by adding downforce producing devices is well established and started in the 1960s when wings were first used. In short, wings enhance the effectiveness of the tires by increasing the load on the tires without adding the equivalent mass. As mentioned earlier, wings increase race car performance by providing a “massless” load to the tires. The wings will add weight to the vehicle, and the performance gain must outweigh the drawbacks of this extra weight and the addition of drag that the wing also cause. As a key characteristic of the vehicle, aerodynamic characteristics have close relationships with handling stability, safety, dynamics, fuel economy, and so on. The aerodynamic characteristics’ influence on the vehicle performance is particularly obvious; for formula cars with exposed wheels, the car wheel resistance accounted for the proportion of the total resistance sometimes can go to over 45%. In the car development process, researchers pay great attention to the car aerodynamic characteristics research and optimization, and aerodynamics package has become an important part of the car. Optimization is one of the most important parts of the aerodynamic devices design because optimization is done by taking into consideration of many parameters. First, the wings are optimized to the maximum downforce and minimum drag individually by altering the angle of attack of both the ME (main element) and FE (flap element) and the position of the flap element concerning the main element. Then the individually optimized wings are incorporated into the CAD (Computer Aided Design) model and further optimized to tune the wings to get the maximum efficiency out of the car.

---

V. S. S. Bavapuram · S. N. Suresh · S. Sharma (✉) · V. Kaushik  
Mechanical Engineering Department, Amity School of Engineering and Technology, Amity University, Noida, Uttar Pradesh, India  
e-mail: [ssharma03@amity.edu](mailto:ssharma03@amity.edu)

V. S. S. Bavapuram  
e-mail: [bavapuram007@gmail.com](mailto:bavapuram007@gmail.com)

S. N. Suresh  
e-mail: [21.narayanansurya@gmail.com](mailto:21.narayanansurya@gmail.com)

V. Kaushik  
e-mail: [vkaushik@amity.edu](mailto:vkaushik@amity.edu)

**Keywords** Aerodynamics · Coefficient of lift · Downforce · Drag · Angle of attack · Airfoil

## 1 Introduction

The main aim of introducing an aerodynamic package in an FSAE (Formula Society of Automotive Engineers) car is to improve its stability and drivability by improving its downforce and traction. Formula Student races are all about design and manufacturing. Speed is not what wins the competition. The clean engineering aspect of the team provides a winning advantage for the team [1].

Aero pack is the result of top-notch engineering design. Teams improvise every year to strive for the best.

As an improvement from the team's previous year's car, the body kit is updated by adding a front wing and rear wing which are designed exclusively for the car. So, the parameters like downforce, lift, and drag are customized with the design of the chassis of the car, and by doing so, aerodynamics helps the car to be faster around corners [2]. Aerodynamics has been a demanding concept of physics for Design Engineers [1]. Formula Student cars are designed and developed by Student Engineers, and they face many challenges in the process of making a car; one such challenge is aerodynamics. Formula Student is governed by a set of well-organized rules. Aerodynamic devices used in an FSAE car are front wings, rear wings, diffusers, and undertray.

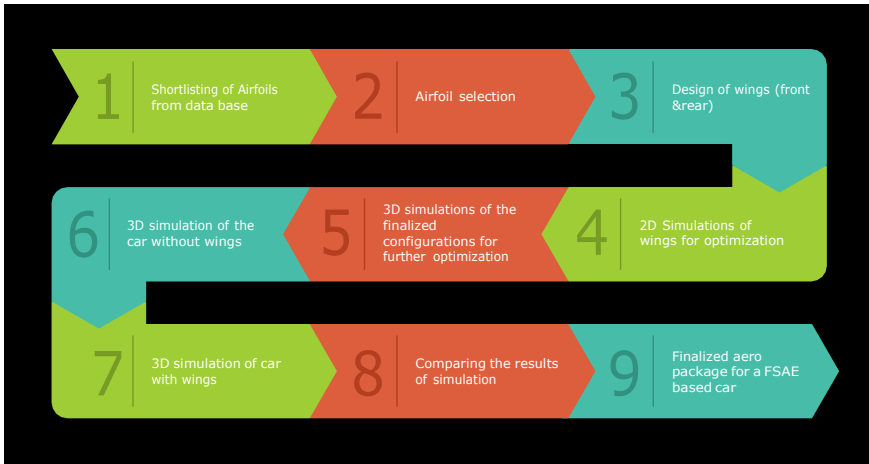
The front wing and rear wing will be the main concentrations for the project. The car must be fast as well as efficient. Performance efficiency plays an important role in this competition. This fueled the idea of introducing aerodynamics in our team's car. It will be a platform for constant learning and development, and improvisation will be eminent in every aspect of the design for upcoming years [2]. Further optimization and design upgradation will ensure the effectiveness of the design for further installments of projects within the team [3].

When air (fluid) flows around an object, the object resists the flow. This phenomenon is called drag [2]. Aerodynamic drag is termed as the sum of pressure and viscosity drag. Pressure drag is the most dominant one and is caused by the shear forces between two fluid layers [2].

## 2 Methodology

First, the airfoils are selected according to the requirements of downforce, then the wings are designed using the airfoils selected from the airfoil database which were then compared using the simulation results from xflr5 and then designed according to the FSAE design constraints of the wings; now the designed wings were then optimized for high downforce configuration comparing multiple simulation results from changing different parameters like angle of attack, vertical height between the





**Fig. 1** Block diagram of work methodology

elements, etc. Firstly, the car without the wings was simulated using Ansys, and the results were analyzed for initial values of  $C_d$  (coefficient of drag) and  $C_l$  (coefficient of lift), then the finalized design of the front and rear wings is incorporated in the design and then simulated together to analyze the results and compared with the results of that without aero package (Fig. 1).

## 2.1 Design Ideology

In the design process of an open-wheel FSAE car, one is exposed to various instances of complex geometry, A-links, wheels, cockpit with a driver, etc. Analytically, the nature of the vehicle makes it too complicated to approach the problem of aerodynamic design and optimization. This is the reason why new methods of simulations like XFLR5, Optiprof, and CFD (Computational Fluid Dynamics) are developed in order to aid in research. We aim to select airfoil, design front, and rear wings and simulate using CFD maximum downforce within the acceptable limits of induced drag and reduced maximum speed [2].

## 2.2 Airfoil Selection

Airfoils are to be selected for both front and rear wings. Both front wing and rear wing comprise main element and flap/side element. The main selection criteria for the main element are done by comparing  $C_l$  versus  $\alpha$  graphs. For the flap airfoil selection, it is done by comparing the  $C_l/C_d$  versus  $\alpha$  graphs as the flaps/side elements are

placed at a relatively higher angle of attack. This makes a huge contribution to the frontal area of the car; thus, coefficient of drag should also be taken into consideration. The airfoil with a higher Cl/Cd ratio is preferred [4].

**Front wing design.** The main element is chosen as FX74 CL5 140.

**Rear wing design.** The main element is chosen as S1223.

**Front wing elements.** Flap element is chosen as E423.

**Rear wing elements.** Flap elements are chosen as GOE464.

## 2.3 Optimization

Optimization of the wing design means modifying the given design configuration from the base design to give the highest possible required parameters by repeated design modification and analysis of the design for the required parameters until we get the required parameters. In the case of the wings, the required parameter for which we will be optimizing the design is maximum downforce and minimum possible drag of the given configuration. So, for achieving the given results, there will be some elements in the wings to constantly modify to compare the required downforce [4]. For wings, they are:

1. AOA—Angle of attack
2. Vertical height
3. Overlap or horizontal distance.

### 2.3.1 Selection of Angle of Attack of the Front Wing

Every single angle geometry is first created in the SolidWorks platform and then imported into Ansys for further analysis. From the simulations, it is evident that the angle of  $45^\circ$  made the maximum downforce when compared to the other angles with downforce of 558.65 N. Hence,  $45^\circ$  is selected as the flap angle for the front wing [5].

### 2.3.2 Overlap and Vertical Height Selection

Similar to the angle of attack, vertical height and overlap distance of flap from the main element affect the lift and drag coefficients. Taking the initial vertical gap and overlap as  $3.8\%c$  and  $5.2\%c$ , respectively ( $c$ —chord length), simulations were performed to obtain optimum configuration. The final configuration of the angle and the distances are given as,  $45^\circ$ , 10 mm overlap, and 15 mm vertical height [6] (Fig. 2).

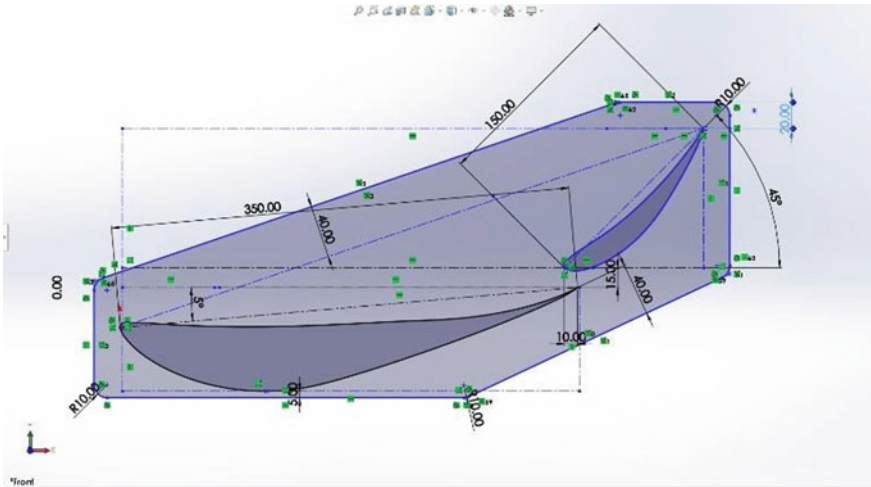


Fig. 2 Front wing—final geometry

### 2.3.3 Front Wing Final Design

The final design of the front wing with the geometry configuration is 45°, 10 mm overlap, and 15mm vertical height along with the second iterative design of endplate [2] (Fig. 3).

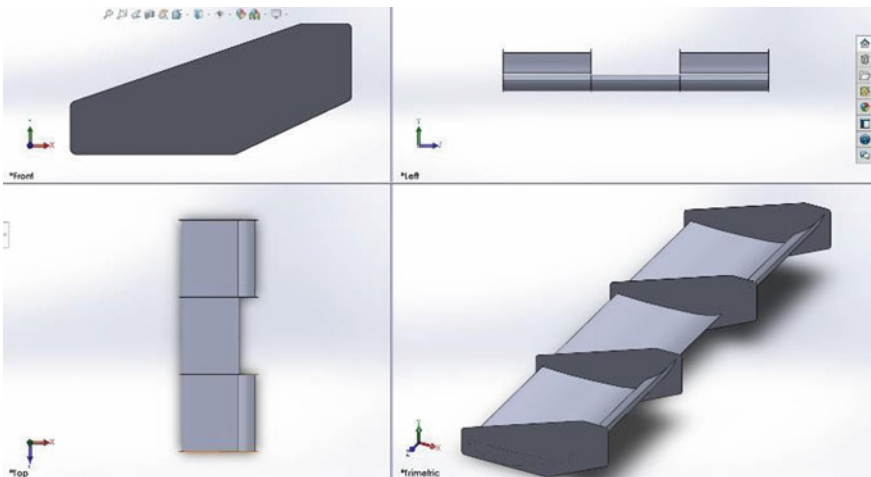
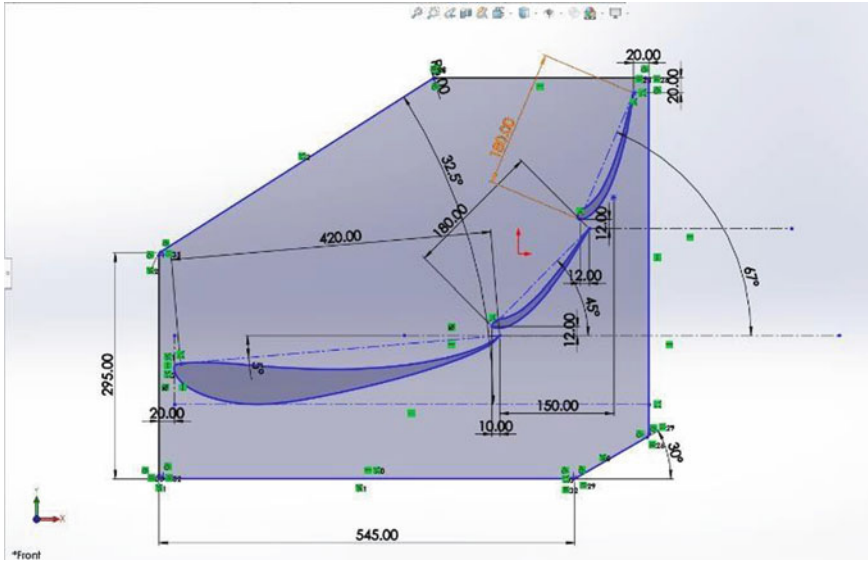


Fig. 3 Front wing final design



**Fig. 4** Rear wing—final geometry

### 2.3.4 Selection of Angle of Attack of the Rear Wing

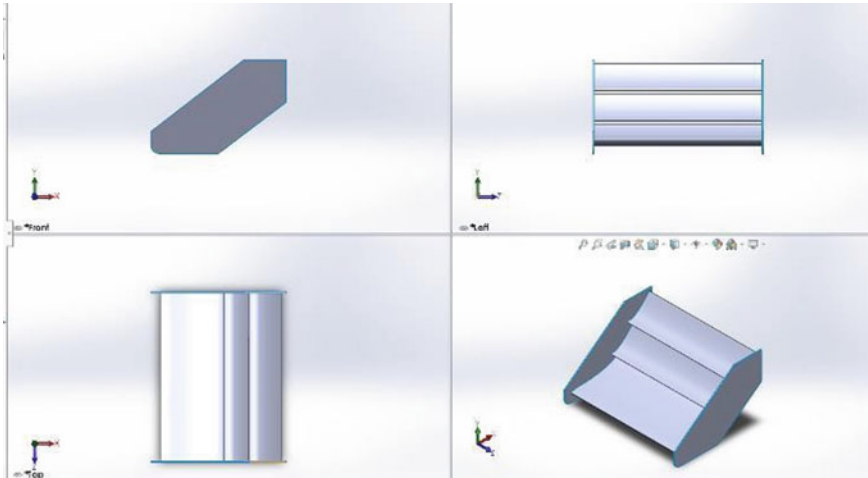
The rear wing has 3-element design. The main element and 2 flap elements sit above the main element progressively. They produce immense downforce on the vehicle which provides grip to the car. The final configuration of the wing elements' angle is found to be, ME  $5^\circ$ , FE1  $45^\circ$ , and FE2  $67^\circ$  [4].

### 2.3.5 Overlap and Vertical Height Selection

Now, just like the front wing, the overlap and vertical height between the elements are found through series of 2D simulations. This gives us the best possible configuration to be put together for achieving the performance output we expect. Since there are 2 flap elements, the overlap and vertical height are found in an order of level to simplify the optimization process. This configuration gives the best possible downforce with the least drag [7] (Fig. 4).

### 2.3.6 Rear Wing Final Design

The final geometric configuration of the rear wing is shown above with the image. The final configuration of the wing is given as, ME  $5^\circ$ , FE1  $45^\circ$ , FE2  $67^\circ$ , FE1 overlap 10 mm and vertical height 12 mm, and FE2 12 mm and vertical height 12 mm [8] (Fig. 5).



**Fig. 5** Rear wing final design

## 2.4 3D Simulation and Analysis of CAD Model

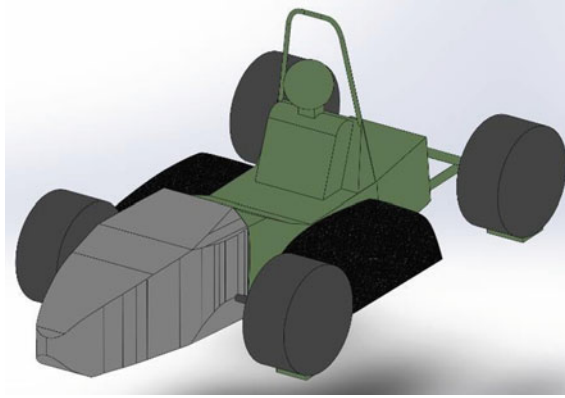
The 3D simulation of the CAD model of the car is done to find the effect of the wings on the overall car's geometry. For this purpose, a simpler model of the car with a driver is made to mimic the actual car's geometry as close as possible. Two CAD models are made, one without any aerodynamic package added and the other with the wings placed in the exact locations allowed as per the rule book. This model will be used to simulate for the aerodynamic effect [9].

### 2.4.1 CAD Model—Without Wings

The CAD model is prepared for simulation analysis in Ansys by beginning with the model assembly. The parts of the model such as nose cone, side pod, wheel rods, chassis, wheels, and driver are modeled as individual parts and are assembled to make a single car model (Fig. 6).

This enables us to customize the positions of the parts and also to set up meshing preferences individually without any complications. The model is imported to the space-claim environment to carry out geometry preparation for meshing. Enclosure is generated, and individual parts are named for flow analysis preparation. Enclosure is a closed volume where the effect of airflow over the car is calculated. Along with the main enclosure, two body of influences are made to make local fine meshing near the car's geometry to obtain exact data of solution in the vicinity of the car [5].

Meshing is done on the surface level to define the surface of the car's geometry. The features are presented as mesh to properly analyze the airflow. Meshing is a very important step in order to obtain results. Poor-quality mesh will not provide the right



**Fig. 6** CAD model—without wings

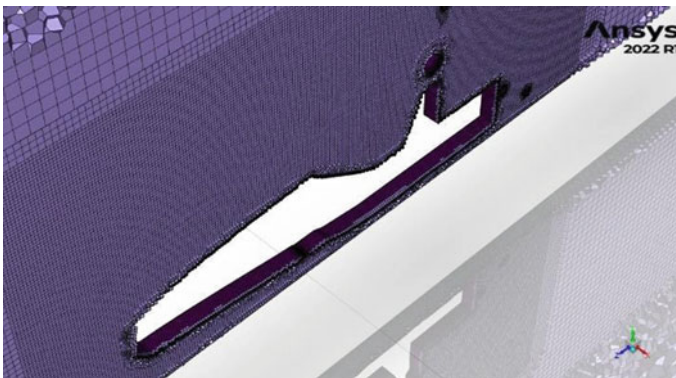
results upon simulation. Hence, each part is carefully meshed to obtain the surface mesh of the model [6].

Volume mesh is to define the car's volume inside the enclosure. It is performed after the surface meshing process [10].

Volumetric meshing is done for the whole model geometry. The highest quality surface meshing will give a flawless volumetric mesh. Further, this mesh is used to obtain the analytical solution (Fig. 7).

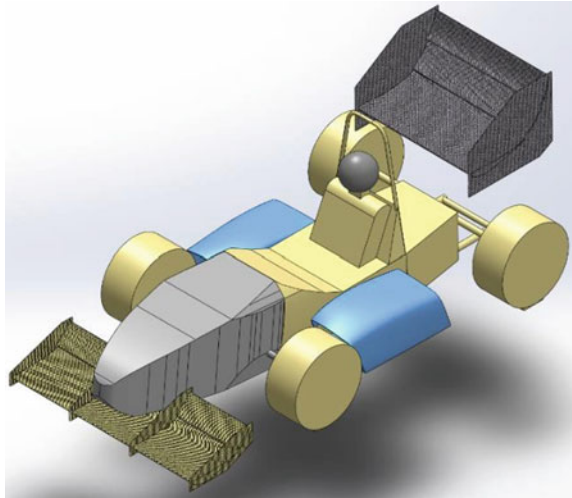
The simulation is set up for analysis in transient state condition to measure the values of  $C_d$  and  $C_l$ . Input parameters are set to obtain the results as follows:

- Frontal area =  $0.353 \text{ m}^2$
- Inlet velocity =  $24 \text{ m/s}$
- Pressure =  $1 \text{ atm}$  (Fig. 7).



**Fig. 7** Volumetric meshing—without wings

**Fig. 8** CAD model—with wings



Simulation is carried out for 650 iterations in total, and the values of coefficient of lift and drag and lift and drag force are noted [6].

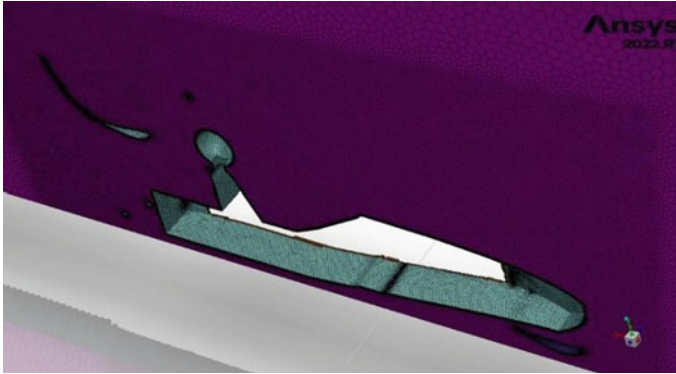
#### 2.4.2 CAD Model—With Wings

The parts of the model such as nose cone, side pod, wheel rods, chassis, wheels, and driver along with front and rear wings are modeled as individual parts and are assembled to make a single car model. This enables us to customize the positions of the parts and also to set up meshing preferences individually without any complications [7] (Fig. 8).

For ease of simulation, the wings are positioned in its destined locations but are not connected to the chassis to avoid interferences and mesh complications. The front wing is set at a height of 70 mm from the ground to the bottom, and the rear wing is set at the maximum allowable height of 1200 mm from the ground to the top. In this arrangement, the wings will have cleaner air flow and minimum contact with the ground.

Enclosure is again made including half of the vehicle only, in order to reduce computational time, and it gives the exact same results because the car is symmetrical.

Along with all the parts as before, wings are selected and named in this model to perform airflow analysis. Surface mesh in this model also includes the wings. The sizes are given as close as possible to that of the wheels to carefully capture the geometry. Since wings have high curvature and smaller face, the mesh quality is taken into account and is modeled in such a way that the edges are not tampered. The perfection of surface mesh will make sure that the volume mesh is generated perfectly [4].



**Fig. 9** Volumetric meshing-with wings

Volumetric meshing is performed the same way as before following all the steps. At the end of volume meshing process, the part features will be captured perfectly in the enclosure volume that will be used to perform the computational study [8] (Fig. 9).

The simulation is set up for analysis in transient state condition to measure the values of Cd and Cl. Input parameters are set to obtain the results as follows:

- Frontal area =  $0.545 \text{ m}^2$
- Inlet velocity =  $24 \text{ m/s}$
- Pressure =  $1 \text{ atm}$  (Fig. 9).
- The parameters are the exact same as the simulation done earlier except the frontal is due to the addition of front wings. Once the FMG initialization is done, the calculation is started to obtain the results [1].

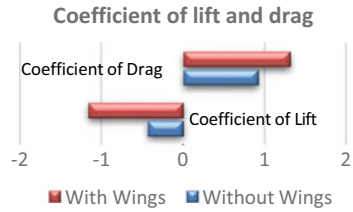
### 3 Results

The aerodynamic study of a Formula SAE car is done in Ansys Fluent software. The main objective of this study is to increase the downforce of the vehicle as a whole and increase the cornering stability of the car [2]. The results obtained are compared with each other to attain a conclusion. The values of coefficient of lift and coefficient of drag are compared, and the values of lift force and drag force are compared in charts.

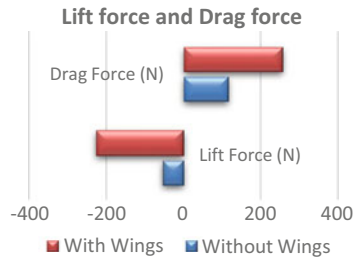
The design procedure for the front and rear wings of the FSAE car began with airfoil selection. Once the basic geometrical design was made, the wings were optimized to its maximum performance output potential. Once the design was complete, it was put through simulation and analysis to obtain the results [5] (Figs. 10, 11; Table 1).



**Fig. 10** Chart for coefficient of lift and drag



**Fig. 11** Chart for lift and drag



**Table 1** Results comparison table

	Without wings	With wings
Coefficient of lift	- 0.43813753	- 1.1665056
Coefficient of drag	0.91761568	1.3111325
Lift force (N)	- 55.183246	- 227.58336
Drag force (N)	115.57333	255.79984

The drag force has increased by 135.3214 Newton. The lift force has decreased from - 55.0273 Newton to - 227.583 Newton. The total downforce gained is 172.555 Newton. Lift force in negative represents the direction and thus means positive downforce. The coefficient of lift has improved from 0.43 to 1.16. This means that the downforce has improved significantly. Also, the drag coefficient has increased from 0.91 to 1.31 which is a 0.394 increase in the value of downforce [9].

## 4 Conclusion

It is concluded that the aerodynamic package provides a performance advantage to the car without any changes in the power unit or chassis. Increase in downforce means that grip of the car’s tires is higher at 86 kmph speeds making it suitable for high speed corners. Improved grip all around the track will significantly improve the lap times of the car. The aerodynamic package is designed to be attached separately to the chassis and not to any body panels and hence gives the flexibility to be attached and detached without disturbing the topology of any part [10].

## References

1. Rehnberg S, Börjesson L, Svensson R, Rice J (2013) Race car aero-dynamics—the design process of an aerodynamic package for the 2012 chalmers formula SAE car. In: SAE technical papers, vol 2. <https://doi.org/10.4271/2013-01-0797>
2. Mariani F, Poggiani C, Risi F, Scappaticci L (2015) Formula-SAE racing car: experimental and numerical analysis of the external aero-dynamics. Energy Procedia 81:1013–1029. <https://doi.org/10.1016/j.egypro.2015.12.111>
3. Shao S, Zhang Y, Zhao J, Tang W (2013) The influence of wheel rotating to FSAE racing car aerodynamic characteristics. Appl Mech Mater 300–301:1054–1057. <https://doi.org/10.4028/www.scientific.net/AMM.300-301.1054>
4. Jagadeep J, Tech RB, Finding the optimum angle of attack for the front wing of an F1 car using CFD
5. Oxyzoglou I, Pelekasis N (2017) Design and development of an aerodynamic package for a FSAE race car
6. Ao S-I, Gelman L, Hukins DWL, International association of engineers, World congress on engineering: WCE 2016: 29 June–1 July, 2016, Imperial College London, London, U.K.
7. Doddegowda P, Bychkovsky AL, George AR (2006) SP-1991
8. Deng Z, Yu S, Wu C (2020) Numerical simulation and analysis for aerodynamic devices of FSAE racing car. J Phys: Con Ser 1600(1). <https://doi.org/10.1088/1742-6596/1600/1/012079>
9. Chen M, Tang W, Yang B, Hu X (2012) Computer-aided front and rear wings aerodynamic design of a formula SAE racing car. Appl Mech Mater 120:20–25. <https://doi.org/10.4028/www.scientific.net/AMM.120.20>
10. View of numerical investigation on the pressure drag of some low-speed airfoils for UAV application

# Numerical Estimation of Base Reactions of an Underwater Manipulator with Variable Drag Coefficients



Chandan Kumar, N. Srinivasa Reddy, Dipankar Chatterjee, Pratik Saha, Sambhunath Nandy, and Soumen Sen

**Abstract** Underwater vehicles play an essential role in marine geosciences, resource exploration, and strategic applications. The addition of a manipulator to the underwater vehicles extends their capabilities for underwater intervention, object handling, and sample collection. When the manipulator interacts with the underwater environment, it experiences different reaction forces, including hydrodynamic forces. These reaction forces may cause destabilization of the vehicle, which would make it difficult to perform the manipulation task. It is important to ensure the stability of the underwater vehicle while the manipulator is interacting with the subsea environment. This paper presents a study of manipulator hydrodynamic forces and base reaction forces, which would be transferred to the underwater vehicle. These reaction forces need to be compensated by the thrusters of the vehicle to achieve stability. In this work, the variation of drag coefficient with velocity and along the length of the manipulator is considered first time in the dynamic modeling of a two-link underwater manipulator. These results would provide input to the design of suitable controllers for the stability of the vehicle.

**Keywords** Underwater manipulator · Hydrodynamic forces · Reaction forces · Underwater vehicle stability · Multi-body dynamics

## 1 Introduction

The development of underwater vehicles has drawn extensive attention due to its great importance in offshore engineering, scientific, and strategic applications. The addition of a manipulator to the underwater vehicles extends their capabilities to

---

C. Kumar · N. S. Reddy · D. Chatterjee (✉) · P. Saha · S. Nandy · S. Sen  
CSIR-Central Mechanical Engineering Research Institute, Durgapur 713209, India  
e-mail: [d\\_chatterjee@cmeri.res.in](mailto:d_chatterjee@cmeri.res.in)

C. Kumar · D. Chatterjee  
Academy of Scientific and Innovative Research, Ghaziabad 201002, India

underwater maintenance works (welding, cutting, drilling, etc.), assembly operations, and scientific sample collection. It also plays an important role in underwater rescue and environmental protection. Therefore, it has become a trend to develop underwater vehicle-manipulator system (UVMS) to achieve complicated tasks in a challenging underwater environment. When the manipulator interacts with the underwater environment, it experiences different reaction forces, including hydrodynamic forces. These reaction forces may destabilize the UVMS, which would make it difficult to achieve the manipulation task. It is important to ensure the stability of the underwater vehicle while the manipulator is interacting with the subsea environment. These reaction forces need to be compensated by the thrusters equipped with the vehicle to achieve stability [1].

In recent years, researchers have taken great interest in designing, studying, and modeling the dynamics of UVMS [2–8]. Wang et al. presented a novel design of a lightweight underwater manipulator and proposed a closed-loop control system with binocular vision for underwater manipulation [2]. Santhakumar Mohan investigated the interaction effects between the manipulator and the underwater vehicle through numerical simulations of vehicle-manipulator system. The dynamics were modeled using recursive Newton–Euler formulation [3]. A model reference control scheme was also proposed for UVMS that compensates for the parameter uncertainties and external disturbances [4]. Tarn et al. employed Kane’s method to derive a closed-form dynamic model of UVMS, which can be utilized for control schemes development [5]. Estimation of hydrodynamic parameters is an equally important factor in accurately modeling the interaction effects between manipulators and vehicles [9]. In addition to these studies, a few experimental and numerical investigations of the hydrodynamic forces and torques acting on underwater manipulator are also available in the literatures. McLain et al. investigated a cylindrical single-link underwater manipulator [10] with variable drag and added mass coefficients. Kolodziejczyk determined transient hydrodynamic coefficients for single-link underwater manipulator [11]. The transient hydrodynamic load was obtained through CFD simulations performed for several kinematic conditions. A preliminary study of an underwater manipulator was presented in [12], carried out to determine the effect of fluid motion on joint torque through CFD simulations. Though there exists some literature on UVMS dynamics [13–16], an accurate hydrodynamic force model is still a challenging task. Most of the works in the literature considered constant hydrodynamic force coefficients and a single-link underwater manipulator for analyses due to its complexity. The present article considers a two-link manipulator for analyzing its hydrodynamic loads and dynamic reaction forces using variable drag coefficient and blade element method, which would be eventually transferred to an underwater vehicle when it is mounted on it. A general block diagram of the overall process is shown in Fig. 1. At first, a series of CFD simulations was carried out to determine hydrodynamic force coefficients at different water flow rate conditions. These variable drag coefficients ( $C_d$ ) obtained through CFD simulations were utilized in the hydrodynamic force formulation of the manipulator dynamic model. A hydrodynamic force model was formulated by using the blade element method (BEM)

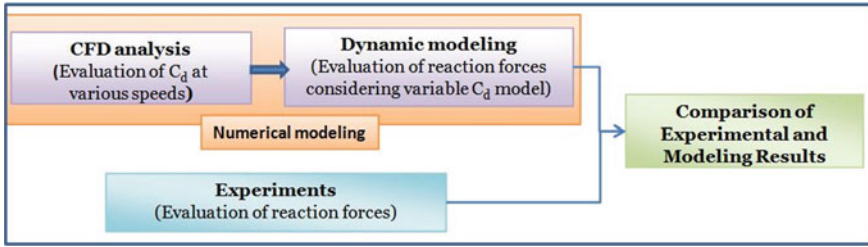


Fig. 1 General block diagram of overall process

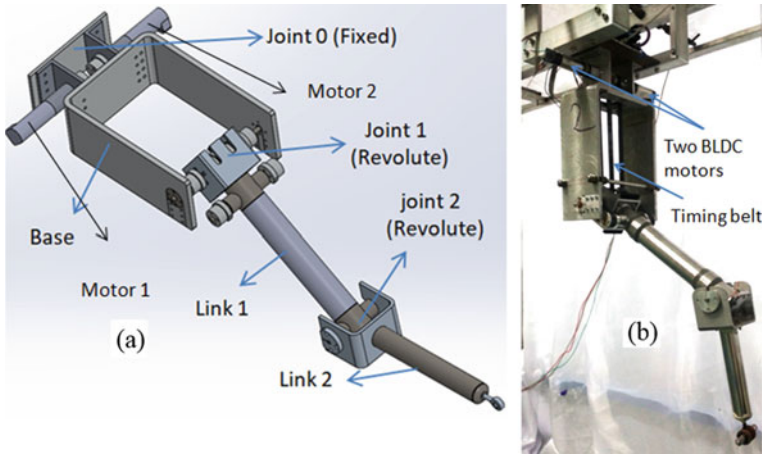
utilizing these predetermined hydrodynamic force coefficients. Finally, this hydrodynamic force model was incorporated in the dynamic simulations of a two-link underwater manipulator by considering the hydrodynamic force as an external force acting on the links. These simulation results were compared with experimental results of the same manipulator configuration and trajectories.

## 2 Underwater Manipulator Description and Experimental Setup

A two-link planar manipulator is considered in the present work. Figure 2a shows the manipulator model with two hollow cylindrical links connected with two revolute joints. These two links were made of stainless steel hollow cylindrical tubes. Two motors were placed at the base to drive these two revolute joints through a timing belts arrangement as shown in Fig. 2b. The timing belt for driving the second link (link 2) was placed inside the first link (link 1), and the two links were sealed to prevent the water from entering. The physical dimensions of the two links are given in Table 1. The experimental setup consists of the two-link manipulator (shown in Fig. 2b) submerged, in a vertical configuration, in a transparent water tank of dimensions—2.5 m × 0.9 m × 1.3 m (length × width × height). The joint torques of the manipulator were calculated with the measured current of the two motors during the experiment (Table 2).

## 3 Determination of Variable Drag Coefficient

A series of steady-state CFD simulations was performed for different velocities ranging from 0.01 to 100 m/s. In each case, the hydrodynamic forces were evaluated, and the corresponding drag coefficient was determined. Commercial software, Ansys Fluent®, was utilized for this purpose. Figure 3 shows the CFD model with a submerged manipulator in the cuboid-shaped fluid domain and boundary conditions.



**Fig. 2** Manipulator assembly. **a** CAD model **b** experimental prototype

**Table 1** Dimension of manipulator links

Parameter/link	Link 1	Link 2
Diameter (m)	0.051	0.038
Length (m)	0.250	0.100

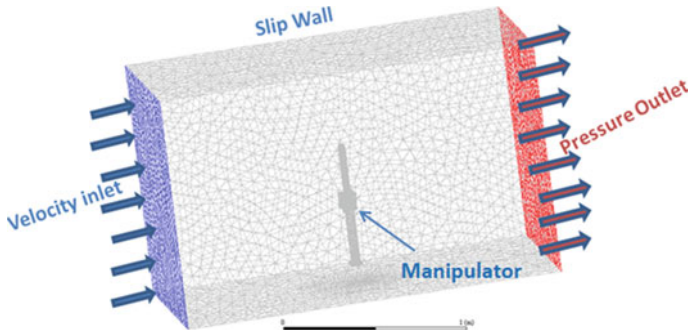
**Table 2** Joint motion trajectories (quintic polynomial) used in dynamic simulations and experiments

	Joint 1	Joint 2
Case 1	$\theta[0-75^\circ]$	$\theta[0-75^\circ]$ in -ve dir
Case 2	$\theta[0-75^\circ]$	$\theta[0-45^\circ]$
Case 3	ZERO	$\theta[0-90^\circ]$
Case 4	$\theta[0-75^\circ]$	Zero

An unstructured grid with tetrahedral elements was used to mesh the fluid domain. A dense grid was created around the manipulator links to capture the behavior of fluid flowing over it. Slip wall boundary condition was used for the domain wall, and the no-slip wall boundary condition was considered at the manipulator’s arm to negate the effect of wall shear on fluid around the manipulator. Initially, a grid independence study was carried out using different domains and sizes. Different sizes of the domain, grid, and corresponding drag coefficient results are given in Table 3. Domain-2 with 2.0 m × 1.0 m × 1.0 m size was chosen for the simulations as it showed no variation in  $C_d$  beyond this size.

The governing equations are described by the following equations of the mass and momentum conservation equations:

$$\nabla \cdot \vec{V} = 0 \tag{1}$$



**Fig. 3** CFD model showing the fluid domain, manipulator, and boundary conditions

**Table 3** Domain and grid sizes for grid independence study

Parameter/domain	Domain-1		Domain-2		Domain-3	
$L \times W \times H$ (m <sup>3</sup> )	1.0 × 0.5 × 0.5		2.0 × 1.0 × 1.0		4.0 × 2.0 × 2.0	
Grid—number of cells	196,400		398,500		560,200	
Velocity (m/s)	1	10	1	10	1	10
Link 1 ( $C_d$ )	0.39	0.39	0.37	0.36	0.37	0.36
Link 2 ( $C_d$ )	0.27	0.32	0.26	0.30	0.26	0.30

$$(\vec{V} \cdot \nabla) \vec{V} = -\frac{1}{\rho} \nabla p + \frac{\mu}{\rho} \nabla^2 \vec{V} + f \tag{2}$$

where  $\vec{V} = [V_x, V_y, V_z]$  is the velocity vector,  $\rho$  represents density of the fluid,  $p$  is the pressure,  $\mu$  represents dynamic viscosity of the fluid, and  $f$  represents body force per unit mass. The fluid in the present study was water with  $\rho = 998.2 \text{ kg/m}^3$  and  $\mu = 0.001003 \text{ kg/m.s}$ . Reynolds-averaged Navier–Stokes (RANS) equations with standard  $k-\epsilon$  turbulence model were used to solve turbulent motion, which is found in the literature [17], best suited for the coarser grid. RANS equations for the incompressible flow are given as

$$\bar{u}_j \frac{\partial(\bar{u}_i)}{\partial x_j} = -\frac{1}{\rho} \frac{\partial \bar{p}}{\partial x_j} + \frac{\partial}{\partial x_j} \left[ \mu_t \left( \frac{\partial \bar{u}_i}{\partial x_j} + \frac{\partial \bar{u}_j}{\partial x_i} \right) - \overline{u'_i u'_j} \right] \tag{3}$$

*k-ε turbulence model:*

For turbulent kinetic energy ( $k$ ),

$$\frac{\partial}{\partial x_i} (\rho k u_i) = \frac{\partial}{\partial x_j} \left[ \frac{\mu_t}{\sigma_k} \frac{\partial k}{\partial x_j} \right] + 2\mu_t E_{ij} E_{ij} - \rho \epsilon \tag{4}$$

For rate of dissipation ( $\epsilon$ ),

$$\frac{\partial}{\partial x_i}(\rho \varepsilon u_i) = \frac{\partial}{\partial x_j} \left[ \frac{\mu_t}{\sigma_\varepsilon} \frac{\partial \varepsilon}{\partial x_j} \right] + C_{1\varepsilon} \frac{\varepsilon}{k} 2\mu_t E_{ij} E_{ij} - C_{2\varepsilon} \rho \frac{\varepsilon^2}{k} \quad (5)$$

where  $u_i$  is the velocity component in direction  $i$ ,  $\overline{\rho u_i' u_j'}$  is the Reynolds stress,  $E_{ij}$  is the rate of deformation, and  $\mu_t$  is the eddy viscosity which is given by,

$$\mu_t = \rho C_\mu \frac{k^2}{\varepsilon} \quad (6)$$

Some adjustable constants  $\sigma_k$ ,  $\sigma_\varepsilon$ ,  $C_{1\varepsilon}$ ,  $C_{2\varepsilon}$  are also present in (4) and (5). These were the default values ( $C_\mu = 0.09$ ,  $\sigma_k = 1.0$ ,  $\sigma_\varepsilon = 1.30$ ,  $C_{1\varepsilon} = 1.44$ ,  $C_{2\varepsilon} = 1.92$ ) present in Ansys Fluent<sup>®</sup>.

Second-order upwind scheme was applied to discretize the momentum equation, and *SIMPLE* algorithm for pressure correction was employed in Ansys Fluent<sup>®</sup>. A maximum relative error value of 0.001 was set between two successive iterations as the convergence criterion. Figure 4 shows the pressure contour plot for the flow velocity case of 2.5 m/s. The pressure difference between upstream and downstream of manipulator (shown in Fig. 4) causes pressure drag, which is the major part of total resistive force acting on links. Figure 5 shows the drag coefficient,  $C_d$ , calculated from the results of hydrodynamic forces obtained from CFD simulations. The variable nature of the drag coefficient can be noticed in Fig. 5. The lower flow velocity cases show higher drag coefficient values and gradually reduce with increase in velocity and stabilize at around 5 m/s flow velocity. These variable  $C_d$  values were used in the hydrodynamic force formulation of the underwater manipulator. This hydrodynamic force was considered as external force acting on the manipulator in the dynamic model, which is presented in the next section.

## 4 Dynamic Modeling of Underwater Manipulator

During the operation of the manipulator, the angular velocity of arms changes continuously, and also the velocity along the manipulator's arm length varies (due to the revolute joint at the base and elbow). The range of velocity of operation of the underwater manipulator is very small (0–6 m/s). In this range of operation, the drag coefficient is found to be variable (discussed in previous section). Therefore, it is important to incorporate the variable  $C_d$  model in the dynamics of the underwater manipulator to evaluate the base reaction forces accurately. This section discusses the dynamic modeling of the underwater manipulator with variable  $C_d$  model.

The governing equations of the two-link underwater manipulator are described by [11]:

$$M(q)\ddot{q} + C(q, \dot{q})\dot{q} + G(q) = \tau \quad (7)$$



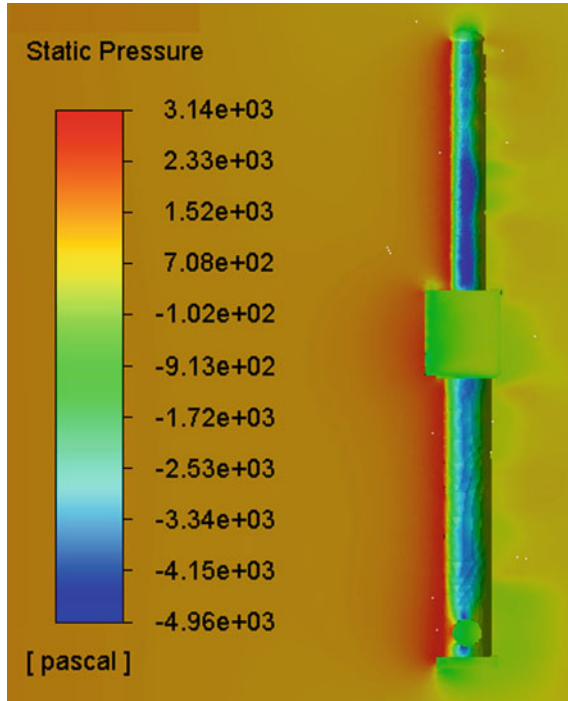


Fig. 4 Pressure contour plot for the flow velocity of 2.5 m/s

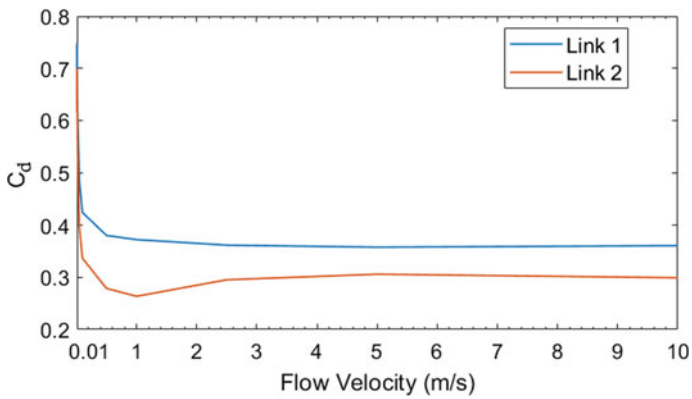


Fig. 5 Variation of the drag coefficient,  $C_d$ , with flow velocity

where  $q$  is the generalized coordinate vector consisting of two joint angles,  $M$  is the generalized inertia matrix,  $C$  is the Coriolis and centripetal matrix,  $G$  accounts for the gravitational and buoyant forces, and  $\tau$  represents the resultant of applied torques, which includes the torque due to hydrodynamic forces,  $\tau_h$ , and torque required to move the weight of the links  $\tau_w$ .

$$\tau = \tau_w + \tau_h \tag{8}$$

The hydrodynamic force acting on the moving links consists of two major components, which are pressure drag and added mass forces. The blade element method was employed to estimate the hydrodynamic forces. This involves the division of a continuous link into small blade elements (see Fig. 6) and the evaluation of forces acting on each of the blade elements. Summing up all the elemental forces yields the total hydrodynamic force.

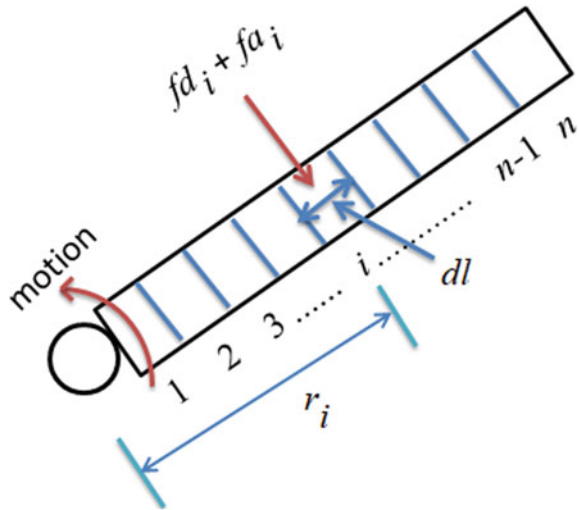
The drag and added mass forces ( $f_{d_i}, f_{a_i}$ ) acting on a blade element  $i$  were calculated as,

$$f_{d_i} = -\frac{1}{2}\rho C_d A_i v_i |v_i| \tag{9}$$

$$f_{a_i} = -\rho\pi \frac{d^2}{4} d a_i \tag{10}$$

where  $A_i$  is the projected area of the element  $i$ ,  $v_i$  is the normal component of the velocity,  $d$  is the diameter of the link,  $dl$  is the length of the element  $i$ , and  $a_i$  is the normal acceleration of the element  $i$ . The negative sign in (9) and (10) indicates that these forces act in a way of opposing the motion. It should also be mentioned that the

**Fig. 6** Division of a link into small blade elements



$C_d$  used to evaluate drag force in Eq. (9) is the function of  $v_i$ . Now, the hydrodynamic torque acting on the element  $\tau_{hi}$  is given by,

$$\tau_{hi} = (f_{d_i} + f_{a_i})r_i \tag{11}$$

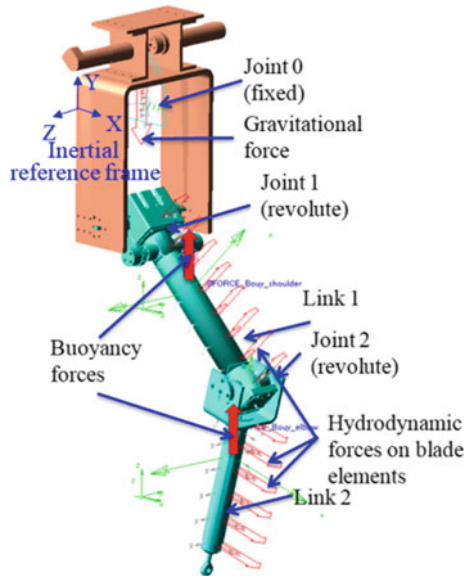
The total hydrodynamic torque acting on the link about the joint is given by,

$$\tau_h = \sum_{i=1}^n \tau_{hi} = \sum_{i=1}^n (f_{d_i} + f_{a_i})r_i \tag{12}$$

where  $r_i$  is the moment arm of the element  $i$  and  $n$  is the number of blade elements of the link.

Commercially available software, MSC ADAMS<sup>®</sup>, was utilized for simulating the dynamics of the underwater manipulator. The blade element forces were defined as functions of element velocity and accelerations (see Fig. 7). Finally, the underwater manipulator dynamics were simulated with a time step of 0.01 s and error tolerances of 0.001 for different motion trajectories (shown in Table 2) of the two links using MSC ADAMS<sup>®</sup> software.

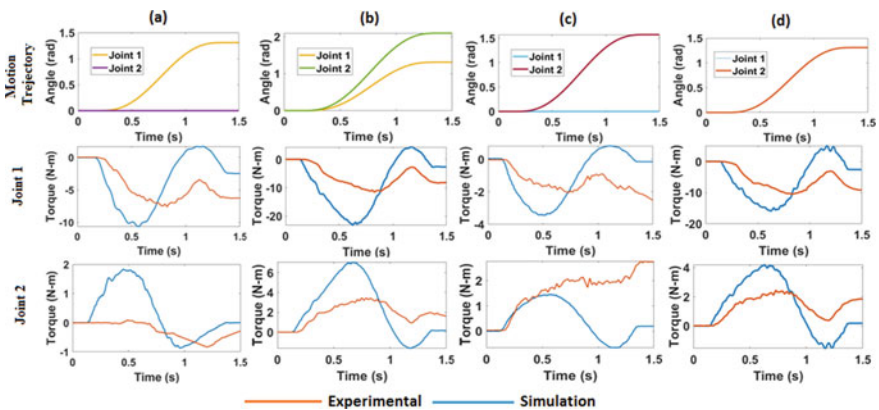
**Fig. 7** Dynamic model in MSC ADAMS<sup>®</sup> software environment



## 5 Results and Discussion

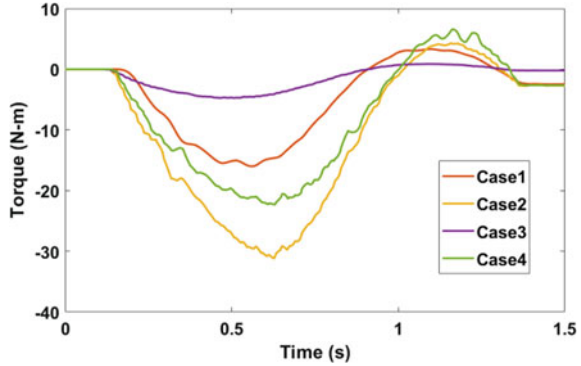
The motion trajectories shown in Table 2 were used in dynamic simulations and experiments to evaluate the hydrodynamic forces through estimation and measurement of joint torques. Figure 8 shows the trajectory plots and joint torques obtained through simulations in MSC ADAMS® software and experiments. Figure 8a shows the result from a trajectory of case 1 in which link 1 rotated by  $75^\circ$  and link 2 also rotated by  $75^\circ$  in opposite direction with respect to the first link. Results from trajectories of case 2 are shown in Fig. 8b. In this case, link 1 was rotated by  $75^\circ$ , but the link 2 was rotated by  $120^\circ$ . Figure 8c shows the joint torques for case 3 in which link 1 was held fixed and link 2 was rotated by  $90^\circ$ . Figure 8d shows the joint torques for case 4 in which link 1 was rotated by  $75^\circ$  and link 2 was held fixed relative to the first link.

It can be seen from the plots (see Fig. 8) that the experimental results and simulation estimates of joint torques are in agreement qualitatively but different in magnitude. This is due to the fact that friction was present in the physical model, which is very challenging to predict and incorporate the same in dynamic model. In addition, accurate estimation of mass, inertia, and center of buoyancy are also difficult. Few of these parameters cannot be directly measured but can be estimated with different modeling techniques and extensive experiments. However, incorporating the variable drag coefficient model in the dynamic modeling of a two-link underwater manipulator has shown a satisfactory agreement with the experimental results. Figure 9 shows the torques transferred to the base while the manipulator was moving as per the trajectories mention against case 1 through case 4. These reaction torques would be transferred to underwater vehicle when the manipulator is mounted on the vehicle. Estimation of these reaction forces is crucial in designing a suitable controller for maintaining the stability of the underwater vehicle—manipulator systems in order



**Fig. 8** Motion trajectories and joint torques obtained through dynamic simulations and experiments for **a** case 1, **b** case 2, **c** case 3, and **d** case 4

**Fig. 9** Torques transferred to the base due to manipulator motion in underwater environment



to successfully complete the manipulation task. The variable  $C_d$  model with BEM used in this work has the great potential to evaluate hydrodynamic forces acting on a two-link underwater manipulator accurately. The modeling technique used in this work can help researchers and engineers in the design and development of multiple link underwater manipulators and their control techniques.

## 6 Conclusion and Future Work

In this paper, the dynamics modeling of an underwater manipulator, simulations, and estimation of base reaction forces due to manipulator movements are presented. A variable drag coefficient model, obtained through CFD simulations, is employed through blade element method in hydrodynamic force formulation of the manipulator. The simulation results are compared with experimental results. These results are found to be in agreement qualitatively but differ in magnitude due to lack of appropriate friction model and few accurate physical parameters of the experimental prototype, which cannot be measured directly. This work serves as a basic framework for determining the underwater manipulator reaction forces, which would destabilize the vehicle on which it is mounted. This framework is crucial for designing the appropriate control system for stabilization of UVMS. Incorporation of appropriate friction models and accurate estimation of physical parameters of the manipulator prototype would constitute our future work.

## References

1. Yoerger D, Cooke J, Slotine J (1990) The influence of thrusters dynamics on underwater vehicle behavior and their incorporation into control system design. *IEEE J Ocean Eng* 15(3):167–178
2. Wang Y, Wang S, Wei Q, Tan M, Zhou C, Yu J (2016) Development of an underwater manipulator and its free-floating autonomous operation. *IEEE/ASME Trans Mechatron* 21(2):815–824
3. Mohan S (2013) Investigation into the dynamics and control of an underwater vehicle-manipulator system. *Model Simul Eng* 839046:1–13
4. McMillan S, Orin D, McGhee R (1995) Efficient dynamic simulation of an underwater vehicle with a robotic manipulator. *IEEE Trans Syst Man Cybern* 25(8):1194–1206
5. Tarn T, Shoults T, Yang S (1996) A dynamic model of an underwater vehicle with a robotic manipulator using Kane's method. *Auton Robot* 3(2–3):269–283
6. Mahesh H, Yuh, Lakshmi R (1991) A coordinated control of an underwater vehicle and robotic manipulator. *J Robot Syst* 8(3):339–370
7. Sarkar N, Podder T (2001) Coordinated motion planning and control of autonomous underwater vehicle-manipulator systems subject to drag optimization. *IEEE J Oceanic Eng* 26(2):228–239
8. McLain T, Rock M, Lee M (1996) Experiments in the coordinated control of an underwater arm/vehicle system. *Auton Robot* 3(2–3):213–232
9. Ryu J, Kwon D, Lee P (2001) Control of underwater manipulators mounted on an ROV using base force information. In: *Proceedings of the IEEE international conference on robotics and automation (ICRA '01)*, pp 3238–3243, Seoul
10. McLain T, Rock M (1988) Development and experimental validation of an underwater manipulator hydrodynamic model. *Int J Robot Res* 17(7):748–759
11. Kolodziejczyk W (2018) The method of determination of transient hydrodynamic coefficients for a single DOF underwater manipulator. *Int J Ocean Eng Ocean Eng* 153:122–131
12. Kolodziejczyk W (2015) Preliminary study of hydrodynamic load on an underwater robotic manipulator. *J Autom Mobile Robot Intell Syst* 9
13. Yusof A, Wasbari F, Ibrahim M (2013) Research development of energy efficient water hydraulics manipulator for underwater application. *Appl Mech Mater* 393:723–728
14. Hyakudome T (2011) Design of autonomous underwater vehicle. *Int J Adv Rob Syst* 8(1):122–130
15. Yoshinada H, Yamazaki T, Suwa T, Naruse T, Ueda H (1991) Seawater hydraulic actuator system for underwater manipulator. In: *Proceeding of the 5th international conference on advanced robotics*, 2, pp 1330–1335, Pisa, Italy
16. Habibah S, Yusof A, Tuan T, Saadun M, Ibrahim M, Nik W (2015) Underwater manipulator's kinematic analysis for sustainable and energy efficient water hydraulics system. *AIP Conf Proc* 1660(1):070112
17. *Ansyst Fluent 15.0—theory guide*. ANSYS Inc, USA, 2010

# A Study on the Reflection Coefficient of Higher Modes of Torsional Wave by Theoretical and Numerical Method



I. Boris, Sunil Kumar Sharma, and Jaesun Lee

**Abstract** Reflection of the fundamental and higher mode of the torsional wave is considered. To evaluate the reflection coefficient, FEM is performed. Simulation result was validated by existing data. For the  $T(0, 2)$  mode, reflection coefficient was calculated in frequency range 300–00 kHz and compared with reflection coefficient for  $T(0, 1)$  in the same frequency range. The results show high rate of  $T(0, 2)$  reflection, which can be used for further studies or damage detection.

**Keywords** Guided wave · Torsional wave ·  $T(0, 2)$  · FEM

## 1 Introduction

Due to their ability to propagate over great distances, guided waves are extremely useful in monitoring elongated items such as pipelines for defects such as cracks or pitting. Torsional waves are unique among guided waves in that the first fundamental mode has a non-dispersive behavior and is unaffected by external factors such as insulation or liquid flowing through a pipe.

The interaction of the first mode of a torsional wave with defects of various shapes is currently being researched extensively. The first mode's interaction with rectangular and trapezoidal defects is discussed in [1–3]. The authors mentioned that the reflection coefficient is proportional to the frequency (the ratio between average defect

---

I. Boris

Department of Smart Manufacturing Engineering, Changwon National University,  
Changwon University Road 20, Changwon 51140, Korea

S. K. Sharma

School of Engineering and Applied Science, National Rail and Transportation Institute,  
Vadodara, Gujarat 390004, India

J. Lee (✉)

School of Mechanical Engineering, Changwon National University, Changwon  
University Road 20, Changwon 51140, Korea

e-mail: [jaesun@changwon.ac.kr](mailto:jaesun@changwon.ac.kr)

length to the wavelength were presented in the article), and that the reflection coefficient drops with increasing frequency in the case of a trapezoidal flaw. If there is a defect on the pipe bend's surface, the reflection amplitude varies depending on the location, and zones of low and high sensitivity on the intrados and extrados, respectively, can be distinguished [4]. In [5, 6], influence of the coating of the pipe with a defect on the torsional wave is studied. Due to the results, fundamental torsional wave mode can be applied for coated or layered pipe inspection.

The number of research papers focuses on the interaction of a guided wave's first mode with defects. Higher modes, on the other hand, have been shown to be more sensitive to specific sorts of imperfections. In [7] mentioned that some bending modes are more sensitive to crack-like defects.  $L(0,4)$  is useful for the detection of deposits on pipe walls, according to [8, 9].

Guided waves are very useful to detect various types of defects such as cracks and pitting on the surface. Their ability to propagate long distances is suitable for pipeline inspection [1–9]. There are 3 types of guided waves in cylindrical structures: longitudinal, flexural, and torsional. It has been found that the torsional wave is very promising for long-range inspection because its lowest fundamental mode is non-dispersive and there is limited interaction between material in- and outside of the pipe.

The occurrence of pipeline flaws is a significant cause for worry in the oil and chemical industries; hence, non-destructive testing (NDT) methods are necessary in order to evaluate the structural soundness of pipes already in use. Ultrasonic testing that is conventional, such as local thickness gauging, employs bulk waves and only examines the section of pipe that is underneath the transducer. The use of guided waves is an additional ultrasonic approach that may be used for long-range examination. This may be accomplished by employing a pulse-echo system on a pipe, and doing so from a single place. With this setup, waves propagate down the length of the pipe in both directions beginning at the place where the wave is initiated, and all of the reflected signals are collected and evaluated as they travel along the length of the pipe. As a result, it is essential to calculate the reflection coefficient from defects of varying sizes and shapes. The issue of the interaction of cylindrically guided waves with discontinuities in the geometry of the waveguide is one that has sparked a significant amount of attention in the recent years. It has been shown that guided waves can identify fractures and notches in pipelines. In addition, the influence that the magnitude of the defect has on the properties of reflection and transmission has been looked at by a number of different studies. In the case of bulk waves, there exist certain accurate closed form analytical solutions to electrodynamic scattering issues. At high frequencies or at low frequencies, it is possible to find closed form solutions for the scattering of bulk waves; however, while working in the mid frequency region, numerical approaches are required.

Many studies of the interaction of torsional wave with defects have been done in the past in different application, i.e., railway [10–55], automobile [56–73], electronics [74], etc. Interaction of the fundamental mode of torsional wave with defects is studied. It is shown that the reflection coefficient is a function of the ratio of the



tapered defect length to the wavelength. Such behavior can be explained by interference between the waves reflected from the two ends of the defect. Influence of the coating of the pipe with a defect on the torsional wave is studied. Due to the results, fundamental torsional wave mode can be applied for coated or layered pipe inspection [2, 75–80].

Unfortunately, most of the studies about focused on the first fundamental mode of the torsional wave. This study aims at the interaction between torsional wave and defect in the case of high frequencies where a  $T(0, 2)$  mode of the torsional wave is exists. The commercial finite element method software [10] is used to investigate the interaction of a torsion wave and a defect.

## 2 Finite Element Analysis

According to [77], the equation of motion for the torsional wave is:

$$\frac{1}{c_t^2} \frac{\partial^2 u_\theta}{\partial t^2} - \nabla^2 u_\theta = 0, u_\theta = \left[ \frac{\partial}{\partial r}, \frac{\partial}{\partial z} \right] \quad (1)$$

where  $u_\theta$ —displacement in  $\theta$  direction,  $c_t$ —shear wave speed,  $r, z$ —coordinates in the cylindrical coordinate system. Presented Eq. 1 solved by finite element (FE) method in the time domain with free surface boundary condition on inner and outer surfaces of the pipe. To reduce the computational time and cost, the coefficient form PDE were used as in Eq. 2.

$$e_a \frac{\partial^2 u_\theta}{\partial t^2} + d_a \frac{\partial u_\theta}{\partial t} - c \nabla^2 u_\theta = f,$$

where  $e_a = 1/c_t^2$ ,  $d_a$ —damping coefficient,  $c = 1, f$ —source term.

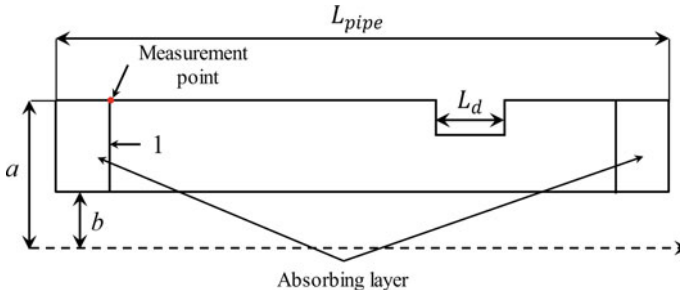
The geometry of the current study is a hollow cylinder with a wall thickness  $d$  (Fig. 1). Length of the pipe  $L_{\text{pipe}} = 90\lambda$  was scalable to reduce a size of the model and depends on frequency.

The excitation impulse is 30 cycles of the sinus with a hamming window function as a source was applied for boundary 1. The reflected waves are monitored in point 1. Additional parameters for the FE simulation are presented in Table 1.

Because of the finite size of the geometry there will be reflections and to avoid them, absorbing layers was added in both sides of the model. Such layers add coordinate dependent damping  $d_e$  to the equation (Fig. 2). The value of damping coefficient was manually defined to absorb all of the mode existing in simulation.

For every FE simulation, it is necessary to make mesh convergence. Time discretization can be calculated using Courant–Friedrichs–Lewy criterion:

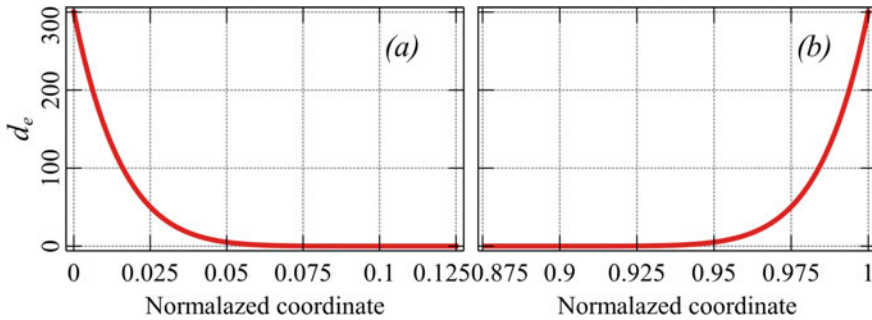
$$\frac{\text{CFL} \cdot \Delta x}{v} = \Delta t \quad (2)$$



**Fig. 1** Hollow cylinder with tapered defect

**Table 1** Parameters for FE simulation

Parameter	Example
$a$	32.6 mm
$b$	38.1 mm
$L_d$	15 mm
$c_t$	3190 m/s
Frequency range $f$	300–400 kHz
Defect depth	50% of wall thickness



**Fig. 2** Damping coefficient  $d_e$  versus normalized coordinate for left (a) and right (b) sides of the pipe

where CFL—constant;  $v$ —wave speed;  $\Delta x$  and  $\Delta t$  spatial and time discretization, respectively.

In Fig. 3, relative “error” is presented for the different CFL numbers. By defining maximum error equal to  $10^{-3}$ , the mesh size and CFL can be defined. For this study, the mesh size equal to  $\lambda/14$  and  $CFL = 0.2$  in order to reduce the computational cost and amount of data generated by the simulation.

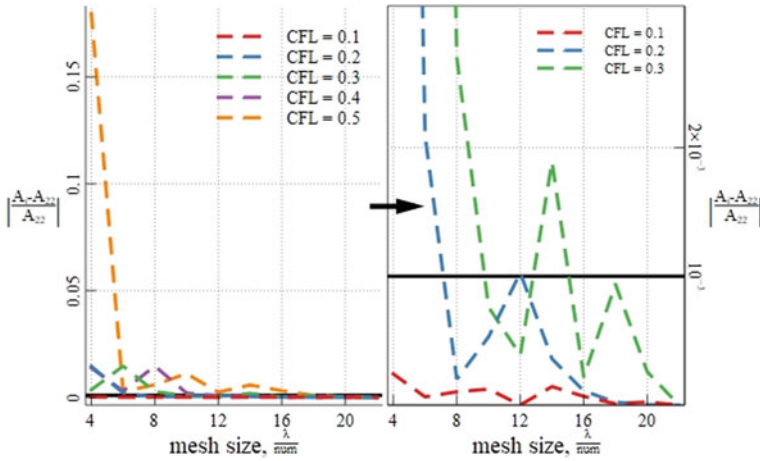


Fig. 3 Relative error versus mesh size

### 2.1 FE Simulation Results

To calculate reflection coefficient  $R$ , FFT procedure was performed for the time track and  $R$  can be defined as ration between the displacement amplitude of incident and reflected waves on the central frequency. To verify the results, simulation in frequency range from 76 to 212 kHz was made. Resulted data were compared with the solution from [2] based on reciprocity theorem. In Fig. 4, reflection coefficient versus  $L_d/\lambda$  ratio is depicted. The graphic shows that the reflection coefficient depends on frequency, with the maximum being a multiple of a quarter of a wave and the minimum being a multiple of half a wave. The graph, however, demonstrates a mismatch in the results, which can be explained by time delay between 2 reflected waves (from near and far boundaries of the defect) in the FEM case. Despite that fact, results show good agreement.

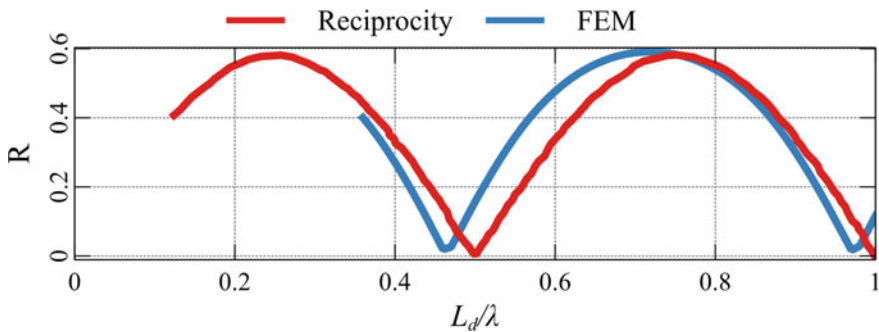
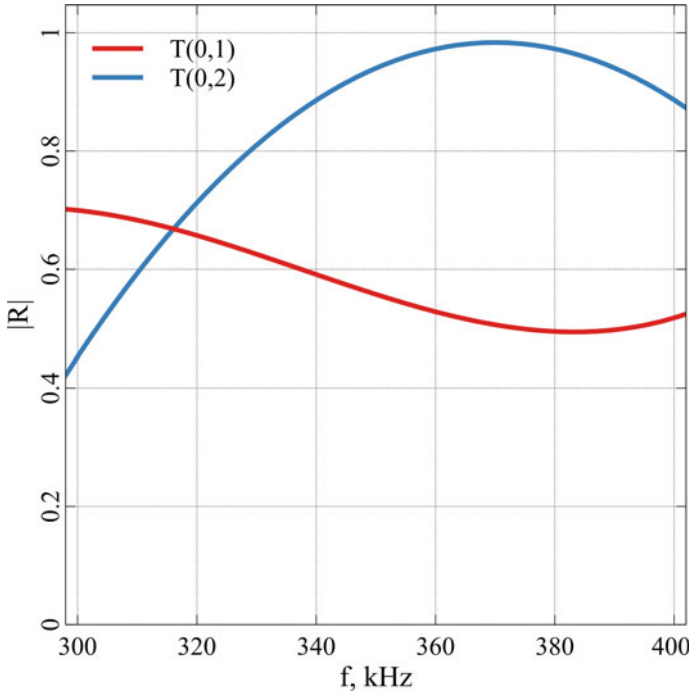


Fig. 4 Reflection coefficient versus  $L_d/\lambda$  ratio for the defect with depth 50% of the wall thickness



**Fig. 5** Reflection coefficient for  $T(0, 1)$  and  $T(0, 2)$  modes versus frequency

In Fig. 5, reflection coefficient for the  $T(0, 1)$  and  $T(0, 2)$  mode is depicted.

The reflection coefficient  $T(0, 2)$  climbs until a frequency of 370 kHz and then begins to fall, whereas the reflection coefficient  $T(0, 1)$  does the opposite. In comparison with the results from Fig. 4, the reflection coefficient for the  $T(0, 1)$  changes its «harmonic» behavior and there is no zero reflection point corresponded to a multiple of the half wave.

### 3 Conclusion

The reflection of the torsional wave was studied by FEM and verified by existing studies. Next the frequency range was shifted to high frequencies to analyze the reflection of the  $T(0, 2)$  mode. Presented results show high values of  $T(0, 2)$  reflection, which can be used for damage detection.

**Acknowledgements** This work was supported by Korea Institute of Energy Technology Evaluation and Planning (KETEP) grant funded by Korea government (MOTIE) (20214000000480, Development of R&D engineers for combined cycle power plan technologies).

## References

1. Carandente R, Ma J, Cawley P (2010) The scattering of the fundamental torsional mode from axi-symmetric defects with varying depth profile in pipes. *J Acous Soc Am* 127(6):3440–3448
2. Lee J, Achenbach JD, Cho Y (2018) Use of the reciprocity theorem for a closed form solution of scattering of the lowest axially symmetric torsional wave mode by a defect in a pipe. *Ultrasonics* 84:45–52
3. Løvstad A, Cawley P (2011) The reflection of the fundamental torsional guided wave from multiple circular holes in pipes. *NDT and E Int* 44(7):553–562
4. Heinlein S, Cawley P, Vogt TK (2018) Reflection of torsional T (0, 1) guided waves from defects in pipe bends. *NDT and E Int* 93:57–63
5. Ma J, Simonetti F, Lowe MJS (2006) Scattering of the fundamental torsional mode by an axisymmetric layer inside a pipe. *J Acous Soc Am* 120(4):1871–1880
6. Kirby R, Zlatev Z, Mudge P (2012) On the scattering of torsional elastic waves from axisymmetric defects in coated pipes. *J Sound Vib* 331(17):3989–4004
7. Zhang X et al (2017) Scattering of torsional flexural guided waves from circular holes and crack-like defects in hollow cylinders. *NDT & E Int* 89(2017):56–66
8. Hay TR, Rose JL (2003) Fouling detection in the food industry using ultrasonic guided waves. *Food Control* 14(7):481–488
9. Chati F et al (2011) Longitudinal mode L (0, 4) used for the determination of the deposit width on the wall of a pipe. *NDT & E Int* 44(2):188–194
10. Sharma SK, Sharma RC (2018) Simulation of quarter-car model with magnetorheological dampers for ride quality improvement. *Int J Veh Struct Syst* 10:169–173. <https://doi.org/10.4273/ijvss.10.3.03>
11. Sharma SK, Lavania S (2013) Green manufacturing and green supply chain management in India: a review. In: *Futuristic trends in mechanical and industrial engineering*. JECRC UDML College of Engineering, pp 1–8
12. Mohapatra S, Mohanty D, Mohapatra S, Sharma S, Dikshit S, Kohli I, Samantaray DP, Kumar R, Kathpalia M (2021) Biomedical application of polymeric biomaterial: polyhydroxybutyrate. In: *Bioresource utilization and management: applications in therapeutics, biofuels, agriculture, and environmental science*. CRC Press, pp 1–14
13. Sharma RC, Sharma SK, Sharma N, Sharma S (2020) Analysis of ride and stability of an ICF railway coach. *Int J Veh Noise Vib* 16:127. <https://doi.org/10.1504/IJNVN.2020.117820>
14. Sharma SK, Kumar A (2017) Ride performance of a high speed rail vehicle using controlled semi active suspension system. *Smart Mater Struct* 26:055026. <https://doi.org/10.1088/1361-665X/aa68f7>
15. Sharma SK, Chaturvedi S (2016) Jerk analysis in rail vehicle dynamics. *Perspect Sci* 8:648–650. <https://doi.org/10.1016/j.pisc.2016.06.047>
16. Sharma SK, Lee J, Jang H-L (2022) Mathematical modeling and simulation of suspended equipment impact on car body modes. *Machines* 10:192. <https://doi.org/10.3390/machines10030192>
17. Sharma SK, Sharma RC (2019) Pothole detection and warning system for Indian roads. In: *Advances in interdisciplinary engineering*, pp 511–519. [https://doi.org/10.1007/978-981-13-6577-5\\_48](https://doi.org/10.1007/978-981-13-6577-5_48)
18. Sharma SK (2019) Multibody analysis of longitudinal train dynamics on the passenger ride performance due to brake application. *Proc Inst Mech Eng Part K J Multi-body Dyn* 233:266–279. <https://doi.org/10.1177/1464419318788775>
19. Goswami B, Rathi A, Sayeed S, Das P, Sharma RC, Sharma SK (2019) Optimization design for aerodynamic elements of Indian locomotive of passenger train. In: *Advances in engineering design. Lecture notes in mechanical engineering*. Springer, Singapore, pp 663–673. [https://doi.org/10.1007/978-981-13-6469-3\\_61](https://doi.org/10.1007/978-981-13-6469-3_61)
20. Sharma RC, Sharma S, Sharma N, Sharma SK (2021) Linear and nonlinear analysis of ride and stability of a three-wheeled vehicle subjected to random and bump inputs using bond graph and Simulink methodology. *SAE Int J Commer Veh* 14. <https://doi.org/10.4271/02-15-01-0001>

21. Sharma SK, Lee J (2020) Finite element analysis of a fishplate rail joint in extreme environment condition. *Int J Veh Struct Syst* 12:503–506. <https://doi.org/10.4273/ijvss.12.5.03>
22. Sharma SK, Kumar A (2016) Dynamics analysis of wheel rail contact using FEA. *Procedia Eng* 144:1119–1128. <https://doi.org/10.1016/j.proeng.2016.05.076>
23. Sharma RC, Palli S, Sharma N, Sharma SK (2021) Ride behaviour of a four-wheel vehicle using H infinity semi-active suspension control under deterministic and random inputs. *Int J Veh Struct Syst* 13:234–237. <https://doi.org/10.4273/ijvss.13.2.18>
24. Sharma RC, Sharma SK (2018) Sensitivity analysis of three-wheel vehicle's suspension parameters influencing ride behavior. *Noise Vib Worldw* 49:272–280. <https://doi.org/10.1177/0957456518796846>
25. Bhardawaj S, Sharma RC, Sharma SK (2020) Development of multibody dynamical using MR damper based semi-active bio-inspired chaotic fruit fly and fuzzy logic hybrid suspension control for rail vehicle system. *Proc Inst Mech Eng Part K J Multi-body Dyn* 234:723–744. <https://doi.org/10.1177/1464419320953685>
26. Sharma SK, Sharma RC, Lee J (2022) In situ and experimental analysis of longitudinal load on carbody fatigue life using nonlinear damage accumulation. *Int J Damage Mech* 31:605–622. <https://doi.org/10.1177/10567895211046043>
27. Sharma SK, Sharma RC, Lee J (2021) Effect of rail vehicle-track coupled dynamics on fatigue failure of coil spring in a suspension system. *Appl Sci* 11:2650. <https://doi.org/10.3390/app11062650>
28. Goyal S, Anand CS, Sharma SK, Sharma RC (2019) Crashworthiness analysis of foam filled star shape polygon of thin-walled structure. *Thin-Walled Struct* 144:106312. <https://doi.org/10.1016/j.tws.2019.106312>
29. Bhardawaj S, Chandmal Sharma R, Kumar Sharma S (2019) A survey of railway track modelling. *Int J Veh Struct Syst* 11:508–518. <https://doi.org/10.4273/ijvss.11.5.08>
30. Sharma SK, Kumar A (2014) A comparative study of Indian and worldwide railways. *Int J Mech Eng Robot Res* 1:114–120
31. Sharma RC, Sharma S, Sharma SK, Sharma N (2020) Analysis of generalized force and its influence on ride and stability of railway vehicle. *Noise Vib Worldw* 51:95–109. <https://doi.org/10.1177/0957456520923125>
32. Sharma SK, Sharma RC, Lee J, Jang H-L (2022) Numerical and experimental analysis of DVA on the flexible-rigid rail vehicle carbody resonant vibration. *Sensors* 22:1922. <https://doi.org/10.3390/s22051922>
33. Sinha AK, Sengupta A, Gandhi H, Bansal P, Agarwal KM, Sharma SK, Sharma RC, Sharma SK (2019) Performance enhancement of an all-terrain vehicle by optimizing steering, powertrain and brakes. In: *Advances in engineering design*, pp 207–215. [https://doi.org/10.1007/978-981-13-6469-3\\_19](https://doi.org/10.1007/978-981-13-6469-3_19)
34. Sharma RC, Sharma SK, Palli S (2020) Linear and non-linear stability analysis of a constrained railway wheelaxle. *Int J Veh Struct Syst* 12:128–133. <https://doi.org/10.4273/ijvss.12.2.04>
35. Kulkarni D, Sharma SK, Kumar A (2016) Finite element analysis of a fishplate rail joint due to wheel impact. In: *International conference on advances in dynamics, vibration and control (ICADVC-2016) NIT Durgapur, India, February 25–27, 2016*. National Institute of Technology Durgapur, Durgapur, India
36. Sharma SK, Lavania S (2011) Skin effect in high speed VLSI on-chip interconnects. In: *International conference on VLSI, communication and networks, V-CAN*. Institute of Engineering and Technology, Alwar, pp 1–8
37. Sharma S, Sharma RC, Sharma SK, Sharma N, Palli S, Bhardawaj S (2020) Vibration isolation of the quarter car model of road vehicle system using dynamic vibration absorber. *Int J Veh Struct Syst* 12:513–516. <https://doi.org/10.4273/ijvss.12.5.05>
38. Sharma RC, Sharma S, Sharma SK, Sharma N, Singh G (2021) Analysis of bio-dynamic model of seated human subject and optimization of the passenger ride comfort for three-wheel vehicle using random search technique. *Proc Inst Mech Eng Part K J Multi-body Dyn* 235:106–121. <https://doi.org/10.1177/1464419320983711>

39. Sharma SK, Sharma RC (2021) Multi-objective design optimization of locomotive nose. In: SAE technical paper, pp 1–10. <https://doi.org/10.4271/2021-01-5053>
40. Sharma SK, Kumar A, Sharma RC (2014) Challenges in railway vehicle modeling and simulations. In: International conference on newest drift in mechanical engineering (ICNDME-14), December 20–21, M. M. University, Mullana, India, pp 453–459. Maharishi Markandeshwar University, Mullana—Ambala
41. Vishwakarma PN, Mishra P, Sharma SK (2022) Characterization of a magnetorheological fluid damper a review. *Mater Today Proc* 56:2988–2994. <https://doi.org/10.1016/j.matpr.2021.11.143>
42. Acharya A, Gahlaut U, Sharma K, Sharma SK, Vishwakarma PN, Phanden RK (2020) Crashworthiness analysis of a thin-walled structure in the frontal part of automotive chassis. *Int J Veh Struct Syst* 12:517–520. <https://doi.org/10.4273/ijvss.12.5.06>
43. Bhardawaj S, Sharma RC, Sharma SK (2020) Development in the modeling of rail vehicle system for the analysis of lateral stability. *Mater Today Proc* 25:610–619. <https://doi.org/10.1016/j.matpr.2019.07.376>
44. Sharma SK, Phan H, Lee J (2020) An application study on road surface monitoring using DTW based image processing and ultrasonic sensors. *Appl Sci* 10:4490. <https://doi.org/10.3390/app10134490>
45. Palli S, Koona R, Sharma SK, Sharma RC (2018) A review on dynamic analysis of rail vehicle coach. *Int J Veh Struct Syst* 10:204–211. <https://doi.org/10.4273/ijvss.10.3.10>
46. Sharma SK, Lee J (2021) Crashworthiness analysis for structural stability and dynamics. *Int J Struct Stab Dyn* 21:2150039. <https://doi.org/10.1142/S0219455421500395>
47. Lavania S, Sharma SK (2011) An explicit approach to compare crosstalk noise and delay in VLSI RLC interconnect modeled with skin effect with step and ramp input. *J VLSI Des Tools Technol* 1:1–8
48. Bhardawaj S, Sharma R, Sharma S (2020) Ride analysis of track-vehicle-human body interaction subjected to random excitation. *J Chinese Soc Mech Eng* 41:237–236. <https://doi.org/10.29979/JCSME>
49. Sharma RC, Palli S, Sharma SK, Roy M (2018) Modernization of railway track with composite sleepers. *Int J Veh Struct Syst* 9:321–329
50. Choppara RK, Sharma RC, Sharma SK, Gupta T (2019) Aero dynamic cross wind analysis of locomotive. In: IOP conference series: materials science and engineering, p 12035
51. Palli S, Sharma RC, Sharma SK, Chintada VB (2020) On methods used for setting the curve for railway tracks. *J Crit Rev* 7:241–246
52. Bhardawaj S, Sharma RC, Sharma SK (2020) Analysis of frontal car crash characteristics using ANSYS. *Mater Today Proc* 25:898–902. <https://doi.org/10.1016/j.matpr.2019.12.358>
53. Sharma SK, Sharma RC, Sharma N (2020) Combined multi-body-system and finite element analysis of a rail locomotive crashworthiness. *Int J Veh Struct Syst* 12:428–435. <https://doi.org/10.4273/ijvss.12.4.15>
54. Sharma RC, Sharma SK (2022) Ride analysis of road surface-three-wheeled vehicle-human subject interactions subjected to random excitation. *SAE Int J Commer Veh* 15. <https://doi.org/10.4271/02-15-03-0017>
55. Sharma SK, Saini U, Kumar A (2019) Semi-active control to reduce lateral vibration of passenger rail vehicle using disturbance rejection and continuous state damper controllers. *J Vib Eng Technol* 7:117–129. <https://doi.org/10.1007/s42417-019-00088-2>
56. Lee J, Sharma SK (2020) Numerical investigation of critical speed analysis of high-speed rail vehicle. *한국정밀공학회 학술발표대회 논문집 Korean Soc Precis Eng* 696
57. Sharma SK, Sharma RC, Kumar A, Palli S (2015) Challenges in rail vehicle-track modeling and simulation. *Int J Veh Struct Syst* 7:1–9. <https://doi.org/10.4273/ijvss.7.1.01>
58. Sharma SK, Mohapatra S, Sharma RC, Alturjman S, Alturjman C, Mostarda L, Stephan T (2022) Retrofitting existing buildings to improve energy performance. *Sustainability* 14:666. <https://doi.org/10.3390/su14020666>
59. Sharma RC, Sharma SK, Palli S (2018) Rail vehicle modelling and simulation using Lagrangian method. *Int J Veh Struct Syst* 10:188–194. <https://doi.org/10.4273/ijvss.10.3.07>



60. Sharma SK (2013) Zero energy building envelope components: a review. *Int J Eng Res Appl* 3:662–675
61. Wu Q, Cole C, Spiriyagin M, Chang C, Wei W, Ursulyak L, Shvets A, Murtaza MA, Mirza IM, Zheliezov K, Mohammadi S, Serajian H, Schick B, Berg M, Sharma RC, Aboubakr A, Sharma SK, Melzi S, Di Gialleonardo E, Bosso N, Zampieri N, Magelli M, Ion CC, Routcliffe I, Pudovikov O, Menaker G, Mo J, Luo S, Ghafourian A, Serajian R, Santos AA, Teodoro ÍP, Eckert JJ, Pugi L, Shabana A, Cantone L (2021) Freight train air brake models. *Int J Rail Transp*:1–49. <https://doi.org/10.1080/23248378.2021.2006808>
62. Sharma SK, Kumar A (2016) The impact of a rigid-flexible system on the ride quality of passenger bogies using a flexible carbody. In: Pombo J (ed) *Proceedings of the third international conference on railway technology: research, development and maintenance*, Stirlingshire, UK. Civil-Comp Press, 2016, Stirlingshire, UK, p 87. <https://doi.org/10.4203/ccp.110.87>
63. Sharma SK, Sharma RC (2018) An investigation of a locomotive structural crashworthiness using finite element simulation. *SAE Int J Commer Veh* 11:235–244. <https://doi.org/10.4271/02-11-04-0019>
64. Sharma SK, Kumar A (2018) Ride comfort of a higher speed rail vehicle using a magnetorheological suspension system. *Proc Inst Mech Eng Part K J Multi-body Dyn* 232:32–48. <https://doi.org/10.1177/1464419317706873>
65. Mohapatra S, Pattnaik S, Maity S, Mohapatra S, Sharma S, Akhtar J, Pati S, Samantaray DP, Varma A (2020) Comparative analysis of PHAs production by *Bacillus megaterium* OUA1016 under submerged and solid-state fermentation. *Saudi J Biol Sci* 27:1242–1250. <https://doi.org/10.1016/j.sjbs.2020.02.001>
66. Bhardawaj S, Sharma RC, Sharma SK, Sharma N (2021) On the planning and construction of railway curved track. *Int J Veh Struct Syst* 13:151–159. <https://doi.org/10.4273/ijvss.13.2.04>
67. Choi S, Lee J, Sharma SK (2021) A study on the performance evaluation of hydraulic tank injectors. In: *Advances in engineering design: select proceedings of FLAME 2020*. Springer Singapore, pp 183–190. [https://doi.org/10.1007/978-981-33-4684-0\\_19](https://doi.org/10.1007/978-981-33-4684-0_19)
68. Sharma SK, Kumar A (2018) Disturbance rejection and force-tracking controller of nonlinear lateral vibrations in passenger rail vehicle using magnetorheological fluid damper. *J Intell Mater Syst Struct* 29:279–297. <https://doi.org/10.1177/1045389X17721051>
69. Sharma SK, Kumar A (2017) Impact of electric locomotive traction of the passenger vehicle ride quality in longitudinal train dynamics in the context of Indian railways. *Mech Ind* 18:222. <https://doi.org/10.1051/meca/2016047>
70. Lee J, Han J, Sharma SK (2021) Structural analysis on the separated and integrated differential gear case for the weight reduction. In: Joshi P, Gupta SS, Shukla AK, Gautam SS (eds) *Advances in engineering design. Lecture notes in mechanical engineering*, pp 175–181. [https://doi.org/10.1007/978-981-33-4684-0\\_18](https://doi.org/10.1007/978-981-33-4684-0_18).
71. Sharma SK, Lee J (2020) Design and development of smart semi active suspension for nonlinear rail vehicle vibration reduction. *Int J Struct Stab Dyn* 20:2050120. <https://doi.org/10.1142/S0219455420501205>
72. Sharma SK, Lavania S (2013) An autonomous metro: design and execution. In: *Futuristic trends in mechanical and industrial engineering*. JECRC UDML College of Engineering, Jaipur, pp 1–8
73. Bhardawaj S, Chandmal Sharma R, Kumar Sharma S (2019) Development and advancement in the wheel-rail rolling contact mechanics. *IOP Conf Ser Mater Sci Eng* 691:012034. <https://doi.org/10.1088/1757-899X/691/1/012034>
74. Sharma SK, Kumar A (2018) Impact of longitudinal train dynamics on train operations: a simulation-based study. *J Vib Eng Technol* 6:197–203. <https://doi.org/10.1007/s42417-018-0033-4>
75. Kirby R, Zlatev Z, Mudge P (2012) On the scattering of torsional elastic waves from axisymmetric defects in coated pipes. *J Sound Vib* 331:3989–4004. <https://doi.org/10.1016/j.jsv.2012.04.013>
76. Demma A, Cawley P, Lowe M, Roosenbrand AG (2003) The reflection of the fundamental torsional mode from cracks and notches in pipes. In: *Dynamic methods for damage detection*



- in structures. Springer Vienna, Vienna, pp 195–209. [https://doi.org/10.1007/978-3-211-78777-9\\_8](https://doi.org/10.1007/978-3-211-78777-9_8)
77. Duan W, Kirby R, Mudge P (2017) On the scattering of torsional waves from axisymmetric defects in buried pipelines. *J Acoust Soc Am* 141:3250–3261. <https://doi.org/10.1121/1.4983192>
  78. Ma J, Simonetti F, Lowe MJS (2006) Scattering of the fundamental torsional mode by an axisymmetric layer inside a pipe. *J Acoust Soc Am* 120:1871–1880. <https://doi.org/10.1121/1.2336750>
  79. Dao DK, Ngo V, Phan H, Pham CV, Lee J, Bui TQ (2020) Rayleigh wave motions in an orthotropic half-space under time-harmonic loadings: a theoretical study. *Appl Math Model* 87:171–179. <https://doi.org/10.1016/j.apm.2020.06.006>
  80. Choi S, Park J, Lee J (2021) A study on the correlation between ultrasonic velocity and stacking thickness of 3D printed specimens. *J Korean Soc Nondestruct Test* 41:102–109. <https://doi.org/10.7779/JKSNT.2021.41.2.102>

# A Comparative Study on Ultrasonic Propagation Characteristics and Defect Detection of Metal Material Additive Manufacturing Using Deep Learning Algorithm



Hyeonsu Song , Junpil Park , Sunil Kumar Sharma, and Jaesun Lee 

**Abstract** The method of measuring the thickness of the specimen using bulk waves is an effective technique for measuring the thickness of the structure in the ultrasonic non-destructive technique. The principle of measuring the bulk wave thickness can be used to determine the thickness of the structure using the correlation between the reciprocating time when the ultrasonic waves pass through the internal material of the specimen and return from the bottom. As interest in 3D printers has increased recently, this paper studied how to process ultrasound A-scan signals reflected from the bottom when measuring the thickness of a structure using the above method. For the experiment, the step wedge manufactured in units of 5 mm from 5 to 25 mm with a 1018 steel material was repeatedly tested using volumetric waves, a result value was derived, and data was generated by imaging it, and then the neural network was trained using MATLAB's Pre-trained Deep Neural Networks. Afterward, the A-scan image of step wedge produced by 3D printer was added to the learned network and used as test data, indicating that the classification according to thickness was very good. Finally, the results were confirmed by training to classify the image results of the defective step wedge produced by the 3D printer. This study is believed to be effective as a basic study in comparing specimens produced with 3D printers through Deep Learning and observing defects.

**Keywords** Deep Learning · Ultrasonic testing · Thickness measurement · 3D printer

---

H. Song · J. Lee (✉)

School of Mechanical Engineering, Changwon National University, Changwon 51140, Korea  
e-mail: [jaesun@changwon.ac.kr](mailto:jaesun@changwon.ac.kr)

J. Park

Extreme Environment Design and Manufacturing Innovation Center, Changwon National University, Changwon 51140, Korea

S. K. Sharma

School of Engineering and Applied Science, National Rail and Transportation Institute, Vadodara, Gujarat 390004, India

## 1 Introduction

The thickness measurement method of a specimen using bulk waves is an effective technique for measuring the thickness of a structure in an ultrasonic non-destructive technique [1–3]. The principle of measuring bulk wave thickness is to know the thickness of a structure by using the correlation between the round-trip time when ultrasonic waves pass through the material inside the specimen and return from the bottom and the ultrasonic speed in the material. If the thickness is known, when an internal defect occurs, the location of the defect may be known through the generation of a reflective signal of the defect part. The method has a disadvantage in that, when measuring the thickness of a structure with various shapes and thicknesses, the time value and the ultrasonic speed in the medium should be checked by section on the ultrasonic A-scan signal reflected from the bottom. In addition, errors may occur due to pressure to press the probe and external environment. In addition, the results of A-scan also differ depending on whether there is a defect in the specimen, so the ability to detect differences even at the same thickness is required. There are many applications of ultrasonic propagation characteristics in different area, i.e., railway [4–45], automobile, [46–66] electronics [67, 68], etc.

Recently, research on artificial intelligence has been actively conducted. Basically, there are many basic studies that classify images, and a typical example is Transfer Learning, which uses data suitable for me as training data in the developed network. Recently, research using images has been actively conducted, and research on image classification learning, such as classification using images of COVID-19-infected patients or transfer learning using damaged images of structures, has been actively conducted. Accordingly, a research was conducted that could immediately know the thickness result only with the A-scan image information using Transfer Learning of Deep Learning [2, 3, 69–74].

In addition, basic studies on thickness and defect detection using ultrasonic measurement have been actively conducted, but studies on using output from 3D printer for ultrasonic non-destructive testing are not well seen. Recently, the 3D printer market has become active and it is used in medical fields such as architecture and healthcare, but recently, research has been conducted on how to quickly and accurately test tensile strength and output power. However, there is not much information on the detection of defects in the output yet [72]. Accordingly, it is necessary to compare and analyze the ultrasonic characteristics of products manufactured by companies and products manufactured using 3D printers and study the problem of whether defects in 3D printer output can be detected.

## 2 Image Classification of Ultrasonic Thickness Measurement Results Using Transfer Learning

### 2.1 Prepare the Data

First, for actual data collection, the step wedge (Fig. 1) produced by the company was measured with a pulser/receiver and an ultrasonic sensor of 5 MHz in units of 5 mm from 5 to 25 mm, and 1000 data were collected, 200 each (Fig. 2). A total of 2000 data were collected, and it was difficult to use it for Deep Learning’s image classification as csv file data consisting of time and amplitude values. Therefore, the work of imaging all data through the data preprocessing process was carried out through coding.

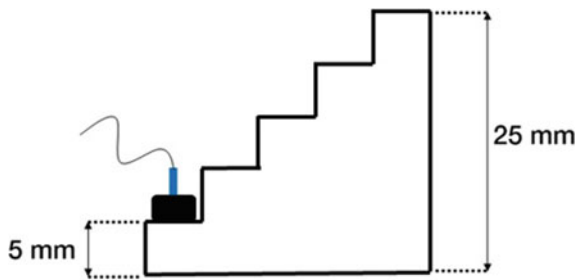


Fig. 1 Step wedge

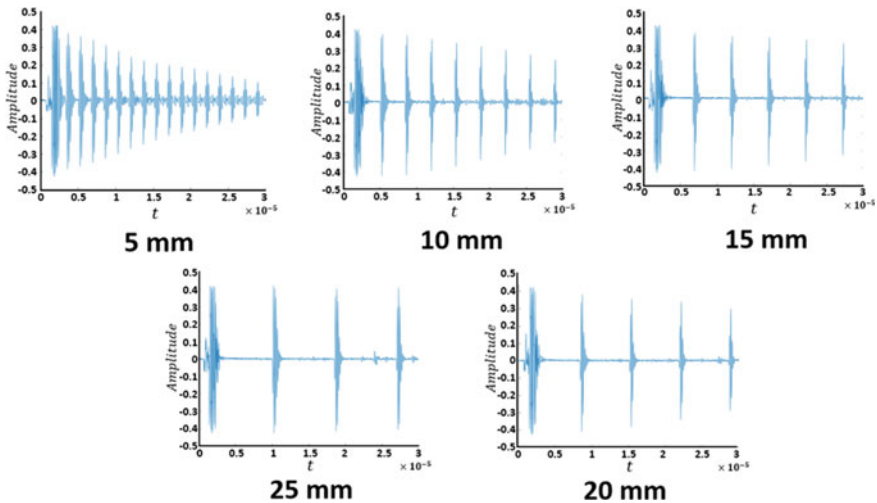


Fig. 2 Step wedge A-scan image result

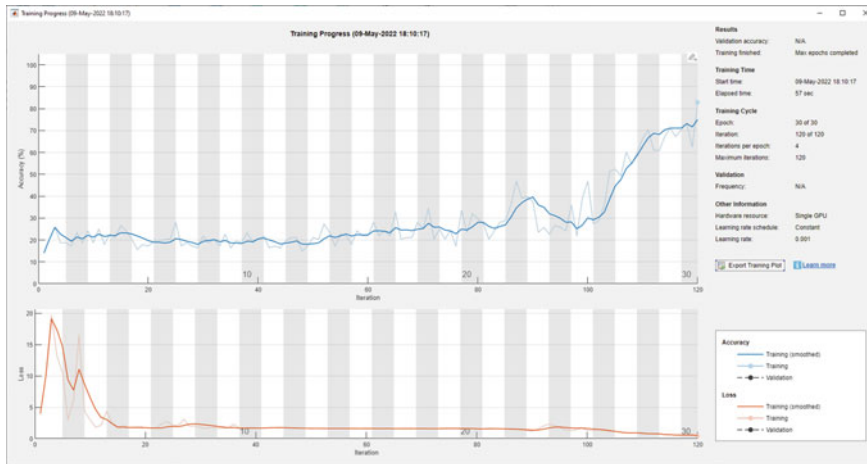


Fig. 3 Training result of the data from the step wedge specimen

## 2.2 Transfer Learning

Transfer learning was conducted through AlexNet. After modifying the network into five classification processes, training was conducted with the default value. The training was conducted with 800 training data and 200 test data, and since it was a network that was not trained with A-scan images, low accuracy was achieved (Fig. 3).

## 2.3 Network Improvement by Changing Options

After dividing the data to be used for training into 600 test data, 200 validation data, and 200 test data, the training options were changed and re-learned, and the successful results were confirmed (Figs. 4 and 5).

# 3 Image Classification of Ultrasonic Thickness Measurement Results Using Transfer Learning

## 3.1 Prepare the Data

Under the same conditions, a total of 1000 data were additionally collected by 200 each of the step wedge specimens made with a 3D printer in 5 mm increments, and converted into images to create data (Fig. 6).

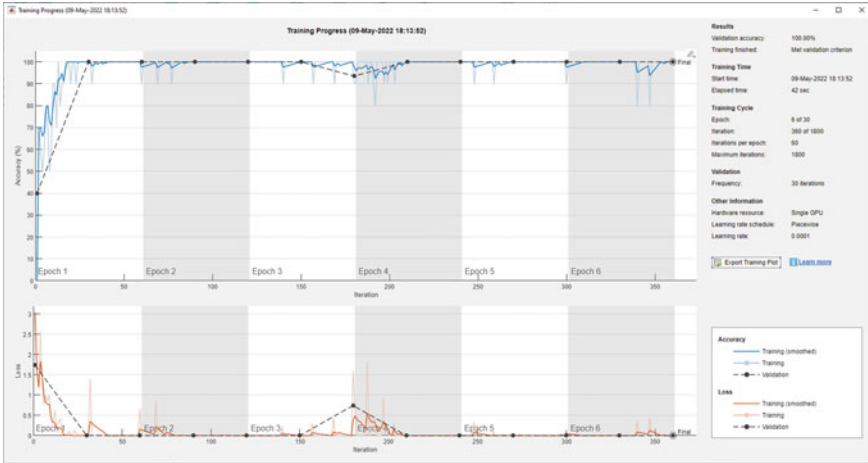


Fig. 4 Re-training result of the data from the step wedge specimen

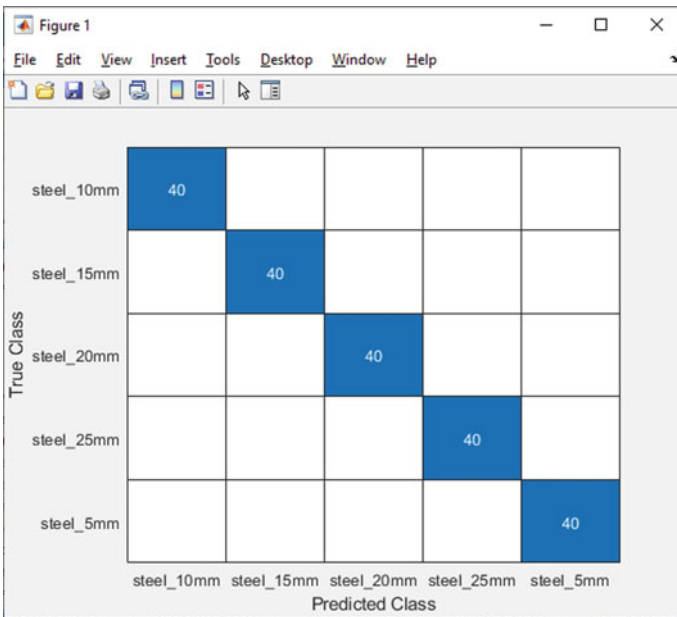


Fig. 5 Test data classification result of the data from the step wedge specimen

### 3.2 Transfer Learning

In the same way as the initial experiment conducted above, Transfer Learning was conducted with the same training options. As a result, validation accuracy achieved

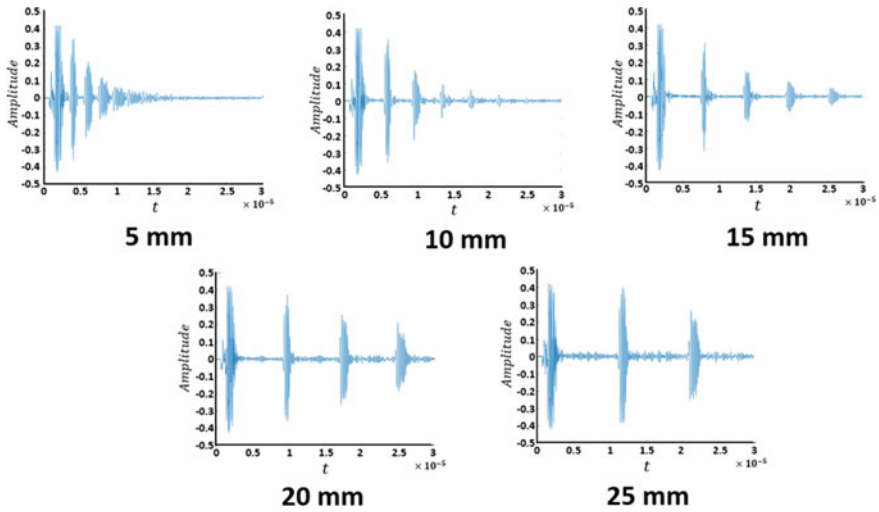


Fig. 6 3D printed step wedge A-scan image result

an accuracy of 94% rather than 100%. As a result of conducting the test using test data, it was confirmed that the accuracy decreased at 20 mm (Figs. 7 and 8).

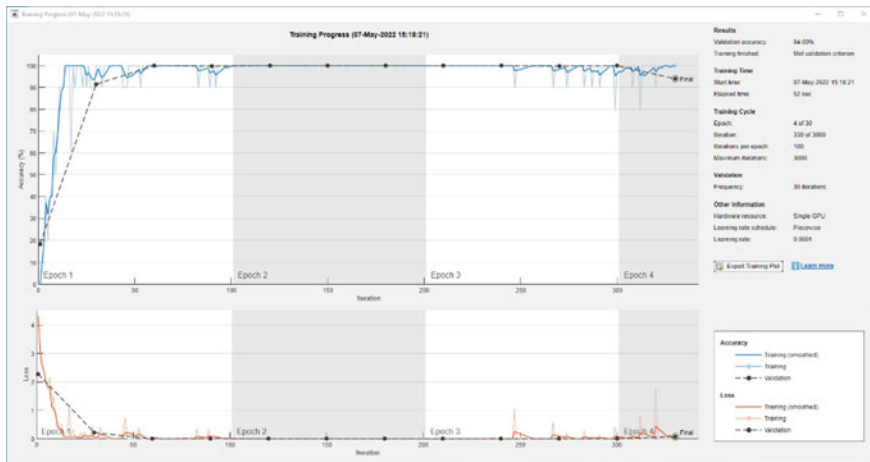


Fig. 7 Training result of the data from the 3D printed step wedge specimen

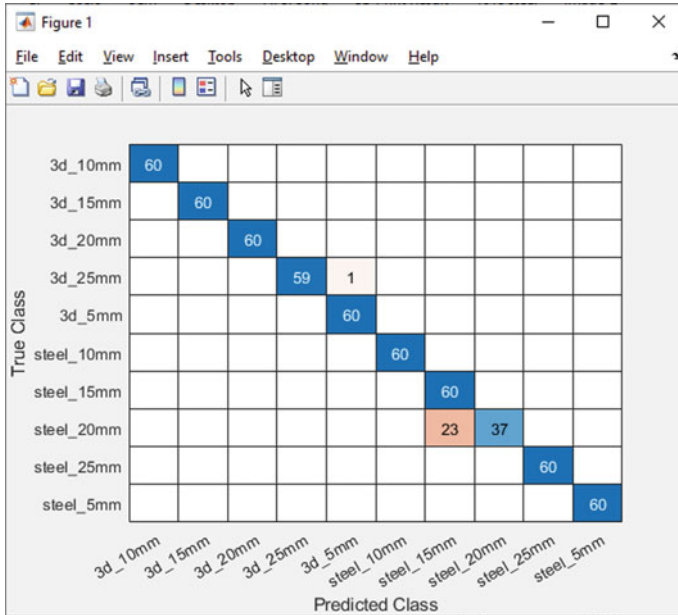


Fig. 8 Test data classification result of the data from the 3D printed step wedge specimen

### 4 Conclusion

In this study, ultrasonic measurements were made to compare and analyze whether the goods manufactured with 3D printers were different from those manufactured by companies, and it was confirmed whether the results could be classified through transfer learning. For signal analysis processing, imaging was performed and used in research, and through this, it was confirmed that basic classification was successfully possible.

However, unlike existing samples, samples manufactured by 3D printers have a difference of 0.7–1 mm for each thickness due to problems that occurred during lamination. As a result, it could be seen that there was a difference in length between the peak points of the two signals, and the difference in ultrasonic signals from the existing sample was large due to severe attenuation.

When Transfer Learning was first attempted, various options such as Initial Learning Rate and Epoch were changed due to low accuracy, and high verification accuracy and test accuracy could be confirmed by training to prevent overfitting by adding validation data.

In addition, when the same training was conducted under the same training option by adding data on specimens made of 3D printer, the validation accuracy was high, but the accuracy was reduced at a thickness of 20 mm due to learning with various signals added. Due to the lack of data, it is determined that sufficient training has not



been conducted or that there may be problems during the training process, so further research on training options is needed before starting training.

**Acknowledgements** This work was supported by Korea Institute of Energy Technology Evaluation and Planning (KETEP) grant funded by the Korea government (MOTIE) (2021400000480, Development of R&D engineers for combined cycle power plant technologies).

## References

1. Seo J-S, Lee B-C, Kim Y-Y (2020) Uniformity and accuracy of mortar layer thickness for the quality evaluation of 3D printer output. *J Korea Concr Inst* 32:371–377. <https://doi.org/10.4334/JKCI.2020.32.4.371>
2. Elsaadouny M, Barowski J, Rolfes I (2019) A convolutional neural network for the non-destructive testing of 3D-printed samples. In: 2019 44th International conference on infrared, millimeter, and terahertz waves (IRMMW-THz). IEEE, pp 1–2. <https://doi.org/10.1109/IRMMW-THz.2019.8874445>
3. Elsaadouny M, Barowski J, Rolfes I (2019) Non-destructive testing of 3D-printed samples based on machine learning. In: 2019 IEEE MTT-S Int Microw Work Ser Adv Mater Process RF THz Applications, pp 22–24
4. Sharma SK, Lee J, Jang H-L (2022) Mathematical modeling and simulation of suspended equipment impact on car body modes. *Machines* 10:192. <https://doi.org/10.3390/machines10030192>
5. Sharma SK, Sharma RC, Lee J (2022) In situ and experimental analysis of longitudinal load on car body fatigue life using nonlinear damage accumulation. *Int J Damage Mech* 31:605–622. <https://doi.org/10.1177/10567895211046043>
6. Sharma SK, Sharma RC, Lee J (2021) Effect of rail vehicle-track coupled dynamics on fatigue failure of coil spring in a suspension system. *Appl Sci* 11:2650. <https://doi.org/10.3390/app11062650>
7. Bhardawaj S, Sharma RC, Sharma SK, Sharma N (2021) On the planning and construction of railway curved track. *Int J Veh Struct Syst* 13:151–159. <https://doi.org/10.4273/ijvss.13.2.04>
8. Mohapatra S, Mohanty D, Mohapatra S, Sharma S, Dikshit S, Kohli I, Samantaray DP, Kumar R, Kathpalia M (2021) Biomedical application of polymeric biomaterial: polyhydroxybutyrate. In: *Bioresource utilization and management: applications in therapeutics, biofuels, agriculture, and environmental science*. CRC Press, pp 1–14
9. Sharma RC, Sharma S, Sharma N, Sharma SK (2021) Linear and nonlinear analysis of ride and stability of a three-wheeled vehicle subjected to random and bump inputs using bond graph and Simulink methodology. *SAE Int J Commer Veh* 14. <https://doi.org/10.4271/02-15-01-0001>
10. Wu Q, Cole C, Spiriyagin M, Chang C, Wei W, Ursulyak L, Shvets A, Murtaza MA, Mirza IM, Zhelieznov K, Mohammadi S, Serajian H, Schick B, Berg M, Sharma RC, Aboubakr A, Sharma SK, Melzi S, Di Gialleonardo E, Bosso N, Zampieri N, Magelli M, Ion CC, Routcliffe I, Pudovikov O, Menaker G, Mo J, Luo S, Ghafourian A, Serajian R, Santos AA, Teodoro ÍP, Eckert JJ, Pugi L, Shabana A, Cantone L (2021) Freight train air brake models. *Int J Rail Transp*:1–49. <https://doi.org/10.1080/23248378.2021.2006808>
11. Sharma RC, Sharma S, Sharma SK, Sharma N, Singh G (2021) Analysis of bio-dynamic model of seated human subject and optimization of the passenger ride comfort for three-wheel vehicle using random search technique. *Proc Inst Mech Eng Part KJ Multi-body Dyn* 235:106–121. <https://doi.org/10.1177/1464419320983711>
12. Lee J, Han J, Sharma SK (2021) Structural analysis on the separated and integrated differential gear case for the weight reduction. In: Joshi P, Gupta SS, Shukla AK, Gautam SS (eds) *Advances*

- in engineering design. Lecture notes in mechanical engineering, pp 175–181. [https://doi.org/10.1007/978-981-33-4684-0\\_18](https://doi.org/10.1007/978-981-33-4684-0_18)
13. Sharma SK, Lee J (2020) Finite element analysis of a fishplate rail joint in extreme environment condition. *Int J Veh Struct Syst* 12:503–506. <https://doi.org/10.4273/ijvss.12.5.03>
  14. Sharma RC, Sharma SK, Sharma N, Sharma S (2020) Analysis of ride and stability of an ICF railway coach. *Int J Veh Noise Vib* 16:127. <https://doi.org/10.1504/IJNVN.2020.117820>
  15. Mohapatra S, Pattnaik S, Maity S, Mohapatra S, Sharma S, Akhtar J, Pati S, Samantaray DP, Varma A (2020) Comparative analysis of PHAs production by *Bacillus megaterium* OUAT 016 under submerged and solid-state fermentation. *Saudi J Biol Sci* 27:1242–1250. <https://doi.org/10.1016/j.sjbs.2020.02.001>
  16. Sharma SK, Mohapatra S, Sharma RC, Altrjman S, Altrjman C, Mostarda L, Stephan T (2022) Retrofitting existing buildings to improve energy performance. *Sustainability* 14:666. <https://doi.org/10.3390/su14020666>
  17. Bhardawaj S, Sharma RC, Sharma SK (2020) Development of multibody dynamical using MR damper based semi-active bio-inspired chaotic fruit fly and fuzzy logic hybrid suspension control for rail vehicle system. *Proc Inst Mech Eng Part K J Multi-body Dyn* 234:723–744. <https://doi.org/10.1177/1464419320953685>
  18. Sharma SK, Phan H, Lee J (2020) An application study on road surface monitoring using DTW based image processing and ultrasonic sensors. *Appl Sci* 10:4490. <https://doi.org/10.3390/app10134490>
  19. Sharma SK, Sharma RC, Sharma N (2020) Combined multi-body-system and finite element analysis of a rail locomotive crashworthiness. *Int J Veh Struct Syst* 12:428–435. <https://doi.org/10.4273/ijvss.12.4.15>
  20. Sharma SK, Lee J (2020) Design and development of smart semi active suspension for nonlinear rail vehicle vibration reduction. *Int J Struct Stab Dyn* 20:2050120. <https://doi.org/10.1142/S0219455420501205>
  21. Bhardawaj S, Sharma RC, Sharma SK (2020) Development in the modeling of rail vehicle system for the analysis of lateral stability. *Mater Today Proc* 25:610–619. <https://doi.org/10.1016/j.matpr.2019.07.376>
  22. Bhardawaj S, Sharma R, Sharma S (2020) Ride analysis of track-vehicle-human body interaction subjected to random excitation. *J Chinese Soc Mech Eng* 41:237–236. <https://doi.org/10.29979/JCSME>
  23. Palli S, Sharma RC, Sharma SK, Chintada VB (2020) On methods used for setting the curve for railway tracks. *J Crit Rev* 7:241–246
  24. Sharma RC, Sharma SK, Palli S (2020) Linear and non-linear stability analysis of a constrained railway wheelaxle. *Int J Veh Struct Syst* 12:128–133. <https://doi.org/10.4273/ijvss.12.2.04>
  25. Acharya A, Gahlaut U, Sharma K, Sharma SK, Vishwakarma PN, Phanden RK (2020) Crash-worthiness analysis of a thin-walled structure in the frontal part of automotive chassis. *Int J Veh Struct Syst* 12:517–520. <https://doi.org/10.4273/ijvss.12.5.06>
  26. Sharma S, Sharma RC, Sharma SK, Sharma N, Palli S, Bhardawaj S (2020) Vibration isolation of the quarter car model of road vehicle system using dynamic vibration absorber. *Int J Veh Struct Syst* 12:513–516. <https://doi.org/10.4273/ijvss.12.5.05>
  27. Vishwakarma PN, Mishra P, Sharma SK (2022) Characterization of a magnetorheological fluid damper a review. *Mater Today Proc* 56:2988–2994. <https://doi.org/10.1016/j.matpr.2021.11.143>
  28. Bhardawaj S, Sharma RC, Sharma SK (2020) Analysis of frontal car crash characteristics using ANSYS. *Mater Today Proc* 25:898–902. <https://doi.org/10.1016/j.matpr.2019.12.358>
  29. Sharma RC, Sharma S, Sharma SK, Sharma N (2020) Analysis of generalized force and its influence on ride and stability of railway vehicle. *Noise Vib Worldw* 51:95–109. <https://doi.org/10.1177/0957456520923125>
  30. Lee J, Sharma SK (2020) Numerical investigation of critical speed analysis of high-speed rail vehicle. *한국경밀공학회 학술발표대회 논문집* Korean Soc Precis Eng 696
  31. Sharma SK, Saini U, Kumar A (2019) Semi-active control to reduce lateral vibration of passenger rail vehicle using disturbance rejection and continuous state damper controllers. *J Vib Eng Technol* 7:117–129. <https://doi.org/10.1007/s42417-019-00088-2>

32. Sinha AK, Sengupta A, Gandhi H, Bansal P, Agarwal KM, Sharma SK, Sharma RC, Sharma SK (2019) Performance enhancement of an all-terrain vehicle by optimizing steering, powertrain and brakes. In: *Advances in engineering design*, pp 207–215. [https://doi.org/10.1007/978-981-13-6469-3\\_19](https://doi.org/10.1007/978-981-13-6469-3_19)
33. Choppa RK, Sharma RC, Sharma SK, Gupta T (2019) Aero dynamic cross wind analysis of locomotive. *IOP Conf Ser: Mater Sci Eng*:12035
34. Goswami B, Rathi A, Sayeed S, Das P, Sharma RC, Sharma SK (2019) Optimization design for aerodynamic elements of Indian locomotive of passenger train. In: *Advances in engineering design*. Lecture notes in mechanical engineering. Springer, Singapore, pp 663–673. [https://doi.org/10.1007/978-981-13-6469-3\\_61](https://doi.org/10.1007/978-981-13-6469-3_61)
35. Sharma SK, Sharma RC (2019) Pothole detection and warning system for Indian roads. In: *Advances in interdisciplinary engineering*, pp 511–519. [https://doi.org/10.1007/978-981-13-6577-5\\_48](https://doi.org/10.1007/978-981-13-6577-5_48)
36. Goyal S, Anand CS, Sharma SK, Sharma RC (2019) Crashworthiness analysis of foam filled star shape polygon of thin-walled structure. *Thin-Walled Struct.* 144:106312. <https://doi.org/10.1016/j.tws.2019.106312>
37. Bhardawaj S, Chandmal Sharma R, Kumar Sharma S (2019) Development and advancement in the wheel-rail rolling contact mechanics. *IOP Conf Ser Mater Sci Eng* 691:012034. <https://doi.org/10.1088/1757-899X/691/1/012034>
38. Sharma RC, Sharma SK (2022) Ride analysis of road surface-three-wheeled vehicle-human subject interactions subjected to random excitation. *SAE Int J Commer Veh* 15. <https://doi.org/10.4271/02-15-03-0017>
39. Sharma SK (2019) Multibody analysis of longitudinal train dynamics on the passenger ride performance due to brake application. *Proc Inst Mech Eng Part K J Multi-body Dyn* 233:266–279. <https://doi.org/10.1177/1464419318788775>.
40. Bhardawaj S, Chandmal Sharma R, Kumar Sharma S (2019) A survey of railway track modelling. *Int J Veh Struct Syst* 11:508–518. <https://doi.org/10.4273/ijvss.11.5.08>
41. Sharma SK, Sharma RC, Lee J, Jang H-L (2022) Numerical and experimental analysis of DVA on the flexible-rigid rail vehicle car body resonant vibration. *Sensors* 22:1922. <https://doi.org/10.3390/s22051922>
42. Choi S, Lee J, Sharma SK (2021) A study on the performance evaluation of hydraulic tank injectors. In: *Advances in engineering design: select proceedings of FLAME 2020*. Springer Singapore, pp 183–190. [https://doi.org/10.1007/978-981-33-4684-0\\_19](https://doi.org/10.1007/978-981-33-4684-0_19)
43. Sharma SK, Sharma RC (2021) Multi-objective design optimization of locomotive nose. In: *SAE technical paper*, pp 1–10. <https://doi.org/10.4271/2021-01-5053>
44. Sharma SK, Lee J (2021) Crashworthiness analysis for structural stability and dynamics. *Int J Struct Stab Dyn* 21:2150039. <https://doi.org/10.1142/S0219455421500395>
45. Sharma RC, Palli S, Sharma N, Sharma SK (2021) Ride behaviour of a four-wheel vehicle using h infinity semi-active suspension control under deterministic and random inputs. *Int J Veh Struct Syst* 13:234–237. <https://doi.org/10.4273/ijvss.13.2.18>
46. Sharma RC, Palli S, Sharma SK, Roy M (2018) Modernization of railway track with composite sleepers. *Int J Veh Struct Syst* 9:321–329
47. Sharma SK, Kumar A (2018) Disturbance rejection and force-tracking controller of nonlinear lateral vibrations in passenger rail vehicle using magnetorheological fluid damper. *J Intell Mater Syst Struct* 29:279–297. <https://doi.org/10.1177/1045389X17721051>
48. Sharma SK, Kumar A (2017) Ride performance of a high speed rail vehicle using controlled semi active suspension system. *Smart Mater Struct* 26:055026. <https://doi.org/10.1088/1361-665X/aa68f7>
49. Sharma SK, Kumar A (2016) The impact of a rigid-flexible system on the ride quality of passenger bogies using a flexible car body. In: Pombo J (ed) *Proceedings of the third international conference on railway technology: research, development and maintenance*, Stirlingshire, UK. Civil-Comp Press, 2016, Stirlingshire, UK, p 87. <https://doi.org/10.4203/ccp.110.87>
50. Sharma SK, Chaturvedi S (2016) Jerk analysis in rail vehicle dynamics. *Perspect Sci* 8:648–650. <https://doi.org/10.1016/j.pisc.2016.06.047>

51. Kulkarni D, Sharma SK, Kumar A (2016) Finite element analysis of a fishplate rail joint due to wheel impact. In: International conference on advances in dynamics, vibration and control (ICADVC-2016) NIT Durgapur, India February 25–27, 2016. National Institute of Technology Durgapur, Durgapur, India
52. Sharma SK, Kumar A (2016) Dynamics analysis of wheel rail contact using FEA. *Procedia Eng.* 144:1119–1128. <https://doi.org/10.1016/j.proeng.2016.05.076>
53. Sharma SK, Sharma RC, Kumar A, Palli S (2015) Challenges in rail vehicle-track modeling and simulation. *Int J Veh Struct Syst* 7:1–9. <https://doi.org/10.4273/ijvss.7.1.01>
54. Sharma SK, Kumar A, Sharma RC (2014) Challenges in railway vehicle modeling and simulations. In: International conference on newest drift in mechanical engineering (ICNDME-14), December 20–21, M. M. University, Mullana, India. Maharishi Markandeshwar University, Mullana—Ambala, pp 453–459
55. Sharma SK, Kumar A (2014) A comparative study of Indian and worldwide railways. *Int J Mech Eng Robot Res* 1:114–120
56. Sharma SK, Lavania S (2013) Green manufacturing and green supply chain management in India: a review. In: *Futuristic trends in mechanical and industrial engineering*. JECRC UDML College of Engineering, pp 1–8
57. Sharma SK (2013) Zero energy building envelope components: a review. *Int J Eng Res Appl* 3:662–675
58. Sharma SK, Kumar A (2018) Impact of longitudinal train dynamics on train operations: a simulation-based study. *J Vib Eng Technol* 6:197–203. <https://doi.org/10.1007/s42417-018-0033-4>
59. Sharma SK, Lavania S (2013) An autonomous metro: design and execution. In: *Futuristic trends in mechanical and industrial engineering*. JECRC UDML College of Engineering, Jaipur, pp 1–8
60. Sharma SK, Sharma RC (2018) An investigation of a locomotive structural crashworthiness using finite element simulation. *SAE Int J Commer Veh* 11:235–244. <https://doi.org/10.4271/02-11-04-0019>
61. Sharma RC, Sharma SK (2018) Sensitivity analysis of three-wheel vehicle's suspension parameters influencing ride behavior. *Noise Vib Worldw* 49:272–280. <https://doi.org/10.1177/0957456518796846>
62. Sharma RC, Sharma SK, Palli S (2018) Rail vehicle modelling and simulation using Lagrangian method. *Int J Veh Struct Syst* 10:188–194. <https://doi.org/10.4273/ijvss.10.3.07>
63. Sharma SK, Kumar A (2018) Ride comfort of a higher speed rail vehicle using a magnetorheological suspension system. *Proc Inst Mech Eng Part K J Multi-body Dyn* 232:32–48. <https://doi.org/10.1177/1464419317706873>
64. Sharma SK, Sharma RC (2018) Simulation of quarter-car model with magnetorheological dampers for ride quality improvement. *Int J Veh Struct Syst* 10:169–173. <https://doi.org/10.4273/ijvss.10.3.03>
65. Palli S, Koona R, Sharma SK, Sharma RC (2018) A review on dynamic analysis of rail vehicle coach. *Int J Veh Struct Syst* 10:204–211. <https://doi.org/10.4273/ijvss.10.3.10>
66. Sharma SK, Kumar A (2017) Impact of electric locomotive traction of the passenger vehicle ride quality in longitudinal train dynamics in the context of Indian railways. *Mech Ind* 18:222. <https://doi.org/10.1051/meca/2016047>
67. Sharma SK, Lavania S (2011) Skin effect in high speed VLSI on-chip interconnects. In: International conference on VLSI, communication and networks, V-CAN. Institute of Engineering & Technology, Alwar, pp 1–8
68. Lavania S, Sharma SK (2011) An explicit approach to compare crosstalk noise and delay in VLSI RLC interconnect modeled with skin effect with step and ramp input. *J VLSI Des. Tools Technol* 1:1–8
69. Dao DK, Ngo V, Phan H, Pham CV, Lee J, Bui TQ (2020) Rayleigh wave motions in an orthotropic half-space under time-harmonic loadings: a theoretical study. *Appl Math Model* 87:171–179. <https://doi.org/10.1016/j.apm.2020.06.006>

70. Park J, Lee J, Le Z, Cho Y (2020) High-precision noncontact guided wave tomographic imaging of plate structures using a DHB algorithm. *Appl Sci* 10:4360. <https://doi.org/10.3390/app10124360>
71. Lee J, Ngo V, Phan H, Nguyen T, Dao DK, Cho Y (2019) Scattering of surface waves by a three-dimensional cavity of arbitrary shape: analytical and experimental studies. *Appl Sci* 9:5459. <https://doi.org/10.3390/app9245459>
72. Park J, Lee J, Jeong S-G, Cho Y (2019) A study on guided wave propagation in a long distance curved pipe. *J Mech Sci Technol* 33:4111–4117. <https://doi.org/10.1007/s12206-019-0806-z>
73. Zhu B, Lee J (2019) A study on fatigue state evaluation of rail by the use of ultrasonic nonlinearity. *Materials (Basel)* 12:2698. <https://doi.org/10.3390/ma12172698>
74. Park B, Kim J, Lee J, Kang M-S, An Y-K (2018) Underground object classification for urban roads using instantaneous phase analysis of ground-penetrating radar (GPR) data. *Remote Sens* 10:1417. <https://doi.org/10.3390/rs10091417>

# Design and Fabrication of an Atmospheric Water Generator for Water Harvesting from Moist Air



Uhinee Banerjee, Harsh Kaushik, Harshit Garg, and Basant Singh Sikarwar

**Abstract** For arid and humid regions, atmospheric water condensation becomes the main water source when the water vapor in moist air is condensed effectively and efficiently. In this manuscript, an atmospheric water generator is designed and fabricated. The vapor compression system is used for cooling moist air. These cooling tubes are arranged in a rectangular shape in a vertical orientation such as pulsating heat pipes arrangement. The refrigerant R-22 flows inside the tubes. However, the condensation of moist air took place over these tubes' surface which is coated by hydrophobic coating. This device was examined at various environmental conditions and condensing water from moist air. It has the maximum capacity to produce 6-L water in a day having a relative humidity of 70% and an atmospheric temperature of 32 °C. However, the average power consumption in a day is 0.89 kWh/liter. This arrangement of the evaporator in vapor compression cooling has a high condensation coefficient as compared to other arrangements.

## 1 Introduction

In the twenty-first century, potable water availability is one of the biggest challenges all over the world humankind [1, 2]. Various approaches have been explored to produce potable water under various environmental conditions. Groundwater extraction and water desalination using thermal energy are the most popular methods for regions that have excess availability of water [2, 3]. However, these methods are not suitable for dry and arid regions of the earth. Hence, water scarcity is a challenging issue in today's world. The severe problem of water scarcity is primarily faced by nations with long coastal areas and island nations that lack sufficient freshwater

---

U. Banerjee (✉) · H. Kaushik · H. Garg · B. S. Sikarwar  
Department of Mechanical Engineering, Amity University, Noida, Uttar Pradesh, India  
e-mail: [Uhineebanerjee2131@gmail.com](mailto:Uhineebanerjee2131@gmail.com)

B. S. Sikarwar  
e-mail: [bssikarwar@amity.edu](mailto:bssikarwar@amity.edu)

sources such as rivers and ponds [1–3]. Most of these nations have to rely on desalination which is costly as well as highly energy consuming [4]. It has been roughly estimated that the atmosphere of the earth consists of 12,800 trillion liters of water in form of moisture [5]. This amount of water is enough to meet the requirement of all the wildlife existing on this planet if extracted methodically and effectively [1–5].

Atmospheric water generator (AWG) is a device that generates water from the atmospheric air. It extracts water from ambient humid air by reducing the temperature of moist air below its dew point temperature, increasing the pressure of air exposure to the desiccant. This method is environmentally friendly, and it is attainable, portable, and compatible with existing systems, with no concentrated hypersaline wastewater discharge. India's warm and humid regions have tremendous amounts of ambient water because of its humid climate throughout the year, and hence, this technology is the best fit [3]. Various cooling methods are approached by scientists to extract water from the atmosphere [6–9]. The most common method used is vapor compression refrigeration (VCR)-based system. The condensate obtained further undergoes microbial and mineral treatment and then its fit for consumption.

A large amount of literature review is present on the design and performance of vapor compression refrigeration-based dehumidifier for the development of AWG device carried out by various scientists around the world. Nandy et al. [10] developed a portable thermoelectric water generator. They designed a system to collect water from the atmosphere using a thermoelectric cooler and depending on solar panels as an energy source. They proposed that use of this device in regions of high humidity would allow users to collect one liter of water per hour during the day. Shourideh et al. [11] and Liu et al. [12] designed AWG based on Peltier cooling. They reported that lower COP and water production are costly by this cooling method. Anbarasu and Pavithra [13] created a water generator made from air-conditioning and dehumidifier parts for producing enough water to meet the drinking water needs of a typical household. They also described the need for access to clean drinking water in remote areas, as well as the approaching insufficiency of potable water in some areas as a consequence of global warming and natural disasters. Bagheri [4] have investigated the performance of commercially available atmospheric generating systems, and his findings revealed that water generation is highly sensitive to ambient air conditions. The humid and warm air conditions were discovered to be critical for significant water generation. Habeebullah [14] developed a refrigeration device to extract potable water from fresh air. The author discovered that at high air velocities, the amount of water extracted decreases due to lower evaporator capacity. Ibrahim et al. [15] investigated in an experimental study of vapor compression system with condensate pre-cooling of incoming air was. They discovered that when the inlet air temperature to the condenser was reduced by circulating the condensate through a pre-cooler, the compressor power input was reduced by 6.1% on average due to the decrease in discharge pressure. On average, the coefficient of performance (COP) increased by 21.4%, and second law efficiency increased by 20.5%. Nada et al. [16] have created a hybrid water desalination and air-conditioning system that employs vapor compression refrigeration. At a temperature of 25 °C and a relative humidity range of 45–57%, the system's desired output quantities were approximately 1.77 and



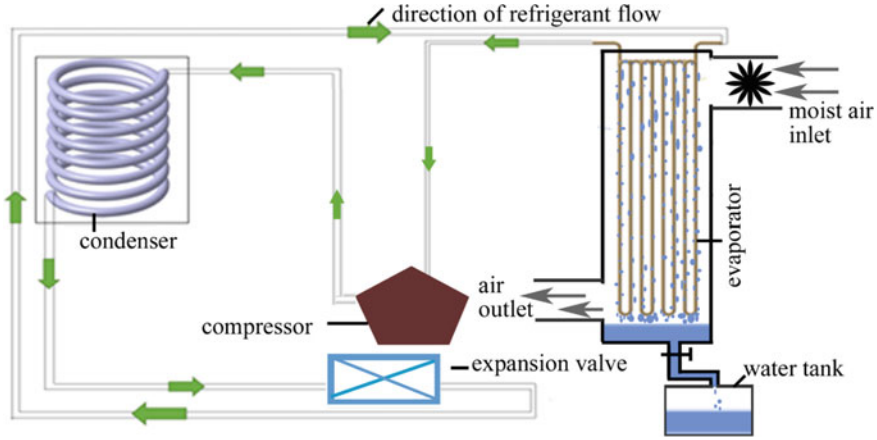
4.74 kg/h. The researcher also proposed that increasing the air specific humidity and inlet temperature, as well as increasing the air mass flow rate, would improve the capacity of desalinated water production. Furthermore, it has been observed that the enhancement of surface by increasing the surface hydrophobicity increases the condensation rate [17, 18]. To improve the superhydrophilicity of the condensing surfaces, low surface energy material modifications to the rough surface may be required [18, 19]. Over the last decade, several methods, including chemical etching [20–24], physical texturing [25, 26], electrodeposition [27, 28], oxidation [5, 28], and sol–gel methods [28–30], have been used to create special hierarchical micro/nano-structures on metal substrates for enhancing the condensing rate of moist air [31].

In this work, vapor compression refrigeration-based system was designed and fabricated for condensing water vapor presence in moist air. The system consists of compressor, condenser, expansion valve, and superhydrophobic copper tube as an evaporator. In the evaporator, the copper tube is encased in the enclosure. A fan is used to facilitate the flow of moist air toward the surface of the tubes. The water vapor condensates over the superhydrophobic surface of the tubes in the form of droplets and then falls down which is transferred to the water tank. However, the superhydrophobic surface of copper tube is fabricated by plasma etching followed by chemical etching which enhances the condensation rate and thermal conductivity resulting in increase of water generation. The aim of this study is to condensate the maximum water quantity achievable for every atmospheric air condition, represented by temperature and humidity.

## 2 Materials and Device

Figure 1 shows the schematic diagram of proposed vapor compression-based atmospheric water generating systems. In this system, the compressor, condenser, and capillary tube of one ton air-condensing unit are used. However, the evaporator of this unit is designed and fabricated as per the enhancing surface area for moist air condensation. In the evaporator, the copper tubes are arranged in a 15 cm × 15 cm × 50 cm acrylic chamber, as shown in Fig. 2a. The total number of tubes is 64, outer diameter of tubes is 6 mm, thickness of tubes is 1 mm, and length of the tubes is 40 cm. The acrylic chamber has an air inlet and an air outlet opening on the opposite faces of chamber at different heights. However, water is collected in bottom of the chamber. Figure 2 shows the photograph of the chamber with arrangement of copper tubes and complete setup of water harvesting. In this device, moist air flows over the evaporator's copper tubes in which outer surfaces were chemically etched for enhancing their hydrophobicity. The details of etching method are reported by authors elsewhere [6, 8, 9]. The obtained contact angle on the pristine and coated copper tube surface were 45° and 135°, respectively. R-22 refrigerant flows through these tubes for maintaining the required cooling condition of water condensation presence in moist air. Condensed water droplets are collected in the tank in which it is processed to filter unit for generating the potable water. The cooled air from





**Fig. 1** Schematic diagram of proposed vapor compression based atmospheric water generating systems

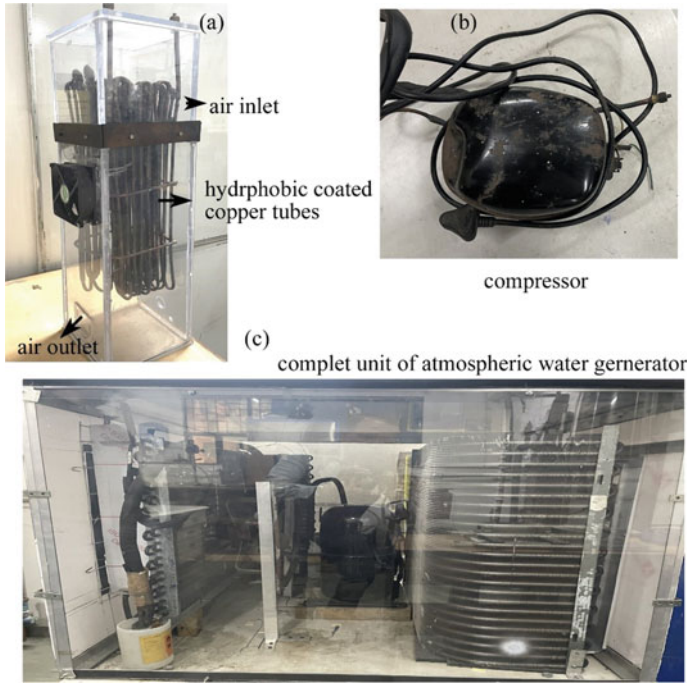
evaporator chamber flows over the compressor. Hence, the sensible cooling of air is used to cool down the compressor for increasing the COP of vapor compression system.

In this study, the proposed atmospheric water generator works on the cooling of vapor compression refrigeration cycle (VCRS). Figure 3a, b shows the  $P-h$  and  $T-S$  diagram of vapor compression cycle. In this cooling method, a refrigerant is compressed by electrically driven compressor to increase its pressure and temperature before entering a condensing unit of refrigerant. The expansion valve decreases the pressure and temperature of the liquid refrigerant before entering the evaporating tubes. The unsaturated moist flows over the evaporating tubes and rejects their heat indirect manner to refrigerant. In this way, the water vapor present in moist air is cooled below the dew point temperature. Hence, moisture in the air to condense and be collected as water.

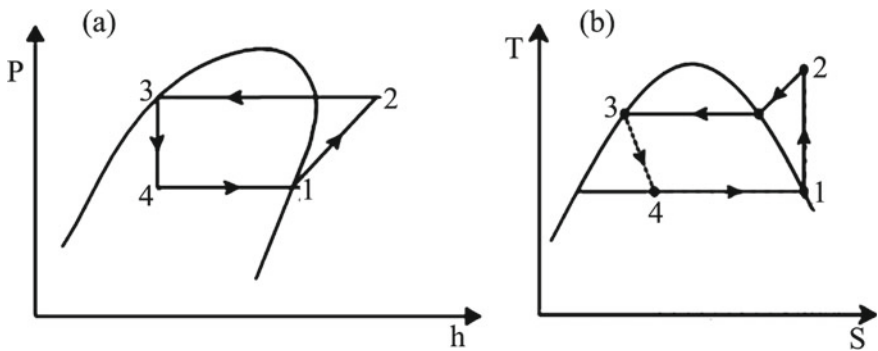
Energy meter is used to measure the power consumption by the vapor compression cycle for given period of water generation. System efficiency is defined as the ratio of the volume of water generated to the total volume of water present in the moist air.

$$\eta = \frac{\dot{m}_w}{\dot{V} \times \phi} \quad (1)$$

Here,  $\dot{m}_w$  is rate mass of condensate (kg/sec),  $\dot{V}$  ( $\text{m}^3/\text{sec}$ ) rate volume of air flow over the tubes, and  $\phi$  is absolute humidity in  $\text{kg}/\text{m}^3$ . Based on the moist air temperature and relative humidity, the absolute humidity is determined by using the following expression [32].



**Fig. 2** a Photographs of evaporator, b compressor, and c complete unit of atmospheric water generator



**Fig. 3** a P-h diagram for vapor compression-based cooling unit and b T-S diagram for vapor compression-based cooling system

$$\phi = \frac{6.112 \times e^{\left(\frac{17.67T}{243.5+T}\right)} \times RH \times 2.1674}{(T + 273.15)}, \tag{2}$$

**Table 1** Details of the experimental date and time with atmospheric conditions

Month/day of experiments	Time period	Average relative humidity (%)	Average temperature (°C)
July 21, 2022	From 9:00 A.M. to 9:00 P.M.	87	30
July 22, 2022		85	29
July 26, 2022		80	29.7
July 27, 2022		81	30.2
July 28, 2022		85.25	28.7
August 16, 2022		77.5	28.8
August 17, 2022		76	29.7
August 18, 2022		75	30
August 23, 2022		70	30.7
September 1, 2022		59.5	31.6
September 2, 2022		59	31.4
September 3, 2022		53	31.6
September 7, 2022		54.5	32
September 9, 2022		65	31.6

where  $T$  is the measured temperature in °C and RH is the relative humidity in percentage (%). The total dissolved solids (TDS) of condensed water are measured periodically with an XSMNER meter. Air velocity flow over the evaporator tubes was measured using hotwire anemometer. The experiments were conducted for various flow rates of air and various relative humidity at different atmospheric temperatures in the months of July, August, and September 2022 in Noida India. The experiment was carried out from 9:30 A.M. to 9:00 P.M. The average relative humidity and temperatures during the experiments date are given in Table 1.

### 3 Result and Discussion

The results obtained after performing the experiment of moist air condensation using the proposed atmospheric water generating are presented in this section. For the months of July, August, and September, hourly water production is shown in Fig. 4.

The graph shows the hourly average water generation from moist from 9:00 A.M. to 4:00 P.M. on 21 at various months (July, August, and September) in the year 2022. The condensation rate during the morning and evening time period is large than the noon time period due the variation of relative humidity and temperature. The average temperature and relative humidity are given in Table 1.

Figure 5 shows the rate of water condensation per day in the months of July, August, and September. Each day, the machine operates for nine hours from 9:00 A.M. to 6:00 P.M. It was observed in the month of August per day condensation rate more than to 10 L for 9 h. Hence, this machine has the capacity to generate water 1.1 L per hour at average temperature 30 °C and relative humidity is 70%. The water generation rate of device was observed large in the month of August. The dependency of water production on the air’s relative humidity was during the month of July. Hence, water production is strongly correlated with the relative humidity values. The average power consumed an average of 1.13kWh/liter which is 304% less than the uncoated copper tubes.

Figure 6 shows power consumption kWh/liter per time period in the month August 9. Although the most important factors affecting water production by proposed machine are the relative humidity and temperature of the environment, the air velocity, altitude, and air quality also play a significant role. These factors have not been experimentally investigated to date in the literature and open to future research. Relative humidity linearly decreases with the increase in altitude at an average of 4% per kilometer. Since wind speed increases and relative humidity decreases at higher elevation, the atmospheric water generation is performed less efficiently at higher evaluation.

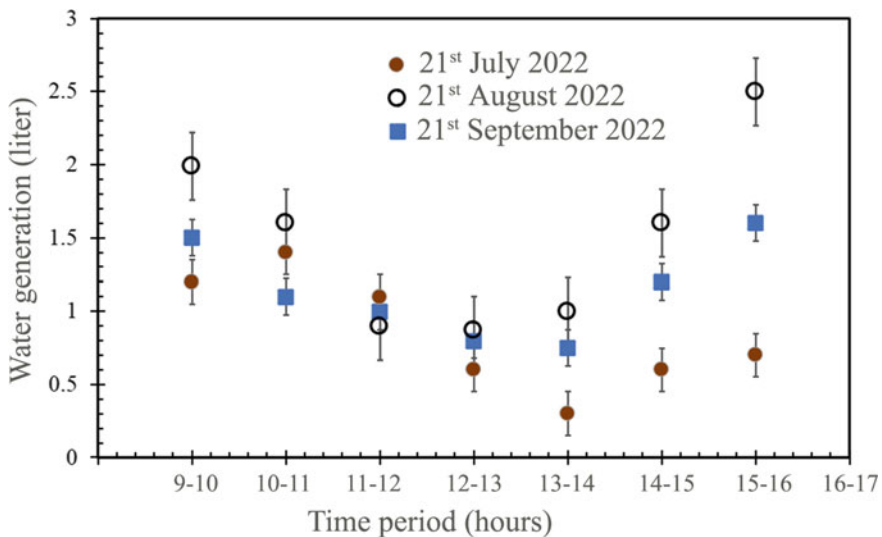
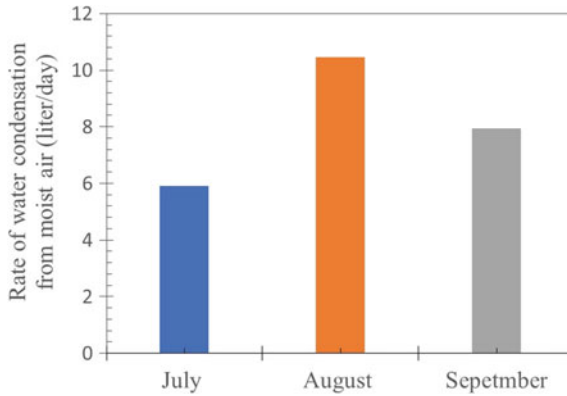
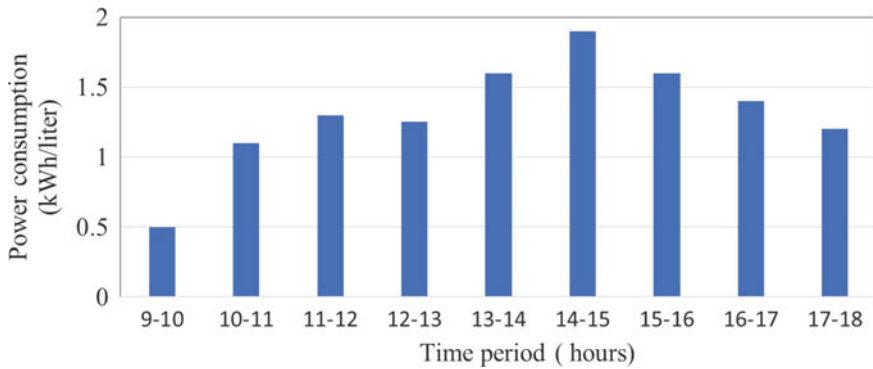


Fig. 4 Average hourly water generation via proposed device in different months in year 2022 at location of Noida, India



**Fig. 5** Average water generation per unit via proposed device in different months in year 2022 at location of Noida, India



**Fig. 6** Hourly average power consumption by the proposed atmospheric water garneting in the month of August in location of Noida, India

### 4 Summary and Conclusions

For arid and humid regions, atmospheric water condensation is one of the pragmatic methods. However, it is an energy-intensive method because water vapor spreads all over the atmosphere and the presence of non-condensable gases provides resistance against its condensation. In addition, the condensation of moist air is a complex process, and it depends on various parameters such as the cooling rate of condensing surface, surface morphology, quality of moist air, and ambient temperature. Large degree of subcooling and high thermal conductivity superhydrophobic surface has a high yield of moist air condensation. Vapor compression refrigeration cycle (VCRC) is used for cooling condensing surfaces. However, superhydrophobic copper tube surface is fabricated by plasma etching followed by chemical etching. This paper

presents the optimization of a refrigeration system for drinking water production through air dehumidification. The system's aim is to condensate the maximum water quantity achievable for every atmospheric air condition, represented by temperature and humidity. The experiment is carried out in humid conditions in Noida, and it claimed that the specific power consumption in stable humid condition is lower than less humid conditions. The environmental impact and economic feasibility have not been estimated for this device.

**Acknowledgements** Basant S. Sikarwar acknowledges the Science and Engineering Research Board (SERB), Government of India (Project number CRG/2021/005669), for providing funds for carrying out this work.

## References

1. United Nations University. Global water crisis: the fact.2019 Water | United Nations
2. Raveesh G, Goyal R, Tyagi SK (2021) Advances in atmospheric water generation technologies. *Energy Convers Manage* 239:114226
3. Dash A, Mohapatra A (2015) Atmospheric water generator: to meet the drinking water requirements of a household in coastal regions of India. Ph.D. Thesis
4. Bagheri F (2018) Performance investigation of atmospheric water harvesting systems. *Water Resour Indus* 20:23–28. <https://doi.org/10.1016/j.wri.2018.08.001>
5. Shafeian N, Ranjbar AA, Gorji TB (2022) Progress in atmospheric water generation systems: a review. *Renew Sustain Energy Rev* 161(2022):112325
6. Singh PL, Sikarwar BS, Ranjan M, Muralidhar K (2022) Enhancing dropwise condensation of vapor from moist air over a copper substrate by temperature-controlled chemical etching. *Therm Sci Eng Progr* 34(2022):101403
7. LaPotin A, Zhong Y, Zhang L, Zhao L, Leroy A, Kim H, Rao SR, Wang EN (2021) Dual-stage atmospheric water harvesting device for scalable solar-driven water production. *Joule*. 5:166–182
8. Baghel V, Sikarwar BS, Muralidhar K (2020) Dropwise condensation from moist air over a hydrophobic metallic substrate. *Appl Therm Eng* 181(2020):115733
9. Baghel V, Sharma DK, Sikarwar BS, Kumar R, Avasthi DK (2019) Tailoring the hydrophobicity of copper surface with ion beam irradiation. *Rad Effects Defects in Solids* 174(3–4):307–319
10. Nandy A, Saha S, Ganguly S, Chattopadhyay S (2014) A project on atmospheric water generator with the concept of Peltier effect. *Int J Adv Comp Res* 4:481
11. Shourideh AH, Ajram WB, Al Lami J, Haggag S, Mansouri A (2018) A comprehensive study of an atmospheric water generator using Peltier effect. *Therm Sci Eng Progr* 6(2018):14–26
12. Liu S, He W, Hu D, Lv S, Chen D, Wu X, Xu F, Li S (2017) Experimental analysis of a portable atmospheric water generator by thermoelectric cooling method. *Energy Proc* 142:1609–1614
13. Anbarasu T, Pavithra S (n.d.) Vapour compression refrigeration system generating fresh water from humidity in the air, 5
14. Habeebullah BA (2009) Potential use of evaporator coils for water extraction in hot and humid areas. *Desalination* 237:330–345. <https://doi.org/10.1016/j.desal.2008.01.025>
15. Ibrahim NI, Al-Farayedhi AA, Gandhidasan P (2017) Experimental investigation of a vapor compression system with condenser air pre-cooling by condensate. *Appl Therm Eng* 110:1255–1263. <https://doi.org/10.1016/j.applthermaleng.2016.09.042>
16. Nada SA, Elattar HF, Fouda A (2015) Experimental study for hybrid humidification–dehumidification water desalination and air conditioning system. *Desalination* 363:112–125. <https://doi.org/10.1016/j.desal.2015.01.032>

17. Baghel V, Sikarwar BS (2019) Moist air condensation on inclined hydrophobic metallic surfaces: simulation & experiments. *J Phys: Conf Ser* 1369(2019):012021. <https://doi.org/10.1088/1742-6596/1369/1/012021>
18. Wang P, Zhang D, Qiu R, Wu J (2014) Super-hydrophobic metal-complex film fabricated electrochemically on copper as a barrier to corrosive medium. *Corros Sci* 83:317–326
19. Savio L, Bhavitha KB, Bracco G, Luciano G, Cavallo D, Paolini G, Passaglia S, Carraro G, Vattuone L, Masini R, Smerieri M (2021) Correlating hydrophobicity to surface chemistry of microstructured aluminium surfaces. *Appl Surf Sci* 542:148574. <https://doi.org/10.1016/j.apsusc.2020.148574>
20. Huang Y, Sarkar DK, Grant Chen X (2015) Superhydrophobic aluminum alloy surfaces prepared by chemical etching process and their corrosion resistance properties. *Appl Surf Sci* 356(2015):1012–1024. <https://doi.org/10.1016/j.apsusc.2015.08.166>
21. Wu R, Chao G, Jiang H, Hu Y, Pan A (2015) The superhydrophobic aluminum surface prepared by different methods. *Mater Lett* 142:176–179. <https://doi.org/10.1016/j.matlet.2014.12.007>
22. Dhanalakota P, Abraham S, Mahapatra PS, Sammakia B, Pattamatta A (2022) Thermal performance of a two-phase flat thermosiphon with surface wettability modifications. *Appl Therm Eng* 204:117862. <https://doi.org/10.1016/j.applthermaleng.2021.117862>
23. Kota AK, Li Y, Mabry JM, Tuteja A (2012) Hierarchically structured superoleophobic surfaces with ultralow contact angle hysteresis. *Adv Mater* 24:5838–5843. <https://doi.org/10.1002/adma.201202554>
24. Liu W, Xu Q, Han J, Chen X, Min Y (2016) A novel combination approach for the preparation of superhydrophobic surface on copper and the consequent corrosion resistance. *Corros Sci* 110:105–113. <https://doi.org/10.1016/j.corsci.2016.04.015>
25. Frankiewicz C, Attinger D (2016) Texture and wettability of metallic lotus leaves. *Nanoscale* 8:3982–3990. <https://doi.org/10.1039/C5NR04098A>
26. Yuan Z, Wang X, Bin J, Peng C, Xing S, Wang M, Xiao J, Zeng J, Xie Y, Xiao X, Fu X, Gong H, Zhao D (2013) A novel fabrication of a superhydrophobic surface with highly similar hierarchical structure of the lotus leaf on a copper sheet. *Appl Surf Sci* 285:205–210. <https://doi.org/10.1016/j.apsusc.2013.08.037>
27. She Z, Li Q, Wang Z, Li L, Chen F, Zhou J (2012) Novel method for controllable fabrication of a superhydrophobic CuO surface on AZ91D magnesium alloy. *ACS Appl Mater Interfaces* 4:4348–4356
28. Zhi C, Limei H, Anqi C, Qingjun S, Changle C (2012) A rapid one-step process for fabrication of superhydrophobic surface by electrodeposition method. *Electrochim Acta* 59
29. Liu L, Xu F, Ma L (2012) Facile fabrication of a superhydrophobic Cu surface via selective etching of high-energy facets. *J Phys Chem C* 116:18722–18727
30. Latthe SS, Rao AV (2012) Superhydrophobic SiO<sub>2</sub> micro-particle coatings by spray method. *Surf Coat Technol* 207:489–492
31. He W, Yu P, Hu Z, Lv S, Qin M, Yu C (2019) Experimental study and performance analysis of a portable atmospheric water generator. *Energies* 13(1):73
32. Bolton D (1980) The computational of equivalent potential temperature. *Mon Weather Rev* 108(7)

# A Comprehensive Survey on Visualization of Human Action Recognition: By Hidden Markov Model and Convolution Neural Network



Aleem Ahmed, Garima Jain, Amritanshu Sharma, Md. Hashim,  
and Aditya Raj

**Abstract** Humanity's recognition action from a visual standpoint content is a difficult task as different types of problems arise in the recognition of human action. In the realm of computer vision, human action recognition (HAR) has reached a significant milestone. The advancement of technology allows us to address this issue and makes it a viable topic of research. A lot of research has already been done on HAR, and still, a lot is left. In this context, the focus of this survey is on the various types of HAR approaches that have been developed in the recent ten years. This paper uses a hidden Markov model based on several algorithms to solve the problem of human action recognition. We are comparing two techniques of HAR to find the best out of them. The hidden Markov model and the convolution neural network are two types of neural network. A convolutional neural network (CNN) capable of recognizing local patterns in input data is trained to recognize human actions from the local patterns in the feature representation. We found out that CNN is a better algorithm for recognizing human actions as it shows the body's movement and body joints in two different aspects of the CNN graph.

**Keywords** Image recognition · Convolution neural network · Action recognition · Feature extraction · Gesture and motion of human action recognition (HAR) · Hidden Markov model (HMM)

## 1 Introduction

Human action recognition is a new computer vision field that recognizes humans' behavioral actions. It can be used for a variety of things, including human-machine interaction, video retrieval, and surveillance. In the fields of machine learning, deep learning, and computer vision, it is a hot topic. As a result, I have opted to focus

---

A. Ahmed · G. Jain (✉) · A. Sharma · Md. Hashim · A. Raj  
Department of Computer Science and Engineering, Noida Institute of Engineering  
and Technology, Greater Noida 201310, India  
e-mail: [garimajain@niet.co.in](mailto:garimajain@niet.co.in)

© The Author(s), under exclusive license to Springer Nature Singapore Pte Ltd. 2023  
R. Sharma et al. (eds.), *Advances in Engineering Design*, Lecture Notes in Mechanical  
Engineering, [https://doi.org/10.1007/978-981-99-3033-3\\_17](https://doi.org/10.1007/978-981-99-3033-3_17)

179



on surveillance in this arena. The primary premise of this research is to identify anomalous human behaviors in front of [1] security cameras [2], surveillance [3], pedestrian monitoring [4], and human-machine interaction which are all examples of applications. Action recognition, on the other hand, seeks to reliably classify [5] the types of query actions, whereas [6] motion prediction projects future movements based on observations. The ability to recognize human behaviors is critical for this. The phrase relates to the classification and recognition of numerous human postures that people take in their daily lives. A few other crucial features, including occlusions, backdrop complexity, diversity in lighting conditions, and the types of analogous movements performed by various people, make the HAR much more difficult, and researchers still encountered enormous challenges [7]. So, primarily, it gives a sense of my proposed solution to the problem of security surveillance, as it would aid us in identifying normal and deviant behaviors. Human activity can be broken down into four categories: gestures, interactions, acts, and group activities.

- **Gesture:** A gesture is a visible body activity that conveys a message. It okay gestures and thumbs up are examples of movements made with the hands, face, or other areas of the body. Rather of verbal or vocal communication.
- **Action:** The term “action” refers to a set of physical actions carried out by a single person, such as walking or running.
- **Interactions:** Interactions are a collection of actions carried out by no more than two actors. One of the subjects the first must be a person, whereas the second might be either a human or an item (hand shaking, chatting, etc.).
- **Groups activities:** It is a blend in a group environment of gestures, movements, and interactions. There must be at least two actors, as well as one or more interactive objects (playing volleyball, obstacle racing, etc.).

Entropy-based, metaheuristic, and heuristic are only a few examples of well-known FS approaches. Finally, supervised approaches such as support vector machine (SVM), K-nearest neighbor (KNN), Bayesian models, and hidden Markov models are used to recognize these features (HMM). Figure 1 depicts a general flow to represent these processes. However, due to a variety of factors such as high dimensionality, redundancy, and others, these approaches do not accurately learn the features. The arrangement of any HAR system is shown in Fig. 2. An extraction of features technique converts data derived from photos or video frames that is numeric or symbolic into numeric or symbolic data. A classifier then applies labels to these retrieved features in accordance. Many processes make up the process, which ensures that actions are described efficiently. As a result, there is a need for periodic surveys to maintain track of the most recent methodologies used, the related outcomes attained, and the challenges that remain in order to assist demonstrate the way forward, which is what this study tries to do. HAR is divided into two types based on the kind of input vectors: unimodal and multi-modal. Unimodal means that the data comes from a single source, while multi-modal indicates that the input dataset comes from multiple sources. The approaches developed for the unimodal HAR in the last decade are covered in this survey. Machine learning ideas were used to classify and characterize the unimodal methods. Furthermore, several deep learning-based HAR models have

been thoroughly studied. This survey also includes a list of distinct feature extractors and a full explanation of some commonly used video and still-image datasets, as well as some relevant insights about future work scope.

- **Human–Robot Interaction (HRI):** This is another key use of vision-based activity recognition. It is critical for HRI to give a robot the ability to recognize human behaviors. As a result, robots can be used in both industrial settings and as personal assistants in the home.

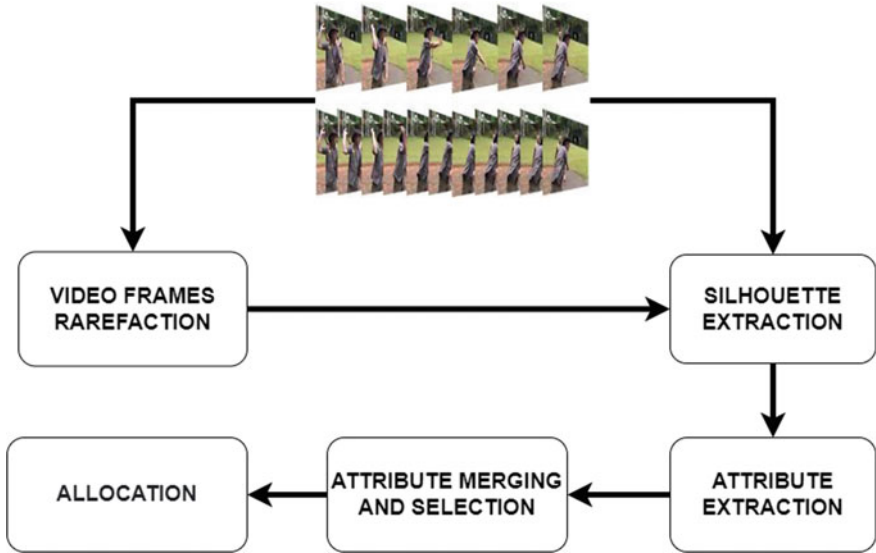


Fig. 1 General flow to represent these processes

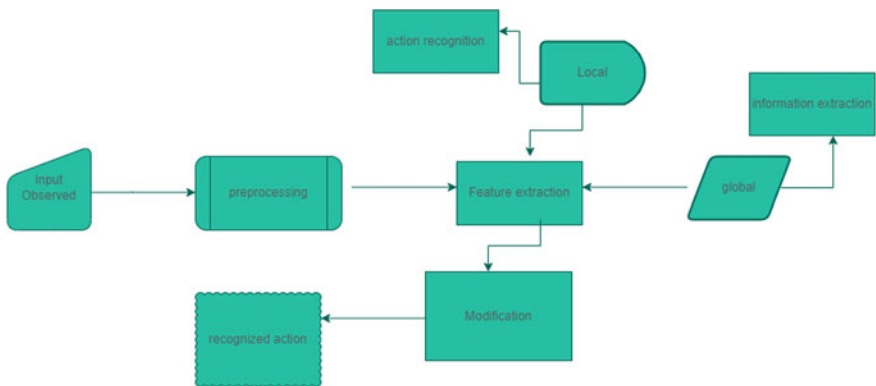


Fig. 2 Working architecture of human action recognition (HAR) system

- Human–Computer Interaction (HCI): In addition to traditional computer interfacing methods such as the mouse and keyboard, it is preferable to have more natural interfaces between the computer and the human operator via recognizing human gesture.

### ***1.1 Research Objectives***

At developing novel strategies for human action recognition using handmade and deep learning-based techniques, we take a vision-based approach.

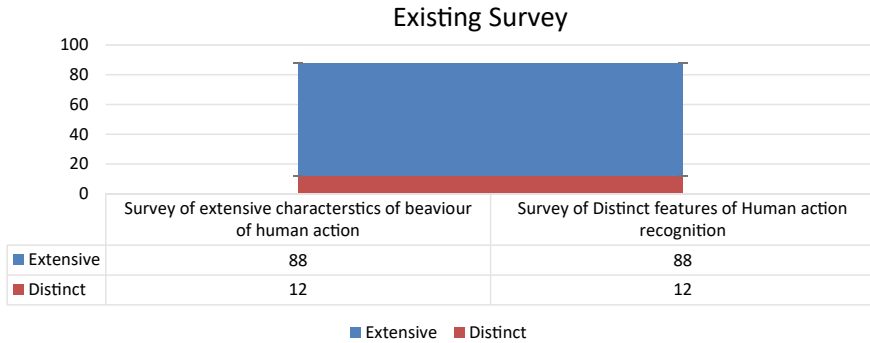
- The creation of a novel approach for view-invariant human action recognition, which is regarded as one of the major problems for human action recognition in several application domains.
- The creation of a novel way for recognizing human actions using an unsupervised deep learning model.
- Producing outcomes that are more accurate and efficient than existing ones on typical benchmark datasets.

### ***1.2 Research Contributions***

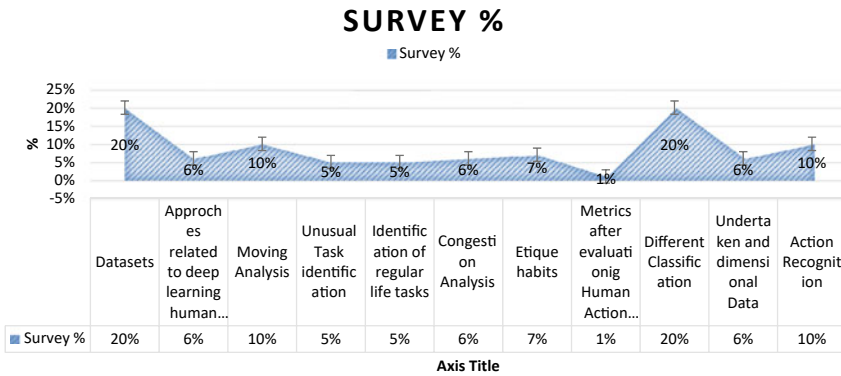
- This study offers a thorough assessment, comparison, analysis, and evaluation of cutting-edge methodologies based on handmade and deep learning approaches.
- This technique is based on a unique view-invariant feature descriptor and can distinguish actions from five various perspectives: front, rear, left, right, and top.
- Supervised deep learning models have generated cutting-edge outcomes in object identification when a massive quantity of labeled data is available. However, when the dataset is small, these models do not generalize effectively.
- This technique makes two contributions: To begin, the suggested technique outperformed similar state-of-the-art methods in terms of accuracy, confirming the promise of a less investigated unsupervised DBNs architecture for modeling complex human behaviors. Second, for learning essential parameters, the suggested technique employs an automated structure learning method.

### ***1.3 Research Survey***

Our study covers both the broad characteristics of human activity recognition and the specialized vision-based HAR systems, and it examines the most notable developments reported recently in the literature. According to Fig. 3, only 9% of available surveys from 2011 to present are devoted to discussing the basic framework of HAR, while 91 percent are committed to providing specific taxonomies or domain specific.



**Fig. 3** Proportion of surveys that offer broad characteristics of HAR versus surveys that present particular taxonomies and application domains of HAR



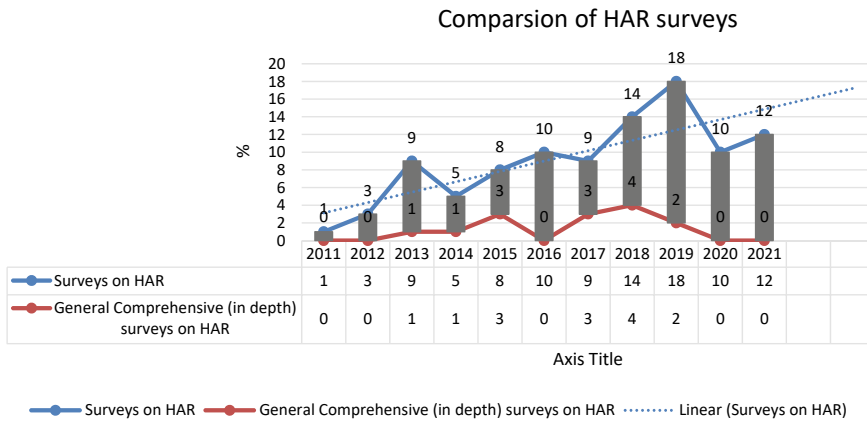
**Fig. 4** Distribution of main HAR issues covered by recent surveys

Furthermore, Fig. 4 depicts the most frequently mentioned HAR topics as well as the proportion of surveys addressing each topic during the previous eleven years.

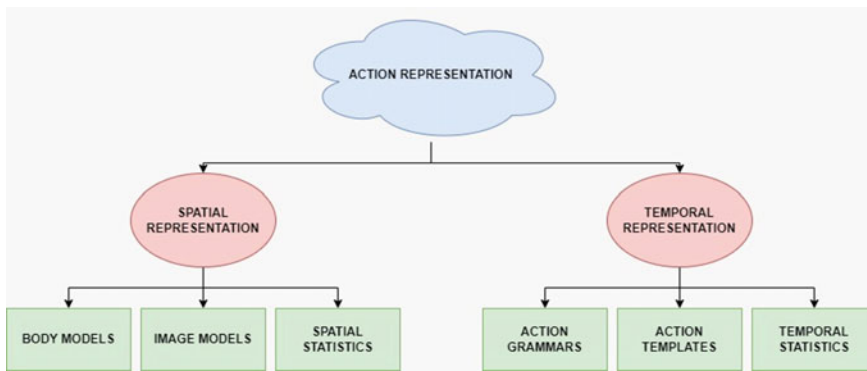
The findings are shown in Fig. 5. This data shows that there are just a few surveys identical to ours, suggesting that there is a need for an updated new thorough study of HAR systems. The HAR approaches are summarized in Fig. 6.

### 1.4 Road Map

The rest of the chapter is organized as follows. The first section introduces human action recognition, related with hidden Markov model and convolution neural network in the paper. Second section gives the background study, review, and the previous works that have been done in the prediction and analysis of human action. The introduction to the hidden Markov model and its general characteristics with the



**Fig. 5** HAR-related surveys from 2011 until 2021



**Fig. 6** Vision-based and action approaches human activities recognition approaches

algorithm is described in next section. Up next section contains a convolution neural network description then neural network description with an algorithm. The results of this study are explained in upcoming section. Finally, concludes the paper.

## 2 Background Study (Literature Review)

They conducted a summary of existing techniques [8] based on the type of problem they deal with a problem. They also compare current datasets in the field of human action recognition. They demonstrate real-world applications in an uncontrolled setting, which makes it more challenging and exciting. They bring valuable information on unsolved HAR real-world difficulties, which might assist and inspire

researchers to work on these hot areas which can use visualization of insufficient data, terrible weather conditions, and cameras to present the outcomes of motion that were promising. But there are still insufficient new HAR systems. It is necessary to consider the generalization of posed approaches. They propose HAR-related issues and solutions, which are a potential HAR research topic. Using the hidden Markov model, a statistical Markov model in which the system is hidden from view, and under consideration, it is assumed that the process is a Markov one. They provide important information about the space and time of interest, such as how difficult and time-consuming annotation of a large dataset is. They also demonstrate the use of efficient energy by utilizing machine learning.

We propose a novel 26-layer convolutional neural network architecture for accurate complicated action recognition in this research [9]. The features are taken from the global average pooling layer and the fully connected (FC) layer, and a suggested high entropy-based technique is employed to fuse them. We have demonstrated that the suggested computer vision architecture outperforms the competition in terms of accuracy and testing compared to existing techniques. Each dataset has an accuracy of 81.4 percent, compared to a SoftMax classifier with 81.2%, 98.3%, and 98.7%. We use CNN and PD for HAR with difficult datasets in this paper. For final recognition, the best features are chosen and submitted to ELM and SoftMax classifiers. For this study, four datasets were used: HMDB51, KTH, Weizmann, and Sports. The suggested HAR method's computing cost was reduced by selecting relevant characteristics. The selection of the final layer for feature extraction is the key constraint. We will also explore the topic of zero paddings in future work and attempt to implement mean padding for parallel feature fusion.

They perform human action recognition by using graph convolutional networks, which signifies the type of architecture that utilizes the structure of data [10]. With its powerful applications, because such data is non-Euclidean, it lacks well-known qualities including global parameterization, common system of coordinates, vector space structure, and shift-invariance. They also compare and contrast existing GCNs datasets in the field of human action recognition. Significant challenges, such as individuals who constantly switch their priorities. This can save the most up-to-date findings in terms of specified metrics. For sampling populations, selected populations, and updating architecture distribution, they use the CEIM algorithm. They also provide important information about the space and time of interest. In this paper, we propose building and exploring the best GCN architecture for skeleton action recognition and using a graph convolutional network for skeleton-based action recognition. By merging the cross-entropy evolution approach with memory-efficient importance-mixing, we developed a unique search technique.

A two-stream convolution neural network model was designed with the goal of enhancing the accuracy of human aberrant behaviors identification [11]. VMHI and FRGB are the two key components of this concept. The VGG-16 is used to extract the motion history pictures. For training, a convolutional neural network is used. The proposed algorithm, region with convolutional neural networks, can recognize not just a single person's behaviors, but also two-person interaction behaviors, and can be improved, and comparable acts can be recognized more easily. The suggested

algorithm has higher accuracy than the previous literature, according to experimental findings on the KTH, Weizmann, UT-interaction, and Tenth Lab datasets. A method for recognizing human behaviors based on MHI, RGB frames, and CNN has been proposed. It is a hybrid of the MHI and the VGG-16 deep neural networks with the Kalman filter and the faster RCNN architecture. To assess its performance, it was subjected to extensive testing on four datasets. The recommended strategy is the following: offers a higher level of accuracy than state-of-the-art techniques and is suitable for recognizing human action, but still has two demerits when dealing with complex multi-person interactions, such as three people fighting. We will endeavor to enhance the proposed technique to solving these difficulties in future work.

Human action recognition based on multi-modality is becoming more popular [12]. Multi-modality can deliver more information in more ways than a single modality. Multi-modality learning, on the other hand, has a hard time efficiently capturing the spatial–temporal information from the complete RGB and depth sequence. We propose a bidirectional rank pooling approach to create RGB visual dynamic images and depth dynamic images in this research to gain improved representation of spatial–temporal information. Furthermore, we develop an effective segmentation convolutional networks architecture for human action detection based on a multi-modality hierarchical fusion technique. Multi-modality-based human activity recognition is getting more common. In comparison with a single modality, multi-modality may convey more information in more ways. Multi-modality learning, on the other hand, struggles to capture the spatial–temporal information from the entire RGB and depth sequence efficiently. In this study, we suggest a bidirectional rank pooling strategy for creating RGB visual dynamic images and depth dynamic images in order to improve spatial–temporal information representation. Furthermore, using a multi-modality hierarchical fusion approach, we construct an effective segmentation convolutional networks architecture for human action detection.

In this research, we introduce the cooperative genetic algorithm, a novel feature selection (FS) model with a cellular-like structure that is suited for hardware implementation [13]. The compact genetic algorithm and the parallel estimate of distribution method were combined to create the CCGA (EDA). The concept and algorithm are given to pick the most relevant and distinguishing traits from the whole feature set in order to achieve two-way reinforcement, and we sought to incorporate notions from cooperative game theory into GA. Four benchmark video datasets, including two sensor-based UCI HAR datasets, are used to test the proposed FS model. It discovered that by utilizing only a tiny part of the original feature vector, overall classification accuracy improved significantly. The experiments were conducted using the GLCM matrix generalized search, histogram of oriented gradient, texturing, and speed up robust features and GIST. They also give crucial details regarding the location and time of interest. CGA performs mutations based on mutual knowledge in order to increase the quality of the solutions. CGA can achieve extremely high accuracy with just employing around 70% of the characteristics. We want to apply this technology to a variety of other disciplines in future, in addition to HAR.

A symbiotic graph neural network was used to address the issues occurring in the previously published works [14]. It is a symbiotic model which is used to handle two tasks jointly. There is a backbone, action recognition heads, and motion prediction heads in this system. These graphs are used to explicitly capture the relationships among body parts and body joints. In conducting extensive experiments, our symbiotic graph neural networks show superior than the current state-of-the-art approach stochastic gradient descent (SGD) which is an iterative approach for solving problems with stochastic gradients. Optimizing an objective function that has the right smoothness qualities the real gradient of  $Q(w)$  is approximated by a gradient in stochastic gradient descent.

$$w := w - n \nabla Q_i(w) \tag{1}$$

A multi-objective scheme is used to learn how to recognize actions and forecast motion simultaneously. Table 1 depicts the analysis of some state-of-the-art comprehensive surveys. The SGD algorithm has been used in it. In this study, we present a new symbiotic graph neural network that performs action identification and motion prediction simultaneously and captures spatial information using graph-based operations. A backbone, an action recognition head, and a motion prediction head comprise our model, with the two heads enhancing each other.

### 3 Hidden Markov Model (HMM)

Because HMM is built on probability vectors and matrices, we will start by defining objects to represent the basic ideas. The objects must reflect on specific attributes in order to be helpful. A probability vector, for example, must have all of its entries be integers  $0 \times 1$  and sum to 1. As a result, let us construct the objects in such a way that the mathematical features are intrinsically protected. The multi-layered hidden Markov model (HMM) was proposed in the early phases of human action identification research to recognize high-level actions hierarchically. Most of the HMM-based researches have been done on single viewpoint datasets. Jegham et al. [7] presented a fundamental form of the multi-layer technique. HMMs were employed at a lower level to recognize sub-events like stretching and withdrawing. The top level takes the lower level's output as input and detects punching activity when stretching and withdrawing happen in a specific order. Hidden Markov Models (HMMs) are statistical models widely used for analyzing sequential data. They are particularly useful for tasks such as speech recognition, natural language processing, bioinformatics, and pattern recognition. In an HMM, we assume that there is an underlying unobservable process, called the hidden state, which generates a sequence of observable outputs. As, shown in Fig. 7 the Working of Hidden Markov Model illustrated.



**Table 1** Analysis surveys

Research paper name	Applied algorithm	Space interest points	Time interest points	Environmental analysis	Energy	Application of machine learning	Graph-based method
Jegham et al. [7]	Hidden Markov model (HMM) algorithm	Yes	Yes	Yes	Yes	Yes	No
Afza et al. [15]	Convolutional neural network (CNN)	No	Yes	Yes	Yes	Yes	No
Peng et al. [16]	CEIM algorithm	Yes	Yes	No	No	Yes	Yes
Liu et al. [8]	Region with convolutional neural networks (RCNNs)	Yes	Yes	No	Yes	No	Yes
Ren et al. [9]	Convolutional networks (CNNs)	No	Yes	No	No	No	No
Guha et al. [10]	Cooperative genetic algorithm (CGA)	Yes	Yes	Yes	No	Yes	Yes
Li et al. [11]	Stochastic gradient descent (SGD)	Yes	Yes	Yes	No	No	Yes

### 3.1 Activity Recognition

It attempts to recognize the behaviors and intentions of one or more agents based on a sequence of observations of the actors' actions and environmental conditions. The flow of sensor-based activity recognition is depicted in Fig. 8.

#### Sensor-based

- Sensor-based activity recognition models a wide variety of human behaviors by combining the developing field of sensor networks with revolutionary data mining and machine learning approaches.
- Agent behaviors may be monitored using ubiquitous computers and sensors.

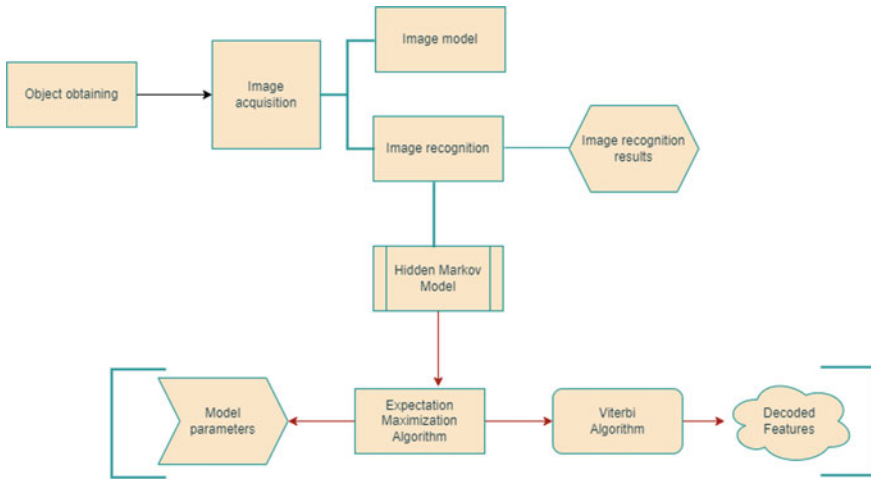


Fig. 7 Working of hidden Markov model (HMM)

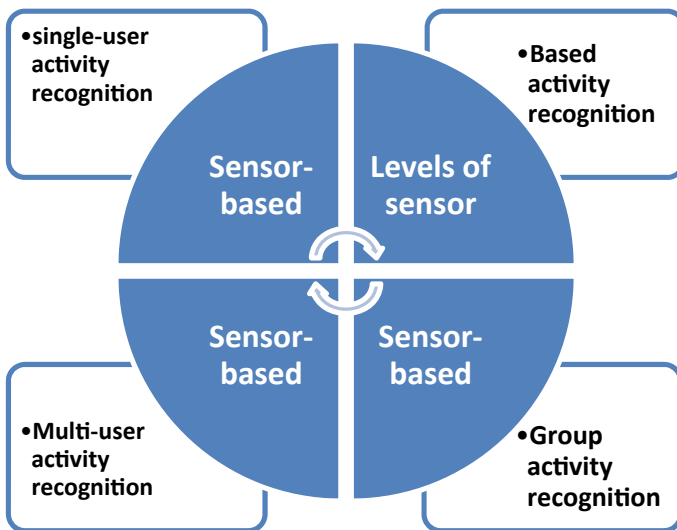


Fig. 8 Flow of activity recognition

**Sensor-based**

- ORL’s work with active badge systems was the first to integrate on-body sensors to recognize actions for numerous users.
- Provide an innovative pattern mining technique for recognizing single-user and multi-user activities in a unified solution.

### Levels of sensor

- Sensor-based activity detection is a difficult process due to the inherent noise in the input.

### Sensor-based

- Group activity recognition differs fundamentally from single or multi-user activity recognition in that the objective is to recognize the group's behavior as an entity, rather than the actions of individual users within it.
- Group activity detection has applications in crowd control and emergency response, as well as social networking and quantified self.

## 3.2 Modeling of the Human Body

To attain better results in specific activities, we should consider precisely simulating the human body. For example [13], in breath detection, the human body was described as a series of concentric cylinders. When individuals inhale, the outside of the cylinder represents the rib cage, and when they exhale, the interior represents the rib cage. As a result, the difference in radius between the two cylinders indicates the moving distance while breathing. The following equation can be used to represent the change in signal phases:

$$\theta = 2\pi \frac{2\Delta d}{\gamma} \quad (2)$$

The findings are shown in Fig. 3. This data shows that there are just a few surveys identical to ours, indicating the necessity for an updated new thorough study of HAR systems. Strictly speaking, the previous quantification (of in-depth survey versus standard survey) is based on the number of technologies and approaches, taxonomic structure, and in-depth comparative analysis done by the highlighted review paper.

## 3.3 Observation on Hidden Markov Model

$$P(Y) = \sum P\left(\frac{Y}{X}\right)P(X) \quad (3)$$

Hidden Markov model is given by

$$M = (A, B, \sqrt{\quad}) \quad (4)$$

$$O = o_1 o_2 \dots o_n \quad (5)$$

where  $O$  is observation sequence

- **Evaluation Problem:** Evaluate the probability that model  $M$  has generated the sequence  $O$ .
- **Decoding Problem:** Calculate the most likely sequence of hidden states  $S_i$  which produced this observation sequence  $O$ .
- **Learning Problem:** HMM parameters,  $M = (A, B, \sqrt{\phantom{x}})$  which best fits the training data.

## 4 Convolution Neural Networks

CNNs have been a prominent deep learning approach in the field of human action recognition due to their ability to learn visual patterns straight from image pixels without any preprocessing. In Pareek and Thakkar, [14] proposed a deep learning model based on a two-step neural network. The first stage uses CNNs to automatically learn spatiotemporal characteristics, while the second employs a recurrent neural network (RNN) to category the sequence. Similarly, in Beddiar et al., [17] presented a 3D CNN for recognizing human actions.

It is advantageous to extract deep CNN characteristics from original video frames using CNN. There is no need to do any preprocessing processes, such as extraction of regions of interest (ROI). The video frames are given immediately to the CNN model, which extracts deeper information from the layers sequence. In comparison with older techniques, CNN models for action recognition have recently been developed, and they have shown to be more accurate. Every picture is represented in the form of an array of values, and the convolution procedure requires matrix arithmetic operations (pixels).

The arrays are multiplied one-by-one element by element in the convolution operation, and the result is aggregated or summed to form a new array that represents  $a * b$ . The components of matrix  $b$  are now multiplied by the first three elements of matrix  $a$ . To acquire the result, the product is added together and saved in a new array of  $c$ .

Figure 9 depicts the shrouded layers of a proposed solution commonly comprise of a progression of convolutional layers that convolve with a duplication or other speck item [18–21]. The enactment work is generally a ReLU layer and is accordingly trailed by extra convolutions, for example, pooling layers, completely associated layers and standardization layers, alluded to as shrouded layers in light of the fact that their sources of info and yields are conceal by the actuation capacity and last convolution. The last convolution, thusly, frequently includes backpropagation so as to all the more precisely weight the final result.

The method is based on the pair-wise data similarity of related data points in low- and high-dimensional spaces. The conditional probabilities are generated to depict

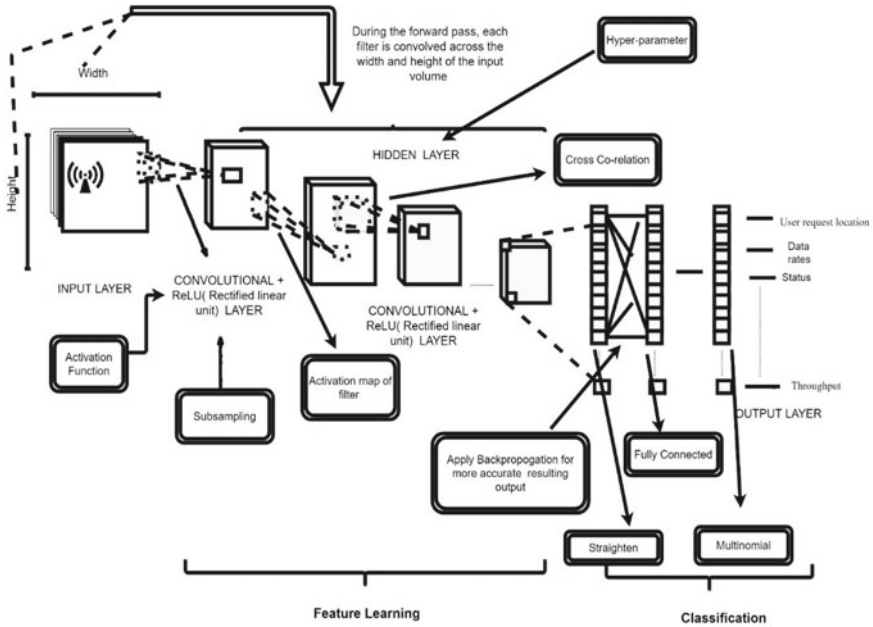


Fig. 9 Shrouded layer of proposed solution

the similarities between data points  $q_i$  and  $q_j$  in a high-dimensional space as

$$z_{ij} = \frac{e\left(\frac{\|q_i - q_j\|^2}{2\sigma_i^2}\right)}{\sum_{l \neq i} e\left(\frac{\|q_l - q_j\|^2}{2\sigma_l^2}\right)} \tag{6}$$

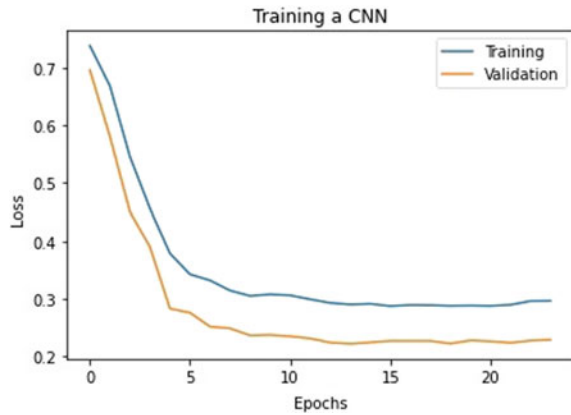
$$r_{ij} = \frac{e\left(\frac{-\|p_i - p_j\|^2}{2\sigma_i^2}\right)}{\sum_{l \neq i} e\left(\frac{-\|p_l - p_j\|^2}{2\sigma_l^2}\right)} \tag{7}$$

where  $i$  is the variance of a Gaussian distribution centered on  $q_i$ . The low-dimensional space analogs of  $q_i$  and  $q_j$ , namely  $r_i$  and  $r_j$ , are first given at random. Similarly, the appropriate conditional probabilities may be given [22].

The difference between  $z_{ij}$  and  $r_{ij}$  between data points  $q$ 's in high-dimensional space must be reduced. The cost function that represents the difference between  $z_{ij}$  and  $r_{ij}$  may be written as the sum of Kullback–Leibler (KL) divergence across all data points:

$$M = \sum_i \sum_j p_{j|i} \log_{r_{j|i}} z_{j|i} \tag{8}$$

**Fig. 10** Graphs of both the actual data and predicted data are approximately similar



## 4.1 Implementation of CNN

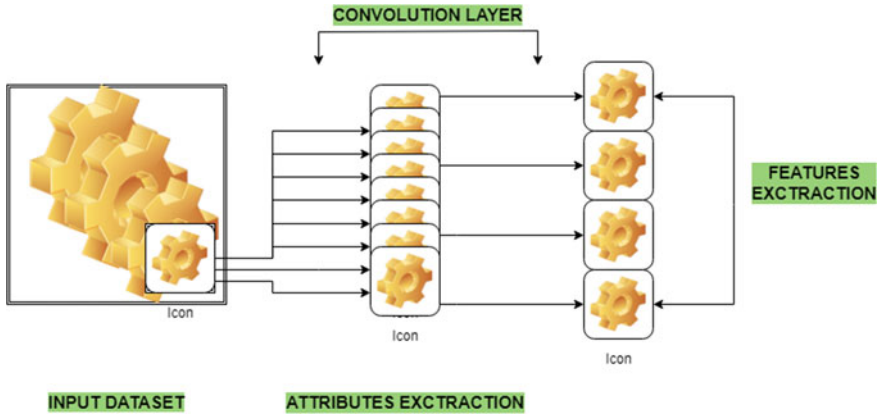
See Fig. 10.

## 5 Neural Network

A neural network is made up of “neurons,” which are linked nodes. The input layer, hidden layer, and output layer are all made up of neurons. Features are represented in the input layer, while our response variable(s) are represented in the output layer.

### 5.1 Neural Network Working

Neurons at the input layer receive data from the hidden layers, which they process and transmit to the hidden layers. This data is then processed by hidden layers before being sent to the output neurons. This artificial neural network (ANN) processes data in terms of a single activation function [23]. The neurons in the brain are imitated by this function. Each neuron has an activation function value as well as a threshold value. The threshold value is the minimal value that an input must have in order to be enabled. The neuron’s job is to do a weighted sum of all the input signals and then apply the activation function to the result before sending it on to the next (hidden or output) layer. Figure 11 discusses the feature extraction in convolution layer.



**Fig. 11** Feature extraction in convolution neural network

## 6 Conclusion

For accurate complex action recognition, a convolutional neural network architecture is used. The features are taken from the global average pooling layer and the fully connected (FC) layer, and a suggested high entropy-based technique is employed to fuse them. The graph shows the body joint and movements on different aspects. On the other hand, hidden Markov model gets out information only regarding its body shapes. So, we concluded that convolution neural network is a better way to recognize human action. As it gives out a better and accurate result.

## References

1. Fujii Y et al (2008) New concept regarding management of security cameras. *J Comm Inform* 4(3)
2. Macnish K (2014) Just surveillance? Towards a normative theory of surveillance. *Surveill Soc* 12(1):142–153
3. Philomin V, Duraiswami R, Davis L (2000) Pedestrian tracking from a moving vehicle. In: *Proceedings of the IEEE intelligent vehicles symposium 2000 (Cat. No. 00TH8511)*. IEEE
4. Johannsen G (2009) Human-machine interaction. *Control Syst Rob Autom* 21:132–162
5. Odijk D et al (2015) Struggling and success in web search. In: *Proceedings of the 24th ACM international on conference on information and knowledge management*
6. Wu P, Chen S, Metaxas DN (2020) MotionNet: joint perception and motion prediction for autonomous driving based on bird's eye view maps. In: *Proceedings of the IEEE/CVF conference on computer vision and pattern recognition*
7. Jegham I et al (2020) Vision-based human action recognition: an overview and real world challenges. *Foren Sci Int: Digit Investig* 32:200901
8. Liu C et al (2021) Improved human action recognition approach based on two-stream convolutional neural network model. *Visual Comp* 37(6):1327–1341
9. Ren Z et al (2021) Multi-modality learning for human action recognition. *Multimedia Tools Appl* 80(11):16185–16203

10. Guha R et al (2021) CGA: a new feature selection model for visual human action recognition. *Neural Comput Appl* 33(10):5267–5286
11. Li M et al (2021) Symbiotic graph neural networks for 3d skeleton-based human action recognition and motion prediction. In: *IEEE transactions on pattern analysis and machine intelligence*
12. Suthar B, Gadhia B (2021) Human activity recognition using deep learning: a survey. In: *Data science and intelligent applications: proceedings of ICDSIA 2020*, pp 217–223
13. Estevam V, Pedrini H, Menotti D (2021) Zero-shot action recognition in videos: a survey. *Neurocomputing* 439:159–175. <https://doi.org/10.1016/j.neucom.2021.01.036>
14. Pareek P, Thakkar A (2021) A survey on video-based human action recognition: recent updates, datasets, challenges, and applications. *Artif Intell Rev* 54(3):2259–2322
15. Afza F et al (2021) A framework of human action recognition using length control features fusion and weighted entropy-variances based feature selection. *Image Vis Comput* 106:104090
16. Peng W et al (2020) Learning graph convolutional network for skeleton-based human action recognition by neural searching. In: *Proceedings of the AAAI conference on artificial intelligence*, vol 34, No 3
17. Beddiar DR, Nini B, Sabokrou M et al (2020) Vision-based human activity recognition: a survey. *Multimed Tools Appl* 79:30509–30555
18. Kumar A et al (2022) Design of a CPW-fed microstrip elliptical patch UWB range antenna for 5G communication application. In: *Intelligent sustainable systems*. Springer, Singapore, pp 801–811
19. Jain G, Prasad RR (2021) Multi-antenna communication security with deep learning network and Internet of Things. In: *Blockchain technology for data privacy management*. CRC Press, pp 61–80
20. Jain G, Prasad RR (2020) IoT enabled multi-antenna communication channel with deep learning network. In: *Proceedings of the international conference on recent advances in computational techniques (IC-RACT) 2020*
21. Jain G, Prasad RR (2020) Machine learning, Prophet and XGBoost algorithm: analysis of traffic forecasting in telecom networks with time series data. In: *2020 8th International conference on reliability, Infocom technologies and optimization (trends and future directions) (ICRITO)*. IEEE
22. Jain G et al (2022) Secure COVID-19 treatment with blockchain and IoT-based framework. In: *Intelligent sustainable systems*. Springer, Singapore, pp 785–800
23. Jain G et al (2021) Securing artificial intelligence applications using protector hiding. *Int J Future Gener Commun Netw* 14(1):3380–3388



# Design and Modal Analysis of an Impact Energy Absorption System for a Four-Wheeler Vehicle



Angat Singh , Surendra Nath Banerjee, Ujjwal Kumar, Rohit Sharma ,  
and Vikas Kumar 

**Abstract** The present research work is aimed at performing modal analysis of an impact energy absorption assembly for a four-wheeler vehicle. In this work, an impact energy absorption mechanism is proposed where the crushing of composites principle is used. With the help of vehicle motion sensors, actuators, and high-speed pumps, the mechanism's bumper will be extended, which will then hit the forward obstacles before the actual collision occurs. The bumper on its way back will crush the composites, which will absorb some of the impact energy, and some of the energy will also be absorbed by the shock absorbers. Thus, the complete mechanism will tend to reduce the damage caused to passengers and vital engine components.

**Keywords** Impact analysis · Automotive · Hydraulic bumper · Fusion 360 · Safety

## 1 Introduction

Car accidents happen every single day. Most motorists think that they can avoid these difficult situations. However, according to the statistics, nearly 13 lakh people perish every year due to the result of automotive related accidents [1]. Hence, development in the safety sector of automobiles is prerequisite to decrease the numbers of accidents and to reduce the injury caused to occupants and pedestrians in these accidents. Car bumper is a structural module which greatly adds to car's crash worthiness/inhabitant protection during collisions.

This work mainly focuses on the design and assembly of a system which uses composite material as an energy absorption device inside front bumper system. Industries are increasing use of composite structures and are gradually replacing metal

---

A. Singh · S. N. Banerjee · U. Kumar · R. Sharma (✉)  
Department of Mechanical Engineering, Amity University Uttar Pradesh, Noida, India  
e-mail: [r25sharma@gmail.com](mailto:r25sharma@gmail.com)

V. Kumar  
Department of Mechanical Engineering, National Institute of Technology Kurukshetra,  
Kurukshetra, India

© The Author(s), under exclusive license to Springer Nature Singapore Pte Ltd. 2023  
R. Sharma et al. (eds.), *Advances in Engineering Design*, Lecture Notes in Mechanical Engineering, [https://doi.org/10.1007/978-981-99-3033-3\\_18](https://doi.org/10.1007/978-981-99-3033-3_18)

materials. This trend is caused by their high strength (and stiffness)—mass ratio. The composite structures can also be used to produce parts with required mechanical properties with ease. The main purpose is to design and perform analysis on a bumper model which can eventually be put into market to produce safer cars for India.

The analysis is done by considering experiments and papers which were carried out from researchers who worked on selection of material in automotive bumper impact analysis.

The researchers have studied on the study “this research paper deals with energy absorption and crushing features of tubes composed of a cylindrical segment with end plain cap, hemispherical cap, and shallow spherical cap.” [2].

The researchers have studied on the study axial crushing of hollow as well as foam filled aluminum tubes [3].

## 2 Objective

The objective of this study is to design and develop a front impact absorption system for passenger vehicles that can be used to protect passenger lives and minimize damage to vital car parts such as engine assembly, transmission by using composite structure as crushing material for energy absorption [4].

The main objectives of the system are

- To increase safety during a crash
- To reduce the level of passenger injury
- To protect the engine components
- To minimize post-accident repair costs.

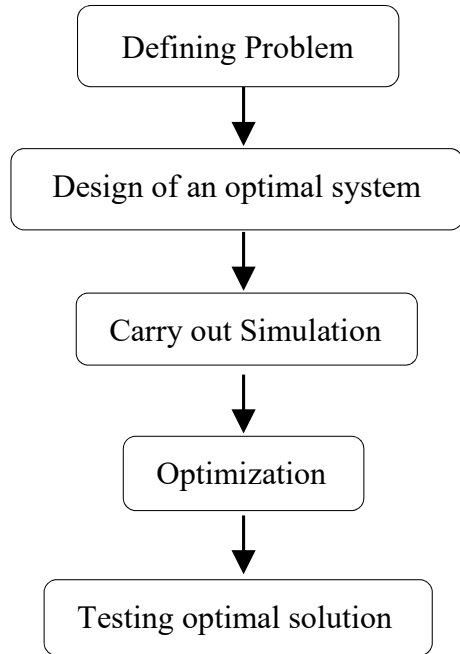
## 3 Methodology

This study puts emphases on designing and developing an active crash absorption system that can be equipped in modern cars bumpers which have a high probability to play a significant role in ensuring vehicle crashworthiness and pedestrian safety. The preliminary design of the model will be done in AutoCAD 2D. 3D modeling of the bumper and simulation is all completed in Autodesk Fusion 360. Components will be chosen depending on required specification and availability. Figure 1 shows a flowchart of methodology followed for this study.

### 3.1 Technical Design

- (1) Actuators/ECU.
- (2) Side cylinders where the fluid is initially filled.

**Fig. 1** Flowchart showing methodology



- (3) Main cylinder where the fluid will enter upon actuation.
- (4) High-speed pump to allow the fluid to flow from side cylinders to main cylinder.
- (5) Metal sheet where the composites are attached.
- (6) Fiber composites which observe the compression.
- (7) Bumper which will initially hit the obstacle.
- (8) Piston with the flat plate arrangement which moves forward due to fluid entering the cylindrical chamber (Fig. 2).

### 3.2 CAD Model

This model has been prepared in Fusion 360 and SolidWorks. The design of the system has been created with manufacturing in mind and uses parts that are can be purchased and manufactured easily. The layout of the design is very straight forward and features swappable parts for maintenance and replacement. The model follows a simple yet innovative design that is not only easy to manufacture but easy to repair/replace (Fig. 3).

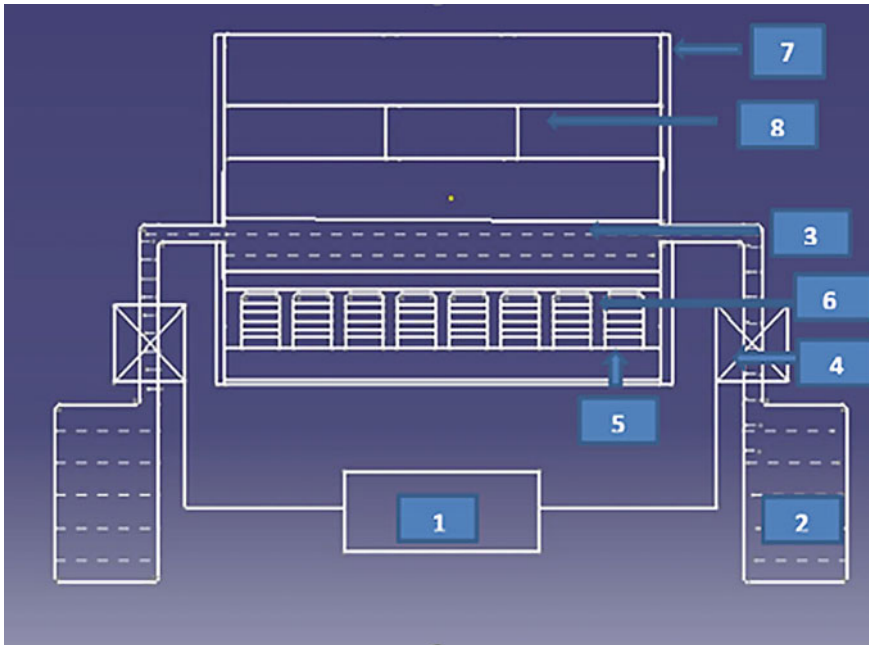


Fig. 2 Preliminary design of the model

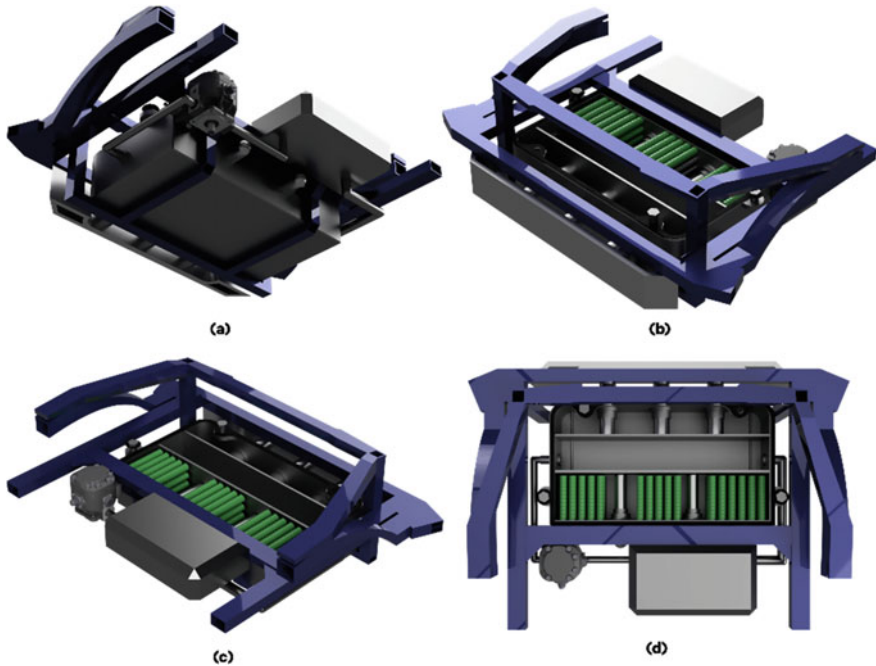
### 3.3 Technical Drawing

Figure 4 showing the detailed technical drawing of an impact energy absorption system.

### 3.4 Structure of Composites

Cylindrical structure is good energy absorbers. The energy absorbing capability varies with its cell size, and hence, a variety of arrangements can be tried. Cylinders are one of those very special structures which have a lot of potential to be applied in the usage of the absorption of shock energy. These are continuous cellular structure consisting of arrangement of open cells. Cylindrical structures also provide repeatable structure which repeats its crushing process [5]. Since being similar structure throughout the body, they have simple design, cost-efficient, and time-efficient in manufacturing.

These cylindrical structures are usually manufactured between two relatively hard surfaces on top and bottom which assists in equal force distribution. These types of structures are typically called as “sandwich panel cylindrical structures.”



**Fig. 3** **a** Bottom view of the assembly showing reservoir and pump. **b** Side view of the system and assembly. **c** Top view of the system showing composite structure placement. **d** Top view showing placement of composite structure

The bumper not only has to provide adequate pedestrian protection, but it should also satisfy the low-speed impact test of 4 kmph to as per regulation. This becomes a difficult task as in order to achieve good lower leg protection, a relatively soft bumper system is required while a relatively stiff system is typically needed to manage barrier and pendulum impacts [6]. The faster the energy absorbing structure responds to the impact event, higher will be the energy management coefficient and therefore, smaller the depth of space needed in order to absorb the impact energy from the event. The composite cylinders have rings along the length to allow axial crushing and prevent bending. This helps to direct the impact force equally through the entire composite structure (Fig. 5).

### 3.5 Material for Composite Structure

#### Physical Properties

After going through multiple different metallic and nonmetallic materials such as steel and aluminum variants [7], different plastics, alloys etc.; aluminum 6061 was

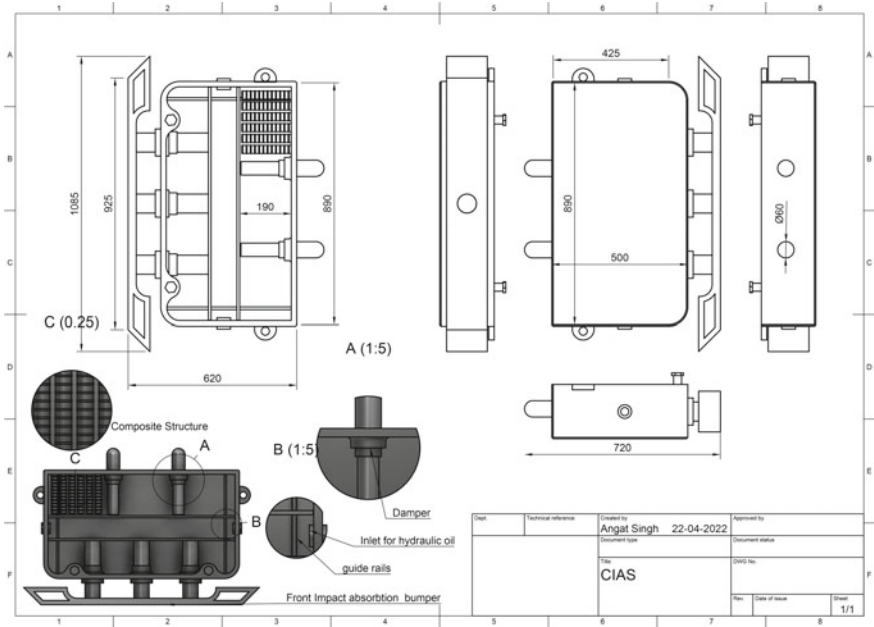


Fig. 4 Technical drawing of the system (all dimensions are in mm)



Fig. 5 Cylindrical structure

**Table 1** Table containing physical properties of aluminum 6061

Mechanical properties	Metric
Ultimate tensile strength	310 MPa
Tensile yield strength	276 MPa
Shear strength	207 MPa
Fatigue strength	96.5 MPa
Modulus of elasticity	68.9 GPa
Shear modulus	26 GPa
Young's modulus	68,900 MPa
Density	2.7E-06 kg/m <sup>3</sup>

selected due to its favorable physical properties. Type 6061 aluminum is from the 6xxx aluminum alloy, which involves those mixtures which uses silicon (Si) and magnesium (Mg) as the primary alloying elements. Second digit in the number specifies the degree of impurity control for the basic aluminum. When this second number is "0," it specifies that the bulk of the alloy is easily available commercial aluminum with its prevailing impurity levels, and no special steps are required to tighten controls. The 3rd and 4th digits are simply designators for individual alloys [3].

The nominal composition of type 6061 aluminum is 97.9% Al, 0.6% Si, 1.0%Mg, 0.2%Cr, and 0.28% Cu. The density of 6061 aluminum alloy is 2.7 g/cm<sup>3</sup>. 6061 aluminum alloy is heat treatable, easily formed, and weld-able and is good at resisting corrosion.

### Mechanical Properties

See Table 1.

## 3.6 Components

### Hydraulic Pump

Everything except the pump has to be manufactured. The pump selected for system is "Dynex PF1000" series high-pressure check-ball piston pump. Fixed delivery PF1000 series pumps provide reliable high-pressure operation which are rated to: 6000 psi (420 bar) continuous and 10,000 psi (700 bar) maximum.

Check-ball pumps use piston check valves to guide flow from the pump inlet to the outlet. Check valves take the place of a valve plate, commonly used in other piston pump designs. The metal-to-metal rotating sealing surface in these other pumps is an inherent leak path, subject to wear and scoring (Table 2).

**Table 2** Engineering specifications for hydraulic pump

Pump model	Output flow (1500 rpm)	Output flow at (1800 rpm)	Rated pressure		Max pressure		Speed rpm	
	L/min	L/min	Psi	Bar	Psi	Bar	Rated	Max
PF1003H	12.9	15.5	6000	420	10,000	700	1800	2800

### 3.7 Working

#### Before Collision

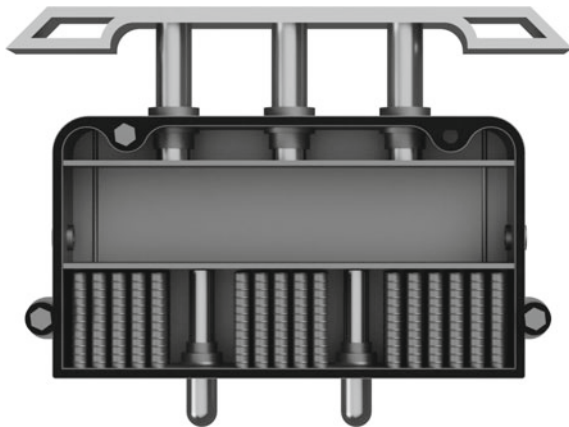
The first step is the detection of imminent collision using LiDAR sensors, radar sensors, and cameras. The control unit (ECU) collects the data from these sensors and calculates the chances of collision and provides appropriate output according to the circumstance.

When an imminent collision is detected, the hydraulic pump is activated, and front bumper is pushed outwards using pistons (Fig. 6).

#### During Collision

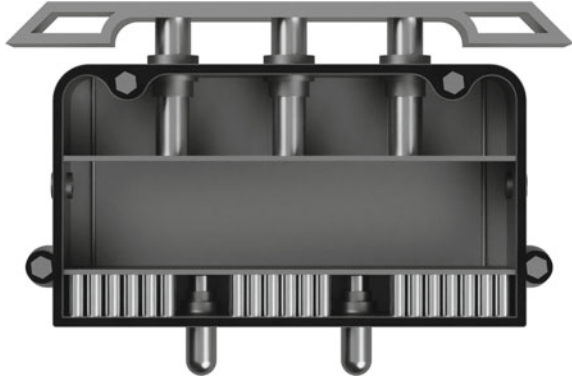
When the collision occurs, the valves in cylinders are closed using one-way valves so the fluid acts as a solid. The impact from the collision is first met with the bumper which is forced backwards into the compartment which is now filled with fluid with closed exit valves, so the middle compartment will now act as a solid system causing the crushing of composite material. Some energy is also redirected toward the rear of the car using chassis, away from the passengers (Fig. 7).

**Fig. 6** System when an impact is imminent





**Fig. 7** System state post collision



### After Collision

Depending on the severity of the impact either composite structure can be replaced or the whole system can be swapped out. This helps in reducing repair cost and repair time.

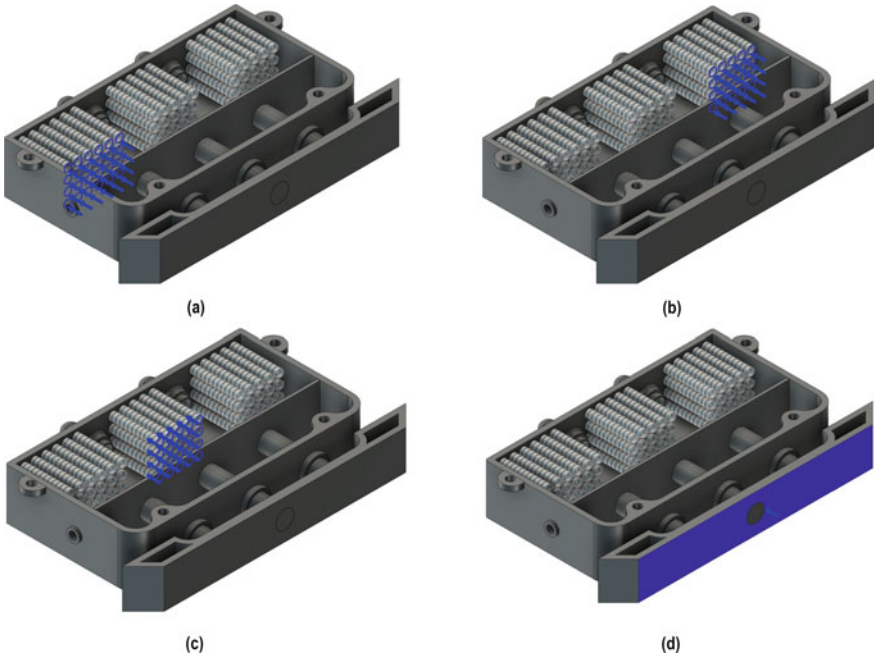
## 4 Simulation

Figures 8, 9, and 10 showing the simulation results of forces applied on composite structure and car bumper of an impact energy absorption system. It shows that how the components absorb the energy while collision.

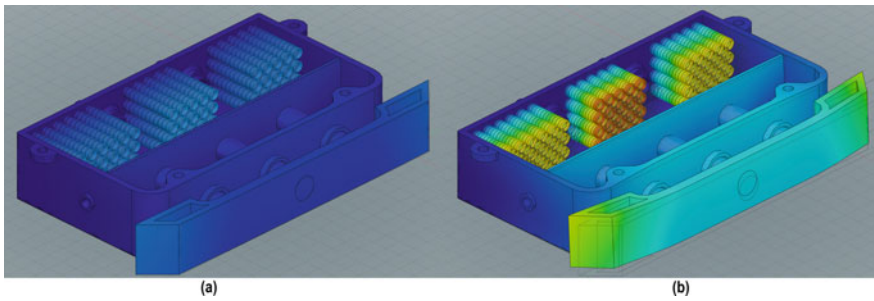
## 5 Result and Discussion

The result shows slight displacement in the front bumper and force absorption in the composite structure with the middle part absorbing the most amount of force. The system is more than capable to withstand and absorb impact energy from light passenger vehicles during crashes of up to 40 km/h.

The composite structure is getting deformed axially as expected. The front bumper also shows slight deformation from sides. The Ring structures along the length of the cylinder help to keep the cylinder upright when under axial stress, without this the cylinders will deform in a more random and unpredictable manner which could cause uneven force distribution.



**Fig. 8** a–c Forces applied on composite structure. **d** Force applied on the bumper



**Fig. 9** Result showing deformation in composite and body

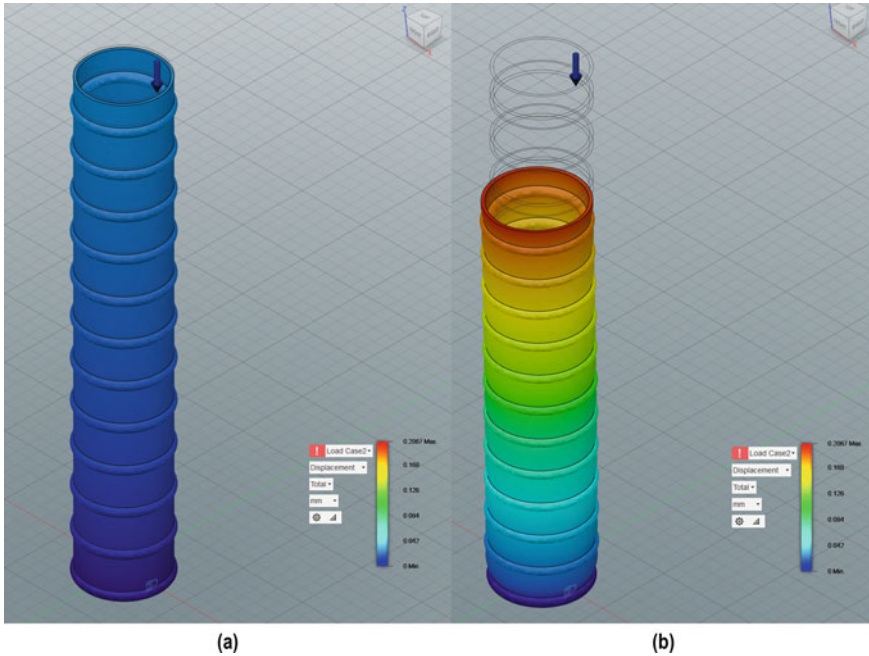


Fig. 10 Axial crushing of composite

## 6 Conclusion

This paper suggests and designs a novel conceptual energy absorption system for vehicles considering the requirements of both passenger safety and engine protection. The design adopts a modular design which can be assembled easily. The model uses crushing of composite structure as an energy absorption tool. The simulation results reveal the ability of aluminum composite’s structure to absorb good amount of energy.

The energy absorption when compared to traditional bumpers is greatly improved. The system shows minimal body deformation, the energy is directly absorbed by the composite structure, and rest of the energy is displaced through the chassis which is connected directly to the system.

## References

1. <https://www.who.int/news-room/fact-sheets/detail/road-traffic-injuries>. Last accessed 14 April 2022
2. Kumar AP, Mohammed MN (2017) Crush performance analysis of combined geometry tubes under axial compressive loading. Proc Eng 173:1415–1422

3. Xu J, Yang X, He C, Yang K, Li W, Sha J, Zhao N (2020) Crushing behavior and energy absorption property of carbon nanotube-reinforced aluminum composite foam-filled 6061 aluminum alloy tubes. *J Mater Sci* 55(18):7910–7926
4. Chawla A, Kulkarni A, Puranik R, Raj A (2018) Automatic pneumatic bumper and braking system. *Int Res J Eng Technol* 5(8)
5. Chen DH, Ozaki S (2009) Numerical study of axially crushed cylindrical tubes with corrugated surface. *Thin-Walled Struct* 47(11):1387–1396
6. Sinha A, Yadav K, Khurana RS (2016) Optimization of bumper beam structure for pedestrian protection and low speed bumper impact (No. 2016-28-0210). SAE Technical Paper
7. Masoumi A, Shojaeefard MH, Najibi A (2011) Comparison of steel, aluminum and composite bonnet in terms of pedestrian head impact. *Saf Sci* 49(10):1371–1380

# Analysis of a Steering Upright for a Three-Wheel Solar Electric Car



Vinayak H. Khatawate, Burhanuddin H. Telwala, and Ayush P. Shah

**Abstract** The upright of the car is one of the most critical components of the car. In this paper, the front upright of a tadpole-shaped three-wheel solar electric car has been designed and analysed. The dynamic forces acting on the upright are calculated considering the extreme condition of braking while cornering, such that the inner front wheel loses contact with the ground, and the car is about to topple. A suitable material has been chosen for the upright, and then the design is analysed using finite element analysis (FEA). Lastly, iterations in the design have been done to achieve the required factor of safety.

**Keywords** Upright · Knuckle · Solar vehicle · FEA · Student solar vehicle competitions · Three-wheel tadpole-shaped car · Dynamic forces

## 1 Introduction

The steering knuckle is among the most important components of a car. It is joined to the hub, suspension A-Arms, steering tie rod and the brake calliper. The uprights carry the weight of the sprung mass of the car. All the traction forces acting on the wheel are transmitted to the chassis of the car through the upright. The steering effort applied by the driver is transferred to the wheels via the upright. The upright also provides the necessary reaction force to hold the brake calliper in place during braking [1].

---

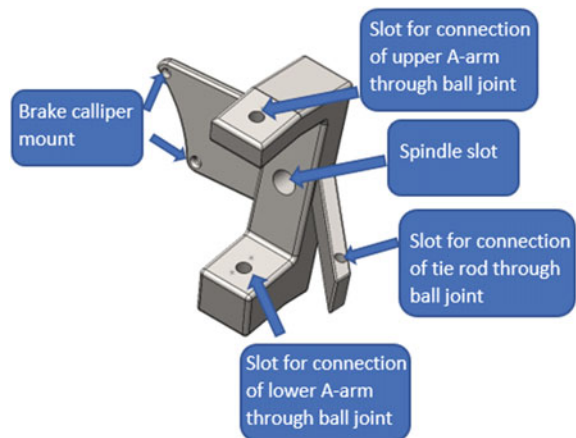
V. H. Khatawate · B. H. Telwala (✉) · A. P. Shah  
Department of Mechanical Engineering, Dwarkadas J. Sanghvi College of Engineering, Mumbai, India  
e-mail: [bhtelwala@gmail.com](mailto:bhtelwala@gmail.com)

V. H. Khatawate  
e-mail: [vinayak.khatawate@djsce.ac.in](mailto:vinayak.khatawate@djsce.ac.in)

A. P. Shah  
e-mail: [shahayush0410@gmail.com](mailto:shahayush0410@gmail.com)

The connection points of various components with the upright have been shown in Fig. 1. With the growing need for sustainability, it is important to reduce the weight of all the components of the car, including the upright. Furthermore, the upright is a part of the un-sprung mass of the car. Therefore, reducing its weight also additionally helps to make the wheels more reactive to bumps and droops, thereby improving comfort and handling for the driver [2]. To reduce the weight of the upright, the forces acting on the upright need to be analysed, the correct material needs to be selected, and finally, iterations to reduce the weight of the component wherever possible need to be carried out. A lot of prior work has been done to design the upright. Kritika Singh and Kanishka Gabel [3] calculated the maximum dynamic forces that act on the upright separately under conditions of braking, cornering, bumps and steering for an ATV vehicle and analysed the upright using FEA analysis. Saksham Bhardwaj et al. [4] used topology optimization using the ANSYS software to optimize the upright design and reduce its weight. They also conducted a detailed comparison of the materials that should be used for the manufacturing of the upright. Dyapa and Shenoy [5] conducted design iterations and argued in favour of using steel over aluminium alloy to manufacture the upright in student vehicle competitions. In this paper, the dynamic forces acting on the front upright of a three-wheel tadpole-shaped car have been calculated, considering the extreme condition of braking while cornering, such that the car is just about to topple, and the entire weight of the car is balanced on two wheels. Not a lot of work has been done to design the upright for a three-wheel tadpole-shaped car considering the above-mentioned extreme condition of loading. The methods used to calculate the dynamic forces are therefore distinct from the previous work done on the upright. Following the calculations of the dynamic forces, FEA analysis using ANSYS 18.1 has been performed and iterations in the design have been done to ensure that the required factor of safety is maintained.

**Fig. 1** Connection points of various components with the upright



**Table 1** Properties of AL-6061-T6

Young's modulus	68 GPa
Poisson's ratio	0.33
Ultimate tensile strength	290 Mpa
Yield strength	240 Mpa
Density	2.7 g/cm <sup>3</sup>

## 2 Selection of Material

Saksham Bhardwaj et al. [4] compared various parameters like specific strength, specific cost and ductility for the materials AL075-T6, Al6061-T6 and AISI 1045, materials which are often used for the upright fabrication, and finally decided to select AL 7075-T6, after making a decision matrix. Aluminium 7075-T6 was difficult to source and is also expensive. Therefore, it was decided to go with Aluminium 6061-T6 due to its smaller density and higher specific strength (yield strength/density) compared to AISI 1045, as the goal was to manufacture a lightweight component. The properties of AL 6061-T6 are mentioned in Table 1.

## 3 Factor of Safety (FOS)

The upright is a critical component of the car. Failure of the upright will cause the sprung mass to fall on the ground and might cause injury to the driver. Although the extreme condition of operation has been considered for analysing the stresses on the upright, larger stresses may be developed during a collision of the front wheel with its surroundings. Therefore, to incorporate safety against such collisions, a factor of safety of two has been considered for the upright. The acceptable stress on the upright is therefore 120 MPa (Yield strength/FOS).

## 4 Calculation of Forces

To design the upright, the extreme condition of braking while cornering is considered, such that the inner front wheel loses contact with the ground and the car is about to topple. During this condition, the entire weight of the vehicle will be balanced on only two wheels, one front and one rear wheel.

### 4.1 Braking Force

A hydraulic braking system is used in the car. It consists of two master cylinders in line with a single pedal. One master cylinder is connected to the brake callipers of the front wheel while the other master cylinder is connected to the brake callipers of the rear wheel. The maximum braking force can be calculated by the equation  $F_{\text{brake}} = \mu N$ , where  $\mu$  is the coefficient of friction between the tyre and the road and  $N$  is the normal force acting on the wheel [3, 5, 6]. However, for the given condition where the entire weight of the car is balanced on two wheels, it will not be possible for the driver to generate enough leg force to completely lock the wheels and utilize the maximum braking force possible. Therefore, to calculate the braking force generated, the maximum leg force by the driver is considered. On experimentation with the driver, in which a weighing scale was placed in the place of the pedal assembly to measure leg force, it was found that the driver can apply a force of 300 N on the pedal assembly.

Parameters listed in Table 2 were considered to calculate the braking force.

$$\begin{aligned} \text{Total force acting on both the master cylinders } (F_{\text{mc}}) \\ = \text{Pedal ratio} \times \text{input leg force} = 6 \times 300 \text{ N} = 1800 \text{ N} \end{aligned} \quad (1)$$

Braking force acting on the front wheel is calculated as follows:

$$\begin{aligned} \text{Force transferred to front master cylinder} \\ = \text{Brake bias for front wheel} \times F_{\text{mc}} = \frac{40}{100} \times 1800 = 720 \text{ N} \end{aligned} \quad (2)$$

$$\text{Master cylinder bore area } (A_{\text{mc}}) = \frac{\pi \times D_{\text{mc}}^2}{4} = 0.000249 \text{ m}^2 \quad (3)$$

**Table 2** Parameters to calculate braking force

Parameter	Value
Disc diameter	245 mm
Disc effective diameter ( $d$ )	220 mm
Master cylinder bore diameter ( $D_{\text{mc}}$ )	17.78 mm
Calliper piston diameter ( $DC$ ) (dual piston calliper is used)	25.4 mm
Pedal ratio	6:1
Input leg force	300 N
Radius of wheel ( $R$ )	232.4 mm
Coefficient Of Friction between brake pad and rotor ( $\mu_p$ )	0.4
Brake Bias Ratio (Front: Back)	40:60



$$\text{Area of the caliper pistons } (A_c) = \frac{\pi \times D_c^2}{4} \times 2 = 0.001013 \text{ m}^2 \quad (4)$$

$$\text{Caliper Piston Force } (F_c) = \frac{A_c}{A_{mc}} \times F_{mcf} = 4.068 \times 720 = 2928.96 \text{ N} \quad (5)$$

$$\text{Frictional Force on brake pads } (F_{bp}) = F_c \times \mu_p = 1171.584 \text{ N} \quad (6)$$

$$\text{Generated Torque } (T_{brakes}) = F_c \times \mu_p \times \left(\frac{d}{2}\right) = 128.87 \text{ Nm} \quad (7)$$

Let the torque generated by the friction on the road about the centre of the wheel be  $T_{road}$ .

$$\text{Net torque on the wheels } (T_{net}) = I(\alpha) \quad (8)$$

$$T_{brakes} - T_{road} = I \times \alpha. \quad (9)$$

Considering  $I\alpha$  is very small compared to  $T_{brakes}$  and  $T_{road}$

$$T_{brakes} = T_{road}. \quad (10)$$

$$T_{road} = \text{Frictional force by road on front wheel } (F_f) \times R \quad (11)$$

$$F_f = \frac{T_{road}}{R} = \frac{128.27}{0.2324} = 552 \text{ N} \quad (12)$$

Since the brake bias ratio is 40:60 (front: rear) and the brake calliper and brake disc diameter of the rear wheel is the same as that of the front wheels, the braking force on the rear wheel is calculated as shown.

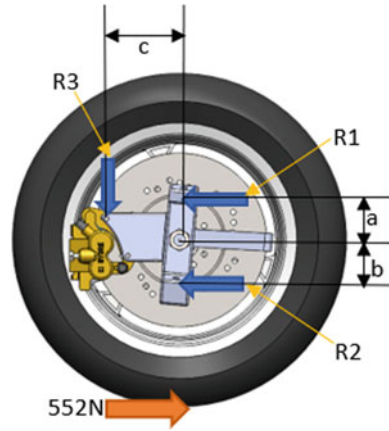
$$F_r \text{ (frictional force by road on the rear wheel)} = \frac{60}{40} \times F_f = 828 \text{ N} \quad (13)$$

$$\text{Total braking force } (F_{brake}) = F_f + F_r = 1380 \text{ N}. \quad (14)$$

**Reaction Forces on upright.** The braking force will be transmitted to the spindle which in turn will be transmitted to the chassis via the upright a-arm joints. The upright will also provide the reaction force to hold the brake calliper in place during braking. Consider the free body diagram showing the reaction forces acting on the upright during braking in Fig. 2.

$$\text{Reaction force on the calipermount } (R3) = F_{bp} = 1171.584 \text{ N}$$

**Fig. 2** Free body diagram indicating reaction forces acting on the upright during braking



Total moment due to the reaction forces on the upright during braking, about the spindle will be zero.

$$(R1 \times a) + (R3 \times c) = R2 \times b. \tag{15}$$

$a = b = 80 \text{ mm}, c = 73 \text{ mm}$

Also,

$$R1 + R2 = Ff. \tag{16}$$

Solving both the equations

$R1 = - 258.53 \text{ N}$  (Direction of force is opposite to that shown in figure)  $R2 = 810.53 \text{ N}$ .

### 4.2 *Weight of the Sprung Mass of the Car Acting on the Upright*

The parameters used to calculate the sprung mass acting on the upright are listed in Table 3.

The vertical distance of the front wheel from the center of gravity =  $d$

$$= \frac{60}{100} \times W = 1.380 \text{ m} \tag{17}$$

The vertical distance of the rear wheel from the center of gravity =  $e$

$$= \frac{40}{100} \times W = 0.920 \text{ m} \tag{18}$$

**Table 3** Parameters to calculate the value of sprung mass acting on upright

Parameter	Value
Total mass ( $m$ )	300 kg
Un-sprung mass of one wheel ( $m_{us}$ )	30 kg
Wheelbase ( $W$ )	2.3 m
Weight distribution (Front:Rear)	40:60
Height of the C.G. ( $h$ )	0.500 m

Let  $N1$  and  $N2$  be the normal reaction forces on the front and the rear wheel, respectively. The values of  $N1$  and  $N2$  can be calculated by balancing the forces and moments about the pitch axis. Consider the following equations,

$$N1 + N2 = m \times g = 300 \times 9.81 \tag{19}$$

$$N1 \times d - N2 \times e = F_{brake} \times h \tag{20}$$

Solving both the equations simultaneously, the values of  $N1$  and  $N2$  comes out to be as follows,  $N1 = 1477.2$  N,  $N2 = 1465.8$  N

$$\begin{aligned} &\text{Downward force acting on upright} \\ &= \text{Normal force on front wheel } (N1) \\ &\quad - \text{weight of un - sprung mass of the front wheel } (m_{us} \times g) \\ &= 1477.2 - 30 \times 9.81 = 1182.9 \text{ N} \end{aligned} \tag{21}$$

The weight of the sprung mass acting on the upright has been shown in Fig. 3.

### 4.3 Cornering Forces

The parameters required to calculate the cornering forces on the upright are listed in Table 4.

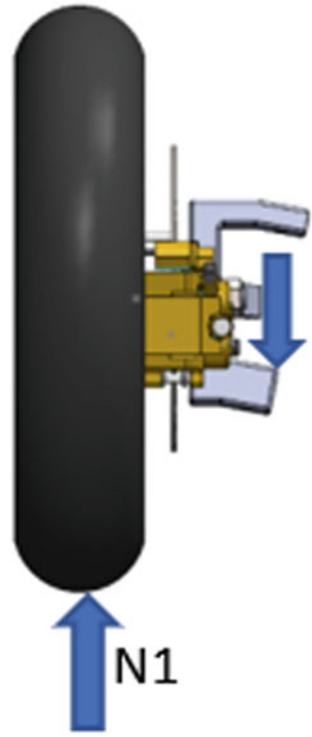
The minimum velocity of the car, when the inner wheel will lose contact with the ground can be found out from the following equation.

$$N1 \times \frac{T}{2} = \frac{mv^2}{r} \times h. \tag{22}$$

From the above equation,  $v = 6.197$  m/s.

$$\text{The total lateral force acting on the wheels} = \frac{mv^2}{r} = 1920.36 \text{ N} \tag{23}$$

**Fig. 3** Free body diagram depicting the weight of sprung mass acting on the upright



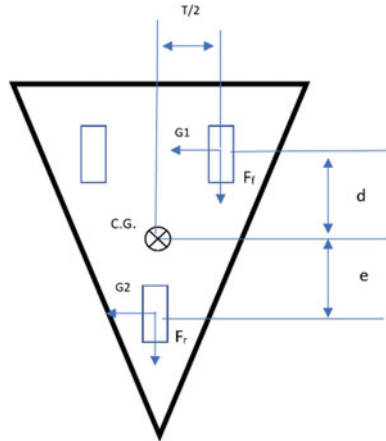
**Table 4** Parameters required to calculate cornering forces

Parameter	Value
Track width ( $T$ )	1.3 m
Min Radius of turn in the track ( $r$ )	6 m
Height of C.G. ( $h$ )	0.5 m
Mass of the car ( $m$ )	300 kg
Radius of the wheel ( $R$ )	0.2324 m
The vertical distance of the front wheel from the centre of gravity ( $d$ )	1.380 m
The vertical distance of the rear wheel from the centre of distance ( $e$ )	0.920 m
Normal reaction force on front wheel ( $N1$ )	1477.2

Consider the free body diagram shown in Fig. 4. Let  $G1$  and  $G2$  be the lateral force acting on the front and rear wheel, respectively. Balancing forces and moments about the axis perpendicular to the road and passing through the centre of gravity we get,

$$G1 + G2 = F_{lateral} = 1920.36. \tag{24}$$

**Fig. 4** Free body diagram depicting braking and cornering forces acting on the wheels



$$G1 \times d = F_f \times \frac{T}{2} + G2 \times e \tag{25}$$

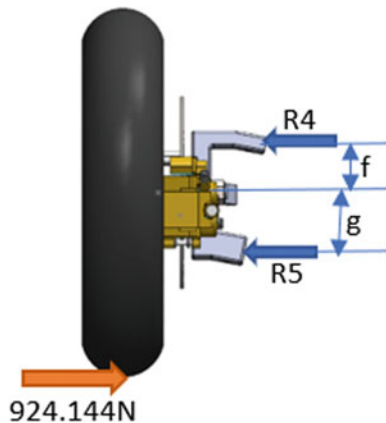
Solving both the equations simultaneously, we get  $G1 = 924.144 \text{ N}$ ,  $G2 = 996.216 \text{ N}$ .

**Reaction forces acting on the upright.** Consider the free body diagram showing the lateral forces acting on the assembly given in Fig. 5. The lateral force on the front wheel will be balanced by the reaction forces on the upright

$$R4 + R5 = G1. \tag{26}$$

Also, sum of the moments on the assembly acting about the spindle will be zero.

**Fig.5** Free body diagram depicting reaction forces acting on the upright during cornering



$$R5 \times g - R4 \times f = G1 \times R. \quad (27)$$

$f = g = 80 \text{ mm (0.08 m)}$ .

Solving both the equations simultaneously we get,

$R4 = - 880.24 \text{ N}$  (Direction opposite to that shown in Fig. 5).  $R5 = 1804.39 \text{ N}$ .

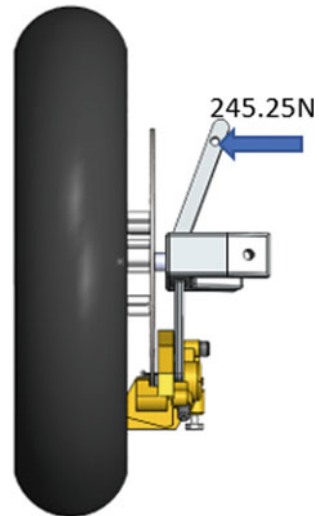
#### 4.4 Steering Forces

A rack and pinion system is used in the car. Taking the moment applied by the driver  $M$ (driver) on the steering wheel as  $50 \text{ kgf cm}$  and radius of pinion as  $2 \text{ cm}$  then,

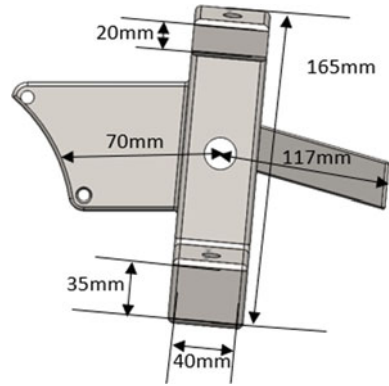
$$\text{Force on the rack} = \frac{M_{\text{driver}}}{R_p} = \frac{50 \text{ kgf cm}}{2 \text{ cm}} = 25 \text{ kgf} = 245.25 \text{ N}. \quad (28)$$

The force on the rack will be transferred to the upright via the tie rod. The moment produced by the driver will be balanced by the opposite moment produced by the braking force about the axis of rotation of the wheel (braking force on front wheel  $\times$  scrub radius), and the reaction force of the ground on the wheel, due to the tendency of the wheel to press into the ground on turning, due to the king-pin inclination angle of the wheel assembly [3]. The force will act on the upright as seen in Fig. 6.

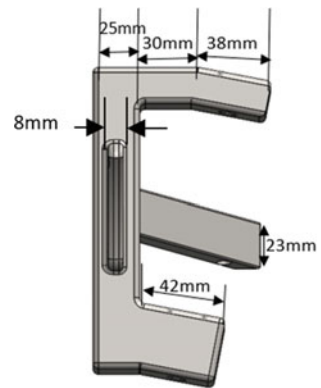
**Fig. 6** Steering force acting on the upright



**Fig. 7** Dimensions of upright in the front view



**Fig. 8** Dimension of the upright in the side view



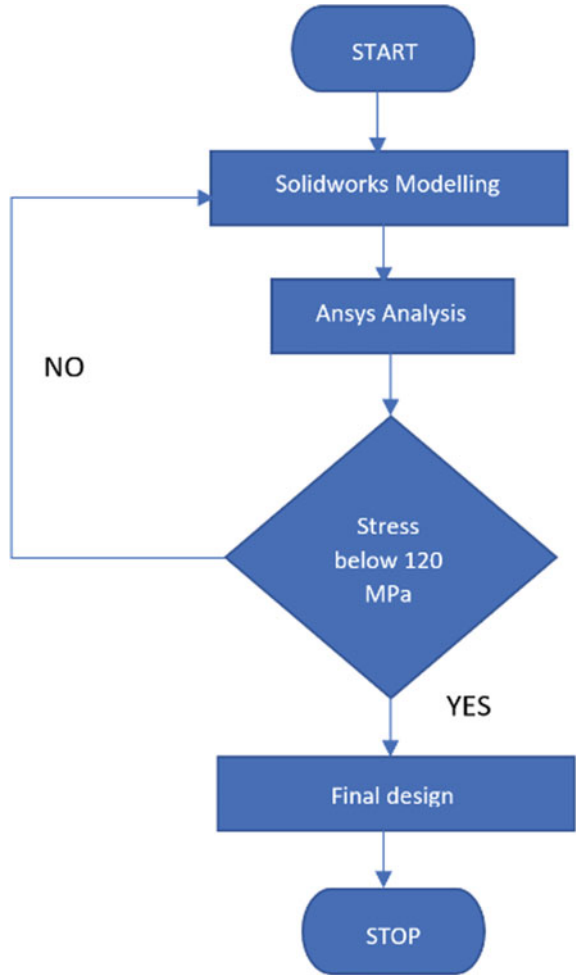
## 5 Dimensions of the First Design of the Upright

The broad dimensions of the upright, like the distance between lower and upper ball joints and the length of the steering arm, are obtained from the suspension and steering geometry. The design and dimensions of the upright used for the first iteration in ANSYS workbench are shown in Figs. 7 and 8.

## 6 Methodology for FEA Analysis

Having selected the material and the desired factor of safety in Sects. 3 and 4, respectively, the goal of the structural analysis was to ensure that the stress produced in the component was within the acceptable limit of 120 MPa. The methodology followed during FEA analysis has been shown in Fig. 9.

**Fig. 9** Methodology for structural analysis



## 7 Results and Discussions

The FEA analysis of upright has been performed in ANSYS Workbench. The proximity and curvature functions were selected in the global mesh settings for meshing the part to capture the stresses at the curves and edges accurately. The region where the spindle passes through the upright has been taken as the fixed support. The forces acting on the upright, as calculated in Sect. 4, are applied to the part as shown in Fig. 10.



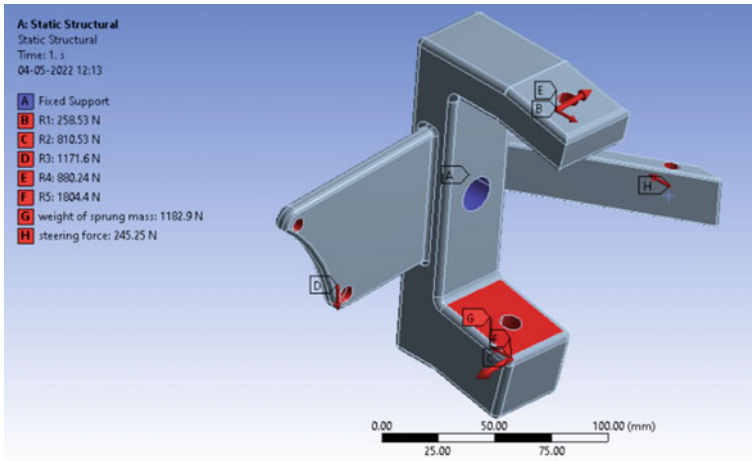


Fig. 10 Application of forces and supports in ANSYS mechanical

### 7.1 Results of the Analysis

The results from the FEA analysis of the first design of the upright are shown in Fig. 11.

The maximum von-Mises stress induced in the upright, close to the region where the spindle passes through the upright is 292.77 MPa as shown in Fig. 11. Since the maximum stress in the component exceeds the maximum allowable stress of

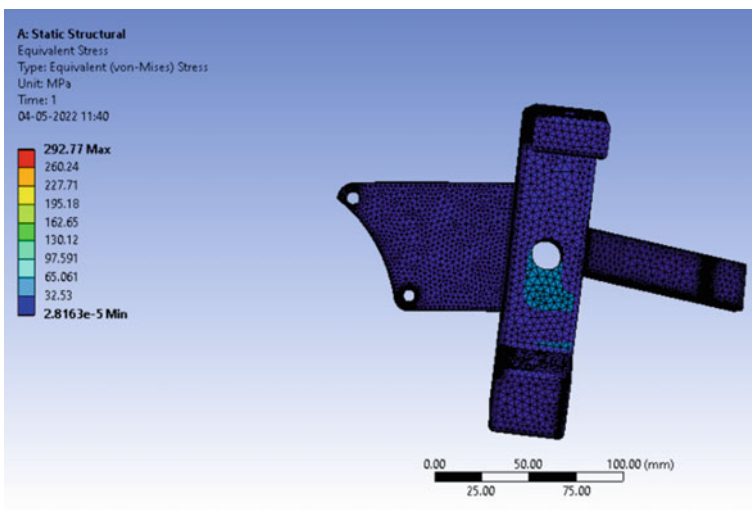
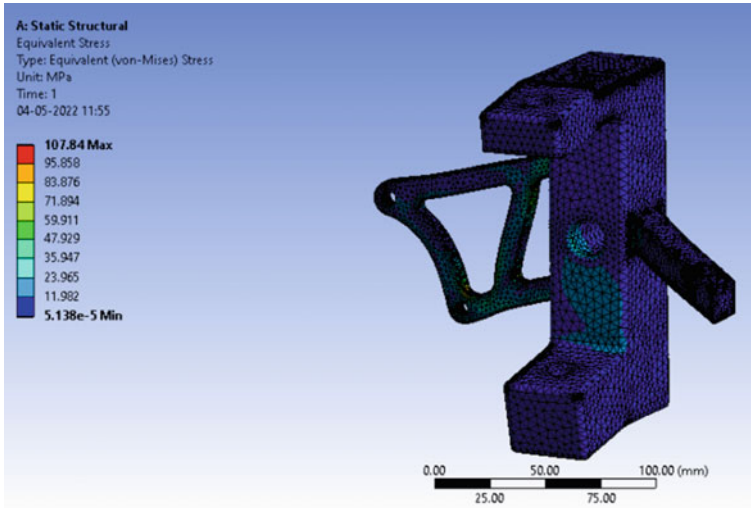


Fig. 11 Maximum von-Mises stress = 292.77 MPa



**Fig. 12** Maximum von-Mises stress = 107.84 MPa

120 MPa, the thickness of the central part of the upright is increased in the second design.

Increasing the thickness increases the area over which the forces are distributed, thereby decreasing the stresses induced in the part. The thickness of the region is increased from 25 to 42 mm for the second iteration. Also, the region of the calliper mount has very low stresses developed. Therefore, material has been deducted from the region in the second design. The result of the FEA analysis of the second design is shown in Fig. 12. On making the changes in the design, the maximum von-Mises stresses developed decreases to 107.84 MPa. Since the maximum von-Mises stress developed is less than the maximum allowable stress of 120 MPa, the design is safe and is finalized.

## 8 Conclusion

The goal of this project was to design a lightweight upright for a three-wheel tadpole-shaped solar electric car. Aluminium 6061-T6 was selected as the material of choice for the upright, due to its availability and high strength-to-weight ratio. A factor of safety of two was decided, to account for the impact forces that might act on the upright during a collision of the wheel with its surroundings. All the forces acting on the upright were calculated, considering the extreme condition of braking while cornering, such that the car is just about to topple and only two wheels remain in contact with the ground. FEA using ANSYS was carried out on the initial design of the upright by applying the calculated forces on the component and taking the

slot for the spindle as the fixed support. The maximum stress on the component came out to be 292.77 MPa. The design was then modified by adding material in the high stress regions and removing material from other low stress regions of the upright. The maximum stress in the component in the second iteration was reduced to 107.84 MPa. Since the stress developed was less than the acceptable stress limit of 120 MPa, the design was safe and finalized.

## References

1. Khatawate VH, Sheth J, Tulasyan P (2020) Structural analysis of the upright of a FSAE race car. In: Vasudevan H, Kottur V, Raina A (eds) Proceedings of international conference on intelligent manufacturing and automation. Lecture notes in mechanical engineering. Springer, Singapore
2. Hrovat D (1988) Influence of unsprung weight on vehicle ride quality. *Journal of Sound and Vibration* 124(3):497–516
3. Singh K, Gabel K (2020) Calculation of dynamic forces and analysis of front upright for ATV. *International Research Journal of Engineering and Technology (IRJET)* 7(4):6314–6319
4. Bhardwaj S, Ashok B, Lath US, Agarwal A (2018) Design and optimization of steering upright to reduce the weight using FEA. <https://doi.org/10.4271/2018-28-0081>
5. Dyapa A, Shenoy V (2014) Design and analysis of upright of an FIA regulated cruiser class solar electric vehicle. *IJERT* 3(10):1062–1066
6. Sindhukavi M, Arun Kannan C, Sowmya S (2020) Design and fabrication of an upright for student formula car. *Int J Res Eng, Sci Manage* 3(8):599–606

# Advanced Helmet System



Rupam Dahe and Ram Bansal

**Abstract** Road crashes have been one of the most frequent causes of death in recent years. The majority of these accidents include two-wheelers, where the chances of survival are very low, but wearing protective gear and obeying traffic laws can reduce the chances of death. The idea of an advanced helmet system is an effective approach which forces a rider to wear a helmet and avoid the consumption of alcohol before or during the ride. The system consists of two units, i.e. the helmet unit and the vehicle unit. The helmet unit consists of a force-sensing resistor to check if the rider is wearing the helmet and an alcohol sensor which detects the consumption of alcohol. Both the signals are sent to the vehicle unit, and if the rider fulfils the criteria (wearing a helmet and NOT consuming alcohol), then only the unit allows the ignition of the vehicle. If the rider is drinking at any point of time throughout the ride, the unit will cut off the ignition. The helmet unit also includes a DRL system that reflects the LED indications (brakes, turning indicators) from the vehicle to the back of the helmet to make the rider more visible to others at night. The main highlight of this system is the introduction of a wireless dongle receiver, which comes with the helmet unit and can be plugged into the vehicle at the time of riding. In countries like India, the majority of the population can only afford two-wheelers, so implementing this system will make it compulsory for riders to wear a helmet, thus making these roads a safer place.

**Keywords** MQ3 sensor · FSR · DOT · ISI · RF

## 1 Introduction

Most countries now require their residents to wear helmets while riding bikes and to not ride a bike while intoxicated, yet restrictions are still broken. The real-world issues we confront on the roadways are the motivating factor behind this initiative. As per a World Health Organization report, road traffic injuries resulted in roughly 1.24

---

R. Dahe · R. Bansal (✉)

Department of Mechanical Engineering, Medicaps University, Indore, India  
e-mail: [ram.bansal@medicaps.ac.in](mailto:ram.bansal@medicaps.ac.in)

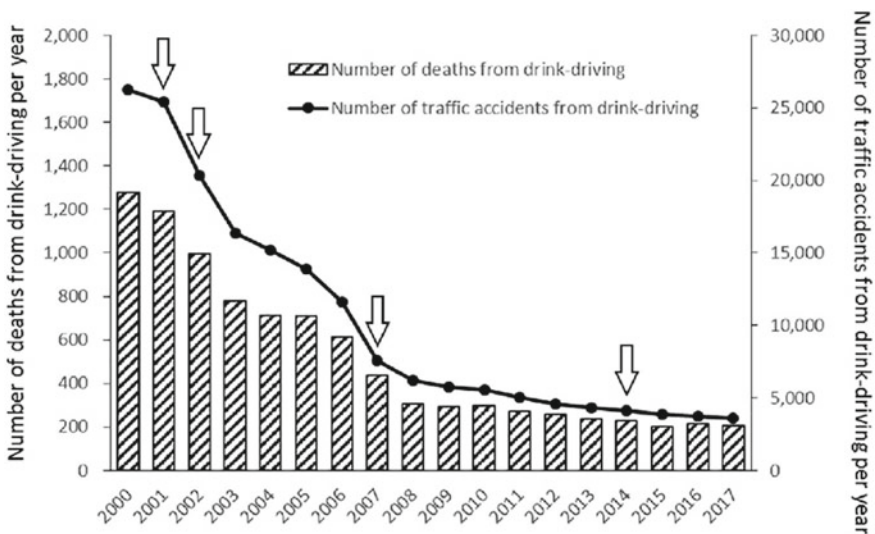
© The Author(s), under exclusive license to Springer Nature Singapore Pte Ltd. 2023  
R. Sharma et al. (eds.), *Advances in Engineering Design*, Lecture Notes in Mechanical Engineering, [https://doi.org/10.1007/978-981-99-3033-3\\_20](https://doi.org/10.1007/978-981-99-3033-3_20)

225

million deaths in 2010, down slightly from 1.26 million deaths in 2000. According to this research, a vehicle accident kills someone every 27 s. Today, we see several examples of fatality caused by two-wheeler accidents. People do not wear helmets despite the fact that they are easily accessible. According to the World Health Organization, vehicle accidents are the second leading cause of death among those aged 8–35. According to recent studies by the National Crime Records Bureau (NCRB), the overall number of deaths caused by traffic accidents has already surpassed 135,000 each year (Fig. 1).

In India, the current system is severely flawed, with many motorcyclists refusing to wear helmets. The only reason they wear helmets is because they are routinely stopped by traffic cops. Similarly, drunk-driving instances are fairly common, particularly at night. Drunk riders lack discipline, and they pose a danger to others on the road. Fines for these offences are also not a concern. People prefer bikes to cars for a number of reasons, including lower component pricing and a wider range of options on the market. As a result, there is a considerable concern, and it has also become a big issue of road safety. The idea of this research is to establish a circuit that will increase motorcycle safety, as well as to develop an intelligent safety helmet for the overall rider and make it mandatory for all riders.

A system is created that checks two conditions before starting the bike engine. The system features FSR, which detects whether or not the rider is wearing a helmet. The system also contains an alcohol sensor, which informs the vehicle unit whether or not the rider is intoxicated. If one of the two prerequisites is not met, the engine will not start. The vehicle unit has the ability to cut off the ignition of the vehicle at



**Fig. 1** Drink-driving-related traffic accidents and deaths (2000–2017) (National Police Agency, KEISATSU HAKUSHO). The years of amendments to the traffic/road law are indicated by white arrows [1]

any point of time throughout the ride if the sensor detects alcohol from the breath of the rider. The helmet back is also equipped with a LED DRL, which indicates the brake and turning signals to the other drivers on the road, so that the person wearing the helmet can be noticed even at night and in foggy conditions. This is another safety feature on this system. The whole system is designed for the improvement of riders' experience while considering the safety laws.

## 2 Previous Literature

To gain a deeper understanding of the problem domain, I conducted research in which I looked at a variety of examples: research articles, previously constructed systems, and systems that are already in use. I looked into a lot of accident cases. The causes of injuries sustained in these events, as well as the failure of safety systems, were explored [2]. Weak legal enforcement, unpleasant aesthetic impressions, some do not consider seat belts as safety gear, and others do not use them because their family and friends do not wear or encourage them were all identified as reasons for the underuse of seat belts. While reviewing study articles, we discovered that various concepts and research have been conducted in this field to make cars safer. However, the ideas and techniques presented in those articles were never implemented or evaluated in the real world [3, 4].

### **Smart Helmet [5]**

By Shreyas Ghule, Sumedh Dorwat, Ashish Shende

The project carried out by these authors was focused on creating a helmet which detects the presence of alcohol from rider and cuts off the engine supply. It was also focused on accident detection and alert system with the help of GPS and GSM. The system is capable of sending an alert message to the emergency contact in case of the road accident which is detected by the vibration sensor in the helmet.

### **Ignition Interlocking Seat Belt [6]**

By Dr. Harshal Shah, Kishankumar Patel, Nitya Patel, Nishil Patel, Rutvik Patel

The proposed solution intends to maximize the effectiveness of seat belts in order to assure passenger safety. The system suggested here employs a variety of sensors to collect data on a variety of characteristics in order to recognize occupants and track seat belt status. By monitoring the human body's weight and temperature, sensors track the status of the seat belt to ensure proper use. Data from these sensors is then sent to microcontroller, which only allows the engine to start if the occupant is properly buckled in.

### 3 Working Methodology

A prototype is being created to demonstrate how the proposed system works. This prototype aids in better understanding the proposed system's functioning principle. It takes inputs and processes them in real time. To supply the necessary inputs to the system, various physical parameters are measured. It is a novel concept that eliminates the possibility of riding a bike without a helmet and avoids drunk driving. A biker's helmet also serves as the second key.

The system's operation is fairly straightforward. The entire system is divided into two components: the helmet unit and the vehicle unit. In the helmet, the helmet unit is mounted. FSR sensor, MQ3 sensor, and DRL LED lights are included. All of these components are connected to the RF system as well as the helmet's output connector. The vehicle unit, on the other hand, is a switch that connects the power source (ignition or battery) to the load (engine or motor). The data is received by the RF system in the vehicle unit and processed by the alcohol unit. The information from the alcohol unit is subsequently sent to the cut-off relay, which regulates the motor. The relay allows power to the motor if the rider correctly fits the helmet and is not intoxicated by drinking. The sensors will detect and send information to the vehicle unit if the rider fails to meet any of the above conditions at any stage before or during the ride. The power is then cut off with the help of a relay. Throughout the travel, the technology ensures the rider's safety. At the same time, the vehicle unit captures LED indicator data from the vehicle and provides it to the helmet DRL display.

Since the helmet must be connected to the vehicle unit at all times to complete the system, it also serves as a key to the vehicle, making it an excellent security solution. The helmet and vehicle units communicate with each other using an RF transmission system; however in this project, I have introduced a wired connection option for the units. Both units have their own output ports for connecting the cable (just like headphones). If the RF system fails, the cable system serves as a backup. The helmet will be provided with a connection dongle (similar to a wireless mouse) [7] and the vehicle unit in this system. The vehicle unit will be installed in the vehicle, and the dongle will be hooked up to the vehicle unit during the ride. This ensures the helmet's portability and allows the rider to use different helmets for different occasions because each helmet has its own unique dongle. The system was created with the rider's comfort and safety in mind.

### 4 Working Components

The system components listed below are being used to create this prototype and to demonstrate the operation of the proposed system in a practical manner.

**Fig. 2** FSR [8]

### ***4.1 Force-Sensing Resistor (FSR)***

Inside the helmet is a force-sensing resistor, which detects actual human touch. Before starting the bike, the helmet unit determines if it is worn or not. If this condition is met, the signal to start the bike unit is sent. FSRs are robust polymer thick film (PTF) devices whose resistance is inversely proportional to the force applied to the sensor's face. In medical systems, automotive electronics, robotics, and industrial applications, this sensor is employed as a human touch control. A force-sensing resistor is a two-wire sensor with a resistance that changes depending on the amount of force applied (Fig. 2).

### ***4.2 MQ3 Alcohol Sensor***

The MQ3 gas sensor is used to detect the presence of alcohol in the breath. It can be placed just in front of your mouth. The sensor detects numerous compounds in alcohol and assesses whether or not the rider is inebriated. A potentiometer is also included in the sensor to alter the gas concentration. We utilize a resistance of 200 K to calibrate the detector for 0.4 mg/L of alcohol content in air. GND, VCC, A out, and D out are the four pins. Both analogue and digital outputs are supported by the sensor. This sensor's digital output is used here (Fig. 3).

### ***4.3 RF Technology***

A frequency or rate of oscillation in the range of 3 Hz–300 GHz is referred to as radio frequency (RF). The frequency of alternating current electrical impulses used to produce and detect radio waves falls within this range. Because most of this range is too high for most mechanical systems to handle, it usually relates to oscillations in electrical circuits or electromagnetic radiation. The RF receiver receives data from



**Fig. 3** MQ3 sensor [9]



**Fig. 4** Wireless dongle [7]



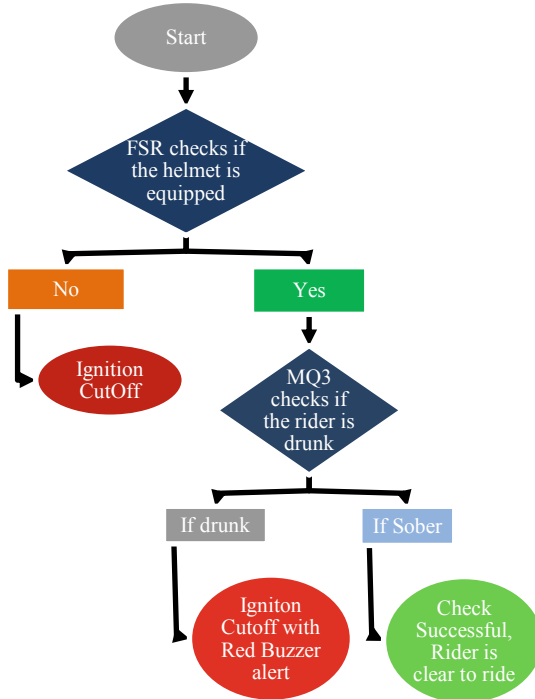
the antenna pin, which is then available on the data pins. The receiver module includes two data pins. As a result, this information can be used in other ways (Fig. 4).

#### ***4.4 Relay Module***

The single-channel relay module is used to control high-voltage current loads such as solenoid valves, motors, AC loads, and lighting. This module is primarily designed to interact with various microcontrollers such as PIC, Arduino, and others.

## 5 Project Architecture

The flow chart below explains the working of the whole system.



A prototype was made to demonstrate the working of the idea (Figs. 5 and 6).

**Helmet Module.** The block diagram shows the overview of the connections at the helmet module of the system (Fig. 7).

**Vehicle Module.** The block diagram shows the overview of the connections at the vehicle module of the system (Fig. 8).

## 6 Conclusion

We successfully created a smart helmet system using alcohol detection technologies in this project. To start the vehicle, the system makes it mandatory to wear a helmet. The project’s findings revealed that wearing a helmet causes the motorcycle to start. As a result, the impact of an accident will be reduced automatically, and bike thefts

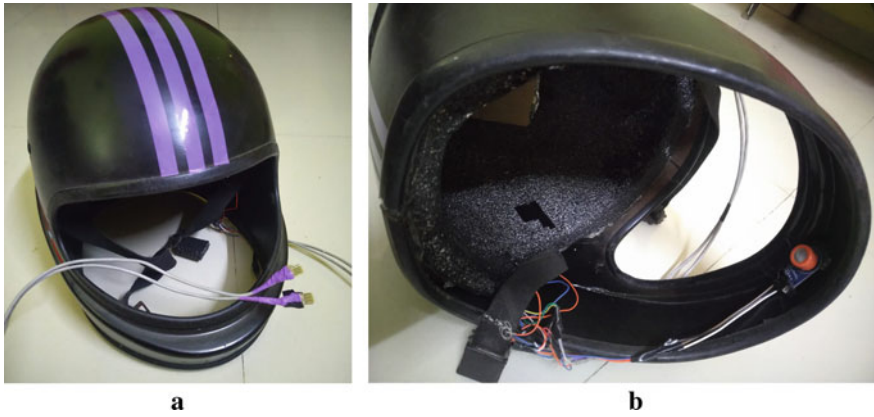


Fig. 5 a and b Helmet unit

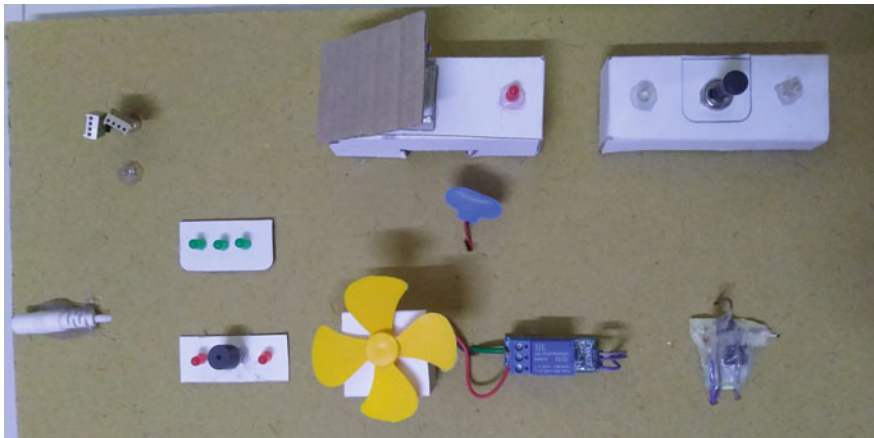
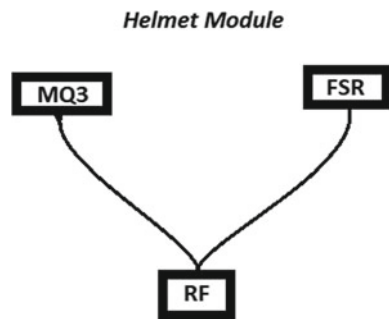
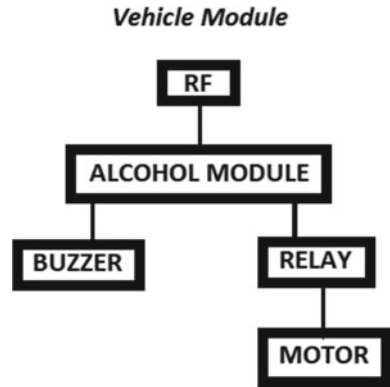


Fig. 6 Vehicle unit

Fig. 7 Helmet module block diagram



**Fig. 8** Vehicle module block diagram



will be avoided. Using a radio frequency module to convey a signal from the helmet unit to the bike unit, the wireless dongle system is being implemented.

In the event of RF failure, a wired backup system is included. The DRL system on the helmet has been introduced to make the rider more visible at night and in hazy conditions. The following characteristics can be added to the proposed methodology to make it even better.

- (a) GSM and GPS technology can be added for accident detection and rescue system.
- (b) Over speed limitation devices can be placed to prevent the rider from going too fast. If the motorcyclist exceeds the speed limit, his registration number will be reported to the traffic enforcement authorities, who will take the appropriate measures.
- (c) A mind wave kit can be used to read brain waves for attention and meditation to boost the sensitivity of the skin potential.
- (d) Various bioelectric sensors can be installed on the helmet to track various activities.
- (e) Small cameras can be used to capture the driver’s actions.
- (f) It can be used to communicate messages from one bike to another via wireless transmitter.
- (g) We may utilize a solar panel to power our helmets and charge our cell phone batteries using the same power source.
- (h) Similar technology can be used in other vehicles like cars to eliminate the chances of accidents (example is seatbelt ignition system)

## References

1. [https://www.researchgate.net/figure/Number-of-traffic-accidents-and-deaths-from-drink-driving-2000-2017-National-Police\\_fig2\\_333908432](https://www.researchgate.net/figure/Number-of-traffic-accidents-and-deaths-from-drink-driving-2000-2017-National-Police_fig2_333908432)
2. Vyas M, Rajee MK, Warghade SS, Arunkumar KR (2017) Active Seat Belt System. IEEE 3(17):1–5
3. Bhardwaj DR, Jogdhankar SR (2014) Seat belt safety features using sensors. International Review of Applied Engineering Research 4(4):349–354
4. Nandakumar C, Muralidaran G, Tharani N (2014) Real time vehicle security system through face recognition. International Review of Applied Engineering Research 4(4):371–378
5. Journal of Emerging Technologies and Innovative Research (JETIR), Issue 4, April 2019. ISSN: 2349-5126
6. International Research Journal of Engineering and Technology (IRJET), vol 07 Issue 04, April 2020. e-ISSN: 2395-0056
7. <https://www.indiamart.com/proddetail/wifi-dongle-11795714273.html>
8. <https://www.sparkfun.com/products/9375>
9. <https://www.indiamart.com/proddetail/mq-3-alcohol-gas-sensor-module-12392978548.html>
10. International Journal of Science and Research (IJSR), vol 3, Issue 3, March 2014. ISSN (Online): 2319-7064
11. International Journal of Computer Science and Applications, vol 6, No.2, Apr 2013. ISSN: 0974-1011 (Open Access)
12. Article from The Hindu [online] 10 Feb 2011. Available from <http://www.hindu.com/2011/02/10/stories/2011021063740500.htm>
13. International Journal of Scientific & Engineering Research, vol 2, Issue 12, 1 Dec 2011. ISSN: 2229-5518
14. Bishop R (2002) The road ahead for intelligent vehicle system: what's in store for riders? In: 8th annual Minnesota motorcycle safety conference
15. Sayeed A, Perrig A (2008) Secure wireless communications: secret keys through multipath. In: Proceedings of IEEE international conference on acoustics, speech signal processing, pp 3013–3016
16. Reagen WR (1979) Auto theft detection system|| US4177466 (US Patent) Computer, May 2011

# Modelling and Stress Analysis of Connecting Rod Using Fusion 360



Riya Pal, Shweta Mitra, Rahul, and Neetu Kanaujia

**Abstract** To ensure that any structure manufactured by the industry operates satisfactorily without breaking under the specified load requirements, it is extremely important to do stress analysis after designing a component as it will reduce a lot of time during design, by avoiding the redesign procedure due to structural verification during failure tests. Stress analysis plays an important role in today's era. In today's competitive market, every part that is manufactured requires proper designing and correct material selection because every part has to undergo various forms of stresses on applying load. Thus, through our research we have tried to demonstrate the importance of stress analysis on a connecting rod and the right material for the manufacturing of it. In this paper, we carried out with the structural static stress analysis of a connecting rod with different materials, using software called Autodesk Fusion 360. By doing this we were able to make a comparison among factors of safety, stress, strain and displacement with our selected materials.

**Keywords** Connecting rod · Fusion 360 · Stress analysis · Stainless steel

## 1 Introduction

The rod that joins the piston to the crankshaft to transfer combustion pressure or to transmit the tensile and compressive forces to the crank pin is known as a connecting rod. It mainly comprises a small end, a large end and an I-beam (shank), and the other parts like the bushing, bearing inserts, bolts and nuts and bearing cap. The small cease is supplied to deal with the piston pin, and the big cease is split into elements to hold the crank pin [1]. Connecting rod is of different types and shapes, but an I-shape connecting rod is preferred for lightness, low inertia force and can

---

R. Pal · S. Mitra · Rahul (✉)

School of Mechanical Engineering, KIIT University, Bhubaneswar, Odisha, India  
e-mail: [rahulkumar589@gmail.com](mailto:rahulkumar589@gmail.com)

N. Kanaujia

School of Computer Application, KIIT University, Bhubaneswar, Odisha, India

resist (or withstand) high gas pressure. The materials used for the connecting rod should be chosen wisely as it is one of the most severely stressed parts for many vehicles and engines (like IC engines). Its miles subjected to the force of gas stress and the inertia pressure of the reciprocating element. Thus, the material used for making connecting rod should be very lightweight and of very high fatigue strength (resistance) to reduce forces. The materials used for connecting rod varies from industry to industry depending on their different applications and uses. Common materials are medium carbon steels containing 0.35–0.45% carbon, alloy steels which include nickel–chromium or chromium–molybdenum steels, iron base sintered metal, spheroidized graphite cast iron (ductile), aluminium and titanium alloy (Ti-6Al-4V). There is always a high chance of facing failure in the connecting rod due to the high heat and pressure given to it. As a result, mostly it gets torn from the lock of the piston pin. The forces acting on the connecting rod are shear force (due to bending) and axial forces, that is compression force and tensile force.

## 2 Materials Used in Present Research

One of the key components of the engine is the connecting rod, which joins the piston to the crankshaft and transfers the piston's reciprocating action into the rotation of the crankshaft. The connecting rod needs to be sturdy enough to sustain the piston's forces during combustion. It experiences several tensile and compressive loads during the course of its lifespan. The selection of proper materials in the designing of the connecting rod is extremely important. Here in our paper, we have done a comparative study of a few materials and using them we did the stress and thermal analysis. Before using any particular material, the properties of that material should be focused on. Thus, given below is a small description of the physical, mechanical and chemical properties of the materials that we have used in designing the connecting rod (Table 1).

**Table 1** Properties of the material [2]

Materials name	Density (kg/mm <sup>3</sup> )	Modulus Young's (GPa)	Poisson's ratio	Strength yield (MPa)	Strength ultimate tensile (MPa)	Thermal conductivity (W/mm C)
Grey cast ASTM A48 grade 35, Iron	7.395E-06	109.6	0.244	251.7	334	0.04804
Aluminium 7075	2.81E-06	71.7	0.33	145	276	0.173
Carbon steel (for pressure vessel)	7.85E-06	200	0.29	350	420	0.0476
Aluminium 6061	2.70E-06	68.90	0.33	275	310	0.167

### 3 Chemical Composition of Materials Used

#### Iron, Grey Cast ASTM A48 Grade 35

This is a special grade of iron used to produce castings that require high tensile strength and hardness (Table 2).

This is a special grade of iron used to produce castings that require high tensile strength and hardness.

#### Aluminium 7075

Aluminium 7075 is widely used for making connecting rods and other industrial appliances [3] (Table 3).

#### Carbon Steel (for Pressure Vessel)

In the recent years, the use of carbon steel has been constantly increasing in the construction industry. Carbon steel requires low investments, but all production capabilities can be achieved. Also, it is very easily available and rust-free usually, thus

**Table 2** Chemical composition of grey cast iron A48 grade 35

Element	Range (wt%)
Sulphur	≤ 0.16%
Manganese	0.5–0.8%
Silicon	1.7–2.4%
Nickel	0.5–0.2%
Molybdenum	0.5–0.15%
Chromium	0.05–0.5%
Copper	0.15–0.5%
Iron	91–94%
Phosphorus	≤ 0.12%
Carbon	4.40–4.0%

**Table 3** Chemical composition of Aluminium 7075

Element	Range (wt%)
Aluminium	Balance
Titanium	0.3%
Chromium	0.15%
Silicon	0.5%
Zinc	5.5%
Iron	0.5%
Magnesium	3.0%
Copper	1.5%
Manganese	0.4%



**Table 4** Chemical composition of carbon steel

Element	Range (wt%)
Carbon	0.10–0.22%
Manganese	1–1.7%
Phosphorus	0.04%
Sulphur	0.03%
Silicon	0.6%
Chromium	0.4%
Nickel	0.3%
Titanium	0.03%
Molybdenum	0.09%
Aluminium	0.02%
Copper	0.3%

making it an excellent alloy for industrial application. Its chemical composition is as follows: [3] (Table 4).

### Aluminium 6061

Usually utilized for the manufacturing of aircraft structures like aeroplane wings and fuselage. Aluminium 6061 has an excellent strength to weight ratio, making it very useful in the automobile as well as the aerospace industry. The demand for Aluminium 6061 alloy has been continuously increasing these days as they are crack resistant as well as corrosion-resistant [4] (Table 5).

**Table 5** Chemical composition of Aluminium 6061

Element	Range (wt%)
Magnesium	0.9%
Silicon	0.62%
Iron	0.33%
Copper	0.28%
Chromium	0.17%
Manganese	0.06%
Zinc	0.02%
Titanium	0.02%
Aluminium	Balance

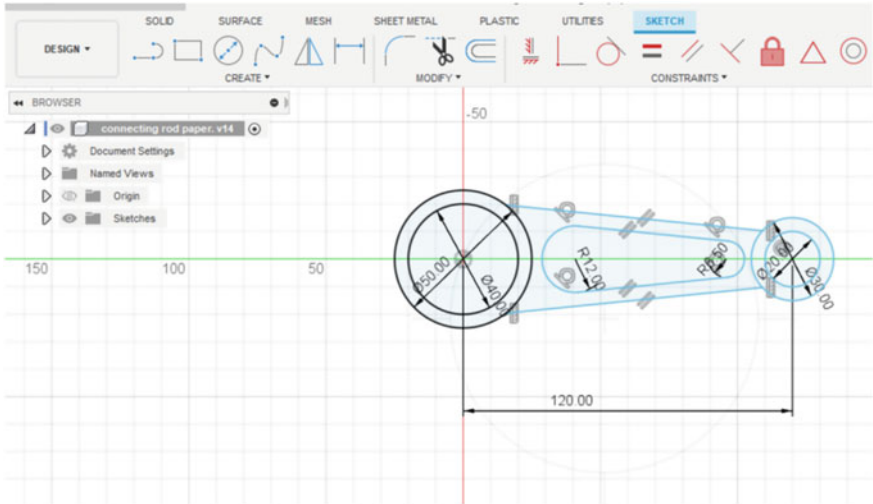


Fig. 1 Sketch of a connecting rod using Autodesk Fusion 360

### 4 Design of Connecting Rod

Fusion 360 is a software that has been introduced by Autodesk as a design platform that allows cloud collaboration and sharing. Fusion 360 is a flawless design that helps in solving technical challenges of cross-platform data sharing, enables effective cross-regional cooperation, presents a top-level view of collaboration, and breaks down the obstacles among art and production, in addition to obstacles between design and processing [5]. To design the connecting rod, some steps are involved which is briefly described below.

Step 1: Make a sketch of the required small end and the big end using proper dimensions as shown in Fig. 1. The length of the connecting tool can be set by using the dimension tool [6, 7].

Step 2: First we have extruded the small end and the bigger end by 25 mm. Next is to extrude the connecting rod portion by 23 mm, keeping the direction symmetric. The screenshot has been attached in Fig. 2 [8].

### 5 Modelling and Analysis

In our paper, we performed the modelling and analysis of the connecting rod using Fusion 360. After designing the connecting rod in the ‘design’ section of Fusion 360, we have moved to the ‘Simulation’ section of Fusion 360 for the simulation part (Analysis) which is our next step. After entering the ‘Simulation’ section, we

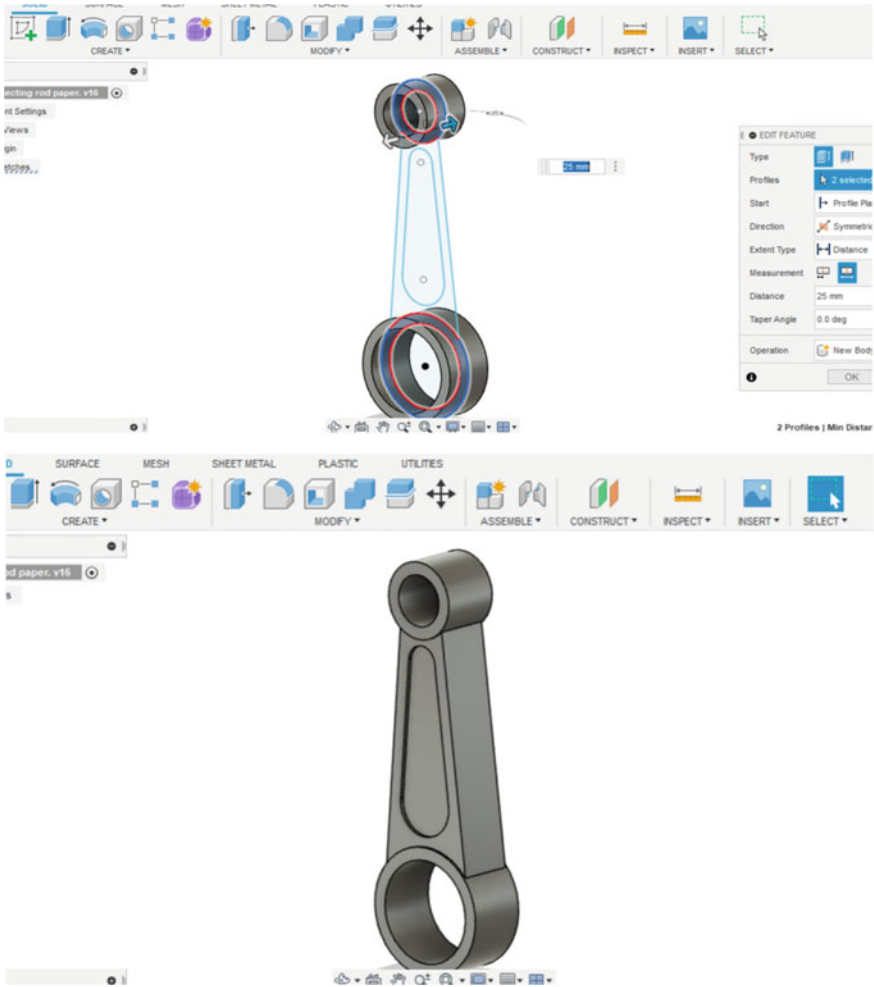


Fig. 2 Design of connecting rod

will select ‘Static Stress’ for the stress analysis of the connecting rod. Four different materials are taken that is Grey cast iron of grade 35, Aluminium 7075, Aluminium 6061 and carbon steel. Each of these four materials is undergone the following boundary conditions.

Boundary Conditions:

1. Load: A load of 5000 N (5 kN) is applied at the crank side, i.e. the larger end of the connecting rod at tensile condition.
2. Constraints: A fixed support is provided to the inner portion of the small end (piston side) of the connecting rod.

After when the boundary conditions (as shown in Fig. 3) are applied and checking all the prerequisites (needed conditions), we will move to the ‘solve simulation study’. After the completion of the simulation study, we get the following result of four different materials in terms of factor of safety (FOS), stress, deformation (displacement) and strain (as shown in Figs. 4, 5, 6, 7 and Tables 6, 7, 8, 9).

1. Grey cast iron (ASTM A48 Grade 35)
2. Aluminium 7075
3. Aluminium 6061
4. Carbon steel (for pressure vessel)

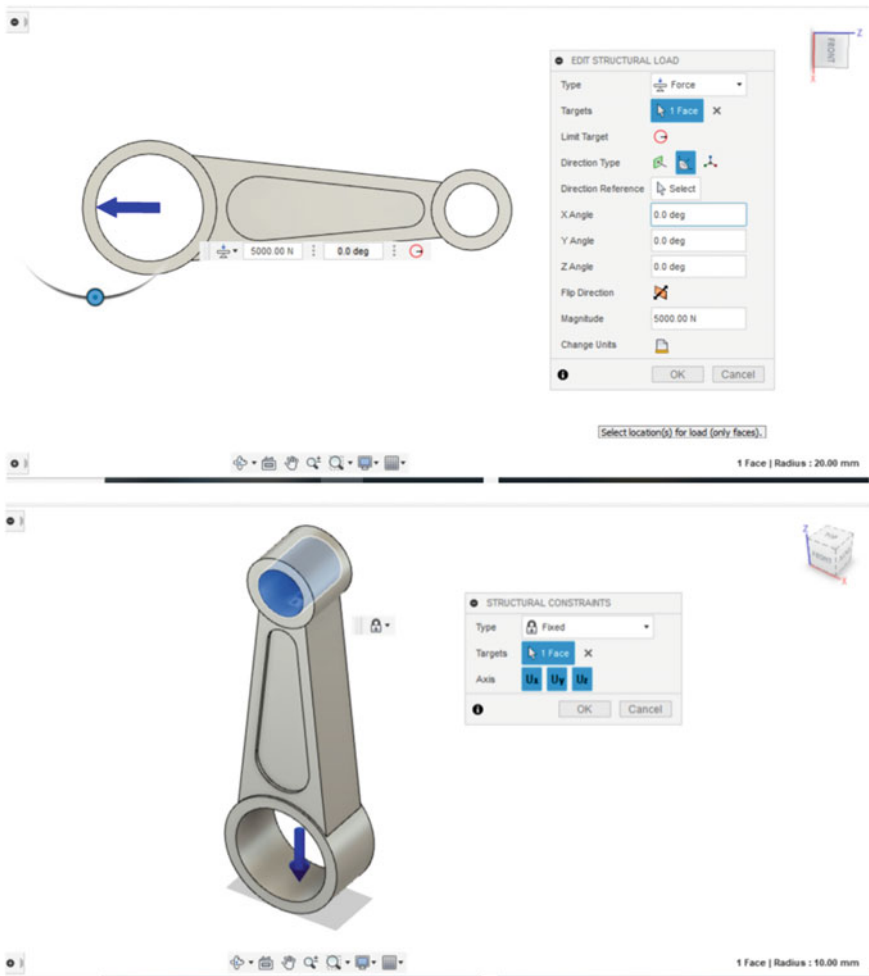


Fig. 3 Boundary conditions (load and constraints)

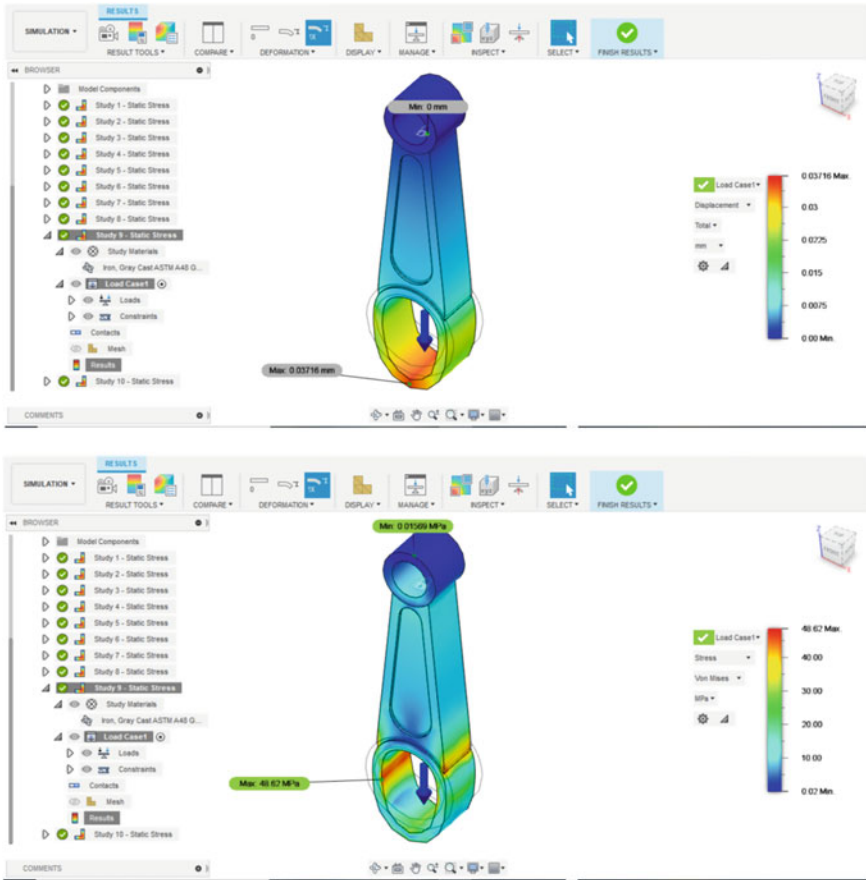


Fig. 4 Displacement and stress analysis of grey cast iron

## 6 Results and Discussion

We have done the stress analysis of a connecting rod and obtained the result. And from the analysis, we found that our design is safe for materials that we have chosen which are grey cast iron, Aluminium 7075, Aluminium 6061 and carbon steel since the values of factor of safety of each material that we have used lie within a range of 3–6. A comparison has been drawn between all the materials based on the result obtained. The result is shown in Table 10 and Fig. 8.

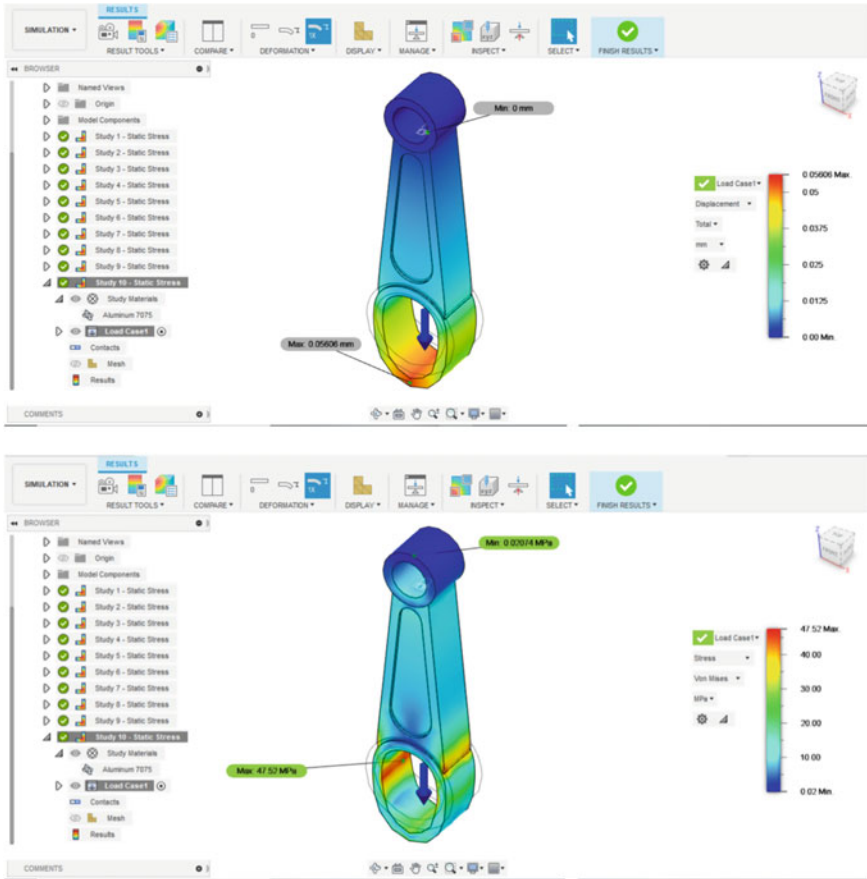


Fig. 5 Displacement and stress analysis of Aluminium 7075

## 7 Conclusions

1. We have compared different possible materials that are used for making connecting rods with the help of analysis (by applying a force in tensile conditions) using Fusion 360 and observed that grey cast iron, Aluminium 6061, Aluminium 7075, carbon steel and some other materials (which is not shown in this paper) like stainless steel is safe and can be used for further analysis and work.
2. On the other hand, materials like Titanium 6Al-4 V, Steel AISI 4340 350A QT and Ductile Iron (SG Cast Iron), who's factor of safety (FOS), is coming out of range (15) for the same design with the same dimensions which is not safe for working and for any industrial purpose.

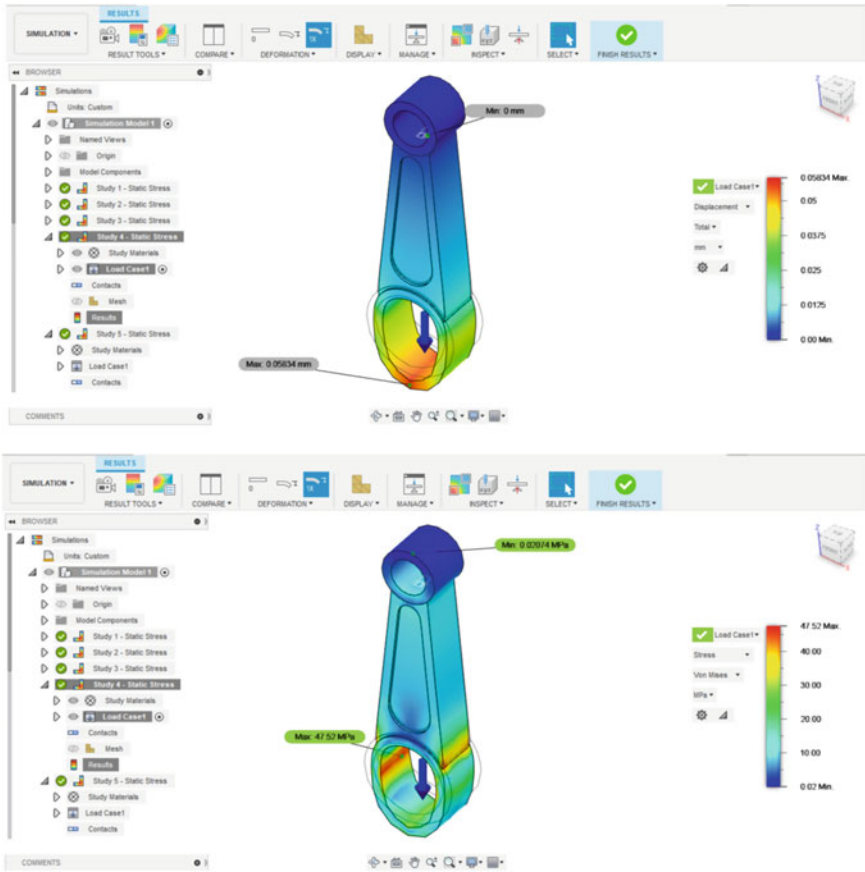


Fig. 6 Displacement and stress analysis of Aluminium 6061

3. From our analysis, we get, that grey cast iron can endure maximum stress in comparison to the other selected materials. In terms of factor of safety (FOS), Aluminium 7075 is better as it has the least FOS value among other materials.

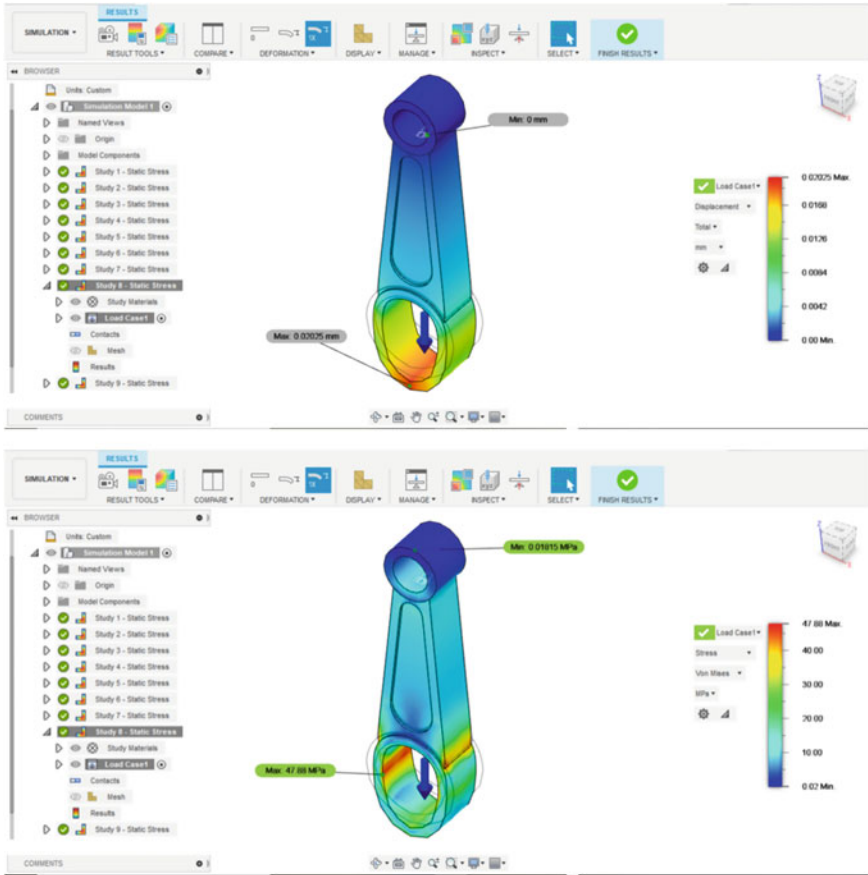


Fig. 7 Displacement and stress analysis of carbon steel

Table 6 Result table for Grey cast iron

FOS	Max. stress (MPa)	Max. displacement (mm)	Strain	Design
5.177	48.62	0.03716	0.0004769	Safe

Table 7 Result table for Aluminium 7075

FOS	Max. stress (MPa)	Max. displacement (mm)	Strain	Design
3.051	47.52	0.05606	0.0007541	Safe

Table 8 Result table for Aluminium 6061

FOS	Max. stress (MPa)	Max. displacement (mm)	Strain	Design
5.787	47.52	0.05834	0.000785	Safe

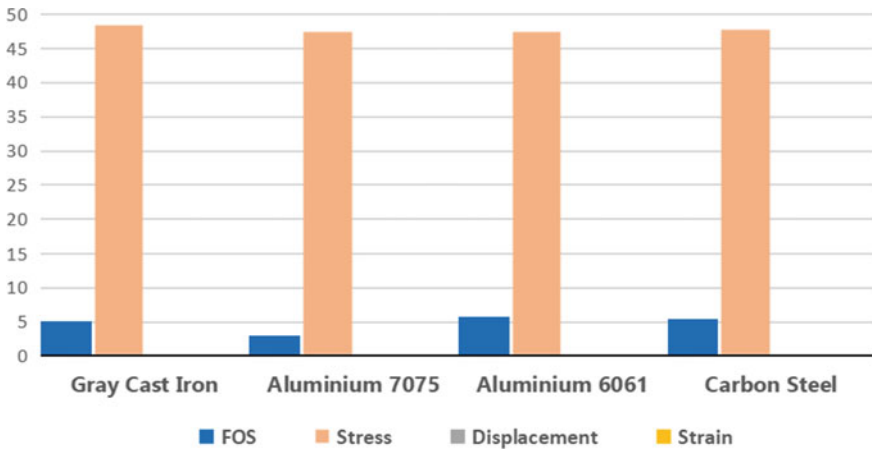


**Table 9** Result table for carbon steel

FOS	Max. stress (MPa)	Max. displacement (mm)	Strain	Design
5.472	47.88	0.02025	0.000266	Safe

**Table 10** Comparison between different materials

Material	FOS	Max. stress (MPa)	Max. displacement (mm)	Strain	Design
Grey cast iron	5.177	48.62	0.03716	0.0004769	Safe
Aluminium 7075	3.051	47.52	0.05606	0.0007541	Safe
Aluminium 6061	5.787	47.52	0.05834	0.000785	Safe
Carbon steel	5.472	47.88	0.02025	0.000266	Safe



**Fig. 8** Comparison between different materials

## References

1. Bhandari VB (2021) Design of machine elements, 5th edn. McGraw Hill Education Private Limited, India
2. Vannan SE, Vizhian SP (2014) Microstructure and mechanical properties of as cast aluminium alloy 7075/basalt dispersed metal matrix composites. Journal of Minerals and Materials Characterization and Engineering 2(03):182
3. Gardner L (2005) The use of stainless steel in structures. Prog Struct Mat Eng 7(2):45–55
4. Song PP, Qi YM, Cai DC (2018) Research and application of Autodesk fusion360 in industrial design. In: IOP conference series: materials science and engineering, vol 359, No. 1. IOP Publishing, p 012037
5. Witek L, Zelek P (2019) Stress and failure analysis of the connecting rod of diesel engine. Eng Fail Anal 97:374–382
6. Shanmugasundar G, Dharanidharan M, Vishwa D, Kumar AS (2021) Design, analysis and topology optimization of connecting rod. Materials Today: Proceedings 46:3430–3438

7. Sriharsha B, Rao PS (2020) Design considerations for connecting rods. IJEAT 9(3):2368–2373
8. Sathish T, Muthulakshmanan A (2018) Design and simulation of connecting rods with several test cases using AL alloys and high tensile steel. IJMPERD 8(1):1119–1126

# Numerical and Experimental Study of Vortex Generator



K. Balaji, Mayuri R. Gore, and S. V. Khandal

**Abstract** This paper aims to study the vortex generators, placed near the separation point over various aerofoils to enhance the aerodynamic performance. The numerical and experimental study was conducted by placing minute-sized vortex generators to overcome parasite drag which improves the aerodynamic performance. Symmetrical and cambered aerofoil with the same thickness of 21% are chosen and analyzed at different angle of attack with a free stream velocity of 15 m/s and Reynolds number of 140,625. Simulation results of 0.2C showed that stalling angle of attack enhanced by 18 and 16% and drag increased by 1% for cambered and symmetrical aerofoil, respectively. Validation experimental results showed a good agreement with simulation results with a difference of 10%. The vortex generators are efficiently working on symmetrical aerofoil as compared to a cambered aerofoil.

**Keywords** Aerofoil · Boundary layer · Drag coefficient · Lift coefficient · Stall angle of attack · Vortex generators

## 1 Introduction

Worldwide growth of aviation sector is forcing to improve the performance and design of an aircraft. One of the major areas to enhance the aerodynamic performance is achieved by controlling the boundary layer. To control the boundary layer, various active and passive mechanisms are used. Passive mechanisms are having a lot of advantages as compared to the active method in terms of less power consumption besides lower maintenance cost. Vortex generators implemented on the top surface of the aerofoil result in enhancement of overall aerodynamic performance.

---

K. Balaji (✉) · M. R. Gore  
Department of Aerospace Engineering, Sanjay Ghodawat University, Kolhapur,  
Maharashtra 416118, India  
e-mail: [arobalaji@gmail.com](mailto:arobalaji@gmail.com)

S. V. Khandal  
Department of Mechanical Engineering, Sanjay Ghodawat University, Kolhapur,  
Maharashtra 416118, India

Al-Jabari and Feszty [1] studied the performance by controlling the flow in a 2D dynamic stall of a novel passive approach. It showed that reduced peak drag by 8–20% and peak negative moment by 9–23%. Arunvinthan et al. [2] carried out research with the new shape of vortex generators. The obtained results showed a reduction in drag and improvement in maximum coefficient of lift. Ayudia [3] studied the effect of vortex generators (VGs) on NACA 4412 aerofoil using computational fluid dynamics (CFD). Results showed that the lift coefficient changes concerning the angle of attack. The optimum lift increase is 13% at the angle of attack of  $5^\circ$ . Chalia and Bharti [4] researched to enhance the aerodynamic characteristics and delay the flow separation and stall angle using the vortex generators and dimples models. The main purpose of this study was to check lift coefficient and drag coefficient by implementing dimples and vortex generators on the surface of the aerofoil. Chillon et al. [5] reported that VGs were one of the flow control devices which control the flow and increase the demand for wind power. The results showed that placing the VGs on the aerofoil can effectively increase the aerodynamic performance. Da Silva and Malatesta [6] studied the influence of vortex generators on the NACA 0015 symmetrical aerofoil. The VGs used at an angle of attack of  $3^\circ$  strongly influence the reduction of recirculation of the bubble which reduces drag up to 1.43%. Fouatih [7] studied the aerodynamic characteristics of the NACA 4415 aerofoil by mounting passive vortex generators. The results showed that at a lower angle of attack there was an increase in the aerodynamic performances by increasing the span-wise separation length. Gutiérrez [8] studied the effect of leading-edge roughness on the aerofoil the aerodynamic performance of a thick aerofoil. This paper reported that at high angles of attack, both zig-zag tape and sandpaper provide significant variations in lift and drag coefficients, whereas at low angles of attack it provided comparable lift and drag coefficients. Himo et al. [9] discussed trapezoidal VGs used to control and delay the flow separation. The effect of non-conventional trapezoidal VGs on the performance was compared with classical triangular winglets which proved an increment in lift over drag by 21%. Hares et al. [10] performed tests with Gothic-shaped vortex generators that have been used to mount on the upper surface. The results showed an increment in the lift coefficient and optimal dimensions and positions of the VG. Kc et al. [11] tested the use of conformal vortex generators (CVGs), which control the flow in a commercial aircraft. The CVGs were able to generate a strong coherent structure and making these CVGs smaller weakened the coherent structure. Li [12] studied the energy improvement using vortex generators installed on DU91-W2-250 wind turbine aerofoil. During the dynamic stall condition, the pressure fluctuation was observed by boundary layer turbulence. Li [13] conducted an experimental and numerical study to realize the effect of vortex generator height in controlling the boundary layer flow. The results showed that the vortex generator intensity and VG height present a relationship and vortex intensity which was found to be proportional to the average kinetic energy. Merryisha and Rajendran [14] studied the differences in the aerodynamic behavior, and comparative experimental and CFD analyses have been carried out with various surface modifiers. These results in pressure drag reduction and also an enhancement in lift coefficient and stall angle of attack. Namura et al. [15] utilized CFD analysis of the swept-back wing by mounting vane-type vortex generators. As result,

the shape optimization revealed that the VG height and incidence angle control the aerodynamic performance and the vortex generators with higher length-to-height ratios show better performance. Zulkefli [16] performed an experimental study with and without passive vortex generators mounted on the surface of the NACA 4415 aerofoil. The results indicated that there is an improvement in lift and drag coefficients and lift-to-drag ratio when the sharkskin-shaped VGs have been used. Kumar [17] introduced a new vision toward the VGs by comparing them with the flat plates which are placed at an angle to the relative flow. The study concludes that the vortex generators provide additional lift over the wing when compared to the flat plate VGs. Yan et al. [18] investigated the effect of microvortex generators on the NACA 0018 aerofoil. The final results showed an increment in lift coefficient and also stall angle, which further increases the stall margin. Zhu et al. [19] investigated the influence of deep dynamic stall on NREL S809 aerofoil. It proved that the maximum coefficient of lift is increased by 40%. This paper also predicted that single- and double-row VGs make a great difference when the aerofoil pitches down. Zulkefli and Mohdnur [20] investigated the performance of the NACA 4415 aerofoil with an inward dimple, outward dimple, and triangular VGs. The inward dimple shows a reduction in drag coefficient as well as it has better aerodynamic efficiency as compared to outward dimple and triangular vortex generators.

This literature survey proved that vortex generators are used to enhance aerodynamic performance. There is no research work explained about the behavior of vortex generators on a symmetrical and cambered aerofoil in a combined manner. This paper studied the behavior of aerofoils with 21% thickness of the symmetrical and cambered aerofoil with minute vortex generators which are placed at 0.2 Chord locations.

## 2 Methods

Vortex generators are used to increase the overall aerodynamic performance by implementing over the top surface of the aerofoil. Vortex generators are placed at 20% of the chord where the boundary layer separation starts. In this work, both numerical and experimental studies are carried out to compare the results. Both the simulation and experimental work are carried out at a free stream velocity of 15 m/s and the Reynolds number of 140,625.

### 2.1 Numerical Methods

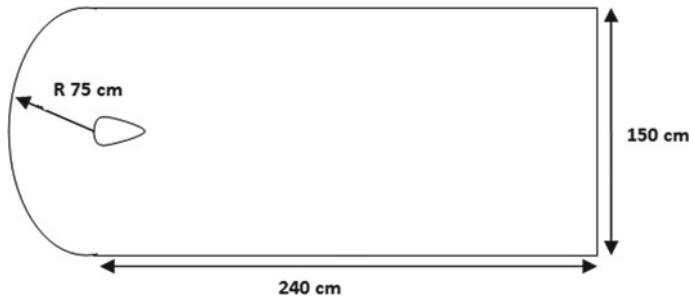
#### Geometry

The design of both NACA 0021 and NACA 6321 aerofoils baseline and VGs model is created in SOLIDWORKS software with the specifications listed in Table 1. Also,

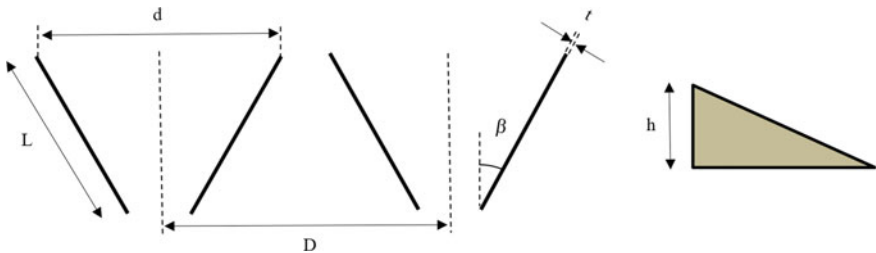
**Table 1** Specification of models

Sr. No	Specifications	Dimension
1	Aerofoil	NACA 6321, NACA 0021
2	Span	23 cm
3	Chord	15 cm
4	VG location	0.2C
5	VG length ( $L$ )	2.2 mm
6	VG height ( $h$ )	0.8 mm
7	VG vane angle ( $\beta$ )	16°
8	VG thickness	0.1 mm
9	Distance between pair vanes ( $d$ )	5 mm
10	Distant between each pair ( $D$ )	11.3 mm
11	Number of VG placed	20

to predict the flow analysis over an aerofoil the domain parameters used are 240 cm \* 150 cm and the radius 75 cm as shown in Figs. 1 and 2.



**Fig. 1** Domain over aerofoils



**Fig. 2** Vortex generators specification



**Fig. 3** Computational mesh of NACA 6321

### **Meshing**

Meshes are used to discretize the elements to produce the accuracy of the results. Mesh for the design is made by using ICEM CFD software as shown in Fig. 3. The meshes used for this work are unstructured tetrahedral mesh. Mesh size was finalized based on the grid-independent study. NACA 6321 aerofoil is divided into 2,954,214 elements with the node of 531,247. NACA 0021 aerofoil is split into 2,714,801 elements into the nodes of 461,785. A height of  $1.2 * 10^5$  mm is set for the first layer near the VG, with wall  $y^+$  less than 1.

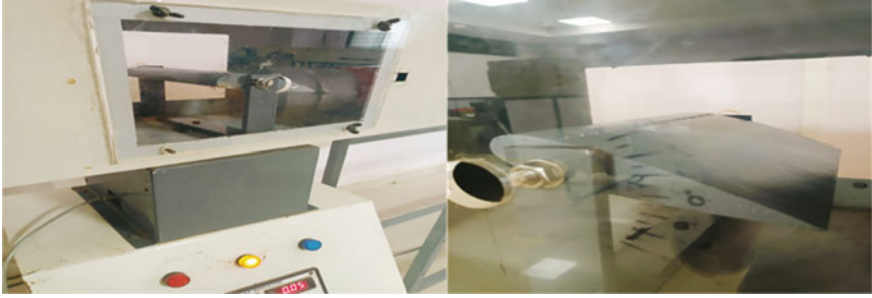
### **Numerical Studies**

Fluent software is used to conduct the numerical analysis of vortex generators and baseline aerofoil. The finite volume method was used to discretize the Navier–Stokes equation using central differences and second-order accuracy with a SIMPLE algorithm to handle pressure–velocity coupling. The K- $\omega$  SST model was selected for this study based on the turbulence model study.

## **2.2 Experimental Studies**

The NACA 0021 and NACA 6321 Baseline and VG models of both aerofoils are fabricated using high-density foam sheets, and the minute VGs are made of the same metal, for good strength. VGs are located at the location of  $0.2C$  from the leading edge based on the numerical study. Four different models have been made of which two are the baseline models and two are models with VGs.

An experimental test was conducted in the open-circuit wind tunnel facility available at Sanjay Ghodawat University Kolhapur, Maharashtra. The baseline and VG aerofoil dimensions are placed into the wind tunnel and tested at the speed of 15 m/s. The lift and drag coefficients are measured by using three-component balancing systems. Before conducting the test, the wind tunnel was calibrated to get an accurate



**Fig. 4** NACA 6321 and NACA 0021 model with VGs at 0.2C placed in wind tunnel

reading. Figure 4 shows the images of models NACA 6321 and NACA 0021 with VGs at 0.2C placed in the wind tunnel.

### 3 Results and Discussions

The simulation and graphical results of numerical and experimental study are presented to report the aerodynamics behaviors of different aerofoils with vortex generators.

#### 3.1 Analysis of Simulation Results

It shows that in both cases, baseline aerofoils are creating the wake region downstream due to the control of the boundary layer. Vortex generators are used to create the circulation flow over an aerofoil. This circulation flow is used to control the boundary layer and make the flow attached due to that wake regions are avoided. Based on the literature survey, both VG aerofoils are used to control the boundary layer and make the flow attached over the entire aerofoils.

#### Velocity Vector

Figures 5 and 6 show the velocity vector over aerofoils at a higher angle of attack. It shows that the flow on the baseline aerofoils is creating a wake region at the trailing edge of the aerofoils at a higher angle of attack. But, in the case of aerofoils with VGs at 0.2C from the leading edge, the flow stays attached near the trailing edge of the aerofoil, compared to the baseline models. In both the symmetrical and cambered aerofoil, the boundary layer controlled and flow attachment at the trailing edge is shown in Figs. 5 and 6, respectively.



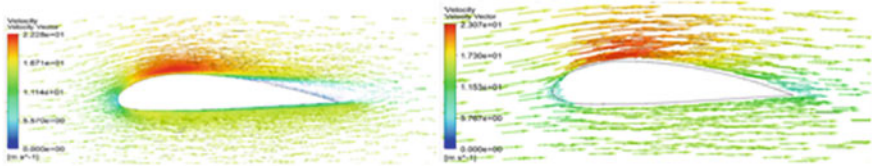


Fig. 5 NACA 6321 Baseline and VG velocity vector

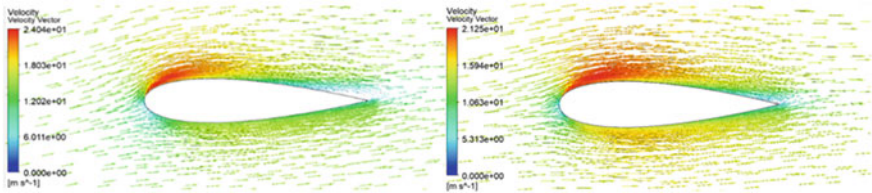


Fig. 6 NACA 0021 Baseline and VG velocity vector

**Lift Coefficient**

Figure 7 shows the lift coefficient of symmetrical and cambered aerofoil at a different AOA range of 0°–25°. It shows that stalling AOA has improved in NACA 6321 and NACA 0021 aerofoil respectively 18% and 16% with 4°. The maximum lift coefficient was enhanced by 10–32%. It proved that vortex generators are used to control the boundary layer and improve the aerodynamics efficiency. In symmetrical aerofoil, VGs are providing good performance as compared to cambered aerofoil.

**Drag Coefficient**

Figure 8 depicts the variation of drag coefficient with different angles of attack for symmetrical and cambered aerofoil. It was observed that for both cambered and symmetrical aerofoil increased the drag coefficient by a closely negligible amount of about 1%. Also, both aerofoils at a low angle of attack produced an equal amount of

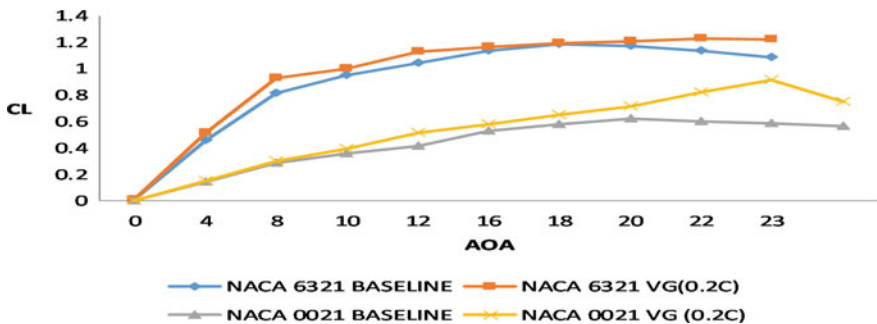


Fig. 7 Simulation analysis of lift coefficient

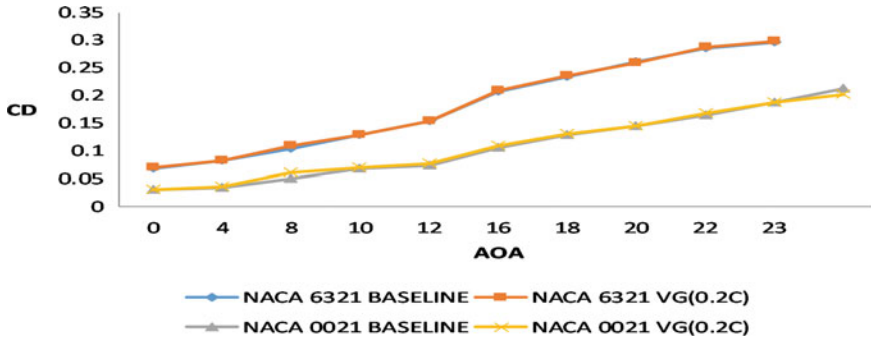


Fig. 8 Simulation analysis of drag coefficient

drag to the baseline model. At the higher angle of attack, it is producing less amount of drag up to stalling angle of attack. Therefore, when VGs are mounted at 0.2C, the produce drag coefficient is equal to or of negligible amount compared to the baseline.

### 3.2 Experimental Analysis

Simulation results showed that the VG on symmetrical and cambered aerofoil is used to enhance the aerodynamic performance without increasing the weight. For experimental work models are made as used for simulation. Symmetrical and cambered aerofoil are made of lightweight and high-density foam materials with VG installed at 0.2C with a height of half of boundary layer thickness, and the results are discussed.

#### Lift Coefficient

Figure 9 shows the coefficient of lift at the different AOA, and it experimentally proved that VG is used to enhance the aerodynamics performance on both aerofoils. Especially at higher AOA, VG performances are good and used to improve the stalling angle of attack by 2° which are 9% and 10%, respectively. The maximum lift coefficient increased by 5% for cambered aerofoil and by 17.5% symmetrical aerofoil. It concluded that VG placed at 20% of chord with the height of half of the thickness of the boundary layer is used to enhance the aerodynamic efficiency of both aerofoils.

#### Drag Coefficient

Figure 10 illustrates the drag coefficient of symmetrical and cambered aerofoil at different angles of attacks. It could be seen that cambered and symmetrical aerofoils reduced the drag by 6% and 9% respectively in comparison with baseline aerofoil, whereas at lower angles of attack the produced drag is almost equal to the baseline values. Once reached the higher AOA, drag coefficient increased due to the circulation

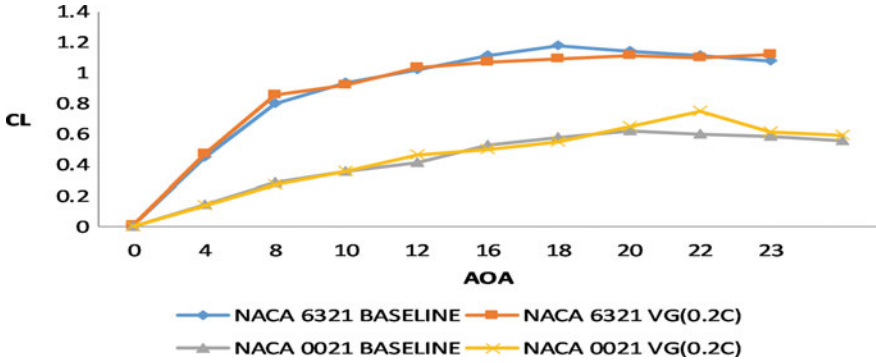


Fig. 9 Experimental analysis of lift coefficient

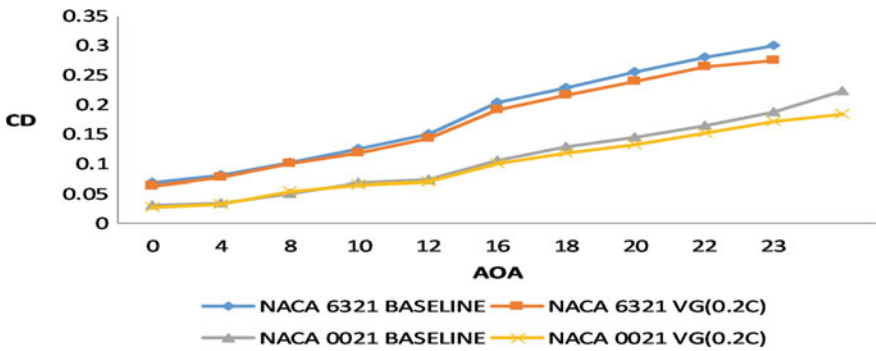


Fig. 10 Experimental analysis of drag coefficient

from the VG. So, it could be revealed that the vortex generators mounted at 0.2C on symmetrical and cambered aerofoil are used to reduce the parasite drag.

### 4 Validation of Results

The validation of the results is done based on the experimental results of the symmetrical and cambered aerofoil, with baseline and VGs models. Figure 11 depicts the graphical representation of the lift coefficient of both results. The lift coefficient of the experimental result is little lower by 10–12% as compared to the simulation results, whereas the stalling angle of attack decrement for experimental data is about 2°.

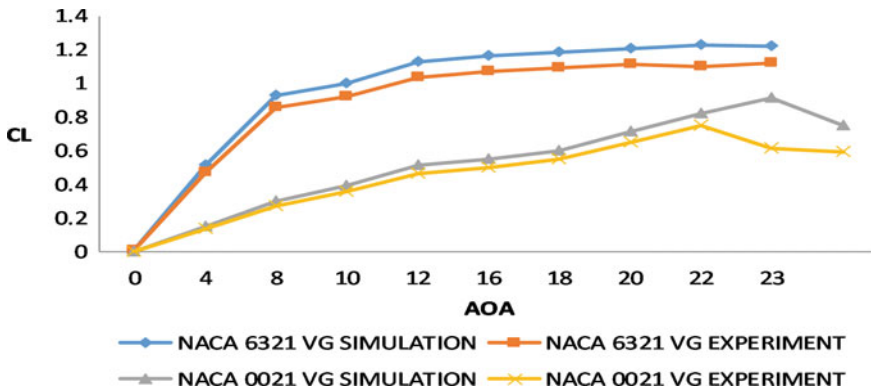


Fig. 11 Lift coefficient of simulation versus experimental results

## 5 Conclusion

Vortex generators are implemented to control or delay the boundary layer separation in order to increase the aerodynamic performance of an aircraft. Generally, the VGs increase the lift coefficient but simultaneously contribute to decreasing the parasite drag. Therefore, this study involves to aims toward decrement in parasite drag, which will eventually decrease the drag coefficient with a significant amount of increase in lift coefficient.

Simulation results have proved that vortex generators worked efficiently in a symmetrical aerofoil to improve the aerodynamic efficiency and stalling AOA by 17% and 16%, respectively. The reduction in drag coefficient is about 1%. Cambered aerofoils improved the stalling AOA and the lift coefficient by 18% and 20% respectively as compared to baseline aerofoil and the overall drag coefficient increased by 1%.

Experimental results revealed that cambered aerofoils with VGs placed at 0.2C improved the stalling AOA and lift coefficient by 10% and 2% respectively as compared to baseline aerofoil. Drag increment for symmetrical aerofoil is about 1% at higher angles of attack. Symmetrical aerofoils produced the stalling AOA and the lift coefficient by 9% and 18% respectively with a drag increment is 1%.

Experimental results showed that cambered aerofoil results differed by 11% and symmetrical aerofoil differed by 10% as compared to the simulation results.

This paper concluded that vortex generators placed at the boundary layer separation point of 0.2 location of chord length and height half of boundary layer height on symmetrical and cambered aerofoils improved the aerodynamic efficiency with a negligible amount of increment in drag coefficient.

## References

1. Al-Jaburi K, Feszty D (2022) Passive flow control of shock-induced dynamic stall via surface-based trapped vortex generators. Proceedings of the Institution of Mechanical Engineers, Part G: Journal of Aerospace Engineering 236(2):308–323. <https://doi.org/10.1177/09544100211011281>
2. Arunvinthan S, Raatan VS, Nadaraja Pillai S, Pasha AA, Rahman MM, Juhany KA (2021) Aerodynamic characteristics of shark scale-based vortex generators upon symmetrical airfoil. *Energies* 14(7). <https://doi.org/10.3390/en14071808>
3. Ayudia SA, Arkundato A, Rohman L (2020) Study of vortex generator effect on airfoil aerodynamics using the computational fluids dynamics method. *Computational And Experimental Research In Materials And Renewable Energy* 3(2):23. <https://doi.org/10.19184/cerimre.v3i2.23547>.
4. Chalia S, Naagar, M (2020) Design and analysis of vortex generator and dimple over an airfoil surface to improve aircraft performance. *International Journal of Advanced Engineering Research and Applications* 3(173)
5. Chillon S, Uriarte-Uriarte A, Aramendia I, Martínez-Filgueira P, Fernandez-Gamiz U, Ibarra-Udaeta I (2020) JBAY modeling of vane-type vortex generators and study on airfoil aerodynamic performance. *Energies* 13 (10). <https://doi.org/10.3390/en13102423>
6. Da Silva D, Malatesta V (2020) Numerical simulation of the boundary layer control on the NACA 0015 airfoil through vortex generators. *J Aerosp Technol Manag* 12(1):1–13. <https://doi.org/10.5028/jatm.v12.1102>
7. Fouatih OM, Imine B, Medale M (2019) Numerical/experimental investigations on reducing drag penalty of passive vortex generators on a NACA 4415 airfoil. In: *Wind energy*, vol 22, Issue 7. Wiley, pp. 1003–1017. <https://doi.org/10.1002/we.2330>
8. Gutiérrez R, Llórente E, Echeverría F, Ragni D (2020) Wind tunnel tests for vortex generators mitigating leading-edge roughness on a 30% thick airfoil. *Journal of Physics: Conference Series* 1618(5). <https://doi.org/10.1088/1742-6596/1618/5/052058>
9. Himor R, Bou-Mosleh C, Habchi C (2021) Aerodynamic performance enhancement of an airfoil using trapezoidal vortex generators. *Aircr Eng Aerosp Technol* 93(1):76–84. <https://doi.org/10.1108/AEAT-01-2020-0021>
10. Hares H, Mebarki G, Brioua M, Naoun M (2019) Aerodynamic performances improvement of NACA 4415 profile by passive flow control using vortex generators. *Journal of the Serbian Society for Computational Mechanics* 13(1):17–38. <https://doi.org/10.24874/jsscm.2019.13.01.02>
11. Kc RJ, Lucido NA, Wilson TC, Alexander AS, Elbing BR, Jacob JD, Ireland P, Black JA (2019) Experimental investigation of conformal vortex generators via wake survey. *AIAA Scitech 2019 Forum*. <https://doi.org/10.2514/6.2019-0578>
12. Li S, Zhang L, Xu J, Yang K, Song J, Guo G (2020) Experimental investigation of a pitch-oscillating wind turbine airfoil with vortex generators. *Journal of Renewable and Sustainable Energy* 12(6). <https://doi.org/10.1063/5.0013300>
13. Li X, Yang K, Wang X (2019) Experimental and numerical analysis of the effect of vortex generator height on vortex characteristics and airfoil aerodynamic performance. *Energies* 12(5). <https://doi.org/10.3390/en12050959>
14. Merryisha S, Rajendran P (2019) CFD letters experimental and CFD analysis of surface modifiers on aircraft wing: a review. *CFD Lett* 11:46–56
15. Namura N, Shimoyama K, Obayashi S, Ito Y, Koike S, Nakakita K (2019) Multipoint design optimization of vortex generators on transonic swept wings. *J Aircr* 56(4):1291–1302. <https://doi.org/10.2514/1.C035148>
16. Zulkefli NF, Ahamat MA, Mohd Safri NF, Mohd Nur N, Mohd Rafie AS (2019) Lift enhancement of NACA 4415 airfoil using biomimetic shark skin vortex generator. *IJRTE* 8(4):9231–9234. <https://doi.org/10.35940/ijrte.d9222.118419>

17. Kumar R, Architha N, Deodhar R, Tejas N, Menon R (2020). Analytical testing of vortex generators with an airfoil profile. *International Journal of Engineering Research & Technology (IJERT)* Ncetesft—2020 8(14)
18. Yan Y, Avital E, Williams J, Cui J (2019) CFD analysis for the performance of micro-vortex generator on aerofoil and vertical axis turbine. *Journal of Renewable and Sustainable Energy* 11(4):043302. <https://doi.org/10.1063/1.5110422>
19. Zhu C, Wang T, Chen J, Zhong W (2020) Flow analysis of the deep dynamic stall of wind turbine airfoil with single-row and double-row passive vortex generators. *IOP Conference Series: Earth and Environmental Science* 463(1). <https://doi.org/10.1088/1755-1315/463/1/012118>
20. Zulkefli NF, Mohdnur N (2020) Dimples and vortex generator performance on airfoil surface. *International Journal of Advanced Science and Technology* 29(6):208–213

# Performance Comparison of Cryptographic Algorithms Used in Cloud Computing



Neha Juyal, Eeshita Deepta, and Dolly Sharma

**Abstract** Cloud computing is a rapidly growing technology, but because of its distributed nature, it is also susceptible to attacks. To ensure security, data transferred uses cryptographic algorithms to encrypt the data. These algorithms' performance is vital as data needs to be available quickly and accessible to users. A reliable way to compare performance that is normalized is through throughput. This paper compares some of the state-of-the-art used algorithms in cryptography to newer algorithms depending on the file size based on their throughput (kilobyte per millisecond). The algorithms were divided depending on their file size into three different groups. The conclusion was that different algorithms perform best for different file sizes. Algorithms, on average, work best on data between 1 and 10 MB in size, according to this research.

**Keywords** Cryptography · Algorithms · Cloud computing · Encryption

## 1 Introduction

Cloud computing is gaining rapid traction owing to its cost-effectiveness and convenient service [1]. Customers can access a virtual data management and service platform via cloud computing [2]. Individuals and corporations can store data without paying additional charges in the cloud's data center [3].

Advantages it provides when compared to typical online computing or backup methods are adaptability, availability, and scalability [4]. These kinds of distributed applications are far more vulnerable to attacks. It contains the flaws associated with

---

N. Juyal (✉) · E. Deepta · D. Sharma  
Amity University, Uttar Pradesh, Noida, India  
e-mail: [neha.juyal@s.amity.edu](mailto:neha.juyal@s.amity.edu)

E. Deepta  
e-mail: [eeshita.deepta@s.amity.edu](mailto:eeshita.deepta@s.amity.edu)

D. Sharma  
e-mail: [dsharma17@amity.edu](mailto:dsharma17@amity.edu)

internet usage, as well as the additional hazards posed by integrated, virtualized, and redistributed resources [5, 6]. Cloud computing raises a slew of data privacy risks. Because of its virtual nature, traditional security techniques are ineffective [3].

Cyber-attackers can now simply access the information saved. When private data is backed up on a private cloud store, security of data is an issue in cloud computing because it is given to a service provider [7]. The unethical disclosure of data utilized in firms in the cloud to outsiders is an impediment [8]. To combat these security concerns, cryptography is used. It refers to the encryption methods used to protect cloud-based storage [6, 9].

The scrambling of data material, such as pictures, audio, video, text, and so on, to render it unreadable, undetectable, or meaningless during transmission or storage is known as data cryptography. Encryption is the technical term for it [1, 10]. Symmetric key algorithms encrypt and decode data using the same key, whereas asymmetric key algorithms employ distinct keys for encryption and decryption [1]. Data Encryption Standard (DES), Advanced Encryption Standard (AES), Triple Data Encryption Standard (3DES), and Blowfish are some examples of symmetric key algorithms while asymmetric contains algorithms like Rivest–Shamir–Adleman (RSA), and Diffie–Hellman Key Exchange [11]. Cryptography is divided into three categories: secret-key cryptography, public cryptography, and hash algorithms [12].

Here, we've looked at many cryptographic methods and compared them depending on their encryption time by calculating throughput; i.e., size of the file in kilobyte (kB) is divided by the time taken for encryption for each algorithm [13]. The performance of algorithms can be directly compared through their throughputs [14].

For text files, cryptographic algorithms take a plain text file as input and give ciphertext as output. Plain text is the first input or knowledge that is entered into algorithms to code from an intuitive source. The ciphertext is a random flow of unintelligible coded data generated by the mixed message [6, 10].

DES, 3DES-128, AES-256, AES-128, Blowfish, RSA-64, RSA-2408, Rivest Cipher (RC2), new lightweight cryptographic algorithm (NCLA), DNA, BDNA, Message Digest (MD5), Hybrid [15], and Paillier have been analyzed.

The goal of our study is to analyze and contrast various modern cryptographic encryption techniques on the basis of their throughput. Multiple experiments were used to determine the file size and the encryption time for each technique.

## 2 Literature Review

The authors in [1] compare various algorithms and their hybrids: 3DES and Krishna Hybrid, AES and Krishna Hybrid, 3DES and RSA Hybrid, and Blowfish and Krishna Hybrid. Encryption time was least for 3DES and Krishna Hybrid, taking 3.13 s.

Reference [2] to protect cloud data files, an elliptic curve encryption technique was applied. The ECC encryption algorithm, that is used for encryption, adds to the efficiency of the encryption–decryption process.



To achieve multilayer security, [3] presents a data security system that combines cryptography and steganography techniques. The picture is first encoded utilizing AES encryption technique, then masked with the cover picture using the SVD-DWT hybrid steganography system, assuring data security.

Authors in [4] devise a new encryption/decryption strategy. The suggested framework offers improved protection of the data. The double-round key feature alters the 128 AES method to boost the encryption process speed to 1000 blocks per second [4].

An algorithm, NCLA, for securing the data that can be utilized to protect cloud's applications has been developed. It is a 16-byte (128-bit) block cipher, and the data must be encrypted with a 16-byte (128-bit) key [5].

The authors in [6] have reviewed various encryption techniques, such as lattice-based cryptography, multivariate-based cryptography, hash-based signature, and software cryptography.

Reference [7] presents a methodology for improving data privacy in cloud computing cryptography of text files. The proposed model's key generation is also explained. The AES algorithm has been found to be six orders of magnitude faster than the DES algorithm.

A comparison has been done of five cryptographic algorithms that are DES, 3DES, Blowfish, RSA, and AES. The conclusion was that Blowfish was the fastest while RSA was the slowest [8].

In [9], LabView was used to perform a 1 time evaluation of various cryptography algorithms. For symmetric encryption methods, AES, DES, 3DES, and RC2 were used, whereas the asymmetric encryption process RSA was utilized.

As suggested by Thabit et al. [10], NLCA demonstrates low complexity symmetric key in comparison with the other algorithms based on the architecture, durability, and security standards.

Discussed in reference [11], the author discusses the symmetric encryption algorithms (AES, DES, Blowfish), asymmetric algorithms like (RSA, Diffie–Hellman Key Exchange), and hashing algorithms (MD5).

The study in reference [12] is a comparative investigation of DES, AES, and Blowfish which has been concluded on the parameters like E-CPU, D-CPU, E-Memory, and D-Memory on various file sizes.

Reference [13] presents the analysis performed on different cryptographic methods used in the security of cloud computing. The paper also gives a result with the proposed frameworks to mitigate the integrity issues in cloud computing.

The BDNA symmetric technique is discussed in this publication. The DNA cryptography approach is the inspiration for this technique. For a given plaintext size, a comparison of ciphertext size, encryption time, and throughput among various [14].

Reference [15] describes a data security strategy in which the encryption of the data has been done using a hybrid cryptographic method that combines AES, Blowfish, and the message-digest algorithm (MD5).

A study has been concluded based on the comparison of present state-of-the-art technologies has also been carried out. The results reveal that with decompression,

Paillier and Blowfish algorithms take roughly three times as long as Paillier and Blowfish with compression [16].

As concluded by the paper [17] a comparative study on variables such as key size, bandwidth, encryption, decryption, and computational overheads has been concluded between elliptic curve cryptosystem (ECC) and RSA. ECC can also minimize computational complexity and optimize memory space, resulting in reduced energy usage for smart devices.

Reference [18] review various strategies for data security in the time period 2011–2019. On the basis of secrecy, integrity, and authenticity, the authors conducted an examination of cryptographic approaches used to protect data in cloud computing. It concluded that every plan is unique in its approach.

The goal of reference [19] is to propose a novel DNA-based cryptography method that uses dynamic sequence table for ASCII characters. The suggested technique provides greater security than existing similar techniques.

In order to make a comparison, a study was conducted in [20] between algorithms Kaunda, Pramanik, Paul, and the proposed algorithm. The proposed scheme's time complexity is  $O(n)$  for all the four parameters making it much faster and more dependable than the others.

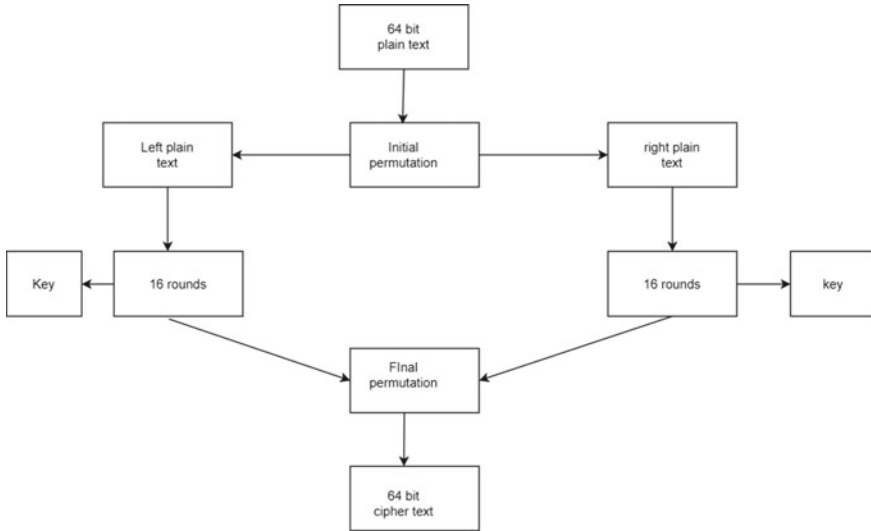
### 3 Methodology

The purpose of this study was to compare cryptographic encryption algorithms. Because individual file throughputs vary greatly depending on file size, the algorithms were separated into three groups: files less than 1 MB, files between 1 and 10 MB, and files between 10 and 100 MB. We used throughput for comparison purposes. It was calculated in kB/ms. This is a standard method of calculating the performance of an algorithm, normalizes the values, and is used to compute the performance and speed of an algorithm [13]. The higher the throughput is, the better the performance is thought to be [14]. We calculated the encryption throughput for the algorithms, and the files considered were text files. Equation 1 is the throughput formula. These were then plotted as a high-low-value chart, and the average was calculated for the different groups.

$$\text{Throughput} = \frac{\text{File size (in kB)}}{\text{Encryption time (in ms)}} \quad (1)$$

### 4 Overview of the Algorithms

A brief overview of all symmetric and asymmetric cryptographic algorithms that we have used in our paper along with their working diagram has been discussed below.



**Fig. 1** Working of the DES algorithm

## 4.1 DES

IBM created the data encryption system in 1972 [9]. It's an algorithm with symmetric keys. DES is currently considered insecure because a brute force attack is possible on it. However, 3DES is considered secure. The distinction between the DES and the 3DES algorithm is that in 3DES, and the algorithm is run 3 times with 3 separate keys. Figure 1 shows the working of the DES algorithm.

## 4.2 AES

This symmetric key block cipher was developed in 1998. Data in it can be up to 128 bits, and key lengths can vary [8]. It can encrypt a data block of up to 128 bits and does so in four operational blocks. AES-128 has 10 rounds and AES-256 has 14 rounds [8, 9]. One round consists of either delivering or retrieving the ciphertext [8]. Figure 2 shows the working of the AES algorithm.

## 4.3 Blowfish

It is a symmetric key algorithm developed in 1992 by Bruce Schneider [16]. Based on the feista network, it contains two phases: data encryption and key expansion. The

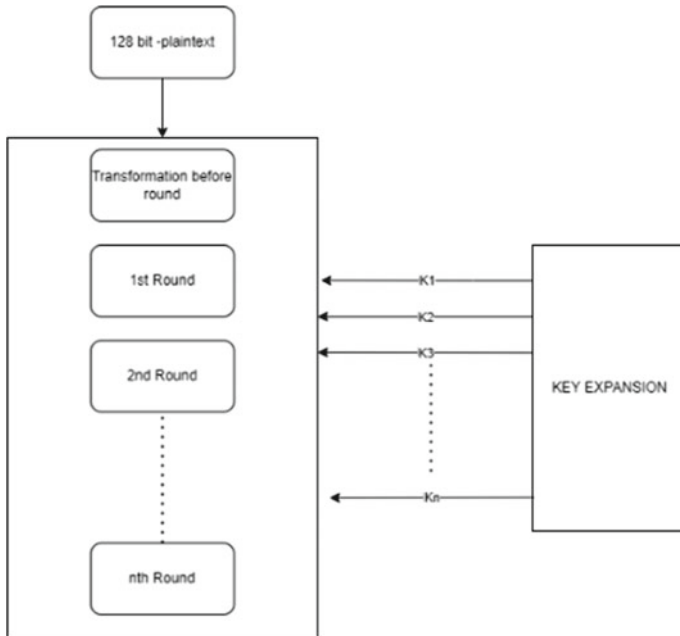


Fig. 2 Depiction of the working of the AES algorithm

latter phase transforms a variable-length key into an array of sub-keys called P-array consisting of 18 32-bit keys. The data encryption phase is done. The F function will split the 32-bit input into four equal portions. These four values are used to look up their corresponding S-boxes [14, 16]. Figure 3 shows the working of the Blowfish algorithm.

### 4.4 RSA

One of the most well-known asymmetric key algorithms, it was created by Rivest, Shamir, and Adleman in 1977, hence the name [9]. It has a public key ecosystem [8]. RSA is based on integer factorization [17]. RSA provides confidentiality, authentication, and integrity [18]. Figure 4 shows the working of the RSA algorithm.

### 4.5 RC2

It stands for Rivest Cipher and was developed in 1987 by Ron Rivest. It is a symmetric key algorithm [9]. In RC2-40, the synoptic key is created using an initialization vector

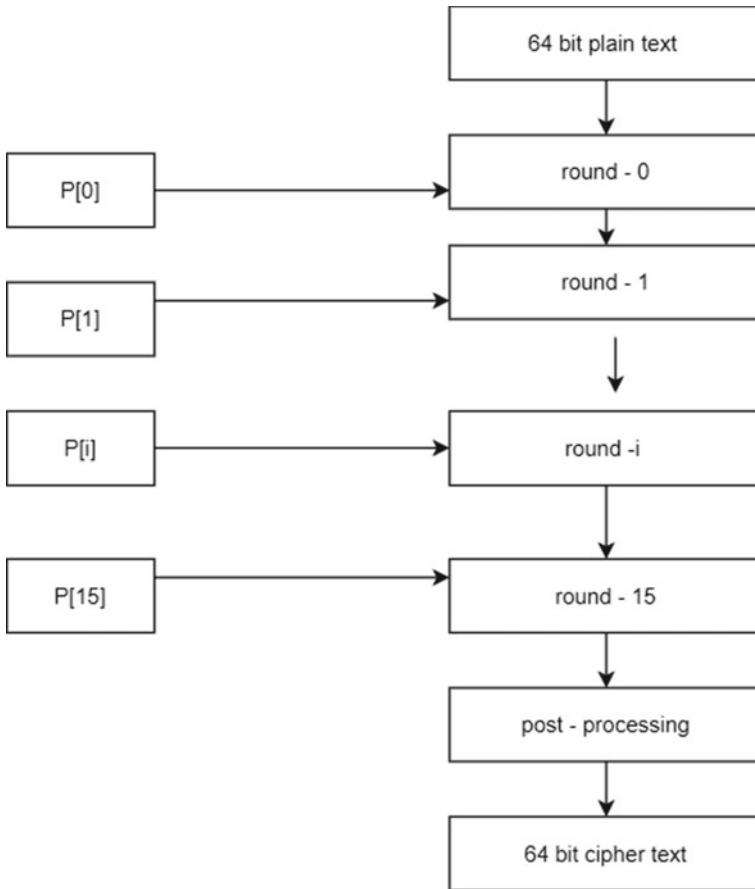


Fig. 3 Working of the Blowfish algorithm

and a separate key. This separate key has 96 bits of characters while the vector has 64 bits of characters which combine to form the synoptic key [9].

### 4.6 NLCA

It stands for new lightweight cryptographic algorithm and is a symmetric key algorithm. A combination of SP and Feistel architectural methods is used to improve its complexity. It is limited to using only 5 rounds for energy efficiency [5].

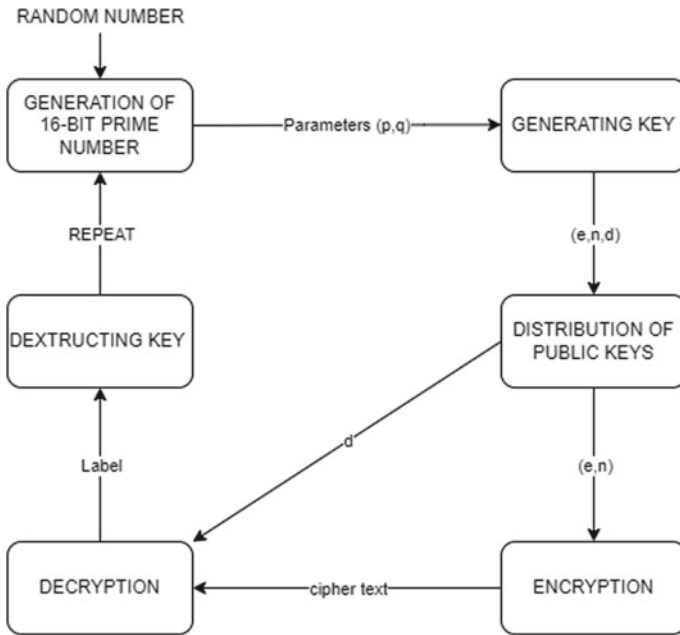


Fig. 4 Depiction of the working RSA algorithm

### 4.7 DNA

In [19], a cryptographic algorithm was proposed based on DNA which was used by [14] and [20]. It uses DNA sequences to enhance the level of security. A DNA sequence table is allotted ASCII, and a finite number of iterations are used to update the ASCII letters dynamically. The ciphertext is handled using genome conversion and processed using an amino acid table, which further confuses the ciphertext [14, 19, 20]. Figure 5 shows the working of the DNA algorithm proposed in [19].

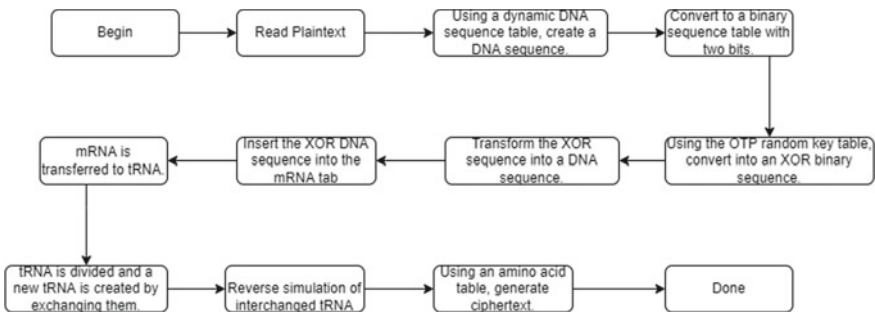


Fig. 5 Depiction of the working of the DNA-based algorithm

## 4.8 *BDNA*

It is a symmetric key algorithm and basically based on the DNA sequence in [19]. Here, two encoding tables are required—a 14-bit encryption key and a random number  $N$ . The plaintext is then converted into a binary sequence using these tables, and then the encryption key is applied to it. The binary sequence is then converted into ciphertext [14, 19].

## 4.9 *Message Digest (MD5)*

It stands for Message Digest 5 and was developed in 1991 by Ron Rivest. It was made to replace the MD4 algorithm, its predecessor. It is a type of hashing algorithm and takes input data of any size. The data blocks are of 512 bits and have 16 subblocks, where each subblock is of 32 bits [11].

### 4.9.1 Hybrid

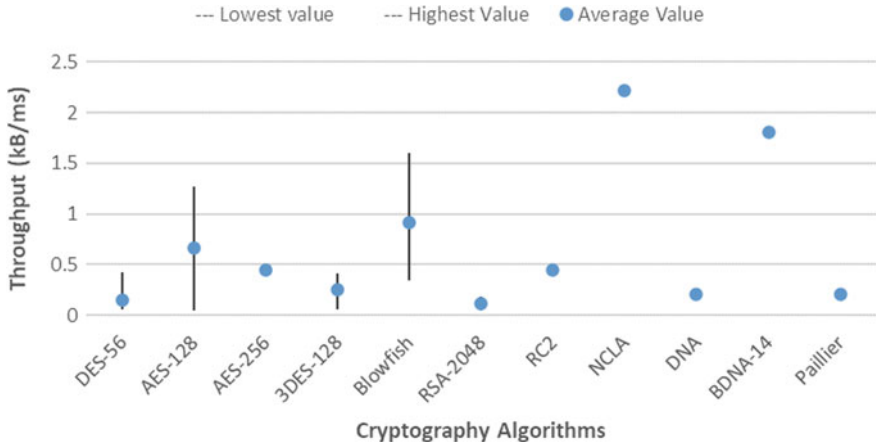
To boost the performance of the encryption process, hybrid cryptography employs more than one algorithm and combines symmetric and hashing encryption. AES, Blowfish, and MD5 algorithms are proposed for hybrid cryptography [15].

### 4.9.2 Paillier

The Paillier cryptosystem is a probabilistic asymmetric method for public key cryptography that was designed by and named after Pascal Paillier. The additive homomorphism attribute is facilitated by the Paillier cryptosystem. In this cryptosystem, the product of two ciphertexts decrypts to the aggregate of their corresponding plaintexts [16].

## 5 Result

The file size and time for encryption for all of the algorithms were taken from multiple studies. For a single algorithm, the calculated throughputs from different studies were then averaged and the comparison was done on that basis for better accuracy.



**Fig. 6** Comparison of DES, AES, 3DES, Blowfish, RSA, RC2, NCLA, DNA, BDNA, and Paillier algorithms for file sizes less than 1 MB

### 5.1 Files Less Than 1 MB

The majority of the algorithms were tested on files that were below 1 MB in size. The NCLA algorithm, with a throughput of 2.214 kB/ms, had the greatest throughput. All of the methods have a throughput of 0.639 kB/ms on average. Figure 6 uses a high-low-value chart to highlight the comparison of algorithms when the file size is smaller than 1 MB.

### 5.2 Files Between 1 and 10 MB

The algorithm with the highest throughput is the hybrid algorithm proposed in [15]. Its value is 4.556 kB/ms. The average throughput of all the algorithms is 2.357 kB/ms. Figure 7 shows the comparison for algorithms when the file size is between 1 and 10 MB through the high-low-value chart.

### 5.3 Files Between 10 and 100 MB

AES-256 is the algorithm with the highest throughput with a value of 2.483 kB/ms. The average throughput of all the algorithms is 1.726 kB/ms. Figure 8 shows the comparison for algorithms when the file size is between 10 and 100 MB through the high-low-value chart.



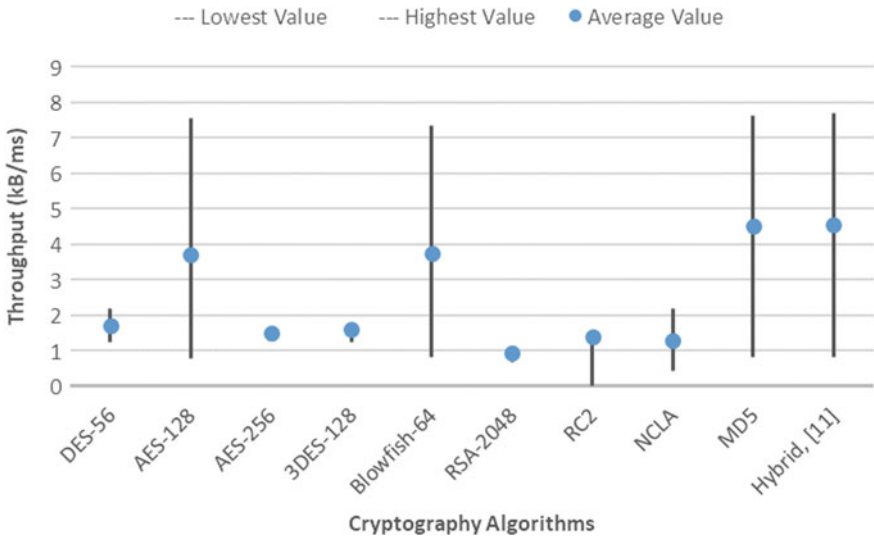


Fig. 7 Comparison of DES, AES, 3DES, Blowfish, RSA, RC2, NCLA, MD5, and Paillier algorithms for file sizes between 1 and 10 MB

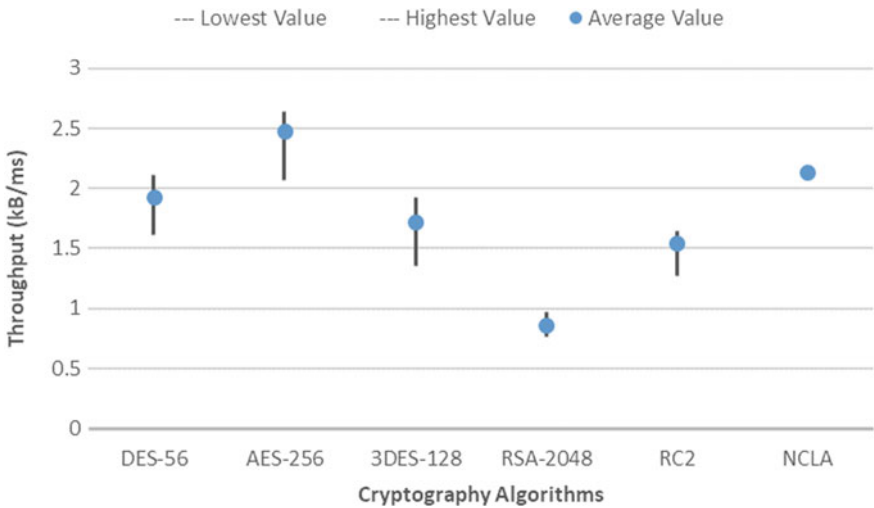


Fig. 8 Comparison of DES, AES, 3DES, RSA, RC2, and NCLA algorithms for file sizes between 10 and 100 MB

## 6 Conclusion

Throughput is an especially important factor to consider when comparing and deciding which algorithm to use for cloud computing and security. It has been seen that different algorithms are suitable for different file sizes. This paper compared algorithms for three groups of file sizes and found that for small file sizes, NCLA is the best algorithm in terms of throughput, while for medium-sized files, is the hybrid algorithm. For large-sized files, the AES algorithm has the highest throughput. It can also be noted that the highest average throughput for all the algorithms was for files with sizes between 1 and 10 MB, while it was the lowest for files with sizes less than 1 MB. Generally, it can be seen that there is no one algorithm that is best for the different file sizes, and that the throughput also is not directly related to the size of the files. The comparison of different algorithms based on other metrics, such as key size, number of rounds, and time and space complexity has not been included in this paper and can become the grounds for future research. Some of the newer algorithms have also not been compared due to the lack of data.

## 7 Future Work

There is a lack of hybrid models combining state-of-the-art algorithms with the newly proposed algorithms, especially DNA-based algorithms. Most of the algorithms have been tested on files with sizes less than 50 MB. The newer models can also be tested on files with large sizes. Algorithms also need to be tested with different media types, other than text files, like video, audio, and images.

## References

1. Ahmad SA, Garko AB (2019) Hybrid cryptography algorithms in cloud computing: a review. In: 2019 15th international conference on electronics, computer and computation (ICECCO). IEEE, pp 1–6
2. Rupa P, Rani GS, Sarika S (2021) Study and improved data storage in cloud computing using cryptography. In: AIP conference proceedings, vol. 2358, No. 1. AIP Publishing LLC, p 080015
3. Mahmood GS, Huang DJ, Jaleel BA (2019) Achieving an effective, confidentiality and integrity of data in cloud computing. *Int J Netw Secur* 21(2):326–332
4. Awan IA, Shiraz M, Hashmi MU, Shaheen Q, Akhtar R, Ditta A (2020) Secure framework enhancing AES algorithm in cloud computing. *Security and Communication Networks*
5. Thabit F, Alhomdy S, Al-Ahdal AH, Jagtap S (2021) A new lightweight cryptographic algorithm for enhancing data security in cloud computing. *Global Transitions Proceedings* 2(1):91–99
6. Kaur H, Kaur A (2021) Cryptography in cloud computing. *Indian Journal of Cryptography and Network Security* 1(1)
7. Sharma Y, Gupta H, Khatri SK (2019) A security model for the enhancement of data privacy in cloud computing. In: 2019 amity international conference on artificial intelligence (AICAI). IEEE, pp 898–902

8. Nazeh Abdul Wahid MD, Ali A, Esparham B, Marwan MD (2018) A comparison of cryptographic algorithms: DES, 3DES, AES, RSA and blowfish for guessing attacks prevention. *J Comp Sci Appl Inform Technol* 3(2):1–7. <https://doi.org/10.15226/2474-9257/3/2/00132>
9. Latif IH (2020) Time evaluation of different cryptography algorithms using labview. In: IOP conference series: materials science and engineering, vol 745, No. 1. IOP Publishing, p 012039
10. Thabit F, Alhomdy S, Jagtap S (2021) Security analysis and performance evaluation of a new lightweight cryptographic algorithm for cloud computing. *Global Transitions Proceedings* 2(1):100–110
11. Chatterjee R, Roy S, Scholar UG (2017) Cryptography in cloud computing: a basic approach to ensure security in cloud. *International Journal of Engineering Science* 11818
12. Kaviya K, Shanthini KK, Sujithra M (2019) Evolving cryptographic approach for enhancing security of resource constrained mobile device outsourced data in cloud computing. *IJSRCSEIT* 5(1)
13. Oruganti R, Churi P (2022) Systematic survey on cryptographic methods used for key management in cloud computing. In: International conference on innovative computing and communications. Springer, Singapore, pp 445–460
14. Sohal M, Sharma S (2022) BDNA-A DNA inspired symmetric key cryptographic technique to secure cloud computing. *Journal of King Saud University-Computer and Information Sciences* 34(1):1417–1425
15. Bermani AK, Murshedi TA, Abod ZA (2021) A hybrid cryptography technique for data storage on cloud computing. *Journal of Discrete Mathematical Sciences and Cryptography* 24(6):1613–1624
16. Seth B, Dalal S, Jaglan V, Le DN, Mohan S, Srivastava G (2020) Integrating encryption techniques for secure data storage in the cloud. *Transactions on Emerging Telecommunications Technologies* e4108
17. Khan IA, Qazi R (2019) Data security in cloud computing using elliptic curve cryptography. *International Journal of Computing and Communication Networks* 1(1):46–52
18. Maryoosh AA, Mohammed RS, Mustafa RA (2019) Subject review: cloud computing security based on cryptography. *IJERAT* 5(9):20–23. ISSN: 2454-6135
19. Hossain EMS, Alam KMR, Biswas MR, Morimoto Y (2016) A DNA cryptographic technique based on dynamic DNA sequence table. In: 2016 19th international conference on computer and information technology (ICCIT). IEEE, pp 270–275
20. Pavithran P, Mathew S, Namasudra S, Lorenz P (2021) A novel cryptosystem based on DNA cryptography and randomly generated Mealy machine. *Comput Secur* 104:102160

# Modern Generative Design Tools: Siemens NX's Algorithmic Feature and Rhinoceros 3D's Grasshopper



Amit Singh Rawat and Gaurav Tiwari

**Abstract** Generative design is a new approach to breaking creative barriers that involve having the computer-generated various design options. These generative designs are created by employing geometrical and mathematical algorithms, which require the use of textual and visual programming languages to express. A non-programmer CAD designer will find it easier to use a visual programming language than a textual language. Two modern visual programming tools, Siemens NX's Algorithmic Feature and Rhinoceros 3D's Grasshopper were contrasted in this paper. In order to compare and demonstrate the two visual programming tools, a conical spiral tubular structure is modeled in Algorithmic Feature and Grasshopper using the identical algorithm. The user interface and several keywords used to implement algorithms are also explained in the paper, including an example of an algorithm to model a conical spiral tubular structure in Algorithmic Feature and Grasshopper. The numerous aspects of both modern visual programming tools such as usability and functionality were reviewed and summarized in this paper. The associativity and custom feature functionality of Siemens NX's Algorithmic Feature was also explored in this paper.

**Keywords** Generative design · Visual programming · Algorithmic Modeling · Grasshopper

## 1 Introduction

The use of computer-aided applications to assist in design processes is known as computer-aided design (CAD). Various sorts of designers and engineers regularly utilize CAD software. Two-dimensional (2D) drawings and three-dimensional (3D) models can both be created with CAD software. The goal of CAD is to improve

---

A. S. Rawat (✉) · G. Tiwari  
Visvesvaraya National Institute of Technology (VNIT), South Ambazari Road, Nagpur,  
Maharashtra 440010, India  
e-mail: [amitrawat057@gmail.com](mailto:amitrawat057@gmail.com)

the designer's workflow, boost productivity, improve design quality and amount of detail, and often contribute to a manufacturing design database [1].

Some models are simpler to design analytically than they are to design manually with CAD software. One type of these designs is generative design. A design exploration technique is referred to as generative design. Designers or engineers enter design goals, as well as characteristics like efficiency or structural requirements, materials, production techniques, and cost limitations, into generative design software [2].

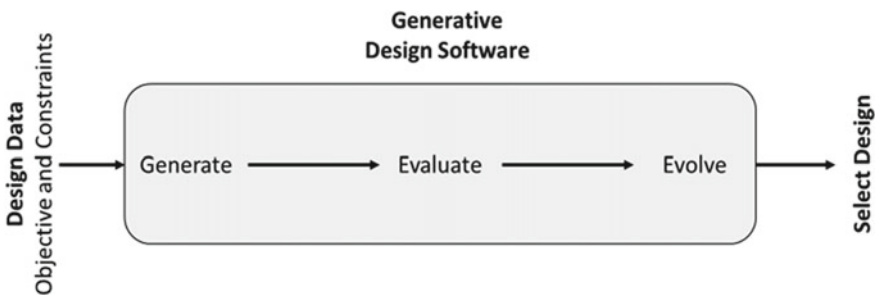
Generative design is related to computational design methodologies that can undertake design exploration automatically under designer-defined limitations and constraints. For example, topology optimization-based generative designs aim to explore different topology designs that cannot be expressed by traditional parametric design methodologies [3].

The use of generative design is rapidly altering the way manufacturers produce the next new and innovative products. This approach is for innovative designs that provide their users with originality and personalization by leveraging new manufacturing techniques. Generative design technology is much more accessible than ever before, providing designers with affordable programming tools which can easily and efficiently develop numbers of designs in less time than a more traditional approach would take [4].

In other sectors, such as industrial design and mechanical design, it is a relatively recent discipline. It is more common in architecture, where the computational nature of the created geometry blends in seamlessly with modern construction aesthetics.

Designers need a set of inputs and limitations to produce generative design, and then they utilize an iterative process to create numerous alternative designs depending on these inputs. As shown in Fig. 1, designers can evaluate the generated design at various iterations and then decide whether to undertake additional iterations to fine-tune the design and evolve it in accordance with design standards and requirements.

Visual programming generative tools are becoming very popular among researchers and industries. These visual generative tools are required for visually representing the geometric algorithm for generating designs. The study explored two modern visual programming generative design tools, Siemens NX's Algorithmic



**Fig. 1** Evolution of designs using generative design software

Feature and Rhinoceros 3D's Grasshopper, by employing a sample algorithm for conical spiral tubular structure.

## 2 Literature Review

In the recent years, it has become increasingly prevalent to use generative design to solve complex design challenges.

Since generative design may also produce models programmatically, CAD designers can quickly generate a large number of design solutions, explore them in a large design space, and evaluate their performance using a pre-defined framework. As a result, the generative design will evolve into a process of experimenting with designs, which is crucial throughout the conceptual design stage [5].

In the recent times, many researchers used generative designs as a complementary solution for topology optimization as it provides a wide range of design sets and ideas to users based on varying inputs, which can be used to perform topology optimization of models [3].

Many studies are performed to explore the various tools and methodologies for generative designs and their applications. The majority of the study points to algorithm-based design as a primary approach.

### 2.1 Algorithmic Aided Design

Algorithmic design is more than just using a computer to create designs and objects. Algorithms enable designers to get over the constraints of standard design software and 3D modelers, allowing them to achieve levels of refinement and complexity that are beyond the individual manual capabilities [6].

Algorithmic design can be employed as a digital representation method for complicated designs, and it can be evaluated using numerous use cases for complicated design models. Researchers emphasized algorithmic design in the study and suggested that, because of its flexibility, algorithmic design is far more than a depiction of design but rather of a complex design space [7].

### 2.2 Programming Languages for Algorithmic Design

Programming has been used to describe rules, limitations, and systems that are significant to the designing process throughout history. Programming in aesthetic design can be considered as the depiction of algorithmic techniques that express design ideas or solve design challenges.

Programming languages for generative design are categorized into two based on their usability.

**Textual Programming Language:** A textual programming language provides the ability to define algorithms by writing programs that are made up of a linear character sequence, pre-defined keywords, mathematical expressions, and numbers. Textual programming languages are identified as one-dimensional languages [7].

**Visual Programming Language:** A visual programming language permits the formulation of programs in a two-dimensional presentation comprised of iconic symbols that can be handled proactively by the programmer according to certain special semantics [8].

Visual programming languages have the potential to encourage creative freedom in new ways, and the CAD designers' capabilities are now allowing for more complicated models via parametric modeling. While textual programming languages may continue to be useful for developing more complicated designs, visual programming languages are also arguably expanding CAD designers' capacity to create a variety of models using an iterative approach [9].

Visual programming has gained in popularity among designers in the recent years as a means of creating a wide range of complicated models. Many scholars have utilized Grasshopper, a popular visual programming tool, to develop iterative models in the architectural domain [10].

Visual programming eliminates the enormous complications that come with software programming while allowing algorithmic connection with the underlying technologies of CAD platforms. One of the most important benefits of this form of programming is that it allows for automating and modularizing complex modeling operations [11].

### 3 Tools for Visual Programming

Several CAD systems have recently included built-in visual programming environments that enable generative functionalities without the need to write textual code. These applications have a diagrammatic window where the user can manage entities by using analog representation in addition to the standard geometric display [12].

The most widely used modern visual programming CAD tools for computational designs are listed below.

#### 3.1 *Grasshopper—Rhinoceros 3D*

Grasshopper is a visual graphical interface for the Rhinoceros 3D modeling software. By creating diagrams that link data to functions, a designer can computationally generate geometric features with visual programming. Designers can use an

algorithmic approach to produce complicated forms and quickly develop alternate designs. Grasshopper is more well-known in the field of architecture designs.

### 3.2 Algorithmic Feature—Siemens NX

Siemens NX is also a popular CAD system among mechanical engineers and designers. Siemens NX used Parasolid as CAD kernel. Solid modeling, generalized cellular modeling, and freeform surface and sheet modeling are all supported by Parasolid. Parasolid additionally supports model creation, advanced surfacing, Boolean modeling, and feature modeling.

Furthermore, Siemens NX offers the ability to define complex mechanical designs computationally, allowing for an iterative approach. To generate computational designs, Siemens NX provides a visual programming tool called Algorithmic Feature. The “Algorithmic Modeling” environment is another name for the “Algorithmic Feature” environment. Similar to Grasshopper, designers can use an iterative and algorithmic approach to develop complicated computational designs using Algorithmic Feature.

## 4 Methodology

Both Siemens NX's Algorithmic Feature and Grasshopper have the ability to produce a generative design using visual programming. To study the various characteristics of both visual programming tools for generative designs, we created a simple generative design in each tool and compared the design and usability of both tools.

A conical spiral tube is modeled in Siemens NX's Algorithmic Feature and Grasshopper to compare the two visual programming tools. In both cases, the same algorithm is employed to develop the conical spiral tube.

### 4.1 Parametric Equation of Conical Spiral

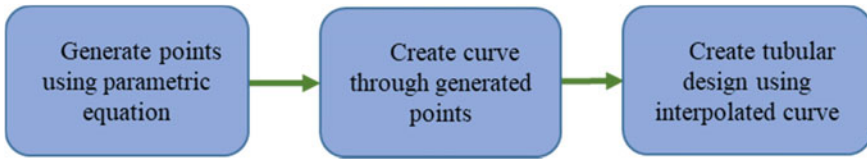
$$x = r(\varphi) * \cos(\varphi) \tag{1}$$

$$y = r(\varphi) * \sin(\varphi) \tag{2}$$

$$z = m * r(\varphi) \tag{3}$$

where  $m$  is the slope of the cone's curves with respect to the  $x$ - $y$ -plane.





**Fig. 2** Sample algorithm flowchart to model conical spiral tube

## ***4.2 Sample Algorithm to Model Conical Spiral Tube***

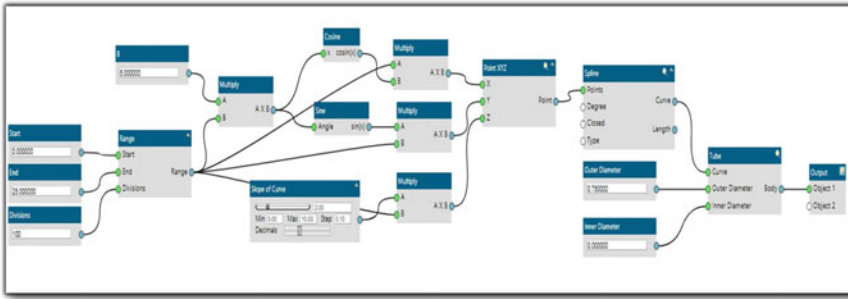
1. Using parametric Eqs. (1), (2), and (3), evaluate the point coordinates in 3D space.
2. Draw an interpolation curve through the points that have been evaluated.
3. Construct a tubular design using the interpolated curve.

The above-mentioned algorithm (refer to Fig. 2) is used in both visual programming environments to compare the different capabilities of Siemens NX’s Algorithmic Feature and Rhinoceros 3D’s Grasshopper.

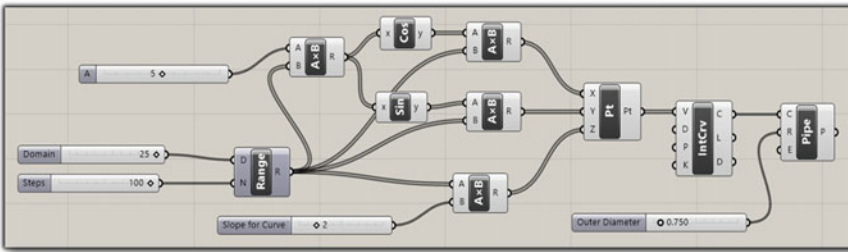
The Algorithmic Feature’s program is shown in Fig. 3a creating a conical spiral design using the above-mentioned sample algorithm. Specific kinds of blocks are interconnected to represent the algorithm, as shown in Fig. 3a, and these building blocks are referred to as “Nodes” in the Siemens NX Algorithmic Feature environment. CAD users can select an appropriate node from Node Library. Algorithmic Modeling environment comprises two windows, the first is called Logic Editor and the second one is the Model Preview window.

In the Logic Editor window, users define the algorithm by identifying suitable nodes and appropriate logic to generate output. The preview button is included on every node that contains any geometrical or topological output. When the user activates the preview from the nodes, the second model preview window displays the corresponding model preview.

Similarly, the Grasshopper program for the same sample algorithm is shown in Fig. 3b. Building blocks that create algorithms and compute output design are referred to as “Components” in the Grasshopper visual programming environment. These components may be used by the user to define the algorithm. “Canvas” refers to the area where users connect these components to generate output. Because the Grasshopper is a 3rd party additional plugin that provides a visual programming environment in Rhinoceros 3D, therefore the visual program is shown in the Grasshopper’s windows, while the model preview of the generated output is displayed in the model window of Rhinoceros 3D.



(a)



(b)

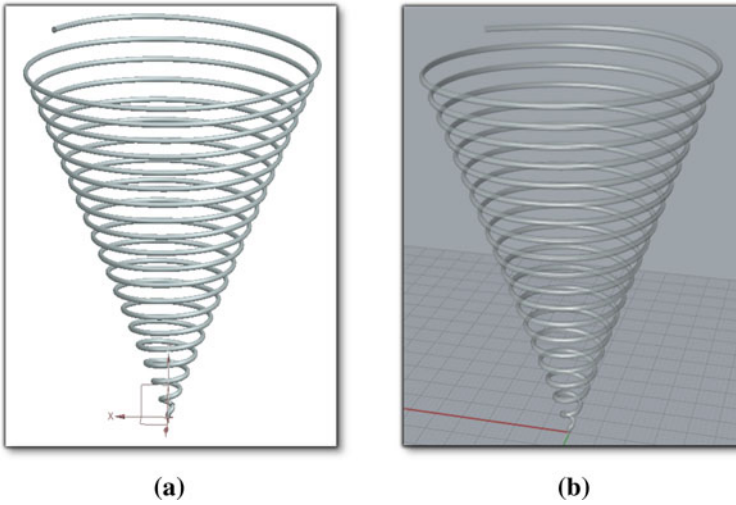
**Fig. 3** a Algorithmic Feature’s program to model conical spiral tube. b Grasshopper’s program to model conical spiral tube

## 5 Discussion

The design developed using the example algorithm in both visual programming environments is shown in Fig. 4a and b. When it comes to the output provided by both tools, the design is comparable in both, implying that both tools generate similar designs given the same algorithm, input, rules, and constraints. This confirms that both environments are really a means of defining the algorithm and that both tools will simply provide output following the routine defined by the user.

Rhinoceros 3D’s Grasshopper has more components or building blocks, which offered more capabilities and flexibilities to the designers because Grasshopper has been developing since 2007, which makes it a mature solution. Therefore, Grasshopper has been a popular generative design tool in the architectural areas.

However, Siemens NX’s Algorithmic Feature offers a complementary solution, allowing users to build custom features using the Algorithmic Modeling environment nodes. This custom feature may be dependent on the geometrical and mathematical output of another feature, and another feature may be dependent on this custom feature as well. When the model is updated by the parent feature, its child features (including custom features) are updated in the same order, and vice versa. This



**Fig. 4** **a** Model with Algorithmic Feature. **b** Model with Grasshopper

complimentary solution is also referred to as “Associativity” in Algorithmic Environment. Users have the flexibility to create an associative feature or non-associative feature.

For CAD users, this functionality includes feature-based modeling as well as parametric modeling. Users do not have to rely on the features provided by CAD software to build any design; instead, they can define their single custom features for any design. As shown in Fig. 5, the custom feature for conical spiral design in part-navigator (enclosed in a rectangle) and the corresponding edit window for that feature to tweak the parameters. This custom feature can now be used in the same way as any other feature supplied by CAD software.

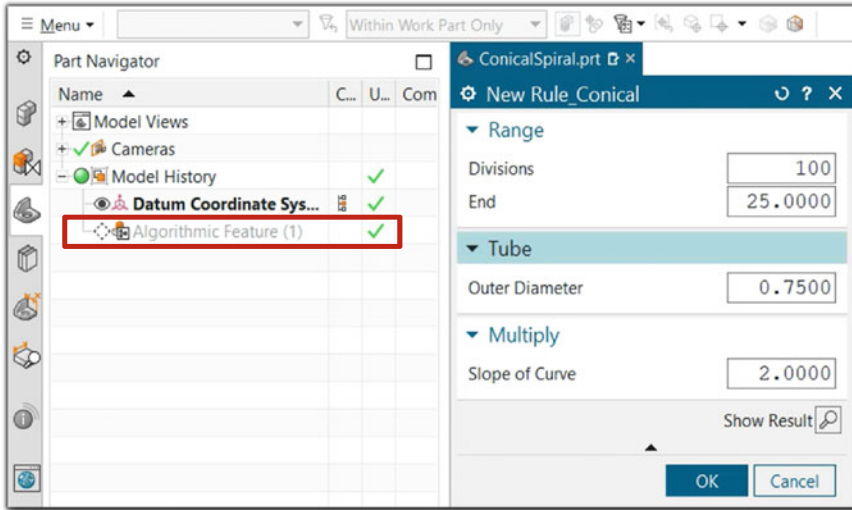


Fig. 5 Conical spiral design as custom feature

## 6 Conclusion

This paper discussed the modern visual programming tools for computational design and contrasted the two tools using a conical spiral design as a case study.

Siemens NX's Algorithmic Feature and Rhinoceros 3D's Grasshopper are both visual programming tools that offer the capabilities to produce a computational design using some geometrical algorithm. However, because Rhinoceros 3D's Grasshopper is a more mature generative design system and is popular in the architectural profession, it offers a wider range of capabilities and components than Siemens NX's Algorithmic Feature.

However, Siemens NX includes certain functionality, such as associativity and the ability to define custom features for any computational design. Therefore, it can be useful in the production of complex designs and automate the process using an iterative approach. But besides that, Algorithmic Feature is an integrated solution for algorithmic aided design, requiring no additional 3rd plugins to employ visual programming, whereas Grasshopper is a 3rd party plugin linked with Rhinoceros 3D, which may require additional licenses.

As Rhinoceros 3D's Grasshopper has more capabilities in terms of functionalities and building blocks for algorithms and it has been a stable solution for generative design for years, therefore it is widely used by architecture industries where generative design is not a new topic. But Siemens NX's Algorithmic Feature is a recent tool in the area of generative design, which development is going on release by release. But Algorithmic Feature offer is easier to use or provides much better usability than Grasshopper. Algorithmic Feature provides associativity, custom feature support as

well an inbuilt solution for the generative design within CAD software Siemens NX, which makes it a better solution for the mechanical design engineers to use for generative design sectors such as automotive, electronics, and industrial designs.

## References

1. Xu X (2008), Integrating advanced computer-aided design, manufacturing, and numerical control: principles and implementations, Information Science Reference
2. What is generative design, its benefits and applications (2020). Available: <https://www.sml ease.com/entries/technology/what-is-generative-design-benefits-applications/>
3. Seowoo Jang SYNK (2022) Generative design by reinforcement learning: enhancing the diversity of topology optimization designs. Computer-Aided Design
4. McKnight M (2017) The international conference on design and technology
5. Hardi K Abdullah JMK (2013) Parametric design procedures: a new approach to generative-form in the conceptual design phase
6. Tedeschi (2014) AAD algorithms-aided design. parametric strategies using grasshopper
7. Renata Castelo-Branco CAL (2021) Digital representation methods: The case of algorithmic design. Frontiers of Architectural Research
8. Antonio Leitao LS (2011) Programming languages for generative design. Textual or Visual?
9. Myers B (1990) Taxonomies of visual programming and program visualization
10. James Novak L (2017) Recoding product design education: visual coding for human machine interfaces. In: DesTech Conference Proceedings
11. Woojae Sung YJ (2022) Site planning automation of apartment complex through grid-based calculation in grasshopper. Automation in Construction
12. Reitz (2019) Modeling through visual programming. Available: <https://www.machinedesign.com/3d-printing-cad/article/21838123/modeling-through-visual-programming>

# Farming System: Quadcopter Fabrication and Development



Rajat Yadava and Anas Aslam

**Abstract** The scope of this study is discussion of a methodology for designing and manufacturing quadcopters for use in agricultural settings. This particular quadcopter is equipped with a pesticide spraying tank that is attached to it. Because pesticides pose a risk not just to the insects they are intended to kill but also to humans. Pesticides are harmful to humans because they alter the nervous system and induce sickness. An unmanned aerial vehicle, often known as a UAV, may be used to spray pesticides and fertilizers, therefore reducing the risk to humans in the area. As a direct result of this, the goal of this project is to design and construct a quadcopter that is equipped with a spraying unit for use in agricultural applications. This will have a competitive advantage in terms of area coverage because to the speed of the UAV, and it will also reduce the amount of pesticide that is wasted. By reducing the amount of manual labor that must be performed by humans, this tactic helps save both time and money. However, a number of issues, including crop area that is not covered in the spraying process, overlapping spraying, and other challenges that are typical in manual spraying, have the potential to reduce productivity or possibly cause harm. The load-carrying capability of the UAV and the spraying unit will serve as the foundation for the design plan. It is planned to build and evaluate a radio-controlled quadcopter, also known as an RC Quadcopter.

**Keywords** Pesticides · Quadcopter · Spraying unit · Unmanned aerial vehicle (UAV) · LQR controllers

## 1 Introduction

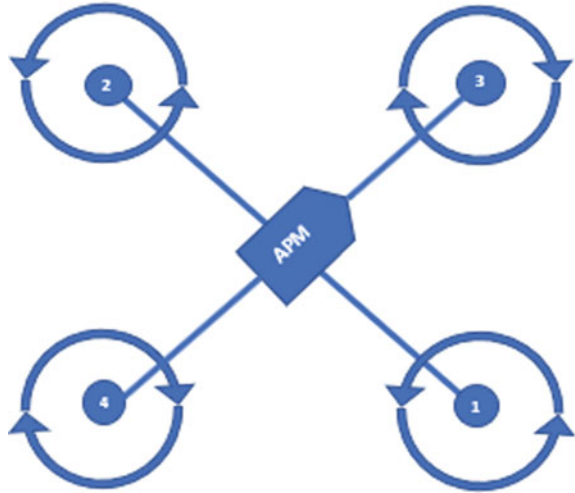
A quadrotor helicopter is another name for a four-rotor helicopter. The quadcopter's rotors are placed upward and set in a square shape at the same distance from the quadcopter's center of mass. The angular velocities of the quadcopter's rotors, which are spun by electric motors, are optimized for power. Because of its simple design, the

---

R. Yadava (✉) · A. Aslam  
IET, GLA University, Mathura, India  
e-mail: [rajat.yadav@gla.ac.in](mailto:rajat.yadav@gla.ac.in)

quadcopter is well-known for lightweight, impersonal aerial vehicles (UAVs) [1, 2]. Monitoring, study and rescue, building inspections, and other applications are possible. Quadcopters are employed. All of the studies begin with a simple dynamic model of the quadcopter, but they progress to more complex aerodynamical properties. PID controllers, backstepping control, nonlinear H1 control, LQR controllers, and nonlinear controllers with nested saturations are among the control methods investigated. Many quadcopters use two sets of identical fixed-pitch propellers: the CW and the CCW [3–5]. Counter-clockwise eliminates torque-induced control problems, and the comparatively short blades are much simpler to design. A small tank is mounted to the quadcopter for carrying pesticides for agricultural purposes. The pesticides are sprayed from the tank, which is connected to the spraying unit. The motor and pumps are used to operate the spraying machine. The pump is used to create pressure to suction the fluid from the tank, and the nozzle is used to spray it on the ground. In this paper, Teresa Donateoa et al. will investigate the problem of developing an electric hybrid multi-copter and comparing its tolerance in electrical and thermal power systems [6–8]. Two multi-copters were compared and built to reach a target mass: a quadcopter (11.2 kg) and a hexagonal cup (12.4 kg) (16.8 kg). The thermal power system had the best endurance for the smaller multi-copter, while the hybrid electric series system fared even better for the hexacopter. Both quadcopter and the hexacopter had more endurance with the hybrid power system than with the electric power system. However, it worked worse for the quadcopter, where a thermal power system had the best endurance. The results, however, are highly dependent on battery charging capacity, threshold of SOC. describe through this paper, they do something different with the digital design life cycle [9–11]. Centered on the unified UML modeling language, this approach employs graphically oriented design languages. And also have many benefits, including fewer interfaces between modeling and simulation tools and a formal, consistent language that eliminates type and content differences between engineering models. A quadcopter was used as an example to demonstrate the efficacy of this device. More research is needed and planned to clarify, information, and strengthen the strategy's feasibility. According to the author, precision farming (PA) is a game-changing trend in farm management. Although there are many benefits to using UAS for precision farming applications, the safety risk must be identified and monitored [12, 13]. The ASRM PA Notional Scenario provides a system sense by incorporating social and technological risks associated with UASs, crop dusters, operations, and the climate. Geo-fencing, also known as "virtual barrier" construction in the sky, is one of the prevention techniques for avoiding mid-air collisions. Geo-fencing mitigation is effective in this hypothesis scenario, according to preliminary ASRM findings. This paper presents a control scheme for a two-level hierarchical quadcopter UAV trajectory monitoring. The angles necessary for orientation control and the main thrust are generated by variable changes in posture control. There is no approximation to the vehicle's initial nonlinear dynamics in the regulatory legislation [14–17]. The LQR method is used to choose parameter gains to shorten input time and thus save energy. Their paper shows how to use a sophisticated adaptive fluid control approach and compare it to the fluid-looking Mamdani controllers.

**Fig. 1** Simple representation of quadcopter



## 2 Design

### 2.1 Frame Selection

This X-configuration quadcopter is made entirely of aluminum. Both frames are strong and lightweight, and they can be fixed easily. Since the parts are made of flat aluminum, they easily bend and can be flattened with a hammer even when struck hard. Because of its simplicity and maneuverability, the multi-copter design is a quadcopter. The quadcopter's configuration is X due to its ease of orientation and low cost. The pitch and roll axes in the 'X' configuration have two counter rotary propellers on both sides. It explains why the "X" configuration is more comfortable and maneuverable than the "+" configuration. In case heavy lifting is required, then octocopter may have opted. Simple representation of quadcopteris shown in Fig. 1.

### 2.2 Components

- Aluminum frame
- Brushless DC motor (A2212)-1000 kV
- Electronic Speed Controller (ESC)-30 A
- Propeller-10" × 4.5
- Lipo battery-3000 mah
- Flight controller
- Transmitter and receiver
- Pump 12 V DC



- Pesticide tank
- Arduino board

### 2.3 *Spray Tank Design*

The sprayer unit consists of a 12 V DC pump, pesticide/fertilizer tank, and nozzle. The 12 V DC pump is used to generate pressure to suck the fluid which is in the tank and the nozzle is used to spray onto the field. The specification of the sprayer unit is as follows: Specifications

- Rated voltage: DC 9 V
- Size: 14\*6 cm
- Noise: < 60db
- Rated current: < 150 mA
- Water flow: 0.4–0.7 L/ min
- Operation temperature range: 5–45 °C
- 350 ml tank
- 0.4 mm nozzle

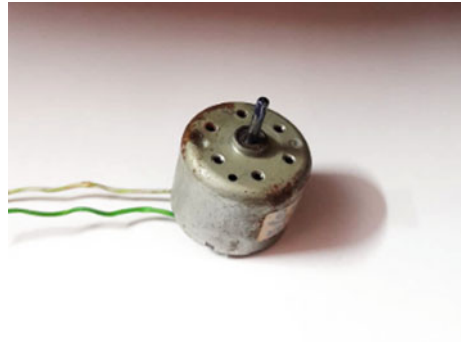
## 3 Frame

The center plate has been framed with aluminum frames of similar size. Quadcopter frames are available in a range of sizes and weight capacities. The majority have the same basic form—a hazy X. In Fig. 2, quadcopter frames are setup for different ranges of sizes as shown.

**Fig. 2** Quadcopter frames setup for different ranges of sizes



**Fig. 3** Brushless DC electric motor



### ***3.1 DC Motor (Brushless)***

Brushless DC electric motors, also known as electronically commutated motors, are synchronous motors operated by an electric AC signal provided by an integrated inverter/shift power supply. Brushless DC electric motor is shown in Fig. 3.

### ***3.2 Propeller***

The function of flight necessitates the use of two types of propellers in quadcopters. A pair of propellers that rotate clockwise (CW) and anticlockwise (ACW) is needed. The measurements of the propellers should be finalized with caution. Both Bernoulli's theory and Newton's third law can be used to model propeller dynamics. The pitch can also be described as the distance traveled by a single prop rotation. Propellers are shown in Fig. 4.

### ***3.3 Speed Controller***

The frequency, not the voltage, is used by the ESC to regulate the speed of an AC motor. If you plug an 11.1V battery into your power device, the motor will receive 11.1V with the battery's full amperage capacity backing it up. We use real 3-phase AC brushless motors in our AC brushless motors. The DC motors are powered by AC. The motor's speed has little to do with the voltage or amps. The ESC allows the motor to spin faster or slower by changing the wavelength (frequency) of the trapezoidal wave in the three phases. To generate waves, the ESC reverses the polarity of the phases. This implies that the voltage passing through each winding alternates. This creates a push-pull effect in the magnetic field of each winding, increasing motor

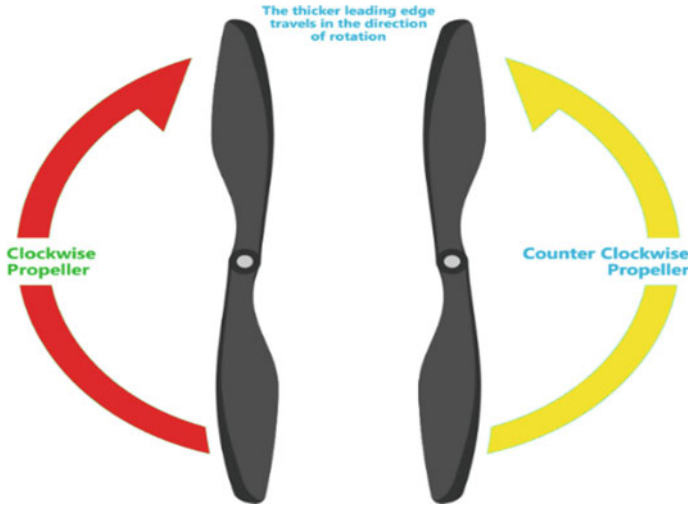


Fig. 4 Propellers

strength as weight and height increase. The engine and load decide the ESC amplifier and battery. Electronic speed controller is shown in Fig. 5.

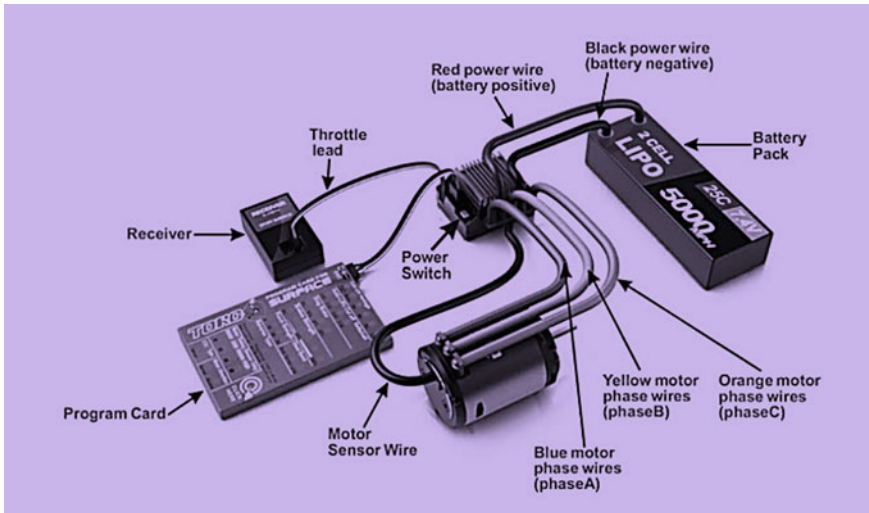


Fig. 5 Electronic speed controller

### **3.4 *Controller (Flight)***

The controller is essentially a small device that controls the quadcopter and interprets the signals sent by the transceiver. In several ways, selecting a flight controller for a quadcopter is more of a personal option, similar to choosing between different PC processors in the same power range. Each manufacturer has different preferences, which may or may not be customizable. If this is a problem that needs to be addressed, start reading forums and listening to hobbyists who suggest inexpensive, dependable controllers that work with a wide range of components.

### **3.5 *Transmitter and Receiver***

The CT6B Fly Sky Transmitter and Receiver that we are using has six channels. It necessitates the use of a computer to adjust channel variables, mix, and reverse servos. The quadcopter can be controlled using the radio transmitter and receiver. There are several suitable models available, but a simple quadcopter with the CC3D control board would need at least four channels. A radio transmitter is an electronic system that emits radio waves with the aid of an antenna in electronics and telecommunications.

## **4 Result**

The parts, such as the motor, electronic speed controller, flight controller, battery, and receiver, are mounted on an aluminum frame with Arduino plates. Figure 6 shows the basic configuration of the quadcopter with various parts.

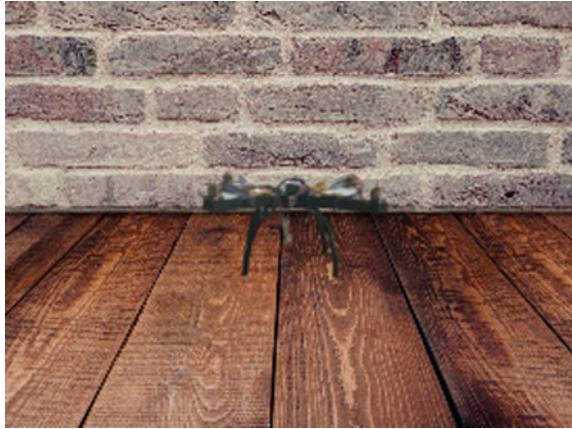
For safety and proper landing, the landing gear is also mounted to the quadcopter. Figure 7 depicts the entire setup of the quadcopter without the spraying device.

The ESC calibration should be performed immediately after building the quadcopter and whenever we assume that the motor speeds are not properly balanced. It aims to have the speed controllers respond to the APM and RC commands in the same way. Automatic calibration is the simplest method since all that is required is to hear the APM's tones and move the remote sticks 1 as a result. The sprayer unit is attached to the quadcopter because the pesticide tank has a capacity of 350 ml, and the quadcopter's pump can last for 10–15 min. This model will aid in the spraying of the desired area.

**Fig. 6** Basic configuration of quadcopter with various parts



**Fig. 7** Entire setup of the quadcopter without the spraying device



## 5 Conclusion

This paper aimed to design and fabricated a multicomputer with a spraying unit for agricultural use. Due to the UAV's altitude, this provided an advantage in terms of faster land coverage and decreased pesticide waste. This approach saved time and money by reducing the amount of work that humans had to put in. However, some factors, such as crop area not covered in the spraying process, overlapping spraying, and other issues that are typical in manual spraying, can reduce yield or even cause harm. The UAV and spraying unit's load-carrying ability was the subject of the design methodology. A radio-controlled quadcopter (RC quadcopter) was designed and tested.

## References

1. Donateo T, Spedicato L, Placentino DP (2017) Design and performance evaluation of a hybrid electric power system for multicopters. *Energy Procedia* 126:1035–1042
2. Ramsaier M et al (2017) Digital representation in multicopter design along the product life-cycle. *Procedia CIRP* 62:559–564
3. Shukla MK, Sharma K (2019) Improvement in mechanical and thermal properties of epoxy hybrid composites by functionalized graphene and carbon-nanotubes. *Materials Research Express* 6(12):125323
4. Hernandez-Martinez EG et al (2015) Trajectory tracking of a quadcopter UAV with optimal translational control. *IFAC-PapersOnLine* 48(19):226–231
5. Laryukhin V, Skobelev P, Lakhin O, Grachev S, Yalovenko V, Yalovenko O (2019) Towards developing a cyber-physical multi-agent system for managing precise farms with digital twins of plants. *Cybernetics and Physics* 8(4):257–261
6. Sharma A, Chaturvedi R, Sharma K, Saraswat M (2022) Force evaluation and machining parameter optimization in milling of aluminium burr composite based on response surface method. *Advances in Materials and Processing Technologies* 1–22
7. Domingos D, Camargo G, Gomide F (2016) Autonomous fuzzy control and navigation of quadcopters. *IFAC-PapersOnLine* 49(5):73–78
8. Cawthorne D, Cenci A (2019) Value sensitive design of a humanitarian cargo drone. In: 2019 international conference on unmanned aircraft systems (ICUAS). IEEE, pp 1117–1125
9. McCabe B, Kroebel R, Pezzaglia M, Lukehurst C, Lalonde C, Wellisch M, Murphy JD (2020) Integration of anaerobic digestion into farming systems in Australia, Canada, Italy, and the UK. *IEA Bioenergy Task 37(2020):8*
10. Sharma A, Chaturvedi R, Singh PK (2022) Efficient activated metal inert gas welding procedures by various fluxes for welding process. In: *Computational and experimental methods in mechanical engineering*. Springer, Singapore, pp 419–427
11. Olivares V et al (2015) Modeling internal logistics by using drones on the stage of assembly of products. *Procedia Computer Science* 55:1240–1249
12. Verma SK et al (2020) Performance comparison of innovative spiral shaped solar collector design with conventional flat plate solar collector. *Energy* 194:116853
13. Sharmaa K, Sharmaa A, Chaturvedia R, Islama A (2020) Automatic mobile patrolling robot for continuous monitoring using DVR algorithm. *European Journal of Molecular & Clinical Medicine* 7(4):2020
14. Dupont, QFM et al (2017) Potential applications of UAV along the construction's value chain. *Procedia Engineering* 182:165–173
15. Criado RM, Rubio FR (2015) Autonomous path tracking control design for a comercial quadcopter. *IFAC-PapersOnLine* 48(9):73–78
16. Bortoff SA (2000) Path planning for UAVs. In: *Proceedings of the 2000 American control conference, ACC (IEEE Cat. No. 00CH36334)*. 1(6):364–368. IEEE
17. Doherty P, Granlund G, Kuchcinski K, Sandewall E, Nordberg K, Skarman E, Wiklund J (2000) The WITAS unmanned aerial vehicle project. In *ECAI*. pp. 747–755

# Development of a Drone with Spraying Mechanism for Agricultural Work



Pratejas Tomar and Sumit Krishnan

**Abstract** UAV or unmanned aerial vehicle is perhaps the most niche and sophisticated means of aviation tech that has evolved to a greater degree in the past few years. Today, drones are employed to serve a wide range of applications, among them military operations, emergency medical supplies, firefighting, thermal image processing, and mapping are the major areas of operations. Further, the marked improvements in drone technology in the last few decades have ensured that the drone can be successfully put into practice in the field of agriculture. The design of a UAV is the most important element which determines how a UAV will phase-in in its general practice. The mechanical and electronic facets that comprise a drone must ensure synchronous working so that the final design delivers a stable flight. This paper not only describes the various use-case scenarios of drones in the field of agriculture but also details the design of a hexacopter with a spraying mechanism, specifically meant to ease agricultural work. Additionally, it encompasses the layout of various design steps that are required to build such a hexacopter. Also, a custom spraying mechanism that sits at the heart of this hexacopter is comprehensively discussed in this paper. The hexacopter design presented has a payload-carrying capacity of 1 L and a maximum flight time of 10–15 min. Apart from this, the various shortcomings and challenges have also been duly addressed to give a wider perspective to not only the readers but also to the researchers working on future drones.

**Keywords** UAV · Drone · Hexacopter · Spraying mechanism · Agriculture

---

P. Tomar · S. Krishnan (✉)  
Amity University Lucknow Campus, Uttar Pradesh, Lucknow, India

P. Tomar  
e-mail: [pratejas4435@gmail.com](mailto:pratejas4435@gmail.com)

# 1 Introduction

Drone, the acronym exerted for dynamic remotely operated navigation equipment, has forged much wider implications in today’s world of aviation. Whether it be fixed-wing or multi-rotor drones, its widespread applications have ensured that we have found a worthy contender for almost any type of aviation job possible. Figure 1 gives the graphical representation of drones being used in various sectors. An equally widespread term is UAV or unmanned aerial vehicle which signifies that there is no human pilot onboard, and at the same time, it is being controlled by a person remotely on the ground or autonomously by a computer program.

One of the most widely used applications of drones in the twenty-first century has emerged to be in the field of agriculture. Drones are being employed for a variety of purposes such as pest control, crop irrigation, aerial mapping among others. More than 60% of the planet’s population naturally depends on agriculture for survival in the current world [2]. Agriculture drones appropriately operate on the feed of image processing to predict various parameters pertaining to the plant’s growth, quality of active area, etc. The human population’s brisk extension increases the fundamental need for high productivity, high performance, and sustainable farming [3].

One of the foremost advantages of a drone is that it can survey an area as large as several kilometers very quickly if it is equipped with long-range capabilities. To achieve a 70% increase in food production means that farmers will need higher technological tools to help them better analyze the agricultural data [4]. In the present day and age, the use of drones has significantly increased in both developing and developed countries. Further, the University of Southern Queensland has over the years invested in drone technology with the intention of making it traditional farming equipment by 2025 [4].

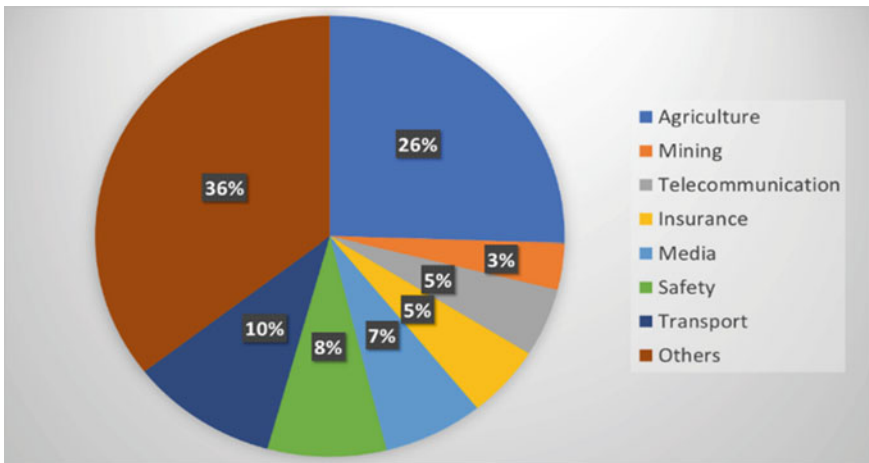


Fig. 1 Use of drones in various sectors [1]



In order to plan and build a drone (or a hexacopter in the present case) specifically meant for agricultural purposes, one needs to plan the entire project in a comprehensive manner so as to ensure that all the bases are covered since agriculture is not only essential in feeding the population of a country, but the yields generated can also be exported in order to boost the GDP of a country. There are multiple configurations that can be considered for an agricultural drone such as a quadcopter, hexacopter, and octocopter. The configurations can be altered depending on whether the need of the hour is stability or speed. Further, the quality of equipment also plays an important role. Therefore, quality controllers like PIXHAWK, ARDUPILOT, and KK 2.1.5 must be employed to overcome the shortcomings. A similar approach must be followed for selecting other equipment like ESC, motors, and propellers. The spraying system is yet another integral part of an agricultural drone, and a custom design must be devised. The upcoming sections discuss the approach which must be deployed while designing the hexacopter and its spraying mechanism. Further, the various shortcomings and challenges associated with the hexacopter have also been addressed.

## 2 Historical Antecedents

The first use of drones in history was reported in 1839, wherein the city of Venice was attacked with explosives carried within the unmanned balloons. In 1916, the first unmanned fixed-wing aircraft, Ruston Proctor Aerial Target, was developed that could be controlled through radio signals [5]. Hewitt-Sperry Automatic Airplane, which was the first unmanned aircraft to have an automatic stabilization system, was developed in 1917 with the intention to be used as a flying bomb during World War I. Talking about modern warfare, in 1982 the UAVs were employed by Israel to identify the ground positions and attack the Syrian fleet.

In 2006, it was the first time when drones began to be used for non-military operations like firefighting, disaster relief, surveillance, pipeline inspection, and pesticide spraying. Also, it was the same year when the Federal Aviation Association (FAA) issued the first permit for commercial use.

The very recent applications include that of Ehang 184, the first taxi drone, which was launched in Dubai in 2017 [6]. Also, in 2017, NASA announced the dragonfly concept, a robotic rotorcraft, to explore the possibilities of life on Saturn's moon Titan [7]. In February 2021, the Ingenuity Mars Helicopter landed on Mars aboard the NASA Perseverance Missions which has the sole purpose of demonstrating the rotorcraft flight in the thin atmosphere of Mars [8].

Moving onto the agricultural field, the first use of a drone dates back to the 1980s. The application of advanced technologies like aerial mapping of agricultural areas for crop growth monitoring and spraying of fertilizers and pesticides using drones received a lot of attention and appreciation over the years [9]. It was in 1983 when Japan became the first nation to use the drone for the purpose of fertilizer spraying owing to the development of the remote-controlled aerial spraying system (RCASS)



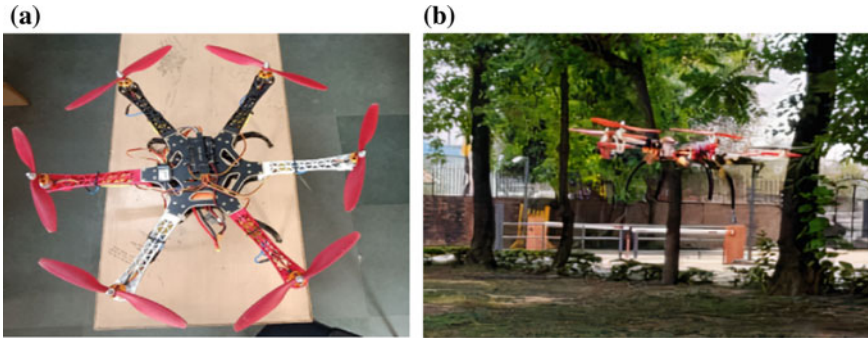
**Fig. 2** Drones showcasing their robustness. **a** Yamaha RMAX [12]. **b** Ingenuity Mars helicopter [13]

by the Yamaha Motor Corporation. In 1990, Yamaha developed the R50UAS helicopter with a payload capacity of 44 lb. Later, the RMAX unmanned helicopter was introduced in 1997 and was modified in the year 2000 to accommodate the DGPS sensor system [10]. The RMAX showed remarkable performance during the California study where it was observed that even at its slow flying speed of 12 mph, it was able to cover the area 10 times faster than tractors [11]. At present, about 90% of crop protection in Japan has been achieved using drones. Figure 2 illustrates the images of drones showcasing their robustness.

### 3 Design of the Hexacopter

The structure of the hexacopter consists of six arms, and the frame should be a balance between lightweight and strength to host a variety of components like a lithium-polymer (Li-Po) battery, six brushless motors (AC or DC), flight controller, six propellers, electronic speed controller (ESCs), and miscellaneous components like a video camera, and sensors. To ensure the stability of the frame, the battery must be conveniently placed to facilitate a lower center of gravity (CG). This location is preferably at the lower half of the frame. Secondly, the motors must be placed at an equidistance from each other in opposite directions for the ‘X’ configuration or right angles concerning one another for ‘+’ configuration and this must be comprehended in a way to avoid any collision of the propellers. After this, all the components are mounted onto the frame of the hexacopter. Figure 3 shows the assembled hexacopter with the components installed on the airframe.

The selection of components is the most significant part of the design as the overall performance of the rotorcraft is going to depend upon it, and this requires technical knowledge. Each component and the principle behind their selection is discussed in detail.



**Fig. 3** a Complete assembly of Hexacopter. b Hexacopter hovering in the air

### 3.1 Drone Aerodynamics

In rotorcraft, the propeller produces an aerodynamic force which is used to oppose the weight and generates thrust for forward motion and maneuver. However, for other types of aircraft there are separate components for the same.

Basically, a drone is acted upon by four types of forces during the flight which are thrust, drag, lift, and weight. As the propeller rotates, it experiences an upward aerodynamic force due to the difference in static pressure across the rotor disk. This force produced by the rotor is a result from Newton's second and third laws.

**Hovering Flight.** To hover, rotors must generate an inflow of air through its disk with a streaming velocity that could support its weight. The hovering speed or streaming velocity ( $v_s$ ) of designed drone is 5.170 m/s. For reference, the formula used, and the calculations are as follows [14]:

$$v_s = \sqrt{\frac{2mg}{n\rho A}} \quad (1)$$

where takeoff weight of the drone =  $mg$ ,  $n$  = number of motors,  $\rho$  is the density of air, and  $A$  is the area of one motor.

On substituting the values in the above formula, we get:

$$v_s = \sqrt{\frac{2 * 2.5}{6 * 1.225 * 0.02544}} = 5.170\text{m/s}$$

[Data of our drone: weight = 2.5 kg,  $n$  = 6, area of one motor = 0.02544 m<sup>2</sup>].

### 3.2 *Choosing an Airframe [15]*

The basic functionality of an airframe is just to hold everything together; therefore in broader terms, it should be judiciously rigid, strong, and lightweight. There are wooden airframes, plastic ones, and even metal ones. One airframe is chosen over the other because it offers some considerable advantage over the former one. For example, an aluminum airframe may be chosen over a wooden one due to its considerable lightweight [16].

$$W_0 = W_{st} + W_{pp} + W_{sys} + W_{bat} + W_{pay} \quad (2)$$

where  $W_0$  = Takeoff weight,  $W_{st}$  = Frame weight,  $W_{pp}$  = Power plant or motor weight,  $W_{sys}$  = Systems weight,  $W_{bat}$  = Battery weight,  $W_{pay}$  = Payload weight,  $W_e$  (or empty weight) =  $W_{st} + W_{pp} + W_{sys}$

Now after finalizing the weight of the frame and various components, the other aspect comes into the picture, i.e., the sizing of the frame. To proceed with this, one must know the size of the propeller to be used for a particular rotorcraft. The propeller is chosen based upon two design elements, the diameter, and the pitch. Accordingly, the formula for the frame size is:

$$X = 2 \times R \quad (3)$$

where  $X$  is the arm length of a frame from center and  $R$  is the radius of a propeller. For this hexacopter, an F550 frame was used.

### 3.3 *Motor*

The motor rotates the propeller which in turn provides the hexacopter the required lifting thrust. To select a proper motor for the hexacopter, it is very important to know the different types of motors that are available in the market. In most cases, DC brushless motors are preferred because of their high power coupled with excellent efficiency. The different types of motors are outrunner, inrunner, brushed, or brushless.

Motors are usually rated in kilovolts, and a higher kV rating corresponds to a faster spinning motor. The main criterion for choosing the motor is the thrust-to-weight ratio, and it is an indicator of the performance of the rotorcraft. Usually, the value of thrust is provided by the manufacturer in grams or kilograms but still one must know how to calculate the thrust. It can be done using the following formula [17]:

$$T = 2 \times \pi \times R^2 \times \rho \times \Delta v^2 \quad (4)$$

**Table 1** Thrust-to-weight ratio for different applications [18]

Thrust-to-weight ratio	Application
1.5–2	Slow flight (minimum)
3	Payload transport; photography
4	Surveillance
5+	Aerobatics; high-speed video
7+	Racing

where  $R$  is the radius of the propeller,  $\rho$  is the density of the air in  $\text{kg/m}^3$ , and  $\Delta v$  is velocity accelerated by the propeller.

Further [17],

$$\Delta v = \frac{P}{T} \quad (5)$$

where  $P$  is the power of motor transmitted to propeller and  $T$  is thrust in Newton,  $N$ . The power component can be further calculated using the equation [17]:

$$P = \text{Propellerconstant} \times \text{RPM}^{\text{powerfactor}} \quad (6)$$

The power factor is nothing but the pitch/diameter ratio of the propeller which can be easily calculated. The RPM is calculated based on supplied voltage to the motor, i.e., [17].

$$\text{RPM} = kV \times \text{Voltage}(\text{battery}) \quad (7)$$

Accordingly, the modified formula for Eq. 3 becomes [17]:

$$T = \sqrt[3]{(2 \times \pi \times R^2 \times \rho \times P^2)} \quad (8)$$

Now, the thrust-to-weight ( $T/W$ ) ratio can easily be obtained (Table 1).

### 3.4 Propellers

A propeller is a type of fan that converts rotational motion into thrust. Generally, the propellers are characterized by three parameters which are the diameter, pitch, and the number of blades. A long, slow-spinning, 2-blade propeller is more aerodynamically efficient than a small, fast-spinning, multi-blade one. In a rotorcraft, basically, two types of propellers are used which are pushers and pullers. The former rotates in the clockwise (CW) direction while the latter rotates in counterclockwise (CCW) direction [19].

The propeller efficiency is defined as:

**Table 2** Propeller size according to various frame and motor sizing

Frame size	Prop size	Motor size	kV
150 mm or smaller	3" or smaller	1305 or smaller	3000 or higher
180 mm	4"	1806	2600
210 mm	5"	2204–2206	2300–2600
250 mm	6"	2204–2208	2000–2300
350 mm	7"	2208	1600
450 mm	8", 9", 10"	2212 or larger	1000 or lower

$$\eta = \frac{P_A}{P} \quad (9)$$

where  $P$  is the power delivered by shaft of the motor and  $P_A$  is the power available from the propeller.  $P_A$  can be determined from the relation,

$$P_A = T_A \times V_\infty \quad (10)$$

Thrust available,  $T_A$ , depends upon pitch angle ( $\beta$ ), free stream velocity ( $V_\infty$ ), number of propeller revolutions per second ( $n$ ), and the diameter of the propeller, ( $D$ ) [20].

Table 2 lists the propeller size according to various frame and motor sizing [21].

Since the frame size is greater than 450 mm for this hexacopter, 10" propellers were used.

### 3.5 Electronic Speed Controller (ESC)

This component curbs the speed of the motor; i.e., it directs the motor as to how fast can it spin at a given time. It deploys an electronic circuit to vary the speed, direction, and possibly as a dynamic brake of a brushless motor. Usually, the current flowing in ESC is in the range of 30–40 A. In the case of a hexacopter, six ESCs are used which are directly connected to the motor and a battery through a power distribution system.

### 3.6 Battery

A battery supplies electrical power to the motors as well as the various electronic modules of the hexacopter. Lithium-polymer (Li-Po) are widely used and are most popular due to their lightweight, energy density, longer run times, and rechargeable

ability. The care must be taken that the voltage of the battery during the discharge must not fall below the safe operating value else it can damage the battery. The capacity of the battery is generally indicated in milliamp-hours (mAh) and indicates the battery draw per hour. Discharge of the battery is indicated with the letter 'C' and indicates the safety rating of its discharge rate. These batteries are packed in the form of cells ranging from 1 to 10, and the voltage of a single cell is  $\sim 3.7$  V [22]. The cells are typically connected in series which results in a higher voltage but a similar amount of battery draw. A 3S 4200 mAh Li-Po battery was used in the present case.

### ***3.7 Transmitter–Receiver and Remote Control***

The main objective of this component is to control the rotorcraft through radio-controlled signals. A series of channels are mapped to perform various maneuvers like rolling and yawing [23]. The controllers available in the market are 4-channel, 6-channel, 8-channel, and so on depending on the number of required functions.

### ***3.8 Flight Controller***

It is the brain of the drone which is installed to convey various sets of commands to the drone. The basic components of a flight controller include a microcontroller with a host of sensors like an accelerometer, compass, and GPS. The main function of a flight controller is to auto-level the drone so that the operator can focus on maneuvering the drone. Further, it can also take some precautionary measures in case of a malfunction like deploying a parachute in the instance of a fall. These controllers can be calibrated using the onboard computer (e.g., KK 2.1.5) or via connection to the computer through a software like Mission Planner. PIXHAWK and ARDUPILOT flight controllers can be calibrated using this software.

## **4 Design of a Spraying Mechanism**

The spraying mechanism for a hexacopter is a custom-designed in the present work and is the most important component of the agricultural drone shown in Fig. 4. It is designed for the purpose of spraying fertilizers on crops. The spraying system has a reservoir capacity of 1 L and consists of a DC pump, servo motor, DC motor driver, reservoir, connecting pipes, and a nozzle.

**Fig. 4** Hexacopter with a spraying mechanism



### ***4.1 DC Pump***

The DC pump transfers pressurized liquid from a reservoir to the nozzle. It has two components, i.e., an impeller and a brushless DC motor. The shaft rotates an impeller, thereby producing the desired output. The DC pump used in making the spraying system delivers an output of 8 W at 110 psi of pressure and can pump the liquid at rate of 10 L/min.

### ***4.2 Servo Motor and DC Motor Driver***

The work of the DC motor driver is to provide sufficient energy to the water pump to continue the pumping of fluid, whereas the servo motor, which works on the Pulse width modulation (PWM) principle translates the power from the battery to the DC motor driver.

### ***4.3 A Nozzle***

The basic function of a nozzle is to break the liquid into fine droplets and then ejects them in a specific direction. In the present work, a hollow cone nozzle is used which is connected to the outlet of the DC pump to spray the fertilizer. The operating pressure of a hollow cone nozzle ranges from 40 to 100 psi, and this depends on the type of hollow cone nozzle being used. Apart from this, hollow cone nozzles are also available in a variety of spray angles like 30, 80–110° [24]. This allows the end-user to extract maximum results for any plant height. Figure 5 shows the hollow cone nozzle. The spraying mechanism is controlled through the transmitter and receiver using a separate channel.



**Fig. 5** Hollow cone nozzle

## 5 Present Challenges

### 5.1 Power and Battery Life

An operator must ensure before a flight that the battery is charged, and the health of the battery is within the optimal working range. Most of the commercially available agricultural drones top out at 20–60 min of flight time [25]. Consequently, a small proportion of land is covered in a single flight. Thus, currently, the end consumer has to pay a big cost for longer flight durations.

### 5.2 Knowledge and Expertise

The farmer must learn the skill pertaining to the operation of drones or must hire a skilled worker to perform the job which can further add up the expenses. In few cases, the analysis of images captured by the drone is also required which needs a specialized skill set. Such analysis cannot be done by an average farmer, and this means that the extraction of any useful information from that data is simply not possible [25].

### 5.3 Weather Dependence

Most of the drones that are being used are weather dependent. They cannot be operated in challenging weather conditions like heavy wind or rain [25].

## 5.4 Connection Issues

The availability of online coverage is almost nil in the arable farms [25]. This means that before buying a drone a farmer must invest in secondary technologies like local data storage, Internet solutions. All these things add up and increase the cost manifold for the average farmer.

## 5.5 Legal Obscurity

Currently, very few countries have a proper law mechanism with regard to flight of a UAV. Consequently, UAVs are being used by terrorists for lethal applications like bombing and warfare. In the USA, it is mandatory to register a UAV with the FAA and go through ‘The Recreational UAS Safety Test’ or TRUST to be able to fly the UAV in the public domain. Thus, a drone user must register their equipment with the certifying agency for secure and safe operation [26].

## 6 Conclusion

In this paper, the design and development of a drone that can be used by farmers for fertilizer spraying on crops have been discussed in detail. Each design element is elaborated as a separate subsection to provide comprehensive knowledge to the reader. The drone has a custom-designed spraying system having a hollow cone nozzle for effective spraying and a hexacopter configuration for better payload-carrying capacity and stability. In the end, difficulties and challenges that could affect the performance of a drone were also presented.

## References

1. Zaychenko I, Smirnova A, Borremans A (2018) Digital transformation: The case of the application of drones in construction. MATEC Web of Conferences 193. <https://doi.org/10.1051/mateconf/201819305066>
2. Rahman MFF, Fan S, Zhang Y (2021) Chen L (2021) A comparative study on application of unmanned aerial vehicle systems in agriculture. *Agriculture* 11(1):1–26. <https://doi.org/10.3390/agriculture11010022>
3. Popescu D, Stoican F, Stamatescu G, Ichim L, Dragana C (2020) Advanced UAV–WSN system for intelligent monitoring in precision agriculture. *Sensors (Switzerland)* 20(3). <https://doi.org/10.3390/s20030817>
4. Naji I (2019) The drones’ impact on precision agriculture. Master of Science Thesis. The University of Texas at EL PASO. [https://scholarworks.utep.edu/cgi/viewcontent.cgi?article=3879&context=open\\_etd](https://scholarworks.utep.edu/cgi/viewcontent.cgi?article=3879&context=open_etd)

5. Herwitz SR, Johnson LF, Arvesen JC, Higgins RG, Leung JG, Dunagan SE (2002) Precision agriculture as a commercial application for solar-powered unmanned aerial vehicles. *AIAA* 2002–3404
6. Gordijn H (2017) Drones in passenger and freight transport. <https://www.researchgate.net/publication/321162396>
7. Scott CJ, Ozimek MT, Adams DS, Lorenz RD, Bhaskaran S, Ionasescu R, Jesick M, Laipert FE (2018) Preliminary interplanetary mission design and navigation for the dragonfly new frontiers mission concept. NASA jet propulsion laboratory. <https://trs.jpl.nasa.gov/handle/2014/48626>. Retrieved 22 Dec 2021
8. NASA (2021) Mars helicopter ingenuity landing press kit—NASA Mars exploration. Mars helicopter ingenuity landing press kit. <https://mars.nasa.gov/resources/25530/mars-helicopter-ingenuity-landing-press-kit/>. Retrieved 10 Jan 2022
9. Chavan PS, Jagtap KT, Nimbalkar AS, Mone PP (2017) Agriculture drone for spraying fertilizer and pesticides. *International Journal for Research Trends and Innovation* 2(6)
10. Sadeghi M, Jones SB, Philpot WD (2015) A linear physically based model for remote sensing of soil moisture using short wave infrared bands. *Remote Sens Environ* 164:66–76
11. CBS Sacramento (2014) Dreams of drone-assisted farming are taking flight. <https://sacramento.cbslocal.com/2014/11/13/dreams-of-drone-assisted-farming-are-taking-flight/>. Retrieved 2 Jan 2022
12. Watts AC, Ambrosia VG, Hinkley EA (2012) Unmanned aircraft systems in remote sensing and scientific research: classification and considerations of use. *Remote Sensing* 4(6):1671–1692. <https://doi.org/10.3390/rs4061671>
13. NASA (2020) Ingenuity Mars helicopter on the Martian surface (artist’s concept)—NASA mars exploration. NASA Science MARS exploration program. <https://mars.nasa.gov/resources/25117/ingenuity-mars-helicopter-on-the-martian-surface-artists-concept/>. Retrieved 10 Jan 10
14. Reid JS (2020) Drone flight what does basic physics say? Homepages. University of Aberdeen. <https://homepages.abdn.ac.uk/nph120/meteo/DroneFlight.pdf>. Retrieved 29 May 2022.
15. Baichtal J (2016) Building your own drones. A beginner’s guide to drones, UAVs, and ROVs. Que Publishing
16. Abishini AH, Priyanka BB, Raque BA, Kumar HA (2018) Design and static structural analysis of an aerial and underwater drone. *International Research Journal of Engineering and Technology*. <https://www.researchgate.net/publication/344821504>
17. Shen CH, Albert FYC, Ang CK, Teck DJ, Chan KP (2017) Theoretical development and study of takeoff constraint thrust equation for a drone. In: *IEEE 15th student conference on research and development (SCORED)*
18. Biczyski M, Sehab R, Whidborne JF, Krebs G, Luk P (2020) Multirotor sizing methodology with flight time estimation. *Journal of Advanced Transportation*
19. Parihar P, Bhawsar P, Hargod P (2016) Design & development analysis of quadcopter. *Compusoft: An International Journal of Advanced Computer Technology* 5(6)
20. Anderson JD (2012) Introduction to flight, 7th edn. McGraw Hill, New York
21. Reid J (2019) Multirotor motor guide. RotorDronePro. <https://www.rotordronepro.com/guide-multirotor-motors/>. Retrieved 17 Feb 2022
22. Tatala O, Anekar N, Phatak S, Sarkale S (2018) Quadcopter: design, construction and testing. *International Journal for Research in Engineering Application & Management*. <https://doi.org/10.18231/2454-9150.2018.1386>
23. Okasha Elnady A, Jamal Al-zoghy O, Ibrahim Khalil O, Monir reda A (2019) Design and manufacturing of quadcopter aerodynamic characteristics of GOE 387 airfoil view project autonomous airplane view project design and manufacturing of quadcopter. <https://www.researchgate.net/publication/334965767>

24. Johnson MP, Swetnam LD. Sprayer nozzles: selection and calibration. PAT-3 University of Kentucky. College of Agriculture. <https://entomology.ca.uky.edu/files/nozzles.pdf>. Retrieved February 25, 2022.
25. Pathak H, Kumar G, Mohapatra SD, Gaikwad BB, Rane J (2020) Use of drones in agriculture: potentials, problems and policy needs
26. Fields NR (2012) Advantages and challenges of unmanned aerial vehicle autonomy in the Postheroic age. <https://commons.lib.jmu.edu/master201019>

# Modeling and Performance Evaluation of Pelamis Wave Energy Converter Considering Indian Economic Estimates



Krishnakant Dixit and Kanchan Yadav

**Abstract** The ways of electrical power generation are a burning issue worldwide. Today, the world is realizing the benefits of substituting former fossil fuels with new renewable energy methods. Sea waves are an untapped energy resource that provides a strong, predictable, and environmentally friendly renewable energy source. Along its 6000 km of coastline, India has a potential of around 40,000 MW. The purpose of this research is to determine the economic viability of Indian coastal sites when converting wave energy into electricity. The electricity generated at each site is calculated for Pelamis wave energy converter (WEC) technology, which is supported by comparisons of the plants and their optimized electrical generation. The world is now seeing the advantages of replacing old fossil fuels with modern renewable energy sources. Sea waves, e.g., can provide powerful, predictable, environmentally sustainable, and easily accessible renewable energy. India's capacity along its 6000 km of coastline is estimated to be around 40,000 megawatts. In order to calculate the electricity costs generated in each plant for the application of Pelamis WEC technology. The goal of this assessment is to include current Indian economic estimates.

**Keywords** Cost of electricity (COE) · Wind energy · Pelamis wave energy converter · (Life-cycle cost (LCC) · Operating cost and wave energy flux

---

K. Dixit (✉) · K. Yadav  
Department of Electrical Engineering, GLA University, Mathura, India  
e-mail: [krishnakant.dixit@gla.ac.in](mailto:krishnakant.dixit@gla.ac.in)

K. Yadav  
e-mail: [kanchan.yadav@gla.ac.in](mailto:kanchan.yadav@gla.ac.in)

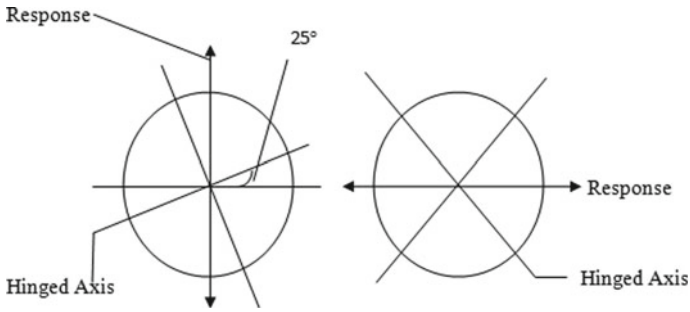
## 1 Introduction

Emphasize energy demand that has risen in recent years as a result of rising population and industrialization. And there is a finite amount of fossil fuel. It is for this purpose that the use of renewable energy resources became essential. Pelamis [1] wave power built and manufactures the Pelamis wave energy converter when a wave moves through the unit, the hinged segments move relative to one another. Hydraulic rams avoid the relative motion of the divided segments. The power conversion modules attach the separated cylindrical units [2]. Pelamis technology is based on hydrodynamic principles and theory, which provides it with some advantages and makes it more effective. It has undergone various modifications and arrangements in order to ensure its survival in adverse conditions [3]. Furthermore, the long thin shape has the highest water plane area-to-volume ratio, which aids in flotation.

Important costs associated with providing an alternative source of reaction are eliminated. Its resonant response can be adjusted to fit our needs and the conditions at sea. The Gulf of Cambay and the Gulf of Kutch on the west coast, where the long wave in the deeper Arabian Sea complements this operation [4, 5], are the most appealing locations. The northern Indian Ocean, including the coast of south-eastern Tamil Nadu and the national waters surrounding the Andaman and Nicobar Islands, is also included. Aside from tidal energy, India also has slow wave energy in deep water with short frequencies. We may try out this new technology right here [6]. There is a pressing need to shift to renewable energy sources, so this was an effort to look at new possibilities in India. The aim of this paper is to assess the power output and economic viability of the latent form of ocean energy in India using a Pelamis wave energy converter [7, 8]. We assessed the methods and equipment needed to exploit this resource, as well as the underlying guiding theory. By observing two sites on India's eastern and western coasts, Vishakhapatnam and Gulf of Khambhat, Gujarat, respectively [9, 10], we analyzed the produced power and measured the Cost of Electricity and Life Cycle Cost.

## 2 Power Production Methods

The Pelamis system, which is the nearest to commercial activity of the offshore devices, deserves more attention. The Pelamis is a floating system made up of five degree-of-freedom hinged joints that link cylindrical hollow steel segments (diameter 3.5 m). Each hinged joint, like a universal joint, is connected to the entire transmission unit of each joint. These joints' wave-induced movement is resistant to ten hydraulic cylinders with horizontal and vertical movement [11, 12]. These cylinders function as pumps, pumping fluid with an electric motor via a hydraulic engine. Circuit accumulators are used to isolate the primary (pump) circuit from the secondary system (the motor), as well as to help regulate fluid flow for more consistent generation, power takeoff (PTO) system is illustrated [13, 14].



**Fig. 1** Mooring system with hinged axis

**Table 1** Specifications of benchmark device

Device total length (m)	66
Floating bodies count	6
Spacing (m)	0.5
Diameter of bodies (m)	3.3
Front-end diameter (m)	0.36
Device total weight (t)	378
Stiffness of hinged (Nm/rad)	4.47E6
Damping (hinged) (Nm/rad/s)	2.26E7
Draft (m)	2
Gravity center height (m)	2
Depth of water (m)	38

### 2.1 Basic Parameters of the Device

In both states, the plane  $xoy$  is parallel to the water plane and passes along the cylinder’s center axis, while the  $z$  axis is vertical. Figure 1 shows mooring system with hinged axis, while Table 1 lists the main dimensions and parameters.

### 2.2 Mooring System (Parameters)

Pelamis’ mooring mechanism is a linear mooring with stiffness  $2E6$  in the numerical simulation. The mooring lines 1, 2, 3 connected with Structure 1, while the lines 3, 4, 5 connected with Structure 5. The angle is  $45^\circ$ .

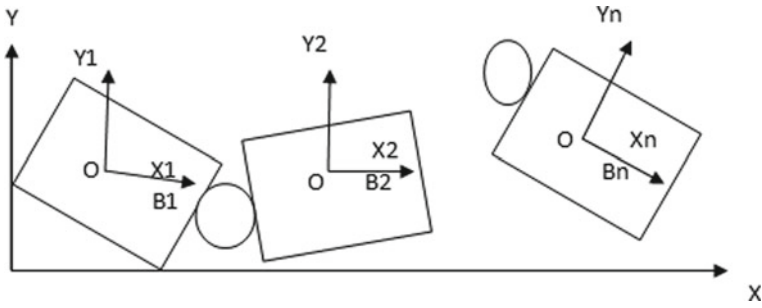


Fig. 2 Coordinate system

### 2.3 Principles

It is called linear when a wave in deep water has a negligible height, as we all know. Assume the fluid is rotational and viscous. Since a wave in deep water has such a small height, it is called linear. Overall coordinates and local coordinates for a structure composed of n hinged floating fragmented bodies Fig. 2 shows coordinate system.

### 2.4 Power Generated

Relative angle [2]

$$\theta = \frac{x}{r}, \theta = \frac{v}{r}$$

Hinged equation can be written as

$$M = K_{\theta}\theta + C_{\theta}\dot{\theta} \tag{1}$$

$r$  represents distance,  $X$ -axis of segment,  $V$ -linear velocity

Pneumatic cylinder position,  $K_{\theta}$ ,  $C_{\theta}$  is rotation stiffness and damping.

$$P = M \times \dot{\theta} = (C_{\theta} \times \dot{\theta})\dot{\theta} = \frac{C_{\theta}\dot{\theta}^2}{r^2} \tag{2}$$

Assuming that the relative angular velocity is and average power can be written as follows

$$\dot{\theta}(t) = A_0 \sin \sin(\omega t) \tag{3}$$



$$P_T = \sum_{i=1}^N n_i P \quad (4)$$

$$E = 0.422 H_s^2 T_p \quad (5)$$

where  $T_p$  is wave period (dominant) and  $H_s$ , is wave height (significant). The annual energy production can be express as follows:

$$E_{\text{avg}} = \sum P_{\text{abs}}(H_{s,p}) \times d(H_s, T_p) \quad (6)$$

where  $P_{\text{abs}}$  is average absorbed power.

## 2.5 Calculation of Life Cycle Cost (LCC) and Cost of Energy (COE)

In addition to the current market COE, the LCC and COE have been chosen to allow comparisons with wave energy converter (WEC) sites and configurations. Dunnitt's methods have been modified for this project.

Wallace and Szonyi et al., e.g., are quite straightforward. The year 2009 will cost the entire life cycle of a 25 MW wave power plant over a 25-year period (LCC). Total cost of capital (CC), total cost of operation and maintenance, and sales are all significant factors ( $R$ ).

$$LCC = CC + OC - R \quad (7)$$

Total power plant capital cost can be calculated as:

$$CC = q[D + (C_{ML} \times L_{ML}) + (C_{UW} \times d_{UW}) + (C_{OL} + D_{OL}) + Z] \quad (8)$$

Underwater transmission cable lengths (dUW), overland transmission cable lengths (dOL), and mooring line lengths per WEC unit (IML) are all measured in meters. The costs of decommissioning a wave power plant ( $Z$ ) are calculated in USD at net-present value, with interest received during the operating duration taken into account.

Under Eq. 5, total operating costs are calculated over a 25-year plant operating period (OC). The costs of operation and maintenance are calculated based on the amount of power produced. Because the outputs of each site and WEC configuration wave power plant are measured annually, the total electricity generated during one year ( $k$ ) is used for the OC calculation in kilowatt-hour units (kWh).

**Table 2** Wave energy convertor designs specifications

Pelamis wave energy converter	
Output power (kWh)	755
Capacity factor	0.182

### 3 Result and Analysis

In India, there is enough opportunity to extract this latent form of energy by using Pelamis wave energy converter. The specification of the device that we used here for observation is given in Table 2.

In India, we observed the potential of extracting power by this process and the conclusion is illustrated in the following Table 3, though the amount of electricity is not more but inviting.

Figure 3 depicts the distribution of wave energy along the Indian coast. Proper generation and distribution of renewable energy resources to land through underwater power transmission cables will result in a massive increase in the field of renewable energy production.

These two locations are subjected to observation for potentiality of power production and economic assessment.

The result is illustrated in the following Table 4.

The COE and LCC completely depend on the power production, operating, and maintenance costs.

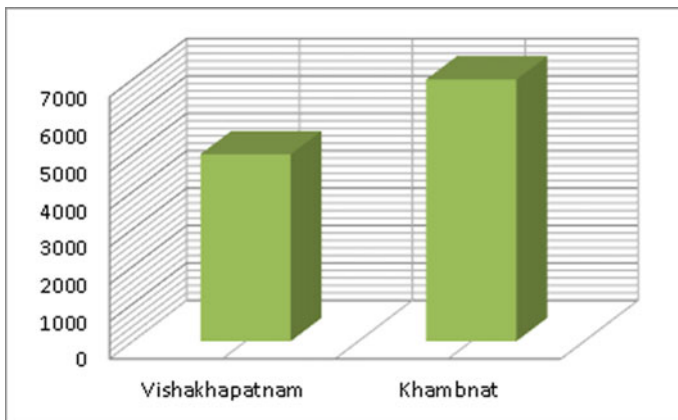
**Table 3** Specifications of coastline wave

Madras 10–15° N and coast-85° E			
	Power of wave	Height of wave (mean) (m)	Period of wave (mean) (s)
Non-monsoon	7.2	5.9	2.1
North-east monsoon	14.2	6.1	2.1
South-west monsoon	17.2	6.0	1.1
Kolkata 20–25°N and coast-85-95E			
	Power of Wave	Height of wave (mean) (m)	Period of wave (mean) (sec)
Non-monsoon	19.1	5.1	2.1
North-east monsoon	14.1	8.1	1.1
South-west monsoon	27.1	6.1	2.1
Visakhapatnam 15–20° N and coast-85 E			
	Power of wave	Height of wave (mean) (m)	Period of wave (mean) (sec)
Non-monsoon	11.1	8.1	2.1

(continued)

**Table 3** (continued)

Madras 10–15° N and coast-85° E			
North-east monsoon	16.1	7.1	2.1
South-west monsoon	32.1	7.1	3.1
Cochin 10–15° N and coast-70° E			
	Power of wave	Height of wave (mean) (m)	Period of wave (mean) (s)
Non-monsoon	6.1	6.1	1.1
North-east monsoon	6.1	5.1	2.1
South-west monsoon	26.1	5.1	1.1
Cape Comorin 5–10° N and coast-75–80° E			
	Power of wave	Height of wave (mean) (m)	Period of wave (mean) (s)
Non-monsoon	9.1	6.1	1.1
North-east monsoon	8.1	6.1	1.1
South-west monsoon	20.1	5.1	2.1
Bombay 15–25° N and coast-70° E			
	Power of wave	Height of wave (mean) (m)	Period of wave (mean) (s)
Non-monsoon	6.1	5.2	1.1
North-east monsoon	5.4	5.4	2.1
South-west monsoon	45.1	5.1	2.1



**Fig. 3** Wave energy distribution

**Table 4** Production and economic assessment

	COE	$E$	$E_{ave}$
Khambhat	33,000 cr.	8.405	6990
Vishakhapatnam	28,000 cr.	14.475	6138

## 4 Conclusion

The aim of this paper is to assess the power output and economic viability of the latent form of ocean energy in India using a Pelamis wave energy converter. We assessed the methods and equipment needed to exploit this resource, as well as the underlying guiding theory. By observing two sites on India's eastern and western coasts, Vishakhapatnam and Gulf of Khambhat, Gujarat, respectively, we analyzed the produced power and measured the cost of electricity and life-cycle cost. There is a pressing need to shift to renewable energy sources, so this was an effort to look at new possibilities in India. We came to the conclusion that the Indian sea coast would generate about 40,000 MW of electricity. The cost of energy and life-cycle cost mean that we would pay 0.04% more than we would for traditional electricity, but considering the advantages and difficulty of harnessing this resource, it may prove advantageous in the long run due to its low maintenance and lack of mechanical moving parts. This system produces no emissions or waste material erosion, making it an efficient and cost-effective method of extracting renewable energy. To become an act, this definition requires some further development and scope.

## References

1. Zhang Y, Zhao Y, Sun W, Li J (2021) Ocean wave energy converters: technical principle, device realization, and performance evaluation. *Renew Sustain Energy Rev* 141:110764
2. Coe RG, Ahn S, Neary VS, Kobos PH, Bacelli G (2021) Maybe less is more: considering capacity factor, saturation, variability, and filtering effects of wave energy devices. *Appl Energy* 291:116763
3. Retzler C (2006) Measurements of the slow drift dynamics of a model Pelamis wave energy converter. *Renewable Energy* 31(2):257–269
4. Choupin O, Andutta FP, Etemad-Shahidi A, Tomlinson R (2021) A decision-making process for wave energy converter and location pairing. *Renew Sustain Energy Rev* 147:111225
5. Rasool S, Muttaqi KM, Sutanto D, Hemer M (2022) Quantifying the reduction in power variability of co-located offshore wind-wave farms. *Renewable Energy* 185:1018–1033
6. Chandrasekaran S, Sricharan VVS (2020) Analysis of a floating wave energy converter with hydraulic-mechanical power take-off using WEC-Sim and SIMSCAPE. In: International conference on offshore mechanics and arctic engineering, vol 84416, p V009T09A032. American Society of Mechanical Engineers
7. Jahangir MH, Fakouriyani S, Rad MAV, Dehghan H (2020) Feasibility study of on/off grid large-scale PV/WT/WEC hybrid energy system in coastal cities: a case-based research. *Renewable Energy* 162:2075–2095
8. Falcão AFDO (2007) Modelling and control of oscillating-body wave energy converters with hydraulic power take-off and gas accumulator. *Ocean Eng* 34(14–15):2021–2032

9. Thomson RC, Chick JP, Harrison GP (2019) An LCA of the Pelamis wave energy converter. *The International Journal of Life Cycle Assessment* 24(1):51–63
10. Babarit A, Guglielmi M, Clément AH (2009) Declutching control of a wave energy converter. *Ocean Eng* 36(12–13):1015–1024
11. Kamranzad B, Hadadpour S (2020) A multi-criteria approach for selection of wave energy converter/location. *Energy* 204:117924
12. Shahriar T, Habib MA, Hasanuzzaman M, Shahrear-Bin-Zaman M (2019) Modelling and optimization of Searaser wave energy converter based hydroelectric power generation for Saint Martin's Island in Bangladesh. *Ocean Eng* 192:106289
13. Kumar A, Sharma K, Dixit AR (2020) Role of graphene in biosensor and protective textile against viruses. *Med Hypotheses* 144:110253
14. Henderson R (2006) Design, simulation, and testing of a novel hydraulic power take-off system for the Pelamis wave energy converter. *Renewable Energy* 31(2):271–283

# Review and Development of Thermal Design of a Cryogenic Dewar



Pranav Pandharpatte, Kartik Kurkure, Sandeep Kore, Avinash Shinde, and K. V. Shrinivasan

**Abstract** The way in which the fluid is to be kept and transferred is a vital component of any cryogenic system. These vessels to store cryogenic fluids can be categorized into low-performance insulations and high-performance insulations. Low-performance insulations include cork, foam, or fibrous insulation, high-performance insulations consist of multilayer insulation system and the container is evacuated. Selection of appropriate insulation method is an important task. A liquid helium Dewar is a storage vessel with advanced thermal insulations techniques. In today's date, the most common way of insulating these vessels is using multilayer insulation (MLI). This paper will throw light on different insulation concepts used in storage systems and give an approach for selection of proper insulation method. The present work deals with 120 l capacity liquid helium cryostat which uses a multilayer insulation system which uses evaporated cold vapour of cryogenic system to reduce heat leak and gives an approach for design of aluminium alloy-based liquid helium cryostat. This work is carried out by calculating heat leak from vessel and neck tube due to solid conduction, fluid conduction, radiation heat leak and heat leak by residual gas conduction in vacuum space, etc.

**Keywords** Dewar · Liquid helium · Cryogenic insulation

## Nomenclature

$Q_{acc}$	Heat loss due to accessories
$C_S, C_G, C_K$	Coefficients of solid conduction, gas conduction and radiation heat transfer
$q$	Heat leak (KJ)

---

P. Pandharpatte · K. Kurkure (✉) · S. Kore  
Vishwakarma Institute of Information Technology, Pune 411048, India  
e-mail: [kartikkurkure13@gmail.com](mailto:kartikkurkure13@gmail.com)

A. Shinde · K. V. Shrinivasan  
Tata Institute of Fundamental Research, Mumbai 400005, India

$T_h$	Cold boundary temp
$T_c$	Warm boundary temp (K)
$p$	Environmental pressure ( $p \leq 10^{(-4)}$ Torr)
$\varepsilon$	Emissivity
$Q_{RLateral}$	Heat loss due to radiation in lateral direction
$Q_{Rcol}$	Heat loss due to radiation in neck
$Q_{Cond}$	Heat loss due to conduction from neck
$Q_{gas}$	Heat loss due to gas conduction
$Q_{gascol}$	Heat loss due to gas conduction in neck
$\varepsilon_i$	Emissivity of first surface
$\varepsilon_e$	Emissivity of second surface
$S_i$	Shape factor of first surface
$S_e$	Shape factor of second surface
$T_i$	Temperature of first surface
$T_e$	Temperature of second surface
$\sigma$	Stefan–Boltzmann constant, $\sigma = 5.6704 \times 10^{-8} \text{ W/m}^2 \text{ K}$

## 1 Introduction

### 1.1 Introduction

The range of cryogenic temperatures varies from  $-150$  to  $-273$  °C. Compared to normal physical processes, cryogenic temperatures are very much lower. Ductility, material strength, thermal conductivity and other properties of the material change below these temperatures. As heat is created by the arbitrary movement of molecules, this states that at cryogenic temperatures molecules of material are very near to a highly ordered state and static state. The advancement in the field of cryogenics is because of the improvement in refrigeration technology. Introduction to the property of the supercooled metals to lose resistance to electricity led to the discovery of superconductivity. In the study of the properties of helium, research laboratories require temperature below 4 K. Temperatures below 3 K are mostly used in laboratories, especially in the research of the properties of helium. Helium is converted into liquid at 4.2 K, and this liquid is called helium I. Helium is converted into liquid at 4 K, which is called helium I. At the temperature of 2 K, it is called helium II [1].

Cryogenic liquids including helium have a small heat of vaporization. For example, liquid helium has a heat of vaporization of 20.7 kJ/kg at a pressure of 1 atm. While for water it is 2260 kJ/kg. Specific high-performance insulations are required to limit the boil-off rate of cryogenic liquids in storage tanks due to the high cost of liquefaction, safety concerns and low heat of vaporization. Today liquid helium has many applications: in the medical field, semiconductors, cryogenic manufacturing. Storing it has always been a challenge. The boiling point of LHe is 4.2 K,

which is what makes it hard to store. Storing it requires advanced thermal insulation techniques, which can reduce its boil-off rate to its minimum. Heat in-leak through these different insulations can take place by different modes of heat transfer, but mainly involves convection, solid conduction, gas conduction and radiation. The main objective of any insulation is to reduce the transfer of heat by various heat transfer modes. The best way to compare the different forms of insulation is to evaluate the apparent thermal conductivity of an insulation for liquid helium systems in an experimental setting to account for all these heat transfer mechanisms [1].

A literature review has been proposed to provide adequate solutions for thermal design. The current work emphasizes on thermal design of liquid helium Dewar. A proper approach for choosing an appropriate insulation method for liquid helium Dewar. Manufacturing of storage vessel is quite limited, and hence, a proper methodology for thermal design calculations has been proposed. A SciLab code has been developed to find a temperature profile of the neck which has a vital role for anchoring of multilayered insulation. In order to minimize the vessel's heat infiltration leak, a correct strategy has been provided for the positioning of the anchoring the layers of multilayered insulation on the glass fibre neck.

## 1.2 Liquid Helium

The two common isotopes are Helium-3 and Helium-4. Normal helium gas consists of around  $1.3 \times 10^{-4}\%$  helium-3. When we refer to helium in general, it is actually Helium-4 having molecular weight 4.002 kg/kmol [2]. It has no solidification point at normal atmospheric pressure. Liquid helium-4 is odourless and colourless and difficult to see in a container.

Table 1 presents the different properties of liquid helium.

**Table 1** Physical properties of liquid helium

Molecular weight	4.0026
Critical temperature	5.2 K (−267.95 °C)
Boiling point	4.2 K (−268.95 °C)
Minimum melting pressure	25 bar (360 psi)
Density	124.96 kg/m <sup>3</sup>
Index of refraction	1.02
Heat of vaporization	20.73 kJ/kg



## 2 Literature Review

### 2.1 Cryogenic Dewar

The rate of heat transmission through the insulation in a Dewar intended for land-based service must be as low as reasonably possible. Cryogenic insulations are usually evacuated to minimize gaseous conduction. To reduce conduction through the solid, low-thermal-conductivity spacers are used, while radiation heat transmission is minimized by using floating radiation shields (MLI). While supporting the inner vessel's and its contents' combined weight, the heat that is conveyed via the support must be reduced by the suspension system used to sustain the inner vessel inside the outer vessel. High-strength stainless steel rods are widely used in vessel suspension systems because stainless steel has a low heat conductivity. The inner vessel of Dewars developed for space applications may be protected by both actively cooled and vapour-cooled radiation shields. To reduce the pace at which the cryogenic liquid evaporates, radiant heat transmission is collected by the shields and sent outside the system. Graphite-epoxy and glass-epoxy composite straps are used to support the inner vessel within the outer vessel.

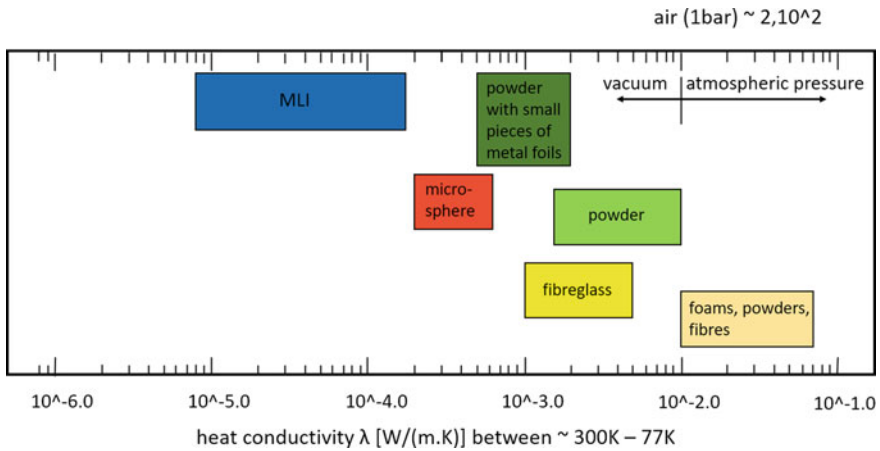
### 2.2 Types of Insulation

The shielding possesses distinguishing characteristics that may be weighed against its cost and design constraints. Total heat conductivity of the insulation is the most essential of these parameters. Porosity, humidity, flammability, evaluability and emissivity should also be taken into account [2]. Insulation used in the storage and transmission of cryogenic liquids can simply be classified as follows:

1. Only vacuum
2. Microsphere insulation
3. Evacuated powders and fibrous materials
4. Opacified powders
5. Aerogel insulation
6. Microsphere insulation
7. Expanded closed-cell foams
8. MLIs
9. Gas-filled powders and fibrous materials.

The insulations are listed above in order of increasing performance, and generally, increasing cost. The specific insulation to be used for a particular application is determined through a compromise between costs, ease of application, weight, ruggedness, availability and so on, in addition to the effectiveness of the insulation. It cannot be stressed upon enough, but selection of the correct type of insulation for the correct

application is perhaps the single most important aspect of the cryogenic equipment set-up (Fig. 1; Table 2).



**Fig. 1** Diagram comparing thermal conductivity of various insulation methods

**Table 2** Different types of insulation

Insulation type	Characteristics	Examples
Expanded foams (mass)	<ul style="list-style-type: none"> <li>• Low-density cellular structure</li> <li>• Solid-gas matrix with void spaces</li> <li>• Only Solid Conduction</li> </ul>	Polyurethane foam, Polystyrene foam, rubber, silica glass
Gas-filled powders and fibrous materials (mass)	<ul style="list-style-type: none"> <li>• Gas conduction is primary and dominant</li> <li>• Disjoins solid conduction</li> <li>• Low k, Low density, Rammed insulation</li> </ul>	Fibreglass, silica powder, santocel, rockwool
Evacuated powders (mass + vacuum)	<ul style="list-style-type: none"> <li>• Vacuum = <math>10^{-3}</math> to <math>10^{-5}</math> Torr</li> <li>• Solid conduction and radiation</li> </ul>	Fine and coarse perlite, lampblack, fibreglass
Opacified powders (mass + vacuum + reflective)	<ul style="list-style-type: none"> <li>• Flakes of Al and Cu added to evacuated powders</li> <li>• Tiny radiation shields</li> <li>• <math>K_A</math> reduced by 5 times</li> </ul>	Cu santocel (60%) Al santocel (40%) Cu $\gg$ Al
Radiation shields (reflective)	<ul style="list-style-type: none"> <li>• Emissivity factor reduced by radiation shield of high reflectivity and low emissivity</li> <li>• As <math>N</math> increases, FN (effective emissivity decreases)</li> </ul>	Aluminium foils

### 2.3 Multilayer Insulation

Multilayer insulation is made up of alternate layers of low conductivity spacer material, such as fibreglass paper, Dacron fabric, or silk net and a highly reflective foil, such as aluminium or copper foil. Aluminized Mylar has essentially replaced the foil material, which was highly delicate and prone to developing pinholes when crinkled. A sheet of Mylar (polyester) that is 6–10  $\mu\text{m}$  thick has an aluminium reflective coating between 40 and 30 nm thick which is deposited by the method of vacuum deposition and is called aluminized Mylar. To avoid the brittle fibreglass paper separator, to separate the reflecting layers, some MLI utilize an embossed or crinkled sheet of aluminized Mylar [2] (Fig. 2).

P. Peterson of Sweden invented multilayer insulation for the first time in 1951. Since that time several investigators have studied various types of multilayer insulation analytically and experimentally with varying the reflector materials, spacer materials and temperature range (Fig. 3).

In multilayer insulation (MLI) blankets for low-temperature applications, materials of polyethylene terephthalate (PET or polyester) sheets that have been aluminized on both sides can be utilized as first surface mirrors. Low solar absorption and emittance are provided by these goods.

**Fig. 2** A photo showing cut section of LHe Dewar (from TIFR, Mumbai) revealing the inside multilayer insulation blanket and four VCS copper plates)



**Fig. 3** Double-aluminized Mylar and netting used as spacer

To be successful, pressures lower than 10 mPa must be evacuated for multilayer insulations ( $8 \times 10^{-5}$  Torr). A graph showing the relationship between residual gas pressure and the typical MLI's mean apparent thermal conductivity.

Experimental research on several MLI kinds was conducted by Bapat et al. [3]. The focus of these studies is on how the number of layers and layer density affect MLI performance. Aluminized Mylar (12  $\mu\text{m}$ ) and glass fabric (76.2  $\mu\text{m}$ ) were proven to be the ideal shield and spacer material combination after evaluating several combinations.

On this combination, more thorough studies are done. Theoretical values and experimental values of effective thermal conductivities are compared. As the number of layers increases, the heat flow rate decreases; however, the heat flow rate increases with an increase in layer density because an increase in layer density raises both the interstitial pressure and the contact pressure between the layers. With an accuracy range of 5–30%, we can estimate MLI performance.

#### ***2.4 Use of Vapour-Cooled Shields as MLI***

The VCS are typically copper sheets between 1 and 2 mm thick that are mounted to the Dewar neck at a certain location. In LHe Dewars, there must be adequate thermal contact between the helium boil-off vapour and the VCS. This occurs because the VCS diverts radiation that would otherwise strike the inner vessel (IV) and transfers the heat it collects to the neck. At the shield-neck junction, this heat is subsequently transferred to the vapour element (SNJ). As a result, the helium that has already been evaporated becomes heated and is released into the environment. The entire boil-off contained in the IV is thus decreased.

If a thermal shield is attached very near to LHe (to get lower shield temperature), He vapour will not get sufficient area to extract heat by convection therefore heat coming from thermal shield will be conducted to LHe through the neck instead of being carried away by He vapour. Lower shield temperature also increases radiation load from outer vessel to shield which in turn increases shield temperature. Therefore, there is an optimum position where a shield shall be attached to the neck to get minimum LHe evaporation. The same logic can be extended for multi-shields.

Calculating the neck size and ideal placement of vapour-cooled radiation shields (VCS) for the lowest possible NER of LHe requires an extension of the solution methodology algorithm which was proposed by Goyal and Attrey [4]. The vapour-cooled shield material is assumed to be copper sheets with a 1 mm thickness, while the neck material is assumed to be SS304L. It is assumed that layer density ( $N$ ) = 32 layers/cm for heat infiltration via SI. The effects of optimum positions, optimum positions on the NER, shield number, neck size and shield number for a liquid helium Dewar are quantitatively examined.

### 3 Thermal Design of Storage Vessel

#### 3.1 Assumptions Made for Thermal Design

1. Heat flow is assumed to be steady state.
2. Heat transfer between neck and vapour is considered to be laminar.
3. Funnelling effect is neglected.
4. The neck material is taken as G10 glass fibre tube, and MLI (reflector as aluminium foil and spacer as paper) acts as vapour-cooled shields.

#### 3.2 Main Focus of Thermal Design

Thermal design discussed in this paper gives a brief idea about MLI selection for helium cryostat, vacuum considerations, etc. A code has been developed to compute the temperature profile of glass fibre neck which plays an important role in layer-by-layer calculations of Heat leak. A proper approach to calculate heat leak by numerical method is also discussed.

#### 3.3 Optimization of Layer Density and Effect of Number of Layers on MLI

In addition to selection of materials for spacers and radiation shields, selecting a suitable density for its layers is important for the optimum performance of the blanket [5]. Heat transferred through the MLI is radiation dominated, therefore we have to put in a greater number of shields, but let's not put in an excessive number of layers because that will increase the solid conductance through the spacers between the radiation. There is a density for each MLI where the heat transmission is the least. Furthermore, increasing the layer density will result in a greater heat flow for a fixed number of layers, whereas for constant thickness of the MLI blanket, it will decrease till a specific, lowest point of layer density and then it will start increasing again due to increasing solid conductance. This lowest point is what we desire to calculate for optimum layer density. For instance, taking the perforated Lockheed equation it has quasi-empirical equations which consist of number of layers  $[N]$  and layer density  $[N]$ . For the purpose of layer density optimization, the heat flux is written in terms of thermal conductivity. The equation for double-aluminized Mylar and Dacron net is shown below, where Mylar has a perforation rate of 0.54%; using perforated Lockheed equation (Figs. 4 and 5).

$$q = \frac{C_S * N^{2.63} (\dot{T}_h - T_c)}{2 * (N + 1)} + \frac{C_S * \varepsilon * (\dot{T}_h^{4.67} - T_c^{4.67})}{N}$$

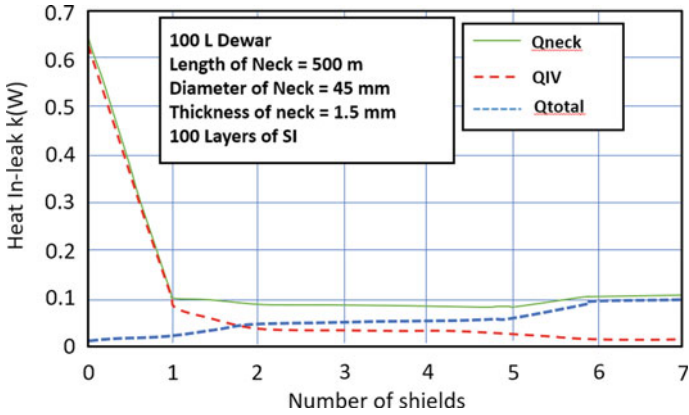
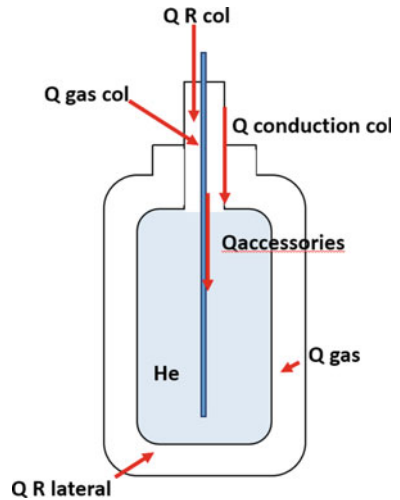


Fig. 4 A graph showing the effect of VCS on the heat leak

Fig. 5 Schematic diagram of heat in-leak sources in a Dewar



$$+ \frac{C_G * p * (\dot{T}_h^{0.52} - T_c^{0.52})}{N}$$

### 3.4 Heat Load Calculation

Modes of heat transfer in liquid helium Dewar:

$Q_{RLateral}$  = Heat loss due to radiation in lateral direction.

$Q_{Rcol}$  = Heat loss due to radiation in neck.

$Q_{\text{Cond}}$  = Heat loss due to conduction from neck.

$Q_{\text{gas}}$  = Heat loss due to Gas conduction.

$Q_{\text{gascol}}$  = Heat loss due to Gas conduction in neck.

$Q_{\text{acc}}$  = Heat loss due to accessories.

$$Q_{\text{Total}} = Q_{\text{Rcol}} + Q_{\text{Cond}} + Q_{\text{gas}} + Q_{\text{RLateral}} + Q_{\text{acc}} + Q_{\text{gascol}}$$

$Q_{\text{gas}} \sim 0$  (as vacuum is maintained between inner and outer vessel).

$Q_{\text{acc}}$  fixed by experiment.

$Q_{\text{gascol}} \ll Q_{\text{Cond}}$

$$Q_{\text{Total}} \text{ effectively becomes } = Q_{\text{RLateral}} + Q_{\text{Conduction col}}$$

First, we find  $Q_{\text{Lateral}}$

$$Q_{\text{RLateral}} = \frac{S_i}{\frac{1}{\epsilon_i} + \left(\frac{1}{\epsilon_e} - 1\right) \frac{S_i}{S_e}} \sigma (T_e^4 - T_i^4)$$

$$\sigma = 5.7 * 10^{-12} \frac{\text{W}}{\text{cm}^2} / \text{K}^4$$

Heat transfer between 2 neighbouring surfaces.

In general,  $T_i^4$  is negligible compared to  $T_e^4$ .

$S_i/S_e$  is in the interval between 0.5 and 0.9.

Layer-by-layer calculation has been done for each layer of radiation shield (MLI) and added up (Table 3).

$$Q_{\text{RLateral}} = 2.79 \times 10^{-5} \text{W}$$

For  $Q_{\text{Conduction col}}$  (Heat loss due to conduction from neck)

A computer program has been developed on SciLab software as shown in Fig. 6 [7] (Table 4).

$$Q_{\text{Conduction col}} = 0.056 \text{ W}$$

$$Q_{\text{total}} = Q_{\text{RLateral}} + Q_{\text{Conduction col}} = 0.056279 \text{ W}$$

**Table 3** Calculation of heat loss due to radiation ( $Q_{RLateral}$ )

POS. from base	Temp for 20 div	Radiation	$Q$
0	40	0–1	1.60E–07
1	48.347438	1 and 2	2.40E–07
2	55.985966	2 and 3	3.30E–07
3	63.091529	3 and 4	4.40E–07
4	69.775242	4 and 5	5.50E–07
5	76.113558	5 and 6	6.70E–07
6	82.16204	6 and 7	7.90E–07
7	87.962671	7 and 8	9.30E–07
8	93.548116	8 and 9	1.10E–06
9	98.944389	9 and 10	1.20E–06
10	104.17261	10 and 11	1.40E–07
11	109.2502	11 and 12	1.50E–06
12	114.19171	12 and 13	1.70E–06
13	119.00947	13 and 14	1.90E–06
14	123.71402	14 and 15	1.00E–06
15	128.31443	15 and 16	2.20E–06
16	132.81862	16 and 17	2.40E–06
17	137.23349	17 and 18	2.60E–06
18	141.56517	18 and 19	2.80E–06
19	145.81906	19 and 20	3.00E–06
20	150		2.79E–05

## 4 Conclusions and Discussions

1. A detailed literature review of the multilayer insulation is done, and the vessel is initially insulated as per the MLI specification for the thermal calculations. A proper approach for insulation method including vacuum conditions, insulation material, insulation technique and heat in-leak calculations has been discussed.
2. Method for thermal design calculations has been discussed.
3. Temperature profile of glass fibre neck has been calculated using SciLab code considering the material thermal properties and its variation with temperature.
4. Further, to decrease the heat in-leak anchoring of layers of multilayered insulation is found useful with respect to temperature gradient of the neck.
5. A numerical model will be finally employed for determining the optimization of VCS.
6. Total boil-off as per heat leak calculations is 1.6% of vessel capacity, and this value will be decreased; when the numerical model for thermal design of neck using VCS is developed, at present calculations considering only neck conduction are used.



clc();		67.099867
clear();	//Obtain the initial temperature	69.727056
//Inputs	profile	72.299573
n=input("no of divisions=");	for j=1:4000 do	74.821204
l=input("enter the length of neck in m=");	for i=2:n	77.295315
d1=input("enter the internal diameter of neck=");	t(i)={((Acn/dy)*t(i+1)+k(i)+t(i-1)*k(i-1))}/((Acn/dy)*(k(i)+k(i-1)));	79.724910
d2=input("enter the outer diameter of neck=");	k(i)=10^(-	82.112691
t(1)=input("temperature at neck base at bottom k=");	2.64827+8.80228*(log10(t(i))-	84.461092
t(n+1)=input("temperature at the neck face top k=");	24.8998*(log10(t(i)))^2+41.1625*	86.772320
//Areas and constants	(log10(t(i)))^3-	89.048381
dy=(l/n);	39.8754*(log10(t(i)))^4+23.1778*(log1	91.291106
Acn=(%pi/4)*((d2)^2-(d1)^2);	0(t(i)))^5-7.95635*(lo	93.502170
//initialise the properties	g10(t(i))^6+1.48806*(log10(t(i)))^7-	95.683112
for i=2:n+1	0.11701*(log10(t(i)))^8);	97.835350
t(i)=150;	end	99.960192
end	end	102.05885
for i=1:n+1	end	104.13244
	for i=1:n	106.18201
	q(i)=(k(i)*(t(i+1)-t(i)))*Acn/dl;	108.20854
	end	110.21293
		112.19603
		114.15863
k(i)=0;	disp (t, 't=')	116.10147
end		118.02527
//temperatures calculations	disp (q, 'q=')	119.93068
for i=1	INPUT and Result -	121.81831
	no of divisions=50	123.68876
		125.54258
k(i)=10^(-	enter the length of neck in m=0.4	127.38029
2.64827+8.80228*(log10(t(i))-	enter the internal diameter of	129.20239
24.8998*(log10(t(i)))^2+41.1625*	neck=0.048	131.00934
(log10(t(i)))^3-	enter the outer diameter of	132.80160
39.8754*(log10(t(i)))^4+23.1778*(log1	neck=0.054	134.57959
0(t(i)))^5-7.95635*(lo		136.34371
g10(t(i))^6+1.48806*(log10(t(i)))^7-	temperature at neck base at bottom	138.09434
0.11701*(log10(t(i)))^8);	k=40	139.83186
end	temperature at the neck face top	141.55661
for i=n+1	k=150	143.26893
	<b>Results</b>	144.96913
	40.	
k(i)=10^(-	43.428279	146.65751
2.64827+8.80228*(log10(t(i))-	46.721681	148.33438
24.8998*(log10(t(i)))^2+41.1625*	49.897552	
(log10(t(i)))^3-	52.969552	"t= 150."
39.8754*(log10(t(i)))^4+23.1778*(log1	55.948735	
0(t(i)))^5-7.95635*(lo	58.844231	"q= 0.0564421"
g10(t(i))^6+1.48806*(log10(t(i)))^7-	61.663714	
0.11701*(log10(t(i)))^8);	64.413717	
end		

Fig. 6 SciLab code to calculate temperature profile of neck heat leak due to conduction

**Table 4** Aspects of thermal design

Reflector (radiation shield)	Aluminium foils (one side polished)
Number of layers	20
Spacer	Paper
Vacuum	$10^{-5}$ Torr
Neck material	Glass Fibre (G10)
Length of neck	400 mm
Adhesive used for joining neck and aluminium vessel	Stycast epoxy

## References

1. Timmerhaus KD, Flynn TM (2013) Cryogenic process engineering
2. Barron RF (1985) Cryogenic systems
3. Bapat SL, Narayankhedkar KG, Lukose TP (1990) Experimental investigations of multilayer insulation. [https://doi.org/10.1016/0011-2275\(90\)90235-5](https://doi.org/10.1016/0011-2275(90)90235-5)
4. Goyal M, Attrey M (2016) Optimum design of liquid helium Dewar with vapour cooled shields
5. Johnson WL (2010) Optimization of layer densities for multilayered insulation systems
6. <https://neel.cnrs.fr/en>
7. Goyal M, Menon RS, Singh T (2012) Development of vapour shielded liquid helium Dewar. Cryo-Technology Division, Bhabha Atomic Research Centre, Trombay, Mumbai

# Static Analysis of a Low-Pressure Stage Blade of a Steam Turbine Using ANSYS



Pooja Rani and Atul Kumar Agrawal

**Abstract** Under normal working conditions, the turbine blades are subjected to a steam load and centrifugal force. The steam load acts on the blade surface in the form of a pressure load. This steam load does, in fact, have dynamic components. The flow dynamics of the steam as it travels past the rotating blades cause the steam loading to fluctuate over time. The measurement of these time-varying steam loads, on the other hand, necessitates specialised instrumentation. The steam loading acting on the pressure side of the turbine blade is presumed to be constant with time due to lack of data about the time-variable nature of the steam load. So, a static analysis of the turbine blade subjected to this pressure loading is carried out in this study.

**Keywords** Steam pressure load · Stress evaluation · Finite element analysis

## 1 Introduction

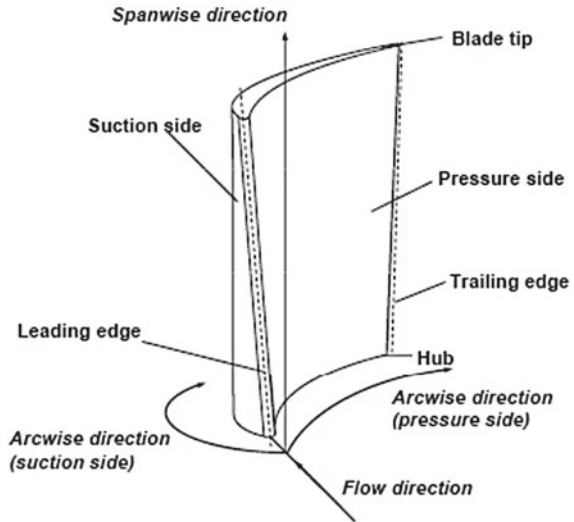
In a thermal plant, the blades of a steam turbine are the critical components, as they are subjected to high pressure and temperature. Most of the power plant failure occurs due to blade failure. So, the blade and its root design are the most important task. Stress evaluation is a very important factor for blade design [1]. There has been a history of stress failure in steam turbine low-pressure stage blade rows. Due to centrifugal force generated by high spinning speeds, along with steam forces, they are susceptible to tensile and bending strains [2]. The root of a 0.9-m-long low-pressure turbine blade is subjected to a centrifugal force of 3000 rpm, which results in nominal stress of 120 MPa [3]. Sadanandam et al. analysed the stress distribution at different rotational speeds and found that the rotor's speed and stress are intimately related [1]. Static stress analysis of turbine blade was conducted by Prabhunandan and Byregowda to check static and fatigue strength [4].

Excessive stress can reduce the useful life of rotating blades and endanger turbo-machinery safety, especially the last stages' blades of turbines, where the steam forces

---

P. Rani (✉) · A. K. Agrawal  
Delhi Technological University, Delhi, India  
e-mail: [pooja1322.ymca@gmail.com](mailto:pooja1322.ymca@gmail.com)

**Fig. 1** Steam turbine blade terminology [4]



can greatly increase rotating blade stresses. As a result, predicting the strength performance of the rotating blades is of tremendous practical significance in the design of wet steam turbines [5]. Gukendran et al. performed the static structural analysis of a wind turbine blade for different materials to look at the blade structure's performance qualities [6].

The blades of turbines are designed with a safety margin in mind, and calculating blade stresses can help you understand how they perform in real-world situations [3]. Knowing how important it is to understand the forces and stresses acting on turbine blades, we will estimate the stresses at a last-stage low-pressure (LP) blade and root of a large steam turbine rotating at 3000 rpm in this exemplar. Steam turbine blade terminology is shown in Fig. 1.

In this paper, the static stresses that occur due to steady steam force and centrifugal force on a low-pressure stage steam turbine blade in service are discussed. Total deformation, equivalent Von-Mises stress, maximum shear stress and directional deformations are measured on the turbine blade materials, and the results are reported.

## 2 Structural Analysis Using ANSYS

A 3D model of the blade of the turbine has been developed using solid works based on the technical drawings. The steam turbine blade is then imported into ANSYS to perform structural analysis. The geometric model of the steam turbine blade is shown in Fig. 3 with the zoomed view of the root section. ANSYS auto-meshing tools are used to build a triangular surface mesh, followed by volumetric meshing. There are 808,878 nodes and 529,431 elements in the developed finite element model. The

**Table 1** Properties of blade material

Modulus of elasticity (N/m <sup>2</sup> )	2.15e+11
Poisson’s ratio	0.31
Density (kg/m <sup>3</sup> )	7750
Shear modulus (N/m <sup>2</sup> )	8.2061e+10
Tensile strength (N/mm <sup>2</sup> )	800–950
Bulk modulus (N/m <sup>2</sup> )	1.886e+11

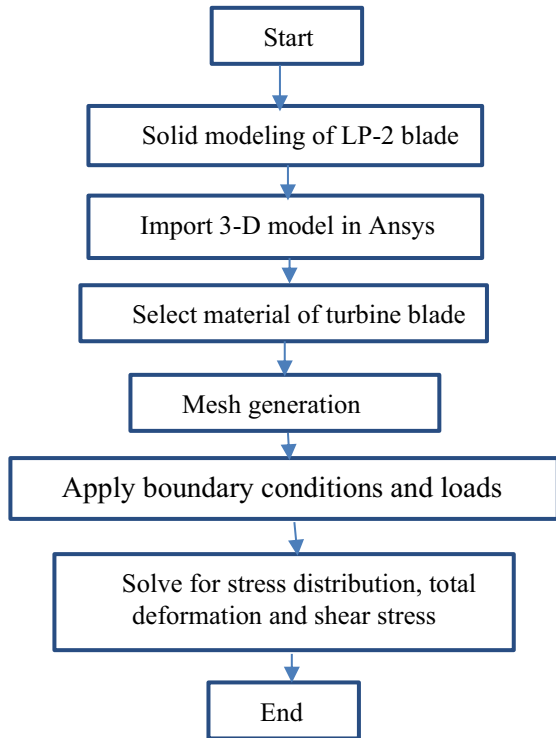
**Table 2** Steam turbine blade dimensions (bounding box size)

Dimensions	Turbine blade
Length X	0.116 m
Length Y	8.6311e–002 m
Length Z	0.49495

meshed model is shown in Fig. 4. Tables 1, 2 list the material qualities and dimensions of the turbine blade. A flowchart of FEA analysis is shown in Fig. 2.

Boundary conditions used for analysis are provided by the plant and are listed in Table 3. The equivalent steam load is applied in the form of pressure force. The

**Fig. 2** Flowchart for FEA analysis



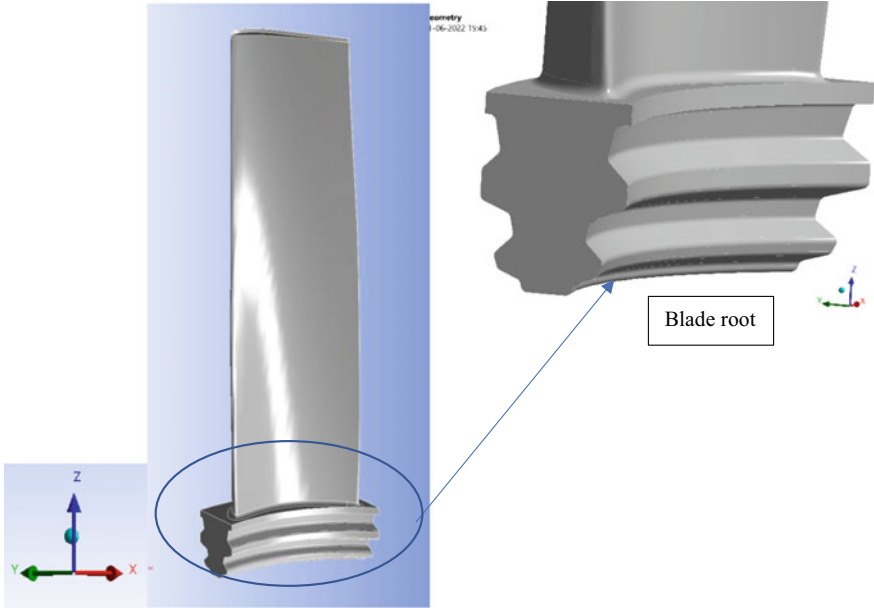


Fig. 3 Geometrical model of steam

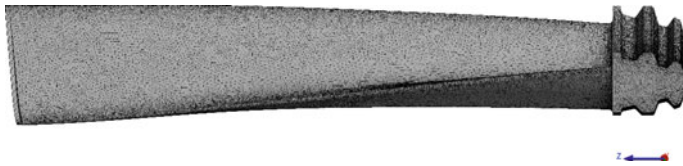


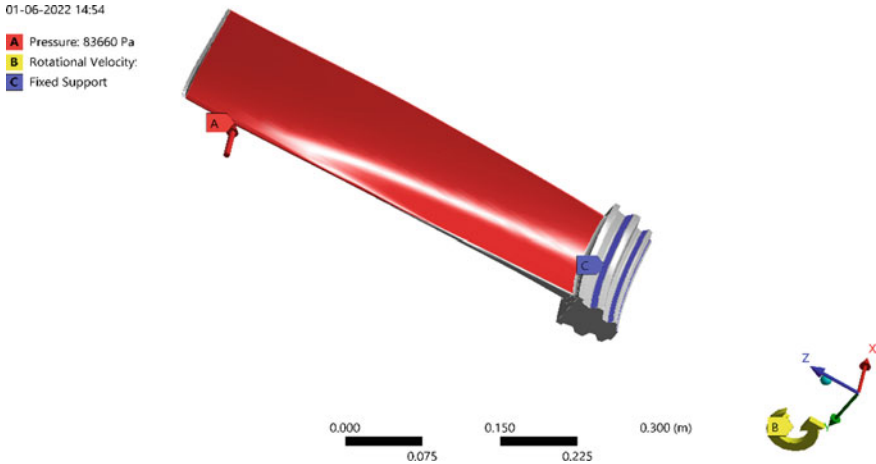
Fig. 4 Meshed view

pressure side of the turbine blade was considered to have a homogeneous distribution of this equivalent steam load.

Figure 5 depicts the boundary and loading conditions applied to the turbine blade for analysis. Fixed support was employed to provide a boundary condition at the fir-tree section of the turbine blade. The last stage steam turbine blade revolves at

Table 3 Boundary conditions

Type	Load and support location	Value
Fixed support	Applied at the root of the blade	
Rotational velocity	Applied to the whole body	3000 (rpm)
Steady steam load	Applied at the pressure side of the blade	83,660 (Pa)



**Fig. 5** Loading conditions for stress analysis of steam turbine blade

3000 rpm, with a steam pressure of 83,660 pa contacting the leading edge of the turbine blade. The axis of rotation is at a distance of 0.7 m from the blade root.

The next sections illustrate the results of ANSYS and the readings received. Maximum and minimum parameter values for the blade material under investigation are discovered.

For the evaluation, these factors are taken into consideration:

- Equivalent von Mises stress;
- Maximum principal stress;
- Directional deformation;
- Total deformation.

### 3 Results and Discussion

ANSYS workbench was used to analyse a turbine blade comprehensively.

The contour plot of the von Mises stresses on turbine blades owing to the above loading is shown in Fig. 6. At the position at the root of the rotor blade, the maximum von Mises stress of 220 MPa is measured. Also, it was noticed that the area where the material’s cross section is smaller results in increased stress. The maximum and minimum total deformation values are 2.49 mm and 0.277 mm, as shown in Fig. 7. It can be seen that the deformation increases as we move towards the tip of the blade, and maximum deformation occurs at the tip.

The directional deformation in X, Y and Z is 1.96 mm, 1.52 mm and 0.30 mm, respectively, as shown in Fig. 8. It can be concluded that the maximum directional deformation occurs in the X-direction. At the tip of the blade, there is a maximum displacement of 1.96 mm transversely, which is quite minor. The maximum shear

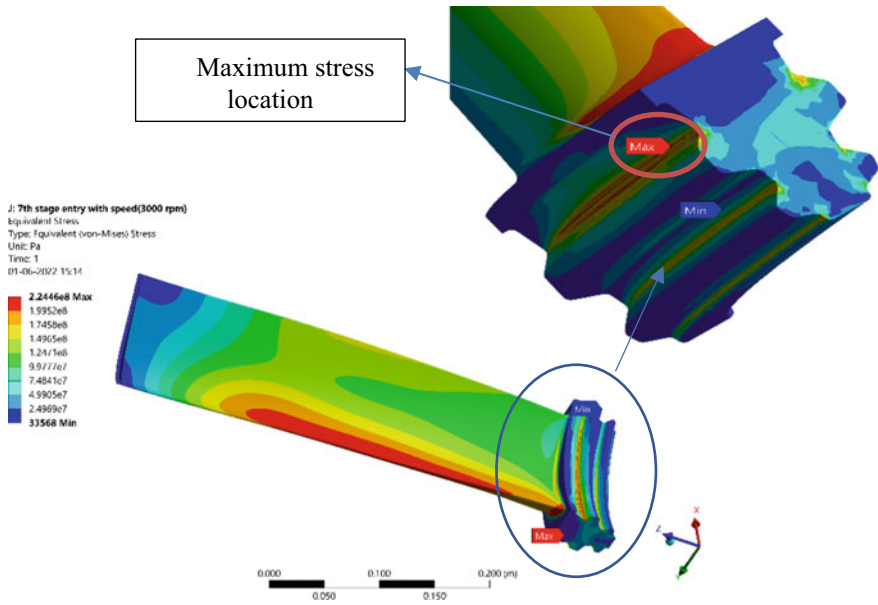


Fig. 6 Von Mises stress plot of steam turbine blade

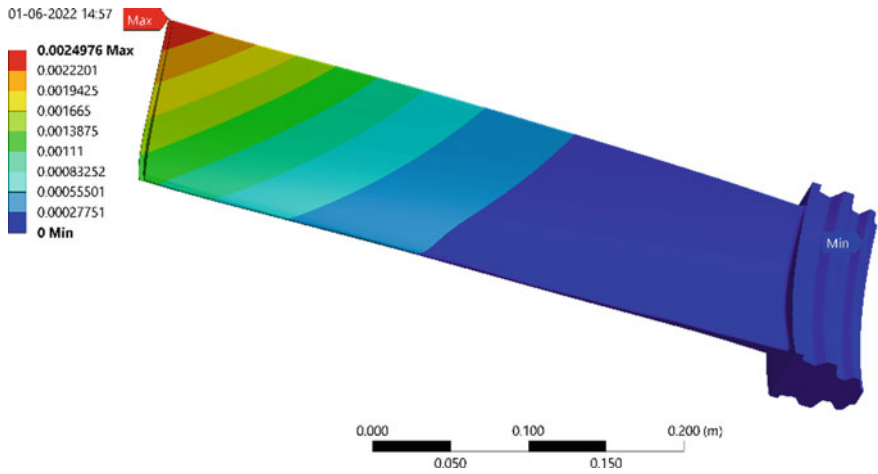


Fig. 7 Total deformation in steam turbine blade

stress calculated by FEA under the applied loading for the blade is 126 MPa, shown in Fig. 9, which is within the acceptable limit.



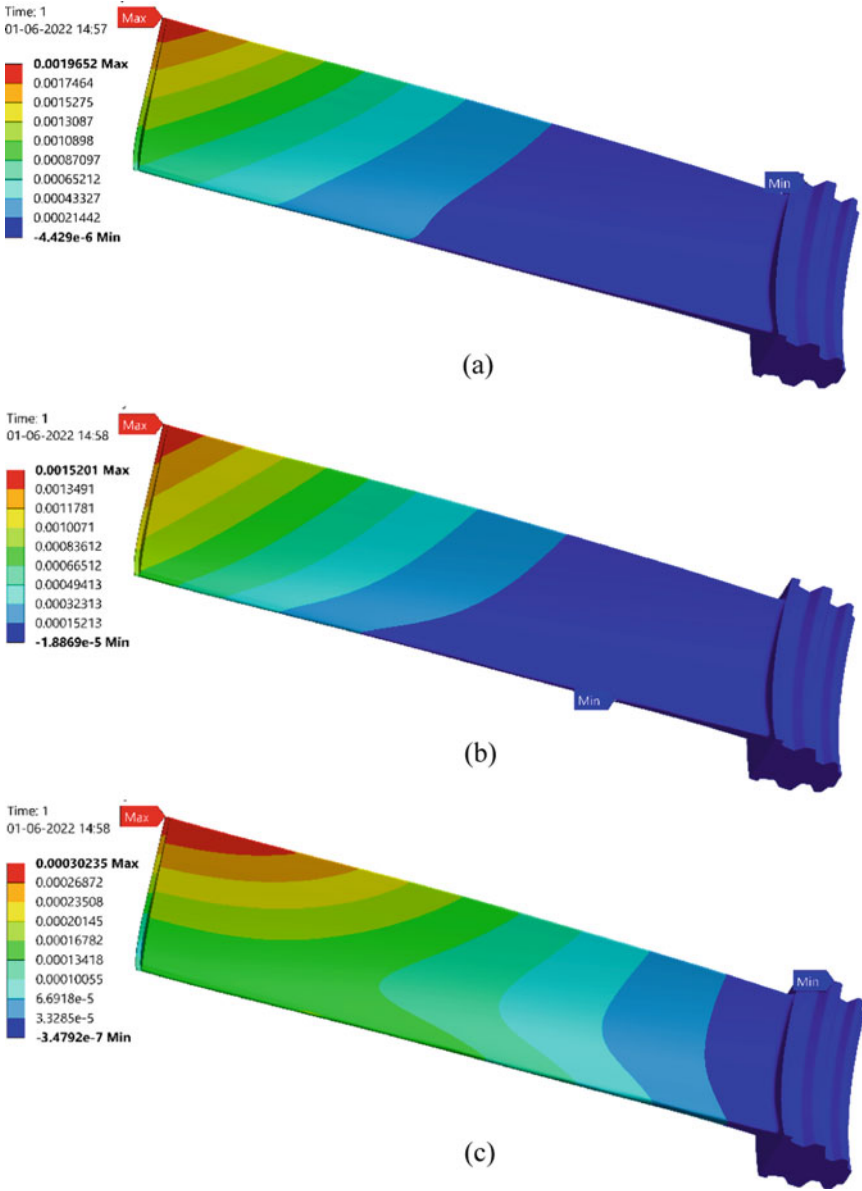
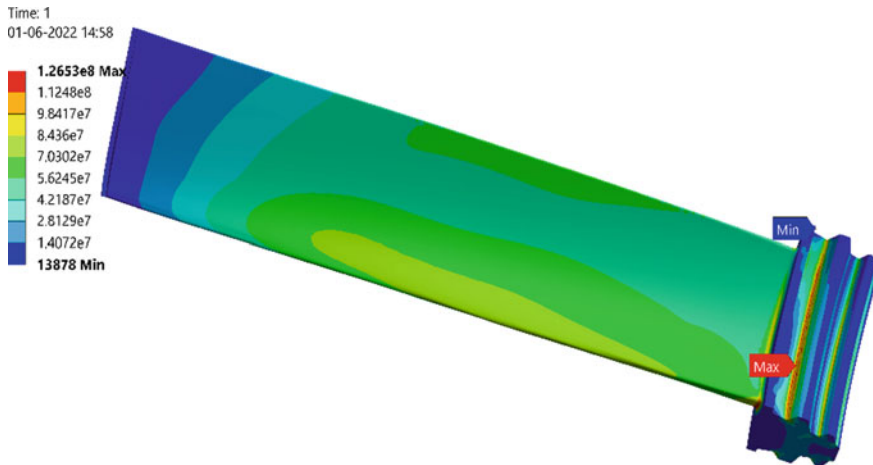


Fig. 8 Deformation a X-direction. b Y-direction. c Z-direction



**Fig. 9** Maximum shear stress

## 4 Conclusions

The turbine blade was analysed for stress evaluation under operating conditions. The crucial region or crack zone on the blade was determined using static stress analysis. It can be seen from the ANSYS results that the maximum stressed zone is near the blade root. So, it can be concluded that the area near the blade root is the crucial region for cracking under the action of stresses generated because of the loading and boundary conditions detailed above. It can also be seen from the results that the maximum total deformation of the steam turbine blade is 2.49 mm. Turbine blade deformation due to applied loading can also be seen in three different directions.

## References

1. Sadanandam P, Srinivas Reddy P, Timmapuram VS (2021) Stress distribution on turbine blade along with root at several operating speeds. IOP Conf Ser Mater Sci Eng 1057:012026. <https://doi.org/10.1088/1757-899x/1057/1/012026>
2. Al-Taie A (2008) Stress evaluation of low-pressure turbine rotor blade and design of reduced stress blade. Eng Tech 26(2)
3. RWE Npower (2008) Forces on large steam turbine blades. R Acad Eng 4. Available: [http://www.raeng.org.uk/education/diploma/maths/pdf/exemplars\\_advanced/22\\_Blade\\_Forces.pdf](http://www.raeng.org.uk/education/diploma/maths/pdf/exemplars_advanced/22_Blade_Forces.pdf)
4. Prabhunandan GS, Byregowda HV (2016) Static and fatigue analysis of a steam turbine blade. Int J Latest Technol Eng V(6):3989–3996. Available: [www.ijltemas.in](http://www.ijltemas.in)
5. Saxena S, Pandey JP, Solanki RS, Gupta GK, Modi OP (2015) Coupled mechanical, metallurgical and FEM based failure investigation of steam turbine blade. Eng Fail Anal 52:35–44. <https://doi.org/10.1016/j.engfailanal.2015.02.012>

6. Gukendran R, Sambathkumar M, Sabari C, Ranjith Raj CR, Ranjeeth Kumar V (2022) Structural analysis of composite wind turbine blade using ANSYS. Mater Today Proc 50:1011–1016. <https://doi.org/10.1016/j.matpr.2021.07.341>

# Behavioral Simulation of Biological Neuron Using VHDL



Sarthak Sharma and V. K. Tomar

**Abstract** In this proposed work, the piecewise linear approximation technique has been used to get a simpler digitally implemented hardware, i.e., a biological neuron with a nonlinear activation function. This design included the sigmoidal function that has been utilized as an activation function. In this artificial model, the neuron is able to distinguish between the two input attributes in terms of their weights. The suggested digitally implemented neuron hardware could be utilized as a fundamental building component in the creation of a general digital network of neurons or neural networks. The inputs are formatted in a specified way, which is required for the piecewise linear approximation technique. The text of the paper includes an overview of the fundamental component required as well as issues encountered during the design of neuron architecture.

**Keywords** Digital hardware implementation · Artificial neural network · Sigmoidal function · Piecewise linear approximation

## 1 Introduction

In the last two decades, artificial neural networks (ANN) have acquired popularity in a wide range of applications like recognition and classification of patterns, controlling techniques, and artificial perception. Artificial neural network architectures are possibly implemented in analog or digital [1, 2]. The sigmoidal function can be created and replicated through analogue implementation by utilizing a trans-conductance amplifier's function or another equivalent circuit, which does not require a large amount of silicon [3]. On the other hand, the implementation of analogue frequently suffers from noise sensitivity and drift issues. However, physical constraints inherent in the chosen technology limit the neural connection model

---

S. Sharma · V. K. Tomar (✉)

Department of Electronics and Communication Engineering, GLA University, Mathura, India

e-mail: [vinay.tomar@gla.ac.in](mailto:vinay.tomar@gla.ac.in)

implementation on digital technology. For the digital applications, there are three major obstacles to consider:

- (a) The network's interconnection complexity in many circumstances and ONb2c connections [4] are required.
- (b) The enormous size of storage space needed to store weight.
- (c) Synchronization between process blocks.

These problems get major attention and become the thrust area of research. In this work, the authors have mainly concentrated on the complexity of the circuit and their interconnections which required large space and synchronization to process input and output. Authors have proposed the architecture of neuron with necessary modification and used bit level logic. A lot of research works [5–10] have also been reported to design static random access memory cells which are being utilized in the embedded processor to process the data at a very high speed. In this proposed work, neuron structure in digital hardware domain along with the behavioral architecture has been explained in detail. Behavioral architecture consists of a finite state machine, addition and accumulation, counter, register, multiplier, multiplexers, de-multiplexers and an activation function.

The rest of the paper is organized in the following manner. Section 2 describes the detailed architecture of the proposed neuron. The associated weight and activation function are explained in Sect. 3. VHDL synthesis and simulation results are discussed in Sect. 4. Finally, Sect. 5 presents the concluding remarks.

## 2 Architecture

The block diagram of the proposed neuron is shown in Fig. 1. In this diagram, different blocks are connected to each other in such a manner that the output of one block is input of other one or more blocks.

The blocks involved in the diagram are basic and can be understood by their names also. Here, FSM objectives to control the synchronization between the blocks by generating the signals of different pulses in such a way to make the system more synchronized and strict to the timing for many actions are carried out by a neuron. The defined input signals used to initialize the neuron circuit are  $a_1$ ,  $a_2$  and  $w_1$ ,  $w_2$ . Further, various input signals like START, CLK, END and RESET are used in FSM to initiate all the process blocks in the circuit. CLK acts as the basic timing clock for block triggering. When RESET signal is activated to high level, everything in FSM becomes stop. The START signal permits the neuron to start work again when RESET signal is low. Every signal is multiplied with its own corresponding weight and sent to the multiplier block for multiplication using a multiplexer circuit. The obtained every multiplication results are added to another result for further processing till the end of the operations. The FSM makes the activation function module get its accumulated output, when the most recent multiplication is done. In this manner, multiplexers along with counter 0–1 are employed to transfer the inputs along with

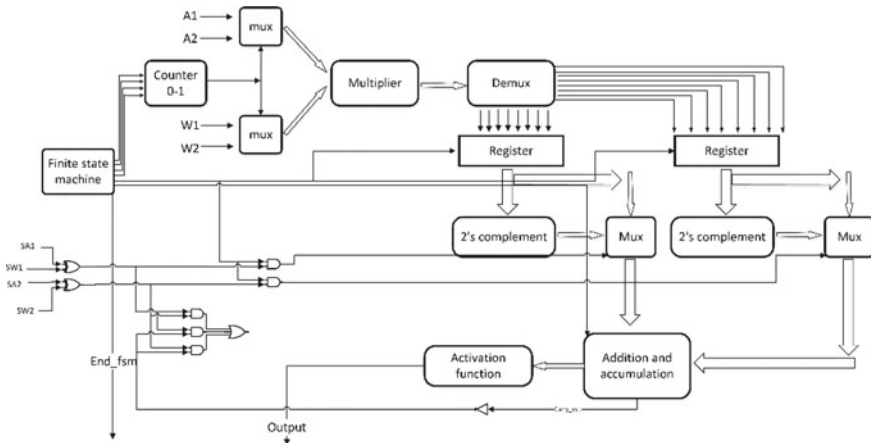


Fig. 1 Architecture of proposed neuron

their weights one by one to the multiplier block for multiplication. After this process, they are distributed by de-multiplexer to their registers to store till the FSM enables the register to transfer the result to accumulator. A counter 0–1 is employed to work with two inputs, whereas for three inputs, counter 0–2 will be utilized as illustrated in Fig. 2.

The multiplier is employed in such a way that it will provide 8 bits output due to the input of addition block which is required to be 8 bits. The cumulative results with its sign are placed into the activation block to obtain its equivalent sigmoidal output. A gate-level logic circuit is employed with sign bits like positive for logic ‘0’ and negative for logic ‘1’ along with their accompanying weights i.e. SA<sub>1</sub>, SW<sub>1</sub>, SA<sub>2</sub> and SW<sub>2</sub> as shown in Fig. 3. The inputs and their weights are independently processed for their sign convention with the help of a logic circuit of two Ex-OR gates and two AND gates. This circuit assists in making the correct decision when multiplication of any integer with a weight gives digital HIGH and the two’s complemented value

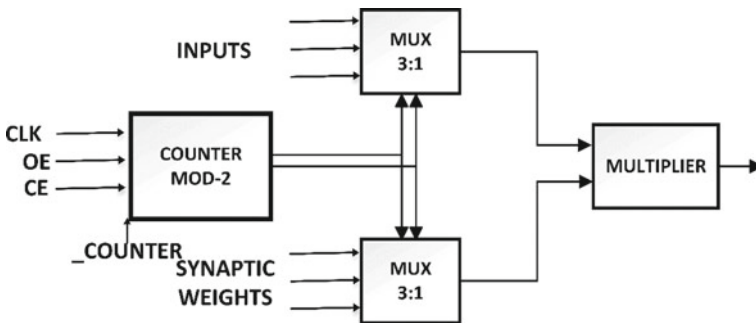
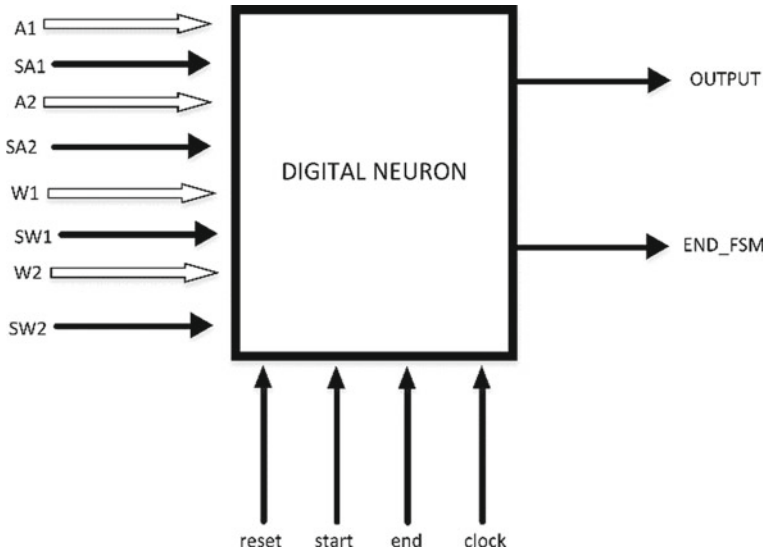


Fig. 2 Counter connection for a three-input port neuron



**Fig. 3** Raw design of circuit integrated on a single piece

of the output must be added to the accumulator. The most difficult part in creating the neuron is remembering to maintain the track of sign, i.e., digital LOW as + ve and digital HIGH as – ve for the processed number received from the accumulation block.

This is due to the sign required, when feeding the number into the sigmoid block. To resolve this situation, a logic circuit is used consisting of three AND and one OR gate [4]. The carry generated through the accumulator is used to maintain the sign of output of activation block. Finally, the FSM generates the end\_fsm signal to end the circuit function.

### 3 Activation Function and Weight

The relevance of each feature is conveyed through associated weights to determine the most accurate output. While processing the inputs according to weights, inputs with lower weights are less important than those with higher weights. Weights are very important for orientation of the separation line that lie between the stimulus and attributes.

- The value of weights indicates the relevance of the input feature.
- Its value is the relationship among the input attribute and desired value.

A sigmoid function is a frequent form of nonlinear function which is presented by Eq. (1), where  $x$  represents the input and  $y$  denotes to sigmoidal output. This sigmoid

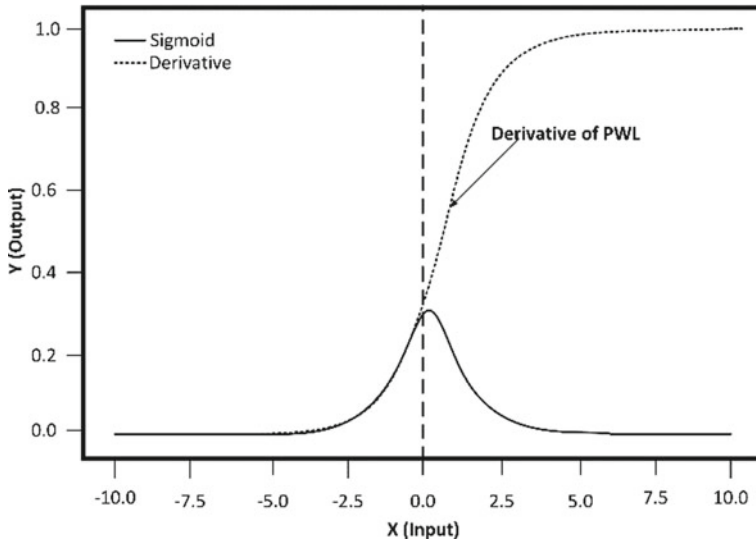


Fig. 4 Approximation using sigmoid function

function remains less complex in differential form as presented by Eq. (2).

$$y = \frac{1}{1 + e^{-x}} \tag{1}$$

$$\frac{dy}{dx} = (1 - y). \tag{2}$$

In digital implementations, multiple techniques can be used to get the sigmoidal approximation. Using the piecewise linear approach, the approximated sigmoidal function is illustrated in Fig. 4.

## 4 VHDL Synthesis, Simulation and Results

The proposed work is implemented with Xilinx ISE simulator. Figure 5 shows the technology schematic of the artificial neuron. FSM module has four inputs like clock, start, reset, end function and seven outputs. The six output ports are connected to other blocks and one output port, i.e., end\_fsm, gives logic high ('1') when all process is done. Further, this block is responsible for generating six different timing clock signals that could synchronize the blocks together by triggering them on the rising edge of their separate clock. The counter module has four input ports and one output port. Its inputs are derived through FSM that processes the output. This block is responsible for counting 0–1, and it is used in the diagram to input attributes



with their respective weights with no synchronization problem, as both the inputs attributes have their separate destination.

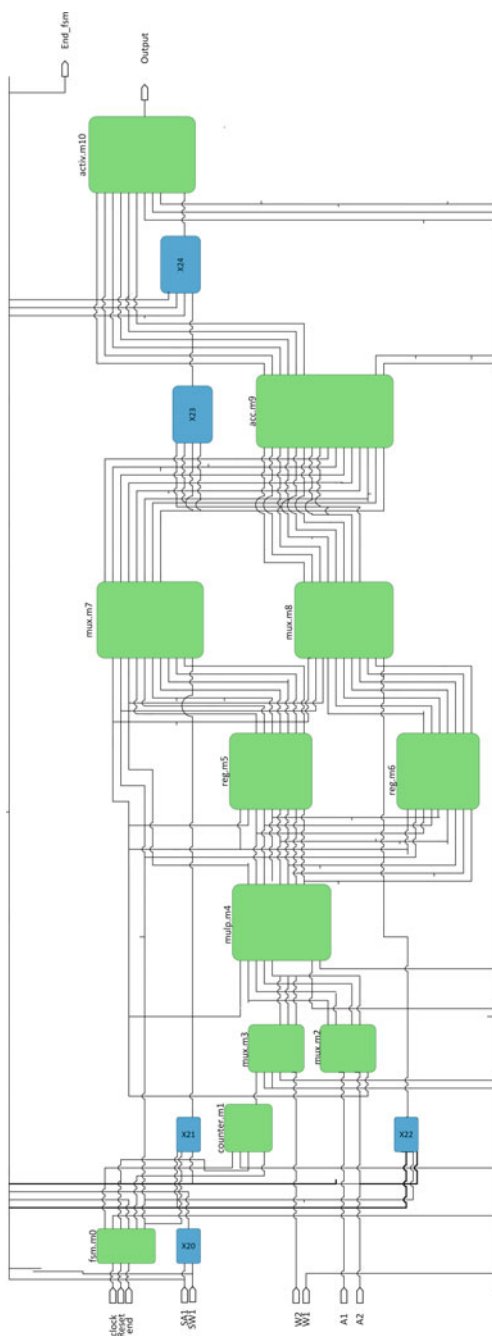
Mux/multiplexer block has three input ports and one output port. The inputs can be applied either from the user directly (if it is four-bit  $A_1, A_2, W_1, W_2$  mux) or may be applied from another block. Its output will be one selected input which is forwarded accordingly. Multiplier block has two input ports and one output port. The inputs are applied through multiplexer blocks. This block is responsible for the multiplication of the input attribute with its weight. Demux/de-multiplexer block has two input ports and two output ports. The input will be coming from multiplier blocks. This block is responsible for distribution output product of multiplier block to the registers according to the clock input.

Register block has two input ports and one output port. The input is applied through de-multiplexer block. This block is responsible to hold the multiplied results till the time it is called from the next block. Two's complement block has one input port and one output port. The input is applied through the register block. This block is responsible for two's complementing input binary code. The addition and accumulation block has three input ports and one output port. The inputs are applied through the mux block. This block is responsible for adding the input binary codes and accumulated results separately.

Activation function block has two input ports and one output port. The input will be coming from addition and accumulation block and logic gates. This block is responsible for applying sigmoidal function over the input. Figure 6 shows the simulated test bench for all the set of input vector. In this simulation test bench, values and inputs are defined with two separate synoptic values. It is interesting to note that all the signals are working according to expecting behavior, and the desired output is achieved at the second last position with an indication of end\_fsm.

## 5 Conclusion

In this work, the authors have simulated the behavior of a digital neuron with a piecewise linear approximation technique. The functions implemented in this simulation are basic mathematical functions. The sigmoidal function is used as an activation function to drive the output and subsequently added and accumulated. The simulated neuron behavior shall be useful in the development of a neural network.



**Fig. 5** Technology schematic of artificial neuron

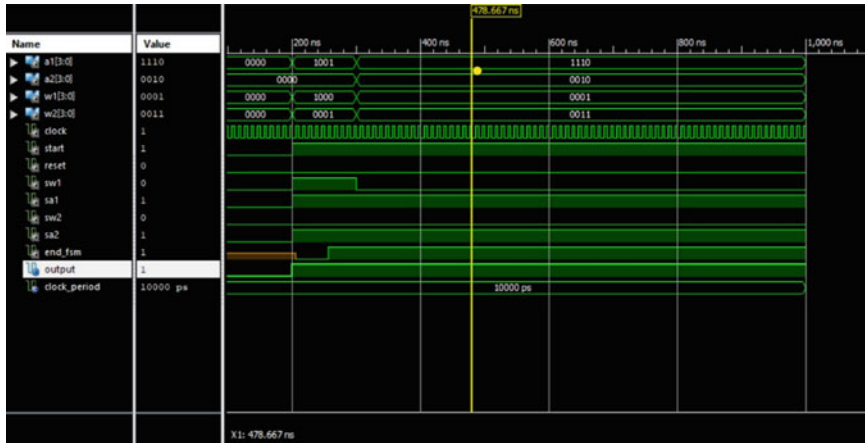


Fig. 6 Simulated waveform

## References

1. Teo SY, Ong SE (2020) Artificial neuron hardware IP verification. In: 2020 IEEE 29th Asian test symposium (ATS). IEEE, pp 1–2
2. Fan D, Shim Y, Raghunathan A, Roy K (2015) STT-SNN: a spin-transfer-torque based soft-limiting non-linear neuron for low-power artificial neural networks. *IEEE Trans Nanotechnol* 14(6):1013–1023
3. Faiedh H, Gafsi Z, Besbes K (2001) Digital hardware implementation of sigmoid function and its derivative for artificial neural networks. In: ICM 2001 proceedings. The 13th international conference on microelectronics. IEEE, pp 189–192
4. Mishra A, Raj K (2007) Implementation of a digital neuron with nonlinear activation function using piecewise linear approximation technique. In: 2007 International conference on microelectronics. IEEE, pp 69–72
5. Yadav V, Tomar VK (2022) A low leakage with enhanced write margin 10T SRAM cell for IoT applications. In: Lenka TR, Misra D, Biswas A (eds) *Micro and nanoelectronics devices, circuits and systems*. LNEE, vol 781. Springer, Singapore, pp 201–211
6. Bansal S, Tomar VK (2022) Simulation and analysis of 11T SRAM cell for IoT-based applications. In: Dhar S, Mukhopadhyay SC, Sur SN, Liu CM (eds) *Advances in communication, devices and networking*. LNEE, vol 776. Springer, Singapore, pp 329–340
7. Bansal S, Tomar VK (2022) Challenges & security threats in IoT with solution architectures. In: 2022 2nd International conference on power electronics & IoT applications in renewable energy and its control (PARC). IEEE, pp 1–5
8. Singh T, Tomar VK (2022) Post simulation of high speed sense amplifiers using 45 nm CMOS technology used in IoT application. In: 2022 2nd International conference on power electronics & IoT applications in renewable energy and its control (PARC). IEEE, pp 1–6
9. Sharma R, Goswami A, Tomar VK (2021) Review: parametric variations in analog-to-digital converters using different CMOS technologies. In: Goyal V, Gupta M, Trivedi A, Kolhe ML (eds) *Proceedings of international conference on communication and artificial intelligence*. LNNS, vol 192. Springer, Singapore, pp 101–110
10. Kumar V, Tomar VK (2020) A comparative performance analysis of 6T, 7T and 8T SRAM cells in 18 nm FinFET technology. In: 2020 International conference on power electronics & IoT applications in renewable energy and its control (PARC). IEEE, pp 329–333

# Flexible Manufacturing System By Mechanized Guided Vehicles Through Genetic Algorithms Approach



Aman Sharma and Rishabh Chaturvedi

**Abstract** Mechanized guide vehicles are one of the many innovative methods of handling materials that are being developed daily. Other processing and storage devices may be used to interact with and operate an intelligent computer control system. Multiple low-volume components may be processed at once by FMS. The FMS components must work together, and the planning issue has become more complicated. Mechanized guide vehicles are increasingly being used in today's lines of work. The improved material transfer quality is the goal of the present initiative, which intends to boost output by 20%. Machine control is still required in many applications, despite the advancements in MGV technology. The preparation of MGVs and the scheduling of activities on machine centers are critical to the overall productivity of the FMS. A genetic algorithm (GA) method is used to finish this task in a particular FMS environment. Mechanized guided vehicles greatly assist in material handling during loading and unloading. Analytical and numerical methods are used to estimate loading/unloading in a material handling system using MGV. In an MGV multi-load behavior, more than one job can be completed. When using a flexible production system, the dispatching rule is used to transmit the product.

**Keywords** FMS · MGV · Genetic algorithm · Control system · Numerical methods

## 1 Introduction

Productivity and versatility are the key goals of today's automation systems. A well-planned and well-maintained material handling system is required for this necessary integration. Mechanized-driven trucks are one of the fastest-growing equipment

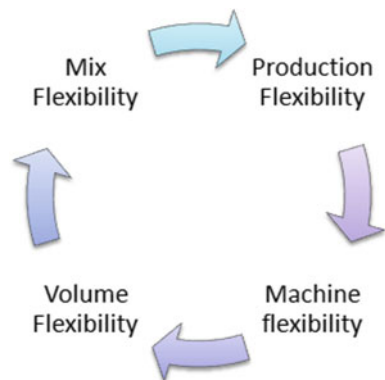
---

A. Sharma (✉) · R. Chaturvedi  
Department of Mechanical Engineering, GLA University, Mathura, India  
e-mail: [aman.sharma@gla.ac.in](mailto:aman.sharma@gla.ac.in)

R. Chaturvedi  
e-mail: [rishabh.chaturvedi@gla.ac.in](mailto:rishabh.chaturvedi@gla.ac.in)

types in the material handling sector [1, 2]. They are self-driving, battery-powered vehicles that can program and position themselves. They can be easily adapted to rapidly changing transportation trends and integrated into fully automated smart control systems. Mechanized guide cars (MGVs) are increasingly being used for material transportation in modern manufacturing plants' production lines. The aim is to increase demand while improving the efficiency of material transport. Although MGv hardware is improving, software for controlling a convoy of MGVs remains in many areas lacking [3–5]. The aims of this study are as follows: figure out how many MGVs are needed for complete supply control and come up with and evaluate different rules for the transportation of personnel carrying MGVs. We join guidelines for managing complex shipping regulations in terms of material quality and DP delivery continuity. The design is then scheduled to divide the entire region into special zones, to minimize route distribution among the MGVs and hence avoid difficulties, one was created for each. To reduce the panic outcome, attempts are made to simultaneously reflect on the arrangements of the FMS system and vehicle and in the analytical and numerical phases, to focus on the problem. The programming deals with the distribution of time to task resources and is a decisive mechanism that connects processes, time, costs, and the company's overall purpose [6–10]. In today's mechanized manufacturing environments, FMS is flexible and adaptable. FMS is suitable for processing a wide range of low-volume component types quickly. Workstations, mechanized, and MGVs are all part of an FMS. Figure 1 illustrates different methods of treating materials. Planning becomes more complex because the FMS components can operate asynchronously. Furthermore, the networks are tightly coupled, and the aggregation incorporates a diverse set of components and alternative routings. It is possible to improve FMS's productivity [11–13].

**Fig. 1** Flexible manufacturing system



## 2 Genetic Algorithm

The machining optimization problem necessitates the use of a powerful search tool. First and foremost, the genetic algorithm approach was chosen because of its robust and well-organized operations. Second, several disciplines are increasingly concentrating on GA. John Holland, on the other hand, was present [14–16]. They wrote a book called "Adaptation in Artificial and Natural Systems," which explained both of the most important ideas behind GA systems today. In his schematic theory, he explains how easy it is to change bit strings and how this can also be done in animal populations with the right amount of control. Goldberg maintains an extensive list of GA-related posts [17–19].

### 2.1 Operations of GA

Consider the problem

$$\begin{aligned}
 & f(x) \text{ minimization} \\
 & x_i^{(L)} < x_i < x_i^{(U)}, \quad i = 1, 2, \dots, N.
 \end{aligned}
 \tag{1}$$

### 2.2 Coding

Before being described in equations using GAs, the variables  $x_i$  are encoded (1). GAs are used directly on the variables in certain tests.

For example, if each variable in Eq. (2) is coded with four bits, the points will be represented by the strings (0000 0000) and (1111 1111).

$$(X1^L, X2^L)(X1^U, X2^U)
 \tag{2}$$

Lowest decoded values of the sub-strings (0000) and (1111). A fixed mapping rule can generate any number of eight-bit strings to represent a search field. The linear mapping rule described below is widely used.

$$x_i = x_i^L + \left[ x_i^u - \frac{x_i^L}{2^{(Li-1)}} \right] * \text{Decoded values of (Si)}
 \tag{3}$$

The vector  $x_i$  is coded with the length  $Li$  sub-string in the preceding Eq. (3).  $2jbj$  is the  $Si$  binary sub-string decoding value, where  $bj$  can be 0 or 1 from the string. In this case,  $j$  is a number ranging from 1 to  $Li$ , and each variable has four bits for coding;

there are either 24 or 16 distinct sub-strings since the value for each bit position is 0 or 1.

### 2.3 Fitness Function

GAs use a “survival of the fittest” design to carry out a quest operation. The  $F(x)$  fitness function is derived from  $f(x)$  and then used in genetics. Some genetic operators require a positive fitness function, even though this is not a requirement for others. Fitness function is

$$F(X) = 1/(1 + f(X)) \quad (4)$$

String fitness refers to the fitness of a string.

### 2.4 Generation

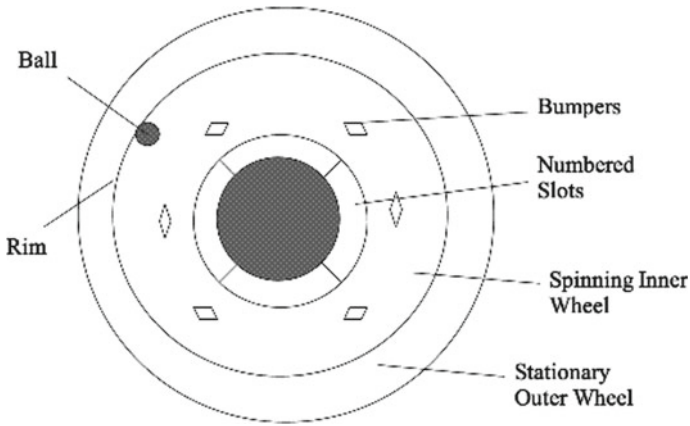
The fitness value for each string is computed. The population is then repeated, crossover, and mutated by three key operators to create a new population of dots. Additional estimations and monitoring of the new population were performed [20]. If no termination criteria, such as highest generation or predefined fitness are met, the population will be run and evaluated iteratively by the aforementioned operators. The assessment process described below is known as a gene one loop of these operations [21].

#### 2.4.1 Operators of GA

Operator 1: (Reproduction)

Figure 2 portrays a roulette wheel with five people on it, each of whom receives a different health gain. Since the third person is more competent than the others, the roulette wheel is supposed to favor the third person over the others. The scheme of this roulette-selection wheel is easily simulated. The fitness value  $F_i$  of all strings can be used to compute the probability of choosing a string  $P_i$ . Following that, the likelihood grew [22–24].

A string is then copied into the matching pool, which represents the random number selected from the string’s total range (evaluated based on the fitness values in Table 1).



**Fig. 2** Roulette wheel

**Table 1** Fitness range

Points	Fitness
1	25
2	5
3	42
4	10
5	18

**Table 2** Representing crossover

Parents	Before crossover	After crossover
1	00000	00111
2	11111	11000

Crossover

The crossover operator generates new strings by transferring information among the strings in the mating pool. There are several different types of crossover operators that can be found in GA literature. It is common practice to choose two strings from a pairing pool at random, then exchange the first few numbers in each string. To execute a single-point crossover, all the bits on the right side of the crossing location are switched. The crossover is given in Table 2.



### *Mutation Operator*

The mutation operator flips from 1 to 0 when there is a low risk of mutation and vice versa when there is a high chance of mutation (pm). The mutation is carried out in stages by flipping a coin with the following probability:

- Select a random number from 0 to 1. After a coin toss, only if the random number is less than pm will the result be right.
- If the result is right, the bit will be distorted; if the result is incorrect, the bit will remain unchanged. The need for mutation stems from the need to establish a point in the current neighborhood and search for the current solution locally. Mutation is also used to keep populations diverse.
- In the above population, all four strings have a 0 at the leftmost point. If the best solution in this situation is 1, they cannot produce 1 using either the replication or crossover operators described above. The only way out is to use the mutations operator.

## **3 Flexible Manufacturing System Forecasting**

### ***3.1 Material Handling System***

A mechanized guided vehicle (MGV) is a mobile robot commonly used to take loads in material handling systems (MHS). Material handling is a process, or a combination of processes, services, initiatives, and equipment used to transport, cover, and store products to achieve specific goals. Furthermore, in recent years, a material handling model has developed. Material handling is described as the movement of materials from the beginning to the end of an operation. Material handling, on the other hand, is not solely described.

Technology associated with material handling has changed. Computerization and automation are being implemented. Today, we have a greater understanding of the importance and function of material processing. Figure 3a–c shows the material handling system. Productivity and adaptability may be achieved in fully integrated material handling settings using modern automation technology's major goals. From the above overview, the material can be conveyed in three types:

- Freely moving
- With fixed position
- Cranes.

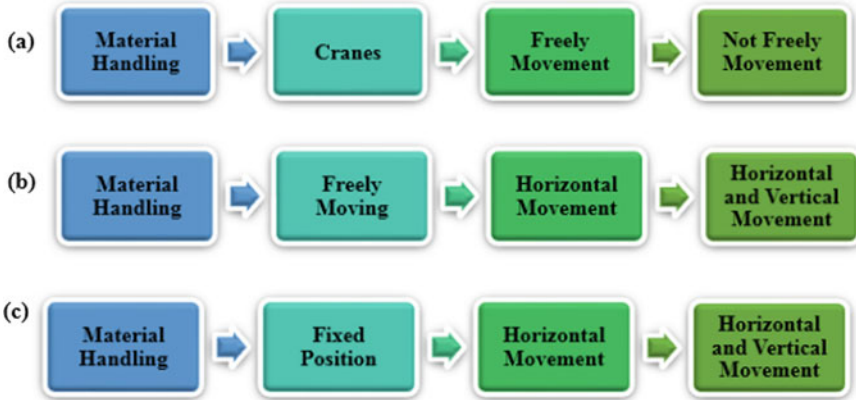


Fig. 3 a–c Classification of material handling system

### 3.2 Dispatch Rules

The timestamp of the DP shows how long it takes for its stock to vanish if no other supply enters. Where  $k$  is the DP’s consumption rate, the current stock amount is ‘ $x$ ’ units, and the time scales are calculated by  $T = x/k$ . These shipping regulations determine which DPs will be served by the MGVS when the next trip begins. The distribution and production of materials were highly manipulated. Direct and indirect dispatches are the two types of dispatch.

- This rule indicates that all MGVS capabilities should be given to the DP with the greatest priority for MGVS operation. MGVS will deliver all plastic container stacks to this one DP, with the same load.
- There will be several destinations for the MGVS under this provision. The MGVS conveyor bay number is assigned to this code. The following are the four guidelines: in all, there are four laws.
- MD1: MGVS prioritizes three DPs and feeds them on the same train, which is split into three parts for each DP. When visiting DPs, the minimum order of MD-travel is followed.

- MD2: In this situation, MGV chooses three DPs, the first with the highest priority, the second and third from reasonable competitors to keep travel to a minimum.
- MD3: Similar to MD2, but the MGVs only recognize the top six qualifying candidates (in order of priority).
- MD4: To optimize the ordering ( $p * L$  separated by MD-travel), MGV chooses the order for three DPs from the top six qualifying contenders (there are  $6P$  3 such commands). The focus here is on 'p,' and the 'L' represents the SD trip of the selected DP.

This dispatch rule aims to eliminate the distortions in MD2/MD3 by weighting the goals with SD flight.

### 3.3 Gain Scheduling Roles in Problem

In combinatorial optimization, the genetic algorithm (GA) is a stochastic search approach that uses natural selection and genetics to find the best solution. A GA is a collection of methods that, when repeated, solves a given issue. GAs produce successive populations of different solutions until an acceptable solution is identified. Individuals with a specific chromosome are subject to genetic operations, crossover, and mutation based on their fitness and the individuals selected. In current populations, a small number of existing chromosomes are replaced by newly created chromosomes, and the population is formed.

## 4 Formulation of Problem

The following are some of the most common loading/unloading operational issues that material handlers face as a result of mechanized-driven vehicles:

- Define nodes and monitor parts on the floor, with a defined number of LPs and DPs and available areas for vehicle movement. Typical activity issues, preparation, and controls.
- Determine the number of MGVs needed to reach the prescribed DP customer levels.
- Create output parameters for a device using different dispatch rules. Making shipping rules for MGVs. A dispatch rule is a way to figure out which DPs will be served based on the current stock levels.
- MGVs are designed to be routed.

### 4.1 Analytical Process

By comparing the total TL-loaded vehicle to the total work time loading/unloading  $T_u$  and the entire  $T_e$ -Vacant (including idle/stretching), the MGVS problem can be solved. In other words, essential vehicle requirement  $V$  can be expressed mathematically (5).

$$V = (T_l + T_U + T_e) / T_a \tag{5}$$

$T_a$  denotes the overall effectiveness of the time frame in which a vehicle occurs in this observation and is set to be.  $T$  denotes the time interval for which car behavior is generated and denotes the following estimation models address some fundamental nomenclature principles. At the front center, when a work is ready to be processed by the system, Eq. (1) shows the  $k-l$  task flow.

$$F_{kl} = \sum_{l=1}^V VL \cdot \delta_{ikl} \tag{6}$$

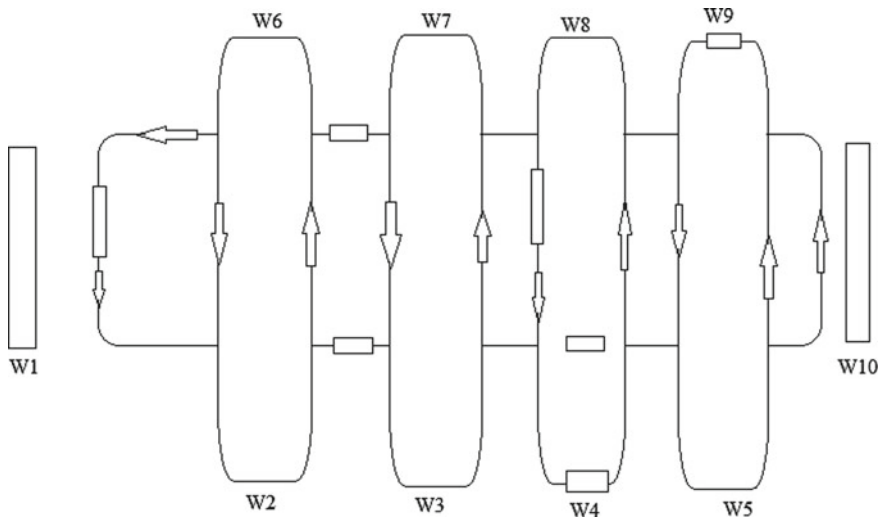
where  $l$  if center  $ll =$  is visited immediately after the visitation center  $k$ ; if this is not the case, a value of 0 is given. As a result, when the employment rate is computed as seen in the equation, the total number of workers  $mkl$  shifts from the midpoint  $k$  to the half point,  $mkl$  is the estimated number of cargo journeys (pick-ups) in a single load MGVS from midpoint  $k$  to midpoint  $l$ . As a result, as seen in the equation, the total workload/discharge time required for vehicles can be calculated.

$$KI = \lambda, fkl, k, 1 = 1, 2 \dots M \tag{7}$$

$$Tu = (tu + tl) \cdot \sum_{t=1}^M m_{ij} \tag{8}$$

### 4.2 Numerical Process

A theoretical workshop production scheme was devised to evaluate the feasibility of the future model. The solution to this quandary is depicted in Fig. 4. It has a single-entry point (S1), a single exit point (S10), and eight processing centers (S2, S3, S4, S2, S6, S7, S8, S9), for a total of  $M = 10$ . Each processing center has three of the same equipment. In the center, there is an endless production queue and an infinite input queue. If it is assumed that another row has infinite potential, it will most likely inspect the maximum airfield needed to accommodate the WIP in the production path.



**Fig. 4** Layout of an illustrative system

## 5 Result and Discussion

According to Table 3, when job arrival rate  $\lambda = 40jh - 1$  and job movement  $T = 480$  min, then the total minimum time is taken for the process and conveyed by a mechanized guided vehicle. In the Table 3, the output of entrance center S1 is the input of center S2 and, respectively, for another process. After that, the result shows we put minimum input (160) and get maximum output (1952) jobs. Determination of a suitable conveying process is an important issue in a flexible manufacturing system for loading and unloading material by using MGCV. The operating efficiency of a random system is difficult to determine due to the various loading and distribution points. In this study, the genetic algorithm method was used on the previously used decision variables. These studies aimed to estimate the vehicle requirement in material handling systems for multiple loads/unload MGCV. A new bulk and multi-load/unload MGCV model, as well as several simple models to support a single MGCV load/unload, were proposed. Two factors are used in this new model: the power consumption factor for charging/unloading vehicles and the additional transport factor for employment. In this analysis, they were both probable in terms of experiential and rough values. To monitor the process of MGCV, it is useful to investigate moving freely, fixed locations, or cranes in material handling systems. Different vehicle dispatch rules apply in a load/unload situation, for example. The distribution points that the MGCV will use when it begins its next journey are determined by the dispatch rules. The efficiency and evenness of material distribution were heavily manipulated using different types of dispatch laws.

**Table 3** Job matrix showing movement

	W1	W2	W3	W4	W5	W6	W7	W8	W9	W10	Total
W1	–	0	0	64	32	96	64	32	32	0	320
W2	0	–	0	64	0	0	64	0	32	0	1601
W3	0	32	–	32	0	0	0	32	0	32	128
W4	0	0	32	–	32	32	32	0	64	32	224
W5	0	32	0	32	–	32	32	0	32	0	160
W6	0	32	32	0	0	–	32	96	32	64	288
W7	0	32	0	0	32	64	–	32	0	96	256
W8	0	32	32	32	0	32	0	–	0	96	224
W9	0	0	32	0	64	32	32	32	–	0	192
W10	0	0	0	0	0	0	0	0	0	–	0
Total	0	160	128	224	160	288	256	224	192	320	

## 6 Conclusion

In this work, there is one complex material handling problem with conveying the material from the loading point to delivery point through many operations, and solved by analytical and numerical processes. Mechanized guided vehicle (MGV) can be used to increase production in the limited period in different modern manufacturing industries. Mechanized guided vehicle (MGV) must be suitable for carrying the unit load as well as bulk load also. In the modern material handling system multi-loaded mechanized guided vehicle (MGV) is more appropriate for obtaining more output within a certain limit. Mechanized guided vehicle (MGV) makes plans for getting more accuracy in uniform distribution of material in warehouses. Multi-load mechanized guided vehicles are more economical, beneficial, and more accurate when compared with single load mechanized guided vehicles and man.

The following two aspects of the future’s scope can be considered:

Since the time required for transportation and setup is deemed constant, additional work can be completed while utilizing these resources. The work is regarded as being of the atomic nature. It is possible to accomplish more work by arranging timetables for the production of various components using various machines.

## References

1. Lyu X, Song Y, He C, Lei Q, Guo W (2019) Approach to integrated scheduling problems considering optimal number of automated guided vehicles and conflict-free routing in flexible manufacturing systems. *IEEE Access* 7:74909–74924
2. Chawla VK, Chanda AK, Angra S, Rani S (2019) Effect of nature-inspired algorithms and hybrid dispatching rules on the performance of automatic guided vehicles in the flexible manufacturing system. *J Braz Soc Mech Sci Eng* 41(10):1–17

3. Karimi B, Niaki STA, Haleh H, Naderi B (2018) Bi-Objective optimization of a job shop with two types of failures for the operating machines that use automated guided vehicles. *Reliab Eng Syst Saf* 175:92–104
4. Jiang Z, Yuan S, Ma J, Wang Q (2021) The evolution of production scheduling from Industry 3.0 through Industry 4.0. *Int J Prod Res*:1–21
5. Fazlollahtabar H, Saidi-Mehrabad M (2015) Methodologies to optimize automated guided vehicle scheduling and routing problems: a review study. *J Intell Rob Syst* 77(3):525–545
6. Duinkerken MB, Ottjes JA, Lodewijks G (2006) Comparison of routing strategies for AGV systems using simulation. In: *Proceedings of the 2006 winter simulation conference*. IEEE, pp 1523–1530
7. Fazlollahtabar H, Rezaie B, Kalantari H (2010) Mathematical programming approach to optimize material flow in an AGV-based flexible job shop manufacturing system with performance analysis. *Int J Adv Manuf Technol* 51(9):1149–1158
8. Badakhshian M, Sulaiman SB, Ariffin MKABM (2012) Performance optimization of simultaneous machine and automated guided vehicle scheduling using fuzzy logic controller based genetic algorithm. *Int J Phys Sci* 7(9):1461–1471
9. Kumar A, Sharma K, Dixit AR (2020) Carbon nanotube-and graphene-reinforced multiphase polymeric composites: review on their properties and applications. *J Mater Sci* 55(7):2682–2724
10. Udhayakumar P, Kumanan S (2010) Task scheduling of AGV in FMS using non-traditional optimization techniques. *Int J Simul Modell* 9(1):28–39
11. Gondran M, Huguet MJ, Lacomme P, Tchernev N (2019) Comparison between two approaches to solve the job shop scheduling problem with routing. *IFAC-PapersOnLine* 52(13):2513–2518
12. Gutjahr M, Kellerer H, Parragh SN (2021) Heuristic approaches for scheduling jobs and vehicles in a cyclic flexible manufacturing system. *Procedia Comp Sci* 180:825–832
13. Shukla MK, Sharma K (2019) Effect of functionalized graphene/CNT ratio on the synergetic enhancement of mechanical and thermal properties of epoxy hybrid composite. *Mater Res Exp* 6(8):085318
14. Zhang L, Hu Y, Guan Y (2019) Research on hybrid-load AGV dispatching problem for mixed-model automobile assembly line. *Procedia CIRP* 81:1059–1064
15. Heger J, Voss T (2019) Reducing mean tardiness in a flexible job shop containing AGVs with optimized combinations of sequencing and routing rules. *Procedia CIRP* 81:1136–1141
16. Singh PK et al (2020) Effect of sonication parameters on mechanical properties of in-situ amine functionalized multiple layer graphene/epoxy nanocomposites. *J Scien Indus Res (JSIR)* 79(11):985–989
17. Islam A, Dwivedi V, Sharma K (2020) FEM analysis of robotized arc welded joint. *E3S Web Conf* 184:01032
18. Scholz M, Steinkamp J, Zwingel M, Hefner F, Franke J (2020) Distributed camera architecture for seamless detection and tracking of dynamic obstacles. *Procedia CIRP* 91:342–347
19. Singh PK et al (2020) Synthesis and characterization of carbon nanotube hydroxypropyl methylcellulose composites. *IOP Conf Ser: Mater Sci Eng* 988(1)
20. Herrero-Perez D, Matinez-Barbera H (2008) Decentralized coordination of autonomous AGV's in flexible manufacturing systems. In: *International conference on intelligent robots and systems*, pp 3674–3679
21. Anees VV, Nazar KP, Sridharan R (2021) Simulation modelling and analysis of due date assignment methods and scheduling decision rules in a flexible manufacturing system. In: *Advances in science and technology*, vol 106. Trans Tech Publications Ltd, pp 99–108
22. Zacharia PT, Xidias EK (2020) AGV routing and motion planning in a flexible manufacturing system using a fuzzy-based genetic algorithm. *Int J Adv Manuf Technol* 109(7):1801–1813
23. Tóth N, Kulcsár G (2021) New models and algorithms to solve integrated problems of production planning and control taking into account worker skills in flexible manufacturing systems. *Int J Ind Eng Comput* 12(4):381–400
24. Bányai T (2021) Optimization of material supply in smart manufacturing environment: a metaheuristic approach for matrix production. *Machines* 9(10):220

# Investigation of Two-Stage Epicyclic Gearbox for an Automobile for Energy Regeneration



Aditi Namdeo, Ashok Atulkar, and R. K. Porwal

**Abstract** This paper identifies the problem of discharge of a battery because of the frequent operation of brake lights in an automobile. This problem is solved through the investigation of a two-stage epicyclic gear train for a vehicle. The revolving axis of certain gears in mesh with numerous gears at the same time and co-axiality of input and output shafts are all properties of the epicyclic gearbox, which is commonly used in tractors, high-speed gas turbines, and construction equipment. In order to regenerate the energy that is emitted during the process of braking, an epicyclic gearbox is used, which uses the emitted energy to regenerate energy and produce electricity using a dynamo. This electricity is used to illuminate the brake lights. The automatic brake light ignition system is developed using the process of regeneration. The existing system requires a charge from the battery present in an automobile, in order to make the automobile futuristic and efficient. A small gearbox has been developed that operates during the time of braking only. The article examines a regenerative braking system, a clear mechanism that includes a dynamo, a planetary gear system, and brake lights as one of the key parts, while keeping size and weight restrictions in mind. Kinetic energy is converted into elastic potential energy in this system. In the system, mechanical energy is transformed into electrical energy. This electrical energy is used in brake lights to operate them and can be fed to the battery itself to recharge it.

**Keywords** Regenerative braking system · Modelling · Two-stage epicyclic gearbox · Brake · Lights

## 1 Introduction

Motion is transmitted by gears through the engagement of gear teeth, resulting in speed reduction and acceleration. The gears use the involute gear tooth profile, which is the most common gear tooth profile. These gears form a “gear train,” which is a

---

A. Namdeo (✉) · A. Atulkar · R. K. Porwal  
Department of Mechanical Engineering, SGSITS, Indore 452001, India  
e-mail: [namdeoaditi1309@gmail.com](mailto:namdeoaditi1309@gmail.com)

© The Author(s), under exclusive license to Springer Nature Singapore Pte Ltd. 2023  
R. Sharma et al. (eds.), *Advances in Engineering Design*, Lecture Notes in Mechanical Engineering, [https://doi.org/10.1007/978-981-99-3033-3\\_32](https://doi.org/10.1007/978-981-99-3033-3_32)

363



transmission system that uses a mating of gears to convey motion. The epicyclic gear train is used in places where we have to accomplish a substantial reduction in speed in a compact area.

An epicyclic gear train is commonly known as a planetary gear train. A planetary gear train employs the axes of relative motion to operate. It consists of four parts: the carrier, planet gear, ring gear, and sun gear. Planet gears are mounted on the carriers, and the planet gears are associated with the ring gear and the sun gear. The quantity of planet gear depends on the assemblage of the framework [1]. This planetary gear train is used to regenerate energy in an automobile using a dynamo. It is worth noting here that energy regeneration is a process of recovering and reusing wasted energy from conventional machinery. The energy is liberated during the braking process and wasted into the atmosphere. This wasted energy could be used in the generation of electricity. Regenerative braking mechanisms involve the transfer of the kinetic energy of an object in motion into potential energy to slow down the vehicle, resulting in an increase in fuel efficiency. The wasted energy from the process of slowing down a car is used in regenerative braking, which uses this energy to recharge the batteries of the car or operate the auxiliary parts. On the other hand, Hsu TR used flywheel-based regenerative braking for regenerative energy recovery, in which system recovers energy using a generator with intermittent rotary velocity [2].

In the present investigation, a system has been developed in which kinetic energy is converted into electrical energy using a dynamo, where the dynamo works as a reverse DC motor. This dynamo takes mechanical power and converts it into electricity. The generated electricity produced via the regenerative system can be used to operate auxiliaries in the vehicle. An epicyclic gear train can be employed in a variety of vehicles, such as all-terrain vehicles (ATVs). A gearbox was developed for the ATV. It is designed, analysed, and manufactured [3]. Peng et al. designed multiple degrees of freedom in functioning planetary gear train in which a technique is described for planetary gear trains (PGTs) with multiple operational degrees of freedom (DOFs) using the variable structure method to create a variety of speed ratios [4]. Regenerative braking is a technology that was designed for human-powered vehicles like bicycles, according to Khokhri et al. A regenerative braking system based on planetary gears and spiral springs has been developed [5]. A three-stage planetary gearbox has been designed for aeroplane use. The construction of a strategy to create an epicyclic gearbox is proposed and analysed in this work [6]. A unique actuator system was created by Lee and Choi for use in mobile robot applications. The proposed actuator system, which consists of dual motors and a planetary gear (DuPG), is known as the dual-motor system with a planetary gear (DuPG) [7]. On the other hand, Hwang and Huang put forward a synthesis to determine suitable clutch layouts for a particular planetary gear train clutching sequence. For the first time, the approach of creating coded diagrams for a planetary gear train is described [8]. A theoretical study has been proposed by Chen and Ling presenting the epicyclic gear train, a basic mechanical transmission with a wide range of applications. The study of these trains' efficiency is essential for their design, optimisation, and operation [9]. To reduce the design cost of planetary gear trains (PGTs) with torque converters, a methodical synthesis of seven-speed PGTs based on six-speed PGTs for heavy-duty commercial vehicles is

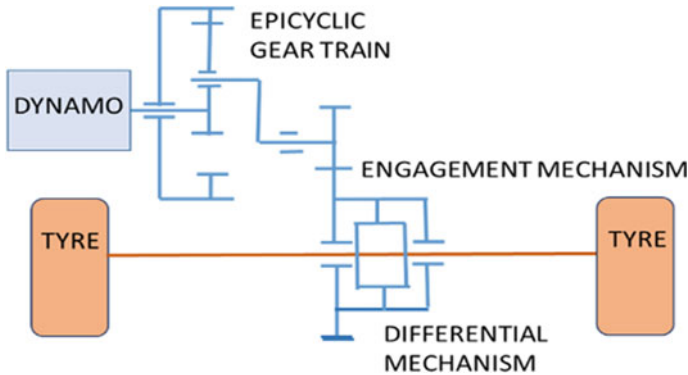
given [10]. In the process of developing an epicyclic gear train, a hybrid transmission system is developed under this research as a plug-in hybrid electric car solution [11].

Energy regeneration is majorly found in electric vehicles. A two-speed seamless transmission and regenerative braking algorithm are proposed in a research study for use in electric vehicles. The transmission is made up of two brakes, helical gear sets, and planetary gear sets with two stages [12]. In order to solve the range problem in an electric vehicle for energy regeneration, instead of an epicyclic gear train, a dual-clutch transmission system is used for braking power-on shifting control [13]. A dual-motor planetary gear transmission system has been developed to improve the efficiency of an electric vehicle. In this paper, two small motors are coupled through planetary gear employed in an electric vehicle, which is used for energy regeneration [14]. Electric vehicles have received a lot of attention in this trend. The trend of emission reduction and energy conservation. The research study that presents a way for a planetary gear electric powertrain's abrupt torsional oscillation reduction develops a novel regenerative braking technique [15]. Carlo and Mantriota suggested combining two electrical motors using a planetary gear train. The electric motors of the sun and the ring of the planetary gear perform at a higher efficiency than a single motor due to the combination of torques and speeds. In urban cycles, average efficiency increases by 9.34% with a single motor and by 11.6% during regeneration of power [16].

Much research has gone into the development of various epicyclic gear trains and much has been done in the area of modelling and analysis. In a dynamic analysis, Liu and colleagues used a hybrid model that combines reduced finite element models (FEMs) for the ring and carrier with lumped-parameter dynamic models for the sun and planets to study the flexible helical planetary gear [17]. This paper offers a generalised dynamic model for multi-stage planetary gear trains used in automatic gearboxes for automobiles. The forced vibration response to gear mesh excitations is obtained using the modal summation method [18]. Virtual power analysis is used to develop an analytical formula for the Simpson gear train's overall efficiency. When overall efficiency is 100%, this formula corresponds to intuitive [19]. As we have seen above, most of the regenerative braking development is done in the field of electric vehicles. As we are moving towards electric vehicles, we also need to update our traditional automobiles to fulfil the needs of the future and represent them efficiently in the market. After knowing all the cons of an electric vehicle, especially the negative effects of the batteries of an electric vehicle. It motivates us to update the features of conventional IC engine automobiles and make them sustainable products in the near future.

## 2 Methodology

The purpose is to eliminate the supply of battery voltage to the brake lights and to develop a regenerative mechanism that helps to absorb the waste kinetic energy during braking and uses it to regenerate electricity. With this power, the brake lights



**Fig. 1** Schematic of regeneration mechanism using epicyclic gear train in an automobile

work independently. There is no battery drainage due to the activation of the brake lights. This reduces battery drain by employing a two-stage epicyclic gearbox in an automobile to assure longer battery life. The devised engagement mechanism is smooth and efficient enough to convey kinetic energy from braking. The main purpose of the research is to develop a two-stage epicyclic gearbox. This gearbox is employed at the rear end of a car at the differential through an engaging mechanism. The first-stage ring gear of epicyclic gear is in mesh with engaging mechanism which imparts the acceleration from the rear axle to the ring gear, resulting in a large increase in the rotation of the sun gear. The sun gear of stage-1 is connected to the ring gear of stage-2, resulting in very high rpm along the sun gear of stage-2 of the epicyclic gearbox. This rpm is transmitted to the dynamo and rotates the axle along with the dynamo. This results in the generation of electricity along the dynamo. The dynamo is connected to the brake light, which results in illuminating the brake lights independently (Fig. 1).

### 3 Design Constraints

To develop a design for a gearbox for an automobile (XUV 500MT) which is run by an engine having the following specifications (Table 1).

**Table 1** Specifications of the vehicle XUV 500MT

Features	Value	Features	Value
Capacity	1997 cc	Tangential force	294 kN kg
Maximum torque	360 Nm @ 1750–2800 rpm	Weight of car	1860 kg
Maximum power	152.87 bhp @ 3750	Radius of wheel	0.3075 m
Acceleration	17.36 m/s <sup>2</sup>	Brake (HP)	313 kN kg
Time taken to reach 27.77 m/s-0 m/s	1.6 s		

Brake light—12 V; current—1.5 A; power—6 W  
 Dynamo model (GMP36-555PM); source—DC; voltage—12 V; power—16 W; RPM—1500

## 4 Design of Components of a Gearbox Assembly

### 4.1 Design of Gears

After the development of the engagement mechanism, the engagement mechanism is connected to the gearbox. The mechanism transmits the kinetic energy to the gearbox. The stopping distance of a car is 44.66 m, and the linear travel of a car is 1.9311 m.

$$\begin{aligned} \text{The rotation of the gear along the axle} &= \frac{\text{Stopping Distance}}{\text{Distance covered in 1 rotation}} \\ &= 44.66/1.9311 = 23 \end{aligned} \tag{1}$$

A dynamo is needed to operate at 1500 rotations per min.

$$\text{Gear Ratio} = \frac{\text{RPM of output}}{\text{RPM of input}} = 1500/23 = 64 \tag{2}$$

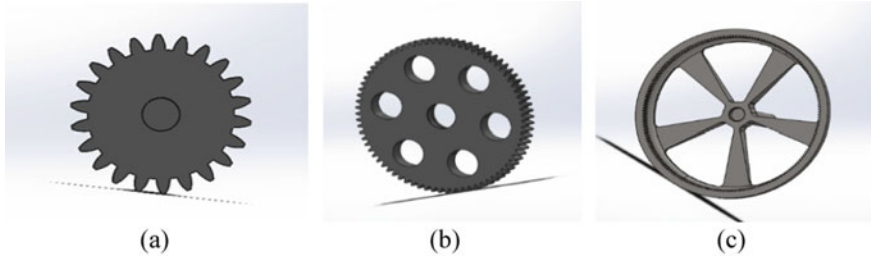
The carrier is being fixed, in order to achieve maximum rpm along the sun gear. Input is given to the ring gear, and output is obtained from the sun gear. Along with the sun gear of second stage, the axle of the dynamo is in mate, which transmits the increased rpm. Using the gear design process, iteration, and studying the above-mentioned mechanism, the number of teeth on the sun, planet, and ring gear is 22, 76, and 174, respectively, as the required gear ratio is 64.

In order to maintain the proper meshing between the gears, all the gears are taken to be of 2 mm module, 20° full-depth involute profiles, and a face width of 12 mm. Two planet gears are chosen as ideal combinations in order to reduce tangential forces. Along with weight reduction, the combination is easy to assemble and disassemble with the set of two planet gears.

- Calculating the diameter of a gear using module and number of teeth (Table 2):

**Table 2** Value of diameter and teeth of sun, planet, and ring gear

Gear	Sun	Planet	Ring
Teeth	22	76	174
Diameter pitch (mm)	44	152	348



**Fig. 2** CAD model of **a** sun gear, **b** planet gear, **c** ring gear designed in SolidWorks 2021

$$\text{Module} = \frac{\text{Diametrical Pitch}}{\text{Teeth}} \text{ where, Module} = 2 \tag{3}$$

- Gear specification (Fig. 2):

Value of module  $m = 2$ , Addendum  $= 1 \times m = 1 \times 2 = 2 \text{ mm}$ ;  
 Dedendum  $= 1.2 \times m = 1.2 \times 2 = 2.4 \text{ mm}$ ;  
 Tooth height  $= 2.5 \times m = 2.25 \times 2 = 4.5 \text{ mm}$ ;  
 Tooth Thickness  $= m\pi/2 = 2 \times 3.14/2 = 3.14 \text{ mm}$  (4)

#### 4.1.1 Forces and Stress Calculations

- Brake force:

$$B_f = M a g = 313 \text{ kN kg} \tag{5}$$

- Tangential force:

$$F_t = F \cos \alpha = 294 \text{ kN kg} \tag{6}$$

where  $\alpha = \text{pressure angle} = 20^\circ$

- According to Lewis equation:

$$\sigma = Ft/bmY \tag{7}$$

**Table 3** Value of tooth bending stress for sun, planet, and ring gear

Gears	Sun	Planet	Ring
Tooth bending stress ( $\sigma$ ) kMPa	37.178	21.948	15.709

**Table 4** Values of diametrical pitch, torque, tangential, radial, and axial load for gears

Stages	Stage-1			Stage-2		
Gears	Ring (174)	Planet (76)	Sun (22)	Ring (174)	Planet (76)	Sun (22)
$D_p$ (mm)	348	152	44	348	152	44
Torque (Nm)	3.925	1.7146	0.4963	0.4963	0.21680	0.06276
$F_t$ (N)	22.56	22.56	22.56	2.85	2.85	2.85
$F_r$ (N)	8.211	8.211	8.211	1.0381	1.0381	1.0381
$F_a$ (N)	0	0	0	0	0	0

(Tooth bending stress is shown in Table 3) where,  $Y$  = Lewis factor— $Y(22) = 0.330$ ,  $Y(76) = 0.559$ , and  $Y(174) = 0.781$ .

### 4.1.2 Diametrical Pitch, Torque, Tangential, Radial, and Axial Load Calculation

For torque calculation:

$$\frac{N1}{N2} = \frac{T2}{T1} \tag{8}$$

For tangential force calculation:

$$T = Ft \times r, \quad \text{Radial Force: } Fr = Ft \sec \beta \tan \alpha \tag{9}$$

where pressure angle  $\alpha = 20$ , helix angle  $\beta = 0^\circ$ , and  $Ft$  = tangential force (N)  
Axial force:

$$Fa = Ft \tan \beta \tag{10}$$

where  $Ft$  = tangential force and helix angle  $\beta = 0^\circ$  (Table 4).

## 4.2 Bearing Design

Equivalent load  $P$ :

$$P = C1(X V Fr + Y Fa) = 1.6515 \text{ N} \tag{11}$$

where  $C1$  = factor on nature of shock load,  $X$  = radial load factor = 1 (from catalogue),  $V$  = outer race rotation factor (1 for fixed and 1.2 for rotation) = 1.2,  $Y$  = thrust factor,  $Fr$  = radial load acting on bearing = 1.37628, and  $Fa$  = axial load acting on bearing = 0.

- The relationship between the life in millions of revolutions and the life in working hours is:

$$Ln = 60 N Lh / 1,000,000 = 5.58, \tag{12}$$

where  $Lh$  = 500 h and  $N$  = speed in rev/min.

- Life factor:

$$Fn = \sqrt[3]{Ln} = 1.7736, \tag{13}$$

where  $Ln$  = relationship between the life in millions of revolutions and the life in working hrs.

- Specific capacity:

$$C = Fn P = 2.929, Fn = \sqrt[3]{Ln}, \text{ life factor, } P = \text{Equivalent load}(N) \tag{14}$$

- Calculation of RPM on the respective gears is: sun = 23, planet = 186, and ring = 1500.

The bearing selected for the planet gear after the calculations is a spherical roller ball bearing, deep groove ball bearing, 6200 Series. Furthermore, the dimensions of the shaft are taken from the catalogue. Another bearing named 6202 ball groove bearing is used along the bigger shaft of 30 mm to prevent oil leakage from the gearbox. The number of bearing = 2 bearing along the planet gear of second stage as result equivalent load = 1.0006 kN and value of  $P = 2$  (ball bearing).

Table 5 shows the dimensions of a shaft that are represented taken from the catalogue. Weight of shaft, tangential load on shaft, load on shaft, rotation per minute of shaft, etc. are discussed below.

**Table 5** Dimensions of the shaft are taken from the catalogue

Features	Value	Features	Value
Weight of shaft (gm)	2000	Load (kN)	2.0012
Tangential load on shaft (N)	6.9736	RPM of shaft	186
Speed factor	0.177419	Life hours of bearing (h)	10,000
Dynamic load (kN)	1409.09	FI (from graph)	125
Outer diameter of shaft (mm)	30	Inner diameter of shaft (mm)	10

### **4.3 Design of Casing**

The casing is designed in such a way that the ball groove can be provided to the ring gear. A sphere jacket is provided along with the ring gear and casing. A ball groove is provided to align the ring gear in its respective position. It also ensures the co-axiality of the ring gear, which is parallel to the axis of the planet and sun gear. By providing a spherical jacket, wear is reduced and the vibration tends to decrease. Thus, the casing is designed in three halves and attached using M6 nut bolts. These three halves are joined together by 18 nut bolts. On the upper side of the casing, a drill is provided for the inlet of the oil into the casing, and at the lowermost part of the casing, a drill is provided to drain the lubricant. By means of tapping, a screw is tightened to the drill.

## **5 Material and Lubrication**

Various materials have been investigated for simulating epicyclic gears. Copper alloy has been shown to be an excellent material for working conditions with higher modes of vibration. Copper alloys are ideal for low-load environments. Its natural properties include corrosion and wear resistance. The inclusion of copper alloy increases the wear resistance as well as stiffness. The copper alloy is lighter in weight [20]. For the gear drive's long-term efficiency, it is vital to utilise the correct industrial gear lubricant. Temperature is critical when selecting an industrial gear lubricant for any application. Because the gearbox must work in an Indian atmosphere where temperatures might reach 45 °C. As a result, the gearbox was lubricated using SAE30 lubricating oil depending on the highest ambient temperature during operation [21].

## **6 Assembly of an Epicyclic Gear Train**

Figures 3, 4, and 5 show a rendered image of the casing and a cut-section view of the epicyclic gear train. Figure 6 depicts the assembly of a two-stage epicyclic gear train in an exploded view of the gearbox, displaying each component of a gearbox. The SolidWorks 2021 software is used to create various components. All of the components are depicted above, along with the calculations.



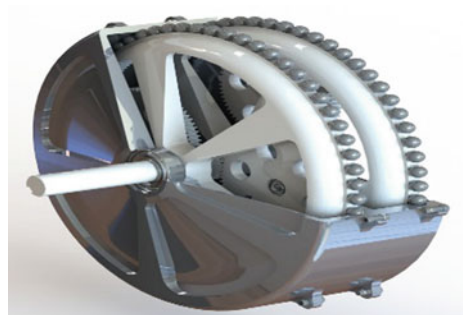
**Fig. 3** Rendered image of casing



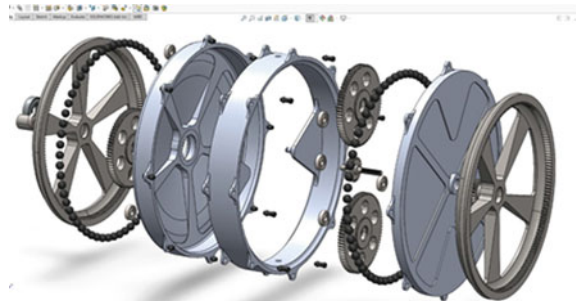
**Fig. 4** Rendered image of epicyclic gear train



**Fig. 5** Cut-section view of two-stage epicyclic gearbox



**Fig. 6** Exploded view of two-stage gearbox



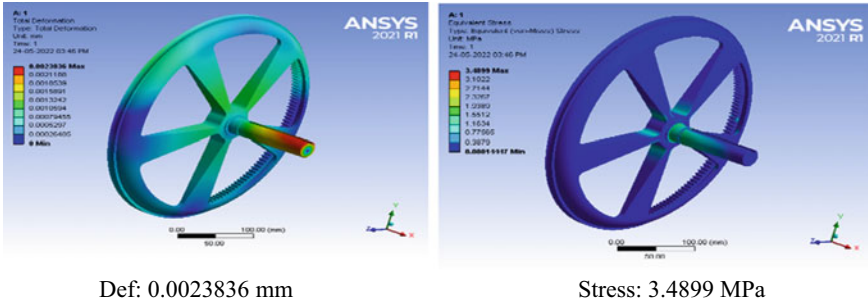


Fig. 7 Simulation of carrier (ring gear of stage-1)

## 7 Modelling

Because of its dominating feature, we choose Ansys Workbench 2021R1 for analysis. Because of the improved aspect ratio, we use quadrilateral dominating as a mesh approach. Determining whether or not a certain structural design will be able to handle the projected external and internal loads and pressures. As previously stated, finite element analysis is required for a specific planetary gearbox design under design loading circumstances. Static analysis of the following has been carried out, and they are shown below.

### 7.1 Simulation of Carrier (Ring Gear of Stage-1) with Input Shaft

See Fig. 7.

### 7.2 Simulation of Planet Gear (Stage-1)

See Fig. 8.

### 7.3 Simulation of Carrier (Ring Gear of Stage-2) and Sun Gear (Stage-1)

See Fig. 9.

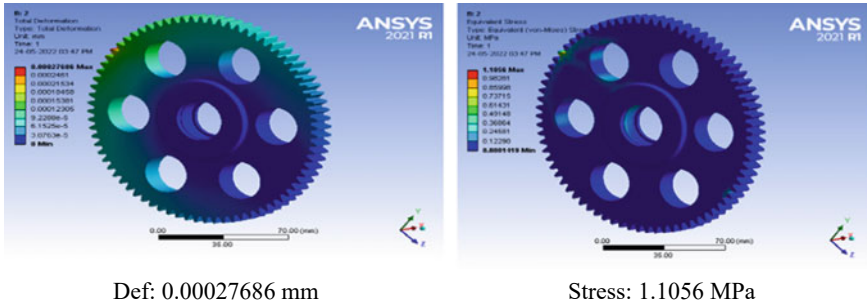


Fig. 8 Simulation of planet gear (stage-1)

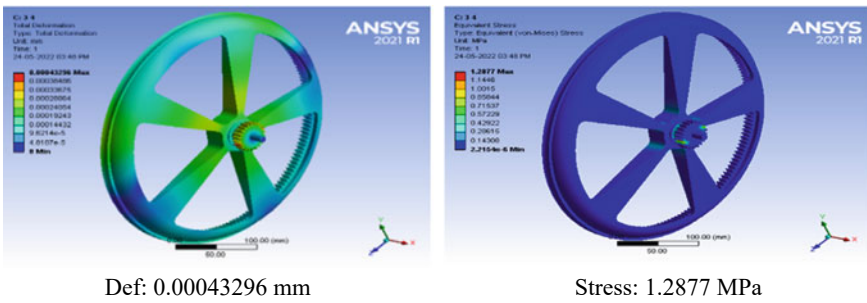


Fig. 9 Simulation of carrier (ring gear of stage-2) and sun gear (stage-1)

### 7.4 Simulation of Planet Gear (Stage-2)

See Fig. 10.

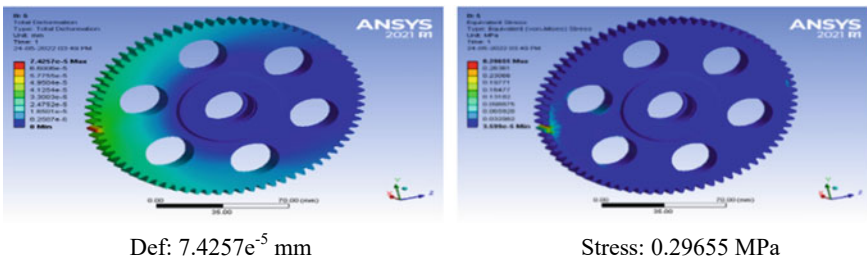


Fig. 10 Simulation of planet gear (stage-2)

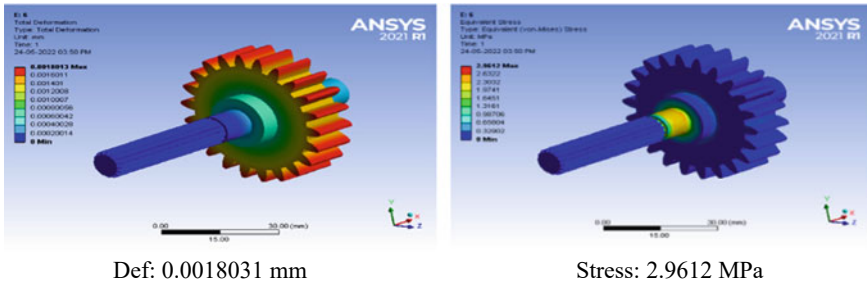


Fig. 11 Simulation of planet gear (stage-2)

### 7.5 Sun Gear (Stage-2) with Spline (Output Axle)

See Fig. 11.

## 8 Conclusion

As a result, the epicycle gearbox is designed and analysed. It resulted in the required amount of reduction (64). It was successfully analysed for Mahindra XUV 500MT. To get the lightest design possible, we went through an iterative design process in which all mechanical drivetrain components were evaluated and researched. The gearbox is constructed and assessed in this project under static and wear stress conditions, with the goal of achieving the lightest possible design. For the gearbox, a lubrication mechanism and suitable lubricating fluid, as well as suitable bearings, are chosen. Regenerative braking is studied using a two-stage epicyclic gearbox with brakes. As the brakes are applied, the gearbox operates and converts the mechanical energy of the braking process into electrical energy, which is used to illuminate the brake lights. Thus, the brake lights in a vehicle are operated independently, instead of using the electric charge from the battery. It reduces the amount of battery drainage. As a huge amount of work on the electric vehicle has been done, knowing how poisonous the batteries of the electric vehicle are to the environment. Electric vehicles also have the problem of heating, which results in explosions. Thus, conventional vehicles come to the rescue with more futuristic components.

## References

1. Akhila K, Reddy AN (2014) Design, modelling and analysis of a 3 stage epicyclic planetary reduction gear unit of a flight vehicle. *Int J Mech Eng Robot Res* 3(4):658–666

2. Hsu TR (2013) On a flywheel-based regenerative braking system for regenerative energy recovery. In: Proceedings of green energy and systems conference 2013, California. arXiv preprint 1311.6012
3. Zhang N, Cao Y, Du J, Li Q (2016) Epicyclic gear train parametric design based on the multi-objective fuzzy optimization method. In: 4th international conference on information systems and computing technology, vol 64. Atlantis Press, pp 1–7
4. Peng ZX, Hu JB, Xie TL, Liu CW (2015) Design of multiple operating degrees-of-freedom planetary gear trains with variable structure. *J Mech Des* 137(9):093301
5. Khokhri A, Agarwal S, Yashwardhan SS, Routh B (2021) Spiral spring and planetary gear based regenerative braking system design for bicycles. In: AIP conference proceedings 2021, vol 2341. AIP Publishing LLC, pp 020046
6. Botman M (1980) Vibration measurements on planetary gears of aircraft turbine engines. *J Aircr* 17(5):351–357
7. Lee H, Choi Y (2011) A new actuator system using dual-motors and a planetary gear. *IEEE/ASME Trans Mechatronics* 17:192–197
8. Hwang WM, Huang YL (2011) Connecting clutch elements to planetary gear trains for automotive automatic transmissions via coded sketches. *Mech Mach Theory* 46(1):44–52
9. Chen C, Liang TT (2011) Theoretic study of efficiency of two-dofs of epicyclic gear transmission via virtual power. *J Mech Des* 133:031007–031017
10. Xie T, Hu J, Peng Z, Liu C (2015) Synthesis of seven-speed planetary gear trains for heavy-duty commercial vehicle. *Mech Mach Theory* 90:230–239
11. Szumanowski A, Liu Z, Chang Y (2010) Design of planetary plug-in hybrid powertrain and its control strategy. *World Electr Veh J* 4(3):544–549
12. Zhou Z, Huang M (2019) Regenerative braking algorithm for the electric vehicle with a seamless two-speed transmission. *Proc Inst Mech Eng Part D J Automobile Eng* 233(4):905–916
13. Liang J, Walker PD, Ruan J, Yang H, Wu J, Zhang N (2019) Gearshift and brake distribution control for regenerative braking in electric vehicles with dual clutch transmission. *Mech Mach Theory* 133:1–22
14. Mantriota G, Reina G (2021) Dual-motor planetary transmission to improve efficiency in electric vehicles. *Machines* 9(3):58
15. Wang F, Ye P, Xu X, Cai Y, Ni S, Que H (2022) Novel regenerative braking method for transient torsional oscillation suppression of planetary-gear electrical powertrain. *Mech Syst Signal Process* 163:108187
16. De Carlo M, Mantriota G (2020) Electric vehicles with two motors combined via planetary gear train. *Mech Mach Theory* 148:103789
17. Liu C, Yin X, Liao Y, Yi Y, Qin D (2020) Hybrid dynamic modeling and analysis of the electric vehicle planetary gear system. *Mech Mach Theory* 150:103860
18. Inalpolat M, Kahraman A (2008) Dynamic modelling of planetary gears of automatic transmissions. *Proc Inst Mech Eng Part K J Multi-body Dyn* 222(3):229–242
19. Chen C (2011) Power flow analysis of compound Epicyclic gear transmission: Simpson gear train. *ASME J Mech Design* 133(9):094502
20. Saravanan A, Suresh P (2019) Finite element analysis of bending and dynamic response of a power transmission spur gear. In: *Advances in manufacturing technology*. Springer, Singapore, pp 511–525
21. Boness RJ, McBride SL (1991) Adhesive and abrasive wear studies using acoustic emission techniques. *Wear* 149(1–2):41–53

# Securing Network Address in PingER and IOS Application Development



Palak Gupta and Purushottam Sharma 

**Abstract** The main objective of this research is to study the Internet network performance across many countries including India in last few years. Comparisons are drawn between the various conditions that existed in the nation at that period and how the network in those regions was most affected. Ping end-to-end reporting is known by the acronym PingER. This study, which began in 1995, set out to gauge Internet performance for a number of different reasons. To enhance the monitoring experience, I have designed an IOS application for researchers to help them remotely monitor and encryption of the server's geolocation to protect it from various malicious attacks. This paper discusses the same in detail. PingER (ping end-to-end reporting) is the name given to the Internet end-to-end performance measurement (IEPM) project to monitor the end-to-end performance of Internet links. Hence to secure the data that is being transferred around the world, there is an urgent need to maintain its integrity as well, without doing so the credibility of the data can be tampered with or worse re-routed and manipulated. Not only this since it is a project to improve and identify the bad links between the networks, but the users also provide a direct link to access and review them, thus creating a need to build an application that is readily available to the audience to use and monitor. Since PingER measurements are conducted for more than 700 targets in over 160 countries, which indeed constitutes 99% of the world's population. This paper discusses the necessity for and creation of an IOS application that will attempt to give capabilities similar to a PingER MA to aid researchers in real-time pinging and monitoring. Also, to avoid information hijacking and manipulation, enable encryption and IP spoofing on the SLAC PingER server.

**Keywords** Network · IOS · Cloud computing · Encryption · IP address · PingER · App development · Server · Network security

---

P. Gupta · P. Sharma (✉)  
Amity University Uttar Pradesh, Noida, India  
e-mail: [puru.mit2002@gmail.com](mailto:puru.mit2002@gmail.com)

© The Author(s), under exclusive license to Springer Nature Singapore Pte Ltd. 2023  
R. Sharma et al. (eds.), *Advances in Engineering Design*, Lecture Notes in Mechanical Engineering, [https://doi.org/10.1007/978-981-99-3033-3\\_33](https://doi.org/10.1007/978-981-99-3033-3_33)

377

## 1 Introduction

The PingER project got its start at the SLAC laboratory in 1995. The laboratory had to transfer a sizable amount of information from all across the world. The network performance was tracked with the help of this project. The sites on the beacon list are pinged by many MAs spread out over the world, and the ping data is stored in servers. This information was gathered over a number of years. This information is excellent for identifying network underperformance nationally and regionally. It can be helpful in assisting less developed nations to access high-quality telecom services and a developing market for such services [1, 2]. Agents must be available 24/7, 365 days a year. This results in high energy consumption which further leads to more expenses. The traditional desktop computer consumes between 80 and 250 W, depending on the devices and components installed. The cost of running a typical 130-W computer and monitor system with the uptime criteria of an MA is \$129.73. A smartphone has a substantially lower annual running cost of about \$1.36. Furthermore, when compared to the size of a smartphone, a desktop and peripherals require a significant amount of room. This project offers an IOS application that will attempt to give capabilities like a PingER MA to aid researchers in real-time pingging and monitoring while also encrypting the location of servers [3].

### 1.1 History of PingER

The SLAC laboratory's PingER project got underway in 1995. Huge amounts of data from all across the world have to be transferred to the laboratory. This initiative made it easier to keep an eye on network performance [4]. Numerous MAs dispersed throughout the world ping the sites listed on the beacon list and save the ping data in servers. These statistics were gathered over a number of years. The performance of the network country- and region-wise can be determined using these data. It can be helpful in providing less developed nations with high-quality telecom services and a growing market for those services.

### 1.2 PingER Process

PingER uses measurement agents which will periodically ping target sites and are responsible for the storage and analysis of the received data. The data can be used for deriving various metrics, which can be useful for the purposes of determining throughput, Voice over Internet Protocol (VoIP), streaming, haptic, and more. Another interesting field this can be used in is in the determination of the geolocation of a host by sending pings to it from well-known landmarks [5].

### ***1.3 Scope***

There was not any previous application developed for IOS, which helped users remotely install it on their devices and ping the servers to measure the short- and long-term response time, packet loss percentages, the variability of the response time (jitter), and the lack of reachability (no response for a succession of pings). By developing the application and possibly removing the use of all MAs, the project saves a lot of power and increases efficiency.

### ***1.4 Constraints***

- **DNS:** After an IP address change to the iepm-maggie.niit.edu.pk host at NIIT, nodes at SLAC were unable to access content off of it reliably. When accessing web content from the server, blank pages or 404 errors would be returned.
- **Unreachable server:** Due to COVID-19, many SLAC servers were shut down; due to this, there is no sync between the ping and reachability. And the sites cannot be monitored with disturbance of one or more unreachable beacons.
- **Software restriction:** IOS being a closed UNIX environment can propose difficulties in connecting with the pinging site or not being able to accept the new IOS versions. Also, an IOS device is needed and to build the software a MACOS device might be needed.
- **Tools:** Lack of tools to support future development for IOS devices.
- **Cost:** If open source is not available, then the cost of building software might be high.
- **Encryption:** To implement encryption, new VPN creations are needed, which can be time- and power consuming.

### ***1.5 IOS System***

IOS Apple's ecosystem contains around 24.49% of the market that is because the consumers of IOS have more or less always been sophisticated. IOS is challenging to break into as it provides secured but limited functionality which makes it difficult for the attackers to access. Also, it has a more user-friendly and richer GUI than Android with limited customizability.

Kernel-resident device drivers and other kernel extensions have APIs and support provided by the Kernel Framework. It provides the class name (IO Service) for I/O kit device drivers, as well as various utility classes and families that support a variety of devices. The IOS kernel is a flexible group of elements and functions that work together as a peer instead of a supervisor with the remainder of IOS. No special kernel mode exists. Everything runs in user mode on the CPU, including the kernel [6], and has complete administrator privileges. Processes are scheduled, memory is



managed, service routines to trap and handle hardware interrupts are provided, and timers are maintained by the kernel [7].

The Darwin operating system includes the XNU kernel, which is used in macOS and iOS. XNU stands for “X is Not Unix.” XNU is a hybrid kernel that combines the Carnegie Mellon University Mach kernel with FreeBSD elements and the IO Kit C++ API for developing drivers. For single or multi-systems, XNU operates on x86 64.

## 2 Methodology

### 2.1 Implementation

The execution of the project takes place in two parts:

- (i) IOS application development
- (ii) IP encryption of servers.

#### IOS Application Development

The IOS application [8] is built to provide users and the networking team with the functionality to ping the servers and collect data on the application itself. This provides the testers with precise results [9] with data formatting which was not possible on the website as the website could not store the data on-site, besides it provided poor formatting options which made the data hard to read and understand. This methodology will present the step-by-step making of the IOS application using Flutter.

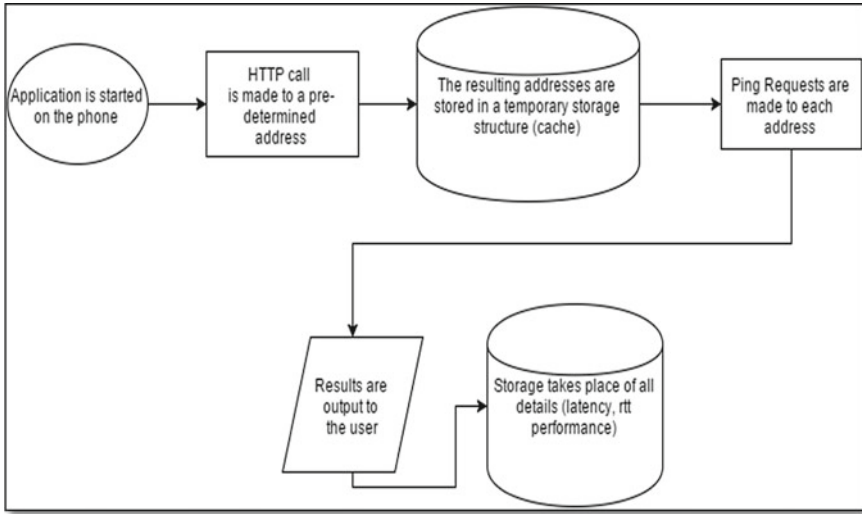
The process followed is kept parallel to the working of the PingER application and is abridged below; refer Fig. 1.

The application on IOS devices, specifically mobile phones, will be started and connected for ping to the server. All general requirements and allowances are given prior to ping. Then as soon as the tester or the user clicks on “Start Ping”, the mobile gadget will send an HTTP call to the predetermined address as shown in Fig. 1, and these predetermined addresses are stored in a temporary database structure, also called cache. After this, the ping request that was sent from the mobile device is made to each of the addresses stored in the temporary database (cache). The result of ping to each of the addresses is presented on the smartphone phone in a pre-defined style, allowing network performance to be monitored consecutively.

#### Assumptions and Simplifications

Several assumptions were performed to confirm that the application prototype worked well, and various optimizations were done to allow the process to run without explicitly managing exceptions or failures.

- (a) The device is linked to the Internet via a secure and consistent connection.



**Fig. 1** Process flow of model

- (b) The handset is charged or is plugged into a charger.
- (c) IOS 13 or above is downloaded on the device prototype.
- (d) Root access has been provided to the application.
- (e) The Internet and power supply are never interrupted.

**Environment Setup**

Tools for developing, designing, and testing the application. The equipment used for the same is listed below.

- (a) Visual Studio code, version 1.65.2 (Universal), the language used was Flutter.
- (b) XCode for MACOS, development of IOS application.
- (c) IOS simulator with IOS version as 13 and above, and any model (here chosen iPhone 11 Pro) as the test device.
- (d) The application has been made on a macOS Monterey which has an i5, 8 Gb of RAM, and 128 GB SSD.

**The IOS Application**

On the iPhone 11 Pro simulator, the app is compiled and tested. The application displays the installation phase on the screen like any other app being downloaded on an iPhone. Following installation, the application will prompt you for specific permissions, such as location permissions, which are also shown in Fig. 2.

Upon launch, the PingER application of the IOS device displays the first page of the application, “Start Pinging”, as shown in the picture below. When the application is started, the target domain names are retrieved from the website where they are stored. Whenever the application is running in the foreground, the list of these



Fig. 2 Permissions upon app installation

domains is stored locally. The application has been kept simple to ensure ease of use. Refer to Fig. 3.

Now, the application currently consists of three pages, namely Start/Stop Pinging, Ping Data Screen, and Contact US, all of these pages provide their own functionality, which is yet to be fully developed as and when the need exists (Fig. 4).

For this project, we will be focusing on the first page, that is, Start/Stop Pinging and the functionality it provides. The Start/Stop Pinging page of the mobile application



Fig. 3 Result of PingER app on iPhone 11 Pro



**Fig. 4** Display of other two app pages

in the iPhone 11 Pro with IOS 15.4 helps in sending the ping packets to the server, which then captures the data into the macOS machine in real time (Fig. 5).

The image depicted above shows that after the tester has clicked on “Start Ping”, the application starts “Pinging” to a particular server requested, by sending HTTP requests to it. Then the data is simultaneously received on the system [10] running the IOS simulator and response time, time to live, and total time taken for the ping to go and come back are noted. This is how the application on IOS devices will work as well, but just instead of catching the ping on PC, we will be able to display it on the second page of the application, Ping Data Screen.

Although the application is complete, it needs a little more work to be installed on an actual IOS device, which is also kept as future work later in this project.

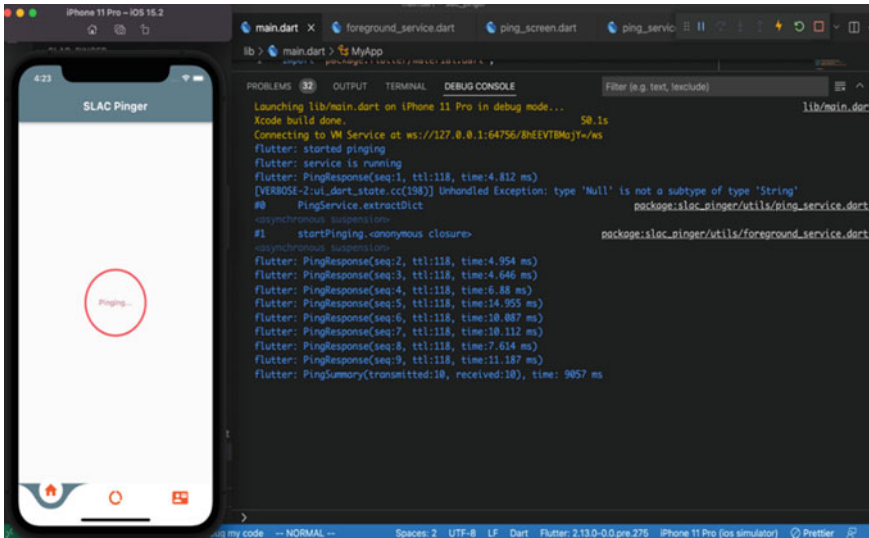


Fig. 5 Output after pinging

### IP Encryption of Servers

IPsec is a collection of protocols that work together to create encrypted communications amongst devices. It aids in the security of data exchanged over public networks. IPsec is frequently used to set up VPNs, and it operates by encrypting IP packets and validating the sender of the packets. The most extensively used routing method on the Internet is the Internet Protocol, which employs IP addresses to determine where data should be transmitted. IPsec secures the procedure by including encryption\* and authentication.

Encryption is the process of hiding data by computationally modifying it to make it appear unpredictable. To put it simply, encryption is the use of a “secret code” that only authorised users can decode. This makes data delivered over IPsec secure and private by encrypting the data packets throughout each packet as well as the IP header (unless routing protocol is used instead of tunnel mode).

The IP encryption is done using a Cloudflare, as it is a great online free tool for making corporate and other websites spoof free, and provides great encryption while at the same time identifying the weak spots on the nameservers and IP addresses.

The Cloudflare encryption takes place in a few steps:

- (i) Creating a free account on Cloudflare’s website (Fig. 6).
- (ii) Get Stanford University accredited SLAC project hosting nameserver and DNS (Fig. 7).
- (iii) Complete the steps by replacing Cloudflare’s nameserver with SLAC’s nameserver and vice versa to protect and encrypt them (Fig. 8).

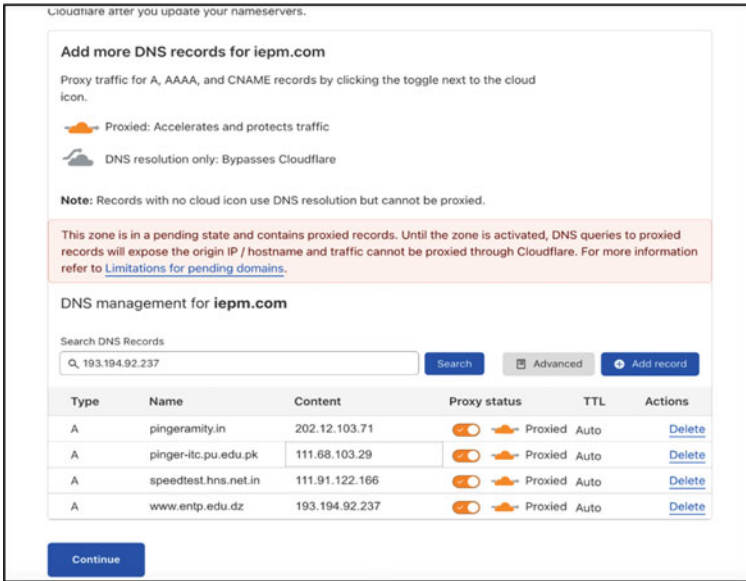


Fig. 6 Adding sites to be encrypted

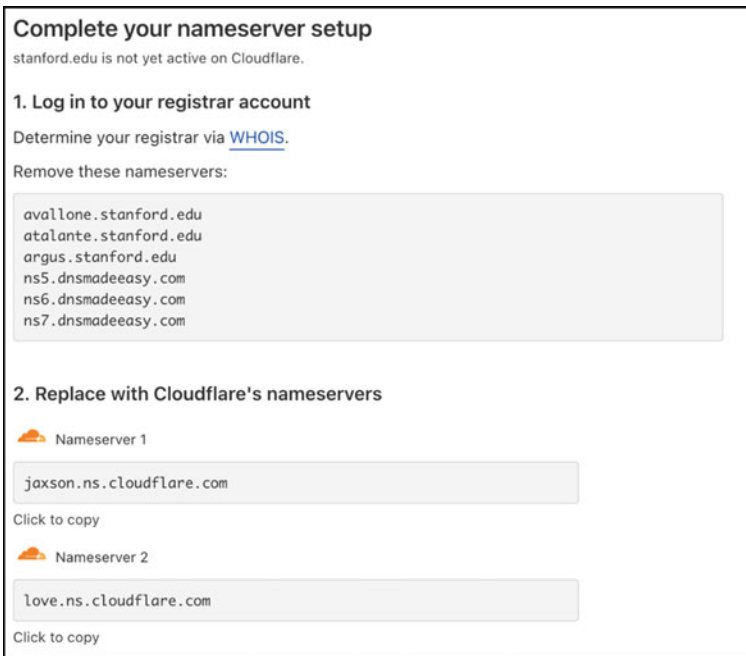


Fig. 7 Encrypting SLAC servers in Cloudflare

```

#####
#Current as of: Sun May 8 23:00:02 2022
#Written by Script: /afs/slac/package/pinger/write_offsitenodes.pl for pinger. It works under account cottrell
# Beacons requirements: Monitoring site
# Beacons requirements: < 28 unreachable for several months
# Beacons requirements: Can find lat/long of site
# Beacons requirements: interest to ESnet or ICFA/SCIC
# e.g. a Beacon could be in Particle Data Group (PDG) book,
# or a collaborator in major HEP experiment
# or represents country or region or community
# (community includes the Digital Divide).
# Beacons preferences: web site
# Beacons preferences: Educational (.edu, .ac) or government site
# The current master list is kept at:
# http://www-lepms.slac.stanford.edu/pinger/beacons.txt
#Location of Historical offsite.nodes: /afs/slac/g/scs/net/pinger/bin/offsite-nodes/offsite.nodes
#####
www.entp.edu.dz 193.194.92.237 #[Beacon - Ecole Nationale Supérieur de travaux public]
www-05.nexus.ao 41.221.254.23 #[Beacon - Nexus Telecom Angola]
www.uac.bj 196.192.16.5 #[Beacon - Université d'Abomey-Calavi]
nsl.btc.bw 168.167.168.34 #[Beacon - Botswana Telecommunications Corporation]
www.cnrst.bf 212.92.137.27 #[Beacon - Centre National de Recherche Scientifique et Technologique]
www.assemblee.bi 173.249.1.93 #[Beacon - National Assembly of Burundi]
www.minepat.gov.cm 195.24.199.65 #[Beacon - Ministère de l'Economie, de la Planification et de l'Aménagement du Territoire]
www.uniteltdmais.cv 41.79.124.84 #[Beacon - Unitel T+]
www.afrinet.cd 41.222.216.214 #[Beacon - The African Society of Communication and Internet]
www.univ.edu.dj 196.201.198.139 #[Beacon - University of Djibouti]
www.mvp.gov.eg 212.103.189.124 #[Beacon - Egyptian Meteorological Authority]
www.alagecollege.edu.et 213.55.96.149 #[Beacon - Alage Agricultural Technical Vocational Educational Technical College]
www.tresor.ga 217.77.72.249 #[Beacon - Tresorerie Generale du Gabon, Libreville]
mail.qanet.gn 196.46.232.3 #[Beacon - QuantuNET]
www.ug.edu.gh 197.255.125.213 #[Beacon - University of Ghana]
www.afribone.net.gn 41.77.187.10 #[Beacon - Afribone Guinea]
www.polymed.ci 164.160.35.253 #[Beacon - PolyMed]
www.kenet.or.ke 41.204.160.5 #[Beacon - Kenya Education Network-KENET]
www.leo.co.ls 64.57.112.1 #[Beacon - Leo Internet Service Provider]
www.orange.com.lr 154.68.9.46 #[Beacon - Orange]
mail.litnet.net 41.208.70.33 #[Beacon - Libya Telecom and Technology]
www.cnaps.mg 102.16.9.71 #[Beacon - National Social Insurance fund]
www.poly.ac.mw 41.77.11.147 #[Beacon - University of Malawi - Malawi Polytechnic]
www.cnrst.edu.ml 197.155.158.21 #[Beacon - Centre National de la Recherche Scientifique et Technologie]
www.nic.mr 82.151.64.726 #[Beacon - NIC Mauritanie]

```

Fig. 8 List of servers that are pinged

Not only this but the Cloudflare application enables users to advanced API protection and under attacker mode with a lot of advanced security features which can help the future application to help and protect them against data breaches and malicious attacks.

### 3 Problems with the Existing System and Techniques for Improving

#### 3.1 PingER Procedure

PingER uses measuring agents, which pests targeted activity on a regular basis and stores and analyses the data they get. The data can be used to calculate numerous metrics, such as throughput, Voice over Internet Protocol (VoIP), streaming, and haptic. Another intriguing application for this is determining a host’s geolocation by sending pings to it from conventional locations [11].

### **3.2 Web Vulnerabilities**

Initially, the SLAC website provided a zero-encryption policy, through which the servers that are located all around the world could have faced some serious consequences such as an XSS attack which is a flaw that allows the attacker to insert client-side scripts into a website page in order to get direct access to sensitive information, deceive the user, or dupe the user into exposing sensitive data, not only this but DoS attack as well, through which attackers are able to overload the target server with a lot of traffic consisting of various attacks, which ultimately leads to denial of service to users [12].

### **3.3 Memory Corruption**

Nearly sixty MAs take PingER assessments. They take measures for over seven hundred targets in over a hundred and sixty nations, which account for nearly all of the world's connected people. Agents must be available 24 h a day, 365 days a year. This results in the potential loss of huge amounts of data all over the world where SLAC servers collect and implant data. This leads to memory corruption which plays a crucial role when there is a lot of data to be collected. It happens when a region in memory is accidentally changed, potentially leading to unanticipated software behaviour. Bad actors will use exploits like code implants and buffer overflow attacks to sniff out and leverage memory corruption.

## **4 Results and Discussions**

The objective of this study to run the PingER application on IOS devices comes from the fact that Apple's ecosystem has been a curse and a boon both, where we have captured the disadvantages of IOS devices and the need to bring change.

Additionally, apart from addressing the more common problems, this device will give consumers/testers the luxury of salient features of drag-drop, which was only available on laptops and desktops for easy transfer of files. The second feature is split-screen where users would be able to view both the operating systems at the same time. A third unique feature is its availability on the cloud as well as remote installation according to users' needs and choices. Although there is still a lot of progress and research to be established for this kind of IOS application, we have made an implemented working model of application through which we can ping web applications, with partial implementation of encryption.



## 5 Conclusion

The above study successfully explains the methodology of building an IOS application for the networking team to help them remotely send pings to the servers to monitor data and other information; the application is built using Flutter which will be further helpful to develop an android application. The built application may be accessed via a simulator on MACOS devices, and the ping time data is gathered using the IOS simulator on the device, which provides the servers' RTT, TTL, and IP address. The SLAC server location was encrypted using the Cloudflare platform, which assists with reverse-proxy and enables fast, reliable, and private connections to websites.

## 6 Future Works

This study concentrates on developing and building an IOS application for the SLAC project networking team to help them ping the SLAC servers worldwide in real time, without losing any data. The application also facilitates the reduction of power-consuming MAs and desktops. The design can be tweaked to accommodate unexpected events, and data from multiple MAs can be uploaded to shared servers for a central backup repository [13]. Furthermore, the programme must be downloaded on a physical IOS device because it works properly on the IOS simulator to gather data rather than on the macOS device as it now does. Lastly, enhance server–client encryption of the locations and information to prevent data loss and manipulation of the SLAC servers, which can be easily tampered with and changed [12].

**Acknowledgements** Authors are grateful to our respectful Prof. Bebo White, Prof. Les Cottrell, Prof. Saqib Ali, Prof. Umar Kalim, and Prof. Abhay Bansal for providing to be a part of the esteemed Stanford University's SLAC project.

## References

1. Madan N, Sabitha AS, Bansal A, Cottrell L, White B (2019) Network performance of PingER data with respect to the growth of the Telecom industry in India. In: 2019 9th international conference on cloud computing, data science & engineering (confluence). IEEE, pp 75–78
2. Matthews W, Cottrell RL (2000) The PingER project: active internet performance monitoring for the HENP community. IEEE Communications Magazine
3. Thorvaldsen ØE (2006) Geographical location of internet hosts using a multi-agent system
4. <https://www-iepm.slac.stanford.edu/monitoring/bulk/sc2005/pinger.pdf>
5. Cottrell RL, Logg C, Chhaparia M, Gngonev M, Haro F, Nazir F, Sandford M (2006) Evaluation of techniques to detect significant network performance problems using end-to-end active network measurements. In: Network operations and management symposium, 2006. NOMS 2006. 10th IEEE/IFIP. IEEE, pp 85–94

6. Sharma P, Saxena K, Sharma R (2016) Heart disease prediction system evaluation using C4.5 rules and partial tree. In: Behera H, Mohapatra D (eds) Computational intelligence in data mining—volume 2. Advances in intelligent systems and computing, vol 411. Springer. [https://doi.org/10.1007/978-81-322-2731-1\\_26](https://doi.org/10.1007/978-81-322-2731-1_26)
7. Lee Y (2014) Design and implementation of smart virtual machine on iOS platform for mobile game portability. *Int J Smart Homes*
8. Gupta P, Sharma P, Prabhakar S (2022) Virtual machine for IOS devices. *Int Mob Embed Technol Conf (MECON) 2022*:627–631. <https://doi.org/10.1109/MECON53876.2022.9752125>
9. Agarwal A, Sharma P, Alshehri M, Mohamed AA, Alfarraj O (2021) Classification model for accuracy and intrusion detection using machine learning approach. *PeerJ Comput Sci* 7:1–22. <https://doi.org/10.7717/PEERJ-CS.437>
10. Aashkaar M, Sharma P (2016) Enhanced energy efficient AODV routing protocol for MANET. Paper presented at the international conference on research advances in integrated navigation systems, RAINS 2016. <https://doi.org/10.1109/RAINS.2016.7764376>
11. Hilbert M (2014) Technological information inequality as an incessantly moving target: the redistribution of information and communication capacities between 1986 and 2010. *J Am Soc Inf Sci* 65(4):821–835
12. Cottrell RL, Logg C, Mei IH (2003) Experiences and results from a new high-performance network and application monitoring toolkit. In: Passive and active measurement workshop
13. Cheng B, Buzbee B (2010) A jit compiler for android's dalvik vm. In: Google I/O developer conference, vol 201, No 0

# Atlas Generation of Planar Flapping Wing Mechanism with Higher Pair



Pankaj Vinayak Dorlikar, Nikhil Belhekar, and Sujit Suresh Pardeshi

**Abstract** The use of unmanned aerial vehicle (UAV) in commercial and military fields has risen exponentially. The flapping of birds has always been one of the prominent topics of research. The flapping motion of birds gives the basic idea behind the propulsion of flapping UAV. This work starts with the study of available flapping mechanisms. Followed by the design process based on creative design theory. We have found out an atlas of 10 planar mechanisms with 4, 5, 6, 7 bar linkages. This atlas can be used for design and development of flapping UAV.

**Keywords** Unmanned aerial vehicle · Flapping · Creative design theory · Planar mechanism

## 1 Introduction

Because of its agility and dexterity, the flapping unmanned aerial vehicle is commonly utilized in the sectors of surveillance, reconnaissance, and rescue operations. An unmanned aerial vehicle (UAV) is a motorized aerial vehicle that does not require a human operator and is either expendable or recoverable. An unmanned aircraft system includes unmanned aerial vehicles (UAVs). The UAV is controlled remotely by a human operator.

Disaster management, geographic mapping, shipping delivery, machine learning, weather forecast are just a few of the modern technologies employed by autonomous drones to complete tasks without the need for human intervention.

---

P. V. Dorlikar (✉)  
College of Engineering, Affiliated to SPPU, Pune, India  
e-mail: [pvdorlikar@aitpune.edu.in](mailto:pvdorlikar@aitpune.edu.in)

P. V. Dorlikar · N. Belhekar  
Department of Mechanical Engineering, Army Institute of Technology, Pune 411015, India

S. S. Pardeshi  
Department of Mechanical Engineering, College of Engineering, Pune 411005, India

Flapping wing UAV mimics like insect or birds and are able to generate high lift at low speeds. The bio-inspired hummingbird-like unmanned aircraft by AeroVironment effectively proved the advantages of UAV [1]. Professor Hong-Sen Yan has already given classical mechanical design theory which is called as 'Creative Design of Mechanical Devices' [2] that was used to generate different types of mechanisms. With the help of this theory, we have generated atlas of planar kinematic flapping mechanism for UAVs.

Various asymmetric flapping kinematics in UAVs that are employed to generate significant aerodynamic loads are investigated. Dynamic stall is one of the main load production processes utilized by hovering insects. Polhamus [3] did substantial research on dynamic stall and its role in lift augmentation and later explored it in relation to flapping wings. By conducting experiments on basic mechanisms, Maxworthy [4] changed Weis-Fogh and Lighthill's explanation of the 'clap and fling' mechanism slightly for acquiring higher lift when hovering by insects. The wing turns near the end of a half-stroke and enters the vortical area created by the preceding half-stroke, resulting in enhanced lift and known as wake capture. Dickinson et al. [5] attempted to fill knowledge gaps in insect flight by coupling the lift and drag for simultaneous flow in a two-dimensional model and summarizing the results with respect to angle of attack and chord lengths.

Based on creative design approach, Zhang et al. [6] presented 31 unique designs of flapping wing mechanisms. Yusoff et al. [7] constructed a compliant flapping wings mechanism with an electronic control system for emulating bat wing motion. They also fabricated and tested the wings in a wind tunnel using titanium alloy based on three different bat species and their measurements. Srigrarom et al. [8] created an ornithopter prototype that mimics a bird's flapping action, and they conducted experimental evaluations of lift and thrust characteristics for varied flapping frequencies and three different prototype materials. Bin Abas et al. [9] researched on micro-aerial vehicle development in low Reynolds number regions, as well as the idea of using a transmission to provide wing motion in nano-aerial vehicles to replace the motorized flapping wing transmission.

Based on design requirements set using unstable blade element theory, Jeon et al. [10] conducted structural analysis of a newly built six-bar pair linkage flapping mechanism. Yang et al. [11] investigated the kinematic reliability of a flapping wing mechanism with variable hinge clearances, flutter angle variation, angular velocity, and acceleration of the wing tip with different clearances. Hassanalian et al. [12] presented a technique for designing actuation components for a micro-aerial vehicle, followed by a discussion of the benefits and downsides of traditional flapping mechanisms. After analysis, a revolutionary hybrid flapping wing micro-aerial vehicle dubbed 'Thunder I' is conceived and built based on optimal actuating mechanism features.

Ji et al. [13] created a spatial six bar flapping wing mechanism for converting a single rotation into flapping swing and twist movements that resembled pigeon landing flight motion. A comparison of theoretical and experimental twist amplitudes was also provided. Yousaf et al. [14] evaluated numerous micro-aerial vehicle

subsystems and discovered research gaps in micro-aerial vehicle subsystem evaluations. Shi et al. [15] studied the flapping motion of birds in the literature to determine the sources of lift and thrust, then optimized the double crank and double rocker mechanisms, as well as the relative position of the driving and flapping mechanisms for determining proper wing size. A pitch mechanism with ball hinges was also incorporated for pitch motion-induced trust.

## 2 The Nomenclature

Symbolic representation for kinematic links and joints in this paper are as follows:

<i>Symbol</i>	<i>Description</i>
$K_F$	Fixed link
$N_L$	Total links count
$N_E$	Number of joints having lower pair
$N_F$	Number of joints having higher pair
$N_J$	Total joints count
$J_G$	Gear joint
$J_T$	Trunnion joint
$A_L$	Link assortment
$F_P$	Degree of freedom

## 3 Analysis of Existing Flapping Mechanism

The mechanism shown in Fig. 1 is gear driven by gears 33 and 32, which creates a symmetric motion that drives the rockers 42 and 41. Figure 2 depicts the generalized kinematic chain and Fig. 3 depicts generalized mechanism.

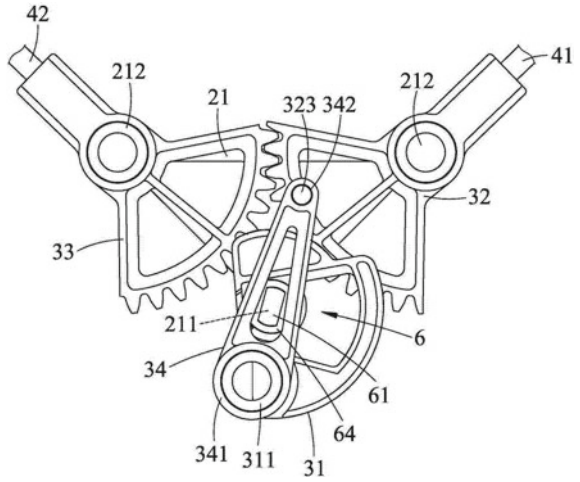
$K_F$  signifies a fixed link,  $L_3$  and  $L_4$  are moving links, and  $L_1$  is the crank in the kinematic chain. There are 5 links and 6 joints in this mechanism, with 5 lower joints and one higher joint.

The calculation of the above mechanism’s degree of freedom is done using (1).

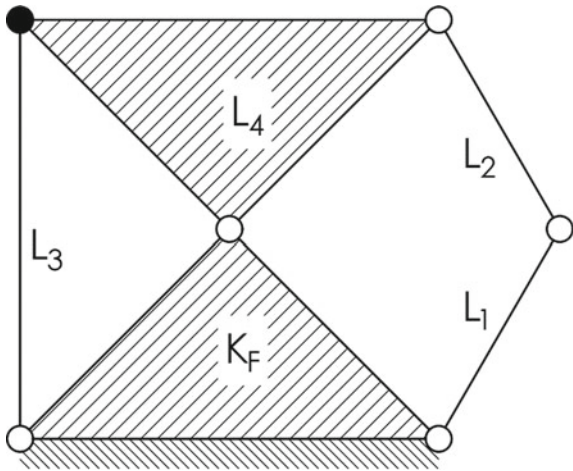
$$\begin{aligned}
 F_P &= 3(N_L - 1) - 2N_E - N_F \\
 F_P &= 3(5 - 1) - (2 \times 5) - 1 \\
 F_P &= 1
 \end{aligned}
 \tag{1}$$

According to Eq. (1), the DOF of the given mechanism is 1

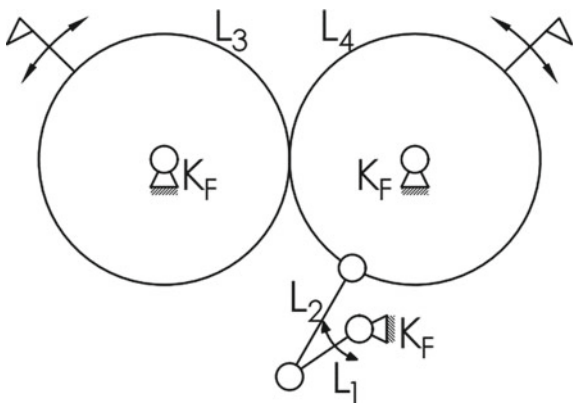
**Fig. 1** Original mechanism [16]



**Fig. 2** Generalized kinematic chain



**Fig. 3** Generalized mechanism



$$\begin{bmatrix} K_F & 1 & 1 & 0 & 1 \\ & K_{L1} & 1 & 0 & 0 \\ & & K_{L2} & 1 & 0 \\ & & & K_{L3} & 1 \\ & & & & K_{L4} \end{bmatrix} \quad (2)$$

The mechanism's topology matrix can be found in Eq. (2). Mechanisms with the same kinematic functionality but different arrangements can be identified and built using this topology matrix.

#### 4 Atlas Generation Objective and Constraints

Based on the design consideration and restrictions for a planar flapping mechanism, this work must fulfill the following objectives:

1. The kinematic links in flapping mechanism should be restricted in the range of 4 to 7 bar linkages.
2. To avoid the complexity of mechanism, the types of links in the mechanism are limited to pentagonal link.
3. The flapping mechanisms should have only one DOF and output motion by two links (wings).

In this study, we have used revolute joint, gear joint, and prismatic joint. Also according to H.S. Yan's theory, we have considered to replace one higher joint by two lower joints as and when required in mechanism.

#### 5 Procedure of Creative Design

- Step 1 Identify any topological properties linked with existing designs that have the requisite design standards.
- Step 2 Using the rules of generalization, transform any one existing design to its corresponding generalized chain.
- Step 3 As mentioned in step 2, synthesize a set of atlas of generalized chains having the number of links as mentioned above.
- Step 4 According to the required design constraints, use the specialization process, and obtain all generalized chains by assigning different links and joints.
- Step 5 To make the atlas of mechanisms use particularization process for each obtained specialized chain and its corresponding schematic representation of mechanism.
- Step 6 To create an atlas of new mechanisms, identify, and eliminate all current mechanisms from the atlas.

**Table 1** Link assortments  $[A_L]$  obtained for 4, 5, 6, and 7 links

$N_L$	$N_E$	$N_F$	$N_J = N_E + N_F$	$m$	$[A_L]$	Schematics
4	3	2	5	3	[2, 2]	Fig. (a <sub>1</sub> )
5	5	1	6	3	[3, 2]	Fig. (b <sub>1</sub> )
5	4	3	7	4	[3, 0, 2], [2, 2, 1]	Fig. (b <sub>2</sub> to b <sub>4</sub> )
6	6	2	8	4	[3, 2, 1], [4, 0, 2]	Fig. (c <sub>1</sub> to c <sub>3</sub> )
7	8	2	10	5	[3, 3, 1]	Fig. (d <sub>1</sub> , d <sub>2</sub> )

### 5.1 Kinematic Number Synthesis

The number synthesis procedure of the mechanisms is as follows:

1. By considering 1-degrees of freedom, for 4, 5, 6, and 7-bar linkages, the number of joints in the mechanism is found out by

$$N_J = [3(N_L - 1) - F_P]/2 \tag{3}$$

where  $N_J$  is the total joints count ( $N_E$  and  $N_F$  are number of joints having lower pairs and higher pairs, respectively),  $N_L$  is the total links count, and  $F_P$  is the degrees of freedom.

2. To find the link assortment ( $A_L$ ), the formulations are

$$\begin{aligned} N_{L2} + N_{L3} + N_{L4} + \dots + N_{Lm} &= N_{L1} \\ 2N_{L2} + 3N_{L3} + 4N_{L4} + \dots + mN_{Lm} &= 2N_J \end{aligned} \tag{4}$$

where  $m$  is maximum number of joints on any link.

From the outputs of the above equations, link assortment is noted for each possibility of each link type as;

$$[A_L] = [N_{L2}/N_{L3}/N_{L4}/\dots] \tag{5}$$

Using the link assortment, atlas of mechanisms with 1-degrees of freedom for 4, 5, 6, and 7 links is generated. From the research objectives, design constraints and using the above steps the results obtained for link assortments  $[A_L]$  are stated in Table 1.

### 5.2 Specialized Kinematic Chains

After kinematic number synthesis, specialization is the process of dispersing discrete links and joints into practical generalized chains. The obtained specialized kinematic



chains are shown in Fig. 4. In Fig. 4, the ground links are marked by  $K_F$ , whereas the remaining links are denoted by  $L_1, L_2, L_3$ , and so on. The higher pair is the gear pair, which is used for flapping wing mechanics and is marked by  $J_G$ .

### 5.3 Mechanisms After Particularization

The process of designating specific links and joints is known as particularization. Using specialized kinematic chains, Fig. 5 illustrates the mechanisms that follow specialization.

## 6 Conclusion

Ten various and innovative style flapping mechanisms have been constructed using Hong-Sen Yan's theory, which can be used to design a planar flapping micro-aerial vehicle. Application of number and type synthesis is used to find feasible planar specialized kinematic chain for 4, 5, 6, and 7 bar linkages. The flapping motion generated by the planar mechanism is prescribed, and the motor input in this mechanism can only change the flap rate as it has only one degree of freedom. This will reduce down motor requirements to only one motor, which will also avoid other control-related issues of micro-aerial vehicles.

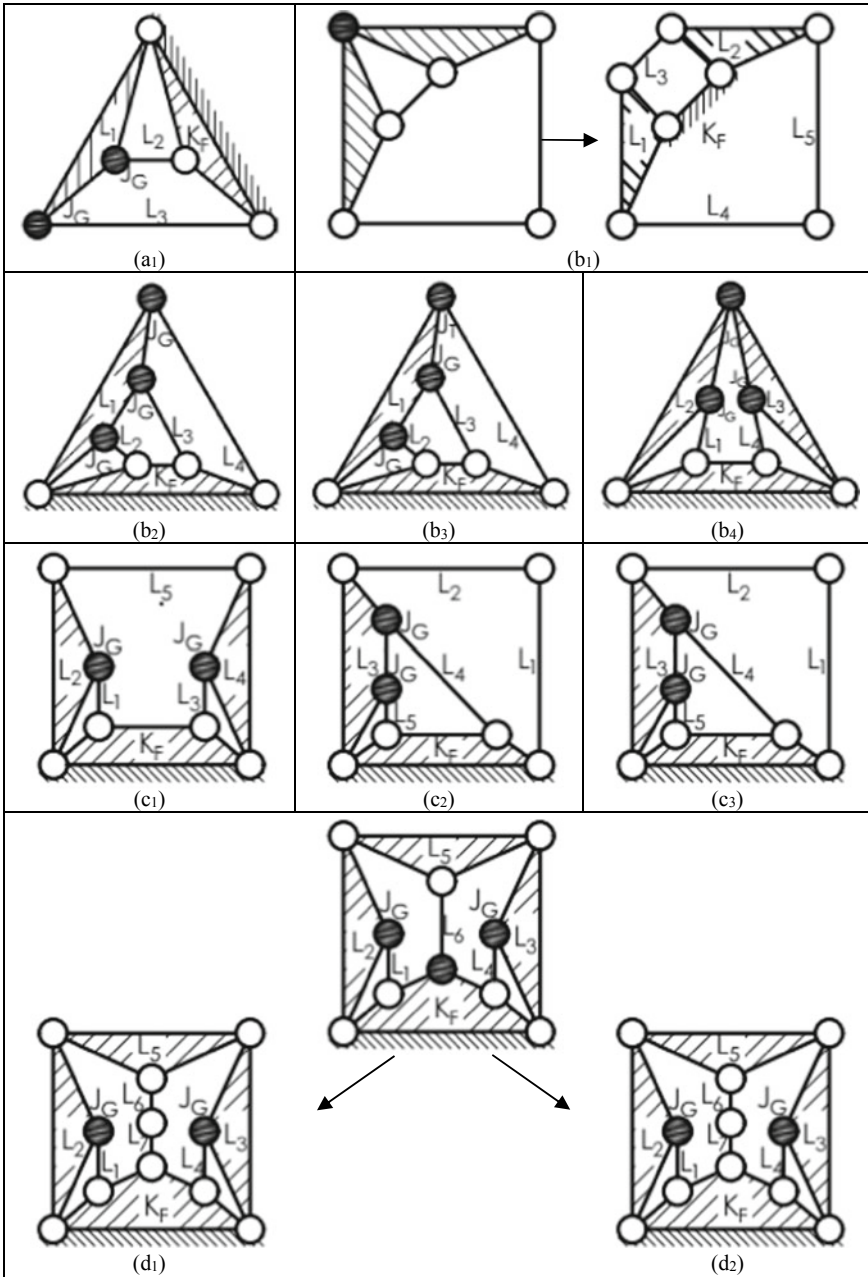


Fig. 4 Specialized kinematic chains

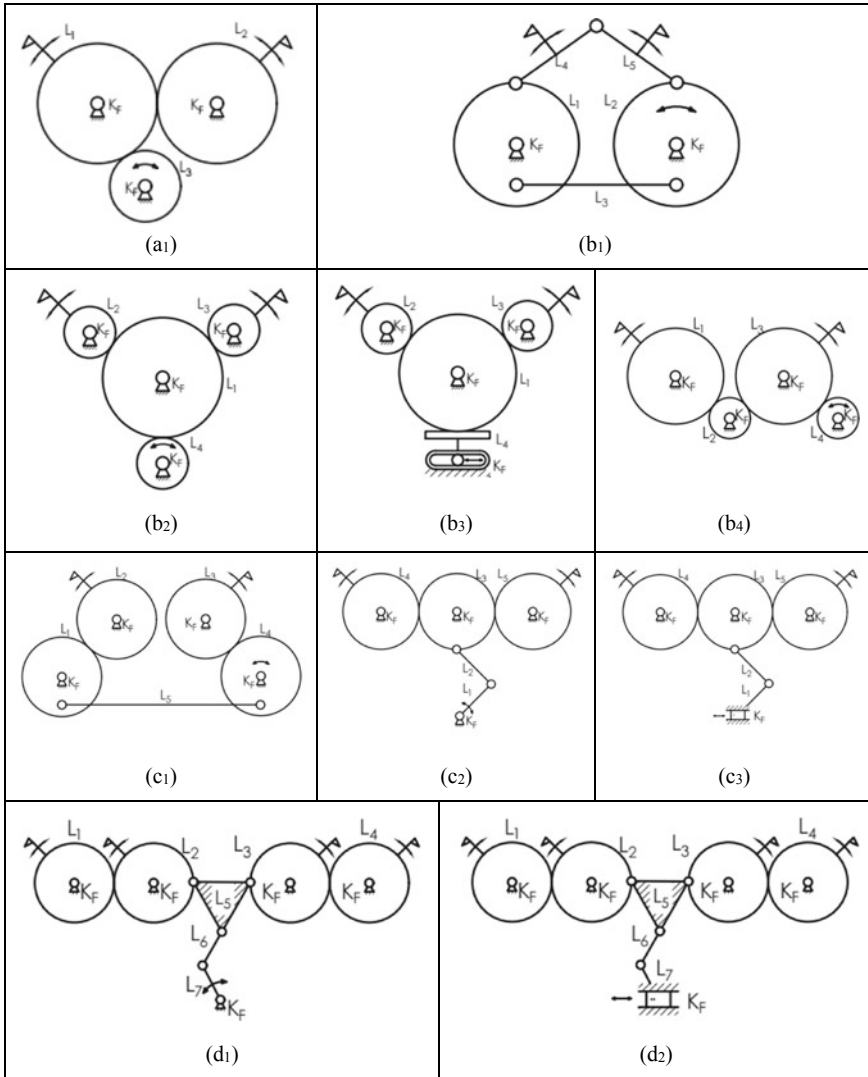


Fig. 5 Innovative flapping mechanism atlas

References

1. AeroVironment Inc, AeroVironment develops world’s first fully operational life-size hummingbird-like unmanned aircraft for DARPA. <https://investor.avinc.com/static-files/1a651d30-80cc-4f11-aace-1f57f9a6a6be>. Accessed 15 Apr 2022
2. Yan H-S (1998) Creative design of mechanical devices. Springer, Singapore
3. Polhamus EC (1971) Predictions of vortex-lift characteristics by a leading-edge suction analogy. J Aircraft 8(4)

4. Maxworthy T (1979) Experiments on the Weis-Fogh mechanism of lift generation by insects in hovering flight part I, dynamics of the 'fling'. *J Fluid Mech* 93:47–63
5. Dickinson MH, Gotz KG (1993) Unsteady aerodynamic performance of model wings at low Reynolds numbers. *J Exp Biol* 174:45–64
6. Zhang T, Zhou C, Wang C, Zhang X (2011) Flapping wing mechanism design based on mechanical creative design theory. In: 2011 International conference on mechatronic science, electric engineering and computer (MEC), August 19–22, 2011, Jilin, China, pp 2237–2240
7. Yusoff H, Abdullah MZ, Mujeebu MA, Ahmad KA (2013) Development of flexible wings and flapping mechanism with integrated electronic control system, for micro air vehicle research. *Exp Tech* 37:25–37
8. Srigrarom S, Chan W-L (2015) Ornithopter type flapping wings for autonomous micro air vehicles. *Aerospace* 2:235–278
9. Bin Abas MF, Bin Mohd Rafie AS, Bin Yusoff H, Bin Ahmad KA (2016) Flapping wing micro-aerial-vehicle: kinematics, membranes, and flapping mechanisms of ornithopter and insect flight. *Chin J Aeronaut* 29(5):1159–1177
10. Jeon JH, Cho H, Kim Y, Lee JH, Gong DH, Shin S, Kim C (2017) Design and analysis of the link mechanism for the flapping wing MAV using flexible multi-body dynamic analysis. *Int J Micro Air Veh* 9(4):253–269
11. Yang Z, Xuan J (2018) Research on kinematic reliability of flapping mechanism for flapping wing flight. In: Haugen et al (eds) *Safety and reliability—safe societies in a changing world: proceedings of ESREL 2018*, June 17–21, 2018. CRC Press, Trondheim, Norway
12. Hassanalian M, Abdelkefi A (2019) Towards improved hybrid actuation mechanisms for flapping wing micro air vehicles: analytical and experimental investigations. *Drones* 3:73
13. Ji B, Zhu Q, Guo S, Yang F, Li Y, Zhu Z, Chen S, Song R, Li Y-B (2020) Design and experiment of a bionic flapping wing mechanism with flapping–twist–swing motion based on a single rotation. *AIP Adv* 10:065018
14. Yousaf R, Shahzad A, Mumtaz Qadri MN, Javed A (2021) Recent advancements in flapping mechanism and wing design of micro aerial vehicles. *Proc Inst Mech Eng Part C J Mech Eng Sci* 235(19)
15. Shi Y, He W, Guo M, Luo X, Ji X (2022) Mechanism design and motion analysis of a flapping-wing air vehicle. *Math Probl Eng* 2022(7920914)
16. Yiming Y (2017) Flutter its wings up and down flying toy. China Patent CN107080957A

# Structural and Dynamic Analysis of an Aluminium Alloy Piston Using Finite Element Method



Prayas Gupta, Manish Kumar, Kuldeep Narwat, and Vivek Kumar

**Abstract** The functionality of an engine relies on the efficient working of its piston. The piston is always acted upon by cyclic stresses and dynamic loads which directly affects its performance. Therefore, it is imperative to study its static and modal characteristics. The present study has been carried out to analyse the natural frequencies of vibration of a mechanical piston. The piston model used in the study has been modelled for two different aluminium alloys AA6105 and A7075-T6. Honda Activa 110 cc BS-IV Engine has been used for standard piston dimensions. Finite element analysis solver ANSYS has been used to perform static structural analyses. The equivalent stress, shear stress, and deformation in the solid model of the piston were obtained for two different aluminium alloys. The von Mises stress is computed as 163.87 MPa and 157.75 MPa for AA6105 and A7075-T6, respectively, which were below the yield value of the material. Six vibration modes were computed by performing modal analysis on piston considering both the aluminium alloy materials. The lowest natural frequencies reported for AA6105 and A7075-T6 were 8320.8 Hz and 8185.6 Hz, respectively. The piston skirt shows maximum deformation under different modes of natural frequencies. The solid model showed improvement in static and dynamic capabilities of a piston. Findings of this study will serve as a reference and framework for piston design.

**Keywords** Piston · Dynamic analysis · Static structural analysis · AA6105 · A7075-T6

---

P. Gupta · M. Kumar · K. Narwat (✉)  
Department of Mechanical Engineering, Galgotias University, Greater Noida, India  
e-mail: [kuldeep.narwat@galgotiasuniversity.edu.in](mailto:kuldeep.narwat@galgotiasuniversity.edu.in)

V. Kumar  
Department of Mechanical Engineering, Netaji Subhas University of Technology, New Delhi, India

## 1 Introduction

The power transmission in a mechanical system requires the efficient operation of rotating and reciprocating parts. A piston is one of the parts that undergo cyclic loads during its operation. The piston design involves the calculation of stresses, which should not exceed the allowable values prescribed in design manuals. The performance of an engine is directly associated with the safe and reliable operation of the piston. In order to better understand the realistic situation of working piston, it becomes imperative to perform static and dynamic analysis. This study has been conducted to calculate von Mises stresses for two aluminium alloy materials (AA6105 and A7075-T6.) used for a piston design. Aluminium alloy has a good thermal conductivity and exhibits excellent wear resistance. Due to its lightweight, it offers a high strength-to-weight ratio and becomes a suitable choice for piston material. There are several aluminium alloys available in the material library which are categorized from series of alloys ranging from 1000 to 8000 based on the percentage of base material and the chemical composition of alloying material. Aluminium alloy 6000 is wrought alloy series alloyed with magnesium and silicon to provide hardness to a mechanical component. 6000 series possess property of good machinability; AA6105 material is used from this series as it a suitable choice for heat resistant application [1]. Aluminium alloy 7000 series is alloyed with zinc to improve its hardness. Magnesium and copper are also used in the 7000 series of aluminium which provides corrosion resistivity. It provides high strength, ductility, toughness, fatigue strength, and good machinability [2]. Aluminium alloy 7075 have nearly 5.5–6% of zinc composition. Due to their excellent mechanical properties, these materials AA6105 and A7075-T6 have been selected to carried out research on piston design. Dynamic studies are required to understand different modes of vibration which in turn provide valuable information regarding the natural frequencies of a component. Vibration analysis is generally carried out to ensure that structural natural frequencies or resonant modes are not excited by the frequencies present in the applied load. Natural frequency helps us to find out whether resonance will occur or not. It is very necessary to find natural frequency because, if resonance will occur in the system, then a component will fail under these dynamic conditions. To perform these analyses, a Honda Activa 110 cc BS-IV Piston dimensions have been used. The part modelling has been done using SolidWorks 2016, and finite element analysis has been performed using ANSYS 2022. In order to numerically simulate the piston model, suitable boundary conditions are to be applied to the piston geometry.

Jadhav et al. [3] analysed a piston using two different alloys of aluminium (A4032, A3618) materials to predict its failure. In their analysis, they have observed that maximum stress would be generated near the piston's bottom side and near the piston pinhole. Critical temperature zones were observed on the piston head. They found that both piston results were approximately the same, i.e., deformation for A4032 and A3618 is 0.051 mm and 0.055 mm, respectively. Zheng et al. [4] performed finite element analysis on a WP10 series diesel engine piston using ANSYS software. Their analysis showed that maximum stress generated in the piston component

as 10.564 MPa, and it was observed on the piston's top land. Their dynamic analysis result showed a maximum deformation as 220.73 mm for fourth mode of vibration. The study findings serve as a reference and foundation for piston research and to provide better alternatives for piston design. Their results of dynamic analysis reported natural frequencies of six vibrational modes. Bin et al. [5] performed a reliability analysis on a solid model of a brake drum. Their findings suggested optimized design parameters and computed the natural frequencies. The first ten natural frequencies and vibration shapes were calculated, and they analysed that first and second modes show radial deformation in two different directions. Fourth mode of vibration reported large deformations where the piston deforms elliptically, the study serve as a guide for brake drum analysis and design. Singh and Sharma [6] investigated the stress distribution and thermal stresses of three distinct aluminium alloy pistons using finite element techniques. For their study, they used a piston from a four-stroke single-cylinder Bajaj Kawasaki motorbike. Comparative analysis for three different aluminium alloy materials (A2168, A4032, Al-GHS 1300) was performed, and it was found that Al-GHS 1300 has the minimum weight among the three materials. As a result of weight optimization, the inertia forces were reduced, which resulted in improving the engine's performance and its fuel efficiency. A high factor of safety [6] was obtained for Al-GHS 1300 than other materials which suggested its usage for high-performance engines. Daniel Vaczko et al. [7] have provided a design modification. They provide 2–3 skewness in inner surfaces. Two pockets were modelled on the piston head, and two ring grooves were provided on the piston; a fillet was provided on the edge to facilitate the flow of stress lines in geometry. The design modification has led to an improvement in the engine efficiency. Zhang et al. [8] conducted a study on a 1.6-L gasoline engine; a three-dimensional model of the connecting rod was created on SolidWorks 2016. Finite element analysis was done using ANSYS solver to compute the stress and eigen frequencies of connecting rod. The maximum tensile stress for the solid model was found to be 42.59 MPa, and the maximum compressive stress was calculated as 74.21 MPa. The above primary stresses were found to be less than the material's allowable stress suggesting the design to be safe. The dynamic analysis was performed on the part to obtain natural frequencies for six modes. The results of modal analysis showed that the middle section of the connecting rod was prone to bending and distortion. Distortion of the connecting rod would have serious implications on the working of an engine, and it needs careful examination to predict failure of a piston. Rahman et al. [9] in their research studied the effect of dynamic frequency on fatigue life of a piston model. Model of cylinder block approximates the model of a free piston engine, and it was subjected to frequency response fatigue studies. A Goodman mean stress correction method is used to predict life cycle of the model. Furthermore, a vibration fatigue study has been performed to understand the system behaviour in terms of structure, load, and coupling frequency. Srikanth Reddy et al. [10] made a study on pistons; their analysis was based on two different conditions, i.e., thermal analysis with/without ceramic coating. They have predicted the critical regions experiencing high thermal stress. In the study, they found that the piston skirt may appear deformed during operation and that the deformation would cause stress on the top end of the piston.

Therefore, to overcome stresses, the piston crown must be rigid enough to minimize deformation and thereby reduce the stress concentration in its critical regions. The coated material resulted in an overall reduction of about 35% in maximum stress in the piston. Piston design models are replicated using iterations to find the safe design based on the application of load. Kumar and Govindarajulu [11] conducted their study on V6 engine. Static and thermal analyses were performed on the piston model. Layers of zirconium and silicon dioxide were applied to a ceramic piston to investigate their effect on its thermal efficiency. The analysis reported that both materials were able to withstand a maximum pressure of 14 Mpa, and a factor of safety of around 1.5 was obtained due to the applied load. The findings of the thermal investigation revealed that the total temperature distribution and heat transfer rate values were approximately the same for these materials. The coating with silicon dioxide ceramic on Al-6065 resulted in a significant improvement in the piston's performance for static and thermal analysis. Yeqing et al. [12] performed structural and modal analysis on a water hydraulic reciprocating piston pump driven by a linear motor. The results of the dynamic analysis show that the natural frequency of the piston pump is less than the excitation frequency of motor. Therefore, the system would not experience any resonance. Bhutto et al. [13] analysed an automotive piston of an engine based on piston shapes. In thier study comparative analysis a shallow depth combustion chamber reported excellent wear and corrosion resistance due to its low density, high specific strength, and low thermal expansion coefficient. Chougule and Khatawat [14] conducted a study on a piston of a two-stroke cylinder engine of a motorbike. Finite element techniques were used to investigate the stress distribution of the piston during its combustion process. During the investigation, the effect of various parameters such as crown thickness, barrel thickness, and piston head height was analysed to understand the distribution of stress in a piston. Venkataraman et al. [15] studied a coated piston and computed its von Mises test using ANSYS solver. Due to coating provided on piston's crown, von Mises stress is increased by 16%. The literature review discussed above has been utilized to understand the selection of material and selection of design parameters to model the piston component.

## 2 Design and Modelling of a Piston

In order to design a piston for an IC engine, the basic design instructions are to be followed. Aluminium alloy AA6105 and A7075-T6 are used as piston material as they offer sufficient strength and thermal conductivity. During the combustion process piston resists pressure loads and hence a suitable material should be selected which can resist these deformations and stresses generated during the combustion process. A compact piston design is useful as it would result in material reduction and lowering the mass moment of inertia of the engine. The mechanical and chemical properties for Aluminium Alloy AA6105 and A7075-T6 are listed in Tables 1 and 2, respectively.



**Table 1** AA6105 aluminium alloy mechanical and chemical properties

Aluminium alloy-AA6105				
Mechanical properties			Chemical properties	
Properties		Unit	Material	Weightage
Density	2.69	g/cm <sup>3</sup>	Aluminium	97.2–99.0%
Young’s modulus	70	GPa	Chromium	0.1% max
Yield strength	260	MPa	Copper	0.1% max
Poisson ratio	0.3		Iron	0.35% max
UTS	270	MPa	Magnesium	0.45%
Density	2.69	g/cm <sup>3</sup>	Manganese	0.1% max
Young’s modulus	70	GPa	Silicon	0.6%
			Titanium	0.1% max
			Zinc	0.1% max
			Residual	0.15% max

**Table 2** A7075-T6 aluminium alloy mechanical and chemical properties

Aluminium alloy-A7075-T6				
Mechanical properties			Chemical properties	
Properties		Unit	Material	Weightage
Density	2.81	g/cm <sup>3</sup>	Aluminium	88.8–89.7%
Young’s modulus	71.7	GPa	Chromium	0.1% max
Yield strength	430	MPa	Copper	1.2–1.6% max
Poisson ratio	0.33		Iron	0.35% max
UTS	510	MPa	Magnesium	2.1–2.5%
Density	2.81	g/cm <sup>3</sup>	Manganese	0.1% max
Young’s modulus	71.7	GPa	Silicon	0.6%
			Titanium	0.1% max
			Zinc	5.6–6.1% max
			Residual	0.15% max

The Honda Activa 4-T single-cylinder BS-IV 110 cc engine piston is studied in this study. The engine’s parameters are listed in Table 3.

- $V_0$  Cylinder Volume
- $A_0$  Area of piston head
- $h_0$  Stroke
- $t_h$  Piton thickness
- $P$  Maximum pressure
- F.O.S Factor of safety
- $\sigma_t$  Permissible tensile stress

**Table 3** Engine specification

Type	Value
Description	4-stroke, single-cylinder, air-cooled
Engine volume	109.51 cc
Max. power	5.73 kW @ 8000 RPM
Max. torque	8.79 N-m @ 5250 RPM
No. of cylinders	1
Emission standard	BS4
Bore	47 mm
Stroke	63.1 mm

- $k$  Heat conductivity = 174.15 W/m – °C  
 $\mu$  Higher calorific value of fuel (KJ/Kg)  
 $m_f$  Mass of the fuel  
 $T_r$  Radial thickness of the ring  
 $T_a$  Ring's axial thickness  
 $T_e$  Piston barrel width at the free end  
 $\sigma_w$  Pressure on the cylinder wall  
 $b_a$  Top land thickness  
 $N$  Number of rings  
 $b_b$  Piston ring thickness  
 $T_b$  thickness at barrel's upper end  
 $d_r$  Radial depth of the piston ring clearance  
 B.P. Brake power  
 TDC Top dead centre  
 BDC Bottom dead centre.

## 2.1 Piston Dimension

The piston dimensions have been calculated using standard design catalogues [16, 17]. To calculate the diameter of the piston, we are using the volumetric capacity of a Honda Activa engine used in our study from Table 3.

$$\begin{aligned}
 V_0 &= \text{Engine volume} \\
 V_0 &= A_0 \times h_0 \\
 V_0 &= 109.51 \text{ cc} \\
 \pi r^2 \times 63.1 &= 109.51 \times 10^3 \text{ mm}^2 \\
 r &= 23.5 \text{ mm, hence } D = 47 \text{ mm}
 \end{aligned}$$

The strength of the piston head is calculated by its ability to bear stress and transfer combustion heat. All mathematical equations used for analytical calculations have been referred from Reddy [18].

**Piston Thickness**

The thickness of the piston is calculated based on the capacity of the piston, in which the Grashoff’s aluminium alloy formula is mainly used.

$$t_h = D \sqrt{\frac{3P}{16\sigma_t}}$$

where  $P = 6 \text{ N/mm}^2$  is the maximum pressure that an aluminium alloy can sustain. Maximum  $\sigma_t = (122.7 \text{ N/mm}^2$ , by taking into consideration the maximum tensile yield strength =  $276 \text{ N/mm}^2$ )

F.O.S = 2.25

$$t_h = 47 \times \sqrt{\frac{3 \times 6}{16 \times 122.7}}$$

$$t_h = 4.5 \text{ mm}^2.$$

Piston’s thickness may also be quantified in terms of combustion heat dissipation.

$$t_h = \frac{I \times 1000}{12.56k(t_c - t_e)}$$

where

- $t_c - t_o$  75 °C for aluminium alloy
- $I$  [ $\alpha \times \mu \times m_f \times \text{B.P}$ ] in KJ/s
- $\alpha$  heat absorbed by the piston as a percentage of total heat generated in the cylinder = 5% or 0.05
- $\mu$  47,000 kJ/Kg (petrol)
- $m_f$  0.15 kJ/BP/Hr
- B.P.  $2\pi NT/60 = 2 \times \pi \times 5250 \times 8.79/60 = 4.83 \text{ KW}$
- $I$   $0.05 \times 47,000 \times 0.15 \times 4.83/3600.$
- $I$  0.47318 kJ/s

$$t_h = \frac{0.4738 \times 1000}{12.56 \times 174.15 \times 75}$$

$$t_h = 2.88 \text{ mm}.$$

The maximum value of dimension is used while designing for safe design, i.e., 4.5 ~ 5 mm.

**Ring's Radial thickness ( $T_r$ )**

The formula below is used to compute the ring's radial width.

$$T_r = D \sqrt{\frac{3\sigma_w}{\sigma_t}}$$

where  $\sigma_w = 0.0251 \text{ N/mm}^2$  to  $0.0421 \text{ N/mm}^2$ .

$$T_r = 47 \times \sqrt{\frac{3 \times 0.042}{122.7}},$$

$$T_r = 1.51067 \sim 2 \text{ mm.}$$

**Ring's Axial Thickness ( $T_a$ )**

The breadth of the rings may be calculated as follows:

$$T_a = 0.7T_r \text{ to } T_r = 0.7 \times 2 = 1.05 \text{ mm.}$$

For the safe design, we take maximum  $T_r$ , so  $T_a = 1.5 \text{ mm}$ .

**Number of rings ( $N$ )**

$$N = \frac{D}{10 \times 1.5} = \frac{47}{10 \times 1.5} = 3.$$

**Top land thickness ( $b_a$ )**

$$b_a = t_h \text{ to } 1.2t_h,$$

$$b_a = 1.2t_h = 1.2 \times 4.5 = 5.4 \text{ mm.}$$

For the safe design, we consider a 6 mm top land thickness.

**Piston ring thickness ( $b_b$ )**

$$b_b = 0.75T_2 \text{ to } T_2,$$

$$b_b = T_a = 1.5 = 1.5 \text{ mm.}$$

**Upper end of the barrel, the maximum thickness ( $T_b$ )**

$$T_b = [(0.030 \times D) + d_r + 4.500] \text{ mm.}$$

The circumferential width ( $d_r$ ) of the piston ring is about 0.4 mm larger than the piston rings' radial thickness ( $T_r$ ).

$$d_r = 0.4 + T_r = 0.4 + 1.5 = 1.9 \text{ mm,}$$

$$T_b = [(0.03 \times 47) + 1.9 + 4.5 = 7.8 \sim 8 \text{ mm.}$$

For safe design, we consider  $T_r = 2$  (max.)

So,  $T_b = 8.5$  mm.

**Barrel width at the free end ( $T_e$ )**

$$T_e = 0.250T_b \text{ to } T_b,$$

$$T_e = 0.250 \times 8.50 = 2.125 \sim 2.5 \text{ mm.}$$

## 2.2 Methodology

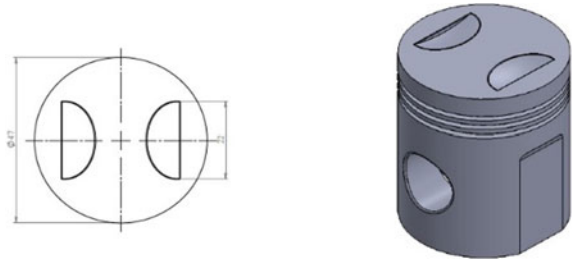
SolidWorks 2016 Software was used for solid modelling of the piston. Figure no. shows two-dimensional and three-dimensional designs of the piston. Dimensions are taken from Table 4 which was calculated through the analytical method. 2.5-mm-thick rib is placed on the inner side of the piston head to withstand bearing pressure. Model Save as in.igs Format. Solid model is shown in Fig. 1 and 2D sketch of piston model is shown in Fig. 2.

ANSYS 2022 has been used for finite element analysis of the piston. ANSYS workbench used for static structural analysis and modal analysis. Engineering data add on the workbench for AA6105 and A7075-T6 material. Geometry import is saved in.igs format. Mesh generation, boundary condition, and solution are done in the model section. Under static analysis, we get results on deformation, von Mises stress, maximum principal stress, shear stress, and under dynamic analysis, we get results up to six modal frequencies. Mesh quality is shown in Table 5

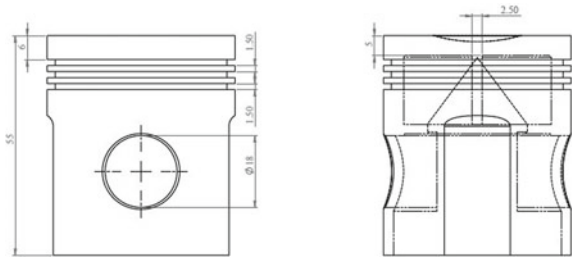
**Table 4** Piston dimension

Part name	Measurement (mm)
Cylinder bore ( $D$ )	47
Top land thickness ( $b_a$ )	6
Radial thickness of ring ( $T_r$ )	2
Ring's axial thickness ( $T_a$ )	1.5
Upper end of the barrel ( $T_b$ )	6
Width of other land ( $b_2$ )	8
Barrel width at the free end ( $T_e$ )	2.5
Piston thickness (th)	5

**Fig. 1** Three-dimensional solid modal of piston



**Fig. 2** Two-dimensional diagram of piston



**Table 5** Mesh quality

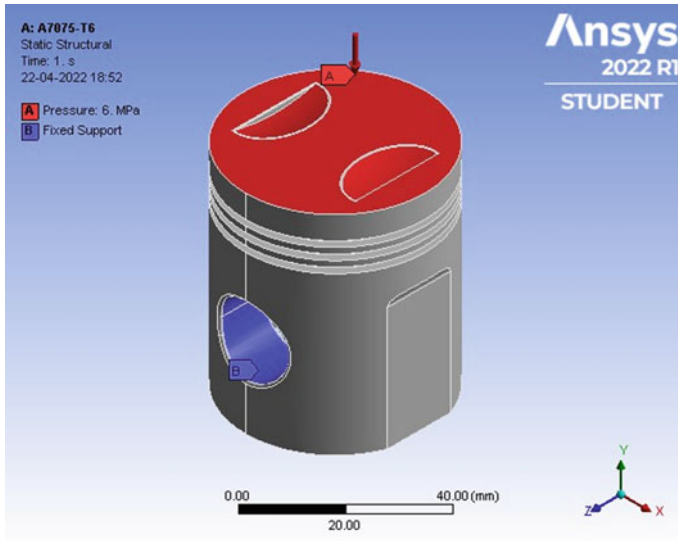
Mesh quality details	
Element order	Quadratic
Element size	1.4 mm
Resolution	5
Span angle	Fine
Smoothing	High
Nodes	94,768
Element	55,748

### 2.3 Load and Boundary Conditions

A load of 6 MPa is applied on top of the piston’s head. Fixed support is provided at the pinhole of the piston. The applied boundary conditions can be visualized in Fig. 3.

## 3 Results and Discussion

During the power stroke, due to the air–fuel mixture, combustion takes place in the cylinder. These burnt gases exert pressure on the piston’s head and push it towards to bottom dead centre. At the surface of the pinhole, fixed support has been provided to



**Fig. 3** Boundary condition

restrict all the degree of freedom. The fixed support at the pinhole enables the piston to travel from TDC to the BDC.

### 3.1 *Static Structural Analysis*

#### **AA6105 Aluminium Alloy Piston**

See Figs. 4, 5, 6, and 7.

#### **A7075-T6 Aluminium Alloy Material**

See Figs. 8, 9, 10, and 11.

Static structural analysis has been performed on the piston considering both aluminium alloys. Finite element techniques have been used to compute total deformation, von Mises stress, shear stress, and maximum principal stress. The von Mises stress for AA6105 is found to be 163.87 MPa as shown in Fig. 4, and its yield stress is 190 MPa, The von Mises stress for A7075-T6 is found to be 157.75 Mpa shown in Fig. 8, and its yield stress is 430 MPa. The result clearly indicates that calculated stress value is below the permissible value. Piston design is safe to withstand the load value used in the analysis. Von Mises stress of A7075-T6 is down by 6.12 MPa which helps significant reduction in total deformation of the piston which are shown in Figs. 5 and 9, respectively. Shear stress and the maximum principal stress values are calculated for AA6105 and A7075-T6 aluminium alloy which are shown in Figs. 7

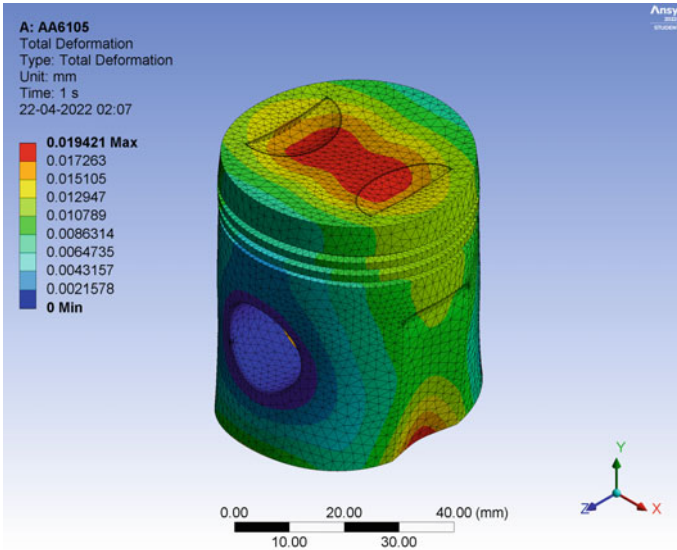


Fig. 4 AA6105 von Mises stress

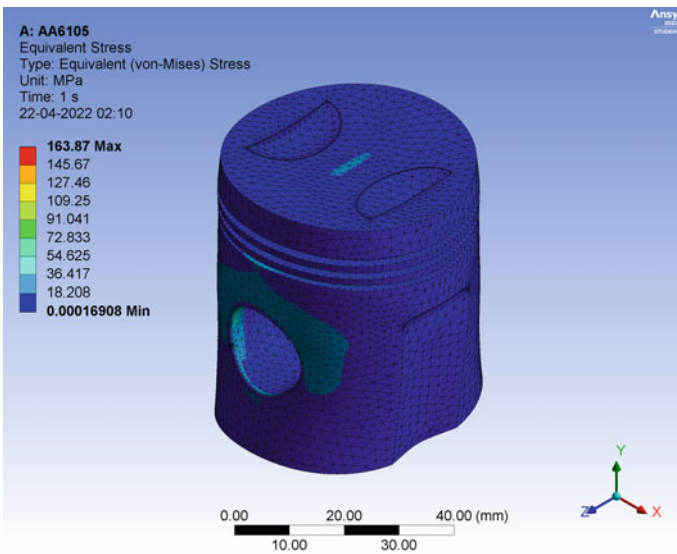


Fig. 5 AA6105 total deformation



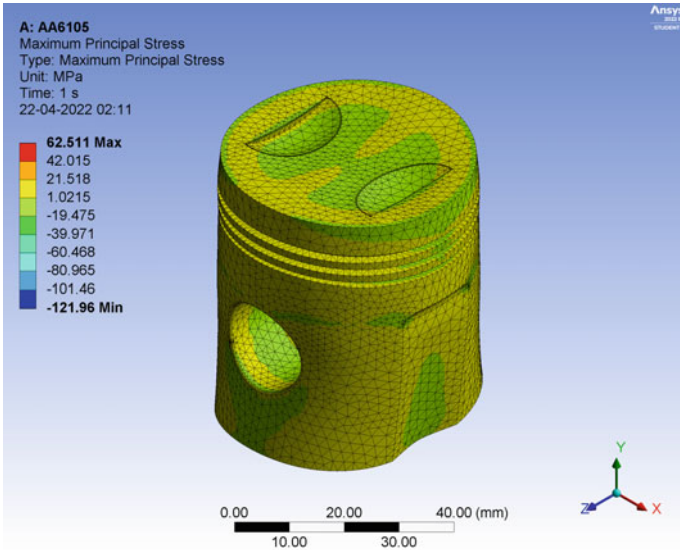


Fig. 6 AA6105 maximum principal stress

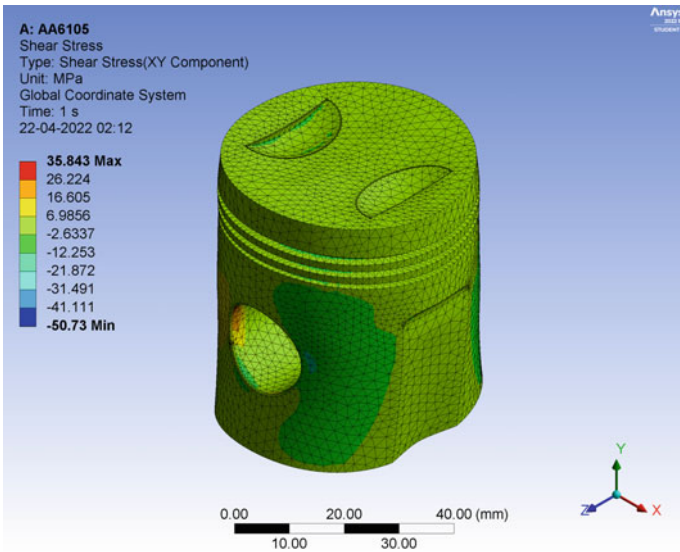


Fig. 7 AA6105 shear stress

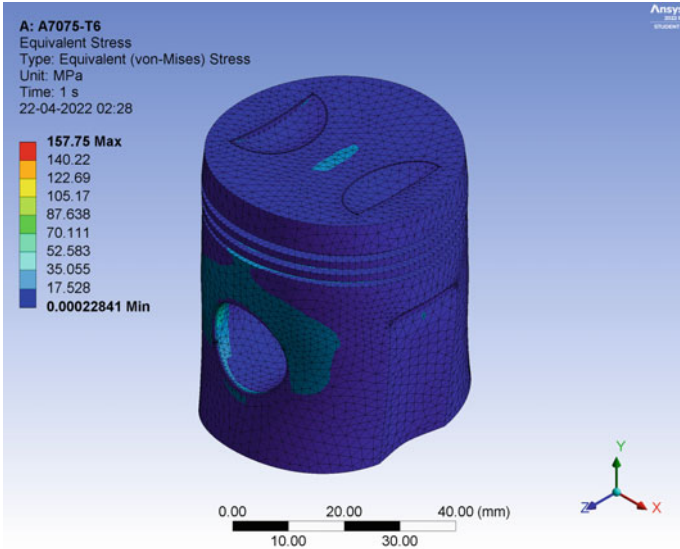


Fig. 8 A7075-T6 von Mises stress

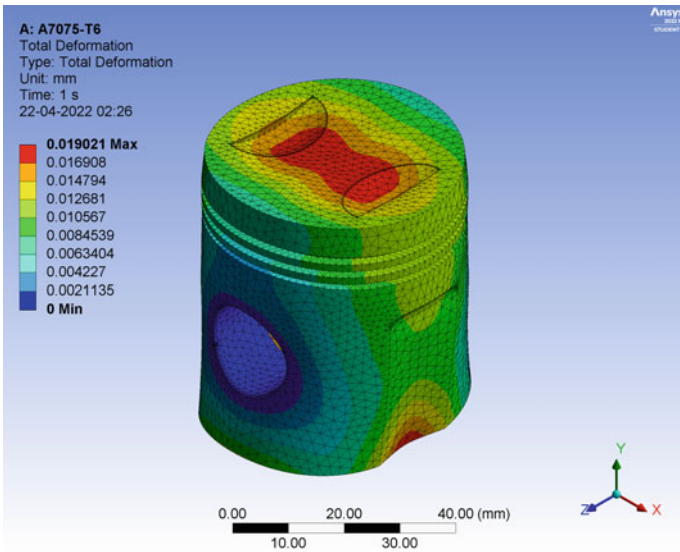


Fig. 9 A7075-T6 total deformation

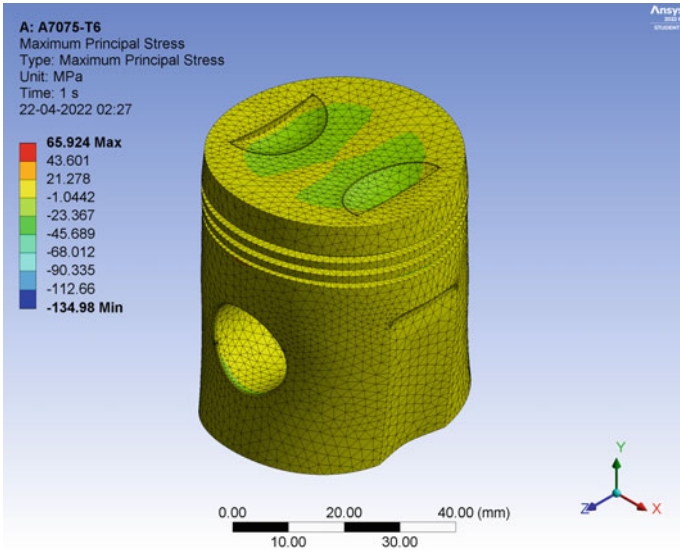


Fig. 10 A7075-T6 maximum principal stress

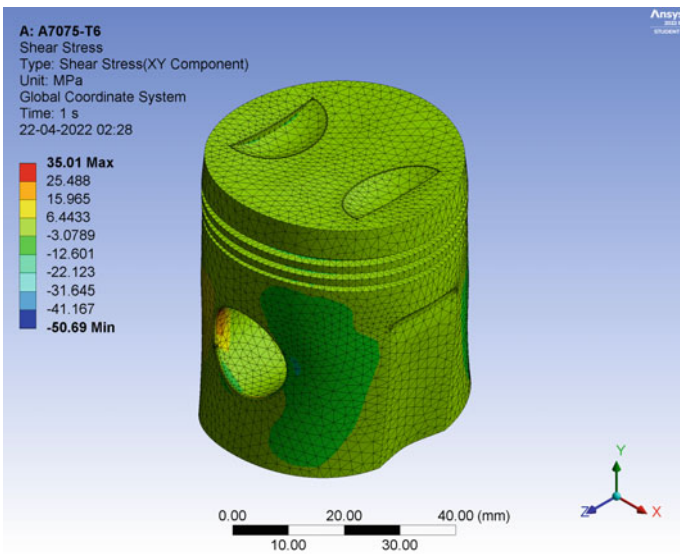


Fig. 11 A7075-T6 shear stress

**Table 6** Static analysis result

S. No	Parameter	AA6105	A7075-T6
1	Total deformation (mm)	1.94E-02	1.90E-02
2	Von Mises stress (MPa)	163.87	157.75
3	Shear stress (MPa)	35.8430	35.01
4	Max. principal stress (MPa)	62.511	65.924

and 10, respectively. The calculated values are within the allowable limits; maximum shear stress generated was observed near the piston pin hole. The static structural analysis result for both piston materials is tabulated in Table 6.

### 3.2 Modal Analysis

A mechanical component when subjected to dynamic loads exhibits frequency due to the amplitude of vibration. When this excitation frequency matches with the fundamental natural frequency of the system, then resonance takes place. The piston when subjected to time-varying load experiences different modes of vibrations; therefore, the natural frequency values are of utmost importance to avoid failure due to resonance in a mechanical component. To better understand this phenomenon, a linear dynamic analysis using ANSYS software is performed, and various mode shapes of the model have been observed. The first six natural frequencies are retrieved after doing a modal analysis on the solid model for both aluminium alloys.

#### AA6105 Aluminium Alloy

The first-order mode's natural frequency is 8320.8 Hz as shown in Fig. 13; the deformation was found to be maximum on the piston skirt. The second mode has a natural frequency of 10,864 Hz shown in Fig. 12, whereas the third-order modal analysis' natural frequency is 10895 Hz as shown in Fig. 15. The fifth-order mode's natural frequency is 13938 Hz as shown in Fig. 17, whereas the sixth-order mode's natural frequency is 14531 Hz as shown in Fig. 16. The sixth mode reported the highest natural frequency among the other modes of vibration. All modes of frequencies and descriptions are shown in Table 7 (Fig. 14).

#### A7075-T6 Aluminium Alloy

The first-order mode's natural frequency is 8185.6 Hz as shown in Fig. 19; the deformation was found to be maximum on the piston skirt. The second mode has a natural frequency of 10,760 Hz as shown in Fig. 18, whereas the third-order modal analysis' natural frequency is 10799 Hz as shown in Fig. 21. The natural frequency for fifth mode was calculated as 13,810 Hz shown in Fig. 23. The sixth mode reported the highest natural frequency of 14,396 Hz among the other modes of vibration as shown in Fig. 22. All modes of frequencies and descriptions are shown in Table 8 (Fig. 20).

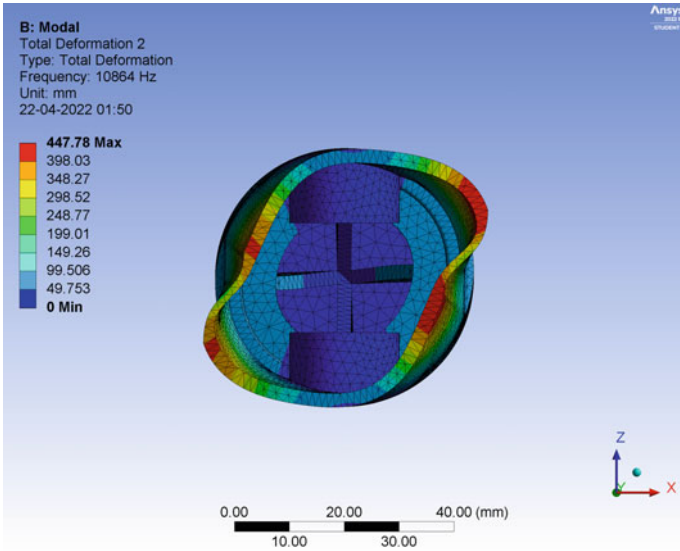


Fig. 12 AA6105 mode-2

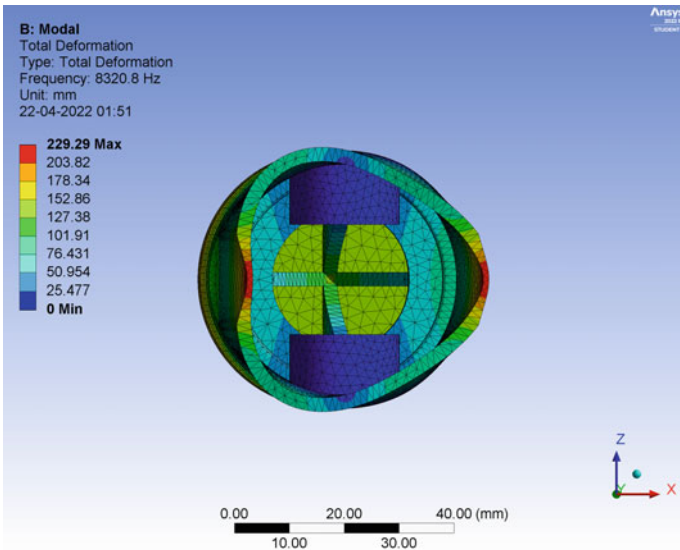
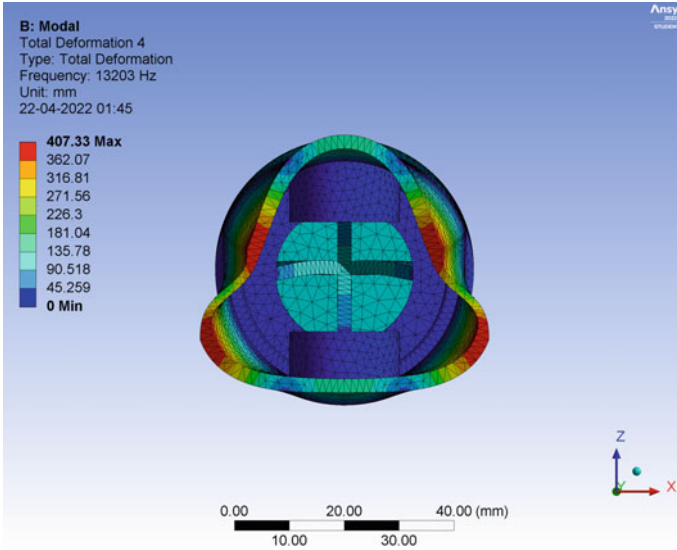


Fig. 13 AA6105 mode-1

**Table 7** AA6105 modal analysis result

Order	Natural frequency (Hz)
1	8320
2	10,864
3	10,895
4	13,203
5	13,938
6	14,531



**Fig. 14** AA6105 mode-4

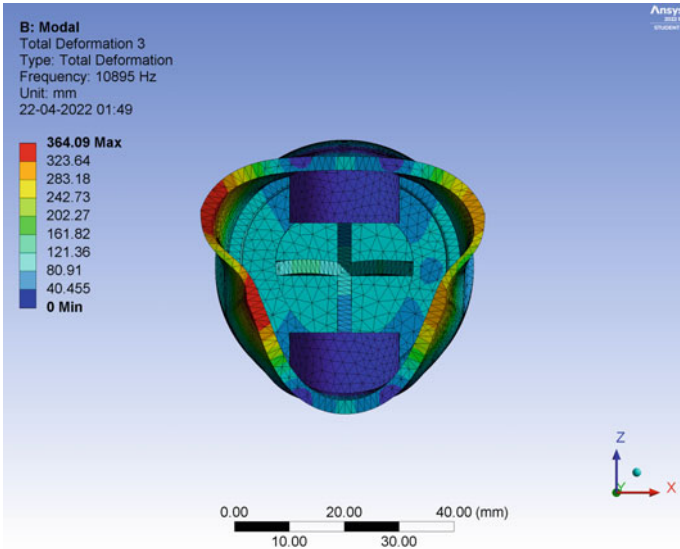


Fig. 15 AA6105 mode-3

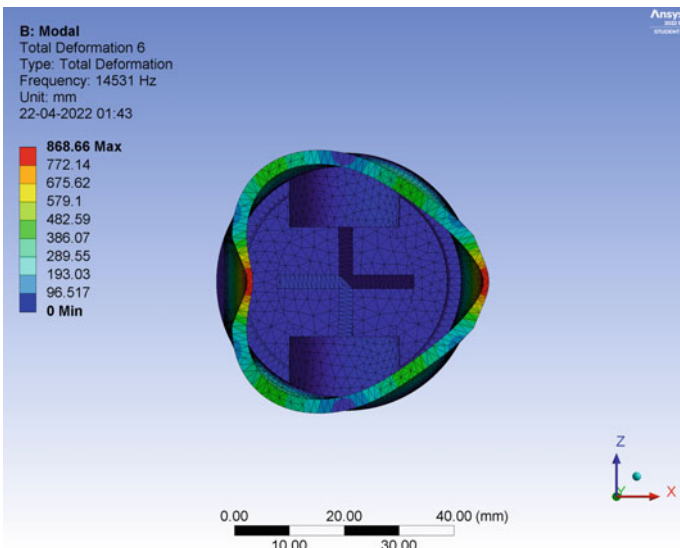


Fig. 16 AA6105 mode-6

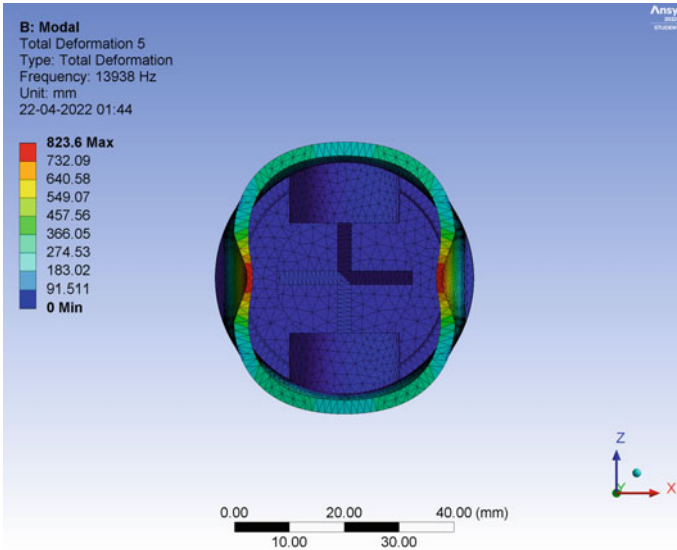


Fig. 17 AA6105 mode-5

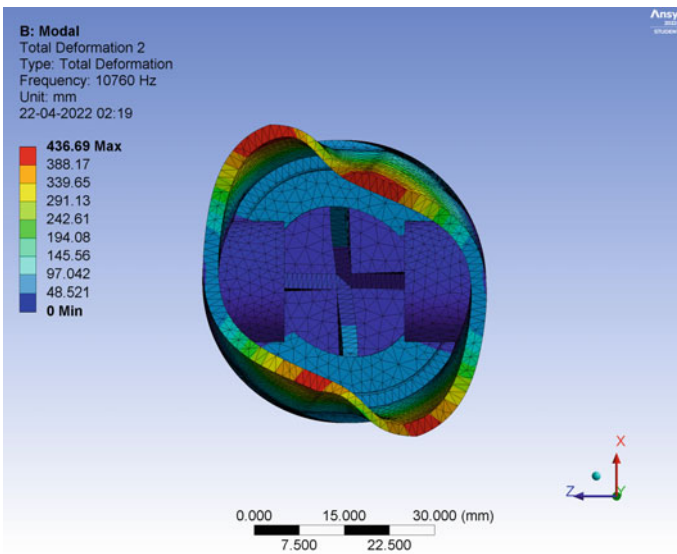
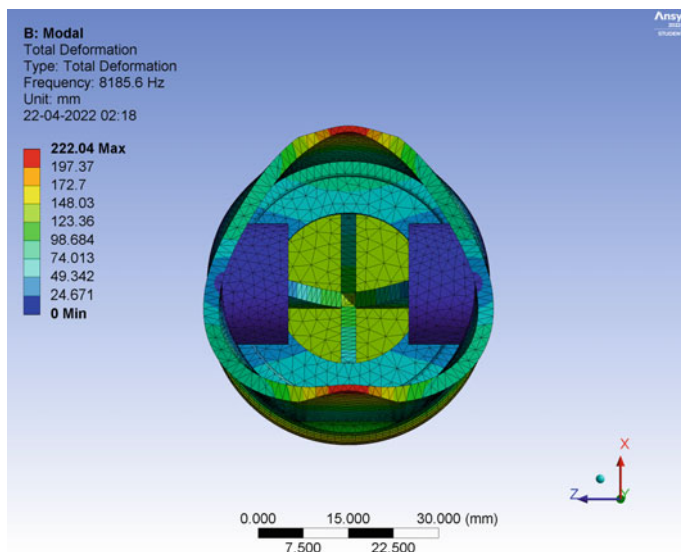


Fig. 18 A7075-T6 mode-2





**Fig. 19** A7075-T6 mode-1

**Table 8** A7075-T6 modal analysis result

Order	Natural frequency(Hz)
1	8185
2	10,760
3	10,799
4	13,025
5	13,810
6	14,396

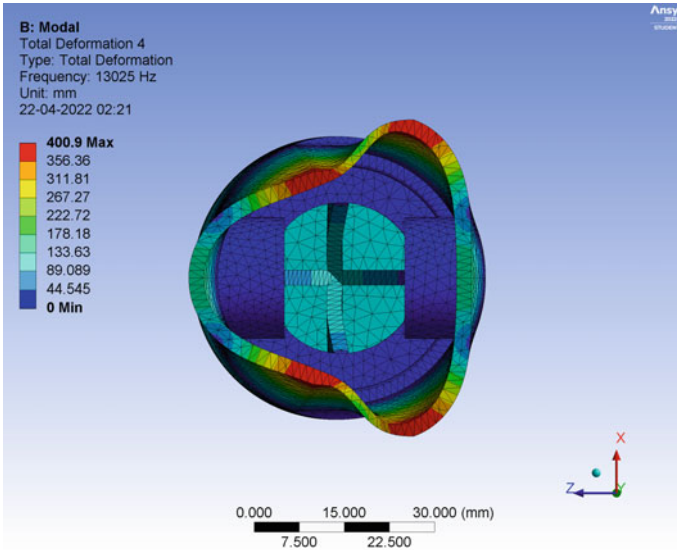


Fig. 20 A7075-T6 mode-4

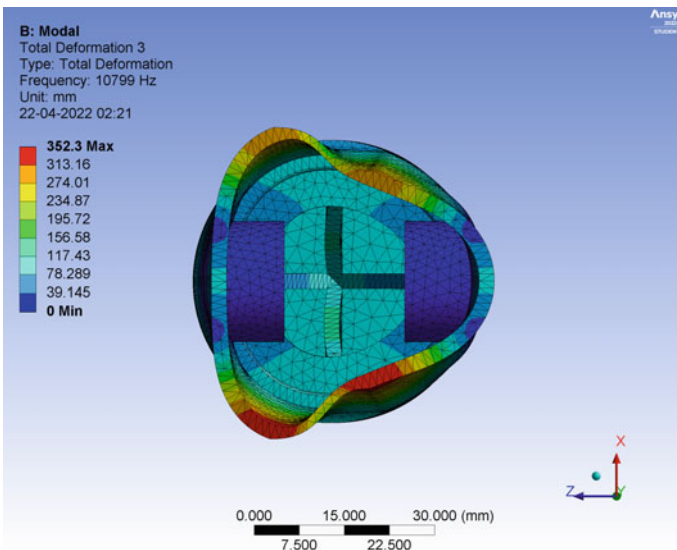


Fig. 21 A7075-T6 mode-3

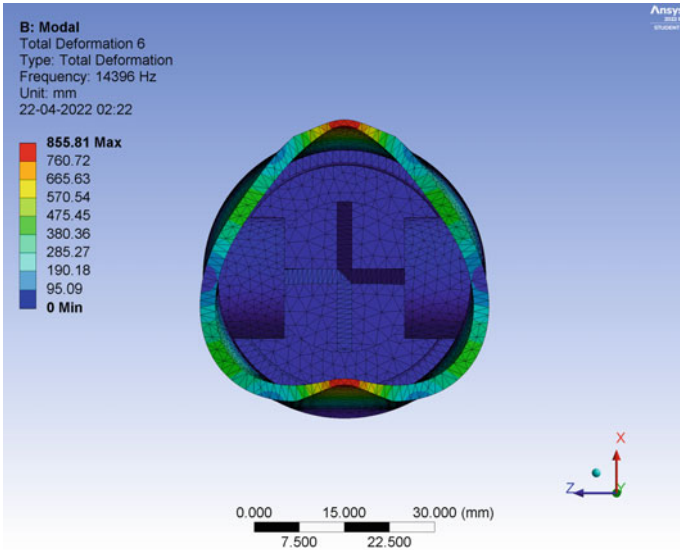


Fig. 22 A7075-T6 mode-6

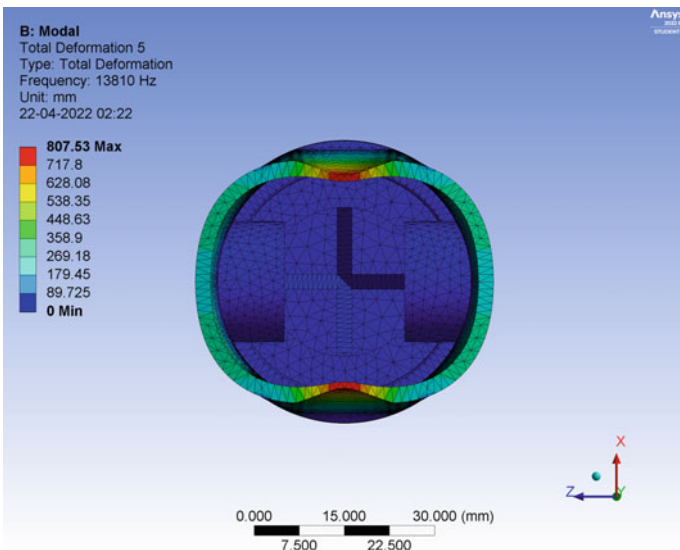


Fig. 23 A7075-T6 mode-5

## 4 Conclusion

The piston has a significant influence on the engine's performance, and the materials with which the piston is manufactured play a key role in its selection for a particular operation. In this study, dynamic and static analyses were done on two different aluminium alloy materials, i.e., AA6105 and A7075-T6. Finite element analysis solver ANSYS 2022 has been used to perform static analysis on the piston part. Calculated stress was below the yield stress of the material which shows that the design is safe for the applied load. The factor of safety for aluminium alloy AA6105 is computed as 1.15 which represents that the design is safe under the above loads. The aluminium alloy A7075-T6 reported a higher factor of safety than AA6105 attributed to lower von Mises stress in A7075-T6. The critical region where stress was calculated to be maximum was near the piston skirt surface, and both the selected materials showed similar results. The maximum deformation is found to be on the top of the piston of AA6105 and A7075-T6.

In the context of dynamic analysis, modal analysis has been performed on piston by using finite element analysis solver ANSYS, and natural frequencies were calculated for six modes for both the alloy materials. The natural frequency is proportional to the parts' quality and strength. The natural frequency of the piston was investigated, as well as the impact of structural changes on the natural frequency. Piston skirt shows maximum deformation on different modes of frequencies. A considerable distortion has been observed on the piston head.

**Acknowledgements** The authors would like to acknowledge the support of the Department of Mechanical Engineering, Galgotias University, Greater Noida, India.

## References

1. ASM Handbook (1990) Properties and selection: nonferrous alloys and special-purpose materials 2:137–38 (7075)
2. Gale WF, Totemeier TC (2003) 22 mechanical properties of metals and alloys. In: Smithells metals reference book, 8th edn. Elsevier Butterworth-Heinemann, Burlington, MA, p 22. ISBN 0750675098. (6105)
3. Jadhav V, Jain RK, Yogendra SC (2016) Design and analysis of aluminium alloy piston using CAE tools. IJESRT ISSN: 2277-9655
4. Zheng B, Zhang J, Yao Y (2019) Finite element analysis of the piston based on ANSYS, ITNEC. IEEE China. ISBN:978-1-5386-6244-1
5. Bin Z, Jing-dong Z (2017) Modal analysis of the brake drum of heavy-scale automobile. In: 3rd information technology and mechatronics engineering conference. IEEE China
6. Singh AR, Sharma PK (2014) Design: analysis and optimization of three aluminium piston alloys using FEA. IJERA 4(1):94–102. ISSN: 2248–9622
7. Reddy SS, Kumar BSP (2013) Thermal analysis and optimization of I.C. engine piston using finite element method. Int J Innovative Res Sci Eng Technol 2(12). ISSN: 2319-8753
8. Zhang M, Zhao C et al (2019) The structure, stress, and modal analysis of 1.6-liter gasoline engine connecting rod based on finite element analysis. In: IOP conference series 677-2019-032094, IMMAGE

9. Rahman MM, Ariffin AK, Jamaluddin N, Haron CHC (2009) Finite element analysis base on vibration fatigue analysis for a new free piston engine component. *Arab J Sci Eng* 34(1B)
10. Floweday G, Tait RB, Petrov S, Press J (2011) Thermo-mechanical fatigue damage and failure of modern high performance piston. *Int J Fail Anal* 18:1664–1674
11. Kumar BB, Govindarajulu C (2021) Design and optimization analysis of V6 engine piston by using ceramic coating *IJSRT* 11(02):122. ISSN: 2457-0362
12. Yeqing H, Songlin N, Kai M, Fan L, Lei L (2015) Static stress and modal analysis of water hydraulic reciprocating piston pump driven by the linear motor. In: *International conference on fluid power and mechatronics, IEEE*. 978-1-479987702/15
13. Bhutto A, Raus AA, Wahab MS, Kamarudin K (2016) Mechanical properties, material and design of the automobile piston: and ample review. *Indian J Sci Technol* 6(36). ISSN: 0974-6846. <https://doi.org/10.17485/ijst/2016/v9i36/102155>
14. Chougule SS, Khatawat VH (2013) Piston strength analysis using FEM. *Int J Eng Res Appl (IJERA)* 3(2):1724–1731. ISSN: 2248-9622
15. Rajam CV, Murthy PVK, Murali Krishna MVS (2013) Linear static structural analysis of optimized piston for bio fuel using Ansys, *Int J Mech Prod Eng Res Dev (IJMPERD)* 3(2):11–20. ISSN 2249-6890
16. Khurmi RS, Gupta JK (2005) *Internal combustion engine in machine design* Eurasia publishing house private limited, 25th edn. pp 1125–1210
17. Sonar DK, Chattopadhyay M (2015) Theoretical analysis of stress and design of piston head using CATIA & ANSYS. *Int J Eng Sci Invent* 4:52–61
18. Reddy KS, Senthil Kumar KR, Jeykrishnan PR (2013) Study of stability of honeycomb structured piston *IJERA* 3(5):1984–1988. ISSN: 2248–9622

# Design and Simulation of PV Solar Cell System with Microgrid and Fuel Cell Using Discrete PID and FUZZY Controller



Gunjan Taneja, Vijay Kumar Tayal, and Kamlesh Pandey

**Abstract** Electrical energy is an important parameter for the economy and development of society in any country. An energy crisis is faced by almost one-third of the world's population today. The power issues can be alleviated by utilizing renewable energy resources in the modern power system. These energy sources are modular in nature and environment friendly. This work entails connecting fuel cells, a PV array system, and a battery with the grid. Discrete PID and fuzzy controllers are used to ensure the desired voltage/current outputs. The simulation results indicate that discrete PID controller output yields in distortion and disturbances. However, a modified fuzzy controller with increased membership function width results in far better outputs. The obtained output voltage and current waveforms are uniform with the reduction in overshoot.

**Keywords** Discrete PID · Modified fuzzy controller · Photovoltaic system · Microgrid · Fuel cell · Modeling · MATLAB · Simulink

## 1 Introduction

Rising energy demand as a result of population growth, industrial expansion, and technological advancement has prompted researchers to look into other alternatives for the generation of energy. Environmental concerns, such as greenhouse gas emissions, global warming, and the depletion of natural resources including natural gas, fossil fuels, and coal, are motivating researchers to develop technologies that can yield power from renewable energy sources. Renewable energy can be defined as energy based on natural resources that can be renewed such as wind, solar radiation,

---

G. Taneja · V. K. Tayal (✉) · K. Pandey  
Department of Electrical and Electronics Engineering, Amity University Uttar Pradesh, Noida,  
Uttar Pradesh, India  
e-mail: [vktyal@amity.edu](mailto:vktyal@amity.edu)

K. Pandey  
e-mail: [kpandey@amity.edu](mailto:kpandey@amity.edu)

rainfall tides, and geothermal heat. Alternative energy is a term used to describe an energy source that is not derived from fossil fuels. In general, it denotes nontraditional energy sources with low environmental impact. Under the current energy crisis, energy sources such as solar, wind, and fuel cells are an important alternative for improving power system reliability. It also aids in the reduction of CO<sub>2</sub> emissions and the mitigation of global warming issues [1]. Solar energy is the collection of the sun's radiant light and heats through a variety of ever-evolving technologies such as solar heating, solar thermal, architecture, and photosynthesis through the artificial method. Due to low operation cost, cleanliness, and minimal maintenance requirement, solar photovoltaic (PV) systems are widely used. PV has risen in importance as a source of energy for a variety of applications. The ability to the conversion of energy along with reducing costs has led to its growth. Since the early 1990s, researchers have been working on developing fuel cells for use in a variety of applications. Portable, backup, transportation, and stationary power applications are all possible with fuel cells. The use of fuel cells has also grown in popularity as a means of producing clean energy. The microgrid is a key concept for incorporating distributed energy resources. A microgrid can handle unexpected fluctuations while maintaining system reliability. When the connection to the alternating current grid is no longer available due to faults, a microgrid can operate in both grid-connected and autonomous modes.

Reshmi and Joe Nigel [2] worked on a photovoltaic system using PI, PID, and different control methods. Incorporating fuzzy method for simulating fuel cells is done by Khubchandani et al. in [3]. The involvement of the fuzzy method for MPPT control is shown in [4]. Khaled et al. [5] focused on the implementation of the PID technique for tracking maximum PowerPoint. The alternative source of energy is discussed by Harabbi et al. [6]. The use of FIS and PID techniques is explained in [7]. Sachin et al. [8] described the effect on peak load while working on a PV array. Suresh et al. [9] emphasize fraction-order PI control of the hybrid system. Frequency control of microgrid in island operation is done in [10]. Balancing of frequency of load by PID tuning is done by Nayak and Maharana [11]. PID control-based microgrid is discussed in [12]. Dwivedi and Laxmi focused on PV system efficiency improvement [13]. Optimization of the photovoltaic system using the bee colony algorithm is explained in [14]. The fractional control technique is described in [15].

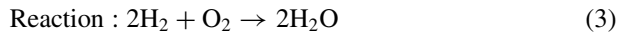
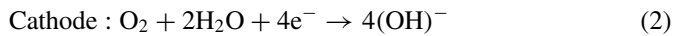
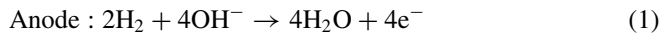
The proposed work includes the design and simulation of a PV array with a fuel cell and a microgrid. This modeling is completed with the support of MATLAB Simulink. Power management is done by the use of the battery. To achieve the best results, the discrete PID controller is compared along with the fuzzy controller. A modified fuzzy controller is used in which the width of the membership function is increased to get the desired response. To optimize the voltage from the source side and the grid side, a Mamdani-type fuzzy-based controller is used. This paper is organized as follows—the description of the system is given in Sect. 2. Different control schemes used for designing the system are then described. Simulation models and results are then added in Sect. 3. Lastly, the conclusion is added followed by the references used.

## 2 System Description

The system model comprises fuel cells, PV array, battery, inverter, filters, AC source, grid, and loads integrated as a single system.

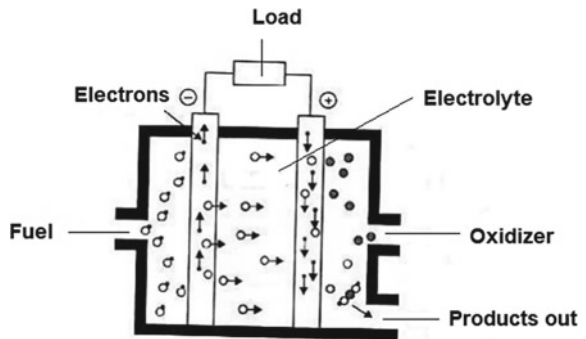
### 2.1 Fuel Cell System

The conversion of energy takes place in the fuel cell. Because of the versatile nature of hydrogen, it is possible to use it in various applications. Clean energy is driven by the hydrogen-based fuel cell. A fuel cell works more simply. In this, conversion of fuel into electricity takes place. The process of this conversion is referred to as an electrochemical reaction. Transportation of electrons takes place on the electrolyte. The fuel cell provides a clean and viable option in nature. Figure 1 represents the schematic representation of the fuel cell. The following equations represent reactions in fuel cell

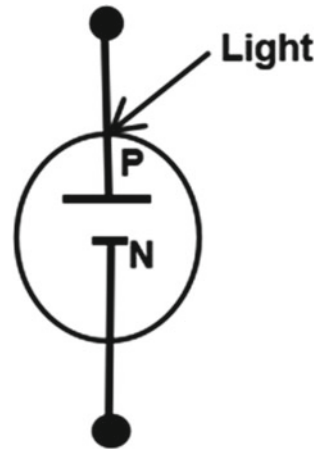


Two fuel cell stacks of 2.5 KW and 48 V each are used for designing an integrated Simulink model. Hydrogen-based fuel cells are used in the system.

**Fig. 1** Fuel cell schematic diagram





**Fig. 2** Solar cell symbol

## 2.2 Photovoltaic System

Scientists refer to solar cells as photovoltaic (PV) cells because sunlight is converted directly to electricity. PV name is derived from the PV effect, in which light is obtained by the conversion of photons. Traditionally, silicon-based solar cells were used. Nowadays, solar dyes and conductive plastics are used in manufacturing solar cells. A solar photovoltaic module is made up of a series and parallel connection of solar cells to accomplish the optimum voltage and current rating. It operates based on the photovoltaic effect. According to this effect, current flows once light strikes the semiconductor. Light is made up of photons with varying wavelengths. Electron hole pair formation takes place. The predetermined electric field is there to allow the flow of current through external circuits. The symbol for a solar cell is represented in Fig. 2.

FS-272 Module of PV array is used in the building of model in MATLAB. Two series-connected and ten parallel-connected strings, along with 110 cells per module are selected for this model. One PV array of 1 KW is involved in systems design.

## 2.3 Microgrid

With the development of microgrids, the conflict between the big power grid and distributed generation technologies has been reduced. It improves the efficiency of renewable sources. Microgrid is a tiny modular and decentralized power generation and distribution system. The major features are included in microgrid are that it can work in both island mode and grid-connected mode and act as a controlling element and clean resource. Microgrids provide a way to balance the requirement to minimize the emission of gases with the need to maintain reliable electric power in absence

of other sources of energy. Microgrids are also assured of being resistant to harsh weather and natural disasters.

### 3 Control Schemes

Different control schemes used in designing and simulating the systems are described as follows.

#### 3.1 Discrete PID Controller

A discrete PID controller is used in the system. It is the most common controller used in industries. As compared to PID controller, it has a high-rise time and is faster in response. It is distinct from the PID controller in such a way that time-based parameters are set to discrete values. Different methods are used for discretizing the PID controller like forward Euler, backward Euler, and trapezoidal method. The following equation is used for the controller in discrete-time form:

$$C = K_p + K_i * IF(z) + K_d/(T_f + DF(z)) \quad (4)$$

$$IF(z) = DF(z) = T_s/z - 1 \quad (5)$$

Here,  $K_p$  is the proportional gain,  $K_i$  is the integral gain,  $K_d$  is the derivative gain,  $T_f$  is the time constant for first-order derivative filter, and  $T_s$  is the sample time

In designing of system,  $K_p$  is considered to be 1,  $K_i$  to be 1,  $K_d$  to be 5, and filter coefficient is 100. The selection of parameters is done on basis of trial methods. Based on these parameters, output waveforms are obtained for three-phase bus voltage and current, load voltage, and source voltage.

#### 3.2 Fuzzy Logic Controller

Fuzzy control system (FCS) is a mathematical and scientific system. It supports analog input written as logical variables with continuous values ranging from 0 to 1. Modified fuzzy logic is used in this system.

Fuzzy logic is utilized in a variety of applications, the most common of which is machine control. In place of “true” or “false,” fuzzy says “partially true.” In various studies, both GA and NN can perform similarly to fuzzy logic, but fuzzy logic has the advantage over these in that it can deal resolve problems that can be comprehended by a human operator, which is why it is involved in the design of controllers. This

unique property makes it ideal for human use. In this system, fuzzy logic controller is implemented for system design. Mamdani-type FLC is used.

Modified fuzzy logic is used in this system. In this model, width of the membership and the function are increased to get desired results. The input and output values are defined using the following variables NB (negative big), NM (negative medium), NS (negative small), ZE (zero), PS (positive small), PM (positive medium), and PB (positive big). For comparison purposes, three-phase bus voltage and current waveforms, load voltage and AC source voltage are considered. The FLC block diagram is shown in Fig. 3. Figure 4 represents fuzzy rules used to design the system.

Fig. 3 Block diagram of fuzzy logic controller

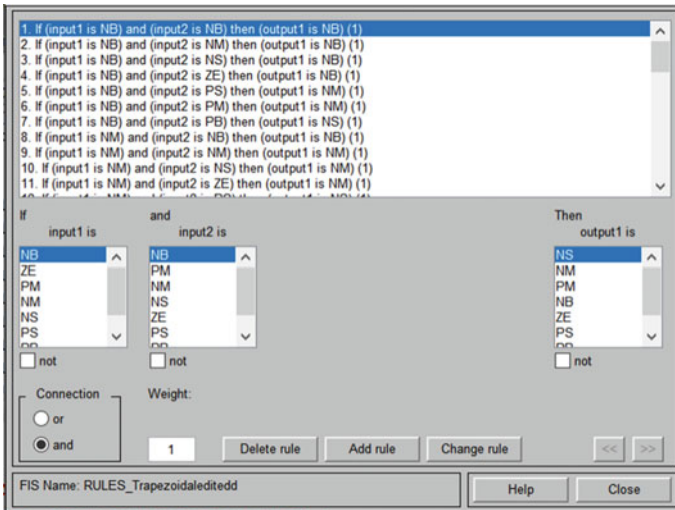
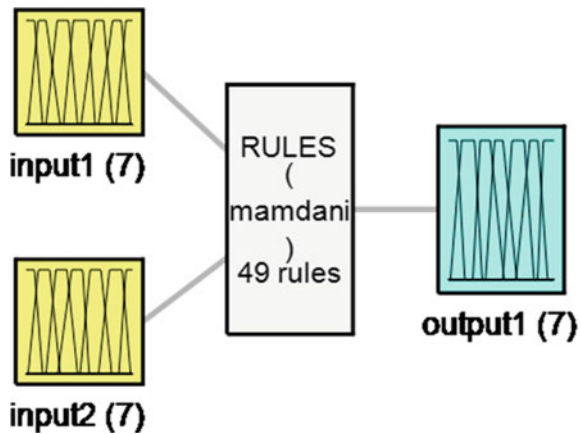


Fig. 4 Fuzzy rules

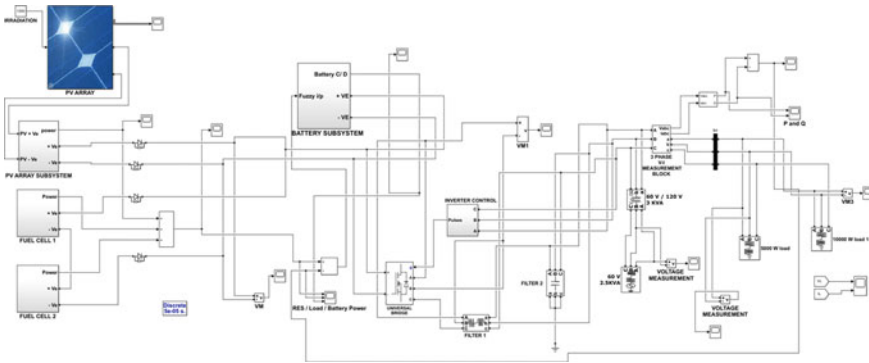


Fig. 5 Simulink model

## 4 System Model

Four energy sources are used to design this system. They are two fuel cells of 2.5 KW and 48 V DC, a PV array of 1 KW, 96 V DC, and 1 AC source of 2.5 KVA. The selection of the PV array module is done as FS-272. Irradiation (1000) acts as input to the PV array. A Li-ion-based battery is used in the system for power management. Batteries max capacity is 30Ah, and nominal voltage is 400 V. The inverter is used for the conversion of DC to AC. PI controller and PWM generator are used for control of the inverter. To avoid noise, two filters of RL type and C type are connected with the inverter. Three-phase V-I measurement block is present in the system. Now the grid side consists of two RL loads of 5000 W and 10,000 W active power and inductive power (as reactive) of 8000 and 1000 W, respectively. Thus, in this way, the entire system is connected. The controlling is done with the help of a discrete PID and fuzzy controller. The basic Simulink model of the integrated system is shown in Fig. 5.

## 5 Simulation Results

The simulation model involves the use of different controllers for designing the integrated system of PV array, fuel cell, and microgrid. Simulink command in MATLAB software is utilized. For comparison, two types of controllers are employed. Firstly, discrete PID controller is used for controlling the fuel cell, PV array, and battery. Figures 6, 7, and 8 represent the waveforms obtained using a discrete PID controller. Secondly, FLC-based control of the system is done. Mamdani-type FLC is used. Figure 9 represents the modified fuzzy membership function of the trapezoidal type. The output waveforms for the fuzzy logic controller are shown in Figs. 10, 11, and 12. From the comparison of outputs, it is observed that the modified fuzzy controller gives a better response than discrete PID controller. Also, overshoot and distortion are reduced using FLC. Tables 1 and 2 are used to compare the parameters of source

voltage and load voltage, respectively. By observing the parameters of source voltage and load voltage, it is concluded that FLC leads to a better response of the system as rise time and overshoot are reduced in both cases by the involvement of a fuzzy controller.

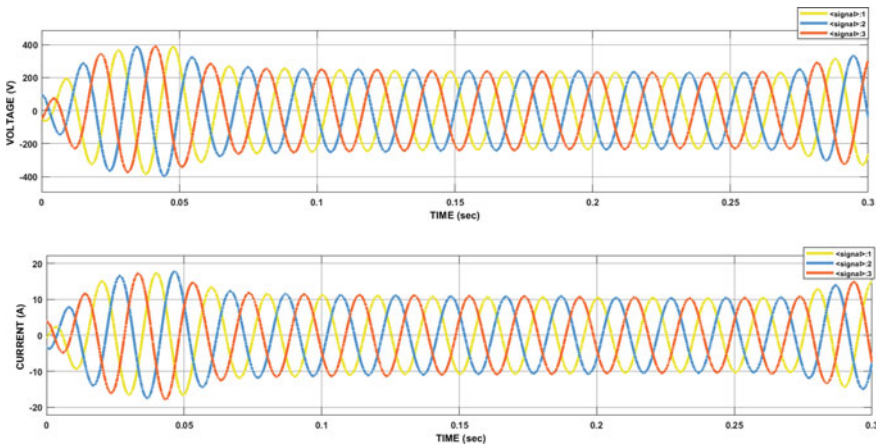


Fig. 6 Three-phase bus V-I measurement using discrete PID controller

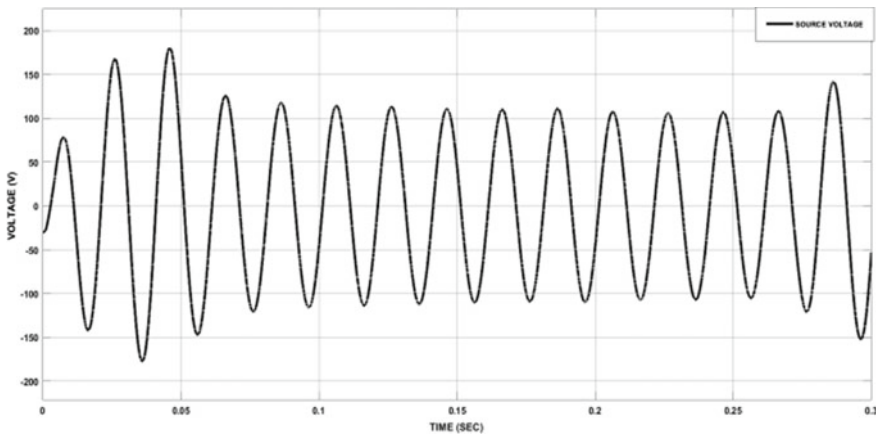


Fig. 7 AC source voltage measurement using discrete PID controller

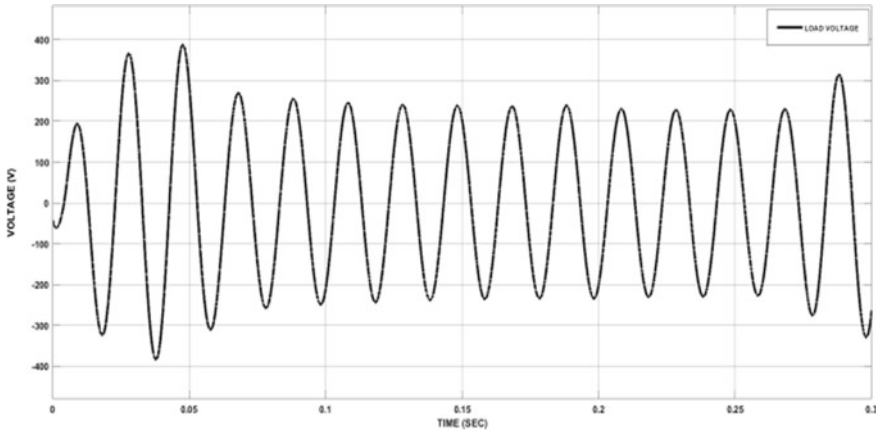


Fig. 8 Load voltage measurement using discrete PID controller

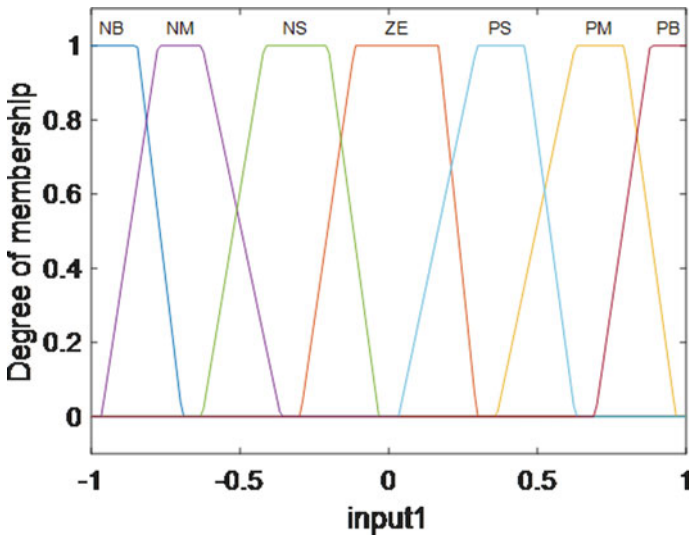
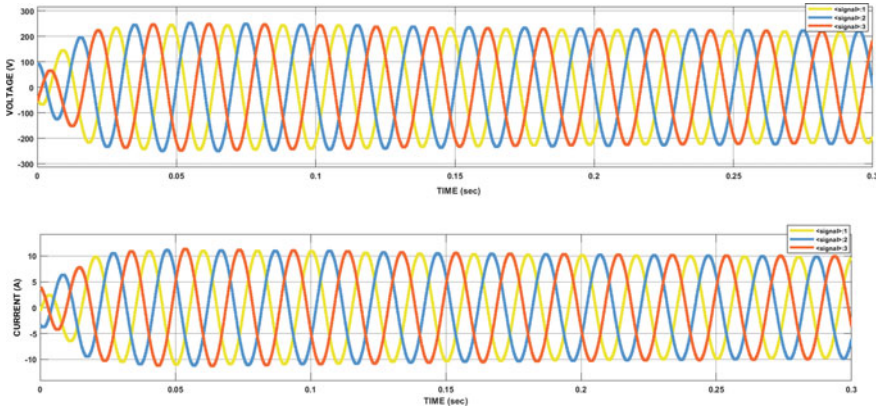
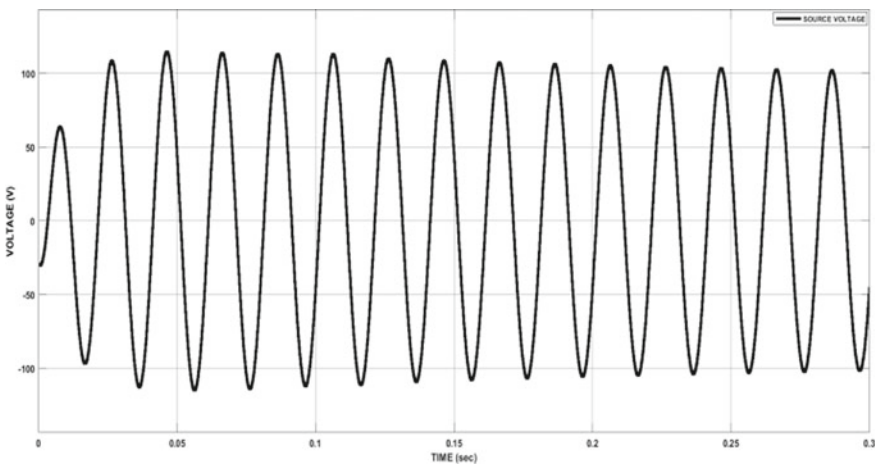


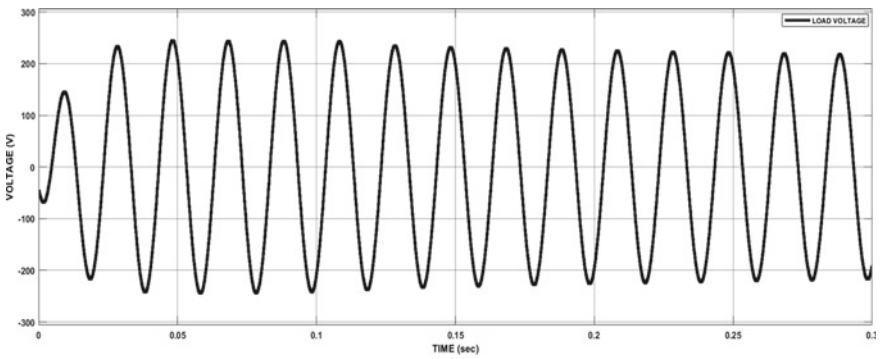
Fig. 9 Modified fuzzy membership function



**Fig. 10** Three-phase bus V-I measurement using modified fuzzy controller



**Fig. 11** AC source voltage measurement using modified fuzzy controller



**Fig. 12** Load voltage measurement using modified fuzzy controller

**Table 1** Source voltage parameter

Parameters	Discrete PID controller	Modified fuzzy controller
Rise time (s)	4.9454e-04	4.4349e-04
Settling time (s)	0.2999	0.2999
Overshoot (%)	236.4456	158.2000
Peak time (s)	0.0460	0.0563

**Table 2** Load voltage parameters

Parameters	Discrete PID controller	Modified fuzzy controller
Rise time (s)	0.0022	0.0159
Settling time (s)	0.2998	0.2997
Overshoot (%)	45.9912	28.9819
Peak time (s)	0.0477	0.0482

## 6 Conclusion

In this paper, the design of the PV array system integrated with fuel cell and microgrid is carried out. Different controllers are used to obtain the best output. With discrete PID controller, this has been observed that there exists distortion in bus voltage, bus current, load voltage, and source voltage. However, no distortion is present with modified fuzzy controller. Further, for the AC source voltage, the fuzzy controller gives less overshoot, whereas discrete PID controller leads to an unstable system because of a very high overshoot. The overshoot obtained for load voltage waveform is reduced from 45.9% (discrete PID) to 28.9% by using a fuzzy controller. Thus, it can be concluded that a modified fuzzy logic controller is far superior compared to a discrete PID controller for the proposed renewable energy system.

## References

1. Shah R, Mithulananthan N, Bansal RC, Ramachandaramurthy VK (2015) A review of key power system stability challenges for large-scale PV integration. *Renew Sustain Energy Rev* 41:1423–1436
2. Reshmi S, Joe Nigel K (2014) Comparative study of photovoltaic system employing PI, PID and sliding mode controller. *Int J Eng Res Technol* 3
3. Khubchandani V, Pandey K, Tayal VK, Sinha SK (2016) PEM fuel cell integration with using fuzzy PID technique. In: *IEEE 1st international conference on power electronics, intelligent control and energy systems (ICPEICES)*. pp 1–4. <https://doi.org/10.1109/ICPEICES.2016.7853450>
4. Sankar R, Velladurai S, Rajarajan R, Thulasi JA (2017) II. PV system description: maximum power extraction in PV system using fuzzy logic and dual MPPT control. In: *International*



- conference on energy, communication, data analytics and soft computing (ICECDS). pp 3764–3769. <https://doi.org/10.1109/ICECDS.2017.8390168>
5. Khaled A, Aboubakeur H, Mohamed B, Nabil A (2018) A fast MPPT control technique using PID controller in a photovoltaic system. In: International conference on applied smart systems (ICASS). pp 1–5. <https://doi.org/10.1109/ICASS.2018.8652062>
  6. Harrabi N, Mansour S, Abdel A, Chaabane M (2018) Modeling and control of photovoltaic and fuel cell-based alternative power systems. *Int J Hydrogen Energy* 43. <https://doi.org/10.1016/j.ijhydene.2018.03.012>
  7. Al-Saeedi AAK, Ali NG, Yaser MJ (2018) New approach of intelligent technique to optimize maximum power point tracking with PID controller by using the algorithm of fuzzy inference system
  8. Tayal VK, Sinha SK, Ranjan P (2016) Impact of solar PV modules on existing power system peak load demand. In: Second international innovative applications of computational intelligence on power, energy and controls with their impact on humanity (CIPECH). pp 119–122. <https://doi.org/10.1109/CIPECH.2016.7918750>
  9. Suresh V, Pachauri N, Vigneysh T (2021) Decentralized control strategy for fuel cell/PV/BESS based microgrid using modified fractional order PI controller. *Int J Hydrogen Energy* 46(5):4417–4436
  10. Mishra D, Sahu PC, Prusty RC, Panda S (2021) A fuzzy adaptive fractional order-PID controller for frequency control of an islanded microgrid under stochastic wind/solar uncertainties. *Int J Ambient Energy* 1–17. <https://doi.org/10.1080/01430750.2021.1914163>
  11. Nayak A, Maharana MK (2017) Tuning of PID controller to maintain load frequency for hybrid power system. In: International conference on innovative mechanisms for industry applications (ICIMIA). pp 24–28. <https://doi.org/10.1109/ICIMIA.2017.7975623>
  12. Srinivasan KG, Sivalingam R (2020) Design, analysis, and real-time validation of type-2 fractional order fuzzy PID controller for energy storage-based microgrid frequency regulation. *Int Trans Electr Energy Syst* 31. <https://doi.org/10.1002/2050-7038.12766>
  13. Dwivedi L (2017) Improve the efficiency of Photovoltaic (PV) system based by PID controller. *Int Res J Eng Technol (IRJET)* 4:2273–2277
  14. González-Castaño C, Restrepo C, Kouro S, Rodriguez J (2021) MPPT algorithm based on artificial bee colony for PV system. *IEEE Access* 9:43121–43133. <https://doi.org/10.1109/ACCESS.2021.3066281>
  15. Singh S, Tayal VK, Singh HP, Yadav VK (2020) Fractional control design of renewable energy systems. In: 8th international conference on reliability, infocom technologies and optimization (trends and future directions) (ICRITO). pp 1246–1251. <https://doi.org/10.1109/ICRITO48877.2020.9197902>

# Modeling, Analysis, and Comparison of Two Materials for Universal Joint by Using Ansys Software



Bishnu Bishwakarma , Devyanshu Raj Singh , Rohit Chaudhary ,  
and Brahma Nand Agrawal 

**Abstract** In this paper, the study has been done for modeling of universal joints and analysis by using Ansys software for structural steel and titanium alloy as materials used. After that performed meshing and gives three possible solutions which are total deformation, equivalent stress, and safety factor. Finite elements analysis is done in the universal joint by considering and applying the average load on it. The analysis confirms the successful design of the universal joint. The study is done by providing real data for the experiments. The safety factor and equivalent stress are more, and total deformation is less in Universal joint-2. So, according to analysis, titanium alloy is the best material for the universal joint and is long-lasting. Because it is lightweight as compared to other materials used for automobile parts manufacturing.

**Keywords** Universal joint · Ansys software · Structural steel · Titanium alloy · Total deformation · Equivalent stress

## 1 Introduction

Universal joints are the main part of the transmission system. Universal joints are used when there needs to be an angular deviation in the rotating shaft [1]. All the inclusive joints such as U-joint, Cardon joint, Tough Spicer joint, or Hooke's joint are the joints or couplings in any path, and in an inflexible bar that enables all the bars to "bend" toward any path, and is usually utilized as the part of shafts that transmit revolving its movement [2, 3]. It is also an important part of the vehicles needed to be considered while designing any vehicles. The universal joint is a critical part of the engine and transmission system of vehicles [4]. In automotive systems, it allows moving down and up for the driveshafts with suspension and the moving shaft so power can be transmitted while the drive shaft isn't in a straight line [5, 6]. It is important to design the universal joint by considering its durability, strength, efficiency, and noise [6]. A pair of hinges in the universal joints consist that are

---

B. Bishwakarma · D. R. Singh · R. Chaudhary · B. N. Agrawal (✉)  
Department of Mechanical Engineering, Galgotias University, Greater Noida, Uttar Pradesh, India  
e-mail: [brahma.agrawal@galgotiasuniversity.edu.in](mailto:brahma.agrawal@galgotiasuniversity.edu.in)

located close to each other and oriented at  $90^\circ$  to each other and also connected by a cross shaft [7]. It consists of components such as

1. Cross shaft
2. Four-point cross.

The cross shaft of the universal joint is used for the power transmission, while the input and output shaft aren't on the same line [6, 8]. It is the main component of the vehicle transmission system which has several features, such as [9]

- (a) Simple structure
- (b) Low wear
- (c) High transmission power
- (d) It can bear a large load and strong torque.

The challenges while analyzing with titanium are

- (a) Titanium is highly reactive, so it needs a different type of management required.
- (b) While providing a high value for the element size and magnitude at the moment, it shows an error or couldn't be able to calculate the value.

The objective or purpose of the study is as follows:

- To design and model the universal joint using Ansys software.
- To analyze and comparison of two materials (Structural Steel and titanium) for the universal joint.

## 2 Methodology

- Designing and modeling by using Ansys software (Ansys 2022R1).
- Material specifying and setting parameters.
- The meshing of the model.
- Analysis setting for the model.
- Result.

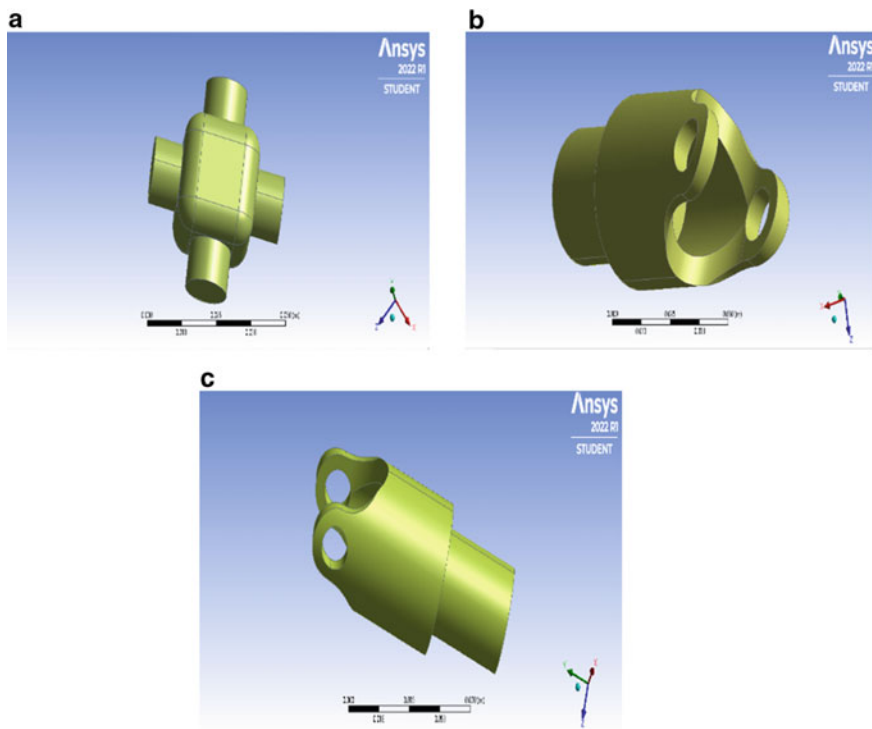
### 1. CAD Model

Ansys software is used for designing the model of the universal joint as shown in figures (Fig. 2) to analyze the data [10]. In the model, three parts are used such are two cross shafts (Fig. 1b and c) and one four-point cross (Fig. 1a).

### 2. Materials

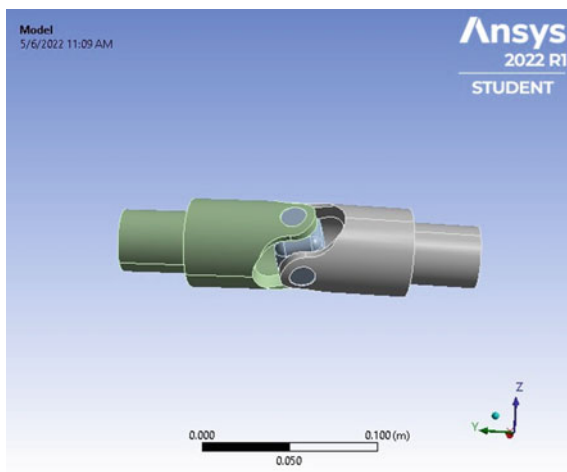
The materials which are used for modeling the universal joint are

- (a) Structural steel
- (b) Titanium alloy.



**Fig. 1** a Modeling of a four-point cross. b Modeling of cross shaft of one side. c Modeling of cross shaft of side

**Fig. 2** Model of the universal another joint after assembly



## 2.1 Material Properties

### (a) Structural Steel

- Name: Structural Steel
- Specific Heat:  $434 \text{ J kg}^{-1} \text{ C}^{-1}$
- Resistivity:  $1.7 \times 10^{-7} \text{ } \Omega \text{ m}$
- Density:  $7850 \text{ kg m}^{-3}$
- Thermal Conductivity:  $60.5 \text{ W m}^{-1} \text{ C}^{-1}$
- Coefficient of Thermal Expansion:  $1.738061806 \text{ C}^{-1}$

### (b) Titanium Steel

- Name: Titanium Alloy
- Specific Heat:  $522 \text{ J kg}^{-1} \text{ C}^{-1}$
- Resistivity:  $1.7 \times 10^{-6} \text{ } \Omega \text{ m}$
- Density:  $4620 \text{ kg m}^{-3}$
- Thermal Conductivity:  $21.9 \text{ W m}^{-1} \text{ C}^{-1}$
- Coefficient of Thermal Expansion:  $9.4 \times 10^{-6} \text{ C}^{-1}$ .

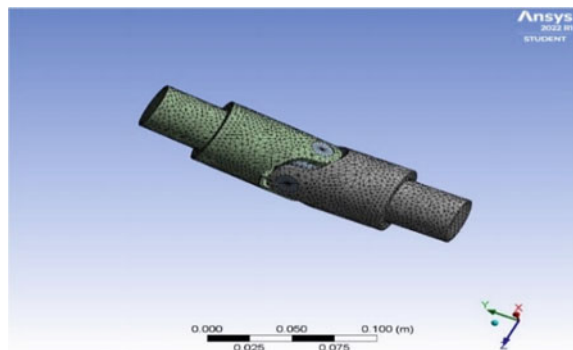
## 3 Meshing

In meshing, the universal joint is divided into the number of elements which helps in engineering equations to give an exact result as required for problems. The meshing is as shown in Fig. 3.

### 3.1 Meshing Properties

- Name: Mesh

**Fig. 3** Meshing of the model universal joint designed in Ansys



- Element: 23,416
- Node: 41,385
- Element Size: 5.154845485 m
- Growth Rate: 1.2
- Transition Ratio: 0.272
- Average Surface Area: 12.14740955 m<sup>2</sup>
- Minimum Edge Length: 7.751348288 m
- Maximum Layer: 5
- Bounding Box Diagonal: 0.24686 m.

## 4 Analysis Setting

- Element Order: Program Controlled
- Physic Preference: Mechanical
- Element: 23,416
- Node: 41,385
- Element Size: 5.154845485 m
- Growth Rate: 1.2
- Transition Ratio: 0.272
- Average Surface Area: 12.14740955 m<sup>2</sup>
- Target Element Quality: 11.59140914
- Minimum Edge Length: 7.751348288 m
- Maximum Layer: 5
- Bounding Box Diagonal: 0.24686 m.

## 5 Result and Discussion

The results of structural steel and titanium alloy used as universal joint materials are calculated and listed below (Table 1):

From the total deformation of both of the materials used for universal joints, the maximum value of titanium alloy is lower and structural steel is higher (Table 2).

From the equivalent stress of both of the materials used for universal joints, the minimum value of titanium alloy is higher and the maximum value is lower than structural steel (Table 3).

**Table 1** Comparison of total deformation

Materials	Total deformation (m)	
	Min	Max
Structural steel	0	7.5706e-005
Titanium alloy	0	1.5845e-004

**Table 2** Comparison of equivalent (von Mises) stress

Materials	Equivalent (von Mises) Stress (Pa)	
	Min	Max
Structural steel	1755.8	1.8924e+008
Titanium alloy	2709.4	1.8803e+008

**Table 3** Comparison of safety factors

Materials	Safety factors	
	Min	Max
Structural steel	1.3211	15
Titanium alloy	4.946	15

From the safety factor of both of the materials used for universal joints, the minimum value of titanium alloy is higher than structural steel and has the same maximum values.

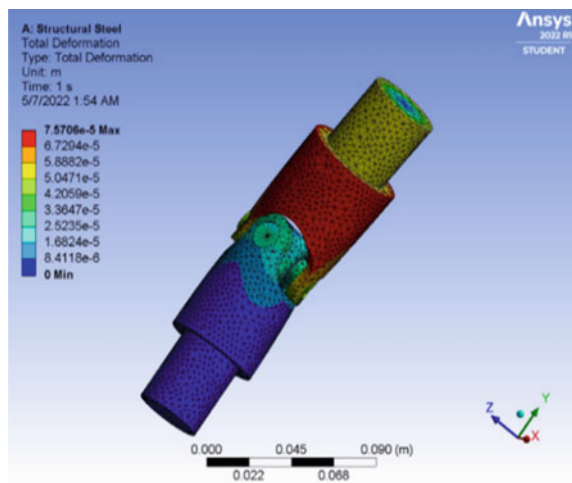
Analysis of universal joint using structural steel as shown in Figs. 4, 5, and 6 consists of minimum and maximum reading of every parameter.

Analysis of universal joint using titanium alloy as shown in Figs. 7, 8, and 9 which consists of minimum and maximum reading of every parameter.

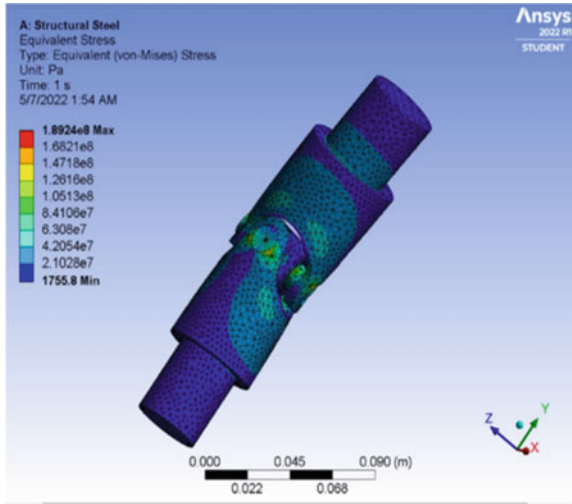
So, according to the analysis,

- (a) The total deformation is shown in Figs. 4 and 7. The higher deformation is shown in the cross shaft (Fig. 2c) in which load is provided is Universal joint-1 which is done by using structural steel as material.
- (b) The equivalent stress is shown in Figs. 5 and 9. The equivalent stress is shown at the moving parts where the cross shaft and four-point cross are connected to the universal joints. The less equivalent stress is in Universal joint-1

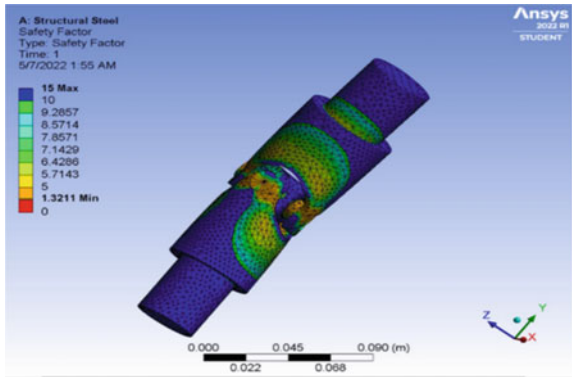
**Fig. 4** Total deformation of Universal joint-1



**Fig. 5** Equivalent (von Mises) stress of Universal joint-1



**Fig. 6** Safety factor of Universal joint-1



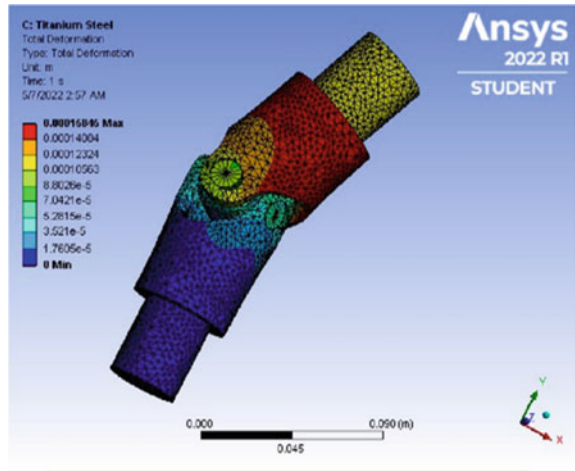
(c) The safety factor is shown in Figs. 5 and 9. The safety factor is shown all the body of the Universal joint-1 and only movement areas of the Universal joint-2.

## 6 Conclusions

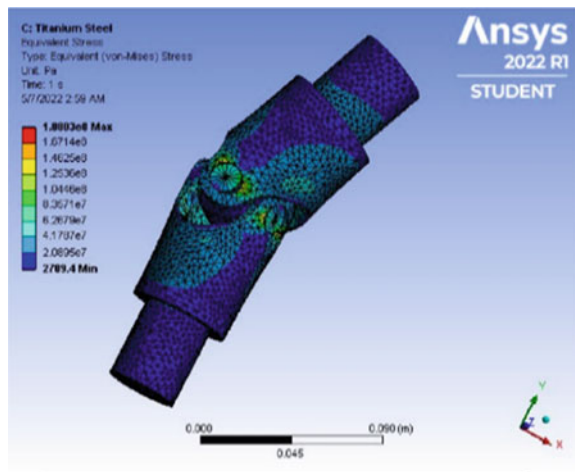
In this paper, the study successfully analyzed the design with different materials. Finite elements analysis is done in the universal joint to calculate total deformation, equivalent stress, and safety factor by considering and applying average load on it. The universal joint is an important part of the automotive system to transfer speed/torque from engine to wheel. In simulating, two materials are used in universal joints named Universal joint-1 and Universal joint-2, respectively. So, titanium alloy is the best material for the universal joint and also for long-lasting. Because it is



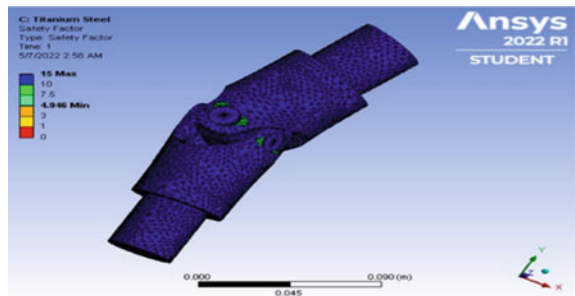
**Fig. 7** Total deformation of Universal joint-2



**Fig. 8** Equivalent (von Mises) stress of Universal joint-2



**Fig. 9** Safety factor of Universal joint-2



lightweight as compared to other materials used for automobile parts manufacturing. It can analyze the following from the figures and the values.

- (i) The modeling is done on Ansys to understand better the design and working points.
- (ii) In this paper, we have studied the conditions that occur while analysis of the universal joint.
- (iii) The part of the modeling works properly while providing load to it.
- (iv) Universal joint-1 shows less equivalent stress and safety factor as compared to Universal joint-2.
- (v) The total deformation of Universal joint-2 is less than Universal joint-1.
- (vi) The values of colors (i.e., red, green, and blue) are less in Universal joint-2 than in Universal joint-1.

## References

1. Yadav K, Jain H Modeling and finite element analysis of universal joint. *Adv Mech Eng Technol* 4(1). <https://doi.org/10.5281/zenodo.4624800>
2. Kohli A, Hombalmath M, Patil AY, Aruna Kumara PC (2022) Analysis of universal joint using virtual simulation method. *Mater Today: Proc.* <https://doi.org/10.1016/J.MATPR.2022.01.213>
3. An K, Wang W (2017) Transmission performance and fault analysis of a vehicle universal joint. *Adv Mech Eng* 9(5). <https://doi.org/10.1177/1687814017707478>
4. Lu Y, Wang W, Zhang K, Zhao Z (2021) Studying on the design of automobile constant velocity universal joint based on mass customization. *Int J Adv Manuf Technol.* <https://doi.org/10.1007/s00170-021-07866-x>
5. Li S, Hao G, Wright WMD (2021) Design and modelling of an anti-buckling compliant universal joint with a compact configuration. *Mech Mach Theory* 156. <https://doi.org/10.1016/j.mechmachtheory.2020.104162>
6. Li S, Hao G (2022) Design and nonlinear spatial analysis of compliant anti-buckling universal joints. *Int J Mech Sci* 219. <https://doi.org/10.1016/j.ijmecsci.2022.107111>
7. Arora R (2017) Modeling and failure analysis of universal joint using ANSYS. *Int J Emerg Technol Eng Res (IJETER)* 5(8). [Online]. Available: [www.ijeter.everscience.org](http://www.ijeter.everscience.org)
8. An Y, Liu J, Li Z (2022) Dynamic load analysis of the connecting bolts in a universal joint. *Eksplotacja i Niezawodność—Maintenance Reliab* 24(2). <https://doi.org/10.17531/ein.2022.2.2.3>
9. Yanda S, Bala Murali G, Shankar Raju S, Jason Duckworth B, Sen C, Singh Chadha S (2021) Design optimization of universal joints for all-terrain vehicles. *IOP Conf Ser: Mater Sci Eng* 1123(1). <https://doi.org/10.1088/1757-899x/1123/1/012012>
10. Vijayan K, Barik CR, Sha OP (2021) Shock transmission through universal joint of cutter suction dredger. *Ocean Eng* 233. <https://doi.org/10.1016/j.oceaneng.2021.109185>

# Small-Scale Electricity Generation from Biogas in Third World Countries



Coddell Tanaka Mutate, Artwell Jairos Kanjanda, and Gitanjali Mehta

**Abstract** Biogas is a relatively clean source of energy that can be used to generate small scale electrical power at an affordable cost. This technology is still new in most African countries which are heavily depended on electricity generated from fossil fuels but is well known in industrialized countries like Germany. In Zimbabwe, a Southern African country, there was no biogas plant that generates electrical power at the time of this compilation. The main objective of this research is to produce electricity from biogas using a simple system that can easily be adopted in African countries. In this project, a model is proposed which enables the generation of electricity from biogas using a spark ignition engine coupled to a synchronous generator. The biogas fuels the spark ignition engine which drives the generator. Two generators and two engines with the same properties are used to illustrate the process of synchronization. Matlab simulation software is used to illustrate the coupling of the engine to the generator. A sinusoidal three-phase alternating voltage is observed from each generator when the simulation is run. This is a key finding showing the viability of the low-cost system. An online biogas calculator designed by the Indian Biogas Association is also used to show that different substrates produce different amounts of electrical power. This crucial realization should be kept in mind when choosing a suitable substrate for the project. The electricity produced will be used by the rural communities of third world countries which do not have direct access to grid power and depend on fossil fuels.

**Keywords** Biogas · Anaerobic digestion · Spark ignition engine · Synchronous generator

---

C. T. Mutate · A. J. Kanjanda (✉) · G. Mehta  
Department of Electrical and Electronics Engineering, Galgotias University, Greater Noida, Uttar Pradesh, India  
e-mail: [artwell\\_kanjanda.secebtch@galgotiasuniversity.edu.in](mailto:artwell_kanjanda.secebtch@galgotiasuniversity.edu.in)

# 1 Introduction

Many third world countries like Zimbabwe suffer from an energy crisis, and this is mainly due to the fact that the national grid is not that extensive. This leaves the greater majority of the rural population energy deprived. Schools and hospitals in the outskirts of the country are greatly affected by this lack of electrical energy which in turn stalls the development of a nation. This results in the greater reliance on other sources of energy like firewood and charcoal which pose great harm to the environment. Biogas is a versatile source of energy which can be used to generate electrical power in the third world countries. Biogas is a clean energy source which is produced through a process known as anaerobic digestion in which organic matter is fermented in the absence of oxygen. The anaerobic digestion process occurs in a series of sequential steps that include hydrolysis, acidogenesis, acetogenesis and methanogenesis. Zimbabwe is a landlocked country which relies on hydro-electricity and thermal power for its energy demands. Biogas energy is less affected by weather conditions unlike wind and solar; a continuous supply of electrical power is guaranteed at any time as long as there is sufficient feedstock to feed in the digester. Generation of electrical power from biogas is a well-known technology in industrialized countries like Germany, China, etc., but is still foreign in most African countries [1]. In the 1990s, the first biogas plants were constructed in East African countries like Tanzania and Kenya with the help of foreign expertise to generate biogas which could be used for cooking, heating and lighting purposes. The standard technology for biogas production was not established during this time, so these plants were not in operation for long because of lack of expertise, maintenance and poor workmanship [1]. The first biogas plant to generate electrical power in Africa was Gorge Farm Energy Park in Naivasha, Kenya, which was only launched in August 2015 [2]. In most African countries, this technology is still in its infancy and there is heavy reliance on foreign expertise as well as their technology. In Zimbabwe, there are a number of biogas digesters with a majority of them being household digesters that generate biogas for cooking, lighting and heating only [3]. The technology being used in most of these digesters is outdated and needs improvement [4–6]. There is not a single biogas plant that generates electrical power in Zimbabwe. This project is focusing on designing a simple system that produces electrical power from biogas using a spark ignition engine coupled to a synchronous generator. The biogas produced in the digester will be used as a fuel for the engine which produces mechanical energy to drive the generator. Matlab simulation is used to illustrate the engine-generator set. An online biogas calculator is also used to estimate the amount of biogas, electrical energy and digestate to be produced from a specific feedstock. The scope of this project is limited on the engine-generator set that is simulated on Matlab and the online biogas calculator.

## 1.1 Literature Survey

In Africa, there exist a significant number of biogas plants in the different countries of the continent. The most common biogas plants in operation are household, municipal and industrial biogas digesters. The biogas generated from these plants is mainly used for cooking, lighting and heating [6]. In some municipal biogas plants, the digesters are used for waste treatment only and the generated biogas is just released into the air [3]. The technology of generating electricity from biogas energy is foreign in most African countries. The first grid-connected biogas plant to generate electricity from biogas is located in Naivasha, Kenya. The plant has a capacity of generating 2 MW of power and was launched in August 2015 [2]. The plant also produces heat and fertilizer as a by-product. The plant was developed by Tropical Power which is incorporated in the United Kingdom and has a subsidiary in Kenya [2]. Jenbacher gas engines are used in the plant, and these are of Austrian origin manufactured in the town of Jenbach [2]. This technology is well known in developed countries like Germany and China. In Europe, the biogas is converted to biomethane which is being used in hybrid heat pumps to heat up buildings, as a fuel in the transport sector and used in the generation of power to balance out intermittent sources of energy like wind and solar [7]. There are no issues in the existing system per se, but the technology is not well known in most third world countries. There is a lot of reliance on foreign equipment and expertise. Jenbacher gas engines are used in Naivasha, Kenya, which are manufactured in Austria. There is limited knowledge on the Internet and in books on how to adopt this technology effectively. Simulation software that are used for the designing of the plants like Aspen Plus and the Anaerobic Digestion Model of Simulink are not easily accessible. Most African universities and institutions especially those in Zimbabwe do not have access to the software.

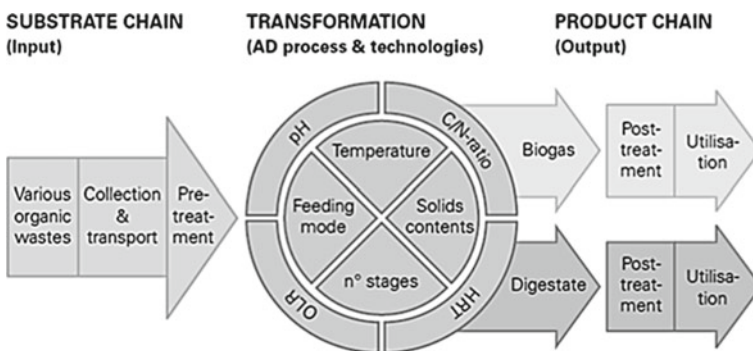
## 2 Biogas Production and Electrical Power Generation

Biogas is a versatile clean energy source which is produced through a process known as anaerobic digestion. AD is a process in which organic biodegradable matter is fermented in airtight reactor tanks to produce two main products which are biogas and the digestate. The biomass fed into the biogas digester is referred to as the feedstock or substrate. The feedstock has to go through a substrate chain before it is fed into the biogas digester, and this involves the waste generation, collection, transportation and pre-treatment process [5]. Different types of feedstocks given in Table 1 can be fed into the reactor depending on their availability, and these include agricultural by-products like manure, energy crops, sewage sludge, human excreta, kitchen and industrial waste. Complex bacterial activity will convert the organic matter into biogas through a series of sequential steps under suitable conditions in the digester. The products of this anaerobic digestion process are biogas and a digestate which can be used as a natural fertilizer by farmers. The products also go through a

post-treatment process before they are utilized. The biogas is treated of its impurities like water vapour and hydrogen sulphide, and the digestate is also treated before it can be used for agricultural purposes [5]. Biogas has a diverse spectrum of applications which include cooking, lighting, heating and generation of electricity. The upgraded version of biogas known as biomethane can also be used as a vehicle fuel the same way compressed natural gas (CNG) is used in countries like India [8–13]. In this project, the main focus is on using biogas to generate electrical power in third world countries like Zimbabwe [14]. After the treatment process of removing impurities from the biogas is completed, it is suitable to be used as a fuel in a desired engine. A spark ignition engine or a diesel engine in dual fuel mode can be used. The engine generates mechanical energy which is used to drive the synchronous generator to which it is coupled [12]. The generator rotates and produces electrical energy which can be used by consumers. This system will be a non-grid connected system to reduce the complexity of equipment required. The electrical power generated will be used by farmers, hospitals, schools and households in the outskirts of the country that lack access to grid power. The process is divided into three sections showing information on the anaerobic digestion processes. The three components being addressed are substrate chain, transformation process and product chain as shown in Fig. 1.

**Table 1** Feedstock from different sources

Municipal	Agriculture	Industry
Organic fraction of municipal solid waste (“Biowaste”)	Manure	Slaughterhouse waste
Human excreta	Energy crops	Food processing waste
	Algal biomass	Biochemical waste
	Agro-industrial waste	Pulp and paper waste



**Fig. 1** Process chain of anaerobic digestion

**Table 2** Typical composition of biogas from biowaste

Component		Concentration (Vol %)	Component		Concentration (Vol %)
Methane	CH <sub>4</sub>	55–70	Nitrogen	N <sub>2</sub>	< 2
Carbon dioxide	CO <sub>2</sub>	35–40	Oxygen	O <sub>2</sub>	< 2
Water	H <sub>2</sub> O	2 (20%)–7 (40%)	Hydrogen	H <sub>2</sub>	< 1
Hydrogen sulphide	H <sub>2</sub> S	20–20,000 ppm (2%)	Ammonia	NH <sub>3</sub>	< 0.05

- **Substrate chain:** This process involves the generation of waste, collection from source, mode of transportation and the necessary pre-treatment required before it is fed into the digester. The type of substrate to be used has to be identified, and the distance between source and digester has to be measured. The source of the feedstock has to be close to the digester to cut down transport costs. The feedstock undergoes a pre-treatment process which includes sorting, reduction in particle size and addition of water before it is fed into the digester [5–9].
- **Transformation process:** In this process, the organic matter is converted to biogas through a series of chemical and biological processes in the digester. This conversion of organic matter to biogas and a digestate occurs through a series of sequential steps that include hydrolysis, acidogenesis, acetogenesis and methanogenesis in that order. Operational parameters such as temperature, pH, carbon-to-nitrogen ratio, organic loading ratio (OLR) and hydraulic retention time (HRT) have to be controlled to maximize the efficiency of bacterial activity [15].
- **Product chain:** The biogas that is produced has to be stored in airtight tanks at the right pressure. The stored biogas can then be used for future purposes. The storage system can be low-pressure storage, medium-pressure storage and high-pressure storage. The generated biogas has impurities that can damage the engine material through corrosion. Impurities such as carbon dioxide, hydrogen sulphide, nitrogen oxides and water vapour are commonly present in the biogas. The composition of biogas from biowaste is given in Table 2. Dewatering is carried out to remove the water vapour from biogas which can cause corrosion and condensation. Desulphurization is carried out to remove hydrogen sulphide; this can be wet or dry desulphurization [5]. Carbon dioxide is removed by bubbling the gas through water which contains an alkaline chemical. In many cases, the effluent also known as the digestate can be directly used as a fertilizer, but in cases where human excreta were used as a substrate the effluent has to go through a post-treatment process [11].

### 3 Research Methodology

In this research, the feasibility of generating electricity from biogas energy in third world countries is to be illustrated. Matlab simulation software is used to illustrate the coupling of a generic engine to a synchronous generator. Biogas is used as a fuel for

the engine which generates mechanical energy to drive the generator which produces electrical power. Quantitative analysis of data is carried out when the simulation is run. The three-phase output voltage from the synchronous generator will determine the feasibility of generating electricity from biogas. The simulation will only illustrate the coupling of a generic engine to a synchronous generator and not the process of generating biogas which is fed into the engine. Two engines and two generators with the same properties will be used to show the process of synchronization. This system will have advantages over a single unit system. An application designed by the Indian Biogas Association is used to show the amount of biogas, electrical power and digestate quantity from a desired substrate. The application has an online biogas calculator that is designed in such a way that you select your desired feedstock at a specific quantity, and it will calculate the estimated amount of biogas and electricity to be produced. The Biogas Application is used to show that different substrates produce different amounts of biogas, and this should be kept in mind when designing a system in which biogas is used to generate electricity.

### **3.1 Simulation**

Quantitative methods of data collection are used in this research. When the Matlab simulation is run, the graphs being shown by the scopes connected to the synchronous generators are analysed to observe if a three-phase alternating voltage is produced. Different substrates are selected on the Biogas Application to show that different amounts of biogas and electrical power are produced, and the values are observed and analysed. Matlab simulation software was used because it can simulate complex electrical circuits and is easier to use. The generation of biogas cannot be illustrated in Matlab as this requires Anaerobic Digestion Model (ADM) which can be embedded on Simulink. ADM is not easily accessible and has to be purchased online. Other software which shows the chemical reactions leading to the generation of biogas include aspenONE software which is also not free and is used mainly by chemical engineers. The online Biogas Application designed by IBA is chosen because it is easily available on Play Store, easy to operate and reliable. The Biogas Application only provides an estimate and not the actual amount of biogas to be produced from a selected substrate. It only serves as a guideline when choosing a substrate for the project. The first part of the proposed model of this project is a Matlab simulation of a generic engine coupled to a three-phase synchronous generator which is shown in Fig. 2. The simulation has two engines and two generators with the same properties to show the principle of synchronization which is possible when the biogas is used to drive two generators. The generic engine type used is a spark ignition engine with a maximum power of 7500 W. The speed at maximum power is 1900 rpm, and the maximum speed is 2450 rpm. The synchronous generator has an apparent power of 7000 VA and a rated voltage of 240 V. The rated frequency is 50 Hz, and the machine has two pole pairs. The second step is the use of a biogas calculator designed by the Indian Biogas Association (IBA). The biogas calculator is accessible



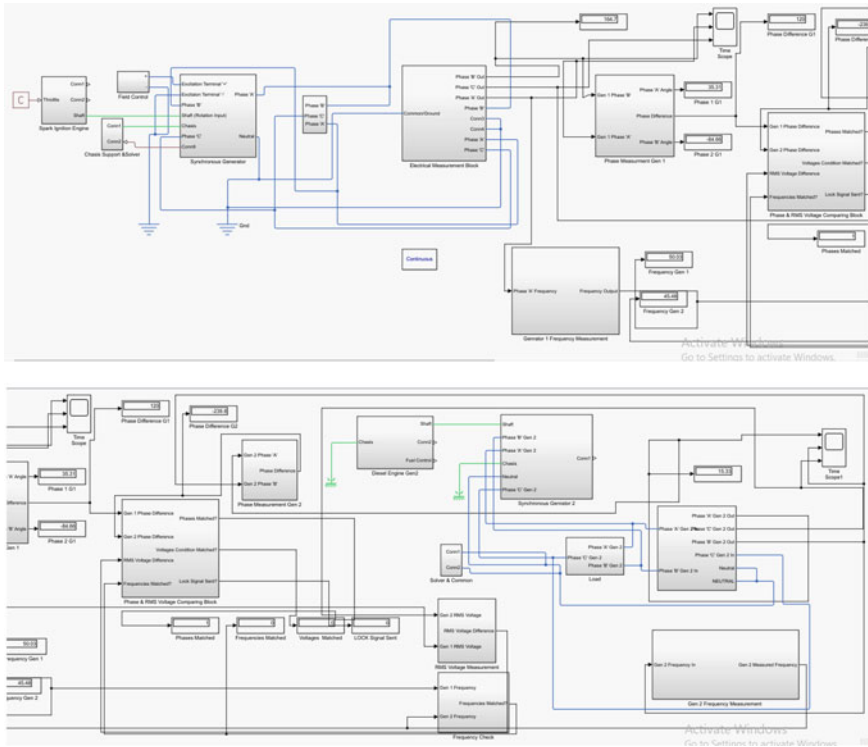


Fig. 2 Simulink model of the engine-generator set

on IBA’s Biogas Application that is available on Play Store. The biogas calculator is designed in such a way that you select your desired substrate and then it calculates the estimated amount of biogas output, electricity output in kWh and biofertilizer in tones. The biogas calculator only calculates the estimated amount of products to be produced and not the actual amounts.

### 3.2 Synchronization Process

This is a process of matching parameters such as phase sequence, phase angle, frequency, voltage and waveform of synchronous generator or a different source with a power system that is running. Once synchronization is achieved between two synchronous generators, the system runs smoothly. The parameters of the two generators have to be matching. When two or more synchronous generators work together to supply power to a common load the need of synchronization comes in the picture. Loads are always not constant; hence, having two or more generators interconnected in parallel is an advantage in handling larger loads. This setup of

having generators working in parallel connection has significant advantages over the one in which only a single generator is used. The advantages are listed below:

**Reliability:** The setup of having two or more generators connected in parallel is more reliable than single unit systems because when one generator fails the whole system is kept active by other generators. In single unit systems if the generator fails, there is no electrical power flowing to the load until the fault is detected and repaired.

**Continuity:** When one unit needs maintenance, the other generators can supply power to the load and there is no need of shutting down the whole system.

**Load:** Load varies throughout the day, with a parallel system adjustment can be done to cater for low and higher loads. The number of active systems can be determined depending on the load.

**Efficiency:** If generators operate at their load rating, they are more efficient. The system remains efficient because it can adapt to variations in the load.

In the procedure of synchronizing generators, four parameters should be aligned between the generators. The parameters are:

**Phase sequence:** The three phases of the synchronous generators must have the same phase sequence as the phases of the bus bar.

**Voltage magnitude:** None of the generators should have a higher or lower voltage than the other as this can pose safety concerns and potential failure of the whole system.

**Frequency:** There is an unstable flow of energy when the frequencies are not equal. This can cause damage to the equipment.

**Phase angle:** The phase angle of the synchronous generator, and bus bar must be zero.

The root mean square (RMS) voltage of each generator is measured and the difference between these values is also measured. The frequencies of the two generators are measured and matched if there is a difference. A circuit is built to compare the phases of the two generators, and the circuit also checks to verify if they are matching.

## 4 Results and Discussions

The purpose of this experiment is to determine if electrical energy is generated from a synchronous generator when it is coupled to a generic engine. The engine generates mechanical energy which drives the generator. Biogas is used as a fuel to power the spark ignition engine. The generated electricity will be used by the rural community in third world countries. Matlab simulation software is used to illustrate the coupling of the generic engine to the synchronous generator. The process of feeding biogas into the engine is not shown in this experiment. The generation of biogas is also not shown in this experiment. Two engines and two generators with the same properties are used to show the process of synchronization. A Biogas Application designed by

the Indian Biogas Association team is used to show that different substrates produce different amounts of biogas and electrical power.

The first generator produces a three-phase alternating voltage as observed in Fig. 3. This shows that the spark ignition engine is generating mechanical energy to drive the synchronous generator which produces electricity. The y-axis of the graph represents the amplitude of the output voltage, and the x-axis represents the time in seconds. The second generator driven by the second engine also produces a three-phase alternating voltage as shown in Fig. 4.

Three different substrates were selected on IBA’s biogas calculator as shown in Fig. 5. The different substrates produce different amounts of biogas and electrical output as given in Table 3. The same mass was used for all substrates that is 1000 kg. The first substrate selected was cattle dung which produced a gas output of 0.05109

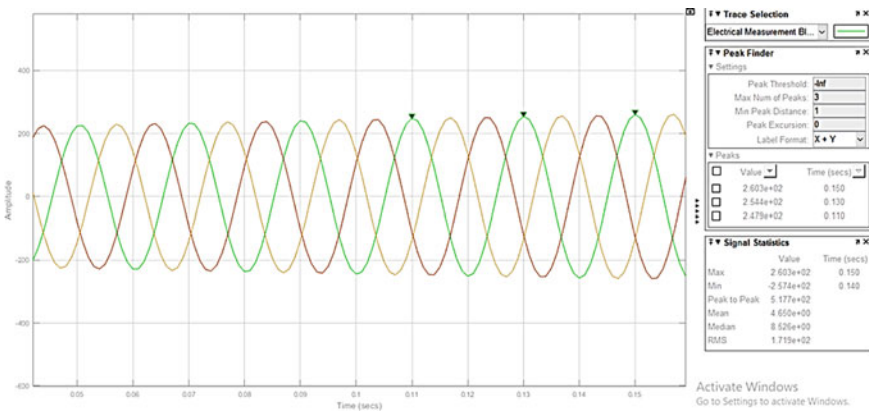


Fig. 3 Output from generator 1

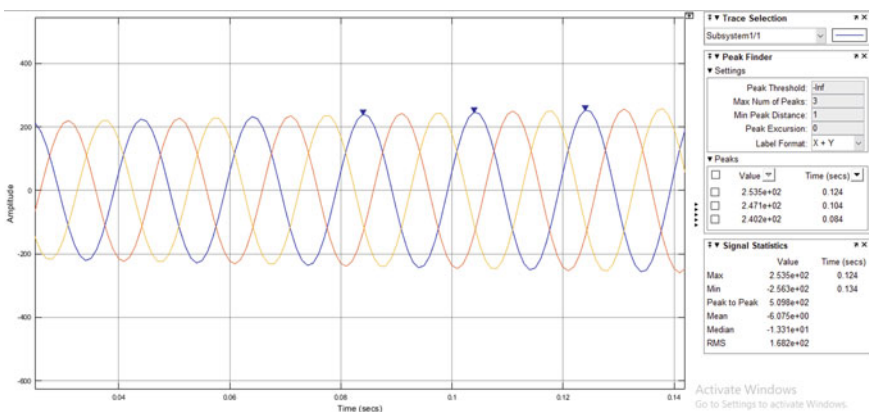


Fig. 4 Output from generator 2

in percentage and an electricity output of 107.8668 kWh. The second substrate selected was maize silage which produced a gas output of 0.19853 in percentage and an electrical output of 419.11467 kWh. The last substrate selected was poultry dung which produced a gas output of 0.23052 in percentage and electrical output of 486.65232 kWh.

The process of synchronization was successfully shown. The two generators produced a three-phase alternating voltage which can be used to supply a load. The signal statistics which include the mean, median and RMS voltage can be observed in the two figures. Focus was only on the gas output and electricity output, but there are also other products like slurry output and biofertilizer as shown in the screenshots. From the results, we can observe that different types of substrates produce different amounts of biogas, and this should be kept in mind when choosing a substrate for generation of biogas. The amount of biogas produced will determine the total electrical power to be generated. This biogas calculator is a rough guide in choosing the right substrate for the project. A three-phase alternating voltage was generated from each generator coupled to a spark ignition engine. The electrical power produced

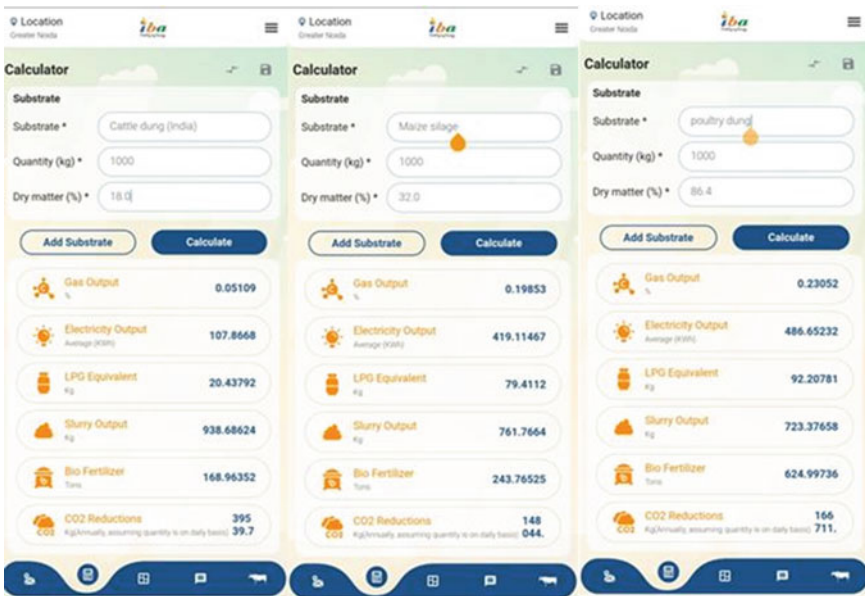


Fig. 5 Outputs from the Biogas Application using three different substrates

Table 3 Gas output and electricity output from different substrates

Substrate (1000 kg)	Gas output (%)	Electricity output (kWh)
Cattle dung	0.05109	107.8668
Maize silage	0.19853	419.11467
Poultry dung	0.23052	486.65232

can be stepped up by transformers and utilized by the community. A synchronous generator is chosen because alternating current is easier to transmit and can easily be stepped up and down. Many electrical appliances also use alternating current. When different substrates (cattle dung, maize silage and poultry dung) were selected on the Biogas Application, it was noticed that they produce different amounts of biogas and electricity. This is a major observation which should be kept in mind when choosing substrate for a biogas project. The strengths of this research include the detailed illustration of the engine-generator set in Matlab and the realization that different substrates produce different amounts of biogas. The simulation of the engine generator set is a crucial and fundamental step in the generation of electricity from biogas energy. The limitations of this research include the non-inclusion of the chemical processes of biogas production in the reactor. After observing the results, it is therefore concluded that if biogas is used as a fuel for the spark ignition engine coupled to a generator electrical energy is produced. The technology of generating electricity from biogas is possible in third world countries like Zimbabwe. Full adoption of this technology in African countries will be a major breakthrough for the rural population that is energy deprived and relies on fossil fuels. The system illustrated in this project is a non-grid connected system which can be used by independent schools and hospitals. In the future, the governments of third world countries can set up suitable policies and favourable feed in tariffs to make this system grid connected. This will greatly increase the grid power and mitigate power shortages in third world countries.

## 5 Conclusion and Future Scope

The objective of this project is to generate electrical power from biogas energy using a spark ignition engine that is coupled to a synchronous generator. The system is a non-grid connected system. Many third world countries suffer from an energy crisis. This is mainly because the grid only supplies major cities and urban areas. People living in the rural areas rely on fossil fuels for their energy needs. This technology will enable the people to have easy access to electricity to power their homes. The rural electrification scheme will come to fruition. The schools and hospitals in the outskirts of the country will operate smoothly without any hustles for energy. Students will be able to study at night, and experiments that require electrical power will be conducted easily. Preserving medicines in hospitals will become easy, and a lot of lives will be saved when patients are on life support. From the results, it is observed that a simple system consisting of an engine-generator set can produce electricity. A three-phase alternating voltage was produced from each generator. This technology can easily be adopted by the rural population of African countries. The clean energy produced from biogas will greatly improve the lives of the people. A biogas calculator designed by the Indian Biogas Association (IBA) which is accessible on their Biogas Application was used to show that different substrates produce different amounts of biogas. This important realization should be kept in mind when choosing a suitable substrate for


the project. In conclusion, there will be less deforestation and the development of the country in the rural areas will be improved. In the coming years, electricity generated from biogas can be connected to the grid if the government lays out suitable feed in tariffs and policies. This will boost the energy sector of African countries and improve their industries. Biogas can also be upgraded to biomethane which can be used as a fuel for vehicles the same way natural gas is used in countries like India. This will reduce pollution from car exhausts in third world countries. Use of biomethane as fuel is becoming common in most European countries.

## References

1. Dimpl E (2010) Small-scale electricity generation from biomass, part-II biogas. In: Experience with small-scale technologies for basic energy supply. pp 2–11
2. <https://africanreview.com/energy-a-power/renewables/kenyan-farm-converts-harvest-waste-into-electricity>. African Review (2016)
3. Kaifa J, Parawira W (2019) A study of the current state of biogas production in Zimbabwe. Lessons for Southern Africa. *Adv Biotech Micro* 13(3):555865. <https://doi.org/10.19080/AIBM.2019.13.555865>
4. Kajau G, Madyira D (2019) Analysis of the Zimbabwe biodigester status. In: 2nd international conference on sustainable materials processing and manufacturing. pp 561–566
5. Vögeli Y, Lohri CR, Gallardo A, Diener S, Zurbrügg C (2014) Anaerobic digestion of biowaste in developing countries. Binkert Buag AG, Laufenburg, Switzerland
6. (2011) Biogas simply the best. European Biogas Association
7. (2022) The future role of biomethane. European Biogas Association
8. Pesuit M, Proietti S, Paolucci L, Kovacs A, Stambasky J, Wellinger A et al (2017) Fuelling the use of biomethane for grid injection and as transport fuel. In: Biomethane as sustainable and renewable fuel
9. Statistical report of the European Biogas Association (EBA) (2021) The role of biogas production from industrial wastewaters in reaching climate neutrality by 2050. pp 3–6
10. Abanades S, Abbaspour H, Ahmadi A, Das B, Ehyaei MA, Esmailion F, El Haj Assad M, Hajilounezhad T, Jamali DH, Hmida A, Ozgoli HA, Safari S, AlShabi M, Bani-Hani EH (2021) A critical review of biogas production and usage with legislations framework across the globe. *Int J Environ Sci Technol* 2–20
11. Antonio AS, Oliveira Filho D, da Silva SC (2018) Electricity generation from biogas on swine farm considering the regulation of distributed energy generation in Brazil: a case study for Minas Gerais. pp 2–6
12. Barragan-Escandon A, Miguel Olmedo Ruiz J, David Curillo Tigre J, Zalamea-Leon EF (2020) Assessment of power generation using biogas from landfills in an equatorial tropical context. 2–7
13. Korbag I, Mohamed Saleh Omer S, Boghazala H, Ahmeedah Aboubkr Abusasiyah M (2020) Recent advances of biogas production and future perspective. In: Recent advances and intergrated approaches, laws and guidelines concerning biogas plants. [issa.omar@uob.edu.ly](mailto:issa.omar@uob.edu.ly) pp 2–38
14. Uddin W, Khan B, Shaukat N, Majid M, Mujtaba G, Mehmood A, Ali SM, Younas U, Anwar M, Almeshal AM (2015) Biogas potential for electric power generation in Pakistan: a survey. *Renew Sustain Energy Rev*
15. Esmailion F, Ahmadi A, Dashti R (2021) Energy-economic-environment optimization of the waste-to-energy power plant using multi-objective particle swarm optimization (MOPSO). *Scientia*

# Design and Implementation of a Gesture-Controlled Car with Arduino Nano Board



Pawan Kumar, Prabhat Kumar Singh, Vaibhav Nijhawan , and Harsh Khanna

**Abstract** Robots today are being controlled in various ways. One of the ways on the frontier of robotics is controlling them via gestures, and when wearable technology is incorporated, then it becomes more intelligent, more capable, and much more user-friendly. This paper is all about movement of robots using gestures that are quick and responsive. We have discussed the idea through a model of car (robot chassis) that can be very easily controlled by simple human hand gestures. Gesture-controlled car is for concept validation; simple user interactions can be used for the movement of the robotic vehicle. The hand glove worn by the user comprises an accelerometer and transmitter, and it allows the sensor worn by humans to stay compact. The technique and technology discussed will facilitate better military applications, medical use, disaster rescue operations, and monitoring and operation of industrial and research equipment in hazardous zones.

**Keywords** Gesture · Arduino · Robot · Accelerometer

## 1 Introduction

In today's era, the human phase of manual repetitive labor work is going to change as robotic systems are taking over every industry. Most of them are fully automated as most repetitive tasks require high speed and efficiency and don't require around the clock human intervention. But there's also a need for robots that are semi-automatic or non-autonomous robots as some decision making is based on the human sense of judgments (some judgments' might be based on human morals) which is quite

---

P. Kumar (✉) · V. Nijhawan · H. Khanna  
Department of Electronics and Communication Engineering, MAIT, GGSIPU, Delhi, India  
e-mail: [chauhanpawan000@gmail.com](mailto:chauhanpawan000@gmail.com)

V. Nijhawan  
e-mail: [vaibhavnijhawan@mait.ac.in](mailto:vaibhavnijhawan@mait.ac.in)

P. K. Singh  
Department of Electronics and Communication Engineering, MSIT, GGSIPU, Delhi, India

difficult to code into a robot (use of artificial intelligence). Suppose a fully automated vehicle must make a choice between saving one of two people. In situations of such moral quandary, a human can make judgment based on their morals, but fully automated robots might run into problems when dealing with such morally ambiguous situations [1].

The manually controlled robots could either be controlled by joysticks, or we can make the controls feel more natural and control them by gestures. This way the user doesn't have to deal with the steep learning curve that comes with joysticks. Although there are robots available that can be controlled using gestures, but we have made the system much more responsiveness, much faster and accurate and not only that we have reduced the power consumption by eliminating constant data transmission and instead only transmitting data when movement is detected [2, 3]. The purpose of the proposed system is to be more user-friendly and provide a better human machine interaction. It's a robotic vehicle in which human gestures control its movement. The movement of the robotic vehicle in a specific direction is based on the hand's movement in a specific direction. The user can interact with the robot very easily, and the device worn by the user connects with the receiver using radio waves.

## 2 Literature Review

Meenatchi Sundaram et al. [4] discussed about robotic vehicle movement and control through hand gestures using Arduino in 2018; it describes an Arduino-based gesture-controlled robot that can have hospital and hazardous environment applications. Robot used in the study is based on Arduino Uno platform which makes the system less user-friendly due to its larger size. Moreover, the motors are driven by L293D motor driver [2] which is limited to draw 600 mA of current from both channels, hence limiting the use of higher performance motors.

In 2018, Atre et al. [5] described the idea of gesture-controlled robots by presenting a model of gesture-controlled robotic arm. In this paper, they describe the various fields where gesture technology can evolve. Now, with the never-ending development in technology, there is a rise in demand for more convenience and greater degree of freedom. This ideology has led to the rise of gesture-controlled robotic technologies. Moreover, the paper gives a brief introduction about the benefits of gesture robots over the remote-controlled robots.

Accelerometer Based Gesture Robot for Medical Assistance [6] by Arpita Ghosh et al. in 2018, the work talks about a wirelessly controlled (via gestures) medical assistance system that can be used to help especially abled people. A patient can use the robot to call for assistance by making a gesture that changes the sensor (accelerometer) value upon which a microcontroller will command for the desired action. The whole process comprises two parts, namely a transmitting and a receiving circuit. The part associated with the patient and is also the most important in the medical assistance system is the transmission circuit; hence, it needs to be transportable and user-friendly. Arduino Lily pad makes transmitting circuits compact and wearable



by the patient. This makes it convenient for the patient as the only thing needed to be worn by the patient is the transmission circuit.

In 2021, Zou et al. [7] explained about a model of a car that can be controlled by gestures which is formed using Arduino board and Bluetooth. MPU6050 is used as a sensor which comes out to be as major drawback for the new user since it is difficult to interact with. Moreover, if anything goes wrong with this robot the user has to face more difficulty to fix the issue, whereas the sensor used in this project (ADXL335) is very handy and is extremely easy to use with Arduino board. Furthermore, the power consumption of MPU6050 (3–5 V) is greater than ADXL335 (1.8–3.6 V). In addition to that, we have used NRF24L01 in place of Bluetooth which does not requires to be paired every time (but, Bluetooth requires to be paired every time), robot is ready to use as soon as the power gets on. This provides a seamless experience to the user.

Following Sect. 3 discusses proposed system that describes the block diagram, flowchart, and circuit system on both transmission and receiver section with components details. Implementation of the system is covered in Sect. 4 that discusses the interfacing and working of the proposed idea. Conclusion of the study is included in Sect. 5 which gives a brief idea of the system and is followed by Sect. 6 that contains the future scope in the technology. Last section contains the references part in which various papers are mentioned that are also cited in the study.

### 3 Proposed System

This section contains the block diagram that explains the hardware used circuit diagrams of transmitter and receiver section with and describes components and the workflow of the proposed model.

#### 3.1 Block Diagram

The idea is to create a gesture-controlled car that works on the principle of gestures that uses an accelerometer to decode different human hand movements.

The proposed system is divided into three major parts to understand the operation of gesture-controlled car better. As shown in Fig. 1, the initial part is used to get content from the ADXL335 (accelerometer Gyro Sensor) by the Arduino. It sends data to the RF Transmitter, which continuously acquires the data from the Gyro sensor, and it is based on some predefined parameters. The next part contains the wireless communication between the RF-based Transmitter and Receiver using NRF24L01. The role of the RF Transmitter is to transmit the data to the RF Receiver through RF communication when it received the data from Arduino. In the last part of this proposed system, processing of the data is done that is received to RF Receiver and sending the appropriate signals to the motor driver. The main role of this is to activate the wheel motors of the car.

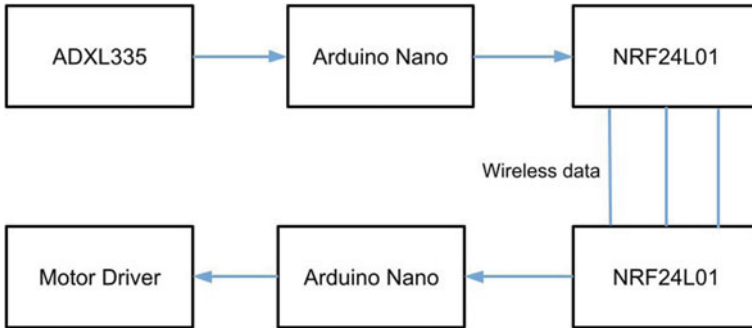


Fig. 1 Block diagram of the proposed model

### 3.2 Flowchart

The flowchart of the proposed system shown in Fig. 2 gives us an understanding of the whole system in much more detail. After ADXL335 picks up the signal, it forwards the signal to Arduino which only forwards the data for transmission when the signal is to move the car. Upon receiving the data wirelessly, receiver section Arduino sends out appropriate commands. The transmission of data only when motion has occurred saves lot on energy by eliminating the need for constant transmission.

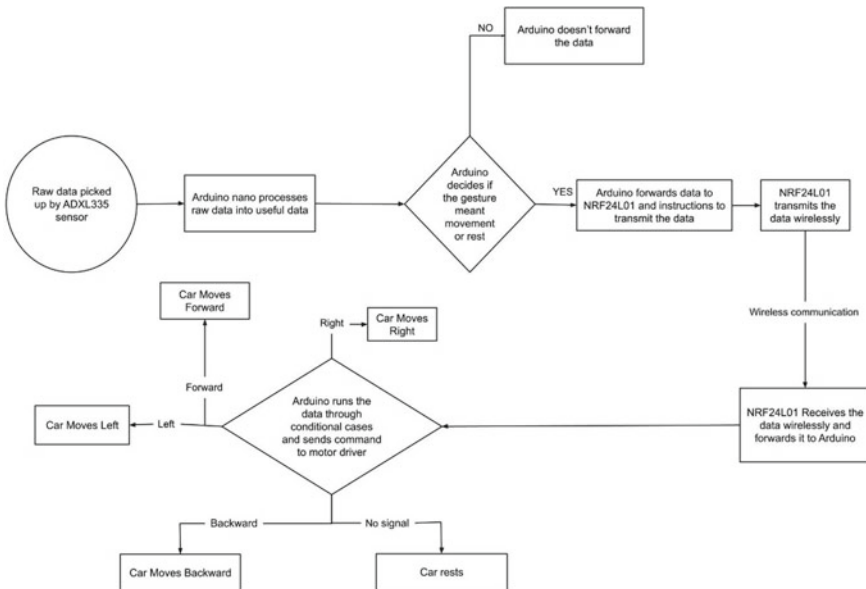


Fig. 2 Flowchart of proposed system

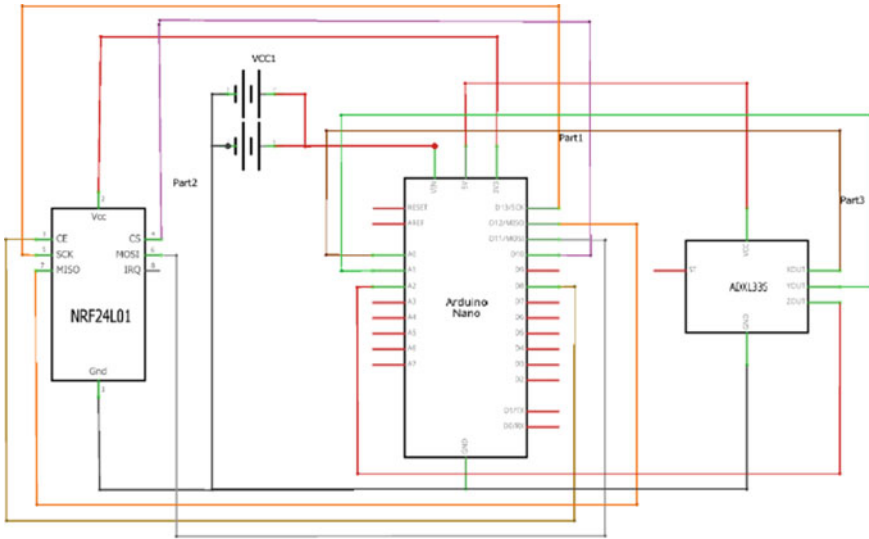


Fig. 3 Circuit diagram of transmitter section

### 3.3 Circuit Diagram

#### Transmitter Section-circuit diagram

The circuit diagram for the transmitter section as shown in Fig. 3 shows the necessary parts and the connections that are done. The Arduino Nano controls the system. ADXL335 is used to sense the motion of hand gestures in XYZ plane, and Arduino processes the incoming signals from ADXL335 [8–10] and sends required commands to be forwarded to receiver sections which will drive the motors. NRF24L01 is responsible for transmission of the commands and data.

#### Receiver Section-circuit diagram

Figure 4 provides the schematic diagram for the receiver section and after receiving data from transmission section NRF24L01 forwards the incoming data to Arduino which processes the data and sends out necessary commands to drive four motors which are driven by L298N motor driver [11].

## 4 Implementation

To implement this idea, we first construct the car, which consists of four wheels and four TT Gear motors mounted on a 5 mm acrylic sheet using glue. The motors are attached to the L289N motor driver on the backside, whereas the Arduino Nano and

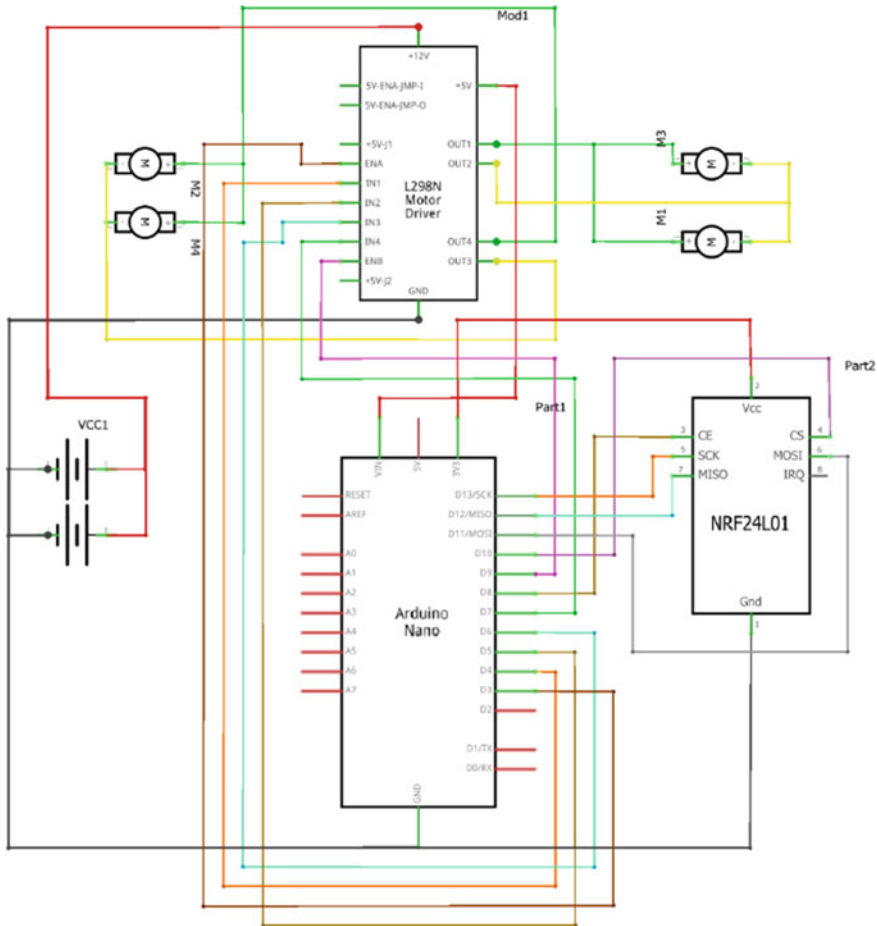


Fig. 4 Circuit diagram for receiver section

NRF24L01 module is mounted on custom Printed Circuit Board which is further powered by 2 18,650 Li-ion batteries.

### The connection of motor driver module with Arduino NANO

The proposed system carries the Direct Current Gearbox motors whose rating is 3–12 V. In the first step, connection of power with motors is to be established, for that connection of external power supply and VCC terminal is carried out. Now, L298N’s logic circuitry would require a 5-V supply. The onboard 5 V regulator will be used by us to deliver the power to Arduino. Six Arduino output pins (9, 7, 7, 5, 4, and 3) are then connected with the input and enable pins of the module. Note that output pins 9 and 3 of the Arduino board are both PWM-enabled. To get a clearer picture of wiring of motor drivers, battery, Arduino and four motors refer to Fig. 5.

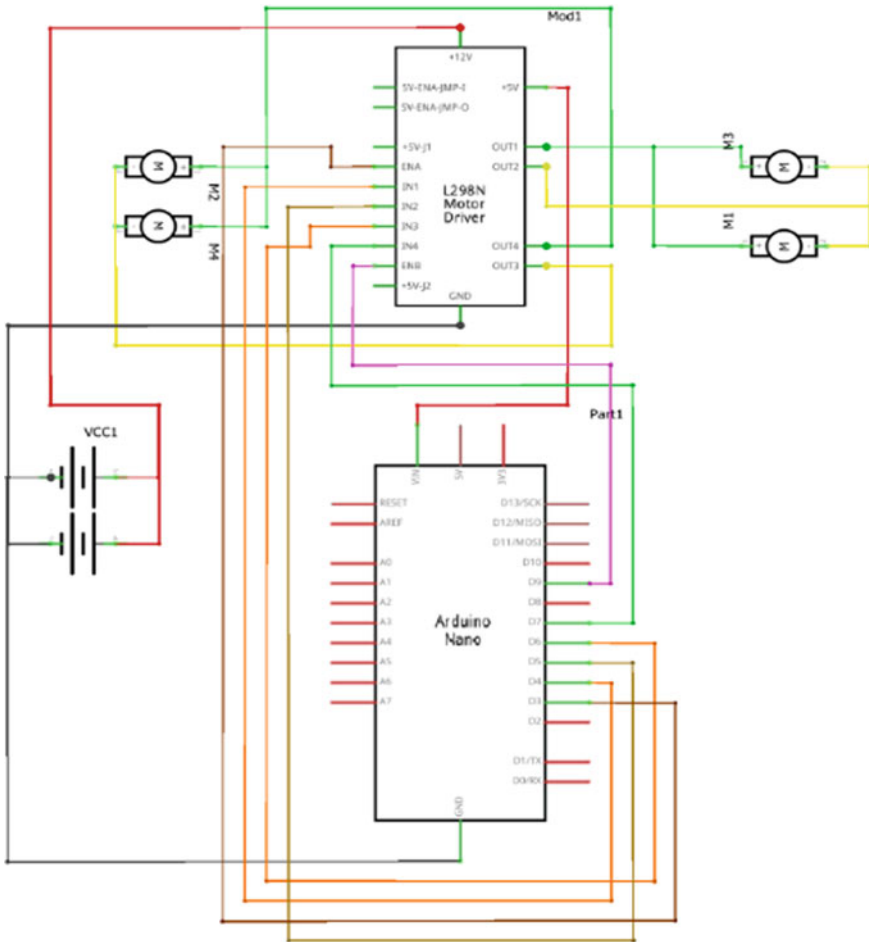


Fig. 5 Wiring L298N motor driver

The serial parallel interface (SPI) communication protocol is used for communication between NANO and nRF24L01. As seen in Fig. 6 which details interfacing of Arduino with NRF24L01, the Ground and VCC of the nRF24L01 are connected to GND and 3.3 V of the NANO.

**The connection of pins as**

- MISO—Master in slave out—connects to pin D12 of NANO
- MOSI—Master out slave in—connects to pin D11 of NANO
- SCK—serial clock—connects to pin D13 of NANO
- CE connects to pin D8 of NANO
- CSN connects to pin D10 of NANO.

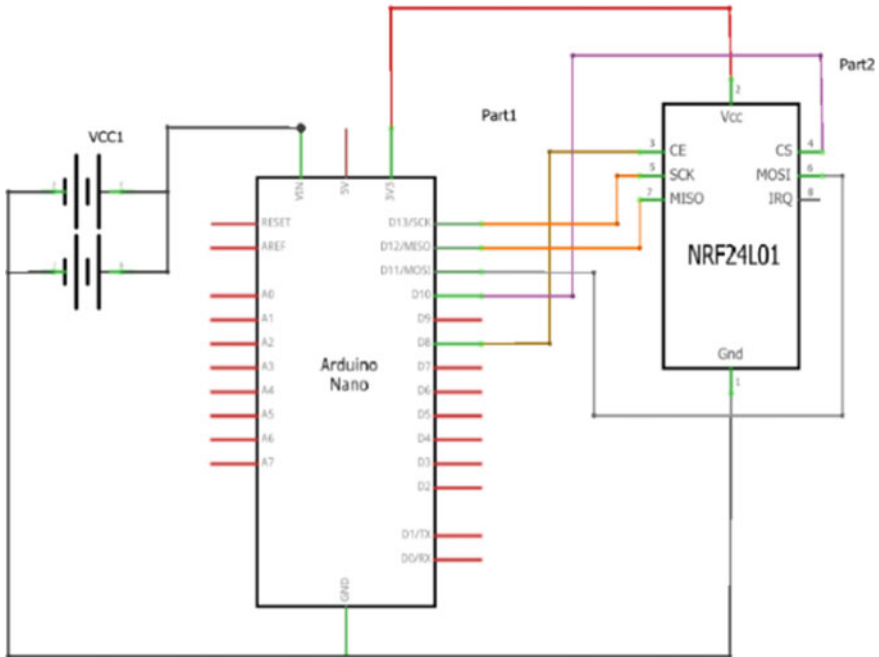


Fig. 6 Interfacing Arduino with Nrf24L01

### Interfacing Arduino with ADXL335

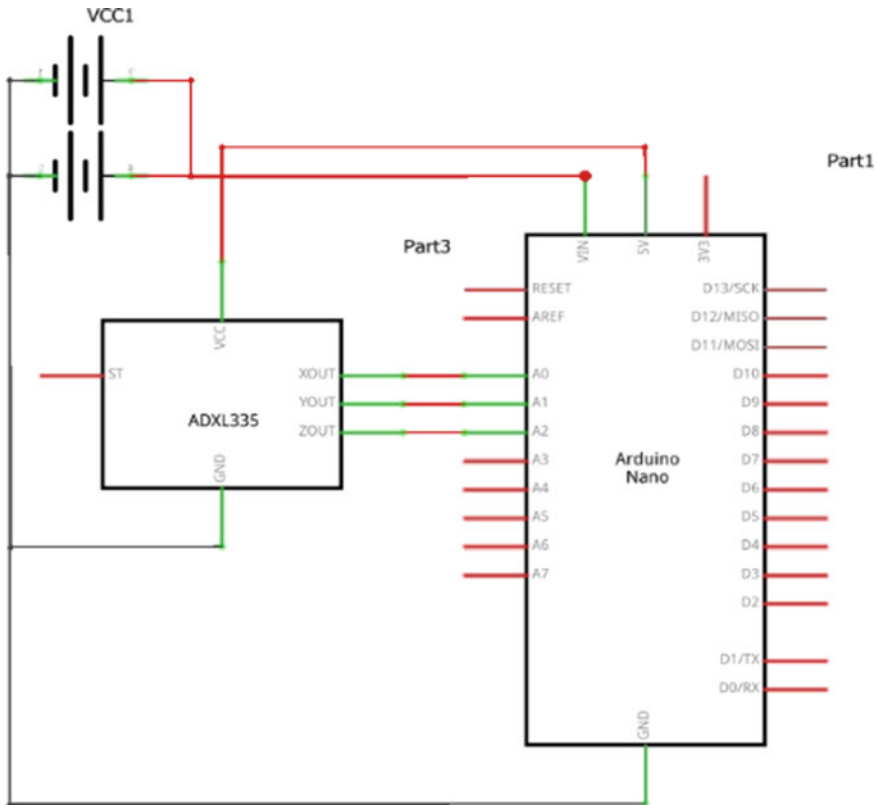
As shown in Fig. 7, we connect VCC pin of ADXL335 to the 5 V pin on the Arduino and connect GND pin to the Ground pin on the Arduino. Following analogue pins A0, A1, and A2 of the Arduino board is connected to X, Y, and Z output of ADXL335 [3, 8].

#### Working: Receiver section

Based on data of X and Y axes received from transmitter section, the Arduino goes through a series of case checks and determines the direction the car should be rolling or if the car should be at rest.

Table 1 gives us an idea of how the hand direction is translated to accelerometer orientation which when sent to receiver section is used to move the robot.

Using the direction control pins, direction of motor toward forward or backward is controlled. The switches of H Bridge inside the L298N IC are controlled by these control pins [12]. Using the direction control pins, direction of motor toward forward or backward is controlled. The switches of H Bridge inside the L298N IC are controlled by these control pins.



**Fig. 7** Interfacing Arduino with ADXL335

**Table 1** Accelerometer I/P shows the accelerometer orientation according to the hand detection

Hand direction	Accelerometer orientation
Forward	+ y axis
Backward	- y axis
Right	+ x axis
Left	- x axis
Stop	Rest

**Working: Transmission section**

The incoming raw data from output ports of ADXL335 is processed by Arduino Nano and turned into meaningful useful data as seen in Fig. 8.

Now, instead of constantly transmitting and receiving data, the data is only transmitted when a movement is detected hence reducing the power consumption considerably. After Nano determines if data needs to be transmitted, it forwards data to NRF24L01 which transmits the data.

**Fig. 8** Converting RAW data into useable data

```
int xAng = map(xRead, minVal, maxVal, -90, 90);
int yAng = map(yRead, minVal, maxVal, -90, 90);
int zAng = map(zRead, minVal, maxVal, -90, 90);

x = RAD_TO_DEG * (atan2(-yAng, -zAng) + PI);
y = RAD_TO_DEG * (atan2(-xAng, -zAng) + PI);
z = RAD_TO_DEG * (atan2(-yAng, -xAng) + PI);
```

## 5 Conclusion

The purpose of this concept is to guide and direct a car using an accelerometer sensor attached to a hand glove. The development of robotic car and its source code to analyze the movements is discussed above. To implement the experiment, hand gestures were used which acted as the input for accelerometer. Meanwhile, the software part was developed in Arduino IDE environment which is used for programming wherein the hand gestures were analyzed to extract the actual direction. The direction when identified is sent with the use of transceiver as characters to the robot to analyze the action. Further, the movement of sensor is realized on Arduino IDE serial monitor. The working reiteration of transmitter and beneficiary is 433 Megahertz based on interfacing. The proposed model is faster and accurate than many existing models. Using the same principle of this analysis various, other possibilities arise which can help people in each industry from medicine to help disabled people till defense to produce robots with vaster capabilities helping minimize human risk. Automation not only increases the degree of control but also improves the ease of usage in every aspect.

## 6 Future Scope

The future scope of this analysis realizes a different way of maneuvering. For disabled people, it is one of the technologies that can make their life easy helping them move better. This technology will provide opportunity to improve accuracy of medical procedures as well. The gesture recognition technology can also diminish some of the unnecessary manual labor. There are numerous entertainment applications possible as today most video games are played on consoles, gesture recognition could be used to truly immerse a player in game providing an experience mirroring reality. Automation using gestures will make life easier in each setting that requires human interaction.



## References

1. Jadhav M (2018) Hand gesture controlled robot using Arduino. *Int J Res Appl Sci Eng Technol* 6(3):2868–2870. <https://doi.org/10.22214/ijraset.2018.3629>
2. Agarwal D, Rastogi A, Rustagi P, Nijhawan V (2021) Real time RF based gesture controlled robotic vehicle. *IEEE conference ID: 51348*
3. Bhirud L, More N, Shekh S, Dhande H (2021) Gesture controlled mouse using Arduino. *Int J Innovations Eng Sci* 6(10):175. <https://doi.org/10.46335/ijies.2021.6.10.36>
4. Meenatchi Sundaram N, Shiva Rama Krishnan R, Suraj Kamal TK, Rajeswari J (2018) Robotic vehicle movement and arm control through hand gestures using Arduino. *Int Res J Eng Technol* 05(04). e-ISSN: 2395-0056 p-ISSN: 2395-0072
5. Atre P, Bhagat S, Pooniwala N (2018) Efficient and feasible gesture controlled robotic arm. Institute of Electrical and Electronics Engineers. ISBN: 978-1-5386-2843-0
6. Mukherjee S, Dhar M, Ghosh A (2018) Accelerometer based wireless gesture controlled robot for medical assistance using Arduino Lilypad. *IJETS* 5(3):2394–3386
7. Zou Z, Wu Q, Zhang Y, Wen K (2021) Design of smart car control system for gesture recognition based on Arduino. In: *IEEE international conference on consumer electronics and computer engineering (ICCECE)*, pp 695–699. <https://doi.org/10.1109/ICCECE51280.2021.9342137>
8. Jawalekar PA (2018) Robot control by using human hand gestures. *Int Res J Eng Technol (IRJET)* 05
9. Fulara N, Vashistha N, Bhullar PS, Kumari N (2019) Hand gesture controlled vehicle. *Int J Adv Eng Res Appl* 4(11). ISSN: 2454-2377
10. Gomathy CK, Niteesh G, Sai Krishna K (2021) The gesture controlled robot. *Int Res J Eng Technol* 08(04). e-ISSN: 2395-0056 p-ISSN: 2395-0072
11. Shukla A, Jain A, Mishra P, Kushwaha R (2019) Human gesture controlled car robot. *SAMRIDDHI: J Phys Sci Eng Technol* 11(02):115–122. <https://doi.org/10.18090/samriddhi.v11i102.5>
12. Srijith B (2021) Gesture controlled robot using Arduino. *Int J Res Appl Sci Eng Technol* 9:2758–2765. <https://doi.org/10.22214/ijraset.2021.3555>

# Design and Fabrication of a Solar-Powered Unmanned Aerial Vehicle (UAV)



Izhaan Shaikh, Mahmoud Abdelrazag Salih Suliman, Nour Alaa Elsonbaty, Sarath Raj Nadarajan Assari Syamala , and Apurv Yadav 

**Abstract** The aeronautics community has long hoped to enjoy a nonstop flight at high altitudes for long durations. The features of such an aircraft would enable it to carry out a wide range of tasks for a wide range of potential users. With the integration of solar photovoltaic (PV) technology for powering the aircraft, military surveillance, traffic control, environmental and meteorological monitoring, civil border patrol, and a wide range of civil communication applications are possible missions. This work presents the design and implementation of a functional solar unmanned aerial vehicle (UAV) aircraft. The aircraft configurations were compared using a decision matrix that was based on the aircraft's required characteristics.

**Keywords** Unmanned · Aerial vehicle · Solar · Aircraft · Flight

## 1 Introduction

With the continued use of renewable energy sources and rising temperatures on our planet, most parts of the world are turning to green energy resources [1]. Many countries are increasing their investment in solar unmanned aerial vehicles (UAV) since the United States was reported to have created the first solar UAV called the Solar Challenger [2]. Solar UAVs provide several advantages over standard UAVs, including environmental protection, great stability, exceptional load capacity, high flight altitude, and a large coverage area [3]. These types of UAVs can carry out many of the activities currently performed by small low-earth-orbit satellites, all at a much cheaper rate [4]. The method of propulsion is a crucial design consideration in the construction of these aircraft because of the long endurance requirements as well as altitudes where they might operate [5]. Solar photovoltaic (PV) units combined

---

I. Shaikh · M. A. S. Suliman · N. A. Elsonbaty · S. R. N. A. Syamala · A. Yadav (✉)  
Amity School of Engineering and Technology, Noida 201301, India  
e-mail: [apurv0210@gmail.com](mailto:apurv0210@gmail.com)

S. R. N. A. Syamala · A. Yadav  
Amity University, Dubai 345019, UAE

with a device for storing energy are an appealing technique for supplying electricity for this kind of aircraft. Using all-electric technology presents key benefits over conventional power systems [6]. It removes the need to transport fuel, as is the case with air-breathing fuel cells [7]. In addition, it removes the requirement to extract and compress air at oxygen scarce high altitudes, as is the case with the open-cycle combustion engines [8]. Furthermore, electrically powered aircraft with military uses would have a very low thermal signature, which would help them avoid detection. While a solar-powered UAV has numerous benefits, it as well encounters significant design challenges, particularly in the areas of too much stress on the wing root and too much wing root deformation [9]. The first solar aircraft, Sunrise I, made a couple of test flights during the winter of 1974 but encountered several harsh winds, which lead to its crash. In the September of 1975, Sunrise II was released featuring a lighter and aerodynamic body with more power when compared to its predecessor. However, after many weeks of testing, the aircraft had many flight controls issues and the test program was ended [10]. Extreme stress upon the wing root is a frequent source of material failure of the wing root beam [11]. When the wing becomes extremely deformed, its aerodynamic efficiency reduces, and the battery gets damaged. This causes reduced aircraft endurance. The aerodynamic layout of a solar UAV, along with solar cells' conversion efficiency, has a significant impact on it [12]. Each design has its distinctive features. Most solar UAVs have recently adopted a conventional layout to address issues such as wing deformation with a large aspect ratio, aeroelasticity, and flight control hurdles. This project discusses the design and implementation of a functional solar UAV.

Energy system of a solar UAV comprises solar array, batteries and energy distribution system. Most of the existing solar UAVs have conventional multi-crystalline silicon solar cells. Advances in solar cells have resulted in thinner and lighter solar cells, but their welding onto the wing will also increase fragmentation rate. The deformation of wing during flight will also affect the laying of solar cells. The UAV presented in this work utilizes flexible solar cells. These cells align with the curvature of the wing and will have minimum effect on flight due to wing deformation.

## 2 Design and Simulation

Various aircraft configurations were evaluated to finalize the UAV design. The pod and boom fuselage configuration are selected due to their lightweight as needed in a solar UAV. For wing configuration, the high wing option is selected as it provides better lateral stability and provides more maneuverability. The most important trait is that it saves a lot of space under the wing for accommodating payload. In addition to that, a high wing configuration produces zero to no shading by the fuselage, especially to the cells that are close to it. This allows for the generation of more power due to less shading. Among conventional tail, V-tail, and T-tail, the conventional tail structure was selected. The V-tail has the least stability and the T-tail configuration is not suitable because of its deep stall problems which lead to losing pitch control at



**Fig. 1** Solar UAV prototype

higher angles of attack. A single tractor propulsion system is selected as it provides higher efficiency. For landing gear, tail dragger configuration is selected as it creates lesser drag and gives more rotational clearance, helping in shorter takeoff. NACA 2412 Clark Y SM airfoil design is selected as it provides a coefficient of lift  $C_L$  of 1.3584 and coefficient of drag  $C_D$  of 0.06036, with a higher angle of attack ( $15.75^\circ$ ). The higher lift to drag coefficient gives efficient and stable flight. A total of 24 monocrystalline flexible solar cells (Sunpower  $C_{60}$ ) with a rated voltage of 0.6 V and a rated current of 5.2 A were used for the design. The image of the prototype is shown in Fig. 1.

The initial parameters of the aerodynamic simulation were set up in the Wizard toolbox and the aerodynamic simulation was performed in Solidworks. The fluid type used for this simulation is air. The initial conditions were set as ambient conditions. The pressure and temperature were kept standard. However, the velocity is set as  $-100$  m/s in the  $z$ -direction. This is due to the  $z$  axis being opposite in direction of the aircraft model. The domain for the computational fluid dynamics (CFD) analysis was selected as a non-uniform box shape. It is done to achieve flow trajectories later.

### 3 Results and Discussions

The simulation results listed a lift to drag ratio of 7.44 and the measured value was found to be close, at 7.38. This high value of lift to drag ratio is due to the use of aerodynamically efficient airfoil and streamlined aircraft shape, which creates low aerodynamic drag. The pressure is highest at the leading edge of the wing and the first point of contact at the front fuselage. However, the upper surface of the wing comprises lower pressure than the lower surface, which eventually creates aerodynamic lift. The pressure contour could be observed in Fig. 2.

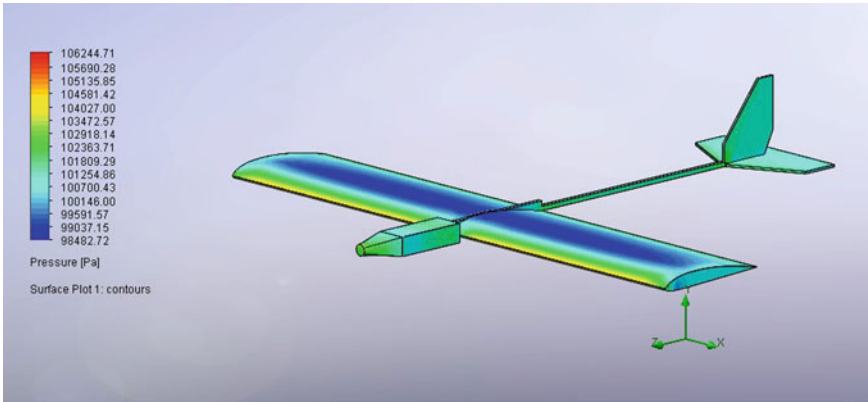


Fig. 2 Pressure contours

Figure 3 shows the incoming flow trajectory of the aircraft. The incoming flow is at a speed of 100 m/s. It can be seen that air flows smoothly over the wing surface which eventually creates less induced drag and produces higher lift.

The UAV required 10 m taxi mode to takeoff and 15 m for landing to halt. A maximum altitude of 23 m and a top speed of 75 km/h were obtained. Both simulations and the prototype values were in synchronization, in terms of stability of the model and working of avionics. Smooth air flow on wing surface can be attributed to the proper aerofoil selection. The net weight of the UAV due to solar panels limited the flight altitude of 23 m. Advancement in solar cell design can lead to a higher altitude as well as speed.

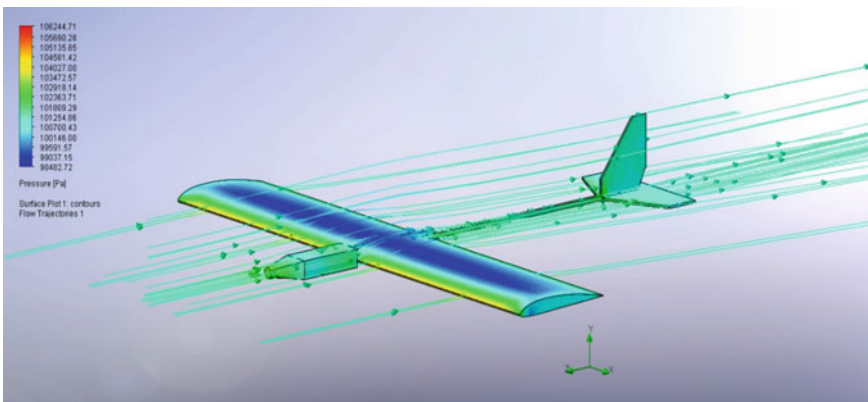


Fig. 3 Incoming flow trajectory

## 4 Conclusion

Solar power technology is now used in several well-proven autonomous vehicles and aircraft systems. There can be many applications of solar UAV as follows:

1. These UAVs can have applications in cinematography and videography.
2. Wildlife documentaries normally spend days just to capture a few-second shot. If they use helicopters, it will affect the behavior of these animals.
3. Another application that can involve solar planes is solar farms monitoring, using thermal cameras that will be mounted on the plane and it can monitor entire fields without landing to recharge.
4. Law enforcement can also benefit from the solar UAV in traffic and street surveillance.

Solar cells in UAVs can reduce their payback period, and also increases the flight duration. More research on solar UAVs can lead to many new applications.

## References

1. Owusu PA, Asumadu-Sarkodie S (2016) A review of renewable energy sources, sustainability issues and climate change mitigation. *Cogent Eng* 3. <https://doi.org/10.1080/23311916.2016.1167990>
2. North A, Siegart R, Engel W Autonomous solar UAV for sustainable flights. In: *Advances in unmanned aerial vehicles*. pp 377–405
3. Delavarpour N, Koparan C, Nowatzki J et al (2021) A technical study on UAV characteristics for precision agriculture applications and associated practical challenges. *Remote Sens* 13:1204
4. Pelton J (2020) High altitude platform systems (HAPS) and unmanned aerial vehicles (UAV) as an alternative to small satellites. In: *Handbook of small satellites*. pp 1–16
5. Sadraey MH (2013) *Aircraft design: a systems engineering approach*. *Choice Rev Online* 51:51-0912
6. Abbe G, Smith H (2016) Technological development trends in solar-powered aircraft systems. *Renew Sustain Energy Rev* 60:770–783
7. Flade S, Stephan T, Thalau O et al (2016) Air breathing PEM fuel cells in aviation. *ECS Trans* 75:471–477
8. Chen L, Li Y, Sun F et al (2004) Power optimization of open-cycle regenerator gas-turbine power-plants. *Appl Energy* 78:199–218
9. Wang X, Zhou W, Mu R et al (2020) A new deformation control approach for flexible wings using moving masses. *Aerosp Sci Technol* 106:106118
10. Boucher RJ (1985) Sunrise, the world's first solar-powered airplane. *J Aircr* 22:840–846
11. Lunia A, Isaac KM, Chandrashekhara K et al (2000) Aerodynamic testing of a smart composite wing using fiber-optic strain sensing and neural networks. *Smart Mater Struct* 9:767–773
12. Romeo G, Frulla G, Cestino E (2007) Design of a high-altitude long-endurance solar-powered unmanned air vehicle for multi-payload and operations. *Proc Inst Mech Eng Part G: J Aerosp Eng* 221:199–216

# Screw-Based Extruder Design for 3D Printing of Food Using Food Layered Technology



Moin Khan, Abid Haleem, Mohd Javaid, Shashi Bahl, Chander Prakash, Rajesh Singh, and Ashok Kumar Bagha

**Abstract** Additive food manufacturing can help provide fast-paced customised food with specified nutritional values. This advanced process can be used to manufacture food items with predetermined quality. 3D food printing technology development requires unique extruder designs for fluid food ingredient deposition. The study of the rheological properties of food material is critical for determining the various factors that influence food printing. This research aims to develop an extruder that can print various food materials. For this, various rheological properties of food have been studied. A literature-based review is done on the correlations between the parameters affecting the printability of the formulations and the rheological properties of the end product. The results thus obtained show the various components of the screw-based extruder for 3D printing of food and the correlations between various rheological properties of food. A non-Newtonian, non-isothermal viscosity model has been used to describe the material's rheology. The nozzle diameters required for printing various types of food were also studied. The screw-based 3D printer was constructed using SOLIDWORKS 2021, and simulation was done using COMSOL Multiphysics V.6.0.0.318 for velocity profile and pressure contour using wheat flour as the ink material.

---

M. Khan · A. Haleem · M. Javaid

Department of Mechanical Engineering, Jamia Millia Islamia, New Delhi 110025, India

S. Bahl (✉)

Department of Mechanical Engineering, I. K. Gujral Punjab Technical University Jalandhar, Kapurthala 144603, India

e-mail: [shashi.bahl@ptu.ac.in](mailto:shashi.bahl@ptu.ac.in)

C. Prakash

School of Mechanical Engineering, Lovely Professional University, Phagwara 144411, India

R. Singh

Division of Research and Innovation, Uttaranchal University, Dehradun, Uttarakhand 248007, India

A. K. Bagha

Department of Mechanical Engineering, Dr B R Ambedkar National Institute of Technology, Jalandhar 144027, India

**Keywords** 3D printing · Screw-based extruder · Additive manufacturing of food · Rheological properties

## 1 Introduction

3D printing technology can create the geometrical representation of a part by the successive addition of material. It originated from the layer-by-layer technology used to fabricate the 3D structures [1]. Traditionally, 3D printing technology has primarily been used to produce prototypes of parts in the engineering field. However, this technology has extended to more diverse fields like ophthalmology, dental implants, fuel injectors for rockets, etc. [2]. 3D printing of food can help revolutionise the food manufacturing processes. Using 3D printers for manufacturing food can control various factors to fabricate food like nutritional value, shapes, quality of food, etc. [3]. 3D printing of food primarily aims to provide custom-designed food by using layer-by-layer method without requiring human intervention. The platform used in the 3D printing of food primarily consists of an X, Y, and Z Cartesian coordinate system and a user interface [4]. There is three essential factors for the rational choice of 3D printing techniques used in the designing of food: (1) printability, (2) applicability, and (3) post-processing feasibility. This process primarily depends upon the materials that have been chosen in the extrusion processes and the required binding mechanisms. In this case, it occurs with the accommodation of layers. These layers are primarily controlled by the rheological properties and solidification achieved upon cooling. Thus, it becomes crucial to study the various rheological properties of the food for effective 3D printing [5]. Various important factors for precise 3D printing of food are binding mechanisms, rheological properties, thermodynamic properties, pre-treatment of the food material, and post-processing methods [3]. Additive manufacturing of food has various applications, including providing food to the military, maintaining nutritional balance for the elderly, and improving the appearance and quality of food. People suffering from dysphagia, a disease that causes difficulty in swallowing, can also be helped by this method by maintaining the standard consistency of food by ensuring the repeatability of this process [6]. The present study aims to design a screw-based extruder that can be used in production to print a wide range of materials at a much faster rate. This study used wheat dough as the ink material, and the model's velocity profile and pressure contour were studied.

## 2 Need for Study

3D printing can solve a wide array of problems. Its application ranges from ordinary household meals to more complex foods with specified nutritional values. It is capable of printing and manufacturing almost any kind of food. Traditional cooking techniques are quite costly and involve raising animals and providing them with



food and water [7]. However, printing meat can even be printed using 3D printers [8]. With the boundaries of space exploration being pushed, it is becoming more and more important to cut down the monetary aspects of food production by eliminating the need for food production and packaging [1]. Even though this technology has much potential, it still faces many problems like increasing the complexity of the structures. The introduction of more ingredients would require more sophisticated 3D printing technologies [9]. It was found that the consumption of 3D-printed food can lead to various problems such as food poisoning. In contrast, long-term consumption can also lead to various permanent changes and health-related difficulties within the human body [7].

### **3 Types of Extruders**

There are mainly three types of extruders that are used in 3D printers.

#### ***3.1 Filament-Fed Extruders***

The extruder serves as one of the most crucial parts of a 3D printer, and this part is primarily responsible for delivering the correct amount of the filament to the hot end of the filament-fed extruder, where it is finally melted and deposited layer-by-layer as thin layers on the surface of the bed [10]. The filament reel is directly fed to the extruder for extrusion. It uses fused-deposition modelling (FDM) to make the required product [11].

#### ***3.2 Syringe/Plunger-Based Extruders***

In these extruders, a dispersion is required. This dispersion is then subsequently deposited with the help of a syringe. These extruders can be controlled with the help of a controller to allow the control of the machine by using specified machine codes [12]. Generally, a pneumatic system is used for simplicity in these types of extruders but pulling back of material in this extruder is not possible. Thus, these types of extruders are less precise. They can be used for bioprinting [13]. In syringe-based extruders, the materials are transported, heated, and pressurised in a chamber. After this, it is dripped onto the bed of the 3D printer. In this process, the material used is stacked layer-by-layer, and this process is continued until the final product is obtained [14].

### 3.3 *Screw-Based Extruders*

In screw-based extruders, the screw in the extruder is driven by a motor that is programmed, and it continuously brings down the ink from the cartridge that further passes through the nozzle. Nevertheless, there are certain limitations to these types of extruders. Firstly, they have been reported to be unsuitable for inks with high viscosity, and it is also not possible to achieve high mechanical strength [15]. It utilises the screw mechanism that uses continuous feeding of granulated materials. This method is more precise as it allows pressure control, mixing materials, and making the mixture more homogeneous [16]. Screw extruders are divided into single-screw extruders and multi-screw extruders. Single-screw extruders are relatively cheaper, have simple designs, and are more reliable. In twin-screw extruders, the mixing of different ingredients is more efficient, and the product obtained is more homogeneous [17].

**Twin-screw extruders** can be primarily used in 2 processes, first in processing polymers that do not easily flow and hence are difficult to process. Secondly, they can be used for more specialised operations such as compounding materials, devolatilisation and chemical reactions. The transport in these types of extruders is the degree of positive displacement, and it depends on how efficient the flight of one of the screws closes the opposing channel of the subsequent screw. The flow patterns of twin-screw extruders are more complex and are difficult to predict using mathematical models. As a result, design calculations of such extruders become quite difficult since predicting the performance of extruders using geometric features becomes difficult [17].

**Single-screw extruders** use drug-induced transport as a transportation medium for the ink material. The polymers are pushed to the solid-conveying medium in these extruders due to friction between the barrel walls and the solid pellets. For rubber extrusion, serrated barrels are introduced to aid the mixing procedure [18]. The mixing process in the extruder is an important criterion for determining the quality of the product obtained from extrusion. The analyses of such extruders have primarily relied on the laminar shear mixing in the metering zone of the single-screw extruder. It is found that if the length of the metering zone is increased and if the striations and plane of shear are aligned, the extruder will be more efficient [19]. Single-screw extruders majorly have five important components [20]:

- Drive system that contains the gearbox.
- The feed system comprises the hopper, which contains the ink material.
- The screw, barrel, and heating system are the part where the ink is melted and mixed.
- Head and die assembly, the transportation of the extrudate, takes place in this component.
- The control system controls the extrusion process parameters, such as pressure, rpm, and temperature.

## **4 Parameters Affecting 3D Food Printing**

### ***4.1 Rheological Properties of Food***

This science branch is used to describe qualitatively and quantitatively the materials' deformation and flow behaviour. The food may be described as viscous, viscoelastic, or as elastic materials. They can be used for determining the flow behaviour over varying temperatures and shear conditions. They are also helpful in determining the processability of the food materials, stability of the manufactured product, and the sensory texture of the processed food. Rheological properties serve as an important criterion in determining the flow behaviour of a given raw material, which can be further utilised to determine the nozzle diameter for food extrusion. Determination of these behaviours and how they change under different operating conditions helps design the industrial processes and the extruder in the food processing industry [21].

### ***4.2 Shear Stress, Strain, and Shear Rate (Rheological Testing)***

The rheological testing for the semisolid foods is carried out by placing the food between two parallel plates. The upper plate can move while the lower plate is kept stationary. The upper plate experiences a shear force during testing. This shear force causes the upper plate to move with a velocity, resulting in the edge of the plate travelling a distance at a given time. Accordingly, shear stress, shear strain (unit less), and shear rate are determined from the force, deformation, and deformation rate placed on the sample [21].

### ***4.3 Creep (Use of Rheological Properties in the Industry)***

Rheological properties are an important criterion in the industry for determining the quality of food products. Rheological properties are modelled and analysed by the industries to create more efficient extruders and determine the printing conditions. They are important in determining the creep of the food materials. Regarding creep, the creep-relaxation test is carried out in the industries. They are two tests which involve stress analysis. It is a quick test, and it is also different from oscillatory testing, in which constant stress is used. It is a very low-frequency oscillatory testing mechanism, as it identifies the material's tendency to flow over for an extended period [21].

**Table 1** Nozzle diameter requirement for various food products

Food used for fabrication	Nozzle diameter (mm)
Dark chocolate	1.25
Egg yolk and egg white	0.84
Mushroom products	1.28

#### 4.4 Nozzle Diameter for Printing Various Food Items

Table 1 gives the nozzle diameter requirement for various food items [22]:

#### 4.5 Various Process Parameters Affecting the Printing of Food

The various parameters affecting the printability of food include [22]:

- Nozzle diameter
- The layer thickness of the printed material
- The printing speeds
- And the printing temperature.

Design parameters to be taken into consideration

- Nozzle depth height
- Tip diameter of the nozzle
- The deposition rates
- The intensity of radiation provided
- And the temp of hot air given.

## 5 Screw-Based Extruder Design

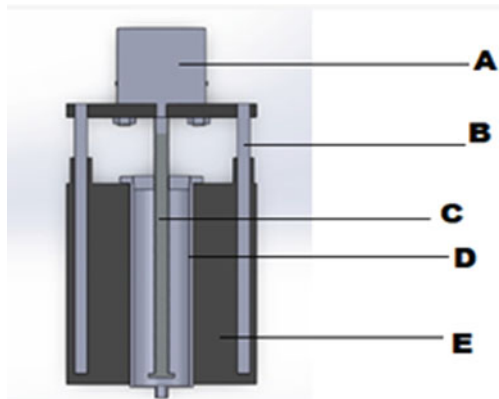
Figure 1 shows the final rendered image of the proposed screw-based extruder. Figure 2 shows the cross-sectional view of the extruder. The various components that are involved in the making of the extruder are:

- Stepper motor (A)
- Support rods (B)
- Screw spindle (C)
- Fluid holder (D)
- 3D-printed frame (E)
- Piston
- Rubber rings.

**Fig. 1** Rendered image of the extruder for food printing



**Fig. 2** Cross-sectional view of the extruder

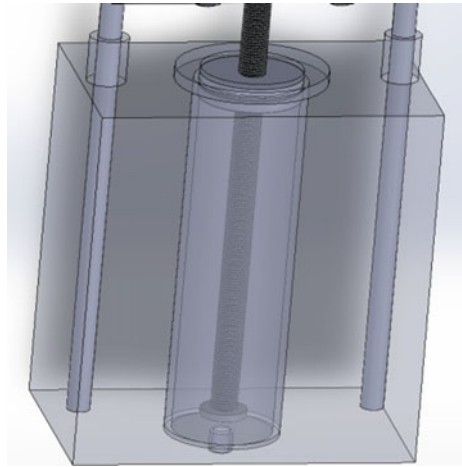


The stepper motor is used for controlling the extruder. No feedback mechanism is required for positioning or control in stepper motors since the stepper motor precisely controls these operations. They can also change the direction according to the pulse signal. This stepper motor will control the motion of the piston. The stepper motor is further connected to the screw spindle to which the piston is attached through the screw mate. As the stepper motor rotates with a certain rpm, the piston would move up and down in the 3D-printed frame. The pressure variations can also be controlled by varying the rpm of the stepper motor. The piston is provided with rubber rings to avoid slipping between the piston and the fluid holder walls. This slipping can also be eliminated with the help of the grooves. The piston is provided with an inlet hole to facilitate the entry of the mixed ink from the hopper.

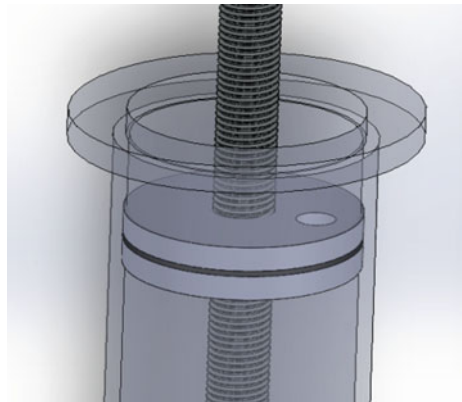
Figure 3 shows the inside view of the screw-based extruder showing how the fluid holder, piston, and the screw spindle are arranged. Figure 4 shows the detailed view of the piston. The rubber ring and the inlet hole are visible in the figure.

This extruder can be used for printing multiple food products as it allows the entry of both the mixed ink material and the single ink material. The advantage of using such an extruder is that it ensures the continuous flow of ink material into the extruder. It makes the production faster and more convenient as the need to change the link after each step would be eliminated since it will allow the flow of mixed and single ink flow. The above model has been made using SOLIDWORKS 2021.

**Fig. 3** Inside view of the extruder spindle and ring



**Fig. 4** View showing the piston



## 5.1 Design Calculations

The equations used for the calculation of the extruder are given by Zheng [23]

Flow rate in the orifice of the extruder in  $\text{m}^3/\text{sec}$ .

$Q_f = \frac{K_f}{\mu} * p$ , where  $K_f$  is the dimension coefficient for the orifice in  $\text{m}^3$ .

$K_f = \frac{(\pi D+h)*h^3}{12l_1}$   $D$  is the average of the hole's diameter of the ring orifice.

$D = 2R - h$ , where  $h$  is the width of the ring of the orifice.

$$k_f = \frac{C^3 \pi * R^3 * r^3 * (R - r)}{8l_1 (R^3 - r^3)}$$

The flow rate can be calculated as

$$Q_T = K_{T1} * \frac{\omega - (K_{T2})}{\mu} * \Delta P$$

where geometric coefficients  $K_{T1}$  and  $K_{T2}$  are given by

$$K_{T1} = \frac{\pi * Dk * B * H * \cos \phi}{2}$$

$$K_{T2} = B * H^3 / 12 * L_2$$

where  $L_2$  is the length of the screw channel in metres

$$L_2 = \sqrt{S^2 + (\pi(Dk - H))^2}$$

The pressure that is made by the extruder can be calculated as

$$\Delta P = \frac{\mu * K_{T1} * \omega}{(K_{T2} + K_f)}$$

The equation gives the extruder productivity

$$Q_{\text{ex}} = \frac{K_{T1} + K}{(K_{T2} + K_f)} * \omega$$

in  $\text{m}^3/\text{sec}$ .

## 6 Numerical Simulations for Extrusion Process Using Power Law

See Table 2.

The above simulations were carried out using COMSOL Multiphysics (V.6.0.318.) for non-Newtonian inelastic conditions. The CFD module of COMSOL is used by setting the physics as laminar flow. The model is taken to be a 2D axisymmetric for considering the pressure and velocity profile on the cross section of the extruder, along with isothermal contour. The results for the simulation were obtained, as shown in Figs. 5 and 6. The complete meshing of the model was done. Bread dough was taken as the material, and the yield stress was taken as 65.75 N/m<sup>2</sup> and the viscosity as 235.79 poise. The inelastic model analysis was done using power law, and a no-slip condition was considered between the piston walls and the fluid holding device. The average inflow velocity was taken to be 0.2 m/s; choosing such a low velocity would allow more uniform mixing of the ink material. It is seen that the maximum velocity was achieved at the nozzle at 1.8 m/s, while the velocity for most parts of the extruder was found to be constant with slight variations at the centre. The maximum pressure was achieved at the convergence of the nozzle. The pressure at this part was found to be 388.44 Pa; it is also seen that there is slight coagulation at the convergence of the nozzle. The equations used were as follows:

For boundary stress

$$[-pl + k]n = F$$

For analysis

$$\rho(u \cdot \nabla)u = \nabla \cdot [-\rho l + k] + f$$

$$\rho \nabla \cdot u = 0$$

**Table 2** Mesh statistics

Description	Value
Status	Complete mesh
Mesh vertices	2901
Triangles	4675
Quads	408
Number of elements	5083
Minimum element quality	0.2115
Average element quality	0.8228
Element area ratio	0.0039195
Mesh area	0.0506 m <sup>2</sup>



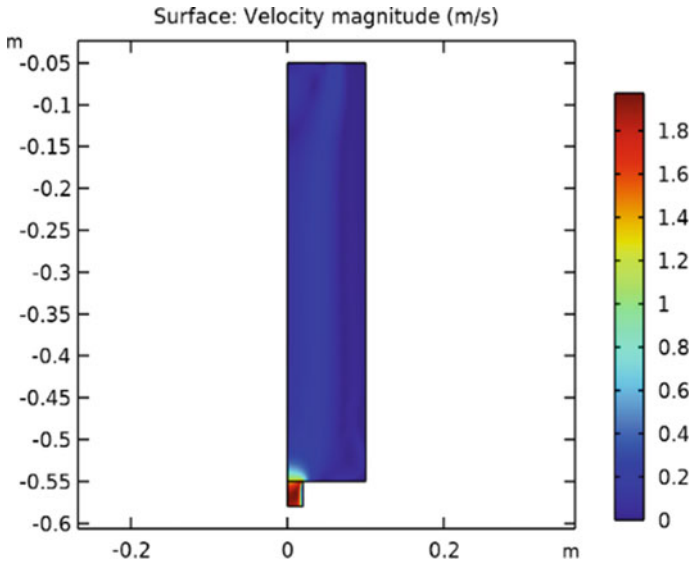


Fig. 5 Surface: velocity magnitude (m/s) streamline: velocity field

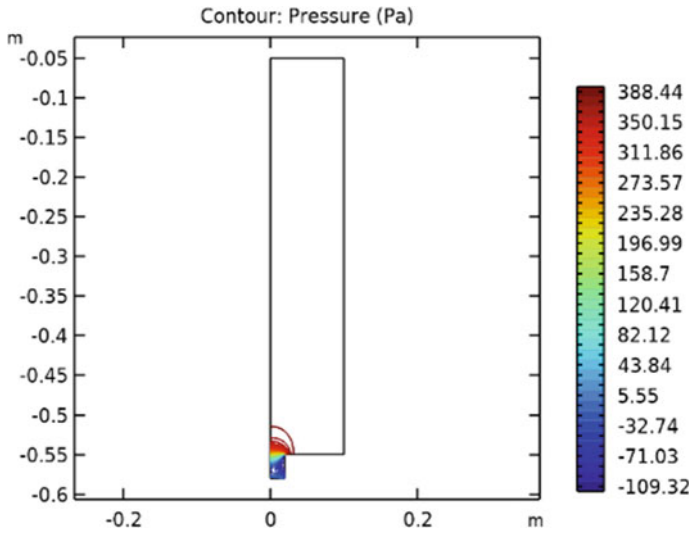


Fig. 6 Contour: pressure (Pa)

$$K = \mu(\nabla u + (\nabla u))^T$$

$$\mu = m \left( \frac{\gamma}{\gamma_{\text{net}}} \right)^{n-1}$$

$$\gamma = \max \left( \sqrt{2S : S}, \gamma_{\text{min}} \right)$$

In past research, the velocity was 0.03 mm/s, and tomato paste was the ink material. The compression distance was taken to be 10 mm. A trial-and-error approach is mostly used to determine the ideal nozzle size and inflow velocity [24].

## 7 Results and Discussions

Screw-based extruder design for additive manufacturing of food was discussed. It was found that the screw-based extruders were not efficient for printing food with high viscosity and led to low mechanical strengths. The various parameters affecting the printing process were also discussed. It was found that the rheological properties of food played an important role in the determination of the extruder design and the nozzle diameters. Nozzle diameter requirements were also listed in Table 1. The equations for design calculations based on the flowrate, the dimension coefficient, geometric coefficients and the length of the screw were studied. The equations governing the extruder pressure and the extruder productivity were also noted. The model of the screw-based extruder was designed using SOLIDWORKS 2021 software.

The numerical simulation of the model was done using COMSOL Multiphysics (V.6.0.318.). A non-Newtonian inelastic laminar model was considered. The graphs for the velocity profile and pressure contour were plotted. The complete meshing of the model was done. The inflow velocity of the ink into the extruder was taken to be 0.2 m/s to allow the uniform mixing of the ink material. The highest velocity was achieved at the nozzle, the velocity was 1.8 m/s, and the highest pressure was found to be at 388.44 Pa. The velocity was constant near the walls, while the velocity at the mid-section of the extruder was found to be a bit higher. The pressure was found to be maximum at the convergence of the nozzle, which could lead to slight coagulation; this is the reason that the screw-based extruders are not found to be more suitable for high viscosity fluids. Nevertheless, the pressure limits obtained in this case were enough for suitable extrusion.

## 8 Future Scope

Additive manufacturing of food depends on the materials used for extrusion, nozzle diameter, rheological properties, nozzle depth height, etc. Recent data shows a significant growth in the 3D food printing industry. There is no human intervention; hence

the end products are more reliable and have fewer nutritional values. However, there are several problems that this industry face. Firstly, the technology has not yet advanced, and the quality of the food produced from this method is also not found to be satisfactory. Screw-based extruders need to be developed since the current models are inefficient for fluids with high viscosity. In the coming future, work may be carried out on creating new materials suitable for 3D printing. People prefer eating nourishing food with an enhanced taste like rice, bread, etc. However, the printing of these materials is complex. Thus, in future, research can be carried out on finding a method that can be used to print more materials and formulate constituents and various particles in 3D printing that will help in the optimisation.

## 9 Conclusion

Several factors influence the 3D food extrusion process like rheological properties, nozzle diameter, nozzle depth height, material and nature of the food, temperature, and pressure given to the extruder. The highest velocity was found to be 1.8 m/s, whereas the pressure was 388.44 Pa at the convergence of the nozzle. This resulted in slight coagulation. That is why screw-based extruders are not found to be efficient for high viscosity fluids. The various parts for the proposed food extruder are stepper motor (A), support rods (B), screw spindle (C), fluid holder (D), 3D-printed frame (E), piston, and rubber rings, as seen in Fig. 2. The future of the 3D food printing process lies in developing new materials suitable for food printing.

## References

1. Shahrubudin N, Lee TC, Ramlan R (2019) An overview on 3D printing technology: technological, materials, and applications. *Procedia Manuf* 35:1286–1296
2. Schubert C, Van Langeveld MC, Donoso LA (2014) Innovations in 3D printing: a 3D overview from optics to organs. *Br J Ophthalmol* 98(2):159–161
3. Nachal N, Moses JA, Karthik P, Anandharamakrishnan C (2019) Applications of 3D printing in food processing. *Food Eng Rev* 11(3):123–141
4. Sun J, Peng Z, Zhou W, Fuh JY, Hong GS, Chiu A (2015) A review on 3D printing for customised food fabrication. *Procedia Manuf* 1:308–319
5. Godoi FC, Prakash S, Bhandari BR (2016) 3d printing technologies applied for food design: status and prospects. *J Food Eng* 179:44–54
6. Kouzani AZ, Adams S, Whyte DJ, Oliver R, Hemsley B, Palmer S, Balandin S (2017) 3D printing of food for people with swallowing difficulties. In: *DesTech 2016: proceedings of the international conference on design and technology*. Knowledge E, pp 23–29
7. Tran JL (2016) 3D-printed food. *Minn JL Sci Tech* 17:855
8. Dick A, Bhandari B, Prakash S (2019) 3D printing of meat. *Meat Sci* 153:35–44
9. Jandyal M, Malav OP, Chatli MK (2021) 3D printing of meat: a new frontier of food from download to delicious: a review. *Int J Curr Microbiol Appl Sci* 10:2095–2111
10. Landry T (2016) Extruders 101: a crash course on an essential component of your 3D printer
11. Poudel B (2015) How to make portable homemade filament extruder

12. Faes M, Valkenaers H, Vogeler F, Vleugels J, Ferraris E (2015) Extrusion-based 3D printing of ceramic components. *Procedia Cirp* 28:76–81
13. Tashman JW, Shiwarski DJ, Feinberg AW (2021) A high performance open-source syringe extruder optimised for extrusion and retraction during FRESH 3D bioprinting. *Hardware* 9:e00170
14. Diagne M, Krstic M (2015) State-dependent input delay-compensated bang-bang control: application to 3d printing based on screw-extruder. In: American control conference (ACC). IEEE, pp 5653–5658
15. Liu Z, Zhang M, Bhandari B, Yang C (2018) Impact of rheological properties of mashed potatoes on 3D printing. *J Food Eng* 220:76–82
16. Justino Netto JM, Idogava HT, Frezzatto Santos LE, Silveira ZDC, Romio P, Alves JL (2021) Screw-assisted 3D printing with granulated materials: a systematic review. *Int J Adv Manuf Technol* 115(9):2711–2727
17. Shrivastava A (2018) Introduction to plastics engineering. William Andrew
18. Wilkes CE, Summers JW, Daniels CA, Berard MT (2005) PVC handbook, vol 184. Hanser, Munich
19. Edwards MF (1992) Laminar flow and distributive mixing. In: *Mixing in the process industries*. pp 200–224
20. Giles Jr HF, Mount III EM, Wagner Jr JR (2004) Extrusion: the definitive processing guide and handbook. William Andrew
21. Zheng H (2019) Introduction: measuring rheological properties of Foods. In: *Rheology of semisolid foods*. Springer, Cham, pp 3–30
22. Soni R, Ponappa K, Tandon P (2022) A review on customised food fabrication process using food layered manufacturing. *LWT* 113411
23. Ibrahim SE, Mohammed MA, Ahmed YE (2018) Single screw extruder design calculations using MatLab and visual basic. In: International conference on computer, control, electrical, and electronics engineering (ICCCEEE). IEEE, pp 1–5
24. Zhu S, Stieger MA, van der Goot AJ, Schutyser MA (2019) Extrusion-based 3D printing of food pastes: correlating rheological properties with printing behaviour. *Innov Food Sci Emerg Technol* 58:102214

# Finite Element Analysis of Residual Stresses During Incremental Sheet Forming of Ti-6Al-4V Alloys Using Different Tool Path Profiles



Gianender Kajal , M. R. Tyagi , and Gulshan Kumar 

**Abstract** The incremental sheet metal forming is highly flexible and a die-free production method for fabricating various sheet metal components using a CNC spindle tool. Compared to the conventional process, it is beneficial for small-batch components. In biomedical and aeronautical sectors, titanium grade-5 (Ti-6Al-4V) is highly recommended due to its optimal specific strength, biomedical applications, and excellent resistance rate against corrosion. This paper simulates a truncated conical, hemisphere, and hyperbolic geometry in the incremental sheet metal forming process. MATLAB programming is then used to compute the profile, modify, and export the data to the Abaqus input file format for further FE analysis. This research uses an explicit-based computational approach to simulate SPIF and determine the output response parameters such as residual stresses, von Mises stress distribution, and variation in sheet thickness along the deforming depth. The Johnson–Cook (J-C) parameters have been used for carrying out the incremental forming simulations. Compared to other tool path profiles, more compressive stresses were observed in the conical shape profile. The distribution of effective residual stresses and part thickness were also explored in a detailed comparison of various tool path profile predictions.

**Keywords** Residual stress · Finite element analysis · MATLAB programming · Titanium grade-5 · Incremental sheet forming (ISF)

---

G. Kajal (✉) · M. R. Tyagi  
Department of Mechanical Engineering, Manav Rachna University, Faridabad, Haryana 121004, India  
e-mail: [kajal2321@gmail.com](mailto:kajal2321@gmail.com)

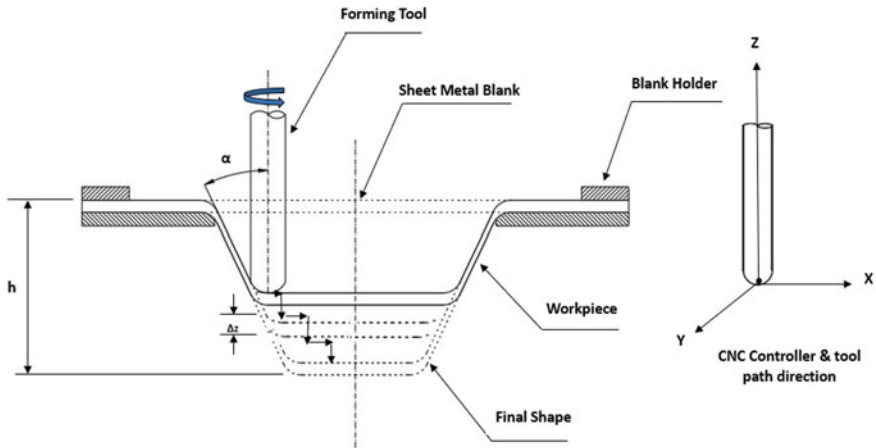
G. Kumar  
Department of Mechanical Engineering, Birla Institute of Technology and Science, Pilani—Dubai Campus, 345055 Dubai, United Arab Emirates

## 1 Introduction

Sheet incremental forming (ISF) is a type of flexible manufacturing technique normally used as batch type and prototype due to economical production cost with less lead time (see Fig. 1). In this process, a hemispherical tool is used for incremental forming on a CNC machine. The movement is controlled by CNC programming. In the plastic zone of the component material, the tool causes smaller, localized deformation. As a result, the part's final form is created [1]. ISF has substantially superior formability than traditional forming processes such as deep drawing, stretching, and stamping [2]. Due to lightweight and heavy demands in biomedical sectors, titanium alloy is normally used [3]. Titanium alloy has a greater average strain hardening exponent than aluminum alloy. As a result, titanium alloy has far higher stretching capability than aluminum [4]. The response surface approximation approach can be utilized to optimize the J-C parameters of Ti-6Al-4V for machining simulation work [5]. Li et al. [6] investigated a truncated pyramid shape's thickness distribution and mechanical properties using numerical modeling simulation and tensile testing produced by incremental forming. The results indicate that the sheet thickness is correlated with tool diameter during the process. Nguyen et al. [7] implemented the combination of computer-aided manufacturing (CAM) and finite element modeling (FEM) simulation. They evaluated stress and strain value by finite element analysis in order to improve the incremental sheet forming process for the product of human face complex shapes. The tool step down was found as a significant component for increasing the formability of the incremental sheet forming process as a result of FE simulations based on the Taguchi orthogonal array. Park et al. [8] investigated the detailed comparison of different tool paths to generate a truncated conical shape simulation of the single-point incremental forming of AA7075-O material. It was observed that the helical tool path is an optimal condition for incremental forming. Sbayti et al. [9] presented the possibility of producing a customized titanium hip prosthesis by assessing FE modeling of a hot SPIF process for an acetabular component. It showed that forming temperature and punch diameter are the most influenced parameters for biomedical components using titanium grade 5 material. Reddy et al. [10] observed that sheet thickness is a major parameter that highly influences the formability limit diagram in incremental forming. They conducted an experimental study to determine the yield stresses under the formability limit diagram of phosphorus-bronze material. Shim et al. [11] determined the deformation characteristics along the tool path and performed a numerical simulation of the single-layer manufacturing in the truncated pyramid. Major and minor strains of different shapes were also measured. Iseki [12] focused on simple geometry models such as rectangular or circular geometries or a combination of both in a simulation model for the incremental forming process. A numerical simulation and experimental study were used to discuss process parameters and their effect on the forming force, sheet thickness, and deformation behavior during the incremental forming process. Several researchers investigated the properties of CP-Ti grade 1 metal sheet and performed FEM with experiments to evaluate the feasibility of customized skull implants and also studied

the forces required to deform the sheet, reduction in thickness, dimensional inaccuracy, and surface finish of the material used [3, 9, 13]. Dobecki et al. [14] examined the tool path planning, i.e., unidirectional and bidirectional, influence on the residual stress development state using numerical simulation processed by the SPIF process. It was found that the impact of residual stresses can be neglected during the variation of the tool path strategy. Kotkunde and Gupta [15] considered the hardening model using Johnson–Cook (J-C) hardening to find out the forming limit diagram (FLD) for titanium grade 5 alloy and stated that the precision of theoretical FLD greatly depends on the hardening model and yield. The formability results of the sheet are compared using theoretical and experimental approaches. Alavala [16] observed that the lowering of sheet thickness is also particularly prevalent in the side walls of the cups. Hahn et al. [17] discussed that tool path strategy directly influences the amplitude of residual stress in the ISF process. It was observed that residual stresses are the most influencing parameters on the mechanical and metallurgical behavior of sheets during the ISF process. Alinaghian et al. [18] investigated that smaller step-down size values produce smaller residual stresses in SPIF. It was also examined that large tool diameter influences residual stresses' impact. Qin et al. [19] explored the impact of pre-heat treatment on deformation behavior of the different type of shapes and their metallurgical behavior changes in the forming process. The improvement in the blank sheet formability without deteriorating the mechanical properties after formed component was investigated. Kumar et al. [20] observed that steepness of forming angles and increment of forming depth leads to residual formation for SPIF process. Golabi and Khazaali [21] analyzed the forming depth in the SPIF process on conical frustums of SS304 sheet. It was determined that the blank thickness is directly correlated to the forming depth of conical frustum shape. Fajoui et al. [22] discovered the impact of residual stress caused by microstructure and static load produced during hot forging process. It showed that the magnitude of residual stress produced by microstructure of hot steel has substantial influence on stress behavior of hot forging under static load. Rashid et al. [23] showed that the nature and magnitude of residual stresses (RS) (tensile and compressive) is directly influencing the performance and capability of the formed sheet. It observed that less stresses are induced in the lower region of pyramid shape component in SPIF process.

The primary purpose is to conduct a preliminary numerical analysis of SPIF technology utilizing the viable finite element computer program ABAQUS and tool path development using MATLAB programming. The present research focuses on determining the sheet thickness feasibility and residual stresses analysis in producing different types of components using titanium alloy (titanium grade 5) sheet. Many studies found that the residual stress conditions may be directly influenced by changing the process variables during manufacturing. A reliable numerical process model is required to gain vital knowledge of residual stress production produced by the SPIF process.



**Fig. 1** Basic principle of ISF process

## 2 Materials and Methodology

In this finite element modeling of the SPIF process, titanium grade 5 sheet was used. The mechanical properties of Ti-alloys are given in Table 1.

In this investigation, a frustum of the truncated cone, hemisphere, and hyperbolic shape has been created from a blank sheet of Ti alloy (Ti-6Al-4V) with a size of 200 mm × 200 mm × 1 mm. The dimensions of different geometrical profiles considered for this study are described in Table 2.

**Table 1** Mechanical properties of material used [2]

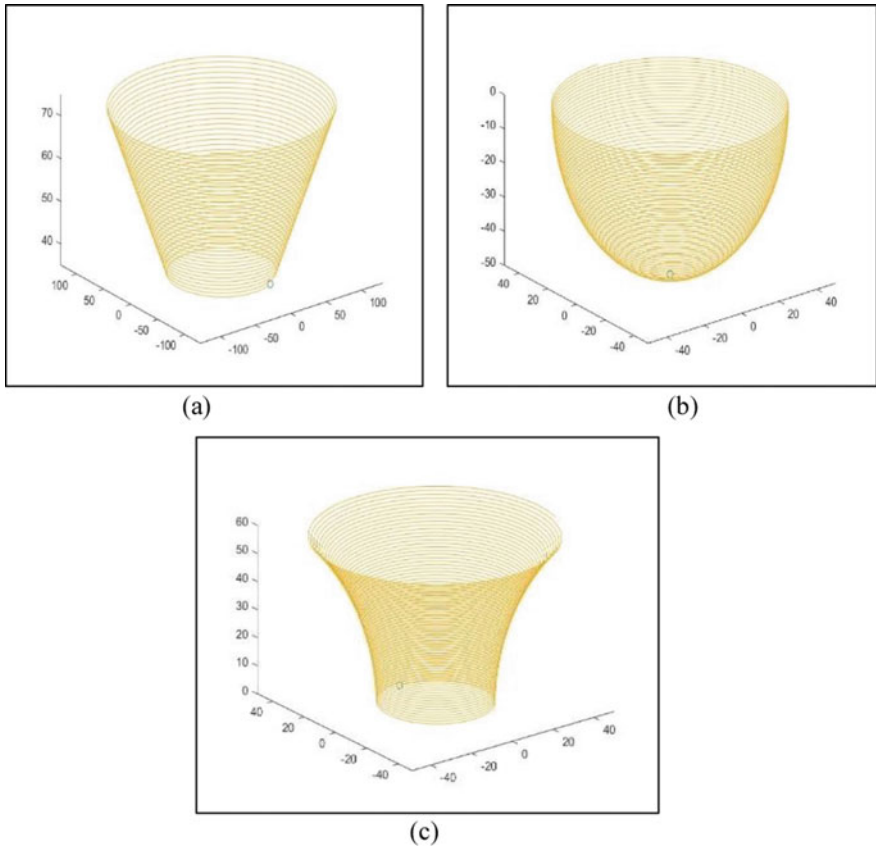
Material	Young’s modulus, E (GPa)	Poisson ratio ( $\mu$ )	Density ( $\text{Kg/m}^3$ )	Thermal conductivity ( $\text{W/m-k}$ )
Ti-6Al-4V	105	0.15	4430	7.4

**Table 2** Dimensions of various geometrical profiles

Geometry	Dimensions
Truncated cone	Wall angle = 30°
	Radius = 90 mm
Hemisphere	Height of cone = 75 mm
	Height of hemisphere = 70 mm
	Radius = 50 mm
Hyperbolic shape	Radius of curvature = 85 mm
	Radius = 50 mm
	Height = 60 mm



The hemispherical-shaped tool used for incremental forming simulation comprises high-speed steel (HSS) grade material with a diameter of 10 mm. As illustrated in Fig. 2, a constant Z spiral tool path method was adopted for the tool path trajectory. MATLAB software was used to generate the tool path. In this analysis, 0.1 mm vertical step down has been considered for tool profile shapes. The shapes have been created corresponding to the tool trajectory shown in Fig. 2. The tool path is made up of different contours produced in the transverse direction to the vertical axis of the actual component. The hemisphere-shaped forming tool follows a programmed tool path, shaping the sheet metal in successive steps until the appropriate depth is attained.



**Fig. 2** Tool paths profile generated using MATLAB and integrated into Abaqus in the ISF process: **a** truncated cone shape (wall angle 30°) **b** hemisphere shape **c** hyperbolic shape

### 3 Finite Element Modeling

The Abaqus/explicit software was utilized to create a three-dimensional elastic-plastic finite element model. This model is used to solve nonlinear problems of the SPIF process [24]. In the case of a cup shape deformation, this software may give elastic-plastic and rigid-plastic simulations of single-point incremental forming, considerably lowering the expense and associated time with the tool and die design. FEM simulation helps to find equivalent stress–strain distribution, forming limit diagram, residual stresses, and fracture zone. This leads to identifying the factor of safety and desired properties of the component for other purposes. The blank (sheet metal) was considered to be isotropic, and meshing was done with shell elements (S4R) in this model. The binder and tool were viewed as hard bodies. The coefficient of friction ( $\mu$ ) between the blank and the tool was taken as 0.15, corresponding to Coulomb’s friction law. The modeling interaction between tool, punch, and sheet is an important parameter to obtain correct simulation results in SPIF using Abaqus/Explicit. The interaction properties between these are characterized by Coulomb’s friction law as described below:

$$\tau_f = \mu p \quad (1)$$

where “ $\tau_f$ ” is the frictional shear stress, “ $\mu$ ” is the friction coefficient between punch and sheet, and “ $p$ ” is the normal contact pressure.

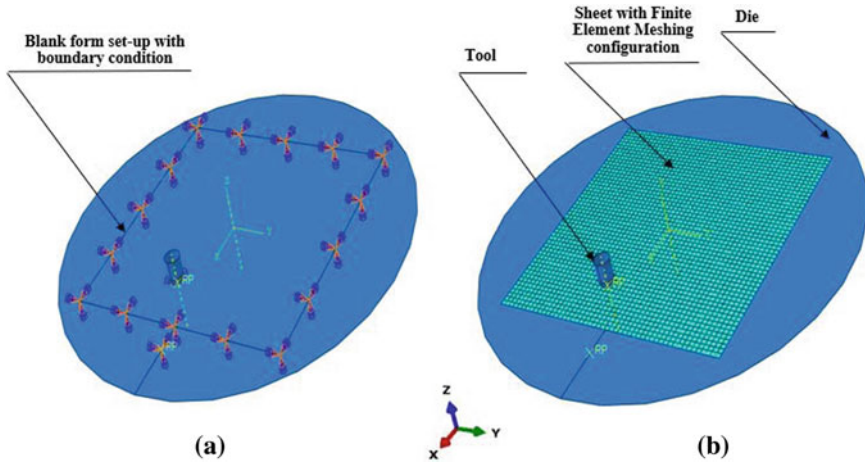
Here, the Johnson–Cook (J-C) model is implemented to explain the plastic behavior of the material used, which can be specified by below equation:

$$Yield\ Stress(\sigma_y) = (a + b \cdot \epsilon^n) \cdot \left[ 1 + c \cdot \ln\left(\frac{\dot{\epsilon}}{\dot{\epsilon}_0}\right) \right] \cdot \left[ 1 - \left( \frac{T_{workpiece} - T_{room}}{T_{melting} - T_{room}} \right) \right] \quad (2)$$

where initial yield strength (in MPa), hardening modulus (in MPa), strain rate correlation coefficient (constant), work hardening coefficient (constant), and thermal softening coefficient (constant) are represented by “ $a$ ,” “ $b$ ,” “ $c$ ,” “ $n$ ,” and “ $m$ ,” respectively, in J-C constitutive model.  $T_{workpiece}$  is workpiece material temperature (in °C), normal room temperature is  $T_{room}$  (in °C), and  $T_{melting}$  is melting temperature (in °C);  $\epsilon$  is equivalent plastic strain rate;  $\epsilon_0$  is reference plastic strain rate (in  $s^{-1}$ ). The parameters of this model are taken from the literature study for this material [25] (see Table 3). The incremental forming simulation is achieved on three distinct tool path profiles, i.e., truncated conical part with wall angle  $\alpha = 30^\circ$ , hemisphere, and hyperbolic shape. The blank form is set up with boundary conditions and meshing with tool position during SPIF simulation, as shown in Fig. 3.

**Table 3** Johnson–Cook constitutive model constants for material used [25]

'a'	'b'	'c'	'm'	'n'	$\epsilon_0$	'Tm'	'Tr'
790	478	0.032	1	0.28	1	1674	25



**Fig. 3** a Representation diagram of the sheet blank form setup in FEA simulations during the SPIF process b finite element meshing with tool position during SPIF simulation

### 4 Results and Discussions

This study has considered the sheet thinning and residual stresses using different path profiles. The outputs and a parametric study of the explicit solver approach using Abaqus are reported here. In SPIF, the impact of an incremental step down and sheet thickness is generally explained by sine law [26]. A sine law predicts the final thickness ( $t_f$ ) by the relationship between the forming angle ( $\varnothing$ ) and original wall thickness ( $t_i$ ) stated in Eq. 3.

$$t_f = t_i \cos \varnothing \tag{3}$$

#### 4.1 Investigation of Conical Profile

As a result, the effect of path profiles' conical shape forming angle ( $30^\circ$ ), hemisphere, and hyperbolic shape on section thickness has been investigated. The remaining process parameters are maintained constant in this study. It has been observed that the section thickness is substantially nonuniform for different tool profiles. Unlike

the cosine law, which showed a uniform change in the thickness, it decreases along the forming depth.

For 1 mm thickness sheet, the maximum equivalent stress induced is 1142.0 MPa, and the minimum sheet thickness distribution is 0.85 mm, respectively, as shown in Figs. 4a and b for truncated cone shape. In this study, von Mises (V-M) stress contour plot has been used to exhibit the stress distribution in the forming sheet, as V-M theory is most appropriate for considering yielding in material while experiencing the plastic behavior of metal sheet. The maximum equivalent stress is recorded in the side and corner walls of the cups with a conical shape. To substantiate the simulation results, 2 mm size of the element has been considered.

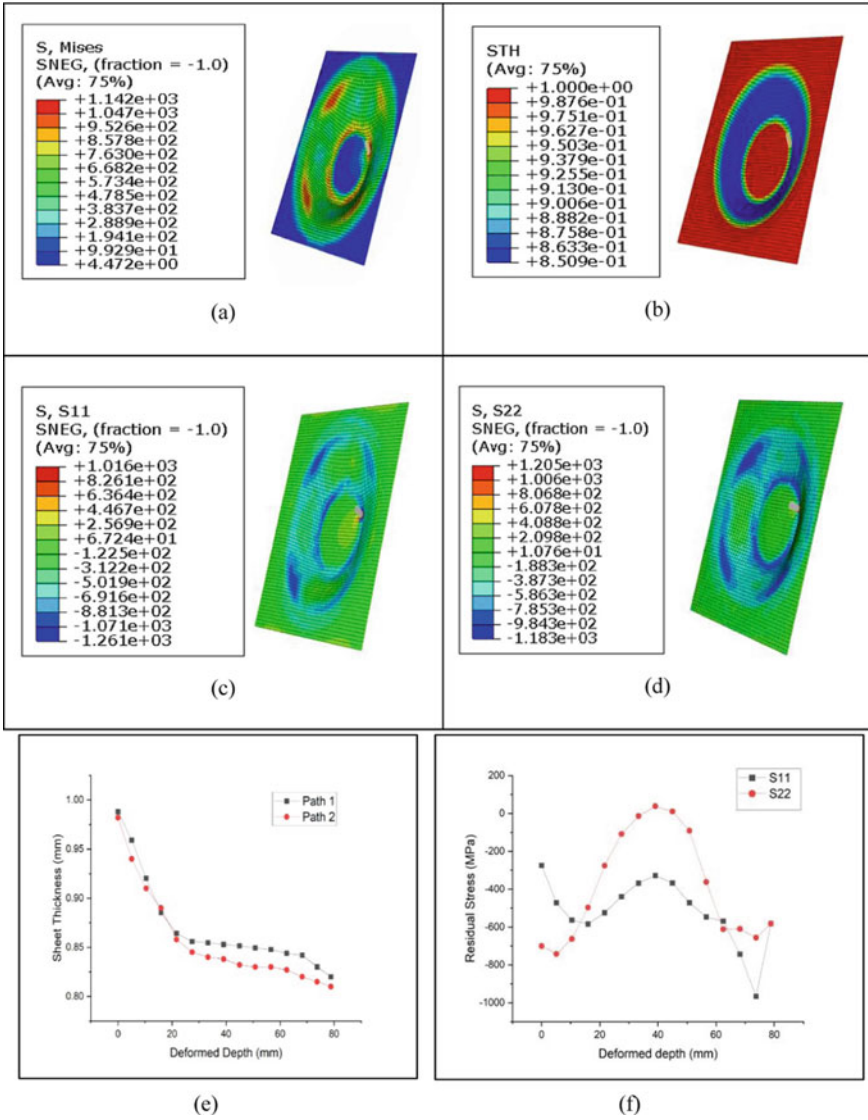
The residual stress values in conical tool path side direction ( $x$ -direction) S11 are 1016 MPa (tensile) and 1261 MPa (compressive) (see Fig. 4c). The residual stress values normal to the tool path direction ( $y$ -direction) S22 are 1205 MPa (tensile) and 1183 MPa (compressive) (see Fig. 4d). A comparison of the magnitude and directions with deformed depth for both the residual stresses is shown in Fig. 4f.

A complete assessment of the residual stress amplitudes demonstrates a very small variation in starting and end points of the tool path wall in the conical section except in the midpoint of the wall. A sudden reduction in section thicknesses up to 20 mm deformed depth has been observed due to evolution from bending (initial) zone to truncated cone shape in forming along paths 1 and 2 (see Fig. 4e). The residual stresses from the mid-region surface of parts are higher than the residual stresses from the interior surface and the initial surface. In SPIF, a variation in the thickness of the deformed components highly influences the product quality and shape. Continuous deformation of the sheet metal exceeding a threshold value may lead to fracture. FEA aids in the simulation of the process to estimate the decrease in the thickness to avoid fracture. The nonuniform thickness distribution is largely caused by the change in deformation mechanics of sheet profiles from plane strain to biaxial thinning with increasing forming depth during SPIF.

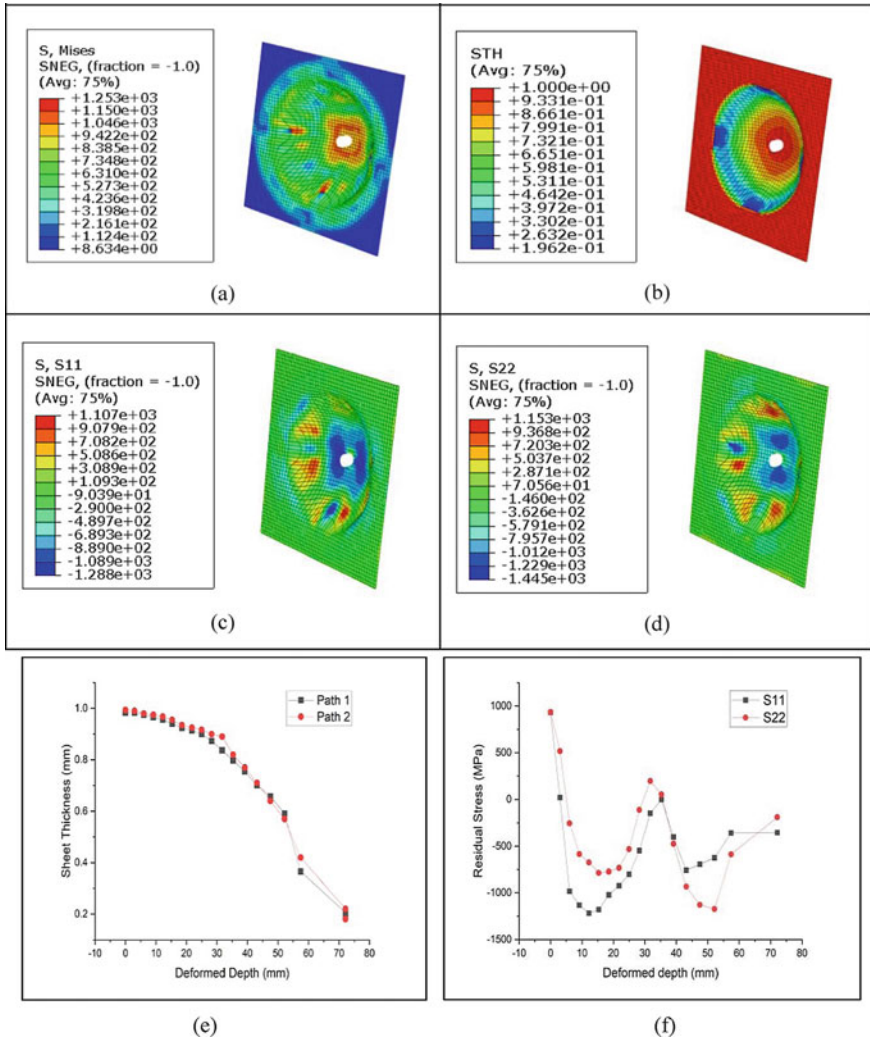
## 4.2 Investigation of Hemisphere Profile

For the hemisphere tool profile, the maximum equivalent stress induced is 1253.0 MPa, and the minimum sheet thickness distribution is 0.19 mm, respectively, as shown in Figs. 5a and b.

The residual stress values in hemisphere tool path side direction ( $x$ -direction) S11 are 1107 MPa (tensile) and 1288 MPa (compressive) (see Fig. 5c). The residual stress values normal to the tool path direction ( $y$ -direction) S22 are 1153 MPa (tensile) and 1445 MPa (compressive) (see Fig. 5d). The comparison in magnitude and directions with respect to deformed depth of both residual stresses has been studied (see Fig. 5f). Figure 4f shows a very small deviation along the deformed depth (top-to-bottom region) in S11 and S22. In this profile, the RS value from the initial region (top surface) of parts is observed to be larger than the mid-region and the lower surface. A sharp reduction in section thicknesses up to 60 mm deformed depth has been



**Fig. 4** For conical shape **a** equivalent stress induced in sheet thickness **b** thickness variation induced in profile **c** stress-induced along the *x*-direction (tool path direction) **d** stress induced along the *y*-direction (transverse to tool path direction) **e** sheet thickness distribution along deformed depth for Path 1 and Path 2 **f** residual stresses versus deformed depth along the shape of the wall

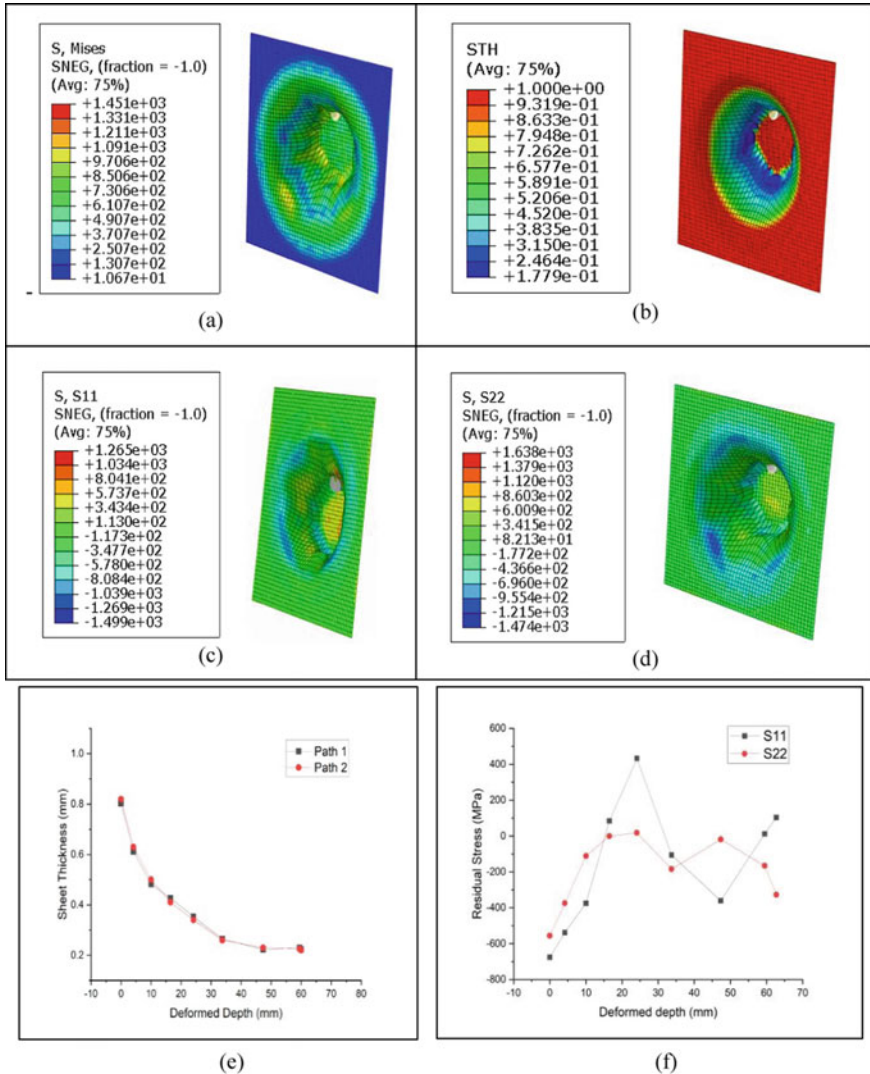


**Fig. 5** For hemisphere shape **a** equivalent stress induced in sheet thickness **b** thickness variation induced in profile **c** stress-induced along the  $x$ -direction (tool path direction) **d** stress induced along the  $y$ -direction (transverse to tool path direction) **e** sheet thickness distribution along deformed depth for Path 1 and Path 2 **f** residual stresses versus deformed depth along the shape of the wall

observed owing to conversion from the initial point to hemisphere shape in forming process (see Fig. 5e).

### 4.3 Investigation of Hyperbolic Profile

The maximum equivalent stress induced for the hyperbolic profile is 1451.0 MPa, and the minimum sheet thickness distribution is 0.177 mm, respectively, as shown in Figs. 6a and b.



**Fig. 6** For hyperbolic shape **a** equivalent stress induced in sheet thickness **b** thickness variation induced in profile **c** stress-induced along the x-direction (tool path direction) **d** stress induced along the y-direction (transverse to tool path direction) **e** sheet thickness distribution along deformed depth for Path 1 and Path 2 **f** residual stresses versus deformed depth along the shape of the wall



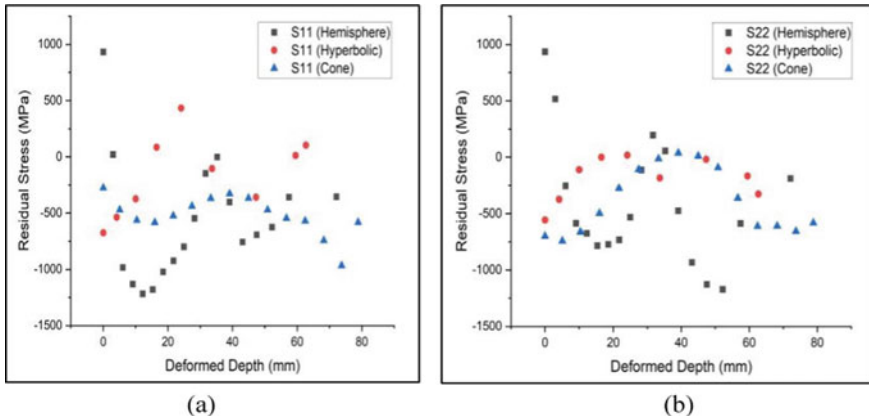
The residual stress values in hyperbolic tool path side direction ( $x$ -direction) S11 are 1265 MPa (tensile) and 1499 MPa (compressive) (see Fig. 6c). The residual stress values normal to the tool path direction ( $y$ -direction) S22 are 1638 MPa (tensile) and 1474 MPa (compressive) (see Fig. 6d). The comparison of both residual stresses' magnitude and directions with respect to deformed depth has been studied (see Fig. 6f). In this profile, the RS value for the mid-region surface of the parts is observed to be larger than the initial and bottom surface. A sharp reduction in section thicknesses up to 60 mm deformed depth has been observed owing to conversion from the initial point to hyperbolic shape in forming process (see Fig. 6e).

## 5 Conclusions

This paper presents a numerical investigation of the ISF of titanium alloy (grade 5) sheet. The finite element modeling is utilized to form a truncated cone, hemispherical shape, and hyperbolic profile based on the use of Abaqus and MATLAB software for finding the stress behavior and thickness distribution on the wall shape. The impact of the tool path technique on the residual stresses was examined. It has been observed that the tool profile directly influences the residual stresses for the analyzed component geometry. In terms of residual stress generation, the truncated conical form produces larger compressive stress than the hyperbolic and hemispheric profiles. The compressive stress enhances the bending strength, reduces the effect of applied tensile stresses, and is also resistance to stress-corrosion cracking of the component. A comparison of residual stresses along the different directions with respect to deformed depth for (S11) with varying path profiles for different forming depths (see Fig. 7a) and deformed depth for (S22) with varying path profiles for different forming depths (see Fig. 7b) is depicted.

The forming region's wall sheet thickness distribution values were determined under varied shape profiles using the finite element analysis technique. The effects of tool path profiles with forming angles on the variation of thinning distribution were also investigated. The present study observed that the favorable stress (compressive stress) ratio is higher than unfavorable stress (tensile stress) for truncated cone shapes in the SPIF process. Hence, a truncated cone shape is an optimal selection for the ISF process, which other studies also investigated [8].





**Fig. 7** **a** Residual stresses distribution (S11) with varying path profiles for different forming depths **b** residual stresses distribution (S22) with varying path profiles for different forming depths

**Acknowledgements** The authors acknowledge support from the Manav Rachna University, Faridabad, India, 121004, which leads to the completion of this manuscript.

## References

1. Sajjad M, Joy JA, Jung DW (2018) Finite element analysis of incremental sheet forming for metal sheet. *Key Eng Mater* 783:148–153
2. Saidi B, Giraud Moreau L, Cherouat A, Nasri R (2020) Experimental and numerical study on warm single-point incremental sheet forming (WSPIF) of titanium alloy Ti-6Al-4V, using cartridge heaters. *J Brazilian Soc Mech Sci Eng* 42(10)
3. Deokar S, Jain PK, Tandon P (2018) Formability assessment in single point incremental sheet forming through finite element analysis. *Mater Today Proc* 5(11):25430–25439
4. Djavanroodi F, Ebrahimi M, Janbakhsh M (2019) A study on the stretching potential, anisotropy behavior and mechanical properties of AA7075 and Ti-6Al-4V alloys using forming limit diagram: an experimental, numerical and theoretical approaches. *Results Phys* 14:102496
5. Xinjian L, Guigen Y, Zhimin W, Shifeng X, Yi Z (2020) Optimization on the Johnson-Cook parameters of Ti-6Al-4V used for high speed cutting simulation. *J Phys Conf Ser* 1653(1)
6. Li JC, Li C, Zhou TG (2012) Thickness distribution and mechanical property of sheet metal incremental forming based on numerical simulation. *Trans Nonferrous Met Soc China* 22(1):s54–s60
7. Nguyen DT, Park JG, Lee HJ, Kim YS (2010) Finite element method study of incremental sheet forming for complex shape and its improvement. *Proc Inst Mech Eng Part B J Eng Manuf* 224(6):913–924
8. Esmailpour R, Pourboghra F, Kim H, Park T (2019) Finite element analysis of single point incremental forming (SPIF) of aluminum 7075 using different types of tool-path. *IOP Conf Ser Mater Sci Eng* 521(1)
9. Sbayti M, Ghiotti A, Bahloul R, Belhadjsalah H, Bruschi S (2016) Finite element analysis of hot single point incremental forming of hip prostheses. *MATEC Web Conf* 80

10. Chennakesava Reddy A (2017) Numerical and experimental investigation of single point incremental forming process for phosphorus bronze hemispherical cups. *Int J Sci Eng Res* 8(1):957–963
11. Shim MS, Park JJ (2001) The formability of aluminum sheet in incremental forming. *J Mater Process Technol* 113(1–3):654–658
12. Iseki H (2001) An approximate deformation analysis and FEM analysis for the incremental bulging of sheet metal using a spherical roller. *J Mater Process Technol* 111(1–3):150–154
13. Hou X, Liu Z, Wang B, Lv W, Liang X, Hua Y (2018) Stress-strain curves and modified material constitutive model for Ti-6Al-4V over the wide ranges of strain rate and temperature. *Materials (Basel)* 11(6)
14. Maaß F, Gies S, Dobecki M, Brömmelhoff K, Tekkaya AE, Reimers W (2018) Analysis of residual stress state in sheet metal parts processed by single point incremental forming. *AIP Conf Proc* 1960
15. Kotkunde N, Gupta AK (2015) Analysis of forming limit diagram for Ti-6Al-4V alloy. *Mater Today Proc* 2(4–5):3762–3769
16. Alavala CR (2016) Fem analysis of single point incremental forming process and validation with grid-based experimental deformation analysis. *Int J Mech Eng* 5(5):1–6
17. Maaß F, Hahn M, Dobecki M, Thannhäuser E, Erman Tekkaya A, Reimers W (2019) Influence of tool path strategies on the residual stress development in single point incremental forming. *Procedia Manuf* 29:53–58
18. Alinaghian M, Alinaghian I, Honarpisheh M (2019) Residual stress measurement of single point incremental formed Al/Cu bimetal using incremental hole-drilling method. *Int J Light Mater Manuf* 2(2):131–139
19. Mohammadi A, Qin L, Vanhove H, Seefeldt M, Van Bael A, Dufloy JR (2016) Single point incremental forming of an aged AL-Cu-Mg alloy : influence of pre-heat treatment and warm forming. *J Mater Eng Perform* 25(6):2478–2488
20. Kumar R, Kumar G, Singh A (2019) An assessment of residual stresses and micro- structure during single point incremental forming of commercially pure titanium used in biomedical applications. *Mater Today Proc* 28(xxxx):1261–1266
21. Golabi S, Khazaali H (2014) Determining frustum depth of 304 stainless steel plates with various diameters and thicknesses by incremental forming. *28(8):3273–3278*
22. Fajoui J, Kchaou M, Sellami A, Branchu S, Elleuch R, Jacquemin F (2018) Impact of residual stresses on mechanical behaviour of hot work steels. *Eng Fail Anal* 94(July):33–40
23. Rashid H, Hussain G, Rehman K, Khan S, Alkahtani M, Abidi MH (2020) Characterization of residual stresses in an asymmetrical shape produced through incremental forming. *CIRP J Manuf Sci Technol* 31(2019):478–491
24. ABAQUS (2010) ABAQUS theory manual. ABAQUS Doc., p 1176
25. Sekar KSV, Kumar MP (2011) Finite element simulations of Ti6Al4V titanium alloy machining to assess material model parameters of the Johnson-Cook constitutive equation. *J Braz Soc Mech Sci Eng* 33(2):203–211
26. Jeswiet J, Micari F, Hirt G, Bramley A, Dufloy J, Allwood J (2005) Asymmetric single point incremental forming of sheet metal. *CIRP Ann—Manuf Technol* 54(2):88–114

# A Comparative Analysis of Plane and Corrugated Designs of Soft Pneumatic Actuators Based on Finite Element Method



Narendra Gariya and Pushpendra Kumar

**Abstract** Several soft robots consist of pneumatic actuators which are developed by using rubber-like materials such as silicone rubber, dragon skin, elastosil, and ecoflex. The complex geometry and nonlinearity in the soft pneumatic actuator (SPA) make the analytical model very difficult to predict the bending behavior of the SPA. The computational simulation technique also known as the finite element method (FEM) is an alternative and effective way to determine the bending behavior of soft actuators. In this work, two SPAs with the plane and corrugated structures are designed and compared in terms of bending angle using FEM. Ecoflex 0050 hyperelastic material model is considered for the analysis. From the FEM simulation results, it has been observed that the SPA with corrugated structure is more efficient because it shows a higher bending angle even at low pressure as compared to the plane-structured SPA. Moreover, a finer mesh led to the accurate distribution of stress and bending angle of the SPA.

**Keywords** FEM · SPA · Plane · Corrugated · Bending · Mesh

## 1 Introduction

Soft robotics is the branch of engineering and science, that deals with robots made up of soft and smart materials. The soft robot provides a safer interaction and can adapt to the surrounding environment compared to the conventional hard robots [1, 2]. The components or links of the conventional hard robots are connected through a number of single degrees of freedom joints like a hyper-redundant manipulator. In this type of robot, each joint is operated independently to complete a particular task [3, 4]. Contrary to that, soft robots show infinite degrees of freedom and require complex algorithms to control their movements as well as their interaction

---

N. Gariya (✉) · P. Kumar

Department of Mechanical Engineering, Graphic Era Deemed to Be University, Dehradun, India  
e-mail: [navigk05@gmail.com](mailto:navigk05@gmail.com)

with the surrounding environment. With the advancement in the additive manufacturing techniques as well as in the soft materials, soft robotics developed continuum structures having soft sensors, actuators, batteries, and transmission mechanisms in order to reduce the requirement of the control and feedback systems. These soft robots have variable stiffness, which generates the required force during interaction with the various physical objects in different environments. Whenever an application requires adaptability to the surroundings as well as safer human–machine interaction, there is a requirement for soft robotic technology. Introducing morphological computation into the soft robotic designs is one of the important features [5]. The aim of the introduction of morphology is to reduce the robot's dependency on the controller. For example, by employing the under-actuation concept, a two–three or multi-actuator gripper or prosthetic hand can be activated [1].

Actuation is the most essential feature of soft robotic technology [6, 7]. Hydraulic and pneumatic actuators can generate high-density power [8, 9]. Soft pneumatic actuators (SPAs) are lightweight, easy to manufacture, low-cost and provide soft contact with physical objects [1]. They are of high interest because of their easy manufacturing using molding and additive manufacturing techniques. Therefore, many multi-actuator soft grippers or prosthetic hands articulated with soft pneumatic actuators have been proposed [10, 11]. SPAs consist of small chambers entrapped inside the slender body of hyperelastic material such as silicone rubber [12, 13]. The chambers are also known as pneu-nets, placed in the continuum body having gaps between their external walls. These gaps will reduce the constraining effects of the continuum body and produce large bending deformation under the same amount of input pressure. The performance of SPAs has been quantified experimentally as well as numerically using the FEM technique [14]. The characterization of fabrication, analysis, and performance of discrete chamber actuators of silicone rubber has been presented in [6]. FEM and quasi-static analytical model of the fiber-reinforced soft pneumatic bending actuator have been proposed in [15]. SPAs having vertical micro-balloon fin having trapezoidal shape developed using 3D printed mold have been reported in [16]. Recently, in rehabilitation or medical centers, many exoskeleton devices are upgraded to soft assistive gloves which are connected to the actuators either by cables or by soft elastomeric actuators [6, 17]. They provide support for the actuator bending. This soft robotic technology combines the designs and control of classical robots with soft and smart materials to develop a new class of applications [18].

In the existing literature, different types of soft pneumatic actuators have been developed. They have been developed in the form of the soft helical actuator, soft bellow actuator, fiber-reinforced soft actuator, and many more. In the present work, two popular designs of SPAs are compared computationally using FEM. The plane and corrugated designs of SPAs are compared based on their bending angles. The remaining paper is organized in the following sections: Sect. 2 presents the computer-aided design (CAD) of the two considered designs of SPAs i.e., plane and corrugated; in Sect. 3, the designed SPAs are analyzed computationally using FEM; finally, the paper is concluded in Sect. 4.

## 2 Computer-Aided Design

Two designs have been developed as soft actuators using CAD software—Solid-Works. One has been developed as a plane actuator with a uniform square cross-section, while the other has been developed as a corrugated actuator with varying square and rectangular cross-sections, also known as pneu-nets. Both the actuators are hollow to provide passage for the compressed air. The dimensions of the two actuators are the same and are taken as the average of different studies [19–21], having lengths of 120 mm, a width of 20 mm, and a height of 19 mm. The sectional and isometric views of the plane actuator (Fig. 1) and the corrugated actuator (Fig. 2) are shown below.

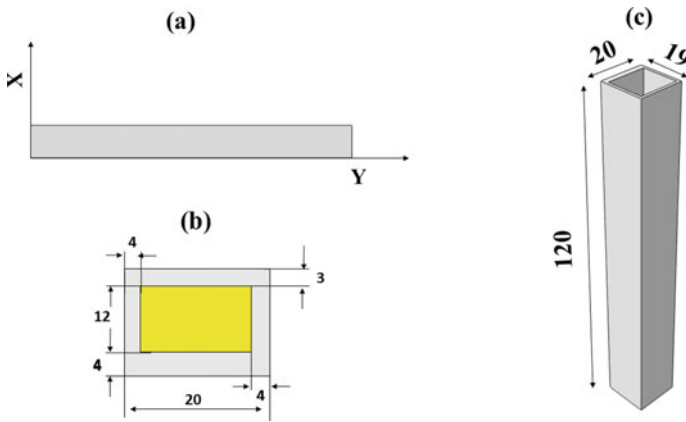


Fig. 1 Plane SPA with **a**  $x$ - $y$  plane view, **b** chambers' cross-sectional view, and **c** isometric view

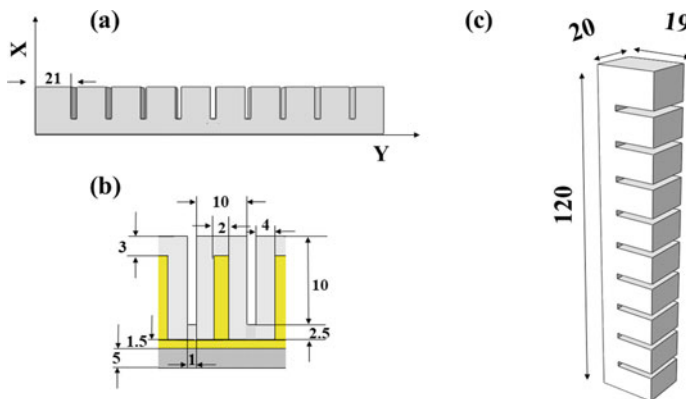


Fig. 2 Corrugated SPA with **a**  $x$ - $y$  plane view, **b** chambers' cross-sectional view, and **c** isometric view

In Fig. 1, different views of the plane-structured actuator are shown, the side walls' thicknesses are taken the same, i.e., 4 mm, while the upper and the lower thicknesses are different to provide the stiffness difference. The difference in the stiffnesses of the upper wall (low stiffness with 3 mm thickness) and the lower wall (high stiffness with 4 mm thickness) results in the bending of the actuator in one direction only, i.e., toward the high stiffness side.

In Fig. 2, different views of the corrugated structured actuator are shown, and the side walls' thicknesses are taken the same, i.e., 4 mm. In the right-side sectional view of the actuator (Fig. 2b), the upper and the lower thicknesses are 1 mm and 2 mm, respectively. The air passage of 1.5 mm is provided just above the lower wall. It can be seen that the lowest and the topmost walls are having thicknesses of 5 mm and 3 mm, respectively (for the stiffness difference). The horizontal wall, just above the horizontal air passage, is of 2.5 mm thickness. Two adjacent chambers are separated by 1 mm. In Figs. 1 and 2, the yellow color represents the air passage, while the gray color represents the material.

### 3 Finite Element Method (FEM)

The hyperelastic materials, it is difficult to analyze using analytical methods due to their complexity and nonlinearities. FEM is a suitable tool for analyzing complex problems numerically. Different models are available for soft hyperelastic materials, which are described here.

#### 3.1 *Soft Material Models*

A hyperelastic material is a rubber or rubber-like soft material. The difference between the elastic and the hyperelastic materials is the elastic deformation. In an elastic material, stress varies linearly with respect to the strain such as in paper, metal, wood, if the deformation is very small. But in the case of hyperelastic materials, elastic deformation could be extremely large and the stress–strain relation is nonlinear [16].

A hyperelastic material uses strain energy density function or strain energy potential ( $U$ ) to establish a relationship between the stress and the strain, even when the strains are 100–700% high [22]. These material models are accurate over different strain ranges. Some of the hyperelastic material models for the numerical simulations are explained below. Depending upon the type of experimental (uniaxial, equi-biaxial, or planar) test data available, different hyperelastic material models can be used for accurate curve fitting [23], which are as follows.

- (i) **Arruda–Boyce Model:** The strain energy density potential  $U$  relation is,

$$\begin{aligned}
 U = \mu \left\{ \frac{1}{2} (I_1^- - 3) + \frac{1}{20\lambda_m^2} (I_1^{-2} - 9) + \frac{11}{1050\lambda_m^4} (I_1^{-3} - 27) \right. \\
 \left. + \frac{19}{700\lambda_m^6} (I_1^{-4} - 81) + \frac{519}{673,750\lambda_m^8} (I_1^{-5} - 243) \right\} \\
 + \frac{1}{D} \left( \frac{J_{el}^{-2} - 1}{2} - \ln J_{el} \right), \tag{1}
 \end{aligned}$$

where  $\mu$ ,  $D$ , and  $\lambda_m$  are material constants, and the shear modulus  $\mu_0$  is given by,

$$\mu_0 = \mu \left( 1 + \frac{3}{5\lambda_m^2} + \frac{99}{175\lambda_m^4} + \frac{513}{875\lambda_m^6} + \frac{42,039}{67,375\lambda_m^8} \right). \tag{2}$$

And the bulk modulus  $K_0$  is given by  $K_0 = 2/D$ .

(ii) **Marlow Model:** The strain energy density potential  $U$  relation is,

$$U = U_{dev}(I_1^-) + U_{vol}(J_{el}), \tag{3}$$

where  $U_{dev}$  is the deviatoric part and evaluated using uniaxial, planar, or equi-biaxial test data and  $U_{vol}$  is the volumetric part and evaluated by considering Poisson’s ratio or by considering the lateral strains with the uniaxial, planar, or equi-biaxial test data.

(iii) **Mooney–Rivlin Model:** The strain energy density potential  $U$  relation is,

$$U = C_{10}(I_1^- - 3) + C_{01}(I_2^- - 3) + \frac{1}{D_1}(J_{el} - 1)^2, \tag{4}$$

where  $C_{10}$ ,  $C_{01}$ , and  $D_1$  are the temperature-dependent material constants. The initial shear modulus  $\mu_0$  and bulk modulus  $K_0$  are given by,  $\mu_0 = 2(C_{10} + C_{01})$  and  $K_0 = \frac{2}{D_1}$ .

(iv) **Neo-Hookean Model:** The strain energy density potential  $U$  relation is,

$$U = C_{10}(I_1^- - 3) + \frac{1}{D_1}(J_{el} - 1)^2, \tag{5}$$

where  $C_{10}$  and  $D_1$  are temperature-dependent material constants, and the shear modulus is defined by,  $\mu_0 = 2C_{10}$ , and the bulk modulus is defined by,  $K_0 = \frac{2}{D_1}$ .

(v) **Ogden Model:** The strain energy density potential  $U$  relation is,

$$U = \sum_{i=1}^N \frac{2\mu_i}{\alpha_i^2} (\lambda_1^{-\alpha_i} + \lambda_2^{-\alpha_i} + \lambda_3^{-\alpha_i} - 3) + \sum_{i=1}^N \frac{1}{D_i} (J_{el} - 1)^{2i}, \tag{6}$$

where  $\alpha_i$  and  $D_i$  are the temperature-dependent material constants,  $N$  is a material constant, the initial shear modulus,  $\mu_0 = \sum_{i=1}^N \mu_i$ , and the bulk modulus  $K_0 = \frac{2}{D_1}$ .

(vi) **Polynomial Model:** The strain energy density potential  $U$  relation is,

$$U = \sum_{i+j=1}^N C_{ij} (I_1^- - 3)^i (I_2^- - 3)^j + \sum_{i=1}^N \frac{1}{D_i} (J_{el} - 1)^{2i}, \quad (7)$$

where  $D_i$  and  $C_{ij}$  are temperature-dependent material constant, initial shear modulus is defined by,  $\mu_0 = 2(C_{10} + C_{01})$ , and the bulk modulus is defined by,  $K_0 = \frac{2}{D_1}$ .

(vii) **Reduced Polynomial Model:** The strain energy density potential  $U$  relation is,

$$U = \sum_{i=1}^N C_{i0} (I_1^- - 3)^i + \sum_{i=1}^N \frac{1}{D_i} (J_{el} - 1)^{2i}. \quad (8)$$

The initial shear modulus is defined by,  $\mu_0 = 2(C_{10})$ , and the bulk modulus is defined by,  $K_0 = \frac{2}{D_1}$ , whereas  $D_i$  and  $C_{i0}$  are material constants.

(viii) **Van der Waals Model:** The strain energy density potential  $U$  relation is,

$$U = \mu \left\{ -(\lambda_m^2 - 3) [\ln(1 - \eta) + \eta] - \frac{2}{3} a \left( \frac{\tilde{I} - 3}{2} \right)^{3/2} \right\} + \frac{1}{D} \left( \frac{J_{el}^2 - 1}{2} - \ln J_{el} \right), \quad (9)$$

where

$$\tilde{I} = (1 - \beta)\bar{I}_1 + \beta\bar{I}_2 \quad \text{and} \quad \eta = \sqrt{\frac{\tilde{I} - 3}{\lambda_m^2 - 3}}. \quad (10)$$

Here,  $\mu$  is the initial shear modulus,  $a$  is the global interaction parameter,  $\lambda_m$  is the locking stretch,  $D$  governs the compressibility, and  $\beta$  is an invariant mixture parameter and can be temperature-dependent, the initial shear modulus,  $\mu_0 = \mu$ , and the bulk modulus  $K_0 = \frac{2}{D}$ .

(ix) **Yeoh Model:** The strain energy density potential  $U$  relation is,

$$U = C_{10} (I_1^- - 3) + C_{20} (I_1^- - 3)^2 + C_{30} (I_1^- - 3)^3 + \frac{1}{D_1} (J_{el} - 1)^2 + \frac{1}{D_2} (J_{el} - 1)^4 + \frac{1}{D_3} (J_{el} - 1)^6. \quad (11)$$



The initial shear modulus is defined by,  $\mu_0 = 2C_{10}$ , and the bulk modulus is defined by,  $K_0 = \frac{2}{D_1}$ .

The terms,  $I_1^-$  and  $I_2^-$  are the first and second deviatoric strain invariants for all the above equations and are given by,

$$I_1^- = \lambda_1^{-2} + \lambda_2^{-2} + \lambda_3^{-2} \quad \text{and} \quad I_2^- = \lambda_1^{-(-2)} + \lambda_2^{-(-2)} + \lambda_3^{-(-2)}. \quad (12)$$

And the deviatoric stretches  $\lambda_i^-$  are given by,

$$\lambda_i^- = J^{-\frac{1}{3}} \lambda_i, \quad (13)$$

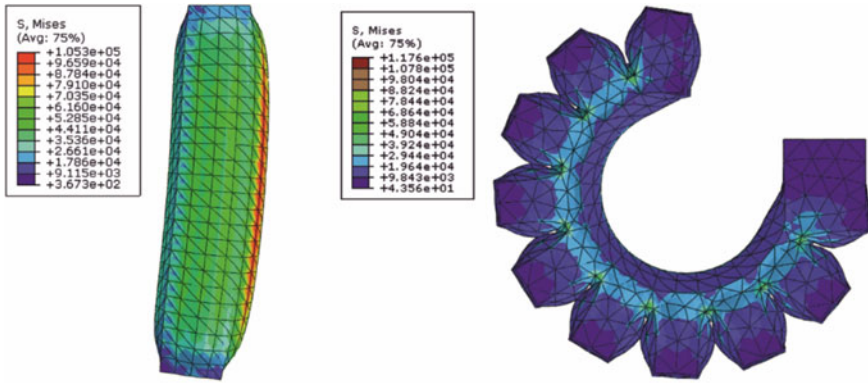
where  $J$  is the total volume ratio and  $\lambda_i$  is the principal stretches.

Out of the above-stated nine models (1)–(13), Ogden model (6) has been considered for the simulation as it provides accurate results over larger strains [24]. In addition, the commercially available hyperelastic material, namely ecoflex 0050, has been considered for the SPA material. For the evaluation of the model parameters, the ecoflex 0050 material is subjected to uniaxial tensile test using INSTRON 3366 universal testing machine (UTM). Utilizing Eq. (6) and uniaxial test data of ecoflex 0050, material constants (in the form of  $\alpha$ ,  $\mu$ , and  $D$ ) are calculated to define the shear and compressibility behaviors of the hyperelastic material. The calculated material constants using the Ogden model with strain energy potential of order,  $n = 3$ , are  $\mu_1 = 1.1704$ ,  $\mu_2 = 0.8632$ ,  $\mu_3 = -1.92$  MPa,  $\alpha_1 = 1.058$ ,  $\alpha_2 = -1.13$ ,  $\alpha_3 = 0.143$ ,  $D_1 = 0.6027$ ,  $D_2 = 0$ , and  $D_3 = 0$  MPa<sup>-1</sup>. Since it is assumed that the ecoflex is an incompressible material; hence, the second term ( $D$ ) in Ogden model (6) is neglected.

### 3.2 FEM Results

In this paper, the dedicated software for FEM analysis called Abaqus has been utilized. The developed CAD models have been imported in Abaqus for further FEM analysis. Then, the two designs have been meshed using quadratic tetrahedral elements of C3D10H type. For the boundary condition, the soft actuators are assumed to behave like cantilever beams. One end of the soft actuator is constrained to move in any direction, while the other end is allowed to move freely under the pneumatic pressure of 25 kPa. The air in the vector form acts perpendicular to the internal surface or chamber's surface. The Ogden model is used to solve the problem. The bending and stress distribution of two SPAs (plane and corrugated) for type 1 meshing are shown in Fig. 3.

In the first case (Fig. 3), both the actuators are subjected to similar pneumatic pressure of 25 kPa. In plane SPA, the total number of nodes and elements for type 1 meshing are 4296 and 2140, respectively. The SPA produces a bending of around 80 and experiences a maximum stress of 105.3 kPa. In corrugated SPA, the total number

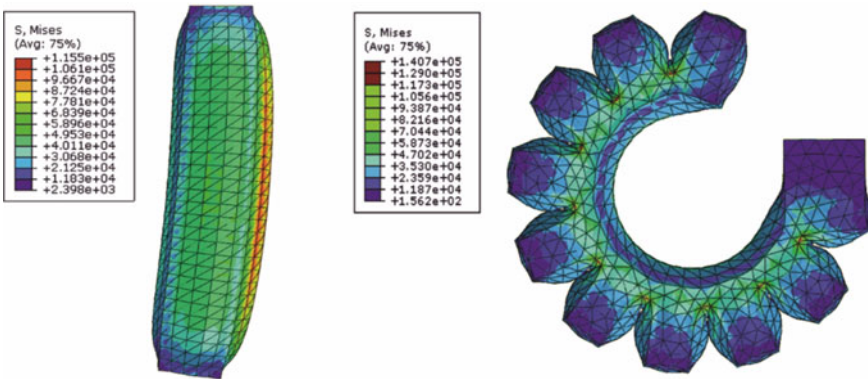


**Fig. 3** Bending and stress distribution for type 1 meshing

of nodes and elements for type 1 meshing are 6995 and 3530, respectively. The SPA creates a bending angle of approximately 1180 and experiences a maximum stress of 117.6 kPa.

In the second case (Fig. 4), both the actuators are subjected to similar pneumatic pressure of 25 kPa. In plane SPA, the total number of nodes and elements for type 2 meshing are 6782 and 3362, respectively. The SPA produces a bending of around 80 and experiences a maximum stress of 115.5 kPa. In corrugated SPA, the total number of nodes and elements for type 2 meshing are 12,060 and 6130, respectively. The SPA creates a bending angle of approximately 1200 and experiences a maximum stress of 140.7 kPa.

In the third case (Fig. 5), both the actuators are subjected to similar pneumatic pressure of 25 kPa. In plane SPA, the total number of nodes and elements for type 3 meshing are 11,897 and 5910, respectively. The SPA produces a bending of around



**Fig. 4** Bending and stress distribution for type 2 meshing

8.50 and experiences a maximum stress of 121.5 kPa. In corrugated SPA, the total number of nodes and elements for type 3 meshing are 20,317 and 10,443, respectively. The SPA creates a bending angle of approximately 1350 and experiences a maximum stress of 159.1 kPa.

In the fourth case (Fig. 6), both the actuators are subjected to similar pneumatic pressure of 25 kPa. In plane SPA, the total number of nodes and elements for type 4 meshing are 28,034 and 14,078, respectively. The SPA produces a bending of around 90 and experiences a maximum stress of 127.1 kPa. In corrugated SPA, the total number of nodes and elements for type 4 meshing are 36,982 and 18,534, respectively. The SPA creates a bending angle of approximately 1380 and experiences a maximum stress of 181.3 kPa.

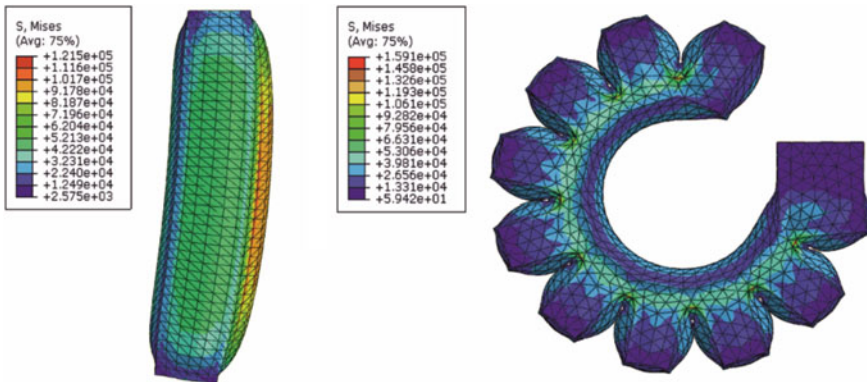


Fig. 5 Bending and stress distribution for type 3 meshing

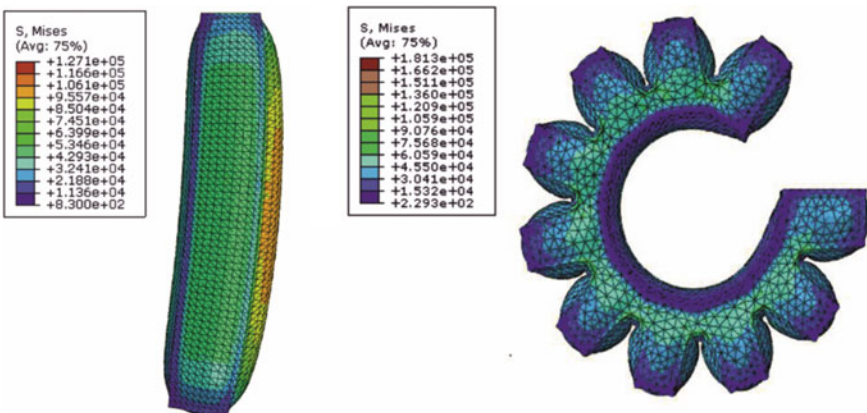


Fig. 6 Bending and stress distribution for type 4 meshing

The SPA with the plane structure shows the surface expansions in the side and the top walls with noticeable bending. The actuating pressure of 25 kPa is enough to produce the noticeable bending in the plane SPA, and it produces a bending angle of approximately 8–90. But in case of the corrugated SPA, same pressure of 25 kPa causes the pneu-nets to expand and the presence of depth of cuts causes the side wall to expand freely. This expansion of chambers develops a bending moment in the direction of the layer of higher thickness or high stiffness and produces a bending angle of approximately 118–1380. The values of stress and bending angle for different type of meshing are provided in Tables 1 and 2.

Based on the synthesis presented in Tables 1 and 2, it can be observed that with increasing nodes and element, both the SPAs create higher bending angle and experience larger stresses. The bending angle of the plane SPA is increased from 80 to 90, whereas experienced stress increases from 105.3 to 127.1 kPa. The bending angle of corrugated SPA is increased from 1180 to 1380 and experienced stress increases from 117.6 to 181.3 kPa. The results of bending angle and stress distribution are improved with the finer mesh. At finer mesh, the small elements of fine mesh can accurately capture stress gradient. Thus, led to the development of much precise results. However, when the meshing is changed from type 3 to type 4, results are not much changed, but computational effort increases highly, due to increase in number of nodes and elements approximately three time. Therefore, results with type 3 are more efficient and sufficiently accurate.

**Table 1** Grid independency of plane actuator using quadratic tetrahedral elements of C3D10H type

Parameters	Nodes	Elements	Bending angle (°)	Max. stress (kPa)	Max. deformation (mm)
Type 1	4296	2140	8	105.3	11.11
Type 2	6782	3362	8	115.5	11.83
Type 3	11,897	5910	8.5	121.5	12.42
Type 4	28,034	14,078	9	127.1	12.56

**Table 2** Grid independency of corrugated actuator using quadratic tetrahedral elements of C3D10H type

Parameters	Nodes	Elements	Bending angle (°)	Max. stress (kPa)	Max. deformation (mm)
Type 1	4296	2140	118	117.6	147.20
Type 2	6782	3362	120	140.7	148.80
Type 3	11,897	5910	135	159.1	154.00
Type 4	28,034	14,078	138	181.3	154.80

## 4 Conclusion

Two parameters have strong impact on the bending angle configuration of SPAs, which are side wall thickness and hardness of the silicone rubber. For silicone rubber material, lower hardness and wall thickness led to the higher bending angle and low stress, at low actuating pressure. Low pressure is very essential for the actuation of biomedical devices due to their delicate applications. The bending angle can be maximized by thickening one of the layers two or three times than the others, which creates stiffness variation between layers for bending. The SPA with a single chamber (plane structure) exhibits more ballooning or swelling effect rather than bending. The ballooning effects refer to the high radial expansion. Due to this effect, actuators even at high pressure show lower bending angle and are subjected to very high stresses. The corrugated structured SPA resists radial expansion. In corrugated structures, factors which affect the bending angle are thickness of the bottom layer, gap between the chambers, and the thickness of the side walls. Particularly, small gap between the chambers leads to the higher bending configurations but also can damage the channel as well. Over a fixed length of an actuator, a greater number of chambers provides higher bending angle even at low pressure. In the obtained results, corrugated structured SPA produces largest bending of 1380 which is larger than the bending produced by the plane-structured SPA (90) under similar pneumatic pressure.

Based on the simulation results, corrugated SPA is found to be more efficient due to its suitable structure for bending, while the plane SPA shows more swelling effect rather than bending. For the future work, it is interesting to improve the corrugated design of SPA by including strain limiting layer of different materials. In addition, it is equally important for future work to fabricate a SPA for experimental study.

## References

1. Bao G, Fang H, Chen L, Wan Y, Xu F, Yang Q, Zhang L (2018) Soft robotics: academic insights and perspectives through bibliometric analysis. *Soft Rob* 5(3):229–241
2. Kovač M (2014) The bioinspiration design paradigm: a perspective for soft robotics. *Soft Rob* 1(1):28–37
3. Whitesides GM (2018) Soft robotics. *Angew Chem Int Ed* 57(16):4258–4273
4. George Thuruthel T, Ansari Y, Falotico E, Laschi C (2018) Control strategies for soft robotic manipulators: a survey. *Soft Rob* 5(2):149–163
5. Coyle S, Majidi C, LeDuc P, Hsia KJ (2018) Bio-inspired soft robotics: material selection, actuation, and design. *Extreme Mech Lett* 22:51–59
6. Wang J, Fei Y, Pang W (2019) Design, modeling, and testing of a soft pneumatic glove with segmented PneuNets bending actuators. *IEEE/ASME Trans Mechatron* 24(3):990–1001
7. Fei Y, Wang J, Pang W (2019) A novel fabric-based versatile and stiffness-tunable soft gripper integrating soft pneumatic actuators and wrist. *Soft Rob* 6(1):1–20
8. Ellis DR, Venter MP, Venter G (2021) Soft pneumatic actuator with bimodal bending response using a single pressure source. *Soft Rob* 8(4):478–484
9. Kim Y, Cha Y (2020) Soft pneumatic gripper with a tendon-driven soft origami pump. *Front Bioeng Biotechnol* 8:461

10. Hu W, Alici G (2020) Bioinspired three-dimensional-printed helical soft pneumatic actuators and their characterization. *Soft Rob* 7(3):267–282
11. Zolfagharian A, Mahmud MP, Gharai S, Bodaghi M, Kouzani AZ, Kaynak A (2020) 3D/4D-printed bending-type soft pneumatic actuators: fabrication, modelling, and control. *Virtual Phys Prototyping* 15(4):373–402
12. Gariya N, Kumar P (2021) A review on soft materials utilized for the manufacturing of soft robots. *Mater Today: Proc* 46:11177–11181
13. Zhong G, Hou Y, Dou W (2019) A soft pneumatic dexterous gripper with convertible grasping modes. *Int J Mech Sci* 153:445–456
14. Dharbaneshwer SJ, Thondiyath A, Subramanian SJ, Chen IM (2021) Finite element-based grasp analysis using contact pressure maps of a robotic gripper. *J Braz Soc Mech Sci Eng* 43(4):1–11
15. Zhang H, Kumar AS, Fuh JYH, Wang MY (2018) Design and development of a topology-optimized three-dimensional printed soft gripper. *Soft Rob* 5(5):650–661
16. Xiao W, Hu D, Chen W, Yang G, Han X (2021) A new type of soft pneumatic torsional actuator with helical chambers for flexible machines. *J Mech Robot* 13(1):011003
17. Barbosa IM, Alves PR, Silveira ZC (2021) Upper limbs' assistive devices for stroke rehabilitation: a systematic review on design engineering solutions. *J Braz Soc Mech Sci Eng* 43(5):1–16
18. Takayama T, Sumi Y (2021) Self-excited air flow passage changing device for periodic pressurization of soft robot. *ROBOMECH J* 8(1):1–12
19. Shintake J, Cacucciolo V, Floreano D, Shea H (2018) Soft robotic grippers. *Adv Mater* 30(29):1707035
20. Hughes J, Culha U, Giardina F, Guenther F, Rosendo A, Iida F (2016) Soft manipulators and grippers: a review. *Front Robot AI* 3:69
21. Shintake J, Rosset S, Schubert B, Floreano D, Shea H (2016) Versatile soft grippers with intrinsic electroadhesion based on multifunctional polymer actuators. *Adv Mater* 28(2):231–238
22. Meaney DF (2003) Relationship between structural modeling and hyperelastic material behavior: application to CNS white matter. *Biomech Model Mechanobiol* 1(4):279–293
23. <https://abaqus-docs.mit.edu/2017/English/SIMACAEMATRefMap/simamat-c-hyperelastic.htm>
24. Kim B, Lee SB, Lee J, Cho S, Park H, Yeom S, Park SH (2012) A comparison among Neo-Hookean model, Mooney-Rivlin model, and Ogden model for chloroprene rubber. *Int J Precis Eng Manuf* 13(5):759–764

# Study of Anti-Tetra Chiral Auxetic Cluster Under Biaxial Loading Using FEM



G. Siva Prasad, Ch Jaya Krishna, and M. P. Hariprasad

**Abstract** Auxetics are the structures that exhibit a negative Poisson's ratio. When subjected to axial tensile loading, they expand in the transverse direction similarly when subjected to compressive loading contracts in the transverse direction. Investigation of the response of auxetic structures under biaxial stress fields is an important factor, and not much work has been done to explore its behaviour under biaxial loading. This paper brings out a typical cruciform specimen comprising of the auxetic cluster in its central region. Anti-tetra chiral structures with different orientations of  $0^\circ$ ,  $30^\circ$ ,  $45^\circ$  and  $60^\circ$  degrees are embedded in the central region of a cruciform and are subjected to biaxial loading conditions. Four different biaxial ratios are investigated. It has been observed that  $45^\circ$  orientated auxetic cluster has shown minimum strain when compared to other orientations under different biaxial ratios.

**Keywords** Auxetics · Anti-tetra chiral · Biaxial loading of auxetics · Negative Poisson's ratio · Biaxial ratio · Cruciform · Cluster orientations

## 1 Introduction

In recent years, auxetic structures have found their place in engineering applications and researchers are trying to utilize its unconventional response mechanism. When a material is subjected to tensile loading, it gets compressed laterally. In case of auxetic structures, when subjected to tensile loading, the structure expands in both longitudinal and lateral directions. On similar lines, when subjected to compressive loading, the structure compresses both longitudinally and laterally. This is a unique response mechanism of auxetic structures and as a result of which they possess a negative Poisson's ratio.

Potential applications of auxetic structures include energy absorption entities, lightweight engineering structures, body armours, packing materials and many more. As they gain popularity among engineering structures, it is essential to evaluate the

---

G. Siva Prasad · C. Jaya Krishna · M. P. Hariprasad (✉)  
Department of Mechanical Engineering, Amrita Vishwa Vidyapeetham, Amritapuri 690525, India  
e-mail: [hariprasadm@am.amrita.edu](mailto:hariprasadm@am.amrita.edu)

structural performance under multiple of loading scenarios. Major works on auxetic structures were done by analysing their deformation characteristics. Yang et al. [1] compared conventional and auxetic structures ratio under different loading conditions and showed that auxetic materials have excellent shock absorption capacity over conventional structures. The energy absorption potential of auxetic structures was further explored by Najafi et al. [2] wherein they pointed out the superior performance of anti-tetra chiral auxetics tested under quasi-static compression test and low velocity impact. Inspired from honeycomb structures, a study on 3-D-printed auxetics with voids filled by photo-sensitive polymers was suggested for enhancing the indentation resistance considering various volume fractions [3]. Compression tests were carried out by Shruti et al. [4] in order calculate the energy absorption by metamaterials; they compared energy absorption values of auxetic structure with diamond, hexagon structures and with hybrids like auxetic-diamond, auxetic-hexagon and diamond-hexagon structures and concluded that auxetic structure and auxetic hybrids has shown better energy absorption. Load bearing aspects of engineering auxetic structures are studied by Dutta et al. [5]. Menon et al. [6] proposed designs for novel and lightweight auxetic beams exhibiting a comparable load-bearing capacity as that of a homogenous beam but with a significant 64% reduction in material usage. On similar lines, detailed studies on auxetic-cored beams over the stress development aspects as well as on the performance after introduction of filler materials in its voids carried out by Menon et al. [7]. Most of the studies in the field of auxetic structures has been over the evaluation of its response under uniaxial loading. In this context, investigation on the response mechanisms of auxetic structures in biaxial stress fields becomes important. However, not much work has been done in this direction. A comparative study of the in-plane biaxial and uniaxial crushing of mixed honeycombs, hexagonal and re-entrant was done by Li et al. [8]. Even though there are experiments done to observe the porous soft solids under different biaxial ratios [9] and the effect of the arrangement of pores on pattern transformation in soft solids under different biaxial conditions [10], very few experiments were done related to biaxial loading with auxetic structures with different orientations.

Traditional uniaxial testing is inadequate in real-world scenarios in which the material can be simultaneously loaded in multiple directions [11]. As auxetic cluster orientation was observed to be advantageous in the context of its load-bearing capacities under a four-point bending scenario [6], it becomes imperative to also gauge its performance under biaxial loading conditions in terms of the internal stress development and the following strains. Unlike in fracture mechanics and vibration analysis, where the analytical formulation is readily available [12, 13], this study needs experimental or numerical investigations. This work is aimed to develop the methodology to explore the biaxial response mechanism of auxetic clusters. Auxetic structures with anti-tetra chiral unit cells having different orientations are subjected to distinct biaxial ratios. The influence of biaxial ratios and cluster orientation is investigated using finite element analysis.



## ***1.1 Biaxial Testing Specimen for Auxetic Clusters***

Different types of biaxial loading machines have been developed over the years. Stand-alone type and Link mechanism attachments for biaxial testing. Stand-alone biaxial testing machines uses hydraulic actuators on both axes to prevent movement at the centre of the specimen during testing [14]. Both actuators are commonly connected to ensure to get equal but opposite force. A mechanism similar to the Pantograph type is also used for biaxial testing. In the Pantograph mechanism, four links are attached to crosshead of the compression tester and load is applied by the movement two different links.

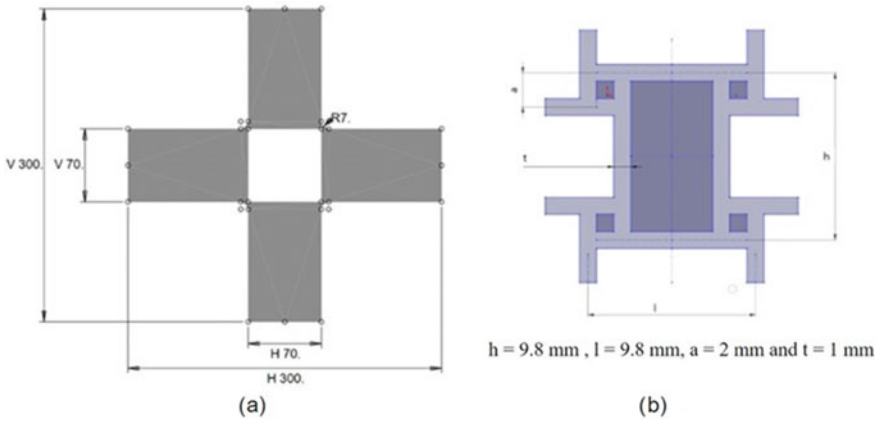
In any of the biaxial testing mechanisms, a cruciform specimen is used to study the behaviour of the material under biaxial loading. Cruciform specimen plays a major role in the biaxial tensile testing method. Various cruciform designs have been studied, and some specimens have a uniform thickness (fabricated from an as-received flat sheet sample). However, because these specimens lack a definite gauge area, determining biaxial stress components accurately would be difficult. Other specimens have slotted arms and uniform thickness to for the uniform traction distribution in the testing region. Others have test sections with reduced thickness to avoid the failure at the arms rather than the test section itself [11, 15–18]. As an extension to the conventional biaxial stress studies, this work proposes a method of testing auxetic clusters using a cruciform specimen embedded with auxetic clusters in its central region.

## **2 Design and Methodology**

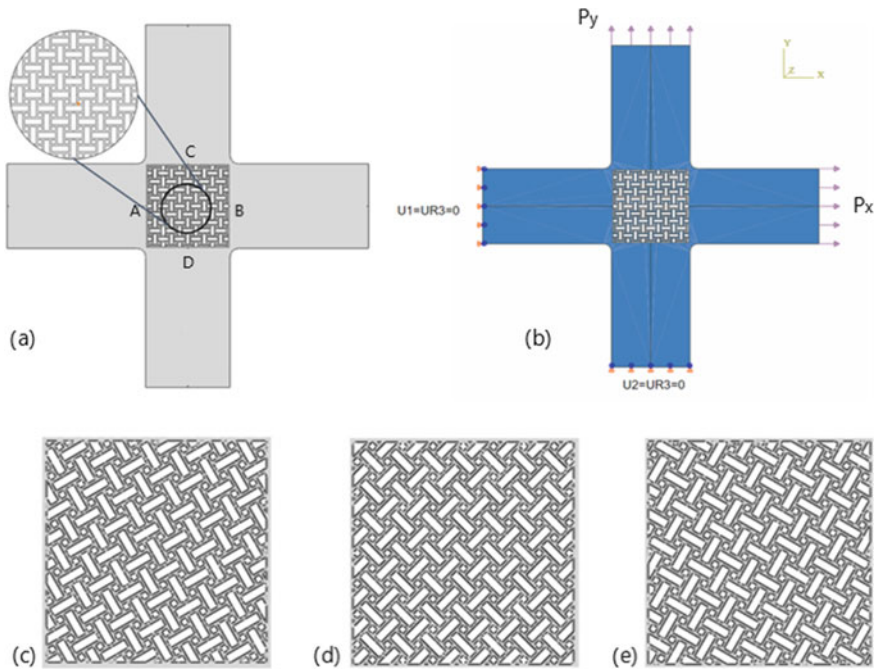
### ***2.1 Design of Cruciform Specimen***

A simple cruciform  $300 \times 70$  mm, with fillet radius at sharp corners of 7 mm, was considered. The central region of  $70 \times 70$  mm is considered to embed the auxetic cluster as shown in Fig. 1a. The fillet radius plays an important role in the design of cruciform. The fillet radius can be 0.04–0.1 times of arm width [15]. As the radius increases, the stress concentration will decrease at those corners. Unit cell dimensions of the anti-tetra chiral structure are shown in Fig. 1b.

An array of anti-tetra chiral cells has been modelled and placed at the centre of cruciform specimen. Menon et al. [6] explored behaviour of auxetic beams with  $30^\circ$ ,  $45^\circ$  and  $60^\circ$  orientations. On similar lines, similar orientations are studied under biaxial loading. Figure 2a shows the specimen with a  $0^\circ$  orientation. Similarly, specimens with  $30^\circ$ ,  $45^\circ$  and  $60^\circ$  cell orientations are also studied here.



**Fig. 1** a Dimensions of cruciform specimen and b dimensions of anti-tetra chiral cell



**Fig. 2** a Cruciform specimen embedded with auxetic cluster, b boundary conditions, c  $30^\circ$  oriented cluster, d  $45^\circ$  oriented cluster and e  $60^\circ$  oriented cluster

**Table 1** Material properties

Property	Unit	Value
Young's modulus	GPa	210
Poisson's ratio	–	0.30

## 2.2 Numerical Analysis of Auxetic Cruciform Specimen

Plane stress conditions are assumed, and a linear elastic model is developed for this analysis. Steel is chosen as material for the analysis, and its properties were listed in Table 1.

A biaxial stress state or biaxial ratio is defined as the ratio of the force applied on the  $y$ -direction to the  $x$ -direction and denoted by “ $R$ ”.

$$R = P_y/P_x (P_z = 0) \quad (1)$$

where  $P_x$ ,  $P_y$  and  $P_z$  are load applied on  $x$ ,  $y$  and  $z$  directions, respectively, and  $R$  is biaxial ratio. Biaxial ratios  $-1$ ,  $-0.5$ ,  $0$ ,  $0.5$  and  $1$  were taken for the analysis. It is important to note here that only loading conditions on the  $y$ -axes are altered while keeping the loading conditions on  $x$ -axis constant. 1 MPa pressure is applied in the  $x$ -direction in all biaxial ratios, and pressure applied on  $y$ -direction is given by the product of biaxial ratio and pressure applied on  $x$ -direction. On vertical arms, load has been applied on one arm, and on another arm, boundary condition is applied such that its motion as well as rotation is restricted along the  $y$ -direction and  $z$ -direction respectively. Similarly on horizontal arms, load has been applied on one arm and the other arm is restricted for motion and rotation along the  $x$ -direction and about the  $z$ -direction respectively as shown in Fig. 2b. As shown in Fig. 2, all orientations are embedded in cruciform structure, and analysis was done and compared with homogenous specimen.

## 3 Results and Discussions

Finite element analysis of all cruciform specimen was carried out in ABAQUS 6.14. To avoid any errors all loading and boundary conditions were kept constant for all variants. All the models were analysed using plane stress assumption and meshed using CPS4R (4-node bilinear plane stress quadrilateral) and CPS3 (3-node linear plane stress triangle). Using the software paths were created along AB and CD (from Fig. 2a), AB is considered as  $x$ -path, CD is considered as  $y$ -path, and paths were created only in the auxetic region. After meshing was done, nodes along the path were considered for the analysis.  $Y$ -directional strains are considered along the path AB, denoted by  $\varepsilon_{yy}$  similarly  $x$ -directional strains are evaluated along the path CD denoted by  $\varepsilon_{xx}$ . Strains of the auxetic clusters were observed and compared with different biaxial ratios as shown in Figs. 3 and 4.

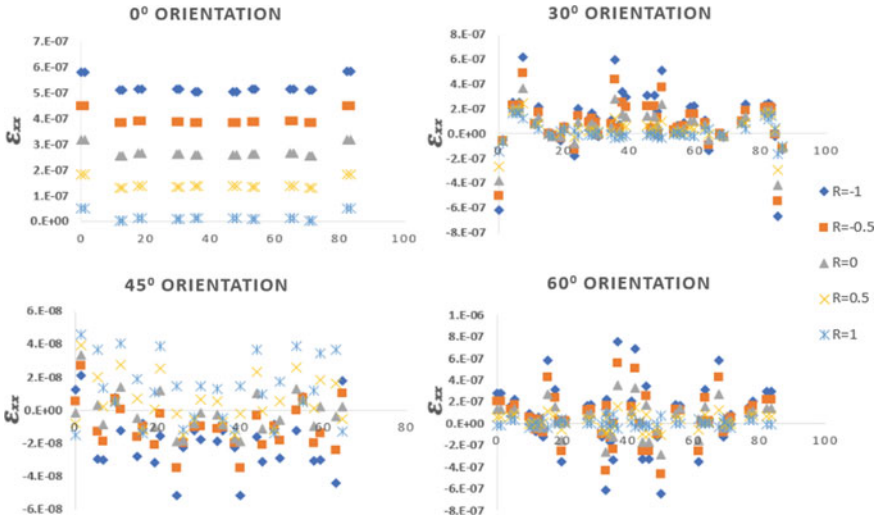


Fig. 3  $\epsilon_{xx}$  along CD. Under different biaxial ratios and different orientations

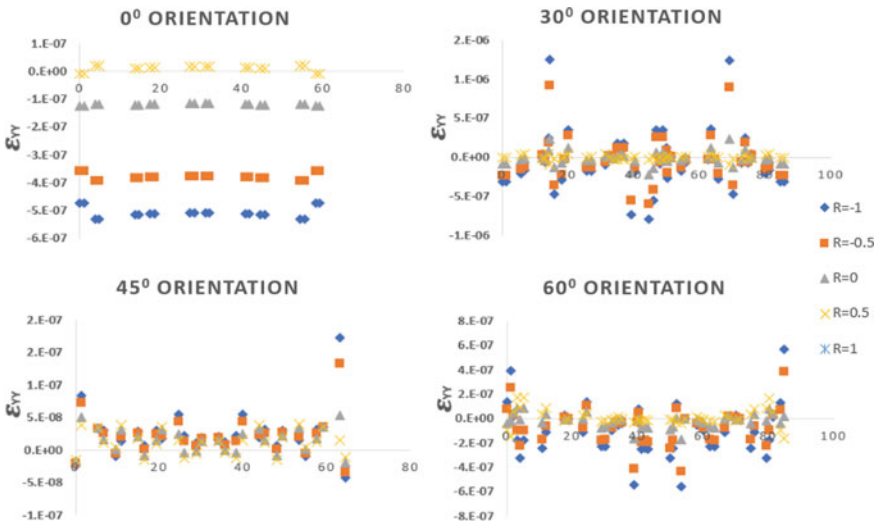
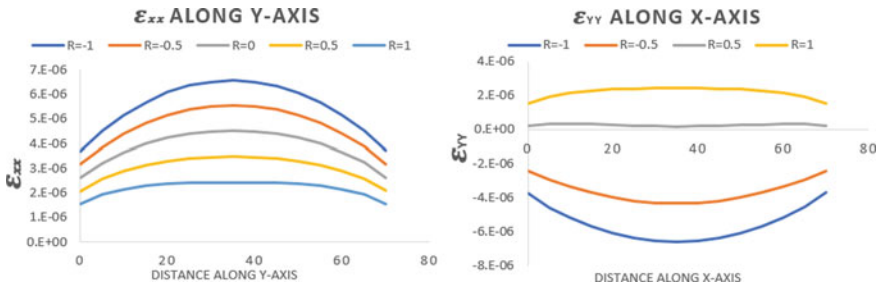


Fig. 4  $\epsilon_{yy}$  along AB. Under different biaxial ratios and different orientations

Similarly, a homogenous structure was considered, and strains were plotted along the path to observe the behaviour of homogenous structure under biaxial loading (Fig. 5).

When we compare strains of homogenous cluster with anti-tetra chiral strains of 0° orientation, we can observe that they are similar to each other, strain changes with



**Fig. 5** Strains of AB and CD for homogenous structure **a**  $\epsilon_{xx}$  along CD, **b**  $\epsilon_{yy}$  along AB

respect to change in loading condition but when we compare homogenous structure with other orientations there is a catastrophic difference.

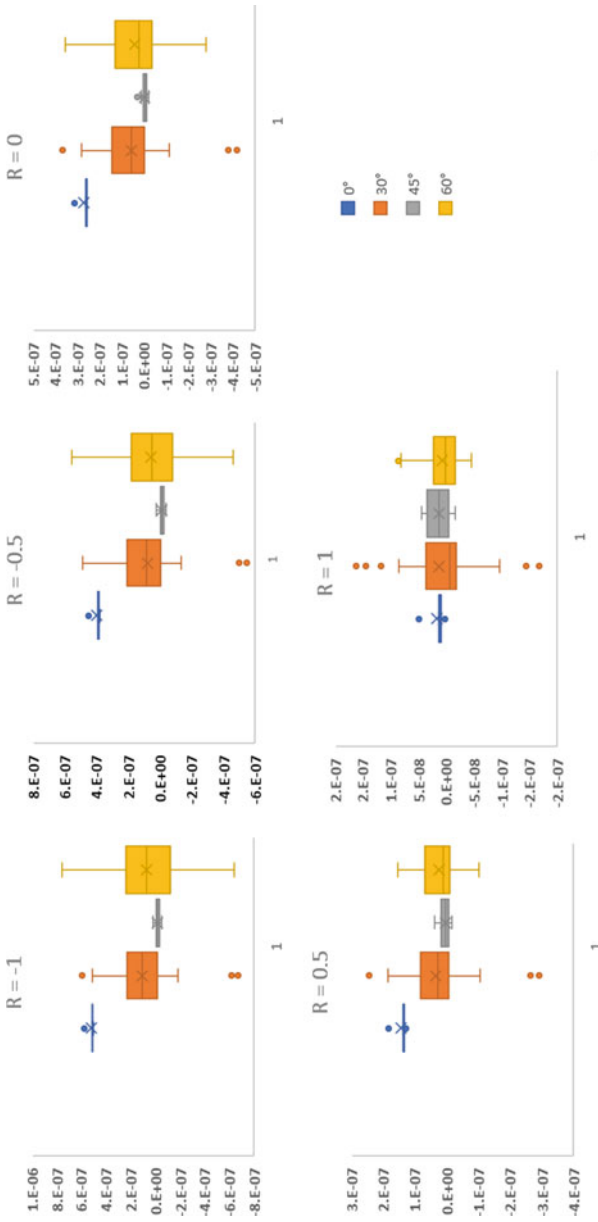
Box whisker plots for a better understanding of the strains under different biaxial ratios. Box whisker plot is a data analysis method through which we can easily interpret the data and compare the results here the data we considered is strains along AB and CD of different biaxial ratios and compared it with different orientations so that we can easily understand under which biaxial ratio the strains are minimum.

From Fig. 6, anti-tetra chiral with  $0^\circ$  degree orientation shows maximum strain compared to other orientations in all cases except when biaxial ratio is 1.  $30^\circ$  and  $60^\circ$  degree orientation shows maximum strain value and the interquartile range is more. But  $45^\circ$  degree orientation shows minimum strain possible in all biaxial ratios except when  $R = 1$ .

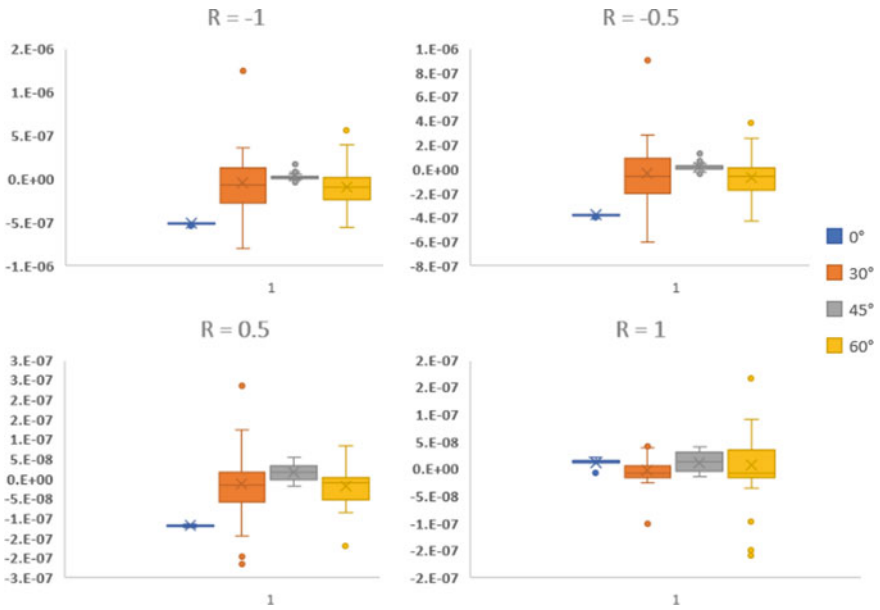
From Fig. 7, we can interpret that  $45^\circ$  orientation shows minimum strain possible except biaxial ratio is 1. From Figs. 6 and 7 when  $R = 1$ ,  $0^\circ$  orientation shows minimum strain but in all other biaxial ratios  $45^\circ$  orientation shown the optimum strain.

## 4 Conclusion

This work focuses on the behaviour of an anti-tetra chiral auxetic cluster of various orientations subjected to different biaxial ratios. As an extension to conventional biaxial stress studies, this paper proposes a method for testing auxetic clusters using a cruciform specimen. Simulations were done in Abaqus CAE. It is shown that the Anti-tetra chiral structure with a  $45^\circ$  orientation has the slightest strain compared to other orientations. It is noted that when the biaxial ratio is 1,  $45^\circ$  orientation has high strain compared to the biaxial ratio  $-1$  and observed that strains of  $45^\circ$  orientation reduced with the reduction of biaxial ratios. In other orientations, the strains are found to be inconsistent, and the  $45^\circ$  orientation has minimum strain when the biaxial ratio is  $-1$ . It is observed that the structure with  $0^\circ$  orientation shows strains similar to that of a homogenous structure. From the plots, it is evident that there is a possibility



**Fig. 6** Box whisker plot of  $\epsilon_{xx}$  along CD of different orientations under different biaxial ratios



**Fig. 7** Box whisker plot of  $\epsilon_{yy}$  along AB of different orientations under different biaxial ratios

of using an anti-tetra chiral cluster with  $45^\circ$  can be used in engineering applications as it provides minimum strain significantly when compared to other clusters.

## References

1. Yang C, Vora HD, Chang Y (2018) Behavior of auxetic structures under compression and impact forces. *Smart Mater Struct* 27(2):025012
2. Najafi M, Ahmadi H, Liaghat G (2021) Experimental investigation on energy absorption of auxetic structures. *Mater Today: Proc* 34:350–355
3. Li T, Liu F, Wang L (2020) Enhancing indentation and impact resistance in auxetic composite materials. *Compos B Eng* 198:108229
4. Shruti M, Hemanth NS, Badgayan ND, Sahu SK (2021) Compressive behavior of auxetic structural metamaterial for lightweight construction using ANSYS static structural analysis. *Mater Today: Proc* 38:12–17
5. Dutta S, Menon HG, Hariprasad MP, Krishnan A, Shankar B (2021) Study of auxetic beams under bending: a finite element approach. *Mater Today: Proc* 46:9782–9787
6. Menon HG, Dutta S, Krishnan A, Hariprasad MP, Shankar B (2022) Proposed auxetic cluster designs for lightweight structural beams with improved load bearing capacity. *Eng Struct* 260:114241
7. Menon HG, Dutta S, Hariprasad MP, Shankar B (2022) Investigation on deflection characteristics of auxetic beam structures using FEM. In: *Recent advances in manufacturing, automation, design and energy technologies*. Springer, Singapore, pp 621–628
8. Li Z, Gao Q, Yang S, Wang L, Tang J (2019) Comparative study of the in-plane uniaxial and biaxial crushing of hexagonal, re-entrant, and mixed honeycombs. *J Sandwich Struct Mater* 21(6):1991–2013
9. Qiu H, Li Y, Guo TF, Guo X, Tang S (2018) Deformation and pattern transformation of porous soft solids under biaxial loading: experiments and simulations. *Extreme Mech Lett* 20:81–90
10. Qiu H, Li Y, Guo T, Tang S, Xie Z, Guo X (2021) The effect of void arrangement on the pattern transformation of porous soft solids under biaxial loading. *Materials* 14(5):1205
11. Moreno MS, Muñoz SH (2020) Elastic stability in biaxial testing with cruciform specimens subjected to compressive loading. *Compos Struct* 234:111697
12. Kushwaha YS, Hemanth NS, Badgayan ND, Sahu SK (2022) Free vibration analysis of PLA based auxetic metamaterial structural composite using finite element analysis. *Mater Today: Proc* 56:1063–1067
13. Kottara AA, Padmanabhan G, Kumar MM, Rohit K, Hariprasad MP (2021) Revisit on the analytic formulations of principal stress orientation in fracture mechanics. *Mater Today: Proc* 46:4765–4770
14. Hannon A, Tiernan P (2008) A review of planar biaxial tensile test systems for sheet metal. *J Mater Process Technol* 198(1–3):1–13
15. Kuwabara T (2014) Biaxial stress testing methods for sheet metals
16. Deng N, Kuwabara T, Korkolis YP (2015) Cruciform specimen design and verification for constitutive identification of anisotropic sheets. *Exp Mech* 55(6):1005–1022
17. Shiratori E, Ikegami K (1968) Experimental study of the subsequent yield surface by using cross-shaped specimens. *J Mech Phys Solids* 16(6):373–394
18. Hanabusa Y, Takizawa H, Kuwabara T (2013) Numerical verification of a biaxial tensile test method using a cruciform specimen. *J Mater Process Technol* 213(6):961–970



# Cross-Correlation of Schlieren Images to Retrieve Velocity Information



Louther Charl Flores David, Jhoffanel Pazo, Efstratios L. Ntantis,  
and Kizhakkelan Sudhakaran Siddharth

**Abstract** Schlieren imaging has been utilized in experimental fluid mechanics as a tool in quantifying flow characteristics of gas flows. This non-intrusive technique when coupled along with cross-correlation turns to be effective in estimating velocity information. This study is an attempt to study the flow occurring around an airfoil, by cross-correlating successive schlieren images after seeding the flow with appropriate tracer particles with the aid of open-source software PIVlab<sup>®</sup>. Velocity variation at multiple spatial locations in a particular region of interest of flow around the airfoil was estimated in the study. The different possible reason(s) of error and necessary precautions while incorporating the method that should be followed have also been abridged.

**Keywords** Schlieren imaging · Cross-correlation · Velocity estimation

## 1 Introduction

Schlieren imaging is flow visualization technique that uses the changes in the indices of refraction of the fluid to visualize the fluid motion. This disturbance of the light rays due to the changes of the index of refraction causes patterns and images to be created. Unlike other fluid flow visualization techniques, it accounts for the changes in the indices of refraction of the fluid as it moves around the body, which is an airfoil in the case of this study. Since the changes in the indices of refraction cause a shift in the paths taken by the light rays, these patterns and images are visible to the naked eye. As changes in the index of refraction occur, this results in a deviation of the original path taken by the light rays that are converging through the usage of a parabolic mirror that focuses light rays into a singular point of finite diameter. It is this deviation from the original path which causes images to be formed on the basis of the extent of the changes in the index of refraction which occurred. Upon this

---

L. C. F. David · J. Pazo · E. L. Ntantis · K. S. Siddharth (✉)  
Amity University Dubai, Dubai, United Arab Emirates  
e-mail: [ssudhakaran@amityuniversity.ae](mailto:ssudhakaran@amityuniversity.ae)

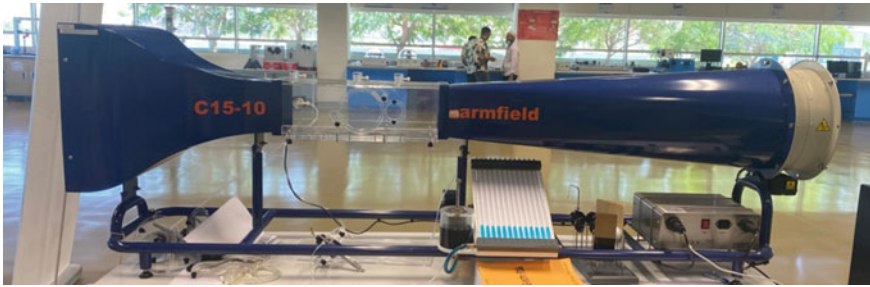
principle is what the basis of this study is built upon while incorporating Point Image Velocimetry software and contrasting the results for further understanding [1].

The object under test in this study is NACA 0015, which is a symmetrical airfoil. This is a NACA 4-digit series airfoil, which has four digits each corresponding to certain characteristic of the airfoil. The first digit shows the maximum camber of the airfoil with respect to the chord length hence it is in percentage. The chord is the length of the line that connects the leading edge to the trailing edge of the airfoil. The second digit dictates the location of in which the maximum camber is to be found, again it is in percentage of the chord length of the airfoil. The last two digits indicate the maximum thickness of the airfoil with respect to the chord length hence it is once again in percentage. Using the aforementioned details of a NACA 4-digit series airfoil it can be surmised that the airfoil utilized for this study is an airfoil which has the characteristic of being symmetrical on either side of the chord line since there is no maximum camber or location for this nonexistent camber. The maximum distance between the upper and lower chambers of this airfoil is 15% of the chord length, for this scenario the distance between the leading edge and trailing edge of the airfoil is 63 mm which means that the maximum thickness is 9.45 mm. This airfoil was chosen due to its availability in the laboratory in which the experiments are conducted [2]. Using Schlieren imaging alongside Point Image Velocimetry lab (PIVlab<sup>®</sup>), which tracks the displacement of a particle between two images and correlates it with the corresponding time frame in which the aforementioned displacement occurred it can acquire the velocity of that specific particle. It is able to track the displacement of a particle by comparing two sets of images in which this particle exists within a certain region. Given a specific region of interest within the sets of images and a denser population of particles which can be tracked, PIVlab<sup>®</sup> can give the mean velocity within a certain region of interest by correlating all images and tracking the displacement of all particles which existed in the first frame; hence, it yields vectors that can indicate the velocity within this region [3].

## 2 Experimental Setup

### 2.1 Wind tunnel

The wind tunnel is an Armfield C-15 model. It is a subsonic wind tunnel that operates using a software package by Armfield. It has a range of speeds from 0 to 34 m/s that can be set in terms of percentage. One of its primary components is a honeycomb flow straightener which is incorporated at the inlet and a 9:4:1 contraction ratio which ensures a uniform airflow through the working section. Refer to Fig. 1 for the wind tunnel image. Implementation of schlieren imaging is possible with the transparent throat available in the wind tunnel model.



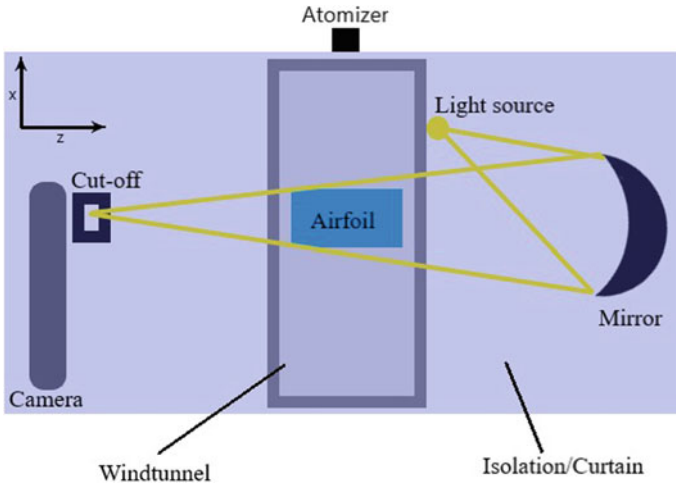
**Fig. 1** Image that shows the wind tunnel Armfield C-15 used for this research

## 2.2 *Schlieren Setup*

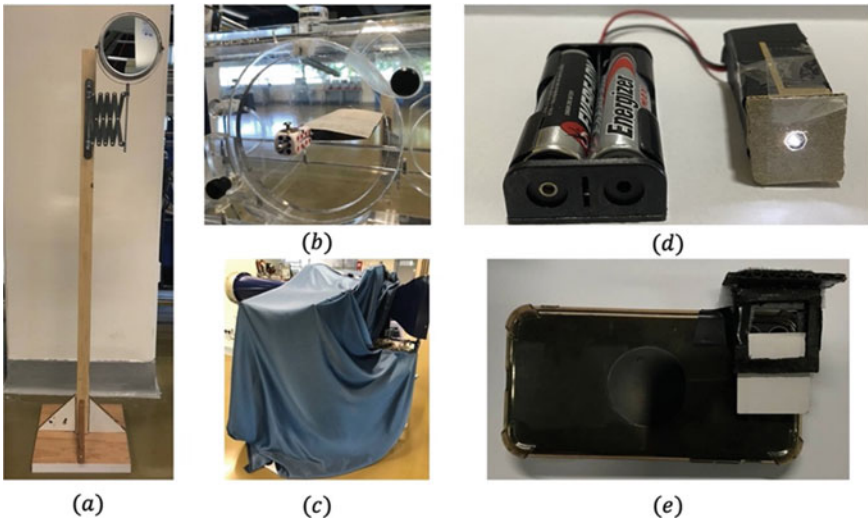
This schematic diagram shows a single-mirror coincident system which is the simplest setup where only one parabolic mirror is used. A light source is positioned at a distance facing toward the parabolic mirror. The setup consists of four subsystems; the isolation chamber, light source, mirror, and recording subsystem. The placement of each setup is shown in Fig. 2. It must be noted that the relative positioning of the recording subsystem and the mirror subsystem varies depending on which section of the airfoil is being studied [4, 5]. The isolation chamber spans the entirety of the experimental setup and refer to Fig. 3d, and its position is shown in Fig. 2. The mirror setup is shown in its entirety in Fig. 3a, and its location in the setup is shown in Fig. 2. The light source is placed on the latter end of the test section opposing the recording subsystem fixed to the wall of the wind tunnel and refer to Fig. 2. Lastly the recording subsystem, it is the camera which is an iPhone-11 fixed to a tripod that has been altered to accept a mobile holder. Just ahead of the camera the cutoff is placed so that it can be placed at the focal point and the light which has been cutoff can be received by the camera lens of the iPhone. The recording subsystem is shown in Fig. 3e [6, 7].

**Mirror Stands:** A stand was fabricated out of wood which was originally made with two components: the base which was intended to be the platform upon which the stand was placed and the pillar which serves as the mounting point for the mirror holder. After these two components were fabricated, it was found that the stands were completely unstable; hence, right-angled triangular components were made as supports to mitigate the instability as shown in Fig. 3a. The mirror holders were salvaged from scrap cosmetic mirror holders which are inherently stable. This permits a certain flexibility to the setup which meant that minor adjustments could be made to further increase the quality of the data captured. Its position in the setup is shown in Fig. 2.

**Acrylic Hatch:** The wind tunnel test section has an access port through which models can be fixed, thus allowing the user to perform tests accordingly. This access port has a 15 cm diameter with a 2 cm thickness with a knob that can be used to alter the angle of the model with respect to the direction of the mean airflow. Apart



**Fig. 2** Schematic of the schlieren imaging setup employed in the current study. All the subsystems are indicated. The general flow direction is at a negative  $x$ -axis



**Fig. 3** a Stands, b acrylic hatch, c light source, d isolation, e recording subsystem with cutoff

from this feature, it has two knobs that are protruding from the hatch; hence for this reason, an acrylic hatch of a similar dimensions was fabricated which permits tests to be done with less disturbances coming from the hatch. This fabricated hatch has an externally fixed device that allows it to hold the models placed through this as shown in Fig. 3b.

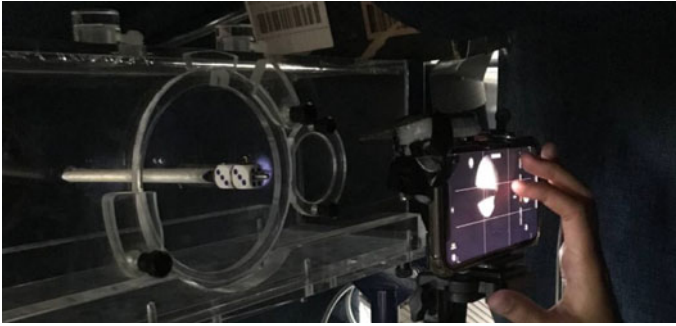
**Cutoff:** The cutoff is designed such that the upper side of the frame has a slit through which cutoffs could be slid through and used. The base is fixed allowing it to be held on a tripod which provides a certain level of mobility and stability, thereby further reducing the errors which could be encountered. The cutoff used for this research is shown in Fig. 3e. Its position is shown in Fig. 2.

### **Point source and Isolation**

This light source consists of an LED housed in a black cardboard box with an adjustable frontal face through which the size of the point or slit can be modified according to the specifications of the user. Its positive and negative are soldered to an external power source using two double-A batteries. The entire light source setup is shown in Fig. 3c. The location is shown in Fig. 2. This chamber was made to ensure that minimal environmental light penetrates through the setup which allows thereby further reducing the errors encountered by the system. It is made of two poles of equal lengths which are passed through boxes that are used as connection points for the wind tunnel's upper sections. These poles then served as mounting sectors for the isolation fabrics which allowed almost no penetration of external visible light. It has two primary components: the box with the poles and the isolation fabric, refer to Fig. 3d. The location is shown in Fig. 2.

## **3 Experimental Procedure**

The procedure consists of four main phases: the light source positioning phase, mirror positioning phase, recording system positioning and alignment phase, and finally the running of the experiment phase. First, the light source is positioned so that it is able to project its light toward the concave mirror. This light must cover the entire surface of the concave mirror [1, 8]. Phase 2 is initiated, and aligning of the converging light must cover the region of interest. The focal point must fall on the latter end of the test section opposing the mirror where the recording subsystem is placed. Phase 3 is initiated, and as previously mentioned, the converging light should fall on the cutoff and therefore the recording setup must be placed on the focal point. Finally, phase 4 which is running the test is done with a fan speed of 90% (30 m/s), while the recording is simultaneously done with the particles introduced to the flow through the use of an atomizer and refer to Fig. 4 [9, 10]. A photograph of the final schlieren imaging setup is shown in Fig. 4. The introduction of spray droplets in the flow enhances the possibility of better cross-correlation among successive images for velocity estimation. Alcohol droplets were chosen for its superior flow following capabilities [3]. This will prove useful during the analysis in PIVlab® (discussed in Sect. 4.1).



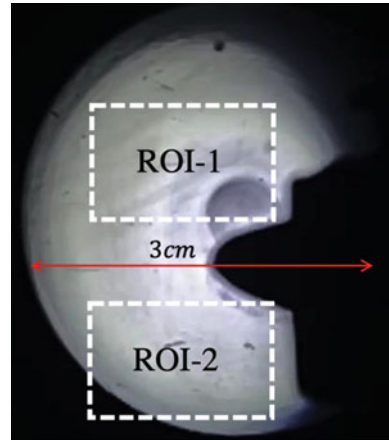
**Fig. 4** Photograph showing positioning of converging light toward the cutoff and recording subsystem (phase 3)

## 4 Results and Discussion

### 4.1 *Post-processing with PIVlab<sup>®</sup>*

Upon setting the speed of the fan at the diffuser end of the wind tunnel, a uniform flow of air is achieved in the test section of the tunnel. The droplets sprayed from the atomizer get advected along with the flow due to its ability in almost faithfully following the gas flow. The flow, once the droplets are introduced, is recorded as discussed previously. Based on the advection pattern of the droplets near the airfoil, the instantaneous velocity values at different spatial locations are obtained when cross-correlated. The cross-correlation of successive images is performed using the open-source MATLAB<sup>®</sup> software—PIVlab<sup>®</sup> [11–14]. The software utilizes the advection of particles/patterns in a flow, for obtaining the velocity information. Depending on the frame rate of recording and the position of the particle(s) from the successive images, the software determines the velocity values at each spatial location of the frame by cross-correlating the images. The primary benefits of utilizing PIVlab<sup>®</sup> for velocimetry research include the user-friendly features such as pre-conditioning the image, sub-pixel peak estimators, its data validation procedures, interpolation algorithms, and smoothing methods allowing the user to acquire better and accurate results and have been implemented successfully in similar studies as well [15–17]. ROI-1 covers the particles getting deflected above the airfoil, while ROI-2 covers the ones that get deflected below the airfoil. Also, shown in the figure is the calibration scale for actual getting velocity values. A raw image obtained from the experiment is shown in Fig. 5. The spherical light source can be clearly seen in the image. The uneven distribution of light across the image can be attributed to the scratches present on the transparent test section of the wind tunnel. Also, it should be noted that the particles (spray droplets) are not clearly visible in the figure due to its relatively smaller diameter compared to the image dimension and also its higher velocity of advection. Two region of interests (ROIs) as depicted in Fig. 5 were

**Fig. 5** Two region of interests (ROIs) considered in the present study. The calibration scale is also shown in the image



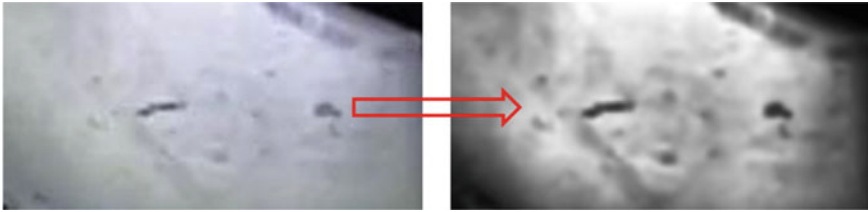
considered for analysis in the present study. The steps involved in post-processing with PIVlab<sup>®</sup> are as follows:

#### **4.2 Batch cropping**

This involves cropping the required region of the raw image for cross-correlation. This step is performed mainly for avoiding the poor cross-correlation which might happen due to the blank regions in the frame. The chosen ROIs only consist of the droplets carried along with the air flow. This avoids erroneous vectors that might come post cross-correlation. Another advantage is the save in computational time required for analysis.

#### **4.3 Prefiltering**

Increasing the contrast of the tracer particles is performed for enhanced results. High pass filtering is employed in the current study for increasing the sharpness of the droplets, compared to the background. Figure 6 shows the advantage of prefiltering the cropped image. As can be seen, contrast of the individual droplets as well as the cluster of droplets is enhanced.



**Fig. 6** Prefiltering the cropped image to enhance the tracer droplets

#### 4.4 *Cross-correlation*

Following the prefiltering of the raw images, the filtered images are cross-correlated for retrieving the displacement information of the particles across the ROI. The dimension of cropped image was  $200\text{px} \times 100\text{px}$ . Four passes with interrogation windows  $32\text{px} \times 16\text{px}$ ,  $24\text{px} \times 12\text{px}$ ,  $16\text{px} \times 8\text{px}$ , and  $12\text{px} \times 6\text{px}$  were provided during the analysis. The increased number of passes provides accurate results [14]. A total of 200 images were considered for the study, thus providing with 199 sets. The pass sizes were chosen to be the biggest possible for the particular frame size.

#### 4.5 *Vector Validation and Calibration*

After the cross-correlation, the erroneous vectors from each frame were eliminated manually based depending on the unusual readings compared to its surrounding vectors. This was done from the scatter plot of the results. Also, the negative vectors (if any) were also eliminated, and the missing data were interpolated. Finally, the vectors were calibrated with the scale (as shown in Fig. 5), to obtain the velocity values in m/s from px/s. A mean of the vector values at all the spatial locations (depending on the size of the passes) was finally performed to obtain the mean velocity values at all of the locations in each ROI. The standard deviation of the readings at each spatial location provides the fluctuation of the flow at the same locations. A total of  $8 \times 18$  vectors were obtained based on the cross-correlation employed. Each vector represented a spatial location at which the velocity value could be retrieved from the analysis. Figure 8 displays the mean of the velocity values at each spatial location. N aN represents the location(s) where velocity values could not be obtained due to the poor cross-correlation. It should be noted that  $8 \times 8$  vectors have only been shown in the figure due to space constraints. The top table in Fig. 8 represents the mean velocity values in  $x$ -direction, while the bottom one that in the  $y$ -direction. A snapshot of the mean vectors obtained is shown in Fig. 7. As similar to Fig. 8, the vectors can be seen visible only in certain locations. The direction can be seen along the flow near the airfoil. The flow can be seen to be getting deflected in the downward-right direction (as expected), since the ROI is chosen near the bottom



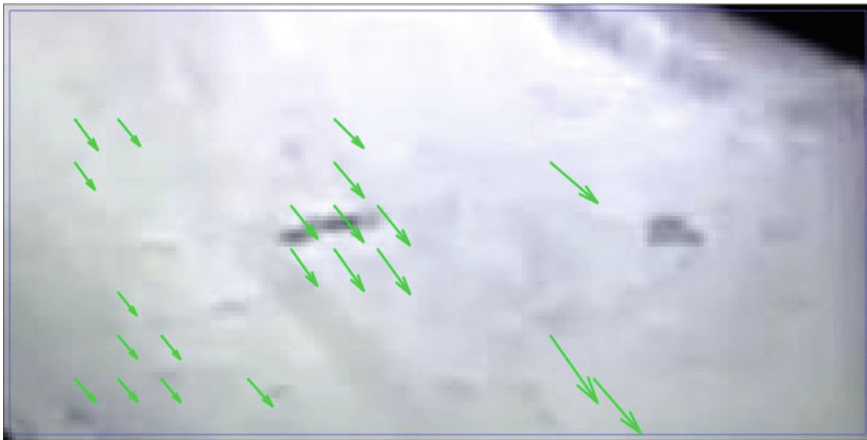
end of the airfoil. A disadvantage of the using the cross-correlation algorithm with respect to schlieren images would be the error in values obtained that might arise due to the motion of particles in the  $z$ -direction [18]. Within the ROI considered, the technique employed assumes that the tracer particles only move in the imaged  $x$ - $y$  plane, though a minimal traversal should be expected. This could be the reason for the general deviation in obtained velocity values to be relatively lower than the theoretical values at the same flow conditions. A deviation of 5% can be expected based on the ROI currently taken, with the inaccuracy likely to increase when a bigger ROI is considered.

NaN	NaN	NaN	NaN	NaN	NaN	NaN	NaN	NaN
9.43414379	9.23540292	NaN	NaN	NaN	NaN	9.85313211	NaN	NaN
8.50188017	NaN	NaN	NaN	NaN	NaN	9.70037968	NaN	NaN
NaN	NaN	NaN	NaN	NaN	8.99389445	9.00135088	9.2218886	NaN
NaN	NaN	NaN	NaN	NaN	8.68552393	8.92067827	9.2581122	NaN
NaN	8.25157503	NaN	NaN	NaN	NaN	NaN	NaN	NaN
NaN	8.34040625	8.51706285	NaN	NaN	NaN	NaN	NaN	NaN
8.35419594	8.39094763	8.59036518	NaN	10.8869724	NaN	NaN	NaN	NaN

NaN	NaN	NaN	NaN	NaN	NaN	NaN	NaN	NaN
11.8070179	10.4460455	NaN	NaN	NaN	NaN	10.2933158	NaN	NaN
10.1780084	NaN	NaN	NaN	NaN	NaN	11.1572004	NaN	NaN
NaN	NaN	NaN	NaN	NaN	10.1356168	10.644037	10.931599	NaN
NaN	NaN	NaN	NaN	NaN	10.7681601	11.7570202	12.0340162	NaN
NaN	9.72910497	NaN	NaN	NaN	NaN	NaN	NaN	NaN
NaN	9.79253837	9.86021553	NaN	NaN	NaN	NaN	NaN	NaN
9.73638458	9.82498455	9.89216348	NaN	10.085271	NaN	NaN	NaN	NaN

**Fig. 7** Velocity values obtained post cross-correlation. The top set shows the variation in  $x$ -direction, while the bottom set that in the  $y$ -direction



**Fig. 8** Mean vector map obtained after post-processing in PIVlab® for ROI-1. All the vectors across the frame could not be generated due to poor cross-correlation

## 5 Conclusion

Schlieren imaging has been used for a long time in visualizing gas flows. The current study is an attempt to quantify the dynamics of flow past an airfoil by cross-correlation of schlieren images obtained from a GoPro<sup>®</sup> camera. The open-source MATLAB<sup>®</sup> developed by Thielecke and Stamhuis—PIVlab<sup>®</sup> has been used for the purpose in the study. The technique provides velocity values at different spatial locations as well as different temporal instants, depending on the interrogation passes provided. Results show that cross-correlation of schlieren images captured from a non-sophisticated action camera is successful in retrieving velocity information at different locations of the frame considered. Utmost care should though be taken during every step in processing which includes—apt preprocessing of images and optimum dimension of interrogation passes employed. Further refining in the experimental procedure as well the imaging technique (i.e., the uniform distribution of tracer particles in the ROI) would yield better results.

## References

1. Settles GS (2013) Schlieren and shadowgraph techniques: visualizing phenomena in transparent media
2. Lai DRTEKLWT (2006) Time resolved PIV analysis of flow over a NACA 0015 airfoil with gurney flap. *Exp Fluids* 1(1):242–243
3. Melling A (1997) Tracer particles and seeding for particle image velocimetry. *Meas Sci Technol* 8(12):1406
4. Venkatakrishnan L, Meier GEA (2004) Density measurements using the background oriented schlieren technique. *Exp Fluids* 1(1):240–243
5. Mazumdar A (2013) Principles and techniques of schlieren imaging systems. 1–14
6. Gearhart B (2020) MacIsaac: a practical classroom iPad shadowgraph system. *Phys Teacher* 58(1):2–11
7. Travers N (2012) Schlieren z-type flow visualization system—visualization of negatively buoyant plumes in water 5
8. Thielicke W, Stamhuis E (2014) Pivlab—towards user-friendly, affordable and accurate digital particle image velocimetry in matlab. *Open Res Softw* 2(1):2–7
9. Raffel M (2015) Background-oriented schlieren (BOS) techniques. *Exp Fluids* 1(1):5–7
10. Kook S, Le M, Padala S, Hawkes E (2011) Z-type schlieren setup and its application to high-speed imaging of gasoline sprays. 3
11. Thielicke W, Sonntag R (2021) Particle image velocimetry for MATLAB: accuracy and enhanced algorithms in PIVlab. *Open Res Softw* 9(1):5–13
12. Thielicke W, Stamhuis E (2014) Pivlab—towards user-friendly, affordable and accurate digital particle image velocimetry in MATLAB. *J Open Res Softw* 2(1)
13. Thielicke W (2014) The flapping flight of birds. Dissertations University of Groningen
14. Thielicke W, Sonntag R (2021) Particle image velocimetry for MATLAB: accuracy and enhanced algorithms in PIVlab. *J Open Res Softw* 9(1)
15. Siddharth KS, Panchagnula MV, Tharakan JT (2017) Feature correlation velocimetry for measuring instantaneous liquid sheet velocity. *J Fluids Eng* 139(9)
16. Siddharth KS, Panchagnula MV, Tharakan TJ (2017) Effect of gas swirl on the performance of a gas-centered swirl co-axial injector. *Atomiz Sprays* 27(8)

17. Siddharth KS (2021) Dynamics of annular liquid sheets using feature correlation velocimetry (FCV). In: *Advances in engineering design*. Springer, pp 211–219
18. Westerweel J (1995) *Digital particle image velocimetry: theory and application*

# Design and Fabrication of a Small-Scale Solar Aircraft



Chaithanya Reddy, Mohammed Hisham,  
and Kizhakkelan Sudhakaran Siddharth

**Abstract** A few years ago, flying with just solar power was a dream but in recent times many of the major challenges have been overcome and solar planes have become a reality. In the last forty years, numerous unmanned solar-powered aircraft has been developed and flown. Most of the research already done has focused on glider design or the conventional aircraft design, and most of the emphasis is given to the technological aspect. To capture solar radiation for use at daytime of the flight, solar-powered aircraft use solar panels but also save the remaining portion for the produced energy on the onboard battery for the night flight. The current study demonstrates a viability and feasibility of a solar aircraft with the design of a flying wing. It also demonstrates the different technologies that have already been developed, working together to form a solar aircraft.

**Keywords** Unmanned · Flying wing · Solar powered

## 1 Introduction

When the wright brothers made their first flight to a wind-swept beach with a powered aircraft in 1903 that was the beginning, it took almost 70 years for a solar aircraft to take flight. The basic principle of a solar aircraft to make the conventional engine obsolete and power the aircraft with energy harnessed from the sun is easier said than done [1]. The “Sunrise 1” was one of the first solar planes which was designed by Ray Burchard, it had its first maiden flight on November 4, 1974, it flew for about twenty minutes at an altitude of roughly 100 m, and this plane was an unmanned vehicle [2]. Another solar-powered flight was again an unmanned aircraft named “Solaris”; a total of three flights were performed by Fred Militky and Hellmut Bruss. Larry Mauro had an idea which was to charge the batteries of the plane on the ground with the help of solar energy and then perform short flights. The Gossamer Penguin discovered what could be considered the world’s first piloted, solar-powered plane.

---

C. Reddy · M. Hisham · K. S. Siddharth (✉)  
Amity University Dubai, Dubai, United Arab Emirates  
e-mail: [ssudhakaran@amityuniversity.ae](mailto:ssudhakaran@amityuniversity.ae)

On July 7, 1981, the next version, Solar Challenger, had crossed the English Channel using solar panels as its sole source of energy [3]. Unlike the conventional aircraft which relay atmospheric air for the production of energy, solar-powered aircraft do not. So there is no pollution or emissions and therefore does not contaminate the air, and it is very ecofriendly [4, 5]. This is not the only advantage of solar-powered planes, the end goal of a solar-powered plane is to fly continuously. The concept is simple: The wings are covered with solar panels, and as the sun is not present all the time, a rechargeable battery system is required to keep the aircraft flying during the nighttime, as at night there is no sun to providing the energy required for maintaining level flight [6, 7]. The solar panels on the aircraft should be able to charge as well as being able to power the engines during the daytime for flight, so most of the development is being done on the improvement of high-density battery storage technology, improving the efficiency of solar panels [8, 9]. When designing a plane that only uses the sun as the energy source, it should maintain a balance between energy consumption and energy production, as a system that has many subsystems that are constantly dependent on one another to stay flying [10–12].

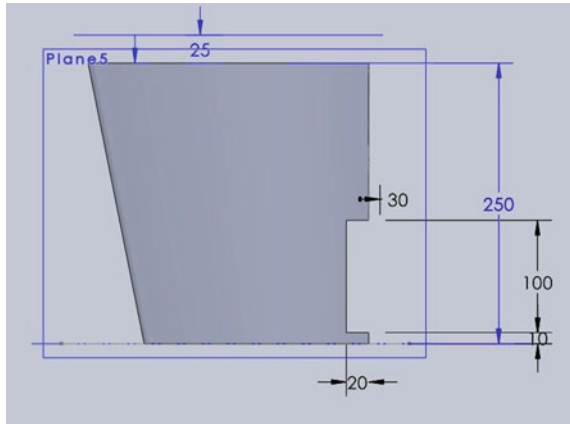
The main applications of using a solar drone include inspection operations, agriculture purpose [13–15] planetary exploration purposes [16, 17], mining purposes [18], etc. The current study is aimed in the design and fabrication of a small-scale solar-powered drone. The fabrication will be mainly done using 3D printing owing to its superior advantages [19, 20].

## 2 Design

### 2.1 Wing Design

In this project, we have selected the flying wing design for the aircraft, as it has a higher lift to drag ratio and increased payload carrying capacity as coined in the article by Martinez-Val and Schoep [21]. As per this report, the flying wing design's main advantages are in the field and cruise performances, with takeoff and landing field lengths comparable to those of much smaller planes. The flying wing design is 10–20% more efficient when considered as a transport vehicle when compared to conventional airplane. Since in this design the body also acts as a part of the wings, the total weight is reduced and thus a higher lift can be produced. The design is successful in balancing the flow of air and the center of gravity (CG) such that there is no need for a tail section. This flying wing design is created by us for our small-scale solar aircraft by keeping in mind our parameters which are easier to 3D print, lesser complicated joints, larger wing area to incorporate the solar panels, using PLA plastic for weight reduction, and to build a stronger body. Keeping in mind to design efficiently, creating a smaller but functional design can incorporate our required power plant while fixing the battery inside the aircraft. Figure 1 shows

**Fig. 1** Wing design and dimensions



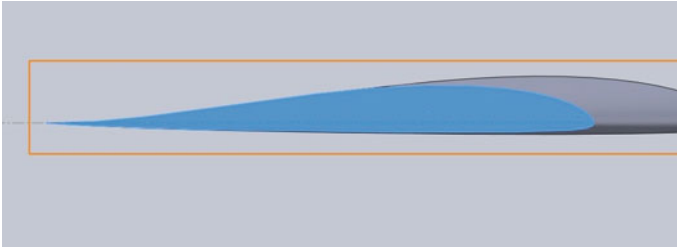
us the design of the wing as well as the dimensions required for our design keeping in mind the parameters to be considered.

## 2.2 Airfoil Design

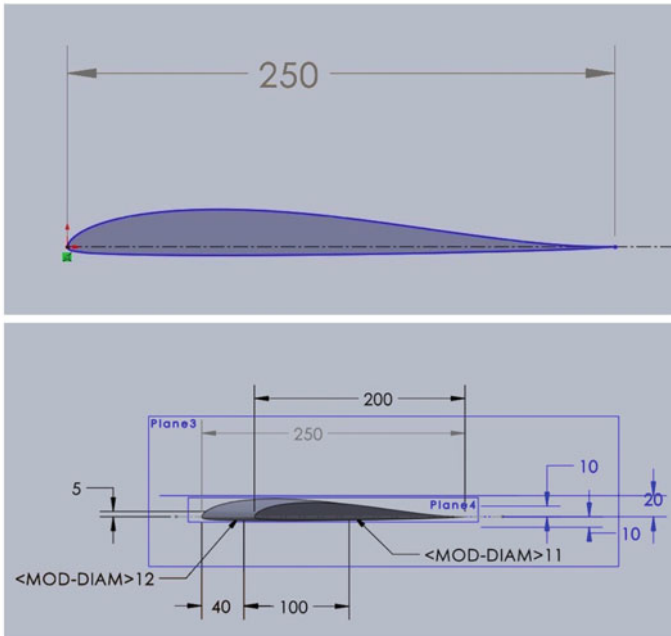
The airfoil design we opted here for our small-scale solar aircraft is flying wing airfoil s5010. This airfoil design was opted based on our study of the report by Selig [22]. As mentioned in the report design of flying wing, s5010 helps in supporting our flying wing design of small-scale solar aircraft by providing a higher lift and drag coefficient, meanwhile staying true to the aerodynamics of the aircraft. The report also states that flying wing airfoil s5010 along with the narrow s5020 was created for flying wings that require a near zero pitching moment. The airfoils performance is limited by the pitching moment required. For example, when compared to the s7012, which has a similar lift range, the s5010 drag is somewhat higher practically everywhere.

Figure 2 shows the airfoil S5010 and the one we are using for our project. S5010 airfoil, together with the thinner S5020, was designed for Alying wings where a near zero pitching moment is usually desirable. The pitching moment requirement does constrain the airfoil performance. For instance, compared with the S7012, which has a similar lift range, the drag of the S5010 is almost everywhere slightly higher. The dimensions of the airfoil design are shown in Fig. 3. This dimension was set by us keeping in mind the parameters to be considered for our small-scale solar aircraft.

The conceptual design of a 300 seat, wingspan-limited C-wing has been carried out. The results obtained with simple analytical and semi-empirical methods have been corroborated, in some validation computations, by those of more complex methods. The main findings of the design process and the subsequent analysis are summarized in the next statements. The medium size flying wing configuration is



**Fig. 2** Airfoil design S5010



**Fig. 3** Dimensions of the airfoil

technically feasible and operationally efficient and can beat conventional airplane of similar size. No infrastructure compatibility problems exist, if the maximum span is kept below 80 m.

### ***2.3 Selection of Electrical and Electronics Component***

The small-scale solar aircraft that we designed requires a power plant of 10 kW. The selection of the electronics components was made keeping in mind the power plant requirements.

The components used in the aircraft are

1. centloT-SG90g 360 servo motor
2. A2212 motor: 1000 kV
3. 30A brushless ESC
4. 1045 propellers
5. MPPT charge controller
6. Battery management system (BMS)
7. Li-ion battery
8. Pixhawk mini flight computer
9. Radio controller receiver
10. GPS module.

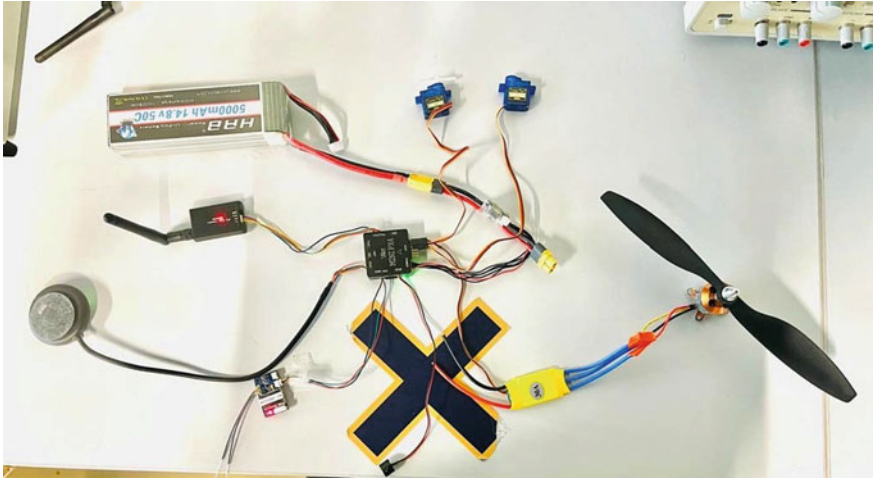
### ***2.4 Solar Panel Arrangement***

In order to achieve the power plant requirement of 10 W, we have selected the polycrystalline silicon photovoltaic solar cells which is connected in a combination of series and parallel connection. While keeping in mind the limited space available for the placement of the solar cells on to the wing and the curvature of the airfoil, we have used a set of 28 solar cells on each wing arranged in way that keeps the shape of the airfoil and the wing in check and connected all the cells in a series connection on each wing to generate a higher voltage which provides a total output of 14 V; the same system was followed on the other wing. The set of solar panels on each wing were connected in parallel to each other in order to increase the amps. These two wings then combined produced 14 V and 0.8 amp, and it was connected to the battery incorporated in the fuselage of the aircraft to charge the battery. The dimension of the solar panel cell is  $52 * 19 \text{ mm} / 2 * 3/4$  inches where each cells produces 0.5 V.

### ***2.5 Flight Control***

The brain of the flight control is the Mini PX4 which is an Arduino-based flight computer. This computer has the provision of an autopilot which can be programmed and controlled using the Mission Planner software. The flight computer has onboard gyroscopes which help keep the aircraft flying in the desired direction. One of the advantages of a fixed wing design is that it has fewer control surfaces on the aircraft; by eliminating the tail, we are left with the ailerons on each wing. The wings house a





**Fig. 4** Flight control system

9 g servo motor each, which actuates the aileron when decided by the flight computer or the pilot. The flight computer has a GPS module attached to it; this helps the autopilot to fly the aircraft in a predetermined trajectory assigned by the ground station using the mission planner software.

Figure 4 shows the flight control system and how the connections of each component were made. These components, namely the wiring, battery, flight controller, the telemetry transmitter, radio receiver, and the GPS module, were incorporated inside the fuselage of the aircraft, and the motor was attached to the rear of the aircraft.

### 3 Fabrication

#### 3.1 3D Printing

Throughout this project, the fabrication of our design has been done using 3D printed components which includes the fuselage, two wings, and control surfaces. All of these parts were printed separately and assembled later as per our design. The design has the provision for installing the electrical components such as the battery, flight computer, receiver, and the telemetry transmitter inside and on the fuselage. The wings are printed with an infill of 10% and a three-layer wall thickness of (0.0 mm) each as shown in Fig. 5. This eliminates the need for ribs and spars. The skin of the wing is the load bearing structure, and the infill keeps the form of the airfoil in check. The fuselage is a two-piece design which is printed with a wall thickness of four layers of (0.0 mm) each with a 0% infill to be able to accommodate the electrical components.

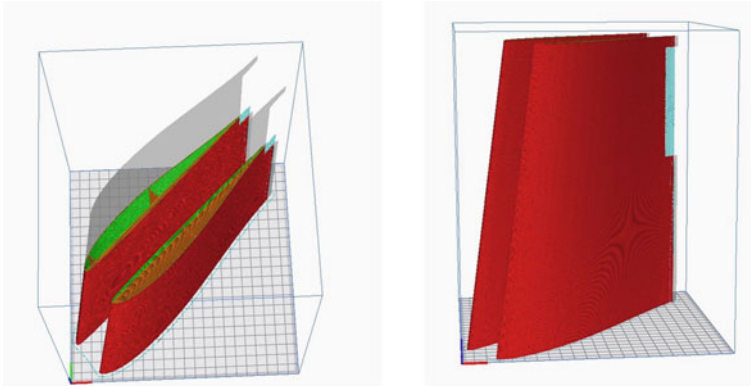


Fig. 5 CURA slicer

**Limitations.** The limitation we faced while 3D printing was material selection. Initially, we selected ABS plastic to print because of its comparatively better durability and resistance to UV radiation than PLA and other types. The reason why we changed the material to PLA from ABS is because ABS plastic is a difficult material to print bigger models. Our model initially failed to print; when we used ABS plastic, the cause of failure was a lack of print bed adherence and layer adherences as shown in Fig. 6, which caused the model to warp on the print bed and also the layers started to separate. After switching to PLA+ which is a variation of PLA plastic, we did not face print bed adherence and layer adherence.

PLA has a tendency of warping and deforming under the harsh conditions of UAE summer as shown in Fig. 7. This resulted in our first prints to fail; this problem was resolved by making a few tweaks to the design such as adding a double wall with air gap, increasing the wall thickness, and by changing the printing filament from PLA to PLA+ which has a higher resistance to UV radiation.

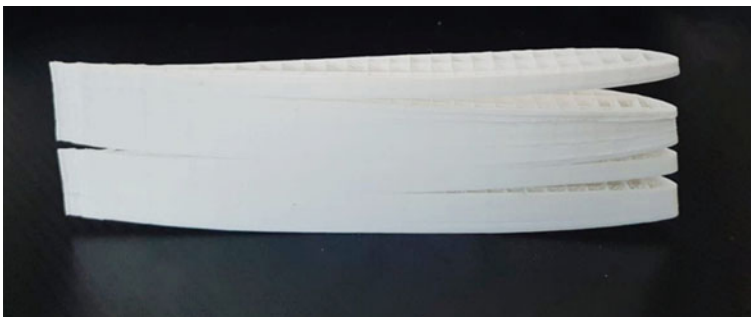


Fig. 6 Layer separation

**Fig. 7** Warping of the wing material used PLA

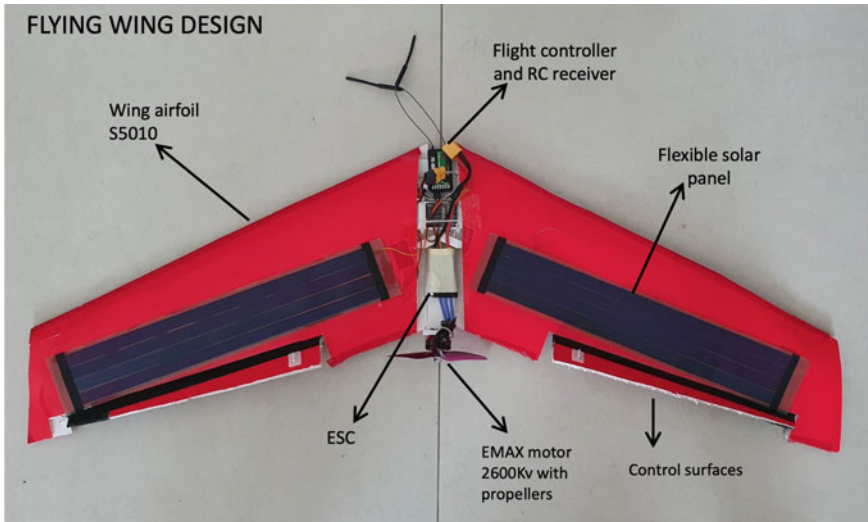


### 3.2 *PLA+*

PLA+ which is a variation of PLA plastic has improved material properties than that of PLA. As per our findings from the report of Singh, D.D. stated it is simple to print with PLA which requires no heating bed because it prints at a lower temperature than ABS and does not distort as easily. Another advantage of using PLA plus is that it does not emit an unpleasant odor when printing. The PLA+ can withstand as solid up to the temperature of 60 °C. PLA+ is also highly durable.

## 4 Conclusion

The current project resulted in the development of our first prototype as shown in Fig. 8. The prototype is fully powered by a 10-W solar power plant, which allows the prototype to be able to fly continuously in the daytime. As the prototype has a built-in autopilot, a human operator is not required to be present throughout the flight time as the prototype is designed to be modular parts which can be easily painted and replaced; this model was tested to be able to carry up to 1.5 kg of payload without losing considerable amount of flight time. The second prototype will be focused on reducing the overall power consumption and increasing the efficiency of the aircraft by improving the lift to drag ratio. This project also demonstrates the viability of using a 3D printer to fabricate the aircraft components. The future plans for the study are to use different materials and different printing techniques to further reduce the overall weight of the aircraft.



**Fig. 8** Photograph of the fabricated solar aircraft

## References

- Hassanaliam M, Abdelkefi A (2017) Classifications, applications, and design challenges of drones: a review. *Prog Aerosp Sci* 91:99–131
- Boucher RJ (1985) Sunrise, the world's first solar-powered airplane. *J Aircr* 22(10):840–846
- Beard J, Iachetta F, Lilleleht L, Huckstep F, May Jr W (1978) Design and operational influences on thermal performance of “solaris” solar collector
- Kim J, Kim S, Ju C, Son HI (2019) Unmanned aerial vehicles in agriculture: a review of perspective of platform, control, and applications. *Ieee Access* 7:105100–105115
- Macrina G, Pugliese LDP, Guerriero F, Laporte G (2020) Drone-aided routing: a literature review. *Transp Res Part C Emerg Technol* 120:102762
- Nonami K (2016) Drone technology, cutting-edge drone business, and future prospects. *J Robot Mech* 28(3):262–272
- Boukoberine MN, Zhou Z, Benbouzid M (2019) Power supply architectures for drones—a review. In: *IECON 2019-45th annual conference of the IEEE industrial electronics society*, vol 1. IEEE, pp 5826–5831
- Boukoberine MN, Zhou Z, Benbouzid M (2019) A critical review on unmanned aerial vehicles power supply and energy management: solutions, strategies, and prospects. *Appl Energy* 255:113823
- Wóznia W, Jessa M (2021) Selection of solar powered unmanned aerial vehicles for a long range data acquisition chain. *Sensors* 21(8):2772
- Alsharoua A, Ghazzai H, Kadri A, Kamal AE (2017) Energy management in cellular hetnets assisted by solar powered drone small cells. In: *2017 IEEE wireless communications and networking conference (WCNC)*, IEEE, pp 1–6
- El-Atab N, Mishra RB, Alshambari R, Hussain MM (2021) Solar powered small unmanned aerial vehicles: a review. *Energ Technol* 9(12):2100587
- Klesh AT, Kabamba PT (2009) Solar-powered aircraft: energy-optimal path planning and perpetual endurance. *J Guid Control Dyn* 32(4):1320–1329
- Mogili UR, Deepak B (2018) Review on application of drone systems in precision agriculture. *Procedia Comput Sci* 133:502–509

14. Tsouros DC, Bibi S, Sarigiannidis PG (2019) A review on uav-based applications for precision agriculture. *Information* 10(11):349
15. Quaglia G, Visconte C, Scimmi LS, Melchiorre M, Cavallone P, Pastorelli S (2020) Design of a ugv powered by solar energy for precision agriculture. *Robotics* 9(1):13
16. Hassanalian M, Rice D, Abdelkefi A (2018) Evolution of space drones for planetary exploration: a review. *Prog Aerosp Sci* 97:61–105
17. Hassanalian M, Rice D, Johnstone S, Abdelkefi A (2018) Planetary exploration by space drones: design and challenges. In: 2018 aviation technology, integration, and operations conference, p 3027
18. Shahmoradi J, Talebi E, Roghanchi P, Hassanalian M (2020) A comprehensive review of applications of drone technology in the mining industry. *Drones* 4(3):34
19. Berman B (2012) 3-d printing: the new industrial revolution. *Bus Horiz* 55(2):155–162
20. Noorani R (2017) 3D printing: technology, applications, and selection. CRC Press
21. Martinez-Val R, Schoep E (2000) Flying wing versus conventional transport airplane: the 300 seat case. In: Proceedings 22nd ICAS congress
22. Selig MS (1995) Summary of low speed airfoil data. SOARTECH publications

# Numerical Study on the Influence of Shape Parameters on Aerodynamic Performance of a Trapezoidal Cylinder



S Aiswarya Lakshmi, Parvathy Rajeev, Manu Sivan, and Ajith Kumar S

**Abstract** The influence of changing the aspect ratio on the aerodynamic characteristics of flow over a trapezoidal cylinder is numerically explored. The study is conducted for a Reynolds number (Re) of 100,  $0.0 \leq d/D \leq 1.0$ , and  $0.5 \leq h/D \leq 2.0$ . The governing equations of fluid flow are discretized using the finite volume approach and solved using the PISO algorithm with the open-source CFD package OpenFoam. The effect of varying  $d/D$  and  $h/D$  on the mean coefficient of drag  $\overline{C_d}$ , rms value of lift coefficient  $Cl_{rms}$ , and Strouhal number St are discussed. For all cases of side length ratios, consider the  $\overline{C_{dp}}$  dominates over the  $\overline{C_{df}}$  and trend of  $\overline{C_d}$  is similar as that of  $\overline{C_{dp}}$ . For all  $h/D$  and  $d/D$  values investigated in this study, the  $\overline{C_d}$ ,  $Cl_{rms}$ , and St were found to be decreasing.

**Keywords** Trapezoidal cylinder · Drag coefficient · Rms of lift coefficient · Strouhal number

## 1 Introduction

Flow over bluff bodies is characterized by the associated wake, vortex formation, shedding, etc. This phenomenon of vortex shedding induces alternating hydrodynamic forces; hence, vibrations on the bodies which when not controlled may lead to structural failures. Because of its importance and applicability, the flow has attracted the attention of scholars, who have explored it experimentally and numerically. Out of different types of bluff bodies, circular cylinders received more attention from researchers. A detailed review of wake transition behind the circular cylinder kept in a flow is discussed by Williamson [1] and Zdravkovich [2]. Unlike circular cylinders which do not have a fixed separation point, non-circular cylinders like square, rectangle, triangular, and trapezoidal have their separation that occurs from the corners. Sohankar et al. [3] studied numerically laminar flow across a square cylinder with

---

S Aiswarya Lakshmi · P. Rajeev · M. Sivan (✉) · S Ajith Kumar  
Department of Mechanical Engineering, Amrita Vishwa Vidyapeetham, Amritapuri, India  
e-mail: [manusivan@am.amrita.edu](mailto:manusivan@am.amrita.edu)

various incident angles. The variation in Strouhal number and aerodynamics coefficients variations are discussed for various values of  $Re$  and incident angles. Tamura and Kuwahara [4] investigated the 2D and 3D flow past a square cylinder for various aspect ratios. They observed 3D structures emerging from near wake due to vortex instabilities, which has a strong influence on the aerodynamic behaviour. The flow past rectangular cylinder over a wide range of aspect ratios and  $Re$  was investigated by Islam et al. [5]. It is reported that increasing the streamwise cylinder length has notable effects on the aerodynamic coefficients and vortex shedding patterns. The influence of  $Re$  and aspect ratio (AR) on the aerodynamic parameters and flow structures were studied numerically (2D and 3D) for rectangular cylinder by Mashhadi et al. [6]. The critical  $Re$  associated with flow transitions was calculated for each value of AR, and the variation of critical  $Re$  with AR is found out to be linear. Also, the authors reported that the normal and shear stresses, as well as fluctuating forces, increase with rising  $Re$  but decrease with increasing AR.

Flow over a triangular cylinder for a  $Re$  ranging from 10 to 250 was conducted by De and Dalal [7]. The steady symmetrical vortices were observed at a critical  $Re$  of 39.9, and in the subcritical regime, the reattachment length and  $Re$  are linearly dependent. Due to the dominance of pressure drag over viscous drag in the range above the subcritical regime, the drag coefficient is observed to be decreasing in the subcritical regime and increasing subsequently. For two triangular prism configurations, apex and base facing the flow, Prasath et al. [8] explored the influence of aspect ratio (AR) and  $Re$  on the reattachment length  $L_r$  and force coefficients. For a constant  $Re$ , a monotonic drop in  $L_r$  was found with a rise in AR in the subcritical regime. The drag coefficient is found to be decreasing with an increase in AR for both cylinder configurations at a constant  $Re$ . Compared to square and triangular cylinders, literature pertaining to trapezoidal cylinders is quite less. For three different angle of attacks at  $Re = 150$ , Zhu et al. [9] numerically studied the flow over a trapezoidal cylinder with varying base length ratios. The hydrodynamic forces are found to be very sensitive to the angle of attack. The  $\overline{C_d}$  and  $Cl_{rms}$  values corresponding to the different base length ratios are compared with that of a square cylinder, and the maximum rise in the  $\overline{C_d}$  and  $Cl_{rms}$  is found to be 54.5% and 451.3%, respectively. For any value of angle of attack, changing the values of the base length ratio has a major impact on the distribution of pressure across the cylinder, vortex formation length, recirculation bubble length, and the vortex shedding frequency. To understand the different numerical methodologies adopted for solving fluid flow problems like that of present study, authors referred numerical works of Sivan et al. [10], Sourav et al. [11], and Kumar et al. [12, 13]. The purpose of this research is to better understand how the aerodynamic coefficient varies for flow over a trapezoidal cylinder at various base length ( $d/D$ ) and side length ( $h/D$ ) ratios.

## 2 Numerical Methodology

### 2.1 Governing Equations and Solutions Methodology

The flow over the trapezoidal cylinder is governed by two-dimensional laminar unsteady incompressible continuity (1) and momentum equations (2) and can be expressed in the vector form as

$$\nabla \cdot \mathbf{V} = 0 \quad (1)$$

$$\frac{\partial \mathbf{V}}{\partial t} + (\mathbf{V} \cdot \nabla) \mathbf{V} = -\nabla p + \frac{1}{\text{Re}} \nabla^2 \mathbf{V} \quad (2)$$

The governing Eqs. (1) and (2) are discretized using the finite volume method, and PISO algorithm is employed for decoupling pressure and velocity fields. For this purpose, we used the pisoFoam solver, available in the open-source software package OpenFOAM.

### 2.2 Problem Description and Computational Domain

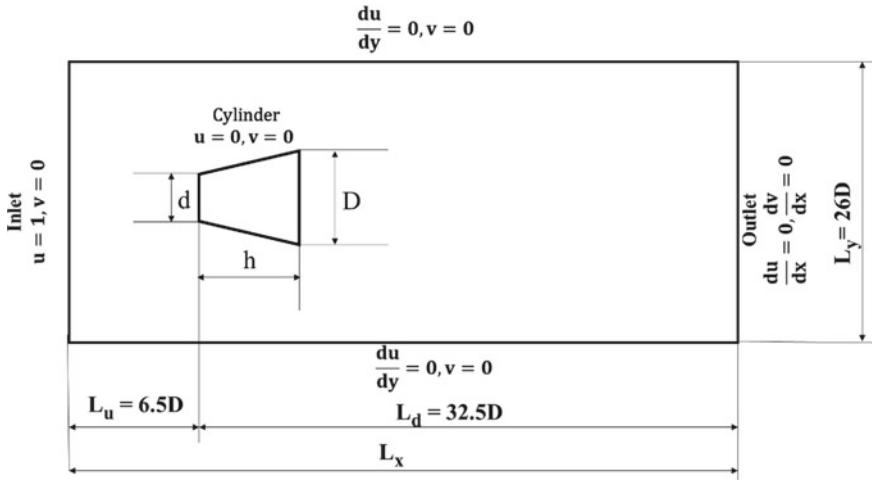
Incompressible 2D laminar flow over a single trapezoidal cylinder is examined for different  $d/D$  and  $h/D$  ratios at a Reynolds number (Re) of 100. Figure 1 shows the computational domain along with boundary conditions used for the current study. The  $d/D$  ratio is varied by 0.25 increments from 0.0 to 1.0, while the  $h/D$  ratio is varied by 0.25 increments from 0.5 to 2.0.

The different configurations of the trapezoidal cylinder for various  $d/D$  and  $h/D$  values are shown in Fig. 2. To avoid the influence of inlet and outlet boundary conditions, the cylinder is placed at an upstream distance of  $6.5D$ , and the downstream distance is taken as  $32.5D$ . A transverse distance of  $13D$  is taken to each side of the cylinder to eliminate any blockage effects. These domain dimensions are selected based on the domain independence test conducted, which is explained in the next section.

### 2.3 Domain Independence Test

A domain-independent test is conducted with different domain sizes starting with  $24D$  along the streamwise direction and  $16D$  along the transverse direction. The test was conducted at  $\text{Re} = 100$  on a square cylinder for which  $d/D$  and  $h/D$  ratio equals 1. The mesh density is kept constant for cases of domain size considered. The test's boundary conditions are the same as those illustrated in Fig. 1. Table 1 lists the





**Fig. 1** Computational domain along with the boundary conditions used for the present work

$d/D = 0$ $h/D \neq 0$	$0 < d/D < 1$ $h/D > 0$	$d/D = 1$ $h/D = 1$	$d/D = 1$ $h/D \neq 1$

**Fig. 2** Different configurations of the trapezoidal cylinder for various side ratios ( $h/D$  and  $d/D$ ) considered for the present study

various domain sizes employed in the test, as well as the related values of aerodynamic parameters determined from the domain independence test. It is observed that after the domain size of  $39D \times 26D$ , there is not much appreciable change in the flow parameters. Therefore, the computational domains having a transverse length of  $26D$ , upstream length of  $6.5D$ , and downstream length of  $32.5D$  are chosen to simulate the unbounded flow past the cylinder.

### 2.4 Grid Independence Study

The optimum grid for the present study is found by conducting a grid independency study on the domain selected after the domain independence test ( $39D \times 26D$ ). Figure 1 depicts the computational domain as well as the boundary conditions employed for grid independence study. The test is conducted for  $Re = 100$ ,

**Table 1** Domain independence test at  $Re = 100$

Domain dimensions		Upstream distance	$\overline{C_d}$	St	$Cl_{rms}$
$L_x$	$L_y$	$L_u$			
24	16	4	1.676	0.161	0.204
27	18	4.5	1.634	0.158	0.199
30	20	5	1.610	0.156	0.195
33	22	5.5	1.578	0.152	0.195
36	24	6	1.560	0.152	0.195
<b>39</b>	<b>26</b>	<b>6.5</b>	<b>1.545</b>	<b>0.152</b>	<b>0.195</b>
42	28	7	1.545	0.152	0.195

**Table 2** Grid independency test

No. of cells $N$	$\overline{C_d}$	St
10,400	1.55	0.1501
15,300	1.548	0.1503
24,950	1.547	0.1506
30,000	1.547	0.1515
37,800	1.546	0.1515
<b>44,750</b>	<b>1.545</b>	<b>0.152</b>
60,000	1.545	0.152
74,410	1.545	0.152

on a square cylinder. A total of eight different cases involving different numbers of quadrilateral cells ( $N$ ) were analysed. Table 2 shows the results of the grid independency test. It is observed that for  $N = 44,750$ , and above,  $\overline{C_d}$  and St are not changing, so for the rest of the numerical simulation, we took the grid with  $N = 44,750$  as the optimum grid.

### 2.5 Code Validation

For the present study, as discussed in Sect. 2.1, we make use of OpenFOAM source code pisoFoam, and the code validation is done for the flow across a square cylinder at a  $Re = 100$ .

Table 3 compares the  $\overline{C_d}$  and St values obtained during validation with those reported in the literature. The value in the brackets indicates the percentage deviation in the aerodynamic parameters obtained from that in the literature. The maximum deviation is found to be less than 4.47%, and it is concluded that the present numerical simulation predicts the values reported in the literature very closely.

**Table 3** Code validation

Literature	$\overline{C_d}$	St
Sohankar et al. [3]	1.477 (4.40%)	0.146 (3.95%)
Robichaux et al. [14]	1.530 (0.97)	0.154 (1.32%)
Darekar and Sherwin [15]	1.486 (3.82%)	0.146 (3.95%)
Sharma and Eswaran [16]	1.493(3.33%)	0.1488 (2.11%)
Singh et al. [17]	1.51 (2.27%)	0.147 (3.29%)
Sahu et al. [18]	1.487 (3.70%)	0.1486 (2.24%)
Sen et al. [19]	1.528 (1.06%)	0.1452 (4.47%)
<b>Present study</b>	<b>1.545</b>	<b>0.152</b>

### 3 Results and Discussions

The unsteady flow across a trapezoidal cylinder is studied at a  $Re = 100$  for different values of  $d/D$  and  $h/D$  ratios. For the cases considered in this study, with an increment of 0.25,  $d/D$  and  $h/D$  are increased from 0 to 1.0 and 0 to 2, respectively. The numerical simulation is carried out on the grid selected after the grid independence study using the pisoFoam solver to understand the influence of varying  $h/D$  and  $d/D$  on  $\overline{C_d}$ ,  $C_{l,rms}$ , and St.

#### 3.1 Effect of Varying Side Length Ratios on the Mean Coefficient of Drag $\overline{C_d}$

Figure 3 depicts the change of mean drag coefficient with  $d/D$  ratio for various  $h/D$  ratio values. The  $\overline{C_d}$  is found to be decreasing up to  $d/D = 0.75$ , and then there is a slight increase after that for all values of  $h/D$ . Comparing all the cases of  $h/D$ , the lowest value of  $\overline{C_d}$  is observed for  $h/D = 2$  and the highest value is observed for  $h/D = 0.5$ .

The graphs of mean pressure drag coefficient ( $\overline{C_{dp}}$ ) and mean friction drag coefficient ( $\overline{C_{df}}$ ) are plotted in Figs. 4 and 5, respectively, to understand how the aspect ratio variation influences the  $\overline{C_{dp}}$  and  $\overline{C_{df}}$ . Figures 3 and 4 indicate that the trends of  $\overline{C_d}$  and  $\overline{C_{dp}}$  are identical, indicating that the pressure drag coefficient dominates in all the instances investigated in this study. The higher values of  $\overline{C_d}$  are observed for the smaller values of  $h/D$ , and as the values of  $h/D$  increase,  $\overline{C_d}$  decreases. The skin friction drag increases as the  $h/D$  grows due to the increased longitudinal area of the cylinder, which decelerates the flow over the cylinder’s surface, reducing the wake region behind the cylinder and hence the wake pressure. As a result, the pressure drag coefficient decreases, which is reflected in the overall drag coefficient.

A decrease in the  $\overline{C_d}$  up to  $d/D = 0.75$ , and a gradual increase afterwards, as seen in Fig. 3, can be interpreted as a trade-off between the trends of  $\overline{C_{dp}}$  and  $\overline{C_{df}}$  based on the relation  $\overline{C_d} = \overline{C_{dp}} + \overline{C_{df}}$ . For all cases of  $h/D$ , the decreasing trend of mean

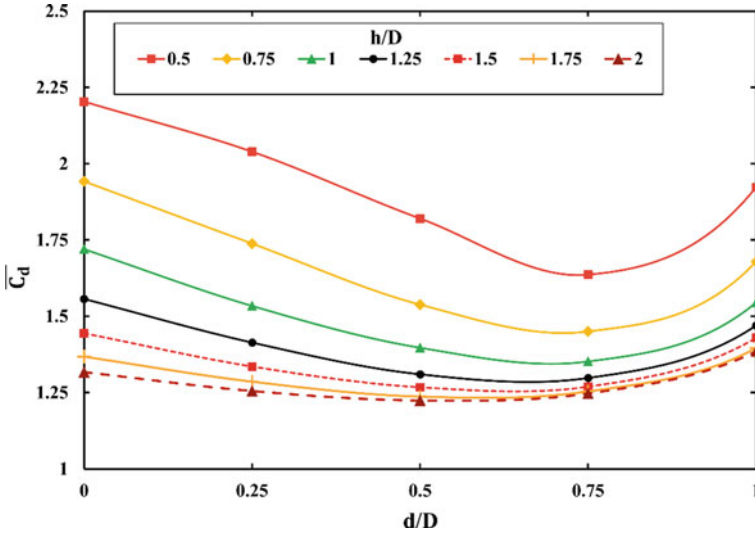


Fig. 3 Variation of mean drag coefficient versus  $d/D$  for various values of  $h/D$

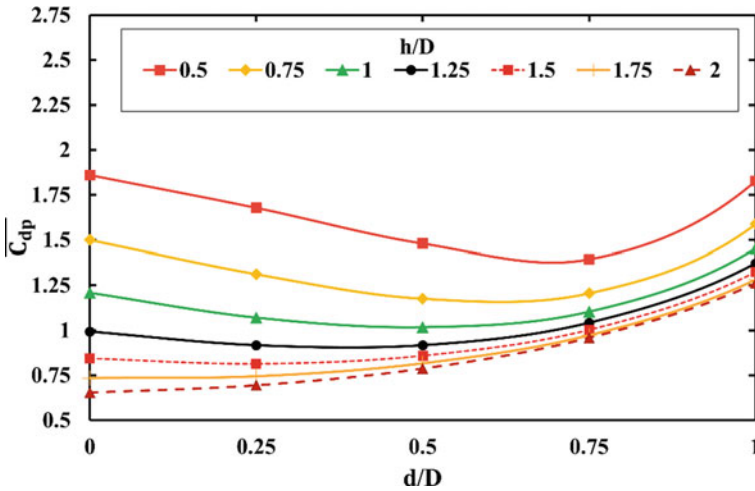


Fig. 4 Variation of mean pressure drag coefficient versus  $d/D$  for various values of  $h/D$

friction drag coefficient as  $d/D$  increases, and the decreasing and then increasing trend of mean pressure drag coefficient creates a local minimum for  $\overline{C_d}$  at  $d/D = 0.75$ .

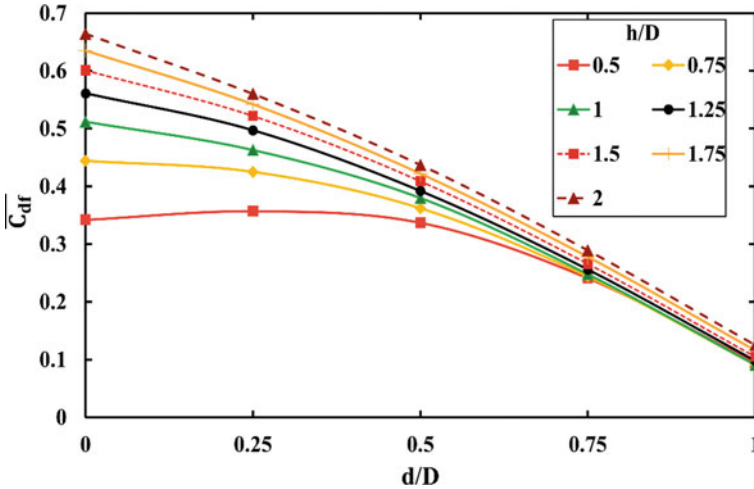


Fig. 5 Variation of mean friction drag coefficient versus  $d/D$  for various values of  $h/D$

### 3.2 Effect of Varying Side Length Ratios on $Cl_{rms}$

The variation in the  $Cl_{rms}$  is shown in Fig. 6. Excluding for some values of  $h/D$  and  $d/D$ , all the curves show a common trend. The curves show a gradual decrease in the  $Cl_{rms}$  value up to  $d/D = 0.75$  and an increasing trend afterwards, which diminishes as  $h/D$  increases. As the  $h/D$  increases for a given  $d/D$ , the fluid particles need to encounter higher shear stresses as they glide along the surface of the cylinder, which results in increased momentum loss, resulting in a lower rate of vortex shedding, and a reduction in the  $Cl_{rms}$  value.

### 3.3 Effect of Varying Side Length Ratios on $St$

Due to the increased momentum dissipation at higher values of  $h/D$  as discussed above, the rate of vortex shedding will also get reduced, and thus the  $St$ , which is evident from Fig. 7. With increasing values of  $d/D$ , the  $St$  is found to be decreasing for all values of  $h/D$ . For  $d/D = 0$ , which is the case of the triangle with the apex facing the flow, the vortex shedding starts from the lower corners, but as the  $d/D$  increases from zero, the shedding will shift to the front corners. This can result in an increased wake width and reduces the interaction between shear layers, and consequently vortex shedding gets delayed.

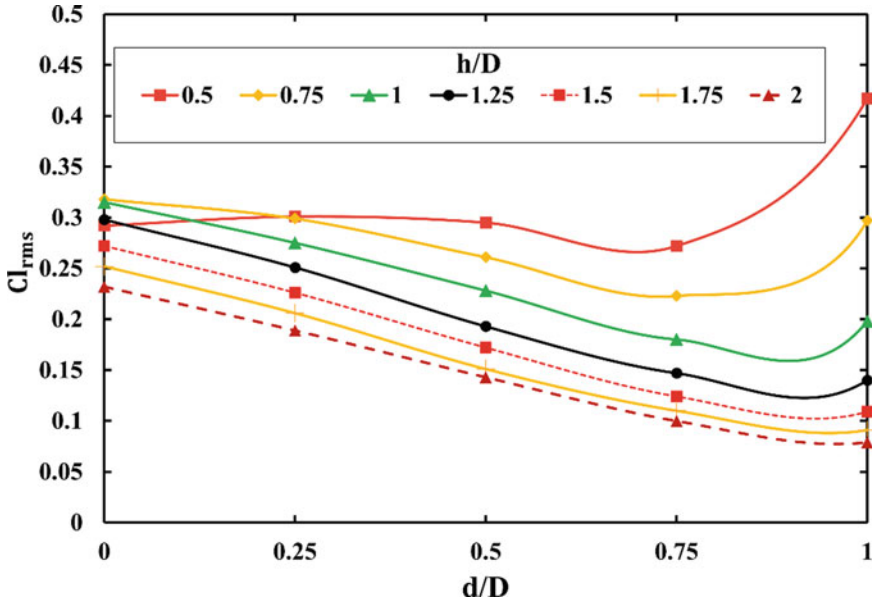


Fig. 6 Variation of  $Cl_{rms}$  versus  $d/D$  for various values of  $h/D$

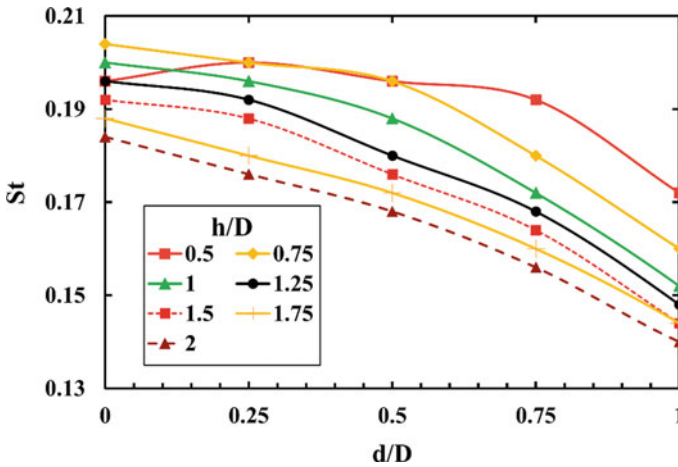


Fig. 7 Variation of  $St$  versus  $d/D$  for various values of  $h/D$

### 4 Conclusions

The flow over a trapezoidal cylinder is numerically simulated in this study at  $Re = 100$ . The effect of varying the side length ratios on the aerodynamic parameters and  $St$  is studied. The  $d/D$  ratio is varied from 0 to 1, and the  $h/D$  ratio is varied

in the range of 0.25 to 1, both with an increment of 0.25. In order to solve the 2D incompressible laminar problem numerically, the PISO algorithm is employed. For all cases of side length ratios, consider the  $\overline{C_{dp}}$  dominates over the  $\overline{C_{df}}$  and trend of  $\overline{C_d}$  is similar as that of  $\overline{C_{dp}}$ . The largest value of  $\overline{C_{dp}}$  is observed for the lowest value of  $h/D$  and  $d/D$ , which is the case where the flow gets deflected by a greater angle. This results in a larger wake and thus pressure drag increases. As the  $h/D$  increases, the  $\overline{C_{df}}$  is found to be increasing since the fluid undergoes higher shear stresses due to increased surface area of the cylinder in the streamwise direction. The deceleration of the flow results in momentum losses of the shear layer which in turn reduces the wake region. The reduction in the wake region leads to the reduction of pressure drag and hence the total drag. Due to increased momentum losses of the fluid and the associated deceleration of the shear layer as the  $h/D$  and  $d/D$  increase, both the  $Cl_{rms}$  and  $St$  are reduced over all the range of  $h/D$  and  $d/D$  considered for this study. It can be inferred that changing the aspect ratio of a trapezoidal cylinder has a significant impact on the aerodynamic coefficients and Strouhal number, similar to other cylinders studied in the literature.

## References

1. Williamson C (1996) Vortex dynamics in the cylinder wake. *Ann Rev Fluid Mech* 28:477–539
2. Zdravkovich MMD (1997) Flow around circular cylinders, vol 1: fundamentals. Oxford University Press, New York
3. Sohankar A, Norberg C, Davidson L (1998) Low Reynolds number flow around a square cylinder at incidence: study of blockage, onset of vortex shedding and outlet boundary condition. *Int J Numer Meth Fluids* 26:39–56
4. Tamura T, Kuwahara K (1990) Numerical study of aerodynamics behavior of a square cylinder. *J Wind Eng Ind Aerodyn* 33:161–170
5. Islam S, Zhou C, Shah A, Xie P (2012) Numerical simulation of flow past rectangular cylinders with different aspect ratios using the incompressible lattice Boltzmann method. *J Mech Sci Technol* 26:1027–1041
6. Mashhadi A, Sohankar A, Alam MM (2021) Flow over rectangular cylinder: effects of cylinder aspect ratio and Reynolds number. *Int J Mech Sci* 195
7. De AK, Dalal A (2006) Numerical simulation of unconfined flow past a triangular cylinder. *Int J Numer Meth Fluids* 25:801–882
8. Prasath S, Sudharsan M, Kumar V, Diwakar SV, Sundararajan T, Shaligram T (2014) Effects of aspect ratio and orientation on the wake characteristics of low Reynolds number flow over a triangular prism. *J Fluids Struct* 46:59–76
9. Zhu H, Tang T, Liu H, Zhou T, Zhong J (2020) Flow structures around trapezoidal cylinders and their hydrodynamic characteristics: effects of the base length ratio and attack angle. *Phys Fluids*
10. Sivan M, Ajith Kumar S (2020) Numerical study on flow over two inline triangular cylinders— influence of gap ratio on vortex shedding. In: Proceedings of international conference on thermofluids. Lecture notes in mechanical engineering, Springer
11. Kumar SN, Akhilesh Vishnu H, Ajith Kumar S (2019) Influence of extending the height on the vortex structures generated inside a lid driven cavity. *IOP Conf Series Mater Sci Eng* 577:012151

12. Kumar R, Nandan G, Dwivedi G, Shukla AK, Shrivastava R (2021) Modeling of triangular perforated twisted tape with V-Cuts in double pipe heat exchanger. *Mater Today Proc* 46(11):5389–5395
13. Kumar A, Saini RP, Saini G, Dwivedi G (2020) Effect of number of stages on the performance characteristics of modified Savonius hydrokinetic turbine. *Ocean Eng* 217
14. Robichaux J, Balachandar S, Vanka SP (1999) Three-dimensional floquet instability of the wake of square cylinder. *Phys Fluids* 11:560
15. Darekar R, Sherwin SJ (2001) Flow past a square-section cylinder with a wavy stagnation face. *Int J Fluid Mech* 426:263–295
16. Sharma A, Eshwaran V (2004) Heat and fluid flow across a square cylinder in the two-dimensional laminar flow regime. *Numer Heat Transfer Part A Appl* 45:247–269
17. Singh AP, De AK, Carpenter VK, Eswaran V, Muralidhar K (2009) Flow past a transversely oscillating square cylinder in free stream at low Reynolds numbers. *Int J Numer Meth Fluids* 61(6):658–682
18. Sahu AK, Chhabra RP, Eshwaran V (2009) Two-dimensional unsteady laminar flow of a power law fluid across a square cylinder. *J Nonnewton Fluid Mech* 160(2):157–167
19. Sen S, Mittal S, Biswas G (2011) Flow past a square cylinder at low Reynolds numbers. *Int J Numer Meth Fluids* 67(9):1160–1174



# Transosonde Balloon Aerial Mapping with APRS Module and GPS Tracking



Sarath Raj, Ali Asgher, Mohamed Sufyan Shafi, and Nour Alaa Elsonbaty

**Abstract** The hot air balloon is the man's earliest attempt to take off from the ground and be able to fly. The story of human flight started with hot air balloons, which are lighter than air aircraft. The modern aerospace industry can still use the technology that was developed in the olden time in an attempt to fly. Today, high-altitude balloons are used in various fields ranging from reconnaissance, recreational activities to high-altitude atmospheric and near-space atmospheric researches and high-altitude measuring hardware developments. The weather balloon or high-altitude balloon is one of the earliest aeronautical inventions which generally ferry instruments/equipment to higher altitudes to measure temperature readings and map out weather patterns with the help of Automatic Packet Reporting System (APRS, transmitters) or Global Positioning System (GPS) and can be tracked with the help of radio stations and radar. This technology is widely used in the meteorological department by using balloons that can send meteorological data from high atmospheric altitudes to the operators on the ground. This paper attempts to represent the construction of an aerial mapping transosonde-type balloon fitted with a GPS tracker, which was formulated in the university, and terminate with few insights into high-altitude balloons in the near-space atmospheres.

**Keywords** Transosonde · APRS · High-altitude balloon · Aerial mapping · Landing predictor · Remote sensing

## 1 Introduction

The balloons are the lighter than air type of aircraft and were the first major payload-carrying aircraft that mankind ever created [1, 2]. Then, we gradually moved on to controllable and fuel-propelled aircraft with reciprocating engines. Then, the aeronautics/aviation manufacturing industry is rapidly progressed to much more advanced technology to make humans fly. The long-forgotten balloon is still can

---

S. Raj (✉) · A. Asgher · M. S. Shafi · N. A. Elsonbaty  
Amity University, Dubai, UAE  
e-mail: [sraj@amityuniversity.ae](mailto:sraj@amityuniversity.ae)

© The Author(s), under exclusive license to Springer Nature Singapore Pte Ltd. 2023  
R. Sharma et al. (eds.), *Advances in Engineering Design*, Lecture Notes in Mechanical Engineering, [https://doi.org/10.1007/978-981-99-3033-3\\_48](https://doi.org/10.1007/978-981-99-3033-3_48)

563

be pretty much used today as well, and it is being used. According to the national oceanic and atmospheric administration of the US Department of Commerce, an average meteorologist uses six tools to acquire meteorological data, and one of the most important tools is the high-altitude balloons [3]. High-altitude balloon technology can be utilized in various fields of practical research such as aerial mapping of small-to-medium range area coverage, tracking of a military convoy, international reconnaissance, field analysis during a natural or a manmade disaster such as an aircraft crash, tsunami, earthquake, ordinance test field radius evaluation, and fire-fighting and various other civil defense services. The transosonde-type balloon uses radio transceivers to transmit and receive information [4]. Transosonde-type balloons can be tracked on the ground with the help of radio technologies such as Automatic Packet Reporting System (APRS) or the Global Positioning System (GPS). These balloons, which are used in the meteorological departments, can go beyond the Armstrong limit which is about 18–19 km above mean sea level. These balloons can go up to even 100 km above mean sea level that is the Kármán line [5]. This height is sometimes referred to as the transition height from the Earth's atmosphere to the inter-planetary (or Inter-Stellar space), where we can get aerial photos transmitted by these balloons [6]. The transosonde balloons have a characteristic method of fabrication and are referred to as the typical 'tear drop'-shaped balloons. These balloons were designed specifically to minimize circumferential stresses to check in-flight or operational shortcomings. The construction of a typical transosonde balloon consists of 14 sections of gore made with 2–2.5 mm of plastic polymer (polythene) that is again laminated with the same plastic polymer [7]. Polyethylene is a suitable balloon material because of its low brittle temperature (about  $-80^{\circ}\text{C}$ ), its chemical stability (property by being unaffected by ultraviolet light and ozone), its low permeability (about 7 L of helium per mil per square meter per 24 h), its high tensile strength (about 1900 lb/in.<sup>2</sup>), and its small radiation absorption capacity [8]. The balloon can carry about 295 kg mass payload to about 35,000 ft. [9]. The transosonde balloons may have an approximated volume of about 765 m<sup>3</sup> and a fully erect standing height of about 12 m. Sometimes, keeping these flights at a constant level above ground of interest is important and causes a major challenge in keeping it balanced. The contingency of flight level depends on several factors such as heat flux changes within the hot air balloon, outside temperature, wind currents, diffusion of minor airborne particulates into or outside the skin of the balloon, solar radiation effects [10]. Out of these factors that affect the contingency of a transosonde balloon's leveled flight, the solar radiation plays a significant role [11]. The heat fluxes throughout the skin of the aircraft vary differently throughout the course of the day. This variation of heat flux and hence the level of the flight of the aircraft is corrected by either increasing the volume of air flow inside the balloon or by dropping off the ballasts [12]. In the present time, however, to conduct researches in the fields of space science, aerial mapping, advanced meteorology, land terrain and geography analysis, military reconnaissance, aerial internet services, the institutions require the balloon-based aircraft to go beyond the Armstrong limit and up to the Kármán line [13]. To achieve this goal, we no longer use the transosonde high-altitude balloon aircraft. Instead, now, the super-pressure aero-static balloons are being used, where

the balloon's weight is equated with the vertical buoyant force [14].

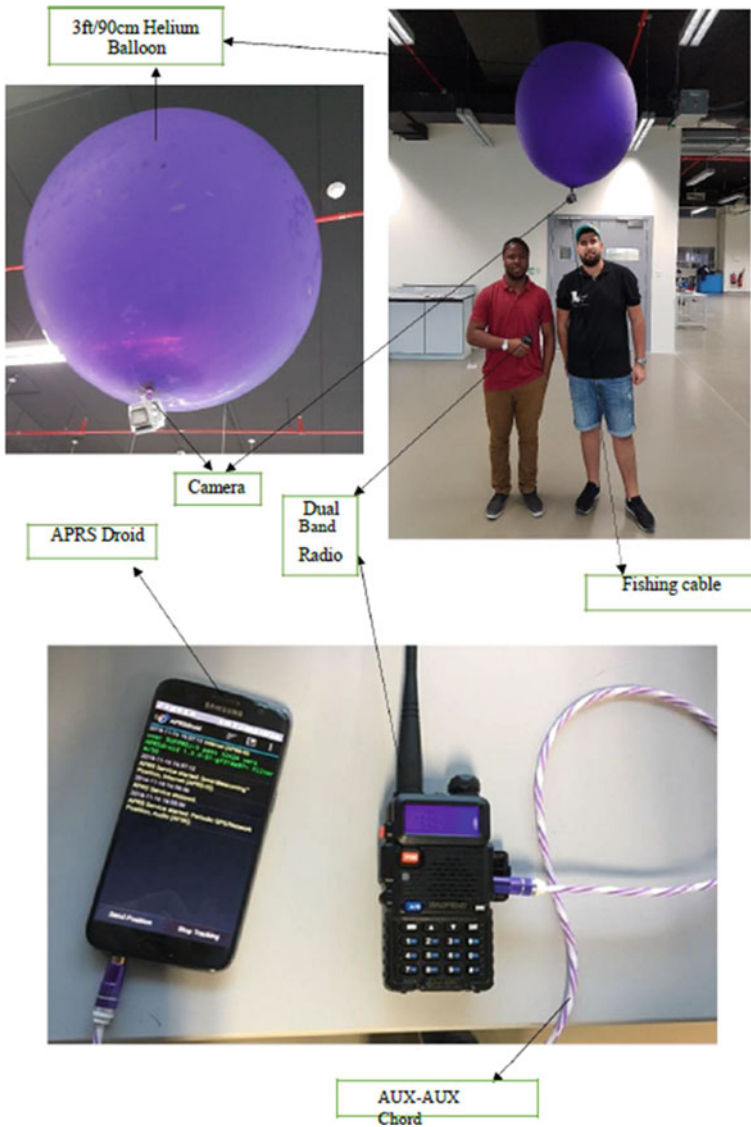
$$V_b(P_a - P_h) = W, \quad (1)$$

where  $V_b$  is the vertical buoyant force obtained by the hot air supplied,  $P_a$  is the density of ambient air,  $P_h$  is the density of helium, and  $W$  is weight of the aircraft. High-altitude balloons have a substantial prospective in being utilized by various institutions at all levels in near-space atmosphere experiments. There are several instances of several educational as well as commercial institutions going forward to experiment on high-altitude balloons. For example, in 2018 an Italian company MBI checked on levels of noise in the Industrial, Scientific, and Medical (ISM) bands at an orbital altitude from the surface of earth while inspecting the practicality of the LEO constellation [15].

## 2 Construction and Characterization of the Balloon

The construction of the balloon involved the use equipment such as camera, helium-filled balloon, APRSdroid app on our cellular devices, dual-band radio (citizen band), APRS.fi website, and a 300 m fishing wire. Since the balloon we are operating on was the of the transosonde (constant altitude) one, the balloon was tied to the camera through a fishing line. This was done further in compliance with the local municipality rules and regulation related to aviation and private aircraft [16]. The movement of the aircraft was thus regulated to the campus itself with restricted movements. The dual-band Baofeng radio was configured to the APRSdroid app via auxiliary-to-auxiliary cable. The transmission and receiving bands of the dual-band radio were set to appropriate channels, respectively. This configuration and set channels enabled the AFSK feature of the application on the cell phones with GPS tracking relayed information accessible through the APRS.fi website (Fig. 1).

The balloon was made to ascent to at least 300 m above the ground level once the weather conditions deemed perfect for the operation. The balloon was tied to the fishing cable that was of the same length. The flight path was remained constant and was continuously tied to the string/cable the entire time of the running of the experiment. This was done to avoid the balloon setting into free flight and violate the law of the nation. However, the experimentation clearly elucidates the objectives of the project by making the balloon traceable to the ground trackers using APRS and GPS tracking facility. Figure 2 portrays the starting point of the balloon's track at the beginning of the experimentation. This was done on switching on the APRSdroid application on the smartphone. The APRS was used to evaluate the current position on the ground. The coordinates of the actual positions were sent to the APRS.fi website to actively track the balloon's movement on the GPS. The callsign of the balloon was 'SUFPROJ'. Then, the balloons' location was moved by pulling the fishing cable in hand on the ground. This caused the balloon's position to change. The change in the balloon's location is shown in Fig. 3. The operators on the ground



**Fig. 1** List of components used

then followed the same route back to the starting point of the experimentation. The final portrayal of the trajectory covered by the balloon is shown in Fig. 4.

A circular track along the football field of the university was chosen to demonstrate the tracking of the balloon via the APRS. In reality, aerial tracking is usually done by letting the balloon free with constant altitude (if it is a transosonde) to travel from one position to another recording different atmospheric variables along its



Fig. 2 Snapshot of the initial position of the balloon with APRS tracker as shown on APRS.fi



Fig. 3 GPS tracking of the balloon

path. Then, the balloon is retrieved and the data are recorded and compared. In case of variable altitude balloons (non-transosonde), the balloon goes beyond the stratosphere and bursts. The payload then enters a free fall but is protected from impact via a pre-attached parachute. The data are retrieved, recorded, and compared.

### 3 Flight Dynamics of Lighter than Air Balloons

Landing predictors are especially programmed computer softwares that are designed to help operator predict the flight path and conditions in the atmosphere that may affect the overall performance of a balloon in a flight [16, 17]. As the name suggests,



Fig. 4 Final destination of the balloon

landing predictors are usually used to determine conditions that are factors for an efficient landing that helps the operator to perform perfect landing of the aircraft. The predictor is usually written in the Python code. It is always advisable to custom code the predictor to account to any flight conditions prevalent in the area. Flight conditions can depend area to area such as variable air density affiliated to humidity in the atmosphere, rainfall, land surface temperature. The code should account for mathematical models for ascent and horizontal motion phases of the flight. Data should be imported from NOAA GFS [18]. Hence, it is always beneficiary to elucidate the dynamics of flight of lighter than air aircraft.

### 4 Mathematical Modeling of the Vertical Motion of the Flight

In balloon flight dynamics, importance is placed on three primary forces: gravity, buoyancy, and drag. The buoyant force is equal to the weight of the balloon and the apparatus. Furthermore, the balloon is lift off the ground by the action of the lifting gases that are less dense than the atmospheric gases (air), and this adds to the buoyant force, exceeding the weight force of the aircraft hence, lifting the balloon off the ground. The buoyant force in the  $z$  direction (upwards) is mathematically described as:

$$\vec{F}_b(z) = V_z * \rho_{air}(z) * g(z) * \hat{z}. \tag{2}$$

$V_z$  is the volume of the balloon. The above-described buoyant force is normalized by the weight force which acts opposite to the buoyant force acting downward:

$$\vec{F}_g(z) = -m_T * g(z) \hat{z} \tag{3}$$

$$m_T = m_{\text{balloon}}, m_{\text{payload}}, m_{\text{helium}}$$

The drag force is described as follows:

$$\vec{F}_d(z) = -\frac{1}{2} \rho_{\text{air}}(z) * C_D * A(z) * |V_{\text{rel}}| * \vec{V}_{\text{rel}}. \tag{4}$$

$C_D$  is the drag coefficient,  $A(z)$  is the cross-sectional area and  $\vec{V}_{\text{rel}} = \vec{V} - \vec{V}_W$ .

Total vertical force acting on the balloon would be evaluated by adding Eqs. (1), (2), and (3):

$$\vec{F}_t(z) = [V(z) * \rho_{\text{air}}(z) - m_T] * g(z)\hat{z} - \frac{1}{2} \rho_{\text{air}}(z) * C_D * A(z) * |V_{\text{rel}}| * \vec{V}_{\text{rel}}. \tag{5}$$

The vertical motion of the aircraft is evaluated by Newton’s laws of motions and by inducing burst conditions of the balloon. The burst conditions can either be of burst diameter or the burst altitude, which is provided by the manufacturer.

## 5 Mathematical Modeling of the Horizontal Motion of the Flight

The horizontal motion takes place in the  $x$ - $y$  plane. During the horizontal motion, the aircraft will have to be modeled along the  $x$ - $y$  plane. The motion of lighter than air aircraft in the horizontal plane widely depends on the direction of wind. The  $x$  component is directly parallel to the local parallel, while the  $y$  component is parallel to the aircraft’s local meridian line (as stated by the manufacturer). The wind components to which the aircraft depends solely for its horizontal motion are provided by the data libraries of institutional entities such as NOAA for any locale in the world with a final resolution of 1° or as low as 0.5°.

Assuming that  $\Delta t$  is the time taken for the compilation/interpretation of the code (which involves integration operation of all the possible parameters), the horizontal displacements can be computed as follows:

$$\Delta_x = V_{x,w} * \Delta t, \tag{6}$$

$$\Delta_y = V_{y,w} * \Delta t. \tag{7}$$

Variations along the latitude and longitudes are as follows:

$$\Delta_{\text{lat}} = a \sin\left(\frac{V_{y,w} * \Delta t}{r_e}\right), \tag{8}$$



$$\Delta_{\text{long}} = a \sin\left(\frac{V_{y,w} * \Delta t}{r_e * \cos(\text{lat})}\right). \quad (9)$$

$r_e \cos(\text{lat})$  is the radius of the circle chosen which is relative to the chosen latitude of travel. This mathematical modeling of the aircraft flight dynamics can be programmed into the custom landing predictor software for pre-planning the aircraft path and reassuring the safety of the aircraft in adverse conditions, if persist.

## 6 Results and Discussions

The following figures describe the results obtained from performing the experimentation.

Initial location of the balloon was evaluated using the APRSdroid application on the smartphone. Furthermore, through the APRS.fi website, the exact position of the balloon was depicted via the GPS. The purple dot in Fig. 2 represents the exact location of the balloon as shown on the website which is configured by the APRS sent coordinates of the balloon.

The above figure illustrates the path covered by the balloon along the perimeters of the football field in the university campus. This was portrayed on the APRS.fi website as it was continuously tracked by the APRSdroid application on the smartphone while traversing the pre-determined path.

The balloon is brought back from the mid-point back to the starting point while being continuously tracked by the APRSdroid and positions continuously shared to the APRS.fi website as shown in Fig. 4. These are some of the many recent projects done by different entities and individuals across the world and by performing this experiment helps understand more about the weather pattern and wind resistance. It also shows the mechanics behind how the transosonde balloons maintain the same altitude but move around in the direction of the wind. Though the balloon was never set free in the air due to legal obligations, the experiment tends to demonstrate the real working behind the tracking of the balloon and the dynamics of changing atmospheric conditions. High-altitude balloons provide preferable/optimum utility for smaller area coverages and that too with less cost. Comparison for different remote sensing platforms is shown in Fig. 5.

## 7 Conclusion

This experiment's aim was to show the importance and the practicality of high-altitude balloons and as the components are getting easier accessibility to ordinary people. The main purpose of the project was to show that the weather balloon/high-altitude balloons are very practical to set up.



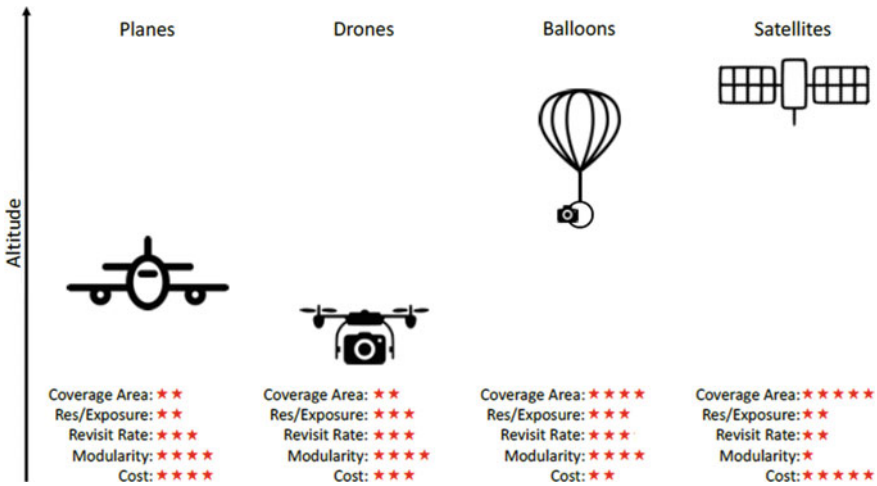


Fig. 5 Utility comparison of different remote sensing platforms

The first gas-filled balloons were flown in the late-eighteenth century by Jacques Charles and Nicolas-Louis Robert in France on December 1, 1783, marking the birth of human flight. The balloon was filled with hydrogen. Since then, gas ballooning has advanced to include high-altitude ballooning, with hundreds of flights providing valuable data and stunning views of Earth in the last 50 years. High-altitude ballooning has also been used as a model for the development of human spaceflight, as it is a reliable and dependable way to explore the upper reaches of the atmosphere, allowing enthusiasts to gather information.

Due to the versatile nature of the high-altitude balloons, there can a potential in improving the standards of service that can be achieved using transosonde or high-altitude balloons. High-altitude balloons can be used in areas of research such as remote sensing. The task of remote sensing done using various available platforms depending on the various contexts and parameters required (parameters such as area coverage, modularity, resolution/scalability and budget). Satellites are the most common means of gathering surface emission data but has its own disadvantages when it comes to sensing a small area of land. Therefore, satellites cannot be declared as the only means of retrieving surface emission data in remote sensing tasks. Efficiency of remote sensing can be improved by the observer/operator by choosing the correct platform depending on the parameters needed to conduct a survey.

## References

1. Watson EC (1949) Science in art: man's first aerial Voyage. *Eng Sci* 12(8):19–20
2. Bowman DC, Albert SA, Dexheimer D (2018) Solar hot air balloons for terrestrial and planetary atmospheres (No. SAND2018-7168R). Sandia National Lab. (SNL-NM), Albuquerque, NM (United States)
3. Purdom JF, Menzel WP (1996) Evolution of satellite observations in the United States and their use in meteorology. In: *Historical essays on meteorology 1919–1995*. American Meteorological Society, Boston, MA, pp 99–155
4. Anderson AD, Mastenbrook HJ (1956) A new upper air data system—the transosonde. *Bull Am Meteor Soc* 37(7):342–350
5. McDowell JC (2018) The edge of space: revisiting the Karman Line. *Acta Astronaut* 151:668–677
6. Stone LM (2014) Outer space and beyond. *Britannica Digital Learning*
7. Angell JK (1961) Use of constant level balloons in meteorology. In: *Advances in geophysics*, vol 8. Elsevier, pp 137–219
8. Haig TO, Lally VE (1958) Meteorological sounding systems. *Bull Am Meteor Soc* 39(8):401–409
9. Taylor HJ, Sitaramaswami M, Krishnamoorthy PN (1952) High altitude balloon experiments and measurement of the heavy primary radiation flux at the geomagnetic equator. In: *Proceedings of the Indian academy of sciences-section A*, vol 36, No 1. Springer, India, p 41
10. Gordon AH (1962) Transosonde studies of the atmosphere. *Nature* 195(4841):552–553
11. Dai Q, Fang X, Li X, Tian L (2012) Performance simulation of high altitude scientific balloons. *Adv Space Res* 49(6):1045–1052
12. Angell JK (1959) The use of transosonde data as an aid to analysis and forecasting during the winter of 1958–1959. *J Geophys Res* 64(11):1845–1853
13. Aragon-Zavala A, Cuevas-Ruiz JL, Delgado-Penín JA (2008) *High-altitude platforms for wireless communications*. Wiley
14. Witze A, NASA launches next-generation scientific balloon. *Nature News*
15. Massaro F, Bergmann M, Campo R, Thiebaut M, Finocchiaro DV, Arcidiacono A, Eutelsat S, Goussetis G, Garcia-Perez J, Amendola G, Riva C (2017) QV-LIFT project: using the Q/V band Aldo Paraboni demonstration payload for validating future satellite systems. In: *23rd Ka and broadband communications conference*
16. Raj NS, Varghese J, Chandra GR (2017) Drones take-off towards legal regime in the United Arab Emirates. In: *2017 international conference on Infocom technologies and unmanned systems (trends and future directions) (ICTUS)*. IEEE, pp 689–693
17. NS, SR, Varghese J, Chandra GR, Iqbal J (2016) Are drones a threat to civil aviation? A retrospective on policies of drones in the United Arab Emirates
18. Fields T, Heninger M, LaCombe J, Wang E (2013) In-flight landing location predictions using ascent wind data for high altitude balloons. In: *AIAA balloon systems (BAL) conference*, p 1294

# Analysis of Water Indices' Level in Nile River over the City of Cairo Using Landsat 8 Satellite Imagery



Sarath Raj, Anusha Santhosh, and Sathiyagayathiri Ramamoorthy

**Abstract** Water level analysis is performed over a water body to find out the changes that have been occurred during a certain span of time. This analysis is done using Normalized Difference Water Index (NDWI) which is considered to be one of the most efficient methods as it provides accurate data. It uses near-infrared and visible green light for this purpose. The analysis is done to get the changes in the water index of the area over 10 years. The study is based on remote sensing data from the Landsat series. This paper's research is based on pictures of the Nile River flowing through Cairo, Egypt, received from Landsat 8, and is accomplished by employing short-wave infrared sensors using Google Earth Engine.

**Keywords** NDWI · Nile River · GEE · QGIS · Landsat 8 · Surface reflectance

## 1 Introduction

The solid-propellant rocket engine is an engine that uses solid fuel as its propellant. They contain both the fluid and oxidizer together in the chemical itself. The solid-propellant rocket technology got a boost in the mid-twentieth century when the government initiatives were developing military missiles [1]. The basic design of the engine consists of the fuel grain or the solid fuel, motor casing, and the nozzle. The fuel grain is placed inside the motor casing where the combustion process takes place. The combustion process of the solid-fuel engine contains multiple phases of which when the propellant changes from solid to liquid to gas state [2]. They are mainly used in various applications because of their easy storage, it is easily handled compared to other types of propellants, and due to their high-density property, and it has a compact size [3].

Solid rocket motors are utilized on aerial and air-to-ground rockets, on model rockets, and as sponsors for satellite launchers. In this type of rocket, the fuel and oxidizer are combined as one into a strong charge which is stuffed into a strong

---

S. Raj (✉) · A. Santhosh · S. Ramamoorthy  
Amity University, Dubai, UAE  
e-mail: [sraj@amityuniversity.ae](mailto:sraj@amityuniversity.ae)

chamber [4]. An opening through the chamber fills in as an ignition chamber. At the point when the blend is touched off, burning happens outside of the charge [5]. Solid rocket engines are consistent with four main parts; initial part is the motor casing which is acting as the engine's protective shell. The second part is the combustion chamber designed to withstand the combustion process load. The third component is the fuel grain (solid propellant), and last part is the nozzle used to increase, expand, and accelerate the combusted gas to produce the desired thrust [6].

Solid-fuel rocket engines are also used in experimental rockets used in the aviation industry to prove the concept of rocket engines and estimate the developments required in the design and performance [7]. It is beneficial for research and aerospace students to conduct various tests and help visualize the concept of any rocket engine. Solid fuels are mainly used as experimental rockets due to their simple design and favorable results [8]. It is also the safest among other experimental rockets because it can be made or bought based on the quantity needed; however, precaution is always needed with any experimental rocket engines, and they also are powered by a solid oxidizer-fuel mixture which makes its ignition easier, prevents leakage issues, and helps decrease the delay time [9].

## 2 Area of Interest

The capital city of Egypt is Cairo which is considered to be the largest city in the Arab world. It is located in northern Egypt also known as Lower Egypt, which is 165 km south of the Mediterranean Sea and 120 km west of the Gulf of Suez Canal and is positioned at 30.0444 N (latitude) and 31.2357 E (longitude). It is metropolitan area with a population of over 20 million and is located near the Nile Delta. The Nile is resuming its ancient path beneath the Aswan High Dam, on the northern side of Lake Nasser. The Nile is separated into two streams north of Cairo, which feed the Mediterranean [6]. Approximately 96% of Egypt's geographic region is desert, with the remaining 4% being agricultural territory. About 98.6% of Egypt's water supplies originate from the Nile's floods. Egyptian farmers have always relied on rainfall since drought signifies a lack of rain, which is just a few millimeters each year. It only rains on the north coast and in Sinai, which occurs often throughout the winter in Egypt's northern shore and the Sinai Peninsula. It was always the result of depressions originating in the Mediterranean Sea [7] (Fig. 1).

## 3 Methodology

The satellite images collected for the data analysis are from Landsat 8, which is an earth observation satellite. It was launched as a collaboration project between the National Aeronautics and Space Administration (NASA) and the US Geological Survey (USGS) on February 11, 2013. The satellite has two payload sensors, the

**Fig. 1** Map of Cairo City



Operational Land Imager (OLI) and the Thermal Infrared Sensor (TIRS) [8]. It offers metadata for bands, such as rescaling. Factor value, thermal constant, etc., which is used for calculations like the temperature of the ground surface. There are 11 different bands, and each band has a different wavelength and resolution. The coastal/aerosol band has a wavelength between the range 0.433–0.453  $\mu\text{m}$ , blue band with a wavelength of 0.450–0.515  $\mu\text{m}$ , and 30 m resolution. The green band has a wavelength of 0.525–0.600  $\mu\text{m}$ , and red band has a wavelength of 0.630–0.680  $\mu\text{m}$ . All these four bands come with a 30 m resolution.

The near-infrared band has a wavelength range of 0.845–0.885  $\mu\text{m}$  with 30 m resolution, there are two types of short-wavelength infrared which has different wavelength ranges, but the same resolution short-wavelength infrared (SWIR)-1 has a wavelength of 1.560–1.660  $\mu\text{m}$  and short-wavelength infrared 2 has a wavelength of 2.100–2.300  $\mu\text{m}$ , and the only difference being that SWIR-1 is used to differentiate moisture content of soil and vegetation and SWIR-2 is used to an improved moisture content of soil and vegetation. The panchromatic band and Cirrus band have a resolution of 30 m with a wavelength of 0.500–0.680  $\mu\text{m}$  and 1.360–1.390  $\mu\text{m}$ , respectively. The Thermal Infrared Sensors in the satellite have wavelengths of 10.60–11.19  $\mu\text{m}$  and 11.50–12.51  $\mu\text{m}$ , but the resolutions remain the same that is 100 m, and the only difference between these sensors is that one is used for thermal mapping and

estimated soil moisture and the other is for improved thermal mapping and estimated soil moisture.

In this research, band 5 and band 6 were utilized to study the water index of the river Nile in the city of Cairo. Data from the year 2011 to 2021 were collected for the water index and surface reflectance analysis. Every time Landsat 8 sends a satellite image, along with it contains the metadata with it. Metadata contains all of the parameters and information about the image quality, including the quantity of reflection and radiation, elevation and azimuth values, thermal constant, and rescaling factor value, among other things.

## 4 Tools

### 4.1 *Google Earth Engine (GEE)*

Google Earth Engine (GEE) is a web portal offering satellite and vector images, cloud-based computing, machine connectivity, and algorithms for data analysis across the global sequence of time series. The data archive is a worldwide array spanning satellite images of over 40 years of several sites that have repeated data for two weeks throughout the whole period and a sizeable collection of regular and sub-daily data. The available information is obtained by various satellites, such as the full sequence Landsat, Modis, Advanced Land Observation Satellite (ALOS). Advanced Oceanographic and Atmospheric Radiometer (THRR), Sentinels 1, 2, and 3 [9]. Data from Landsat 8 have been used for Normalized Difference Water Index.

### 4.2 *QGIS*

QGIS is an open-source, cross-platform, portable Geographic Information System (GIS) tool with Python and C++ plugin development. This is one of the open-source foundations' official initiatives aimed at helping and promoting the collaboration of open-source geometric applications. It was developed in the year 2002 for better visualization of the satellite images collected [10, 11]. Using this software, it will be easier to calculate various data such as water index, vegetation index.

### 4.3 *Mathematical Formulation*

The normalized differential water index (NDWI) standardization is used for the study of water systems. The index uses remote sensing images of green and near-infrared bands for better visualization of the images. In most situations, the NDWI

can efficiently improve water detail. It is susceptible to ground construction and leads to an excessive estimation of water sources. Water bodies with low reflectance reflect only the visible component of the electromagnetic spectrum. Water bodies in liquid form have a higher reflectance on the blue (0.4–0.5 m) continuum than on the green (0.5–0.6 m) and red (0.6–0.7 m) spectrums. Clearwater with the highest reflectance in the visible spectrum's blue region. As a consequence, the water looks blue. In the visible spectrum, turbid water has a greater reflectance.

The formula used for calculating NDWI for Landsat 8 is:

$$\text{NDWI} = (\text{Band 5} - \text{Band 6}) / (\text{Band 5} + \text{Band 6}), \quad (1)$$

where Band 5 is near-infrared and Band 6 is short-wavelength infrared.

These bands are used to get a better image of the reflected areas and the changes that occurred over time. The values of NDWI range from (– 1 to 1) depending upon the tested satellite image, research location, and season. The lower the value, the less water there is. The positive values of NDWI or the values that are equal to 1 refer to deep water quality, while negative values other than 0 refer to characteristics other than water.

## 5 Analysis

For the analysis, GEE was used for the data processing and Landsat 8 is used as it is the latest satellite to be launched and along with that surface reflectance was also used to get a better and clear visualization of the wetland. Once the data have been processed, the downloaded images were imported to QGIS so that the bands are changed for a clear image. The bands used here are B1, B4, and B7 through which the Nile River in the city of Cairo is visualized properly.

The following images have used surface reflectance for better and clear visualization. The band combinations used here include B7, B6, and B11. Figures 2, 3, 4, 5, 6, 7, 8, 9, 10, 11, and 12 show the water index in Nile over Cairo for the year from 2010 to 2021 (Fig. 13).

Figures 14, 15, 16, 17, 18, 19, 20, 21, 22, 23, 24, and 25 show the water index in Nile over Cairo for the year from 2010 to 2021.

## 6 Results and Discussions

In the year 2010, NDWI was calculated to be around 0.45, and it remained almost constant till 2012. There was a sudden decrease in the year 2013 which was about 0.399, and during the years 2014 and 2015, there was an increase in the water index, and it was found to be 0.4. The water index during the years 2016 and 2017 has been increased to 0.5. During the years 2018, 2019 2020, and 2021, the results were found

**Fig. 2** Water index for 2010

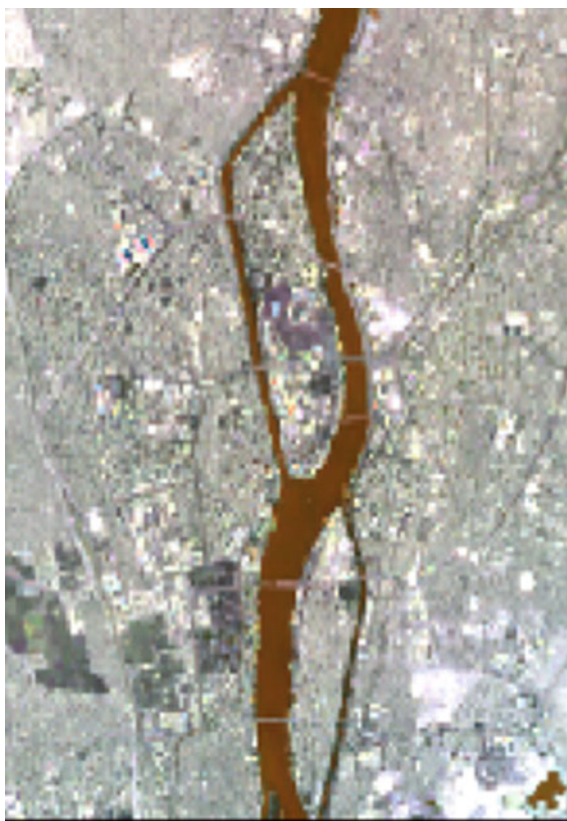
to be 0.45, 0.42, 0.40, and 0.535, respectively, where there was a 12% decrease in the water index from 2018 to 2020 and a 33% increase in water index in the year 2021.

This decrease in the river is due to wastewater and garbage being dumped directly into it, as well as farm runoff and industrial waste, with negative implications for wildlife, especially fishing and human health. Rising sea levels are expected to bring Mediterranean saltwater deep into the rich Nile River delta as a result of climate change. Despite the injection of various forms of waste into the Nile, the water quality does not yet show contamination levels high enough to pose health hazards, except locally, where the prevalence of bacteria suggests unhealthy levels for direct irrigation and fisheries' use.

In addition to surface reflectance, land cover analysis was also performed using QGIS. The band combinations used here are B2, B3, and B5 for surface reflectance land cover and the band combinations used for NDWI land cover were B2, B4, and B5. The NDWI image shows the water level of the river Nile in the city of Cairo, and the surface reflectance image supports the NDWI and provides a clear picture (Fig. 26).



**Fig. 3** Water index for 2011



**Fig. 4** Water index for 2012



**Fig. 5** Water index for 2013



**Fig. 6** Water index for 2014



**Fig. 7** Water index for 2015





**Fig. 8** Water index for 2016



**Fig.9** Water index for 2017



**Fig. 10** Water index for 2018





**Fig. 11** Water index for 2019



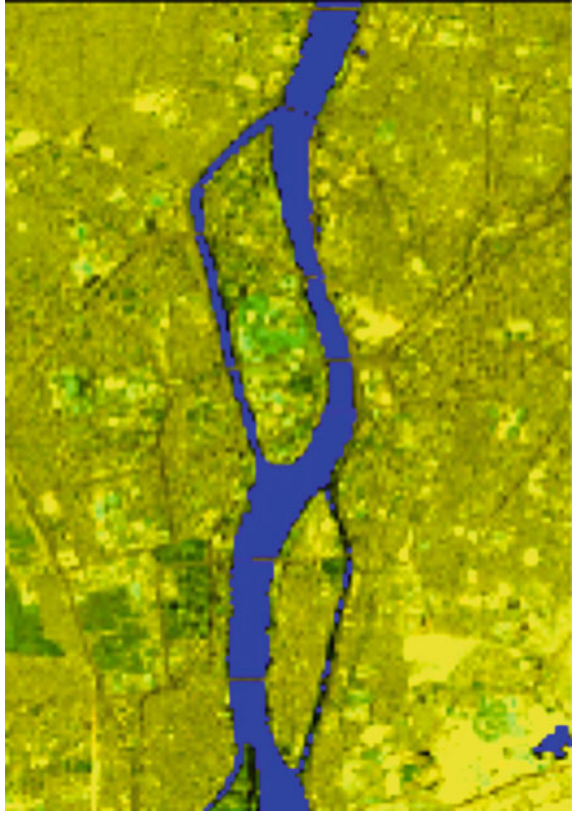
**Fig. 12** Water index for 2020



**Fig. 13** Water index for 2021



**Fig. 14** Surface reflectance for 2010



**Fig. 15** Surface reflectance for 2011



**Fig. 16** Surface reflectance for 2012

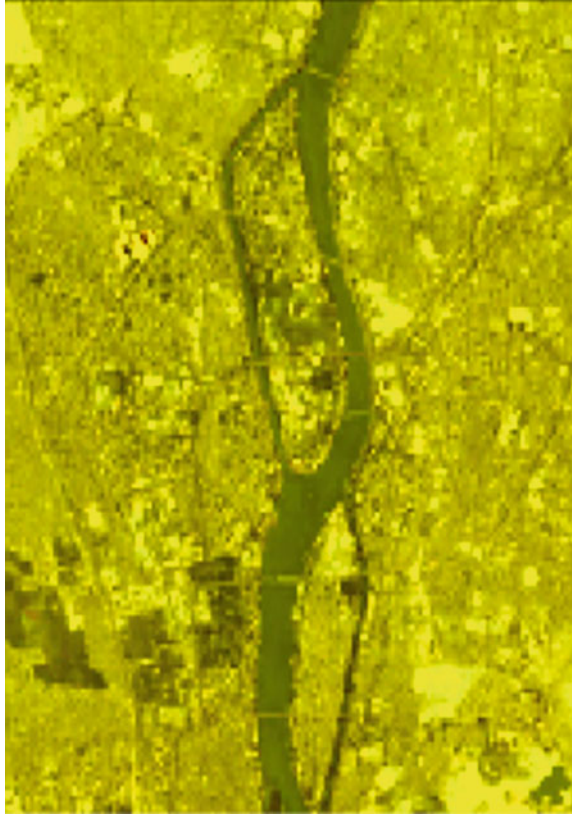




**Fig. 17** Surface reflectance for 2013



**Fig. 18** Surface reflectance for 2014





**Fig. 19** Surface reflectance for 2015



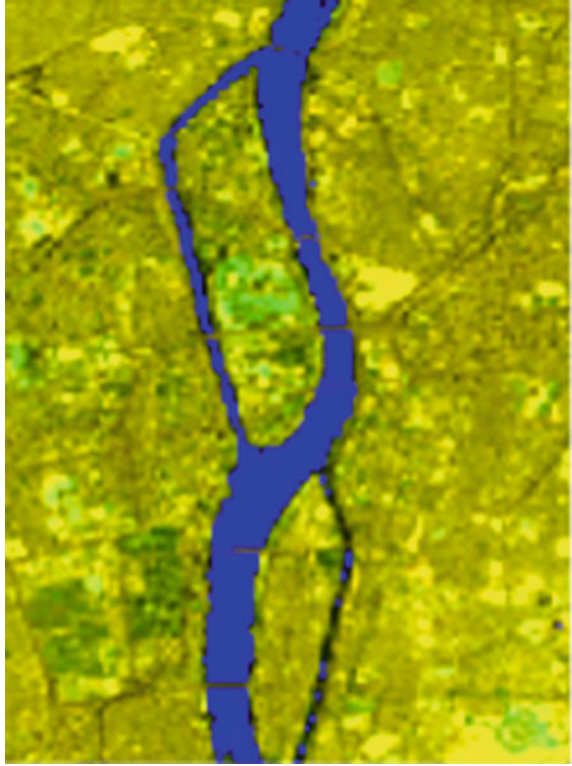
**Fig. 20** Surface reflectance for 2016



**Fig. 21** Surface reflectance for 2017



**Fig. 22** Surface reflectance for 2018



**Fig. 23** Surface reflectance for 2019



**Fig. 24** Surface reflectance for 2020





**Fig. 25** Surface reflectance for 2021



**Fig. 26** Water index level in the Nile over a period of 2011–2021



## 7 Conclusion

This paper deals with the study of the changes in the Nile River flowing through the city of Cairo in Egypt from the year 2010 to 2020. Images from Landsat 8 were collected and a thorough study was done on the Normalized Difference Water Index (NDWI) and surface reflectance was also used to provide clarity on the data collected.

QGIS software was used to change different band combinations and also to calculate the NDWI.

At the end of the study, it can be concluded that after the year 2013, there is a drastic decrease in the water level which is about 30.23%. During the years 2014 and 2015, the water level rose to 0.4 which is a 33.33% increase, whereas there is a 20% decrease in the water level during 2016 and 2017. The water level further decreased from 2018 to 2020 to around 12%, and during the year 2021, it rose up to 33%. The changes in the water levels can be due to dumping wastes in the water body, industrial waste runoff into the river.

## 8 Auxiliary Data

Data type	Data recorded	Sources used
Satellite data	Landsat 8 and band	Tri Dev Acharya, Intae Yang (2015) Exploring Landsat 8, volume 4 edn., South Korea: International Journal of IT, Engineering and Applied Sciences Research (IJIEASR)
Water index	Rainfall patterns and drought levels	El-Asmar, H M, M E. Hereher, and S. B. El Kafrawy. "Surface area change detection of the Burullus Lagoon, North of the Nile Delta, Egypt, using water indices: a remote sensing approach." <i>The Egyptian Journal of Remote Sensing and Space Science</i> 16(1) (2013): 119–123

## References

1. Adam E, Mutanga O, Rugege D (2010) Multispectral and hyperspectral remote sensing for identification and mapping of wetland vegetation: a review. *Wetlands Ecol Manage* 18:281–296
2. Nasser Mohamed Eid A, Olatubara C, Ewemoje T, Talaat El-Hennawy M (2020) Inland wetland time-series digital change detection based on SAVI and NDWI indices: Wadi El-R yan lakes, Egypt, 2nd edn. Remote Sensing Application Society, Egypt
3. Stowe LL, Jacobowitz H, Ohring G, Knapp KR, Nalli NR (2002) The advanced very high resolution radiometer (AVHRR) pathfinder atmosphere (PATMOS) climate dataset: initial analyses and evaluations. *J Clim* 15(11):1243–1260
4. Information sheet on Ramsar Wetlands to designate of Wadi El Rayan and Qaroun lakes as new Ramsar sites. Convention on Wetland of International Importance (Ramsar Convention), 2012: 2009–2012 version, 33p
5. Woodward RT, Wui YS (2001) The economic value of wetland services: a meta-analysis. *Ecol Econ* 37(2):257–270
6. Khalifa MA, El-Khateeb SM, Fayoum oasis between problems and potentials: towards enhancing ecotourism in Egypt. In: 4th international congress on environmental
7. El-Asmar HM, Hereher ME, El Kafrawy SB (2013) Surface area change detection of the Burullus Lagoon, North of the Nile Delta, Egypt, using water indices: a remote sensing approach. *Egypt J Remote Sens Space Sci* 16(1):119–123



8. Reuter D, Irons J, Lunsford A, Montanaro M, Pellerano F, Richardson C, Smith R, Tesfaye Z, Thome K (2011) The operational land imager (OLI) and the thermal infrared sensor (TIRS) on the landsat data continuity mission (LDCM). In: Algorithms and technologies for multispectral, hyperspectral, and ultraspectral imagery XVII, vol 8048. International Society for Optics and Photonics, p 804812
9. Gorelick N (2013) Google earth engine. In: EGU general assembly conference abstracts, vol 15, p 11997
10. Moyroud N, Portet F (2018) Introduction to QGIS. QGIS and generic tools 1:1–17
11. Sarath RNS, Varghese JT, Bhatkar R (2020) Effect of global climate change on land surface temperature over Dubai, United Arab Emirates with the Aid of Landsat 8 Satellite imagery. In: 2020 8th international conference on reliability, Infocom technologies and optimization (trends and future directions) (ICRITO), pp 1289–1292. <https://doi.org/10.1109/ICRITO48877.2020.9197858>

# Design and Analysis of Load Stiffness Tester for Dual Applications in Measurement of Spring Stiffness and Walnut Shell Stiffness



Shivam Aggarwal, M. L. Aggarwal, and Krishan Verma

**Abstract** Load stiffness tester possess an inevitably prominent position in the vast applications of mechanical systems. It is found during experimental investigation that the helical springs possess a linear behaviour, while the conical spring displays nonlinear behaviour. A new methodology based on stiffness measurement and cracking of walnuts is presented in this paper. This experimental setup measures not only stiffness of springs but also measures the stiffness of walnut shell. Stiffness of wide variety of walnuts varies due to number of factors and walnuts can be hard or soft. Stiffness was also assessed using same experimental setup with the load applied and corresponding deflection. Walnut shell stiffness of 90 samples was tested in broadly three categories: hard, medium hard, and soft. Measurement of stiffness provides good estimation whether walnut is soft, medium hard, or hard, besides convenient method of cracking of walnuts by machine. In the present work, manufacturing of single machine and its stiffness tester results are analysed for dual applications in measurement of walnut stiffness and spring stiffness.

**Keywords** Spring · Stiffness · Load cells · Walnut

## 1 Introduction

Springs are very important mechanical components that find a variety of indispensable applications everywhere including industries, automobiles, educational institutes, and many products of day-to-day use. Springs are elastic bodies which have ability to distort or deflect when a load is externally applied, and as soon as the load is removed, the spring tends to regain its initial structure. Springs are used to absorb and release the energy as per the application.

In our setup, we make use of load cells that detect the load applied in form of change in electrical signal which is displayed on digital display unit. The deflection

---

S. Aggarwal (✉) · M. L. Aggarwal · K. Verma  
Department of Mechanical Engineering, JCBUSTYMCA, Faridabad, Haryana 121006, India  
e-mail: [shivamaggarwal231@gmail.com](mailto:shivamaggarwal231@gmail.com)

is measured from the pointer scale fixed on the tester. Load exerted on the spring is transmitted to lower anvil from where it is detected by load cell resulting in a change in shape of strain gauge incorporated into it. The induced strain results in change of resistance and electrical output. Load (Newton) corresponds to deflection (mm).

Aouraze et al. [1] developed a hydraulic spring stiffness tester. Through the suction valve, oil rushes in to exert a load on ram that compresses the spring and reading is obtained. Ayodeji et al. [2] designed and constructed a spring stiffness testing machine for stiffness measurement. Kumar et al. [3] designed spring testing machine for metal analysis of metal springs. In a paper presented by Belapurkar and Jadhav [4], presented a new approach to calculate stiffness of springs. They have used a spring with known dimensions and adjusted it within the machine plates. The upper plate exerted some force on the seated spring and machine is given a vibration. Vibration measuring instruments are employed to take the frequency of spring. The stiffness and frequency of master springs are used to give the stiffness of spring at any other random frequency. Using the ratio of master springs, other springs are tested for stiffness. Nagre et al. [5] developed a hydraulic spring stiffness testing machine. In this machine, a hand-operated hydraulic jack is used to cause movement to hydraulic piston rod that compresses the spring to be tested. This force applied for compression is measured through a pressure gauge and deflection of spring is read in units of length. These readings are used to calculate stiffness of machine. McGranahan and Leslie [6] developed the “DURHAM” variety of a walnut with different properties.

The available literature on the walnuts is very limited. The work on walnut stiffness measurement is rare. This research paper deals with the novel concept of finding stiffness of walnuts using the same machine setup as that of helical springs. This paper presents a novel approach for analysis of load stiffness tester for dual applications in measurement of spring stiffness and walnut shell stiffness using a single machine.

## 2 Experimental Setup and Materials

### 2.1 Experimental Setup

The fabricated experimental setup (Fig. 1) is used for testing the stiffness of spring. It was designed and manufactured using the following main components:

1. Frame or structure.
2. Base or platform.
3. Hand wheel.
4. Upper and lower anvil.
5. Scale with pointer.
6. Digital display unit.



**Fig. 1** Spring load stiffness tester

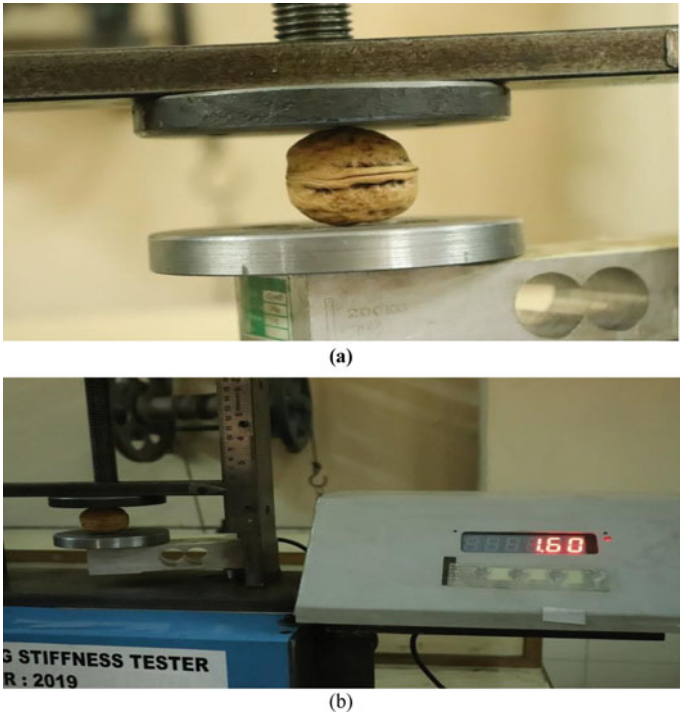
The digital display is both batteries operated as well electricity operated through electrical cable. The setup is designed to take a load in the range of 1–1980N. The same range and setup were used for checking stiffness of walnuts as well as springs (Fig. 2).

Then, the hand wheel is further rotated to apply load on the spring through upper anvil to take multiple readings of load from the display unit of walnuts cracking in order to avoid error. The corresponding readings of deflection are taken in the unit of length from the scale.

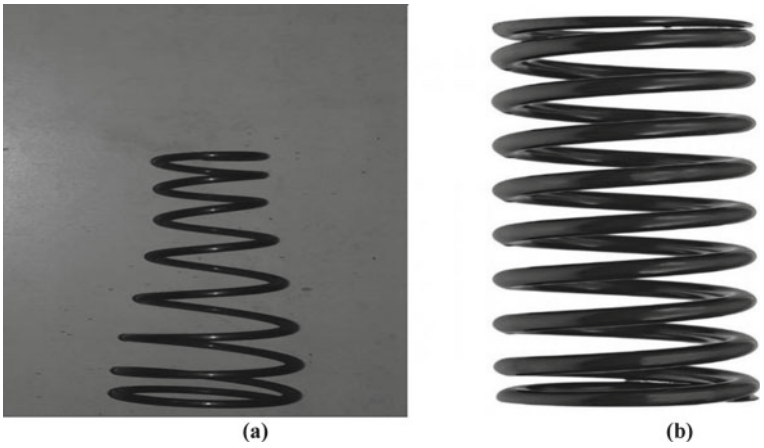
## **2.2 Spring Data (Fig. 3)**

### **Constant Rate Helical Spring:**

- Material: cold drawn steel wire.
- Diameter of wire: 2.5 mm.
- Coil diameter: 28 mm.



**Fig. 2** Spring load stiffness tester for walnut **a** walnut gripping, **b** load and displacement measurement



**Fig. 3** **a** Conical springs, **b** standard rate helical springs

- Spring length: 100 mm.
- Number of turns: 9.

**For Conical:**

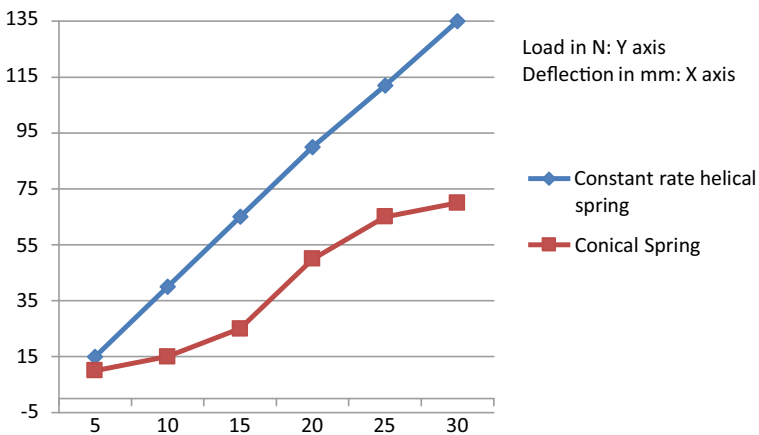
- Material: cold drawn steel wire.
- Wire diameter: 2.5 mm.
- Small end diameter: 20 mm.
- Large end diameter: 38 mm.
- Spring length: 100 mm.
- Number of turns: 9.

### 3 Results and Discussion

#### 3.1 Constant Rate Helical Springs

When a load v/s deflection graph is plotted with load on vertical axis and deflection on horizontal axis, the slope of the graph at any point will give the value of stiffness as it straight in case of helical springs (Fig. 4).

For the same load, the conical spring deflects more as compared to the straight helical springs and shows nonlinear trend. This is due to fact that bigger end of conical is deflected more in the beginning.



**Fig. 4** Comparison of deflection between conical and helical springs

### 3.2 Walnut Stiffness

Force is applied manually by rotating a handle and it pushed moving jaw against walnut to the lower jaw. The applied force was exerted on the load cell which is calibrated to read load on the digital indicator. Its accuracy was  $\pm 0.01$  N. The displacement was measured with the fixed linear scale and its least count was 0.5 mm. Stiffness is load per unit displacement and walnut shell stiffness was measured by a load stiffness tester by measuring load and displacement.

Walnuts are produced in several countries but instead of with China, United States and Iran are major contributors. Total of 90 samples (30 each) of three varieties (hard, medium hard, and soft walnut) were tested. They were purchased from distributor who is selling in these three varieties. A person is adopting various methods of walnut cracking depending upon experience. Stiffness test results of walnuts of samples are shown below (Table 1).

It can be concluded that as stiffness increases, hardness of walnut increases. As there is demand of customer for soft walnuts, customer can be made aware of hardness by marking specifications on walnuts' packets. It will assist in selection of quality walnuts. This load stiffness tester for dual applications in measurement of spring stiffness and walnut shell stiffness provides an economical and simple substitute to costly and complicated spring stiffness machines available for each product stiffness measurement. This electromechanical system is easy to understand and operate with higher accuracy even by a less skilled operator. The digital display unit gives a direct reading, thereby decreasing the time involved in process completion. The provision of battery operation further adds on to the advantages by facilitating the operator to take the reading anywhere, even in absence of proper electrical supply.

**Table 1** Stiffness test results of walnuts of samples

S.No.	Walnuts' sample	Average deflection just before the point of cracking, mm	Average range maximum load to Minimum load, N	Average range maximum stiffness of walnut/Minimum stiffness of walnut, N/mm
1	Sample1: hard walnuts	2.0	720–268	360.0/134.0
2	Sample2: medium hard walnuts	3.5	267–142	76.28/40.57
3	Sample3: soft walnuts	5.5	141–92	25.63/16.72

## 4 Conclusion

This novel load stiffness tester for dual applications provides precise estimation stiffness measurement. Following conclusions were drawn from the present work:

1. For the same load, the conical spring deflects more as compared to the straight helical springs and shows nonlinear trend. This is due to fact that bigger end of conical is deflected more in the beginning.
2. Stiffness of walnut was measured using fabricated machine in the present work. It was found that as stiffness of walnut increases with increase in walnut hardness. As there is demand of customer for soft walnuts, customer can be made aware of hardness by marking specifications on walnuts' packets. It will assist in selection of quality of walnuts.
3. It can be concluded that the fabricated machine is suitable for dual applications in measurement of walnut stiffness and spring stiffness, resulting in cost reduction.

## References

1. Aouraze PM, Dastagir PS, Balu PS, Bajirao LS (2017) A review on spring stiffness testing machine. *Int Res J Eng Technol (IRJET)* 4(01)
2. Ayodeji OO, Abolarin MS, JonathanYisa J, Muftau AG, Kehinde AC (2015) Design and construction of a spring stiffness testing machine. *Am J Eng Res* 4(4):79–84
3. Kumar P, Tisekar N, Sakunde A, Patil S (2017) Design of Spring testing machine. *International conference on advances in thermal system*, pp 1–5
4. Belapurkar PD, Jadhav SS (2015) A new methodology for testing spring stiffness. *Int J Sci Res (IJSR)* 4(12):867–869
5. Nagre NP, Bhosale MS, Patil SC (2017) Hydraulic Spring stiffness testing machine. *International conference on ideas, impact and innovation in mechanical engineering (ICIIME)* 5(6):572–576
6. McGranahan G, Leslie C (2017) Walnut variety named 'DURHAM', Patent No.: 20170215313



# A Review of Vehicle Automation Using Artificial Intelligence



Sudhanshu Sharma, S. A. Khan, Sachin Sharma, Vishal Gupta,  
Yatharth Rajput, and Surya Pratap Singh

**Abstract** Vehicle automation is of interest to researchers; there are many works done in this field, and many things have been achieved in all those researches in this field; this paper represents the chronological order of the details. This paper helps to understand the trend of vehicle automation. The research on vehicle automation starts in the 1920s, when the first vehicle was controlled using a radio controller and in subsequent decades, there have seen many attempts for developing an electric vehicle. The next big milestone was achieved in the 1960s when the first vehicle was automated using vision-guided technology. With the vision-guided system, many semi-automated systems were made which was the base of a fully autonomous vehicle. Automation was done to reduce human work and reduce human error in driving and following. This also saves time and the efficiency of the work is also increased. With the demand for more efficient and easier to use vehicles, this method was introduced. With this mechatronics system, one can achieve full automation driving in less than a decade. In this project, the objective is to create an easy to install system where vehicle can run autonomously without any human interaction with high precision. It can track the object and determine its path. A color tracking system is to be installed to decide the moving path trajectory.

**Keywords** Autonomous vehicle · Cars · Mechatronic system · Automation

## 1 Introduction

Vehicle automation is the term used for controlling vehicles without or with minimum human interference only initial command is required for this to achieve much different hardware and software are used with this the trust between human and machine is also required. To start with automation image processing is to take place where data is taken from the image and then compare to another image this image comes from the

---

S. Sharma (✉) · S. A. Khan · S. Sharma · V. Gupta · Y. Rajput · S. P. Singh  
Department of Mechanical Engineering, Galgotias College of Engineering and Technology, Gr.  
Noida, Uttar Pradesh 201306, India  
e-mail: [sudhanshu.shr@gmail.com](mailto:sudhanshu.shr@gmail.com)

frames from the camera. Many software(s) are used to do image processing (Table 1). Hardware used to operate software and then convert data sent by the software to physical use if software sends a left command, then to turn left, motors are used and vice versa. Artificial intelligence (AI) is used to differentiate different categories of the things like cars, humans, trees, roads, lanes, shadows, etc. Differentiation is required because this can help in determining the size of the object and on which object driving is safe on which object must be avoided. To achieve automation, many types of research are taking place.

The objective of this paper is to review the technology used in automated vehicles. The main focus is identification of the objects by color coding, deciding the path of movement, accuracy, and minimum power consumption. Python code will be used for tracking the object with color coding. System will be enabled to identify the color with high precision and identify the path which requires minimum efforts and energy in the movement.

**Table 1** Methods comparison

S. No.	Method	Pros	Cons
1	Background subtraction method	A generally utilized technique that is easy to carry out	Exceptionally mistaken
		Objects are permitted to turn into a piece of the foundation without obliterating the current foundation	Can't manage fast changes
		It learns itself and shouldn't be reinvented	Instating the Gaussian
		Can be executed in any application	When shadow and other impediments are present, this is not a good deduction
		Give quick recuperation	Gives bogus upsides
		Low memory prerequisite	It doesn't get by with a multimodal foundation
2	Real-time background Subtraction and shadow Detection technique theory	This method has a higher precision than the outline contrast It recognizes shadow as well	The calculation dependent on this technique is very perplexing
3	Template matching	Best method for a specific environment	Possibly happens when there's a one-toon match

## 2 Methods Comparison

### 3 Detailed Review

#### 3.1 *Vehicle Automation Using the Object Tracking System*

In 2016, an automated vehicle was developed using a global positioning system (GPS) where the vehicle drive according to a map but does not know the status of traffic and other objects which is an issue for an automated vehicle. Later on, AI and the Internet of Things (IoT) were combined where an internal system is used for emergency purposes and sending data to cloud service for real-time processing, and this also saves power used for processing data. The problem there was the loss of data and time delay for processing and much additional hardware required for the automation [1]. Similarly, in 2021 Hanying Guo addressed another issue for vehicle automation driver trust. The most important factor of vehicle automation was addressed which is trust between humans and machines since the vehicle must be run automatically. Therefore, it becomes an important factor, and a driver with high trust has fewer accidents [2, 3]. It also detects whether the person is awake and keeping the eye on the road which can occur due to any problem in processing the data; thus, this program is run separately on different cores or threads of the processor, thus giving extra security during driving. With the solution to the trust issue, a technology was invented for Connected and Autonomous Vehicles (CAV) where vehicles communicate with each other; thus, automation will be easy and safe, but there will be a privacy issue for the person [4]. It also uses many sensors in the steering wheel and lidar technology to predict the course of action, thus decreasing the driver's responsibility and checking if the driver keeps his focus on road without distraction. All the above tracking systems and autonomous vehicles are not fully automated. They require constant human interference to drive. There was an attempt for automatic video surveillance for an aircraft which was a European Union (EU) project AVITRACK. Here, algorithm was applied to a multi-camera environment with an overlapping field of view [5].

In 2016, Society of Automotive Engineers (SAE) J3016 had defined the levels of automation from level 0 to level 5. Level 0 denotes complete manual control, whereas level 5 denotes complete automation with no human intervention [6]. In the current situation, maximum vehicles are at level 1 or level 2 because of many traffic rules and the cost of sensors, many companies are working on level 3 automation. Only a few have attained level 3 automation in the laboratory environment [7]. Level 3 automation vehicles work perfectly in many situations, but in some situations, AI gives control to the driver, or in certain situations, the driver wants to take over the control it lets the user decide that, in a special case [8].

Fatigue in driving forms bit by bit with driving time [9]. It was recognized that driving exhaustion can be brought about with lack of sleep and rest limitation, and dull driving errands that request a high mental burden [10]. Analysts have divided

driving fatigue into two categories: rest-related and task-related, based on the causal variables that contribute to the fatigued condition. An abstract propensity associated with normal human circadian cycles is rest-related weakness [11]. Task-related weariness is further divided into dynamic and detached exhaustion, with dynamic exhaustion being triggered by high-thickness traffic or mental overburden, and aloof exhaustion appearing in exceptionally typical settings with little intricacy [12]. Level 3 automation also checks on driver fatigue and helps with that by stopping the vehicle and giving time to the driver.

### ***3.2 Object Tracking in Different Places***

In 2008, visual object tracking was used in robotics where robots were made automated. In this project, a robot was used to track the object's color and place. This type of tracking was used in the delivery and part management systems [13]. Similarly in 2013, motion tracking was used in surveillance cameras where if the object moves an inch from its previous position the camera records the data otherwise discards the recording. During this time, the frames of the camera for surveillance were low; thus, any small changes detection was not possible; thus, 1 inch's movement was used. This system keeps the data of the recording only for the time when the first movement was detected after 30 s from the time when the movement was stopped. Thus, it saves the space in storage and the data can be kept for a long time [14]. In 2015, moving object tracking was improved for changes in pixel for the ground, and underwater object tracking was also introduced, and character recognition was developed this year. Before this program was made the accuracy of tracking underwater was less than 46% which gives many false alarms. Underwater tracking was important in many places like for military use or tracking any rare species of the underwater creature or keeping security in many underwater facilities [15]. Moving object detection for surveillance is the system that was developed to increase security. It uses the background subtraction method to get a clear image of the target to track the subject and text detection. In video, AI was introduced in 2015 which uses the same method, but instead of any person and object, it checks the text which is run by the pre-trained program which has many samples [16, 17].

### ***3.3 Using Raspberry Pi as Processing***

In 2010, a project based on object detection and color-based tracking was created which was the base for Raspberry Pi integration as it requires less memory to run the program [18]. It was further developed in 2014 after the introduction of the first Raspberry Pi which improves the tracking accuracy and speed of the previous generation [19]. In 2016, background subtraction method was developed [20] that creates the foreground of the image. Using this method, processing power was reduced

with a subsequent reduction in processing time and memory for the Raspberry Pi as mentioned in Table 1.

### ***3.4 Programs Develop for Object Tracking and Vehicle Automation***

In 2009, first time background subtraction method was developed which improves the runtime of the program, and it can avoid noises in the image. It improves accuracy from its previous counterpart. This method uses a static camera to capture the frame, and then the background is removed which is already in the program. First background subtraction method uses a temporal average filter which uses many images to create the base of the background. This method requires the user to enter the images during the programming and execution of the program. If the user wants to change the location of the camera, it will be a long process [21]. After the introduction of the background subtraction method, a new method was introduced which was the Gaussian matrix method (GMM) which is superior to the background subtraction method because it is much fast in removing noise from the image and results in better performance. Every pixel in the image is represented by  $p(x, y, t)$ , where  $x$  and  $y$  are image pixels that are coordinated and  $t$  is the time. A GMM value of  $k$  is obtained, and a value of  $k$  between 3 and 5 is employed [22].

In 2012, real-time motion detection techniques were developed. To improve performance, the algorithm combines the temporal differencing method, optical flow method, double background filtering (DBF) method, and morphological processing methods. It comprises three methods.

- (i) Optical flow detection, which detects frame-to-frame optical flow.
- (ii) Double background filtering, here background and foreground information is separated,
- (iii) Region-based matching, here the moving object is detected as alarming [23].

In 2013, a computation was performed in order to work on the presentation of normal component determination. It was also utilized to speed up the extraction of highlights from live versatile camera photos using strong high lights and robust features (SURF) [24].

The design and development of multi-color graphics that was developed in 2014 relied heavily on three-dimensional visual tracking of multi-colors [25, 26]. The previous programs used to take monochrome color, but this program can take color which gives the camera more information. In 2015, two papers were released on the first technique for walker recognition where the program isolates the foreground with image pixel force [27]. The second study was on an objected tracking and

extracting system that used frame differencing and template matching, with the algorithm detecting objects frame by frame. It explains

- (i) Frame differencing is a technique in which the computer compares two video frames to see how they differ. If the pixels have altered, something in the image has obviously changed.
- (ii) Each frame passes the generated templates to the tracking module, which begins tracking the object with an input reference template.

The module searches for the input template in the camera-captured scene using template-matching search [28]. Here, AI was developed which was smart enough to detect the changes in frames and thus only use program to compare the frame which is different thus reducing the processing time.

The researchers created a model that combines tensor features with the Scale Invariant Feature Transform (SIFT) to detect and classify objects in films. Images were blurred first, and then the image was processed in this technique. SIFT is an image descriptor for image recognition that was developed in 1999 [29–31]. It is used in various computer vision fields to match the points in 3D scenes and view-based recognition. As a tool in computer vision technology, a deep neural network (DNN) approach to classifying detected objects was developed. Here, the graphic API of nodes represents the network, and the link represents data that is implementing DNN with OpenVX. The OpenVX Kernel Integrate Extension [32] and a methodology utilizing a non-all-encompassing foundation demonstrating [33] are two more ways to import a neural network into OpenVX that are superior to the prior version. Before the development of SIFT approximate reach of the maximum accuracy in tracking was 87%, but after this development, the efficiency moved to 89% which was of better performance and a low false rate.

In 2018, a dynamic threshold technique based on mathematical morphology was re-released for efficient motion detection and people counting using background subtraction [34]. Object detection for following the object in video frames has come up with the solution of human identification using recorded video. Dynamic Tactile Object Recognition (TOR) uses different tactile sensors to receive additional data which is interrupted by many real-world conditions is used to compute the recognition, and then tracking is done [35]. Some tactile senses using temperature sensor, ultrasound, infra-red, etc., procedure is generated in urgent situations or in situations where the Operational Design Domain (ODD), ODD decides the domain at which the automated vehicle can run safely. This also controls the runtime of the machine. It is the concept that will take the automated vehicle research platform to level 4, when a threshold will be crossed. As a result, the time it takes for a vehicle to move from automated to manual driving mode, known as the handover period, is crucial, as a smooth transition is required to ensure road safety [36, 37].

The year 2021 was the year in which much research was done on this topic which leads to many new methods and improvements of the previous methods. Some of them are using Python for object tracking and the creation of an Open CV-based system to identify and track items on tape. Algorithms for single item tracking based

on deep learning mechanisms [38], Learning Dynamic Compact Memory Embedding (CME) for Deformable Visual Object Tracking (VOT) was developed. This object tracking is not fixed to the grid which can be changed with the requirement that helps with several appearance problems in video recognition system [39–41]. Self-supervised multi-object tracking with cross-input consistency was utilized to create an unsupervised high-performance tracker [42]. It has been demonstrated that a robust, totally unsupervised multi-object tracker can be trained using a new self-supervisory learning signal and cross-input consistency, which ensures that tracking outputs are consistent across different input variants of a single video sequence [43]. In all these processes, a neural network has been trained. AI for various detection and tracking method which incorporates automation in various field has been used. The two-branch network employs classification for foreground separation and an anchor-based method that employs the Siam Region proposal network (SiamRPN). It consists of a Siamese subnetwork for feature extraction and a region proposal subnetwork for prediction, which includes classification and regression branches. In the inference phase, the proposed framework is constructed as a local one-shot detection issue, and SiamDW where SiamDW and SiamRPN++ [44] improve ResNet [45] and successfully apply to Siamese network-based tracking. These types of methods will achieve flexible bounding box regression and the best performance. In Siamese tracking, use template matching for tracking the objects tracking. All the tracking software uses the same basic principle as shown in Fig. 1. As the research in this field increases, then more advancement will happen; thus, autonomous tracking and the controlling system can be achieved, thus advancing the mechatronics field of research. Figure 2 shows the block diagram of object detection and tracking.

Davis et al. focused primarily on ground-based mobile surveillance, which can monitor large areas for people’s activities. The surveillance system can detect movements and recognize objects belonging to different categories, like vehicles, people, and even animals. This system can detect one to several persons simultaneously and analyze their movements to recognize their actions. This paper was focused on the method for detecting motion that is independent of directional motion estimation. This paper explains the use of the theory to identify independent motion within long images. This technique is based on two easy geometric visual inspections of directional components. Because of the projection technique, the difficult task of

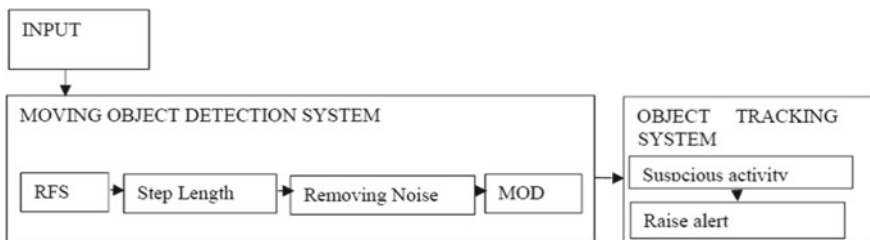


Fig. 1 Moving object tracking flowchart

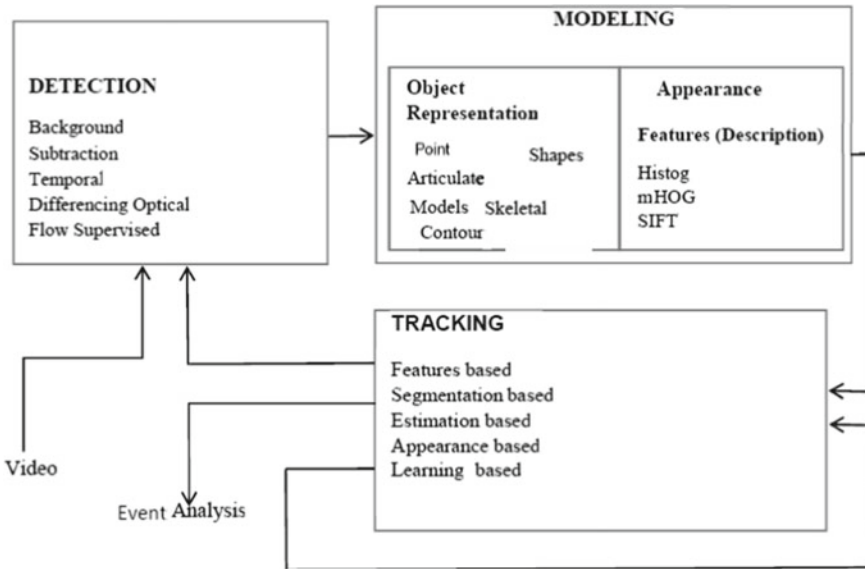


Fig. 2 Block diagram of object detection and tracking

identifying independent movement is decreased to an amalgamation of a robust line [46].

Khan et al. have suggested in their article that Ecumenical GIST may be used to identify the kinetics patterns in videos. This feature allows you to determine the corner of every moving body within each frame. A summary of the results of various videos involving only one or two persons is available. Human kinetics identification is a difficult task and is to be trained on the huge amount of data. Each dataset can be used by only one individual or two. Gist description of features and skeleton detection is extremely effective in locating the flexible forms of the kinetics of the body in the video. The next task is to determine the non-clash or clash between two persons or several individuals and design sensors as violence on the particular clash video [47].

## 4 Hardware and Software Description

### 4.1 Raspberry Pi

Raspberry Pi is the microcomputer which has both CPU and GUP. It is the small size computer. Its size is almost the size of the credit card. It is used in this project because the module which will be used should small because for vehicles like drones, cart, car, etc., has space constrain so to manage in this space we use this computer. It uses



5v DC power supply so it also solves the power problem and since it is available in market anyone can use it.

## ***4.2 Web Camera***

Web camera is the input device which gives images to the computer which can be further analyzed and since camera gives 30 frames per second it also gives more data for the tracking.

## ***4.3 Raspbian OS***

Raspbian OS is the main OS used in Raspberry Pi. It is based on Linux which is an open-source OS. Since the storage and ram is fixed and less so we use this OS because it is light weight software and gives many useful software which helps in controlling Raspberry Pi.

## ***4.4 Python***

Python is a general-purpose programming language with a high level of abstraction. Programmers can now write code in less lines due to this application. It was chosen for this project because it is easy to use and compatible with the Raspberry Pi.

## ***4.5 RPi.GPIO Python Library***

The RPi.GPIO is a Python library that facilitates communication between the Raspberry Pi's General-Purpose Input and Output (GPIO) pins and Python programs.

## ***4.6 OpenCV***

Open CV (Open-Source Computer Vision) is a programming library that focuses on real-time computer vision. It's used since it comes with a pre-programmed object tracking library.

## 4.7 NumPy

NumPy is the fundamental package in the Python, and it is the short form of numerical Python which deals with the numerical value of the program. NumPy is used to perform mathematical operations on array. It guarantees efficient calculation.

## 4.8 Servomotor

A servomotor is the motor with gears attached to it which helps the motor to control its rotation angle and no of turns with its rotation speed. Since user can control these factors of the motor, it becomes most suitable part to control action of vehicles.

The required hardware is mentioned in Table 2.

**Table 2** Required hardware

S.No.	Hardware and software	Specification
1	Raspberry Pi	Raspberry Pi 3 model B 1 GB RAM
2	Web camera	Crystal clear 3p camera
3	SD Card	32 GB 120 mbps
4	Servomotor	SG90 180-degree rotation motor
5	Mobile Phone	For Wi-Fi controlling and external display
6	Raspbian OS	Raspberry Pi OS 64 bit 2022-04-04
7	Python	Python 3.7.0
8	RPi.GPIO Python Library	V0.7.1
9	OpenCV	V4.5.5.64
10	NumPy	V1.21

## 5 Required Hardware

## 6 AI Parameters for Training the Model

### 6.1 Gaussian Matrix Method (GMM)

It uses Gaussian matrix to find the correct value of the color. To do this, we convert all the pixels of the image to matrix form where each pixel is given some value according to the color.

### 6.2 Rule-Based Method

A rule-based AI system is one that aims to develop artificial intelligence (AI) through a model that is exclusively based on pre-determined rules. This simple system is made up of a series of human-coded rules that lead to pre-determined outputs.

### 6.3 Neural Network Method

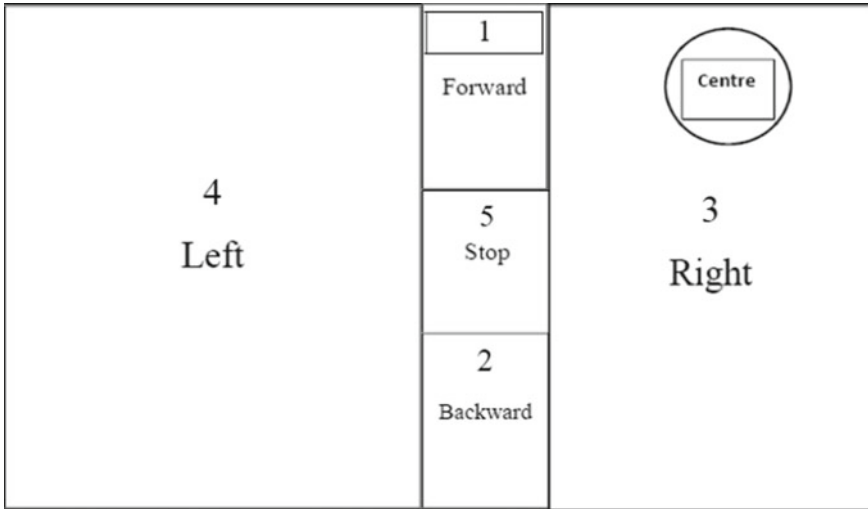
A neural network is an artificial intelligence technique for teaching computers to analyze the data in the same way that the human brain does. Deep learning is a form of machine learning technique that employs interconnected nodes or neurons in a layered structure to mimic the human brain functioning.

Figure 3 and Table 3 depicts how vehicle sees the plane at which it has to move toward the object at desired location. With the movement of motors on left and right, the movement and direction can be changed by changing the rotational movement and direction of the motor.

Figure 4 shows the flowchart of the hardware design.

## 7 Results and Discussions

During the review, it was discovered that the reaction time was long in the early stages of object tracking implementation. Techniques for reducing processing time and improving accuracy and efficiency were investigated. Use of Raspberry Pi addresses these issues significantly. In this study, the operating environment is considered to be without constraints. Real-time surveillance, motion detection technique with color tracking have been studied as a combined technique to track any object of a specified color without any error. Drone used for a specified work is equipped with all these



**Fig. 3** Different segment of image plane

**Table 3** Movement of the vehicle

No.	Status	Command	Left wheel	Right wheel
1	Center in segment 1	Forward	Forward	Forward
2	Center in segment 2	Backward	Backward	Backward
3	Center in segment 3	Right	Forward	Backward
4	Center in segment 4	Left	Backward	Forward
5	Center in segment 5	Stop	Stop	Stop

technologies which results in accuracy and ease of movement with low consumption of energy and minimum response time. The same technology has been studied to be implemented in the automation of a shopping cart in a supermarket. The reviewed work where the object tracking robot was used on Raspberry Pi produced false results. Therefore, it has been explored how to use color tracking and AI which can predict the next frame and thus increases efficiency and reduce total time for processing. In all the previous work, the no. of frames used were 27 fps and, in this project, 30 fps were used which was limit of the camera, and it can work till 44 fps which gives us more data to track the object. In this project, the aim is to improve the efficiency and the object tracking and increase the total no. of frames that can be processed per second. It has also been studied how to make a versatile module which can be installed at many places with plug and play features with minimum changes in the programming section.

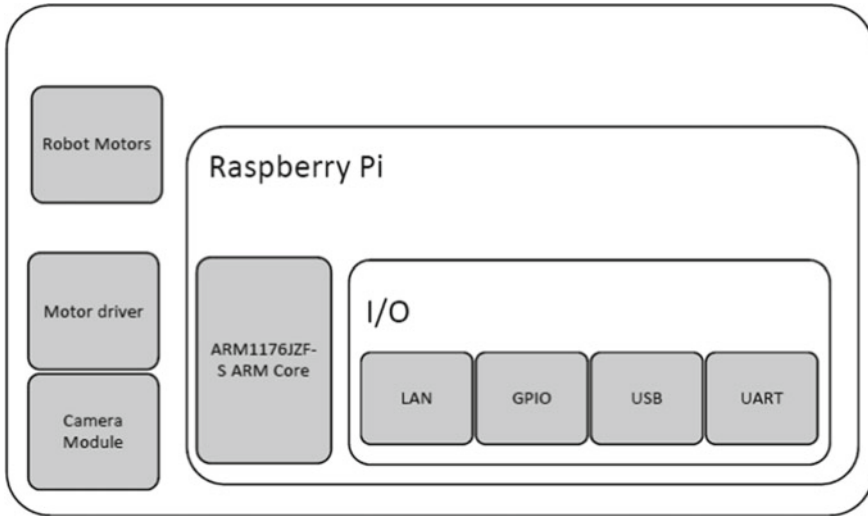


Fig. 4 Flowchart of hardware design

## 8 Conclusion

As complex processes consume large amount of time and energy, they can be automated in order to conserve high amount of energy and time. The conserved quantities can be used to be utilized in several other important tasks. A close monitoring of the difficulties aroused in automated system is a must. Efficient methods need to be discovered to overcome such difficulties so that the required output can be achieved within given time frame. In order to achieve desired output from an automated system, a need to understand the necessary requirements needed is also recognized. Necessary requirements include the machinery needed, skills required, power required, other resources required like platform that includes hardware platform as well as software platform, documents, licensing requirements, etc. The one of the major objectives behind modifying a system is to get the better version of it that must be deployed or integrated within other existing system to enhance the quality of product and services. Suitable environment or deployment is a must to get the best out of the modified system and to reach its ultimate objective. The objective of this project is to explore the method to automate the carts used in supermarkets. The automation system once used in a cart for automatic tracking may reduce the human efforts up to a great extent. An automated cart may track the dress code of store employee and thus simplify the movement. Monitoring needs to be ensured at software level as hardware level. At software level, whether program is serving its required objective is to be ensured. The modified libraries and keywords that may hamper the result of programs needs to be taken care of at all levels. Error needs to be overcome. On the other hand, at hardware level the integrated mechanical systems and resources

should be taken care of. Their replacement with the suitable systems and resources should be ensured in case of failure of any old system integrated within or with it.

## References

1. Gurram R, SweathaSuresh B, Sneha BR, Sushmitha R (2016) Object tracking robot on raspberry Pi using opencv. *Int J Eng Trends Technol (IJETT)* 35(4)
2. Guo H, Zhang Y, Cai S, Chen X (2021) Effects of level 3 automated vehicle drivers' fatigue on their take-over behaviour: a literature review. *J Adv Transp*
3. Rana M, Hossain K (2021) Connected and autonomous vehicles and infrastructures: a literature review. *Int J Pavement Res Technol* 1–21
4. Borg M, Thirde D, Ferryman J, Fusier F, Valentin V, Brémond F, Thonnat M (2005) Video surveillance for aircraft activity monitoring. In: *IEEE conference on advanced video and signal based surveillance*. IEEE, pp 16–21
5. Gkartzonikas C, Gkritza K (2019) What have we learned? A review of stated preference and choice studies on autonomous vehicles. *Transp Res Part C Emerg Technol* 98:323–337
6. Van Brummelen J, O'Brien M, Najjaran H (2018) Autonomous vehicle perception: technology of today and tomorrow. *Transp Res Part C Emerg Technol* 89:384–406
7. Gold C, Happee R, Bengler K (2018) Modeling takeover performance in level 3 conditionally automated vehicles. *Accid Anal Prev* 116:3–13
8. Useche SA, Ortiz VG, Cendales BE (2017) Stress-related psychosocial factors at work, fatigue, and risky driving behavior in bus rapid transport (BRT) drivers. *Accid Anal Prev* 104(April):106–114
9. May JF, Baldwin CL (2009) Driver fatigue: the importance of identifying causal factors of fatigue when considering detection and countermeasure technologies. *Transp Res Part F Traffic Psychol Behav* 12(3):218–224
10. Davenne D, Lericollais R, Sagaspe P et al (2012) Reliability of simulator driving tool for evaluation of sleepiness, fatigue and driving performance. *Accid Anal Prev* 45:677–682
11. Saxby DJ, Matthews G, Warm JS, Hitchcock EM, Neubauer C (2013) Active and passive fatigue in simulated driving: discriminating styles of workload regulation and their safety impacts. *J Exp Psychol Appl* 19(4):287–300
12. Angelov P, Ramezani R, Zhou X (2008) Autonomous novelty detection and object tracking in video stream using evolving clustering & Takagi-Sugeno type neuro-fuzzy system. In: *IEEE international joint conference on neural networks within the IEEE world congress on computational intelligence*, Hong Kong, pp 1457–1464
13. Lavanya MP (2014) Real time motion detection using background subtraction method and frame difference. *Int J Sci Res (IJSR)* 3(6):1857–1861
14. Guo H, Zhang Y, Cai S, Chen X (2021) Effects of level 3 automated vehicle drivers fatigue on their take-over behaviour: a literature review. *J Adv Transp*
15. Ayed AB, Halima MB, Alimi AM (2015) Map reduce based text detection in big data natural scene videos. *Proc Comput Sci* 53:216–223
16. Hussien HM (2014) Detection and tracking sys. of moving objects based on MATLAB. *Int J Eng Res Technol (IJERT)* 03(10)
17. Angelov P, Sadeghi-Tehran P, Ramezani R (2011) A real-time approach to autonomous novelty detection and object tracking in video stream. *Int J Intell Syst* 26(3):189–205
18. Amir S, Siddiqui AA, Ahmed N, Chowdhry BS (2014) Implementation of line tracking algorithm using Raspberry pi in marine environment. In: *IEEE international conference on industrial engineering and engineering management*. IEEE 2014, pp 1337–1341
19. Ayed AB, Halima MB, Alimi AM (2015) MapReduce based text detection in big data natural scene videos. *Proc Comput Sci* 53:216–223

20. Kim C, Lee J, Han T, Kim YM (2018) A hybrid framework combining background subtraction and deep neural networks for rapid person detection. *J Big Data* 5(1):1–24
21. Lu N, Wang J, Wu QH, Yang L (2008) An improved motion detection method for real-time surveillance. *IAENG Int J Comput Sci* 35(1)
22. Weng ENG, Khan RU, Adruce SAZ, Bee OY (2013) Objects tracking from natural features in mobile augmented reality. *Proc Soc Behav Sci* 97:753–760
23. Fu Q, Chen XY, He W (2019) A survey on 3D visual tracking of multicopters. *Int J Autom Comput* 16(6):707–719
24. Soundrapandiyan R, Mouli PC (2015) Adaptive pedestrian detection in infrared images using background subtraction and local thresholding. *Proc Comput Sci* 58:706–713
25. Abdul Malik A, Khalil A, Ullah Khan H (2013) Object detection and tracking using background subtraction and connected component labeling. *Int J Comput Appl* 75(13):1–5
26. Ramya P, Rajeswari R (2016) A modified frame difference method using correlation coefficient for background subtraction. *Proc Comput Sci* 93:478–485
27. Risha KP, Kumar AC (2016) Novel method of detecting moving object in video. *Proc Technol* 24:1055–1060
28. Zhang J, Cao J, Mao B (2016) Moving object detection based on non-parametric methods and frame difference for traceability video analysis. *Proc Comput Sci* 91:995–1000
29. Najva N, Bijoy KE (2016) SIFT and tensor based object detection and classification in videos using deep neural networks. *Proc Comput Sci* 93:351–358
30. Viswanath A, Behera RK, Kuttly K (2015) Background modelling from a moving camera. *Proc Comput Sci* 58:289–296
31. Prabhakar N, Vaithiyanathan V, Sharma AP, Singh A, Singhal P (2012) Object tracking using frame differencing and template matching. *Res J Appl Sci Eng Technol* 4(24):5497–5501
32. Bhuvanawari P, Kumar TS (2014) Moving object tracking using background subtraction technique and its parametric evaluation
33. Liu L, Ouyang W, Wang X, Fieguth P, Chen J, Liu X (2018) Deep learning for generic object detection. *A Survey*
34. Morales-Alvarez W, Sipele O, Léberon R, Tadjine HH, Olaverri-Monreal C (2020) Automated driving: a literature review of the take over request in conditional automation. *Electronics* 9(12):2087
35. Zhang XQ, Jiang RH, Fan CX, Tong TY, Wang T, Huang PC (2021) Advances in deep learning methods for visual tracking: literature review and fundamentals. *Int J Autom Comput* 18(3):311–333
36. Zhu P, Yu H, Zhang K, Wang Y, Zhao S, Wang L et al (2021) Learning dynamic compact memory embedding for deformable visual object tracking. *arXiv preprint [arXiv:2111.11625](https://arxiv.org/abs/2111.11625)*
37. Ye J, Chen Y, Wang N, Wang X (2021) Adaptation for implicit object tracking and shape reconstruction in the wild. *arXiv preprint [arXiv:2111.12728](https://arxiv.org/abs/2111.12728)*
38. Pan X, Yang TY (2021) Image-based monitoring of bolt loosening through deep-learning-based integrated detection and tracking. *Comput-Aided Civil Infrastruct Eng*
39. Zhou Z, Fu H, You S, Borel-Donohue CC, Kuo CCJ (2021) UHP-SOT: an unsupervised high-performance single object tracker. In: 2021 international conference on visual communications and image processing (VCIP). IEEE, pp 1–5
40. Bastani F, He S, Madden S (2021) Self-supervised multi-object tracking with cross-input consistency. *Adv Neural Inf Process Syst* 34
41. Li B, Yan J, Wu W, Zhu Z, Hu X (2018) High performance visual tracking with Siamese region proposal network. In: Proceedings of IEEE conference computer pattern recognition (CVPR), pp 8971–8980
42. Fan H, Ling H (2019) Siamese cascaded region proposal networks for real-time visual tracking. In: Proceedings of IEEE conference computer pattern recognition (CVPR), pp 7952–7961
43. Li B, Wu W, Wang Q, Zhang F, Xing J, Yan J (2019) Siamrpn++: evolution of Siamese visual tracking with very deep networks. In: Proceedings of IEEE conference on computer vision pattern recognition (CVPR), pp 4282–4291

44. Zhang Z, Peng H (2019) Deeper and wider siamese networks for real-time visualtracking. In: Proceedings of IEEE conference on computer vision pattern recognition (CVPR), pp 4591–4600
45. He K, Zhang X, Ren S, Sun J (2016) Deep residual learning for image recognition. In: IEEE conference on computer vision pattern recognition (CVPR), pp 770–778
46. Davis L, Fejes S, Harwood D, Yacoob Y, Hariatoglu I, Black MJ (1998) Visual surveillance of human activity. In: Asian conference on computer vision. Springer, Berlin, Heidelberg, pp 267–274
47. Khan A, Janwe NJ (2017) Review on moving object detection in video surveillance. *Int J Adv Res Comput Commun Eng* 6:664–670



# Ultra-Broadband with High Absorption Rate Metamaterial Absorber on Thin Substrate for Airborne Radar Applications



Maxon Okramcha and Malay Ranjan Tripathy

**Abstract** In this paper, the design and simulation results of an ultra-broadband with high absorption rate metamaterial absorber known as MMA are presented. The structure of this material is composed of rectangular copper patches that are arranged on top of an FR-4 Epoxy dielectric substrate with a thickness of 2.7 mm. The relative bandwidth above 90% absorption rate is 73.3%, which covers X-band and middle section of the Ku-band of microwave frequencies. In order to better understand the absorption mechanism and optimize the design, the electric field, magnetic field, and surface current distributions of the MMA, as well as the effects of many important structural parameters on the absorber, are studied. The high absorption rate and ultra-broadband characteristics of the X-band and middle section of Ku-band enable it to be used for a wide range of applications, such as secret detection, thermal sensor, electronic-clocking devices, electromagnetic stealth, and shielding.

**Keywords** Ultra-broadband metamaterial absorber · Polarization-insensitive · High absorption rate · X-band · Ku-band · Stealth

## 1 Introduction

The term metamaterial refers to materials that have been engineered to have needed qualities which are not found in natural materials. They are made up of numerous elements made of composite materials including metals and polymers. Metamaterials, due to their surprising properties in sub-wavelength scale, have been studied experimentally in various applications at different EM spectra [1]. With the introduction of “perfect metamaterial absorber” in 2008, the interests among many researchers have skyrocketed in the last few years. Electromagnetic (EM) properties of metamaterials are largely determined by the materials’ characteristics along with their size and layout [2].

---

M. Okramcha (✉) · M. R. Tripathy  
Department of Electronics and Communication, Amity University, Noida, Uttar Pradesh, India  
e-mail: [maxonokram8@gmail.com](mailto:maxonokram8@gmail.com)

As a result, metamaterial-based EM absorbers can attain better absorption rates of electromagnetic waves of a certain frequency by constructing sizes and structures that have arbitrary permittivity and permeability. Because of its thin thickness, compact size, simple construction, reduced weight, and high absorption rate, metamaterial absorbers (MMA) have advantages over traditional absorbers [1, 2]. They may be utilized in antennas, super lenses, cloaking, absorbers, sensor, filter, and other domains.

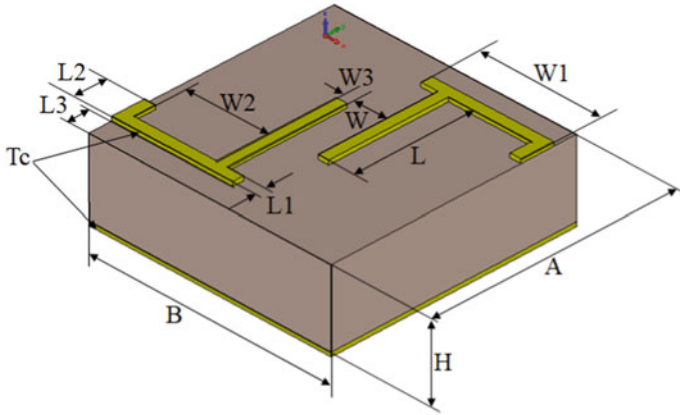
The structures of metamaterial absorbers usually consist of a metallic frequency selective surface (FSS) which are arranged in periodic pattern and then the structure is printed on a very thin grounded dielectric substrate [3]. Narrow-band absorbers, such as single-band and dual-band/multi-band, are used for narrow-band applications. However, a broadband metamaterial absorber is required in many practical applications such as broadband sensing, broadband thermal radiometers, and so on. Therefore, the broadband absorber has long been a hot topic. Here are two strategies which were commonly used by researchers for designing broadband metamaterial absorbers. The first method is to sum up multiple sub-units within a co-planar super-unit resonant structure, and the second approach is to construct alternating multiple patterning metallic structures and dielectric layers with different geometric variables assembled vertically [4–6]. A stack of two or more layers of metal construction are used to increase the absorption bandwidth [7]. Furthermore, a full dielectric metamaterial absorber can likewise accomplish broadband absorption [8].

The suggested study aims to achieve a greater absorption rate with increased bandwidth that covers X-band and the middle of the Ku-band. In this paper, an MMA on a 2.7 mm thick FR-4 Epoxy substrate is proposed, which qualifies for a compact absorber with a high absorption bandwidth ranging from 7.9 GHz to 17.06 GHz, suited for both X-band and Ku-band applications. Section 2 gives a brief idea about design and simulation technique for the proposed structure, Sect. 3 analyzes the results, and Sect. 4 wraps up the article.

## 2 Design and Simulation

The suggested MMA unit cell is shown in Fig. 1 with the dimensions listed in Table 1. The suggested structure has  $9 \times 9 \times 2.7 \text{ mm}^3$  and has three layers: (1) The design started with two L-shaped copper patches (with the conductivity of  $5.8 \times 10^{13} \text{ S}/\mu\text{m}$ ) on the opposite to each other with the longer side coupled in a broadside manner, (2) FR-4 substrate ( $\epsilon_r = 4.39$  and  $\tan \delta = 0.02$ , with thickness 2.7 mm) as a dielectric layer is placed in the middle layer, and (3) a copper plane acting as a ground metallic layer at the bottom. Briefly, the FR-4 dielectric is sandwiched by a copper sheet having 0.035 mm thickness. The resonator structure is attached to the top layer of the substrate and the ground sheet on the bottom layer.

CST Microwave Studio is used to calculate and analyze the design. Simulation multiplier is a frequency domain solver (FDS) with a limited frequency range of 7–19 GHz and a normal background. In the  $x$ -direction and in the  $y$ -direction, the



**Fig. 1** Unit cell of the suggested UMMA structure

**Table 1** Designed parameters of the suggested UMMA

Parameters (mm)					
A	B	H	L	W	Tc
9	9	2.7	4.4	1.26	0.035
L1	W1	L2	W2	L3	W3
0.4	4.5	1.2	3.08	0.85	0.4

boundary condition is set to unit cell, and in the  $z$ -direction, the boundary condition is set to open. The total structure’s absorption can be determined using a formula [9],

$$A(\omega) = 1 - |S_{11}(\omega)|^2 - |S_{21}(\omega)|^2, \tag{1}$$

where  $|S_{11}(\omega)|^2$  is the reflected power and  $|S_{21}(\omega)|^2$  is transmitted power. As the MMA structure has a complete metallic layer on the ground, the transmittance becomes zero ( $|S_{21}(\omega)|^2 = 0$ ) [9]. So, Eq. (1) is reduced as

$$A(\omega) = 1 - |S_{11}(\omega)|^2 \tag{2}$$

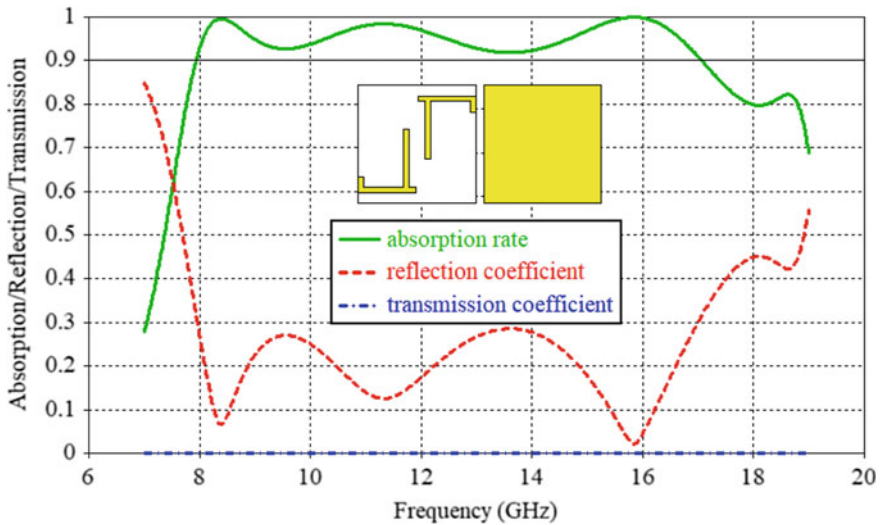
### 3 Simulation Results and Discussion

Figure 2 depicts the MMA’s simulated absorption, reflection, and transmission response over a frequency range of 7–19 GHz. We see an ultra-broadband property from 7.9 GHz to 17.06 GHz below  $-10$  dB in reflection coefficient, and the

absorption rate at 8.392 GHz, 11.332 GHz, and 15.844 GHz is found to be 99.5%, 98.4%, and 99.9% for the suggested structure, respectively.

When compared to the previously reported broadband MMA in the microwave range (Table 2), the suggested MMA has demonstrated its superiority in terms of compactness, bandwidth coverage, and absorption rate. Table 2 shows that the absorption rate is only 80–90% with reduced bandwidth coverage for the pre-existing work; however, we prove that the suggested ultra-broadband MMA outperforms the reference works [10–14].

In actuality, incident EM waves frequently have many polarization components; hence, the absorber must be polarization-insensitive. As a result, the recommended ultra-broadband MMA's polarization-insensitivity is explored (Figs. 3 and 4). The absorption response under the incidence of traverse electric (TE) and traverse magnetic (TM) polarization waves minimally altered during the reported frequency



**Fig. 2** Simulated absorption, reflection, and transmission response of the suggested ultra-broadband metamaterial absorber

**Table 2** Comparison of several broadband MMA in microwave range

S.No.	Reference no	Unit cell size (mm <sup>2</sup> )	Frequency range (GHz)	Absorption rate (%)
1	[10]	11 × 11	7.8–14.7	90
2	[11]	9 × 9	8.85–14.17	90
3	[12]	12 × 12	4.98–12.58	90
4	[13]	6.67 × 5.33	8.71–11.44	80
5	[14]	10.3 × 10.3	13.40–14.25	90
6	This work	9 × 9	7.9–17.06	> 90

range, as shown in Fig. 3. The effects of different polarization angles on the absorption of ultra-broadband MMA are then investigated in TE mode, as shown in Fig. 4.

As we see in Fig. 4, the incident angles in TE mode are varied by  $10^\circ$  and taken the variation from  $0^\circ$  to  $30^\circ$ . In this, we see that up to  $15^\circ$ , there is less variation in the response, but when the angle reaches  $20^\circ$ , we see a slight deviation in the middle

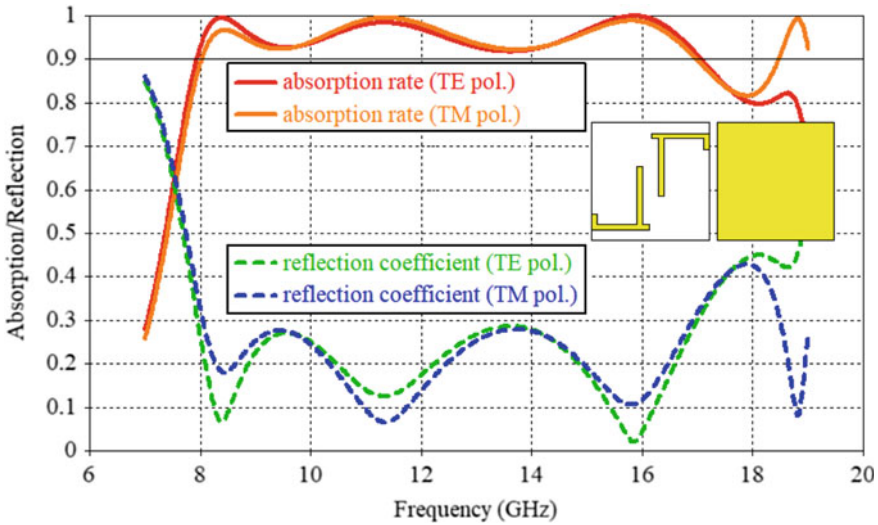


Fig. 3 Simulated absorption and reflection response for TE and TM at normal incident

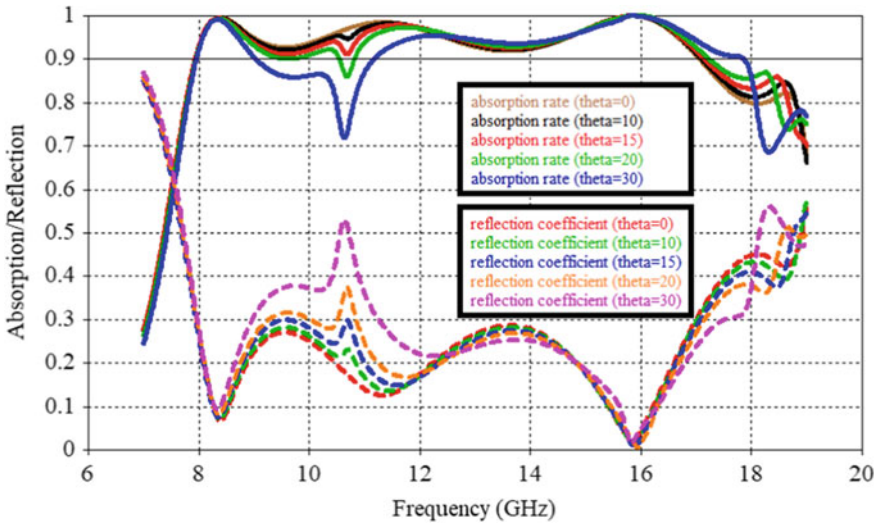
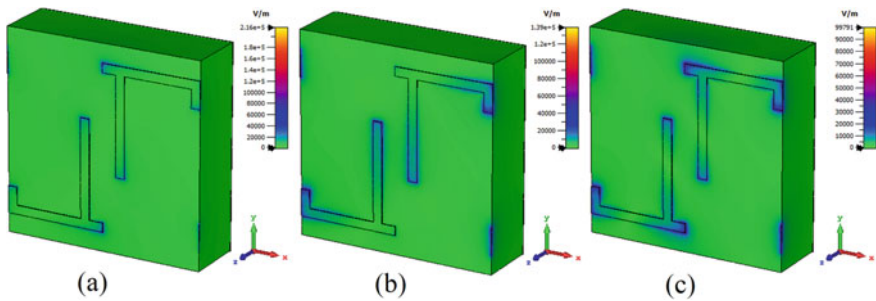


Fig. 4 Effect of different polarization angle on the absorption rate in TE mode of suggested UMMA

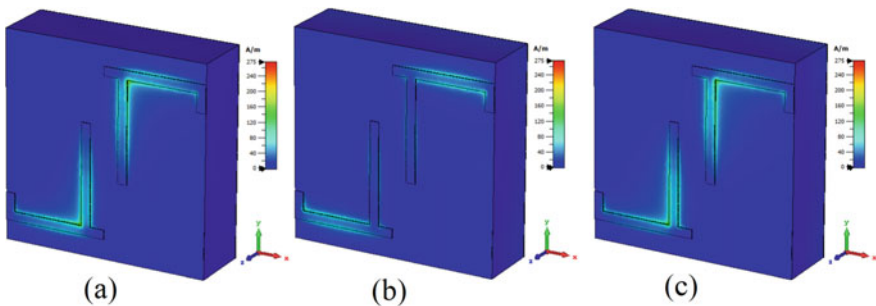
portion of X-band, but the absorption rate is above 80% overall. When the angle reaches  $30^\circ$ , we see a major deviation this is due to the lack of fourfold symmetry in the resonating patch and mainly responsible by the dimension of  $L$ . In conclusion, we can say that up to  $20^\circ$  variation in the incident angle, there is polarization-insensitivity, but if the variation goes above  $30^\circ$ , we see polarization sensitiveness.

For better understanding of the absorption mechanism, the electric field distribution, magnetic field distribution, and surface current distribution of the MMA are investigated (see Figs. 5, 6 and 7). To make the study easier, three different frequencies of EM waves in TE mode have been chosen for discussion: 8.392, 11.332, and 15.844 GHz. The electric fields are spread throughout the terminal area of the patch, as shown in Fig. 5. The extended base section in broadside of the L-shaped patch is accountable for the 8.392 GHz radiation (Fig. 5a). The top side and lower corner of the base of the L-shaped patch are accountable for 11.332 GHz radiation (Fig. 5b), and the combination of resonating points of 8.392 and 11.332 GHz is responsible for 15.844 GHz (Fig. 5c).

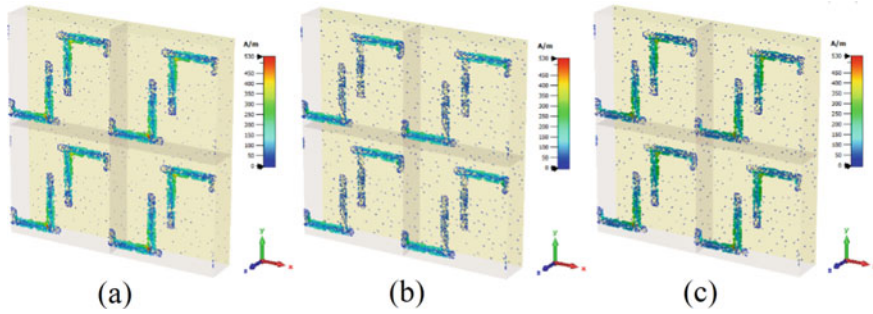
The magnetic field distribution of the suggested MMA is depicted in Fig. 6. Here, we see that most of the distribution lies in the middle portion of the L-shaped patch. The resonance and radiation of 8.392 GHz is caused by the connecting area and the vertical portion of the L-shaped patch (Fig. 6a). The magnetic field of 11.332 GHz



**Fig. 5** Electric field distribution at **a** 8.392 GHz, **b** 11.332, and **c** 15.844



**Fig. 6** Magnetic field distribution at **a** 8.392 GHz, **b** 11.332, **c** 15.844



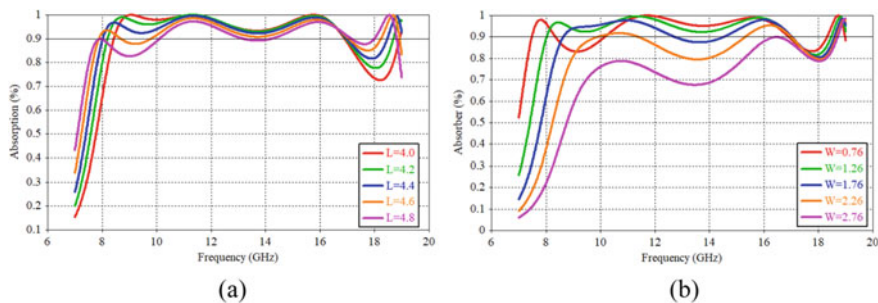
**Fig. 7** Surface current distribution at **a** 8.392 GHz, **b** 11.332, and **c** 15.844

mostly lies in the base portion of the L-shaped patch (Fig. 6b) and for 15.844 GHz, it has some similarity with 8.392 GHz but mostly lies in the base portion of the L-shaped patch (Fig. 6c).

Figure 7 gives a brief idea about the surface current distribution of the suggested MMA. The resonance and radiation of 8.392 GHz is caused by the connecting area and the vertical portion of the L-shaped patch (Fig. 6a). The surface current of 11.332 GHz mostly lies in the base portion of the L-shaped patch (Fig. 6b), and for 15.844 GHz, it has some similarity with 8.392 GHz but mostly lies in the base portion of the L-shaped patch as well (Fig. 6c).

For further understanding of the resonance and radiation at the operating frequencies, we perform parametric study to show which parameter is responsible for the absorption at 8.392 GHz, 11.332 GHz, and 15.844 GHz.

Figure 8 illustrates rate of absorption for the suggested MMA by changing vertical dimension ( $L$ ) in Fig. 8a and base dimension ( $W$ ) in Fig. 8b of the suggested MMA. In Fig. 8a, due to the increase in dimension of  $L$ , the bandwidth in the lower frequency tend to shift toward left side and the rate of absorption in the mid-frequency range keeps on decreasing. When the dimension of  $W$  is increased in Fig. 8b, the absorption performance degrades with increasing frequency.



**Fig. 8** Changing the parameters of **a** vertical dimension of L-shaped ( $L$ ) and **b** base dimension of the L-shaped ( $W$ ) for the suggested UMMA



Figure 9 illustrates rate of absorption for the suggested MMA by changing the base width ( $L1$ ) in Fig. 9a and base length ( $W1$ ) in Fig. 9b of the suggested MMA. In Fig. 9a, when the base width ( $L1$ ) increase, we see the rate of absorption increases but when the value decreases, the absorption at the middle frequency range decreases below 90% but above 80% which is also desirable. When the length of the base ( $W1$ ) varies, we saw undesirable absorption rate when the value increases. But when we decrease the value of  $W1$ , we saw that at the lower portion of the frequency range the absorption rate decreases proving that the parameter that we have taken exhibits greater absorption performance.

Figure 10 illustrates the rate of absorption for the suggested MMA by changing the arm length ( $L2$ ) in Fig. 9a and arm width ( $W2$ ) in Fig. 10b. In Fig. 10a, when we increase the arm length from 1 to 1.4 mm, we see rate of absorption in the lower frequency increases, and when  $L2 = 1$  mm, the absorption at the middle portion decreases. But overall, the absorption rate stays at 90% for the entire frequency range. In Fig. 10b, we vary the arm width by 0.1 mm. In this, there is not much of the change in the rate of absorption concluding that the change in the arm width ( $W2$ ) doesn't influence much in the absorption of the MMA.

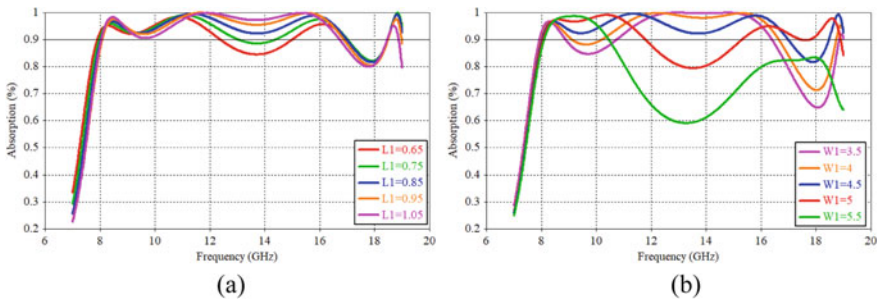


Fig. 9 Changing the parameters of **a** base width of the L-shaped ( $L1$ ) and **b** base length of L-shaped ( $W1$ ) for the suggested UMMA

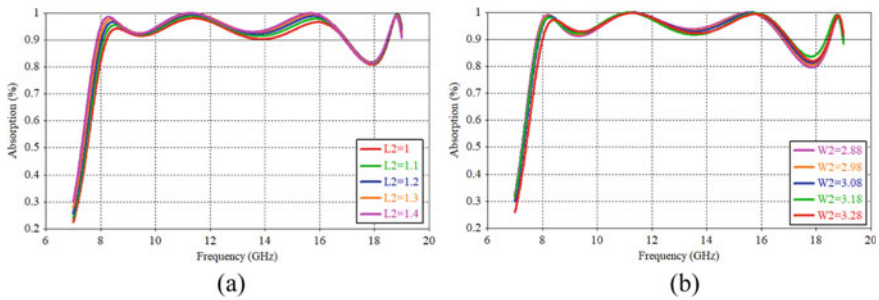
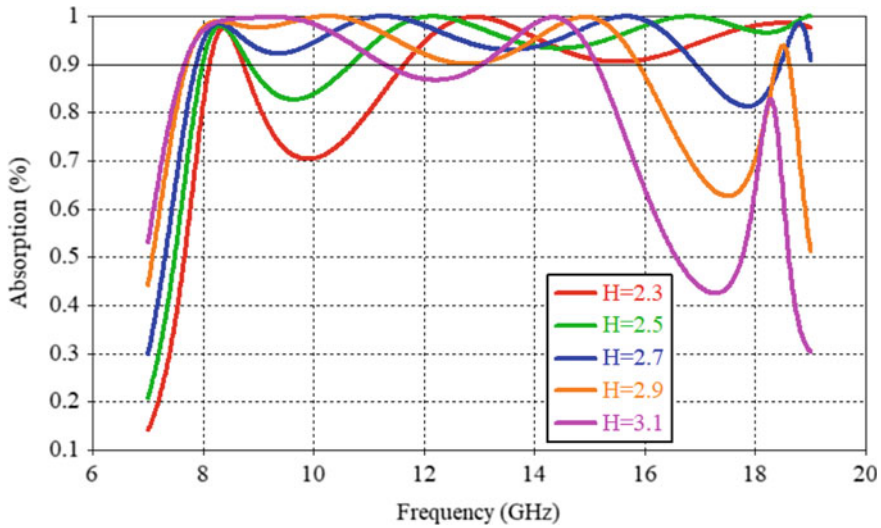


Fig. 10 Changing the parameters of **a** small arm length of the L-shaped ( $L2$ ) and **b** small arm width of L-shaped ( $W2$ ) for the suggested UMMA





**Fig. 11** Changing the substrate thickness ( $H$ ) of the suggested UMMA

Figure 11 illustrates the variation in the substrate thickness ( $H$ ) and change in the rate of absorption by MMA. We start off the simulation when  $H = 2.3$  mm, in this we see that the ultra-broadband property is reduced giving only dual-band. From the figure, we can conclude that if we decrease the thickness, it will affect the rate of absorption in the lower frequency. Then when  $H = 3.1$  mm, it also exhibits dual-band property leading to the decrease in the rate of absorption in the higher frequency. When  $H = 2.7$  mm which is the proposed dimension, we see that the ultra-broadband property is maintained from 7.9 GHz to 17.06 GHz with absorption rate above 90%, proving that the best thickness is 2.7 mm.

## 4 Conclusion

An ultra-broadband with very high absorption rate is proposed in this paper. The frequency range is taken from 7 to 19 GHz for this simulation. In the simulation results, we see the radiation below  $-10$  dB from 7.9 to 17.06 GHz with absorption rate over 90% in the entire frequency region. We have taken 8.392, 11.332, and 15.844 GHz as the reference frequency and found that the rate of absorption is 99.5, 98.4, and 99.9% at the respective frequencies. The absorption bandwidth covers entire X-band and up to middle portion of Ku-band. Since the structure lag fourfold symmetry, the polarization-insensitive occurs up to  $20^\circ$  of the incident angles. We perform different parametric studies presenting that the suggested design has the best absorption rate out of all the possible parameters. The substrate thickness is

only 2.7 mm adding a feature of this design, making it a low profile and less bulky component that can be widely used for appropriate microwave applications.

## References

1. Okramcha M, Tripathy MR (2021) Design and analysis of multi-band polarization-insensitive annular ring metamaterial absorber. In: 2021 8th international conference on signal processing and integrated networks (SPIN), pp 108–111
2. Ji S et al (2019) An ultra-broadband metamaterial absorber with high absorption rate throughout the X-Band. *Physica Status Solidi (b)* 256.11:1900069
3. Sen G, Islam SN, Banerjee A, Das S (2017) Broadband perfect metamaterial absorber on thin substrate for X-band and Ku-band applications. *Prog Electromagnet Res C* 73:9–16
4. Wang AX, Qu SB, Dai HL, Zhang GP, Wang WJ, Yan MB (2019) Design of ultrathin five-band polarization insensitive metamaterial absorbers. In: 2019 IEEE 2nd international conference on electronic information and communication technology (ICEICT). IEEE, pp 658–661
5. Arezoomand AS, Zarrabi FB, Heydari S, Gandji NP (2015) Independent polarization and multi-band THz absorber base on Jerusalem cross. *Optics Commun* 352:121–126
6. Huang L, Chowdhury DR, Ramani S, Reiten MT, Luo SN, Taylor AJ, Chen HT (2012) *Opt Lett* 37:154
7. Ye YQ, Jin Y, He S (2010) *J Opt Soc Am B-Opt Phys* 27:498
8. Pu M, Wang M, Hu C, Huang C, Zhao Z, Wang Y, Luo X (2012) *Opt Express* 20:25513
9. Bağmancı M, Akgöl O, Özak Türk M, Karaaslan M, Ünal E, Bakır M (2019) Polarization independent broadband metamaterial absorber for microwave applications. *Int J RF Microwave Comput Aided Eng* 29(1):e21630
10. Sun J, Liu L, Dong G, Zhou J (2011) *Opt Express* 19:21155
11. Wang BY, Liu SB, Bian BR, Mao ZW, Liu XC, Ma B, Chen L (2014) *J Appl Phys* 116:094504
12. Ma JJ, Tong WH, Shi K, Cao XY, Gong B (2014) *Prog Electromag Res* 49:73
13. Ozden K, Yucedag OM, Kocer H (2016) Metamaterial based broadband RF absorber at X-band. *AEU-Int J Electron Commun* 70.8:1062–1070
14. Stephen L, Yogesh N, Subramanian V (2019) Realization of bidirectional, bandwidth-enhanced metamaterial absorber for microwave applications. *Sci Rep* 9.1:1–9

# Experimental Design of a Novel Winglet for Aircraft



Sarath Raj, Shone George Kurian, and Sathiyagayathiri Ramamoorthy

**Abstract** Winglets are basically nonplanar lifting surfaces that help in reducing wingtip vortices and induced drag associated with it. Winglets help to improve the lift to drag ratio ( $L/D$ ) without significantly increasing the wing span. This paper attempts to design a novel winglet for aircraft, and parameters like lift, drag, and vortex intensity will be analyzed using CFD software ANSYS CFX. Design software SolidWorks is used in modeling the wing and winglet geometry. Extensive CFD simulations of selected winglets and the newly designed winglet will be conducted, and its results will be compared against the results of the CFD simulations conducted for a base wing without any winglets. These simulations will be carried out with the winglets at various angles of attack to understand the performance of each of the designs under various flight conditions. The results obtained by these CFD simulations will be validated by verifying with the results obtained theoretically. Other parameters will be kept constant so as to get consistent results without the influence of external conditions other than the angle of attack. A potential new and optimized winglet can help reduce fuel consumption, which also helps to reduce the emission levels. At the same time, it can also increase the service life of engines and reduce maintenance frequency as the thrust output required by the engine can be reduced (reduced load on the engines) as drag is reduced.

**Keywords** Aircraft · Winglet · CFD · SolidWorks · Vortex · Drag

## 1 Introduction

It has been a known fact for many years that a lifting system with a nonplanar surface should have less induced drag than a planar wing. One of the earliest known patent for vertical surfaces at the wingtips were obtained by Lancaster in the year 1897. Years following that, scientists and engineers conducted critical theoretical analysis and research into this matter and concluded that significant improvements are possible in

---

S. Raj (✉) · S. G. Kurian · S. Ramamoorthy  
Amity University, Dubai, UAE  
e-mail: [sraj@amityuniversity.ae](mailto:sraj@amityuniversity.ae)

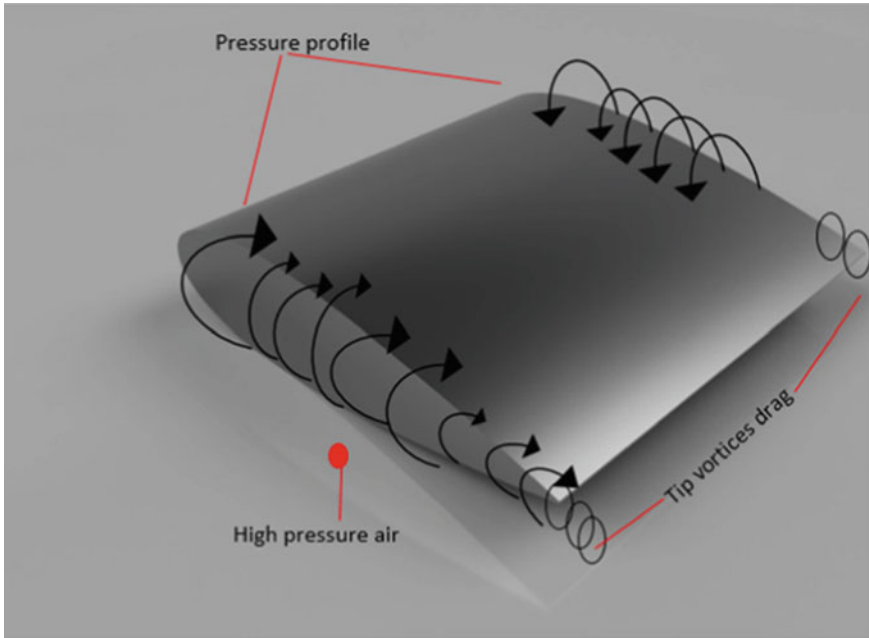
© The Author(s), under exclusive license to Springer Nature Singapore Pte Ltd. 2023  
R. Sharma et al. (eds.), *Advances in Engineering Design*, Lecture Notes in Mechanical Engineering, [https://doi.org/10.1007/978-981-99-3033-3\\_53](https://doi.org/10.1007/978-981-99-3033-3_53)

639

this field with nonplanar vertical surfaces at the wingtips. Most of these studies were conducted with flat plates, and they offered a significant reduction in drag at mostly high lift coefficients only. In cruise lift coefficient values, they only accounted for a limited reduction in drag and that was offset by the gain in viscous drag caused by the flat plate in these conditions. The fact that significant amount of side force is required for the vertical surfaces to be fully effective was overlooked by them. For this reason, something which was a bit more aerodynamic in shape than a flat plate was used as the vertical surfaces at the wingtip. These vertical surfaces at the wingtips were what later came to be known as winglets. One of the pioneering studies on winglets was done by Richard T. Whitecomb, in fact he was the one who termed the name winglet. Winglets are extremely useful in improving the efficiency of an aircraft by reducing drag, thereby reducing the fuel consumption of the aircraft. Winglets are also useful in reducing the intensity of wingtip vortices, which is formed by the pressure difference in the upper and lower surfaces of the wing [1].

Over the course of time, different types of winglets were developed by the engineers in the aviation sector with focus on reduction of wingtip vortices and the drag associated with it, which ultimately improves the fuel efficiency. Wingtip vortices are one of the major causes of inefficiency in aircraft performance due to the drag associated with it. Wingtip vortices are an indirect result of the difference in pressure between the lower and upper surface of the wing. When an aircraft travels through the air, the airfoil shape of the wing causes a pressure difference between the lower and upper wing surfaces. The lower surface of the wing experiences a higher pressure compared to the upper surface. This pressure difference is the cause of the lift force that's being generated. This difference in pressure, which is necessary for the generation of lift causes formation of vortices at the tip of the wing as the high pressure air spills over to the low pressure area at the upper surface. As it moves toward aft of the wing, it begins to swirl and forms a vortex at the tip. These wingtip vortices can develop into wake vortices or wake turbulence, which can be hazardous to nearby or following aircrafts, especially if they are smaller in size as it can lead them into uncontrollable rolls. These tip vortices can also increase drag; hence to counter both of these issues, winglets are used [2] (Fig. 1).

As a result of various studies and researches conducted, it is widely accepted that wings without winglets produces the most amount of induced drag in comparison. Hence, winglets have now become a staple in the aviation industry as airlines are becoming more and more cost conscious, especially in today's post pandemic world. There is also a reduced environmental toll as a result of the reduced carbon footprint due to the improved fuel efficiency. Years of research and design innovations by the engineers have led to the development of different types of winglets. Numerous studies have been conducted comparing the performance of various types of winglets using both CFD as well as wind tunnel.



**Fig. 1** Cause of wingtip vortices [30]

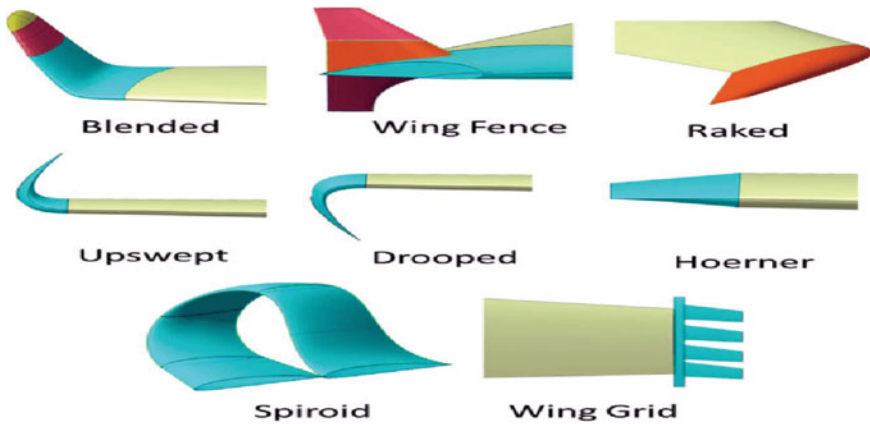
### ***1.1 Types of Existing Winglets***

**Raked winglets:** They have an extreme angle of sweep, which reduces the flow of air from the high pressure region to the low pressure region. It also gives rise to small vortices at the tips, which counteracts the effect of wingtip vortex, reducing its intensity [3].

**Spiroid winglet:** These winglets work in a way which might seem counter intuitive when compared to the other types of winglets, as they direct the flow from the tip to the root being a closed or looped system. It also forms small vortices which interfere with the wingtip vortex, reducing its intensity. According to some studies, they are one of the most effective type of winglet in reducing wingtip vortices [4].

**Dual feather winglet:** These winglets were developed by Boeing as part of their effort to improve efficiency by reducing drag. This winglet design is a hybrid combination of blended winglet, wingtip fence and raked tip as these are some of the most commonly used and efficient winglets out there [4].

**Blended winglet:** This winglet is shown to be the most efficient of all winglets by the numerous studies that have been conducted. It reduces the induced drag and increases the L/D ratio significantly when compared to wing without winglets. It is one of the most widely used winglets in commercial aviation sector [5].



**Fig. 2** Different types of winglets [31]

**Hoerner tip:** This is a sharp-edged wingtip with the upper surface extending to the outer surface of the wing. The lower surface is “undercut” and canted at an angle to the horizontal surface. This allows for a better diffusion of the tip vortex. This configuration, even though not very efficient, is slightly better than conventional round tips [6].

**Upswept and Drooped winglets:** These winglets have a slight upward or downward twist by curving upward (upswept) or downward (drooped), thereby increasing the effective wing span. This promotes a better diffusion of the tip vortex and thereby aids in the reduction of induced drag [6].

**Wing Grids:** These winglets, in structure, are a group of several wing extensions attached to the tip of the wing. They are attached in different orientations or angles to prevent the tip vortices of each of these sections from interacting with each other and form a stronger vortex. These smaller sections help to dissipate the vortex energy as multiple smaller vortices are formed, which leads to the energy being distributed into multiple smaller vortices instead of a single concentrated vortex. As a result, this leads to induced drag reduction [7].

**Wingtip fence:** These winglets help to increase coefficient of lift and reduce the induced drag by generating a nonplanar lift due to its delta shape. It also helps to reduce the formation of downwash [8] (Fig. 2).

## 1.2 Computational Fluid Dynamics

Computational Fluid Dynamics or CFD for short is one of the most widely used tool for solving problems related to fluid flow, heat transfer, mass transfer, and chemical reactions. CFD is used for analyzing systems that have fluid flow or heat transfer and

related phenomenon that arise as a result, by using computer simulation to replicate these situations and acquire simulated results in a controlled environment, which can be compared to the results in real life scenarios. CFD works by employing a set of mathematical equations which solve for parameters related to viscosity and turbulence, generally, in most cases, the Navier–Stokes equations or other variations of it are used. CFD has practical application in many fields like aerospace engineering, automotive engineering, mechanical engineering, biomedical engineering, etc. The advantage of CFD is that it is useful especially in situations where there is a large number of design variations that is to be analyzed or when there are limitation for physical testing due to factors like scale or budget constraints, as results can be achieved in a fraction of cost and time required by actual physical testing. However, the disadvantage of using CFD is that there could be inaccuracies associated with the boundary conditions, inlet values, and truncation errors due to approximation in the numerical models [9].

### ***1.3 Objective***

The objective of this study is to design an optimized and efficient winglet that has improved vortex reduction capabilities and lift to drag ratio, by comparing the performance and aerodynamic parameters of some of the major existing winglets used in the aviation industry today using Computational Fluid Dynamics (CFD), and utilizing this data, a new and optimized winglet will be designed by combining the positive aspects of these winglets. This new design will be compared to the other winglets in terms of performances at various angle of attacks to identify its performance strong points and weakness at different flight conditions.

## **2 Literature Review**

Aerodynamic optimization of winglet models plays a major role in improving the efficiency [10]. Various aspects affecting the design of winglets are discussed, ranging from airfoil characteristics to the shape and importance of correctly designing the transition surface between the wing and the winglet [11]. Addition of winglets also helps to save fuel and reduce the noise levels during takeoff [12]. The drag affecting a wing is the combination of parasitic drag and induced drag. Spiroid winglet is acknowledged as one of the most efficient winglets in terms CL/CD ratio [13]. The analysis performed at multiple flow velocities indicates that wing with winglets has reduced induced drag and better L/D ratio compared to a wing without any winglets [14]. Winglets are effective in reducing the fuel consumption, decreasing the takeoff distance and ultimately increased operational life for the engine as a result of less thrust requirement during takeoff and cruising conditions [15]. The sweep angles of 60° were concluded to have the least minimum drag compared to other winglet sweep

angles. Also analysis shows that a cant angle of  $15^\circ$  was the most suitable for cruise condition due to the least amount of drag at low AoA and a cant angle of  $45^\circ$  was more suitable for higher AoA [16]. After comprehensive analysis and evaluation, it was concluded that the version with max thickness at 40% of chord compared to the reference aerofoil was the most optimized overall out of all the other designs, as it had the highest L/D ratio in multiple AoA [17]. After performing analysis at various (AoA), and comparing the results, it was concluded that the blended winglet was more efficient than a wing without any winglets as well as the blended winglet with a cant angle of  $90^\circ$  is the most optimized of all [18]. The performance parameters of an optimized spiroid winglet were compared to that of a simple winglet and a wing without any winglets. Results indicated that the spiroid winglet had the most vortex reduction and range improvement [19]. The winglet with a cant angle of  $45^\circ$  was the most optimized as it had the highest L/D ratio overall [20]. Performance of a multi-winglet, blended winglet, and a split blended winglet are compared with the performance of a base wing without winglet using CFD with k-epsilon turbulence model solver. It can be assumed from the results that the split blended winglet was the most optimized in comparison as it exhibited overall consistent performance [21]. NACA series airfoils were the most sensitive to the change in Reynolds number when compared to other airfoils like thin cambered plates and flat plate airfoils [22]. Wing with winglets had exhibited improved performance in comparison with the wing without any winglets [23]. Each cant angle was effective at a particular stage of flight, i.e., no cant angle can perform effectively at all flight conditions [24]. The multi-tipped winglet with three tips were the most optimum of all as it had the highest L/D value, and it was effective in reducing the intensity of the tip vortices as the energy of the vortices was transferred among the three tips, thereby preventing it from being concentrated at a single point [25]. Increase in Reynolds number caused an increase in CL, max while an increase in Mach number caused a decrease. The 13% thickness airfoil was the most optimum as it provided the best performance of all the airfoils that were tested [26]. A new concept design introduces a hyperbolic curved transition from the wing to the winglet. The curved concept winglet was the most optimized and efficient of all the designs tested, but there was added structural toll on the entire structure as a result of this, and to tackle this, a multi-disciplinary approach is needed [27]. Wake vortices caused by commercial aircrafts are a hazard to commercial air transportation. There are regulatory process in place to avoid encountering wake vortices and steps to be taken in case of an encounter [28]. The C-Wing has improved efficiency in situations where the maneuver lift coefficient is same as lift coefficient at cruising conditions. Even though it performs better at maneuvering situation, more research has to be done on the structural aspect of the wing [29].

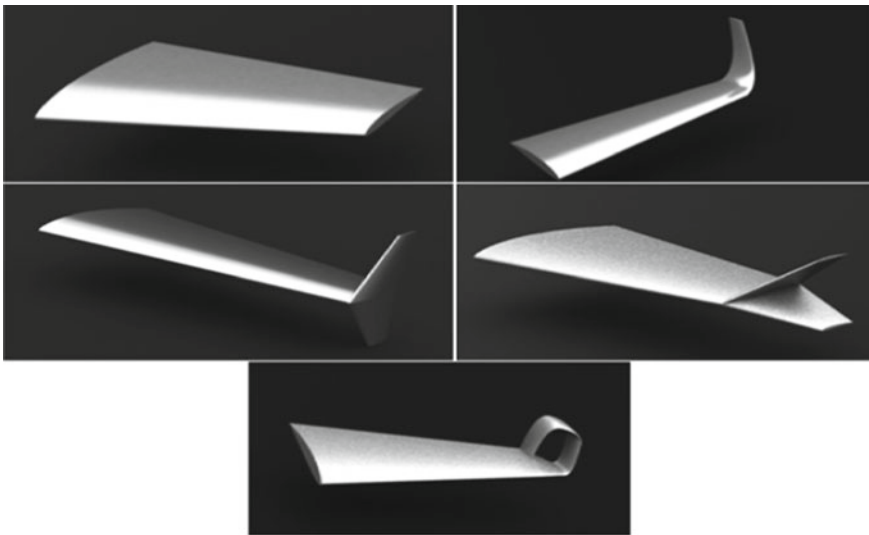


### 3 Methodology

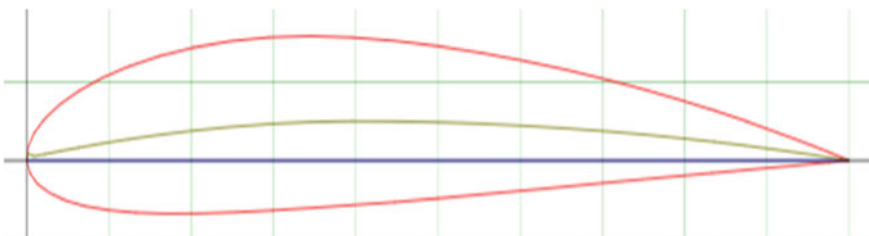
#### 3.1 Design and CFD Analysis

Some of the most commonly used winglets like the blended winglet, wingtip fence, dual feather winglet, spiroid winglet, and a baseline wing without any winglets were modeled from a NACA2411 airfoil using SolidWorks. CFD analysis of these winglets and baseline wing was performed using ANSYS CFX (Figs. 3, 4, 5, 6, 7, 8, and 9).

Some of the most commonly used winglets like the blended winglet, wingtip fence, dual feather winglet, spiroid winglet, and a baseline wing without any winglets were modeled from a NACA2411 airfoil using SolidWorks. CFD analysis of these

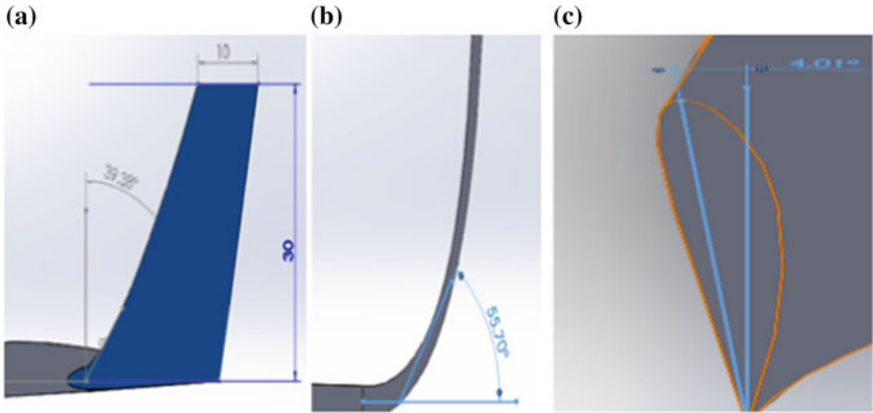
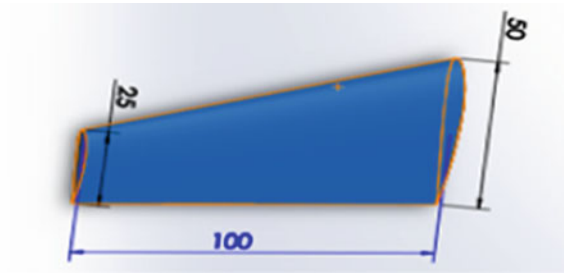


**Fig. 3** Winglets chosen as part of the analysis **a** baseline wing, **b** blended winglet, **c** wingtip fence, **d** dual feather winglet, **e** spiroid winglet

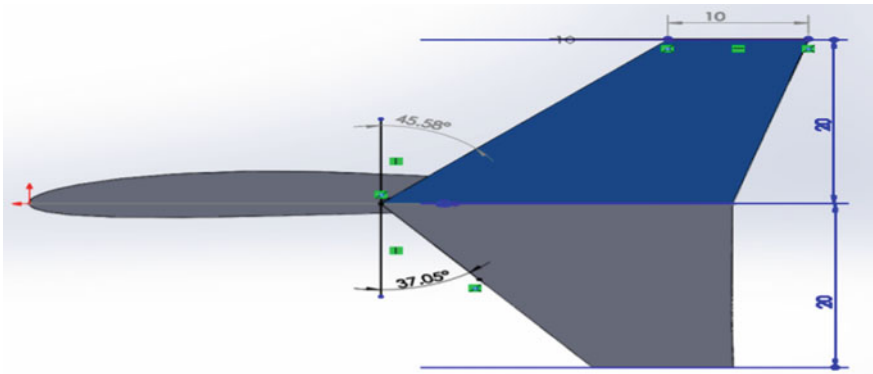


**Fig. 4** NACA2411 airfoil (max thickness-11% at 29.5% of chord and max camber-2.5% at 39.6% of chord)

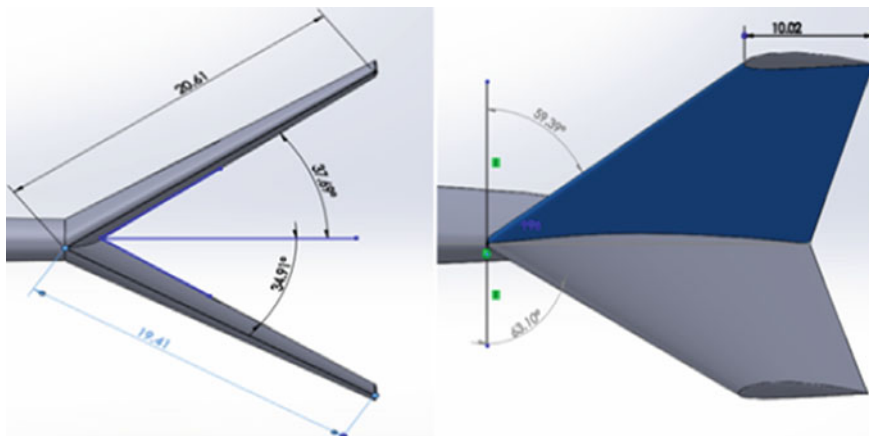
**Fig. 5** Baseline wing dimensions (root chord-50 mm, tip chord-25 mm, and semi-span-100 mm)



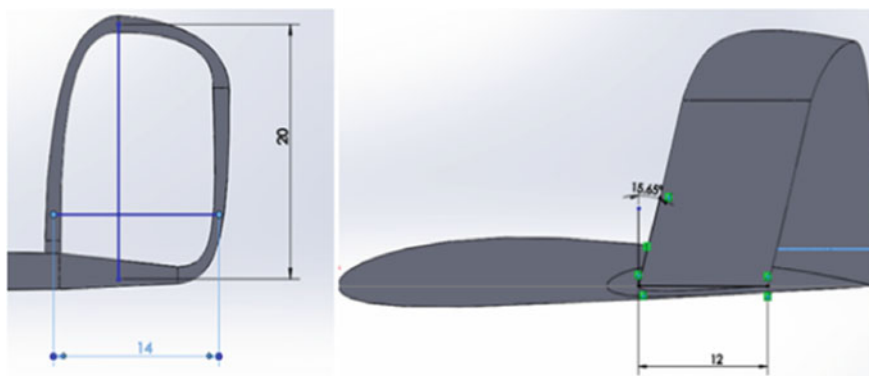
**Fig. 6** Blended winglet dimensions **a** tip chord-10 mm, height-30 mm, sweep angle-39.38°, **b** Cant angle-55.70°, **c** tip outward twist-4.01°



**Fig. 7** Wingtip fence dimensions (all length dimensions in mm)

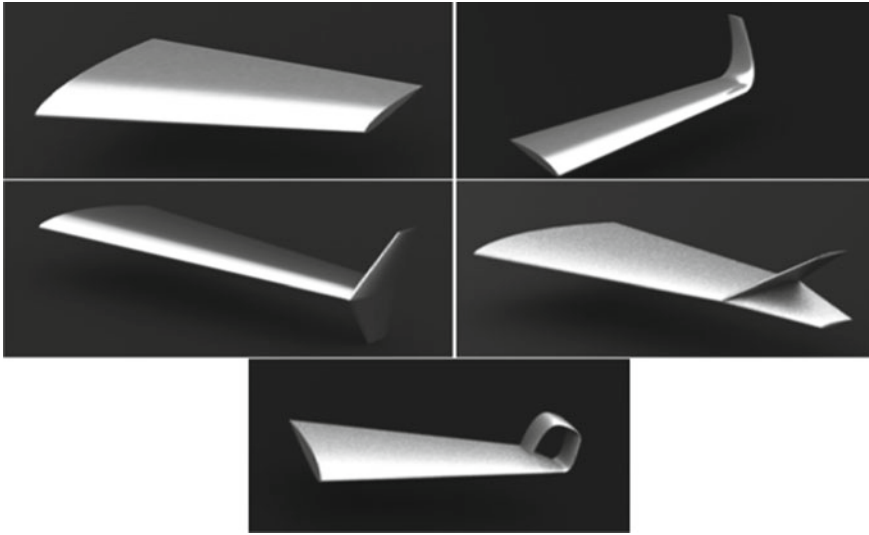


**Fig. 8** Dual feather winglet dimensions (all length dimensions in mm)

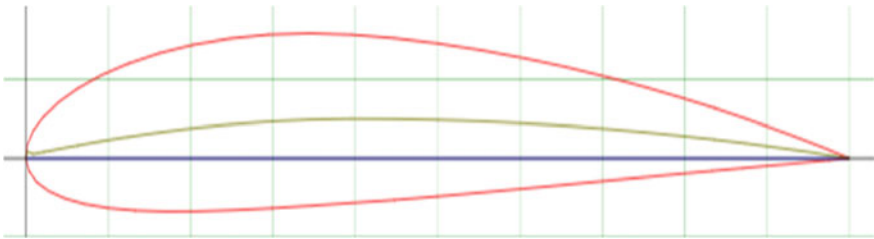


**Fig. 9** Spiroid winglet dimensions (all length dimensions in mm)

winglets and baseline wing was performed using ANSYS CFX (Figs. 10, 11, 12, 13, 14, 15, and 16).



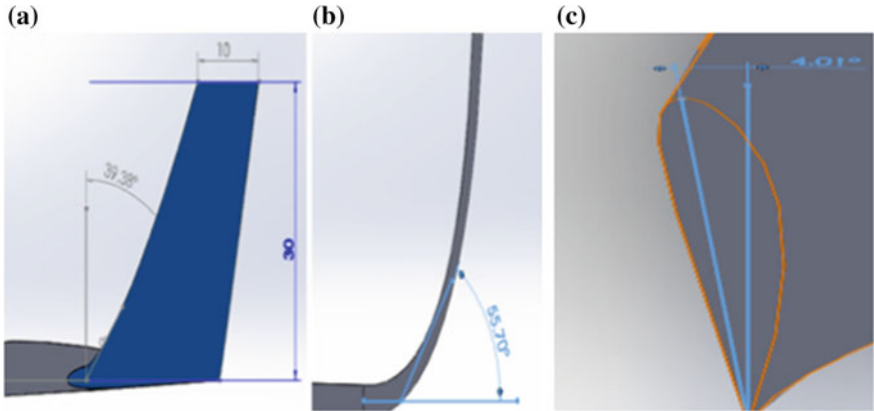
**Fig. 10** Winglets chosen as part of the analysis **a** baseline wing, **b** blended winglet, **c** wingtip fence, **d** dual feather winglet, **e** spiroid winglet



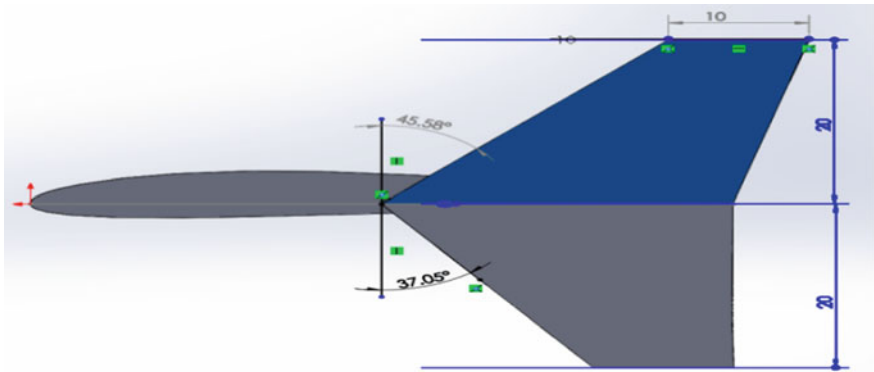
**Fig. 11** NACA2411 airfoil (max thickness-11% at 29.5% of chord and max camber-2.5% at 39.6% of chord)

**Fig. 12** Baseline wing dimensions (root chord-50 mm, tip chord-25 mm, and semi-span-100 mm)





**Fig. 13** Blended winglet dimensions **a** tipchord-10 mm, height-30 mm, sweep angle-39.38°, **b** cant angle-55.70°, **c** tip outward twist-4.01°



**Fig. 14** Wingtip fence dimensions (all length dimensions in mm)

### 3.2 Mesh Settings and Boundary Conditions Used for CFD Analysis

Computational Fluid Dynamics (CFD) analysis of these winglets and the baseline wing was analyzed using ANSYS CFX for understanding the aerodynamic performance and to observe the aerodynamic parameters of these winglets. All the simulations were done with the following mesh and solver settings (Fig. 17; Tables 1 and 2).

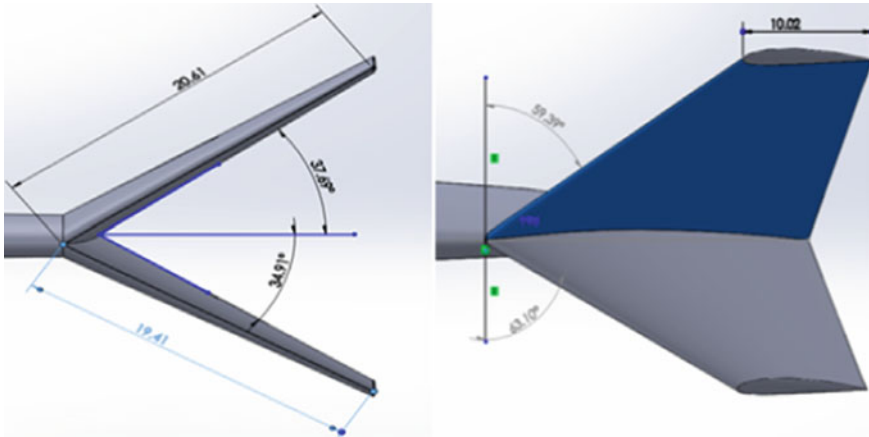


Fig. 15 Dual feather winglet dimensions (all length dimensions in mm)

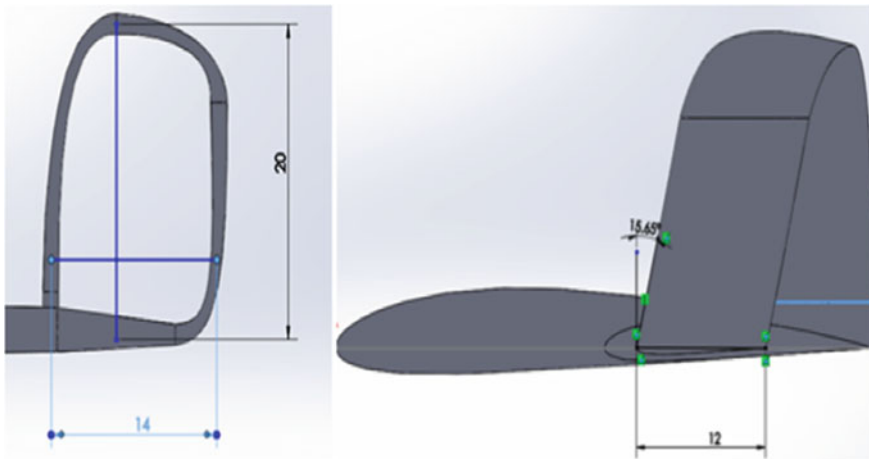
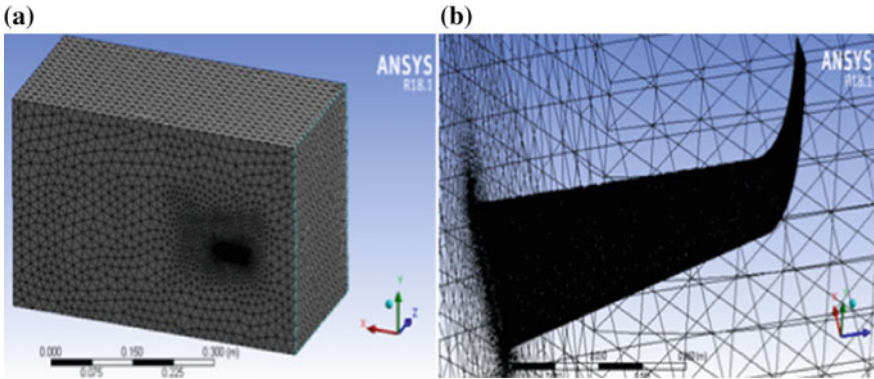


Fig. 16 Spiroid winglet dimensions (all length dimensions in mm)

### 3.3 Design of the New Winglet

After analyzing the performance, design advantages and disadvantages of these winglets, a new type of hybrid winglet was designed incorporating some of the design advantages of these winglets. Before finalizing on a preliminary design, seven designs were tested and analyzed for their performance before choosing a preliminary design. Three variations of the chosen preliminary design were created and tested, after observing the results, one of the designs were chosen to be the final design for further CFD analysis to be compared with other winglets in terms of performance. This new winglet is a hybrid combination a spiroid winglet (for its vortex reduction



**Fig. 17** a Mesh structure, b wireframe view of winglet mesh

**Table 1** Mesh settings and statistics

Advanced sizing function	Proximity and curvature
Relevance center	Medium
Smoothing	Medium
Transition	Slow
Element size for winglets	0.5 mm
Element size for body of influence 1 (area surrounding the wing)	6.0 mm
Element size for body of influence 2 (area surrounding the wingtip/winglet)	1.25 mm
Total number of elements	7,400,000 (average)
Total number of nodes	1,500,000 (average)

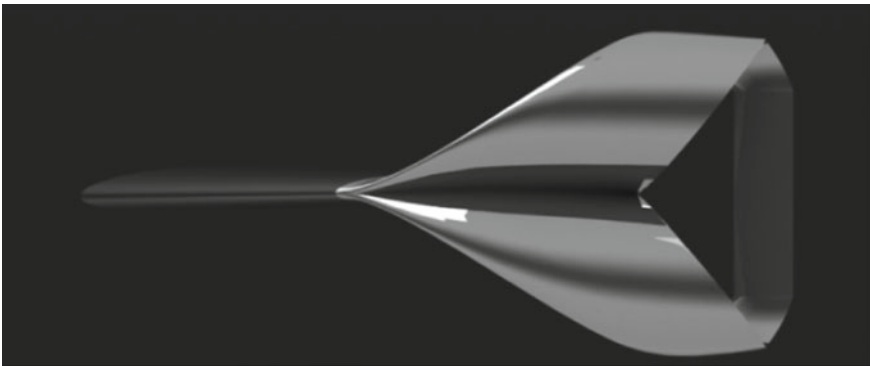
**Table 2** Boundary conditions and solver settings

Inlet velocity	200 m/s
Inlet temperature	300 K
Outlet pressure	0 Pa
Wall settings	No-slip, smooth wall
Winglet/wing	Same as wall
Atmospheric conditions	Sea level atmospheric conditions
Turbulence model	$K-\omega$ turbulence model
Number of iterations	500–1000 iterations

capacity), blended winglet, and the dual feather winglet (for their overall efficiency). The new winglet design was named XT-6 (Figs. 18 and 19).



**Fig. 18** XT-6 winglet



**Fig. 19** Side view of the XT-6

### ***3.4 Dimensions of the New Winglet***

The XT-6 winglet when viewed from front has a semi-circular shape with the following dimensions. When viewed from side, the upper winglet section has a sweep angle of  $58.33^\circ$ , and the lower section has a sweep angle of  $58.10^\circ$ . The upper most airfoil section of the upper winglet has an upward twist angle of  $2.30^\circ$  and a chord length of 10 mm. The straight section of the winglet with 20 mm length has a chord length of 5 mm. Since the upper section and lower section of the winglets are symmetric in nature, the dimensions are same for the lower section also, except the twist angle of  $2.30^\circ$  as the lower section has no twist (Figs. 20 and 21).



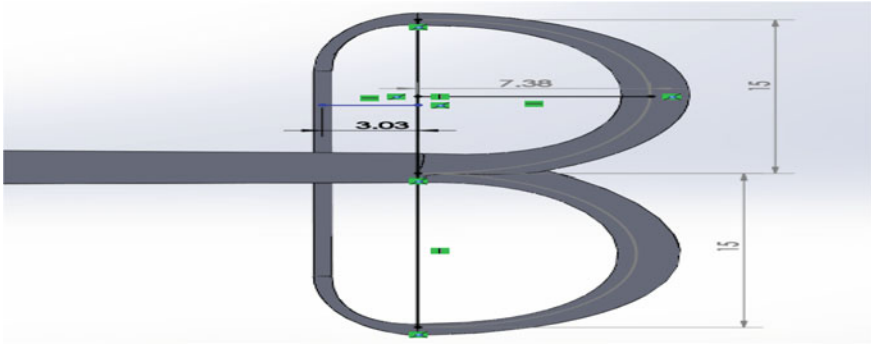


Fig. 20 Dimensions of XT-6 winglet (front view)

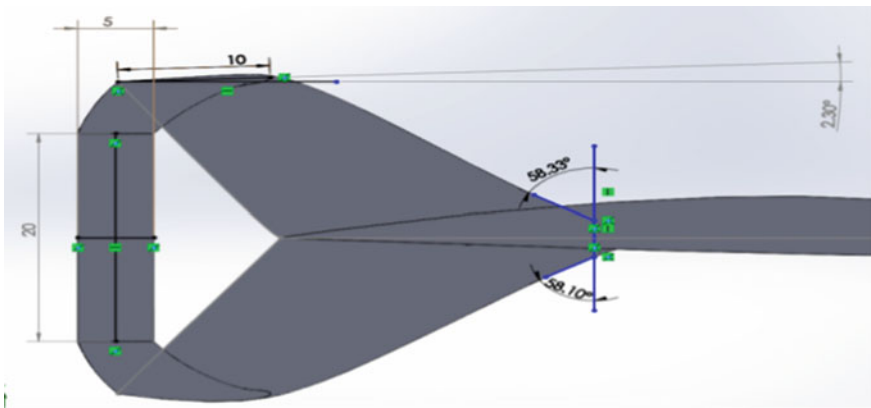


Fig. 21 Dimensions of XT-6 winglet (front view)

### 4 Results

The performance of these winglets and the baseline wing were analyzed, and aerodynamic parameters like lift, drag, and vortex intensity were observed and recorded. Main parameters that were considered for this study as an indicator of efficiency were lift to drag (L/D) ration vortex intensity (Tables 3, 4, 5, and 6).

From these results of CFD simulation, it is clear that blended winglet and the dual feather winglet has the highest L/D ratio compared to other winglets at 0° and 5° angle of attacks. And spiroid winglet has the least vortex intensity of all. Since the new winglet XT-6 is a combination of these three winglets, we can see that its vortex intensity is also comparatively less when compared to most other winglets that was analyzed. At  $\alpha = 0^\circ$ , L/D ratio of winglet XT-6 is not ideal. At  $\alpha = 5^\circ$ , L/D ratio of winglet XT-6 is improved compared to the baseline wing and most of the other type of winglets. At  $\alpha = 10^\circ$ , we can see that XT-6 winglet has the highest L/D ratio of

**Table 3** L/D ratio and vortex intensity at  $\alpha = 0^\circ$  (angle of attack)

Type of winglet (at $\alpha = 0^\circ$ )	L/D	Vortex intensity (1/s)
Base line wing	13.1715	5231.33
Blended winglet	14.0343	2894.8
Wingtip fence	13.317	2304.82
Dual feather winglet	15.141	3658.55
Spiroid winglet	13.678	2198.22
XT-6 winglet	12.651	2500.01

**Table 4** L/D ratio and vortex intensity at  $\alpha = 5^\circ$  (angle of attack)

Type of winglet (at $\alpha = 5^\circ$ )	L/D	Vortex intensity (1/s)
Baseline wing	16.608	4804.89
Blended winglet	19.0412	4230.18
Wingtip fence	18.094	6563.24
Dual feather winglet	19.1881	8870.16
Spiroid winglet	18.0414	2325.04
XT-6 winglet	18.334	3273.194

**Table 5** L/D ratio and vortex intensity at  $\alpha = 10^\circ$  (angle of attack)

Type of winglet (at $\alpha = 10^\circ$ )	L/D	Vortex intensity (1/s)
Baseline wing	11.2471	4111.04
Blended winglet	11.320	5314.45
Wingtip fence	11.906	10,787
Dual feather winglet	11.676	7557.19
Spiroid winglet	11.739	2902.37
XT-6 winglet	12.401	3379.91

**Table 6** L/D ratio and vortex intensity at  $\alpha = 15^\circ$  (angle of attack)

Type of winglet (at $\alpha = 15^\circ$ )	L/D	Vortex intensity (1/s)
Baseline wing	8.4602	4367.61
Blended winglet	5.6779	5306.28
Wingtip fence	4.6145	9649.55
Dual feather winglet	6.029	7125.87
Spiroid winglet	5.5893	4876.24
XT-6 winglet	6.298	4923.04

all. It is also evident that vortex intensity is controlled and better than all the other winglets except the spiroid winglet (Figs. 22 and 23).

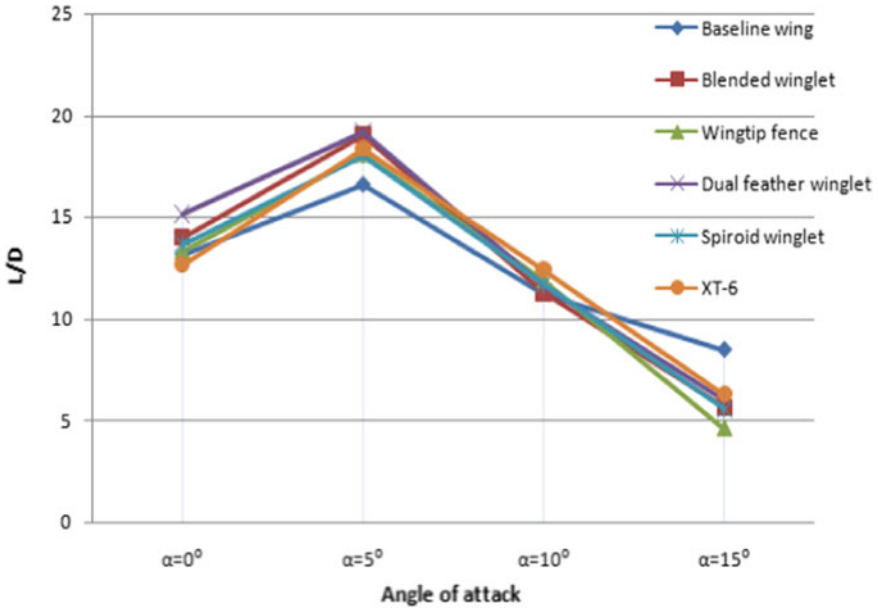


Fig. 22 L/D versus angle of attack comparison graph

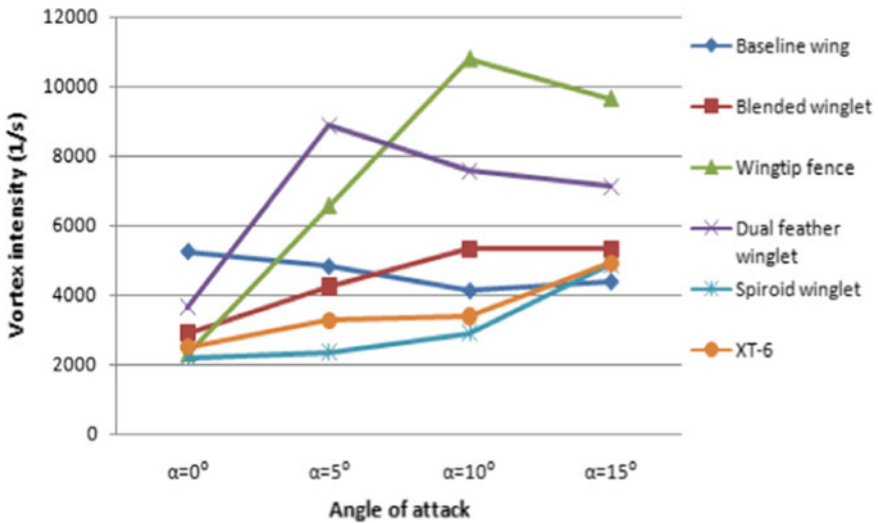
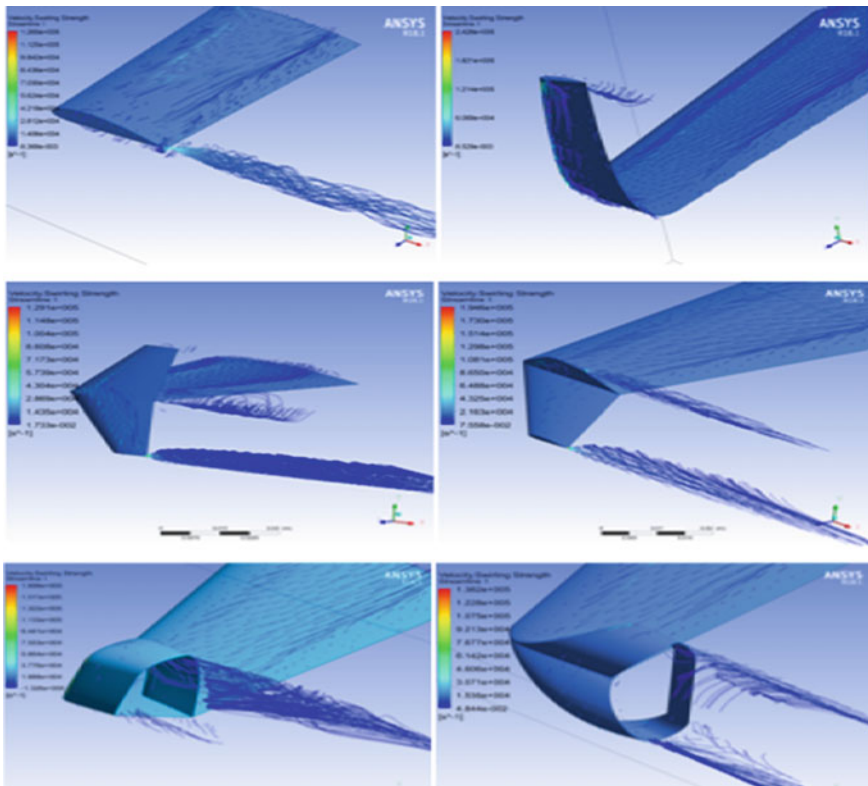


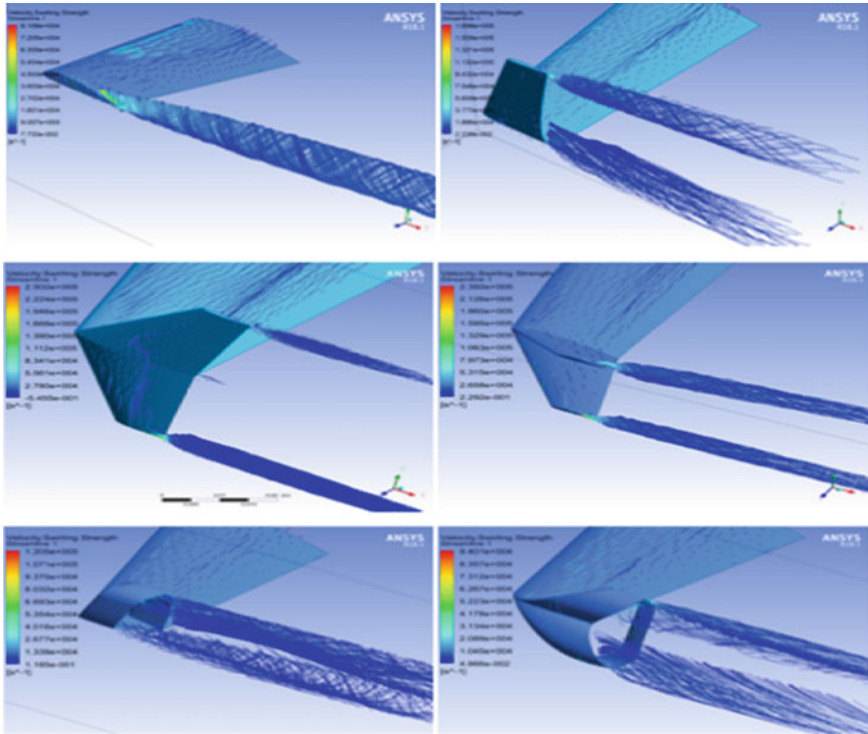
Fig. 23 Vortex intensity versus angle of attack graph

From analyzing the above results and graphs, it is clear that the newly designed winglet, XT-6 is more efficient at higher angle of attacks and hence more suitable for short to medium range flights (Figs. 24, 25, 26, and 27).

After analyzing the vortex swirling strength stream lines at various angle of attacks, it was observed that the maximum swirling strength of the new winglet XT-6 is lower than the maximum swirling strength of the spiroid winglet at all AoAs except at  $\alpha = 15^\circ$ . It was also observed that all the winglets are in stall condition at  $\alpha = 15^\circ$  and hence the unstable flow visible in the streamlines. It is also clear that these winglets and the baseline wings were most efficient at the angle of attack of  $\alpha = 5^\circ$ , as all the winglets exhibited highest lift to drag (L/D) ratio. It was observed that the swirling strength stream lines were more dense and concentrated for all the winglets indicating strong vortex formation, except for the spiroid and XT-6 winglets. These vortices were formed at tips and junctions with sharp angle transitions at the surface and since the spiroid and XT-6 winglets are closed systems, effectively meaning they had no tips, was one of the main reasons of the reduced vortex intensity. Analysis of L/D ratio at various angle of attacks simulating various flight condition revealed



**Fig. 24** Vortex swirling strength streamlines at  $\alpha = 0^\circ$ , **a** baseline wing, **b** blended winglet, **c** wingtip fence, **d** dual feather winglet, **e** spiroid winglet, **f** XT-6 winglet



**Fig. 25** Vortex swirling strength streamlines at  $\alpha = 5^\circ$

that almost all the winglets had improved L/D ratio than baseline wing at all angle of attacks except at  $\alpha = 15^\circ$ . It can be inferred from this that wings with winglets reach stall conditions faster than the baseline wing. It was also observed that the blended and dual feather winglets were efficient and had balanced performance in terms L/D ratio at all angle of attacks. Analysis of the CFD simulation results of the newly designed winglet XT-6 revealed that it inherited the vortex reduction capability of the spiroid winglet, which was one of the major design goals. Analysis of the L/D ratio revealed that the performance of the XT-6 winglet was not ideal at  $\alpha = 0^\circ$ , which was a drawback of the design. At all the other angle of attacks, it was observed that the L/D ratio significantly improved for the new winglet. XT-6 had the highest L/D ratio value of all the winglets and the baseline wing compared at  $\alpha = 10^\circ$ . It can be inferred from these results that the new design is more efficient at higher angle of attacks and hence more efficient at take-off and landing conditions. It can also be observed that the new winglet was able to successfully reduce the vortex intensity at all flight conditions. Hence, it can be inferred that the newly designed winglet XT-6 is more suitable for short to medium range flights.

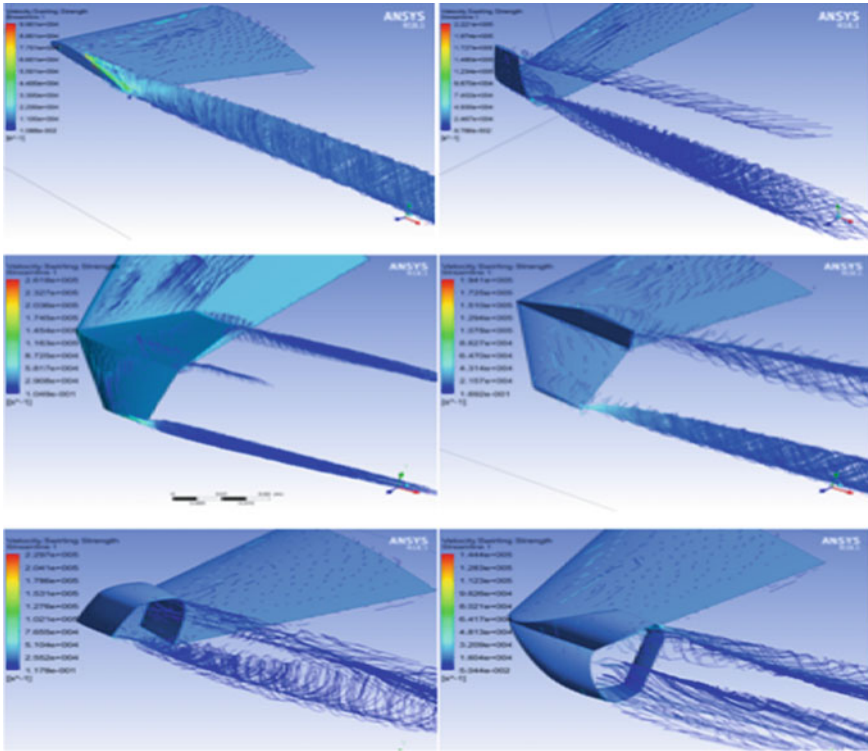


Fig. 26 Vortex swirling strength streamlines at  $\alpha = 10^\circ$

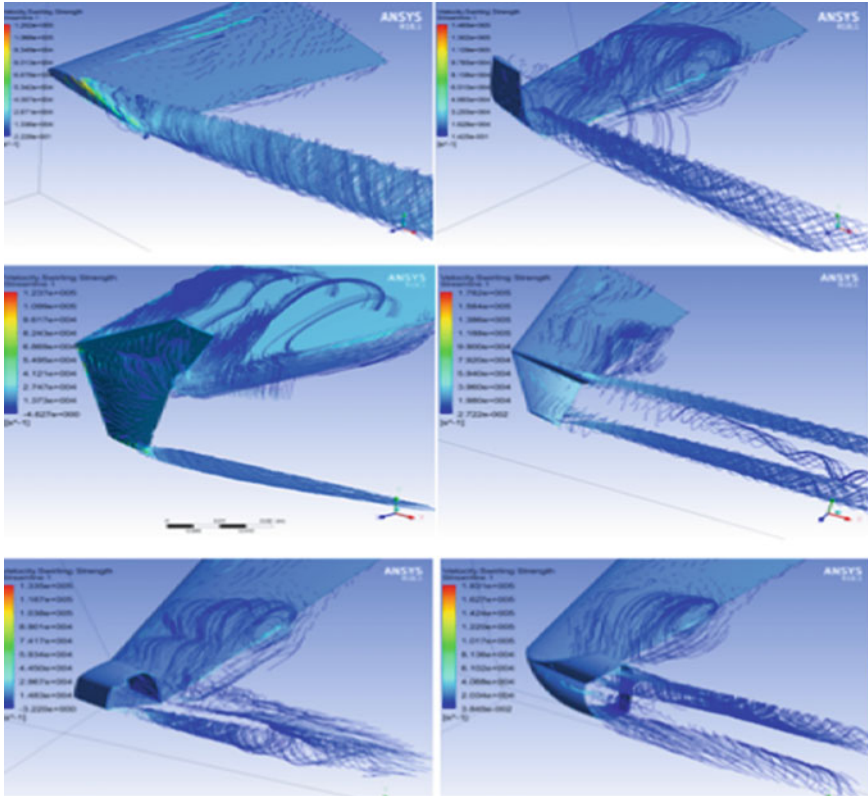


Fig. 27 Vortex swirling strength streamlines at  $\alpha = 15^\circ$

## 5 Conclusion

Winglets are one of the most staple design accessories in the commercial aviation sector today. Winglets are used to increase the efficiency of the aircraft and reduce its fuel consumption. Winglets achieve this by reducing the wingtip vortices and reducing the associated induced drag. Engineers are trying to push the limits and improve efficiency of winglets even further. This project was done to design a winglet by combining positive aspects of some of the most commonly used winglets. The goal was to design a winglet with improved efficiency in terms of L/D ratio and excellent vortex reduction capability. After analyzing the results, it can be concluded that the blended winglet and the dual feather winglet were suitable for long distance cruise conditions, and the newly designed XT-6 winglet is more suitable for short-medium range flights. The XT-6 winglet was also efficient in reducing the wingtip vortices at all flight conditions; as a result, it will only lead to weaker wake vortices, effectively reducing the risk posed by wake vortices. Hence, the separation distance between aircrafts, which was maintained to avoid wake vortex encounters, can be



reduced. But the additional structure could increase the structural toll on the wing as it could lead to increased wing loading and structural stress and would also require the need for additional structural reinforcements, which could again add to the weight. Structural analysis for the design was not conducted as it is beyond the scope of this project at this stage. Further research on structural aspect needs to be done for the complete optimization process.

## References

1. Whitcomb RT (1976) A design approach and selected wind-tunnel results at high subsonic speeds for Wing tip mounted winglets. NASA TN D-8260
2. Rohit B, BASU S (2017) Influence of wingtip devices in reducing induced drag—a review. *Int J Mech Prod Eng Res Develop* 7(3)
3. TMAM, Seetloo S (2014) Wingtips and multiple wing tips effects on wing performance: theoretical and experimental analyses. In: 10th international conference on heat transfer, fluid mechanics and thermodynamics. University of South Wales, Orlando
4. Kumar Bada V, Monika K, Hussain Md A (2016) CFD analysis and comparison of spiroird and dual feather winglets. *Int J Eng Res* 5(Issue No.8). ISSN: 2319-6890
5. Pragati P, Baskar S (2015) Aerodynamic analysis of blended winglet for low speed aircraft. In: *Proceeding of the world congress on engineering 2015, vol II*
6. Raymer D (1992) *Aircraft design, 2nd edn.* American Institute of Aeronautics and Astronautics, Inc.
7. Smith MJ, Komerath N, Ames R, Wong O, Pearson J (2001) Performance analysis of a wing with multiple winglets. *AIAA paper*, 2001–2407
8. Chakravarthy M, Sudhakar U (2015) Numerical investigation of winglet angles influence on vortex shedding. *Int J Res Eng Technol* 04(12):11–17. <https://doi.org/10.15623/ijret.2015.0412003>
9. Raman RK, Dewang Y, Raghuvanshi J (2018) A review on applications of computational fluid dynamics. *Int J LNCT* 2(6). ISSN (Online): 2456-9895
10. Reddy S, Sobieczky H, Dulikravic G, Abdoli A (2016) Multi-element winglets: multi-objective optimization of aerodynamic shapes. *J Aircr* 53(4):992–1000. <https://doi.org/10.2514/1.c033334>
11. de Mattos S, Macedo A, da Silva Filho D (2003) Considerations about winglet design fluid dynamics and co-located conferences
12. Najafian Ashrafi Z, Sedaghat A (2014) Improving the aerodynamic performance of a wing with winglet. *Int J Nat Eng Sci* 8(3)
13. Manikandan G, Rajashree V, Gràcia S (2017). Design and performance analysis of spiroird winglet with normal wing. *Imperial J Interdisc Res* 3(4)
14. Sawale A, Khaleel MD, Jaswanth S (2017) Design and analysis of winglet. *Int J Civil Eng Technol* 8(5):842–850
15. Al Sidairi KA, Rameshkumar GR (2016) Design of winglet device for aircraft. *Int J Multidiscip Sci Eng* 7(1). ISSN: 2045-7057
16. Guerrero J, Sanguineti M, Wittkowski K (2018) CFD study of the impact of variable cant angle winglets on total drag reduction. *Aerospace* 5(4). <https://doi.org/10.3390/aerospace5040126>
17. Prasad KS, Krishna V, Kumar BA (2013) Aerofoil profile analysis and design optimisation. *J Aerosp Eng Technol* 3(2). <https://doi.org/10.37591/v3i2.656>
18. Khalil EE, Helal H, Abdellatif O, Elharriri GM (2016) Aerodynamic analyses of aircraft-blended winglet performance. *IOSR J Mech Civil Eng (IOSR-JMCE)* 13(3). <https://doi.org/10.9790/1684-1303046572>



19. Mostafa S, Bose S, Nair A, Raheem MA, Majeed T, Mohammed A, Kim Y (2014) A parametric investigation of non-circular spiroid winglets. EPJ Web of Conferences 67:02077. <https://doi.org/10.1051/epjconf/20146702077>
20. Khalil EE, Abdelghany ES, Elharriri GM, Abdellatif OE (2016) Air craft winglet design and performance: cant angle effect. In: 14th international energy conversion engineering conference. <https://doi.org/10.2514/6.2016-4821>
21. Kishan PM (2016) CFD analysis of aerodynamic characteristics of scimitar winglets in lighter aircrafts. J Basic Appl Eng Res 3(9):2350
22. Winslow J, Otsuka H, Govindarajan B, Chopra I (2018) Basic understanding of airfoil characteristics at low Reynolds numbers (104–105). J Aircr 55(3):1533–3868, 1050–1061. <https://doi.org/10.2514/1.c034415>
23. Rabbi M, Nandi R, Mashud M (2015) Induce drag reduction of an airplane wing. Am J Eng Res (AJER) 4(6):2320-0847, 219–223
24. PC, S., Sanjid M, EA, M., Krishnan A, Jacob T (2018) Performance analysis of winglet using CFD. Int Res J Eng Technol (IRJET) 5(4):2395-0056
25. Narayan G, John B (2016) Effect of winglets induced tip vortex structure on the performance of subsonic wings. Aerosp Sci Technol 58:328–340. <https://doi.org/10.1016/j.ast.2016.08.031>
26. McGhee RJ, Beasley WD (1976) Effects of thickness on the aerodynamic characteristics of an initial low-speed family of airfoils for general aviation applications. In: McGhee RJ (ed) Free download, borrow, and streaming. Retrieved 20 May 2020, from [https://archive.org/details/ails/nasa\\_techdoc\\_19790004829](https://archive.org/details/ails/nasa_techdoc_19790004829)
27. Gueraiche D, Popov S (2017) Winglet geometry impact on DLR-F4 aerodynamics and an analysis of a hyperbolic winglet concept. Aerospace 4(4). <https://doi.org/10.3390/aerospace4040060>
28. Gerz T, Holzäpfel F, Darracq D (2002) Commercial aircraft wake vortices. Prog Aerosp Sci 38(3):181–208. [https://doi.org/10.1016/s0376-0421\(02\)00004-0](https://doi.org/10.1016/s0376-0421(02)00004-0)
29. Ning S, Krooy I (2008) Tip extensions, winglets, and C-wings: conceptual design and optimization. <https://doi.org/10.2514/6.2008-7052>
30. Raj W, Thomas (2015) Design and analysis of spiroid winglet. Int J Innov Res Sci Eng Technol 4(3). 2319-8753:1140–1140. <https://doi.org/10.15680/IJIRSET.2015.0403070>
31. Rajendran S (2012) Design of parametric winglets and wing tip devices: a conceptual design approach, MA thesis. Linköping University, Linköping

# Design and Analysis of PLA and Carbon Fiber Mono Leaf Spring for Small Commercial Vehicles



Lavepreet Singh, Shreyansh Gupta, and Rahul Katiyar

**Abstract** Finite Element Analysis (FEA) has been used to study and analyze a single leaf of the steel spring used in the Tata Ace© as its rear suspension. To compare the result, a single leaf composite spring has been designed by 3D modeling and optimized. Main consideration was to optimize the spring geometry to obtain spring that has maximum stress and is able to withstand the external static forces without failure. Deformation and stresses are the design constraints whereas width at the points and area of the cross section are the variables of the design. The comparison between PLA (Polylactic Acid), Carbon Fiber (390 GPa) and High Carbon Steel will be the primary objective of this paper in order to analyze max. and the min. stress on the mono leaf spring using different category of Materials.

**Keywords** Composites · Carbon fiber · Leaf spring

## 1 Introduction

People nowadays can't imagine moving without automobiles. One of the issues that come to mind in this case is comfort, which is dependent on the suspension system [1]. The most likely matter that follows the word "suspension system" is the use of springs. The most common spring is the 'Leaf Spring,' which is made of numerous metal strips fixed in a sequence of increasing length one on top of the other, also slightly curved upwards in shape [2]. When the weight, stress, natural frequency, and corrosion of metal springs are compared to springs made of different composites, an engineer should choose the composite made ones. Because composite materials out-perform all other metals in terms of weight, stress due to a given load, and corrosive behavior [3]. The use of animated composites in the manufacturing industries is increasing with each passing day because of the properties that they exhibit like minimum density, high strength, and elevated stiffness [4]. Mechanical structures have improved torsional rigidity hence making them ideal for shell structures [5].

---

L. Singh (✉) · S. Gupta · R. Katiyar

Department of Mechanical Engineering, Galgotias University, Greater Noida, Uttar Pradesh, India  
e-mail: [punstu@gmail.com](mailto:punstu@gmail.com)

When compared to metallic springs, Flexural strength at lower mass and increased damping is the primary characteristics of composite leaf springs. Approximately 60% of the weight can be reduced by the use of composite leaf springs in place of metallic springs [6]. Composite leaf springs have shown 180% maximum proof strength of that of steel while the stress level was 22% lower [7]. Various materials have been used to manufacture composite leaf springs out of which carbon fiber reinforced polymer (CFRP) showed stress of about 43.2% [8]. The use of E-glass fiber composites showed a weight redirection of 72% while E-glass showed a 62% weight reduction as compared to steel [9]. The reinforced hybrid composites of 30% glass fiber and 30% carbon fiber showed better results than other composites [10]. The tests conducted on Glass Fiber Reinforced Polymer (GFRP) provided more flexibility to it and significantly improved noise and harshness in the test drive [11]. 55% fiber volumetric fraction and higher frequency of the composite springs provide optimum results as well [12]. Preference of carbon fibers over glass fibers is not surprising as the material for composite leaf spring development despite its good insulating properties, high strength, and better chemical resistance [13, 14]. The tensile limit of the fiber composites is also increased by the addition of minimal quantities of aluminum in carbon fiber composite along with boron carbide [15]. The most basic and cheaper manufacturing technique is hand layup [16]. Improved damping properties were shown by CFRP bodies in the first three resonance frequencies. Higher resonance frequencies are achieved by the low masses of the composites [17]. A higher frequency than steel is achieved [18]. CFRP is proven to be better than GFRP in its shock-absorbing properties; still, it cannot replace steel yet [19]. Therefore the layering of the CFRP on top of GFRP has provided better results after exposing it to compressive loads in comparison with metallic or steel springs and can be used to replace it, hence proving the additional benefits of hybridization [20]. The aramid composite was tested and investigated because of its mechanical properties and it provided with desirable results when compared to the otherwise common metallic material for spring [21].

Several articles focused on using composites as materials for various parts in automobiles. Composite structure is being used in automobiles [22]. These materials' potential for use in vehicle structures has been determined. Furthermore, in terms of fabrication advancements, composites possess various properties that make them ideal for types of structural uses. Despite the fact that no specific design or model is introduced [23]. In addition, composite leaf springs are used in big trucks. Because of the higher load acting in these sorts of vehicles, the utilization of composite materials should be thoroughly researched [24]. The primary distinction is the usage of a single leaf. The composite leaf spring provided with extraordinary results when compared to metallic leaf [25].

Material properties like energy absorption, modulus of the material and flexural strength can be altered extensively by incorporating hybridization in the design. The addition of two basalt fiber layers to the surface of the carbon fibers provided the highest flexural strength of the structure [26]. The mechanical properties can also be tailored by shuffling the stacking sequence of the hybrid composites [27]. The amount of water absorption can be significantly reduced by using carbon in

the hybridization process. Alternatively stacking carbon fiber piles between basalt layers will significantly increase the impact resistance when tested under the same force conditions. The benefits of both reinforcements in a hybrid can be observed by setting carbon fiber on the second layer of the stacking arrangement as it increases the energy absorption of the laminate [28].

The bast of the PLA plant provides us with the lax fiber beneath its surface [29]. It is a soft, flexible, and lustrous fiber. The impact resistance of the spring can be increased by sandwiching lax between the consecutive layers [30]. The interface between basalt layers contains delamination in large amount and PLA can be demonstrated by the falling weight impact test [31]. The tensile strength, impact resistance, flexural rigidity can be altered majorly by different sequencing of the layers of the spring [32]. High damping properties are shown by PLA over pure carbon. Internal piles of carbon along with the outer layers of hybrid PLA composites show a decline in the damping coefficient. Damping can otherwise be altered by the fiber direction [33]. A comparison between the composites reinforced with PLA fibers and those reinforced with carbon fiber showed that the damping coefficient was 4 times higher in PLA fibers than in the latter; meanwhile, the elastic modulus and strength were lost [34]. Higher damping coefficients were examined in PLA laminates than those in carbon composites in finite element analysis and experimental investigation [35]. The use of PLA fibers showed an increment in bending modulus was observed from 2 to 10% [36]. Furthermore, an increment in impact resistance was seen when PLA layers were introduced in the middle of the composite [37].

Design of the composite beam and its applications for composite leaf spring have been done through a preliminary approach [38]. The amount of elastic energy that a leaf spring volume unit can store has been shown by Eq. 1 [39].

$$1a^2/2E \tag{1}$$

Here the modulus of elasticity (longitudinal direction) is represented by E while the max. allowed stress imparted into the spring is represented by a. While major load on a leaf spring is the vertical force, above equation reveals that the ideal material for the leaf spring would be the one which has minimum elasticity modulus in the longitudinal direction and maximum strength. Luckily, these properties are possessed by composites [40]. The lighter weight of the composites makes it a better option over steel. Other major features that make composites ideal for leaf springs is lack of friction between the leaf's, high strength by weight ratio, greater resistance to fatigue, "fail-safe" abilities, smoother ride, higher natural frequency, exceptional resistance to corrosion, and so on [41].

## 2 Mono Leaf Spring Dimension

In this paper the required load on the single mono leaf is been calculated manually, the mass of the mini truck is 890 kg with the pay load of 710 kg, so the approx. weight is 1600 kg, the force requirement is 3922.7 N on single mono leaf spring (Table 1).

$$1 \text{ kg} = 9.8\text{N}$$

$$\text{For 4 sheet leaf spring is} = 1600 \times 9.8 \text{ N} = 15,680 \text{ N.}$$

For single mono leaf spring:

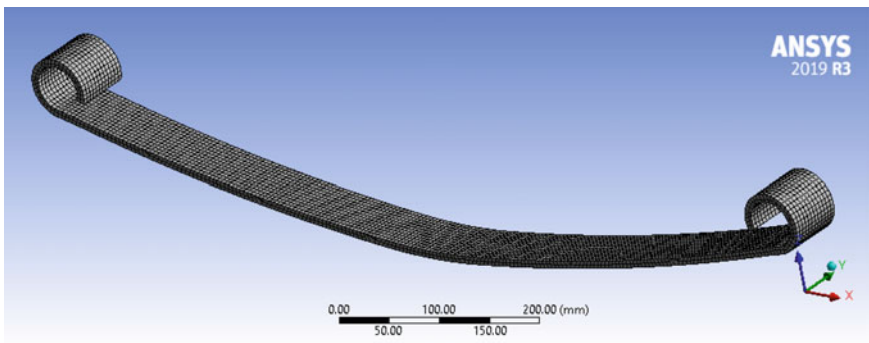
$$1600 \times 9.8/4 = 3922.66 \text{ N (3.9227 kN)}$$

So, on the single leaf spring the force will be applied around 3922.66 N.

Calculated load: The assume weight of the mini truck body is 890 kg with the payload of 710 (Fig. 1; Table 2).

**Table 1** Mono spring leaf sizing and parameters

Parameters	Values
Eye to eye diameter	930 mm
Thickness	8 mm
Width	60 mm
Camber	82.77 mm
Node	35,372
Elements	6180
Mesh size	5 mm



**Fig. 1** Meshing of single mono leaf spring

**Table 2** Load parameters

Load	Value (kg)
Body	890
Payload	710
Total	1600

### 3 Materials Selection

In this study High Carbon steel, carbon fiber (390 GPa) and PLA will be use. High carbon steel has moderate ductility while having extravagant hardness, extreme strength and wear resistance, by which we can measure the load capacity of the material while it does not break but is allowed to deform. FDM (Fused Deposition Modeling) is a method which is used for 3D printing using PLA that is a form of bioplastic. This material as well as ABS (Acrylonitrile Butadiene Styrene) is standardized for this technology. The most frequent alternatives available for consumer printers are these materials only; therefore, there is a tendency to have them compared. PLA material is user friendly and has some mechanical qualities that often interest their users. Carbon fibers are fibers consisting primarily of carbon atoms and measuring 5–10 μm (0.00020–0.00039 in.) in diameter. Carbon fibers provide a number of benefits that include elevated tensile strength, strong chemical resistance, and high stiffness, a high strength by weight ratio, minimal thermal expansion and increased temperature tolerance (Table 3).

**Table 3** Material properties

Material properties	High carbon steel	Carbon fiber 390	PLA (polylactic acid)
Poisson’s ratio	0.29	0.2	0.39
Young’s modulus	2012e+05 MPa	6000 MPa	3450 MPa
Bulk modulus	1.6825e+05 MPa	–	5227.3 MPa
Shear modulus	82171 MPa	8000 MPa	1241 MPa
Isotropic secant coefficient (thermal expansion)	1.1e–05 1/°C	–	0.000135 1/°C
Tensile ultimate strength	1070 MPa	–	59.2 MPa
Tensile yield strength	761 MPa	–	54.1 MPa
Density	7.85e–06 kg/mm <sup>3</sup>	1.8e–06 kg/mm <sup>3</sup>	1.25e–06 kg/mm <sup>3</sup>

### 4 Simulation

The simulation was conducted on ANSYS 2019 R3 In which a single leaf model was made of the eye to eye diameter of 930 mm and thickness of 8 mm. The width of the leaf was taken to be 60 mm while the camber was 82.77 mm. The total number of nodes was taken to be 35,372 with 6180 elements and a mesh size of 5 mm. A manual calculation of the required load on the single mono leaf has been conducted in this paper. The payload was taken to be 710 kg whereas the mass of the truck itself was 885 kg. The total approximate load was 1595 kg which was then rounded off to 1600 kg. This resulted in a force of 3922.7 N applicable on a single mono leaf spring.

Though stresses under different loads have been discovered, the maximum stress under 3922.7 N load for the three types of springs is illustrated in Figs. 2, 3 and 4.

- (a) Carbon fiber 390 GPa
- (b) High Carbon Steel
- (c) PLA.

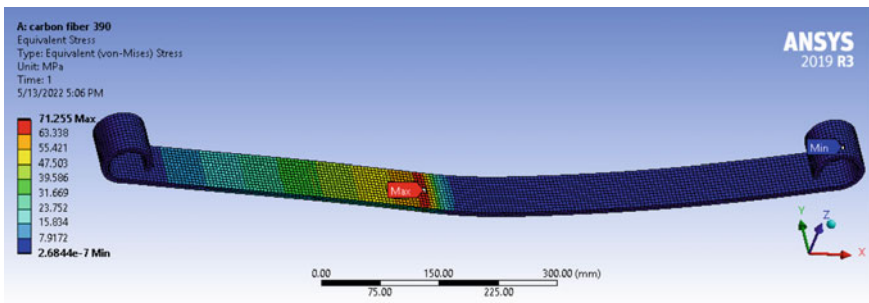


Fig. 2 Maximum stress under 3922.7 N load for carbon fiber 390 GPa

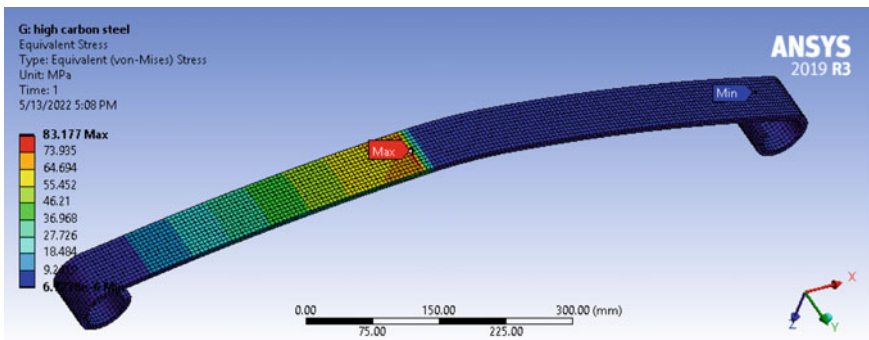


Fig. 3 Maximum stress under 3922.7 N load for high carbon steel

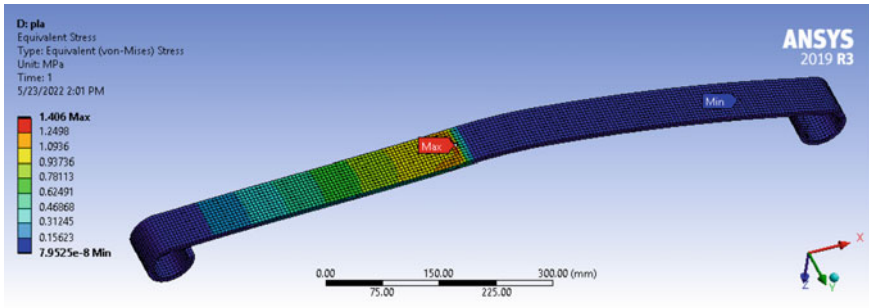


Fig. 4 Maximum stress under 3922.7 N load for PLA

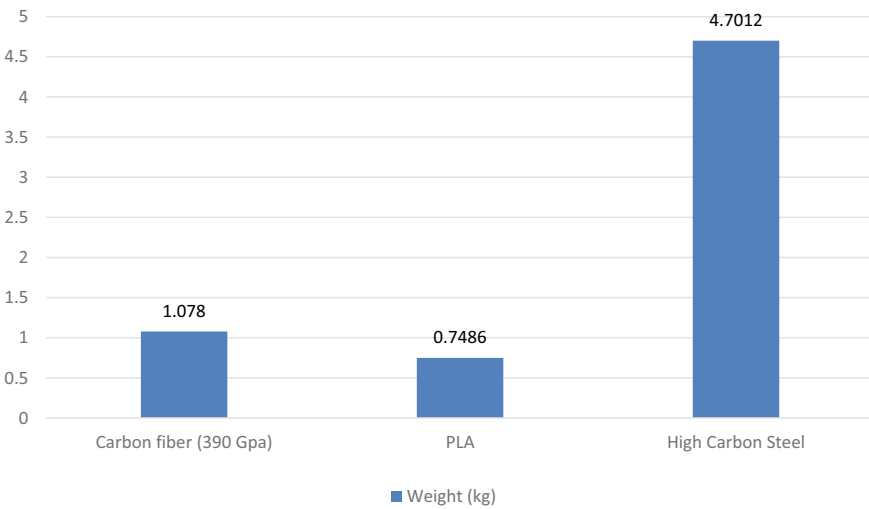


Fig. 5 Weight comparison of single mono leaf spring

Table 4 Weight reduction (for single mono leaf spring)

Properties	Carbon fiber (360 GPa)	Polylactic acid	High carbon steel
Density	$1.8e-06 \text{ kg/mm}^3$	$7.85e-06 \text{ kg/mm}^3$	$1.25e-06 \text{ kg/mm}^3$
Volume	$5.9888e+005 \text{ mm}^3$	$5.9888e+005 \text{ mm}^3$	$5.9888e+005 \text{ mm}^3$
Spring weight (kg)	1.078	0.7486	4.7012

## 5 Result and Discussion

The simulation revealed the maximum stress (equivalent von-mises), maximum equivalent elastic strain and weight variation of leaf springs. The weight was calculated manually based on the density of the components (Fig. 5; Tables 4, 5, 6, 7 and 8).



**Table 5** Stress comparison for carbon fiber 390, PLA and high carbon steel (on 3922.7 N load)

Material	Force (N)	Min. (MPa)	Max. (MPa)	Avg. (MPa)
Carbon fiber 390 (GPa)	3922.7	2.6844e-007	71.255	7.4219
PLA	3922.7	7.9525e-008	1.406	0.13444
High carbon steel	3922.7	6.7278e-006	83.177	8.19

**Table 6** Stress comparison for carbon fiber 390, PLA and high carbon steel (on 5000 N load)

Material	Force (N)	Min. (MPa)	Max. (MPa)	Avg. (MPa)
Carbon fiber 390 (GPa)	5000	3.0302e-007	71.255	7.4219
PLA	5000	1.6546e-007	1.406	0.13444
High carbon steel	5000	7.2635e-006	83.177	8.19

**Table 7** Equivalent elastic strain at 3922.7 N

Material	Force (N)	Min. (mm/mm)	Max. (mm/mm)	Avg. (mm/mm)
Carbon fiber 390 (GPa)	3922.7	2.6844e-007	71.255	7.4219
PLA	3922.7	8.1613e-011	1.279e-003	1.4736e-004
High carbon steel	3922.7	1.8345e-010	3.9279e-004	3.9279e-004

**Table 8** Equivalent elastic strain at 5000 N

Material	Force (N)	Min. (mm/mm)	Max. (mm/mm)	Avg. (mm/mm)
Carbon fiber 390 (GPa)	5000	7.8212e-011	1.279e-003	1.4736e-004
PLA	5000	2.5374e-010	4.0775e-004	3.9629e-005
High carbon steel	5000	1.8921e-010	3.9279e-004	3.9285e-005

## 6 Conclusion

In this research method main compared parameters are design optimization and analyzing the different materials like composite materials and thermoplastic. After the completion of analysis and comparing the result it has been figured out that weight of the thermoplastic material (PLA) as minimum weight and low maximum stress and PLA has the maximum elastic strain which means it has the ability to rebound easily upon the removal of the load.

## References

1. Gonçalves JPC, Ambrósio JAC (2003) Optimization of vehicle suspension systems for improved comfort of road vehicles using flexible multibody dynamics. *Nonlinear Dyn* 34(1):113–131
2. Aized T, Ahmad M, Jamal MH, Mahmood A, ur Rehman SU, Srari JS (2020) Automotive leaf spring design and manufacturing process improvement using failure mode and effects analysis (FMEA). *Int J Eng Bus Manag* 12:1847979020942438
3. Gebremeskel SA (2013) Design, simulation, and prototyping of single composite leaf spring for light weight vehicle. *Global J Res Eng* 12(7-A)
4. Öztoprak N (2013) Design of composite-based leaf spring systems for automotive sector. Master's thesis, İzmir Institute of Technology
5. Campbell FC (2010) Structural composite materials. ASM international
6. Varma N, Ahuja R, Vijayakumar T, Kannan C (2021) Design and analysis of composite mono leaf spring for passenger cars. *Mater Today Proc* 46:7090–7098
7. Kumar MS, Vijayarangan S (2007) Analytical and experimental studies on fatigue life prediction of steel and composite multi-leaf spring for light passenger vehicles using life data analysis. *Mater Sci* 13(2):141–146
8. Saini P, Goel A, Kumar D (2013) Design and analysis of composite leaf spring for light vehicles: 2319-8753
9. Ashwini K, Mohan Rao CV (2018) Design and analysis of leaf spring using various composites—an overview. *Mater Today Proc* 5(2):5716–5721
10. Patunkar MM, Dolas DR (2011) Modelling and analysis of composite leaf spring under the static load condition by using FEA. *Int J Mech Ind Eng* 1(1):1–4
11. Shankar G, Siddaramanna S, Sambagam V (2006) Mono composite leaf spring for light weight vehicle—design, end joint analysis and testing. *Mater Sci* 12(3):220–225
12. Bhattacharjee S, Kanitkar S, Kalasapur N, Patel V (2017) Composite leaf spring. *Int Res J Eng Technol* 4:1534–1541
13. Sureshkumar M, Tamilselvam P, Kumaravelan R, Dharmalingam R (2014) Design, fabrication, and analysis of a hybrid FIBER composite mono leaf spring using carbon and E-glass fibers for automotive suspension applications. *Mech Compos Mater* 50(1):115–122
14. Soliman ESMM (2019) Static and vibration analysis of CFRP composite mono leaf spring. *J Fail Anal Prev* 19(1):5–14
15. Ravi Kumar V, Lalitha Narayana R, Srinivas C (2013) Analysis of natural fiber composite leaf spring. *Int J Latest Trends Eng Technol* 182–191
16. Rajesh S, Bhaskar GB, Venkatachalam J, Pazhanivel K, Sagadevan S (2016) Performance of leaf springs made of composite material subjected to low frequency impact loading. *J Mech Sci Technol* 30(9):4291–4298
17. Raut LB, Katu AR (2016) Experimental analysis of different compositions of carbon fiber/epoxy composite and its application in leaf spring. In: *Techno-Societal 2016, international conference on advanced technologies for societal applications*. Springer, Cham, pp 699–707
18. Singh L, Kumar S, Raj S, Badhani P (2021) Aluminium metal matrix composites: manufacturing and applications. In: *IOP conference series: materials science and engineering*, vol 1149, no 1. IOP Publishing, p 012025
19. Katake KA, Mankar SH, Kale SA, Dabeer PS, Deshmukh SJ (2016) Numerical and experimental stress analysis of a composite leaf spring. *Int J Eng Technol (IJET)*. ISSN (Print): 2319-8613 ISSN (Online): 0975-402
20. Kumar MS, Vijayarangan S (2007) Static analysis and fatigue life prediction of steel and composite leaf spring for light passenger vehicles
21. Zhang B, Jia L, Tian M, Ning N, Zhang L, Wang W (2021) Surface and interface modification of aramid fiber and its reinforcement for polymer composites: a review. *Eur Polymer J* 147:110352
22. Beardmore P (1986) Composite structures for automobiles. *Compos Struct* 5(3):163–176
23. Narula CK, Allura JE, Bauer DR, Gandhi HS (1996) Advanced materials for automobiles. *Chemtech* 26(11)

24. Gumerov IF, Shafigullin LN, Vakhitova SM, Shaekhova IF (2014) Noise absorbing composite materials applied in domestic trucks. *IOP Conf Series Mater Sci Eng* 69(1):012011
25. Al-Salloum YA, Almusallam TH (2003) Rehabilitation of the infrastructure using composite materials: overview and applications. *J King Saud Univ Eng Sci* 16(1):1–20
26. Arpita K, Akhila MJ, Avi Kumar R (2018) Automated headlight intensity control and obstacle alerting system. *Int J Eng Res Technol (IJERT) NCESC-2018* 6 (2018): 13
27. Thippesh L (2018) Fabrication of hybrid composite mono-leaf spring with unidirectional glass fibers. *Mater Today Proc* 5(1):2980–2984
28. Yang M, Ma F, Pu Y, Zhi Y (2018) Response of carbon-basalt hybrid fiber reinforcement polymer under flexural load. *Mater Res Express* 5(8)
29. Raj SS, Kannan TK, Babu M, Vairavel M (2019) Processing and testing parameters of PLA reinforced with natural plant fiber composite materials—a brief review. *Int J Mech Prod Eng Res Develop* 9(2):933–940
30. Gerdeen JC, Rorrer RAL (2011) *Engineering design with polymers and composites*, vol 30. CRC Press
31. Vidya S, Wattal R, Singh L, Mathiyalagan P (2021) CO<sub>2</sub> laser micromachining of polymethyl methacrylate (PMMA): a review. *Adv Manuf Ind Eng* 939–945
32. Ali A, Nasir MA, Khalid MY, Nauman S, Shaker K, Khushnood S, Altaf K, Zeeshan M, Hussain A (2019) Experimental and numerical characterization of mechanical properties of carbon/jute fabric reinforced epoxy hybrid composites. *J Mech Sci Technol* 33(9):4217–4226
33. Flynn J, Amiri A, Ulven C (2016) Hybridized carbon and flax fiber composites for tailored performance. *Mater Des* 102:21–29
34. Dhakal HN, Zhang ZY, Guthrie R, MacMullen J, Bennett N (2013) Development of flax/carbon fibre hybrid composites for enhanced properties. *Carbohydr Polym* 96(1):1–8
35. Ma F, Yang M, Wang G, Yongfeng P, Wang X, Dai W (2019) Response of carbon-basalt hybrid fiber reinforced polymer under low velocity impact load. *Mater Res Express* 6(9):095311
36. Singh L, Kumar S, Raj S, Badhani P (2021) Development and characterization of aluminium silicon carbide composite materials with improved properties. *Mater Today Proc* 46:6733–6736
37. Singh L, Kumar R, Bhardwaj Y, Singh M, Kumar R (2023) Estimation of flyer velocity for Titan 12 (Grade 1) plates by pin contact velocity measurement method. In: Singari RM, Jain PK, Kumar H (eds) *Advances in manufacturing technology and management. Lecture notes in mechanical engineering*. Springer, Singapore. [https://doi.org/10.1007/978-981-16-9523-0\\_49](https://doi.org/10.1007/978-981-16-9523-0_49)
38. Corvi A (1990) A preliminary approach to composite beam design using FEM analysis. *Compos Struct* 16(1–3):259–275
39. Singh L, Nafees A, Dubey K (2022) Hydrogen fuel cell hybrid technology in aviation: an overview. In: *Biennial international conference on future learning aspects of mechanical engineering*. Springer Nature Singapore, Singapore, pp 803–821
40. Abdelgader HS, Jarosław G (2003) Stress-strain relations and modulus of elasticity of two-stage concrete. *J Mater Civil Eng* 15(4):329–334
41. Kalanchiam M, Chinnasamy M (2012) Advantages of composite materials in aircraft structures. *Int J Mech Aerosp Ind Mechatron Manuf Eng* 6(11):2428

# Design and Analysis of a Compliant Microgripper



Anurag T. Vidap, Bhagyesh D. Deshmukh, and Sujit. S. Pardeshi

**Abstract** Microsystems' Technology has proven its utility in a variety of fields, including biomedical, material wisdom, and automotive. To transport/handle micro-sized objects safely, a typical microsystem requires a precise microgripper. The correct absorbing force must be considered when handling the components in order to cover the micro-part from inordinate absorbing force. Researchers have mentioned several tools, but a simple, low-cost, and compact tool is lacking. In this paper, an attempt is made to design a microgripper. A numerical simulation is used to develop and validate a mock rigid-body model (PRBM) of a biddable microgripper, and the issues are respectable.

**Keywords** Compliant microgripper · PRBM · Displacement · Force · Compliant mechanism · Microfabricated · MEMS

## 1 Introduction

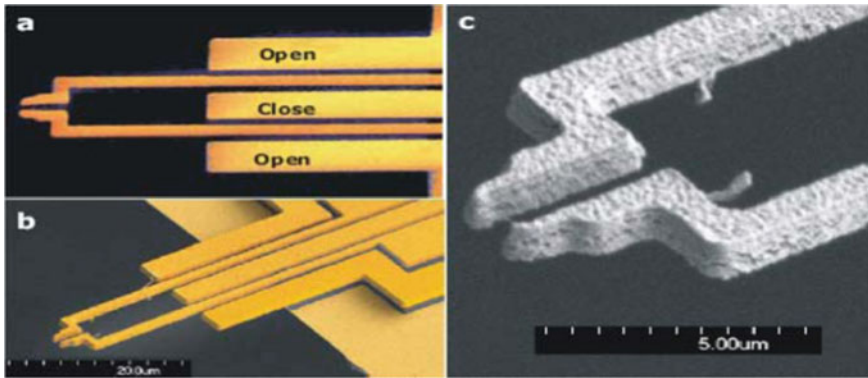
Microgrippers are implicit end-effectors for systems that can grapple and control the micro and nano-gauged objects, with operations in a variety of scientific and artificial fields [1, 2]. Microgrippers have come more important in the MEMS field for a variety of operations. Microgripper structures offer a wide range of uses, including micro-manipulation of micro-patches, micro-factors, and indeed cells, as well as assembly and medicinal operations, and have formerly had a significant impact on current and unborn technology [3], and these may be placed next to each other save space. For illustration, see Fig. 1.

A microgripper could be useful for icing safe carriage of small objects similar as electronic bias, carrying end-effectors for endoscopic manipulations, and grasping

---

A. T. Vidap (✉) · B. D. Deshmukh  
Walchand Institute of Technology, Solapur, Maharashtra 413006, India  
e-mail: [vidapanurag@gmail.com](mailto:vidapanurag@gmail.com)

Sujit. S. Pardeshi  
College of Engineering, Pune, Maharashtra 411005, India



**Fig. 1** Types of microgrippers

cells for bioapplication. The conditions for making such a gripper are to achieve quasi-static stir, high micro-positioning delicacy, and the capability to snare a wide range of objects. Microtechnologies have formerly demonstrated electrostatic microgrippers in the last decade, but their low aspect rate averted safe movement of micro-particulars [4].

### ***1.1 Compliant Mechanism***

Mechanisms that contain entire or partial stir from the deformation of their compliant parts are termed as compliant mechanisms. The compliant mechanisms are the same as the general mechanisms defined by the transmission of the stir, force, or energy. The contradistinction midst them is that flexible material supersedes linkages and hinges. According to Howell [3], compliant mechanism is classified into two types: lumped-compliant mechanism; and distributed-compliant mechanism. The reason for using the compliant mechanism to do this device is because it is just a two-dimensional structure, so it is suitable for microfabrication. Another reason is that it can be designed by specific delineations.

### ***1.2 Historical Background of Compliant Mechanism***

The conception of using flexible members to store energy and produce stir has applied to glories. Archaeological substantiation suggests that curvatures have been in use since before 8000 B.C. and was the primary armament and stalking tool in utmost cultures. Beforehand, curvatures were constructed of fairly flexible materials similar as wood and beast potency. Catapults are another illustration of the early use of

compliant members used by the Greeks as early as the fourth century B.C. Early catapults were constructed of rustic members that were deformed to store energy and also release into propel a gunshot.

### ***1.3 Pseudo-Rigid-Body Model***

A model called Pseudo-Rigid-Body Model (PRBM) has been developed to help designing of similar compliant structures. Through originally made for assembly of several original compliant joints, it have been extended to global compliant systems, and to systems with mixed original and compliant deflections [5].

### ***1.4 Flexure Hinge***

The most important components in FCMs are the flexure hinges (Flexure based Compliant Mechanisms). A flexure hinge is a mechanical element that, rather of a conventional rotational joint, provides relative gyration between conterminous rigid members by flexing (bending). Each flexure hinge should be accompanied by a complete set of compliances (or, in the contrary case, stiffness) that define its mechanical response to quasi-static loading [6].

## **2 Modeling**

A detail literature check was carried out in order to gather in depth knowledge of Compliant Mechanism, their Modeling and analysis. Modeling and analysis of a compliant microgripper is carried out in order to establish the methodology for detail analysis of the mechanism.

### ***2.1 Design Approach***

The conception of the (pseudo-rigid-body mechanism) tactic and other strategies has fortuitously made it possible to design and analyze a wide range of compliant mechanisms in a straightforward manner. Researchers frequently utilize two strategies while creating compliant mechanisms.

## 2.2 Flexure Hinge

The PRBM aims to provide a straightforward framework for studying systems that suffer substantial nonlinear deformations [8]. Design is carried out by synthesizing a rigid-body mechanism. Also, the thing is designed flexible with the use of flexible hinges and tested for its intended function. Both stirs including the force–deflection connection are predicted by the pseudo-rigid-body model. The model employs pin joints and springs, and it is critical to locate the pin joint-associated spring constant locations. The PRBM was already utilized nearly exclusively for something like the design and modeling of goods when the seismic deformation is nonlinear, yet dynamical factors do not play a significant role in mechanism effectiveness. The PRBM seems to have a strong reputation of being a consistent indicator of immobile behavior in compliant systems.

## 2.3 Analytical Formulation for Displacement of a Compliant Microgripper

To find out the relation of force and displacement, a PRBM has to be established. For this, the study of effect of flexure radius, position of flexure, and thickness is needed. Kinematic synthesis approaches are used to design lumped and distributed-compliant mechanism independently.

**Kinematic Synthesis Approach:** Kinematic synthesis approach is also called as design approach of pseudo-rigid-body mechanism, where the design is originally performed by synthesizing a rigid-body mechanism, and also the flexibility is introduced to redesign the hinged joints of rigid-body parts as flexible hinges. The execution of the eventuating compliant element is roughly like a pseudo-rigid-body mechanism when compared to that of a rigid-body mechanism.

As mentioned in [9], the flexural pivot spring constant  $K$  is determined by Equation (i) for miniature length flexible pivot springs,

$$k = \frac{El(l)}{l}, \quad (1)$$

where

$k$  = spring constant,

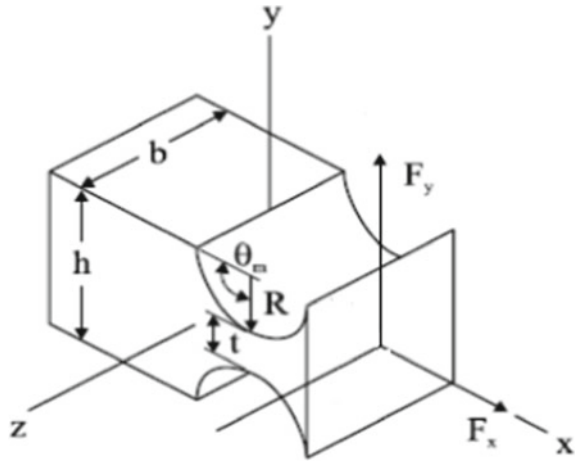
$I$  = beam moment of inertia,

$E$  = Young's modulus,

$l$  = length of flexible segment.

The flexures are replaced by torsional springs with comparable stiffness, as shown in Fig. 2, when developing the compliant mechanism,

Fig. 2 Flexure hinge



$$k_{\theta} = \frac{2Ebt^{2.5}}{9\pi r^{0.5}}, \tag{2}$$

where

- $b$  = thickness of plate used,
- $k_{\theta}$  = torsional stiffness of the hinge,
- $E$  = Young's modulus of material used,
- $t$  = hinge thickness,
- $r$  = flexure radius.

Theoretical Calculation of Compliant Microgripper Displacement: As previously stated, PRBM is advantageous tool for adjudicate the connection amidst force and displacement. Basic modeling of a compliant microgripper is done by employing the (PBRM) concept. The use of PRBM in conjunction with classical cantilever beam theory simplifies the model in order to anticipate mechanism response under prescribed input motion.

Figure 3 exhibits the basic model of compliant microgripper. A pull-type input force makes this device which acts as a gripper as shown in Fig. 3.

$$Y = \frac{Fl^2}{4k_{\theta}}. \tag{3}$$

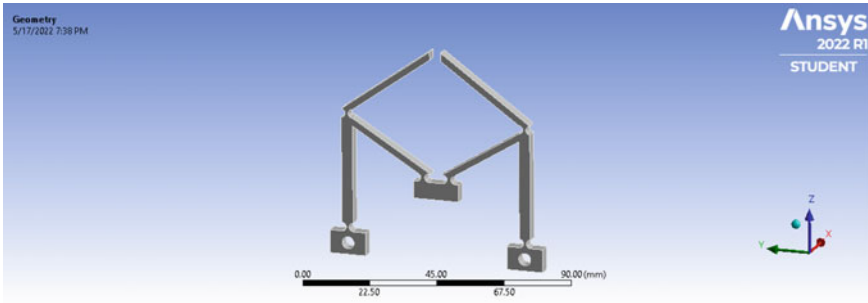
Equation (3) provides the displacement of a compliant microgripper.

The dimensions considered for analysis are  $b = 2.4$  mm,  $t = 1.5$  mm,  $r = 2$  mm, and  $l = 40$  mm. FEA analysis is executed for the compliant mechanism considering plastic, acrylonitrile butadiene styrene (ABS) material ( $E = 1628$  N/mm<sup>2</sup>).

Input force and input displacement are calculated by PRBM and are tabulated in Table 1.

Table 1 shows input displacement of the compliant microgripper versus input force for a thickness of 2.4 mm. The analytical equation obtained is used for carrying out





**Fig. 3** Microgripper model

**Table 1** Input force and displacement

Input force $F$ (N)	Input displacement (mm)
0.1	0.0742
0.5	0.3713
1	0.7426
1.5	1.1133
2	1.4852

displacement analysis for displacement of microgripper which is to be validated by using FEA (ANSYS) and Catia.

### 3 Finite Element Method

Only planar compliant mechanisms are addressed in this study, and its obsolete affirmed that the compliant mechanisms are manufactured from material thick enough to withstand the  $x$ -directional load, with out of plane displacements being negligible.

#### 3.1 Steps in FEM

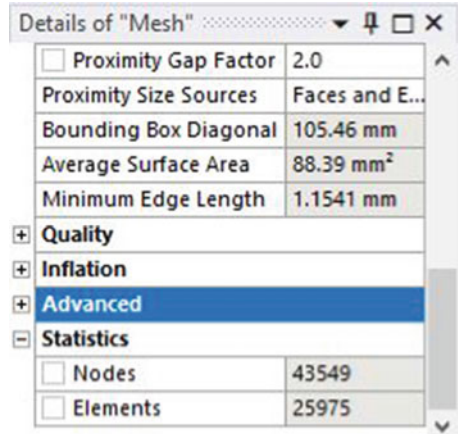
(a) *Preprocessor model generation*

See Figs. 3 and 4.

(b) *Solution application of a load and boundary conditions*

Boundary parameters and load are imposed to the meshed model. To accomplish micro-displacement static structural analysis, module of Catia is considered

Fig. 4 Meshing details



for analysis. Figure 5 shows application of boundary conditions to the model. After specifying boundary conditions, solution is carried out for resulting deformation.

(c) *Postprocessor display results*

The solution obtained by the solution process is a general solution. The displacement plot is obtained for the particular load condition and is represented in (Fig. 6). The displacement analysis is carried out over a range of input force (0.1–0.5–1–1.5–2 N) and the equaling results are represented in Table 2.

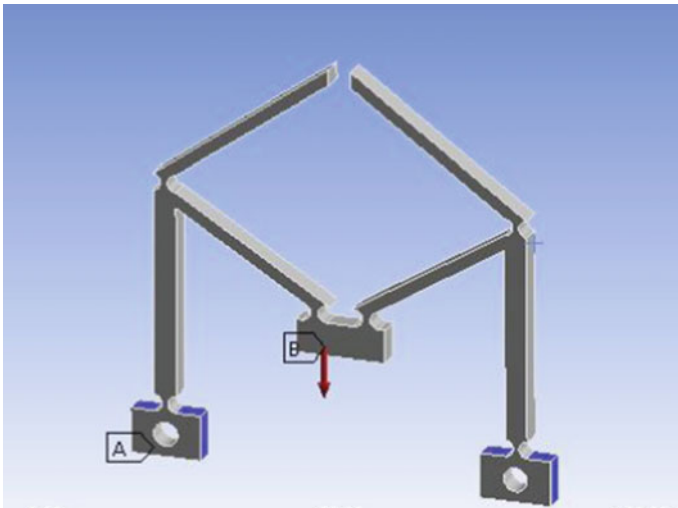
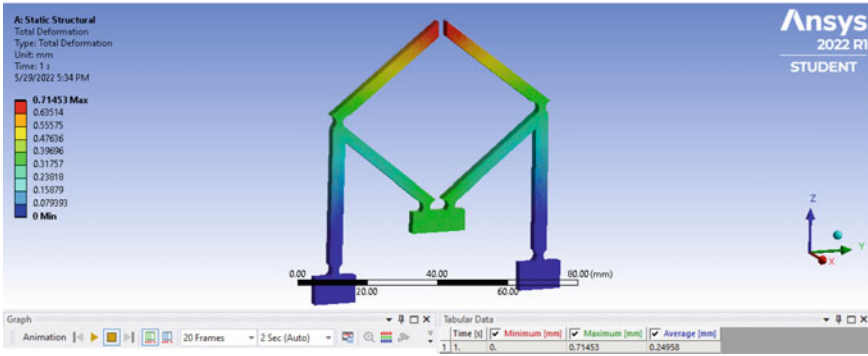


Fig. 5 Boundary conditions



**Fig. 6** Displacement plot

**Table 2** Simulation results

Force	Displacement (mm)
0.1	0.0714
0.5	0.3572
1	0.7145
1.5	1.1071
2	1.4291

In the above table, the displacement is found out by varying the input force. Now from Tables 1 and 2, results obtained by PRBM technique, analysis using ANSYS, and error percent are tabulated in Table 3.

These results exhibit a minimal error, which can be proved to be smaller on further refinement of the model. Figure 6 illustrates the ANSYS results of displacement of the microgripper on which a force of 1N is imposed.

**Table 3** Results by PRBM technique, analysis using ANSYS, and error percent

Force (N)	Displacement (mm) by PRBM	Displacement (mm) by ANSYS	Error %
0.1	0.0742	0.0714	3.78305
0.5	0.3713	0.3572	3.78305
1	0.7426	0.7145	3.78485
1.5	1.1133	1.1071	3.78441
2	1.4852	1.4291	3.78215

## 4 Discussion

The results exhibit that a microgripper can be analyzed using the PRBM technique, and design variations can be easily accommodated for analysis of grippers used for different applications. The procedure and approaches described above help to design novel microgrippers for specific applications.

The displacements are calculated by varying the input force; the results obtained by analytical, and simulations are in close agreement.

## 5 Conclusion

- The PRBM technique was used to investigate a displacement model for a compliant gripper mechanism, then validated through simulation using finite element analysis.
- To demonstrate consistency, simulation trials are run on the model in order for the solution to converge closer to the exact value.
- The results are validated using classical rigid-body equations developed using the PRBM technique and they vary within acceptable limits.
- The simple microgripper analysis demonstrates the variation of displacement at the jaws from its calculated value. The results exhibit a microgripper which can be analyzed using the PRBM technique, and design variations can be easily accommodated for analysis of grippers used for different applications.
- This paper depicts the design and analysis of novel-compliant microgripper using the PRBM technique.

## References

1. Khare P, Madhab GB, Kumar CS, Mishra PK (2007) Optimizing design of piezoelectric actuated compliant Microgripper mechanism. In: 13th National Conference Mechanisms and Machines, Bangalore, India, pp 1–4
2. Feng Z, Zhang W, Su B, Harsh KF, Gupta KC, Bright V, Lee YC (1999) Design and modeling of RFMEMS tunable capacitors using electro-thermal actuators. IEEE MTT-S Int Microwave Symp Dig 4:1507–1510
3. Howell LL (2001) Compliant Mechanisms, Mechanical engineering department Brigham Young University, John Wiley & Sons, Inc, pp 1–180
4. Kim CJ, Pisano AP, Muller R (1992) Silicon-processed overhanging microgripper. J Micro Electro Mech Syst 1:31
5. Sung Alexander E, Slocum H, Ma R (2011) Design of an ankle rehabilitation device using compliant mechanisms. J Med Devices ASME MARCH 5:011001 (1–7)
6. Lobontiu N (2002) Compliant mechanism design of flexure hinges. CRC Press Boca Raton London New York Washington, DC
7. Midha A, Howell LL, Norton TW (2000) Limit positions of compliant mechanisms using the pseudo-rigid-body model concept, Department of Mechanical and Aerospace Engineering and

Engineering Mechanics, University of Missouri Rolla, Rolla, MO, 65409-0050, USA. *Mech Mach Theory* 35:99-115

8. Yong YK, Lu T-F, Handley DC (2008) Review of circular flexure hinge design equations and derivation of empirical formulations, School of Mechanical Engineering, The University of Adelaide, SA 5005, Australia. *Precis Eng* 32:63-70
9. Lee WH, Kang BH, Young SO, Harry S, Arthur CS, George S, Matthew E (2003) Micropeg manipulation with a compliant microgripper. In: *Proceedings of IEEE international conference on robotics and automation*, pp 3213-3218

# Water Logging Analysis over Dubai Using Sentinel-2 Satellite Imagery



Sarath Raj, Ayush Harish, and Sathiyagayathiri Ramamoorthy

**Abstract** Remote sensing techniques are utilized for the analysis of water and land cover. Normalized difference water index (NDWI) is applied for the identification of water-associated characteristics of an area. The technique is used for discovering water covers, moisture over an area, and identifying droughts. Modified normalized difference water index (MNDWI) is capable of removing built-up land noise. This technique is appropriate for analyzing areas with many developed land areas. These techniques are made use of with the help of the SENTINEL-2A series. The area of interest in is Dubai, UAE. The image attained is a Level-1C orthorectified image. Google Earth Engine (GEE) is used to attain the images with the help of Top of Atmosphere Reflectance (TOA). The images are processed with the help of QGIS software. NDWI and MNDWI techniques are used to identify water covers in Dubai and identify places with the possibility of waterlogging.

**Keywords** Normalized difference water index (NDWI) · Modified normalized difference water index (MNDWI) · Top of Atmosphere Reflectance (TOA) · Remote sensing · QGIS · GEE

## 1 Introduction

Remote sensing is acquiring physical data with help of a satellite. It was introduced by Sir William Herschel in 1800 [1]. One hundred and fifty earth observation satellites are in the orbit for earth observation purpose. The selection of the satellite among all these satellites depends on the area of analysis. Each satellite provides different spatial and spectral resolutions. The most commonly used satellite is Landsat and Sentinel because these satellites can be used for free, provide RGB bands, and are suitable for land cover mapping. Since earth observation is the main aim of remote sensing, methods such as Normalized Difference Vegetation Index (NDVI), normalized difference water index (NDWI), and modified normalized difference water index

---

S. Raj (✉) · A. Harish · S. Ramamoorthy  
Amity University, Dubai, UAE  
e-mail: [sraj@amityuniversity.ae](mailto:sraj@amityuniversity.ae)

© The Author(s), under exclusive license to Springer Nature Singapore Pte Ltd. 2023  
R. Sharma et al. (eds.), *Advances in Engineering Design*, Lecture Notes in Mechanical Engineering, [https://doi.org/10.1007/978-981-99-3033-3\\_56](https://doi.org/10.1007/978-981-99-3033-3_56)

683

(MNDWI) were introduced to make this possible [2, 3]. In 1996, a remote sensing indicator by the name of NDWI was developed to elevate and showcase the features of landscapes related to water by McFeeters [4]. Water has the highest absorption of incident energy. The reflectance of water is low and it directly depends on the wavelength. In clear water, the reflectance of a band can be ranked as Blue Band, Green Band, Red Band, Near-Infrared (NIR), and Medium-Infrared (MIR). The reflectance of water is also affected by the turbidity of the water [5].

NDWI is a technique that captures water covers and other features with help of Green and NIR Bands. The bands used vary from  $0.86 \mu\text{m}$  to  $1.24 \mu\text{m}$  [3]. Green Band is used instead of red band which is because soil and vegetation areas are more visible to the Green Band. This is because of the absorption of chlorophyll which makes it have a lower reflectance which only Green Band can capture [6]. MNDWI is a modified method of NDWI introduced by Xu in 2006 [7]. This method can capture water-related features in a built-up area and reduce errors in areas with shadows. The error in NDWI is that instead of considering Clouds and Mountains as the formation of shadows, it also considers lakes as shadows too and this error is reduced by the MNDWI technique [8]. This paper is trying to learn about the change in water covers to identify waterlogged places. Waterlogging is a condition where there is a collection of excessive water which leads to a deficiency of soil nutrients [9]. This condition leads to deprivation of oxygen to the roots. The cause of waterlogging could be natural or man-made. Natural cause is due to blockage in the natural drainage over the lands, while leakage from surface drains or loss of water from improper irrigation systems is the man-made reasons of waterlogging [10].

## 2 Objective

This paper aims to study and witness the water cover changes over the years for avoiding waterlogging issues in Dubai, UAE, using the NDWI/MNDWI technique. The paper has models ranging from 2017 to 2021.

## 3 Area of Interest

United Arab Emirates (UAE) is made up of seven emirates. The seven emirates are as follow: Abu Dhabi, Dubai, Sharjah, Ras Al Khaimah, Ajman Umm al Quwain, and Fujairah. It is located in the Southeast of the Arab Peninsula [11]. Dubai is the second largest emirate with an area of  $4110 \text{ km}^2$  [12]. The coordinates of UAE are  $23.4241^\circ \text{ N } 53.8478^\circ \text{ E}$ , while the coordinates of Dubai are  $25.07725^\circ \text{ N}, 55.30927^\circ \text{ E}$  [13]. Dubai has a sandy desert topography with the southern part being dominated by gravel deserts [14]. According to the 2021 data, the population of UAE is 9,991,089 and there has been an increase of 1.31% in the population from the previous year.



**Fig. 1** Geographic area of Dubai, UAE

Dubai has a population of 1,137,347 and is the most populated among the other emirates [15] (Fig. 1).

## 4 Methodology

European Space Agency (ESA) is leading the Copernicus program which consists of the Sentinel family of satellites. The program Sentinel family of the satellite has a set of six satellites starting with Sentinel-1 up to Sentinel-6. Sentinel-1 has a set of four satellites, Sentinel-2 has a set of two satellites, and Sentinel-3 has a set of four satellites. Sentinel-5 and 6 will be launched by the year 2023 [16]. Sentinel-2 has a swath width of 290 km and can cover an area of  $-56^{\circ}$  to  $84^{\circ}$  in latitude. The Sentinel-2A was launched on June 23, 2015, and Sentinel-2B was launched on March 7, 2017. The Multispectral Instrument (MSI) present in the satellite (Sentinel-2) consists of 13 spectral bands in the wavelength. Visible, Near-Infrared (NIR), and Short-Wave Infrared (SWIR) are the wavelength that is available in Sentinel-2 [17]. The satellites cover the surface every 10 days. The operation cycle of the Sentinel-2 mission involves orbit maintenance followed by image acquisition and downlink of the data [12].



The Sentinel-2 has bands varying from B1 to B12 and three other bands, namely QA10, QA20, and QA60. The scale of bands B1 to B12 is 0.0001. B1 band or also known as Aerosol Band consists of two wavelengths 442.3 nm and 443.9 nm for S2B and S2A, respectively, while B2 band or also called as Blue Band consists of two wavelengths 492.1 nm and 496.6 nm for S2B and S2A, respectively. B3 band or also known as Green Band consists of two wavelengths 559 nm and 560 nm for S2B and S2A, respectively. B4 band or also known as Red Band consists of two wavelengths 665 nm and 664.5 nm for S2B and S2A, respectively. B5 band or also known as Red Edge 1 Band consists of two wavelengths 703.8 nm and 703.9 nm for S2B and S2A, respectively. B6 band or also known as Red Edge 2 Band consists of two wavelengths 739.1 nm and 740.2 nm for S2B and S2A, respectively. B7 band or also known as Red Edge 3 Band consists of two wavelengths 779.7 nm and 782.5 nm for S2B and S2A, respectively. B8 band or also known as NIR Band consists of two wavelengths 833 nm and 835.1 nm for S2B and S2A, respectively. B9 band or also known as Water Vapor Band consists of two wavelength 943.2 nm and 945 nm for S2B and S2A, respectively. B10 band or also known as Cirrus Band consists of two wavelengths 1376.9 nm and 1373.5 m for S2B and S2A, respectively. B11 band or also known as SWIR 1 Band consists of two wavelengths 1610.4 nm and 1613.7 nm for S2B and S2A, respectively. B12 band or also known as SWIR 2 Band consists of two wavelengths 2185.7 nm and 2202.4 nm for S2B and S2A, respectively, while band QA10 and QA20 are usually empty and do not provide any data and QA60 is a band which defines the Cloud Mask which is providing images with or without a cloud cover within a spatial range of 60 m. Cloud could be a Dense or a Cirrus Cloud [13].

The bands which are used for this study are Band 3, Band 8, and Band 11. The data are taken over Dubai, UAE, over the years 2017–2021 (Fig. 2).

## ***4.1 Tools Used***

### **4.1.1 GEE**

Google Earth Engine (GEE) is a powerful, high-performance open-source software found by Google to capture a large array of data for analysis of multisensory, multi-scale, and multitemporal images. It provides Earth Observation (EO) data which are used for purpose of prevention, risk monitoring, and study purposes.

The GEE provides us with the datasets which are data received from satellites such as Landsat Satellite series, Sentinel Satellite series, Moderate-Resolution Imaging Spectrometer (MODIS), and many more. The data received from these satellites are Shapefiles, Digital Terrain Models (DTM), Meteorological Data, Land and Water cover, and more [18].

**Fig. 2** Methodology path of NDWI image



### 4.1.2 QGIS

QGIS is software that is in use to analyze and edit spatial information. The software is advanced and user-friendly. It was found by Gary Sherman in July 2002. QGIS supports two methods [19]. The first method uses vector data. In this method, it represents objects in the elements of polygons, lines, and points. Water bodies such as rivers and pipelines or anything which has a shape to it can be captured by this data.

The second method uses raster data which showcases characteristics that do not have a shape to it such as annual rainfall, depth of water bodies, elevation, and many more. Raster means a matrix of square cells with each of the cells displaying depth with varying color, i.e., the deeper the surface, the darker the color becomes. Raster images' examples are aerial photos and satellite images [20].

## 4.2 Calculation for Analysis

### 4.2.1 Calculation of NDWI

NDWI uses Band 3 to increase the reflectance to capture water bodies, while Band 8 is used to capture water bodies with a minimum reflectance.

$$\text{NDWI} = \frac{\rho_{\text{Green}} - \rho_{\text{NIR}}}{\rho_{\text{Green}} + \rho_{\text{NIR}}},$$

where:

$\rho_{\text{Green}}$  = Top of Atmosphere Reflectance of Green Band.

$\rho_{\text{NIR}}$  = Top of Atmosphere Reflectance of Near-Infrared.

### 4.2.2 Calculation of MNDWI

MNDWI avoids noise signals from the surface. SWIR can absorb the water body better than NIR. This is useful for capturing water bodies in built-up surfaces [21].

$$\text{MNDWI} = \frac{\rho_{\text{Green}} - \rho_{\text{SWIR}}}{\rho_{\text{Green}} + \rho_{\text{SWIR}}},$$

where:

$\rho_{\text{Green}}$  = Top of Atmosphere Reflectance of Green Band.

$\rho_{\text{SWIR}}$  = Top of Atmosphere Reflectance of Short-Wave Infrared.

## 4.3 Analysis of NDWI/MNDWI

See Figs. 3, 4, 5, 6, 7, 8, 9, 10, 11, and 12.

The values of NDWI and MNDWI are as follows (Tables 1 and 2).



**Fig. 3** Normalized difference water index of UAE for 2017



**Fig. 4** Normalized difference water index of UAE for 2018



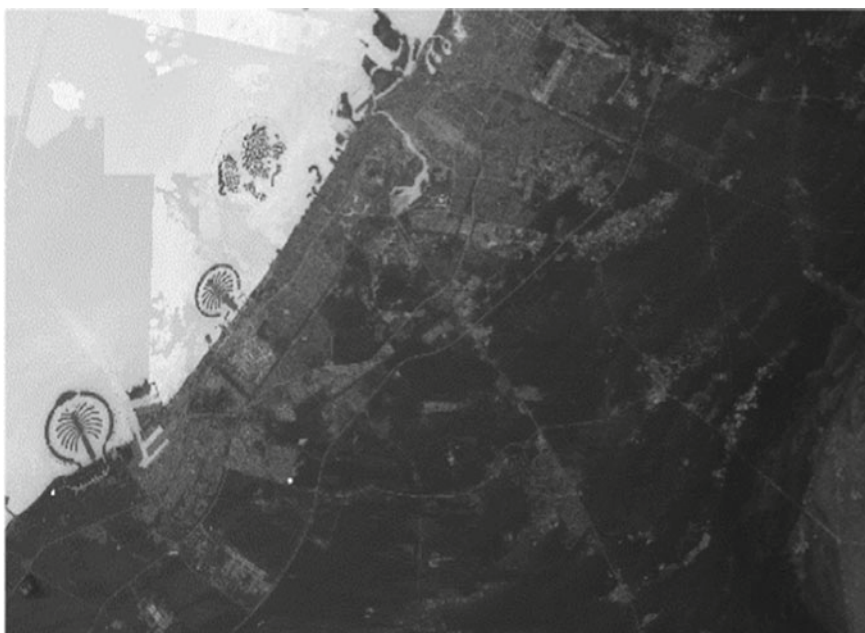
**Fig. 5** Normalized difference water index of UAE for 2019



**Fig. 6** Normalized difference water index of UAE for 2020



**Fig. 7** Normalized difference water index of UAE for 2021



**Fig. 8** Modified normalized difference water index of UAE for 2017

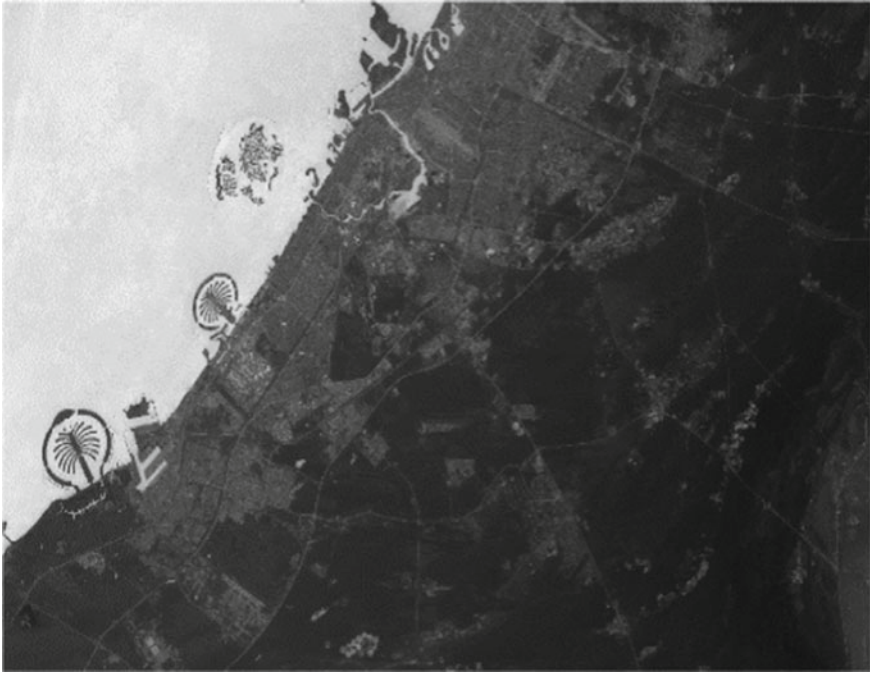


**Fig. 9** Modified normalized difference water index of UAE for 2018



**Fig. 10** Modified normalized difference water index of UAE for 2019



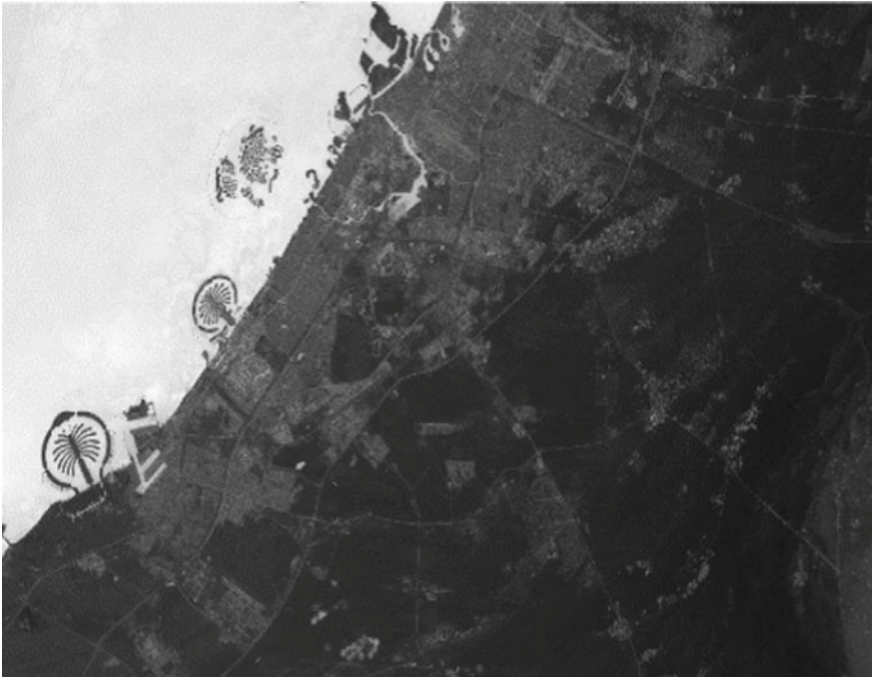


**Fig. 11** Modified normalized difference water index of UAE for 2020

## 5 Results and Discussions

The images were attained with the help of QGIS. The data are received from the Sentinel-2 satellite. According to the images provided, the change over the 4 years in Dubai, UAE, is not very visible. This does not mean that there has been no change over the year. To identify these changes, NDWI and MNDWI formulas are made in use and the changes are visible in the values received in the table. There has been an increase of 6.64% in NDWI value and an increase of 2.33% in MNDWI value in Dubai over the years. Therefore, the water covers over Dubai have been increasing over the years and waterlogging issues are highly possible.



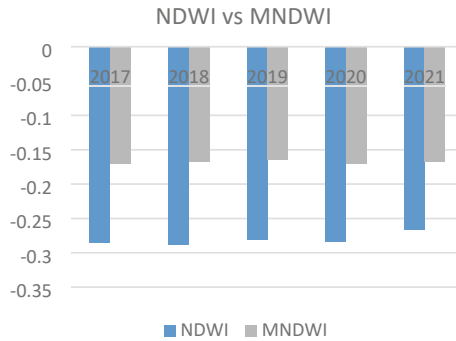


**Fig. 12** Modified normalized difference water index of UAE for 2021

**Table 1** Auxiliary data obtained

YEAR	NDWI	MNDWI
2017	- 0.286	- 0.171
2018	- 0.288	- 0.168
2019	- 0.281	- 0.165
2020	- 0.284	- 0.171
2021	- 0.267	- 0.167

**Table 2** Yearly distribution of NDWI and MNDWI of UAE



## 6 Conclusion

The paper studies the water covers over the Dubai, UAE, for the years 2017–2021. These water cover data can be utilized for understanding possible waterlogging problems in Dubai, UAE. The images seen above were received using the Sentinel-2, where NDWI and MNDWI were utilized to produce data which were then reviewed using QGIS. The analyzed data can be concluded to understand that there has been increment of about 6% over the years. This means that there is possibility of water logging in the city.

## References

1. Campbell JB, Wynne RH (2011) Introduction to remote sensing. Guilford Press
2. Sarath Raj NS, Elsonabty NA, Bhatkar RR (2021) Greenness visualization in Al-Ain using landsat imagery. In: 2021 12th international conference on computing communication and networking technologies (ICCCNT), pp 1–5. <https://doi.org/10.1109/ICCCNT51525.2021.9709623>
3. Szabo S, Gácsi Z, Balazs B (2016) Specific features of NDVI, NDWI and MNDWI as reflected in land cover categories. *Landscape Environ* 10(3–4):194–202
4. Özelkan E (2020) Water body detection analysis using NDWI indices derived from landsat-8 OLI. *Pol J Environ Stud* 29(2):1759–1769
5. Zhou W, Li Z, Ji S, Hua C, Fan W (2014) A new index model NDVI-MNDWI for water object extraction in hybrid area. In: International conference on geo-informatics in resource management and sustainable ecosystem. Springer, Berlin, Heidelberg, pp 513–519
6. Singh SK (2017) Delineation of waterlogged areas in Vaishali district (Bihar) using normalized difference water index. *J Clim Change Water* 34
7. Baig MHA, Zhang L, Wang S, Jiang G, Lu S, Tong Q (2013) Comparison of MNDWI and DFI for water mapping in flooding season. In: 2013 IEEE international geoscience and remote sensing symposium-IGARSS. IEEE, pp 2876–2879
8. Chen Y, Huang J, Song X, Wu H, Sheng S, Liu Z, Wang X (2018) Waterlogging risk assessment for winter wheat using multisource data in the middle and lower reaches of Yangtze River. *Int J Agric Biol Eng* 11(5):198–205
9. Neeraj K, Kamal K (2016) Time series analysis of glacial lake in western Himalayas based on NDWI and MNDWI. *Int J Res Appl Sci Eng Technol* 4(3):527–533
10. Kaushik S, Dhote PR, Thakur PK, Aggarwal SP (2018)
11. Assessing the impact of canal network on surface waterlogging using remote sensing datasets in Rohtak district, Haryana. *Int Arch Photogram Remote Sens Spat Inf Sci*
12. Traganos D, Reinartz P (2018) Mapping mediterranean seagrasses with Sentinel-2 imagery. *Mar Pollut Bull* 134:197–209
13. Wang Q, Atkinson PM (2018) Spatio-temporal fusion for daily Sentinel-2 images. *Remote Sens Environ* 204:31–42
14. Phiri D, Simwanda M, Salekin S, Nyirenda VR, Murayama Y, Ranagalage M (2020) Sentinel-2 data for land cover/use mapping: a review. *Remote Sens* 12(14):2291
15. Wang Q, Shi W, Li Z, Atkinson PM (2016) Fusion of Sentinel2 images. *Remote Sens Environ* 187:241–252
16. Drusch M, Del Bello U, Carlier S, Colin O, Fernandez V, Gascon F, Hoersch B, Isola C, Laberinti P, Martimort P, Meygret A (2012) Sentinel-2: ESA's optical high-resolution mission for GMES operational services. *Remote Sens Environ* 120:25–36

17. Main-Knorn M, Pflug B, Louis J, Debaecker V, Müller-Wilm U, Gascon F (2017) Sen2Cor for sentinel-2. In: Image and signal processing for remote sensing XXIII, vol 10427. International Society for Optics and Photonics, pp 1042704
18. Fattore C, Abate N, Faridani F, Masini N, Lasaponara R (2021) Google earth engine as multi-sensor open-source tool for supporting the preservation of archaeological areas: the case study of flood and fire mapping in Metaponto, Italy. *Sensors* 21(5):1791
19. Lee GL, Han KS, Yeom JM, Pi KJ, Park SJ (2009) Water stress monitoring using NDWI around deserts of China and Mongolia. In: Remote sensing for environmental monitoring, GIS applications, and geology IX, vol 7478. International Society for Optics and Photonics, pp 74780Z
20. Kurt Menke GISP, Smith R, Pirelli L, John Van Hoesen GISP (2016) Mastering QGIS. Packt Publishing Ltd
21. Linuxjournal.com (2019) Getting started with quantum GIS | Linux Journal

# Comparative Deflection Analysis of a Cantilever Beam Fixed at One End by Using Finite Element and Analytical Method



Aditya Pratap Singh, Shrikant Vidya, P. Suresh, and Amresh Kumar

**Abstract** In mechanical and civil engineering, beams are considered as a common feature of many buildings, structures buildings, and the bending beams studies are also a significant part of a comprehensive field of structural mechanics and mechanics of materials. Under the activity of a uniformly dispersed load along its own weight and an outside vertical accumulated load at the free end, the old style issue of deflection of linear elastic material of a cantilever beam is being analytically and numerically analyzed. Material is being presumed to be isotropic with the material AISI1020 Stainless Steel is being taken for the study. For the analytical evaluation of the system and for calculating beam material deflection, the SolidWorks program is being used. Finally, finite elements analysis is used to compare the numerical results with the analytical ones.

**Keywords** Finite element analysis · Cantilever beam · Deflection · Centroid · AISI 1020 · SolidWorks

## 1 Introduction

In terms of structural engineering, a beam is considered to be a component which is made up of several materials (that includes steel, wood aluminum) in order to withstand loads—usually used side by side on a metal axis. Beams can also be referred to as members, elements, planks, shafts, or purlins. In order to carry a direct load, shear load, and sometimes horizontal load, a beam as a horizontal structure is being used. It is the most significant part of the architecture. It is commonly used in the development of extensions, brackets, and different designs that convey a direct load. In comparison with the length, any part of a structure in which the cross-section is very small carries a lateral load which is known as a beam. A beam is a horizontal bar that carries a rear load or a couple that often bends, or a horizontal bar undergoes

---

A. P. Singh · S. Vidya (✉) · P. Suresh · A. Kumar  
Department of Mechanical Engineering, Galgotias University, Greater Noida, Uttar Pradesh, India  
e-mail: [skvrsm@gmail.com](mailto:skvrsm@gmail.com)

curved stress that is known as a beam. In the construction of a building and failure to exercise deflection is an important consideration which can be catastrophic. Beam deviations can be calculated on the structure in a variety of ways: mathematical methods and finite element analysis, etc. [1].

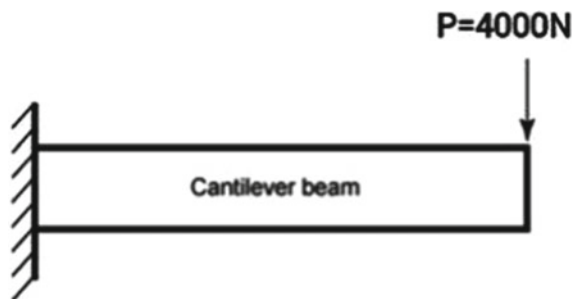
According to engineering terms, the shape of the building changes at the rate of the deflection when a load is applied. The changes that occur include the angle or distance which can be invisible or visible that depends on following factors: severity of load, part shape, also included the material from which they are obtained. The deflection is mainly caused by different types of loads, in which uniform distributed loads, shear loads, point loads, wind loads, and ground pressures along with earthquakes are included. The part may fail when too much deviation is produced by load. Beams, floors, columns, bridge floors, walls, dams, tunnel walls, and more are included in detachable sections. San Francisco's Golden Gate Bridge can move about 15 feet [4 m] alongside strong winds [2].

Deviation is observed in the non-built parts; for example, building lock panels may deviate inside if they are under high air load. In order to ensure the building users safety and the integrity of the structure as a whole while considering the potential for failure related to structures, construction code generally decides maximum deviation to be allowed. In the beam, this is often expressed as part of a span; e.g., beam deviation should not be greater than  $1/360$  span; therefore, if span is 5 m, then deviation should not exceed 13.9 mm. In the center of the beam, it will typically be measured [3].

A lot of research had been published related to the analysis of deflection on different types of engineering structures [4]. In this study, there is a comparative deflection analysis of a cantilever beam fixed at one end by using finite elements and mathematical methods. The point load of 4000 N is supported by beam at one of the ends of the cantilever beam that is manufactured of stainless steel AISI1020 (Fig. 1).

Deviation and the distribution of stress on the long, thin cantilever of a rectangular cross-shaped cross-sectional and isotropic was being examined by Ashish Kumar Samal. Deviation of the cantilever beam in actual is a 3D problem. The stress in perpendicular direction accompanies the stretching on one side. Under the action of three different loading conditions, the beam is being molded: vertical focused. He concluded by using ANSYS the deviation is very accurate when using the 10-node

**Fig. 1** Cantilever beam diagram loaded at the free end



tetrahedral feature but due to the stress, the 8-node brick feature gives better results. Therefore, the 10-node tetrahedral element is being used, to detect deviations, while the stresses 8-node element of the brick is best and most suitable [5].

GT beam is a graphical analysis system that is being developed by Georgia Tech which is used in undergraduate studies. In order to allow students to do 'what if' design conditions in deciding shear/moment and complex deviation beam diagrams, program was being designed that reduces the instructor time which he spend for showing the analysis of beam. This kind of program allows the reader to visualize the impact of the moving foundations or loads in the real-time that has its own design next to the Macintosh graphical interface [6].

Kyungwoo Lee has presented that a large deviation of the cantilever beams made of Ludwick-type material under the combined load that includes load which is distributed uniformly and a single direct load at free end was being examined. Dominant figures were obtained by using the shape of the shear instead of the flexible temporal structure because, in the case of a large, deformed limb, the shear strength formation has certain calculation advantages over the temporal curvature. Since the problem involves both nonlinear geometry and equipment, the rule number is the complexity of dividing a random number, for determining the maximum derivation of the given load numerical solution is required. The fifth Butcher method Runge–Kutta is used to obtain numerical solution that is presented in a table format [7].

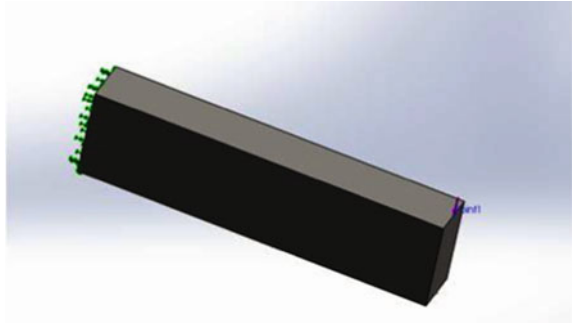
Saeed Moaveni's research has been dedicated to the analysis of problems, stress, and conversion of other members of the structure by such examination. The numerical tests reported here will introduce students to the importance of boundary conditions, power equilibrium conditions, stress/weight relationship of a given object, axial loading, pressure focus, pure bending, opposite loading, and integrated loading. ANSYS and parametric programs are used to set these tests [8].

S. S. Oueini and A. H. Nayfeh verified the result from theoretical analysis by testing. The cantilever steel beam is fitted with piezoceramic actuators, and subject to parametric excitation has a frequency equal to twice the natural frequency of its original mode. A computer and a series of analog filters are used to generate a response signal of cubic velocity. Frequency test and power turning curves are in excellent agreement with quality and theoretical results [9].

In this paper, Wang has focused on analysis numerically of the major cantilever beam deviation problem below the compressive force points to a constant area. The numerical solution obtained from the problem which is then allowed for a comprehensive analysis of different factors impacting on it, which includes the magnitude of the force, the position of fixed point, and length of the beam, includes the nature of the underlying cantilever beam to point to the fixed position. From a practical point of view, our work allows for a more accurate mathematical model development of the design of agreeable designs in regions like as soft robots or intelligent objects [10].

On the examination of deflection by the analytical method, volumes of research papers have been published. A comparative type of study will be done currently between the finite element method and the analytical method. A change in maximum deflection will be observed on the body when the point load is increased, and for three

**Fig. 2** Round shaft with shoulder fillet,  $r = 0.01$  m,  $D = 0.2$  m,  $d = 0.15$  m



different loading conditions, the maximum deflection being calculated and analyzed (Fig. 2).

The above three-dimensional model has been developed with the help of Solid-Works. One of the ends is fixed, and the point load has been generated at the axial position of the free end. There are three iterations have been performed with different loading conditions.

## 2 Materials and Methods

There are several ways to determine the deviation of a beam or frame. The choice of a particular method depends on the loading condition and the type of problem being solved. Some of the methods used in this chapter include the dual integration method, the unity method, the temporary location method, the unit load method, the optical operating method, and the power methods.

In a cantilever beam, the maximum deflection is experienced only in the free end and is calculated using Eq. (1) [11]

$$\delta_{\max} = \frac{PL^3}{3EI}. \quad (1)$$

where

$P$  is a point load applied (in N).

$L$  represents the beam length (in mm).

$E$  represents the material Young's modulus (MPa or N/mm<sup>2</sup>).

$I$  represents the moment of inertia of the cross-section (in mm<sup>4</sup>).

$\delta_{\max}$  is maximum deflection at free end (in mm).

First, let us define the problem to be solved. This consists on a single cantilever beam 1000 mm length ( $L$ ) with a rectangular section ( $a = 150$  mm,  $b = 250$  mm).

**Table 1** Calculation of centroid structure

Segment	Area A (mm <sup>2</sup> )	$\underline{x}$ (mm)	$\underline{y}$ (mm)	$\underline{x} A$ (mm <sup>3</sup> )	$\underline{y} A$ (mm <sup>3</sup> )
1	$150 \times 250 = 37,500$	75	125	2,812,500	4,687,500
Total	37,500			281,250	4,687,500

This beam will support a point load of 4000 N at one of the end of cantilever beam which is manufactured of stainless steel AISI1020. In these conditions, the maximum ( $\delta_{\max}$ ) must be calculated. A scheme of the problem is as follows:



For this particular problem,  $P = 4000$  N,  $L = 1000$  mm, for the value of  $E$ , this value can be obtained by searching the technical datasheet (TDS) of a stainless steel ( $E = 200$  GPa). For the calculation of moment of inertia, first we have to calculate the centroid coordinates of this structure (Table 1).

### 2.1 Centroid Calculation

$$\underline{x} = \frac{\sum \underline{x}A}{\sum A} = \frac{2,812,500}{37,500} = 75 \text{ mm,}$$

$$\underline{y} = \frac{\sum \underline{y}A}{\sum A} = \frac{4,687,500}{37,500} = 125 \text{ mm.}$$

The moment of inertia of a rectangle with respect to an axis passing through its centroid, is given by the following expression:

$$I_x = \frac{1}{12}bh^3 = \frac{1}{12} \times 0.15 \times (0.25^3) = 1.953 \times 10^{-4} \text{ m}^4.$$

The following step is to substitute all the above-mentioned numerical values into the general expression (Eq. 1) to calculate the maximum vertical deflection.

$$\delta_{\max} = \frac{PL^3}{3EI} = \frac{4000 \times 1^3}{3 \times 2 \times 10^{11} \times 1.953 \times 10^{-4}} = 3.41 \times 10^{-5} \text{ m} = 0.0341 \text{ mm.}$$



## 2.2 Finite Element Analysis

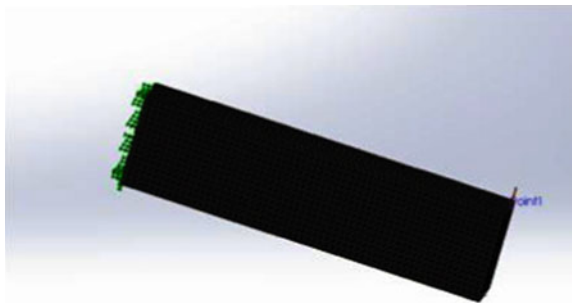
FEA is used by engineers to help simulate real-world scenarios and thus reduce the need for portable prototypes while allowing component development as part of the project design process. In complex geometry, FEA is being most commonly used in which conventional analysis methods can solve issues as FEA partitions complex calculations into more modest parts (components). Examination of the limited feature of the cantilever beam under the free endpoint is done using SolidWorks 19.0. Imitation can provide accurate and reliable results for a wide range of types of research from basic vertical line analysis to complex and flexible indirect analysis. Speed up the repetition and prototyping phase of your imitation design process. The model is built on Solid Tasks, and there is a point load operating at the beam of 4000 N. Accurate results in the FEA model are being obtained from meshing. The information related to meshing is shown in Fig. 3. The best meshing is done in the file area.

The above figure has been developed by the help of SolidWorks functionality, and it is known as the meshing of the geometry. Meshing features an important role once it involves the engineering simulation method. Making a high-quality mesh is one among the foremost important factors that ought to be thought about to confirm simulation accuracy. Meshing is the part of process before the simulation. It helps to give the more accurate results while running the simulation. The finer the mesh, will give the more accurate result. And the meshing of geometry will also depend on the system configuration.

The analytical and finite element methods are being used to calculate the maximum deflection value. The material is presumed as being isotropic that has been taken for the review is AISI1020 Stainless Steel. The low carbon steel is AISI 1020 carbon steel that has as a minimum 0.17%C and 0.3%Mn. Its strength and ductility combination is good which can be carburized. It is difficult to install a solid or fire-resistant due to its low carbon content, and also, it is not suitable for nitriding because of the absence of alloying elements. With the help of traditional methods, the steel can easily be machined and welded. The material mechanical properties are referenced in Table 2.

The results of FEA are found and compared for cantilever beam. Overall, three different point loads are being prepared, analyzed, and simulated. Figures 5, 6, and

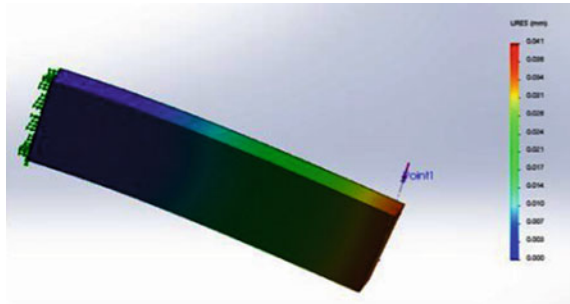
**Fig. 3** Meshed model of cantilever beam



**Table 2** Properties of 1023 carbon steel sheet material

Properties	Values	Units
Density	7900	Kg/m <sup>3</sup>
Poisson's ratio	0.29	N/A
Shear modulus	77,000	MPa
Elastic modulus	200,000	MPa
Strength (tensile)	420.507	MPa
Strength (yield)	351.571	MPa

**Fig. 4** Graphical plot of the numerical simulation by FEA, corresponding to displacements on the beam



7 show FEA results of a cantilever beam with free end point loading for the different point loading. Here, the applied load is considered for examination purpose, the point load as 4000 N, 5000 N, and 6000 N for all iterations with different point loads, and all the variables are same for all iterations except loading. The result is being calculated as the change in maximum deflection from all three various point loading. The resultant deflection denoted as URES (mm). There is a minimum value and maximum value on the side of color scale and is labeled URES (mm) (Fig. 4).

From the above FEA results, resultant deflection of one end fixed cantilever is being identified and then used for comparative review for the maximum deflection at different loading derived from the analytical method. Results of finite element analysis URES for different loading and the result that are being obtained by the analytical method are tabulated in Table 3, and its comparison is performed with maximum deflection that is obtained from analytical method and FEM.

### 3 Results and Discussion

In this work, a point load has been developed at free end of a cantilever beam. The maximum deflection's value is being calculated with the help of finite element analysis. Three loads have been considered for the calculation to get the more clarity about the problem. The main aim of this paper is to compare the variation of the result that has been calculated by the help of finite element method and theoretical

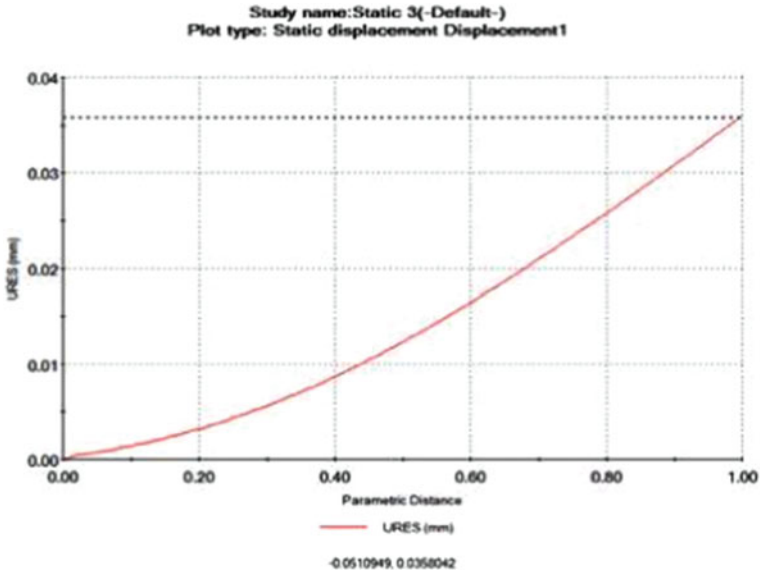


Fig. 5 Maximum deflection graph at the free end for  $P = 4000$  N

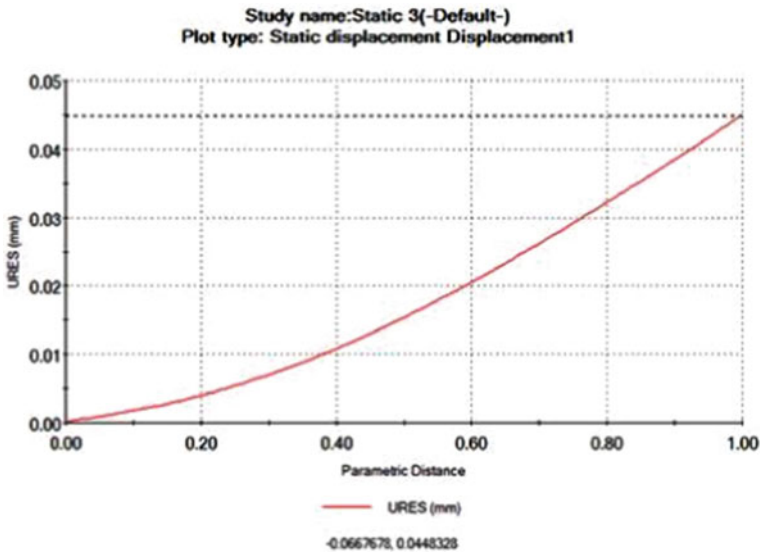


Fig. 6 Maximum deflection graph at the free end for  $P = 5000$  N

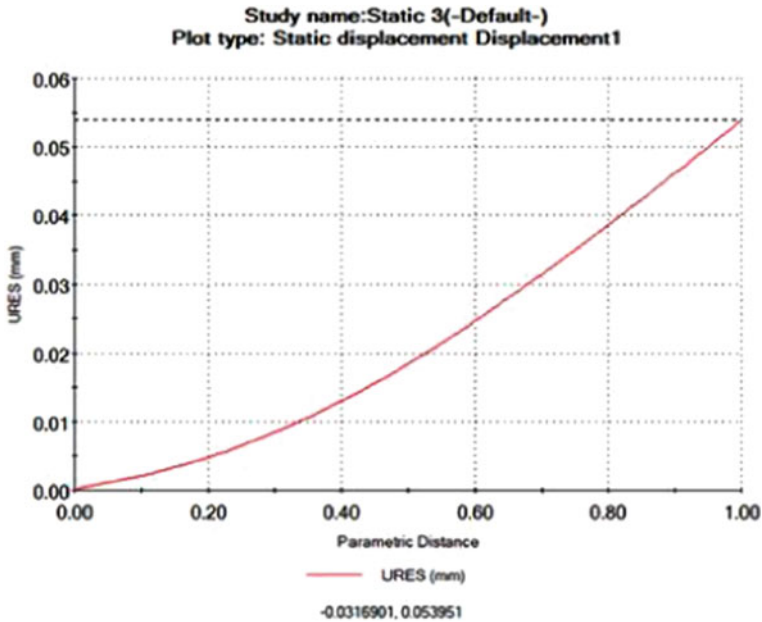


Fig. 7 Maximum deflection graph at the free end for  $P = 6000$  N

**Table 3** Comparison of maximum deflection acquired from FEA, and theoretical maximum deflection acquired from the analytical method under point loading at free end

Load, $P$ (N)	Theoretical maximum deflection (mm)	Equivalent (URES) deflection (mm)	Percentage deviation (%)
4000	0.0341	0.0358	4.98
5000	0.0426	0.0448	5.16
6000	0.0512	0.0539	5.27

method. The accuracy of FEA solution always depends on the density of mesh used. Check with more refined meshes and compare the results with theoretical solution. The chart has been shown below between the parametric distance and deflection. The red curve represents the maximum deflection at the end, and it is represented by the horizontal line.

From Table 3, the both result of the maximum deflection from the FEM and theoretical method have approached toward same as different loading.

The red curve is representing the maximum deflection at the end of the beam that is also known as the total vertical displacement of the beam at the free end. And the above result obtained, when the applied load is 4000 N.

Figures 6 and 7 are representing the total vertical displacement when the applied load is 5000 N and 6000 N.

## 4 Conclusion

The conclusions given below are mainly based on contrast between the maximum deflection results that is obtained by the theoretical method FEA for a cantilever beam point loading at free end.

- The maximum deflection value decreases when the value of point load is increased.
- As you have seen in this article, the solution of a simple engineering problem (single cantilever beam) can be solved by either analytical expressions or finite elements analysis (FEA). The solution is almost the same, but some deviation can occur by using numerical methods by FEA.
- These complex engineering systems are not easy to be solved by analytical expressions, and it is there where FEA takes some advantages. FEA allows simulating complex parts in a reasonable time, so FEA represents an important tool for engineers. The use of FEA tools can positively contribute to reducing the design and development time of an engineering part or assembly.

## References

1. Riley FW, Sturges LD (1993) *Engineering mechanics: statis*. Jonh Wiley & Sons New York
2. Bedford A, Fowler W (1996) *Engineering mechanics: statics*. Addison Wesley, Massachusetts
3. McGill DJ, King WW (1995) *Engineering mechanics: statics*. PWS Publishing Company, Boston
4. Timoshenko SP (1983) *History of strength of materials*. Dover Publications, New York
5. Samal AK, Rao TE (2016) Analysis of stress and deflection of cantilever beam and its validation using ANSYS. *Int J Eng Res Appl* 6:119–126
6. Wu TM (2006) Computer-aided deflection and slope analyses of beams. *J Appl Sci* 6(2):333–339
7. Lee K (2002) Large deflections of cantilever beams of non-linear elastic material under a combined loading. *Int J Non-Linear Mech* 37(3):439–443
8. Moaveni S (1998) Numerical experiments for a Mechanics of Materials course. *Int J Eng Educ* 14(2):122–129
9. Oueini SS, Nayfeh HA (1999) Single-mode control of a cantilever beam under principal parametric excitation. *J Sound Vib* 224(1):33–47
10. Wang CM, Kitipornchai S (1992) Shooting—optimization technique for large deflection analysis of structural members. *Eng Struct* 14(4):231–240
11. Jonnala SubbaReddy M, Kartheek G, Reddy JVS (2018) Influence of parameters on safe design of leaf spring for static and dynamic loading using finite element 5(04)

# Application of Compliant Mechanisms in Various Fields—A Review



Pooja K. Jambhale and Bhagyesh B. Deshmukh

**Abstract** In the world of modernity, there is a need for alternative designs with improved quality, economy, and safety. Compliant mechanisms are single-piece pliable devices that can induce useful work through elastic deformations. Compliant mechanism gains their mobility through deflection of flexible members contrary to the traditional rigid body mechanism. Compliant mechanisms offer significant advantages such as fewer parts, less wear, noise, and backlash. Compliant mechanisms have the potential to solve many of the challenges faced in various fields. The compliant mechanism gives a precise and better solution. Compliant mechanisms have enormous applications in the field of transportation, aerospace, micro-mechanism, biomedical, handheld tools, MEMS, and robotics industry. However, many fields of engineering have started to use flexibility for better, more elegant, and ultimately more satisfying designs. The objective of the current work is to study and understand compliant mechanisms and their applications in various fields communicated by various researchers.

**Keywords** MEMS · Compliant mechanism · Rigid body mechanism · Flexible devices

## 1 Introduction

If we notice the world surrounding us, there are several exemplifications that are naturally compliant such as birds flying in the sky, branches swaying in the wind, and many others. The bow and arrow were the most ancient and simplest example of a compliant mechanism, that was used for war and hunting. The human heart is the best example of a compliant mechanism that started working before you were born. The conventional design methods of the compliant mechanism are simple and do not need notable calculations. After the advancement, complex systems can be

---

P. K. Jambhale (✉) · B. B. Deshmukh  
Walchand Institute of Technology, Walchand-Hirachand Marg, Ashok Chowk, Solapur 413006,  
India  
e-mail: [poojasachink96@gmail.com](mailto:poojasachink96@gmail.com)

designed fluently by using numerical methods [1]. In the mid-1960 due to outstanding benefits, the elastic deformations of materials have been successfully used to create useful motions in many mechanisms and were compatible with then applications. A compliant mechanism is defined as the mechanisms that are prepared to get flexibility from a flexural hinge and relatively long flexible components of mechanisms are referred to as compliant mechanisms [2]. The lack of conventional joints in single-piece flexible structures offers many advantages such as low cost, zero backlashes, ease of manufacture, better efficiency, scalability, the absence of wear debris, pinch points, crevices, and lubrication. Compliant mechanisms are single-piece and flexible structures that use strain energy to convert input energy components into the desired output force or displacement. The compliant mechanisms have a similar function to the traditional rigid body mechanisms, but they gain some or all of their mobility from the deflection of flexible members rather than from movable joints only [3].

The objectives of the current research are:

- To study various aspects of compliant mechanism and their advantages.
- To study the applications of compliant mechanisms in various fields.

## 2 Literature Review

The literature is to be studied in order to gather knowledge about compliant mechanisms. New competitive products must be lightweighted, resource-efficient, durable, and stable and have a low noise emission, so that the product can meet the growing demands of the market. However, it is very difficult to analyze and design compliant mechanisms [4]. Material properties, geometry, loading, and boundary conditions are the three primary ways that affect the flexibility of compliant mechanisms [5].

The design methods of compliant mechanisms are as follows.

### 2.1 *Design Methods of Compliant Mechanism*

The main approaches for designing the compliant mechanisms are as follows:

- (a) Kinematics-based approach: In this method, pin joints are used to join several rigid links together, and to resist torsion, tensional springs are attached. When there is a mechanism with large nonlinear deflections kinematics approach is best suited for that, and it is very easy to analyze as compared to other methods. In this approach, pseudo-rigid body models are used to design compliant mechanisms.
- (b) Structural optimization-based approach: This approach is mainly concentrated on their solution of the topology, shape, and size of the mechanism. It is not necessary to start with known rigid links while designing. There are two

approaches, i.e., ground structure and continuum structure. Continuum structure is designed by three approaches, namely homogenization method, density method, and evolutionary structural optimization [6].

## 2.2 Various Applications of Compliant Mechanism

### (a) Day-to-day life applications

Compliant mechanism design has been used in various fields and increasing research interest among the researchers is now a day. The compliant mechanism gives a precise and better solution [7]. Figure 1 shows some common single-piece examples of compliant mechanism which is used in day-to-day life.

### (b) Hand-held tools

Ananth Suresh and Laxmi Narayana Saggar [8] proposed the design of a single-piece compliant stapler. It is designed to eliminate the component assembly so that the ultimate cost of the stapler is reduced. The injection molding process is best suited for manufacturing staplers at a single stage on a large scale with suitable plastic material. The deformation energy is stored in a compliant beam spring which provides energy to the spring for keeping staples in place. The principal advantage of this design is a significant reduction in production cost, and the stapler is light in



Fig. 1 Examples of compliant mechanisms used in day-to-day life



**Fig. 2** Compliant plier

weight and more amenable to improving upon ergonomic and aesthetic aspects than a traditional stapler.

Howell and Midha [9] demonstrated the design and analysis of compliant pliers. This compliant plier can be built in a single piece when it is manufactured using an injection molding process, and hence, the assembly process is eliminated. The pseudo-rigid body mechanism is used to design and analyze the plier wherein the length of the flexural pivot is very small when it is compared to the rigid section. A fully compliant plier is shown in Fig. 2.

Ibrahim et al. [10] investigated a finite element analysis of compliant pliers. The model-compliant plier is created in CAD, and then it is simulated by using a linear solver in Siemens NX 12. The purpose of this study is to find out the best polymer material for compliant plier application; from the result of the study, it is concluded that ABS is the best material.

(c) Biomechanics and robotics:

Kota et al. [11] designed a compliant kidney manipulator for use in minimally invasive surgery. The objective of this work is to create a compliant mechanism that can pick the object and is relatively stiffer to resist the reaction forces upon gripping the object. The gripping arms have two degrees of freedom and are driven via external cable actuation.

Sun et al. [12] state that metal forceps are replaced by disposable plastic forceps so that the chances of getting infected by these reusable metal forceps are eliminated but the clamping performance of the plastic forceps is lower and hence use is restricted. To resolve this problem, author illustrated the compliant forceps by using bio-inspired topology optimization techniques. The analysis and simulation are done on finite element analysis to assess the clamping performance. After the evaluation, it is proved that the clamping performance of these optimized forceps is much better than the conventional forces. Bio-inspired forceps are widely used in open surgery and physical nursing application.

Bilancia et al. [13] illustrated the bio-inspired compliant wrist, whose flexibility has been gained by employing two pairs of contact-aided cross-axial flexural pivots (CAFP) actuated via remotely placed servo motor and tendon transmission.

The wrist is operated by two servo motors and a set of flexible cables. The proposed 3D model aims at mimicking such natural human wrist motion and its passive stiffness. The deflection of two pairs of CAFPs will result in the movement of a device. Sun et al. [14] present era modeling of bio-inspired compliant mechanisms in MATLAB for medical application, to analyze the mechanics of different

bio-inspired compliant mechanisms. A compliant mechanism has enormous application in medical robotics and devices because of its mobility and joint less structure. Traditional medical devices have some limitations like as complicated assembly work and a little gap between the joints. To solve these difficulties, compliant mechanism is used. There are many examples of bio-inspired compliant mechanisms such as Snake-Like Continuum Manipulator, Flytrap-Like Compliant Forceps, and Fish-Fin-Inspired Adaptive Finger.

Snake-like robots are used in minimally invasive surgery (MIS) because of their pliability and tangible benefits to the patients. Medical forceps are another example of a bio-inspired compliant mechanism that is inspired by the Venus flytrap.

Ai and Xu [15] reported an overview of flexure-based compliant micro-grippers. Micro-gripper is a device used for handling micro-objects in micro-assembly and microsurgery without damage. It is most widely used for pick and place applications in robotics. The author has presented a survey of the latest evolution of flexure-based micro-grippers.

The author has explained the different mechanisms, sensors, and control methods that are used in micro-grippers. Additionally, the author also addressed how to choose the right component in a compliant micro-gripper. Compliant micro-gripper has plenty of application in the field of medicine and robotics. In the field of biomedical, material science, automotive, etc., a typical micro-system requires a precise micro-gripper to accomplish safe transport/handling of micro-sized object [16].

Stutel et al. [17] designed an under-actuated finger. Fully compliant under-actuated mechanisms are used for prosthetic or robotic hands. This type of mechanism can be easily controllable and can take various types of objects when it is compared to conventional hands. Furthermore, it is lightweight, less costly, less friction, backlash, and wear. This proposed work aims to compose a fully compliant under-actuated finger with a single-piece structure.

The designing process begins with a common topology. The best suitable topology was selected based on the rigid body model, and then the most advanced shape of the individual segment was selected based on the pseudo-rigid body model. The whole design of under-actuated fingers with largely distributed compliance was analyzed on finite element analysis.

Arora et al. [18] plotted a method for the stiffness-based design of compliant iris. Mechanical iris has been used in many devices such as the iris diaphragm of a camera, iris valves. It is also used in optical setups to manage the amount of light passing through it. Recently, iris structures have also found use in solar thermal receivers where the amount of light is controlled mechanically.

Mechanical iris has some limitations as many plates move relative to each other resulting in friction and backlash. The compliant iris is a single-piece structure based on large deflections of parts. The thin plates are substituted by flexible beams. Figure 3 shows the 3D prototype of the compliant iris.

Gor et al. [19] presented the entire development process of a compliant quadruped-legged robot. Recently, many quadruped robots are designed such as baby elephants, cheetah cubs, and little dogs. They were used in hazardous and unstructured environments. In a solid model of a compliant legged quadruped robot, each leg has two

**Fig. 3** Compliant iris

links and two motorized revolute joints for moving. The body and upper link of the leg where the rigid and lower link of each leg is compliant. Compliance with the links enhances the movement of the quadruped robot.

(d) Transportation:

Roach et al. [20] differentiate between compliant overrunning clutch and conventional overrunning clutch. When torque is required to be transmitted in only one direction, then overrunning clutch is best suited. These clutches have been used conventionally in vehicle transmissions, engine starters, agricultural equipment, helicopters, and bicycles. There are many types of overrunning clutches, but the four main types include the sprag clutch, the roller or ball clutch, the spring clutch, and the ratchet and pawl clutch. These clutches offer many advantages such as reduced manufacturing cost, assembly time, part count, and weight reduction.

Prof. Patel et al. [21] introduced a compliant centrifugal clutch. The material used for the fabrication of a compliant centrifugal clutch is polypropylene, and there is no anyone connecting part. In this clutch, revolute joint is replaced by flexible segments; hence, the problem of backlash and wear is reduced. The compliant centrifugal clutch contains a rigid body mechanism through dimensional synthesis by graphical method. A mechanism is estimated and synthesized specific force deflection relationship. Another advantage of a compliant mechanism is cost reduction. The compliant clutch is designed by graphical method, and then it is compared with conventional design.

Karakus et al. [22] introduced a novel partially compliant wiper mechanism. The traditional wiper mechanism which is used in automotive vehicles has several linkages and joints. The author makes a compliant wiper design simpler than a conventional one. The wiper mechanism is a partially compliant four bar mechanism. A compliant wiper mechanism is developed for an L7e car. Fatigue calculations and analytical results are verified on finite element analysis. After the experimentation, it is concluded that the compliant wiper mechanism has infinite life. The number of part counts is reduced in the compliant wiper mechanism [23].

Olsen et al. [24] designed a compliant bicycle brake. This work aims to advance the compliant mechanism and to reduce the number of part count; hence, the overall weight is reduced.

Yuvaraja et al. [25] developed the compliant clutch fork by using topology optimization. Modernized clutch fork design was used as a reference. In the modernized clutch design, 50% mass or weight has been reduced by the topology optimization method. Polypropylene has been selected to the compliant clutch fork. Cost of the compliant clutch fork is reduced as polymer-based materials are relatively cheaper than cast iron or steel-based materials. This compliant clutch fork is designed for automotive applications.

Karlekar et al. [26] presented detailed aspects of the compliant mechanism and its applications in the automotive industry. The author has designed a compliant steering mechanism and compliant bicycle brake. PRBM provides the analytical solution for any compliant mechanism problem. For the verification, the FEA analysis is carried out.

(e) Micro-electromechanical systems (MEMS):

The application of MEMS compliant mechanisms is more important for designing micro-actuators. Micro-electromechanical systems (MEMS) are integrated with electronic circuits and fitted with a millimeter scale. Due to the tiny length scale and elimination of assembly, friction and wear compliant mechanism is widely used in MEMS.

Lin et al. [27] described the post-design of topology optimization for mechanical compliant amplifier in MEMS. A single-piece compliant amplifying micro-gripper has been designed to illustrate the design model and presented the presenting approach. In this paper, the author has concluded that the combination of flexure hinges and structural optimization in a phase for designing a single-piece micro-compliant mechanism is practically successful.

(f) Aerospace:

Merriam et al. [28] reported the concept, modeling, and growth of a fully compliant 2 DOF pointing mechanism that is used in spacecraft thruster, antenna, or solar array systems.

The mechanism is designed in such a way that it provides benefits like low part count, small mass, low friction, small volume, and high reliability because of the elimination of articulating components.

Fowler et al. [29] proposed compliant space mechanisms as a new research direction in the field of compliant mechanisms and explained the significant factors of compliant mechanisms applying to space mechanisms. A compliant space mechanism is defined as flexible mechanical assemblies that gain its desired motion, force, or displacement using the deflection of flexible members and that can perform a needed function in the field of launch and space.

Kota et al. [30] designed a compliant mechanism for the application of morphing aircraft structures. The compliant mechanism offers many practical advantages when it is used in aerodynamics; these include minimizing complexity, problems due to

wear, backlash and lubrication being removed, sub-micron accuracy, embedded actuation/sensing, and because of joint less structure additional weight savings. Perfectly designed compliant mechanisms are best for shape morphing applications namely variable geometry leading and trailing edge surfaces, engine inlets, and other aircraft components. The material used for designing compliant mechanisms with the desired stiffness is titanium, aluminum, steel, and composites.

The author highlighted the application of compliant mechanisms. They are:

- (i) Variable geometry wings specifically for leading and trailing edge flaps and
- (ii) High frequency vortex generators for active flow control.

The air vehicle performance has been enhanced by using developed compliant mechanism technologies for shape morphing aircraft.

### 3 Finding of the Study

A review shows that the compliant mechanism offers numerous benefits like as low cost, zero backlashes, reduction in weight, reduced assembly time, ease of manufacture, better efficiency, scalability, and absence of lubrication.

The compliant mechanism has an immeasurable contribution in the field of transportation, MEMS, biomechanics, and robotics, for adaptive structure and aerospace.

After a study of the compliant mechanism, the most used design methods of the compliant mechanism are pseudo-rigid body model and topology optimization.

The full range of a compliant mechanism depends on the type of material used for manufacturing and the geometry of the structure; due to the nature of flexure joints, no purely compliant mechanism can accomplish continuous motion like as found in a normal joint.

A brief review of the compliant mechanism shows that they are restricted to several degrees of freedom or minimal displacement.

### 4 Conclusion

Compliant mechanisms have become an important branch of modern mechanisms. The varied range of modern applications has steered the development of compliant mechanisms. In our study, we focused on the application of compliant mechanisms in various fields such as adaptive structures, components in transportation, hand-held tools, electronics, medical, aerospace industry.

PRBM method provides a better analytical solution for any compliant mechanism problem. Compliant mechanism analysis and design are tougher than those rigid body mechanisms. In the future, there should be an analysis of the fatigue failure to

prevent premature failure in the device. At present, work is being carried out to design a compliant macro-scale gripper that can be used for pick and place applications.

**Acknowledgements** Authors are thankful to the authorities of Walchand Institute of Technology, Solapur, to support this research work.

**Conflict of Interest** In publishing this paper, there is no conflict of interest between the authors.

## References

1. Zhu B et al (2020) Design of compliant mechanisms using continuum topology optimization: A review. *Mech Mach Theory* 143:103622
2. Deshmukh B et al (2012) Conceptual design of a compliant pantograph. *Int J Emerg Technol Adv Eng ISSN* 2(8):2250–2459
3. Phadatare R (2020) Review on design of compliant mechanism for surgical applications. *Int J Future Gener Commun Netw* 13(2):735–741
4. Arumugam P, Kumar A (2016) Design methods for compliant mechanisms used in new-age industries— a review 14(2):223–232
5. Jagtap SP, Deshmukh BB, Pardeshi S (1969) Applications of compliant mechanism in today's world—a review. *J Phys Conf Ser*
6. Shuib S et al (2007) Methodology of compliant mechanisms and its current developments in applications: a Review. *Am J Appl Sci*
7. Tang LB et al (2007) Multi-material compliant mechanism design and hapticevaluation. *Virtual Phys Prototyping* 2(3):155–160
8. Anantha Suresh GK et al (1994) A one-piece compliant stapler, ASME design technical conference, Minneapolis, Minnesota
9. Howell L et al, A method for design of compliant mechanism with small length flexural pivots. *J Mech Des* 116
10. Ibrahim A et al, Finite element (FE) assisted investigation of a compliant mechanism made of various polymeric materials. *Mater Today Proc.* <https://doi.org/10.1016/j.matpr.2020.01.105>
11. Kota S et al (2005) Design and application of compliant mechanisms for surgical tools. *J Biomech Eng*
12. Sun Y et al, Design of a disposable compliant surgical forceps with optimized clamping performance. <https://doi.org/10.1109/EMBC44109.2020.9176027>
13. Bilancia P et al (2021) Design of a bio-inspired contact aided compliant wrist. *Robot Comput Integr Manuf* 67
14. Sun Y et al, FEM-based mechanics modeling of bio-inspired compliant mechanisms for medical applications. <https://doi.org/10.1101/2020.06.15.151670>
15. Aia W, Xu Q, Overview of flexure-based compliant micro-grippers. <https://doi.org/10.12989/arr.2014.1.1.001>
16. Patil MB, Deshmukh BB, Modelling and analysis of flexure based compliant microgripper. *IOSR J Mech Civil Eng.* e-ISSN: 2278-1684, p-ISSN: 2320-334X
17. Steutel P et al, Design of an under actuated finger with a monolithic structure and largely distributed compliance
18. Arora V et al, Design of compliant iris
19. Gor MM et al, Development of a compliant legged quadruped robot. <https://www.researchgate.net/publication/325826581>
20. Roach GM, Howell LL, Evaluation and comparison of alternative compliant overrunning clutch designs, Mechanical engineering department., Brigham young university, Provo, UT 84602

21. Patel N et al (2013) Design of centrifugal clutch by alternative approaches used in different applications. *Int J Innov Res Sci Eng Technol* 1(4)
22. Karakus R et al, Novel compliant wiper mechanism. *Mech Sci* 9:327–336
23. Premanand S et al (2018) Review on the design of a compliant mechanism for automotive application—a topology optimization approach 9(4):748–755
24. Olsen BM et al, Compliant road bicycle brake. In: *Proceedings of the ASME 2011 international design engineering technical conferences and computers and information in engineering 2011*, Washington, DC, USA
25. Yuvaraja S et al (2019) Design and development of a compliant clutch fork using topology optimization. *IJITEE* 8(11). ISSN: 2278-3075
26. Karlekar O et al (2019) Design and analysis of compliant mechanism and their applications in automotive industry. *IRJET* 06(10)
27. Lin CF, Shih CJ (2006) A post-design of topology optimization for mechanical compliant amplifier in MEMS. *Tamkang J Sci Eng* 9(3):215–222
28. Merriam EG et al (2013) Monolithic 2 DOF fully compliant space pointing mechanism. *Mech Sci* 4:381–390
29. Fowler R et al (2011) Compliant space mechanisms: a new frontier for compliant mechanisms. *Mech Sci* 2:205–215
30. Kota S et al (2003) Design and application of compliant mechanisms for morphing aircraft structures, smart structures and materials 2003: Industrial and commercial applications of smart structures technologies. In: Anderson EH (ed) *Proceedings of SPIE*, vol 5054 © 2003 SPIE

# Enhancement of the Machine Safety Using OpenCV



Sumit Raut, Vishal Hase, Shreyas Kotgire, Swapnil Dalvi,  
and Abhijeet Malge

**Abstract** Hand pose detection is the system of recognizing where the joint of the hand is detected which is used to communicate the machine with the outside environment. In industries, 22.9% accidents are caused due to human faults. In order to avoid this accident, the human posture can be used to detect a human error in the industrial area, and when the human limbs enter the operation area, the machine can stop, thus preventing the accident. This can be implemented with the use of TensorFlow, MediaPipe, and OpenCV. This article focuses on the hand pose detection model used to prevent accidents at work. The study shows that the media pipeline hand gesture recognition model has the highest accuracy for recognition with OpenCV. The media pipeline recognizes 21 different locations on the palm that accurately detect the presence of the hand in the environment.

**Keywords** Hand detection · MediaPipe · OpenCV · Industrial accident

## 1 Introduction

Computer vision (CV) is used in image processing as either three dimensional or two dimensional in animal monitoring process, and it plays an important role in animal behaviors. They offer benefits for the monitoring of farm animals due to the wide range of applications, cost, and efficiency. Object detection and recognition are two main areas of application for many decades that are presently within the laptop vision systems. These approaches face challenges akin to scaling, occlusion, the purpose of view, lighting, or background confusion, all topics that may be treated as discussion topics resulting in the introduction of neural networks and convolutional neural networks (CNN). The new another usefulness is formed from differing

---

S. Raut · V. Hase · S. Kotgire · S. Dalvi · A. Malge (✉)  
MIT Academy of Engineering Alandi (D), Pune, Maharashtra 412105, India  
e-mail: [ammalge@mech.mitaoe.ac.in](mailto:ammalge@mech.mitaoe.ac.in)

S. Kotgire  
e-mail: [sskotgire@mitaoe.ac.in](mailto:sskotgire@mitaoe.ac.in)



kinds of layers that take into consideration numerous parameters capable of understanding the choices obtainable throughout a given amount of time. Since then, these architectures have been developed, and a large number of advanced structures with hidden nonlinear layers between the input and output layers of a CNN are called deep convolutional neural network (DCNN), and with it, the amount of information has enabled deep learning to increase performance underneath supervised learning conditions. It seems that once extensive knowledge is gained, which is used by larger models in a faster system, the results are better.

Ding et al. [1] proposed to evaluate for four human postures in that there is different algorithm which can recognize with different human posture effectively. A frequent adage about model interpretability is that as model complexity rises, model interpretability falls at the same rate. The datasets are used in the MSC12 and U+ Kinect activities. The accuracy curve in the sklearn toolbox was generated using the micro-average approach in this study. The Ripper algorithm is a rule-based classification algorithm. It derives a set of rules. It is a widely used rule induction algorithm. Panini and Curcchira [2], in this study, describe the different human posture. It is devised for indoor domestic applications. Approach of this study is to study or explore the things and integrates and improves the human postures. MVOs proved some reliable robust if their working constrained is to be satisfied. Chebila [3], in this study, describes the occurrence of hazardous events or involving dangerous substances in wide range in machine learning tool. In this study, they use nature of information collected in the MARS database. They use conceptualization methodology, software, validation, data curation, writing draft, and other six different algorithms which is used to predict possible occurrence of accident in industry. Dargan et al. [4] state that the methods, motivational features, and properties of deep learning are the subject of this study. This study discusses the distinctions between deep learning, classical machine learning, and convectional learning. There are so many datasets that are used for deep learning, in that visual graphic group net, Google net, Yolo, Resnet RCHH, GAH. Elforaici et al. [5] state that the purpose of this study is creating a challenging posture recognition technique with variety of datasets and conditions. This approach is based on a two-dimensional picture that depicts human postures. This method using depth image are suitable for indoor environments which is having less or limited recognize the postures. Kakhki et al. [6] state that this study is used for artificial neural network methodology to analyze the different incidents of their sources and safety and risk in it. They put in place safety procedures in grain elevators, which has helped the sector decrease accidents. From this study, the data says \$ 78 million US dollars were incurred in that incident according to this study. Different ANN, MLP, and RBF models are also employed in this study. This study provides safety techniques to continue to avoid accidents occurring in industry. Hou et al. [7] state that the objective of this study is to provide safety which is essential in engineering industry. There are traditional method SHM and JSM which are inefficient and also costly. This DL-based application is safely in ACE industry. The main purpose of SHM, JSM, DL, and ML application is more possible solution to research challenges. IBTISAM et al. [8], this paper describe CMOS process technology on graphics Pyxis version is use for simulation of bio-electric using ultra-wide waveform. Bonneau et al. [9] is

to evaluate and use of CNN and segmentation to extract image for four postures kept in it. They use input variable in as sum method to estimate posture. They use this posture prediction from feature sum classification models. Two different datasets are used to change behavior of lightning condition or field view camera. Dzwidrek and Latala [8] explain how additional safety precautions taken by machinery operators might help prevent accidents. It shows that 23–28% of total accidents happened in operation time (400 accidents per year). EUROSTAT model developed distractive level. They minimize or reduce possible dangerous accidents zone and provide safety control methods.

## 2 Working Model

The flow chart of model is shown in the Fig. 1. The data is accumulated in the form of the video taken as an enter from the webcam. Then this data is processed and paperwork a set of the photographs that is may be processed with assist of the OpenCV and can be used for detection of the posture.

For the identification of the hand, utilities from the MediaPipe Holistic module are utilized, and for future upgradation, the detection of the complete body posture is utilized. The distinctive 21 key factors are detected withinside the hand, and the lines of the 3d posture are joined withinside the  $x$ ,  $y$ , and  $z$  coordinates for the 3d posture detection. The distinctive 21 key factors and connection are proven withinside Fig. 2.

The perpendicular distance between the posture key points and the webcam is calculated with the assistance of mathematics and SciPy. Spatial modules. The

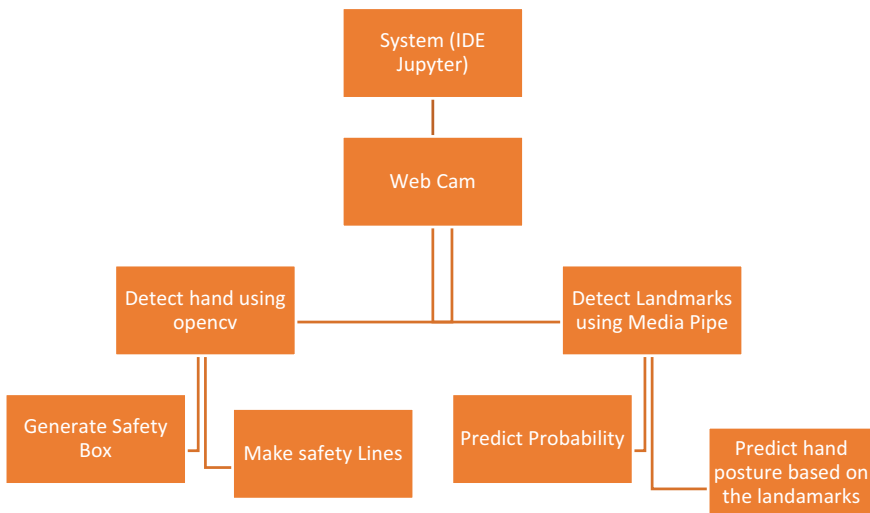
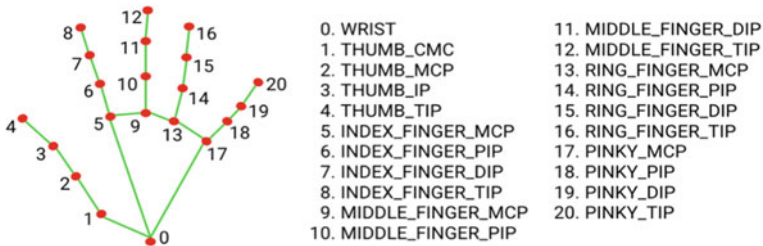


Fig. 1 Flow chart of the model



**Fig. 2** Hand posture key point and connection

distance is calculated to generate an imaginary safety line for the detection and for making an operation region the usage of actual live data.

If the detected palm fingers/key factors crossed these imaginary safety lines, then an emergency signal is generated which stops the system. As soon as the fingers of the hand touch the system, it shuts off the system which in turn prevents the accident from happening. With the assistance of the cv2 function from the OpenCV, the system can capture the data within the frame of the video and process that data within the form of the separate frames. As the different device has different frame sizes, they input the body width and height are designated the use of OpenCV.

The black overlay is created for the detection of the only posture and the safety lines in the system. This black overlay hides everything from our point of view and only shows the key points and the lines. This helps us to evaluate the system module that in the black background.

The confidence value of the module is pre-defined with help of MediaPipe ML. The confidence value is the number that the model can detect and calculate the correct or probable output. The 0–1 is the range of the confidence value used in the machine learning which gives probability of the output. It checks the given value is above or below the 0.5. If the calculate above 0.5, then it is true or else it is false.

With use of MediaPipe Holistic model, the system can detect the separate body skeleton landmarks, left hand connection and key point, right hand connections and key points. The hand separate key points can be detected using try, if and except function in the Python. In the simple terms, if the specified and detected key point crosses the safety lines, the system can detect it as a duct to break the code. If the key point does not cross the line, then the system remains running continuously and detecting the key points.

With help of the OpenCV module, a separate rectangle can be generated on the display around both of the hand covering all the key points that are detected. This rectangle acts as a safety box for the hand in most of the contact with machine. This safety box can help in the evaluation of the model as well as the design of the machine where the posture of the human is needed to detect. This helps in the improvement of the design of the machine to reduce the possibility of the accidents happening in the working area.

### 3 System Model

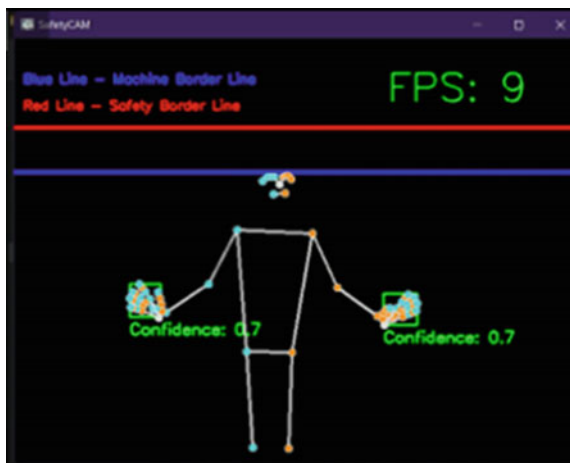
The system uses MediaPipe ML model for better accuracy with body posture detection in OpenCV. OpenCV is mainly used for image processing which helps the system to take input in the form of the image. The main features of the image processing included in the OpenCV are object detection, feature extraction, image filtration, and image transformation. The output obtained using OpenCV are the properties or the characteristics of the image. OpenCV is a programmable function library that is mostly used for image processing and includes a variety of tools for computer vision. OpenCV can be used with machine learning, image processing, computer vision, and deep learning.

The MediaPipe provides various machine learning solutions which are customizable. The MediaPipe solution includes selfie segmentation, face mesh, hand tracking, human pose detection and tracking, object detection, face detection, and holistic tracking. Holistic tracking of the MediaPipe uses different components or models like hand pose, face, mesh, and hand detection and combines them as the holistic tracking. The MediaPipe Holistic model combines different model and works as a multistage pipeline which is shown in Fig. 3.

The built-in library called math is used for the different mathematical functions that are specified by the standard C. The math is mostly used to calculate differentiation, probability, addition, multiplication, subtraction, division, quadratic function, combination, permutation, exponential function, trigonometric function, periodic, and hyperbolic function. This calculation is used to operate and calculate different operation in the module. The mathematics is used to for different numerical problem that are incorporated in the module.

The subprocess utilized in the Python 3.0 module is used to link multiple module input and output signals so that the various modules may operate efficiently and without errors. If any error occurred at specific input output link, it can be identified

**Fig. 3** Full body posture detected with help of MediaPipe



easily. Its main application is to run different program module in the Python. The subprocess can be easily managed in the Python as the input and output.

For the representation of numerical data in Python, the module NumPy package is utilized. The Python consists of the different collection of data like list and dictionaries, but this type of the data cannot be effectively used for the representation of high-level numerical data. The NumPy is the collection of different mathematical function as well as the different arrays used for the calculation. It consists of multidimensional mathematical elements.

The SciPy. Spatial is used in the system for the matrix calculation which contains the distance which is calculated pairwise of the matrices. The Python is equipped with the time module which handles all the task related to the time domain which is required in the module for collecting the data in the organized pattern.

### 4 Results

The software is built using the open-source neural network application programming interface (API) provided by cameras documentation, written in Python programming language. In the area of machine learning as one of the most accurate, prevalent, and well-supported Python language used, Python is a natural choice for running computer vision code.

Initially, the code was run on local host in that the code was set around the two lines; i.e., safety border line and machine border line (stop line). From Fig. 4, red line was safety border line and blue line was machine border line. Hand images dataset was trained on these lines. For local host, frames per second was bit low, so for faster purpose, the model was deployed on AWS Cloud. After implementing the model on cloud, the frames per second was pretty good compared to local host and accuracy was improved.



Fig. 4 Hand posture detected by system with safety lines

On local host, the model detects 6–8 frames per second if hand touches the blue line which is machine border line, then alarm gets started if the hand goes up to red line, then machine automatically gets switch off and danger alert has given to system. Computer vision has numerous applications across various fields. It helps us by bringing out the details in live stream videos and then taking action based on it. Here, use of posture detection can be seen to detect the hand in the machining area. Since availability of more data posed as a challenge to us, SSD model has been used for the detection. In this paper, the implementation and testing of code carried out with dataset of hand images over 11,000 hand images; with the help of this data, high accuracy in hand detection has been ensured.

From Fig. 4, we got to know that even if worker is wearing hand gloves, then model is able to detect it. Also, the confidence score is 0.7 which is same has the hand without gloves.

## 5 Conclusion

In the industry, accidents caused because of the interaction between human and heavy machinery accounts up to 22.6%. The accidents are mostly because the operator is either tired or in a rush of finishing jobs where sometimes, he forgets safety procedure. In most of the cases, the accidents are caused because of the human limbs which are get into the operation area. To prevent these accidents, the machine can be equipped with different sensors like ultrasonic sensor, limit switch, and IR sensor. The problems occurred while using these sensors is that the detects other parts of job and stops the machine. To prevent this from happening, the system is built to detect only the human limbs, so if the human limbs get into the operation area of the machine, then the system sends the emergency signal to stop the machine. In the designed system, the posture of the human hand is detected, and as soon as human hand crosses the safety line or operation line, then the system gives the emergency signal to the machine. In the human hand, 21 different key points are detected using MediaPipe Holistic model which gives 3d hand coordinates. The system also gives which finger crossed the safety line. So that this data can be effectively used to verify design of the machine or the posture of the worker working on thar machine. The posture data of the worker is effectively utilized for the improvement in the design of the system.

## References

1. Ding Y, Wan P, Zhang B (2021) Research on online detection System of lathe tool wear based on Machine Vision. Research Square

2. Panini L, Cucchiara R (2003) A machine learning approach for human posture detection in domestic applications. In: 12th International conference on image analysis and processing, pp 103–108. IEEE
3. Chebila M (2021) Predicting the consequences of accidents involving dangerous substances using machine learning. *Ecotoxicol Environ Saf* 208:111–470
4. Dargan S, Kumar M, Ayyagari MR, Kumar G (2020) A survey of deep learning and its applications: a new paradigm to machine learning. *Arch Comput Methods Eng* 27(4):1071–1092
5. Elforaici MEA, Chaaoui I, Bouachir W, Ouakrim Y, Mezghani N (2018) Posture recognition using an RGB-D camera: exploring 3D body modeling and deep learning approaches. In: 2018 IEEE life sciences conference (LSC). IEEE, pp 69–72
6. Davoudi Kakhki F, Freeman SA, Mosher GA (2019) Use of neural networks to identify safety prevention priorities in agro-manufacturing operations within commercial grain elevators. *Appl Sci* 9(21):4690
7. Hou L, Chen H, Zhang GK, Wang X (2021) Deep learning-based applications for safety management in the AEC industry: a review. *Appl Sci* 11(2):821
8. Dźwiarek M, Latała A (2016) Analysis of occupational accidents: prevention through the use of additional technical safety measures for machinery. *Int J Occup Saf Ergon* 22(2):186–192
9. Bonneau M, Benet B, Labrune Y, Bailly J, Ricard E, Canario L (2021) Predicting sow postures from video images: comparison of convolutional neural networks and segmentation combined with support vector machines under various training and testing setups. *Biosys Eng* 212:19–29

# Implementation of Artificial Neural Network for Prognosis of Photovoltaic Panel Using Python



Neeraj Khera, Komal Rukshar Begum, and Farheen Khan

**Abstract** This paper presents the development of an artificial neural network and two suitable machine learning regression models for prognosis of photovoltaic panel using Python. The objective of this paper is to present the evaluation and comparison of the performances shown by the varying models. Their performances are evaluated in terms of their ability to predict the output voltages of a photovoltaic panel provided the operating values for temperature and irradiance. In order to implement the proposed scheme, a neural network-based approach and two different machine learning-based approach are designed and tested in Jupyter Notebook using Python.

**Keywords** ANN · AdaBoost regressor · Jupyter Notebook · Random forest regressor · Photovoltaic panel

## 1 Introduction

The photovoltaic system (PV) market has grown dramatically in recent years because of a number of stimulants, including considerable cost reductions in the components and the support provided by the government throughout the world for its maximum use. These features have increased the appeal of a solar system's return on investment. The PV system may be prone to flaws and anomalies during fabrication, resulting in a reduction in their overall reliability due to the parametric degradation of their components. These factors undoubtedly diminish a PV system's productivity and, as a result, its profit. Therefore, the early detection of the faults in the critical components of PV system is needed which motivates this work. This paper presents the use of soft computing methods for prognosis of the critical component of PV system that is PV panel. The performance analysis of an individual PV module is performed in the PV system [1]. The open-circuit voltage and the output power of a PV module depend upon the irradiance and temperature values, but their relationship is nonlinear and therefore cannot be mathematically obtained [2]. For this purpose, the artificial

---

N. Khera (✉) · K. R. Begum · F. Khan  
Department of ECE, ASET, Amity University, Uttar Pradesh, Noida, India  
e-mail: [neerajpec@hotmail.com](mailto:neerajpec@hotmail.com)



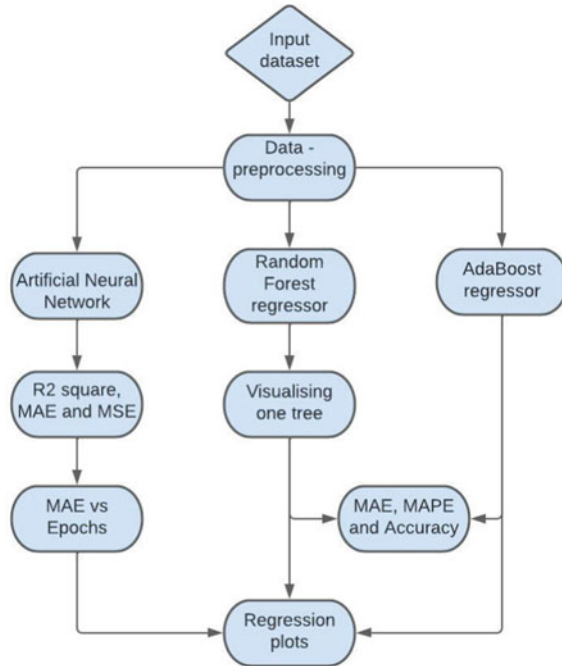
neural network-based approach and two suitable machine learning-based models are applied for determining open-circuit voltage of photovoltaic module at different operating temperatures and irradiance conditions. Machine learning algorithms are better for learning from small datasets in general. While working with small data, a large number of iterations might lead to overfitting. As a result, we employed machine learning models and artificial neural network to compare model performance to see which models perform best. A microcontroller-based testbed is developed to obtain the open-circuit voltage target PV module at different operating temperatures and irradiance [3].

This paper focuses on predicting the variation of open-circuit voltage of PV module with irradiance and temperature using the neural network approach in order to effectively use the PV module in the PV system. Therefore, irradiance and temperature are independent features, and open-circuit voltage is dependent features. The implementation of an artificial neural network designed especially for predicting the output voltage and later aiding in prognosis of a photovoltaic panel is proposed. The photovoltaic module's electrical parameters mainly depend on solar irradiation and temperature, but their relationship is nonlinear and hence cannot be easily expressed in terms of any analytical equation [4, 5]. Therefore, the proposed ANN is trained and tested with the help of calculated target-output curves, and the equivalent circuit parameters are estimated by simply reading the samples of solar irradiation and temperature. Later, data distribution and performance comparison between machine learning model and artificial neural network models are explored to identify significant relations between variables and outliers. From the results obtained, the machine learning-based approach is better in comparison to artificial neural network-based approach. The work done in this paper will aid in future projects related to early fault detection and real-time diagnosis of a photovoltaic panel. This is essential for not only lowering maintenance costs and time but also for avoiding energy loss, equipment damage, and safety risks.

## 2 System Description

An artificial neural network and a machine learning model are created to implement the suggested approach. For comparing model performance and determining which model offers the best outcome, the random forest regressor, AdaBoost regressor, and ANN are used [6]. The proposed models are trained and tested in Python using same dataset, with two independent variables (temperature and irradiance) and one independent variable (open-circuit voltage) that must be predicted. Random forest regression is a supervised learning algorithm that uses ensemble-learning method for regression, whereas AdaBoost builds and ensembles by sequentially adding members, which have been trained on those instances of data, which are proving most difficult to correctly classify/predict. Artificial neural network (ANN) is a computational model that mimics the way nerve cells work in the human brain. ANN consists of three or more layers such as input layer, hidden layer, and output

**Fig. 1** Flow chart for system implementation



layer. The input and output datasets are normalized, and the ANN model is trained using a back-propagation (BP) algorithm with gradient descent and momentum terms [7, 8]. In this paper, a random forest regression, AdaBoost regressor, and artificial neural network model are created to analyze the correlation between temperature, irradiance, and solar panel open-circuit voltage, and to predict photovoltaic panel open-circuit voltage based on temperature and irradiance on a given day. Furthermore, the accuracy of each models is calculated and compared using the regression plots as shown in the flow chart in Fig. 1.

### 3 System Implementation

#### 3.1 Model Implementation

The system implementation started by importing the necessary libraries. Data preprocessing procedure included steps such as checking for missing values, data normalization, and splitting the data into train and test set in the ratio 80:20 [9]. The regressors are imported using the Scikit-learn library, and the ANN is build using the Keras library. The random forest regressor and AdaBoost regressor are then separately fitted into the dataset using fit and predict functions. Performance metrics such as mean

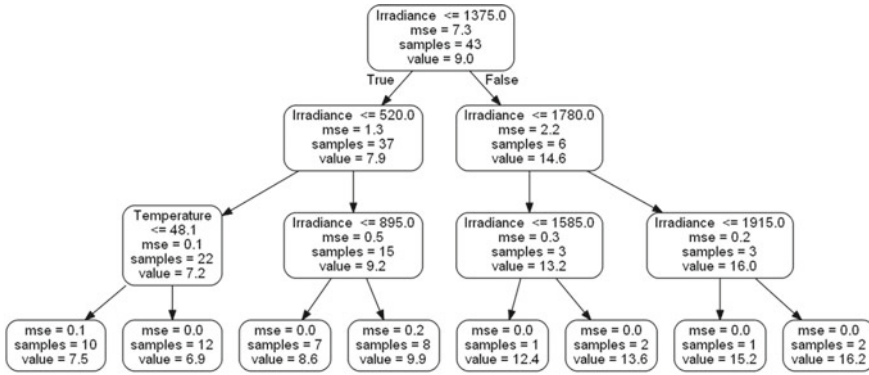


Fig. 2 Decision tree depth level = 3

absolute error (MAE), mean absolute percentage error (MAPE), and accuracy are determined to put the predictions to perspective [10]. Random forest implementation in Scikit-learn offers visualization of a single tree. The depth of trees in the forest is later limited to three levels, and the tree is extracted to produce an understandable image. The reduced size tree annotated with labels is shown in Fig. 2.

### 3.2 Evaluation of Performance Metrics

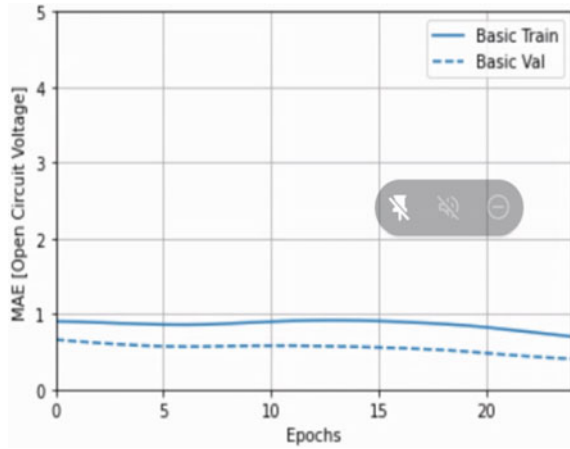
The three models that are ANN, random forest regressor, and AdaBoost regressor are used to predict the open-circuit output voltages, and the results are compared to evaluate the prediction made by each model against the corresponding actual open-circuit output voltages.

Artificial neural network contains 37 layers in total with 325 trainable parameters and 0 non-trainable parameters. ReLu activation function is used in 36 layers and linear activation for the output layer. The model showed smallest loss value after 25 epoch as shown in Fig. 3.

The results obtained from the three model used for predicting the output open-circuit voltages are shown in Fig. 4.

The collective evaluation of the real versus the predicted open-circuit voltages and the performance metrics with respect to the objective of this paper pointed to random forest regressor as the best model closely followed by AdaBoost regressor as the second best.

**Fig. 3** MAE versus epoch curve



S.No.	Artificial Neural Network	Random Forest Regressor	AdaBoost Regressor
	<i>Real OC Voltages</i>	<i>Predicted OC Voltages</i>	
1	7.74	7.044	7.757
2	6.87	7.087	6.908
3	11.11	7.225	11.035
4	14.22	7.267	13.681
5	14.71	7.398	15.070
6	9.22	7.410	9.145
7	14.46	7.432	14.776
8	6.48	7.489	6.489

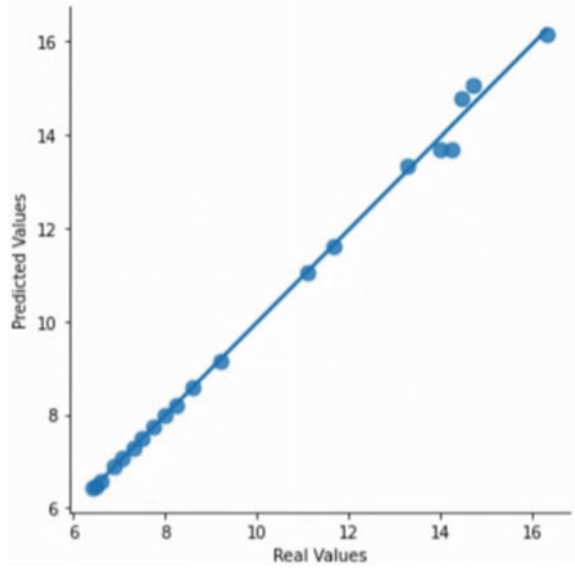
**Fig. 4** Predicted OC voltages of different models

### 3.3 Regression Plots

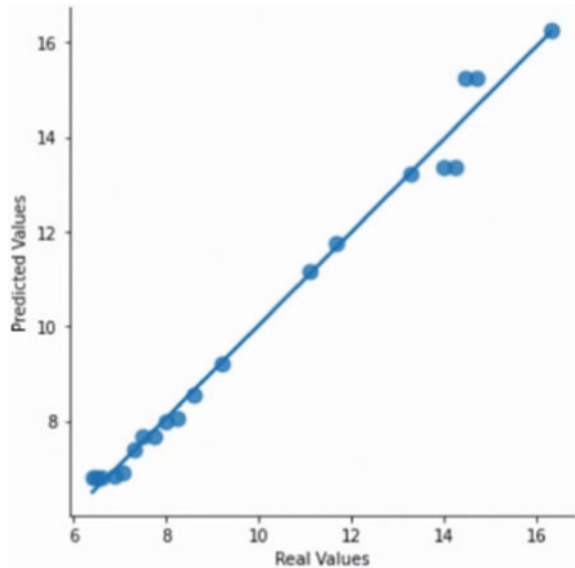
Figures 5, 6, and 7 show regression line between predicted and actual output values of all three models and help to visualize their linear relationships.

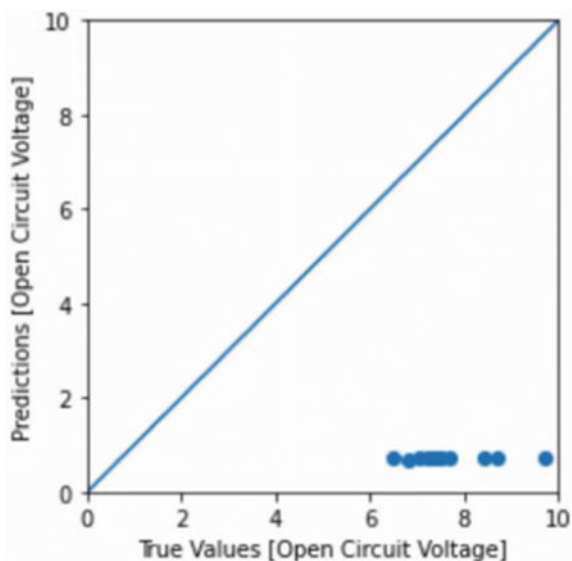
As clearly visible, the regression line obtained from the random forest regressor fits the data points extremely well as compared to the other two models.

**Fig. 5** Random forest regression plot



**Fig. 6** AdaBoost regression plot



**Fig. 7** ANN regression plot

## 4 Conclusion

In this paper, a random forest regression, AdaBoost regressor, and artificial neural network model are created to analyze the correlation between temperature, irradiance, and solar panel open-circuit voltage, and to predict photovoltaic panel open-circuit voltage based on temperature and irradiance on a given day. Furthermore, the accuracy of each models is calculated and compared using the regression plots. From the results obtained, the machine learning-based approach is better in comparison to artificial neural network-based approach. The work done in this paper will aid in future projects related to early fault detection and real-time diagnosis of a photovoltaic panel. This is essential for not only lowering maintenance costs and time but also for avoiding energy loss, equipment damage, and safety risks.

## References

1. Safari A, Ghavifekr AA (2021) International stock index prediction using artificial neural network (ANN) and python programming. In: 7th International conference on control, instrumentation and automation (ICCIA), pp 1–7
2. Khera N, Shukla D, Kumar V (2017) Artificial neural network approach for modelling of photovoltaic module. In: 4th International conference on signal processing and integrated networks (SPIN), pp 237–240
3. Khomdram J, Rita K, Jitu S, Chandrika Y, Basanta N, Sarkar S (2014) Artificial neural network approach for more accurate solar cell electrical circuit model. *Int J Comput Sci Appl (IJCSA)* 4:101–116

4. Hussein K, Muta I, Hoshino T, Osakada M (2005) Maximum photovoltaic power tracking: an algorithm for rapidly changing atmospheric conditions. *IEE Proc Gener Trans Distrib* 142:953–959
5. Hontoria L, Aguilera J, Almonacid F, Nofuentes G, Zufiria P (2006) Artificial neural networks applied in PV systems and solar radiation. In: *Artificial intelligence in energy and renewable energy systems*, pp 163–200
6. Khera N et al (2015) Remote condition monitoring of real-time light intensity and temperature data. In: *Proceedings of IEEE conference on advances in computing and communication engineering*, pp 3–6
7. Karamirad M, Omid M (2013) ANN based simulation and experimental verification of analytical four- and five-parameters models of PV modules. *Comput Sci Eng* 1:86–98
8. Mellit A, Pavan M (2010) A 24-h forecast of solar irradiance using artificial neural Trieste, Italy. *Sol Energy* 84(5):807–821
9. Kumari K, Boiroju N, Ganesh T, Reddy P (2012) Forecasting surface air temperature using neural networks. *Int J Math Comput Appl Res* 3:65–78
10. Mugdha V, Bhavana B, Moharil (2021) Solar photovoltaic technology: a review of different types of solar cells and its future trends. In: *International conference on research frontiers in sciences*

# A Methodology for Optimal Scaling of Unguided and Guided Rockets in a Military Formation



N. Ranjana and Indra Deo Kumar

**Abstract** A novel approach for determining the optimal scaling of unguided and guided rockets as a military decision aid is presented in this paper. The proposed method simulates a rocket model and perturbs key trajectory design parameters determining rocket impact accuracy. A Monte Carlo simulation is used for incorporating variations in input design parameters over a specified bracket and quantifying its effect on impact points of the rockets. Coverage-based solution for determining optimal mix of unguided and guided rockets is determined based on the ratio of these rockets for equal coverage if fired for the same range. Equal coverage is assumed to provide equal damage if warhead unit of both unguided and guided rockets is designed for equal lethal radius.

**Keywords** Rockets · Precision guided rockets · MBRLs · Military decision aid · Area targets · Accuracy · Monte Carlo simulations

## 1 Introduction

Rocket artillery is one of the most versatile firepower added to the conventional artillery options. It is most destructive and has the longest range. Since the rocket artillery does not produce any recoil, it is highly mobile and also can potentially fire on the move. The rocket artillery is generally fired from the multi-barrel rocket launchers. These are called as multiple launch rockets system (MLRS) or multiple barrel rocket launcher system (MBRLS). MBRLS is used in the role of area saturation artillery system capable of delivering free flight rockets in the range bracket of 10–200 km. Due to its long range and wide destructive radius, it is often used in counter-battery operations. It can destroy the adversary targets while staying out of their gun's range. They deliver a high volume of fire in a short period of time but are less accurate than conventional stationary artillery and cannot provide sustained, accurate fire support. The simplicity and ability to deliver massive firepower from a relatively light mobile

---

N. Ranjana (✉) · I. D. Kumar

Directorate of Systems and Technology Analysis, DRDO, New Delhi, India

e-mail: [n.ranjana@gov.in](mailto:n.ranjana@gov.in)



platform have led to the widespread adoption of MBRLS. Although MBRLS is not as common as the tube artillery, the system has certain marked advantages over the artillery guns.

The accepted norm for dispersion of area weapons is 0.5–2% of the rocket range globally [1]. The major advantage is that these conventional area weapons allow shoot and scoot, since these are mounted on mobile platforms. This increases the survivability of the system in the battlefield [2]. However, there are some identified disadvantages associated with these class of weapons like less impact point accuracy, cost and weight of ammunition, not suited for direct fire mode, more pronounced signatures and limited ability to deliver sustained fires [3].

In the recent times, the technology trend has been shifting toward the precision conventional rockets since these rockets can attack targets with high impact accuracy and low collateral damage. Precision guided rockets are primarily autonomous weapons which have an obvious edge over the unguided weapons due to improved accuracy. The precision is improved by adopting various technologies in the rockets. These include navigation system, GPS-aided navigation, terrain contour mapping (TERCOM) and guidance based on target imaging sensors. These systems guide themselves to the target point. However, the homing technology is not yet employed in this class of systems [4, 5].

Due to the emergence of the precision guided rockets, there is a marked shift in battlefield dynamics wherein the area target is becoming a kind of point target [6]. This overcomes some of the disadvantages of the unguided rockets at a reasonable cost, since cost of integration of guidance kits has become within reach.

In an operational scenario, a predetermined mix of free flight and guided rockets is used for the desired damage to be achieved. A method is evolved to estimate the optimum mix of guided rockets and unguided free flight rockets in a battery in order to harass/neutralize/destroy the given distribution of area targets (of specific sizes) in the enemy areas considering maximum coverage with minimum cost. To arrive at the optimal scaling of guided and free flight rockets weapons in a military formation, cost effectiveness of each class of rocket is estimated based on the operational reach and lethal radius of the rockets and area target sizes. The optimal scaling solution can be used for decision making such as optimal combination of guided and unguided rockets and budgetary allocations for artillery resources.

## 2 Coverage as a Measure of Effectiveness of MBRLS

The optimal scaling problem is dependent on multiple factors like range of each type of rocket and the distribution of targets. In this paper, both the types of rockets are assigned the same range, and targets are considered to have equal distribution across all the ranges. Based on these assumptions, the measure of effectiveness (MoE) of a MBRLS is to be identified. Identification of measures of effectiveness is an important and necessary step for any defense system analysis.

An efficient MBRLS is one that requires fewer than specified number of rockets for a given coverage of area target for the identified operational scenario. Coverage based on the rocket's range, accuracy and lethal radius is the prime measure of effectiveness parameter for assessing rocket's operational effectiveness. Due to uncertainties in the impact points of unguided rockets, solution for computation of number of rockets for specific coverage against an area target is probabilistic in nature.

Both analytical and numerical methodologies are applied for computation of coverage against intended area targets. Mathematical properties of various probability density functions are used to solve the coverage problem. The analytical solution to the coverage problem is provided in the second chapter of 'Operations Research in Military Science' by Eckler [7] and 'Military Operations Research Quantitative Decision Making' by Jaiswal [8]. The number of rockets required for the coverage of a specified area target is computed assuming the uniform distribution of key target points in an area target. The coverage requirement could vary based on the strategy of the artillery team operating in the field. Conventionally, artillery teams assume 30% coverage of area as desirable level for damage, and thus, this number is used for this study. Computation of number of guided rockets required for specific coverage against a given area target gets simplified due to its pin-point accuracy to hit the targets.

To arrive at the coverage, dispersion of impact points is to be estimated based on the performance of the rocket. Performance of the rocket is based on propulsion system, accuracy and warhead effectiveness under the given environment. A numerical technique for performance evaluation of free flight rockets and derivation of range table is given in [9]. Methodology for damage assessment of rocket artillery is discussed in [10]. Performance of warhead of the rockets for its operational effectiveness parameters is not considered in this work.

### 3 Rocket Trajectory

Initial range of the rocket is predicted using modeling and simulation. This is correlated and validated with flight trial data. A rocket trajectory is affected by various internal as well as external factors. In a free flight rocket, these effects are more pronounced. However, in a guided rocket, the trajectory is controlled by the guidance and control system to achieve an accuracy of less than 0.05% of range.

Rocket trajectory is controlled by the parameters like launch elevation and bearing angles, structural mass, inertia and propellant mass. Propulsion system performance is dependent on the operating temperature conditions which affects the propellant burn rate and burn time duration. The other important parameter affecting the performance of the rocket is its ballistic coefficient. Wind conditions under which rockets operate also have a major share contributing toward error in elevation and azimuth planes [11].

Rocket performance is acceptable within a specified band of operational parameters. This band of operation is defined to subsume the errors that can occur due

to manufacturing or environmental factors. Adequate numbers of flight trials are conducted to capture the performance variations under various launch and weather conditions. This also helps toward development of an accurate rocket trajectory prediction model.

### 3.1 Trajectory Variation

Error budgets comprise of errors in elevation and azimuth planes due to variations in engineering parameters of rockets primarily attributed to manufacturing process and operation under various environmental conditions. The propellant burnout condition of the rocket in terms of its positional and velocity state vectors and flight path angle in range and line axis translates into errors at impact points. All the contributing errors due to variation in its design parameters are mapped to the key trajectory parameters at burnout conditions. Ballistic coefficient of the rocket is a measure of its ability to overcome air resistance in flight.

The sources of the error defined in the range table have different perturbation effect on the rocket trajectory and the impact point. Trajectory is perturbed by varying the parameters from the range table. The aggregate of all the errors is used to determine the boundary of variations and computing the impact point deviations. Mapping of the various types of error in elevation and azimuth planes to rocket's trajectory shaping parameters is shown in Table 1.

**Table 1** Mapping of errors in elevation and azimuth plane with trajectory shaping parameters

S. No	Design/Operational parameters	Plane in which error translates	Mapping to trajectory determining parameters
1	Elevation	Range	Flight path angle elevation
2	Bearing	Line	Flight path angle azimuth
3	Structural mass	Range	Ballistic coefficient
4	Propellant mass	Range	Velocity
5	Specific impulse	Range	Velocity
6	Burn time	Range	Velocity
7	Charge temperature	Range	Velocity
8	Center of gravity	Range	Flight path angle elevation
9	Ixx and Iyy	Range	Flight path angle elevation
10	Fin cant angle	Line	Flight path angle azimuth
11	Drag coefficient	Range	Ballistic coefficient
12	Ballistic air temperature	Range	Ballistic coefficient
13	Ballistic air density	Range	Ballistic coefficient
14	Wind	Range and line	Flight path angle elevation, azimuth

## 4 Simulation for Estimation of Coverage

A novel approach is adopted based on the fixed amount of coverage to be achieved and estimation of number of rockets to achieve this coverage. To this requirement, rocket trajectory is simulated for calculating the impact points and its dispersion. Rocket trajectory equations are used to incorporate possible variations under flight conditions. On this rocket trajectory equation, Monte Carlo technique is implemented to simulate the variations in the performance. This solution is implemented in Systems Tool Kit (STK) for estimating the coverage of area target by the number of rockets impacting in the specified area target. STK not only provides the physics-based modeling and simulation environment, but it also enables the simulation of the operational environment. For realistic modeling of trajectory, environmental factors are varied using Monte Carlo simulation for evaluation of rocket performance.

### 4.1 Rocket Trajectory Simulation

The high precision orbit propagator module (HPOP) of STK tool has been used to simulate the characteristics of the rocket. The guidance is not built in the models used in the simulation. The rocket model is represented by the differential equations which get solved numerically for generation of its trajectory profiles [12–14]. The trajectory equations include all the force components acting on the rocket including atmospheric drag and gravity. The drag force model provides a variety of options for enabling the atmospheric density variations used in the computation of atmospheric drag accelerations on the rockets. The atmospheric density model existing with the HPOP module and the ballistic parameters ( $C_d$ , area/mass ratio) are configured as per the design specifications of the rockets.

#### Drag Force computation

De-acceleration caused by drag is:

$$a_D = (C_D)(A_D/M)(\rho V^2/2),$$

where:

$C_D$  = coefficient for drag

$A_D$  = satellite/missile/rocket cross-sectional area along velocity vector

$M$  = satellite/missile mass

$\rho$  = atmosphere density

$V$  = rocket velocity

## HPOP—Integrator

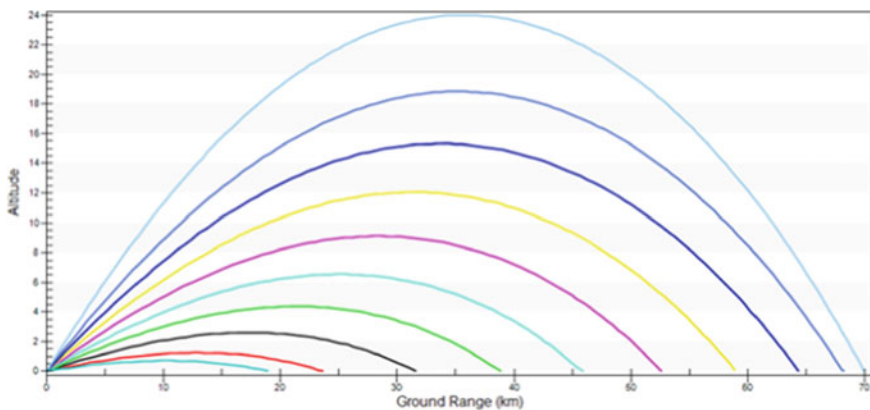
The integrator allows configuring the combination of the formulation of the equations of motion and the numerical integration technique to be used during rocket flight. Here in this case, Runge–Kutta integration method of fourth order (RK4) is used for the numerical integration of trajectory differential equations.

## 4.2 Perturbations

All the rocket parameters are varied between its error boundaries using Monte Carlo simulation. Burnout velocity of a rocket with a solid propulsion unit is fixed. Flight path angle is varied to generate the trajectories for the range brackets. Trajectory profiles for a rocket for various ranges generated by varying flight path in elevation angle are shown in Fig. 1. As shown in the Fig. 1, bands of range are created, and each is run with the Monte Carlo Simulation.

Monte Carlo simulation is configured as normal distribution around the mean point of impact (MPI). Following parameters are set up with its variations specified within a bracket.

- Mean and [Min Max] values of key trajectory parameters
  - Velocity—Mean [Min Max]
  - Flight path angle in range axis—Mean [Min Max]
  - Flight path angle in line axis—Mean [Min Max]
  - Drag—Mean [Min Max]
  - Area/Mass—Mean [Min Max]
- Standard deviation (%)



**Fig. 1** Ground range (km) versus altitude (km) profiles of a rocket

- Size of the area target

Distributed impact points within an area target are generated, and percentage coverage within the area target is computed using specified lethal radius of the rockets (average of 100 runs for each case is carried out).

### 4.3 Design of Experiment

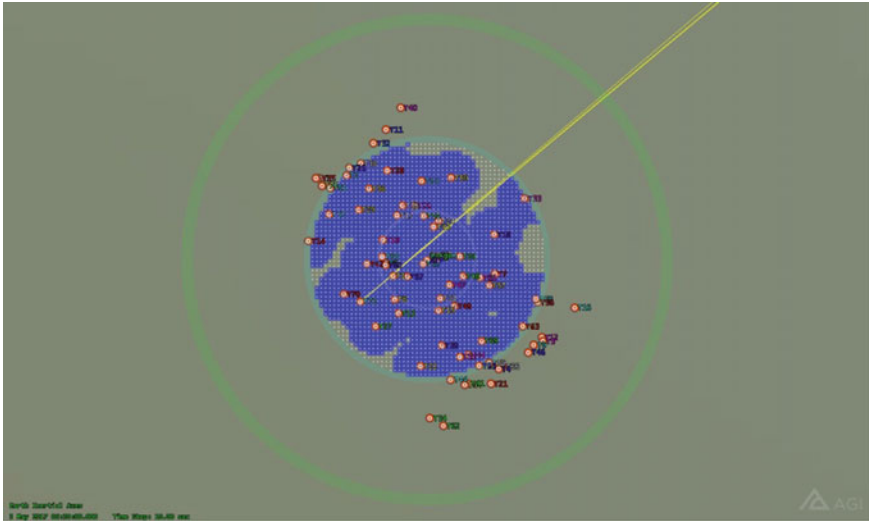
A separate simulation is configured for different range brackets. Circular area targets with radius of 100 m, 250 m and 500 m are considered. For each 5 km increase of range within the minimum and maximum of the full range, a different simulation band is created. For each range and for each area target, three different numbers of rockets (say  $n_1$ ,  $n_2$ ,  $n_3$ ) are fired. These numbers are taken from the salvo firing practice followed by the artillery teams. Number of rockets falling within the target area for each run is multiplied by the assumed lethal radius of the rocket payload (say  $r$ ) and graphically summed up (to remove the overlaps of the circular impact points) to give the coverage achieved by each run. Thus, a large experimental data set is created for each of the circular area target size, ten range brackets and three different salvos, and the trajectories are perturbed based on Monte Carlo settings.

Result of one of the runs is shown in Fig. 2. For each run, different number of rockets fall within the area target giving a different coverage value for the run. Large numbers of runs are conducted to arrive at the number of rockets required for 30% coverage. For any guided rocket, the impact point is same as the trajectory gets controlled using navigation and control mechanisms. To cover the area, exact latitude and longitude positions of the point can be fed to cover an entire area. For calculating the coverage due to guided rockets, numbers of required rockets are arrived at by dividing the area by the standard impact area of individual rocket due to lethal radius.

## 5 Optimal Scaling

To arrive at the optimal number of guided versus free flight rockets, cost ratio factor is estimated for the two variants. Based on this cost factor, ratio of unguided and guided rockets is computed for equal cost effectiveness for different ranges. Boundary of cost effectiveness of unguided rocket over guided rocket for circular area targets with radius of 250 m and 500 m is determined from the coverage values. Number of unguided rockets over guided rockets for equal cost effectiveness for complete range bracket for both the type of area targets is arrived at using these figures. Computation of optimal mix of unguided and guided rockets for 250 m circular area target is used as a median. Other factors which are used as simple multiplication factors for rationalizing these numbers are:

- (a) Target distribution percentage for different range brackets



**Fig. 2** Rockets impacting area target along with coverage

- (b) Weightage of target distribution (user input for re-estimation from proportional division)
- (c) Re-distribution of percentage due to non-reachability of the weapon for a specific range bracket
- (d) Estimation of rockets required for 30% coverage for each range bracket
- (e) Selection of unguided rockets or guided rockets based on the cost versus number factor of 5 times (if no of unguided rockets > 5 number of guided rockets) then guided rocket is cost effective else unguided rocket is cost effective (This computation is based on the assumption that cost of guided rockets is 5 times that of unguided rocket)
- (f) Estimation of optimal parameters using the constraint of configuring specific number of rockets in a launcher and number of rockets required in a battery
- (g) By solving the above constraints and ratio equation, the FFR:GER ratio is computed.

## 6 Conclusion

A systematic methodology for optimal scaling of unguided and guided rockets is developed factoring all the important considerations of the artillery rockets performance as well as operational factors. The concept is implemented using the Systems Tool Kit's modeling and simulation environment. This methodology is a military decision aid specific to optimal operational deployment of unguided and guided rockets in a military formation. More than 10,000 Monte Carlo simulation runs have been executed to capture the desired number of rockets for specified percentage

coverage of area targets. This simulation framework has provided excellent results computing optimal scaling of unguided and guided rockets. The outcomes of the numerical solutions are verified with analytical solutions. The achieved study is utilized for arriving at the numbers of rockets required for a specified coverage of area targets.

## References

1. Williams AG, Dhingra J (2017–2018) HIS Jane's weapons ammunitions, pp 881–927
2. Gordan IV J, Mikolic-Torreira I, Sean Barnett D, Best KL, Boston S, Madden D, Tarraf DC, Willcox J (2019) Army fires capabilities for 2025 and beyond. RAND corporation, pp 77–86
3. Katoch LGPC (2019) MLRS for army and indigenous capability, SP's land forces. SP Guide Publications
4. Runduo C, Xiaobing Z (2018) Multi-objective optimization of the aerodynamic shape of a long-range guided rocket. *Struct Multi Optim* 57:1779–1792 (Springer)
5. Raza A, Wang H (2022) Range and accuracy improvements of artillery rocket using fixed canards trajectory correction. *Aerospace Basel* 9(1)
6. Birkler J, Hura M, Shlapak D, Frelinger D, McLeod G, Kent G, Matsumura J, Chiesa J, Davis B (1996) A framework for precision conventional strike in post-cold war military strategy. RAND corporation, pp 5–32
7. Eckler A, Burr S (1972) Mathematical models of target coverage and missile allocation. Military Operations Research Society, Alexandria, VA
8. Jaiswal NK (1997) Military operations research quantitative decision making, vol 5. Springer, ISOR
9. Raza A, Wang H (2022) Range and accuracy improvement of artillery rocket using fixed canards trajectory correction fuze. *Aerospace*
10. Wang H, Labaria G, Moten C, Zhou H (2017) Average damage caused by multiple weapons against an area target of normally distributed elements. *Am J Oper Res* 7:289–306
11. Kranthi Kumar R (2020) Error modification in trajectory prediction of an unguided rocket, vol 13, no 01
12. Prabhakar N, Kumar ID, Tata SK, Vaithyanathan V (2013) A simplified guidance for target missiles used in ballistic missile defence evaluation. *J Inst Eng India Ser C* 94(I):31–36 (Springer)
13. Siouris GM (2004) Missile guidance and control systems. Springer, New York, pp 365–489
14. Vinh NX (1981) Optimal trajectories in atmospheric flight. ESPC, Amsterdam-Oxford-New York



# Static Analysis of Pick-and-Place Robotic Arm Based on ANSYS



Shikkha Sood and Pramod Kumar

**Abstract** Robotics is creating a revolution in an industrial area because it cuts personnel and manufacturing time. In the present time, robotic arms play a vital role in the industry. To assure the robot's performance before it is used in real-world applications, it must be examined using software to prevent wasting energy and money. Robots' performance determines the stability of the robotic arm. This paper uses SolidWorks and finite element analysis tools to create a pick-and-place robot arm model. The analysis of the robotic arm has been done with ANSYS, and statics analysis is presented in this paper with the robotic arm's stress and strain diagram and deformation diagram.

**Keywords** Robotic arm · SolidWorks · Finite element analysis · ANSYS

## 1 Introduction

Different sorts of robots with countless human people are implemented in the car industry, construction, and many other production areas. A robot is a machine that consists of sensors, control systems, manipulators, power supplies, and software that all work together to complete a task. These robots have different types of robotic arms with different sizes, shapes, materials, and tasks. These robotic arms resemble human arms in appearance and perform a separate industrial purpose. The structure of these robotic arms contains rectangular-shaped links, a gripper, a rotatory table, joints, and a rectangular platform. A servo motor drives the angular rotation of each joint.

A robot's design, construction, programming, and analysis need a mix of physics, engineering, mathematics, and computers. A robot has a mechanical manipulator (MM) and a controller for arm movement, and it performs several interrelated tasks. It has joints and links for orientation, and it places the manipulator's end relative to its base.

---

S. Sood (✉) · P. Kumar

Department of Mechanical Engineering, Galgotias University, Greater Noida, India  
e-mail: [shikhasood0396@gmail.com](mailto:shikhasood0396@gmail.com)

Examination of the finishing SolidWorks design is completed by ANSYS. For examining the structure of the sections of a robot arm, ANSYS can be quite useful. This paper analyses the static analysis of the different sections of a robotic arm by using finite element analysis ANSYS.

## 2 Background

Each robot is designed to do a certain duty. In this paper, we studied the model features and static analysis of seven degrees of freedom articulated monitoring robots in a nuclear atmosphere. The mechanical configuration is designed using CATIA software. To ensure the design is secure, ANSYS is used to carry out stress and deflection analysis. The primary goal of static analysis is to do a stress and deflection study on the manipulator as a result of force and gravity loading. We noticed the examination of the robot's self-weight in this work. The robot is made up of rotational joints, which cause some deflection in the robot system. The robot's arms include two universal joints that allow for adaptable arm movement, allowing the robot to traverse around the steel canister's exterior surface. Here we observed that the deflection of the arm is in the negligible range due to the self-weight of the robot which is calculated using ANSYS. The design calculations for the robots' primary components, the screw-jack mechanism, and universal joint, are quickly discussed in this paper. ANSYS is used to verify the robot's stabilization and to analyze deflections. The result of this paper concluded that according to the static analysis, the robot's design parameter is secure to produce for real examination purposes. The findings show that even after taking into account the factor of safety, the stress value is still within acceptable bounds, allowing for a simple modification in shape or mass optimization for the same loading situation to enhance payload capacity [1].

An articulated robot is one having rotational joints. All examples of articulated robots are simple two-jointed constructs or systems with ten or more interacting joints and materials. One of the various forms of energy for them is electric motors. Some robots, such as robotic arms, are articulated whereas others are not. Assembly, die casting, fettling machines, gas welding, arc welding, and spray painting are all examples of applications. This is a robot with at least three rotary joints on its arm. The generic articulated robotic arm is presented in the paper. The notion of a five-degree-of-freedom robot arm is described in this study. This allows for a broad variety of arm postures for any given target location, allowing for a lot of motion freedom. Further, the modeling and static analysis of the five degrees of freedom articulated robotic arm motivated our work. The robot is built to carry a 5 kg payload, and each link is analyzed to determine the precise stress pattern on each link. The factor of safety value is set to 2, and the robot is evaluated for safety. The maximum shear stress created in the model is presented following a static structural study of the articulated robot arm. The stresses developed and deformation that occurred is also shown in the models of the robot, equivalent stresses and deformation of each link are observed in this paper. The result of this paper concluded that the stress value is limited even after

factoring in the factor of safety, payload capacity can be raised simply by changing the design, or mass optimization can be used for the same payload condition [2].

Concrete pouring robots are widely utilized in the field of building construction due to their extremely intelligent autonomous pouring and self-diagnosis capabilities. The mechanical arm is a crucial actuator in a concrete pouring robot; its effectiveness improves the reliability of the used concrete pouring robot, so you must assess if it can completely fulfill technical requirements. To ensure that the mechanical arm can move the concrete uniformly and accurately to the appropriate casting location, a statics analysis is necessary. The foundation of mechanical design is static analysis. This article's static analysis of the mechanical arm accounts for gravity, the basic load carried by the concrete pouring robot, the weight of the traction on the pipe, the wind load, and the lateral force of the dynamic load. Finally, the mechanical arm's stress and strain diagrams are obtained. In this paper, we studied the stress and strain diagram of the robotic arm, as well as the pivot point connection mode of the robotic arm efficiency strategy using ANSYS statics analysis. Create a model of a concrete pouring robot arm using SolidWorks software and finite element analysis tools. We observed that alloy steel, the material has the benefits of being low weight, having high welding properties, and having a clean and neat look [3].

Robots are frequently used in the industrial sector to produce high-quality goods faster and more precisely. There are several functions, including gathering information and performing research regarding hazardous sites that are too dangerous for humans to approach. Nearly half of the time, robots are utilized to reduce human intervention. Because it is widely employed in automation, particularly for high-precision micromachining, the design of the robot gripper provides an active study topic. In unstructured situations, robot grippers frequently struggle to accomplish sophisticated manipulation tasks. Special robot grippers have recently appeared, posing a threat to the universal grasping capacity of robot grippers. We investigated the SolidWorks 2020 model of a robotic arm with five degrees of freedom and a gripper. By monitoring the maximum stress caused by the applied forces at the different components of the robotic arm and the gripper, the statics assessment of the robotic arm and the gripper aims to estimate the maximum load-carrying capability. We analyzed the behavior of the body upon applied load by computing stress. Forces are delivered to the bodies of the robotic arm and gripper in the statics section, causing stress on those parts. We observed that the collar part carries a maximum 6000 N load safely while the base and shaft can carry a 20,000 N load safely. The collar part is the weakest part of the robotic arm. The base and shaft are the strongest part. Arm 1 can safely handle 5000 N of strain, and the fillet region of the arm shows the most stress. Arm 2 can also carry a safe load of 5000 N, and the highest stress of arm 2 is seen at the point where it is attached to arm 1. During the dynamic study of the robotic arm, the average force acting at revolute joint 1 is about 400 N.

From the above results, we concluded that for the above-mentioned static loads and provided angular velocities at the robotic arm's joints, the robotic arm's design is safe. The gripper's jaws can readily sustain 5000 N weights at the same time. That means the gripper can bear a total force of  $(5000 \times 2)$  N, or 10,000 N [4].

We studied five degrees of freedom robotic arms for stress and deformation evaluation. SolidWorks was used to create the design and model for the five-DOF mechanical arm, and ANSYS software was used to evaluate the entire structure. Robots are utilized in many sectors nowadays, especially those that need accuracy. The finite element analysis (FEA) is used in a model design development technique to create the robotic arm. The modeling, building, and development of robot arms have been particularly active study areas in recent years all around the world. The primary goal is the evolution of a design that can accurately predict the robot arm's position in specific arm postures and high-stress situations. Further structure upgrading should be conceivable if disparate nozzle weights are pressed and final data from diverse conditions are compared to identify the weak areas.

We study the design of the ideal robotic arm in this paper. The perfect mechanical arm, as stated in this article, has a low weight, is capable of withstanding the maximum levels of permissible stresses while carrying various payloads, has a high-performance index, and lowers a robot's total production and maintenance costs. The primary goal is to reduce the structure's mass and physical distortions to improve the stiffness of the design model we choose or any static model by using various force conditions. The weight restrictions, the anticipated number of linkages in the mechanical arm, and a few other external factors have already been determined. By implementing an automatic collaboration between the ANSYS software and the SolidWorks program, this task is made promising. This work supported the industrial mechanical arm with five degrees of freedom as the automation of the optimum design process. When analyzing total deformation and maximum shear stress, the results from the ANSYS program with a mesh size of 0.05 are quite good [5].

A novel, high-performance, semi-direct drive robot arm's mechanical design, structural analysis, and results validation. A finite element analysis (FEA) design optimization process is examined, and the resulting arm design is given. High structural vibration frequencies are predicted by FEA simulations of the final design throughout the workspace for the arms. The projected structural vibration characteristics are confirmed across the workspace of the arm in extensive structural vibration studies using the finished manipulator. To analyze the structural parameters, a modal and structural analysis of the model is conducted. Robots are machines that use sensors to gather data about their surroundings and then autonomously decide what to do. People like using several fields, including industry, which includes certain risky employment involving radioactive impacts. Robots are treated as servers at this stage. They offer several benefits and are simple to administer. The study of robot motion, or kinematics, is known as robot kinematics. Finding the natural frequency and the system's-related vibration mode shapes is the goal of modal analysis for robot arm systems utilizing finite element software. The structural types and constraint conditions absent of loads have the greatest impact on these characteristics. According to the results of the modal analysis, several robot arm structures are examined. It is discovered that circular-shaped robot arm structures, whether hollow or solid, maintain greater natural frequencies than square-shaped robot arm structures. The findings of the structural study indicate that the equivalent stress and deformation of a robot arm with a circular shape are superior in comparison because the stresses

raised are lower. The study is deemed accurate since the findings fall within safe design limitations [6].

The model, analysis, development, and manufacture of a mechanical arm for sorting several components are discussed in this study. The primary issue driving the project's launch is the industrial sector's comparatively greater pace of growth. Most businesses manufacture heavy-duty robotic arms. Few businesses produce lightweight, inexpensive robotic arms. As a consequence, a portable, reasonably priced robot is created to address this problem. The body of the mechanical arm was built out of plastic, and an optical sensor was added to give rudimentary object identification. For general operation, the robotic arm required five servomotors: four for its joints and one for the grasping mechanism. Due to the material's low weight and excellent strength, perspex was chosen for the design and construction of the gripper. The robotic arm's movement was controlled by the basic stamp programming sequence, and the gadget was designed to distinguish between different types of material and other objects using reflective theory before carrying out further actions. SolidWorks was employed to simulate the robotic arm's action and model the intricate design. The project's first goal was to create a functioning robotic arm with sense-pick-and-place capabilities. The robotic arm prototype was successfully created, and it could perceive pick-and-place operations. To provide a fuller picture of its general dependability, it was evaluated. 90% of the robotic arm's total tasks were completed by it. Analyzing the mechanical characteristics of the robotic arm's design is the project's second goal. The necessary shear stress on the finger gripper connecting hole was calculated. The gripper needed to understand this method to understand shear stress. Consequently, the project's second goal was accomplished [7].

### 3 Robot Modeling

SolidWorks software was used to create the whole design of the robotic arm. The entire design consists of many components such as the base, body, upper arm, end nozzle, forearm, and so on. The measurements of each part of the design are different. A servo motor is utilized to produce proportionate motion between these sections. Due to its low power need and small weight, a DC servo motor will be ideal for this design instead of pressure-driven or pneumatic actuators. To complete the work, the assembly of the automated arm design should be coordinated. Awareness, observation, and enactment are three distinct steps in the regulation of a robotic arm. Sensors provide data to the robotic arm about the state of its linkages and end effector, which is then prepared for the control unit, which figures out an acceptable signal for the motor to move accurately.

To begin, the robot's whole design and design portions are created for the operator. Firstly, we create a 2D sketch design of the robotic arm to produce the 3D model of the robotic arm. Then we design a 3D model of the robotic arm using SolidWorks software. After that, we analyzed the model in the ANSYS using finite element analysis.

For FEM analysis, a 3D CAD model of a robotic arm was created as shown in Fig. 1 and the design of the robotic arm with meshing is shown in Fig. 2. The model's whole design is created using the program SolidWorks. The design of each piece of the robotic arm is first constructed, and then each portion is combined to create the final model design. The full design is then imported into the ANSYS software from SolidWorks. Because the model assembly must remain fixed with the surface when in use, the lowest half of the design must serve as a stationary constraint.

The material used for designing the pick-and-place robotic arm is structural steel having a density is  $7.85e-06 \text{ kg/mm}^3$  (Table 1).

The meshing of geometry is done with a boundary box diagonal of 669.08 mm, a minimum edge length of  $1.8311e-002 \text{ mm}$ , and an average surface area of  $526.86 \text{ mm}^2$ . The meshing of geometry is shown in Fig. 2.

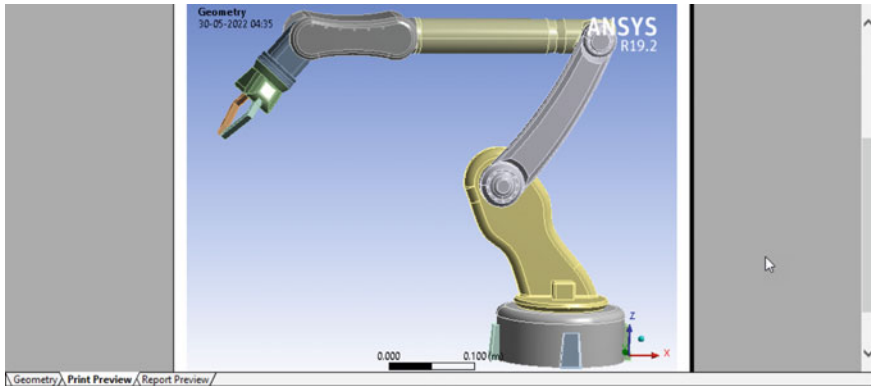


Fig. 1 3D modeling of the robotic arm

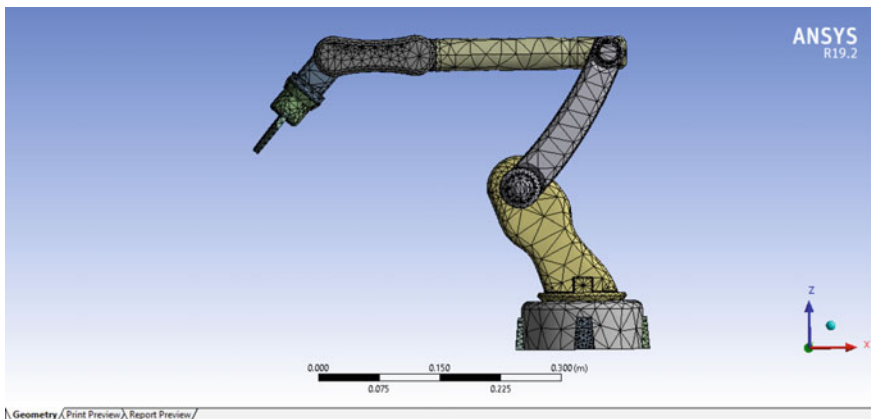
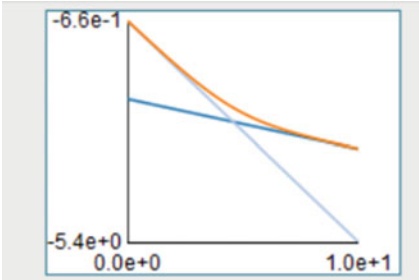
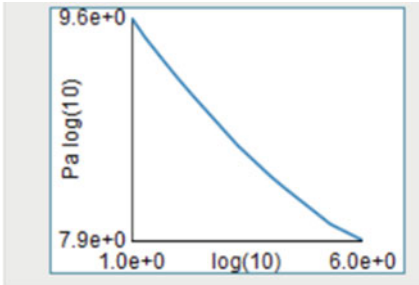


Fig. 2 Robotic arm with meshing

**Table 1** Parameters of robotic arm material

Isotropic elasticity derived	Young's modulus and Poisson's ratio
Young's modulus	2e+11 Pa
Poisson's Ratio	0.3
Bulk modulus	1.6667e+11 Pa
Shear modulus	7.6923e+10 Pa
Thermal expansion isentropic	1.2e-0.5 1/°C
Compressive ultimate strength	0 Pa
Compressive yield strength	2.5e+08 Pa
Yield stress	4.6e+08 Pa
Tensile yield strength	2.5e+08 Pa
Strain life parameter	
S-N Curve	

Following the design of the robotic arm on 2D and 3D models, modal analysis was examined using the FEM approach in ANSYS which help to find the shear and strain stresses and total deformation of the robotic arm. The study’s findings are listed in the result and discussion section below.

### 4 Result and Discussions

The main goal of static analysis is to find out the stress and deformation analysis on the robot due to the effect of force. In this paper, we analyzed the static analysis of the five degrees of the freedom robot arm. The force of 5N is applied to the end effector link. Figures 3 and 4 show the shear stress and shear strain of the robot. The total deformation of the five degrees of freedom robotic arm shows in Fig. 5. When a medium is subjected to a lateral force, shear strain results. It is possible to produce a shear force wave that moves perpendicular to the direction of the applied force. A shear wave’s particle motion is parallel to its path of propagation. By permitting a material to move along a plane or planes parallel to the given tension, shear stress tends to deform it. Due to its close connection to earthquakes and the downslope movement of earth elements, the resulting shear has a significant impact on nature.

Total deformation and both the shear stress and shear elastic strain were analyzed and shown with their maximum and minimum values. The blue part shows the minimum deformation and the red part shows the maximum deformation of the robotic arm (Table 2).

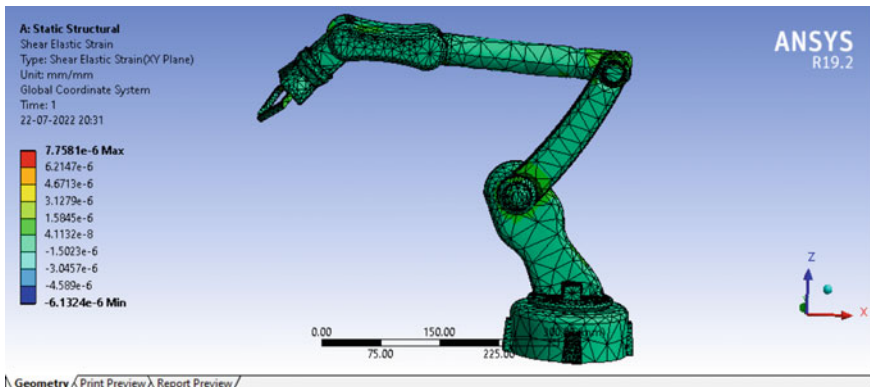


Fig. 3 Shear elastic strain at load 5N of the robotic arm



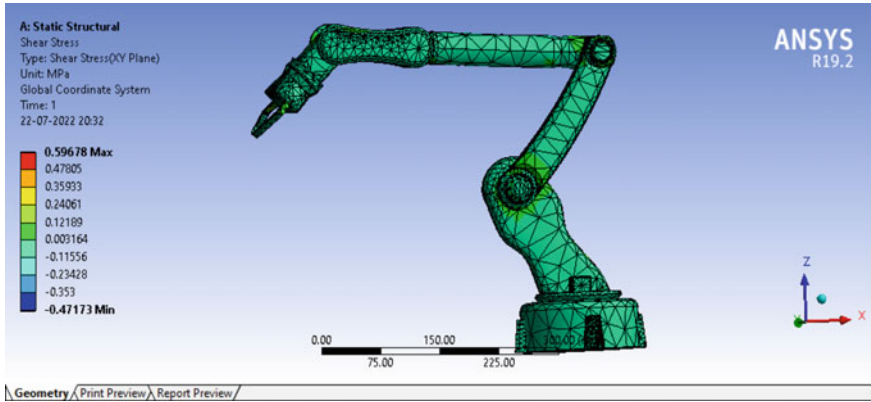


Fig. 4 Shear stress at load 5N of the robotic arm

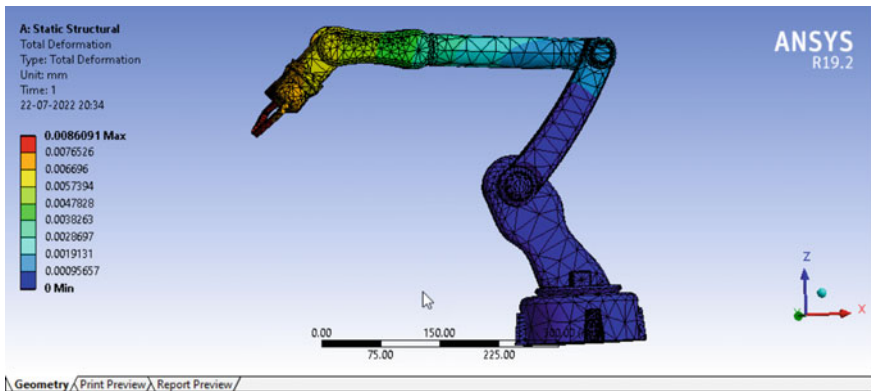


Fig. 5 Total deformation at load 5N of the robotic arm

Table 2 Result analysis

Result	Minimum	Maximum	Average
Shear elastic strain	- 6.1324e-006 mm/mm	7.7581e-006 mm/mm	2.3995e-009 mm/mm
Shear stress	-0.47173 MPa	0.59678 MPa	1.8458e-004 MPa
Total deformation	0	8.6091e-003 mm	2.2976e-003 mm

## 5 Conclusions

We created a simulation environment that was generally accurate in simulating the work settings, and we used that environment to analyze our model. Any design must be shown to be beneficial for the intended goal to be considered a good design. The Static analysis of the Five degrees of freedom robotic arm is carried out. This robot

is employed to pick-and-place objects. This paper focuses on the design and static analysis of the robotic arm for pick-and-place purposes. We applied the 5N load condition to the robotic arm, which is found to be safe. The analysis was done on the robot geometry of the SolidWorks model using ANSYS to evaluate the shear stress, strain stress, and total deformation results.

## References

1. Shanmugasundar G, Sivaramakrishnan R, Venugopal S (2013) Modelling, design, and static analysis of seven degree of freedom articulated inspection robot. In: *Advanced materials research*, vol 655. Trans Tech Publications Ltd, pp 1053–1056
2. Vadhadiya RP, Patel BK, Zala C, Patel CC (2015) Static analysis of five degrees of freedom articulated robot arm. *IJSRD Int J Sci Res Dev* 3(03). ISSN (online): 2321-0613
3. Shuai H, Yuming Q (2018) Static analysis of Concrete pouring robot arm based on ANSYS. *Int J Eng Res Technol (IJERT)* 07(01)
4. Chakravarti S, Sarkar S, Mukherjee S, Biswas M, Static and dynamic analysis of robotic arm with a gripper
5. Singh A, Arora R, Chouhan YS (2020) Design and static analysis of robotic arm using ANSYS. *Int J Recent Technol Eng (IJRTE)* 9(1). ISSN: 2277-3878
6. Jeevan, Rao AM (2015) Modeling and analysis of robot arm using ANSYS. *Int J Sci Eng Technol Res* 4(33):6692–6697. ISSN 2319-8885
7. Yi KZ, Razali ZB (2013) Design, analysis and fabrication of robotic arm for sorting of multi-materials. Project Report, School of Mechatronic Engineering, University of Malaysia Perlis

# Experimental Reduction of Coke Oven Gas by Adjustment of Gas Flow in Pushing and Charging Schedule of Coke Oven Plant



Niranjan Mahato, Himanshu Agarwal, and Jainendra Jain

**Abstract** One of the essential components used in blast furnaces to transform iron ore into hot metal (liquid iron), the majority of which is then processed into steel, is coke. Coke is a reducing agent and a load-handling tool in blast furnaces. Steel is produced at a lower cost because the coke ovens are using less specific energy. The current research article comprises the adjustments of the gas flow with respect to pushing and charging scheduled. This research work saved the coke oven gas up to 500 Nm<sup>3</sup> per hour without affecting the quality of coke. This includes that the specific heating consumption value is also reduced from 640 to 620 (in kcal/kg) of the coke oven battery without any type of additional manpower and the physical type of resources. This type of experimental rectification or modification process of coke oven battery will be making blended coal to coke more energy efficient without any type of extra money addition.

**Keywords** Coke oven heating regime · Coke · Heating chamber · Flues of heating chamber

## 1 Introduction

One of the essential components used in blast furnaces to transform iron ore into hot metal (liquid iron), the majority of which is then processed into steel, is coke. Hot metal is manufactured using the majority of the coke produced. Other industries that employ coke include chemical facilities, nonferrous smelters and iron foundries. It serves as a carburizing component in the manufacture of steel. In [1], this paper developed a model for reducing the variation in burning of coal to coke during the coke-making process and to gain the quality and also to develop the energy in coke

---

N. Mahato (✉) · H. Agarwal  
Department of Mechanical Engineering, Government Engineering College, Jagdalpur, India  
e-mail: [niranjan166mahato@gmail.com](mailto:niranjan166mahato@gmail.com)

J. Jain  
Department of Applied Mathematics, Government Engineering College, Jagdalpur, India

plant. The total length of the coke oven is 100 m, consisting rectangular-shaped chambers of length 16 m, height 7 m and width 0.41 m with removal door ends. In [2] this paper, the recovery type coke-making process takes a periods of eighteen to twenty hours depending on the number of pushing's by indirect heating with the coke oven gas or mixed gas. 7 m tall battery is having the sixty-eight number of heating walls, and each type of walls is having thirty number of burning flues. The total average temperature of each flue is about maintained at about 1200–1300 °C. Maintaining the proper uniform operating conditions is a difficult task due to the dynamic pushing of the operation and to achieve the required production target [3]. In [4], the heating chamber is divided into pairs of vertical flues. Vertical flues of each pair are connected at the top through a window in the partition wall. The gas and preheated air are fed to the base of the flues from where they move upwards under the influence of chimney draught. The hot products of combustion cross over to the adjacent flues and pass on the regenerators where the checker-work absorbs most of the sensible heat [5]. Integrated plants and merchant plants are the two sectors that make up the coke manufacturing business. Blast furnace coke is produced by integrated factories, which are owned by or connected to iron and steel production facilities and is largely used in such facilities' blast furnaces. Furnace and/or foundry coke are produced by independent merchant factories and sold on the open market. The majority of the products these factories produce are sold to businesses that operate foundries, blast furnaces and nonferrous smelting operations. In [6], this describes the gas pressure in the oven chambers should be positive and higher than pressure at any point of adjacent heating chamber during whole coking period. Good quality coking coal is often carbonized to produce high-quality coke. The term “coking coals” refers to coals that, after carbonization, undergo the softening process, the swelling process, and after the re-solidification process to become coke. In [7], a new design of optimum control of temperature of gas coming out of the oven into the standpipe is about 600–700 °C, and it leaves the hydraulic mains at the temperature of 80–85 °C [8]. In [9] in this system of ovens, paired vertical flues are envisaged which are interconnected with each other with a provision for recirculation of products of combustion. The heating chamber is divided into pairs of vertical flues. Vertical flues of each pair are connected at the top through a window in the partition wall [10]. In this paper, the vertical flues are connected with regenerator through short and long inclined flues [11]. In [12], the gas and preheated air are fed to the base of the flues from where they move upwards under the influence of chimney draught. The hot products of combustion cross over to the adjacent flue and pass on to the regenerators where the checker-work absorbs most of the sensible heat contained in the products of combustion. In [13], heating is continued in the same way as started above; i.e. by increasing gas pressure/gas volume till gas volume cannot be increased by increasing gas pressure. In [14], research article comprises that coke oven battery is constructed in different types of groups, with the heating ovens and heating chamber walls containing the heating flues. In [15], coke oven clean gas can be saved up to 300–400 Nm<sup>3</sup> per hour by using reversal cycle modification in coke plant [16]. The coke oven clean gas and preheated type of air are fed to base flues from where they move upwards under the influence of chimney draught [17].

The hot products of combustion cross over to the adjacent flues and pass on the regenerators where the checker-work absorbs most of the sensible heat contained in the product of combustion [17]. In this paper, the cooled gases from the regenerator move to the waste heat flues and then to the chimney. These two currents of heat flow, i.e. the up-current and down-current, are periodically reversed in every 20 min to maintain uniform and state temperature condition throughout the whole battery [18]. A minimum coal ash value and preferred minimum level of sulphur value for bituminous coal is destructively distilled (also known as carbonized) to generate coke, a solid carbonaceous substance. The extra type of contaminants included in blended coal, such type of volatile substances (grease, oil and tars), are to be flushing out during the process of distilling coal in heating chambers for controlling the uniform temperatures is around of 1100–1200 °C. Coke is generated in a controlled manner of desired quantity. For coking purposes, it is thought that coal with a volatile matter (VM) content of about 25% is ideal. The burning of coal's carbon is prohibited by the controlled-temperature distillation process. Readiness of coke at the end of coking period along the length, height and width of coke oven chamber by maintaining uniform temperature throughout the length and height of heating wall all along the battery [19].

However, there is the requirement for the experimentation work; it is observed that the flow of gas cannot be increased for increasing 1–2 pushing and charging target schedule in a day. This type of modification will not be violated daily maintenance and standard operating practices. The decrement of flow of coke oven gas with respect to pushing and charging target schedule and the possible modification works solution is also justified against standard operating practices and of regular-based schedule jobs and schedule maintenance. In this research paper at 83 no. this research article experimentation work reduced the coke oven gas flow up to 500 Nm<sup>3</sup> per hour.

## 2 Experimental Set-up

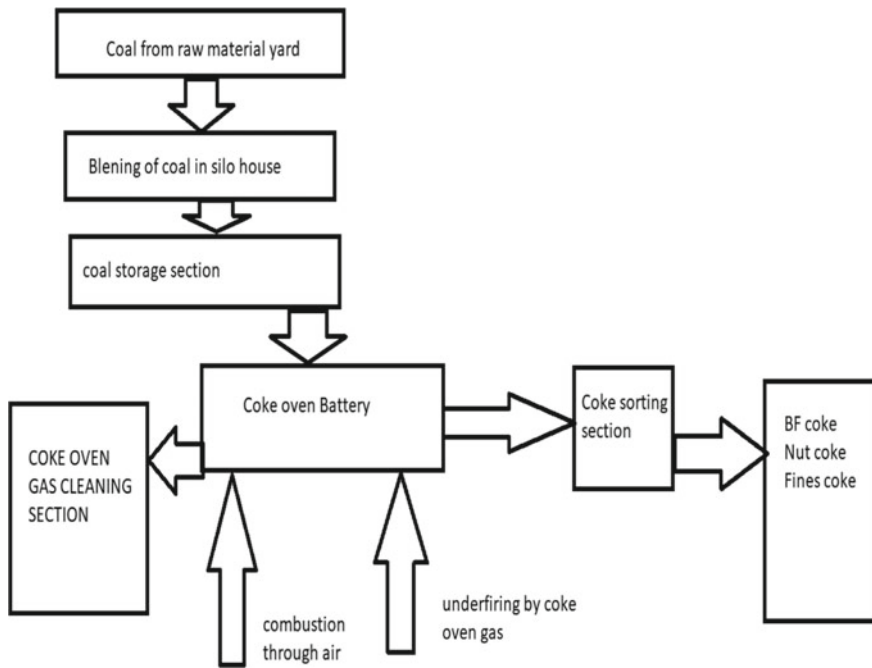
The experimental set-up requires some process parameters of the coke plant which is shown in Table 3. For moving the waste gas tunnel to the chimney, there are sixty-seven heating ovens, sixty-eight heating walls and sixty-nine heating waste boxes. The coking coal can be inserted into the heating oven through one of three charging holes. Desired analysis of typical coal charged to coke oven is also shown in Table 2. Working principal of coke oven plant can be easily classified in coke oven flow chart which is given below.

### 2.1 The Flow Diagram of Coke Oven Plant

The coke oven factory has a total of about 67 ovens, one for each battery. Through charging holes, coal is added to the oven. Following this, the coal is carbonized for

17–18 h, during which time the volatile coal material distils out as coke oven gas and is transferred to the recovery area for the recovery of important compounds. By maintaining a high hydraulic main pressure, the ovens are kept under positive pressure. When the oven’s centre reaches a temperature of between 950 and 1050 °C, coking is said to be finished. The oven is now disconnected from the hydraulic lines, and the doors are opened to push the coke after residual gases have been vented. At the end of coking period, the coke mass has a high volume shrinkage which leads to the detachment of mass from the walls ensuring easy pushing (Fig. 1).

The desired analysis of typical coal charged to coke oven is mentioned in Table 1.



**Fig. 1** Flow diagram of coke oven plant

**Table 1** Desired analysis of typical coal charged to coke oven

Moisture	Volatile matter	Fixed carbon	Sulphur	Phosphorous
7–9%	22–25%	57–60%	0.56%	0.09%

**Table 2** Technical configuration of recovery coke oven battery

Components	Technical value
No. of heating ovens	67
No. of chamber walls	68
Height of the coke oven battery	7 m
Oven length	16 m
Wall width of pusher side	385 mm
Wall width of coke side	435 mm
The total coal feeding in each heating chamber on dry basis	31–32 tonnes
Charging holes per oven	03
Effective height of the battery	6.7 m
Output coke in tonnes of each ovens	25
No. of vertical heating flues of each heating walls	32
Hot coke temperature	1000–1100 °C

**Table 3** Tabulation for before the adjustment of gas flow with respect to production target

S. No	Average value on weekly basis	Average value for specific heating consumption	Average value of day production target	Pause timing	Coking hours
1	First week	640	83	20	19.37
2	Second week	640	83	20	19.37
3	Third week	640	83	25	19.37
4	Fourth week	640	83	25	19.37
5	Fifth week	640	83	20	19.37
6	Sixth week	640	83	20	19.37
7	Seventh week	640	83	20	19.37
8	Eighth week	640	83	20	19.37

## 2.2 Technical Specification of Coke Oven Battery

Table 2 represents the technical specification of coke oven recovery type plant.

## 2.3 Number of Charging/Pushing in a Day

This section describes the advanced mathematical formula for determining the number of production target like pushing and charging schedule. The mathematical equation formula is given below

$$N = \frac{24 \times N_1}{CH} \quad (1)$$

where

$N$  = No. of charging target/pushing target in a day

$N_1$  = Number of heating ovens

CH = coking hours.

#### ***2.4 Coke Oven Gas Flow Requirement of Coke Oven Gas Flow According to Pushing and Charging***

This section comprises that mathematical equation formula for calculating the required coke oven gas flow. The mathematical equation formula is given below

$$F = \frac{Q * 1000 * N * W}{C.V \times T} \quad (2)$$

where  $Q$  = Specific heating consumption in kcal/kg

$F$  = Requirement of gas flow in Nm<sup>3</sup>/h

C.V = coke oven gas desired calorific value.

#### ***2.5 Calculation Formula of Specific Heating Consumption of Coke Oven Gas***

This section describes the mathematical equation formula for evaluating specific heating gas

$$Q = \frac{F * C.V * T}{N * 1000 * W} \quad (3)$$

where  $Q$  = Specific heating consumption in kcal/kg

$F$  = Requirement of gas flow in Nm<sup>3</sup>/h

C.V = coke oven gas desired calorific value in kcal/kg.

These all mathematical equation formulas are taken for proper calculation in Tables 1, 2 and 3 in respective manner.

As per the experimentation work, it is observed that the flow of gas cannot be increased for increasing 1–2 pushing and charging target schedule in a day. This type



of modification will not be violated daily maintenance and standard operating practices. The decrement of flow of coke oven gas with respect to pushing and charging target schedule and the possible modification works solution is also justified against standard operating practices and of regular-based schedule jobs and schedule maintenance. In this research paper at 83 number of production target, the requirement of coke oven flow is 16,800 to 16,900 Nm<sup>3</sup> per hour. The rate of gas consumption is higher in nature; however, there is need of research-based experimental analysis for reducing the coke oven flow without affecting the quality of coke.

Table 3 comprises that the average data is taken on weekly basis before the adjustment of gas flow with respect to pushing and charging schedule of coke oven plant. The first to eight weeks specific heating consumption is around 640 kcal/kg at that time pause timing is twenty second at a constant pushing, and charging target schedule is 83. The requirement of coke oven flow is 16,800 to 16,900 Nm<sup>3</sup> per hour.

### 3 Experimental Results with Discussion

#### 3.1 Adjustment of Gas Flow with Respect to Pushing and Charging Target Schedule

As per the experimentation work, it is observed that the flow of gas cannot be increased for increasing 1–2 pushing and charging target schedule in a day. This type of modification will not be violated daily maintenance and standard operating practices. After the modification as per 83 numbers of target schedules, after adjustment of gas flow with respect to pushing and charging target schedule gas flow is reduced from 16,300 to 16,400 in Nm<sup>3</sup> per hour.

Table 4 comprises that after the adjustment of gas flow with respect to production target, gas flow is reduced up to 500 Nm<sup>3</sup> per hour at same production target for 83. After the rectification process, it will affect the smooth operation of coke oven battery as well as quality of coke. It also includes that coking hour value 19.37 and pause time timing value is also constant after the adjustment process. After the adjustment process, validation of temperature of all chamber flues of pusher side and the coke side should be taken. The temperature reading of both sides like pusher side and the coke side's chamber is taken randomly of three heating walls like 11, 13 and 15 by digital pyrometer. The temperature reading is shown in Tables 5 and 6.

Table 5 describes the temperature reading taken of heating flues number 01 to 16 called as pusher side temperate. It includes the 03 number of heating wall temperature is taken like 11, 13 and 15. Table 5 temperature reading which is taken by pyrometer is shown by graphical representation of Figs. 2, 4 and 6.

Table 6 describes the temperature reading taken of heating flues number 17–32 called as coke side temperate. It includes the 03 number of heating wall temperature is taken like 11, 13 and 15. Table 6 temperature reading which is taken by pyrometer is shown by graphical representation of Figs. 3, 5 and 7.

**Table 4** Tabulation for before the adjustment of gas flow with respect to production target

S. No	Average value on weekly basis	Average value for specific heating consumption	Average value of day production target	Pause timing	Coking hours
1	First week	620	83	20	19.37
2	Second week	620	83	20	19.37
3	Third week	620	83	25	19.37
4	Fourth week	620	83	25	19.37
5	Fifth week	620	83	20	19.37
6	Sixth week	620	83	20	19.37
7	Seventh week	620	83	20	19.37
8	Eighth week	620	83	20	19.37

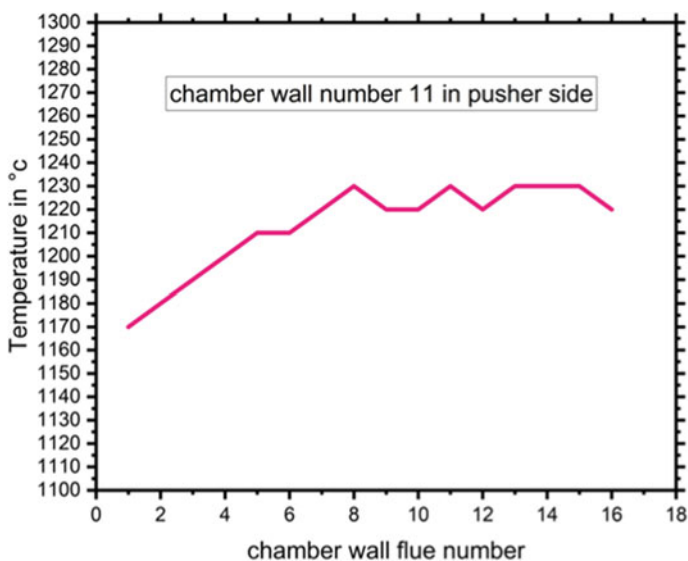
**Table 5** Pusher side flues temperature in °C

S. No	Chamber wall number 11 pusher side temperature in °C	Chamber wall number 13 pusher side temperature in °C	Chamber wall number 15 pusher side temperature in °C
1	1170	1160	1170
2	1180	1170	1180
3	1190	1180	1180
4	1200	1190	1190
5	1210	1210	1200
6	1210	1210	1210
7	1220	1220	1220
8	1230	1230	1230
9	1220	1220	1220
10	1220	1220	1220
11	1230	1230	1230
12	1220	1220	1230
13	1230	1220	1230
14	1230	1230	1220
15	1230	1230	1230
16	1220	1230	1220

Figure 2 comprises that the temperature reading which is taken by digital pyrometer of heating wall number 11 of pusher side. Firstly flue temperature is increased slowly. The minimum temperature is recorded as 1170 °C in pusher side of the chamber wall and maximum temperature is 1230 °C. This temperature parameter is suitable for good health for coke oven battery as well as maintaining the good quality of coke.

**Table 6** Coke side flues temperature in °C

S. No	Chamber wall number 11 pusher side temperature in °C	Chamber wall number 13 pusher side temperature in °C	Chamber wall number 15 pusher side temperature in °C
17	1220	1210	1220
18	1220	1220	1230
19	1240	1230	1240
20	1250	1240	1250
21	1240	1240	1240
22	1250	1250	1250
23	1240	1240	1240
24	1250	1250	1240
25	1250	1240	1250
26	1240	1240	1240
27	1230	1230	1230
28	1220	1220	1220
29	1210	1200	1210
30	1200	1190	1200
31	1190	1180	1190
32	1180	1170	1180



**Fig. 2** Temperature with respect to wall flue number

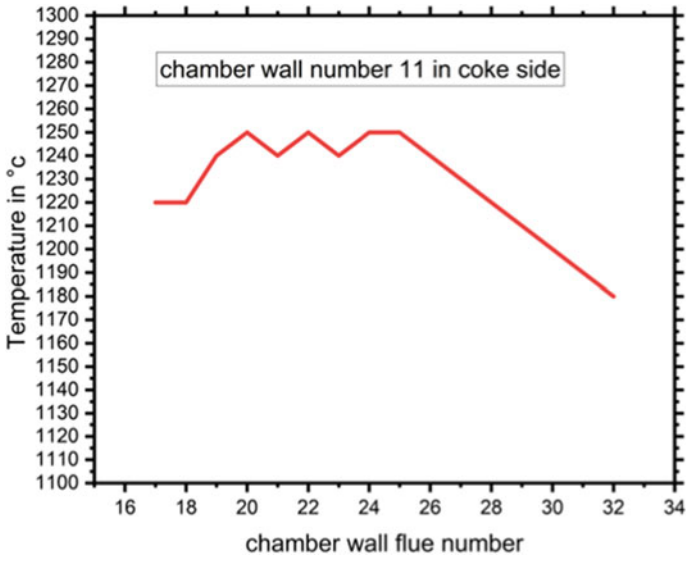


Fig. 3 Temperature with respect to wall flue number

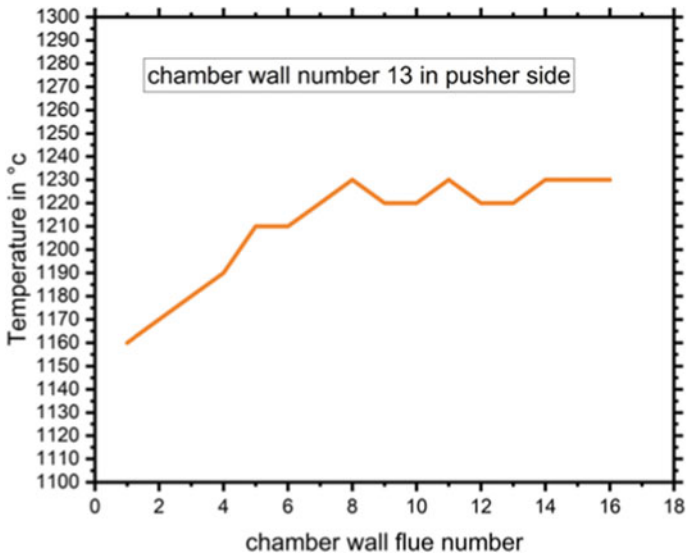


Fig. 4 Temperature with respect to wall flue number

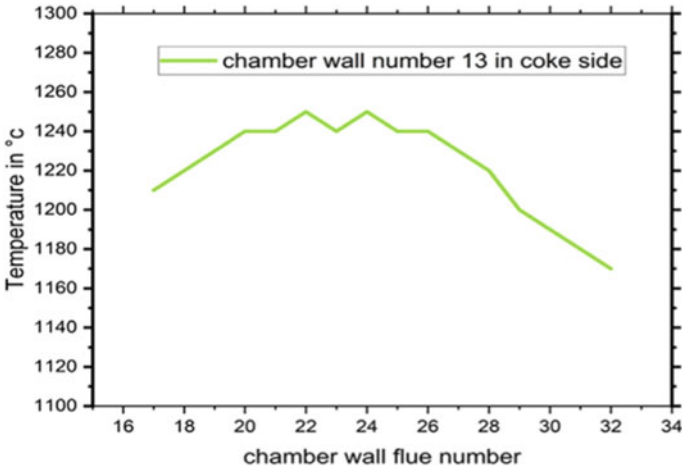


Fig. 5 Temperature with respect to wall flue number

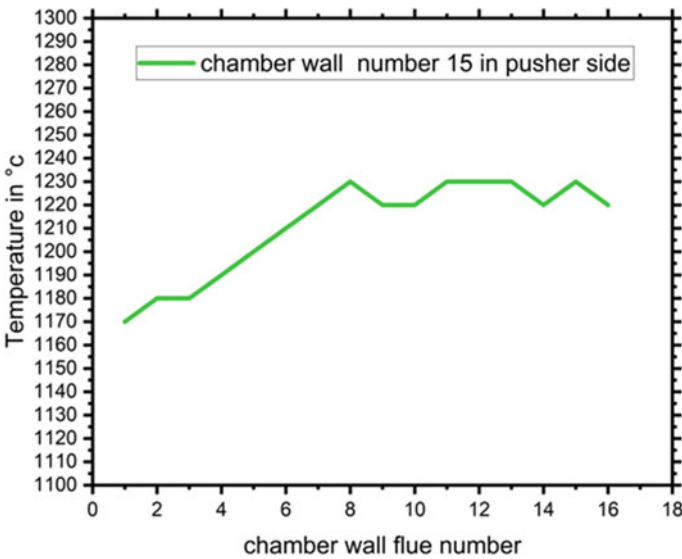


Fig. 6 Temperature with respect to wall flue number

Figure 3 comprises that the temperature reading which is taken by digital pyrometer of heating wall number 11 of coke side of flues. The minimum temperature is recorded as 1180 °C in pusher side of the chamber wall, and maximum temperature is 1250 °C. This temperature parameter is suitable for good health for coke oven battery as well as maintaining the good quality of coke.

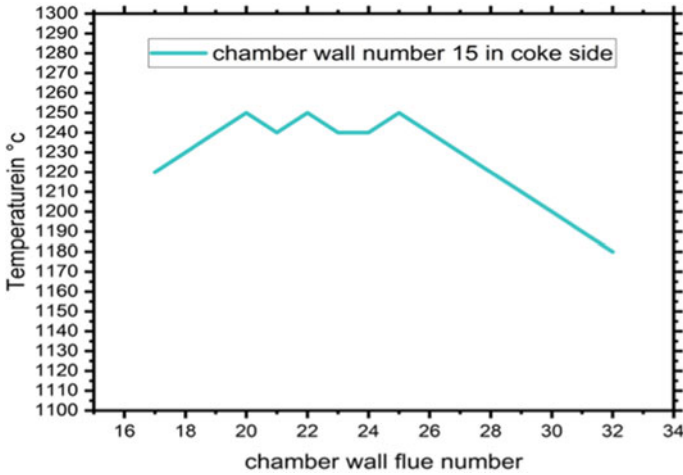


Fig. 7 Temperature with respect to wall flue number

Figure 4 comprises that the temperature reading which is taken by digital pyrometer of heating wall number 13 of pusher side. Firstly flue temperature is increased slowly. The minimum temperature is recorded as 1160 °C in pusher side of the chamber wall, and maximum temperature is 1230 °C. This temperature parameter is suitable for good health for coke oven battery as well as maintaining the good quality of coke.

Figure 5 comprises that the temperature reading which is taken by digital pyrometer of heating wall number 13 of coke side. Firstly flue temperature is increased slowly. The minimum temperature is recorded as 1170 °C in the coke side of the chamber wall, and maximum temperature is 1250 °C. This temperature parameter is suitable for good health for coke oven battery.

Figure 6 comprises that the temperature reading which is taken by digital pyrometer of heating wall number 15 of pusher side. The minimum temperature is recorded as 1170 °C in pusher side of the chamber wall, and maximum temperature is 1230 °C. This temperature parameter will not be affected the quality of coke.

Figure 7 comprises that the temperature reading which is taken by digital pyrometer of heating wall number 15 of the coke side. Firstly flue temperature is increased slowly. The minimum temperature is recorded as 1180 °C in the coke side of the chamber wall, and maximum temperature is 1250 °C. This temperature parameter is suitable for good health for coke oven battery as well as maintaining the good quality of coke.

The average cross-wall temperature of pusher side and coke side reading in Tables 5 and 6 for the A, B and C shifts, respectively, demonstrates that the thermal regime of the coke oven battery was unaffected by the modification of COG gas flow. The cross-wall temperature is measured without deviation during several shifts and at various times. After comparing Tables 3 and 4, it is clear that increasing the pushing/

**Table 7** Desired analysis of typical coal charged to coke oven

Serial No	Before adjustment Average value for specific heating consumption	After adjustment Average value for specific heating consumption	Coke oven gas saving in Nm <sup>3</sup> /hr	Monthly basis saving of Coke oven gas in Nm <sup>3</sup>	Monthly saving in Indian rupees @ 4.5 rupees per Nm <sup>3</sup>
01	640	620	500	360,000	1,620,000

charging as (1–2) no. COG gas flow is not increased, as result in a reduction in the coke oven gas flow of 500 Nm<sup>3</sup>/hour, which will save money. This is illustrated in Figs. 2, 3, 4, 5 and 6 through 5 heating walls show that the cross-wall temperature is measured at various times and that different shifts have no effect on the temperature of the flues.

Table 7 describes that before adjustment the process average value for specific heating consumption is around 640 then after adjustment the process Average value for specific heating consumption is around 6200. On the average basis coke oven gas is saved of around 500 Nm<sup>3</sup>/hr.

## 4 Conclusion

On the adjustment of coke oven gas flow with respect to pushing and charging target schedule, the flow of coke oven gas is saved up to 360,000 Nm<sup>3</sup> per month. The specific heating consumption value is also saved up 20 kcal/kg. The proposed adjustment is also saving in terms of Indian rupees as 1,620,000 rupees per month.

**Acknowledgements** All authors would like to special thanks to S K Biswas (Coke Oven HOD, NMDC Iron & Steel Plant, Nagarnar), Arsh Pandey (AGM, NMDC Iron & Steel Plant, Nagarnar), J Arjun Prasad (Ex General Manager I/C, iron, BSP SAIL), Chandan Bhattacharya (Ex General Manager in Coal, Coke & Coal Chemicals, RSP, SAIL) & RBK Lakra (D.G.M, Coke Oven Operation, RINL, India) for his insights and critical assessment in preparing this Research paper.

## References

1. Bénard C, Berekdar S, Duhamel C, Rosset M-M (1989) Input-output nonlinear model of a coke oven battery. IFAC Proc 22:95–99. <https://doi.org/10.1016/b978-0-08-037869-5.50020-0>
2. Bénard C, Berekdar S, Rosset M-M, Depoux M (1989) A coke oven battery modelization for transient operating conditions. IFAC Proc 22:451–457. [https://doi.org/10.1016/s1474-6670\(17\)53587-9](https://doi.org/10.1016/s1474-6670(17)53587-9)
3. Suzuki G, Mizuno M, Higuchi M, Matsushita T (1978) Development of an automatic computer control system for coke oven operation. Trans Iron Steel Inst Jpn 18:308–316. <https://doi.org/10.2355/isijinternational1966.18.308>
4. Pang S, Lai Y (2011) Hybrid intelligent control of coke oven. Int Rev Comput Softw 6:1313–1319. <https://doi.org/10.5813/www.ieit-web.org/ijadc/2011.4.4>

5. Buczynski R, Weber R, Kim R, Schwöppe P (2016) One-dimensional model of heat-recovery, non-recovery coke ovens: part IV: numerical simulations of the industrial plant. *Fuel* 181:1151–1161. <https://doi.org/10.1016/j.fuel.2016.05.033>
6. Buczynski R, Weber R, Kim R, Schwöppe P (2016) One-dimensional model of heat-recovery, non-recovery coke ovens. Part III: Upper-oven, down-comers and sole-flues. *Fuel* 181:1132–1150. <https://doi.org/10.1016/j.fuel.2016.01.087>
7. Kostúr K (2002) Control system of coking plant. *Metalurgija* 41:121–124. [https://doi.org/10.1016/s0140-6701\(03\)90704-1](https://doi.org/10.1016/s0140-6701(03)90704-1)
8. Razzaq R, Li C, Zhang S (2013) Coke oven gas: Availability, properties, purification, and utilization in China. *Fuel* 113:287–299. <https://doi.org/10.1016/j.fuel.2013.05.070>
9. Kertcher LF, Linsky B (1974) Economics of Coke Oven Charging Controls. *J Air Pollut Control Assoc* 24:765–771. <https://doi.org/10.1080/00022470.1974.10469967>
10. Smolka J, Slupik L, Fic A, Nowak AJ, Kosyrzyk L (2016) CFD analysis of the thermal behaviour of heating walls in a coke oven battery. *Int J Therm Sci* 104:186–193. <https://doi.org/10.1016/j.ijthermalsci.2016.01.010>
11. Poraj J, Gamrat S, Bodys J, Smolka J, Adamczyk W (2016) Numerical study of air staging in a coke oven heating system. *Clean Technol Environ Policy* 18:1815–1825. <https://doi.org/10.1007/s10098-016-1234-8>
12. Nyathi MS, Kruse R, Mastalerz M, Bish DL (2016) Nature and origin of coke quality variation in heat-recovery coke making technology. *Fuel* 176:11–19. <https://doi.org/10.1016/j.fuel.2016.02.050>
13. Tiwari HP, Banerjee PK, Saxena VK, Sharma R, Haldar SK, Paul S (2014) Effect of heating rate on coke quality and productivity in nonrecovery coke making. *Int J Coal Prep Util* 34:306–320. <https://doi.org/10.1080/19392699.2014.896349>
14. Díez MA, Alvarez R, Barriocanal C (2002) Coal for metallurgical coke production: predictions of coke quality and future requirements for cokemaking. *Int J Coal Geol* 50:389–412. [https://doi.org/10.1016/S0166-5162\(02\)00123-4](https://doi.org/10.1016/S0166-5162(02)00123-4)
15. Mahato N, Agarwal H, Jain J (2021) Reduction of specific heat consumption by modification of reversal cycle period of coke oven battery. *Mater Today Proc*. <https://doi.org/10.1016/j.matpr.2021.12.032>
16. Yang K, Gu Z, Long Y, Lin S, Lu C, Zhu X et al (2021) Hydrogen production via chemical looping reforming of coke oven gas. *Green Energy Environ*. <https://doi.org/10.1016/j.gee.2020.06.027>
17. Nag D, Das B, Banerjee PK, Haldar SK, Saxena VK (2013) Methodology to improve the mean size of coke for stamp charge battery. *Int J Coal Prep Util* 33:128–136. <https://doi.org/10.1080/19392699.2013.769436>
18. Van Speybroeck V, Hemelsoet K, Minner B, Marin GB, Waroquier M (2007) The technical achievement which deserves special mention is the optimization of combustion. *Mol Simul* 33:879–887. <https://doi.org/10.1080/08927020701308315>
19. Sutcu H, Toroglu I, Piskin S (2009) Prediction of metallurgical coke strength from the petrographic composition of coal blends. *Energy Sour Part A Recover Util Environ Eff* 31:1047–1055. <https://doi.org/10.1080/15567030801909730>



# Studying Current Safety Systems for Accident Prevention and Wellbeing of Powered Two-Wheeler Community: Prevalence of Safety Components



Gaurav Gupta, Riya Mariam Babu, Ashok Kumar Yadav, Devendra Kumar Sinha, R. K. Tyagi, Sanjeev Kumar Sharma, and Srinivasa Rao Gorrepati

**Abstract** Two-wheelers are the most preferred mode of transport by the majority of the Asians due to its size, price range and fuel requirement. But there is not much safety equipment present in accordance with the fact that the driver is directly in contact with the atmosphere. So, this paper deals with the various technologies under research and development and some safety technologies already in market to ensure safety in two-wheelers. This basically covers the different types of passive safety systems for the protection of the upper body of the rider. A detailed study of each technology including its principle, components, design, working and the advantages and disadvantages of each technology is covered. It covers the pre-requisite design conditions, general types of the safety systems and a detailed study of some of the most effective and feasible safety system.

**Keywords** Powered two-wheelers · Safety device · Air bag · Wearable safety device

## 1 Introduction

As the world progresses toward improved technology as the day succeeds, it has been the greatest source of comfort for the human beings. But these comforts do come with a price on the account of the safety.

---

G. Gupta (✉) · R. M. Babu · R. K. Tyagi · S. K. Sharma · S. R. Gorrepati  
Department of Mechanical Engineering, Amity University, Noida 201304, Uttar Pradesh, India  
e-mail: [15.gaurav@gmail.com](mailto:15.gaurav@gmail.com)

A. K. Yadav  
Raj Kumar Goel Institute of Technology, Ghaziabad, India

D. K. Sinha  
Adama Science and Technology University, Adama, Ethiopia

**Table 1** Survey of the number of registered bikes around the world (2020)

S.No.	Countries	Units sold (per thousand)
1	USA	780 [1]
2	India	1420 [2]
3	China	8260[3]
4	Brazil	1740 [4]
5	England	82 [5]

**Table 2** Survey of the number of people injured and killed in accidents of two-wheelers in various states of India (2019) [6]

S.No.	States	Injured	Fatal
1	Kerala	2362	19,538
2	Uttar Pradesh	6931	5343
3	Gujarat	2755	3744
4	Maharashtra	5894	7769
5	West Bengal	1030	1503

The invention of the wheel has been the greatest life changing innovation and has seen the most technological development. From a wheeled cart to cycle to scooter and then eventually motorcycles and four-wheelers, we have seen how each invention has helped reduce human effort.

India has been one of the largest markets for two-wheelers, and following survey presented in Table 1 would justify the above statement.

But this increased use of motorcycles has come with a very immediate need for development for more safety features for the two-wheelers as can be clearly seen from Table 2.

And thus, it is very important that proper safety system which is reliable too needs to be developed and be equipped to the masses on an immediate basis. Unlike four-wheelers, two-wheelers need a more complicated and thorough system of safety as the driver is exposed more in case of accidents. Before designing any system for an existing technology, the restraints and the limitations of size, weight and other factors need to be considered and only then would the design be actually feasible.

Therefore, the things that need to be kept in mind while designing any form of safety system for two-wheelers are as follows [7–10]:

1. The design of the system needs to be compact which does not hinder with regular functioning of the motorcycle, and the vehicle is able to incorporate the minimum changes in the design of the vehicle as required.
2. The system incorporated should be light weighted as in two-wheelers; it is a pre-requisite as the weight needs to be compatible with the rider.
3. The direction of the fall of the rider in a two-wheelers cannot be predicted as the driver is more exposed to the external environment and has infinite probability of ways of getting hurt. And thus, the design of the safety system needs to incorporate the majority possibility of injuries.

4. It needs to be ensured that the safety systems are only deployed in the case of crash or accidents, as the vehicle may also experience heavy turbulence or disturbances on rough terrains.
5. As most of the collisions result due to frontal collisions, the highest area prone to injury is the upper body and the head, and thus, it needs to be taken in consideration the most while designing the safety system.
6. The most important part of the safety system is the fall predictive algorithm responsible for triggering the concerned responses which needs to be full-proof and deploys the safety system accurately.
7. Usage of legitimate equipment and of perfectly tuned airbags could raise rider insurance to higher level of performance and security.

These are some of the general limitations for the designing that are recommended or included by the engineers who have attempted to study in the same field to develop any advancements in the safety features of two-wheelers. Safety features in automobiles are largely classified into further two types: passive automotive safety system and active automotive safety system [11–13].

**Active safety system** incorporates set of security highlights which diminish the possibilities of an accident or crash in any case. A few manufacturers also call it as the “primary safety system.” Engineers utilize the dynamic security designs principally to keep away from accidents. These systems enact before the accident happens with the goal that they might keep away from the accident. The engineers designed the car with an elevated degree of dynamic wellbeing through superior design. This incorporates attributes, for example, road holding, visibility, comfort, handling and ergonomics.

**Passive safety system** is the system which responds to unusual activity or when the vehicle is way-off its regular course. It implies that these systems actuate during or after the accident occurs. In this way, the passive safety systems help to diminish or reduce the impact of the unusual incidents like an accident. Passive safety systems includes the seatbelts that are pre-tensioned and are active during sudden breaks or stoppage, airbags and the presence of the guard in the front of the vehicle which are prone to frequent deformation.

## 2 Safety Devices

This study focuses on passive safety system for powered two-wheelers; the devices that would be covered are majorly categorized in three categories [14]:

- (i) Vehicle mounted airbags, (ii) headgear, (iii) wearable airbags.

## **2.1 Vehicle Mounted Airbag**

Airbags have always been a concept that has been associated with four-wheelers. In the year 1987, for the first time, Porsche decided to introduce airbags in the model 944 Turbo. An airbag consists of a flexible fabric bag which provides cushioning to the vehicle driver. It thus reduces injuries and substantially decreases the chances of death in case of severe accidents and collisions. The key to the success of this system is the shortest time of deployment. This concept of an inflatable device has inspired one of the existing technologies for two-wheelers with assisted airbags, the Honda Goldwing. Honda was the first company that introduced the concept of Airbags in two-wheelers in its bike model Goldwing 1500 in the year 2006. The company has not seen much success in terms of its sales but still owns the recognition for its concept. Recently, it has filed patent applications for three new designs of airbag systems for two-wheelers.

The motorcycle's airbag system only activates in the event of a severe frontal impact, when forces exceeding a preset value are detected [15, 16]. In principle, it should not be deployed inside or rear impacts or falls. Since a collision can involve a variety of factors, such as an angled impact or a motorcycle being wedged under a truck, an airbag cannot help reducing the severity of injuries in all cases. The airbag may also activate due to a strong impact caused by the front wheel falling into a large hole or ditch or when colliding with a curb or other object [17]. There has also been very wide research ongoing currently in this field bringing up many innovative solutions. Few most feasible is discussed [18–22].

## **2.2 Headgear**

Headgears or helmets more or less have only been associated with two-wheelers. Helmets came into existence when the motorized two-wheelers increased their speeds and started being used in races and the people started getting injured. So, in the year 1914, a British Physician Dr. Eric Garner came up with the idea and a basic sketch of a device then known as a “headgear” to protect the head of the riders during the races. It was introduced for the first time in the Isle of Man TT races and then became successful to gain confidence for regular use. There has been a lot of smart helmets in market, and one of the first companies to introduce the concept of smart helmets in India is the Altor Helmets [23]. It uses Internet of things and machine learning. New age headgears have functionalities like helmet wear detection, touch enabled functions, audio navigation, Bluetooth connectivity, accident detection, emergency SOS.

## 2.3 Wearable Airbags

Wearable airbags have been one of the most recent areas of interest for most of the engineers, and a great deal of work is presently being developed. As this device most closely associates with the body of the driver, this can prove to be the most reliable safety system if developed enough to suit the comfort of the human.

Wearable airbags have a very promising scope in the area of the passive safety systems. As this a system is portable and is jacked on the driver, no major changes are required to be made on the existing design structure of the two-wheeler driver wearable airbags. Some engineers developed a concept of a wearable airbag whose inflation is triggered by the acceleration and the angular velocity. It used two sensors—accelerometer and gyroscope for its fall detection algorithm [24, 25]. Few wearable airbags are already existing in market, but it is mainly for the non-motorized vehicles such as the bicycle. But this concept can be advanced and made suitable even for the motorized and geared vehicles. One of this kind of concept safety device is “Hövding collar” [26].

The decision for deployment is made by the comparison of accelerometer data from bicycle crashes against “typical” cycling. The Hövding contains accelerometers that detect these unusual movements which then deploys the airbag if the movement patterns match the profile of a crash. Each Hövding airbag also contains a “black box” that records the accelerometer data 10 s before a deployment. This data can be used by the Hövding developers to improve the product. The Hövding collar is constructed of a waterproof material and has interchangeable fabric “shells” that allow color customization. There has also been ongoing research for the introduction of a wearable airbag that can be adorned as a jacket [27–29]. Based on available literature, various aspects of safety devices are presented in tabulated form in Table 3.

## 3 Components of Safety Devices

### 3.1 Vehicle Mounted Airbag

The components required for this safety system to work include-

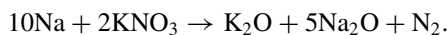
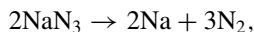
1. **Airbag**—They are constructed using strong leather with grip technology. During deployment, the airbags would inflate to form a semi-circular (D-shaped) structure. The grip technology avoids the possibility of skidding or slipping in case of the presence of oil or water on the surface. While this does not guarantee to prevent absolute injury or demise, it tends to be exceptionally useful in cushioning the travelers.

**Table 3** Latest technological status of safety devices for powered two-wheeler drivers

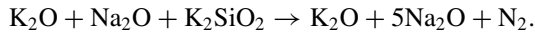
S.No.	Type of safety system	Status	Pros	Cons
1	Vehicle attested airbag [18]	Honda Goldwing	<ul style="list-style-type: none"> <li>• Effective safety system for two-wheelers</li> <li>• Reduce injury effects</li> </ul>	<ul style="list-style-type: none"> <li>• Airbag rupture</li> <li>• Selective performance</li> <li>• Only compatible with selected designs</li> </ul>
		Under research	<ul style="list-style-type: none"> <li>• May prevent skidding</li> <li>• Suitable for low CC vehicles too</li> </ul>	<ul style="list-style-type: none"> <li>• Not compatible with all bikes</li> <li>• Intervention of the inflation of the airbag with the human</li> </ul>
2	Helmets [30]	Altor headgear	<ul style="list-style-type: none"> <li>• Reduce cases of head injuries</li> <li>• SOS system ensures instant alert</li> <li>• User enhancing facilities</li> </ul>	<ul style="list-style-type: none"> <li>• Expensive</li> <li>• Might get bulky</li> <li>• Chances of initiation failure</li> <li>• Analytical problems</li> </ul>
		Under research	<ul style="list-style-type: none"> <li>• Reduce cases of drunk and driving accidents</li> <li>• Endure wearing of helmet</li> <li>• More advanced data encoding</li> </ul>	<ul style="list-style-type: none"> <li>• Expensive</li> <li>• Might get bulky</li> <li>• Chances of initiation failure</li> <li>• Analytical problems</li> </ul>
3	Wearable Airbags [31]	Hodvings Collar	<ul style="list-style-type: none"> <li>• Reduce head injuries</li> <li>• Follows youngsters trend of not wearing helmet</li> <li>• Light weight</li> <li>• Easy to use</li> </ul>	<ul style="list-style-type: none"> <li>• Design not advanced for motorized vehicle</li> <li>• Chances of initiation Failure</li> <li>• Not suitable for high speed vehicles</li> </ul>
		Under research	<ul style="list-style-type: none"> <li>• Protects the upper chest region</li> <li>• Effective safety system</li> </ul>	<ul style="list-style-type: none"> <li>• Long response time</li> <li>• Airbag deployment failure</li> <li>• Bulkier jacket</li> </ul>

2. **Chemical Cylinders to release gases**—Actual opening of the airbag is because of the chemical reaction between the two cylinders which are fitted to the vehicle. At the point when an accident or crash of anything with the bike happen, then the gases in the cylinders are allowed to mix and react with one another which in turn inflates the airbag [32–34].

The reactions involved are-



The last response is utilized to take out the  $\text{K}_2\text{O}$  and  $\text{Na}_2\text{O}$  created as the first-period metal oxides are exceptionally reactive. These items react with  $\text{SiO}_2$  to give a silicate glass which is a stable compound



1. **Fitting cage**—As the airbag needs to be contained in something, a structure known as a fitting cage is introduced in the vehicle.
2. **Battery power**—It is already pre-installed in the automobile.
3. **Sensors**—The main parts responsible for the outcome of the airbag system working are the sensors. These little bits of gadgets are intended to tell when the vehicle has been harmed in an accident. They answer a few distinct arrangements of upgrades, including unexpected halting, expanded tension as parts of the vehicle are moved because of the power of the crash and angle between street surface and tires of bike. The sensors transfer signs [35] to the airbag control unit, which dissects the information and can coordinate safety features like seat belt lock, automatic door locks, as well as airbag deployment.
4. **Pyrotechnic device**—In this case, it is an electric conductor wrapped in a combustible material, which has the capability to activate a pulse of about 1–3 A/s. It can bring up about a temperature of about 300 °C (which is the ideal for the activation of the reaction for the inflation of the airbag).

### 3.2 Headgear

Basic components of more advanced “intelligent helmet” are:

**Arduino Uno Micro Controller**—Arduino Uno is a microcontroller board in view of the ATmega328P (datasheet). It has 14 advanced input/output pins (of which 6 can be utilized as PWM outputs), 6 simple data sources, a 16 MHz quartz crystal, a USB association, a power jack, an ICSP header and a reset button. It contains everything expected to help the microcontroller interface it to a PC with a USB link or power it with an AC-to-DC connector or battery to drive the board.

**Radio frequency Communication Circuit**—It is the basis for the wireless communication between two objects. In this case, it is between the input signal from the headgear to the ignition center of the bike. It consists of an encoder and a decoder circuit. The encoder converts parallel data into series signal, which is situated in the helmet, whereas the decoder is present in the control unit of the bike interfacing with the ignition unit and converts the parallel output to series signals [36].

**Sensing Resistor**—It is situated in the inside of the helmet and senses human touch. It has applications in various fields such as medical system, automotive electronics. They are strong polymer thick film (PTF) devices whose resistance is inversely proportional to force applied to the face of the sensor.

**MQ3 Alcohol Sensor**—This is sensor is placed in front inside region of the helmet near the mouth and has the ability to sense alcohol content in the breath of the rider. The calibrated value for the detector is 0.4 mg/L of alcohol concentration in air and

200 K $\Omega$  of resistance is used. Here, we utilize digital result of this sensor which gives an output regarding high or low.

**Magnetic Reed Switches**—It is also known as the speed sensor. The reed switches are electronic or electromechanical parts that work using the technology of the reed contacts. The reed contact switch is a lamina (usually open) which closes inside seeing a magnetic field.

**Helmet Holder**—The headgear holder is a basically a part made of fiber-reinforced plastic which has a state of the headgear's base structure, comprising of a grip and magnetic lock to connect the headgear to the holder. It is attached to the petrol tank of the two-wheeler by permanent or semi-permanent join such as bolts, rivets or welding.

### 3.3 *Wearable Airbags*

As a wearable airbag cannot be generalized and almost have the same components as that of the airbags attested to the vehicles, only a few components need to be introduced.

1. **Mechanical Inflator**—It is an inflator that does not need any external power source for actuation and is designed for the need according to the specifications of the technology requirement.
2. **Jacket**—A jacket of strong tensile material that is comfortable to wear is chosen and has high elasticity, so that no tears develop when the inflator actuates.

## 4 Working Methodology

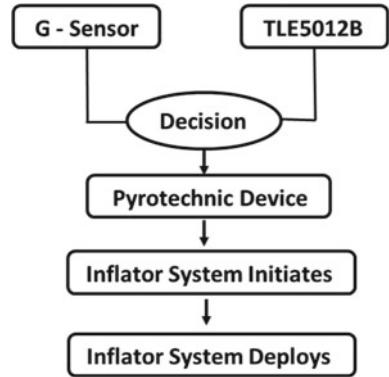
### 4.1 *Vehicle Mounted Airbag*

Flowchart shown in Fig. 1 depicts the process of deployment of airbag [37]

1. The reading from both the sensors is taken, and a decision is made. This decision is made in about 15–30 ms.
2. The decision then signals to the pyrotechnic device which acts as the initiator.
3. In the inflator system, it consists of two cylinders, whose gases are allowed to mix as the pyrotechnic device is set off.
4. These gases then fill the airbags and inflate it.



**Fig. 1** Deployment of airbag



### 4.2 Headgear

Working of headgear in tandem is shown in Fig. 2 where according to the proposed design, the whole system can be divided into two parts—the one fitted, or part of the helmet and the other is attached to the vehicle. The communication between the two parts is wireless through the RF communication circuit [38]. As discussed earlier, the RF circuit consists of two parts: the receiver and the transmitter. The receiver receives the information from the transmitter and the sensor and then displays the same on an LCD screen and to a relay switch which makes the decision regarding the ignition through a Arduino Board. Arduino Board is powered by a rechargeable battery present on the outside of the helmet. The transmitter is part of the control unit attached to the vehicle which generates the information required from the inputs of the alcohol sensor and the FR sensor and transmits the same to the helmet unit. Figure 3 shows decision-making process while rider is with helmet [39].

### 4.3 Wearable Airbags

This is the design structure of the inflator that is used in the vest in order to inflate the vest. It has a mechanical inflator [40], where there is a flexible wire which has a ball on one end and is attached to the two-wheeler on the other side. As the driver is detached or thrown away from the vehicle, the flexible wire is pulled, pulling the ball. The ball is further connected to the flexible wire which directly controls the drilling pin operation. The pin is then released punching the cartridge due to the elastic force of the built-in spring, injecting the compressed gas into the distributor.

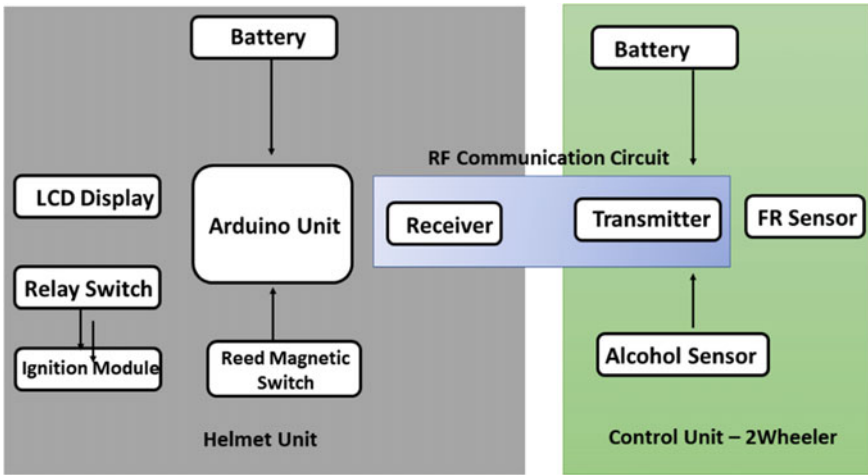


Fig. 2 Depicts the communication between different sensors

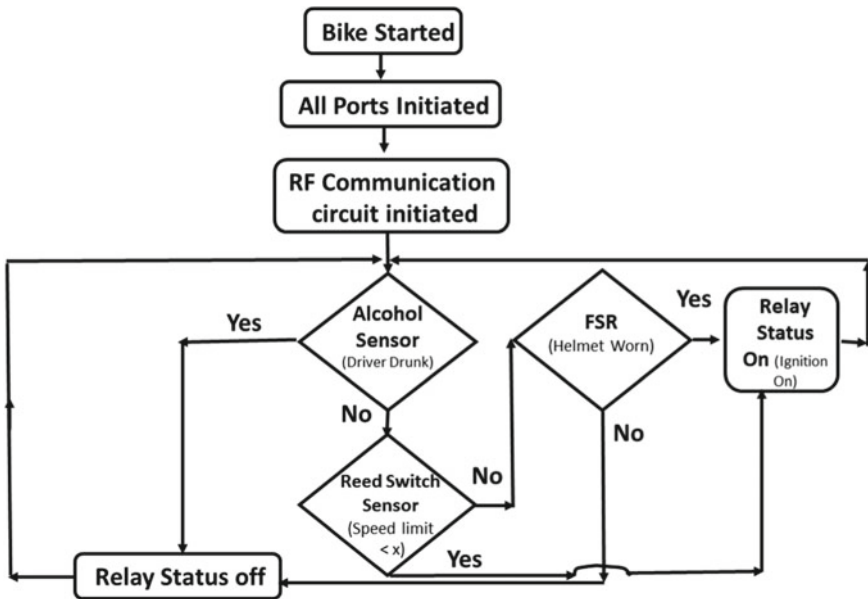


Fig. 3 Depicts the decision-making process

## 5 Conclusion

Two-wheeler drivers have the highest possibilities of fatal injuries during accidents more than in the case of four-wheelers due to the exposure of the driver. Thus, the research and development for more economical, feasible, technologically compact but versatile concepts need to be continuously made to ensure the better safety for the riders. Here, we have tried to accommodate the most comprehensible designs currently under development and innovations that can be of practical use along with their limitations which when overcome can make the technology better. We also tried to cover the different ways and the opportunities for research in the various ways of safety systems and the scope for feasibility of the same.

Airbags attested to the vehicle and tend to use a non-desiccated inflator which on actuation can rupture the airbag defeating the purpose. The airbag serves the purpose only if the individual is in contact with the bike and does not prevent any event of skidding. This design is only compatible with higher CC vehicle, and also, the design of the vehicle should restrict the movement of the driver which might make the vehicle bulky. It does prevent the bike from falling and the sides of the bike from touching the ground and thus preventing skidding.

These designs cannot be incorporated in all bikes as there is not enough space for the introduction of a fitting cage in most of the bikes. The inflation of the airbags may interfere with the positioning of the leg of the driver causing further complications. It might make the helmet bulky due to all the sensor addition. If the helmet is not in the range, the RF communication is not initiated, and thus, the system does not work. The sensors are placed in a series, and if even one of them stops working, the communication circuit breaks off and system does not work. The bike ignition is turned off the moment the sensor conditions are not satisfied which would pose a problem to the rider on a busy road. As the initiator of the airbag solely depends on the tension acting on the string, there are high chances that the airbag is deployed when not required. The insertions of cylinders and the system may make the jacket bulky.

## References

1. Statistics & Facts on the U.S. Motorcycle Industry/Market|Statista. [Online]. Available: <https://www.statista.com/topics/1305/motorcycles-in-the-us/>
2. Two Wheeler Sales in India for the Year 2020—Hero gains the highest Market Share. [Online]. Available: <https://www.autopundit.com/post/two-wheeler-sales-in-india-for-the-year-2020-hero-gains-the-highest-market-share>
3. China Motorcycle Market. [Online]. Available: <https://www.trade.gov/market-intelligence/china-motorcycle-market>
4. Brazil: two-wheeler sales 2020|Statista. [Online]. Available: <https://www.statista.com/statistics/615553/two-wheeler-sales-in-brazil/>
5. UK motorcycle sales leap into fall season as recovery c... | Visordown. [Online]. Available: <https://www.visordown.com/news/industry/uk-motorcycle-sales-leap-fall-season-recovery-continues-september>

6. Road Accidents in India-2019 IR;es oot;rs
7. Bellati A, Cossalter RL, Ambrogi A (2006) Preliminary investigation on the dynamics of motorcycle fall behavior: influence of a simple airbag jacket system on rider safety
8. Aikyo Y, Kobayashi Y, Akashi T, Ishiwatari M (2015) Feasibility study of airbag concept applicable to motorcycles without sufficient reaction structure. *Traffic Inj Prev* 16:S148–S152
9. Savino G et al (2020) Active safety systems for powered two-wheelers: a systematic review. *Traffic Inj Prev* 21(1):78–86
10. Gupta G, Tyagi RK (2019) An experimental evaluation of mechanical properties and microstructure change on thin-film-coated AISI-1020 steel. *Mater Perform Charact* 8(3):20180143
11. Active and passive automotive safety systems. [Online]. Available: <https://www.electronicsoecifier.com/products/sensors/active-and-passive-automotive-safety-systems>
12. Active and Passive Safety Systems in Cars—PathPartnerTech. [Online]. Available: <https://www.pathpartnertech.com/active-and-passive-safety-systems-in-cars/>
13. Gil G, Savino G, Piantini S, Baldanzini N, Happee R, Pierini M (2017) Are automatic systems the future of motorcycle safety? A novel methodology to prioritize potential safety solutions based on their projected effectiveness 18(8):877–885. <https://doi.org/10.1080/15389588.2017.1326594>
14. Safety Data Sheet—Inflatable Life Jackets
15. Honda GlobalMotorcycle Airbag System—Picture Book. [Online]. Available: <https://global.honda/innovation/technology/motorcycle/Airbag-picturebook.html>
16. Kuroe T, Namiki H, Iijima S (2005) Exploratory study of an airbag concept for a large touring motorcycle: further research second report. Honda R&D Co., Ltd. Asaka R&D Cent. Japan, no. Paper Number 05-0316
17. Pallacci T, Baldanzini N, Barbani D, Pierini M (2019) Preliminary effectiveness assessment of an airbag-based device for riders' leg protection in side impacts. *Procedia Struct Integr* 24:240–250
18. Nishigandh G, PMC, Air bag system in two-wheeler vehicle system
19. Ariffin AH et al (2016) Exploratory study on airbag suitability for low engine capacity motorcycles. *J Teknol* 78(4):65–69
20. Rishikesh T, Mukesh C (2014) The airbag system for 2-wheeler vehicle system. *IJRAME* 2(2):96–104
21. Gupta G, Tyagi RK (2021) Theoretical analysis of plasma parameters on film deposition in planer and cylindrical magnetron sputtering. *IJPAP* 59(03):174–179
22. Gupta G, Tyagi RK (2019) Investigation of Titanium as thin film deposited material thereon effect on mechanical properties. In: *Advances in industrial and production engineering*. Springer, Singapore, pp 315–323
23. Buy Smart Helmet with Bluetooth & SOS Emergency Alert in India. [Online]. Available: <https://www.altorsmarthelmet.com/>
24. Tamura T, Yoshimura T, Sekine M, Uchida M (2011) Development of a wearable airbag for preventing fall related injuries. *Lect Notes Comput Sci (including Subser Lect Notes Artif Intell Lect Notes Bioinformatics, vol 6776, LNCS, pp 335–339*
25. Kurosu M (ed) (2011) *Human centered design, vol 6776*
26. Chandra S (2018) *Motorcycle and its aesthetics: a glimpse in history, pp 9–25*
27. Hövding's airbag for cyclists beats all other cycling helmets in independent safety testroad.cc. [Online]. Available: <https://road.cc/content/tech-news/safety-tests-reveal-hovding-airbag-superior-helmets-282023>
28. Hövding 3 Airbag Helmet—Condor Cycles. [Online]. Available: <https://www.condorcycles.com/products/hovding-3-airbag-helmet?variant=30292458766474>
29. Hövding's official websiteHövding—Airbag for urban cyclists. [Online]. Available: <https://hovding.com/>
30. Hartwell PG, Brug JA (2004) Smart helmet, 16-Oct-2004
31. Memane S, Ruiwale VV, An overview of two wheeler airbag system. *Int J Res Eng Appl Manag* 32.
32. Safety Data Sheet. Rearing Kit for Inflatable Life Vests (2014)

33. All about Inflatable Life Vests—NauticEd. [Online]. Available: <https://sailing-blog.nauticed.org/all-about-inflatable-life-vests/>
34. Gas Canister for Inflatable Vest. [Online]. Available: <https://www.sellerie-materiel-equitation.com/en/riding-instruments-and-accessories/1962-gas-canister-for-inflatable-vest.html>. Accessed 28 Oct 2022
35. Gupta G, Tyagi RK (2021) A newer universal model for attaining thin film of varied composition during sputtering. *Lect Notes Mech Eng* 629–638
36. Gupta G, Tyagi RK, Rajput SK (2021) A statistical analysis of sputtering parameters on superconducting properties of niobium thin film. *Evergreen* 8(1):44–50
37. Blackman RA, Haworth NL (2013) Comparison of moped, scooter and motorcycle crash risk and crash severity. *Accid Anal Prev* 57:1–9
38. Bourke AK, O'Brien JV, Lyons GM (2007) Evaluation of a threshold-based tri-axial accelerometer fall detection algorithm. *Gait Posture* 26(2):194–199
39. Campero I, Márquez-Sánchez S, Quintanar J, Rodríguez S, Corchado JM (2020) Smart helmet 5.0 for industrial internet of things using artificial intelligence. *Sensors (Basel)* 20(21):1–27
40. Piantini S, Aathresh VN, Savino G, Pierini M (2022) Assessment of the effect of motorcycle autonomous emergency braking (MAEB) based on real-world crashes, pp 1–7. <https://doi.org/10.1080/15389588.2022.2117983>

# Design and Temperature Measurement of Axisymmetric Heater for Rotor–Stator System



Rakesh Kumar Yadu and Achhaibar Singh

**Abstract** The present study deals with the design and development of an axisymmetric heater for a rotor–stator system. The heater consists of three components: a nichrome heating coil, cellulose fiber cement board (CFCB), and a mica sheet. For making the uniform heater, two spirals are designed in Fusion360 software, and it is processed with a CNC machine called ShopBoat to make a spiral groove on CFCB. Nichrome heating coil is fitted into the spiral groove and covered with a mica sheet. To measure the performance of the heater, experiments are performed with aluminum disk and compared to standard heater used in industry. The result shows the variance of heat distribution of spiral coil heater with respect to the tangential direction at any radius is negligible which reflects the uniform heat distribution in tangential direction. This shows that a double spiral heater is very close to an ideal axisymmetric heater.

**Keywords** Rotor–stator system · Spiral coil heater · Parallel coil heater · Cellulose fiber cement board (CFCB) · Axisymmetric · Heat transfer

## 1 Introduction

In industry, rotor–stator system is a very important part of many machines; because of that, the behavior of heat transfer from the disk is a very much interesting topic for researchers and mathematicians. The present study has various applications in heat exchangers, turbine disks, hard disk drives, and rotor–stator systems. Therefore, it becomes a very popular research topic among researchers.

The behavior of heat transfer between two disks has been investigated by many researchers and engineers. Mochizuki and Yang [1] had an experiment in which they used a radial heater to determine the heat transfer mechanism between two heated disks with radial flow and observed that heat transfer performance increases proportionally to the 0.5 and 0.8 powers of the Reynolds number. Ervin et al. [2]

---

R. K. Yadu (✉) · A. Singh  
Netaji Subhas University of Technology, Delhi, India  
e-mail: [rakesh.yadu93@gmail.com](mailto:rakesh.yadu93@gmail.com)

performed an experimental investigation to find the characteristics of incompressible fluid between two stationary co-axial disks in turbulent, radially outward flow. Velocity components in axial and radial directions were measured by introducing a split film anemometer probe.

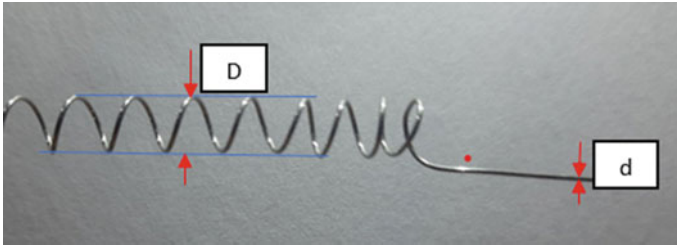
An experimental study for a wide range of flow was performed by Murphy et al. [3]. The measurements range for the acceleration parameter from  $2.6 \times 10^{-8}$  to  $2.2 \times 10^{-4}$ , and the local Reynolds number changes from 210.00 to 68,000.00. The results showed that laminarization of turbulent inward direction flow takes place because of acceleration in the radial channel. From their experiment, they find out that at a Reynolds number of 20,700 transitions of laminar to turbulent flow. Djaoui et al. [4] performed an experiment to examine the behavior of heat transfer of rotor and stator system with help of a heated disk by use of temperature–velocity correlations, the air temperature inside the cavity, radial and circumferential mean velocity components, temperature, and also local Nusselt numbers measured on the stationary disk. They found the flow structure near the axis is strongly affected by the presence of a superimposed radial inflow, as already observed under isothermal conditions. The steady forced convection between two stationary parallel disks was studied by Sorour et al. [5] numerically, with turbulent radial inflow. They investigated the effect of grooved surface and swirling flow on the heat transfer and fluid flow parameters. They used swirl flow and three-dimensional ribs to increase the heat transfer and concluded that the swirl was useful for plain surfaces only. The ribs were beneficial for radial inflow without swirl.

Jones and Launder [6] developed a model for the generality of energy-dissipation of momentum transfer and swirling flows generated in a quiescent atmosphere by rotating disks. This model is used to predict heat transfer, flow, and mass transfer between rotating disks. Prakash et al. [7] analyzed the laminar flow and heat transfer between rotating and stationary disks numerically. For that, complete Navier–Stokes equation is to be solved and provided a prediction of the entire recirculating of the flow. From their study, they found that, in the presence of rotation, the flow is quite complex and characterized by recirculating zones near the inlet and the exit.

In the present study, a spiral coil heater was designed, manufactured, and analyzed, to investigate the heat transfer between rotor–stator systems. To understand the heat transfer from the disk, it is necessary to understand the temperature distribution of the disk.

## 2 Components of the Heater

Heating material—The heating material is nichrome wire, it is non-magnetic material and is commonly used, and it has a composition of nickel (Ni 80%) and chromium (Cr 20%). It has all the necessary and useful properties of heating materials. It has a high melting point of 1400 °C, high resistivity of  $112.2 \times 10^{-6} \Omega\text{-cm}$  at 20 °C, and very low linear expansibility of 0.0000132 cm/°C. The heating coil has coil diameter  $D = 6.5$  mm and wire diameter  $d = 0.5$  mm (Fig. 1).



**Fig. 1** Heating (nichrome) coil

Cellulose fiber cement board (CFCB)—The CFCB is used to support the heating coil and also provides resistance for heat transfer from the back side of the heater. CFCB is the composition of cement, quartz, and cellulose fiber. The CFCB has low density, high strength, high burning temperature, high heat resistivity ( $k_{\text{CFCB}} \leq 0.02 \text{ W/mK}$ ), and high electrical resistivity. The CFCB has a thickness of  $t = 8.5 \text{ mm}$ .

Mica sheet—It has high electrical resistivity and good heat conductance properties, so it is used as a cover on the spiral coil. It is also used to distribute the heat uniformly and provide uniform heat flux as output. It has high fire resistance properties and can sustain at  $1000 \text{ }^\circ\text{C}$ . It has a high electrical resistivity of  $1016 \text{ } \Omega/\text{cm}$  at  $20 \text{ }^\circ\text{C}$  and  $1012 \text{ } \Omega/\text{cm}$  at elevated temperature of  $400 \text{ }^\circ\text{C}$ . It has high heat conductivity of  $3 \text{ W/cm-K}$  along the plane compared to heat conductivity of  $0.54 \text{ W/cm-K}$  perpendicular to the plane. Therefore, the heat is transmitted along the surface rapidly, and it gives uniform heat flux as output.

### 3 Design Procedure of the Heater

It is necessary for a heater that the temperature is uniform at every point on the circumference of any radius for heating to be axisymmetric. To make the heater, following steps had followed:

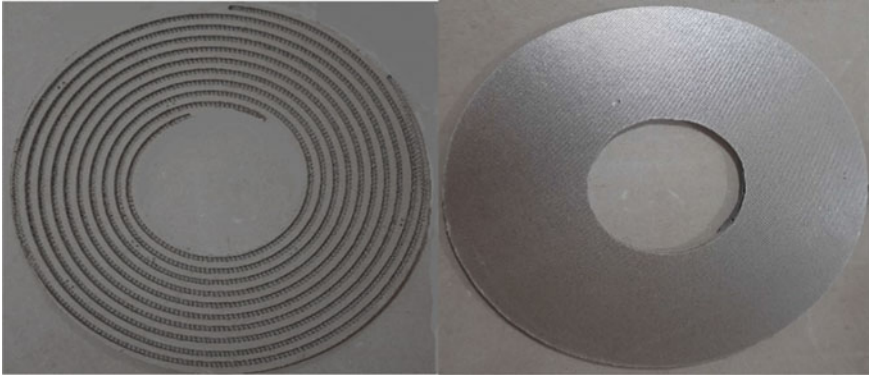
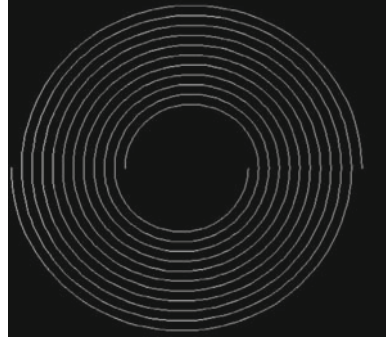
- To generate uniformly distant spirals, semicircles are used and put at an offset along the  $X$ -axis while cutting the semicircle in half. Two spirals are generated for uniformity.
- Drawn the circles in Fusion360, then add a line break cutting the circle in half and offset the bottom half. This gave the shape of a uniform spiral (Fig. 2).

Then the generated spiral was exported as a DXF file and opened in PartWork 3.0 a cam software to generate a toolpath for the CNC being used in ShopBot DesktopPRS. ShopBot made the spiral cut on the cellulose fiber cement board.

- Cut made on CFCB has a dimension of  $7 \text{ mm}$  [width] \*  $7 \text{ mm}$  [depth], and the gap between two consecutive spirals is  $6 \text{ mm}$ .



**Fig. 2** Image of design of uniform spiral of heater 1

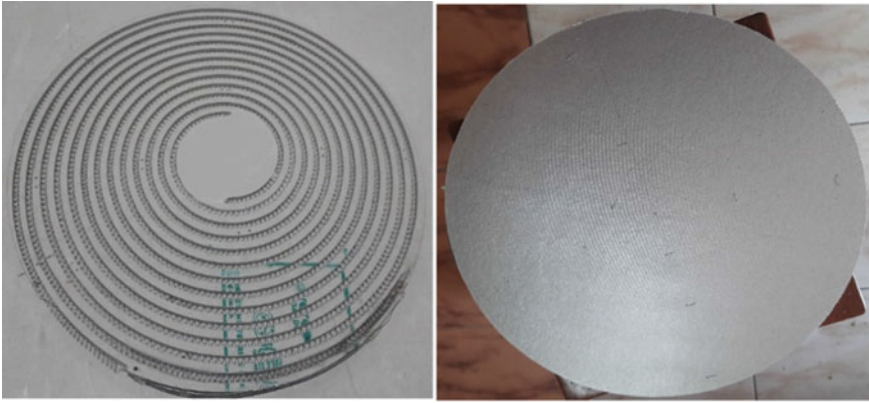


**Fig. 3** Physical image of heater 1

- After the spiral cut on CFCB, the heating coil is installed in the spiral grooves on CFCB. After installation coil is connected to the electrode, one electrode connected at the outer periphery and another connected to the inner periphery. The direction of flow of current is inward direction.
- Then the heater is covered with the mica sheet. The final dimension of heater 1 is outer diameter  $D_{o, 1} = 434$  mm and inner diameter  $D_{i, 1} = 160$  mm (Fig. 3).
- All the procedures repeated for the heater 2 (Fig. 4).

## 4 Experimental Apparatus and Process

To analyze the performance of spiral coil heater, experiments are performed with an aluminum disk (inner radius  $D_i, Al = 160$  mm and outer radius  $D_o, Al = 434$  mm) that replica of part of turbo machines, at the adiabatic environment where no source of heat rather than heater was present. Resistance Temperature Detector, Pt100 (RTD) sensor is used to measure the temperature of the aluminum disk surface. A digital



**Fig. 4** Physical image of heater 2

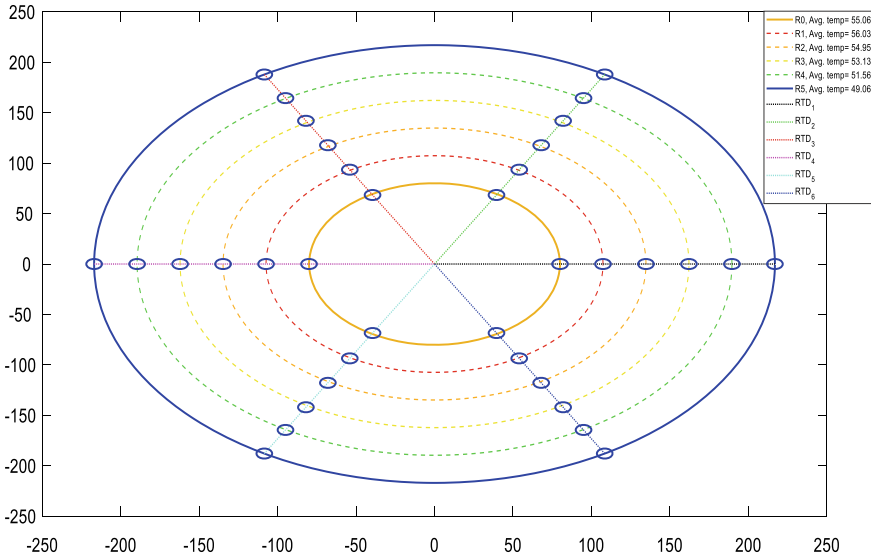
voltmeter and ammeter are used to measure the voltage and current, respectively. The aluminum disk is tightly connected with the heater so there is no gap between the heater and disk, and then RTD sensors are installed on the surface of the aluminum disk through a tiny hole. The temperature was measured for 6 circumferences at 6 angular positions. The position of temperature measurement points is shown in Fig. 5, where  $R_0$ ,  $R_1$ ,  $R_2$ ,  $R_3$ ,  $R_4$ , and  $R_5$  are radii,  $R_0$  is the innermost radius and  $R_5$  is the outermost radius, and all radii are equidistance. RTD1, RTD2, RTD3, RTD4, RTD5, and RTD6 at equiangular positions. The heater and aluminum disk are placed in the adiabatic environment, and then the heater is connected to the power source. The power is controlled by an autotransformer. The power of 108W (current  $I = 3$  A and Voltage  $V = 3$  V) supplied to the heater, so the heater starts to heat up and the aluminum disk's temperature also starts rising.

$$H = I^2RT, \quad (1)$$

where  $H$  = Heat generation,  $I$  = Current in Amps,  $R$  = Resistance in Ohm, and  $T$  = Time. It takes 2 h to come to a steady state. Then temperatures are recorded at a steady state. Then all the processes of the experiment are repeated for a standard parallel coil heater which is used in industries and much equipment in the same environment and all the conditions are also unchanged.

## 5 Results

The spiral coil heater and standard parallel coil heater have equal capacity and surface area. Figure 5 shows the position of temperature sensors and the average temperature of the circumference of the different radius of the spiral coil heaters.



**Fig. 5** Position of the temperature sensor

The temperature distribution of the aluminum disk is shown in in Figs. 6 and 7 for the spiral coil heater and parallel coil heater, respectively. In the graph, different lines represent the circumference of the different radii. The graph shows the temperature of the circumference at a given radius, as a function of angular position. The line of the graph of spiral coiled heater has more linear and organized than standard parallel coil heater that shows spiral coil heater have a uniform or axisymmetric heat distribution and a specific heat zone. Variance is the measured degree of dispersion which is calculated by Eq. 2

$$V = \sigma^2 = (\Sigma(x - \mu)^2)/N, \tag{2}$$

where  $V$  = variance,  $\sigma$  = standard deviation,  $x$  = value at the given point,  $\mu$  = mean value, and  $N$  = total number of values.

Tables 1 and 2 show the variance of temperature on the surface of aluminum disk for spiral and parallel coil heater, respectively. From the table, it can be analyzed that variance of parallel coil heater is more than spiral coil heater. It shows that the spiral coil heater has negligible temperature difference on any circumference of the surface of spiral coiled heater; it has axisymmetric temperature distribution. The parallel coiled heater has large difference on the any circumference of the surface.

Figures 8 and 9 show the temperature distribution in radial direction for spiral coil heater and standard parallel coil heater, respectively, the graph plotted for average temperature of circumference of their respective radius. The plot shows that the temperature shown in Fig. 9 has abrupt and uneven change compared to the temperature shown in Fig. 8. Both the heaters have same power supply and same environment

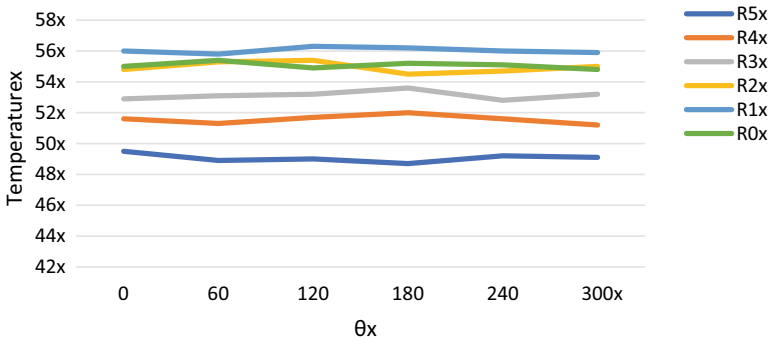


Fig. 6 Angular temperature distribution of different radius of spiral coiled heater

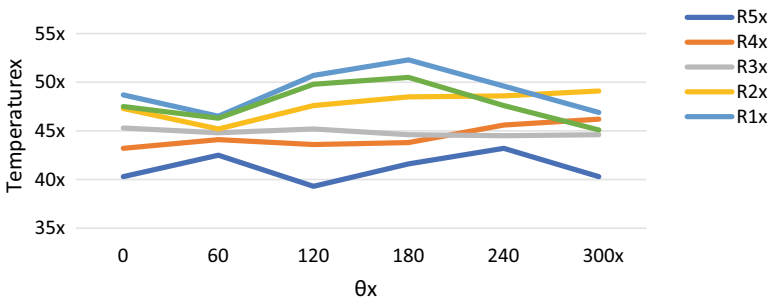


Fig. 7 Angular temperature distribution of different radius of standard parallel coiled heater

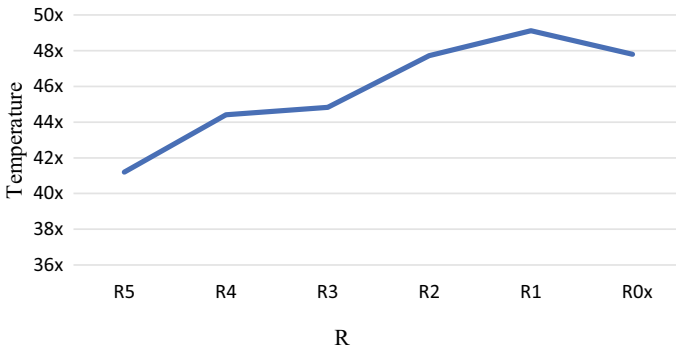
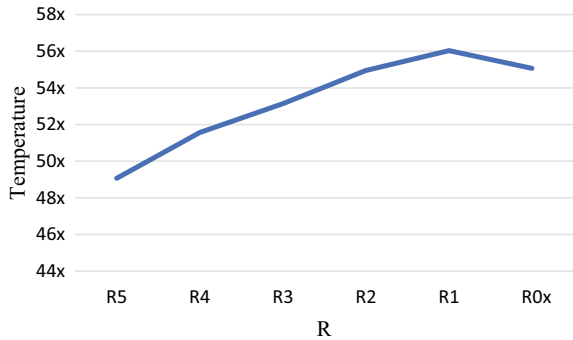
Table 1 Variance of spiral coil heater

Radius	Variance
$R_5$	1.846667
$R_4$	1.201389
$R_3$	0.095556
$R_2$	1.638056
$R_1$	4.134722
$R_0$	3.493333

Table 2 Variance of standard parallel coil heater

Radius	Variance
$R_5$	0.062222
$R_4$	0.068889
$R_3$	0.065556
$R_2$	0.1025
$R_1$	0.028889
$R_0$	0.038889

**Fig. 8** Temperature distribution in radial direction of spiral coil heater



**Fig. 9** Temperature distribution in radial direction of standard parallel coil heater

condition but spiral coil heater attained higher temperature than parallel coil heater due to its design that prevent the access heat loss from the back side and periphery. It shows that spiral coil heater is more efficient.

## 6 Conclusion

Present study dealt with the design and development of axisymmetric electric heater capability of 1 kW to use in rotor stator system. The result shows that the spiral coil heater has very low variance and the standard parallel coil heater has high variance. Therefore, it can be concluded that the spiral coil heater is close to an ideal axisymmetric heater than standard parallel coil heater used in industries. The, the spiral coil heater is more suitable heater for rotor–stator system than the standard heater used in industry.

## References

1. Mochizuki S, Yang W-J (1987) Local heat-transfer performance and mechanisms in radial flow between parallel disks. *J Thermophys Heat Transfer* 1(2):112–116
2. Ervin JS, Suryanarayana NV, Ng HC (1989) Radial turbulent flow of a fluid between two coaxial disks. *Trans. ASME J Fluids Engg* 111:378–383
3. Murphy HD, Chambers FW, McEligot DM (1983) Laterally converging flow, part 1 mean flow. *J Fluids Mech* 127:379–401
4. Djaoui M, Dymont A, Debuchy R (2001) Heat transfer in a rotor–stator system with a radial inflow. *Eur J Mech B/Fluids* 20(3):371–398
5. Sorour MM, Fayed M, El-Din NA (2019) Heat transfer enhancement in a radial turbulent sink flow cooling system. *J Therm Sci Eng Appl* 11(3):031003–031013
6. Jones WP, Launder BE (1972) Prediction of relaminarization with a two-equation model of turbulence. *Int J Heat Mass Transfer* 15:301–314
7. Prakash C, Powle US, Suryanarayana NV (1985) Analysis of laminar flow and heat transfer between a stationary and a rotating disk. *AIAA J* 23(11):1666–1667

# Formulating and Analysing the Effect of Suspension Parameters on Critical Speeds for Various DOFs in Rail Vehicle



Prem Narayan Vishwakarma , Pankaj Mishra, Sunil Kumar Sharma, and Anoop Kumar Shukla

**Abstract** Because of the growing demand for high-speed rail vehicles and the ongoing development of these vehicles, the comfort and safety of passengers have become key criterion for advancement. The critical speeds of various DOFs with respect to suspension properties like stiffness and damping are first formulated, then calculated, and then assessed based on its dynamic equations in order to understand, investigate, and improve the ride stability of rail vehicles. To develop, research, and enhance the ride stability of rail cars, this is done. The secondary lateral damping is the most sensitive sort of suspension damper, according to studies employing dynamic equations. This kind of dampening contributes to the stability and ride comfort of rail vehicles.

**Keywords** Ride stability · Critical speed · DOFs · Lateral damping

## 1 Introduction

With an expansion of railways across the nation, the focus is not only on the connectivity but also on performance. Several parameters can be used to evaluate the performance of railway, out of which comfort of passengers is quite vital. The comfort level of the rail coaches is affected by several parameters, namely rail imperfections and speed of the vehicle. The evaluation of railway in dynamic mode is a challenge in itself [1–4]. The vibration response of such a system having random railway excitation is quite complex, the reason being the multi-DOF and the mechanical system,

---

P. N. Vishwakarma (✉) · P. Mishra  
Department of Mechanical Engineering, Madhyanchal Professional University, Bhopal, India  
e-mail: [prem\\_professional@yahoo.co.in](mailto:prem_professional@yahoo.co.in)

P. N. Vishwakarma · A. K. Shukla  
Department of Mechanical Engineering, Amity University, Lucknow, Uttar Pradesh, India

S. K. Sharma  
School of Engineering & Applied Science, National Rail and Transportation Institute (Deemed to be University), Vadodara, Gujarat, India

which is nonlinear. The passenger railway transport in some of the special line in China has been able to function at an extremely high speed of 360 km/h. This calls for an improved rail vehicle system to stay clear of high perturbations. As of now, the rail vehicle systems are not able to absorb all the perturbations, but only a small fraction of it. The usual passive suspension system has been in use for a long time and has been studied in detail [5–13]. Sharma et al. [14, 15] studied the effect of creep force on the stability and vertical ride for the railway vehicle. Sharma et al. [16, 17] researched the performance of rail wagons in dynamic mode. Nejlaoui [18] worked towards the optimisation of passive suspension which subsequently led to an increase in the comfort level of the passengers; it was done in order to improve the comfort and safety levels. A simulation model was developed by Abood and Khan [17] for analysing the impact of secondary suspension stiffness on the comfort of the passenger. FEM optimisation tool was made use to shortlist the most affecting parameters for passive suspension. The effect of parameters such as load, speed, and damping on the dynamic response was studied by Majka and Hartnett [19]. The aim is to find a compromised value between the suspension deflections and the quality of the ride.

In the current research work, a dynamic model of a high-speed train is created, and its dynamic equation is formulated, based on which further damping ratios are calculated for each degree of freedom. Damping ratio is function of speed. As speed varies, damping ratio varies. Analysis helps to determine critical speed of train.

## 2 Mathematical Model and Calculation of Train Critical Speeds

Throughout the bookshelves of the world, you can find countless models of hypothetical trains. Use a model trained for 18° of freedom to examine how the semi-active suspension system affects the trail vehicle's stability [19, 20]. Liu [8] proposed four distinct train dynamic models using 17-DOF, 19-DOF, 31-DOF, and 35-DOF to improve ride stability. Considering all possible degrees of freedom makes doing computations and analysis more challenging. Many researchers choose a simplified model with fewer degrees of freedom since it is easier to analyse. For describing dynamic behaviour, Garg [21] proposed a model with 15-DOFs. Using a 15-degrees-of-freedom model, the dynamics of a high-speed train are examined in this case. In this study, we investigate the damping ratio and critical speed for each degree of freedom.

Considering both front and rear truck frames, a typical model is created and can be seen in Fig. 1. Each one contains both primary suspension and secondary suspension.



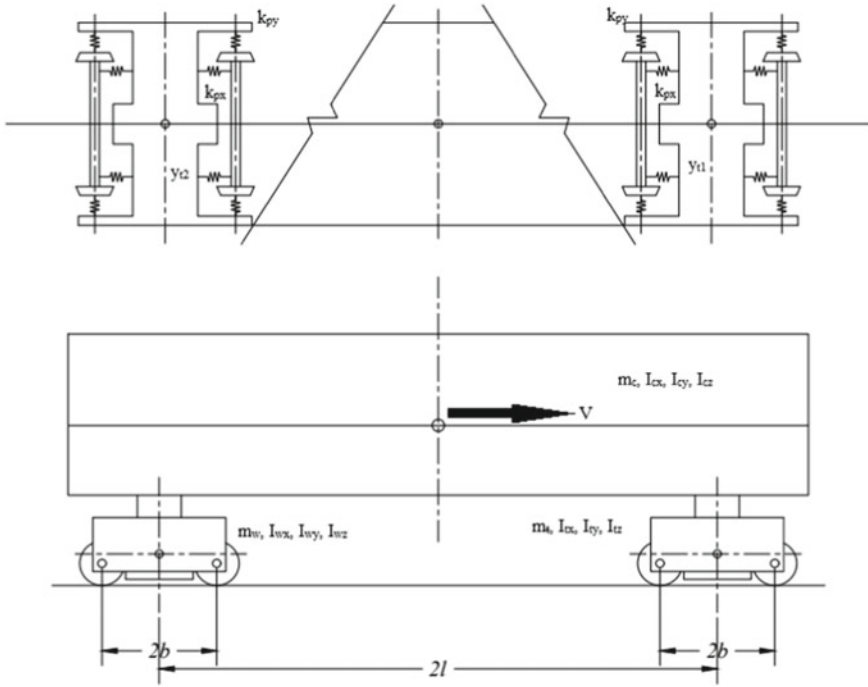


Fig. 1 Rail vehicle model (15-DOFs)

### 2.1 Dynamics of Vehicle Body

Equations are created for the dynamics of a car’s body, which are represented by the lateral ( $y_c$ ), yaw ( $\psi_c$ ), and roll ( $\theta_c$ ) motions [1].

$$\begin{aligned}
 m_c \ddot{y}_c &= 2C_{sy} \dot{y}_c - C_{sy} \dot{y}_{t2} - K_{sy} y_{t1} - C_{sy} \dot{y}_{t1} - K_{sy} y_{t2} \\
 &\quad + 2K_{sy} y_c - 2C_{sy} h_4 \dot{\theta}_c - 2h_4 K_{sy} \theta_c
 \end{aligned}
 \tag{2.1}$$

$$\begin{aligned}
 I_{cz} \ddot{\psi}_c &= -K_{sy} \psi_{t1} + K_{sy} \psi_{t2} + (2K_{sy} l_b^2 + 2K_{sy}) \psi_c - C_{sy} l_b \dot{y}_{t1} \\
 &\quad + C_{sy} l_b \dot{y}_{t2} - K_{sy} l_b y_{t1} + K_{sy} l_b y_{t2} + 2C_{sy} l_b^2 \dot{\psi}_c \\
 I_{cx} \ddot{\theta}_c &= (4K_{sz} b_4^2 + 2C_{sy} h_4^2) \theta_c + (4K_{sz} b_3^2 + 2K_{sy} h_4^2) \theta_c + C_{sy} h_4 \dot{y}_{t1} \\
 &\quad + C_{sy} h_4 y_{t2} + K_{sy} h_4 y_{t1} - 2C_{sy} h_4 y_{tc} + K_{sy} h_4 y_{t2} - 2K_{sy} h_4 y_c
 \end{aligned}
 \tag{2.2}$$

## 2.2 Dynamics of Trucks

The lateral ( $y_{ii}$ ) and yaw ( $\psi_{ti}$ ) motions are taken as characteristics in order to derive governing equation of truck dynamics. The dynamic equations are derived using Newton's method. For the leading truck, equations are as follows:

$$\begin{aligned}
 m_t \ddot{y}_{t1} = & (2K_{pd} + 2K_{py} + K_{sy})y_{t1} - C_{py}\dot{y}_{\omega1} - C_{py}\dot{y}_{\omega2} - C_{sy}\dot{y}_c \\
 & - K_{sy}y_c + (2C_{py} + C_{sy})\dot{y}_{t1} - K_{sy}l_b\psi_c \\
 & - (K_{pd} + K_{py})y_{\omega1} - (K_{pd} + K_{py})y_{\omega2} + C_{sy}h_4\dot{\theta}_c \\
 & - C_{sy}h_4\dot{\psi}_c + K_{sy}h_4\theta_c - K_{sy}l_b\psi_c
 \end{aligned} \quad (2.3)$$

$$\begin{aligned}
 I_{tz}\ddot{\psi}_{t1} = & 2C_{py}\dot{y}_{\omega1} - 2C_{py}\dot{y}_{\omega2} + 8C_{py}\dot{\psi}_{t1} - K_{sy}\psi_c \\
 & + (4K_{px}b_1^2 + 8K_{pd} + 8K_{py} + K_{sy})\psi_{t1} + (2K_{pd} + 2K_{py})y_{\omega1} \\
 & - (2K_{pd} + 2K_{py})y_{\omega2} - 2b_1^2K_{px}\psi_{\omega1} - 2b_1^2K_{px}\psi_{\omega2}
 \end{aligned} \quad (2.4)$$

## 2.3 .

The equations of motions for the trailing truck are as follows:

$$\begin{aligned}
 m_t \ddot{y}_{t2} = & (2K_{pd} + 2K_{py} + K_{sy})y_{t2} - C_{py}\dot{y}_{\omega3} - C_{py}\dot{y}_{\omega4} - C_{sy}\dot{y}_c \\
 & - K_{sy}y_c + (2C_{py} + C_{sy})\dot{y}_{t2} - (K_{pd} + K_{py})y_{\omega3} \\
 & - (K_{pd} + K_{py})y_{\omega4} + C_{sy}h_4\dot{\theta}_c - C_{sy}l_b\dot{\psi}_c + K_{sy}h_4\theta_c + K_{sy}l_b\psi_c
 \end{aligned} \quad (2.5)$$

$$\begin{aligned}
 I_{tz}\ddot{\psi}_{t2} = & 2C_{py}\dot{y}_{\omega3} - 2C_{py}\dot{y}_{\omega4} + 8C_{py}\dot{\psi}_{t2} + K_{sy}\psi_c \\
 & + (4K_{px}b_1^2 + 8K_{pd} + 8K_{py} + K_{sy})\psi_{t2} + (2K_{pd} + 2K_{py})y_{\omega3} \\
 & - (2K_{pd} + 2K_{py})y_{\omega4} - 4b_1^2K_{px}\psi_{\omega3} - b_1^2K_{px}\psi_{\omega4}
 \end{aligned} \quad (2.6)$$

## 2.4 Wheelset Dynamics

There are four wheelsets included in high-speed rail (for both leading and trailing trucks). Motions defined are lateral and yaw. The governing equation for the lateral motion of the wheelsets is given by:

$$m_{\omega1}\ddot{y}_{\omega1} = [C_{py} + (2f_{22})/v]\dot{y}_{\omega1} + (K_c - 2f_{22} + K_{pd} + K_{py})y_{\omega1}$$

$$- C_{py}\dot{y}_{t1} - 2C_{py}\dot{\psi}_{t1} + (2K_{pd} + 2K_{py})\psi_{t1} - (K_{pd} + K_{py})y_{t1} \quad (2.7)$$

$$m_{\omega 2}\ddot{y}_{\omega 2} = [C_{py} + (2f_{22})/v]\dot{y}_{\omega 2} + (K_c - 2f_{22} + K_{pd} + K_{py})y_{\omega 2} - C_{py}\dot{y}_{t1} - 2C_{py}\dot{\psi}_{t1} - (2K_{pd} + 2K_{py})\psi_{t1} - (K_{pd} + K_{py})y_{t1} \quad (2.8)$$

$$m_{\omega 3}\ddot{y}_{\omega 3} = [C_{py} + (2f_{22})/v]\dot{y}_{\omega 3} + (K_c - 2f_{22} + K_{pd} + K_{py})y_{\omega 3} - C_{py}\dot{y}_{t2} + 2C_{py}\dot{\psi}_{t2} + (2K_{pd} + 2K_{py})\psi_{t2} - (K_{pd} + K_{py})y_{t2} \quad (2.9)$$

$$m_{\omega 4}\ddot{y}_{\omega 4} = [C_{py} + (2f_{22})/v]\dot{y}_{\omega 4} + (K_c - 2f_{22} + K_{pd} + K_{py})y_{\omega 4} - C_{py}\dot{y}_{t2} - 2C_{py}\dot{\psi}_{t2} - (2K_{pd} + 2K_{py})\psi_{t2} - (K_{pd} + K_{py})y_{t2} \quad (2.10)$$

The governing equation for the yaw motion of the wheelsets is given by:

$$\begin{aligned} I_{\omega z}\ddot{\psi}_{\omega 1} &= 2b_1^2K_{px}\psi_{\omega 1} - 2b_1^2K_{px}\psi_{t1} + \left[\frac{(2f_{11}l_o^2)}{v}\right]\dot{\psi}_{\omega 1} \\ &\quad + [(2f_{11}a\lambda)/r_o]y_{\omega 1} \\ I_{\omega z}\ddot{\psi}_{\omega 2} &= 2b_1^2K_{px}\psi_{\omega 2} - 2b_1^2K_{px}\psi_{t1} + \left[\frac{(2f_{11}l_o^2)}{v}\right]\dot{\psi}_{\omega 2} \\ &\quad + [(2f_{11}a\lambda)/r_o]y_{\omega 2} \\ I_{\omega z}\ddot{\psi}_{\omega 3} &= 2b_1^2K_{px}\psi_{\omega 3} - 2b_1^2K_{px}\psi_{t2} + \left[\frac{(2f_{11}l_o^2)}{v}\right]\dot{\psi}_{\omega 3} \\ &\quad + [(2f_{11}a\lambda)/r_o]y_{\omega 3} \\ I_{\omega z}\ddot{\psi}_{\omega 4} &= 2b_1^2K_{px}\psi_{\omega 4} - 2b_1^2K_{px}\psi_{t2} + \left[\frac{(2f_{11}l_o^2)}{v}\right]\dot{\psi}_{\omega 4} \\ &\quad + [(2f_{11}a\lambda)/r_o]y_{\omega 4} \end{aligned} \quad (2.11)$$

### 2.5 Determine the Critical Speed of a High-Speed Train

On the basis of equations from 2.1 to 2.11, the governing equation is given as:

$$[M]\{\ddot{q}\} + [C]\{\dot{q}\} + [K]\{q\} = \{0\} \quad (2.12)$$

where

$$\{q\} = [y_c\theta_c\psi_c y_{\omega 1}\psi_{\omega 1} y_{\omega 2}\psi_{\omega 2} y_{\omega 3}\psi_{\omega 3} y_{\omega 4}\psi_{\omega 4} y_{t1}\psi_{t1} y_{t2}\psi_{t2}]^T$$

is called as a generalised coordinate vector.

If we define the state vector as

$$\{y\} = \begin{Bmatrix} q \\ \dot{q} \end{Bmatrix}$$

Governing equations mentioned above can be written as

$$\{\dot{y}\} = [A]\{y\} \quad (2.13)$$

where

$$[A] = \begin{bmatrix} [A_1] & [A_2] \\ [A_3] & [0] \end{bmatrix}$$

which is termed as dynamic matrix, where

$$[A_1] = [M]^{-1} [C]$$

$$[A_2] = [M]^{-1} [K]$$

$$[A_3] = [I]$$

The transformation matrix approach produces the mass matrix  $[M]$ , damping matrix  $[C]$ , and stiffness matrix  $[K]$ . After that, MATLAB is used to determine the dynamic matrix's eigenvalue.

$$\lambda_{2j-1,2j} = \alpha_j \pm i\beta_j \quad (i = \sqrt{-1}, j = 1 - n)$$

Damping ratio can be calculated for each degree of freedom using these Eqs. (2.1–2.13). The formulae show that the damping ratio shifts as the train accelerates. The damping ratios may drop below zero as train speed increases. When the damping ratio crosses zero, that is the critical speed of the train. All the critical velocities for the degrees of freedom can be computed in the same way.

### 3 Results and Discussion

#### 3.1 The Effect of Train Speed on the Damping Ratio

We can infer from the dynamic matrix that train speed is inversely correlated with damping ratio. The damping ratio for degree of freedom likewise increases with speed. This damping ratio is also used to determine the critical train speed. Figures 2,

3, 4, and 5 show the relative damping ratios for the front truck leading wheelsets, the car body reaction, the car body lateral, and the car body roll.

We can see the effect of speed of train on damping ratio of front truck leading wheelsets from Fig. 2. The figure indicates that increase in speed of train from 40 to 160 m/s reduces the  $\xi$  approximately to 8–12%.

From Fig. 3, it can be seen that the effect of speed of train and damping ratio of rear truck wheel axle is having both lateral + yaw motions. It can be noticed that the value of damping ratio decreases to value below zero line at speed approximately of 125–130 m/s, which indicates the critical speed of rear truck wheel.

Effect  $\xi$  of truck frames (lateral + yaw) response modes can be seen in Fig. 4. It can be noticed that damping ratio considerably decreases from 0.6 to 0.3 from speed variation from 40 to 160 m/s. From Fig. 5, we can see that damping ratio of car body

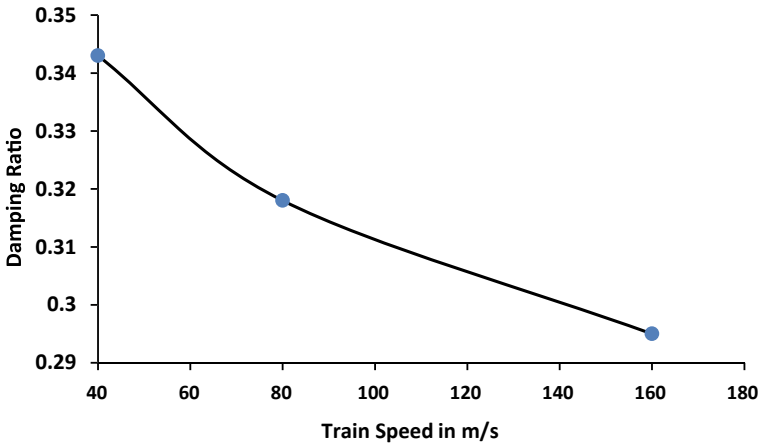


Fig. 2 Damping ratios ( $\xi$ ) of the front truck leading wheelset yaw response mode

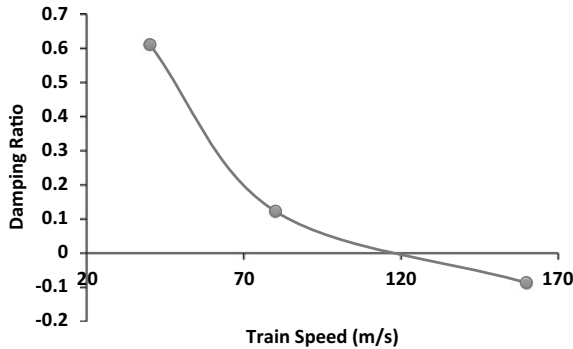


Fig. 3 Damping ratios ( $\xi$ ) of the rear truck wheelset (lateral + yaw) response modes

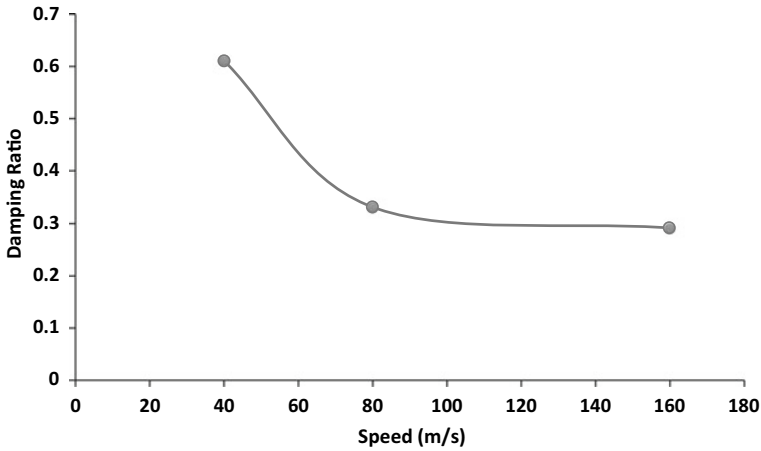


Fig. 4 Damping ratios ( $\xi$ ) of truck frames (lateral + yaw) response modes

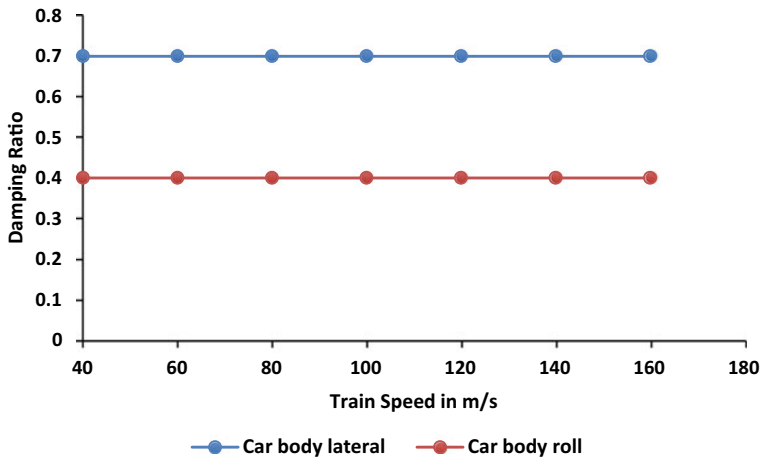


Fig. 5 Damping ratios of car body response modes

is not affected by speed of train. Stability of car body is maintained as speed of train increases. It is above zero mean level.

### 3.2 Effect of Suspension Factors on Critical Speeds

Critical speed is a crucial factor that impacts a number of suspension characteristics. Studying how suspension variables affect critical speed is thus crucial. When a certain degree of freedom exhibits instability, the train is operating at that degree of freedom's

critical speed. In that instance, the entire train maintains the necessary speed. Finding each degree of freedom’s minimal critical speed is essential. Figures 6 and 7 illustrate how the critical speed varies in relation to the principal lateral damping. It can be seen from Fig. 6 that increase in primary lateral damping and critical speed of motions (rear truck trailing wheel lateral and rear truck trailing wheel yaw) decreases slightly and maintained at 110 m/s following same patterns. The increase in primary damping decreases critical speed to some extent.

Figure 7 shows the variation for rear truck leading wheel lateral motion. Figure trend shows that with increase in primary lateral damping to 1.00E+07 Ns/m, the critical speed also increases to 180 m/s.

Figures 8 and 9 illustrate how the critical speed shifts with the secondary lateral damping. Analysis is performed on movements of varied severities. Trend analysis reveals an increase in velocity for both motions, followed by a fall as the value of the

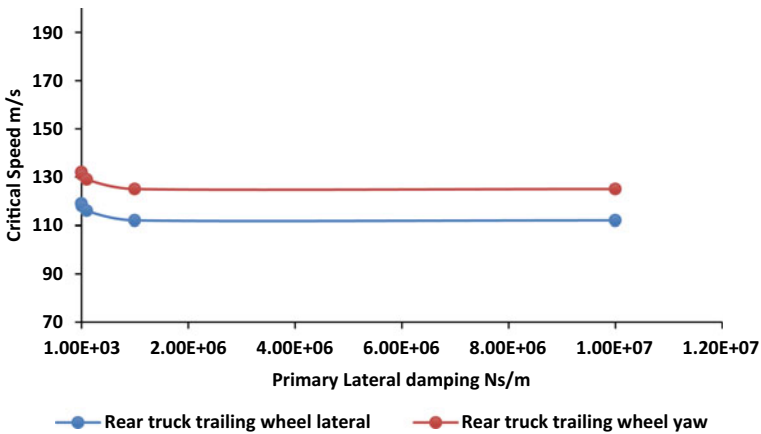


Fig. 6 Effect of primary lateral damping on critical speed

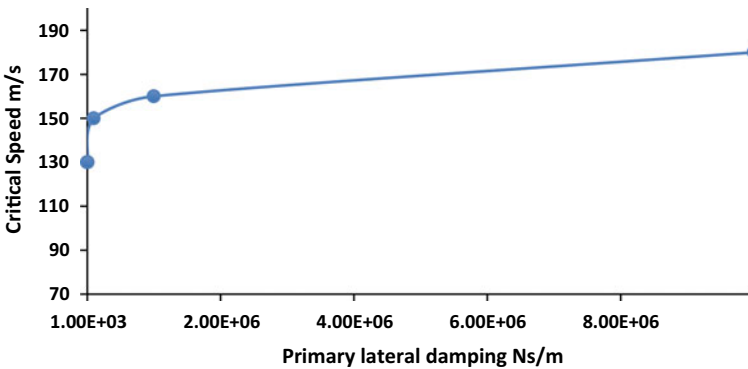


Fig. 7 Effect of primary lateral damping on critical speed

speed reaches a plateau (rear truck frame yaw and rear truck leading wheel yaw). It is evident from the figure that the critical speed of the train is bounded by the lateral and yaw motions of the rear truck frame below  $4.0E5$  Ns/m, despite the variance in secondary lateral damping.

Figure 9 shows the differences between rail vehicle motion, rear truck trailing wheel motion, rear truck wheel lateral motion, and rear truck trailing wheel yaw motion. Secondary lateral damping has been shown to significantly impact critical speed for a wide range of motions. As secondary lateral dampening is increased, the critical speed for trailing wheel yaw motion rises somewhat before returning to its previous, constant trajectory.

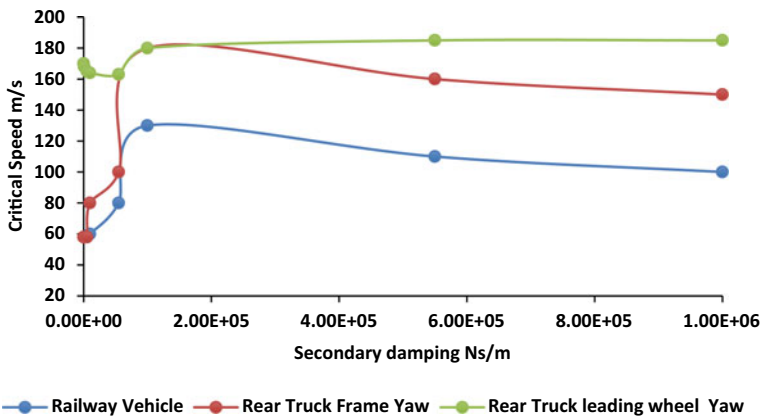


Fig. 8 Effect of secondary lateral damping on critical speed

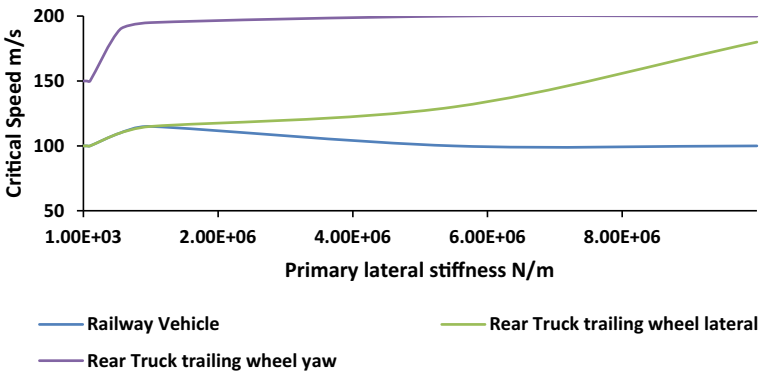


Fig. 9 Effect of primary secondary damping on critical speed



## 4 Conclusion

In this study, dynamic governing equations for 15 degrees of freedom are developed. Based on these equations, damping ratio for various motions and critical speed for various degree of freedom were calculated. Variation of critical speed w.r.t to primary and secondary lateral damping was analysed for various motions. Results indicate that both primary and secondary lateral damping are very sensitive parameters, and they have very significant effect on critical speed of train.

Further, we can replace secondary damping by MR damping and can be analysed for improvement of critical speed and stability of train vehicle.

## References

1. Sun S, Deng H, Li W, Du H, Ni YQ, Zhang J, Yang J (2013) Improving the critical speeds of high-speed trains using magnetorheological technology. *Smart Mater Struct* 22:115012
2. Choi S, Lee J, Sharma SK (2021) A study on the performance evaluation of hydraulic tank injectors. In: *Advances in engineering design: select proceedings of FLAME*. Springer, Singapore, pp 183–190. ISBN 9813346833
3. Sharma RC, Sharma S, Sharma N, Sharma SK (2021) Linear and nonlinear analysis of ride and stability of a three-wheeled vehicle subjected to random and bump inputs using bond graph and Simulink methodology. *SAE Int J Commer Veh* 14. <https://doi.org/10.4271/02-15-01-0001>
4. Bhardawaj S, Sharma RC, Sharma SK, Sharma N (2021) On the planning and construction of railway curved track. *Int J Veh Struct Syst* 13:151–159. <https://doi.org/10.4273/ijvss.13.2.04>
5. Wu Q, Cole C, Spiryagin M, Chang C, Wei W, Ursulyak L, Shvets A, Murtaza MA, Mirza IM, Zheliezov K et al (2021) Freight train air brake models. *Int J Rail Transp* 1–49. <https://doi.org/10.1080/23248378.2021.2006808>
6. Huang C, Zeng J (2021) Suppression of the flexible carbody resonance due to bogie instability by using a DVA suspended on the bogie frame. *Veh Syst Dyn*. <https://doi.org/10.1080/00423114.2021.1930071>
7. Dai L, Chi M, Xu C, Gao H, Sun J, Wu X, Liang S (2021) A hybrid neural network model based modelling methodology for the rubber bushing. *Veh Syst Dyn*. <https://doi.org/10.1080/00423114.2021.1933090>
8. Wang X, Liu B, Di Gialleonardo E, Kovacic I, Bruni S (2021) Application of semi-active yaw dampers for the improvement of the stability of high-speed rail vehicles: mathematical models and numerical simulation. *Veh Syst Dyn*. <https://doi.org/10.1080/00423114.2021.1912366>
9. Yang S, Li F, Shi H, Wu P, Zeng J (2021) A roll frequency design method for underframe equipment of a high-speed railway vehicle for elastic vibration reduction. *Veh Syst Dyn*. <https://doi.org/10.1080/00423114.2021.1899252>
10. Lu Y, Bi W, Zhang X, Zeng J, Chen T, Wu P (2020) Calculation method of dynamic loads spectrum and effects on fatigue damage of a full-scale carbody for high-speed trains. *Veh Syst Dyn* 58:1037–1056. <https://doi.org/10.1080/00423114.2019.1605080>
11. Sun W, Thompson D, Zhou J (2020) The influence of vehicle–track dynamic coupling on the fatigue failure of coil springs within the primary suspension of metro vehicles. *Veh Syst Dyn* 58:1694–1710. <https://doi.org/10.1080/00423114.2019.1643486>
12. Zhang X, Wu G, Li G, Yao Y (2020) Actuator optimal placement studies of high-speed power bogie for active hunting stability. *Veh Syst Dyn* 58:108–122. <https://doi.org/10.1080/00423114.2019.1566556>
13. Ahmed MI, Hazlina MY, Rashid MM (2016) Modeling a small-scale test rig of quarter railway vehicle suspension system. *Int J Robot Mechatron* 2(4):149–153

14. Harak SS, Ravi SK, Sharma SC, Harsha SP (2015) Effect of vertical track irregularities on the dynamics of freight railway wagon. *Int J Veh Noise Vibr* 11(2):133–148
15. Palli S, Koonar R (2015) Analyses of dynamic response of a railway bogie. *Int J Veh Noise Vibr* 11(2):103–113
16. Majka M, Hartnett M (2008) Effects of speed, load and damping on the dynamic response of railway bridges and vehicles. *Comput Struct* 86(6):556–572. <https://doi.org/10.1016/j.compstruc.2007.05.002>
17. Nejlaoui M, Houidi A, Affi Z, Romdhane L (2013) Multiobjective robust design optimization of rail vehicle moving in short radius curved tracks based on the safety and comfort criteria. *Simul Model Pract Theory* 30:21–34. <https://doi.org/10.1016/j.simpat.2012.07.012>
18. Sharma RC, Sharma S, Sharma SK, Sharma N, Singh G (2021) Analysis of bio-dynamic model of seated human subject and optimization of the passenger ride comfort for three-wheel vehicle using random search technique. *Proc Inst Mech Eng Part K J Multi-body Dyn* 235:106–121. <https://doi.org/10.1177/1464419320983711>
19. Abood KHA, Khan RA (2011) Railway carriage model to study the influence of vertical secondary stiffness on ride comfort of railway carbody running on curved tracks. *Mod Appl Sci* 5. <https://doi.org/10.5539/mas.v5n2p11>
20. Sun W, Zhou J, Thompson D, Gong D (2014) Vertical random vibration analysis of vehicle–track coupled system using Green’s function method. *Veh Syst Dyn* 52:362–389. <https://doi.org/10.1080/00423114.2014.884227>
21. Zong L-H, Gong X-L, Xuan S-H, Guo C-Y (2013) Semi-active  $H_{\infty}$  control of high-speed railway vehicle suspension with magnetorheological dampers. *Veh Syst Dyn* 51:600–626
22. Garg VK (1984) *Dynamics of railway vehicle systems*. Academic, Toronto

# Detection of Biofilm on Steel and Plastic Surfaces Using Image Analysis



Manoj Kumar Dewangan, Pulkit Jain, and Gurmeet Singh

**Abstract** We know very little about the structure and function of biofilms and how to control them, despite the fact that they are found in almost every environment. Biofilm production and interspecies interactions are complicated, which is why we don't fully understand them. In this work, the two methods of tube adherence and micro-titer plate method were used to detect infectious biofilms on indwelling devices, and the testing capabilities of these methods were also examined. There's no doubt that a better understanding of biofilm activities will lead to new and better ways to improve human health, as well as the development of biofilm management in biotechnological processes. It is difficult to eliminate complex biofilms due to the creation of EPS and the difficulties involved with cleaning complicated processing equipment as well as the surrounding environment. In this paper, stainless steel and plastic materials were put to the test in squares of  $10 \times 10$  cm ( $100 \text{ cm}^2$ ). For the recognizable proof of biofilm in the beginning stages of improvement, picture surface was surveyed. A co-occurrence gray-level matrix was created using ImageJ software for image analysis (GLCM). Principal component analysis (PCA) was carried out on the data using MATLAB and the PLS\_Toolbox (PCA).

**Keywords** EPS · ImageJ software for image analysis · Gray-level co-occurrence matrix (GLCM) · Principal component analysis (PCA) · MATLAB and PLS\_Toolbox

## 1 Introduction

Biofilms are polymeric lattices created by a local area of microorganisms which will generally tie to biotic and a biotic surface. Biofilm is made out of 1–2% nucleic acids, 1–2% starches, 2.5% bacterial cells, 1–2% proteins including chemicals and 97% water. Biofilm arrangement was at first tracked down restricted to modern and

---

M. K. Dewangan (✉) · P. Jain · G. Singh  
Department of Mechatronics Engineering, Chandigarh University, Gharuan, Mohali,  
Punjab 140413, India  
e-mail: [manojdewangan100@gmail.com](mailto:manojdewangan100@gmail.com)

wastewater frameworks and, however, later acquired significance in clinic settings. As per National Institute of Health (NIH), 65% of microbial diseases were related with biofilms, coming about for around 80% of ongoing contaminations.

Biofilm arrangement includes microorganisms which go through formative cycle, from a moving unicellular to a fixed multicellular state. Biofilm development is a multistep interaction requiring a strong fluid connection point for introductory connection, trailed by a steady restricting. The extracellular polymeric substance created by miniature settlements fosters a three-layered structure with a few water channels for transport of supplements. The biofilm develops, lastly customized separation happens because of end of extracellular polymeric substance creation. During the course of development, microscopic organisms secure majority detecting and new quality articulations by various species implanted in the biofilms. These instruments are expected for nourishing upgrade and to endure ecological pressure.

Recognition of biofilms was at first in view of customary strategies like suitable culture techniques, grasping the microbial variety and phenotypic strategies. Further examinations were centered around atomic techniques like limitation section subcomposing, polymerase chain response and so on. Biofilm arrangement is multi-factorial including the two microorganisms and non-microbes having a place with various genera and species. For instance, in catheter-related contaminations, beginning colonization happens by single creature having a place with same animal categories, for example, *Escherichia coli* or *Proteus mirabilis*, *Staphylococcus epidermidis*, *Enterococcus faecalis* and later the variety and number of organic entities increments, various species having a place with different genera gather, for example, *P. mirabilis*, Providence starter, *Pseudomonas aeruginosa*, *Klebsiella pneumonia*, *Acinetobacter calcaemic*, *Organelle moraine* and *Enterobacter* air qualities. In this way, clinical connection was troublesome requiring rehashed blood societies and examination of anti-infection profile. This prompts a reason for distinguishing putative qualities encoding harmfulness factors which help in line as well as directing biofilms.

## 2 Biofilm Formation

Biofilms are polymeric lattices created by a local area of microorganisms which will generally tie to biotic and a biotic surface. Biofilm is made out of 1–2% nucleic acids, 1–2% starches, 2.5% bacterial cells, 1–2% proteins including chemicals and 97% water. Biofilm arrangement was at first tracked down restricted to modern and waste water frameworks and, however, later acquired significance in clinic settings. As per National Institute of Health (NIH), 65% of microbial diseases were related with biofilms, coming about for around 80% of ongoing contaminations.

Biofilm arrangement includes microorganisms which go through formative cycle, from a moving unicellular to a fixed multicellular state. Biofilm development is a multistep interaction requiring a strong fluid connection point for introductory connection, trailed by a steady restricting. The extracellular polymeric substance

created by miniature settlements fosters a three-layered structure with a few water channels for transport of supplements. The biofilm develops, lastly customized separation happens because of end of extracellular polymeric substance creation. During the course of development, microscopic organisms secure majority detecting and new quality articulations by various species implanted in the biofilms. These instruments are expected for nourishing upgrade and to endure ecological pressure.

### 3 Literature Review

Oleander et al. [1] Methods that are more sensitive to detect microbial populations in biological matrixes, as well as capable of allowing the investigation of their metabolic changes (for example during the development of biofilm) to happen, are fundamental for both human wellbeing and the food businesses' ability to produce safe and nutritious food. Scientists are particularly interested in two techniques: The first is called "bio speckle," and it is an optical technology that may be used to improve food quality and safety, as well as to create nutraceuticals. Biofilm electrostatic testing (BET) is a second method that has a good likelihood of succeeding (BET). After just two hours of incubation with a pyro-electrified carrier, BET is a rapid, simple and highly repeatable method for testing in vitro bacterial adhesion to pyro-electrified carriers. Bacterial resistance among biofilm-producing microorganisms might be evaluated quickly and standardized using BET, a rapid examination of the existence of the biofilm.

Mountcastle et al. [2]. In order to accurately measure biofilm production on a surface, standard microbiological approaches, such as total colony-forming units (CFUs), sometimes need human counting. As a result, these methods are more sensitive to human error than others. High-resolution co-focal laser scanning microscopy (CLSM) provides 3D views of biofilm structures. Using a live/dead stain, it is possible to determine the viability of biofilms on both opaque and translucent surfaces. Co-focal micrograph processing, on the other hand, lacks consensus on the best procedure. A repeatable method for measuring biofilm vitality and surface coverage has been developed in this work. We also show how it may be applied to a wide variety of bacterial species and translational applications. For researchers who are not experts in computational approaches, this methodology was designed to make biofilm micrograph analysis more accessible and user-friendly. In addition, because of its simplicity, the approach may be customized by the user. Automated microbiological analysis has been shown in validation trials to be reliable and accurate across a wide spectrum of bacterial species. Furthermore, the automated approach has been used in translational experiments to show that biomass and cell viability can be accurately measured.

Achinas et al. [3]. Any water-based application in many sectors is plagued by biofouling. To eliminate biofouling issues in bioreactors, it is vital to identify biofilms. The current examination on biofilm location moves toward that can be utilized to distinguish biofouling in bioreactors doesn't give clear supporting realities. There

are several biofilm detection techniques accessible; however, researchers may utilize this research to compare the various biofilm detection methods to help them select the best one for their research. There is more discussion of how typical bioreactor manufacturing materials interact with biofilm development.

Schiebel et al. [4]. Biofilms have a negative impact on both industry and medicine, resulting in significant expenditures and difficulties. Biofilm-resistant bacteria are of great relevance since they typically cannot be eradicated from prosthetic materials because to their high antibiotic resistance. Decreased colonization potential and antibacterial activity in novel materials and coatings are critical for lessening biofilm development. In situ evaluation of bacterial colonization properties in a biofilm does not have a uniform approach. Image capture and quantification of microorganisms were carried out utilizing innovative software after fluorescent staining of bacteria. Compared to glass, titanium has a far larger number of germs adhering to it. We believe this is because titanium has a greater micro roughness. According to the number of adhering bacteria, titanium coupons had a substantially greater colonized area than glass. Glass coupons have a substantially lower maximum 3D biofilm height than steel and titanium. This new technique allows for the standardization and automation of the study of bacterial colonization on various substrates. With this technique, novel material surfaces and their revolutionary coatings may be characterized in situ without the requirement for conventional culture, which is a significant benefit.

Huang et al. [5]. Bacterial biofilms have a negative impact on food quality and safety. Biofilms are an indicator of bacterial adherence to surfaces of processing equipment that come into touch with food. Until recently, nothing is understood about how these films begin to form and how they continue to develop. Biofilms can be caused by a variety of variables, including food-surface interaction, the idea of the food item, the types of microscopic organisms and food handling qualities. Biofilms are challenging to study because of the synergistic effects among them. As part of our effort to get a better understanding of food-related biofilms, we studied the literature on the effects of surface topography on bacteria and their adhesion to substrates. Methods for characterizing biofilms' morphology and identifying substances were specifically explored.

Kleine et al. [6] Pathogenic bacteria, which generally develop on live tissue, such as mucosa and bone, provide a unique difficulty to researchers when it comes to imaging biofilms on opaque surfaces. The problem is that they may also develop on surfaces that are utilized in industrial applications like as food preparation, making it difficult to complete the task. As a result, it is critical to have a better understanding of bacteria in their natural habitat. A custom-built flow cell was used to culture the strain for 18 h, followed by six hours of continuous cultivation. The topography of the biofilm was determined using co-central laser filtering microscopy (CLSM). It was tracked down that the math of the microstructure titanium surfaces greatly affected biofilm improvement in *E. coli* GFPmut2 than the type of metal substrate utilized. There were no interruptions to the formation of a biofilm expressing GFP on metallic surfaces since the most extensively used analytical approach for biofilms (CLSM) was utilized in conjunction with the biofilm culture in flow cells in this investigation.

Grzegorzczuk et al. [7]. It was explored in the Baltic Sea (Gulf of Gdansk) for a long-time utilizing contact point wet capacity, co-central microscopy and photograph acoustic spectroscopy strategies to look at befouling on both fake and normal strong substrates. The pH, dissolved oxygen (DO), phosphate, nitrate and ammonium concentrations were used to determine the trophic condition of a water body as a baseline, and Spearman's rank correlation was used to link these results to the biofilm defining characteristics. Two biologically relevant parameters, the specific growth rate and the induction time, were used to simulate a marine biofilm in steady state, generated from simultaneous multitechnique data. Modern water body trophic status indices might be derived from a collection of well-established biofilm structure and physical properties.

Malegori et al. [8]. Extracellular polysaccharides (EPS) generated by microbes form the backbone of biofilms, a thin coating of microorganisms adhered to a surface. Microorganisms may degrade and damage the food and constitute a health hazard to consumers if they are pathogenic. Disinfection and sanitization of surfaces are challenging because biofilms are particularly resistant to detergents and medicines. Steel, plastic and ceramic specimens of  $10 \times 10$  cm were tested for their suitability for food consumption. *Pseudomonas fluorescens* was chosen as a biofilm-producing bacteria. At regular intervals over seven days, photographs of the specimens were taken in a photography room. Classical bacteriology was used to detect biofilm growth during the picture capture period. ImageJ software was used to analyze the photographs and create a matrix of co-occurrence gray levels (GLCM). Principal component analysis (PCA) was carried out on the data using MATLAB and the PLS\_Toolbox (PCA). Using image analysis, it is possible to detect the formation of biofilms at an early stage. It was necessary to pick GLCM characteristics in order to discriminate between clean and contaminated samples because of the dynamic biofilm growth. On-line and off-line monitoring of the sanitary status of food-contact surfaces might be made possible using this non-destructive, quick technology.

## 4 Material and Method

### 4.1 Specimens

The following food-grade materials were put to the test in squares of  $10 \times 10$  cm ( $100 \text{ cm}^2$ ):

- Stainless steel AISI 304 "Scotch Brite" finished.
- Plastic low-density polyethylene (LDPE) for food.

Low-density polyethylene (LDPE) is a delicate, adaptable and lightweight plastic material. LDPE is noted for its low temperature adaptability, sturdiness and erosion opposition.

## **4.2 Biofilm Formation**

To begin, a consistent approach for creating biofilms on the samples' surfaces was required for this study; therefore, the method proposed by Pan et al. (2006) was used to mimic conditions seen in the food business. A 9:1 ethanol: acetone solution was used to clean the specimens, which were then brooded at 30 °C for 4 h with the microorganism test's suspension. For biofilm growth, the samples were moved to a fresh Petri plate, covered with 1:10 TSB and incubated at 22 °C for 16 h.

After draining for 30 s, the samples were placed on aseptic paper and allowed to dry for 10 min. Under a UV hood, all procedures were carried out aseptically.

## **4.3 Biofilm Data Processing—Gray-Level Co-occurrence Matrix (GLCM)**

GLCM is the orientation, and pitch of the pixels has a significant impact on this post-processing step. A step equal to one was used in this study, allowing for more subtle differences in processing. In order to account for any variations in the material's surface geometry, descriptors derived at all four angles (0°, 45°, 90° and 135°) were averaged.

## **4.4 Microbial Count**

For each substance, there were five specimens positioned beyond the camera's field of view in the shooting room. A thermometer inside the shooting room kept the temperature at  $25 \pm 2$  °C.

For each item, a sample was taken on the day of preparation, as well as 2, 5, 6 and 7 days afterward.

For each substance, there were five specimens positioned beyond the camera's field of view in the shooting room. A thermometer inside the shooting room kept the temperature at  $25 \pm 2$  °C.

For each item, a sample was taken on the day of preparation, as well as 2, 5, 6 and 7 days afterward.



## 5 Results and Discussion

### 5.1 Results

This feature's average values are shown in Tables 1 and 2; in particular, Table 1 shows the element's standard deviation and coefficient of variety. For the qualities introduced, the two catch sessions are averaged together, regardless of time. This study did not take into account the sample variability over time because it proved to be insignificant. The inconstancy of every example over the long haul is comparable to the changeability of the two catch meetings. Since nothing is changing over the long run in the spotless examples (TQ and Br), this is an anticipated outcome. Pseudomonas growth in the two polluted trials (M1 and M2) is hindered by the absence of nutrients, and therefore, no changes are predicted in this situation. Image analysis has shown to be effective in detecting natural material on surfaces and however misses the mark on responsiveness of a microbiological assessment to separate over the long haul the improvement examples of microorganisms.

GLCM features furthermore and their loadings on the main principal component (PC1) are given in Table 2 after autoscaling. Using data autoscaling, we can see how each attribute affects our ability to tell clean from infected samples. To illustrate this point, consider the example of a characteristic that is positive in clean specimens but negative in contaminated ones. In addition, the loading of each feature on PC1 is taken into account when determining the significance of each variable in explaining sample variability.

Figure 2 shows the microbial count for steel and plastic specimens to evaluate how many microorganisms were eliminated.

### 5.2 Steel

#### 5.2.1 Image Texture Analysis

A look at Table 2 reveals how well each of these variables can recognize the polluted examples, M1 and M2, and the perfect examples. All of the factors that may be used to differentiate steel specimens are equally important (huge distinction between the normal worth of M1 and M2 and the typical worth of TQ and Br). All factors are equally essential; as seen by the identical levels of PC1 loadings, it is important to show that no determination.

In Fig. 1, the biofilm-contaminated examples (M1 and M2) are obviously isolated from the uninfected examples (Fig. 1) (Br and TQ). The first component accounts for 92.69% of the variation between the two pairs of samples. According to the results of M1 and M2, the differences between the two trials are insignificant. Along PC2, the GLCM can discriminate between clean surfaces (TQ) and surfaces (BR) polluted with organic residues when applied to steel specimens (6.72% of difference

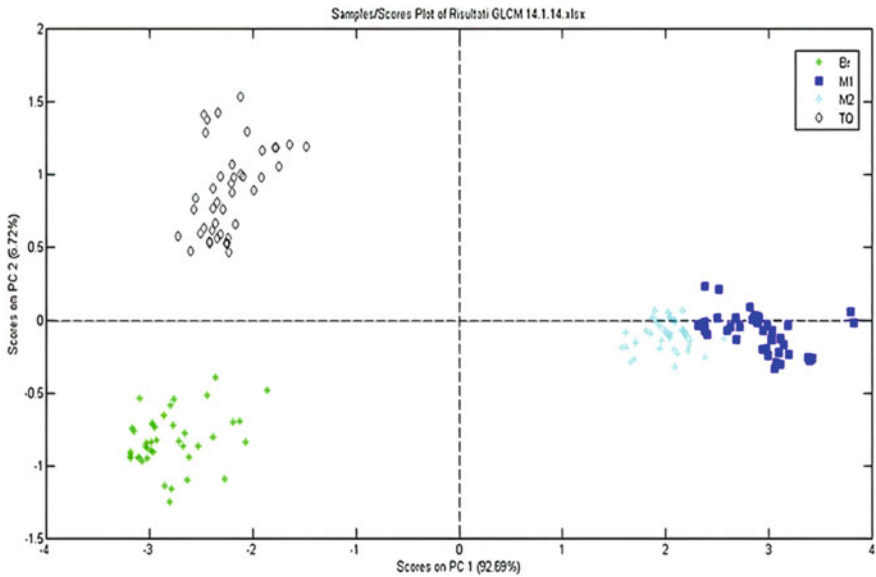
**Table 1** Four samples of each material were used to calculate the GLCM's mean, standard deviation and coefficient of variation

	ASM	DEV.ST	CV%	Homogeneity			Correlation			Energy	DEV.ST	CV%	
				IDM	DEV.ST	CV%	Contrast	DEV.ST	CV%				DEV.ST
Steel	TQ	0.0083	0.0005	5.52	0.4757	0.0026	0.55	0.60	0.22	4.83	0.0083	0.0005	5.52
	Br	0.0072	0.0003	4.43	0.4917	0.0044	0.89	4.07	0.17	4.12	0.0072	0.0003	4.43
	MI	0.0118	0.0003	2.90	0.5664	0.0066	1.17	2.53	0.12	4.56	0.0118	0.0003	2.90
	M2	0.0113	0.0003	2.49	0.5577	0.0034	0.60	3.03	0.08	2.48	0.0113	0.0003	2.49
Plastic	TQ	0.0218	0.0009	4.27	0.5270	0.0023	0.43	4.04	0.08	1.96	0.0218	0.0009	4.27
	Br	0.0212	0.0008	3.59	0.4790	0.0036	0.75	7.44	0.29	3.89	0.0212	0.0008	3.59
	MI	0.0227	0.0012	5.24	0.4316	0.0032	0.75	11.51	0.36	3.09	0.0227	0.0012	5.24
	M2	0.0209	0.0010	4.94	0.4212	0.0017	0.40	14.93	0.25	1.67	0.0209	0.0010	4.94
Entropy		DEV.ST	CV%	Homogeneity			Correlation			DEV.ST	CV%		
	5.17	0.04	0.82	0.530	0.002	0.002	0.41	0.030	0.002	8.35			
	5.29	0.05	0.87	0.543	0.004	0.004	0.66	0.022	0.002	8.30			
	4.82	0.03	0.62	0.604	0.005	0.005	0.90	0.037	0.001	3.03			
	4.91	0.02	0.34	0.596	0.003	0.003	0.46	0.034	0.001	2.76			
	4.90	0.02	0.37	0.574	0.002	0.002	0.32	0.089	0.004	4.22			
	5.22	0.02	0.34	0.534	0.003	0.003	0.57	0.096	0.003	3.28			
	5.42	0.02	0.34	0.495	0.003	0.003	0.57	0.098	0.007	6.93			
5.39	0.02	0.32	0.485	0.002	0.002	0.31	0.085	0.005	5.48				

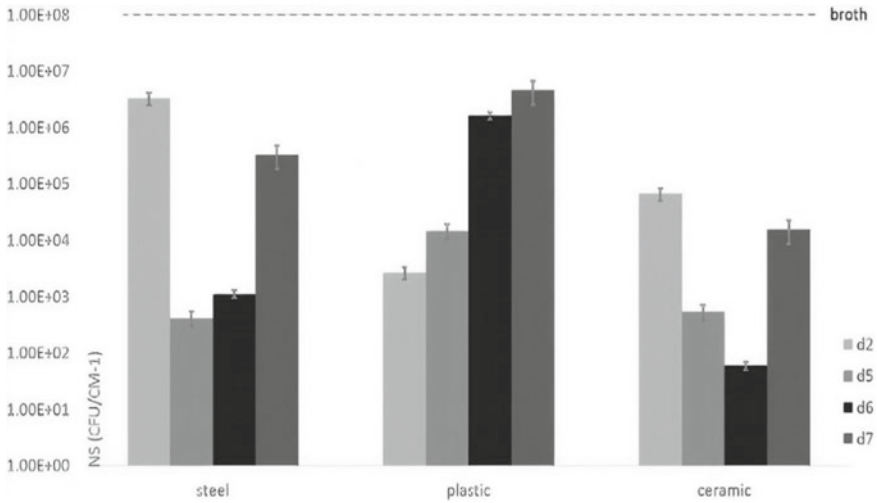
**Table 2** Autoscaled mean qualities and relative PC1 loadings of the four examples, for every material, are given by GLCM

		ASM	IDM	Contrast	Energy	Entropy	Homogeneity	Correlation
Steel	TQ	-0.60	-1.03	1.1	-0.60	0.57	-1.03	-0.16
	Br	-1.09	-0.68	0.55	-1.09	1.1	-0.68	-1.33
	M1	0.95	0.95	-1.09	0.95	-1.04	0.95	0.95
	M2	0.75	0.76	-0.56	0.75	-0.63	0.76	0.55
	PC1	0.39	0.38	-0.37	0.39	-0.39	0.38	0.35
Plastic	TQ	0.19	1.28	-1.15	0.19	-1.39	1.28	-0.57
	Br	-0.55	0.29	-0.43	-0.55	-0.07	0.3	0.68
	M1	1.32	-0.68	0.43	1.32	0.79	-0.66	1
	M2	-0.96	-0.90	1.15	-0.96	0.66	-0.91	-1.10
	PC1	0.04	0.5	-0.49	0.04	-0.49	0.5	-0.01

made sense of). Steel is the most intelligent of the inspected surfaces, and the stock pollution adjusts the textural picture between the two clean examples.



**Fig. 1** PCA score plot of the steel tests, taking into account every one of the seven factors



**Fig. 2** Microbiological count histogram for each example at each testing time

### 5.2.2 Microbiological Analysis

The histogram (Fig. 2) provides a visual representation of the biofilms microbial count. In order to verify the plate count, each analysis was paired with a Safranin-colored picture of the plates.

After 48 h (day 2), the sponge has eliminated most of the bacteria, resulting in the notion that the biofilm has not yet grown on the steel surface. The number of microorganisms eliminated from steel on day 5 is markedly different. Biofilm begins to separate off the steel at day 6, and removal is greater than the day prior to it, increasing till day 7.

## 5.3 Plastic

### 5.3.1 Image Texture Analysis

To begin with, all seven characteristics were used in the PCA, which resulted in an excellent score plot (56% of variance explained). For the time being, it does not appear that the 37% homogeneity of the four groups along the second main component is meaningful.

As can be seen from the average trend of each variable (Table 2), not all of the factors are helpful in identifying the surface of the biofilm; as a matter of fact, a few factors simply add inconstancy and clamor to the lattice of co-event. Opposite difference moment, contrast, entropy and homogeneity are the attributes that might

be utilized to recognize biofilms on plastic examples. The PC1 loading is confirmed by these four properties, which reveal the greater values of the PC1 loading.

### **5.3.2 Microbiological Analysis**

The biofilm has already developed on the plastic examples in Fig. 2, as seen by the diminished number of cells eliminated from the plastic at day 2 contrasted with different materials. After day 5, the value of cells that have been eliminated is nearly constant. Cells begin to seem to separate after six days, and they do so more thoroughly on day seven.

## **5.4 Discussion**

When it comes to biofilm formation, the bond ability of the biofilm fluctuates incredibly relying upon the sort of substance on which microbes are developing. On the second day, typical patterns for the various materials may be observed until the biofilm is removed on the seventh day. This behavior is most likely caused by a lack of nutrients on the specimens' surface, which causes them to separate from it. It takes steel longer to adhere than plastic, but the biofilm that forms is still robust six days later. As a result, the plastic's quick access to the biofilm is offset by its virtually total clearance. In comparison to the other two materials, the adherence of ceramic takes longer, and the detachment phase begins on day seven.

## **6 Conclusion**

The type of substance on the surface has been found to influence the growth of the biofilm. A technique called surface imaging has shown to be a valuable and successful method for detecting biofilm early on. It was possible to distinguish a clean surface from a microbial-infested surface by using the gray-level co-occurrence matrix and principal component analysis, even if the distinctions between the surfaces were not clear to the natural eye. Non-destructiveness is a key point to keep in mind when discussing this strategy. Using this strategy, which is both fast and easy to implement, might be a great way to keep tabs on the cleanliness of industrial surfaces.

## References

1. Oleandro E, Grilli S, Rega R, Mugnano M, Bianco V, Valentino M, Mandracchia B, Nazzaro F, Coppola R, Ferraro P (2021) Biospeckle analysis and biofilm electrostatic tests, two useful methods in microbiology. *Appl Microbiol* 1 <https://doi.org/10.3390/applmicrobiol1030036>
2. Mountcastle S, Vyas N, Villapun V, Cox S, Jabbari S, Sammons R, Shelton R, Walmsley A, Kuehne S (2021) Biofilm viability checker: an open-source tool for automated biofilm viability analysis from confocal microscopy images. *NPJ Biofilms Microbiomes* 7 <https://doi.org/10.1038/s41522-021-00214-7>
3. Achinas S, Yska S, Charalampogiannis N, Krooneman J, Euverink G (2020) A technological understanding of biofilm detection techniques: a review. *Materials* 13:3147. <https://doi.org/10.3390/ma13143147>
4. Schiebel J, Noack J, Rödiger S, Kammel A, Menzel F, Schwibbert K, Weise M, Weiss R, Boehm A, Nitschke J, Elimport A, Roggenbuck D, Schierack P (2020) Analysis of three-dimensional biofilms on different material surfaces. *Biomater Sci* 8. <https://doi.org/10.1039/D0BM00455C>
5. Huang Y, Chakraborty S, Liang H (2019) Methods to probe the formation of biofilms: applications in foods and related surfaces. *Anal Methods* 12. <https://doi.org/10.1039/C9AY02214G>
6. Kleine D, Chodorski J, Mitra S, Schlegel C, Huttenlochner K, MüllerRenno C, Mukherjee J, Ziegler C, Ulber R (2019) Monitoring of biofilms grown on differentially structured metallic surfaces using confocal laser scanning microscopy. *Eng Life Sci* 19. <https://doi.org/10.1002/elsc.201800176>
7. Grzegorzcyk M, Pogorzelski S, Pospiech A, Boniewicz-Szmyt K (2018) Monitoring of marine biofilm formation dynamics at submerged solid surfaces with multitechnique sensors. *Front Mar Sci* 5. <https://doi.org/10.3389/fmars.2018.00363>
8. Malegori C, Franzetti L, Guidetti R, Casiraghi E (2016) GLCM, an image analysis technique for early detection of biofilm. *J Food Eng* 185. <https://doi.org/10.1016/j.jfoodeng.2016.04.001>

# Artificial Hip Prostheses Design and Its Evaluation by Using Ansys Under Static Loading Condition



Gyan Prakash Tripathi, Sumit Agarwal, Ankita Awasthi, and Vanya Arun

**Abstract** Total hip replacement (THR) is one of the most common procedures adopted to maintain the proper functionality of human anatomy due to rapture, sudden impact, osteoporosis, arthritis, inflammatory bones, etc. Biomaterials are indispensable parameters to be looked after before CAD designing prostheses or implants. The hip prostheses should be cost-effective, readily available, light in weight, and good in longevity and strength. This research paper explores the possibility of different biomaterials that qualify as hip prostheses materials. This paper emphasizes developing a synergistic approach toward finite element analysis. The computational design of the proposed hip implant is analyzed by applying different biomaterials such as Ti-based alloys, cobalt and its alloys, and ultrahigh polyurethane. The results show the von Mises stress pattern where Ti- and Zr-based biomaterials show higher load bearing ability as compared to other materials.

**Keywords** Total hip replacement (THR) · Biomaterials · Finite element analysis (FEA) · Hip prostheses · CAD

## 1 Introduction

The demand for hip arthroplasty procedures is growing worldwide, focusing on young people and the medical assistance needed by patients. Abrupt accidents can cause hip dislocations, injuries related to sports (Knee or ankle arm dislocation and

---

G. P. Tripathi · A. Awasthi (✉)

Department of Mechanical Engineering, IILM College of Engineering and Technology, Greater Noida, India

e-mail: [anky22cool@gmail.com](mailto:anky22cool@gmail.com)

S. Agarwal

Department of Automobile Engineering, IILM College of Engineering and Technology, Greater Noida, India

V. Arun

Department of Electronics and Communication Engineering, IILM College of Engineering and Technology, Greater Noida, India

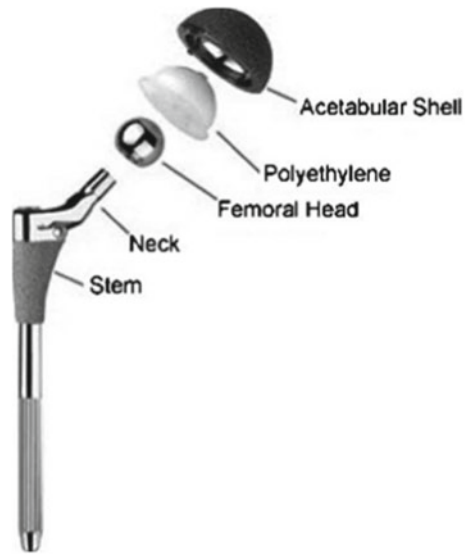
so on), as well as high-intensity collisions [1]. Dislocations or fractures may develop more frequently in older people due to minor accidents or falls, especially in bone diseases like osteoporosis [2]. The hip is one of the body's most critical weight-bearing joints. It comprises two parts: a ball (femur head) just at the upper edge of our femur bone and a rounded socket (acetabulum) for the pelvis. Ligaments are bands of tissue that connect the ball to the socket and provide reliability to the joint. The hip joint can also be destroyed by diseases like arthritis, chronic pain, injuries, and misalignments, along with fatalities. It may lead to a hip fracture, making the person severely disabled [3].

The hip joint can be defined as our body's primary body weight-bearing system, providing stability to the body. In the concept of it, it is a ball and socket joint created by the articulation between the pelvic acetabulum and the femur's head, as shown in Fig. 1. When a hip joint fails and need to be replaced, the artificial hip joint require to place in the designated area [4, 5]. Hip prostheses can repair the damaged or disfigured hip joint as hemi-replacements for joint replacement as part of this surgical procedure. There are two types of fractures generally found in hip arthroplasty. Pins (surgical screws) are used to restore a proximal femur fracture if the person is younger, much more active, and has had a minor injury. If the person is older and much less active, a high-strength material device aligns into the hip joint and substitutes the femoral head through hemiarthroplasty. The broken femur is held in place by a metal device (a compression screw and a side plate) that allows the femoral head to move freely in the hip socket. Total hip replacement is the most popular development as a massive boost to human civilization. The person with a hip injury or who has been in an accident will be helped by a total hip replacement, which will allow them to go back to work. A total hip replacement is a surgical procedure that will alleviate the pain and debilitation caused by osteoarthritis, fractures, dislocations, congenital deformities, and other hip-related problems. The diseased cartilage and bone of the hip joint are surgically replaced with artificial materials. The artificial hip may be made up of different materials, like metals. The hip is in the shape of a ball and socket joint [6]. The socket is a cup-shaped bone of the pelvis, which is called the acetabulum, and the ball is the head of the thighbone, which is also medically termed as the femur. The infected ball and socket shape by surgical intervention are removed and replaced with either a metal ball or stem inserted into the femur bone and an artificial ceramic cup socket. White and Best [7] say that a prosthetic limb is an artificial ball and stem made of metal.

Total hip replacement (THR) was first documented in 1891 by Dr. Gluck, where ivory is used in hip replacement material [8]. Sir John Charnley (1950) considered as a father of modern prosthetic arthroplasty established a prosthetic joint which is built of stainless steel material (SS) and because of the erosion microcracks are developed. Around 1970s, the single solid object stem tail banana-shaped with 32 mm size and femoral head 22.2 mm is prepared. It instantly gained lots of popularity and standardized as a standard implant size. For the first time, polymethyl methacrylate is used as a bone cement is placed in between bone joint and implant. Nowadays,



**Fig. 1** Different sections of THR assembly design [11]



there are many varieties of prosthetic implants, and joints are fabricated depending upon the customer requirements [9]. They are classified as

- Stem-based prosthetic design such as single block and modular block stems.
- Biomaterials-based prosthetic joints/implants.
- Fastening devices, intramedullary nails (cemented, uncemented).

Total hip replacement assembly design is divided into five sections in tail/stem, head, cup liner, neck, and acetabular cup [10].

There are many characteristics possessed by biomaterials that qualify them as implant material. These characteristics are as follows:

1. **Mechanical Characteristics:** Hardness, strength to bear the external load, modulus of elasticity, and elongation are considered critical mechanical characteristics. The response of a material to repeated cyclic loads is determined by its fatigue strength. To obtain better stress, distribution bone is constantly changed and redesigned. Biomaterials are used to replace the bone and are expected to have similar properties to bone. The stiffness is another mechanical characteristic of today's implant materials that prevent the required stresses from being transferred and distributed evenly throughout the bone.
2. **Biocompatibility:** Biocompatible materials must be non-toxic, non-allergic, and non-inflammatory placed over or inside the human body.
3. **Excellent corrosion and wear resistance:** When the implant is inserted into the human body and comes in contact with blood, debris will be generated inside the materials.
4. **Osseointegration:** When bone made up of biomaterial is inserted as a scaffold or implant to replace the missing bone or organ, the body will integrate it as a

similar bone and intend to perform a similar task. Hydroxyapatite is one of the most popular materials which is used to merge with [12].

Special engineered materials known as biomaterials are used to fabricate the implants and orthopedical prostheses. There are many types of implant materials used which can be altered synthetically or biologically [13]. The classification of biomaterials is based on structure, physical properties, and material class, such as metal, ceramic, polymeric, composite, and naturally occurring material. Metallic implant material holds a greater market in terms of popular implant material because of their excellent mechanical properties, good corrosion resistance, and acceptable biocompatibility [14] (Table 1).

## **2 Material and Methodology of Hip Implant**

The basic design of the hip implant was developed with the help of Fusion 360. The set design is then validated with the help of Ansys. Ansys is one of the most popular tools for performing finite element analysis. FEA aims to ensure the safety and relevance of design in terms of its mechanical properties with different boundary conditions [16].

The static analysis was performed on this model using ANSYS-19. Many researchers have done both static and dynamic research under different loading conditions. However, for analyzing the magnitude of load related to the body's weight, the static loading condition is preferred most. Other biomaterials investigate and analyze the hip prosthesis concerning body weight and the load applied under fixed conditions. So, the main objective of this investigation is to analyze the stress distribution pattern of different implant materials [28].

### **2.1 Material Used**

Bio-implant materials have better mechanical properties such as strength, toughness, and wear resistance. They are biocompatible as we know that the hip bears the load from the upper part of the body toward the lower abdomen area. For a healthy adult, the hip bone is designed to be 45 cm long with the synovial ball. This synovial ball arrangement contains an acetabulum and femoral head, which provide an extensive range of movements and increase their load bearing abilities. However, every human body is designed uniquely, and stability is one of the issues that must be ensured during walking, sleeping, running, etc. By comparing the materials listed in table number-1, the list of materials used for this paper is given in table number-2. So, this work focuses on using different bio-implant materials with both biocompatibility and better mechanical properties. The metallic biomaterials such as stainless steel,

**Table 1** Description of popular biomaterials, type, properties, and their ASTM standard

S. no.	International standardization	Type	Properties	Implant category	Citing article
1	ASTM F-1383 16L stainless steel	Metallic materials (SS)	Strength is good, but biocompatibility is not good	Braces, orthopedics implants	Chocholata et al. [1]
2	ASTM F-75 ASTM F-799 ASTM F-1537 Co-Cr-based alloys	Metallic materials (Co-Cr)	Better strength, corrosion, and wear resistance	Dental implants, cardiovascular prosthesis, orthopedics implants	Toh et al. [15]
3	ASTM F1472 ASTM F1295 (Nb-based titanium alloys)	Metallic materials ( $\alpha + \beta$ titanium alloys, Ti-6Al-4 V, $\alpha + \beta$ Ti-6Al-7Nb)	Less density, best mechanical load bearing capacity, excellent corrosion resistance, and better biocompatibility	Orthopedics implants, total knee-hip replacement (KHR-THR)	Su et al. [16]
4	Alloy surface modifications (tantalum-based alloys, hydroxyapatite)	Amalgam of different alloying metals	Good osseointegration, rapid bone healing, resistance to slacking, and loosening of implant	Total joint replacement, orthopedics prosthesis	Wilson [17]
5	Ultrahigh molecular weight polyethylene (UHMWPE)	Thermoplastic (medical grade) D-4020-01a	Less oxidation, good wearing characteristics, but increase slight brittleness	Customized femoral cup, PE liners but not suitable for hip arthroplasty	Singh et al. [18]
6	High crosslinked UHMWPE (XLPE)	Thermoplastic (medical grade)	Higher density but less oxidations, maintains mechanical properties, less wearing	Total hip and knee replacement. (Available in both cemented and uncemented forms.)	Biomaterials and Composite [19]
7	Antioxidant-doped polyethylene	Thermoplastic (medical grade) with vitamin E	Prevents oxidation, good wear resistance	Used as a second-generation polyethylene	Teo et al. [20]

(continued)

Table 1 (continued)

S. no.	International standardization	Type	Properties	Implant category	Citing article
8	Poly(2-methacryloyloxyethyl phosphorycholine) (PMPC)	Thermoplastic	Better abrasive resistance	Bone grafting	Barr et al. [21]
9	Alumina	Ceramics	Better biocompatibility, wear resistance, chemically inert in nature	Dentistry, bridges, cap, etc.	Dini et al. [22]
10	Zirconia	Ceramics	Increased toughness	Femoral head and its base	Özkurt and Kazazoğlu [23]
11	Alumina-zirconia composites	Ceramics, zirconia-toughened alumina (ZTA), which was first commercialized by CeramTec	High hardness and less crack propagation	Al-Zr alloys are popular ceramics for load bearing applications	Zhang et al. [24]
12	Silicon nitride	Ceramic material (non-oxide)	High flexural strength, less hydrothermal decomposition, good biocompatibility	Artificial hip implants	Iyappan et al. [25]
12	Ceramic-Oxinium™	Ceramic layer on metal	High fracture toughness and fatigue strength because of the metal substrate	Treated as a new material in Zr-2.5Nb series, but used for clinical trials only	Donate et al. [26]
13	Ultrahard coatings on metals	DLC, 5000 HV, TiN 2100 HV	Higher weight-to-strength ratio, very hard layer over base material, good biocompatibility	Total hip arthroplasty	Goodman et al. [27]

**Table 2** Materials used in proposed work with their properties

Materials	Elastic modulus (GPa)	Poisson's ratio	Yield strength (Mpa)
Co–Cr	220	0.3	450
Ti6Al4V	110	0.34	895
Titanium zirconium-based alloy (Ti-29Nb-13Ta-4.5Zr)	80	0.33	1000
Ti–commercial (Ti–CP)	113	0.3	900
UHMWPE	1.4	0.46	0
Cortical bone	17	0.3	170
Cancellous bone	0.52	0.29	4
Stainless steel SS316L	193	0.3	1000

titanium-based alloys such as Ti6Al4V but Ti29Nb13Ta, and commercial–Ti (Cp–Ti) are less considerable in terms of popularity.

On the other hand, chromium can be used as a corrosion-resistant material. Co–Cr can also share good biostability. Polymers possess the flexibility and better mechanical properties but are lightweight, making them again suitable to fall in the bio-implant category [29] (Table 2).

## 2.2 Boundary Conditions

ASTM F299-13 standard and ISO 7206-4:2010 are used for applying loading conditions. The designing of bone is done on Fusion 360, as shown in Fig. 2. Stress analysis is done on different materials, and loading conditions are proposed in this research paper. Bone is simulated with or without the muscle forces. About 3, 4, and 5 kN load is applied over implant head at 20° angles from the vertical axis [30, 31] (Fig. 3).

## 3 Results and Discussion

### 3.1 Boundary Condition Applied on Bone Alone

Static structural analysis is done where load is applied at the femur head of 3, 4, and 5 kN in downward direction in Fig. 4. There are two constraints provided over the design labeled as A and B, which is considered as fixed support. This fixed support is provided at femur head and stem area [33]. As shown in Table 3, the average adult femur as per Asian population ranges in between 32 and 48 cm. The proposed computational model of hip implant is designed to sustain the load applied on hip

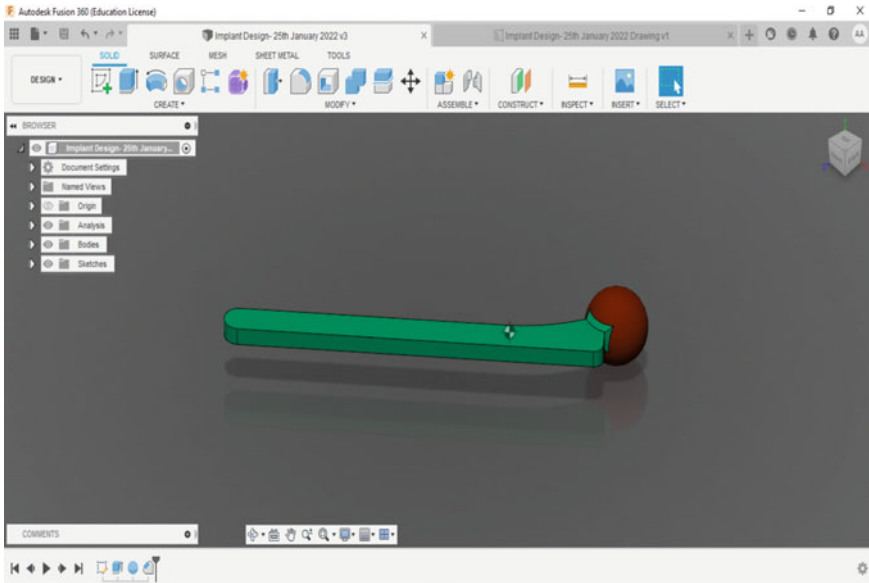


Fig. 2 Geometric model of hip implant

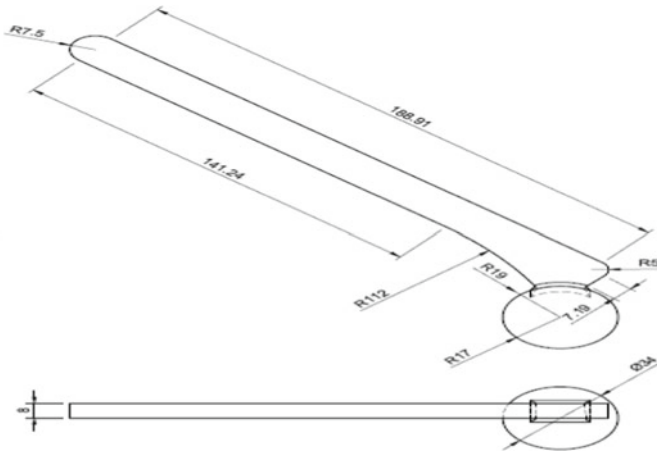
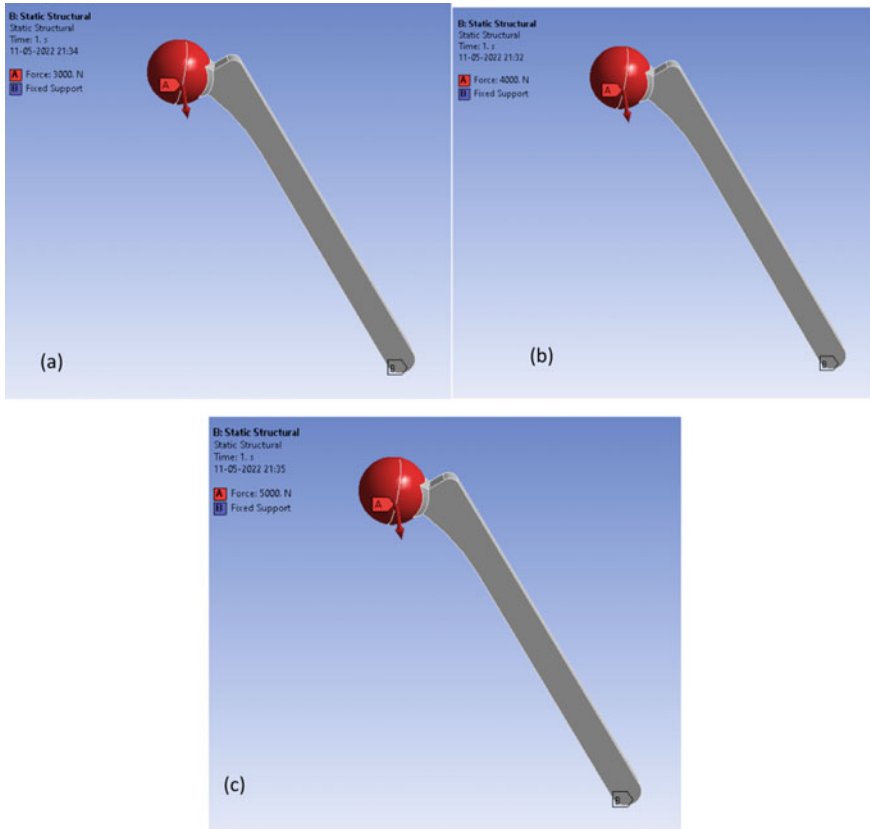


Fig. 3 Detailed drawing of hip implant in mm [32]

during physical activities such as standing, walking, and climbing staircase 3, 4, and 5 kN load will be applied.

As indicated in Figs. 4, 5, 6, 7, 8, 9, 10, 11, and 12 onward, boundary condition and stress analysis of suggested implant are analyzed. The bio-implant material is applied in the neck region where von Mises appears at the femoral head prosthesis.



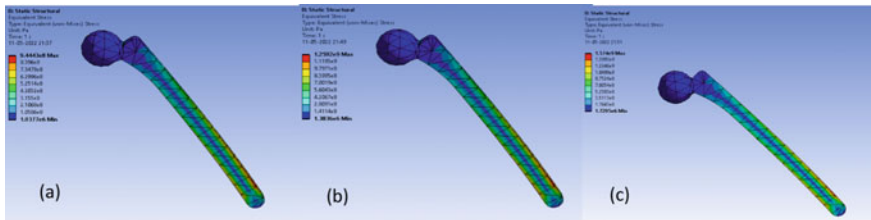
**Fig. 4** Boundary condition for implant alone at 3000, 4000, and 5000 N loading condition (a), (b), and (c)

**Table 3** von Mises stress distribution peak at 3, 4, and 5 kN

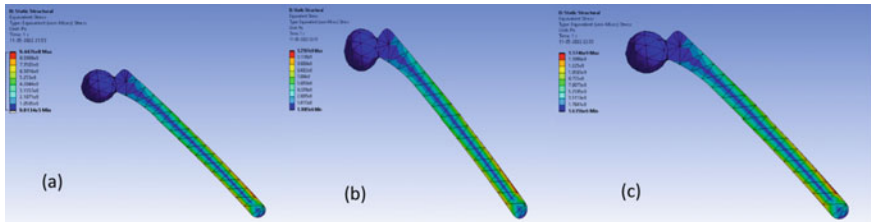
Material	3 kN		4 kN		5 kN	
	Min	Max	Min	Max	Min	Max
Co–Cr	1.0377	9.4443	1.3836	1.2592	1.7295	1.578
Ti6Al4V	9.4476	9.8134	1.2597	1.3085	1.6356	1.5746
Ti-29Nb-13Ta-4.5Zr	9.4375	9.9437	1.3258	1.2583	1.6573	1.5729
CP–Ti	1.03777	9.4443	1.3836	1.2592	1.7295	1.574
UHMWPE	9.5512	9.0135	1.2018	1.2735	1.5022	1.5919
Cortical bone	1.0377	9.4443	1.3836	1.2592	1.7295	1.574
Cancellous bone	1.0535	9.4513	1.4046	1.2602	1.7558	1.5752
Stainless steel	1.3077	9.4443	1.2592	1.3836	1.574	1.7295

The neck is the first part which comes in contact with other bones of body. Stress distribution is well spread from femoral head to stem [16].

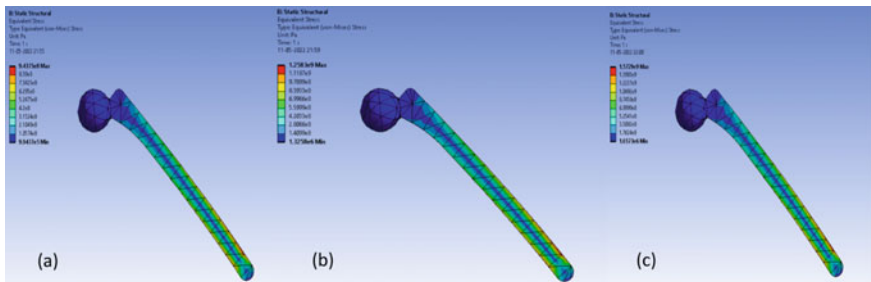
All popular eight materials have shown remarkable results under proposed boundary conditions. From the results obtained from Table 3, Ti-29Nb-13Ta-4.5 Zr and Ti6Al4V possess more strength in comparison with other materials in 3 kN. This preliminary study is conducted to ensure the suitable material for implant. Since titanium-based alloys exhibit better corrosion-resistant property and also ensure its compatibility toward hard tissues. But as the loading condition increases from 3 to 4 and 5 kN, then their ability to resist deformation decreases. Since ultrahigh



**Fig. 5** Stress analysis contour on Co-Cr implant at 3000, 4000, and 5000 N loading conditions (a), (b), and (c)

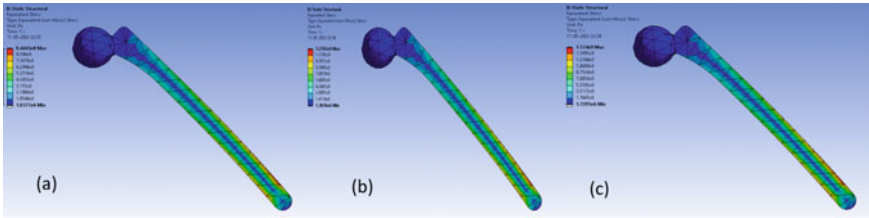


**Fig. 6** Stress analysis contour on Ti6Al4V implant at 3000, 4000, and 5000 N loading conditions (a), (b), and (c)

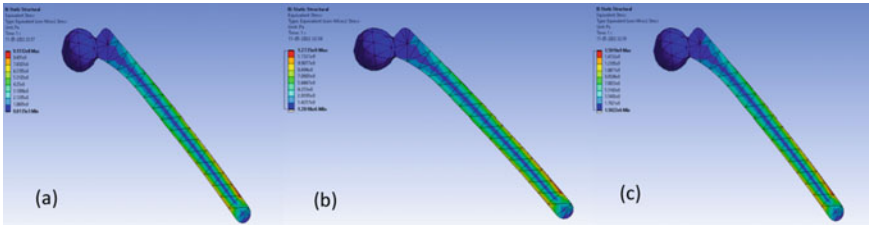


**Fig. 7** Stress analysis contour on titanium zirconium-based alloy (Ti-29Nb-13Ta-4.5Zr) implant at 3000, 4000, and 5000 N loading conditions (a), (b), and (c)

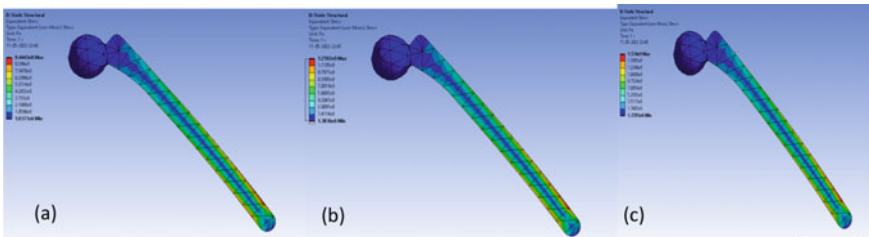




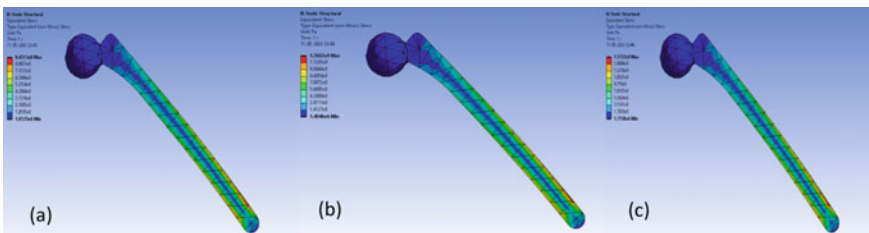
**Fig. 8** Stress analysis contour on Ti-commercial (Ti-CP) implant at 3000, 4000, and 5000 N loading conditions (a), (b), and (c)



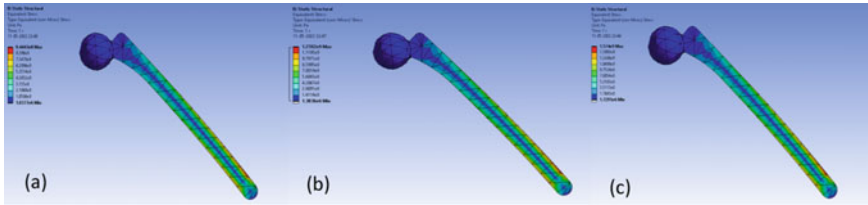
**Fig. 9** Stress analysis contour on UHMWPE implant at 3000, 4000, and 5000 N loading conditions (a), (b), and (c)



**Fig. 10** Stress analysis contour on cortical bone implant at 3000, 4000, and 5000 N loading conditions (a), (b), and (c)



**Fig. 11** Stress analysis contour on cancellous bone implant at 3000, 4000, and 5000 N loading conditions (a), (b), and (c)



**Fig. 12** Stress analysis contour on stainless steel SS316L implant at 3000, 4000, and 5000 N loading conditions (a), (b), and (c)

molecular weight polyethylene (UHMWPE) shows stress peak range from 9.55 kN to 9.01 kN (3 kN), 1.20 kN to 1.27 kN (4 kN), and 1.50 kN to 1.59 kN (5 kN), respectively. These stress distribution patterns are observed in polymer-based biomaterials because of their flexibility, porous structure, etc. Almost every material has given same maximum von Mises stress peak at 3 kN loading conditions. Variation is observed after 3 kN. It is clearly evident from Table 3 that Ti6Al4V and stainless steel have better strength, but titanium-based alloy such as Ti-29Nb-13Ta-4.5Zr, which contain tantalum, zirconium, and niobium, can show both biocompatibility and strength.

## 4 Conclusion

There are plenty of biocompatible materials available that can revolutionize the orthopedic industry. Few of the bio-implant materials are proposed in this study. There are many criteria for selecting the biomaterials, but for hip arthroplasty, mechanical characteristics, biocompatibility, and corrosion resistance are considered to be the main objectives. In this proposed research, eight materials are selected on the basis of the above criteria. From this, the following observations are concluded from their peak stress analysis:

- There are no significant differences observed between cortical bone and cancellous bone materials. However, cancellous bone is found to be stronger than cortical bone.
- Co–Cr- and Cp–Ti-based alloys have the same maximum stress bearing ability at different loading conditions (3, 4, and 5 kN).
- When compared to other Ti-based alloys, such as commercial–titanium and Ti6Al4V, Ti-29Nb-13Ta-4.5Zr is found to be the best.

## References

1. Chocholata P, Kulda V, Babuska V (2019) Fabrication of scaffolds for bone-tissue regeneration. *Materials* 12(4). <https://doi.org/10.3390/ma12040568>
2. Witte F (2010) The history of biodegradable magnesium implants: a review. *Acta Biomater* <https://doi.org/10.1016/j.actbio.2010.02.028>
3. Awasthi A, Saxena KK, Dwivedi RK (2021) An investigation on classification and characterization of bio materials and additive manufacturing techniques for bioimplants. *Mater Today: Proc* 44:2061–2068. <https://doi.org/10.1016/J.MATPR.2020.12.176>
4. AHIRWAR H, Zhou Y, Mahapatra C, Ramakrishna S, Kumar P, Nanda HS (2020) Materials for orthopedic bioimplants: modulating degradation and surface modification using integrated nanomaterials. *Coatings*. <https://doi.org/10.3390/coatings10030264>
5. (2002) For tissue replacement and tissue regeneration. 724:1–11
6. Razavi M, Fathi M, Savabi O, Tayebi L, Vashae D (2020) Biodegradable magnesium bone implants coated with a novel bioceramic nanocomposite. *Materials* 13(6). <https://doi.org/10.3390/MA13061315>
7. White AA, Best SM (2007) Hydroxyapatite—carbon nanotube composites for biomedical applications: a review 13:1–13
8. Nikolova MP, Chavali MS (2019) Recent advances in biomaterials for 3D scaffolds: a review. *Bioactive Mater* 4:271–292. <https://doi.org/10.1016/J.BIOACTMAT.2019.10.005>
9. Geetha M, Singh AK, Asokamani R, Gogia AK (2009) Ti based biomaterials, the ultimate choice for orthopaedic implants—a review. *Prog Mater Sci* <https://doi.org/10.1016/j.pmatsci.2008.06.004>
10. Bussooa A, Neale S, Mercer JR (2018) Future of smart cardiovascular implants. *Sensors (Switzerland)* 18(7). <https://doi.org/10.3390/S18072008>
11. Chethan KN, Satish Shenoy B, Shyamasunder Bhat N (2018) Role of different orthopedic biomaterials on wear of hip joint prosthesis: a review. *Mater Today: Proc* 5(10):20827–20836. <https://doi.org/10.1016/J.MATPR.2018.06.468>
12. Eltom A, Zhong G, Muhammad A (2019) Scaffold techniques and designs in tissue engineering functions and purposes: a review. *Adv Mater Sci Eng* 2019. <https://doi.org/10.1155/2019/3429527>
13. Kang CW, Fang FZ (2018a) State of the art of bioimplants manufacturing: part I. *Adv Manufact* <https://doi.org/10.1007/s40436-017-0207-4>
14. Kang CW, Fang FZ (2018) State of the art of bioimplants manufacturing: part II. *Adv Manufact*. <https://doi.org/10.1007/s40436-018-0218-9>
15. Toh WQ, Tan X, Bhowmik A, Liu E, Tor SB (2017) Tribochemical characterization and tribo-corrosive behavior of CoCrMo alloys: a review. *Materials* 11(1) <https://doi.org/10.3390/ma11010030>
16. Su WL, You KD, Yang CC, Wu JJ, Yeh MK (2020) Stress analysis of improper femur cut in total knee arthroplasty by finite element method. *J Mech* 36(3):315–322. <https://doi.org/10.1017/jmech.2019.45>
17. Wilson J (2018) Metallic biomaterials. *Fundam Biomater: Metals* <https://doi.org/10.1016/B978-0-08-102205-4.00001-5>
18. Singh S, Ramakrishna S, Singh R (2017) Material issues in additive manufacturing: a review. *J Manufact Process* <https://doi.org/10.1016/j.jmapro.2016.11.006>
19. Biomaterials AC, Composite A (2021) Editorial 2–4
20. Teo AJT, Mishra A, Park I, Kim YJ, Park WT, Yoon YJ (2016) Polymeric biomaterials for medical implants and devices. *ACS Biomater Sci Eng* <https://doi.org/10.1021/acsbiomaterials.5b00429>
21. Barr T, McNamara AJA, Sándor GKB, Clokie CML, Peel SAF (2010) Comparison of the osteoinductivity of bioimplants containing recombinant human bone morphogenetic proteins 2 (Infuse) and 7 (OP-1). *Oral Surg Oral Med Oral Pathol Oral Radiol Endodontology*. <https://doi.org/10.1016/j.tripleo.2009.10.027>

22. Dini C, Costa RC, Sukotjo C, Takoudis CG, Mathew MT, Barão VAR (2020) Progression of bio-tribocorrosion in implant dentistry. *Front Mech Eng* 6(January):1–14. <https://doi.org/10.3389/fmech.2020.00001>
23. Özkurt Z, Kazazoğlu E (2011) Zirconia dental implants: a literature review. *J Oral Implantology*<https://doi.org/10.1563/AID-JOI-D-09-00079>
24. Zhang J, Feng Y, Zhou X, Shi Y, Wang L (2021) Research status of artificial bone materials. *Int J Polym Mater Polym Biomater* 70(1):37–53. <https://doi.org/10.1080/00914037.2019.1685518>
25. Iyappan SK, Karthikeyan S, Ravikumar K, Makkar S, Rutvi Uday K, RVM (2020) Mechanical properties and machinability of aluminium and aluminium-silicon carbide composites processed by equal channel angular pressing (ECAP). *Adv Mater Process Technol*<https://doi.org/10.1080/2374068X.2020.1833402>
26. Donate R, Monzón M, Alemán-Domínguez ME (2020) Additive manufacturing of PLA-based scaffolds intended for bone regeneration and strategies to improve their biological properties. *E-Polymers* 20(1):571–599. <https://doi.org/10.1515/epoly-2020-0046>
27. Goodman SB, Yao Z, Keeney M, Yang F (2013) The future of biologic coatings for orthopaedic implants. *Biomaterials*<https://doi.org/10.1016/j.biomaterials.2013.01.074>
28. Nawathe S, Nguyen BP, Barzani N, Akhlaghpour H, Bouxsein ML, Keaveny TM (2015) Cortical and trabecular load sharing in the human femoral neck. *J Biomech* 48(5):816–822. <https://doi.org/10.1016/j.jbiomech.2014.12.022>
29. Kolli RP, Devaraj A (2018) A review of metastable beta titanium alloys. *Metals*<https://doi.org/10.3390/met8070506>
30. Masood MS (2015) Unconventional modeling and stress analysis of femur bone under different boundary condition. *Aust J Basic Appl Sci* 4(12):331–335
31. Nakamura F (1989) Effects of mechanical stress on cytotoxicity of cobalt-chromium alloys for denture base. Shika Zairyo, Kikai = *J Jpn Soc Dental Mater Dev* [https://doi.org/10.18939/jjdm.8.5\\_712](https://doi.org/10.18939/jjdm.8.5_712)
32. Romanò CL, Delia R, Enzo M, Nicola L, Lorenzo D (2011) Two-stage revision surgery with preformed spacers and cementless implants for septic hip arthritis: a prospective, non-randomized cohort study. *BMC Infect Dis*<https://doi.org/10.1186/1471-2334-11-129LK>
33. Kumar K, Prasad RB (2021) Stress analysis of cortical bone of human femur. *Mater Today: Proc* 44:2054–2060